FRACTURE MECHANICS

26TH VOLUME

Walter G. Reuter,
John H. Underwood and
James C. Newman, editors

ASTM STP 1256

STP 1256

Fracture Mechanics: 26th Volume

Walter G. Reuter, John H. Underwood, and James C. Newman, Jr., Editors

ASTM Publication Code Number (PCN)
04-012560-30



ASTM
100 Barr Harbor Drive
West Conshohocken, PA 19428-2959
Printed in the U.S.A.

ISBN: 0-8031-1996-8
ASTM Publication Code Number (PCN): 04-012560-30
ISSN: 1040-3094

Copyright © 1995 AMERICAN SOCIETY FOR TESTING AND MATERIALS, Philadelphia, PA. All rights reserved. This material may not be reproduced or copied, in whole or in part, in any printed, mechanical, electronic, film, or other distribution and storage media, without the written consent of the publisher.

Photocopy Rights

Authorization to photocopy items for internal or personal use, or the internal or personal use of specific clients, is granted by the AMERICAN SOCIETY FOR TESTING AND MATERIALS for users registered with the Copyright Clearance Center (CCC) Transactional Reporting Service, provided that the base fee of $2.50 per copy, plus $0.50 per page is paid directly to CCC, 222 Rosewood Dr., Danvers, MA 01923; Phone: (508) 750-8400; Fax: (508) 750-4744. For those organizations that have been granted a photocopy license by CCC, a separate system of payment has been arranged. The fee code for users of the Transactional Reporting Service is 0-8031-1996-8/95 $2.50 + .50.

Peer Review Policy

Each paper published in this volume was evaluated by three peer reviewers. The authors addressed all of the reviewers' comments to the satisfaction of both the technical editor(s) and the ASTM Committee on Publications.

To make technical information available as quickly as possible, the peer-reviewed papers in this publication were prepared "camera-ready" as submitted by the authors.

The quality of the papers in this publication reflects not only the obvious efforts of the authors and the technical editor(s), but also the work of these peer reviewers. The ASTM Committee on Publications acknowledges with appreciation their dedication and contribution to time and effort on behalf of ASTM.

Printed in Philadelphia
December 1995

Foreword

The Twenty-Sixth National Symposium on Fracture Mechanics was held June 28–30, 1994 in Idaho Falls, ID. ASTM Committee E08 on Fatigue and Fracture was the sponsor. The individuals responsible for organizing the meeting consisted of W. G. Reuter, Idaho National Engineering Laboratory (Lockheed Martin Idaho Technologies), who served as the symposium chairman, J. C. Newman, Jr., NASA Langley Research Center, J. H. Underwood, Army Armament Research/Development and Engineering Center, and Linda L. Reuter, Idaho Falls, ID, who was responsible for developing the women's program and locating the banquet speaker. The symposium chairman would like to express his appreciation to Dorothy A. Cullen at the Idaho National Engineering Laboratory for all her support during the planning of the symposium and the publishing of the STP. The publication was edited by W. G. Reuter, J. H. Underwood, and J. C. Newman, Jr.

Table of Contents

Overview xi

PROFESSOR J. L. SWEDLOW MEMORIAL LECTURE

Patterns and Perspectives in Applied Fracture Mechanics—J. G. MERKLE 3

CONSTRAINT CRACK INITIATION

Two-Parameter (J-Q) Fracture Characterization of Ductile Tearing—S.-X. WU, AND Y.-W. MAI 43

The Relationship Between Constraint and Ductile Fracture Initiation as Defined by Micromechanical Analyses—T. L. PANONTIN AND S. D. SHEPPARD 54

J-Integral for a Semi-Elliptical Surface Crack at a Bimaterial Interface—M. H. SHAROBEAM AND J. D. LANDES 86

Experimental Application of Methodologies to Quantify the Effect of Constraint on J_c for a 3-D Flaw Geometry—W. C. PORR, JR., R. E. LINK, J. P. WASKEY, AND R. H. DODDS, JR. 107

Wide Range CTOD Estimation Formulae for SE(B) Specimens—M. T. KIRK AND Y.-Y. WANG 126

Effects of Constraint on Upper Shelf Fracture Toughness—J. A. JOYCE AND R. E. LINK 142

Effects of 3-D Transverse Constraint on the Evolution of In-Plane Q-Stress—D. K. M. SHUM 178

CONSTRAINT CRACK GROWTH

Tests and Analyses for Fully Plastic Fracture Mechanics of Plane Strain Mode I Crack Growth—F. A. MCCLINTOCK, Y.-J. KIM, AND D. M. PARKS 199

Three-Dimensional CTOA and Constraint Effects During Stable Tearing in a Thin-Sheet Material—D. S. DAWICKE, J. C. NEWMAN, JR., AND C. A. BIGELOW 223

Orientation Effects on the Measurement and Analysis of Critical CTOA in an Aluminum Alloy Sheet—M. A. SUTTON, D. S. DAWICKE, AND J. C. NEWMAN, JR. 243

An Experimental Study of CTOD for Mode I/Mode II Stable Crack Growth in Thin 2024-T3 Aluminum Specimens—B. E. AMSTUTZ, M. A. SUTTON, D. S. DAWICKE, AND J. C. NEWMAN 256

Evaluation of Disk-Shaped Compact Specimen for Determining J-R Curves—K. K. YOON, L. B. GROSS, C. S. WADE, AND W. A. VANDERSLUYS 272

Constraint Effects Observed in Crack Initiation Stretch—D. M. LAMBERT, AND H. A. ERNST 284

Three-Dimensional Crack Growth Assessment by Microtopographic Examination—W. R. LLOYD AND R. S. PIASCIK 303

WELDMENTS

On the Effect of Mismatching on Structural Resistance of Welds—C. ERIPRET, C. FRANCO, AND P. GILLES 321

CTOD (δ_5) Estimate of Mis-Matched Joints Using the ETM-MM Procedure—P. HORNET, M. KOÇAK, S. HAO, A. CORNEC, AND K.-H. SCHWALBE 336

Significance of Locally Intensified Strain Ageing to the Fracture Toughness of Welded Steel Structures—M. G. DAWES 350

Investigation of Fracture Mechanical Behaviour of Nodular Cast Iron and Welded Joints with Parent-Material-Like Weld Metal—W. BAER AND G. PUSCH 361

Fracture Toughness Testing of Bi-Material Joints with High Strength Mis-Match—M. KOÇAK, P. HORNET, A. CORNEC, AND K.-H. SCHWALBE 376

Experiments and Analyses on Undermatched Interleaf Specimens in Bending—D. M. PARKS, S. GANTI, F. A. MCCLINTOCK, J. S. EPSTEIN, L. R. LLOYD, AND W. G. REUTER 391

Fracture Behaviour of Subclad Cracks—L. HODULAK AND D. SIEGELE 417

Stress-Intensity-Factor Influence Coefficients for Semielliptical Inner-Surface Flaws in Clad Pressure Vessels—J. A. KEENEY AND J. W. BRYSON 430

ENGINEERED MATERIALS

Evaluation and Significance of Fracture Toughness in Ceramic Materials—Y. MUTOH 447

Analysis of Damage and Failure in Metal Matrix Composites—F. W. BRUST, B. S. MAJUMDAR, AND G. M. NEWAZ 461

Translaminar Fracture Toughness Test Methods and Results from Interlaboratory Tests of Carbon/Epoxy Laminates—J. H. UNDERWOOD, M. T. KORTSCHOT, W. R. LLOYD, H. L. EIDINOFF, D. A. WILSON, AND N. ASHBAUGH 486

Cyclic Fatigue Mechanisms in Partially Stabilised Zirconia—M. J. HOFFMAN, S. WAKAYAMA, Y.-W. MAI, T. KISHI, AND M. KAWAHARA 509

Predicting Crack Growth in Continuous-Fiber Composite Materials—J. A. CORDES AND R. YAZICI 531

Constraint Effect on Fracture Behaviour of Adhesive Joints with Different Bond Thickness—H. R. DAGHYANI, L. YE, AND Y.-W. MAI 556

Reduction of the Stresses in a Joint of Dissimilar Materials Using Graded Materials as Interlayer—Y. YANG AND D. MUNZ 572

In-Plane Fracture Toughness Measurement of Paper—Y.-W. MAI, H. HE, R. LEUNG, AND R. S. SETH 587

SUBCRITICAL CRACK GROWTH

Fatigue Crack Growth Behavior of Al-Li Alloy 1441—R. V. PRAKASH AND B. K. PARIDA 600

Fatigue Crack Growth Behavior of Ti-1100 at Elevated Temperature—D. C. MAXWELL AND T. NICHOLAS 617

Fatigue Fracture of Thin Plates Under Tensile and Transverse Shear Stresses—M. J. VIZ, A. T. ZEHNDER, AND J. D. BAMFORD 631

The Application of a Logic Framework for Fatigue Crack Growth Analyses to Microstructural Effects—J. G. XU AND H. W. LIU 652

Numerical Modeling and Experiments of Creep Crack Growth Under Cyclic Loading—F. W. BRUST 673

Intermittent Environment-Assisted Crack Growth During Slow Constant Extension Rate Testing—T. W. WEBB AND D. A. MEYN 698

DYNAMIC LOADING

Strain Rate and Inertial Effects on Impact Loaded Single-Edge Notch Bend Specimens—P. M. VARGAS AND R. H. DODDS, JR. 715

Evaluation of Test Methods for Dynamic Toughness Characterization of Duplex Stainless Steel Forgings—M. E. NATISHAN AND R. L. TREGONING 732

APPLICATIONS

Introduction of δ_5 as an Operational Definition of the CTOD and Its Practical Use—K.-H. SCHWALBE 763

Fracture Mechanics Life Prediction Computer Code Verification and Validation—C. D. WILSON 779

Fracture Toughness and Critical Crack Sizes for the Space Shuttle Solid Rocket Motor D6AC Steel Case—J. C. NEWMAN, JR., J. D. BLAND, AND R. F. BERRY, JR. 799

Validation of R6 Defect Assessment Methodology Using Experiments on Plates and Pipes with Surface Cracks—L. HODULAK, D. MEMHARD, AND C. COUTEROT 822

Author Index 835

Subject Index 837

Overview

The ASTM National Symposium on Fracture Mechanics is sponsored by ASTM Committee E08 on Fatigue and Fracture Testing. The original objective of these symposia was to promote technical interchange between researchers from the United States and worldwide in the field of Fracture. This objective was recently expanded to promote technical interchange between researchers in the field of fatigue and fracture. The meeting attracted about 100 researchers covering a broad range of issues in constraint, weldments, advanced materials, and practical applications.

The volume opens with the paper by Merkle who delivered the Fifth Annual Jerry L. Swedlow Memorial Lecture at this symposium. Merkle's presentation provided a brief philosophical and historical overview of applied fracture mechanics, particularly as it pertains to the safety of pressure vessels. The importance of constraint, a fundamental aspect of fracture mechanics in which Jerry Swedlow had a keen interest and made valuable contributions, was presented along with the need for physically realistic analysis. Additional insight into constraint effects on fracture toughness was developed by considering the roles played by the plastic strains, as well as the stresses that develop near a crack tip.

There are 42 papers following the Merkle paper that are broadly grouped in the same categories used to separate the presentation at the symposium. The constraint issue was separated into Crack Initiation with seven papers examining J or CTOD, and Crack Growth with seven papers investigating plane strain or plane stress conditions. Following these papers, there is a section on Weldment with eight papers. These papers are primarily concerned with effects of weld metal mismatch on the fracture process. The remaining papers discuss strain aging and nodular cast iron. The next section on Engineered Materials contains nine papers that cover a variety of topics consisting of monotonic or cyclic loading of ceramics, composites, adhesive joints, graded materials, paper, and an Al-Li alloy. The last three sections consist of Subcritical Crack Growth with five papers that present results of studies on fatigue, creep, or stress corrosion crack growth; Dynamic Loading with two papers; and Applications with four papers.

The technical quality of these papers is due to the authors and to the fine reviews provided by the reviewers. The symposium organizers would like to express our appreciation to all reviewers for a job well done. Because of the large number of papers, camera-ready manuscripts were used to develop the STP. The organizers of the symposium hope that it meets your approval.

The National Symposium on Fracture Mechanics is often used to present ASTM awards to recognize the achievement of current researchers. At the Twenty-Sixth Symposium, the award for the Jerry L. Swedlow Memorial Lecture was presented to Dr. John G. Merkle, Oak Ridge National Laboratory. The Award of Merit was presented to Professor Ashok Saxena, Georgia Institute of Technology. Awards of Appreciation were presented to Dr.

Mark T. Kirk, Dr. James C. Newman, Jr., and to Professor Ad Bakker, Delft University of Technology. The organizing committee would like to congratulate the above award winners as considerable time, effort, and hard work were required to win these awards.

Walter Reuter
EG&G Idaho Ink,
Idaho Falls, ID; symposium
chairman and editor.

John H. Underwood
U.S. Army Armament RD Center
Watervliet, NY; symposium
co-chairman and editor.

James C. Newman, Jr.
NASA Langley Research Center
Hampton, VA; symposium
co-chairman and editor.

Professor J. L. Swedlow Memorial Lecture

John G. Merkle[1]

PATTERNS AND PERSPECTIVES IN APPLIED FRACTURE MECHANICS

REFERENCE: Merkle, J. G., **"Patterns and Perspectives in Applied Fracture Mechanics,"** Fracture Mechanics: 26th Volume, ASTM STP 1256, Walter G. Reuter, John H. Underwood, and James C. Newman, Jr., Eds., American Society for Testing and Materials, Philadelphia, 1995.

ABSTRACT: This fifth Jerry L. Swedlow Memorial Lecture begins with a brief philosophical and historical overview of applied fracture mechanics, particularly as it pertains to the safety of pressure vessels. It then progresses to a more-or-less chronological panorama of experimental and analytical results pertaining to the important subject of constraint, a fundamental aspect of fracture mechanics in which Jerry Swedlow had a keen interest and to which he made valuable contributions. To be truly useful and dependable in application to the safety analysis of real structures, new analysis developments must be physically realistic. That means that they must accurately describe physical cause and effect. Consequently, before useful mathematical modeling can begin, a pattern of cause and effect must be established from experimental data. This can be a difficult and time consuming process, but it is worth the effort. Accordingly, a central theme of this paper is that, consistent with the scientific method, the search for patterns is constant and vital. This theme is well illustrated historically by the development of small, single-specimen, fracture toughness testing techniques. It is also illustrated, at the end of the present paper, by the development, based on two different published large-strain, elastic-plastic, three-dimensional finite-element analyses, of a hypothesis concerning three-dimensional loss of constraint. Specifically, it appears that, at least in standard compact specimens, when a generalization of Irwin's thickness-normalized plastic-zone parameter, β, reaches a value close to 2π, the through-thickness contraction strain at the apex of the near-tip logarithmic-spiral slip-line region becomes the dominant negative strain accommodating crack opening. Because slip lines passing from the midplane to the stress-free side surfaces do not have to curve, once these slip lines are established, stresses near the crack tip are only elevated by strain hardening and constraint becomes significantly relaxed. This hypothesis, based on published three-dimensional elastic-plastic analyses, provides a potentially valuable means for gaining additional insight into constraint effects on fracture toughness by considering the roles played by the plastic strains as well as the stresses that develop near a crack tip.

Keywords: Fracture mechanics, pressure vessels, fracture toughness, small specimen testing, flawed structural components, thickness effects, constraint.

[1]Research Specialist, Oak Ridge National Laboratory, Oak Ridge, Tennessee 37831.

Copyright© 1995 by ASTM International www.astm.org

It is an honor to be invited to present the Fifth Professor Jerry L. Swedlow Memorial Lecture. Jerry Swedlow set a personal example of insight and quality in research, as well as an example of professional service, that we can all admire. I've tried to prepare this paper with these two examples in mind. By fortunate circumstance, this paper develops a focus on one of the very subjects that attracted Jerry's keen interest as a graduate student and held it throughout his career, that of the effects of thickness on fracture toughness, or slightly more generally, the three-dimensional aspects of constraint. This paper begins with some overall philosophy about fracture mechanics. It then progresses to a brief historical overview of some of the important experimental and analytical developments in fracture mechanics, especially as they relate to pressure vessels. Next a more or less chronologically based chain of evidence about what have come to be called constraint effects on fracture toughness is developed. Finally, the paper concludes with some recent evidence, and a hypothesis, about three-dimensional loss of constraint, especially in standard compact specimens.

It is easy to be positive and enthusiastic about fracture mechanics because it is an important and challenging field for several good reasons. It deals with an important real problem, the imperfection of real structures. By means of fracture toughness, it does what stress analysis alone cannot do; it enables the quantification of safety margins against fracture for real, imperfect structures. It makes full use of material science, nondestructive examination, thermal analysis, stress analysis, and probabilistic information. Nothing is overlooked. Interdisciplinary teamwork is essential. An important aspect of the behavior of structural metals is that crack-tip yielding precedes fracture. Therefore, a basic understanding of elastic-plastic metal behavior is required. Furthermore, fracture toughness is a unique material property. Its value cannot be reliably synthesized from other material properties. It must be calculated from sharp-cracked specimen data. With respect to analysis methods, some relationships in fracture mechanics exist in algebraic closed form. Others can only be obtained numerically. A partnership between algebraically direct and iterative numerical analysis is required. Finally, development and application of fracture mechanics requires proper use of the scientific method. Experiments and analyses must be coupled. *The search for patterns is constant and vital.*

To establish a perspective on applied fracture mechanics as it now exists, a look at its history is helpful. Table 1 lists some historically key issues and developments in fracture mechanics, emphasizing those that have been particularly significant with regard to quantifying the safety margins of pressure vessels. There was a time when brittle fracture was described simply in terms of catastrophic failure without warning, due to what was believed to be the reaching of a cleavage stress before yielding, a condition caused by triaxial stress concentration. The realization that, in structural metals, macroscopic cracks are a necessary cause of brittle failure was the key to modern fracture mechanics. From that realization flowed the concepts of elastic strain energy release rate [1], G_I, and the linear-elastic stress-intensity factor [2], K_I, as well as their critical values. In some structural metals, loading rate and crack-front-motion induced strain-rate effects were observed and appropriate analyses were developed [3, 4]. Effects of specimen size, especially thickness, on fracture toughness were observed and provisions made to deal conservatively with these effects [5]. Pressure vessel steels were characterized, first in terms of their thick-section dynamic impact

TABLE 1--Some historically key issues and developments in fracture mechanics for pressure vessels

- Brittle fracture: catastrophic failure without warning (up to early 1950's).
- Basic material behavior; is that all there is to it (up to early 1950's)?
- The involvement of cracks (starting in late 1940's).
- Elastic strain energy release rate; G and G_{Ic} (1954).
- The elastic stress intensity factor; K_I and K_{Ic} (1957).
- Loading rate and strain rate effects (1960's).
- Effects of size, especially thickness, on toughness (1970's).
- Characterizing pressure vessel steels (1970's).
- Initial codes, standards and technical basis documents; ASTM E399, WRC-175, ASME Section III Appendix G (1970's).
- Measuring toughness with reasonably sized specimens (1970's).
- CTOD and the J Integral (1965 and 1970).
- Determining the behavior of cracked structural components (1970's).
- ASME Section XI Appendix A (1974).
- Size and geometry effects (1980's).
- Ductile crack growth (1980's).
- E561, E813, E1152, E1221, and E1290 (1980's).
- ASME Section XI appendices for piping (1990's).
- Computers come of age (1990's).
- Constraint (1990's).
- Shallow cracks (1990's).
- Ductile hole growth and cleavage initiation sites (1990's).
- Statistical variability of cleavage toughness (1990's).

energy [6] and then in terms of their static [7], dynamic [8] and crack arrest [9] fracture toughness values. Initial versions of American Society of Mechanical Engineers (ASME) codes, American Society for Testing and Materials (ASTM) standards, and Welding Research Council (WRC) technical basis documents were written and published, as mentioned in Table 1. It soon became apparent that developing the experimental and analytical methods for measuring fracture toughness with reasonably sized specimens was going to be a major long-term challenge. The crack-tip-opening displacement (CTOD) and J-Integral parameters became prime candidates for this job. As single specimen J-Integral testing techniques were being developed, attention also became focused on determining the performance of cracked structural components, which display various unique behavioral characteristics of their own. Once linear-elastic fracture mechanics (LEFM) had reached a sufficient level of maturity, its essentials were incorporated into Appendix A of Section XI of the ASME Code [10], for the purpose of evaluating flaw indications discovered by nondestructive inspection. The J Integral was used to characterize ductile crack growth, and once again size and geometry effects became apparent [11]. Several more ASTM standards were completed and published, three relating to tearing resistance curves, one for crack arrest and one for CTOD testing. Appendices to the ASME Code were written to describe acceptable methods for performing ductile tearing instability analyses for flawed piping, as well as safety margin calculations for vessels containing materials with relatively low ductile tearing resistance. Then as computers and their software grew in capability, attention focused anew on the details of crack-tip deformation and stress distributions, creating the prospect of finally understanding the subject of constraint. Specimens with shallow cracks were tested and analyzed [12, 13] and the detailed modeling of ductile hole growth began in earnest [14]. Modeling the onset of unstable cleavage may not be far behind. The statistical variability of cleavage fracture toughness has already become a subject in its own right [15] despite the present lack of certainty concerning the exact sequence of events that leads to unstable cleavage.

Because fracture mechanics is a relatively new branch of knowledge within the field of structural engineering, opportunities for the development of new problem solutions and analysis procedures have abounded. However, to be truly useful and dependable in application to the safety analysis of real structures, these new problem solutions must be more than just mathematically or computationally ingenious. They must also be physically realistic. That means that they must accurately describe physical cause and effect. Consequently, before useful mathematical modeling can begin, a pattern of cause and effect must be established from experimental data. This can be a difficult and time consuming process, but it is worth the effort. Table 2 lists some of the analytical aspects of fracture mechanics that have been particularly dependent upon experimental data for their development. The remainder of this paper focuses on a selection of subjects from Table 2, particularly those related to size, geometry and rate effects on fracture toughness.

SMALL SPECIMEN TESTING

In the course of performing the static and dynamic fracture toughness testing of pressure vessel steels described in Refs. 7 and 8, some important fundamental facts about such testing soon became apparent. Because of the crack size dependence of all crack-tip stress

TABLE 2--Analytical aspects of fracture mechanics particularly dependent upon experimental data for their development

- Effects of yielding
  - Small specimen toughness testing
  - Cracks in structural members
  - Warm prestressing
- Constraint
- Stable ductile crack growth
  - Upper shelf
  - Before cleavage
- Strain rate effects, including crack arrest
- Effects of temperature and irradiation
- Effects of environment
- Fatigue
- Calculated versus measured strains and displacements
- Statistical effects of crack length
- Interactions between fracture and plastic collapse

intensity parameters, large specimens were required in order to obtain valid linear-elastic fracture toughness data. For lower and intermediate yield grade steels with adequate toughness for ensuring structural safety, statically loaded fracture toughness specimens of reasonable size will usually yield before fracturing. Therefore, the proper calculation of fracture toughness from laboratory tests of reasonably sized specimens requires inelastic analysis according to an analytically defined and physically meaningful fracture criterion. For practical purposes, laboratory specimens must be analyzable with single-specimen formulae. Such testing and analysis capabilities did not exist in 1970. Consequently, the search began for single-specimen test and analysis techniques applicable to small specimens that yield before fracturing, and results were soon forthcoming.

There were three candidate approaches for calculating fracture toughness from reasonably sized small specimens that yield before fracturing. These were (1) CTOD [16], (2) equivalent energy [17], and (3) the J Integral [18]. The CTOD was physically defined, in terms of single-specimen formulae, for the rigid-plastic behavior of laboratory specimens. However, analytical definitions for flaws in structures were lacking, except for definitions in terms of K_I and G_I that did not have the same analytical basis as the definition for laboratory specimens. Equivalent energy was an empirical concept with no exact physical definition in terms of crack-tip conditions. Although a single-specimen analytical definition existed in terms of global conditions for single load pairs, the definition could become ambiguous for distributed forces and thermal loads. The J Integral had strong potential advantages in terms of its physical meaning and analytical basis, but it was experimentally unproven and there were no single-specimen formulae available. Rice's derivation of the J Integral [19] had begun with an inquiry into the meaning of nonlinear work per unit crack extension area. It turned out that this energy rate was also the integral of work density with vertical distance progressing around the blunted crack-tip contour. Another integral over a connecting arbitrary internal path was formulated in terms of stress and strain to be equal to the blunted crack-tip integral, thus becoming an indirect measure of nonlinear crack-tip conditions. This was the J Integral.

Some key developments occurred at the Westinghouse Research Laboratory (WRL) in 1971. On April 13, 1971, a meeting of WRL staff and consultants took place* at which the general subject of elastic-plastic fracture mechanics was discussed. Topics included Rice's fundamental derivations related to the J Integral, some ongoing multispecimen measurements of work per unit crack surface area, i.e., J-Integral values, being made by Landes and Begley at WRL, and empirically successful applications of the equivalent energy method being made at the Oak Ridge National Laboratory (ORNL). In response to a presentation by Prof. H. T. Corten on ORNL's equivalent energy applications, Rice made an apparently extemporaneous commentary during which he developed the rigid-perfectly-plastic version of his now well known single-specimen J formula for a deeply cracked beam in pure bending.* Soon after the meeting at WRL, Landes and Begley presented their experimental demonstration of the J Integral as a fracture criterion at the 5th National Symposium on Fracture Mechanics (NSFM) [20, 21]. Later in the year, Rice improved his single-specimen beam formula to include strain hardening by adding the reasonable assumption that the net section bend angle depends only on the ratio of the applied moment to the fully plastic moment [22]. Rice's single-specimen beam and other formulae

were presented the following year at the 6th NSFM [23]. Two other developments occurred soon after. Following Rice's lead, Merkle and Corten [24] applied the same class of assumptions to the compact specimen, which carries an axial force as well as bending, to produce a single-specimen J formula for the specimen most commonly used for measuring fracture toughness. Ernst, Paris, and Landes [25] then used the basic concepts of the deformation theory of plasticity to derive a method for adjusting calculated single-specimen J values for crack growth during loading, thus clearing the way for the measurement of J-R curves.

In the case of developing a soundly based method for measuring fracture toughness with reasonably sized small specimens, the pattern was fairly simple, namely, match previously measured valid data where it existed. The perspective, which was all important, involved applying basic principles and keeping all the criteria clearly in mind, namely that the chosen fracture toughness parameter must be (1) physically meaningful, (2) analytically defined, and (3) lead to single-specimen formulae.

CRACKS IN SPECIMENS REPRESENTING STRUCTURAL COMPONENTS

The emergence of the J Integral for measuring material fracture toughness with reasonably sized small specimens, loaded primarily in bending, did provide a satisfactory means of material characterization. However, it did not automatically lead to a sufficient degree of understanding of the behavior of flaws in structural test components, especially in the elastic-plastic range. Some load and geometry combinations tested showed toughness elevations above values obtained under conditions of high constraint. Some of the elevations were gradual, some were sudden. Other load and geometry combinations showed no toughness elevations. The effects of loading mode (tension versus bending; thermal loading), so-called constraint (longitudinal and transverse), and geometry (pressurized cylinders, nozzle corners, tensile bars, shallow cracks, through-cracks, and part-through cracks) remained to be better understood.

The effects of tension versus bending were revealed in a rather striking manner by a series of so-called gross strain tests performed by Randall [26], using long rectangular bars of A533, Grade B, Class 1 steel containing finite-length part-through surface cracks. Flaw tolerance was measured in terms of gross strain, defined as the ratio of axial displacement divided by gage length between two surface points on the centerline perpendicular to the crack plane. As shown in Fig. 1, the critical values of both the net section gross strain (ε_{gnc}) measured across the crack mouth and the gross section gross strain (ε_{ggc}) measured above or below the crack, for uniform tensile loading, underwent rapid increases with temperature between the yield strain and either the strain at the onset of strain hardening (~ 1-2%) or the tensile instability strain (~ 10%). The strain values above yield considerably exceed, and rise faster with temperature, than those calculated by LEFM, although the temperature at which the fracture strain equals the yield strain is roughly consistent with LEFM. By modifying the test fixture it was possible to load the gross strain specimens with a controlled combination of axial strain and bending strain, with the pattern of results [27] shown in Fig. 2. As positive bending strain increased relative to uniform tensile strain, the curve

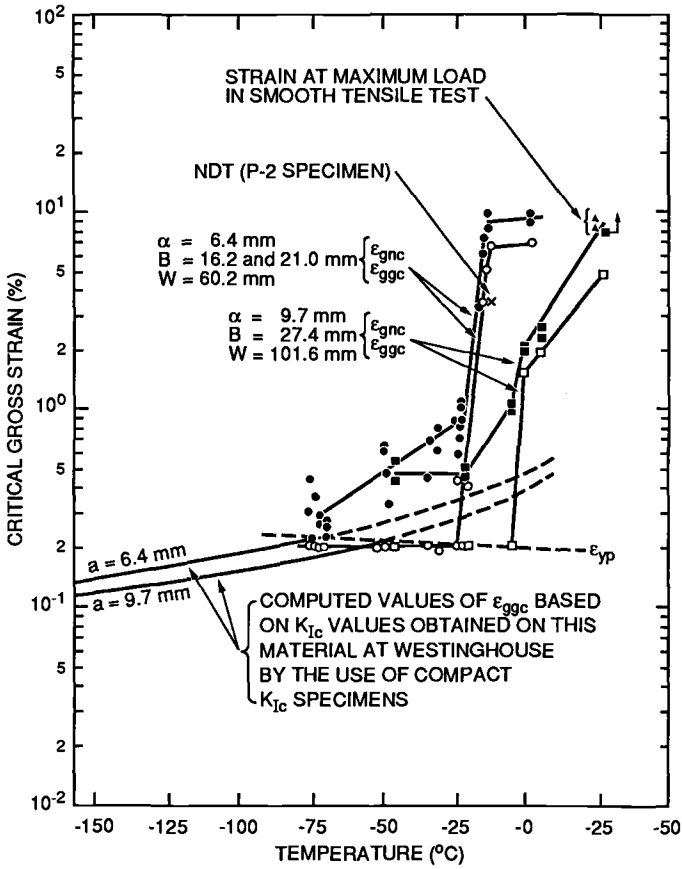


Fig. 1 Critical net and gross-section gross-strain curves for surface-cracked tensile specimens of A533 Grade B, Class 1, steel (from Ref. 26).

of front-face critical gross strain versus temperature decreased in average slope, appearing to approach the curve predicted by LEFM [28]. An apparently systematic effect of bending versus tension on elastic-plastic fracture toughness was experimentally demonstrated.

Following the gross strain tensile tests described in Ref. 26, considerably larger surface cracked tensile bars of the same material were tested at the Southwest Research Institute (SwRI) [29]. These specimens had cross sections 152 mm (6 in.) thick and 457 mm (18 in.) wide and contained fatigue sharpened finite-length part-through surface cracks between 57 mm (2.25 in.) and 111 mm (4.38 in.) deep. As shown in Fig. 3, the pattern of results, plotted here in terms of net section fracture stress versus temperature, was very similar to that for the gross strain tension specimens. The specimens fractured at a net section stress equal to the yield stress over a range of temperature, a

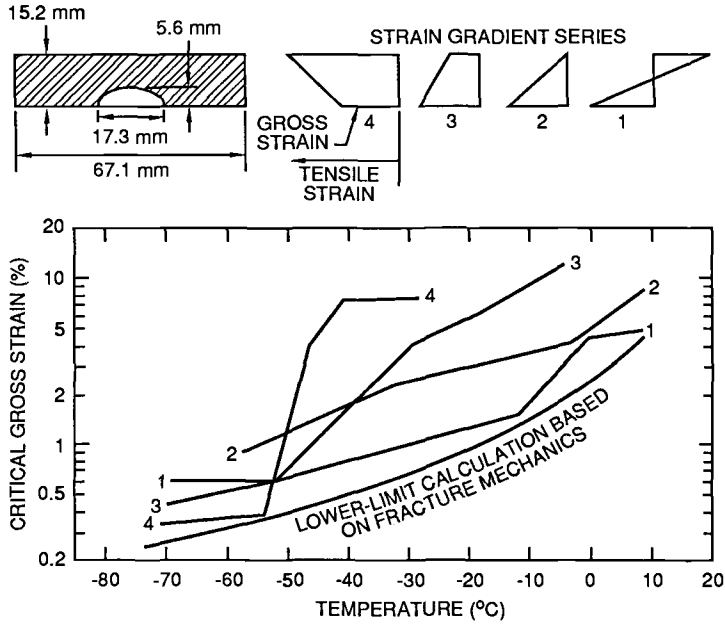


Fig. 2 Effect of strain gradient on critical gross strain curves for A533 Grade B, Class 1, steel (from Ref. 28).

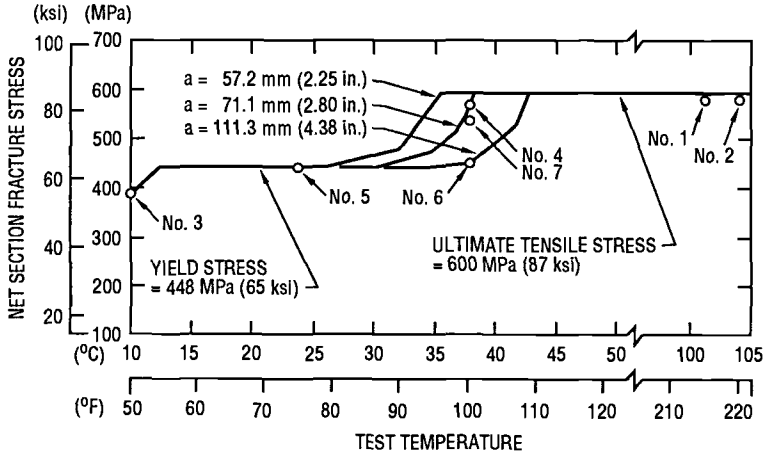


Fig. 3 Net-section fracture stress versus temperature curves for large surface-cracked tensile specimens of A533 Grade B, Class 1, steel tested at the Southwest Research Institute (from Ref. 28).

result qualitatively similar to that obtained two decades earlier in wide plate tests of World War II ship plate specimens [30]. Then, with further increase in temperature, the net section fracture stress rose steeply, with flaw size being a parameter, until it became equal to the ultimate tensile stress. The curves plotted in Fig. 3 were calculated by an approximate method of analysis that considered both yielding and a toughness elevation due to externally unrestrained net section transverse contraction [28]. Had the calculations been based on the plane-strain fracture toughness, they would have underestimated the fracture stresses.

At about the same time a series of geometrically similar drop-weight specimens of A516 and A533B steel, with thicknesses ranging between 9.53 mm (3/8 in.) and 203 mm (8 in.) were tested, both statically and dynamically, by the Martin Marietta Corporation in Denver, Colorado, to investigate thickness and flaw size effects on strain tolerance for flaws in bending [31]. Surface strains were measured with strain gages. In the elastic-plastic range, strain tolerances exceeded elastic predictions, leading to a general conclusion that yielding per se elevates fracture toughness [31, 32]. Although this general conclusion was soon contradicted, the Martin Marietta tests were in reality shallow-crack tests and their results are consistent with more recent similar tests.

Following the SwRI intermediate tensile tests and the Martin Marietta scaled drop weight tests, the Heavy Section Steel Technology (HSST) Program at ORNL performed a series of ten pressure tests to failure of 991 mm (39 in.) outside diameter, 152 mm (6 in.) thick, pressure vessels of A508 or A533B steel with external axial finite-length surface flaws, and two additional tests with axially oriented inside nozzle corner flaws [33]. The vessel diameter was chosen for practicality of fabrication and cost and the wall thickness was chosen to provide constraint conditions typical for full scale vessels [33]. A pair of test results from two vessels tested at room temperature is particularly illuminating with respect to the effects of structural geometry on effective fracture toughness for finite-length surface flaws. Vessel V-4, tested at 24°C (75°F) with a 76.2 mm (3.00 in.) deep, 210 mm (8.25 in.) long, axial surface flaw in an axial weld, failed at an outside hoop strain of 0.168%, close to the LEFM estimate. Vessel V-9, tested at 24°C (75°F) with a 30.5 mm (1.20 in.) deep inside nozzle corner surface crack, failed at an opposite inside nozzle corner strain of 8.4%, about ten times the LEFM estimate. It is apparent that the presence or absence of a transverse tensile stress in the plane of the crack (present for the axial flaw in the cylinder of vessel V-4 and absent, because of the two perpendicular free surfaces, at the inside nozzle corner of vessel V-9) exerted a strong influence on the effective fracture toughnesses. Other intermediate test vessels containing axially-oriented surface cracks in the vessel cylinders and tested at higher temperatures showed no pronounced toughness elevations above plane strain in the elastic-plastic range [34]. Thus the hypothesis that yielding per se elevates fracture toughness was not substantiated for relatively deep surface cracks subject to geometrically induced lateral tensile stress, but it was substantiated when such transverse tensile stresses were absent [28].

Following the intermediate pressure vessel tests, the HSST Program performed a series of thermal shock tests, using liquid nitrogen, on hollow cylinders of A508 steel of two different sizes, the larger of which were identical to the intermediate test vessel cylinders. These cylinders all contained shallow internal axially-oriented surface cracks, all but one of which were initially as long as the cylinders [35]. As shown in Fig. 4, none of these tests produced toughness values

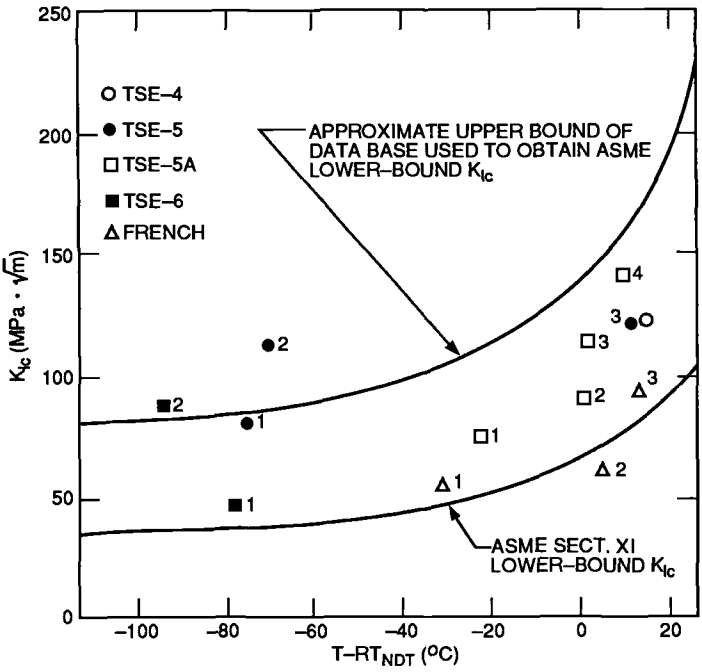


Fig. 4 Static-initiation fracture toughness data from French and ORNL thermal shock tests (from Ref. 35).

for their first or subsequent initiations that implied a consistent toughness elevation above the plane-strain scatter band [35]. Since elastically calculated thermal stresses at the inside and outside surfaces of a free-ended hollow cylinder are equal in the axial and circumferential directions, it is evident that transverse tensile stresses, as well as strain gradients, were once again playing a decisive role in maintaining constraint [36]. Similar results were obtained from subsequent tests of two intermediate test vessels containing shallow axially-oriented long surface cracks subject to pressurized-thermal-shock loading [37, 38].

Considering the small- and large-flawed structural simulation tests just described in their entirety, it is evident that a pattern involving a complex interaction of flaw size, geometry, loading mode, plane-strain fracture toughness and yield stress is emerging. However, this pattern is still incompletely understood, and it is not practical to expect that it can be made entirely clear by means of large structural simulation tests alone. Collectively, the effects described above have come to be called constraint effects and it is clear that these effects need to be studied, per se, analytically as well as experimentally.

INITIAL STUDIES OF CONSTRAINT

Studies of constraint effects actually did begin early in the development of fracture mechanics, as soon as it was recognized that

there were apparent size, geometry, and yield stress effects on measured values of fracture toughness. Irwin [39, 40] reasoned that the ratio of formally calculated plastic-zone radius to specimen thickness, for a through-cracked specimen, must be fundamentally related to crack-tip inelastic constraint effects. Over the course of several years, Irwin made several estimates of the relation between the ratio of plastic-zone radius to thickness and the degree of constraint, expressed in terms of fracture surface appearance and the characteristics of the fracture mode conversion from plane strain to plane stress. These estimates were phrased first in terms of the parameter α, where [39, 40]

$$\alpha = B/(K_{Ic}/\sigma_Y)^2, \tag{1}$$

B is specimen thickness, K_{Ic} is plane strain fracture toughness, and σ_Y is yield stress. Later the estimates were phrased in terms of the parameter β_c, where [41]

$$\beta_c = (K_c/\sigma_Y)^2/B \tag{2}$$

and K_c is the measured non-plane-strain value of fracture toughness. An empirical equation [41, 42],

$$\beta_c = \beta_{Ic}(1 + 1.4\ \beta_{Ic}^2), \tag{3}$$

in which

$$\beta_{Ic} = 1/\alpha, \tag{4}$$

was developed by Irwin for estimating values of K_{Ic} from measured values of K_c, or the reverse. Tables 3 and 4 show estimates made by Irwin of the significance of α and β_c values, in terms of fracture mode, including the references in this paper from which the individual estimates were obtained. It is clear that Irwin's estimates could only be semi-quantitative, but also that they were an important guide to the establishment of conservative criteria for plane-strain fracture toughness testing. Equation (3) was put to an early important application by Wessel [46], that of conservatively but realistically adjusting experimental data to estimate the plane-strain fracture toughness of a heat-treated ASTM A-372, Class 4, steel used for critical U.S. Navy air flasks. The successful outcome of this effort was a key factor in the acceptance of the discipline of fracture mechanics by the U.S. Navy.**

Recognizing that constraint effects on fracture toughness pertain to physical phenomena very close to a blunting crack tip, some investigators, including Lubahn [47] and Weiss [48], attempted to develop stress state dependent ductility relationships for use with elastic or elastic-plastic crack-tip stress analyses. Building on the results of a scaled-up, slow-bend, Charpy test performed by Lequear and Lubahn [49], which demonstrated essentially a plane strain condition at the notch root, Clausing [50] developed a procedure for estimating plane-strain ductility. Plane-strain ductility was measured directly by testing deep doubly-face-notched tensile bars and measuring the final

** E. T. Wessel, personal communication to J. G. Merkle, November 2, 1983.

TABLE 3--Estimated Significance of a in Terms of Fracture Mode.

$\alpha = 1/\beta_{Ic}$	Significance	Reference
0.2	Plane stress	39
0.25	Shear mode	39, 40
0.50	Beginning of transition to plane strain	42
0.67	80% shear	43
1.0	Plane strain; Mid-range of transition; Less than 50% shear	40 42 44
1.2	End of transition to plane strain	42
1.5	Beyond transition to plane strain	42
2.0	Plane strain; Possibly 50% shear	39 43
2.5	ASTM E399	

TABLE 4--Estimated significance of β_c in terms of fracture mode.

β_c	Significance	Reference
0.55	Less than 5% shear	41
1.9	Plane strain; Beginning of fracture mode transition to plane stress	41 42
2.7	45-60% shear	41
π	Near mid-range of fracture mode transition; Still less than 50% shear	41, 43 45
2π	Sometimes 70-80% shear; Sometimes nearly 100% shear	41 43, 44, 45

contraction of the remaining ligament after failure. For convenience in application, this strain was correlated empirically with the energy to maximum load in a slow-bend ordinary Charpy test. Attempts to relate plane-strain ductility to plane-strain fracture toughness were then made empirically by Barsom [51] and analytically by Merkle [52]. Merkle's approach dealt directly with the finite root radius of the physical crack, by using Malkin's and Tetelman's estimate [53] of an initial root radius value for A533B steel and calculating the applied notch root strain by integrating an incremental version of Neuber's equation [54] for notch-tip stresses and strains beyond yield. A resulting estimate of K_{Ic} for A533B steel [52] is shown in Fig. 5, which at least supports some optimism concerning the estimation of K_{Ic} values from Charpy data. Note that the results shown in Fig. 5 are an exception to the postulate

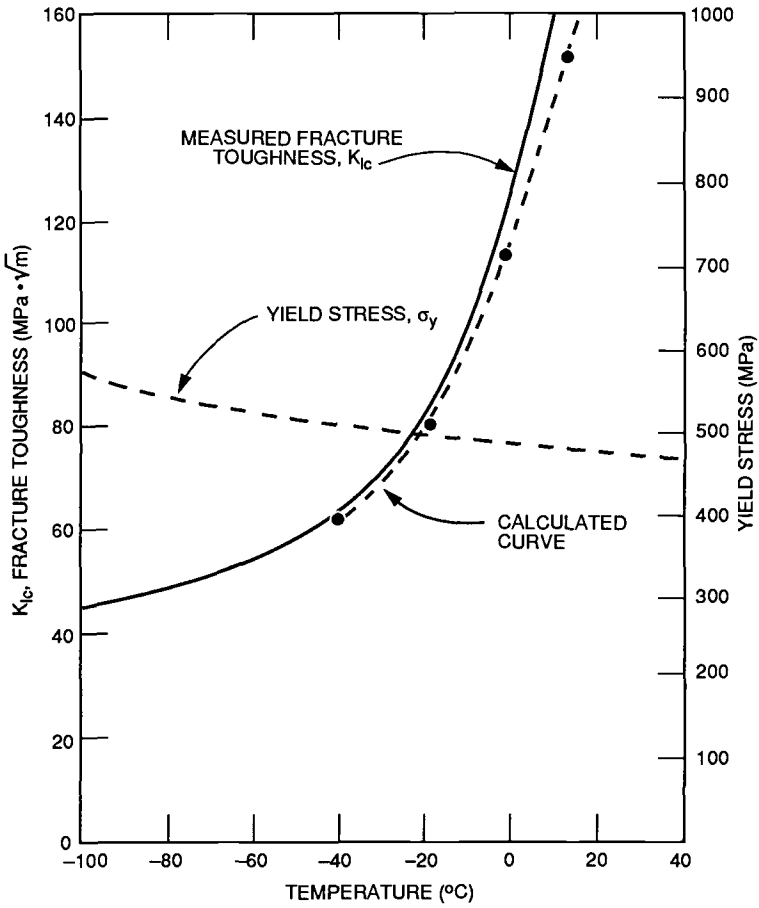


Fig. 5 Comparison of fracture toughness estimated from plane-strain ductility (plotted points and broken rising curve) with the curve based on valid large-specimen directly-measured data (solid curve) for A533 Grade B, Class 1, steel (from Ref. 52).

that determinations of fracture toughness require sharp-cracked specimens. However, the existence of several other useful correlations between Charpy data and fracture toughness also implies that the sharp-crack postulate might not be absolute.

In the course of applying the CTOD and J-Integral analysis methods to laboratory specimens, it was observed, both analytically and experimentally, that the relationship between the two fracture toughness parameters is subject to apparent constraint effects. Table 5 summarizes typical analytically and experimentally calculated values of the constraint parameter, m, in the alternate expressions

$$J = m\,\sigma_Y\,\delta \text{ or } J = m\,\sigma_f\,\delta, \tag{5}$$

where σ_Y and σ_f are the yield and flow stresses, respectively, and δ is the CTOD, demonstrating that as transverse constraint increases, the CTOD value corresponding to a given J value decreases [55-59]. The constraint parameter m is useful in estimating J from δ, or the reverse, for specified conditions, but it has not yet been developed into a means of predicting constraint effects on fracture toughness, per se.

Apparent constraint effects were also observed experimentally in the form of a specimen geometry effect on the magnitude of $J - \Delta a$ ductile tearing resistance curves, where Δa is the amount of crack growth by ductile tearing. Landes, McCabe, and Ernst [60] observed that the $J_M - \Delta a$ tearing resistance curve for a center-cracked tensile specimen of A533B steel was higher than the curve for other geometries. It was deduced that the reason for this difference is that slip lines can extend from the crack tips in a center-cracked tensile specimen to free specimen edges without curving, whereas in the other specimens they cannot do so. Since stress elevation at crack tips increases as the slip lines that intersect at the crack tip become more curved, it follows that the crack tips in the center-cracked tensile specimen are subject to less stress elevation due to yielding than in the other geometries. This is an important observation, and may have a significant bearing on transverse as well as longitudinal (in-plane) constraint effects.

Differences in crack-tip stress distributions under tensile and bending loads were also investigated analytically, using plane-strain, finite-strain, elastic-plastic finite-element analyses to reveal important details. McMeeking and Parks [61] observed that in bending, as J increases, the values of crack opening stress normalized by the flow stress, σ_{yy}/σ_o, remain almost exactly equal to their small-scale yielding values at equal values of normalized distance, $R/(J/\sigma_o)$, at least to $L\sigma_0/J = 42$, where L is the ligament dimension.. However, in tension, the normalized stresses immediately begin to decrease with increasing J, beyond the stress peak, which occurs at a value of $R/(J/\sigma_o)$ about equal to 1.0. These early near-crack-tip stress analyses served both to illustrate and define geometry effects on crack-tip stress distributions, but also to warn analysts that elastic-plastic near-crack-tip stress distributions must be functions of more than one parameter. This warning did not go unheeded.

Early in the development of fracture toughness testing, shallow cracks were avoided, because they were likely to lead to specimen yielding and higher values of fracture toughness than would otherwise be measured with deeply cracked specimens. However, as experience in CTOD testing accumulated, deliberate testing of shallow cracked specimens in bending commenced in order to realistically simulate certain structural

TABLE 5--Values of the constraint parameter m in the relation between J and CTOD, $J = m\ (\sigma_Y \text{ or } \sigma_f)\ \delta$.

Investigator	Ref.	Year	Reference Stress	Plane Stress	3D	Plane Strain	Remarks
Harrison	55	1975	σ_Y	1.3		1.7	
Dawes	56	1977	σ_Y		1.5-2.1		Experimental
Wellman, Rolfe, & Dodds	57	1984	σ_Y	1.0		2.0	
			σ_f	1.2		1.6	
Wilson & Donald	58	1989	σ_Y		1.73		Experimental
Sorem, Dodds, & Rolfe	59	1990	σ_f		1.4		Shallow; E-PP
					1.6		Shallow; A-36
					1.7		Deep; A-36

safety situations [56, 12]. Eventually, such data were also interpreted in terms of numerical calculations of J [59, 13]. Sorem, Dodds, and Rolfe [62] showed conclusively that the shallow-crack toughness elevation in bending is caused by slip lines from the crack tip curving backwards to reach the front-face free surface, which they do not do in a deeply cracked specimen. The detailed effects of such a plastic zone development, in terms of the near-crack-tip stresses, were investigated later by others.

With the aforementioned experimental and analytical information in hand, plus the vast improvements in computing technology that have taken place in recent years, analysts were in a position to economically investigate the details of crack-tip stress distributions, at least in two dimensions, in order to formulate and test hypotheses concerning constraint. Since the analyses of Ref. 61 had illustrated the non-uniqueness of elastic-plastic crack-tip stress distributions with respect to J alone, attention focused on the identification of a practical second parameter. The first candidate was a parameter already routinely calculated from photoelastic data [63], namely the elastically calculated nonsingular horizontal normal stress near the crack tip, σ^{o}_{nn}. In fracture mechanics constraint investigations [64, 65], this stress became known as T_{11}, or more commonly, simply the T stress. Elastic-plastic, large strain, so-called modified boundary layer analyses of circular regions containing crack tips and subject to the elastic boundary tractions or displacements corresponding to K_I and T show that positive values of T raise the near-crack-tip stresses only slightly, while negative T values lower them appreciably [64, 65]. Although predictions of near-crack-tip stresses based on the T stress still seem useful near limit load [65], other investigators [66] have chosen to focus on another second parameter, the definition of which is based on the stresses that develop within a few multiples of the CTOD from the blunting crack tip. This is known as the Q parameter, which represents what in two dimensional analysis turns out to be an approximately constant hydrostatic stress difference in the forward sector, equal to $Q\sigma_o$, between the near tip normal stresses beyond the stress peak and the values which exist under small-scale yielding conditions at the same normalized distance from the crack tip [66]. Figure 6 illustrates the variations of normalized hydrostatic stress on the plane of crack extension with normalized distance, obtained from plane-strain, large-strain, modified-boundary-layer analyses using K_I and T to determine boundary conditions, as presented in Ref. 66. Beyond the stress peak, the curves become virtually parallel, thus supporting the Q parameter concept. The curves in Fig. 6 are therefore labeled with the calculated values of Q. These results show that for two-dimensional analyses, a two parameter characterization closely represents elastic-plastic near-crack-tip stress distributions beyond the stress peak. However, for a given geometry and loading condition, the relation between J and Q is not known in advance, but must be determined numerically. The rising stress distribution between the blunted crack tip and the stress peak is quite insensitive to T and Q, because constraint conditions in this large-strain region are dominated by proximity to the stress-free surface of the blunted crack tip. At least within the limits of a one parameter characterization based on CTOD, this same segment of the normalized stress distribution is also relatively insensitive to uniform variations in the transverse strain [67]. The range of the rising stress distribution, and therefore the magnitude of the stress peak, does depend on constraint, through its effect on the falling stress distribution beyond the stress peak. In particular, a decrease in

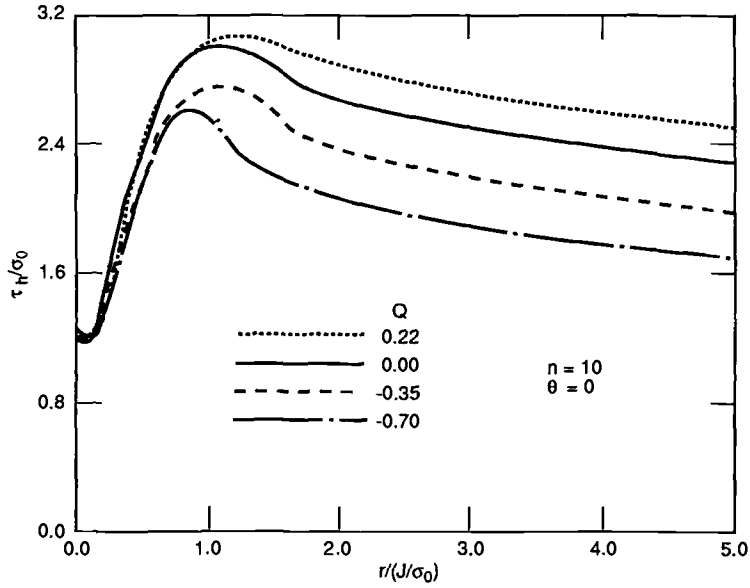


Fig. 6 Effect of variations in the T stress applied to a modified-boundary-layer model, on the near-crack-tip normalized hydrostatic stress, expressed in terms of the Q parameter (from Ref. 66).

constraint lowers the falling stress distribution, thereby lowering the stress peak.

Considering the approximate invariance of Q with the crack-tip polar coordinates r and θ in the forward sector, and the null effect of hydrostatic stress on yielding, it is understandable that Anderson and Dodds [68-70] could observe, in two-dimensional, elastic-plastic, small strain, analyses, that normalized principal stress contours ahead of crack tips in finite bodies, within a range of stress values, tend to remain geometrically similar, although they usually decrease in size as yielding progresses. An example of these observations, for a shallow crack in a beam [70], is shown in Fig. 7. On this basis, Anderson and Dodds [68, 69] proposed to use the absolute area enclosed within an arbitrarily chosen principal stress contour as a fracture criterion. Because of the observed geometric similitude of principal stress contours, the resulting fracture estimates are independent of the chose stress value, as long as it is within the range of similitude. The method of application of this hypothesis is to construct a curve relating the small-scale-yielding values of J_{SSY} and the finite body values of J_{FB} that produce equal areas enclosed by the chosen principal stress contour. Then, measured small-specimen values of J_{FB} at fractur can be adjusted to the corresponding large-specimen small-scale-yieldin values on the basis of equal areas, or the reverse.

Although the normal stresses in the small-strain region of the plastic zone beyond a crack tip in finite bodies at low loads may be describable in terms of J and a hydrostatic stress difference coefficient Q, with respect to a reference small-scale-yielding (SSY)

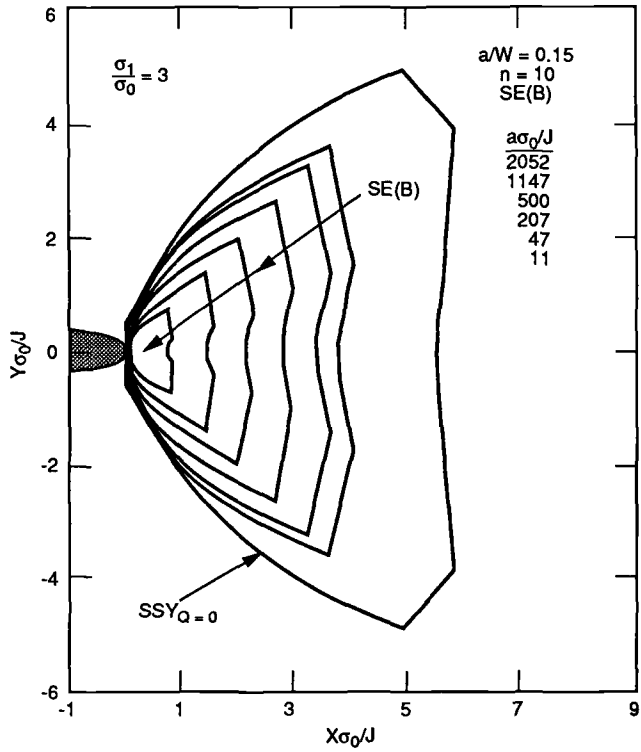


Fig. 7 Normalized principal stress contours for a succession of normalized increasing J values (from Ref. 70).

solution, this does not always remain true at higher loads. At higher loads, significant differences in terms of the shear stresses, and therefore also the plastic strains, sometimes appear with respect to the reference SSY solution [71, 72]. These differences cannot be reconciled by means of a hydrostatic stress change, because hydrostatic stress changes have no effect on yielding, and therefore no effect on the shear stresses and the plastic strains [71, 72]. For this reason, mathematical investigations, at present based on small-strain theory, have recently been undertaken to obtain additional terms in the elastic, power-law strain-hardening, series expansions for which the HRR solution is the set of initial terms [71-76]. Good results have been obtained by means of a three-term, variables-separable, series expansion for all the stresses, strains and displacements near a crack tip in a material with a Ramberg-Osgood stress-strain curve [73]. It turns out that the first three terms are often sufficient to match numerically calculated values of stress at all angles over most if not all of the plastic zone, for deep and shallow cracks and for low to high strain hardening exponents in both plane stress and plane strain [73]. In each case, the first term in the series represents the HRR solution [74, 77-79]. In the case of Mode I, for plane stress, all three stress terms are controlled by J alone, while for plane strain the second and third terms are controlled

by a single independent dimensionless coefficient, termed A_2 [71, 75], which can be numerically calculated by either point matching or least-squares fitting to finite-element data [71-74]. One reason for the sufficiency of a three-term stress series is the empirical observation that, based on the separability of the variables r and θ in each term, the functions of θ in the third and higher order terms are almost proportional at all values of θ, thus allowing, by close approximation, a collection of the third and higher order terms into a single term [73]. In addition, the fourth and higher order stress terms are apparently relatively small in magnitude compared to the third term so that the numerical determination of A_2, which also appears in the second term, is not rendered inaccurate. For small-scale yielding, as modeled by the modified boundary layer (MBL) method, numerically calculated differences in shear and effective stresses in the forward sector between the HRR and the complete solutions are small compared to those for the normal stresses [73, 76]. This implies that normal stress differences are due to a hydrostatic stress, which therefore justifies the J-Q approach for relatively low loads. However, for finite geometries under large-scale yielding, which is typical of laboratory test specimens in the transition range, shear and effective stress differences, and therefore plastic strain differences, can become significant [73]. Such differences cannot be corrected by the J-Q approach, but they generally can be and are well corrected by the $J\text{-}A_2$ approach. Although it is presently still necessary to employ full-field numerical analyses to determine the parameter A_2, in the absence of a single-specimen experimental method, the $J\text{-}A_2$ method does offer an improved mathematically rational method for describing the stress fields in the plastic zones extending from crack tips. Therefore, the parameter A_2 is a good candidate for a constraint parameter for stress-controlled fracture [74]. Similar comparative calculations in terms of strains, displacements, and transverse loading, are feasible but have not yet been published [72, 74]. In addition, the present theory is based on small-strain-theory and the assumption of an infinitely sharp initial crack, so the full extent of crack-tip blunting is not considered. With these limitations in mind, it does appear that higher order term analyses have the potential to be quite helpful in developing improved engineering fracture criteria in terms of either stress or strain [72, 74].

The foregoing examples demonstrate that analysis aspects of constraint for stationary cracks under plane-strain conditions have been greatly clarified by recent computational studies. However, other important aspects of constraint remain to be equally well understood. These include thickness effects, biaxial nominal-stress effects, effects of ductile crack growth prior to cleavage, crack-front-motion induced strain-rate effects and microstructural effects.

PRELIMINARY THICKNESS, BIAXIAL, CRACK-GROWTH AND METALLURGICAL ASPECTS OF CONSTRAINT

Although the recent two-dimensional plane-strain analytical treatments of constraint have certainly revealed the importance of in-plane (longitudinal) constraint effects, especially for shallow flaws, they have not proven that through-thickness (transverse) constraint effects are unimportant. Returning to basic physical reasoning and experimental observations, the fact that the side surfaces of standard through-cracked specimens are free of stress, and the observation of transverse contraction dimples at the crack ends, which grow with

increasing load, strongly imply a loss of stress triaxiality progressing through the thickness from the free surfaces toward the mid-plane with increasing load. Historically, thickness contraction effects were believed to be the main reason that measured fracture toughness values were observed to decrease with increasing specimen thickness, approaching an asymptote which implicitly corresponds to fracture initiation near the mid-plane before significant through-thickness stress reduction has occurred. Such reasoning was the basis for the thickness criterion chosen by ASTM for measuring linear-elastic-fracture toughness [5]. It also served as the qualitative definition of what was considered to be perhaps the most basic unsolved problem in fracture mechanics, that of transverse constraint. Because of its fundamental importance, the thickness effect on fracture toughness attracted Jerry Swedlow's attention and it was the subject of his Ph.D. thesis [80]. Using Irwin's data for 7075-T6 aluminum as an illustration, as shown in Fig. 8, Jerry attempted to formulate the three-dimensional elastic equations for a through-crack in a wide plate, finding that if the near-crack-tip stresses are expressed as products of functions of radius and angle, the transverse stresses would not be singular. This somewhat suspicious and physically unlikely result led to the decision to approach the elastic-plastic problem numerically. Jerry used the finite-element method to solve the plane-stress problem as a first step in understanding free-surface-induced transverse constraint effects. Although not a three-dimensional solution, Jerry's work was an early milestone in computational fracture mechanics.

One preliminary approach to a three-dimensional analysis is a two-dimensional generalized-plane-strain analysis. Such results, obtained

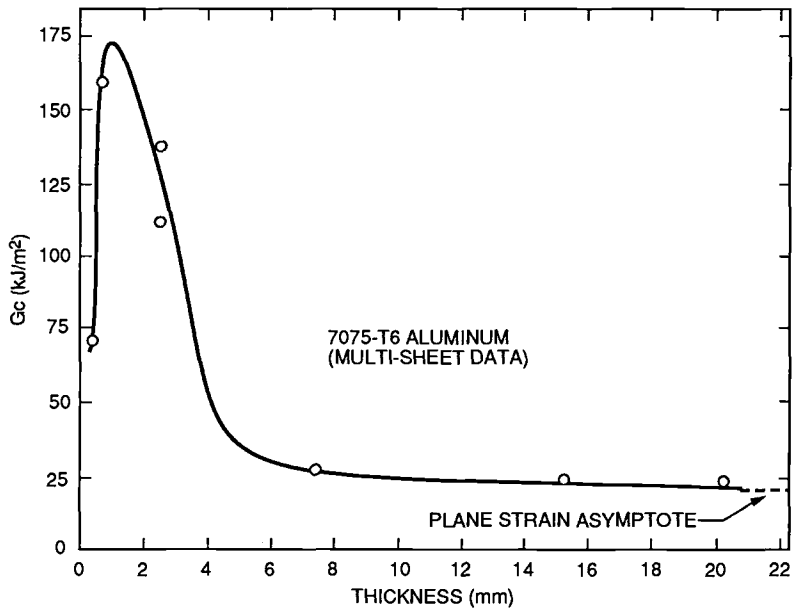


Fig. 8 Variation of critical strain energy release rate values with specimen thickness for 7075-T6 aluminum (from Ref. 80).

by Shum, for an elastic-plastic, large-strain analysis of a single-edge-notched tension specimen with a/W = 0.25, as shown in Fig. 9, show that under nominally LEFM valid conditions, positive variations in transverse strain at a given load have no significant effect on near-crack-tip stresses [81], for $r/(J/\sigma_0) \leq 2.5$. Although results were not presented in Ref. 81 for negative transverse strains, the results presented imply that thickness effects, when they do appear, may be due to phenomena that cannot be well modeled by a two-dimensional analysis. Further experimental and analytical investigations of biaxial-loading effects on the fracture toughness of reactor pressure vessel steels are in progress at ORNL [82]. However, three-dimensional analysis results are not yet sufficient to clearly define the important details of multiaxial stress and strain behavior near crack tips for biaxial loading [82].

The general observation that size effects on dynamic-initiation and crack-arrest fracture toughness are minimal, compared to those on static-initiation fracture toughness, is generally attributed to strain-rate effects on the yield stress. However, the observation made by Milne and Curvey [83] in 1982, as shown in Fig. 10, that stable ductile crack growth prior to cleavage initiation causes a progressive reduction and eventual elimination of size effects on the cleavage fracture toughness implies that something other than general strain rate effects may also be involved in this process. An analytical explanation for this phenomenon was recently developed by Varias and Shih [84] who, using a modified-boundary-layer, small-strain, elastic-plastic finite-element analysis, and equations appropriate for steady-state rate and inertia-independent crack growth, found that a high-constraint

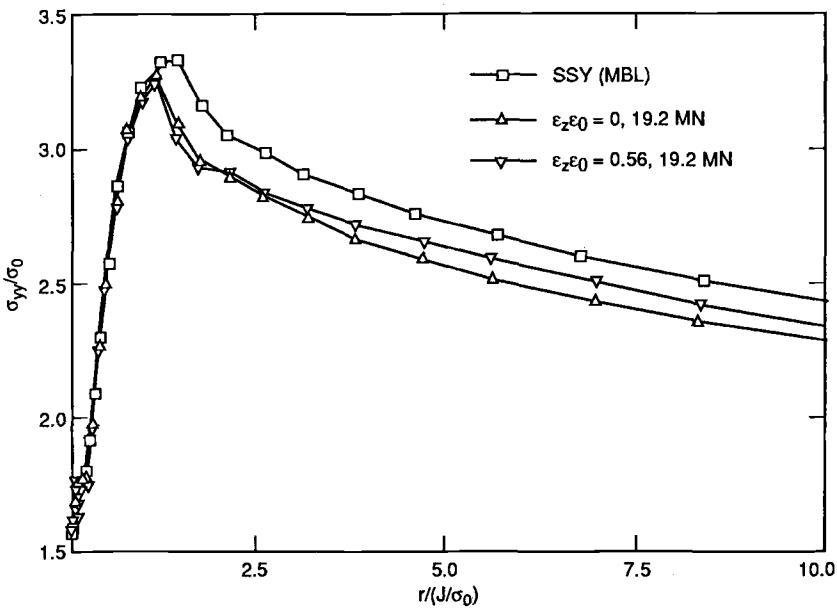


Fig. 9 Comparison of normalized near-crack-tip stresses for two generalized-plane-strain values from full-field analyses of a single-edge-notch specimen with a small-scale-yielding modified-boundary-layer solution (from Ref. 81).

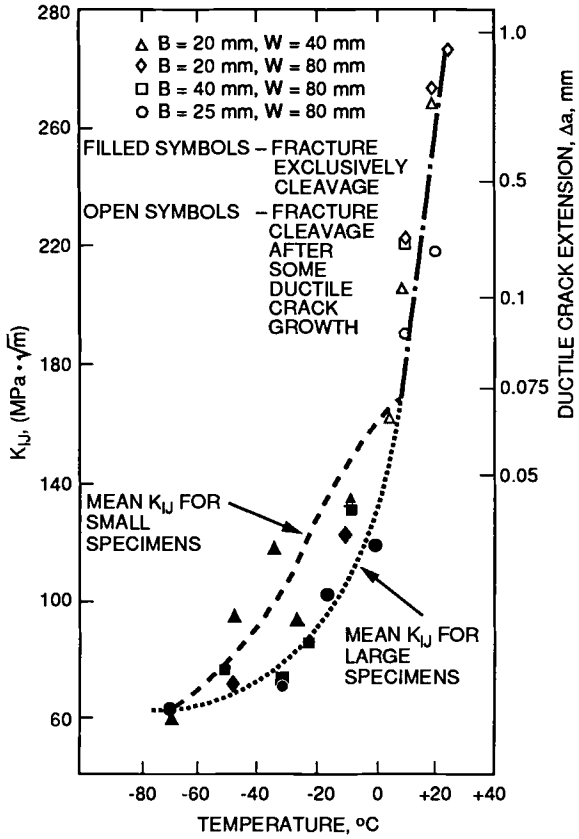


Fig. 10 Illustration of the convergence of small and large-specimen fracture toughness curves in the upper transition region, caused by constraint recovery due to ductile crack growth prior to cleavage (from Ref. 83).

single-parameter stress field always tends to develop during ductile crack growth, regardless of the level of constraint before crack growth. Tang and Dodds [85] confirmed the results of Ref. 84 by analyzing the early transient phase of crack growth. They found a progressive increase of the normal stresses in the region surrounding the crack tip, toward values generally slightly higher than the small-scale-yielding values. In the yielded region behind the growing crack, the horizontal stress was especially increased, apparently because of the resistance to the plastic contraction required to accommodate crack opening. This stress increase could be responsible for the elevation of the hydrostatic stress ahead of the crack tip and the observed reduced opening (so-called crack sharpening) characteristic of growing cracks.

Metallurgical studies have also shown that the effects of moving separations within and between individual grains are also extremely and fundamentally important in the development of unstable cleavage fractures. Averbach [86, 87] and Hahn [88], among others, have

elucidated the requirement for plastic strain in the single digit percent range to form a cleavage microcrack, and the immediate temperature and time-dependent competition that ensues between grain yielding, microcrack blunting and arrest versus continued cleavage propagation through successive grains. More recent research at the University of Maryland [89, 90] has led to the hypothesis that cleavage in reactor pressure vessel steels and welds occurs only when small rapidly moving ductile separations, which develop in vulnerable regions, cause the impingement of very high local strain rates on neighboring ferrite grains. A typical vulnerable region in base material is a local concentration of micron-sized carbide particles which can rapidly debond from the surrounding ferrite. In low-carbon weld metals, broken or debonding silicate particles play the same role [90]. Constraint can become involved in this process via the fact that elastically-releasable strain energy is the only available means of propagating cleavage microcracks, and this quantity depends strongly on the maximum principal tensile stress normal to the plane of the microcrack. In turn, the maximum principal tensile stress is elevated by an increase in the hydrostatic stress. Thus the relevance of stress triaxiality.

ADDITIONAL AXISYMMETRIC AND THREE-DIMENSIONAL CONSTRAINT ANALYSIS RESULTS

Although the assumption of plane strain has often been used for crack-tip stress analysis problems, either because it was believed to represent an actual physical limit approaching the crack tip or simply because it was a computationally expedient and reasonable two-dimensional approximation, not all important facts about constraint are revealed by such analyses. Jerry Swedlow realized this and consequently sought to perform some accurate crack-tip stress analyses involving no arbitrary assumptions about the transverse strain and its effects. Having observed first hand the difficulty of performing numerical three-dimensional elastic-plastic analyses, Jerry decided to take the intermediate step of studying a class of axisymmetric elastic problems. Swedlow and Ritter [91] performed elastic finite-element stress analyses of axially loaded thick-walled hollow cylinders containing either complete (360°) internal or external circumferential surface cracks. They defined positive crack front curvature for an internal surface crack as the ratio of the cylinder thickness to the crack-tip radius, and negative curvature for an external surface crack as the negative of the same ratio. The circumferential strain tangential to the crack front was always negative for an internal surface crack. While it was still negative for shallow external surface cracks it became positive for deeper external surface cracks. Thus it was numerically demonstrated that crack tips do not automatically create plane strain, and that the transverse strain at a crack tip for a given load type depends on specimen and flaw geometry.

As computing capabilities improved, innovations continued in the development and application of computational and analytical techniques to fracture analysis problems. Using the method of lines, Malik and Fu [92] succeeded in analyzing the problem posed by Swedlow in his thesis, the through-crack is a finite-thickness elastic-plastic plate. Elastic K_I calibrations and elastic-plastic crack-tip plastic zone contours and opening-mode strains approaching the crack tip were calculated and plotted as functions of load and thickness positions. These results demonstrated that three-dimensional elastic-plastic fracture analyses were becoming practical. Other available three-dimensional elastic crack-tip stress analysis results for various geometries were examined [93] and it was found that they all imply non-singular non-zero values

of strain tangent to the crack front. These transverse strains were negative for all cases examined, except for the deeply externally notched round tensile specimen, in qualitative agreement with the Swedlow and Ritter [91] results.

A recent series of three-dimensional, small-strain, elastic-ideally plastic finite-element analyses of through-cracked tensile and bending specimens shows vividly the effects of finite thickness that are not portended by two-dimensional analysis results. Newman et al. [94], calculated average constraint factors, α_g, defined as the ratio of the average opening-mode stress on the plane of crack extension within the crack-tip plastic zone, divided by the yield stress. As shown in Fig. 11, values of α_g, plotted versus $K/(\sigma_o\sqrt{w})$, where w is specimen width, tend to fall within the same range as the values of m in Eq. (5), the relation between J and CTOD. Furthermore, partly because they represent through-thickness averages, the curves representing combined transverse and longitudinal constraint effects, as determined by three-dimensional analyses, are noticeably different from, and lower than, those representing longitudinal constraint effects only, as determined by two-dimensional analyses. In contrast to the plane-strain results of Refs. 84 and 85, it was also found that the normal stresses near the crack tip in a through-cracked thin sheet are not greatly affected by crack growth [94]. This could be due to the fact that the transverse contraction strains accommodating crack opening are occurring primarily in the through-thickness direction, which is associated with a plane-stress boundary condition rather than an increasing value of σ_{xx} behind the crack tip. The stationary crack results in Ref. 94 agree qualitatively with other recent results, expressed in terms of J and Q, obtained by Shum [95] from two and three-dimensional elastic-plastic analyses of compact specimens. Consequently, it is clear that the estimation of constraint effects is best accomplished with three-dimensional analyses.

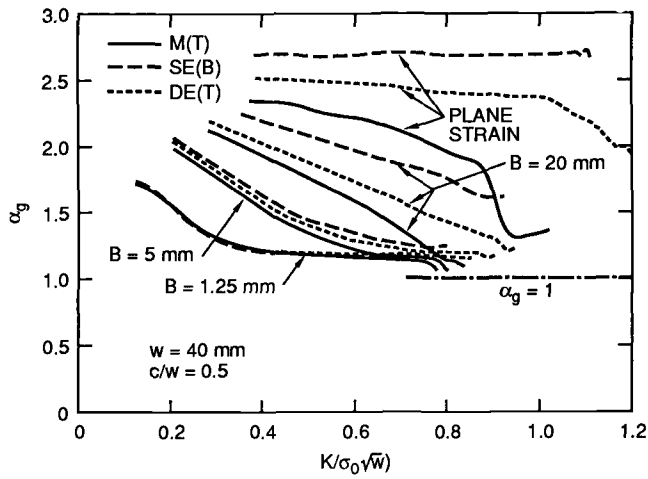


Fig. 11 Curves of α_g, the average normalized crack-opening stress on the plane of crack extension, within the plastic zone, from two- and three-dimensional elastic-ideally-plastic analyses (from Ref. 94).

Two recently obtained sets of two and three-dimensional large-strain, elastic-plastic finite-element analysis results for compact (CT) and other specimen geometries shed considerable light on the details of three-dimensional constraint effects, especially when the two sets of results are considered together. Figure 12 shows two and three-dimensional analysis results obtained by Brocks and presented by Sommer and Aurich [96], for double-edge-cracked tensile, center-cracked-tensile and compact specimens. Based on a reference cited [97], the Ramberg-Osgood stress-strain parameters for Brocks' analyses were σ_0 = 440 MPa, n = 7.7 and α = 1.0. In Fig. 12(a), the lower curve of each pair, for a given specimen geometry, is for J = 12 N/mm and the higher is for

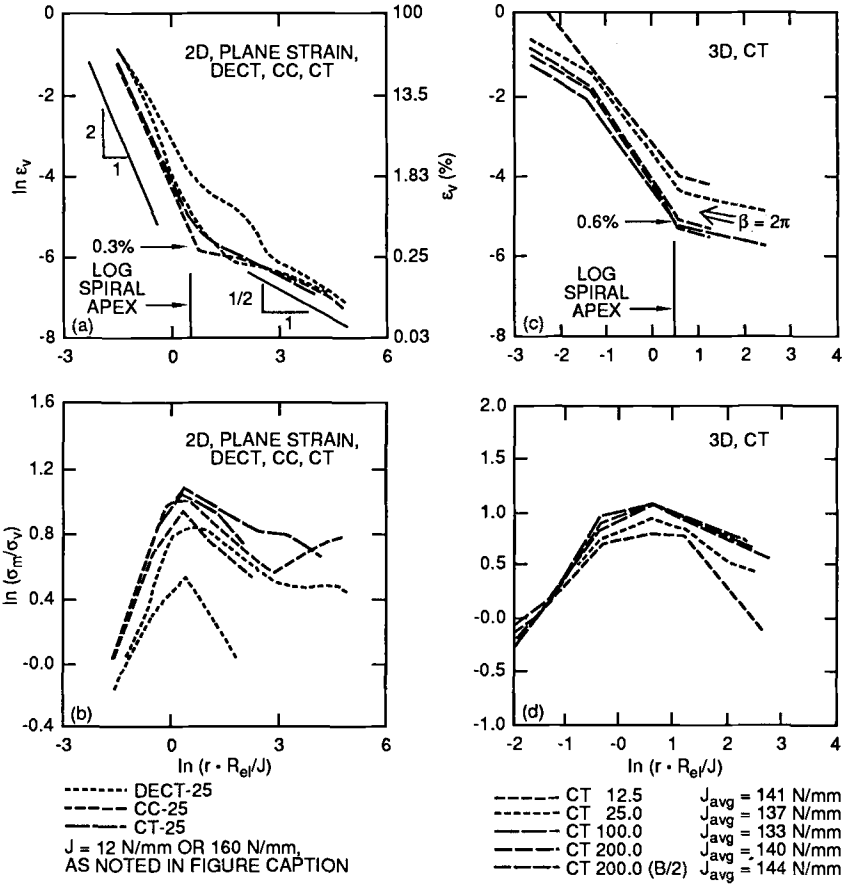


Fig. 12 Logarithmic plots of normalized near-crack-tip strain and stress for two- and three-dimensional large-strain elastic-plastic analyses of double-edge-cracked tensile, center-cracked tensile and compact specimens (from Ref. 96) In (a), the lower curve of each pair, for a given specimen geometry, is for J = 12 N/mm and the higher is for J = 160 N/mm. In (b), the reverse is true [97].

J = 160 N/mm. In Fig. 12(b), the reverse is true [97]. Figure 12(a) shows a log-log plot from two-dimensional plane-strain analyses of equivalent plastic strain versus normalized distance from the crack tip. In these coordinates, the strain curves are quite bilinear, with an abrupt change in slope at a logarithmic normalized distance of about 0.5. Assuming a value of m = 1.5 in Eq. (5) implies that the knee of the strain curves in Fig. 12(a) occurs at about r = 2.47 δ, which is close to the tip of the large-strain logarithmic-spiral slip-line zone [52]. The location of the stress peaks in Fig. 12(b) basically coincides with the knee of the strain plots. The slopes of the strain plots in Fig. 12(a) are nearly -1/2 beyond the knees of the curves, implying that deformations beyond the log-spiral region are still controlled by compatibility with the surrounding elastic material. Within the logarithmic-spiral slip-line region, the strain curves have slopes of about -2, in agreement with the small-plastic-strain solution for a yielded hollow cylinder, which is also characterized by logarithmic-spiral slip lines [52]. In the case of the three-dimensional results for the CT specimens, the strain plots in Fig. 12(c) are still piecewise linear, although they tend to be somewhat trilinear. The slopes of the segments meeting at the apex of the log spiral slip line region are not exactly -1/2 and -2, but they are reasonably close.

In the further examination of the same results, it is useful to employ a logical generalization of Irwin's definition of the β parameter in order to apply it to conditions beyond small-scale-yielding. Using the conversion

$$K^2 = EJ, \tag{6}$$

where differences between plane stress and plane strain are set aside for simplicity, Eq. (2) becomes

$$\beta = \frac{EJ}{\sigma_Y{}^2 B}. \tag{7}$$

In Eq. (7), the subscripts have been dropped in order to represent applied rather than critical values. The physical significance of Eq. (7) can be made clear by employing Eq. (5), which leads to

$$\beta = \frac{m}{\epsilon_Y}\left(\frac{\delta}{B}\right), \tag{8}$$

a relationship which has an easily understood meaning at all levels of loading. With these definitions it is possible to extend Eq. (3) beyond the limits of small-scale-yielding if experimental data substantiate the extension [98]. For Brocks' analysis, using a yield stress of 440 MPa (63.8 ksi), an elastic modulus of 207 GPa (30 × (10^6 psi) and ν = 0.3, it is possible to calculated the β values for each of the strain curves in Fig. 12(c). The strain curves rise as β increases, but only slightly until $\beta > 2\pi$ and then they rise noticeably more. The stress curves in Fig. 12(d) fall as the corresponding strain curves in Fig. 12(c) rise, and to the same relative degree, implying that $\beta > 2\pi$ does empirically correspond to the onset of a significant loss of three-dimensional constraint, as indicated by the "nearly 100% shear" note in Table 4. Until $\beta > 2\pi$, the equivalent plastic strain at the apex of the log-spiral slip-line region is about 0.6%. Afterwards it becomes significantly larger. These observations lend direct analytical support to those of McCabe [99], which were based on statistical analyses of

fracture toughness data in the transition temperature region, and which also independently imply that β reaching a value close to 2π constitutes a loss of constraint criterion.

The second set of results to be considered here are those obtained by Keeney [81] for the calculated values of transverse displacements close to the crack tip in a 1T-CT specimen, for which the yield stress at -75°C was assumed to be 483 MPa (70 ksi) and the elastic modulus 207 GPa (30×10^6 psi). Transverse displacement distributions were calculated for three different loads ranging beyond small-scale yielding, 29, 35, and 50 kN (6.5, 7.9, and 11.2 kips). Fig. 13 shows the plot of transverse displacement versus distance through the thickness for the load of 50 kN (11.2 kips). Notice in Fig. 13 that the curves for three different distances from the crack tip basically coincide, implying a condition of generalized-plane-strain close to the crack tip. Since

$$\varepsilon_z = \frac{\partial w}{\partial z}, \tag{9}$$

the negative slopes of the transverse displacement curves at $z = 0$ give the mid-plane transverse contraction strains. The calculated values of J, ε_z and β for the three loads are listed in Table 6, from which it can be seen that to a first approximation,

$$\varepsilon_z\ (\%) = -\ \beta\ /\ 10\,. \tag{10}$$

Referring to Fig. 12(c), it appears that when β becomes equal to 2π, the transverse contraction strain has become approximately equal to the equivalent plastic strain at the apex of the log-spiral slip-line region. Beyond this value of β, all of the transverse contraction strain needed to accommodate positive crack-opening strain near the

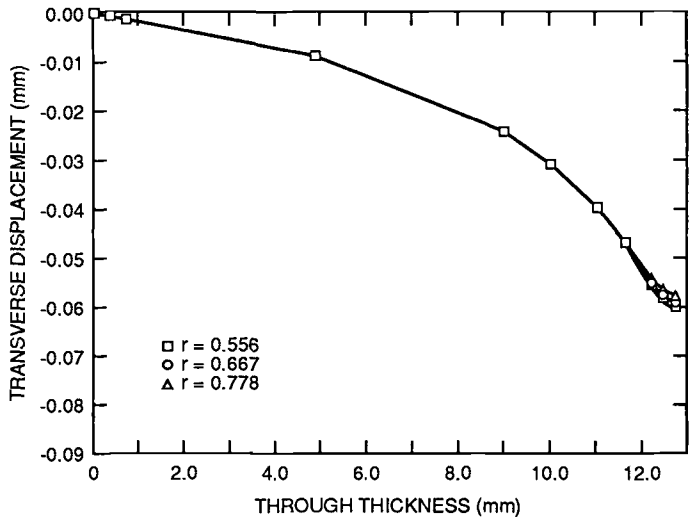


Fig. 13 Calculated near-crack-tip transverse contraction displacements in a compact specimen at three different distances from the crack tip (from Ref. 81).

TABLE 6--Three-dimensional elastic-plastic analysis results for a 1T-CT specimen based on data given in Ref. 81.

$T = -75°C \quad B = 25.4$ mm
$E = 207$ GPa
$\sigma_Y = 483$ MPa

$$\varepsilon_z = \frac{\partial w}{\partial z} \qquad \beta = \frac{EJ}{\sigma_Y^2 B}$$

P (kN)	J (kJ/m^2)		$\varepsilon_z @ z = 0$ (%)	β
29	15.7	-	0.059	0.55
35	23.7	-	0.081	0.83
50	67.3	-	0.191	2.36

stress peak is being supplied from the through-thickness direction. This implies that slip lines have extended from the mid-plane to the free side surfaces without curvature, thus allows plastic tensile strain to develop near the crack tip without stress elevation except for strain hardening.

Some qualitative substantiation of the hypothesis just described can be found in the results of an additional large-strain, elastic-plastic analysis for an axial, external semielliptical surface crack in the cylinder of a pressure vessel, also performed by Brocks [100]. The values of crack-opening stress at a fixed small distance from the crack front, as a function of the parametric angle of the semiellipse, measured from the deepest point, slowly approach a maximum as the angle increases, then drop suddenly, shortly after the tangential contraction strain passes - 0.6% on the way to becoming more negative. Thus, it appears that the ease with which negative plastic strain can occur near the crack tip, in the plane of the crack, and the curvature of the slip lines associated with the directions of its occurrence, are prime determinants of constraint.

CONCLUSIONS

This paper began with a brief philosophical and historical overview of applied fracture mechanics, particularly as it pertains to the safety of pressure vessels. It then progressed to a more-or-less chronological panorama of experimental and analytical results pertaining to the important subject of constraint, a fundamental aspect of fracture mechanics in which Jerry Swedlow had a keen interest and to which he made valuable contributions. A central theme of this paper has been that, in accordance with the scientific method, the search for patterns is constant and vital. This theme is well illustrated historically by the development of small, single-specimen, fracture toughness testing techniques. It is also illustrated here by the development, based on two different published large-strain, elastic-plastic, three-dimensional finite-element analyses, of a hypothesis concerning three-dimensional loss of constraint. Specifically, it appears that, at least in standard compact specimens, when a generalization of Irwin's thickness-normalized plastic-zone parameter, β, reaches a value close to 2π, the through-thickness contraction strain at the apex of the near-tip logarithmic-spiral slip-line region becomes the dominant negative strain

accommodating crack opening. Because slip lines passing from the midplane to the stress-free side surfaces do not have to curve, once these slip lines are established, stresses near the crack tip are only elevated by strain hardening and constraint becomes significantly relaxed. This hypothesis, based on published three-dimensional elastic-plastic analyses, provides a potentially valuable means for gaining additional insight into constraint effects on fracture toughness by considering the roles played by the plastic strains as well as the stresses that develop near a crack tip.

ACKNOWLEDGMENT

This research was sponsored by the Office of Nuclear Regulatory Research, U.S. Nuclear Regulatory Commission under Interagency Agreement 1886-8011-9B with the U.S. Department of Energy under Contract DE-AC05-84OR21400 with Martin Marietta Energy Systems, Inc. The submitted manuscript has been authored by a contractor of the U.S. Government under Contract No. DE-AC05-84OR21400. Accordingly, the U.S. Government retains a non-exclusive, royalty-free license to publish or reproduce the published form of this contribution, or allow others to do so, for U.S. Government purposes.

REFERENCES

1. Irwin, G. R. and Kies, J. A., "Critical Energy Rate Analysis of Fracture Strength," *Welding Journal,* Research Supplement, April 1954, pp. 193-S - 198-S.

2. Irwin, G. R., "Analysis of Stresses and Strains Near the End of a Crack Traversing a Plate," *Journal of Applied Mechanics*, September 1957, pp. 361-364.

3. Pellini, W. S. and Puzak, P. P., "Fracture Analysis Diagram Procedures for the Fracture-Safe Engineering Design of Steel Structures," *Welding Research Council Bulletin No. 88*, May 1963.

4. Irwin, G. R., "Crack-Toughness Testing of Strain-Rate Sensitive Materials," *Journal of Engineering for Power*, ASME, October 1964, pp. 444-450.

5. Brown, W. F. (ed.), *Review of Developments in Plane Strain Fracture Toughness Testing*, ASTM STP 463, American Society for Testing and Materials, Philadelphia, Pennsylvania, 1970.

6. Loss, F. J., "Dynamic Tear Test Investigations of the Fracture Toughness of Thick-Section Steel," NRL Report 7056 (HSSTP-TR-7), Naval Research Laboratory, Washington, D.C., May 14, 1970.

7. Shabbits, W. O., Pryle, W. H., and Wessel, E. T., "Heavy Section Fracture Toughness Properties of A533 Grade B, Class 1 Steel Plate and Submerged Arc Weldment," WCAP-7414 (HSSTP-TR-6), Westinghouse Electric Corporation, Pittsburgh, Pennsylvania, December 1969.

8. Shabbits, W. O., "Dynamic Fracture Toughness Properties of Heavy Section A533 Grade B, Class 1 Steel Plate," WCAP-7623, Westinghouse Electric Corporation, Pittsburgh, Pennsylvania, December 1970.

9. Crosley, P. B. and Ripling, E. J., "Plane Strain Crack Arrest Characterization of Steels," *Journal of Pressure Vessel Technology*, ASME, November 1975, pp. 291-298.

10. *ASME Boiler and Pressure Vessel Code*, Section XI, Rules for Inservice Inspection of Nuclear Power Plant Components, Appendix A, Evaluation of Flaw Indications, July 1, 1974.

11. Merkle, J. G. "A Summary of the Low Upper Shelf Toughness Safety Margin Issue," *Pressure Vessel Integrity - 1991*, PVP-Vol. 213 (MPC-Vol. 32), ASME, June 1991, pp. 89-98.

12. Sorem, W. A., Rolfe, S. T., and Dodds, R. H., Jr., "The Effects of Crack Depth on Elastic-Plastic CTOD Fracture Toughness," *WRC Bulletin 351*, Welding Research Council, New York, New York, February 1990, pp. 12-23.

13. Theiss, T. J. and Bryson, J. W., "Influence of Crack Depth on the Fracture Toughness of Reactor Pressure Vessel Steel," *Constraint Effects in Fracture*, ASTM STP 1171, American Society for Testing and Materials, Philadelphia, Pennsylvania, 1993, pp. 104-119.

14. Shih, C. F. and Zia, L., "Modeling Crack Growth Resistance Using Computational Cells with Microstructurally-Based Length Scales," *Constraint Effects in Fracture: Theory and Applications*, ASTM STP 1244, American Society for Testing and Materials, Phildelphia, Pennsylvania (in press).

15. Wallin, K., "Statistical Aspects of Constraint with Emphasis on Testing and Analysis of Laboratory Specimens in the Transition Region," *Constraint Effects in Fracture*, ASTM STP 1171, American Society for Testing and Materials, Philadelphia, Pennsylvania, 1993, pp. 264-288.

16. Wells, A. A., "Notched Bar Tests, Fracture Mechanics, and the Brittle Strengths of Welded Structures," *British Welding Journal*, January 1965, pp. 2-13.

17. Witt, F. J. and Mager, T. R., "Fracture Toughness K_{Icd} Values at Temperatures up to 550°F for ASTM A533, Grade B, Class 1 Steel," *Nuclear Engineering and Design*, Vol. 17, 1971, pp. 91-102.

18. Rice, J. R., "A Path Independent Integral and the Approximate Analysis of Strain Concentration by Notches and Cracks," *Journal of Applied Mechanics*, ASME, June 1968, pp. 379-386.

19. Rice, J. R., "Mathematical Analysis in the Mechanics of Fracture," Chapter 3 in Vol. 2 of *Fracture, an Advanced Treatise*, H. Liebowitz, ed., Academic Press, 1968.

20. Begley, J. A. and Landes, J. D., "The J-Integral as a Fracture Criterion," *Fracture Toughness*, Part II, ASTM STP 514, American Society for Testing and Materials, Philadelphia, Pennsylvania, 1972, pp. 1-23.

21. Landes, J. D. and Begley, J. A., "The Effect of Specimen Geometry on J_{Ic}," *Fracture Toughness*, Part II, ASTM STP 514, American Society for Testing and Materials, Philadelphia, Pennsylvania, 1972, pp. 24-39.

22. Paris, P. C., "Fracture Mechanics in the Elastic-Plastic Regime," *Flaw Growth and Fracture*, ASTM STP 631, American Society for Testing and Materials, Philadelphia, Pennsylvania, 1977, pp. 3-27.

23. Rice, J. R., Paris, P. C., and Merkle, J. G., "Some Further Results of J-Integral Analysis and Estimates," *Progress in Flaw Growth and Fracture Toughness Testing*, ASTM STP 536, American Society for Testing and Materials, Philadelphia, Pennsylvania, 1973, pp. 231-245.

24. Merkle, J. G. and Corten, H. T., "A. J-Integral Analysis for the Compact Specimen, Considering Axial Force as well as Bending Effects," *Journal of Pressure Vessel Technology*, Vol. 96, No. 4, ASME, November 1974, pp. 286-292.

25. Ernst, H. A., Paris, P. C., and Landes, J. D., "Estimations on J-Integral and Tearing Modulus T from a Single Specimen Test Record," *Fracture Mechanics, Thirteenth Conference*, ASTM STP 743, American Society for Testing and Materials, Philadelphia, Pennsylvania, 1981, pp. 476-502.

26. Randall, P. N. and Merkle, J. G., "Gross Strain Crack Tolerance of Steels," *Nuclear Engineering and Design*, Vol. 17, 1971, pp. 46-63.

27. Randall, P. N. and Merkle, J. G., "Effects of Strain Gradients on the Gross Strain Crack Tolerance of A533-B Steel," *Progress in Flaw Growth and Fracture Toughness Testing*, ASTM STP 536, American Society for Testing and Materials, Philadelphia, Pennsylvania, 1973, pp. 404-420.

28. Merkle, J. G., "Development of the Tangent Modulus Method of Elastic-Plastic Fracture Analysis," *Fracture Mechanics Applications: Implications of Detected Flaws*, IAEA-189, International Atomic Energy Agency, Vienna, 1976, pp. 407-460.

29. Grigory, S. C., "Testing the Six-Inch Thick Flawed Tensile Specimen for the Heavy Section Steel Technology Program," *Nuclear Engineering and Design*, Vol. 17, 1971, pp. 161-169.

30. Hall, W. J., Kihara, H., Soete, W., and Wells, A. A., *Brittle Fracture of Welded Plate*, Prentice-Hall, Inc., Englewood Cliffs, New Jersey, 1967 (see also Prof. Mylonas' written discussion of Ref. 40 cited later in this paper).

31. Loechel, L. W., "The Effect of Testing Variables on the Transition Temperature in Steel," MCR 69-189 (HSSTP-TR-2), Martin Marietta Corporation, Denver, Colorado, November 20, 1969.

32. Merkle, J. G., Koostra, L. F., and Derby, R. W., "Interpretations of the Drop Weight Test in Terms of Strain Tolerance (Gross Strain) and Fracture Mechanics," ORNL-TM-3247, Oak Ridge National Laboratory, Oak Ridge, Tennessee, June 1971.

33. Whitman, G. D., "Historical Summary of the Heavy-Section Steel Technology Program and Some Related Activities in Light-Water Reactor Pressure Vessel Safety Research," NUREG/CR-4489, Oak Ridge National Laboratory, Oak Ridge, Tennessee, March 1986.

34. Merkle, J. G., Whitman, G. D., and Bryan, R. H., "Relation of Intermediate-Sized Pressure-Vessel Tests to LWR Safety," *Nuclear Safety*, Vol. 17, No. 4, July-August 1976, pp. 447-463.

35. Cheverton, R. D., Iskander, S. K., and Ball, D. G., "Review of Pressurized-Water-Reactor-Related Thermal Shock Studies," *Fracture Mechanics: Nineteenth Symposium*, ASTM STP 969, American society for Testing and Materials, Philadelphia, Pennsylvania, 1988, pp. 752-766.

36. Theiss, T. J., Shum, D. K., and Rolfe, S. T., "Experimental and Analytical Investigation of the Shallow-Flaw Effect in Reactor Pressure Vessels," NUREG/CR-5886, Oak Ridge National Laboratory, Oak Ridge, Tennessee, July 1992.

37. Bryan, R. H., Merkle, J. G., Nanstad, R. K., and Robinson, G. C., "Pressurized Thermal Shock Experiments with Thick Vessels," *Fracture Mechanics: Nineteenth Symposium*, ASTM STP 969, American Society for Testing and Materials, Philadelphia, Pennsylvania, 1988, pp. 767-783.

38. Bryan, R. H. et al., "Performance of Low-Upper-Shelf Material Under Pressurized-Thermal-Shock Loading," *Nuclear Engineering and Design*, Vol. 115, 1989, pp. 359-367.

39. Irwin, G. R., Kies, J. A., and Smith, H. L., "Fracture Strengths Relative to Onset and Arrest of Crack Propagation," *ASTM Transactions*, Vol. 58, American Society for Testing and Materials, Philadelphia, Pennsylvania, 1958, pp. 640-660.

40. Irwin, G. R., "Fracture Mechanics," *Structural Mechanics*, Proceedings of the First Symposium on Naval Structural Mechanics, Pergamon Press, 1960, pp. 557-594.

41. Irwin, G. R., "Dimensional and Geometric Aspects of Fracture," *Fracture of Engineering Materials*, American Society for Metals, 1964, pp. 211-230.

42. Irwin, G. R., "Fracture Mode Transition for a Crack Traversing a Plate," *Journal of Basic Engineering*, Vol. 82, No. 2, ASME, June 1960, pp. 417-425.

43. Irwin, G. R., "Plastic Zone Near a Crack and Fracture Toughness," *Proceedings of the Seventh Sagamore Ordnance Materials Research Conference*, Syracuse University Research Institute, 1960, pp. IV-63 to IV-78.

44. Irwin, G. R., "Relation of Crack Toughness Measurements to Practical Applications," *Welding Research Supplement*, Vol. 41, No. 11, November 1962, pp. 519s-528s.

45. Irwin, G. R., "Structural Aspects of Brittle Fracture," *Applied Materials Research*, Vol. 3, No. 2, April 1964, pp. 65-81.

46. Wessel, E. T., "Relation of Laboratory Determinations of Fracture Toughness with the Performance of Large Steel Pressure Vessels," *Welding Journal, Research Supplement*, Vol. 43, No. 9, September 1964, pp. 415s-424s.

47. Lubahn, J. D., "A Review of Engineering Approaches to Brittle Fracture Design," (no document number) Colorado School of Mines, Golden, Colorado, 1961.

48. Weiss, V., "Material Ductility and Fracture Toughness of Metals," *Mechanical Behavior of Materials*, Vol. 1, The Society of Materials Science, Japan, 1972, pp. 458-474.

49. Lequear, H. A. and Lubahn, J. D., "Root Conditions in a V-Notch Charpy Impact Specimen," *Welding Journal Research Supplement*, December 1954, pp. 585-s - 588-s.

50. Clausing, D. P., "Effect of Plastic Strain State on Ductility and Toughness," *International Journal of Fracture Mechanics*, Vol. 6, No. 1, March 1970, pp. 71-85.

51. Barsom, J. M., "Relationship Between Plane Strain Ductility and K_{Ic}" *Journal of Engineering for Industry*, Vol. 93, No. 4, ASME, November 1971, pp. 1209-1215.

52. Merkle, J. G., "An Elastic-Plastic Thick-Walled Hollow Cylinder Analogy for Analyzing the Strains in the Plastic Zone Just Ahead of a Notch Tip," ORNL-TM-4071, Oak Ridge National Laboratory, Oak Ridge, Tennessee, January 1973.

53. Malkin, J. and Tetelman, A. S., "Relation Between K_{Ic} and Microscopic Strength for Low Alloy Steels," Report No. 69-58, Materials Department, University of California, Los Angeles, California, August 1969.

54. Neuber, H., "Theory of Stress Concentration for Shear-Strained Prismatical Bodies with Arbitrary Nonlinear Stress-Strain Law," *Journal of Applied Mechanics*, ASME, December 1961, pp. 544-550.

55. Harrison, J. D., "A Comparison Between Four Elasto-Plastic Fracture Mechanics Parameters," R/RB/E64/75, The Welding Institute, Abington Hall, Cambridge, England, January 1975.

56. Dawes, M. G., "Elastic-Plastic Fracture Toughness Based on the COD and J-Contour Integral Concepts," *Elastic-Plastic Fracture*, ASTM STP 668, American Society for Testing and Materials, Philadelphia, Pennsylvania, 1979, pp. 307-333.

57. Wellman, G. W., Rolfe, S. T., and Dodds, R. H., "Three-Dimensional Elastic-Plastic Finite Element Analysis of Three-Point Bend Specimens," *WRC Bulletin 299*, Welding Research Council, New York, New York, November 1984, pp. 15-25.

58. Wilson, A. D. and Donald, J. K., "Evaluating Steel Toughness Using Various Elastic-Plastic Fracture Toughness Parameters," *Nonlinear Fracture Mechanics: Vol. II - Elastic-Plastic Fracture*, ASTM STP 995, American Society for Testing and Materials, Philadelphia, Pennsylvania, 1989, pp. 144-168.

59. Sorem, W. A., Dodds, R. H., Jr., and Rolfe, S. T., "A Comparison of the J-Integral and CTOD Parameters for Short Crack Specimen Testing," *WRC Bulletin 341*, Welding Research Council, New York, New York, February 1990, pp. 24-34.

60. Landes, J. D., McCabe, D. E., and Ernst, H. A., "Geometry Effects on the R-Curve," *Nonlinear Fracture Mechanics: Vol. II - Elastic-Plastic Fracture*, ASTM STP 995, American Society for Testing and Materials, Philadelphia, Pennsylvania, 1989, pp. 123-143.

61. McMeeking, R. M. and Parks, D. M., "On Criteria for J-Dominance of Crack-Tip Fields in Large-Scale Yielding," *Elastic-Plastic Fracture*, ASTM STP 668, American Society for Testing and Materials, Philadelphia, Pennsylvania, 1979, pp. 175-194.

62. Sorem, W. A., Dodds, R. H., Jr., and Rolfe, S. T., "An Analytical Comparison of Short Crack and Deep Crack CTOD Fracture Specimens of an A36 Steel," *WRC Bulletin 351*, Welding Research Council, New York, New York, February 1990, pp. 1-11.

63. Smith, C. W., Jolles, M., and Peters, W. H., "Stress Intensities in Flawed Pressure Vessels," *Proceedings of the Third International Conference on Pressure Vessel Technology, Part II - Materials and Fabrication*, Tokyo, ASME, April 1977, pp. 535-543.

64. Bilby, B. A., Cardew, G. E., Goldthorpe, M. R., and Howard, D. C., "A Finite Element Investigation of the Effect of Specimen Geometry on the Fields of Stress and Strain at the Tips of Stationary Cracks," *Size Effects in Fracture*, The Institution of Mechanical Engineers, London, 1986, pp. 37-56.

65. Hancock, J. W., Reuter, W. G., and Parks, D. M., "Constraint and Toughness Parameterized by T," *Constraint Effects in Fracture*, ASTM STP 1171, American Society for Testing and Materials, Philadelphia, Pennsylvania, 1993, pp. 21-40.

66. Shih, C. F., O'Dowd, N. P., and Kirk, M. T., "A Framework for Quantifying Crack Tip Constraint," *Constraint Effects in Fracture*, ASTM STP 1171, American Society for Testing and Materials, Philadelphia, Pennsylvania, 1993, pp. 2-20.

67. Shum, D. K. M. and Merkle, J. G., "Crack Initiation Under Generalized Plane-Strain Conditions," *Fracture Mechanics: Twenty-Third Symposium*, ASTM STP 1189, American Society for Testing and Materials, Philadelphia, Pennsylvania, 1993, pp. 37-54.

68. Anderson, T. L. and Dodds, R. H., Jr., "Specimen Size Requirements for Fracture Toughness Testing in the Transition Region," *Journal of Testing and Evaluation*, Vol. 19, No. 2, JTEVA, March 1991, pp. 123-134.

69. Anderson, T. L., Vanaparthy, N. M. R., and Dodds, R. H., Jr., "Predictions of Specimen Size Dependence on Fracture Toughness for Cleavage and Ductile Tearing," *Constraint Effects in Fracture*, ASTM STP 1171, American Society for Testing and Materials, Philadelphia, Pennsylvania, 1993, pp. 473-491.

70. Dodds, R. H., Jr., Shih, C. F., and Anderson, T. L., "Continuum and Micromechanics Treatment of Constraint in Fracture," UILU-ENG-92-2014, Department of Civil Engineering, University of Illinois, Urbana, Illinois, November 1992.

71. Yang, S., Chao, Y. J., and Sutton, M. A., "Complete Theoretical Analysis for Higher Order Asymptotic Terms and the HRR Zone at a Crack Tip for Mode I and Mode II Loading of a Hardening Material," *Acta Mechanica*, Vol. 98, 1993, pp. 79-98.

72. Chao, Y. J., Yang, S., and Sutton, M. A., "On the Fracture of Solids Characterized by One or Two Parameters: Theory and Practice," *Journal of the Mechanics and Physics of Solids*, Vol. 42, No. 4, 1994, pp. 629-647.

73. Yang, S., Chao, Y. J., and Sutton, M. A., "Higher Order Asymptotic Crack Tip Fields in a Power-Law Hardening Material," *Engineering Fracture Mechanics*, Vol. 45, 1993, pp. 1-20.

74. Chao, Y. J., and Ji, W., "Cleavage Fracture Quantified by J and A_2," *Constraint Effects in Fracture: Theory and Application*," ASTM STP 1244, American Society for Testing and Materials, Philadelphia, 1995.

75. Chao, Y. J., "On a Single Parameter Controlled Fracture of Solids Under Plane Stress Conditions," *International Journal of Fracture*, Vol. 62, 1993, pp. R7-R10.

76. Xia, L., Wang, T. C., and Shih, C. F., "Higher-Order Analysis of Crack-Tip Fields in Elastic Power-Law Hardening Materials," *Journal of the Mechanics and Physics of Solids*, Vol. 41, 1993, pp. 665-687.

77. Hutchinson, J. W., "Singular Behavior at the End of a Tensile Crack in a Hardening Material," *Journal of the Mechanics and Physics of Solids*, Vol. 16, 1968, pp. 13-31.

78. Rice, J. R. and Rosengren, G. F., "Plane Strain Deformation Near a Crack Tip in a Power-Law Hardening Material," *Journal of the Mechanics and Physics of Solids*, Vol. 16, 1968, pp. 1-12.

79. Hutchinson, J. W., "Plastic Stress and Strain Fields at a Crack Tip," *Journal of the Mechanics and Physics of Solids*, Vol. 16, 1968, pp. 337-347.

80. Swedlow, J. L., "The Thickness Effect and Plastic Flow in Cracked Plates," ARL 65-216, Aerospace Research Laboratories, Office of Aerospace Research, United States Air Force, Wright-Patterson Air Force Base, Ohio, October 1965.

81. Bass, B. R., Shum, D. K., and Keeney-Walker, J., "Constraint Effects on Fracture Toughness for Circumferentially Oriented Cracks in Reactor Pressure Vessels," NUREG/CR-6008, Oak Ridge National Laboratory, Oak Ridge, Tennessee, August 1992.

82. Pennell, W. E., Bass, B. R., Bryson, J. W., McAfee, W. J., Theiss, T. J., and Rao, M. C., "Biaxial Loading and Shallow-Flaw Effects on Crack-Tip Constraint and Fracture Toughness," *Changing Priorities of Codes and Standards*, PVP-Vol. 286, ASME, 1994, pp. 103-114.

83. Milne, I. and Curry, D. A., "Ductile Crack Growth Analysis Within the Ductile-Brittle Transition Regime: Predicting the Permissible Extent of Ductile Crack Growth," RD/L/2209N81, Central Electricity Research Laboratories, Central Electricity Generating Board, United Kingdom, March 1982.

84. Varias, A. G. and Shih, C. F., "Quasi-Static Crack Advance Under a Range of Constraints: Steady-State Fields Based on a Characteristic Length" *Journal of the Mechanics and Physics of Solids*, Vol. 41, No. 5, 1993, pp. 835-861.

85. Tang, M., Dodds, R. H., Jr., and Anderson, T. L., "Effects of Ductile Crack Growth on Constraint Models for Cleavage Fracture," UILU-ENG-94-2001, Department of Civil Engineering, University of Illinois, Urbana, Illinois, January 1994.

86. Averbach, B. L., "Physical Metallurgy and Mechanical Properties of Materials: Brittle Fracture," Paper No. 2686, *Journal of the Engineering Mechanics Division*, ASCE, Vol. 86, No. EM6, December 1960, pp. 29-43.

87. Averbach, B. L., "Some Physical Aspects of Fracture," Chapter 7 in *Fracture, An Advanced Treatise*, Vol. 1, Academic Press, New York, 1968.

88. Hahn, G. T., "The Influence of Microstructure on Brittle Fracture Toughness," *Metallurgical Transactions A*, Vol. 15A, June 1984, pp. 947-959.

89. Irwin, G. R. and Zhang, X. J., "Cleavage Behaviors in Nuclear Vessel Steels," *Pressure Vessel Integrity*, PVP-Vol. 250, ASME, 1993, pp. 11-17.

90. Irwin, G. R., Zhang, X. J., and Schwartz, C. W., "Small Scale Nonuniformities Related to Cleavage Initiation and their Implications for Constraint Modeling," ORNL/NRC/LTR-94/18, Oak Ridge National Laboratory, Oak Ridge, Tennessee, August 1994.

91. Swedlow, J. L. and Ritter, M. A., "Toward Assessing the Effects of Crack Front Curvature (CFC)," *Stress Analysis and Growth of Cracks*, Part I, ASTM STP 513, American Society for Testing and Materials, Philadelphia, Pennsylvania, 1971, pp. 79-89.

92. Malik, S. N. and Fu, L. S., "Elasto-Plastic Analysis for a Finite Thickness Rectangular Plate Containing a Through-Thickness Central Crack," *International Journal of Fracture*, Vol. 18, No. 1, 1982.pp. 45-63.

93. Merkle, J. G., "Constraint and Strain Rate Effects in Fracture Toughness Testing," *Proceedings of the Fifteenth Water Reactor Safety Information Meeting*, NUREG/CP-0091, U.S. Nuclear Regulatory Commission, Washington, D.C., February 1988, pp. 5-15.

94. Newman, J. C., Jr., Crews, J. H., Bigelow, C. A., and Dawicke, D. S., "Variations of a Global Constraint Factor in Cracked Bodies Under Tension and Bending Loads," NASA Technical Memorandum 109119, National Aeronautics and Space Administration, Langley Reaearch Center, Hampton, Virginia, May 1994.

95. Shum, D. K. M., "Effects of 3-D Transverse Constraint on the Evolution of In-Plane Q-Stress," *Fracture Mechanics*, Vol. 26, ASTM STP 1256, American Society for Testing and Materials, Philadelphia, Pennsylvania, (in press).

96. Sommer, E. and Aurich, D., "On the Effect of Constraint on Ductile Fracture," *Defect Assessment in Components*, ESIS/EGF 9 Mechanical Engineering Publications, London, 1991, pp. 141-174.

97. Brocks, W., Künecke, G., Noack, H. D., and Veith, H., "On the Transferability of Fracture Mechanics Parametes from Specimens to Structures Using FEM," *Nuclear Engineering and Design*, Vol. 112, 1989, pp. 1-14.

98. Merkle, J. G., "An Examination of the Size Effects and Data Scatter Observed in Small-Specimen Cleavage Fracture Toughness Testing," NUREG/CR-3672, Oak Ridge National Laboratory, Oak Ridge, Tennesssee, April 1984.

99. McCabe, D. E., "A Comparison of Weibull and b_{Ic} Analyses of Transition Range Data," *Fracture Mechanics: Twenty-Third Symposium*, ASTM STP 1189, American Society for Testing and Materials, Philadelphia, Pennsylvania, 1993, pp. 80-94.

100. Brocks, W. and Künecke, G., "Elastic-Plastic Fracture Mechanics Analysis of a Pressure Vessel with an Axial Outer Surface Flaw (Part 2)," ORNL/TR-89/48 (translation of BAM Research Report No. 137, Berlin, Germany, June 1989), Oak Ridge National Laboratory, Oak Ridge, Tennessee, 1989.

Constraint Crack Initiation

Shang-Xian Wu[1] and Yiu-Wing Mai[1]

TWO-PARAMETER (J-Q) FRACTURE CHARACTERIZATION OF DUCTILE TEARING

REFERENCE: Wu, S. -X., and Mai, Y. -W., "**Two-Parameter (J-Q) Fracture Characterization of Ductile Tearing,** Fracture Mechanics: 26th Volume, ASTM STP 1256, Walter G. Reuter, John H. Underwood, and James C. Newman, Jr., Eds., American Society for Testing and Materials, Philadelphia, 1995.

ABSTRACT: CTOD tests have been carried out for compact tension specimens with a/W=0.6, double-edge notched tension specimens with a/W=0.9 and 0.5, single-edge notched tension specimens with a/W=0.5, three-point bend specimens with a/W=0.5 and 0.1 and center-cracked tension specimens with a/W=0.5. The results of the CTOD tests show that the crack initiation toughness of the material increases as the in-plane plastic constraint of the specimens decreases. The recently proposed two-parameter (J-Q) fracture characterisation technique has shown that the near-tip fields under very general conditions of loading in finite bodies can be described by two parameters, J and Q. A theoretical model of void nucleation and growth in the J-Q fields ahead of the crack tip is given in this paper. This model predicts the relationship between the crack initiation toughness (J_i or δ_i) and the constraint parameter Q. Comparison of experimental results of CTOD tests gives good agreement with theory.

KEYWORDS: ductile fracture, void nucleation, void growth, crack tip opening displacement, J-integral, constraint.

1. INTRODUCTION

The effects of constraint on fracture have been widely investigated. Many studies [1-3] have found that the fracture toughness for crack initiation is higher for shallow-cracked bend specimens with low constraint than for deeply-cracked bend specimens

[1] ARC research fellow and professor, respectively, Centre for Advanced Materials Technology, Department of Mechanical & Mechatronic Engineering, University of Sydney, Sydney, NSW 2006, Australia.

Copyright © 1995 by ASTM International www.astm.org

with high constraint. Hancock and Cowling [4] observed variations of crack tip opening displacement (CTOD) at ductile tear initiation in HY 80 steel specimens with different constraints by as much as 10 times. Kirk et al. [5] reported about the same amount of variation in cleavage fracture toughness for A515 steel over a range of constraints. It is also found that a ductile-brittle fracture transition takes place in medium carbon steels as the constraint increases [6-7].

By slip-line analysis for nonhardening materials McClintock [8] has shown that the stress and velocity fields around a notch or crack strongly depend on the specimen geometry and the crack depth. Although the introduction of strain hardening creates a region over which the Hutchinson-Rice-Rosengren (HRR) J-singularity dominates [9,10], the size of this region strongly depends on both specimen configuration and crack length. Only in deeply cracked bend geometries with high in-plane constraints is the size of J-dominance region large enough to contain the fracture process zone and the single parameter J-based or δ(CTOD)- based approach approximately valid. However, for specimen geometries with low in-plane constraints or shallow cracks the size of the J-dominance zone is too small to validate the single parameter characteristics of stress-strain fields ahead of the crack tip. A single toughness measurement, J_{Ic} or δ_i, is not sufficent to represent the fracture criterion of materials and it should be combined with a parameter representing the in-plane constraint of specimens or structures. Recently, some researchers have suggested a two-parameter characterization of the crack-tip stress-strain fields. Rice [11] has shown that in the small scale yielding case the second non-singular term T of the elastic crack tip stress field has a significant influence on the shape and size of the crack tip plastic zone. Bilby *et al.* [12], Betegon and Hancock [13], and Al-Ani and Hancock [14] have studied the effects of the T-stress on the stress fields in the crack tip plastic zone. However, in the generally yielding or fully plastic cases both K and T have lost their meaning. O'Dowd and Shih [15-17] have shown that in the forward sector, the near-tip fields under very general conditions of loading in finite bodies can be described by two parameters J and Q. The J-integral sets the scale of deformation at the crack tip (i.e. the CTOD) while the hydrostatic stress parameter, Q, quantifies the level of stress triaxiality ahead of the crack tip. The J-Q fracture methodology has been successfully applied to account for the variation of the cleavage toughness [17] and the dependence of brittle-ductile fracture transition [7,18] with constraint.

Ductile fracture usually involves the nucleation of voids around inclusions or large second-phase particles and the subsequent growth of these voids to a critical size. The final coalescence of the voids and the main crack gives the initiation of ductile fracture. Both the nucleation and growth of voids are promoted by high hydrostatic stress. Analyses of growth of voids given by McClintock [19] for cylindrical voids and by Rice and Tracey [20] for spherical voids show that the growth rate of voids increases exponentially with the hydrostatic stress. Therefore, it is expected that the fracture toughness for initiation of ductile fracture is affected by constraint as

evidenced by experiments. Considering nucleation, growth and coalescence of voids in J-Q fields, Wu *et al.* [21] developed a theoretical model for ductile tearing which can predict the fracture toughness of ductile fracture initiation of a given material in different J-Q fields from one single measurement for a particular specimen.

In the present paper the experimental results of CTOD tests of various specimen geometries on a low carbon steel are reported. The results are compared with the predictions of the theoretical model.

2. CTOD TESTS AND RESULTS

The test material was a plain carbon steel plate 25 mm thick in the as-received condition. The chemical composition of the steel is 0.25% C, 0.82% Mn, 0.005% P, 0.03% S and 0.21% Si and its mechanical properties are given in Table 1. A least-squares fit of its true stress-true strain curve by the Ramberg-Osgood relation gives

$$\epsilon/\epsilon_0 = \sigma/\sigma_0 + \alpha(\sigma/\sigma_0)^n \tag{1}$$

with Young's modulus $E = 206$ GPa, $\sigma_0 = 252$ MPa and $\epsilon_0 = \sigma_0/E$ gives $n = 3.95$ and $\alpha = 5.30$.

TABLE 1–Mechanical properties of test material

Condition	0.2% Proof stress (MPa)	Ultimate tensile strenth (MPa)	Elogation to failure over 50 mm (%)	Reduction in area (%)
As-received	252	456	31.0	65.8

Three-point bend specimens (SE(B)), double-edge notched tension specimens (DE(T)), center-cracked tension specimens (M(T)), single-edge notched tension specimens (SE(T)) and compact tension specimens (C(T)) shown in Table 2 were machined from the steel plate. All specimens had the same thickness B = 23 mm. The specimen width W = 50 mm for SE(B), SE(T) and C(T) specimens and W = 25 mm for DE(T) and M(T) specimens. On each specimen a single notch or double notches were cut and then fatigue precracked such that the total length of notch plus precrack was a. SE(B) specimens with a/W = 0.5 (SE(B)5) and 0.1 (SE(B)1), DE(T) specimens with a/W

= 0.5 (DE(T)5) and 0.9 (DE(T)9), SE(T) specimens with a/W = 0.5 (SE(T)5) and C(T) specimens with a/W=0.6 (C(T)6) were prepared. Centre-cracked tension specimens with a/W = 0.5 (M(T)5) were made by putting together two precracked SE(T)5 specimens of W = 25 mm back to back and loaded with two bolts at the specimen ends.

CTOD tests of SE(B) and C(T) specimens were performed in an Instron 1195 testing machine. Tests on DE(T), SE(T) and M(T) specimens were carried out on a Shimadzu testing machine. A P-V plot was recorded on each SE(B), SE(T), DE(T) and C(T) specimen, where P was the applied load and V was the crack mouth opening displacement for SE(B), SE(T) and DE(T) specimens and the load-line displacement for C(T) specimens. The CTOD values were calculated from

$$\delta = \frac{K^2(1-\nu^2)}{2\sigma_y E} + \delta_p \tag{2}$$

where σ_y is yield strength, E Young's modulus, ν Poisson's ratio, K nominal stress-intensity factor and δ_p plastic component of δ. K-factors for the SE(B) and CT geometries were calculated from the formulae given in ASTM Test Method for Plane-Strain Fracture Toughness of Metallic Materials (E399). For the DE(T) geometry K-factor is given by [22]:

$$K = \frac{P}{2BW}\sqrt{\pi a}\left[1 + 0.122\cos^2(\pi a/2W)\right]\sqrt{\frac{2W}{\pi a}\tan\frac{\pi a}{2W}}, \tag{3}$$

for the SE(T) geometry this is obtained from [23]

$$\begin{aligned} K &= \frac{P}{BW}\sqrt{\pi a}[1.12 - 0.231a/W + 10.55(a/W)^2 \\ &\quad -21.72(a/W)^3 + 30.39(a/W)^4], \end{aligned} \tag{4}$$

and for the M(T) geometry this is calculated by [24]

$$K = \frac{P}{2BW}\sqrt{\pi a}\left[1 - 0.025(a/W)^2 + 0.06(a/W)^4\right]\sqrt{\sec\frac{\pi a}{2W}}. \tag{5}$$

The plastic component δ_p of the CTOD for all specimens was obtained by measuring the relative opening displacement between two microhardness indentations with an initial distance of 0.2 mm across the crack on both surfaces of the specimen and taking the average. The two indentations were located at 0.2 mm behind the crack tip(s). It was observed that these positions were closed to the intersections of the straight and deformed portions of the crack faces for the material and deformation level studied in this work. For the SE(B)5 and C(T)6 specimens the values of δ_p obtained by the indentation method were in good agreement with the values obtained according to ASTM Test Method for Crack-Tip Opening Displacement (CTOD) Fracture Toughness Measurement (E 1290) with the plastic rotation factor $r_p = 0.4$. The unloaded specimens were then broken open at liquid nitrogen temperature and the crack length

and crack extension were measured on the fracture surface by the nine-point average method given in the ASTM Standard E 1290. The CTOD at fracture initiation, δ_i, was obtained by the multiple-specimen R-curve method given by ASTM E1290. and was taken as the value corresponding to Δa=0.2 mm. For DE(T) and M(T) specimens each of the measurements of δ_p and Δa on two crack fronts was treated individually, hence each specimen gives two data points on the R-curve. J-integral values were also measured on each C(T)6 specimen according to ASTM Test Method for J_{Ic}, A Measure of Fracture Toughness (E 813).

The results of the δ_i measured on various specimens are given in Table 2. Fig. 1 shows the R-curves for the SE(B), SE(T) and CT specimens and Fig. 2 shows those for the DE(T) and M(T) specimens. The δ and J values measured on the same group of C(T) specimens are presented in Fig. 3.

It was found that fracture in all specimens was stable ductile tearing except one DE(T)9 specimen where fracture was initiated by stable ductile tearing and then transformed to cleavage fracture when crack growth reached about 0.3 mm.

3. MODEL OF VOID NUCLEATION AND GROWTH

According to the J-Q two-parameter theory, for a material obeying the Ramberg-Osgood relation (1) the stress fields within the forward sector of the crack tip are superposition of the HRR fields and a hydrostatic stress $Q\sigma_0$. Since the hydrostatic stress does not affect yielding of the material, the strain distribution in the forward sector is insensitive to the parameter Q. Therefore, the stress and strain directly ahead of the crack tip are

$$\sigma_{ij}(r) = \sigma_0 \left(\frac{J}{\alpha\epsilon_0\sigma_0 I_n r}\right)^{\frac{1}{n+1}} \tilde{\sigma}_{ij}(0,n) + Q\sigma_0\delta_{ij}, \tag{6}$$

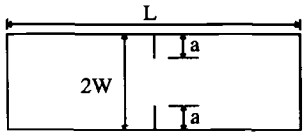
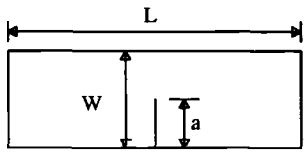
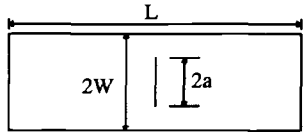
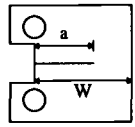
$$\epsilon_{ij}(r) = \alpha\epsilon_0 \left(\frac{J}{\alpha\epsilon_0\sigma_0 I_n r}\right)^{\frac{n}{n+1}} \tilde{\epsilon}_{ij}(0,n), \tag{7}$$

where I_n, $\tilde{\sigma}_{ij}$, $\tilde{\epsilon}_{ij}$ are HRR field constants [25], δ_{ij} is the Kronecker delta and r is distance from the crack tip.

Wu *et al.* [21] considered nucleation and growth of a void from a spherical inclusion of radius R_0 at a distance r_0 ahead of the crack tip. They assumed that debonding of the inclusion from the matrix is stress-controlled, i.e. debonding occurs and a void of initial radius R_0 is nucleated when the local maximum normal stress reaches a critical stress σ_c corresponding to a J-integral, J_N, which can be calculated from Eqn (6). After the void has nucleated, it grows in the J-Q fields of Eqns (6) and (7) following the Budiansky, Hutchison and Slutsky equation [26]

$$\frac{d\bar{R}}{\bar{R}} = 0.853 \left[\frac{3}{2n}\left(\frac{\sigma_m}{\sigma_e}\right) + \frac{(n-1)(n+0.4319)}{n^2}\right]^n d\epsilon_{22}, \tag{8}$$

TABLE 2--test results of various specimens.

Specimen Code	Specimen Type	Dimension (mm)	δ_i (mm) Test	δ_i (mm) Theory	Q
DE(T)9		W=25 L=300 a=22.5	0.23	0.33	- 0.40
DE(T)5		W=25 L=300 a=12.5	0.39	0.39	- 0.79
SE(T)5		W=50 L=300 a=25	0.41	0.32	- 0.49
SE(B)5		W=50 L=120 a=25	0.30	0.31	- 0.48
SE(B)1		W=50 L=120 a=5	0.38	0.39	- 0.90
M(T)5		W=25 L=300 a=12.5	0.46	0.49	- 1.14
C(T)6		W=50 a=30	0.28	0.28	- 0.28

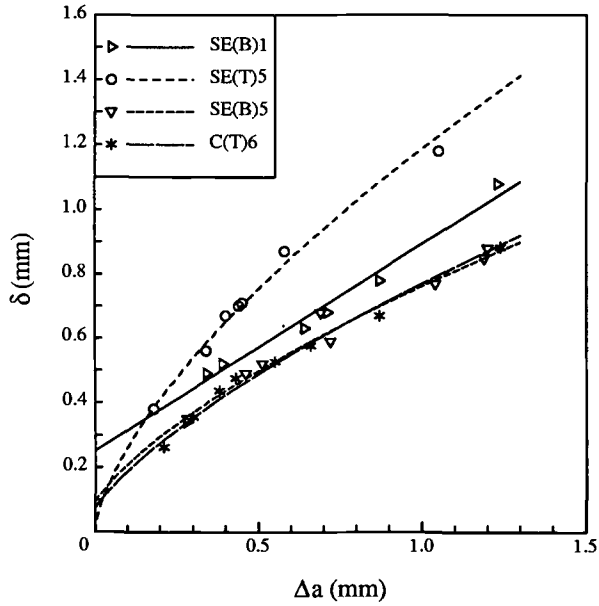


Figure 1: CTOD versus Δa curves for C(T)6, SE(T)5, SE(B)5 and SE(B)1 specimens.

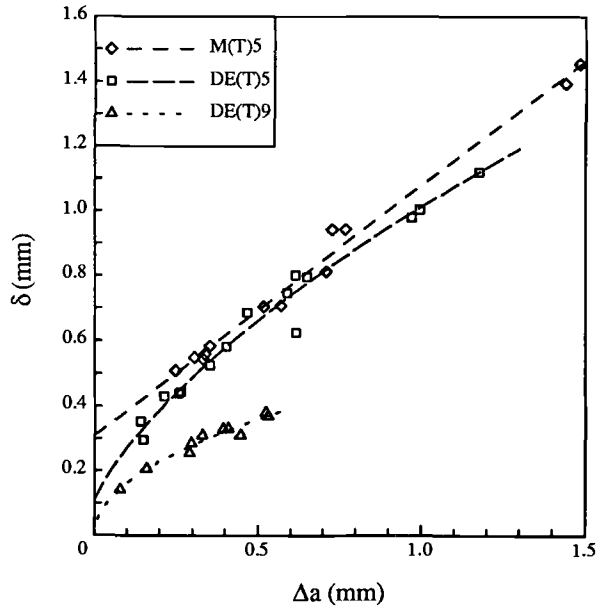


Figure 2: CTOD versus Δa curves for M(T)5, DE(T)5 and DE(T)9 specimens.

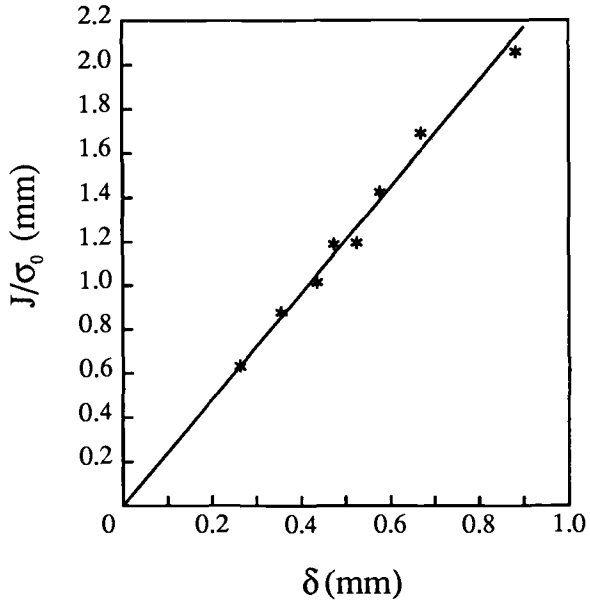


Figure 3: Relationship between CTOD and J-integral for C(T)6 specimen.

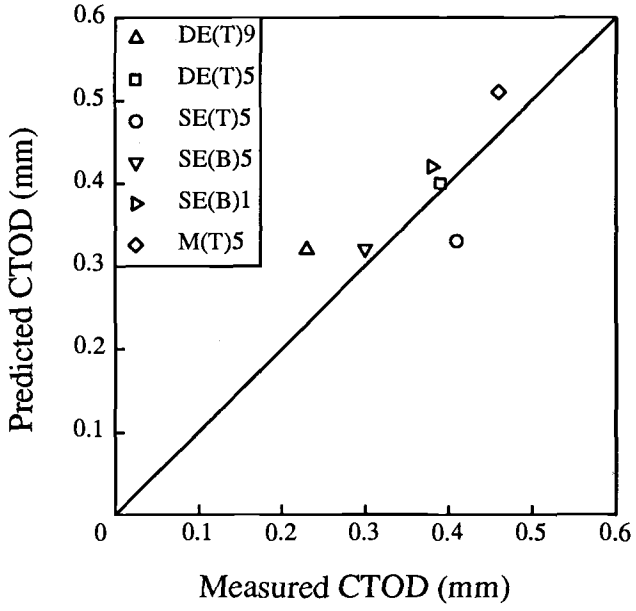


Figure 4: Comparison between theoretical prediction and experiment

where $\bar{R}$ is the average radius of the void, σ_m and σ_e are the hydrostatic and equivalent flow stresses respectively and ϵ_{22} is the tensile strain in the direction perpendicular to the crack line. Assuming that the void coalescence occurs at the same critical size R_c in different J-Q fields for the same material, Wu *et al.* obtained the following equation

$$\int_{J_{N2}}^{J_{i2}} \left[A\left(G + C\frac{Q_2}{J^{\frac{1}{n+1}}}\right) + B \right]^n \frac{dJ}{J^{\frac{1}{n+1}}} = \int_{J_{N1}}^{J_{i1}} \left[A\left(G + C\frac{Q_1}{J^{\frac{1}{n+1}}}\right) + B \right]^n \frac{dJ}{J^{\frac{1}{n+1}}} \tag{9}$$

where

$$A = \frac{3}{2n\tilde{\sigma}_e}, \tag{10}$$

$$B = \frac{(n-1)(n+0.4319)}{n^2}, \tag{11}$$

$$C = (\alpha\sigma_0\epsilon_0 I_n r_0)^{\frac{1}{n+1}}, \tag{12}$$

$$G = \tilde{\sigma}_{11} + \tilde{\sigma}_{22}, \tag{13}$$

and the constant $\tilde{\sigma}_e$ is given in [25], J_{N1} and J_{N2} are the J values corresponding to void nucleation in J-Q_1 and J-Q_2 fields, respectively, and can be calculated from Eqn (6), J_{i1} and J_{i2} are the ductile fracture initiation J-values for specimens J-Q_1 and J-Q_2, respectively. Equation (9) can predict the fracture toughness of ductile fracture initiation of a given material in different J-Q fields from one single measurement for a particular specimen. This model needs two new parameters σ_c and r_0. Usually in a tensile test of metals void nucleates after yielding but before necking of the specimen. Therefore it is expected that $\sigma_c \approx (1.5 - 3)\ \sigma_0$. r_0 is the average distance between the crack front and the centres of large voids and can be measured on the fracture surface with scanning electron microscopy. r_0 can also be interpreted as the mean spacing of big inclusions. An alternative interpretation of r_0 is 0.2 mm, i.e. the crack extension corresponding to the definition of fracture initiation in ASTM Standards E813 and E1290.

4. COMPARISON BETWEEN THEORY AND EXPERIMENT

A relationship between values of CTOD and J-integral is obtained from the results given in Fig. 3

$$J = 2.41\delta\sigma_0. \tag{14}$$

This relationship is used to convert the δ_i of C(T)6 specimen into J_i-values. The C(T)6 specimen is used as the master J-Q_1 field in the model equation (9). SEM observation on the fracture surfaces of specimens shows that the distances between the crack front and the centres of large voids are about 0.1 - 0.2 mm. The parameter r_0 is taken as 0.2 mm. With the Q-J relations given in [21] for a similar material and other parameters $\sigma_0 = 252$ MPa, $E = 206$ GPa, $n = 3.95$, $\alpha = 5.30$, $\sigma_c = 2\sigma_0$, J_i for other specimen geometries can be predicted from the model. The predicted J_i

values are then converted to δ_i values using (11). The predicted δ_i values are given in Table 2. The Q values corresponding to J_i are also given in the last column of Table 2. The predicted δ_i values are compared with the experimental values in Fig. 4. It can be seen that the model clearly indicates the variation of the toughness with the constraint, although the prediction for DE(T)9 specimen is overestimated and for SE(T)5 is underestimated. The underestimate for SE(T)5 may be caused by the elastic components of δ given by Eqn (2) for SE(T)5 specimens which were three times as large as for other specimens. The overestimation for DE(T)9 was also obtained in [21]. Experimental results and observation show that DE(T)9 has higher constraint than C(T)6, but the finite element analysis [21] gives the opposite result. Further work is needed here.

5. CONCLUSIONS

Experimental results of CTOD tests on different specimen geometries show that the initiation toughness of ductile fracture increases as the constraint decreases. The theoretical model of ductile fracture based on void nucleation and growth in the J-Q fields ahead of the crack tip predicts this trend and there is good agreement between theory and experiments. However, further experimental and theoretical work using this approach is needed.

ACKNOWLEDGEMENT

The authors wish to thank the Australian Research Council for the continuing support of this project.

REFERENCES

[1] Chipperfield, C. G., In *Proc. Specialists' Meeting on Elastic-Plastic Fracture Mechanics*, Vol. 2, paper 15, OECP Nuclear Energy Agency, Daresbury, 1978.

[2] Cotterell, B., Li, Q. F., Zhang D. Z. and Mai, Y.-W., *Engineering Fracture Mechanics*, **21**, 1985, 239.

[3] Wu, S. -X., *Advances in Fracture Research, ICF7*, Vol.1, 1989, 517.

[4] Hancock, J. W. and Cowling, M. J., *Metal Science*, **14**, 1980, 293.

[5] Kirk, M. T., Koppenhoefer K. C. and Shih, C.F., "Effect of Constraint on Specimen Dimensions Needed to Obtain Structurally Relevant Toughness Measures", in *Constraint Effects in Fracture, ASTM STP 1171*, E.M. Hackett, K. H. Schwalbe, and R. H. Dodds, Eds., American Society for Testing and Materials, Philadelphia, pp. 79-103, 1993.

[6] Wu, S.-X., Mai, Y.-W., Cotterell, B and Le, C.V., *Acta Metall. Mater.*, **39**, 1991, 2527.

[7] Wu, S.-X., Mai, Y.-W. and Cotterell, B., to appear in ASTM STP for the *US 24th National Symposium on Fracture Mechanics*, American Society for Testing and Materials, Philadelphia,1994.

[8] McClintock, F. A., *Fracture: An Advanced Treatise*, Vol.3, p.47, Liebowitz, H., Ed., Academic Press, New York, 1971.

[9] Hutchinson J. W., *Journal of Mechanics and Physics of Solids*, **16**, 1968, 13.

[10] Rice, J. R. and Rosengren, G. F., *Journal of Mechanics and Physics of Solids*, **16**, 1968, 1.

[11] Rice, J. R., *Journal of Mechanics and Physics of Solids*, **22**, 1974, 17.

[12] Bilby, B. A., Cardew, G. E., Goldthorpe M. R. and Howard I. C., In *Size Effects in Fracture*, The Institution of Mechanical Engineers, London, 1986, 37.

[13] Betegon C. and Hancock, J. W., *Journal of Mechanics and Physics of Solids*, **38**, 1991, 104.

[14] Al-Ani A. M. and Hancock, J. W., *Journal of Mechanics and Physics of Solids*, **39**, 1991, 23.

[15] O'Dowd, N. P. and Shih, C. F., *Journal of Mechanics and Physics of Solids*, **39**, 1991, 989.

[16] O'Dowd, N. P. and Shih, C. F., *Journal of Mechanics and Physics of Solids*, **40**, 1992, 939.

[17] O'Dowd, N. P. and Shih, C. F., to appear in ASTM STP for the *US 24th National Symposium on Fracture Mechanics*, American Society for Testing and Materials, Philadelphia,1994.

[18] O'Dowd, N. P., Shih, C. F. and Dodds, Jr., R. "The Role of Geometry and Crack Growth on Constraint and Implications for Ductile/Brittle Fracture," *Constraint Effects in Fracture: Theory and Applications, ASTM STP 1244,* M. Kirk and A. Bakker Eds., American Society for Testing and Materials, Philadelphia, 1994.

[19] McClintock, F. A., *Journal of Mechanics and Physics of Solids,* **35**, 1968, 363.

[20] Rice, J. R. and Tracey D. M. 1969 *Journal of Mechanics and Physics of Solids*, **17**, 1969, 201.

[21] Wu, S. -X., Mai, Y.-W. and Cotterell, B., "Prediction of the Initiation of Ductile Fracture", *Journal of Mechanics and Physics of Solids,* to be published.

[22] Benthem, J.P. and Koiter, W.T., in *Methods of Analysis and Solutions of Crack Problems, Mechanics of Fracture 1*, p. 157, Sih, G.C. Ed., Noordhoff Int. Pub., 1972.

[23] Brown, W.F. and Srawley, J.E., in *Plane Strain Crack Toughness of High Strength Metallic Materials, ASTM STP 410*, American Society for Testing and Materials, 1966, p.12.

[24] Tada, H., *Engineering Fracture Mechanics*, **3**, 345(1971).

[25] Symington, M., Shih, C. F. and Ortiz, M., Brown University Report MRG/DMR-8714665/1, 1988.

[26] Budiansky, B., Hutchinson, J.W. and Slutsky, S., in *Mechanics of Solids. The Rodney Hill 60th Anniversary Volume*, Pergamon Press, Oxford, 1982, p.13.

Tina L. Panontin[1] and Sheri D. Sheppard[2]

THE RELATIONSHIP BETWEEN CONSTRAINT AND DUCTILE FRACTURE INITIATION AS DEFINED BY MICROMECHANICAL ANALYSES

REFERENCE: Panontin, T. L., and Sheppard, S. D., **"The Relationship Between Constraint and Ductile Fracture Initiation as Defined by Micromechanical Analyses,"** Fracture Mechanics: 26th Volume, ASTM STP 1256, Walter G. Reuter, John H. Underwood, and James C. Newman, Jr., Eds., American Society for Testing and Materials, Philadelphia, 1995.

ABSTRACT: The overall objective of this study is to provide a proven methodology to allow the transfer of ductile fracture initiation properties measured in standard laboratory specimens to large, complex, flawed structures. A significant part of this work involved specifically addressing effects of constraint on transferability under large scale yielding conditions. The approach taken was to quantify constraint effects through micromechanical fracture models coupled with finite element generated crack tip stress-strain fields to identify the local condition corresponding to fracture initiation. Detailed finite element models predicted the influence of specimen geometry, loading mode, and material flow properties on the crack tip fields.

The ability of two local, ductile fracture models (the Rice and Tracey void growth model [1] (VGM) and the stress-modified, critical strain (SMCS) criterion of Mackenzie et al. and Hancock and Cowling [2,3]) to predict fracture initiation were investigated. Predictions were made using experimentally verified, two- and three-dimensional, finite strain, large deformation, finite element analyses. Two, high toughness pressure vessel steels were investigated: A516 Gr70, a ferritic, carbon-manganese mild steel demonstrating high hardening behavior, and HY-80, a martensitic, high strength low alloy (HSLA) steel possessing medium hardening ability. Experimental verification of the ductile fracture initiation predictions was performed in a variety of crack geometries possessing a range of a/w ratios from 0.15 to 0.70 and experiencing a range of load conditions from three point bending to nearly pure tension. The predicted constraint dependence of global ductile fracture parameters in the two materials is shown.

1. Group Leader, Materials and Failure Analysis Group, NASA Ames Research Center, Moffett Field, CA 94035
2. Associate Professor, Mechanical Engineering, Design Division, Stanford University, Stanford, CA 94305

Copyright © 1995 by ASTM International www.astm.org

KEYWORDS: ductile fracture initiation, toughness, constraint, micromechanics, void growth and coalescence, J-integral, CTOD

In October, 1994 a major, national aeronautical facility located at NASA-Ames Research Center, the Unitary Plan Wind Tunnel, was shut down for a duration of 2 years. During this period, the tunnel is undergoing extensive repair of the more than 10 miles of butt welds in its pressure shell. The shut-down comes after 30 years of operation and a failed attempt at recertification of the wind tunnel pressure shell's fitness-for-purpose using a fracture-mechanics-based life assessment. Fracture mechanics analyses could not assure an additional 30 years of life (less than 100,000 pressure cycles) even though the pressure vessel plate and welds were found to demonstrate ductile (upper shelf) fracture behavior in the operating temperature range and possess reasonably high toughness. As a consequence, every linear defect found from the 100% inspection of the welds in the facility must be completely repaired.

One reason for the failure of fracture mechanics to recertify the tunnel lies in the lack of a justified methodology to transfer material properties measured in standard laboratory specimens to large, complex, flawed structures. Specifically, the use of toughness measured in deep, through-cracked, bend fracture specimens to predict the behavior of shallow, part-through cracks in a structure loaded primarily in tension, in many cases, leads to uncertainties in assessments of fitness-for-purpose and remaining life. Such highly constrained specimen geometries generally provide conservative measurements of toughness, and as such do not produce accurate assessments for less constrained structures. The conservatism that is introduced may result in unnecessary and costly repairs, or in the removal from service of an important facility, with a corresponding loss of confidence in fracture mechanics analyses.

The effect of constraint can be eliminated as an explicit issue by testing actual structural configurations or by matching the constraint of a laboratory specimen to that of the structure; however, such an approach is not straightforward and can be prohibitively costly. The recognition that constraint influences the driving force for fracture rather than the material resistance to fracture (toughness) has led to the formalization of methodologies to quantify constraint effects through micromechanical fracture models coupled with finite element generated crack tip stress strain fields [3,4]. In these methodologies, micromechanical models identify the local conditions at fracture initiation using crack tip stresses and strains. Finite element analysis is used to predict the influence of specimen geometry, loading mode, and material flow properties on the crack tip fields. The value of the global parameter associated with satisfying the local conditions needed for fracture initiation is said to be the critical value specific to the particular geometry analyzed. Repeating this type of analysis for a variety of specimens allows for trends in the variation of the critical global parameter due to size, geometry, and loading to be defined. Constraint corrections can then be made to the critical global parameter obtained in toughness testing of standard laboratory specimens.

RESEARCH OBJECTIVES

The current study attempted to extend the use of existing methodologies for ductile fracture initiation [3,4] to large scale yielding conditions. More specifically, this investigation was undertaken to achieve the following objectives:

(1) to characterize the relative effectiveness of a local fracture criterion explicitly incorporating deformation history, such as the void growth model (VGM) based on the work of Rice and Tracey [1], versus that of a criterion considering only the instantaneous values of stress and strain, such as the stress-modified, critical strain (SMCS) criterion after the work of Mackenzie et al. [2] and Hancock and Cowling [3];

(2) to ascertain which global fracture parameter associated with fracture initiation (J-integral or CTOD) exhibits the most constraint dependence;

(3) to quantify the effect of strain hardening on the amount of constraint dependence demonstrated by the global fracture parameters associated with fracture initiation;

(4) to examine the ability of constraint parameters like the m-factor (equal to the ratio of J-integral/ (flow stress*CTOD)) and the triaxiality (equal to the ratio of mean stress, σ_m, to von Mises effective stress, σ_e) to describe the trend demonstrated by the global fracture parameters associated with ductile fracture initiation.

To achieve these objectives, ductile fracture initiation was predicted in thin fracture specimens possessing a range of crack depth to width (a/w) ratios and experiencing a range of load conditions, and in circumferentially cracked pipes of various sizes. The materials investigated were high toughness steels: A516 Gr70, a high-hardening, ferritic, C-Mn pressure vessel steel, and HY-80, a medium-hardening, martensitic HSLA steel.

This paper provides an overview of the work performed. The detailed approach taken, including the specimen geometries investigated, the test procedures used, the materials studied, and the finite element analysis procedures employed, is discussed first. Application of the micromechanical models for fracture initiation prediction is described next. This is followed by the calibration of the models to determine critical local parameters and the characteristic length for ductile fracture for each material. Predictions made using the calibrated models are presented next. Experimental verification is then provided. Finally, the constraint dependencies demonstrated by the predicted initiation values of J-integral and CTOD are shown as a function of the m-factor and the maximum triaxiality.

APPROACH

Two local fracture criteria corresponding to ductile fracture micromechanisms were evaluated: (1) a critical void ratio criterion for void growth based on the Rice and Tracey model [1], and (2) a stress-modified, critical strain criterion for void coalescence proposed by Mackenzie et al. [2] and Hancock and Cowling [3]. Initiation of ductile crack extension was assumed to occur when the critical value of the local fracture parameter

(void ratio or stress-modified strain) was reached over a critical length characteristic of the material microstructure. Critical values of the local fracture parameters were obtained by finite element analysis (FEA) coupled with experimental testing of circumferentially notched tensile specimens of varying constraint (i.e., notch radius) (Step A in Fig. 1). The characteristic length was similarly obtained using a fracture specimen (one with a cracked geometry) and verified through microstructural measurements (Step B in Fig. 1). These values of the critical local fracture parameter and characteristic length were then used to predict initiation in other geometries (Step C in Fig. 1). Large strain, large deformation, two- and three-dimensional finite element analyses were used to predict crack tip stress-strain distributions and the global fracture parameters associated with ductile fracture initiation. These predictions were verified experimentally; precracked fracture specimens were loaded to the predicted initiation load, unloaded, and then examined to measure the CTOD and corresponding amount of ductile crack growth (Step D).

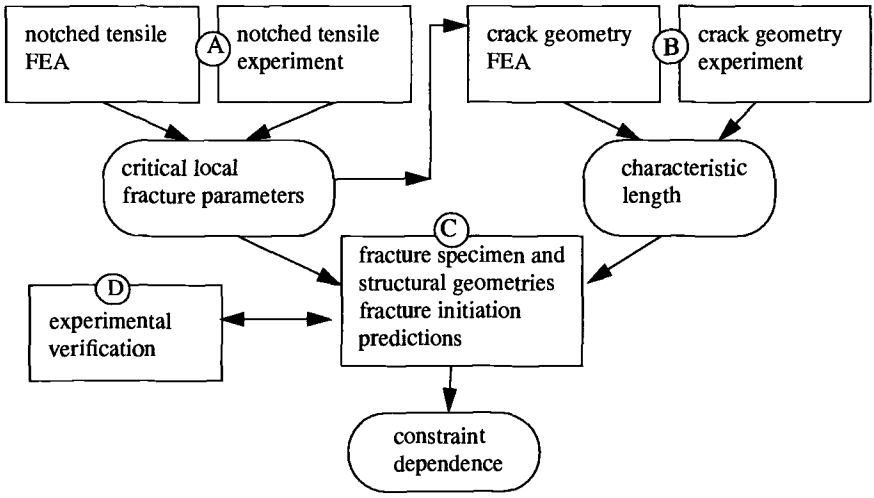


FIG. 1-- Schematic depiction of research approach.

Specimen Geometries

The specimen geometry used to measure engineering and true tensile properties was a standard round bar configuration, possessing a 2 inch (51 mm) gage length, 0.38 (9.6 mm) inch diameter gage section, and threaded ends. A 2 inch (51 mm) extensometer and a diametral gage were used to measure deformations. The specimens were wasted slightly to encourage necking at the diametral gage location. True stress-true strain properties were obtained from measurements of average stress (load divided by current area) and logarithmic strain (2*ln(initial/current diameter)) corrected for necking effects using the Bridgman approach [5].

Notched tensile specimens used to obtain critical values of the local fracture parameters (Step A) employed the same overall design as above, except that the gage section was circumferentially notched. As shown in Fig. 2, a constant minimum section diameter was maintained at 0.25 inch (6.4 mm) while the notch radius, r*, was varied from 0.06 to 0.13 inch (1.5 to 3.3 mm). These notch configurations were patterned after the work of Hancock and Mackenzie [6] to provide a range of triaxiality while still allowing for positioning of the diametral gage.

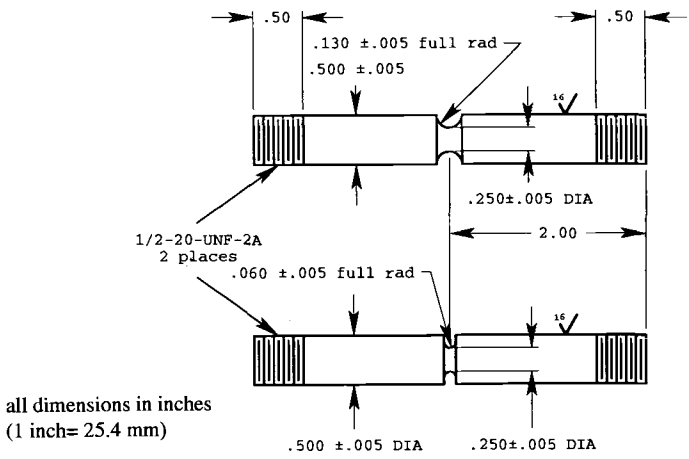


FIG. 2-- Notched tensile specimen geometries

Fracture initiation predictions (Step C) were made in both precracked fracture specimens of A516 Gr70 steel and of HY-80 steel. Fracture specimen geometries consisted of single edge crack tension (SECT) and single edge crack bending (SECB) specimens with varying a/w ratios, and a center crack panel (CCP) specimen. In addition, structural geometries were considered with the A516 Gr70 steel which consisted of circumferentially cracked pressure vessel/pipe of different sizes. Experimental verification was performed on all geometries except the center crack panel and large pressure vessel. The full test and analysis matrix for fracture initiation specimens is shown in Table 1.

The specific SECT specimens investigated were selected so as to allow for variation of the bending to tension loading in the uncracked ligament (it varies with crack depth [7]). Three a/w ratios, 0.15, 0.3, and 0.7, were studied. The specimens possessed a thickness, t, of 0.125 inch (3.3 mm) and a width, w, of 1.0 inch (25.4 mm). Fixed end conditions were imposed at a length of 2.0 inch (50.8 mm) using the grips shown in Fig. 3. Notches were made with a cutter or an EDM to have a 0.003 inch (0.076 mm) maximum radius at the tip for ease of precracking. The overall notch geometry conforms to that specified in ASTM Standard E813 [8]. Four tapped holes placed symmetrically about the notch were used to mount knife edges to hold the extensometer that provided load line displacements (see Fig. 3). A single strain gage was mounted mid-way through thickness on the side opposite the notch to provide longitudinal strain.

TABLE 1--Test and analysis matrix of fracture initiation specimens

		fracture specimen						structural	
		SECT w = 1.0 in (25.4 mm) t = 0.125 in (3.3 mm)			SECB w = 1.0 in (25.4 mm) t = 0.125 in (3.3 mm)		CCP w = 2.0 in (50.8 mm) t = 0.125 in (3.3 mm)	Pressure Vessel R_o = 20 in (508 mm) w =1.0 in (25.4 mm)	Pipe Specimen R_o= 2.5 in (63.5 mm) w =0.125 in (3.3 mm)
		a/w			a/w		a/w	a/w	a/w
Mat'l	**Exam**	0.15	0.30	0.70	0.30	0.70	0.70	0.30	0.30
A516	Analysis	√	√	√	√	√	√	√	√
	Exp.	√	√	√	√	√	...	...	√
HY-80	Analysis	...	...	√	...	√	...	...	...
	Exp.	...	...	√	...	√	...	...	...

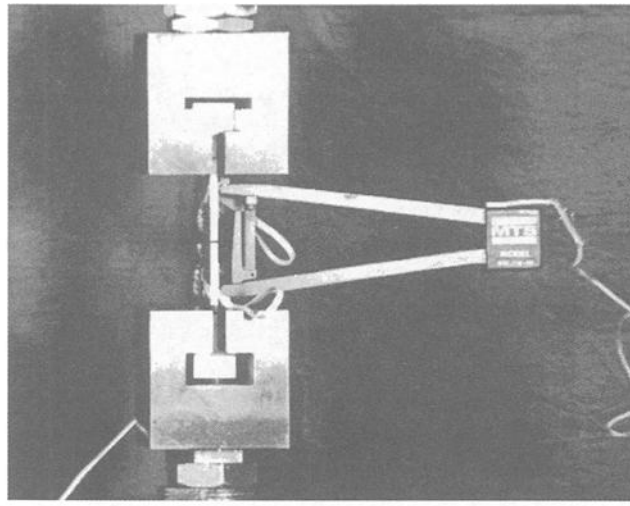


FIG. 3-- Experimental set-up for SECT specimen, showing fixed grip design and extensometer placement

The geometry of the single edge crack bending (SECB) specimens studied is essentially identical to that of the SECT specimens. Only a/w ratios of 0.3 and 0.7 were tested in this case, since the change in constraint arises solely from the change in crack depth in these specimens rather than from the combined effect of changes in loading and

crack depth. Notches were cut as described above. A three point bend loading fixture with a total span of 4.0 inches (101.6 mm) was used and a dial indicator mounted to the bend fixture provided load-line displacements. A single strain gage used to measure longitudinal, in-plane strain was placed approximately midway from the crack tip to the back edge of the specimen.

The center crack panel (CCP) analyzed was 2.0 inch (50.8 mm) wide, 0.125 inch (3.3 mm) thick, and had an a/w = 0.70. Its fracture behavior was not experimentally verified as its performance (as predicted by FEA) was essentially the same as the SECT specimen with the same a/w.

The two structural geometries were selected to investigate the applicability of the fracture criteria to more realistic crack configurations and geometries than those of standard fracture specimens. The configuration of the two geometries analyzed are the same -- an axially-loaded, 360 degree-circumferentially cracked, cylindrical pressure vessel, which idealizes the common case of a continuous lack of penetration defect in welded pressure systems. In addition, both geometries possess an R_o/w ratio of 20 and an a/w of 0.3. The actual dimensions of the two geometries are different. One geometry, a cracked, cylindrical pressure vessel (so-called pressure vessel geometry) with an outer radius, R_o, of 20 inch (508 mm) and a wall thickness, w, of 1.0 inch (25.4 mm), was analyzed so that the behavior of typical, large, welded structures could be compared to that of the fracture specimens. The other, a small, notched pipe (so-called pipe specimen geometry) with R_o=2.5 inch (63.5 mm) and w=0.125 inch (3.3 mm), was analyzed to provide predictions that could be experimentally verified.

As described above, the pipe specimen geometry is an 1/8 scale version of the pressure vessel (PV) geometry; however, the pipe was notched rather than cracked to eliminate the need for precracking prior to testing. The notch had a depth of 0.04 inch (1 mm) and a tip radius of 0.0025 inch (0.06 mm). Fixed end conditions at 2.0 inches (50.8 mm) above and below the notch were attained in the experiment by increasing the wall thickness to twice that in the notched section. Caps bolted to the specimen ends allowed the pipe specimen to be mounted in the test machine and axially loaded. Strain (longitudinal) gages placed symmetrically around the pipe on the front-face, 1.0 inch (25.4 mm) above the notch, and on the backface, straddling the notch, were used to assess the symmetry of the loading and to provide verification data.

Additional details regarding all specimen geometries and design are provided in [9].

Test Procedures

Tests were conducted on servo-hydraulic test machines with tensile load capacities ranging from 20 to 120 kip (89 to 534 kN). All tests for which the maximum load point was to be attained or surpassed, such as the tensile and notch tensile tests, were conducted remotely in stroke control. Verification tests on the fracture specimens were conducted manually in load control so that the predicted load for crack initiation could be accurately applied. In all cases, monotonic, quasi-static tests were conducted at crosshead speeds of approximately 10^{-4} inch/inch to avoid strain rate effects on material tensile properties [10].

Precracking of fracture specimens was conducted in load control at a constant ΔK in accordance with ASTM Standard E813 [8]. Cycling was controlled remotely by computer at frequencies from 4 to 10 hz and at $R = 0.1$. A minimum of 0.050 inch (1.3 mm) of fatigue (pre)crack growth was used.

Load, strain gage, and extensometer data were recorded continuously during quasi-static testing for verification of finite element predictions of the notched-tensile, precracked-fracture, and notched-pipe specimen behaviors. For verification of fracture initiation predictions, fracture specimens were loaded to the predicted initiation loads (and beyond), unloaded, and then examined (following grinding) to measure the CTOD and amount of stable tearing (Δa). Note that this procedure allows only the plastic component of the CTOD to be measured, which is large compared to the elastic component under the conditions considered. The 90° intercept definition of CTOD was used [11]. A minimum of four specimens was tested to obtain the CTOD-Δa curve for a particular (fracture) geometry. A CTOD-Δa curve was not obtained for the pipe specimens because of their notched geometry and the limited number of specimens tested; instead verification of ductile fracture initiation was made by examining the notch tip following loading and sectioning for evidence of void growth and coalescence.

Materials

The two steels selected for this study reflect those typically used in welded structures for which fracture assessments are made. A high toughness-to-strength ratio is an attribute common among the two materials investigated and both steels demonstrate ductile (i.e., upper shelf) fracture behavior at room temperature under all constraint levels studied. However, their hardening behaviors, microstructures, and hence, their response to constraint changes, are quite different. Reported below for each material are the certified material compositions and engineering properties, measured flow properties, published toughness properties, and results of measurements of microstructural features made to verify the (predicted) length-scale characteristic of ductile fracture. The detailed procedures for these measurements are contained in [9].

The first material investigated was a high hardening, ferritic, pressure vessel steel, A516 Gr70, typically used for welded vessels operating at moderate to low temperatures. The notched tensile and fracture specimens were machined from two 1 inch (25 mm) thick, normalized plates (plates #1 and #2 in Tables 2 and 3 and Fig. 4). Specimens were oriented in the LT and TL directions. The pipe specimens were machined from 5 inch (127 mm) thick, normalized plate (plate #3 in Tables 2 and 3). Compositions of the plates are given in Table 2 and the engineering properties in Table 3. The true stress-true strain properties as described above for the 1 inch (25 mm) thick plates are shown in Fig.4. Also shown is the fit to the data used in the finite element analyses (see discussion below). Note the difference between the yield strengths (17%) and flow stresses (~10%) of the two plates. Variability between heats of steel plate is to be expected and is treated in this investigation as a test of the robustness of the predictive techniques. A hardening coefficient of 4 was determined from a Ramberg-Osgood fit to the data. The plane strain fracture toughness, J_{IC}, of normalized A516 Gr70 has been reported to be ~ 750 lb/in (131 kN/m) [12].

TABLE 2--Compositions of A516 Gr70 and HY-80 plates (wt%)

plate	C	Mn	P	S	Si	Ni	Cr	Mo	Al	Cu
A516 plate #1	.20	1.06	.004	.009	.28	.08	.06	.02	.034	.23
A516 plate #2	.20	1.11	.009	.014	.24	...	...	...	.053	...
A516 plate #3	.23	1.05	.009	.009	.21	.20	.19	.06	.051	.267
HY-80	.13	.30	.006	.002	.26	2.19	1.17	.27	...	.13

TABLE 3--Engineering properties of A516 Gr70 and HY-80 plates

plate	yield strength, ksi (MPa)	ultimate strength, ksi (MPa)	elongation (2 in)
A516 plate #1	52.5 (362.1)	78.0 (537.9)	22%
A516 plate #2	44.5 (306.9)	81.0 (558.5)	25%
A516 plate #3	48.8 (336.5)	77.6 (535.2)	27%
HY-80	91.5 (631.0)	106.8 (736.6)	24%

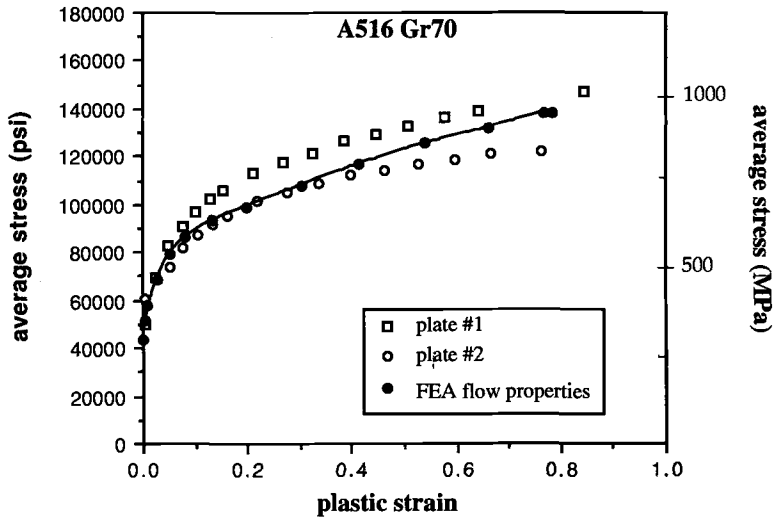


FIG. 4-- Flow properties for A516 Gr 70 steel

The microstructures of all the A516 Gr70 plates were quite similar, displaying the banded, ferritic-pearlitic structure typical of hot rolled plate. Inclusions were primarily manganese sulfide stringers, although small carbides were also present. The mean ferritic grain sizes of the plates ranged from 0.0013 to 0.0017 inch (0.033 to 0.043 mm) (ASTM grain size numbers 7 and 6, respectively).The spacing between large manganese sulfide inclusions averaged 0.0018 inch (0.046 mm) and the mean inclusion diameter was estimated to be 0.00014 inch (0.0035 mm). Dimple sizes measured on the fracture surfaces of failed notched tensile specimens (after the work of Schwalbe [13]) averaged 0.0015 inch (0.038 mm).

The second material investigated was HY-80, a weldable, higher strength steel. It was selected for its high toughness and moderate hardening properties, as well as for its tempered martensitic microstructure. All specimens were fabricated from a single plate, with the composition shown in Table 2. The plate was austenitized at 1800°F (30 minutes), water quenched, tempered at 1250°F (60 minutes), and water quenched to produce the engineering properties listed in Table 3 and the true stress-true strain properties depicted in Fig. 5. The Ramberg-Osgood hardening coefficient is approximately 8 for this material. The reported elastic-plastic, plane strain fracture toughness for HY-80 is approximately 1275 lb/in (223 kN/m) [14].

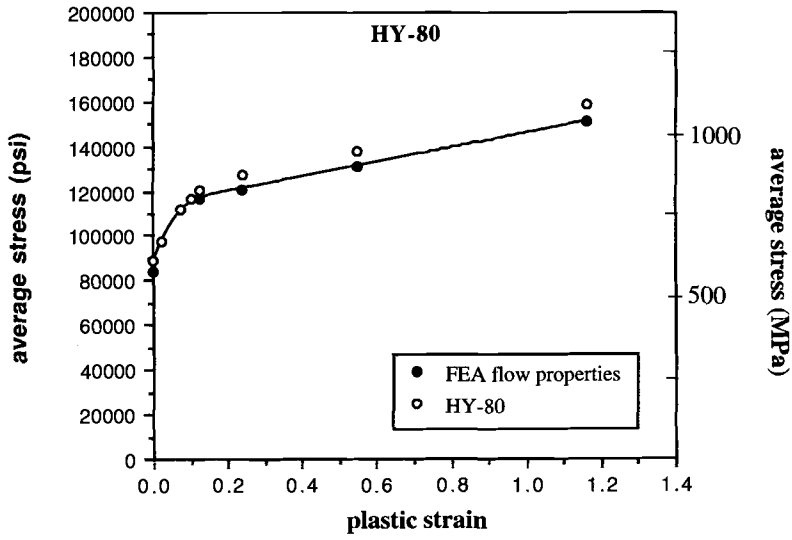


FIG. 5-- Flow properties for HY-80

The microstructure of the HY-80 plate was found to be tempered martensite with a mean prior austenitic grain size of 0.00085 inch (0.021 mm). The reported inclusion compositions were silicon oxides, aluminum carbides, and manganese sulfides (MnS) [6]. The

mean distance between MnS inclusions and mean (large) dimple size were approximately the same at 0.001 inch (0.025 mm), and the MnS inclusion diameter averaged 0.0002 inch (0.0051 mm).

Finite Element Analysis Procedures

All meshes for finite element models were generated using the PATRAN 2.7 modelling package [15]. Elastic-plastic finite element analyses were made utilizing ABAQUS 5.2 [16]. The finite element solutions employed nonlinear, large deformation material and geometry relations. Reduced integration (2x2 for 2-D, and 2x2x2 for 3-D) was used to eliminate artificial locking under incompressible deformation conditions. Incremental theory with a von Mises yield surface, associated flow rule, and isotropic hardening was used to model plasticity. Crack and/or void growth were not simulated in the analyses.

Details of the element mesh for each geometry analyzed are summarized in Table 4. All models which contained cracks possessed the same in-plane, crack tip element mesh. The element size at the crack tip was 0.0005 inch (0.013 mm). The crack tip was modelled with a finite radius of either 0.0005 inch (0.013 mm) or 0.001 inch (0.025 mm) depending on geometry, in anticipation of substantial crack tip blunting. For all geometries, ductile fracture initiation was predicted to occur after blunting of the crack tip exceeded 4.5 times its initial size, which ensured that the effect of the initial radius size on predicted crack tip deformation was small [17]. Four layers of elements were equally distributed through the half-thickness of the three dimensional models. This refinement was sufficient to define deformation on the midplane in all models; however, in the lowest constraint geometries (SECT, CCP with a/w=0.7) some accuracy was lost at the free surface. To insure that the location of fracture initiation was correctly predicted, models possessing six layers of varying thickness were also analyzed. In these more refined models, the layer at the surface is half as thick as that on the midplane to better capture the out-of-plane strain gradient.

TABLE 4--Finite Element Mesh Details

Specimen	Element Dimension	Element Type	Crack Tip Radius	Crack Tip Element Size
notched tensile	axisymmetric	8-noded	n/a	n/a
SECT, SECB, CCP	3-dimensional	20-noded	0.0005 in (0.013 mm) or 0.001in (0.025 mm)	0.0005 in (0.013 mm)
Pressure Vessel	axisymmetric	8-noded	0.001in (0.025 mm)	0.0005 in (0.013 mm)
Pipe	axisymmetric	8-noded	0.0025 in (0.064 mm)	0.00032 in (0.008 mm)

The nominal flow properties used for A516 Gr70 and HY-80, shown in Figs. 4 and 5, are piece-wise linear fits to the measured true stress, log strain curves for each material adjusted for necking effects by the Bridgman correction [5]. Additional, small adjustments (~5% of plastic modulus) were made to match the predicted behavior of one (small)

notched tensile specimen to its experimental behavior. These adjusted properties were then used for the analyses of the second (large) notched tensile geometry and all the fracture initiation geometries.

The J-integral in the crack geometries at each load step was calculated by the virtual crack extension method utilized by ABAQUS [16]. 2-dimensional values were calculated at each element layer through the thickness; layers containing mid-side nodes were ignored in the three dimensional models. A minimum of 25 contours on each layer were used to insure accuracy of the J-integral value obtained. The error between the 25^{th} and 26^{th} contour values was less than 1% in all models. The CTOD was obtained from displacements of nodes at the approximate 90 degree intercept from the crack tip nodes. Note that this procedure considers the current nodes at the 90° intercept. The m-factors (midplane and free surface) were obtained for each geometry from the slopes of J-integral vs. CTOD plots; the plots were linear for a significant portion of the loading in all cases.

The accuracy of the finite element predictions was studied extensively [18]. The effect of variation in flow properties in the notched tensile analyses were examined. Mesh refinement studies of the crack tip region, initial crack tip radius, and through-thickness element distribution in the crack analyses were performed to ensure convergence of the predicted crack tip deformation and associated stress-strain fields. In addition, numerous empirical measurements of load-displacement and load-strain behaviors, and deformed shape, were made for all geometries and compared to finite element predictions. An example comparison of finite element prediction to measured load-load line displacement and load-longitudinal strain for the A516 Gr70 SECT a/w-0.15 specimen is shown in Fig. 6. Although some differences exist, due primarily to differences in precrack length and end conditions, the agreement is generally good. Results for all the specimen geometries tested are reported in [9].

PREDICTION OF DUCTILE FRACTURE INITIATION USING MICROMECHANICAL MODELS

Predictions of ductile fracture initiation were made by examining the distribution of the local fracture parameter (as predicted by the finite element analysis) over a distance ahead of the crack tip as a function of load. The load at which ductile crack initiation occurs is said to be reached when the fracture parameter exceeds the critical value over the critical length. The location of crack initiation, whether on the midplane or free surface, at 0° or 45° from the crack plane, is predicted to be where the fracture parameter first satisfies the initiation criterion.

To obtain the distribution of the VGM parameter (so-called void ratio), the Rice and Tracey equation [1] for void growth (modified for strain hardening)

$$\int_{Ro}^{R} dR/R = 0.283 \int_{0}^{\varepsilon p} \exp(1.5*\sigma_m/\sigma_e) d\varepsilon_p \qquad \text{(EQ 1)}$$

is integrated over the deformation history to the current plastic strain at each point of interest ahead of the crack tip, where R/R_o= void ratio, σ_m/σ_e = triaxiality as defined previously, and ε_p is the von Mises equivalent plastic strain. The values R/R_o from this relation as a function of distance from the crack tip, r, are examined at various loads, P*i*. The fracture initiation load (P=P2 in Fig. 7) is defined as the (smallest) load at which R/Ro exceeds

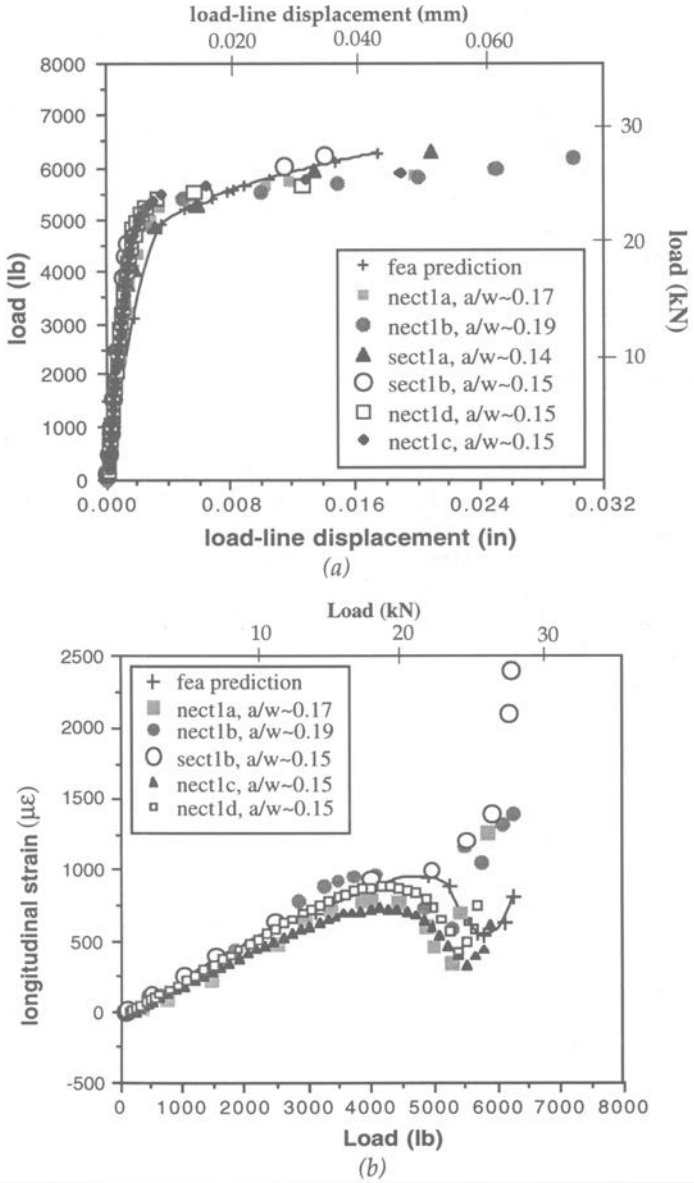


FIG. 6-- Verification measurements of (a) load load-line displacement and (b) load longitudinal strain made for A516 Gr70 SECT a/w =0.15 specimen

the material's critical value, R/R_0^*, over the material's characteristic length, l^*. A schematic of this approach is shown in Fig. 7 and it will be referred to as the VGM-R/R_0^* criterion.

Fracture initiation predictions using the second criterion, the SMCS criterion, can be made by examining the equivalent plastic strain, ε_p, and triaxiality, σ_m/σ_e, at each point of interest as a function of load. As shown in Fig. 8a, each material point ahead of the crack tip demonstrates a similar history of triaxiality and plastic strain as loading or deformation increases. Initiation is predicted to occur when the equivalent plastic strain within the characteristic length (0-to-l*) is equal to or greater than the critical equivalent plastic strain associated with the triaxiality levels at those points [3], or in other words:

$$\varepsilon_p(r) \geq \varepsilon_p)_{crit}(\sigma_m/\sigma_e(r)) \text{ for } r \leq l^*. \quad \text{(EQ 2)}$$

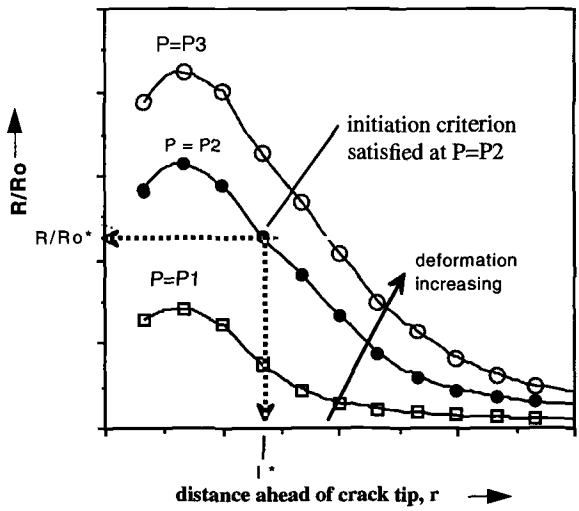


FIG. 7-- Fracture initiation prediction with the VGM /critical void ratio criterion.

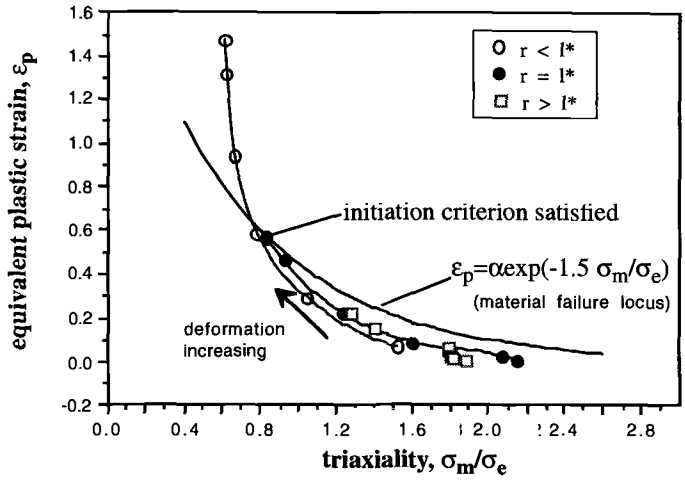
In the current study, the critical plastic fracture strain is assumed to be modeled by the relationship

$$\varepsilon_p)_{crit} = \alpha \exp(-1.5\, \sigma_m/\sigma_e(r)) \quad \text{(EQ 3)}$$

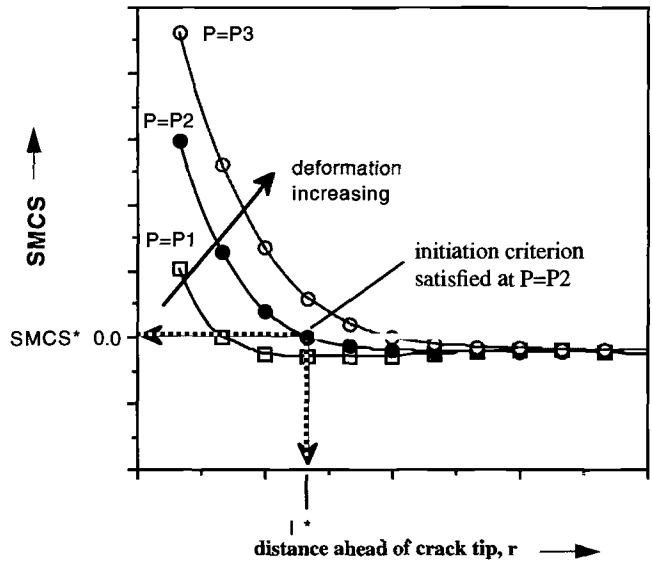
where α is a material constant fit to experimental data obtained from test and analysis of the notched tensile specimens after the work of Hancock and Mackenzie [6]. The SMCS criterion becomes cumbersome when written in this form because there are two variables (plastic strain and triaxiality) to monitor; a locus of failure conditions must be examined at every point ahead of the crack tip. Further, as shown in Fig.8a, both the distance ahead of the crack tip, r, and the load or deformation level, are implicit variables, i.e., suppressed in a plot of plastic strain vs. triaxiality. The fracture initiation prediction procedure can be simplified by rewriting the SMCS parameter as:

$$\text{SMCS} = \varepsilon_p(r) - \alpha \exp(-1.5\, \sigma_m/\sigma_e(r)) \quad \text{(EQ 4)}$$

where the subtracted form of EQ 2 is used and $\varepsilon_p)_{crit}$ has been replaced with EQ 3.



(a)



(b)

FIG. 8-- (a) Ductile fracture initiation locus superimposed on plastic strain and triaxiality history of points ahead of the crack tip
(b) Fracture initiation prediction using SMCS criterion.

Therefore, the criterion becomes

$$\begin{aligned} &\text{SMCS} \geq 0 \text{ between } 0 \leq r \leq l^*\text{: initiation} \\ &\text{SMCS} < 0 \text{ between } 0 \leq r \leq l^*\text{: no initiation} \end{aligned} \qquad \text{(EQ 5)}$$

The prediction of initiation can be made as shown in Fig. 8b, which is analogous to the procedure used with the VGM/critical void ratio criterion, where r is an explicit variable. (Note that in Fig. 8b, the points that do not satisfy the criterion (i.e., at $r > l^*$) all lie approximately the same distance from zero. This is because the trace of plastic strain and triaxiality of each point runs essentially parallel to the fracture initiation locus as shown in Fig. 8a.)

Once the fracture initiation loads were identified using these procedures, the global fracture parameters (e.g., J-integral and CTOD), the amount of ductile crack growth (i.e., the deformed distance corresponding to the characteristic length), and the maximum triaxiality associated with that load were obtained from the finite element analyses. (The m-factor was determined from FEA predictions of J-integral vs. CTOD as discussed above.) The variation of the global parameters with geometry (constraint) was then determined.

DETERMINATION OF CRITICAL LOCAL FRACTURE PARAMETERS

The critical values of the local fracture parameters (e.g., R/R_0^*, α) were determined from the testing and analysis of notched tensile specimens with varying notch severity (Step A in Fig. 1). Tests were conducted to identify the load or displacement corresponding to fracture initiation. Fracture initiation is defined to be the loss of load-carrying capacity, as purported by several investigators and studied in detail by Mackenzie et al. [2], and is indicated on experimental load-displacement curves by a sudden drop in load during testing. Finite element analysis of each notched tensile geometry was performed to calculate the values of the local fracture parameters at the load or displacement corresponding to fracture initiation.

A516 Gr70

The A516 Gr70 notched tensile specimens demonstrated cup-and-cone type fractures, indicating that fracture initiated in the center of the specimens. Sectioning of specimens following tests interrupted before reaching the fracture initiation load verified that voids initiated in the center of the specimen.

First consider determining R/R_0^* of the VGM-R/R_0^* criterion. Examination of the finite element predictions in the notched specimens of the void growth model (VGM) parameter, R/R_0, at the load corresponding to initiation confirms that the site of initiation is indeed the center of the specimen. The data for both specimens are shown in Fig. 9, in which R/R_0 is plotted against specimen radius at the notched section. The data show that the maximum void ratio occurs at the center of both specimens. Further, the gradient in void ratio near the center of the specimens is very shallow, illustrating why it is difficult to identify the length scale associated with ductile fracture in these specimens. The data also indicate that the critical void ratio for fracture initiation, R/R_0^*, in the small notched specimen is 1.75 and that for initiation in the large notched specimen is 1.84. These values are

consistent with those obtained by others in similar specimens and materials [19]. The two values are nearly the same and should be the same if the critical void ratio is a material property. An average value of 1.80 was used as the critical void ratio in the predictions of fracture initiation in the fracture specimen and pipe geometries.

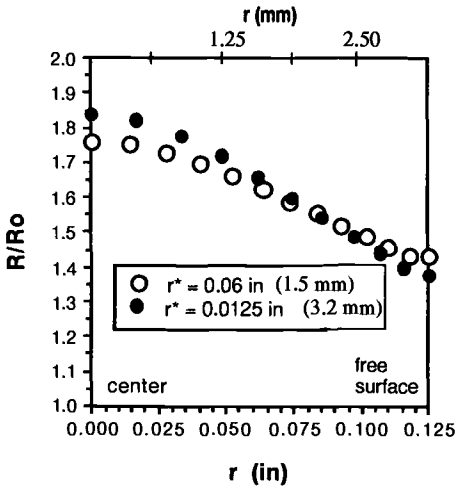


FIG. 9-- Void ratio distribution in A516 Gr70 notched tensile specimens at fracture initiation conditions.

The SMCS parameter is based on combinations of triaxiality (σ_m/σ_e) and equivalent plastic strain (ε_p) at fracture initiation.The combinations were predicted by the FEA at the notched specimen centers at fracture initiation and are shown in Fig.10. Also included in the plot are the data for smooth tensile specimens (the equivalent plastic strain and the triaxiality in the necked region were estimated from Bridgman [5], with the error associated with the triaxiality estimated from the errors obtained by comparison of Bridgman analysis to FEA predictions for notched tensile specimens). Note that the equivalent plastic strain at fracture initiation is strongly dependent on triaxiality. Following the work of Hancock and Mackenzie [6], the relationship in EQ 3 was fit to the points as shown, resulting in

$$\varepsilon_p)_{crit} = 1.995 \exp(-1.5*(\sigma_m/\sigma_e)). \qquad \text{(EQ 6)}$$

HY-80

Cup and cone fractures also occurred in the HY-80 notched tensile specimens. Tests interrupted just after attaining the fracture initiation load produced specimens with cracks in the center of the notched sections. The maximum void ratio is predicted to develop in the center of the notched section in both notched tensile geometries, with distributions of the void ratio similar to those in the A516 Gr70 specimens developing across the notched section in each HY-80 specimen.The critical value of the void ratio, R/R_o*, was found to be 3.12 in the large notched specimen and 2.23 in the small notched speci-

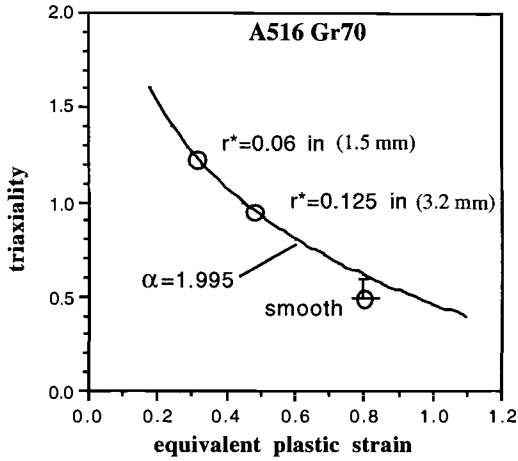


FIG. 10-- Triaxiality and plastic strain predicted at center of A516 Gr70 notched tensile specimens at fracture initiation conditions

men. Note that the difference between the two is quite large, which makes suspect the use of the critical void ratio as a material property. However, in order to proceed, an average of the two values was used as the critical void ratio for HY-80 (i.e., R/R_0*=2.67).

The peak triaxialities and the plastic strain magnitudes that are predicted to occur in the center of the HY-80 notched specimens are somewhat higher than those developed in same specimens made of A516 Gr70 steel. The plastic strain magnitudes at fracture initiation are again observed to be strongly dependent on triaxiality and compare well with data obtained for a similar steel by Mackenzie et al [2]. The stress-modified critical strain, SMCS, relationship for HY-80 was found to be

$$\varepsilon_p)_{crit} = 3.865 \exp(-1.5*(\sigma_m/\sigma_e)). \quad \text{(EQ 7)}$$

DETERMINATION OF CHARACTERISIC DISTANCE

The critical or characteristic distance can be defined from a first principles approach by utilizing physical material characteristics or from a phenomenological approach by adjusting values by trial and error until experimental fracture initiation data can be predicted. Attempts to use the former approach have met with mixed results because of the difficulties in determining appropriate inclusion populations and sizes; not all inclusions are important to the fracture event [20]. The latter approach also has some problems. In order to use it, specimens containing cracks must be tested and analyzed so that the plastic strain gradients are large enough for the critical length to be identifiable [21]. With this approach, the characteristic length becomes dependent on the resolution of the predicted stress-strain fields.

In this investigation, both the metallurgical characteristics of the materials and the phenomenological approach were utilized. Because mesh/modelling effects were minimized and a number of different crack geometries were modelled, the phenomenological approach is believed to be reliable. The critical distance was calibrated by matching the crack initiation load measured in a single fracture geometry (e.g., SECT a/w=0.7) to that predicted by the micromechanical models in the finite element analysis. This distance was then used to predict the fracture initiation loads for other geometries. The value of critical length was also investigated through metallurgical examination of the material and verified by post test microscopic examination of the crack tip region in all specimens. The results are discussed below.

A516 Gr70

The characteristic, critical length, l*, for ductile crack initiation in A516 Gr70 normalized steel was found phenomenologically to be 0.003 inch (0.076 mm) (undeformed length in the original mesh). This length is about 2 times the mean grain size and mean dimple diameter, and 1.67 times the mean void nucleating particle spacing. In the finite element models, there are at least 6 elements within the critical distance from the crack tip, which allows good resolution of the stress-strain fields. In the deformed state, this point in front of the crack tip moves to within 0.0011-0.0013 inch (0.028-0.033 mm) of the crack tip, depending on the geometry. Hence, the definition of ductile fracture initiation used in the current research corresponds to the finite amount of crack growth of 0.0011 to 0.0013 inch (0.028-0.033 mm).

HY-80

By matching the crack initiation load measured in the SECT a/w=0.70 specimen to the finite element predictions of initiation, the characteristic, critical length for HY-80 steel was found to be 0.002 inch (0.051 mm) (undeformed length in the original mesh). This length is about 2.35 times the prior austenitic grain size and 2 times the void nucleating particle spacing or dimple diameter. Within this length, there are four elements in the finite element models. The predicted amount of ductile crack growth corresponding to fracture initiation drops to 0.00015 - 0.00025 inch (0.0038 - 0.0063 mm) in the HY-80, a fifth of that defined for the same A516 Gr70 specimens.

DUCTILE FRACTURE INITIATION PREDICTIONS

Predictions of the load for which ductile crack initiation occurs in the fracture specimens were made using the SMCS and VGM-R/R_0* criteria, which are summarized in the headers of Tables 5 and 6. The distribution of the fracture parameter with distance from the crack tip is obtained from finite element analysis as a function of load; the load at which ductile crack initiation occurs is predicted when the fracture parameter exceeds the critical value over the critical length. In addition, location of crack initiation, whether on the midplane or free surface, at 0° or 45° from the crack plane, is predicted to be where the fracture parameter first satisfies the initiation criterion.

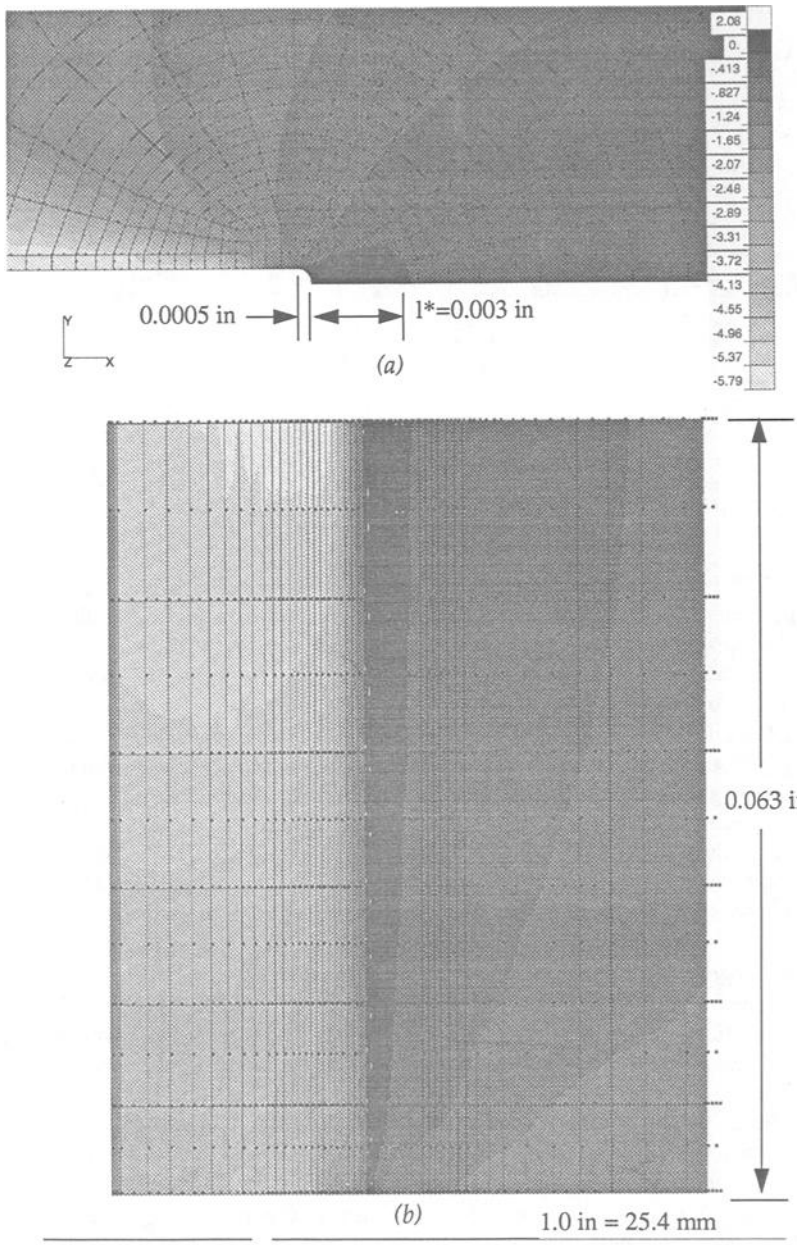


FIG. 11--Contour plots of SMCS criterion at fracture initiation in A516 Gr70 SECT a/w=0.70 specimen (a) on midplane (b) through thickness and (c) on free surface.

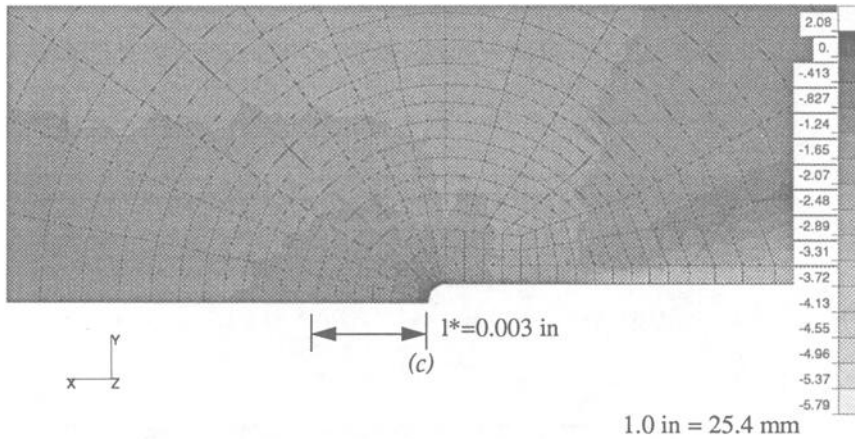
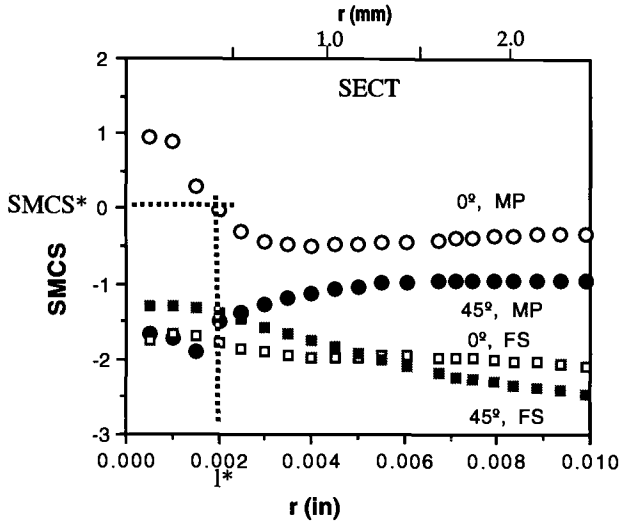


FIG. 11-- Continued. Contour plots of SMCS criterion at fracture initiation in A516 Gr70 SECT a/w=0.70 specimen (c) on free surface.

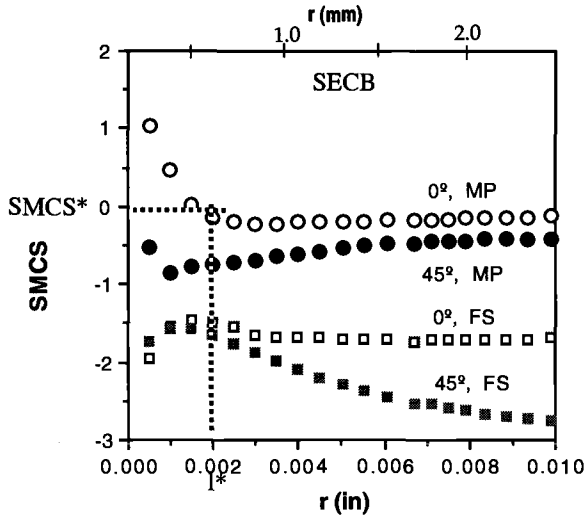
Examination of contour plots of the local fracture criteria indicate that the maximum damage (as described by micromechanical analysis) at a given load/ deformation level occurs on the midplane directly ahead of the crack tip (0° line) in all specimen geometries for both materials. Plots of the SMCS parameter at the deformation level corresponding to fracture initiation in the A516 Gr70 SECT a/w=0.7 specimen are shown in Figs.11a-c for the midplane, through thickness, and free surface.These plots show that damage occurs over a greater distance directly ahead of the crack tip on the midplane than at other angles, even though significant damage surrounds much of the crack tip. The damage is greater at the midplane than on the free surface with the characteristic "thumbnail" profile of ductile crack growth developing through the specimen thickness. Finally, on the free surface, damage appears to accumulate more rapidly an angle near 45°, indicating that shear lips would eventually develop in this specimen.

The same trends are predicted by the VGM-R/R_o* criterion. Further, these conclusions are generally representative of predictions in all other specimens except that shear lips at the free surface are not predicted in some specimens.This is shown quantitatively in Figs.12a and b for the HY-80 SECT and SECB a/w=0.7 specimens. Distributions of the SMCS parameter are shown as a function of distance, r, on the midplane (MP) and free surface (FS) at crack tip angles of 0° and 45°. As is evident from these plots, the SMCS criterion is satisfied first and solely on the midplane directly ahead of the crack tip in both specimens. On the free surface, the fracture criterion would be satisfied first at 45° in the SECT specimen, but at 0° in the SECB specimen.

Accordingly, fracture initiation predictions were made using midplane, 0° line data with the critical values obtained from the notched tensile specimens. The predicted initiation loads for the A516 Gr70 and HY-80 fracture specimen geometries using each criterion are shown in Tables 5 and 6, respectively, with the corresponding predicted midplane values of the J-integral and CTOD. Evident from data presented in Tables 5 and 6 is that the



(a)



(b)

FIG. 12-- Variation of SMCS parameter at fracture initiation on midplane (MP) and free surface (FS) for HY-80 (a)SECT and (b) SECB a/w=0.70 specimens.

VGM-R/R_0* criterion consistently predicts much lower initiation loads and values of J and CTOD than the SMCS criterion. Also evident is that the initiation values of the J-integral and CTOD predicted by either criterion are not constant for each material but vary with specimen geometry.

TABLE 5--Predicted critical global fracture initiation parameters: A516 Gr70
l*=0.003 in (0.076 mm), R/R_0*=1.80, $\varepsilon_{p)crit} = 1.995 \exp(-1.5*(\sigma_m/\sigma_e))$

specimen	Load, lb (kN)		CTOD, in (mm)		J, lb/in (kN/m)	
	SMCS	VGM-R/R_0*	SMCS	VGM-R/R_0*	SMCS	VGM-R/R_0*
SECT, a/w=.15	6516 (29)	5692 (25.3)	0.0056 (0.14)	0.0026 (0.07)	660 (115.5)	306 (53.5)
SECT, a/w=.30	5060 (22.5)	4661 (20.7)	0.0076 (0.19)	0.0046 (0.12)	804 (141)	479 (84)
SECT, a/w=.70	2544 (11.3)	2200 (9.8)	0.0071 (0.18)	0.003 (0.08)	726 (127)	317 (55.5)
SECB, a/w=.30	1094 (4.9)	928 (4.1)	0.0067 (0.17)	0.0022 (0.06)	722 (126)	246 (43)
SECB, a/w=.70	227 (1.0)	194 (0.86)	0.005 (0.13)	0.002 (0.05)	632 (111)	232 (41)
CCP, a/w=.70	5200 (23.1)	4736 (21.1)	0.007 (0.18)	0.0036 (0.09)	710 (124)	384 (67)
pressure vessel, a/w=.30	5.6E06 (25E03)	4.9E06 (21.8E03)	0.0059 (0.15)	0.0026 (0.07)	670 (117)	284 (50)
pipe specimen, a/w=.30	1.2E05 (534)	1.1E05 (489)	n/a	n/a	930 (163)	568 (99)

TABLE 6--Predicted critical global fracture initiation parameters: HY-80
l*=0.002 in (0.051 mm), R/R_0*=2.67, $\varepsilon_{p)crit} = 3.865 \exp(-1.5*(\sigma_m/\sigma_e))$

specimen	Load, lb (kN)		CTOD, in (mm)		J, lb/in (kN/m)	
	SMCS	VGM-R/R_0*	SMCS	VGM-R/R_0*	SMCS	VGM-R/R_0*
SECT, a/w=.70	3726 (16.6)	2946 (13.1)	0.0081 (0.21)	0.002 (0.05)	1033 (181)	320 (56)
SECB, a/w=.70	332 (1.5)	304 (1.3)	0.0056 (0.14)	0.0018 (0.046)	918 (161)	306 (54)

VERIFICATION OF FRACTURE INITIATION PREDICTIONS

A516 Gr70 and HY-80 Fracture Specimens

Experimental verification of the fracture initiation predictions was made for each fracture specimen type from R-curves measured in terms of CTOD vs. the amount of stable tearing (Δa) (see Test Procedures above). A straight line was fit to the measurements of midplane CTOD and Δa made on each specimen tested and the initiation CTOD was identified from the R-curves as the CTOD corresponding to the amount of crack growth equal to the deformed characteristic length, l^*, predicted by finite element analysis. For A516 Gr70, this amount of crack growth ranges from 0.0011 to 0.0013 inch (0.028-0.033 mm) depending on the specimen; for HY-80, from 0.00015 to 0.00025 inch (0.0038 - 0.0063 mm). Example R-curves for the A516 Gr70 and HY-80 SECT a/w=0.7 specimens are shown in Figs. 13 a and b. The data for all fracture specimens are reported in [9].

The experimentally determined initiation CTOD values are tabulated in Table 7 for A516-70 and Table 8 for HY-80 fracture specimens. Also listed are the predicted values using the SMCS and VGM-R/R_0* criteria. The SMCS criterion is shown to predict the experimental initiation CTOD within 17% for all A516 Gr70 specimens and within 20% for HY-80 specimens. The VGM/critical void ratio criterion clearly underpredicts the level of deformation required for initiation when the critical void ratios obtained from the notched tensile calibration are used.

Examination of the void ratio distributions at the known initiation loads indicate that much higher critical void ratios are reached at the crack tips in the fracture geometries (3.5 for A516 Gr70 and 10.3 for HY-80) than were achieved in the notched tensile specimen calibration.This suggests that the critical void ratio is not a material property -- that it may be dependent on the nature of the strain gradient in which the voids grow or highly affected by crack tip-void interaction. The problems associated with use of the VGM-R/R_0* criterion are discussed more fully in [9].

Fractographic evidence of ductile crack initiation was obtained for all specimens and is presented in [9]. An example is shown in Fig. 14 for the A516 Gr70 SECT a/w=0.15 specimen. In only two specimens out of 40 did more ductile crack growth occur on the free surface than on the midplane; these data were not used to determine the R-curves. Crack growth was seen to mostly occur directly ahead of the crack tip rather than angles inclined to the crack tip. Deviations from the 0° line that were observed are thought to be due to the statistical nature of the inclusion distribution rather than error in stress-strain predictions. Much of the crack tip (as shown above in the contour plots) exhibits a high level of damage, so that an inclusion close to the crack tip at a 30° inclination may fall within the damaged region to create a void.

A516-70 Pipe Specimens

Experimental verification of the fracture initiation predictions in the pipe specimens was made by examining the notch tip following loading to the predicted initiation load for evidence of void growth within the characteristic length (see Test Procedures above). After loading a pipe specimen to 90% of the predicted initiation load, unloading, and sectioning, void growth at the notch was observed. As shown in Fig.15, voids are

present within the deformed characteristic length and may have coalesced with the notch, although the coalescence is difficult to determine.The experimentally determined load for fracture initiation, then, was within 10% of the loads predicted by the SMCS and VGM--R/R_0* criteria listed in Table 5. Note that for this geometry the two criteria predict essentially the same initiation load; the notched tensile geometries appear to provide adequate calibration for the void ratio criterion for the (similarly) notched pipe specimen.

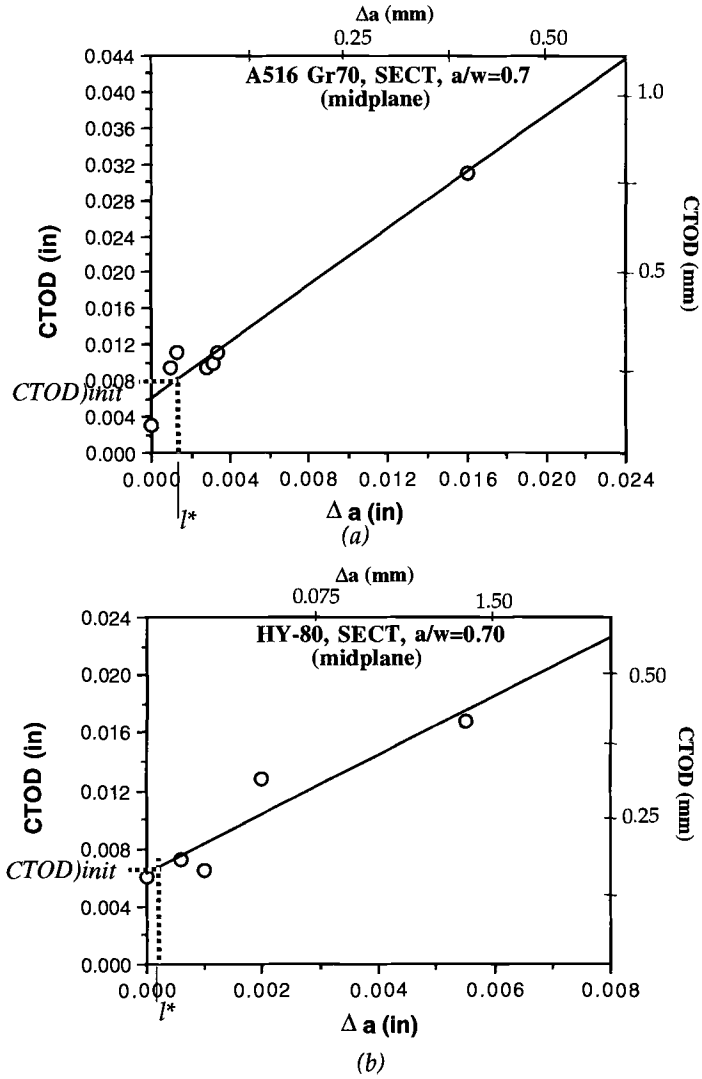


FIG. 13-- Measured R-curves for (a)A516 Gr70 and (b) HY-80 SECT a/w=0.70 specimens

TABLE 7--Predicted vs. Measured Initiation (midplane) CTOD, A516 Gr70

Specimen	measured CTOD, in (mm)	predicted CTOD, in (mm) SMCS	predicted CTOD, in (mm) VGM (R/Ro*=1.8)
SECT, a/w=.15	0.0055 (0.14)	0.0056 (0.14)	0.0026 (0.07)
SECT, a/w=.30	0.0069 (0.17)	0.0076 (0.19)	0.0046 (0.12)
SECT, a/w=.70	0.0078 (0.20)	0.0071 (0.18)	0.0030 (0.08)
SECB, a/w=.30	0.0065 (0.16)	0.0065 (0.16)	0.0022 (0.06)
SECB, a/w=.70	0.0055 (0.14)	0.0050 (0.13)	0.0020 (0.05)

TABLE 8--Predicted vs. Measured Initiation (midplane) CTOD, HY-80

Specimen	measured CTOD (in)	predicted CTOD (in) SMCS	predicted CTOD (in) VGM (R/Ro*=2.67)
SECT, a/w=.70	0.0067 (0.17)	0.0081 (0.21)	0.0020 (0.05)
SECB, a/w=.70	0.0062 (0.16)	0.0056 (0.14)	0.0018 (0.046)

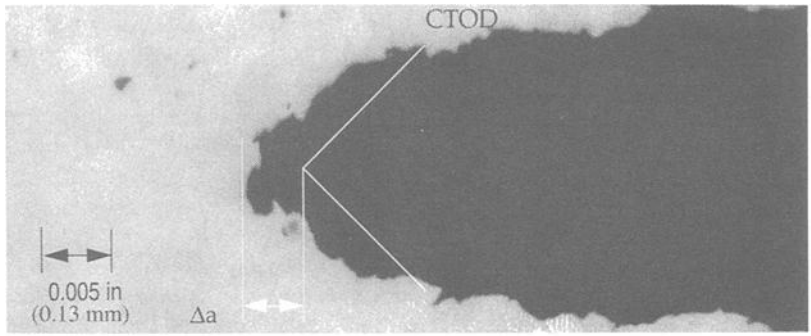


FIG. 14-- Fractograph of midplane of A516 Gr70 SECT a/w = 0.15 after testing to (beyond) fracture initiation load.

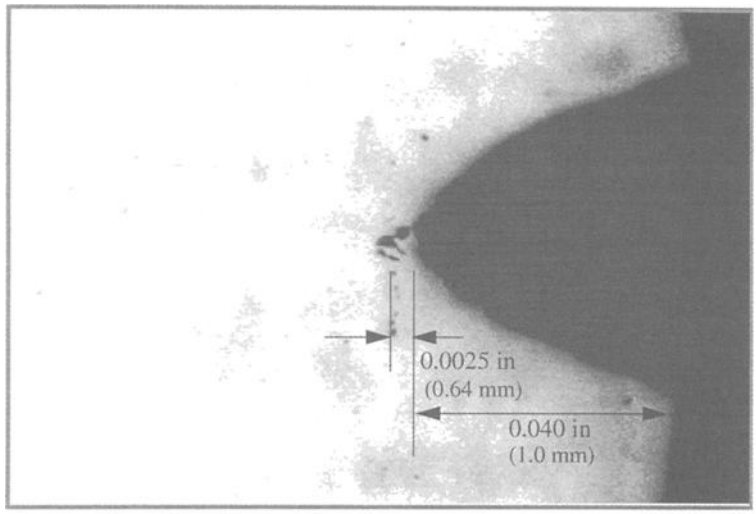


FIG. 15-- Fractographic evidence of void growth in pipe specimen loaded to 90% of the predicted initiation load.

PREDICTED CONSTRAINT DEPENDENCE

As discussed above, the J-integral and CTOD for ductile fracture initiation in the geometries analyzed were not constant for a given material, but varied with geometry. The range in these global parameters, when examined in relation to the constraint levels present in the geometries, indicate the constraint dependence of ductile fracture initiation in each material. Several parameters exist for indicating the level of triaxiality or constraint in a cracked configuration. A local parameter, the maximum triaxiality, and a global parameter, the m-factor were investigated in the current study. The use of the m-factor to represent the constraint of a cracked configuration is attractive because it is a global parameter that requires less computational resources to obtain than the local parameters. However, the m-factor can only rigorously be used on cracked geometries to the exclusion of notched configurations. Further, the m-factor is a constant value for a particular geometry, and does not change with increasing deformation as constraint levels do. This, in conjunction with the small range of m-factor values, makes the m-factor relatively insensitive to constraint changes [22]. In contrast, the maximum triaxiality parameter can represent constraint in notched as well as cracked geometries, and does vary with deformation level. It is a local parameter, however, describing constraint only at a specific point ahead of the crack and requiring highly refined finite element meshes for accurate prediction.

Unfortunately, neither parameter was found to provide a completely consistent representation of the constraint level in the fracture and structural configurations in the present study. Figs. 16 and 17 show the initiation CTOD values predicted by the SMCS criterion vs. the constraint parameters in all the geometries analyzed (including the pressure vessel and center cracked plate geometries which were not experimentally verified).

In Fig. 16 the maximum triaxiality parameter is shown to provide a reasonable representation of the trend in initiation CTOD with constraint. However, some scatter is demonstrated; the highest triaxiality (σ_m/σ_e=2.24) geometry (i.e., the pressure vessel) is seen to require a larger CTOD for initiation than a lower triaxiality (σ_m/σ_e=1.9) specimen. On the other hand, the m-factor, plotted in Fig.17, shows scatter in the lower constraint region where the largest CTOD is not observed to be associated with the lowest m-factor value.

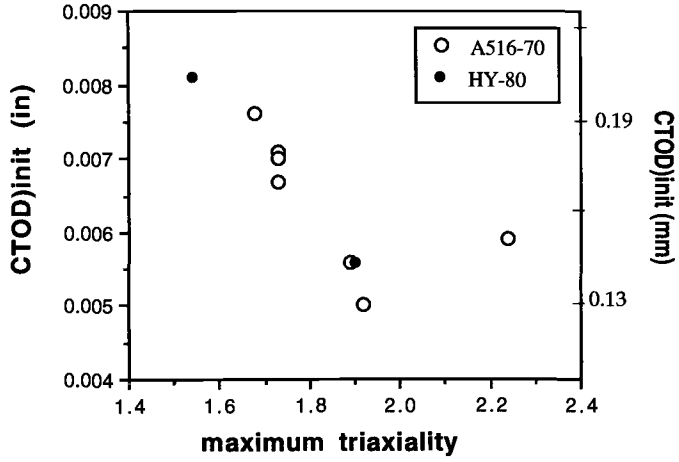


FIG. 16-- Predicted constraint dependence of CTOD as defined by the maximum triaxiality

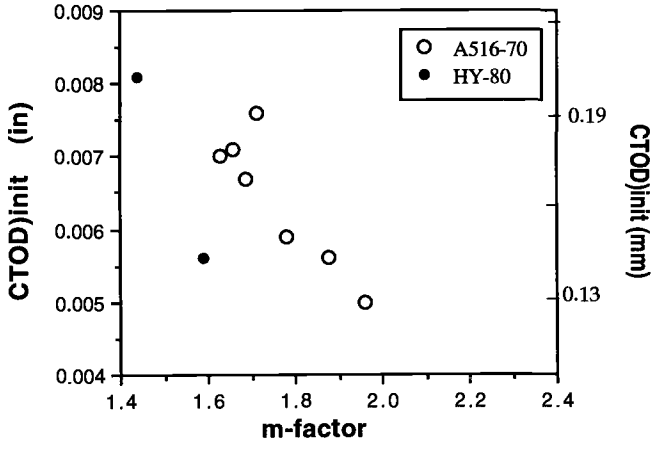


FIG. 17-- Predicted constraint dependence of CTOD as defined by the m-factor

The predicted constraint dependence of both materials is shown in Figs. 17 in terms of CTOD and in Fig. 18 in terms of J-integral. The global parameters shown were predicted by the SMCS criterion (the more accurate criterion) and the maximum triaxiality parameter is used to indicate the constraint level in each specimen geometry. The general trend demonstrated is an increase in the value of the critical global parameter with decreasing triaxiality; however, the J-integral demonstrates less constraint dependence than the CTOD. In the A516-70 steel, the critical J-integral values in the least constrained

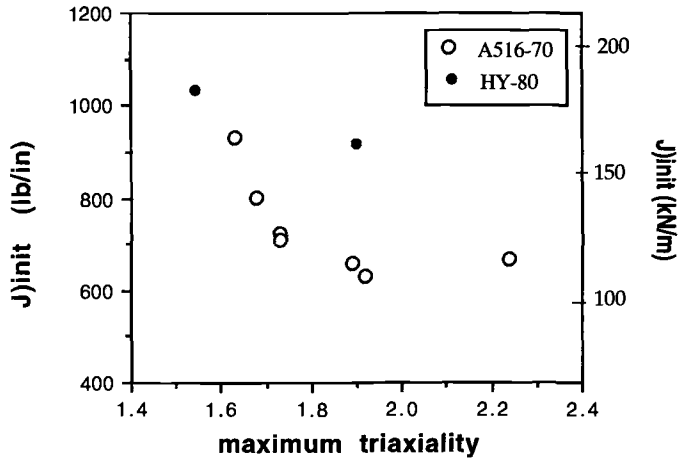


FIG. 18-- Predicted constraint dependence of J-integral as defined by the maximum triaxiality

geometries were 1.27 times higher than those demonstrated by the most constrained geometries. The change in CTOD over the same constraint range is 1.53. The magnitude of the constraint dependence of the CTOD and J-integral parameters is somewhat smaller than that observed in experimental results obtain by other researchers [23, 24]; however, the amount of ductile crack growth associated with initiation values is approximately 0.0012 inch in the current work, about half that used in these other studies. Constraint effects on global parameters tend to increase with ductile crack growth [23].

The variation observed to occur in the global parameters predicted in HY-80 specimens (12.5% in J, 44.5% in CTOD) were about the same as those occurring in the same A516-70 fracture specimens (15% in J, 42% in CTOD). This result is inconsistent with previous experimental studies (e.g., [4]) that have shown an increase in constraint dependence as strain hardening capability decreases. However, this reported increase is small (5%) over the range of strain hardening exponent studied [4]. Further, the amount of crack growth associated with initiation in the HY-80 steel is nearly an order of magnitude smaller than that in the A516-70; at an equivalent amount of crack growth, the variation predicted in the HY-80 specimens should be somewhat larger than those observed in the A516-70 specimens.

CONCLUSIONS

Key findings of the current study are described briefly below:

- A significant difference between the two local fracture models investigated is that the VGM explicitly accounts for deformation history while the SMCS criterion does not. The current study has shown for a range of loading conditions and material strain hardening capability that deformation history is not an important consideration for ductile fracture initiation.
- The SMCS criterion accurately predicts initiation in both steels using critical plastic strains measured in notched tensile specimens. In contrast, the VGM/critical void ratio criterion cannot be calibrated using notched tensile specimens; this leads to severe underpredictions of the deformation needed for fracture initiation in cracked specimens.
- The critical, characteristic length can be calibrated using a crack geometry. In the current study, the critical lengths for both steels were observed to be approximated by 2 times the dimple diameter (after the work of Schwalbe [13]) and by the square root of the hardening exponent times the grain size (after the work of Clayton and Knott [14]).
- The J-integral demonstrated less constraint dependence than the CTOD in both steels. The degree of constraint dependence is consistent with that shown in past experimental work.
- An increase in constraint dependence of the global parameters with declining strain hardening ability was not observed, due in part to the smaller amount of crack growth associated with the definition of initiation in the HY-80 than in the A516-70.
- Neither of the parameters investigated (e.g., maximum triaxiality nor m-factor) provided an entirely consistent representation of constraint. The best correlation between CTOD at initiation and the constraint level in the geometry was given by the maximum triaxiality parameter.

ACKNOWLEDGMENTS

This work was supported by NASA, Engineering and Quality Management Division (Code QW), under RTOP 323-11-03, "Life Prediction Methodology for High Toughness Metal Structures." CRAY computational resources were generously provided by Gwyn Faile at NASA Marshall Space Flight Center. The expertise provided by Dr. Robert Dodds and Dr. Walt Reuter is gratefully acknowledged. Thanks are also due to numerous others who were helpful in completing this work, including Mike Hill for data reduction, Dan Dittman and John Segreto for mechanical testing, Frank Pichay for strain gaging, and Jim Stein for metallographic specimen preparation.

REFERENCES

[1] Rice, J.R. and Tracey, D.M., "On the Ductile Enlargement of Voids in Triaxial Stress Fields." Journal of the Mechanics and Physics of Solids, Vol. 17, 1969, pp. 201-217.

[2] Mackenzie, A.C., Hancock, J.W., and Brown, D.K., "On the Influence of State of Stress on Ductile Failure Initiation in High Strength Steels," Engineering Fracture Mechanics, 1977, Vol. 9, pp. 167-188.

[3] Hancock, J.W. and Cowling, M.J., "Role of state of stress in crack-tip failure processes." Metal Science, Aug.-Sept., 1980, pp. 293-304.

[4] Anderson, T.L., Vanaparthy, N.M.R., and Dodds, R.H., Jr., "Predictions of Specimen Size Dependence on Fracture Toughness for Cleavage and Ductile Tearing," ASTM Symposium on Constraint Effects in Fracture, Indianapolis, 1991.

[5] Bridgman, P.W., Studies in Large Flow and Fracture, McGraw-Hill, New York, 1952.

[6] Hancock, J.W. and Mackenzie, A.C., "On the Mechanisms of Ductile Failure in High-Strength Steels Subjected to Multi-Axial Stress-States." Journal of the Mechanics and Physics of Solids, Vol. 24, 1976, pp. 147-169.

[7] Landes, J.D., McCabe, D.E., and Ernst, H.A., "Fracture Testing of Ductile Steels," EPRI Report NP-5014, Electric Power Research Institute, 1987

[8] ASTM Standard E813, "Test Method for Jic, A Measure of Fracture Toughness," ASTM, Philadelphia, 1989.

[9] Panontin, T.L., Ph.d. Dissertation, Stanford University, Stanford, CA, Aug.1994.

[10] Meyers, M.A. and Chawla, K.K., Mechanical Metallurgy: Principles and Applications, Prentice-Hall, New Jersey, 1984, p.569.

[11] Wilson, A.D., "The Fatigue and Toughness Properties of a C-Mn-Cb Plate Steel," Journal of Engineering Materials and Technology, Vol. 102, 1980, pp. 269-279.

[12] Shih, C.F., "Relationship Between the J-integral and the Crack Opening Displacement for Stationary and Extending Cracks." Journal of the Mechanics and Physics of Solids, Vol. 29, 1981, pp. 305-326.

[13] Schwalbe, K., "On the Influence of Microstructure on Crack Propagation Mechanisms and Fracture Toughness of Metallic Materials," Engineering Fracture Mechanics, 1977, Vol. 9, pp. 795-832.

[14] Clayton, J.Q., and Knott, J.F., "Observations of Fibrous Fracture Modes in a Prestrained Low-Alloy Steel," Metal Science, Feb., 1976, pp. 63-71.

[15] PATRAN, 1992, User's Manual, Version 2.5, PDA Engineering, Inc., Costa Mesa, CA.

[16] ABAQUS, 1993, User's Manual, Version 5.2, Hibbitt, Karlsson, and Sorenson, Inc., Providence, RI

[17] Moran, B., Ortiz, M., and Shih, C.F., "Finite Deformation Plasticity," International Journal for Numerical Methods in Engineering, Vol 29, 1990, pp. 483-514.

[18] Panontin, T.L. and Sheppard, S.D., "An Experimentally-Verified Finite Element Study of the Stress-Strain Response of Crack Geometries Experiencing Large Scale Yielding," manuscript under preparation for the 27th National Symposium on Fracture Mechanics, Williamsburg, VA, June, 1995.

[19] Mudry, F. "Methodology and Application of Local Criteria for the Prediction of Ductile Tearing," Elastic-Plastic Fracture Mechanics, L.H. Larsson, ed., Brussels, 1985, pp. 263-283.

[20] Ritchie, R.O. and Thompson, A.W., "On Macroscopic and Microscopic Analyses for Crack Initiation and Crack Growth Toughness in Ductile Alloys." Metallurgical Transactions, Vol. 16A, 1985, pp. 233-248.

[21] Norris, D.M., Jr., Reaugh, J.E., Moran, B, and Quinones, D.F., "A Plastic-Strain, Mean-Stress Criterion for Ductile Fracture." Journal of Engineering Materials and Technology, Vol. 100, 1978, pp. 279-286.

[22] Dodds, R.H., Jr., private communication

[23] Reuter, W.G., Graham, S.M., Lloyd, R.W., and Williamson, R.L., "Ability of Using Experimental Measurements of δ to Predict Crack Initiation for Structural Components," European Symposium on Fracture Mechanics: Elements of Defect Assessment, Freiburg, FRG 1989.

[24] Sorem, W.A., Rolfe, S.T., Dodds, R.H., Jr.,"The Effects of Crack Depth on Elastic-Plastic CTOD Fracture Toughness," Welding Research Council Bulletin 351, 1990, pp. 12-23.

Monir H. Sharobeam[1] and John D. Landes[2]

J-INTEGRAL FOR A SEMI-ELLIPTICAL SURFACE CRACK AT A BIMATERIAL INTERFACE

REFERENCE: Sharobeam, M. H., and Landes, J. D., **"J-Integral for a Semi-Elliptical Surface Crack at a Bimaterial Interface,"** Fracture Mechanics: 26th Volume, ASTM STP 1256, Walter G. Reuter, John H. Underwood, and James C. Newman, Jr., Eds., American Society for Testing and Materials, Philadelphia, 1995

ABSTRACT: Surface cracks are common defects in welded, bonded, and composite structures. The elastic-plastic fracture of these defects may be analyzed using the *J*-integral. The authors have recently developed a new approach to evaluate the *J*-integral for semi-elliptical surface cracks in panels made of homogeneous materials and subject to remote tension. This approach, which is based on load separation, allows the evaluation of *J* for such a three-dimensional geometry using a single specimen test record. It is analogous to the single specimen technique in two-dimensional geometries. In this article, the authors extend their study to surface cracks at bimaterial interfaces. A three-dimensional finite element model is developed to model such a crack. The *J*-integral is evaluated along the crack front using the virtual crack extension method. The elastic-plastic fracture behavior of the crack is studied. Load separation is also examined and the new single specimen approach for surface cracks in single material panels is extended to those at bimaterial interfaces. The study also includes a comparison between the results of surface cracks in single material panels and those at bimaterial interfaces.

KEYWORDS: interfacial cracks, surface cracks, *J*-integral, load separation, single specimen technique, ductile failure

Introduction

The study of the fracture behavior of cracks at the interface of dissimilar materials is essential for the assessment of the structural integrity and damage tolerance in welded, adhesive, and composite structures. The elastic solutions developed early by Williams [1] indicated that it is a mixed mode problem and is associated with oscillatory

[1] Assistant Professor, Richard Stockton College of New Jersey, Pomona, NJ 08240.

[2] Professor, University of Tennessee, Knoxville, TN 37996.

Copyright© 1995 by ASTM International www.astm.org

singularities at the crack tip. Since then, several investigators [2,3,4] also studied the problem and developed elastic solutions for the stress and strain fields around the crack tip. Related problems such as crack face wrinkling or contact [3,5] and crack kinking [6] also were addressed. The elastic stress intensity factors for the different modes involved were developed using complex analysis or numerical approaches such as finite element and boundary element methods. Several investigators agreed that using the J-integral [7] to evaluate the elastic stress intensity factors provides very reliable results even if a coarse mesh is used in the numerical approach.

Cases that include small scale yielding were recently addressed by Rice [10] and Shih and Asaro [11,12,13,14]. Shih and Asaro [13] discussed also the effects of large scale yielding using a geometry containing an infinite row of collinear cracks at the interface. In their studies, they considered the crack at the interface of an elastic-plastic material and a rigid or elastic substrate in a plane strain geometry. The elastic-plastic material was governed by Ramberg-Osgood Stress-strain relationship,

$$\frac{\epsilon}{\epsilon_y} = \frac{\sigma}{\sigma_y} + \alpha\left(\frac{\sigma}{\sigma_y}\right)^n \tag{1}$$

where σ and ϵ are the stress and strain, σ_y and ϵ_y are the yield stress and strain, α is a material constant and n is the strain hardening exponent. They pointed out that for an interfacial crack subject to remote tension, the crack opens up smoothly at its ends and the oscillatory singularities disappear at a very low level of remote stress. They noticed also that within the plastic zone of the crack tip, the stress fields change from a mixed mode pattern to mode I pattern as the distance from the crack tip increases, load increases, or the size of the plastic zone increases.

The geometries in the above studies were two-dimensional with semi-infinite cracks or center cracks. The studies were also mainly concerned with the stress and strain fields in the crack vicinity. In this paper, the elastic-plastic fracture behavior of a three-dimensional geometry will be studied. This geometry which is shown in Fig. 1, is a semi-elliptical surface crack at a bimaterial interface. The paper will focus on the behavior of the crack opening and the plastic J, J_{pl}. The study will also examine J_{pl} evaluation using a new single specimen form. This new form was recently developed by the authors [15] for surface cracks in single material panels. It is based on load separation which is a dominant criterion in two- and three- dimensional geometries [16,17,18]. In this paper this criterion will be examined and the basis for a single specimen J_{pl} form for an interfacial surface crack will be discussed. The paper will also present a comparison between the crack opening and J_{pl} behaviors for interfacial surface crack and equivalent cracks in single material panels.

The Finite Element Model

The symmetry of the interfacial surface crack allowed the consideration of one half of the geometry. The model contains 4563 nodes and 612 20-node hybrid brick elements. The crack vicinity is modeled by five concentric rings of focused elements. Each ring contains 72 elements; 6 elements along the crack front times 12 elements along the circumference of the ring and perpendicular to the plane of the crack. Figures 2a,b,c show the details of the model. The crack tip sides of the elements in the first ring were collapsed and the mid-side nodes in the first three rings were moved to the quarter point to capture both the plastic and elastic singularities. The bottom and top halves of the model are assigned different elastic-plastic materials. The behavior of these materials is characterized by the Ramberg-Osgood relationship given in Eq (1). A Fortran program was developed to generate the model and write it as an input file to the finite element code, "Abaqus". This Fortran program allows the change of all dimensions and materials involved in the model.

The model was verified by comparing its elastic J, J_{el}, results to Newman and Raju [19] solutions assuming same material for both top and bottom halves of the model. Figure 3 shows the stress intensity factor, K, developed by both the model and Newman-Raju solutions for surface cracks of different sizes at different locations (θ) along the crack front. The stress intensity factor is obtained from J_{el} using the relationship:

$$K = \sqrt{EJ_{el}/(1-\mu^2)} \qquad (2)$$

where E is the modulus of elasticity and μ is poissons' ratio. The model results agree well with Newman-Raju elastic solutions. The elastic-plastic behavior of the model was also verified by comparing its results with experimental test records of three different surface cracks. These experimental records were originally used by McCabe et al [20] in a study on J-evaluation for surface cracks. These cracks were blunt notched in Tungsten arc weld in 2219-T87 Aluminum panels. E and μ for both the weld and base metals are 69 GPa. (10000 ksi) and 0.3, respectively. σ_y, n, and α for the weld metal are 131 MPa. (19 ksi), 4.2, and 0.7, respectively. The material properties for the weld metal were used for both the top and bottom halves of the model. The model should represent the real specimen as long as the plasticity is contained in the weld region which is expected for moderate loading. Figure 4 shows the agreement between the generated load versus crack mouth opening displacement (CMOD) records and their equivalent experimental records. Moreover, we verified the results of this model by comparing its results to another model we developed early [15] to study J_{pl} evaluation for surface cracks in single material panels.

Although the mesh used in this study can be considered as a relatively coarse mesh, the required time for each elastic-plastic run was about 40-60 hours on a DEC3100 workstation. Using a more refined mesh could have been impractical for this study. However, a model with a fine mesh was prepared for one of the studied cases and the

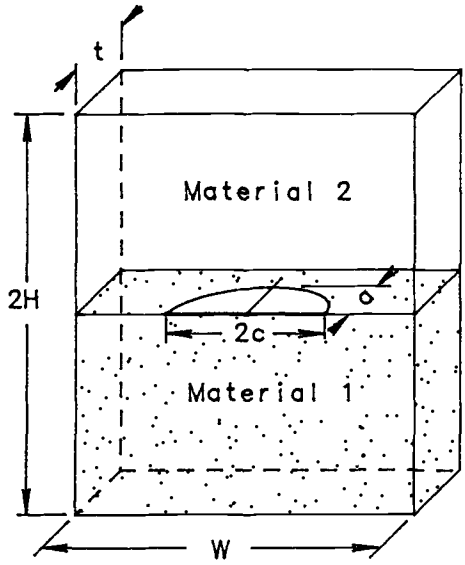


FIG. 1--Semi-elliptical Surface Crack on bimaterial interface.

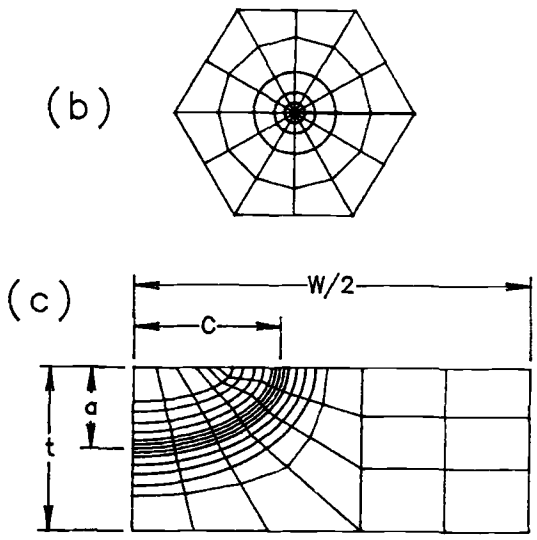


FIG. 2--The finite element Model; (a) an isometric view, (b) the crack fan details, and (c) sectional view at the crack plane.

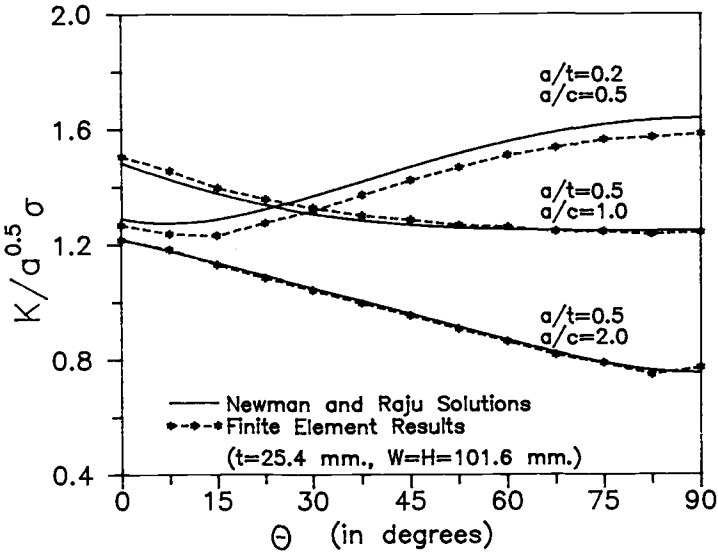


FIG. 3--A comparison between the model results and Newman-Raju solutions.

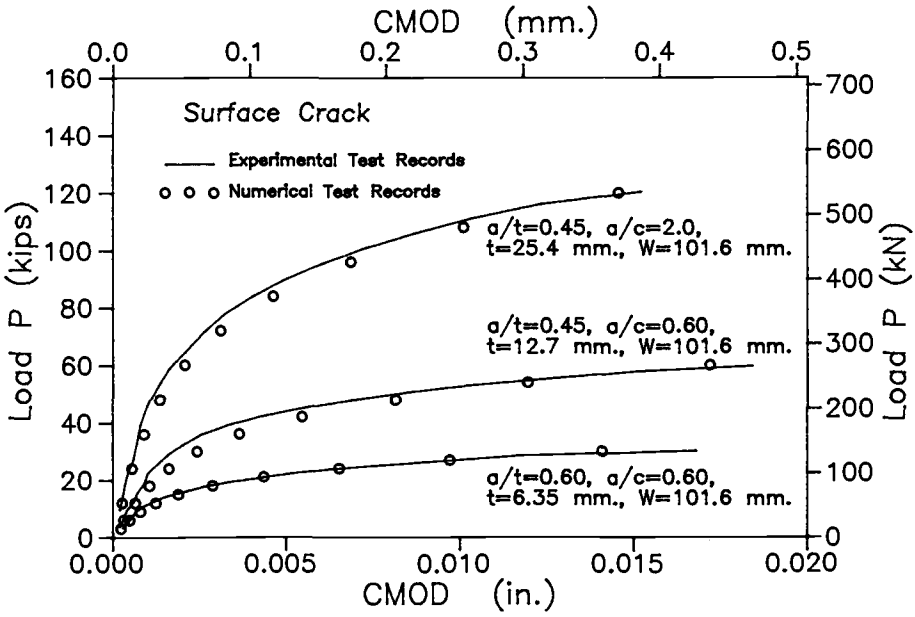


FIG. 4--A comparison between experimental test records and numerical test records developed by the model.

results of both models were compared. The model with the fine mesh contains 1260 elements; 1044 20-node brick elements and 216 15-node triangular prism elements. The crack vicinity in this model included 648 elements more than the model used in the study. Table 1 shows the J values at different locations of the crack front obtained by both models for an interfacial surface crack with $a/t = 0.6$ and $a/c = 1.5$. The top half of both models was assigned a material with a yield stress value of 1.5 times the yield stress of the bottom half material. Both materials are Ramberg-Osgood Materials with $n = 5.0$ and $\alpha = 1.0$. The angle θ is measured from the front surface of the specimen. The J values were estimated at a remote tensile stress of 1.5 times the yield stress of the model bottom half material, σ_{yl}. Table 2 shows the crack mouth opening displacement at different locations obtained by both models for the same geometry under the same applied load. x in this table represents the distance from the center of the crack mouth to any point at the crack mouth measured along the direction of the crack width c. Thus x/c is equal to 0.0 at the center of the crack mouth and 1.0 at the end of the crack. The agreement between the results of both models indicates that the model with the relatively coarse mesh can provide an accurate estimate of the crack tip parameter J and also the crack opening displacement even at locations very close to the crack tip ($x/c \approx 1.0$).

TABLE 1--The $[J/\sigma_{yl}\epsilon_{yl}t]$ values obtained by both models at different θ values.

θ	0.0°	15°	30°	45°	60°	75°	90°
Fine Mesh	7.20	11.95	10.48	8.80	7.52	6.53	6.15
Coarse Mesh	8.71	11.58	10.33	8.73	7.47	6.58	6.40

TABLE 2--The crack mouth opening displacement[1] at different x/c values.

x/c	0.00	0.38	0.63	0.82	0.93	0.97	0.993
Fine Mesh	0.0234	0.0227	0.0210	0.0181	0.0141	0.0108	0.0070
Coarse Mesh	0.0234	0.0226	0.0211	0.0182	0.0142	0.0110	0.0074

1 The displacement values are normalized by the thickness t.

In order to focus on the plasticity effects on the crack opening and J_{pl} behaviors, the materials for the top and bottom halves of the model were assumed to have the same poissons' ratio and modulus of elasticity. Other material properties such as the yield stress σ_y, the hardening exponent n, and the material constant α were assigned different

values for the two halves but one property at a time. The thickness of the model t is considered as 1/8 the width W and half the height H is taken equal to the width. A matrix of several bimaterial models (12 models) was selected. It provides different combinations of material properties for the top and bottom halves of the model and a reasonable range of crack depth to thickness ratios a/t and crack depth to crack width ratios a/c. Eight models additional were also developed using the single material model. Table 3 lists the different models used in the study. For most models, both elastic and elastic-plastic cases were considered. In the elastic runs, a fixed remote tensile stress σ was applied while in the elastic-plastic runs the remote tensile stress σ was augmented incrementally. The parameter J was evaluated using the virtual crack extension method built into the finite element code.

TABLE 3--The different bimaterial and single material models.

Bimaterial Models			Single Material Models	
Case	Material	a/t, a/c	Material	a/t, a/c
Vary n only	n (bot.) = 5.0 n (top) = 10.0 σ_y/E = 0.002 α = 1.0	0.5, 1.0	σ_y/E=0.002, n=5, α=1	0.5, 1.0
		0.5, 1.5	σ_y/E=0.003, n=5, α=1	0.5, 1.0
		0.4, 0.5	σ_y/E=0.002, n=10, α=1	0.5, 1.0
		0.8, 2.0	σ_y/E =0.002, n=5, α=2	0.5, 1.0
Vary σ_y only	σ_y/E (bot.)=0.002 σ_y/E (top)=0.003 n = 5.0 α = 1.0	0.5, 1.0	σ_y/E=0.002, n=5, α=1	0.5, 1.5
		0.6, 1.5	σ_y/E=0.002, n=5, α=1	0.6, 1.5
		0.4, 0.5	σ_y/E=0.002, n=5, α=1	0.4, 0.5
		0.8, 2.0	σ_y/E=0.002, n=5, α=1	0.8, 2.0
Vary α only	α (bot.) = 1.0 α (top) = 2.0 σ_y/E = 0.002 n = 5.0	0.5, 1.0		
		0.6, 1.5		
		0.4, 0.5		
		0.8, 2.0		

The Elastic-Plastic Behavior of the Crack

1 - The Crack Opening

Based on our material selection which avoids any elastic mismatch, we did not expect any crack face contact or wrinkling which is usually associated with the oscillatory singularities in the elastic analysis. Even with elastic mismatch, Shih and Asaro [11,12] indicated that the crack opens up smoothly in small scale yielding cases in two-dimensional tensile geometries. However, we decided to examine the crack face behavior at the front face of the panel and near the crack tip since this is a three-dimensional geometry and may behave differently. Figures 5a,b,c show the shape of the crack opening at the front face of the panels at different levels of loading for three different combinations of materials. x and y here represent the horizontal and vertical coordinates of each point of the crack mouth after deformation. Figures 6a,b,c show the crack opening very close to the crack tip ($r/t = 0.014$) for the same panels. r and θ in these figures represent the distance from the crack tip and the angular location measured from the front face of the panel. v is the displacement of any point at the crack face in the loading direction. From these figures, it is clear that the crack opens up and its faces are smoothly displaced in the loading direction.

We also generated the behavior of similar configurations but in single material panels using both materials used in each of the bimaterial models. Figures 7a,b,c show the shape of the crack at the front face of the panel for the different bimaterial models and their equivalent single material models at a loading level well in the post yield range. The overall trend in the shape of the crack opening is the same in all cases which may imply that mode I is dominant in the case of the interfacial crack. It is clear from the figures, also, that the crack face in the more deformable material half of the bimaterial panel shows much less displacement than if it is in a single material panel while that in the less deformable material half shows slightly more displacement than if it is in a single material panel. This was typical in all of the studied cases.

2 - *J*-Integral

The J-integral for surface cracks is a domain integral with two components: a remote contour integral and an integral over the area bounded by the contour [21]. It is evaluated in this study using the virtual crack extension method built into the Abaqus Code [22]. The main feature of J-integral, since it was first introduced by Rice [23], has been its path-independence which also characterizes all of its equivalent contour or domain integrals. For interfacial cracks in two-dimensional geometries, J was found to be path-independent [7,9] within the elastic region. This still needs to be verified in three-dimensional geometries and particularly in the plastic region.

In this study, J is evaluated over four hexagonal contours around the crack front. These contours were selected on the outside boundaries of the first four rings of elements

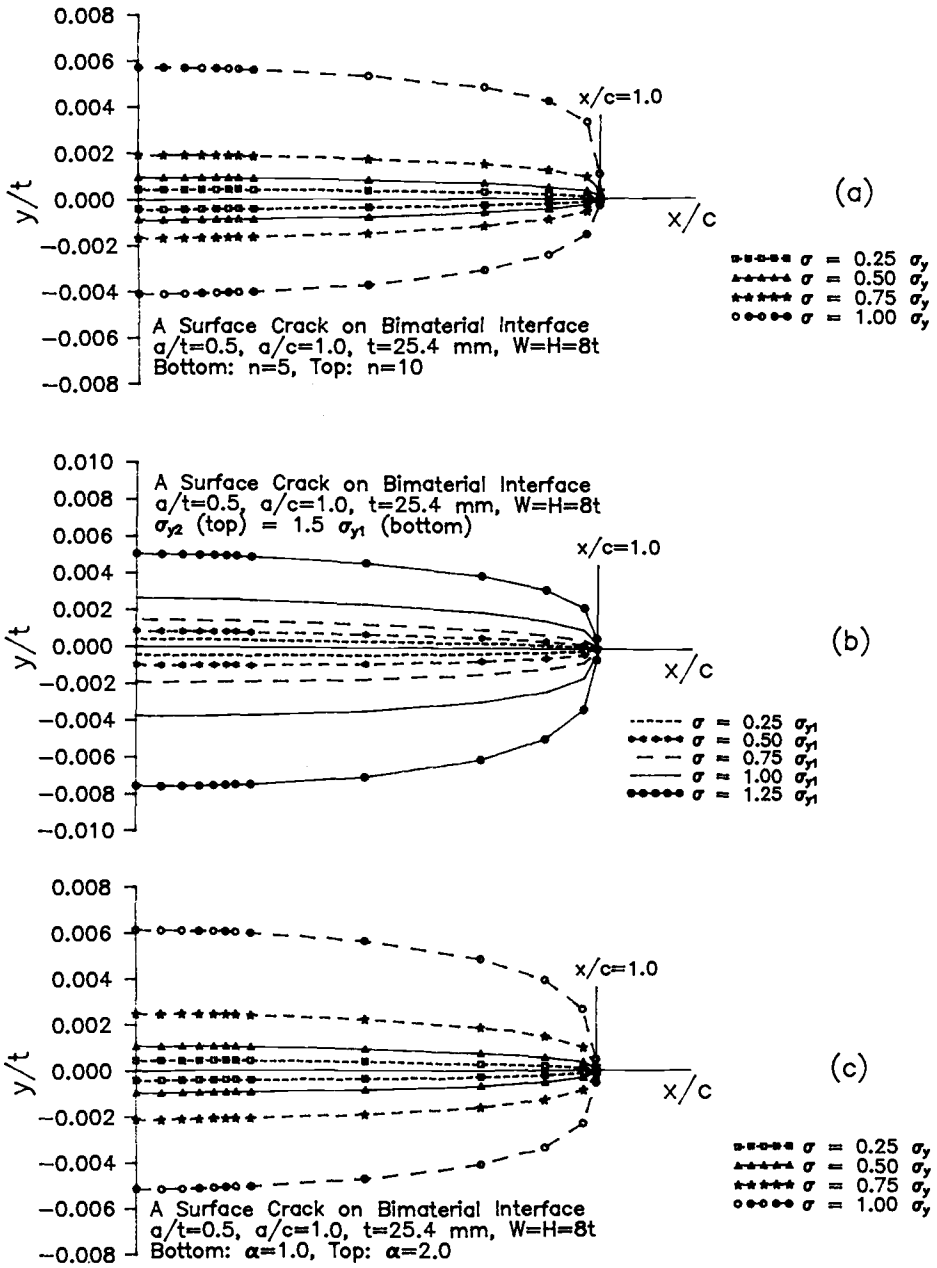


FIG. 5--The crack mouth opening at different load levels for the different bimaterial cases; (a) different n values, (b) different σ_y values, and (c) different α values.

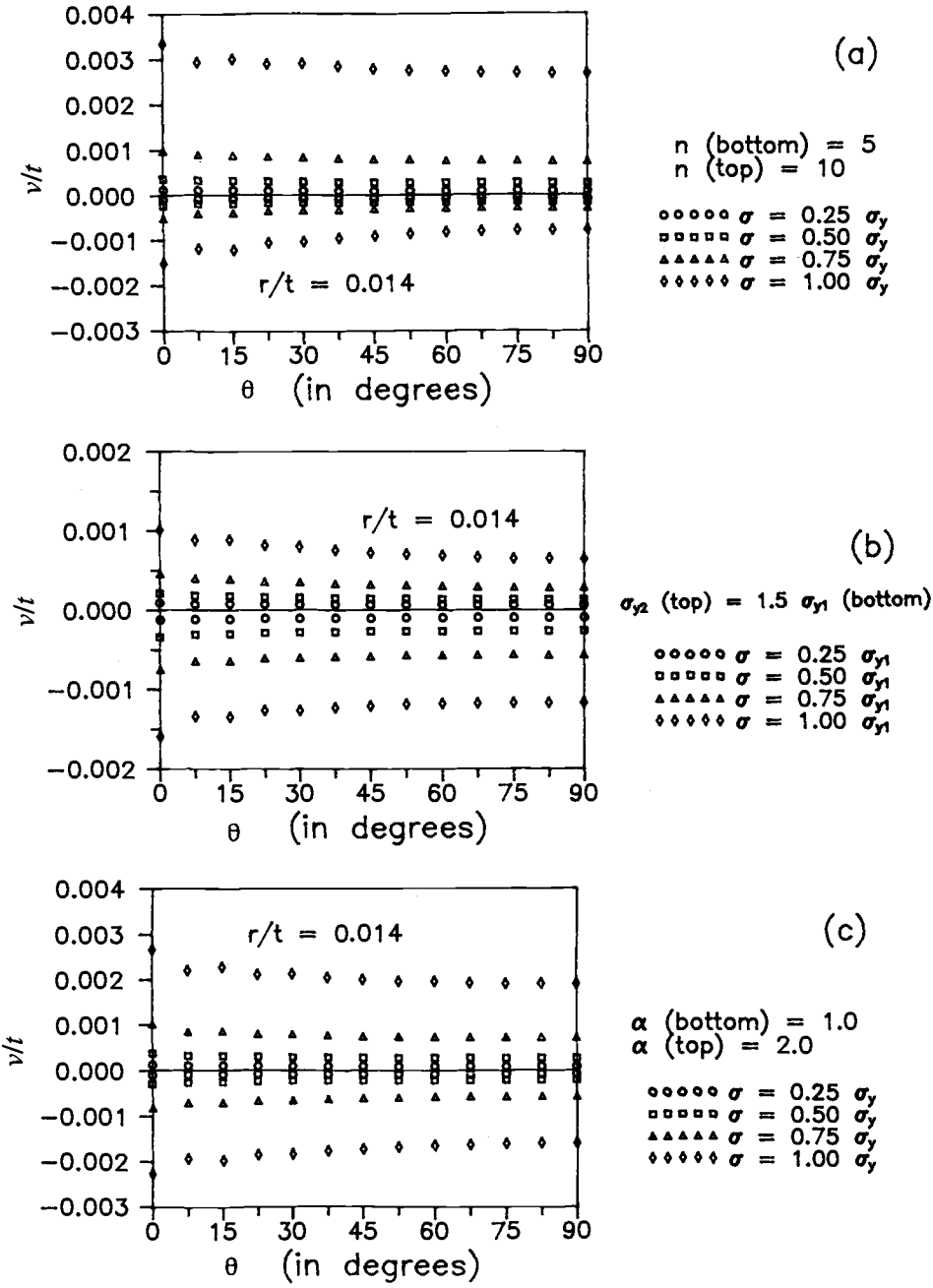


FIG. 6--The crack face opening at r/t= 0.014 behind the crack tip at different load levels for the different bimaterial cases; (a) different n values, (b) different σ_y values, and (c) different α values.

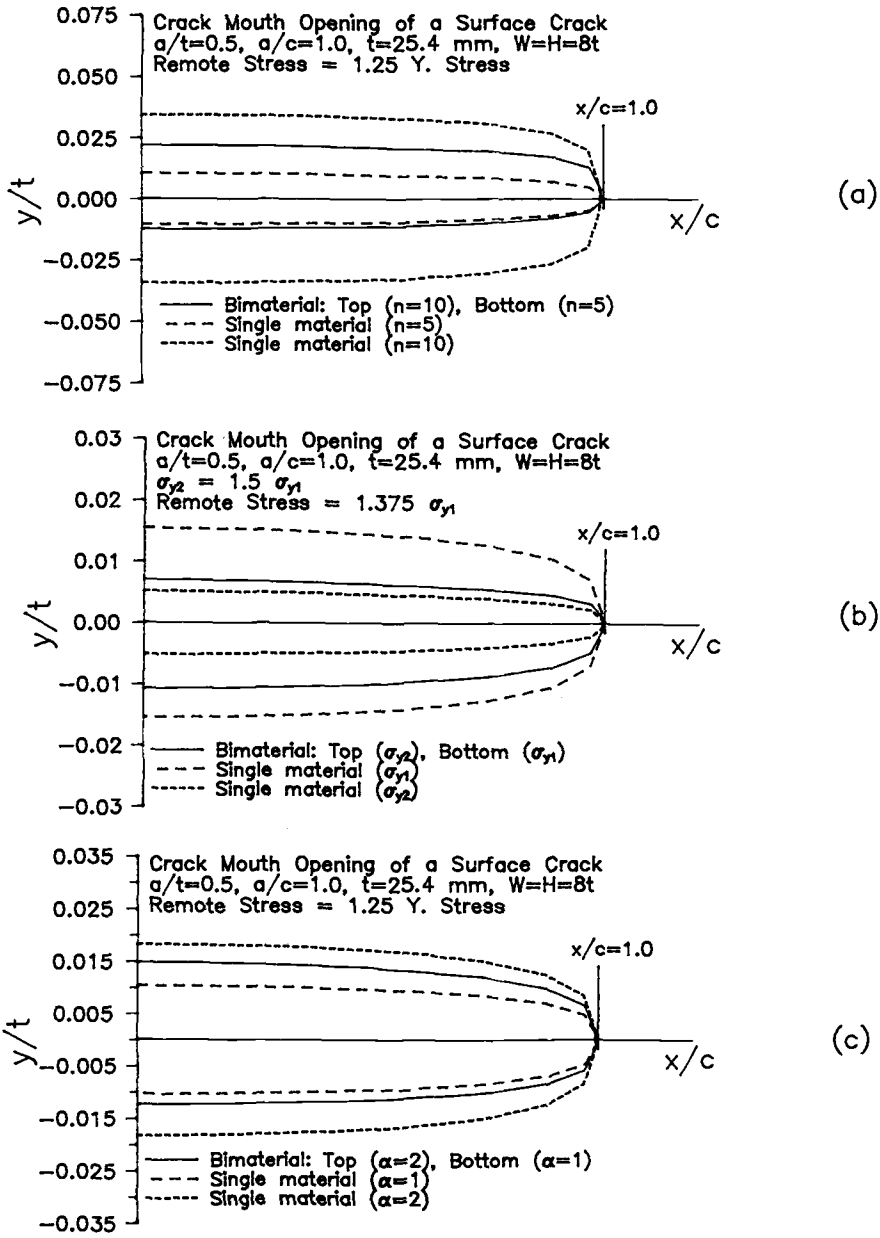


FIG. 7--The crack mouth opening for the interfacial surface crack and similar crack in single material panels with material properties similar to either half of the bimaterial panel for the different bimaterial cases; (a) different n values, (b) different σ_y values, and (c) different α values.

around the crack tip. The generated J values for the semicircular crack case are shown in Figs. 8a,b,c for the three different material combinations. The distance r in these figures represents the radius of the contour and is measured from the crack front. The J values in these figures were obtained at a remote stress about 1.25 times the yield stress if both materials have the same yield stress and 1.375 times the low yield stress if they have different yield stresses. It is evident from these figures that the path-independence of J is maintained in this interfacial surface crack under loading level well in the post yield range. The other interfacial surface crack models in the study also confirmed the path-independence of J.

We examined also the variation of J_{pl} along the front of the interfacial surface crack and compared it with those for similar surface cracks in single material panels under same loading conditions, see Figs 9a,b,c. It seems that the trend of the variation is the same for both the single material and bimaterial models. For the semicircular crack, J_{pl} has a low value at the panel face ($\theta = 0°$), then it increases to a maximum around θ = 22.5° - 30°, then, starts to decreases again. It is also clear from the figures that J_{pl} values for the interfacial surface crack in the bimaterial panels are closer to those of a similar crack in the panels made of the less deformable material than the other. This was also typical in the other interfacial crack cases.

The Single Specimen Plastic *J* form

The single specimen technique developed by the authors [15] for surface cracks is based on the energy balance expression for three-dimensional geometries which can be written as:

$$- \left(\Delta U_{pl}\right)_{v_{pl}} = \int_S J_{pl}(s)\ \Delta a(s)\ dS \tag{3}$$

where ΔU_{pl} is the change in the plastic potential energy for an arbitrary change in the crack size $\Delta a(s)$, v_{pl} is the plastic load line displacement due to crack presence, S is the crack front, and $J_{pl}(s)$ is the plastic J defined as a function of the location. The authors demonstrated [15] that the two parameter surface crack can be treated as a single parameter crack with an equivalent crack length a_e. Thus Eq (3) can be written as:

$$- \left[\frac{\partial U_{pl}}{\partial a_e}\right]_{v_{pl}} = \int_S J_{pl}(s)\ dS \tag{4}$$

The right hand side of this equation can be written as $[SJ_{pl,av}]$ where $J_{pl,av}$ is the average plastic J along the crack front. Hence, an energy rate interpretation form for J_{pl} can be written as:

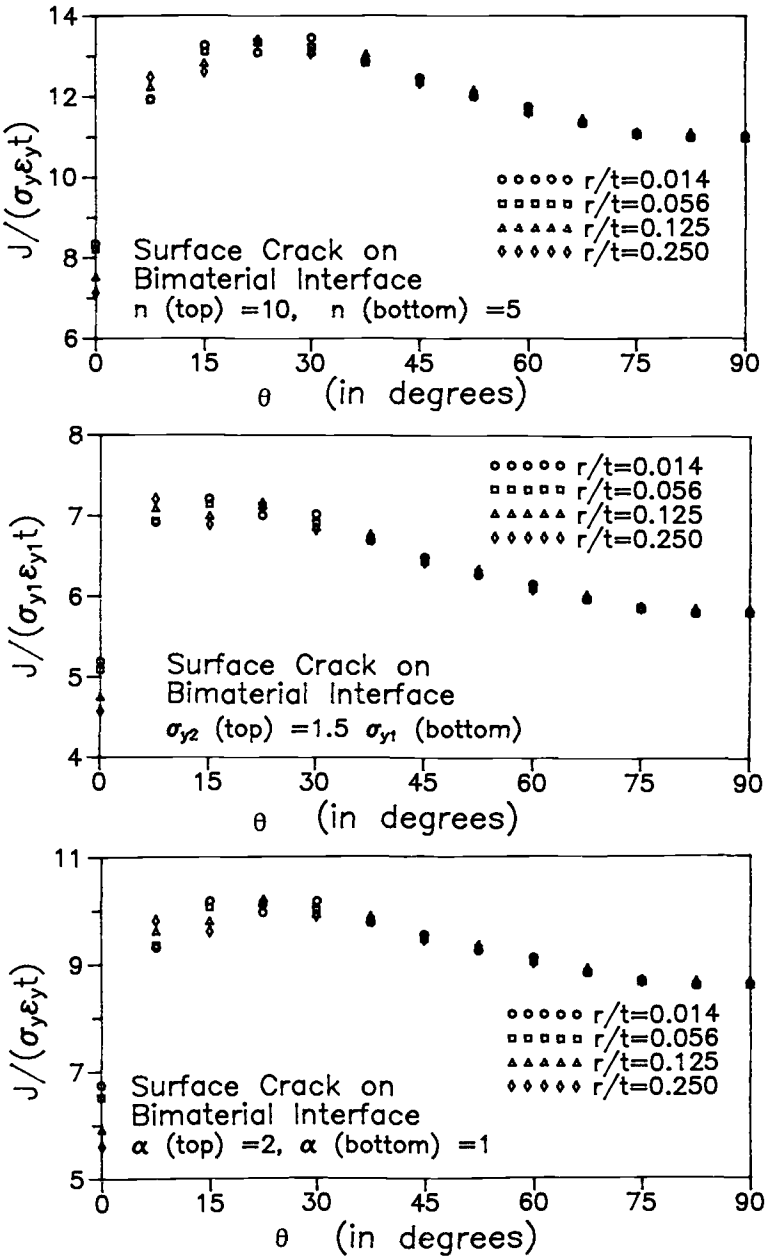


FIG. 8--The *J*-integral values at different contours for an interfacial surface crack in the different bimaterial cases; (a) different *n* values, (b) different σ_y values, and (c) different α values.

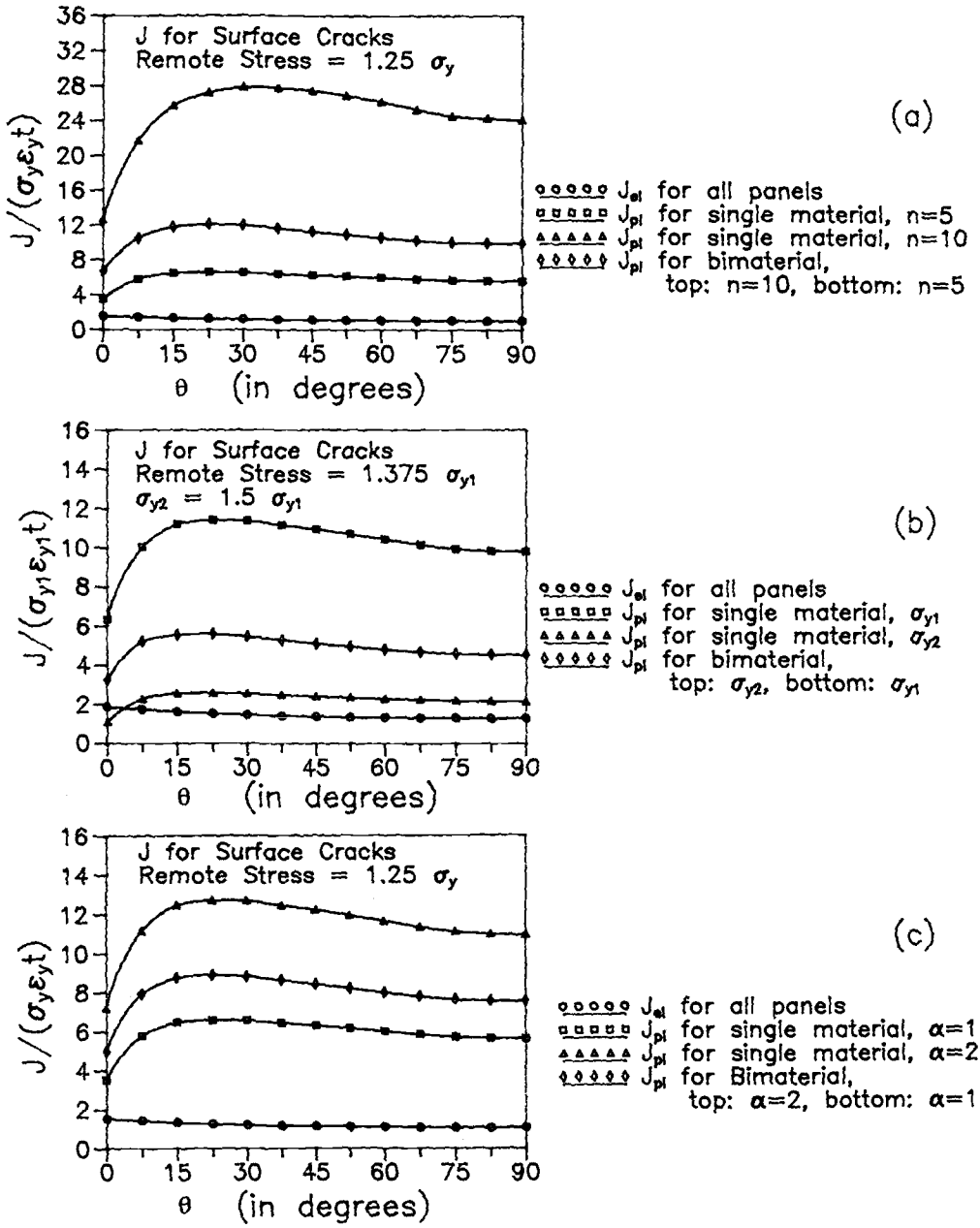


FIG. 9--The J_{pl} variation along the interfacial surface crack and a similar crack in single material panels with material properties similar to either half of the bimaterial panel for the different bimaterial cases; (a) different n values, (b) different σ_y values, and (c) different α values.

$$J_{pl,av} = -\frac{1}{S}\left[\frac{\partial U_{pl}}{\partial a_e}\right]_{v_{pl}} \tag{5}$$

For surface cracks in single material panels under tension, the remote stress can be written in a separable form as [15,18]:

$$\sigma = G(a_e)\ H(v_{pl}) \tag{6}$$

where $G(a_e)$ and $H(v_{pl})$ are the geometry and deformation functions. From Eqs (5) and (6), a single specimen J_{pl} form can be written as:

$$J_{pl,av} = \zeta_{pl} \int \sigma\ dv_{pl} \tag{7}$$

where ζ_{pl} is a factor that depends only on the crack size and geometry. v_{pl} is the plastic load line displacement (LLD) due to the crack presence. This displacement is usually small compared to the total displacement which makes it sensitive to the errors in the measurements. The plastic CMOD, on the other hand, can be more accurately measured. However, in order to use it in Eq (7) instead of the plastic LLD, the ratio between both displacements should be independent of the amount of plasticity. This was well demonstrated for surface cracks in Ref. [15].

For interfacial surface cracks, Eq (4) should hold because it is energy-based. However, the single specimen J_{pl} form in Eq (7) requires the existence of load separation in the test records. Load separation in the test records of the interfacial surface cracks in the different bimaterial panels is demonstrated in Figs 10a,b,c. In these figures, the remote stress in all of the test records of the different configurations with the same material combination is divided by the remote stress in the test record of the configuration with a/c=1 at the same plastic displacement. If these ratios, which are usually defined as the separation parameters S_{ij}'s, maintain constant values over the plastic region, this should indicate the existence of load separation. It is clear from the figures that load separation exists in this geometry.

The validity of Eq (7) for this geometry can be also verified by looking at the ratio $[J_{pl}/\int \sigma dv_{pl}]$ which is already defined as the ζ_{pl} factor. This ratio should be independent of the amount of plastic deformation because Eq (7) implies that J_{pl} is linearly related to the plastic potential energy represented by the integral $\int \sigma dv_{pl}$. Figure 11 shows this ratio for several interfacial surface cracks with different material combinations. The ratio maintains almost constant values over most of the plastic region for all of the studied cases. Hence, the single specimen J_{pl} form given in Eq (7) can be used for interfacial surface cracks as well as for surface cracks in single material panels.

The ζ_{pl} factor still needs to be defined for interfacial surface cracks. An expression for ζ_{pl} for surface cracks in single material panels is provided in Ref [15].

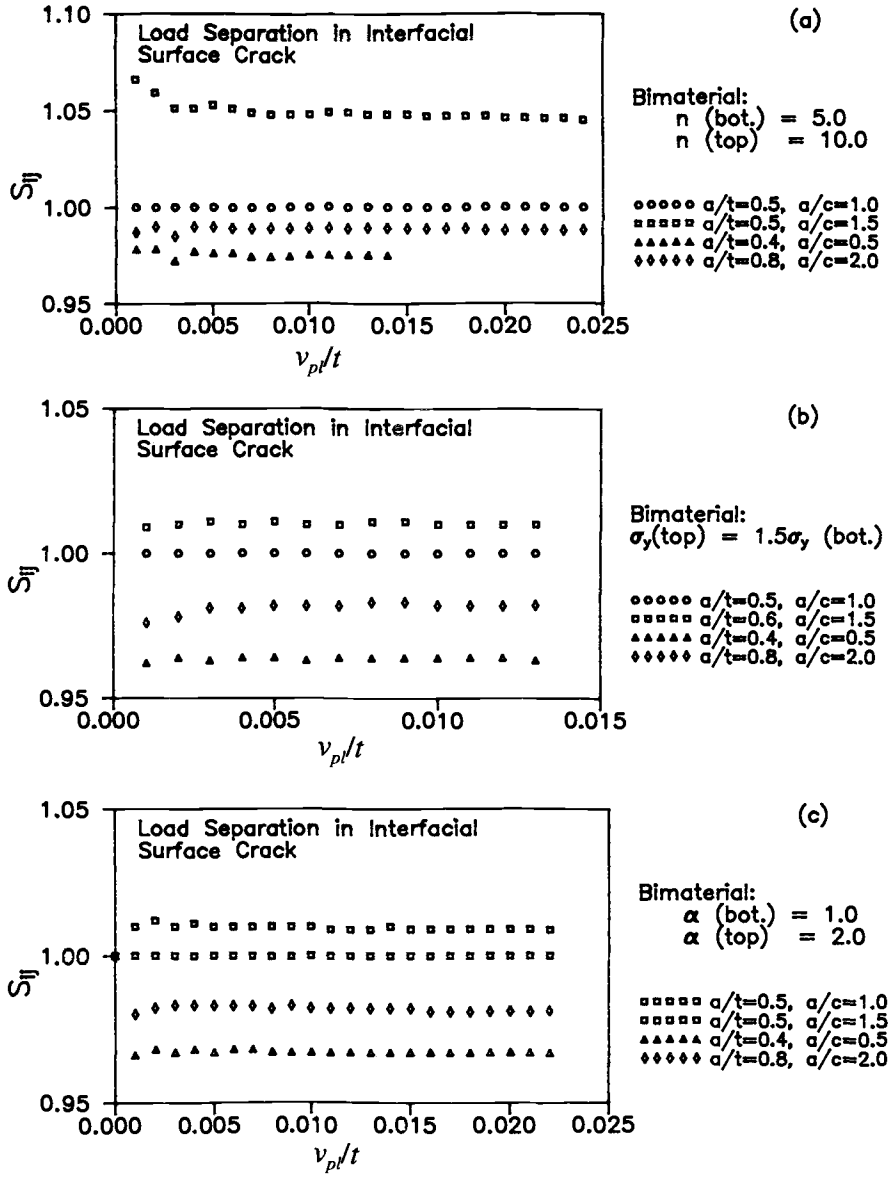


FIG. 10--Load separation parameters in three sets of test records; each for one of the bimaterial combinations: (a) different n values, (b) different σ_y values, and (c) different α values.

Although, ζ_{pl} is independent of the material, its values in single material panels may be different from those in bimaterial panels because of the change in the constraint at the interface due to the plastic mismatch. Table 4 gives the different values for ζ_{pl} factor or, in other words, the ratio $[J_{pl}/\int \sigma dv_{pl}]$ for both the interfacial surface cracks and similar cracks in single material panels. It lists also the values for ζ_{pl} from the approximate expression in Ref [15]. The ζ_{pl} factor for interfacial surface cracks seems to be about 5% to 10% lower than that for surface cracks in single material panels. This means that for the same plastic area under the test record, J_{pl} will be lower for an interfacial surface crack than for a similar crack in a single material panel. This could be due to the plastic relaxation provided by the more deformable material in the bimaterial panels. Low level of constraint usually results in low J_{pl} values. For example, in two-dimensional geometries, the value of J_{pl} at the end of the crack front is usually lower than its value at the middle [24] because of the relaxation at the surface provided by the plane stress conditions. Since the difference in ζ_{pl} is usually less than 10%, we can assume that the single specimen J_{pl} form with the ζ_{pl} expression for surface cracks in single material panels could provide an approximate conservative estimate for J_{pl} in interfacial surface cracks.

As discussed early, the variation of J_{pl} along the interfacial surface crack front is similar to that along an equivalent crack in single material panel. An expression for the ratio between the maximum plastic J, $J_{pl,max}$ and $J_{pl,av}$ has been provided in Ref [15] for surface cracks in single material panels for different a/c values as:

$$\frac{J_{pl,max}}{J_{pl,av}} = \begin{cases} 1.14 + 1.42\left(\frac{a}{t}\right) - 5.09\left(\frac{a}{t}\right)^2 + 4.28\left(\frac{a}{t}\right)^3 & \text{for } \frac{a}{c} = 0.5 \\ 1.01 + 0.41\left(\frac{a}{t}\right) - 1.28\left(\frac{a}{t}\right)^2 + 1.70\left(\frac{a}{t}\right)^3 & \text{for } \frac{a}{c} = 1.0 \\ 1.31 + 0.095\left(\frac{a}{t}\right) & \text{for } \frac{a}{c} = 2.0 \end{cases} \tag{8}$$

This expression could provide an approximate estimate of $J_{pl,max}$ for interfacial surface cracks. Table 5 gives the values for $J_{pl,max}$ obtained from the model and those estimated using Eq (8).

As discussed before, the similarity of the crack opening and J_{pl} behaviors between interfacial surface cracks and those in single material panels suggests that the elastic-plastic fracture behavior of interfacial surface cracks under remote tension is dominated by mode I. The validity of Eq (7) to estimate J_{pl} for interfacial surface cracks may also indicate the dominance of mode I behavior since it is based on the displacement measured in the opening direction of mode I. This agrees with what Shih and Asaro [11,12] observed in interfacial cracks in two-dimensional geometries.

TABLE 4--A comparison between $[J_{pl}/\int \sigma dv_{pl}]$ values for the single material and bimaterial models.

Bimaterial Model	*a/t, a/c*	$[J_{pl}/\int \sigma dv_{pl}]$ for bimaterial model	$[J_{pl}/\int \sigma dv_{pl}]$ for single material model	ζ_{pl} from Ref [15]
n (bot.) = 5.0 n (top) = 10.0 σ_y/E = 0.002 α = 1.0	0.5, 1.0	0.67	0.71	0.718
	0.5, 1.5	0.59	0.66	0.679
	0.4, 0.5	0.69	0.75	0.740
	0.8, 2.0	0.61	0.68	0.640
σ_y/E (bot.) = 0.002 σ_y/E (top) =0.003 n = 5.0 α = 1.0	0.5, 1.0	0.67	0.71	0.718
	0.6, 1.5	0.64	0.68	0.679
	0.4, 0.5	0.69	0.75	0.740
	0.8, 2.0	0.61	0.68	0.640
α (bot.) = 1.0 α (top) = 2.0 σ_y/E = 0.002 n = 5.0	0.5, 1.0	0.68	0.71	0.718
	0.6, 1.5	0.65	0.68	0.679
	0.4, 0.5	0.70	0.75	0.740
	0.8, 2.0	0.61	0.68	0.640

Conclusions

From this study, it was clear that the interfacial surface crack opens up and the crack faces are smoothly displaced in the loading direction. It was also evident from the results that the crack face in the more deformable material half of the bimaterial panel shows much less displacement than if it is in a single material panel while that in the less deformable material half shows slightly more displacement than if it is in a single material panel. The J_{pl} variation along the front of the interfacial surface crack was found to be similar to an equivalent crack in single material panels. However, the values of J_{pl} for the interfacial crack were closer to those for an equivalent crack in a panel made of the less deformable material than the more deformable material. The study indicated also that the overall elastic-plastic fracture behavior of the interfacial surface crack is dominated by mode I. It established the basis for a single specimen J_{pl} form for this geometry. It also indicated that using the single specimen J_{pl} form with the ζ_{pl} expression which was developed for surface cracks in single material panels could provide an approximate conservative estimate of the average J_{pl} for interfacial surface cracks. The maximum plastic J can be also obtained using an expression for the ratio between the maximum plastic J and the average plastic J.

TABLE 5--A comparison between $J_{pl,max}$ values from the numerical model and Eq (8).

Bimaterial Model	*a/t, a/c*	$[J_{pl,max}/\sigma_y\zeta_y t]$	
		from the model	Eq (8)
n (bot) = 5.0 n (top) = 10.0 σ_y/E = 0.002 α = 1.0	0.5, 1.0	12.08	11.94
	0.5, 1.5	5.63	5.72
	0.8, 2.0	21.26	20.55
σ_y/E (bot.) = 0.002 σ_y/E (top) = 0.003 n = 5.0 α = 1.0	0.5, 1.0	5.60	5.50
	0.6, 1.5	11.44	11.66
	0.8, 2.0	11.44	11.16
α (bot.) = 1.0 α (top) = 2.0 σ_y/E = 0.002 n = 5.0	0.5, 1.0	8.90	8.88
	0.6, 1.5	8.99	8.997
	0.8, 2.0	11.21	10.92

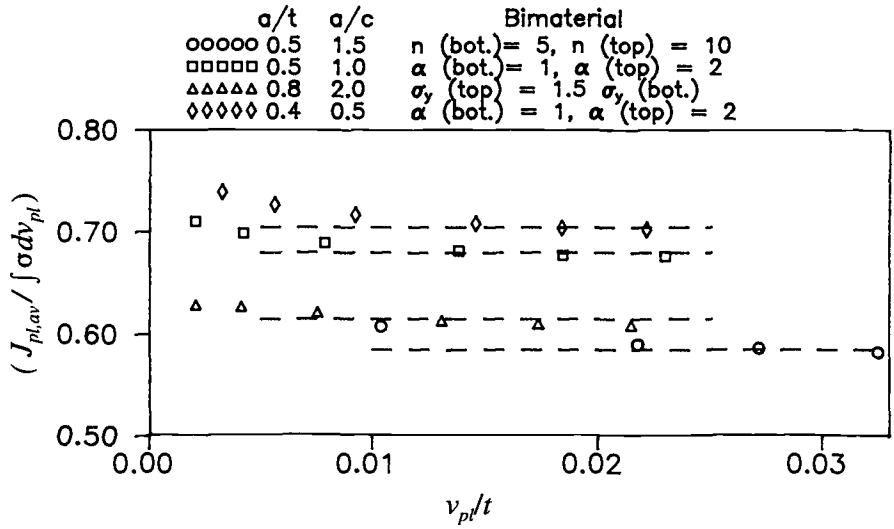


FIG. 11--$[J_{pl}/\int \sigma dv_{pl}]$ versus v_{pl} for several interfacial surface cracks from the different bimaterial combinations.

References

[1] Williams, M. L., "The Stress Around a Fault or Crack in Dissimilar Media," Bulletin of Seismological Society of America, Vol. 49, pp. 199-204, 1959.

[2] Erdogan, F., "Stress Distribution in a Non-homogeneous Elastic Plane with Cracks," Journal of Applied Mechanics, Vol. 30, pp. 232-237, 1963.

[3] England, A. H., "A Crack between Dissimilar Media," Journal of Applied Mechanics, Vol. 32, pp. 400-402, 1965.

[4] Rice, J. R., and Sih, G. C., "Plane Problems of Cracks in Dissimilar Media," Journal of Applied Mechanics, Vol. 32, pp.418-423, 1965.

[5] Comninou, Maria, "The Interface Crack," Journal of Applied Mechanics, Vol. 44, pp. 631-636, 1977.

[6] He, Ming-Yuan, and Hutchinson, J. W., "Kinking of a Crack out of an Interface," Journal of Applied Mechanics, Vol. 56, pp. 270-278, 1989.

[7] Mates, P. P. L., McMeeking, R. M., Charalambides, P. G., and Drory, M. D., "A Method for Calculating Stress Intensities in Bimaterial Fracture," International Journal of Fracture, Vol. 40, pp. 235-254, 1989.

[8] Miyazaki, N., Ikeda, T., Soda, T., and Munakata, T., "Stress Intensity Factor Analysis of Interface Crack Using Boundary Element Method - Application of Contour Integral Method," Engineering Fracture Mechanics, Vol. 45, No. 5, pp. 599-610, 1993.

[9] Raju, I. S., and Shiva Kumar, K. N., "An Equivalent Domain Integral Method in the Two-dimensional Analysis of Mixed Mode Crack Problems," Engineering Fracture Mechanics, Vol. 37, pp. 707-725, 1990.

[10] Rice, J. R., "Elastic Fracture Mechanics Concepts for Interfacial Cracks," Journal of Applied Mechanics, Vol. 55, pp. 98-103, 1988.

[11] Shih, C. F., and Asaro, R. J., "Elastic-Plastic Analysis of Cracks on Bimaterial Interfaces: Part I - Small Scale Yielding," Journal of Applied Mechanics, Vol. 55, pp. 299-316, 1988.

[12] Shih, C. F., and Asaro, R. J., "Elastic-Plastic Analysis of Cracks on Bimaterial Interfaces: Part II - Structure of Small Scale Yielding Field," Journal of Applied Mechanics, Vol. 56, pp. 763-779, 1989.

[13] Shih, C. F., and Asaro, R. J., "Elastic-Plastic Analysis of a Collinear Array of

Cracks on a Bimaterial Interface," Material Science and Engineering, A 107, pp. 145-157, 1989.

[14] Shih, C. F., "Cracks on Bimaterial Interfaces: Elasticity and Plasticity Aspects," Material Science and Engineering, A143, pp. 77-90, 1991.

[15] Sharobeam, M. H., and Landes, J. D., "A Single Specimen Approach for J-Integral Evaluation for Semi-Elliptical Surface Cracks," Fracture Mechanics: 25th Volume, ASTM STP 1220, 1994.

[16] Sharobeam, M. H., and Landes, J. D., "The Load Separation Criterion and Methodology in Ductile Fracture Mechanics," International Journal of Fracture, Vol. 47, pp. 81-104, 1991.

[17] Sharobeam, M. H., and Landes, J. D., "The Load Separation and η_{pl} Development in Precracked Specimen Test Records," International Journal of Fracture, Vol. 59, pp. 213-226, 1993.

[18] Sharobeam, M. H., and Landes, J. D., "A Simplified Approach for Ductile Failure Analysis of Semi-elliptical Surface Cracks," International Journal of Fracture, Vol. 61, pp. 379-395, 1993.

[19] Raju, I. S., and Newman, J. C., "Stress Intensity Factor Equations for Cracks in Three-Dimensional Finite Bodies," Fracture Mechanics: Fourteenth Symposium - Theory and Analysis, ASTM STP 791, Vol. I, pp. 283-295, 1983.

[20] McCabe, D. E. Ernst, H. A., and Newman, J. C., "Application of Elastic and Elastic-Plastic Methods to Surface Flaws," Fracture Mechanics: 22nd Symposium, ASTM STP 1131, Vol. I, pp. 495-518, 1992.

[21] Carpenter, W. C., Read, D. T., and Dodds, R. H., Jr., "Comparison of Several Path Independent Integrals Including Plasticity Effects," International Journal of Fracture, Vol. 31, pp. 303-323, 1986.

[22] Abaqus manuals, Hibbitt, Karlson & Sovensen, Inc.

[23] Rice, J. R., "A Path Independent Integral and the Approximate Analysis of Strain Concentration by Notches and Cracks," Journal of Applied Mechanics, pp. 379-386, 1968.

[24] Schmitt, W., "Three-Dimensional Finite Element Simulation of Post-Yield Fracture Experiments," International Journal of Solids and Structures, Vol. 22, No. 7, pp. 833-843, 1986.

William C. Porr, Jr.[1], Richard E. Link[1], Joseph P. Waskey[1], and Robert H. Dodds, Jr.[2]

EXPERIMENTAL APPLICATION OF METHODOLOGIES TO QUANTIFY THE EFFECT OF CONSTRAINT ON J_c FOR A 3-D FLAW GEOMETRY

REFERENCE: Porr, W. C., Jr., Link, R. E., Waskey, J. P., and Dodds, R. H., Jr., **"Experimental Application of Methodologies to Quantify the Effect of Constraint on J_c for a 3-D Flaw Geometry"**, *Fracture Mechanics: 26th Volume, ASTM STP 1256*, Walter G. Reuter, John H. Underwood, and James C. Newman, Jr. Eds., American Society for Testing and Materials, Philadelphia, 1995.

ABSTRACT: In an effort to validate methodologies to quantify the effect of crack tip constraint on cleavage fracture toughness, a series of experiments were conducted to measure the cleavage fracture toughness, J_c, of an ASTM A515 Grade 70 steel utilizing large plate bend specimens containing semi-elliptical surface cracks, SC(B), (3-D flaw geometry). J_c was estimated with modified EPRI and Turner design curve schemes from load and remote strains measured at initiation. The cleavage toughness of the A515 steel used for this testing was previously characterized using a series of through-cracked single edge notch bend specimens, SE(B), (2-D flaw geometry) with various initial crack-depth to specimen-width ratios, a/W. The toughness values estimated for the surface cracked plate specimens were consistent with the toughness ranges predicted from the SE(B) results using the two parameter fracture mechanics (J-Q) methodology to account for differences in crack tip constraint. This result indicates the applicability of small specimen, constraint adjusted, results to engineering structural integrity predictions for the case of cleavage fracture.

KEYWORDS: A515 steel, J-Integral, fracture toughness, cleavage, surface crack, crack tip constraint, toughness scaling, two parameter fracture mechanics

[1]Materials Engineer, Senior Mechanical Engineer, and Mechanical Engineering Technician, respectively, Fatigue and Fracture Branch, Carderock Division, Naval Surface Warfare Center, Annapolis, MD 21402-5067.

[2]Professor, Department Of Civil Engineering, University of Illinois, Urbana, IL 61801.

Copyright © 1995 by ASTM International www.astm.org

INTRODUCTION

A fracture mechanics assessment of a structure is made by comparing the driving force for fracture with some measure of the materials resistance to fracture. Traditionally, the fracture toughness of the material is expressed in terms of the critical value of a single parameter (eg. K, J, or CTOD). The fracture toughness is measured in the laboratory using small, deeply-cracked specimens with through cracks. This type of specimen is chosen because it has high constraint and is expected to yield a conservative measure of the toughness, provided certain size criteria are met. In calculating the driving force for fracture, it is frequently necessary to employ 2-D idealizations of the structural flaw in order to simplify the analysis and make use of existing tabulated crack solutions. This approach is generally thought to yield a conservative assessment of the fracture safety of a structure; however, there is no way of quantifying the degree of conservatism and such analyses may be overly conservative.

Two parameter fracture mechanics methodologies have been developed over the past several years which attempt to quantify material fracture toughness as a function of constraint [1-4]. The second parameter (Q or T) provides a quantitative measure of the level of constraint present in the structure or specimen. In these approaches, the material fracture toughness is not a single point value, but is described by a locus of toughness that varies with the applied constraint conditions. These approaches show the most promise for application in the ductile-brittle transition range of ferritic steels where the fracture toughness can be greatly influenced by the constraint conditions [3,5]. A related approach that has been developed along with the two-parameter methodologies is the toughness scaling model. The toughness scaling model incorporates a micromechanics-based failure criterion to determine the driving force which must be applied to a crack in a finite body in order to achieve a stressed volume equivalent to the critical stressed volume under small scale yielding conditions [6,7]. The various methodologies have been used to correlate experimentally observed effects of constraint on fracture toughness with some success [3-5,7].

All of the experimental validations of these two methodologies to quantify constraint reported to date have employed data from essentially 2-D, through cracked geometries. The critical test of these approaches will be the more difficult problem of accurately predicting the response of structural elements containing realistic 3-D flaw geometries such as surface cracks. The surface crack introduces several difficulties that are not addressed by a 2-D approach to the problem. For 2-D analyses of through crack geometries, it is generally assumed that the crack tip conditions are uniform along the crack front. This is certainly not the case for the surface crack. For a given loading condition, the value of applied J varies considerably with position around the crack front [8]. The constraint also varies around the crack front, and the constraint variation may be completely different than that of J [9]. In the ductile-brittle transition region, there is also a size effect, related to the length of the crack front and associated with the probability of the incidence of a crack front cleavage initiation site, which is independent of the in-plane constraint effect [10]. No complete methodology

has been developed yet which addresses all of these issues, and there are only very limited J and Q solutions for surface cracks currently available in the literature [8,9]. Nevertheless, experimental measurements of fracture behavior in specimens with surface cracks are needed in order to validate these new predictive models and guide their continued development.

This paper describes experiments conducted to assess the applicability of the toughness scaling and two parameter fracture mechanics methodologies to predicting cleavage fracture behavior of a surface cracked specimen geometry. The driving force, J, and Q were estimated based on available 2-D and 3-D results. The surface crack results were compared with conventional data developed from small laboratory specimens containing two dimensional flaws.

EXPERIMENTAL METHOD

Material

Specimen material used in this study is the same ASTM A515 grade 70 steel used in previous studies [3,4]. A515 is a C-Mn pressure vessel steel that is in transition at room temperature and shows significant plasticity before initiation of cleavage fracture. The microstructure of the material used in this study, illustrated in Figure 1, is mixed ferrite and pearlite, with an average grain diameter of approximately 75 micrometers.

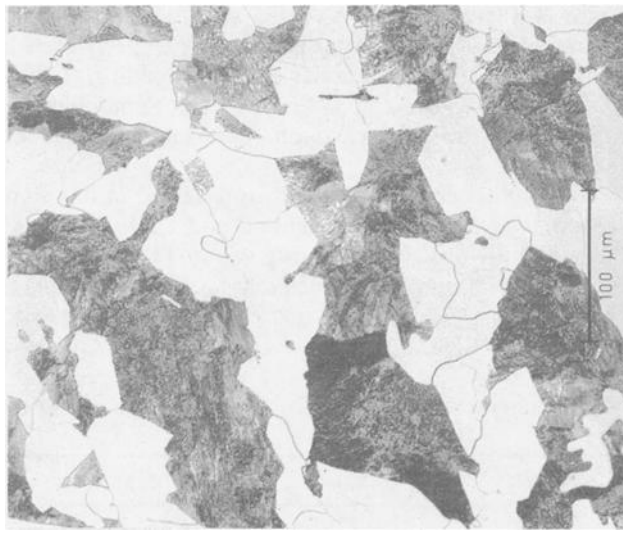


Figure 1--Mixed ferrite and pearlite microstructure of the ASTM A515 Grade 70 steel tested.

The uniaxial tensile properties of the A515 are given in Table 1. For this study, Young's modulus, E, is assumed to be 207,000 MPa. The strain hardening coefficient given in Table 1 is defined by a fit to the stress-strain curve at stresses greater than the yield stress, σ_o, of the form:

$$\epsilon = \frac{\sigma_o}{E}\left(\frac{\sigma}{\sigma_o}\right)^n \quad (1)$$

The lower the value of n, the greater the work hardening behavior of a material. A515, with a strain hardening coefficient of 4, is a high work hardening steel.

TABLE 1--Tensile properties of ASTM A515 Grade 70 steel at 20° C

0.2% Yield strength, MPa	Tensile strength, MPa	Flow strength, MPa	% Elongation, in 25.4 mm	% Reduction in area	Strain hardening coefficient
288	542	415	34	51	4

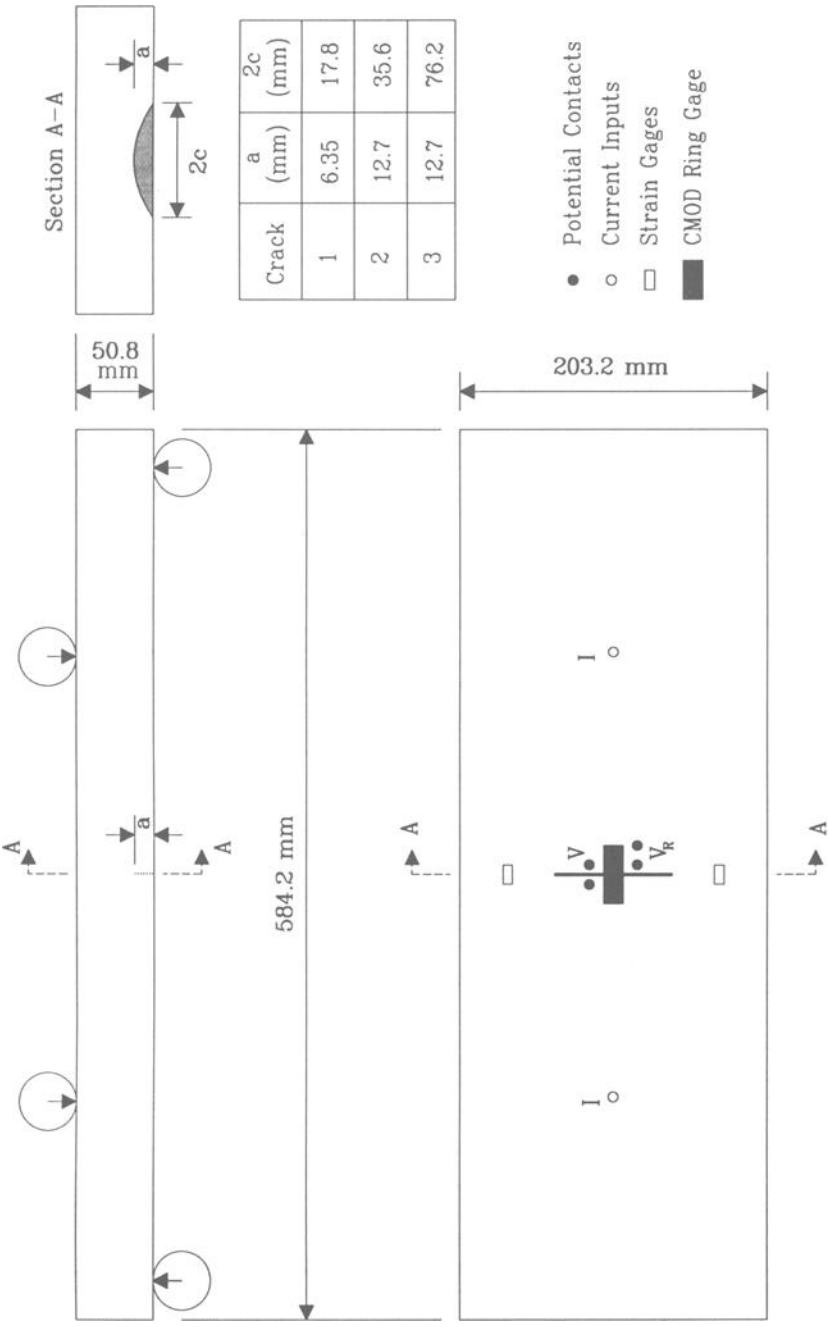
Specimen Geometry

The large plate, surface cracked bend, SC(B), specimen tested in this study is illustrated in Figure 2. Plate dimensions were 50.8 mm in thickness, 203.2 mm in width, and 584.2 mm in length. This approximates a geometry used by the U.S. Navy for hull material qualification under explosive loading. Cracks were oriented in the T-S direction relative to plate processing. Semi-elliptical surface cracks were grown by fatigue from electric discharge machining (EDM) slots in the center of the specimens.

Three different nominal crack geometries were tested in this study. The three different geometries are indicated in Figure 2 and Table 2, with actual crack dimensions for all successfully tested specimens given in Table 3. Crack geometry 1 (a = 6.35 mm and 2c = 17.8 mm), was utilized for only two specimens, GGR2-1 and GGR2-2, with neither test yielding data that could be analyzed in this study.

TABLE 2--Nominal crack dimensions for the SC(B) specimens tested

Geometry	2c/a	a/t	a (mm)	2c (mm)
1	2.8	0.125	6.35	17.8
2	2.8	0.25	12.7	35.6
3	6.0	0.25	12.7	76.2



Crack	a (mm)	2c (mm)
1	6.35	17.8
2	12.7	35.6
3	12.7	76.2

Figure 2 Large plate, surface cracked bend, SC(B), specimen geometry tested in the current study.

Fatigue precracking was performed in three-point bending at a constant load amplitude. The stress ratio, R, was 0.2. The cyclic moment range was approximately 17.2 kN-m, and the stress (moment) ratio, R, was approximately 0.2. This loading resulted in maximum ΔK's of approximately 12.6 MPa$\sqrt{m}$ for crack geometry 2 and 14.8 MPa$\sqrt{m}$ for crack geometry 3, at the end of precracking. Initial EDM slot dimensions were selected to result in specific crack geometries following precracking. Using stress intensity (K) solutions for semi-elliptical surface cracks in plates subjected to bending loads [11] and assuming steady state fatigue crack growth ($da/dN = C\Delta K^m$), EDM slot dimensions required could be inferred from desired final crack dimensions. The stress intensity factor varies around the semi-elliptical crack front for a given remote load:

$$K = S_b\sqrt{\pi a} \bullet f\left(\frac{a}{c}, \frac{a}{t}, \frac{c}{b}, \phi\right) \tag{2}$$

where S_b is the bending stress, a is the crack depth, c is the half surface length, t is the plate thickness, b is the plate half-width, and ϕ is the parametric angle of ellipse. K is typically higher at the maximum depth than at the surface for the cracks examined here. The semi-elliptical crack grew at different rates in the depth and along the plate surface, hence, initial depth (a) to surface length (2c) aspect ratio (2c/a) was not necessarily the same as the desired final aspect ratio. Additionally, EDM slot depth was reduced from that dictated by this method to account for crack initiation at the maximum depth (higher initial ΔK) prior to initiation on the surface.

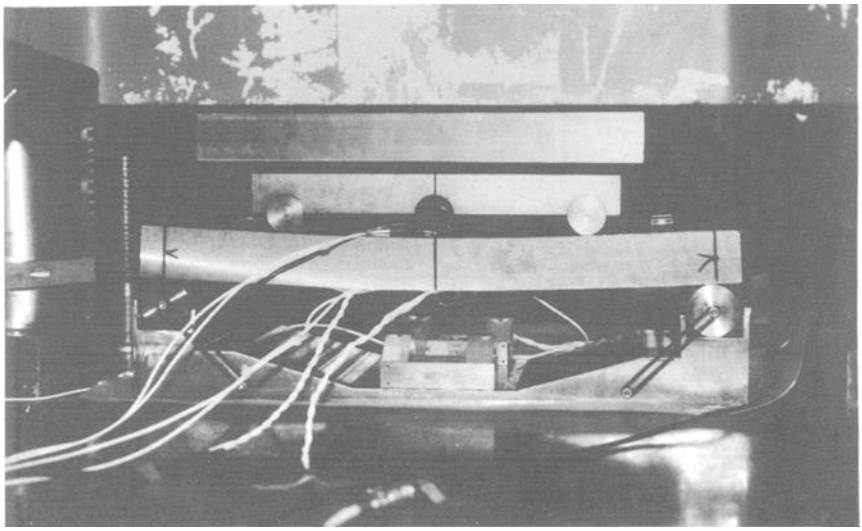


Figure 3--Large plate, SC(B) specimen loaded in four point bending.

Testing Procedure

SC(B) specimens were loaded in four point bending under a constant crosshead displacement rate of 2.12 x 10^{-5} m/s (Figure 3). The moment arm for applied loading was 121 mm. Load, crack mouth opening displacement (CMOD), remote strain, and AC potential difference (ACPD) across the crack mouth were monitored continuously during loading. CMOD was measured by a ring gage inserted at the crack mouth on the center line of the specimen. Remote strain was measured at ±0.5 b on the crack plane, on both the front and back faces of the plate. The parameter b is defined as the distance from the centerline to the plate edge in the plate width. ACPD was measured to indicate any ductile crack extension prior to the initiation of cleavage fracture. Neither the ACPD data nor the CMOD data were necessary for the analyses conducted in his study, but will be used for additional analyses to be conducted in the future.

J Integral Estimation

J integral values at cleavage initiation were estimated using two approximations that had previously been shown to be effective in estimating J for the SC(B) specimen geometries 2 and 3 with a different material response [8]. For the analyses that follow, each approximation was used to determine the J response of the specimen crack geometry that it more accurately described according to 3-D finite element modelling.

For crack geometry 2, an engineering-J design curve formulation [12] was used to estimate J_c from remote strains. The design curve formulation was developed from two-dimensional elastic-plastic plane-strain finite-element analyses of a variety of cracked body geometries and loading conditions, for cracks with $a/W \leq 0.1$ [12]. When yielding has occurred in the 'gross section' of the specimen (i.e. $e/e_y > 1.2$), the engineering-J design curve methodology provides that J can be estimated by:

$$J = 2.5\left[\left(\frac{e}{e_y}\right) - 0.2\right]G_y \tag{3}$$

where e is remote strain for the uncracked body, e_y is the yield strain (σ_o/E), and $G_y = K^2_{Iy}/E$. K_{Iy} is given by solving equation 2 with $S_b = S_o$, the bending stress for outer fiber yielding.

For crack geometry 3, a modified EPRI estimation scheme [13] was used. The EPRI methodology for determining J was developed from consideration of cracks in stressed bodies where material flow behavior is described by:

$$\frac{\epsilon}{\epsilon_o} = \frac{\sigma}{\sigma_o} + \alpha\left(\frac{\sigma}{\sigma_o}\right)^n \tag{4}$$

where α is a constant ($\approx$1) and $\epsilon_o = \sigma_o/E$. J is given by:

$$J = J_e + J_p \tag{5}$$

where J_e is defined as:

$$J_e = \frac{K^2(a_{eff})}{E'} \tag{6}$$

where E' is E for plane stress and $E/(1-\upsilon^2)$ for plane strain, υ is Poisson's ratio, and $K(a_{eff})$ is the stress intensity factor for the given plastic zone corrected crack length and applied loading. Plastic zone corrected crack length, a_{eff}, is given by:

$$a_{eff} = a + \frac{1}{\beta\pi}\left(\frac{n-1}{n+1}\right)\left(\frac{K}{\sigma_o}\right)^2 \frac{1}{1+\left(\frac{P}{P_L}\right)^2} \tag{7}$$

where β is 2 for plane stress and 6 for plane strain, P is applied load, and P_L is the specimen plastic limit load. Limit load was estimated for each specimen by determining an equivalent through edge crack depth, a_{eq} for the surface crack in the plate geometry [14],

$$a_{eq} = \frac{\pi a c}{4c + 2t} \tag{8}$$

and solving for limit load of this through edge crack:

$$P_L = \frac{\sigma_o B (t - a_{eq})^2}{4L} \tag{9}$$

where B is plate width (=2b) and L is the moment arm length. Modification of the EPRI methodology, incorporating a reference stress ($\sigma_o \bullet P/P_L$) and the assumption that a non-dimensional geometry factor is independent of work hardening [13], results in J_p approximated as:

$$J_p = \frac{\mu K^2(a)}{E}\left[\left(\frac{P}{P_L}\right)^{n-1} - 1\right] \tag{10}$$

TABLE 3--Test specimen data

Specimen ID	a_i (mm)	$2c_i$ (mm)	$2c/a_i$	a/t_i	Δa (mm)	a_f (mm)	$2c_f$ (mm)	P_L (kN)	P_o (kN)	e_o	J_o (kJ/m^2)
GGR2-3	11.2	32.5	2.89	0.221	2.36	13.6	35.1	273.6	626.1	0.0498[1]	391.2
GGR2-4	13.3	37.7	2.84	0.261	0.13	13.4	37.7	262.0	419.0	0.0180	154.3
GGR2-5	10.5	31.9	3.03	0.207	1.60	12.1	33.9	276.2	572.5	0.0398[1]	337.0
GGR2-6	11.9	35.2	2.96	0.234	0.00	11.9	35.2	269.1	446.4	0.0218[1]	193.3
GGR2-7	12.2	35.3	2.89	0.240	0.00	12.2	35.3	267.8	453.0	0.0229	105.3[2]
GGR2-8	12.9	38.7	3.00	0.254	0.00	12.9	38.7	262.4	379.6	0.0171	97.5[2]
GGR2-9	13.6	37.1	2.72	0.268	0.00	13.6	37.1	261.2	421.4	0.0180	149.0
GGR6-1	12.2	77.5	6.36	0.240	0.00	12.2	77.5	246.9	338.9	0.0085	55.4
GGR6-2	11.4	78.3	6.88	0.224	0.00	11.4	78.3	250.9	342.7	0.0110[1]	56.4
GGR6-3	10.9	80.3	7.33	0.216	0.38	11.3	80.3	252.6	388.8	0.0193	104.2
GGR6-4	12.8	79.4	6.19	0.253	1.14	13.9	79.4	243.3	453.3	0.0269[1]	242.1
GGR6-5	12.1	76.6	6.34	0.238	0.28	12.4	76.6	247.8	372.7	0.0137	86.9
GGR6-6	12.7	76.4	6.02	0.250	0.64	13.3	76.4	244.6	409.0	0.0197	140.8
GGR6-7	13.4	77.8	5.8	0.264	0.00	13.4	77.8	240.6	330.3	0.0093	51.9
GGR6-8	12.4	77.4	6.22	0.245	0.00	12.4	77.4	245.5	340.3	0.0092	57.3[2]
GGR6-9	13.7	81.5	5.94	0.270	0.00	13.7	81.5	237.5	374.7	0.0131	103.6
GGR6-10	14.5	79.5	5.49	0.285	0.00	14.5	79.5	234.4	335.6	0.0102	60.2

[1] Extrapolated
[2] Pop-in

where μ is 1 for plane stress and 0.75 for plane strain.[3]

RESULTS

J Integral Estimation

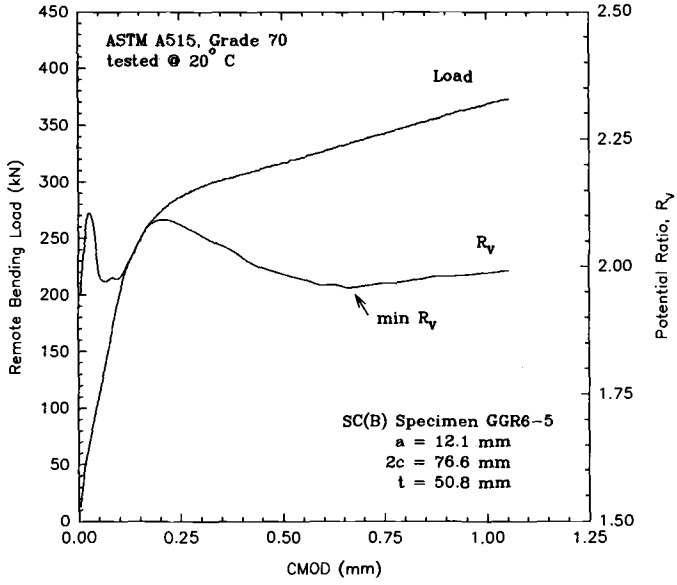
It was determined early in the test program that crack geometry 1, with a ≈ 6.4 mm and 2c ≈ 17.8, would not yield the desired cleavage fracture data at the test temperature, 20°C. Extensive ductile crack extension occurred in the two specimens of this crack geometry tested, GGR2-1 and GGR2-2, without subsequent initiation of cleavage fracture. This geometry was then abandoned for crack geometry 2, with a ≈ 12.7 mm and 2c ≈ 35.6 mm. Crack geometry 2 has approximately the same crack aspect ratio of 2c/a = 2.8 as geometry 1, but is four times larger by area. The load and strain at the initiation of cleavage fracture, P_c and e_c, from the seven successful experiments with specimen geometry 2 and ten experiments with geometry 3 are given in Table 3. One specimen with crack geometry 2 (GGR2-10) did not fail before the displacement (≈50 mm, center-line) and load limits (≈1300 kN) of the test fixtures and load frame were reached.

An example of recorded data is given in Figures 4a and 4b. Applied bending load (½ of load cell output) and ACPD potential ratio, R_V, are plotted versus CMOD for specimen GGR6-5 in Figure 4a. The potential ratio, R_V is defined as V/V_r, where V is the potential across the crack mouth and V_r is the reference potential. Bending load is plotted versus monitored remote strains for the same specimen in Figure 4b. The monitored data were relatively free of noise, with the exception of the ACPD data which are shown after smoothing. The strain at cleavage fracture had to be extrapolated from lower strains in several cases after strain gages debonded from the specimen during loading. In three instances cleavage initiation was indicated by crack "pop-in", where a burst of cleavage cracking occurred without causing total separation of the plate specimen. Total specimen failure then occurred with additional loading.

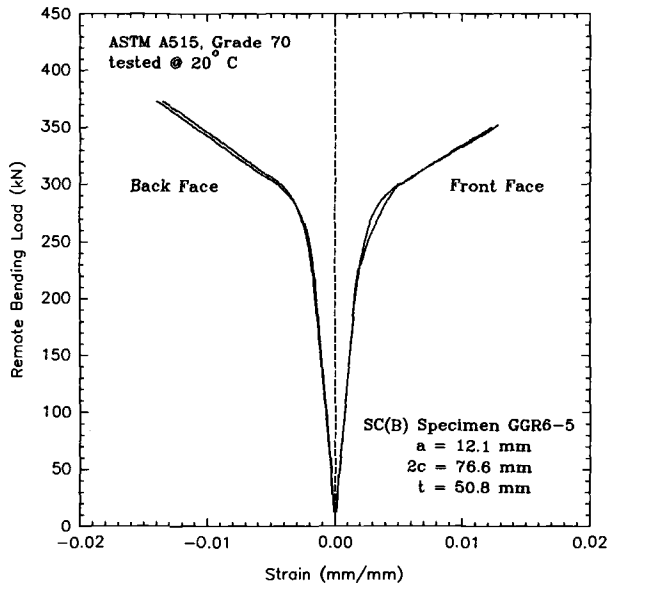
Following specimen failure, fracture surface examination at low magnification confirmed the cleavage fracture mode and allowed accurate precrack measurement (Figure 5). As indicated in Table 3, six of the specimens with crack geometry 3 and four specimens with geometry 2 failed by cleavage with no prior ductile crack extension. The other specimens exhibited varying amounts of crack extension less than 2 mm, with the exception of specimen GGR2-3. Crack extension was measured at the maximum depth. ACPD was successful at indicating the occurrence of ductile crack extension during loading, but unsuccessful in correctly measuring the amount of extension without post-test analysis. For the purposes of the current study, a real time measure of crack extension was not critical. ACPD was used primarily as a condition monitoring

---

[3] Equation 10 varies from that reported in Ref. 13 with $\sigma_o/E*(\sigma_{ref}/\sigma_o)^n$ substituted for ϵ_{ref}, where $\sigma_{ref}=(P/P_L)\sigma_o$.



(a)



(b)

Figure 4--(a) Load and potential ratio versus crack mouth opening displacement (CMOD), and (b) load versus remote strain, for SC(B) specimen GGR6-5.

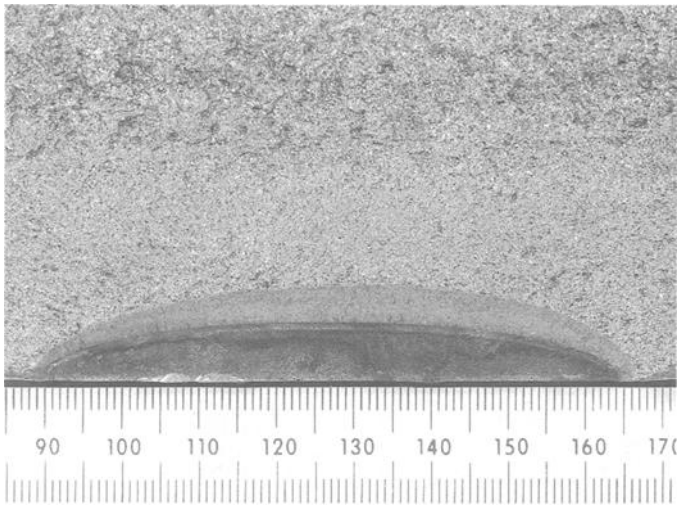


Figure 5--Low magnification image of the semi-elliptical 2c/a = 6 flaw for SC(B) specimen GGR6-8. Scale shown is in units of millimeters (mm).

tool in this study with future analysis of the data to characterize the effect of ductile tearing on cleavage initiation possible.

J_c values for the tested specimens were estimated at the maximum depth ($\phi = \pi/2$) using the techniques described above. The results are indicated in Figure 6 and Table 3. Values shown for geometry 3 are the average of the plane strain and plane stress values determined with the EPRI estimation. This was done to account for the probability that the actual crack tip stress state was somewhere between fully plane strain and fully plane stress. Figure 6 plots the measured cleavage toughness as a function of specimen geometry. Results for the A515 cleavage fracture toughness determined using SE(B) specimens with crack depth ranging from a/W = 0.1 to a/W = 0.55 [3] are also plotted in Fig. 6 for comparison. Toughness values ranged from 51.9 kJ/m^2 to 242.1 kJ/m^2 for crack geometry 3, and from 97.5 kJ/m^2 to 391.2 kJ/m^2 for crack geometry 2. The range of measured toughness values for geometry 3 approximates the range for SE(B) specimens with a/W≈0.3, while that associated with geometry 2 approximates the cleavage toughness range for SE(B) specimens with a/W≈0.1.

Multi-specimen fracture resistance curves developed from the SE(B) data from Reference 3 and the SC(B) data for crack geometries 2 and 3 from this study are presented in Figure 7. J values at cleavage were plotted versus the amount of ductile crack extension prior to cleavage initiation. The R-curve produced this way includes crack tip blunting with the measured crack extension. From these plots, an approximate initiation J, J_i, for ductile crack extension can be determined by the intersection with the blunting line ($J=2\sigma_{flow}\bullet\Delta a$) of a regression line drawn through the data. J_{IC} for ductile crack extension has been

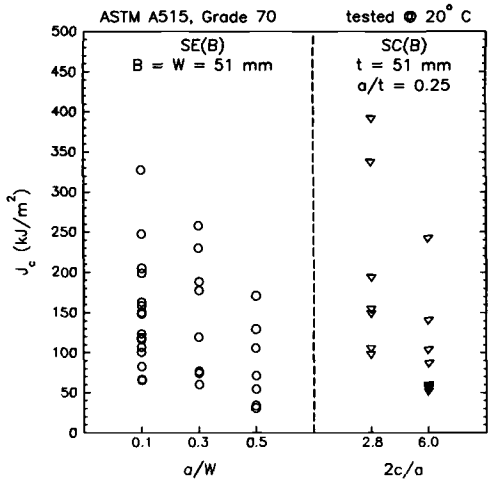
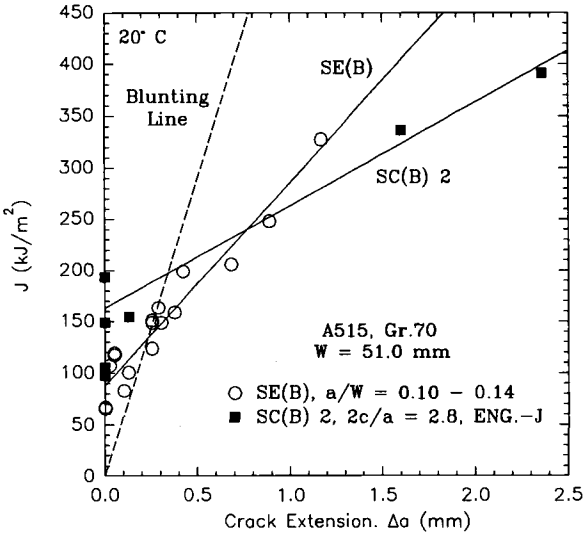


Figure 6--Cleavage toughness (J_c) values for A515, Gr. 70 steel measured using SE(B) [3] and SC(B) specimens with nominal geometries shown.

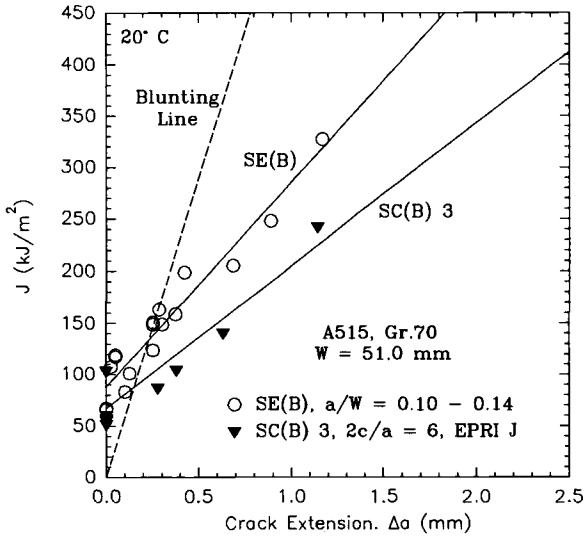
previously shown to be relatively insensitive to specimen geometry for a given material [15]. Therefore, comparison of the J_i for each of the data sets should give an indication of the accuracy of the estimation schemes used for SC(B) J analysis. As indicated in Figure 7, J_i for ductile crack extension in the A515 steel is approximately 135 kJ/m^2 according to the SE(B) data from Reference 3. The J_i indicated by the regression through the SC(B) data for crack geometry 3 from this study is approximately 89 kJ/m^2. This implies that the estimation scheme used to determine applied J for the SC(B) specimen with crack geometry 3 underestimates the true J-integral at the crack front. This result is consistant with a previous analysis of the anticipated effectiveness of the EPRI estimation for an SC(B) specimen at strains well beyond yield [8]. Similarly, the J_i for the SC(B) specimen with crack geometry 2 is approximately 197 kJ/m^2, indicating that the engineering-J design curve overestimates the true applied J-integral in this case.[4]

---

[4] Two different estimation schemes were used to determine J_c for the two SC(B) geometries; if the same estimation technique was used for all of the data, it was found that the engineering-J design curve formulation apparently overestimated the true J at the crack tip for geometry 3 as well. Likewise, the EPRI estimation apparently underestimated the true crack-tip J for geometry 2. A determination as to which technique is more appropriate to use for the SC(B) specimens of this material is not made here.



(a)



(b)

Figure 7--Multi-specimen R-curves for A515, Gr. 70 steel determined with SC(B) specimens for (a) 2c/a = 2.8 with J determined from engineering J design curve, and (b) 2c/a = 6 with J determined from modified EPRI formulation. Data from SE(B) specimens with a/W = 0.1 [3] plotted for comparison.

Application of Constraint Methodologies

Experimental application of constraint methodologies to the data developed in the current study can only be accomplished by making numerous estimations. Future work will include finite element modelling to develop the necessary J integral and constraint solutions for this material and specimen geometry. Finite element modelling has been performed for surface cracked tension, SC(T), specimens of the lower hardening, higher strength, pressure vessel steel ASTM A533B [9], and for SC(B) specimens with different flow properties than the material examined in the current study [8]. Results of that modelling are used here to estimate the applicable Q values for the SC(B) A515 data.

For the J values determined for crack geometry 3 using the modified EPRI estimation scheme described previously, Q values were estimated graphically from the uniaxial tension J-Q driving force curves in Reference 9 and then adjusted to higher constraint values to account for the higher hardening material and bend loading. The amount of the adjustment ($\approx +0.25$) to Q was selected based on previously reported dependence of Q on strain hardening coefficent for the SE(B) geometry [3,9]. The value of Q for a given J_c for crack geometry 2 was estimated as approximately equal to that for the larger surface flaw in the lower hardening material. Prior modelling of this type of flaw [8,9] indicates that the highest J and crack tip constraint for a surface crack is not necessarily at the maximum depth. For the purposes of this study however, initiation is assumed at the maximum depth. The maximum J given by the two J estimation schemes used is at the maximum depth.

Figure 8 shows the application of the two parameter fracture mechanics (J-Q) methodology to assess the effect of constraint on the cleavage fracture toughness. Plotted are the A515 data for the SC(B) specimens of this study and the SE(B) data of a previous study [3] (with a crack growth restriction as indicated). If the nominal J-Q driving force curve for crack geometry 3 is estimated as shown, then SC(B) measured cleavage toughness values should fall along the curve, within the J-Q toughness locus developed from SE(B) specimens with various a/W. Examination of the values estimated indicates that the data for crack geometry 3 are within the range of the SE(B) J-Q locus. Even if the actual J_c values for this geometry are approximately 50% higher than the estimates, as implied by the data in Figure 7, then the data for the SC(B) geometries would still fall within the J-Q locus. The implication from these results is that the cleavage fracture integrity of a structure can be determined using computer modelling to determine the applicable J-Q driving curve, and the J-Q locus for the material developed from standard fracture specimen laboratory tests coupled with the constraint indexing methodology.

Application of the toughness scaling methodology to the SC(B) data is not as straightforward. The general approach to validate any modelling would be to determine the range of J_o for the A515 from constraint corrected SE(B) data, and then determine the range of predicted J_c for the the two SC(B) geometries from toughness scaling driving force curves for cleavage fracture. Measured data would then be compared to these ranges. At this time, however, the finite element

modelling to develop the driving force curves for the A515 SC(B) specimens has not been completed.

Another approach to utilize the toughness scaling approach to quantify constraint effects in cleavage fracture is possible. The toughness scaling driving force curves for the two SC(B) geometries studied could be matched to approximately equivalent driving force curves of SE(B) specimens [9]. If it were assumed that the J values determined for the experiments of this study were accurate, the implication of the data in Figure 6 is that the toughness scaling driving force curve for an SE(B) specimen with a/W of $\approx$ 0.1 could be used to approximate the response of SC(B) specimen geometry 2. Likewise, the driving force curve for the SE(B) specimen with a/W $\approx$ 0.3 could be used to approximate the response of SC(B) specimen geometry 3.

Future Work

Finite element modelling (3-D) will be conducted to determine the appropriate J and Q values, and toughness scaling driving force curves as a function of the material behavior, loading parameters, and position along the crack front for the two SC(B) geometries tested in this study. This will be coupled with measurements of the angle of cleavage initiation site along the crack front of each of the SC(B) specimens, determined from detailed scanning electron microscopy (SEM). In that way, accurate application of the two methodologies to quantify the effect of constraint on cleavage fracture initiation can be conducted to demonstrate that data from small laboratory specimens with 2-D flaws can be

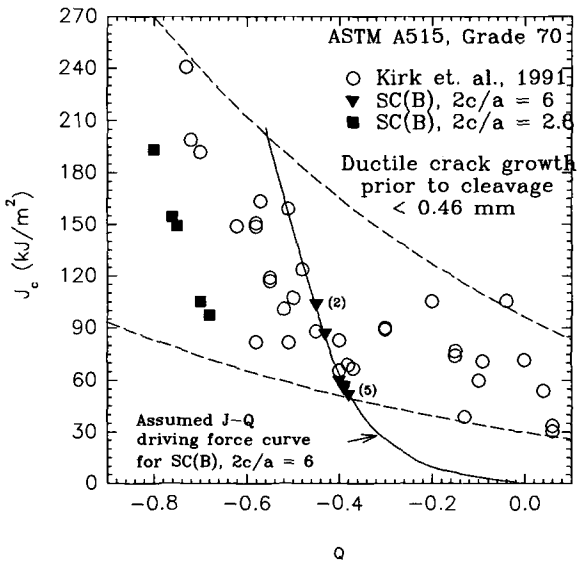


Figure 8--Application of two parameter fracture mechanics methodology. J-Q fracture toughness locus developed from SE(B) data [3].

used to predict the fracture integrity of a structure containing a 3-D flaw. Preliminary SEM has indicated cleavage initiation site angles of approximately 44° and 37° for specimens GGR6-1 and GGR6-2 respectively.

CONCLUSIONS

The following conclusions can be made from the data and analyses presented:

1. Multi-specimen fracture resistance curves for the A515 steel used in this study, developed from SC(B) and SE(B) data, indicated that J_c values estimated for SC(B) specimen geometry 3 were lower than actual J_c values, and those estimated for SC(B) geometry 2 were higher. J_c values estimated are sufficiently accurate for evaluation of methodologies to quantify constraint.
2. Application of the two parameter fracture mechanics (J-Q) methodology to quantify the role of constraint on cleavage fracture toughness appeared effective in predicting the fracture behavior of the structurally relevant surface cracked plate geometry.
3. The data range for SC(B) geometry 2 approximates that of the SE(B) specimen with $a/W \approx 0.1$ and the data range for SC(B) geometry 3 approximates that for the SE(B) specimen with $a/W \approx 0.3$. This result implies that toughness scaling constraint analysis of the SC(B) geometries may be possible by estimating the toughness scaling driving force curves for the two SC(B) geometries from the appropriate SE(B) curves.

ACKNOWLEDGEMENTS

The authors would like to thank Dr. M. T. Kirk for contributing insight to this work through many helpful discussions, and providing the SE(B) data included in this manuscript.

This work was performed at the Carderock Division, Naval Surface Warfare Center, Annapolis Detachment, under the supervision of T. W. Montemarano as part of the program "Fracture Behavior of Naval Alloys Subjected to Explosive Loading Rates". Funding for this work was provided from the Office of Naval Research Ship and Submarine Materials Technology Program administered at CDNSWC by I. L. Caplan.

REFERENCES

1. O'Dowd, N. P. and Shih, C. F., "Family of Crack-Tip Fields Characterized by a Triaxiality Parameter: - Part I. Structure of Fields", *Journal of Mechanics and Physics of Solids*, Vol. 39, pp. 989-1015, 1991.

2. O'Dowd, N. P. and Shih, C. F., "Family of Crack-Tip Fields Characterized by a Triaxiality Parameter: - Part II. Fracture Applications", *Journal of Mechanics and Physics of Solids*, Vol. 40, pp. 939-963, 1992.

3. Kirk, M. T., Koppenhoefer, K. C., and Shih, C. F., "Effect of Constraint on Specimen Dimensions Needed to Obtain Structurally Relevant Toughness Measures." *Constraint Effects in Fracture, ASTM STP 1171*, E. M. Hackett, et al., Eds., American Society for Testing and Materials, Philadelphia, pp. 79-103, 1993.

4. Shih, C. F., O'Dowd, N. P., and Kirk, M. T., "A Framework for Quantifying Crack Tip Constraint," *Constraint Effects in Fracture, ASTM STP 1171*, E. M. Hackett, et al., Eds., American Society for Testing and Materials, Philadelphia, pp. 2-20, 1993.

5. Sumpter, J. D. G., and Forbes, A. T., "Constraint Based Analysis of Shallow Cracks in Mild Steel", *Proceedings of TWI/EWI/IS International Conference on Shallow Crack Fracture Mechanics Test and Applications*, Cambridge, UK, 1992.

6. Anderson, T. L. and Dodds, R. H., Jr., "Specimen Size Requirements for Fracture Toughness Testing in the Transition Region", *Journal of Testing and Evaluation*, Vol. 19, No. 2, pp. 123-134, 1991.

7. Dodds, R. H., Jr., Anderson, T. L., and Kirk, M. T., "A Framework to Correlate a/W Effects on Elastic-Plastic Fracture Toughness (J_c)", *International Journal of Fracture*, Vol. 48, pp. 1-22, 1991.

8. Kirk, M. T., and Dodds, R.H., Jr., "Approximate Techniques of J Estimation Applicable to Part-Through Surface Cracks", *Engineering Fracture Mechanics*, Vol. 43, No. 1, pp. 123-136, 1992.

9. Dodds, R.H., Jr., Shih, C. F., and Anderson, T.L., "Continuum and Micromechanics Treatment of Constraint in Fracture", NUREG/CR-5971, Nuclear Regulatory Commission, Washington, D.C., 36 pp., 1993.

10. Wallin, K., "Statistical Aspects of Constraint with Emphasis on Testing and Analysis of Laboratory Specimens in the Transition Region", *Constraint Effects in Fracture, ASTM STP 1171*, E. M. Hackett, et al., Eds., American Society for Testing and Materials, Philadelphia, pp. 264-288, 1993.

11. Newman, J. C. and Raju, I. S., "Stress-Intensity Factor Equations for Cracks in Three-Dimensional Finite Bodies Subjected to Tension and Bending Loads", NASA Technical Memorandum 85793, NASA Langley Research Center, Hampton, VA, 38 pp., 1984.

Turner, C. E., "Further Developments of a J-Based Design Curve and Its Relationship to Other Procedures", *Elastic Plastic Fracture: Second Symposium, Volume II--Fracture Resistance Curves and Engineering Applications, ASTM STP 803*, C. F. Shih and J. P. Gudas, Eds., American Society for Testing and Materials, pp. II-80--II-102, 1983.

Ainsworth, R. A., "The Assessment of Defects in Structures of Strain Hardening Material", *Engineering Fracture Mechanics*, Vol. 19, No. 4, pp. 633-642, 1984.

Miller, A. G., "Review of Limit Loads of Structures Containing Defects", *International Journal of Pressure Vessels and Piping*, Vol. 32, pp. 197-327, 1988.

Joyce, J. A. and Link, R. E., "Effects of Constraint on Upper Shelf Fracture Toughness", *Fracture Mechanics: 26th Volume, ASTM STP 1256*, Walter G. Reuter, John H. Underwood, and James C. Newman, Jr. Eds., American Society for Testing and Materials, Philadelphia, 35 pp., 1995.

Mark T Kirk[1] *and Yong-Yi Wang*[1]

Wide Range CTOD Estimation Formulae for SE(B) Specimens

REFERENCE: Kirk, M. T., and Wang, Y.-Y., "Wide Range CTOD Estimation Formulae for SE(B) Specimens," Fracture Mechanics: 26th Volume, ASTM STP 1256, Walter G. Reuter, John H. Underwood, and James C. Newman, Jr., Eds., American Society for Testing and Materials, Philadelphia, 1995.

ABSTRACT: Fracture testing of single edge notch bend, SE(B), specimens containing shallow cracks is often undertaken to match constraint conditions between specimen and structure, thereby obtaining a more accurate assessment of structural integrity. However, standardized methods for measuring fracture toughness in terms of the crack-tip opening displacement (CTOD) do not currently provide formulae which relate experimentally measurable quantities to CTOD for shallow cracks. A CTOD estimation equation, based on results from plane-strain finite element analyses, is proposed to fill this gap. This equation applies to specimens having a wide range of crack depths ($0.05 \leq a/W \leq 0.70$) and Ramberg-Osgood work hardening exponents ($4 \leq n \leq 50$). The proposed equation provides CTOD estimates which are up to five times more accurate than those obtained using the procedures recommended by ASTM E1290. This improved accuracy is achieved by estimating the plastic part of CTOD from a work-like quantity rather than as a scalar multiple of $CMOD_{pl}$ (as is done in E1290). Accuracy improvements of the new equation over the E1290 equation are especially notable for materials having a moderate to high work hardening capacity because the linear proportionality that E1290 assumes between $CTOD_{pl}$ and $CMOD_{pl}$ breaks down in the presence of work hardening. A procedure for estimating the value of the work hardening exponent (n) from the results of a simple tension test is presented and validated. Use of this procedure permits routine application of the proposed CTOD estimation equation in the characterization of fracture toughness. The only material property data that is needed to apply this equation in addition to that currently required by E1290 is the ultimate tensile strength.

KEY WORDS: Crack tip opening displacement (CTOD), single edge notch bend (SE(B)) specimen, estimation formula, fracture toughness testing.

Standardized procedures for fracture toughness testing currently require both sufficient specimen thickness to insure predominantly plane strain conditions at the crack tip and a crack depth of at least half the specimen width [1–3]. Within certain limits on load level and crack growth, these restrictions insure the existence of very severe conditions for fracture as described by the Hutchinson Rice Rosengren (HRR) crack-tip fields [4,5]. These conditions make the applied driving force needed to initiate fracture in a laboratory specimen lower than the value needed to initiate fracture in common civil and marine structures where such severe geometric conditions

[1] Manager and Senior Research Engineer, respectively, Numerical Analysis Section, Edison Welding Institute, 1100 Kinnear Road, Columbus, Ohio 43212, USA.

Copyright© 1995 by ASTM International www.astm.org

are not present. As a consequence, structures often carry greater loads without failure than predicted from fracture toughness values measured using standardized procedures.

Fracture testing of single edge notch bend, SE(B), specimens containing shallow cracks is often undertaken to match constraint conditions between specimen and structure, thereby obtaining a more accurate assessment of structural integrity. Both Sumpter [6] and Kirk and Dodds [7] achieved good agreement between the initiation fracture toughness of single edge notched bend, SE(B), specimens and structures containing part–through semi–elliptical surface cracks by matching thickness and crack depth between specimen and structure. These studies show that use of geometry dependent fracture toughness values allows for more accurate prediction of the fracture performance of structures than is possible using more traditional approaches. However, standardized methods for measuring fracture toughness in terms of the crack–tip opening displacement (CTOD) do not currently provide formulae which relate experimentally measurable quantities to CTOD for shallow cracks. Such a formula is developed in this investigation.

Previous Work

Kirk and Dodds [8] performed a comprehensive study of different methods to estimate J and CTOD from test results for SE(B) specimens over a wide range of crack depths and work hardening exponents. This study revealed a fundamental limitation in the applicability of the CTOD estimation formula for SE(B) specimens recommended by ASTM test standard E1290 [2]:

$$\text{CTOD} = \frac{K^2(1-\nu^2)}{m\sigma_{ys}E} + \frac{r_{pl}\,b\,CMOD_{pl}}{r_{pl}\,b + a} \quad \text{for } 0.45 \le a/W \le 0.55 \tag{1}$$

where

K	linear elastic stress intensity factor,
ν	Poisson's ratio,
b	remaining ligament, $W-a$,
m	constraint factor, = 2 for the SE(B) specimen
σ_{ys}	yield stress,
r_{pl}	plastic rotation factor, = 0.44 for the SE(B) specimen,
$CMOD_{pl}$	plastic component of *CMOD*.

Making the substitution

$$\eta_\delta = \frac{r_{pl}\,b}{r_{pl}\,b + a} \tag{2}$$

allows re–expression of eqn. (1) as follows:

$$\text{CTOD} = \frac{K^2(1-\nu^2)}{m\sigma_{ys}E} + \eta_\delta CMOD_{pl} \tag{3}$$

Thus, eqn. (1), which was derived assuming rotation of the arms of the SE(B) specimen about a plastic hinge formed on the uncracked ligament, assumes a linear proportionality between the plastic components of CTOD and *CMOD*. This proportionality breaks down for work hardening materials because the elastic portion of CTOD must increase in proportion to increasing load. The nonlinear relationship between the plastic components of CTOD and *CMOD* for work hardening materials causes

CTOD values estimated by eqn. (1) to err by a considerable margin (Kirk and Dodds [8] report RMS errors of up to 25%). Figure 1 shows the break down in linearity with increasing work hardening level for deeply cracked SE(B)s; this behavior occurs in shallow cracked specimens as well.

Beyond their findings on the ASTM E1290 CTOD estimation formula, Kirk and Dodds [8] also proposed the following new J estimation formula:

$$J = \frac{K^2(1-\nu^2)}{E} + \frac{\eta_{J-C}}{Bb} A_{pl}|_{CMOD} \tag{4}$$

where

K linear elastic stress intensity factor,

ν Poisson's ratio,

η_{J-C} eta factor (here the $-J$ subscript denotes that this is a proportionality factor that relates measurable variables to J while the $-C$ denotes that the measured variable is $CMOD$),

B specimen thickness,

b remaining ligament, $W-a$,

$A_{pl}|_{CMOD}$ area under the load vs. plastic crack mouth opening displacement ($CMOD$) curve.

Use the area under the load vs. plastic–$CMOD$ curve to estimate the plastic part of J, rather than the area under the load vs. plastic load line displacement curve as is more typical, provides a proportionality constant relating the plastic part of J to the experimentally measured area that is insensitive to the material's work hardening capacity. In eqn. (4), η_{J-C} is a function only of crack depth:

$$\eta_{J-C} = 3.785 - 3.101\frac{a}{W} + 2.018\left(\frac{a}{W}\right)^2 \quad \text{for } 0.05 \le a/W \le 0.70 \tag{5}$$

Specific η_{J-C} values are given in Table 1 and in Figure 2. Work hardening insensitivity of the proportionality constant relating J to measurable quantities is desirable

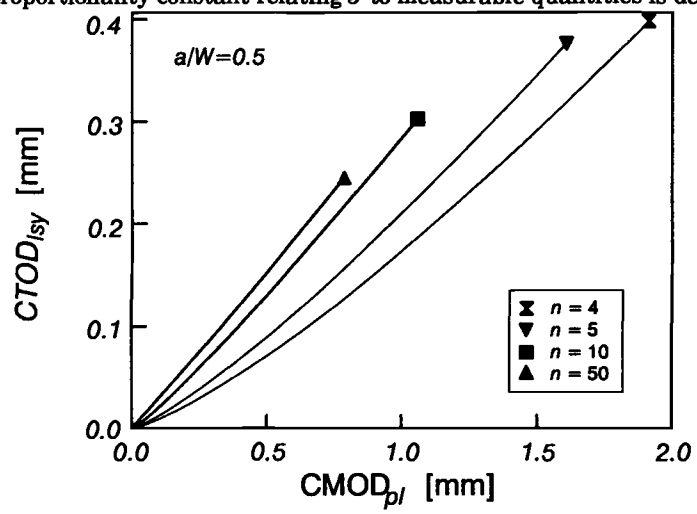


Figure 1: Effect of strain hardening on the linearity of the large-scale yielding part of CTOD ($CTOD_{lsy}$) and the plastic part of $CMOD$ ($CMOD_{pl}$) for an a/W=0.50 SE(B) specimen [8].

so that the selection of a η_{J-C} value corresponding to a specific material does not become a potential error source. In view of the ambiguity attendant to fitting experimental stress–strain data with a power law curve, insensitivity of η_{J-C} to material work hardening is extremely advantageous. Further, material insensitivity of η_{J-C} eliminates the need to perform companion tensile testing as part of a fracture toughness characterization effort.

In their previous work, Kirk and Dodds [8] noted that none of the CTOD estimation strategies they investigated had the desirable characteristic of work hardening insensitivity that the J estimation formula of eqn. (4) has. Their results on CTOD estimation strategies are re–examined herein. While a CTOD estimation strategy with the same work hardening insensitivity of eqn. (4) remains illusive, the uncertainty introduced by imprecise knowledge of the work hardening capacity of the material being tested is not as significant as previously suspected.

Table 1: Summary of η_{J-C} coefficients proposed by Kirk and Dodds [8] for SE(B) Specimens.

	Ramberg–Osgood work hardening exponent (n)			
a/W	4	5	10	50
0.05	3.848	3.793	3.482	3.420
0.15	3.359	3.385	3.322	3.376
0.25	3.152	3.138	3.130	3.137
0.50	2.748	2.749	2.728	2.723
0.70	2.613	2.641	2.595	2.562

Approach

Results from the two dimensional, plane–strain finite–element analyses of SE(B) specimens previously reported by Kirk and Dodds [8] for crack depths from 0.05 to

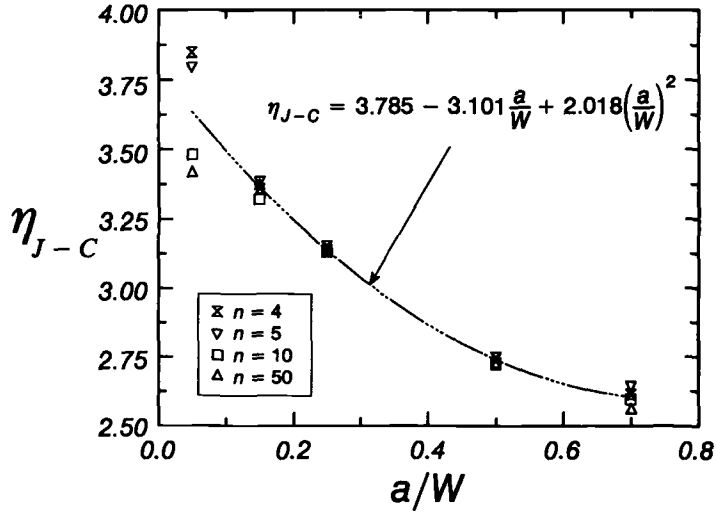


Figure 2: Variation of η_{J-C} with crack depth and material work hardening exponent, after Kirk and Dodds [8].

0.70 a/W with Ramberg–Osgood work hardening exponents (n) between 4 and 50 are re–examined to develop a CTOD estimation formula applicable across this range of conditions. This proposed formula is compared with that recommended by the current ASTM standard for determination of CTOD values from deeply cracked specimens, E1290. Two techniques are examined for estimating the work hardening exponent of a particular material from simple tension test data (i.e. yield and ultimate strength). The influence of imprecise knowledge of the work hardening exponent on the accuracy with which CTOD can be estimated using the proposed formula is then assessed. Finally, the applicability of the proposed CTOD estimation formula to analysis of tests performed using "real" materials, i.e. materials that obey an incremental rather than a deformation plasticity material model, is examined.

Finite Element Modelling

Two–dimensional, plane strain finite–element analyses of SE(B) specimens are performed using conventional small strain theory. The analyses are conducted using the POLO–FINITE analysis software [9] on an engineering workstation.

Uniaxial stress strain behavior is described using the Ramberg–Osgood model

$$\frac{\varepsilon}{\varepsilon_o} = \frac{\sigma}{\sigma_o} + \alpha\left(\frac{\sigma}{\sigma_o}\right)^n \tag{6}$$

where σ_o is the reference stress (0.2% offset yield stress when $\alpha = 1$), $\varepsilon_o = \sigma_o/E$ is the reference strain, $\alpha = 1$, and n is the work hardening exponent. work hardening exponents of 4, 5, 10, and 50 model materials ranging from highly work hardening to nearly elastic – perfectly plastic. Figure 3 illustrates these stress – strain curves.

J_2 deformation plasticity theory (nonlinear elasticity) describes the multi–axial material model. Total strains and stresses are related by

$$\varepsilon_{ij} = \left[\frac{1+\nu}{E} + \frac{3\alpha\varepsilon_o}{2\sigma_o}\left(\frac{\sigma_e}{\sigma_o}\right)^{n-1}\right]s_{ij} + \frac{1-2\nu}{3E}\sigma_{kk}\delta_{ij}, \quad \sigma_e = \sqrt{\frac{3}{2}s_{ij}s_{ij}} \tag{7}$$

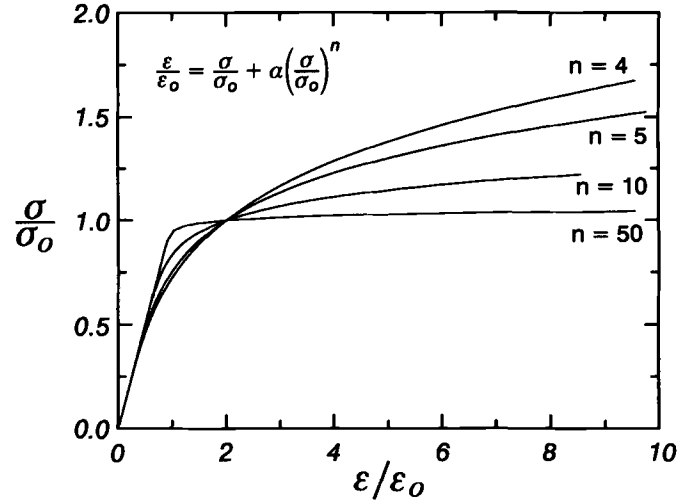


Figure 3 Ramberg–Osgood stress strain curves used in the finite–element

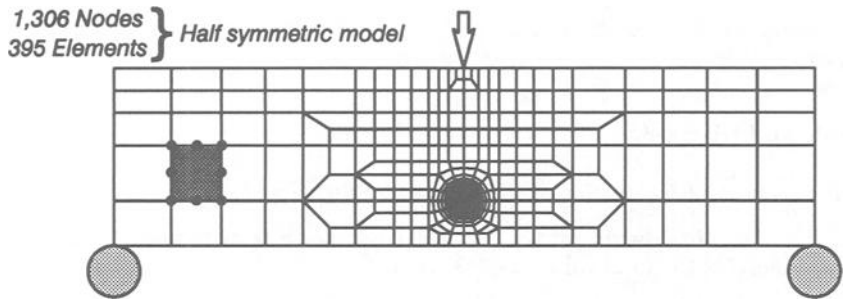


Figure 4: Finite–element model of the a/W=0.25 SE(B) specimen.

where s_{ij} is the stress deviator, σ_e is the Mises equivalent tensile stress, σ_{kk} is the trace of the stress tensor, and δ_{ij} is the Kronecker delta.

Finite–element models are constructed for a/W ratios of 0.05, 0.15, 0.25, 0.50, and 0.70. The SE(B) specimens have standard proportions; the unsupported span is four times the specimen width. Symmetry of both geometry and loading permit use of a half–symmetric model. Each model contains approximately 400 elements and 1300 nodes; the $a/W = 0.25$ model is shown in Figure 4. Eight–noded, plane–strain isoparametric elements are used throughout. Reduced (2 x 2) Gaussian integration is used to eliminate locking of the elements under incompressible plastic deformation. The same half–circular core of elements surrounds the crack tip in all models. This core consists of eight, equally sized wedges (22.5° each) of elements in the θ direction. Each wedge contains 30 quadrilateral elements; the radial dimension decreases geometrically with decreasing element distance to the crack tip. The eight crack–tip elements are collapsed into wedges with the initially coincident nodes left unconstrained to permit development of crack–tip blunting deformations. The side nodes of these elements are retained at the mid–point position. This modelling produces a $1/r$ strain singularity appropriate in the limit of perfect plasticity. Crack–tip element sizes range from 0.2% to 0.02% of the crack length depending on the a/W modelled.

Load is distributed uniformly over two small elements and applied at the center of the compression face of the specimen to eliminate the local singularity effects caused by a concentrated nodal load. Load is increased in 30 to 50 variably sized steps until the CTOD reaches 5% of the crack length. Strict convergence criteria at each step insure convergence of calculated stresses and strains to the third significant figure. Two to three full Newton iterations at each load step are required to satisfy this criteria. As deformation plasticity is strain path independent, converged solutions are load step size invariant.

The J–integral is computed at each load step using a domain integral method [10,11]. J values calculated over domains adjacent to and remote from the crack tip are within 0.003% of each other, as expected for deformation plasticity. CTOD is computed from the blunted shape of the crack flanks using the $\pm$ 45° intercept procedure. The η and m coefficients are determined from these results by calculating the slope of the quantities indicated in Table 2 at each load step. Slope calculation is initiated with data from the final three load steps. Data from earlier load steps are included in this calculation until the linear correlation coefficient (r) falls below 0.999. This procedure eliminates data from the first few load steps, which are predomi-

nantly elastic, and therefore not expected to provide reliable relationships between plastic quantities.

Results and Discussion

A New Proposal for Estimation of CTOD from a SE(B) Test Record

A proportionality coefficient typically referred to as m is often used to relate the total value of J to the total value of CTOD:

$$\text{CTOD} = \frac{J}{m\sigma_{flow}} \tag{8}$$

Table 2 summarizes m values reported by Kirk and Dodds [8] for SE(B) specimens while Figure 5 shows how m varies with crack depth and with work hardening exponent. The trends in Figure 5 suggest a bi–linear variation of m with both a/W and $1/n$. A least squares fit to the data of Figure 5 produces the following relationship:

$$m = 1.221 + 0.793\frac{a}{W} + 2.751\frac{1}{n} - 1.418\frac{a}{Wn} \tag{9}$$

Combination of eqns. (4), (5), (8), and (9) provides the following CTOD estimation strategy for SE(B) specimens having $0.05 \leq a/W \leq 0.75$ and $4 \leq n \leq 50$:

$$\text{CTOD} = \frac{1}{m\sigma_{flow}}\left[\frac{K^2(1-\nu^2)}{E} + \frac{\eta_{J-C}}{Bb}A_{pl}|_{CMOD}\right] \tag{10}$$

where

$$\eta_{J-C} = 3.785 - 3.101\frac{a}{W} + 2.018\left(\frac{a}{W}\right)^2$$

$$m = 1.221 + 0.793\frac{a}{W} + 2.751\frac{1}{n} - 1.418\frac{a}{Wn}$$

The accuracy of eqn. (10) is checked by using it to predict the finite element data from which it was derived. Figure 6 illustrates the variation of CTOD with *CMOD* for an a/W=0.15, n=5 SE(B) determined by finite element analysis. This is compared with the variation of CTOD with *CMOD* predicted by eqn. (10). Figure 7 shows CTOD estimation errors, more clearly illustrating the differences between eqn. (10) and the finite element data . To evaluate the effects of both a/W and n on the estimation accuracy of eqn. (10) across its entire range of applicability, the following error measure is defined:

Table 2: Summary of m coefficients proposed by Kirk and Dodds [8] for SE(B) Specimens.

	Ramberg–Osgood Work Hardening Exponent (n)			
a/W	4	5	10	50
0.05	1.908	1.786	1.496	1.291
0.15	1.963	1.863	1.573	1.423
0.25	2.036	1.938	1.648	1.501
0.50	2.177	2.047	1.788	1.687
0.70	2.200	2.093	1.932	1.810

$$\overline{ERR} = \sum_{i=1}^{N} |E_i CTOD^{fe}{}_i| \Big/ \sum_{i=1}^{N} CTOD^{fe}{}_i \tag{11}$$

where

$$E_i = \frac{CTOD^{est}{}_i - CTOD^{fe}{}_i}{CTOD^{fe}{}_i} 100, \quad \text{percent error at load step } i$$

N total number of load steps

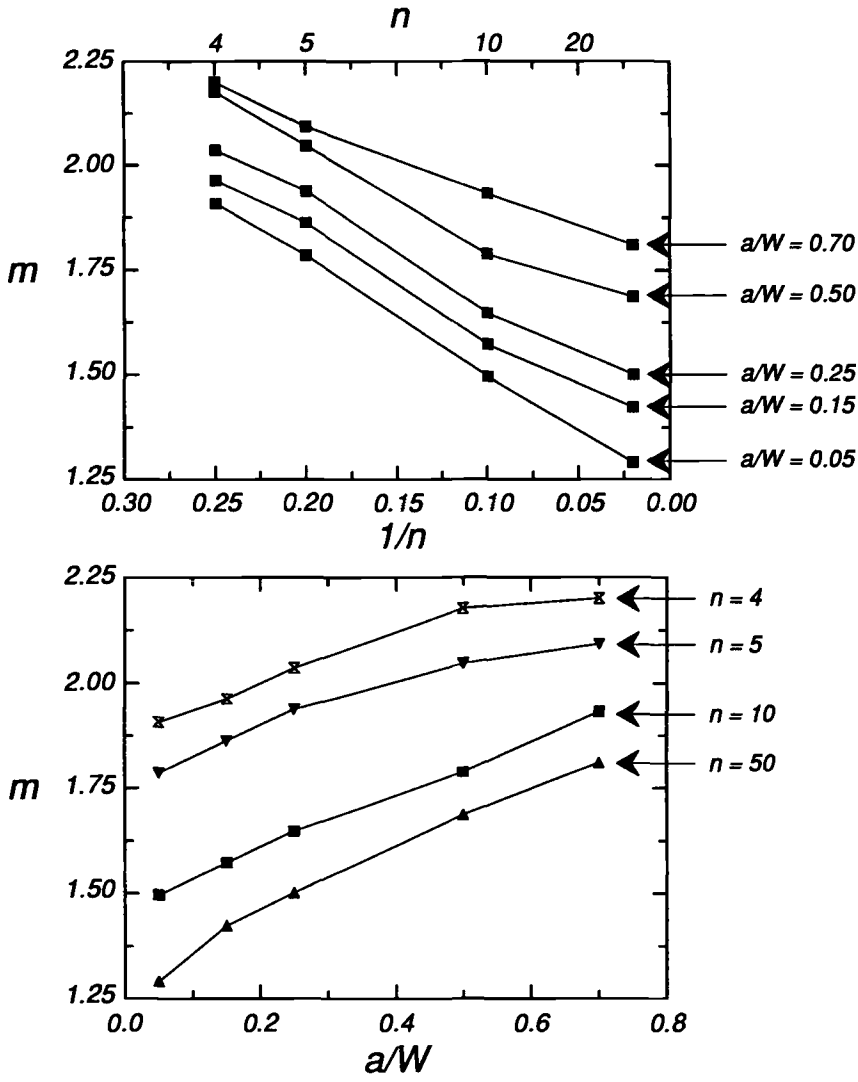


Figure 5: The variation of m values with crack length and work hardening exponent [8].

$CTOD^{est}_i$ estimated CTOD at load step i

$CTOD^{fe}_i$ CTOD at load step i from finite element analysis

For an a/W=0.15 / n=5 SE(B), the $\overline{ERR}$ value for CTOD estimation using eqn. (10) is 5.7%. Comparison of this value with the data in Figure 7 demonstrates that $\overline{ERR}$ is a root mean square error measure. The variation of $\overline{ERR}$ values for eqn. (10) with a/W and n is shown in Figure 8; a similar plot giving prediction errors for the ASTM E1290 equation is shown in Figure 9. Comparison of these data reveals that the new proposal (eqn. (10)) provides estimates of CTOD for SE(B) specimens that are up to five times more accurate than can be achieved using the ASTM E1290 formula (eqn. (1)). Accuracy improvements of the new equation over the E1290 equation are especially notable for materials having a moderate to high work hardening capacity because the linear proportionality that E1290 assumes between $CTOD_{pl}$ and $CMOD_{pl}$ breaks down in the presence of work hardening.

Estimation of the Work Hardening Exponent

The analysis presented in the preceding section demonstrates that eqn. (10) provides a good fit to the data from which it was derived and is far more accurate than eqn. (1) over a wide range of a/W and n. Unfortunately, eqn. (10) depends on the material work hardening exponent through the relation for m of eqn. (9). This dependency can complicate the application of the eqn. (10) due to uncertainties associated with estimation of a value for the Ramberg–Osgood work hardening exponent from stress – strain data, an activity for which no ASTM standard currently exists. As an alternative to direct estimation of n from experimental data, two techniques are examined for estimating n from the ratio of the ultimate strength to the yield strength ($\mathbf{R} = \sigma_{uts}/\sigma_{ys}$). These techniques are as follows:

1. From Constancy of Volume during Plastic Flow: The ultimate tensile strength of a Ramberg–Osgood material is obtained by finding the point on the true stress – true strain curve having a subtangent of unity (i.e. the tensile instability point), converting true stress to engineering stress, and taking the ratio of this value with 0.2% offset yield stress. This approach is described by Dieter [12] and was originally proposed by Considère [13]. These manipulations provide the following relation between the ratio between the ultimate and yield strengths and n:

$$\mathbf{R} = \frac{\sigma_{uts}}{\sigma_{ys}} = \left(\frac{1}{0.002n}\right)^{\frac{1}{n}} \Big/ \exp\left(\frac{1}{n}\right) \tag{12}$$

2. By Empirical Correlation: Barsom and Rolfe [14] provide an empirical relationship between the ultimate to yield strength ratio and the work hardening exponent for pressure vessel and construction grade steels ranging in yield strength from 207 to 1034 MPa (30 to 150 ksi). The mathematical form of this relation is as follows:

$$\mathbf{R} = \frac{\sigma_{uts}}{\sigma_{ys}} = \frac{(1/n)^{0.25}}{0.46} \tag{13}$$

Figure 10 shows the variation of $1/n$ with $\mathbf{R}$ calculated from eqns. (12) and (13). This plot also presents the data from which eqn. (13) was derived as well as more recent data reported by James for A302–B steel [15]. These data demonstrate that neither the empirical correlation, eqn. (13), or the constant volume relation, eqn. (12), provide a good mean fit to all of the available data. Within the mid–range ($1.1 \leq \mathbf{R} \leq$

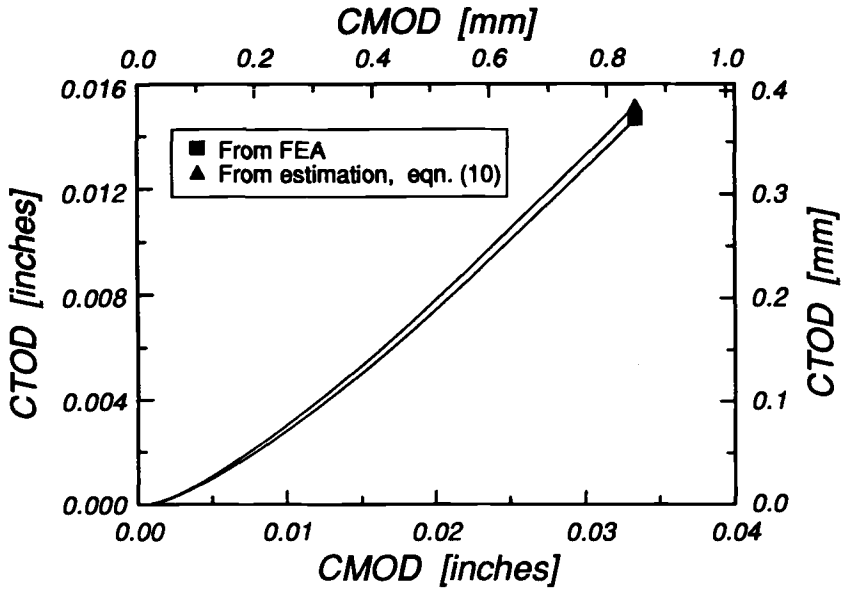


Figure 6: Variation of CTOD with *CMOD* for an a/W=0.15, n=5 SE(B).

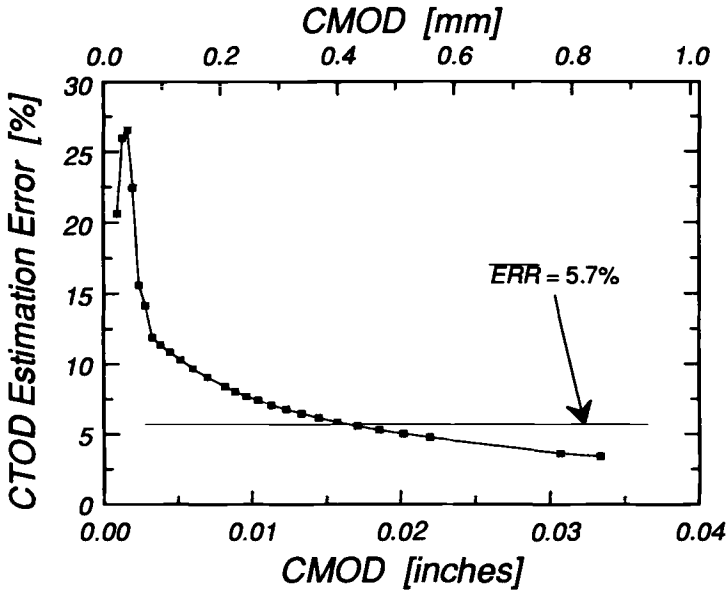


Figure 7: CTOD estimation error from eqn. (10) for an a/W=0.15, n=5 SE(B).

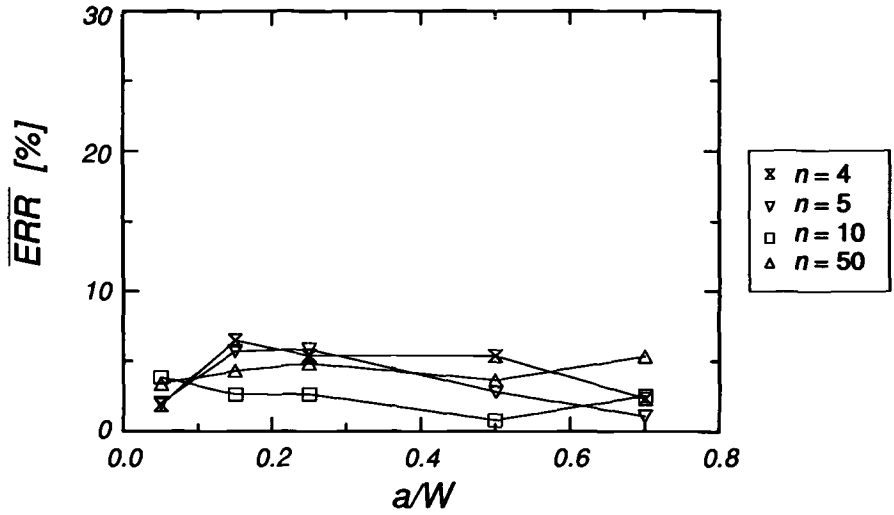


Figure 8: Variation of CTOD estimation errors from the proposed CTOD estimation equation (eqn. (10)) with a/W and n.

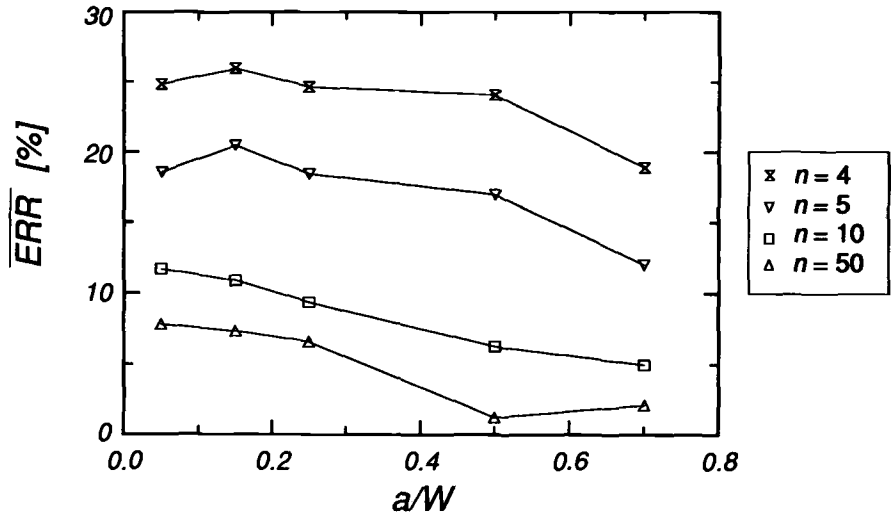


Figure 9: Variation of CTOD estimation errors from the ASTM E1290 CTOD estimation equation (eqn. (1)) with a/W and n [8].

1.6) eqn. (13) appears reasonably accurate. For materials having a post–yield flow behavior that is nearly perfectly plastic ($\mathbf{R} \rightarrow 0$), eqn. (13) under estimates the work hardening exponent. Moreover, the empirical correlation estimates uncharacteristically low values of n for highly work hardening materials ($\mathbf{R} \geq 1.75$) as a consequence of the limited data for these materials. These observations, combined with the scatter exhibited by the experimental data, make it difficult to identify the better

of eqns. (12) and (13) based on this information alone. This issue is examined further in the following section.

Applications of the Proposed CTOD Estimation Strategy to Real Materials

In the preceding section an attempt was made to develop a relationship between the ratio of the ultimate strength to the yield strength and the Ramberg–Osgood work hardening exponent to facilitate routine application of eqn. (10). However, certain ambiguities remain. Furthermore, the issue of the applicability of the proposed CTOD estimation strategy, eqn. (10), which was derived from finite element results for a non–linear elastic material, to "real" materials which obey an incremental plasticity material model, has not been addressed. These issues are reconciled in this section.

Four additional finite element analyses are performed using ABAQUS. An incremental plasticity material model is adopted to represent the two measured stress – strain curves shown in Figure 11. Aside from the material model, all analysis details for these computations are similar to those described previously. These two steels are selected to represent approximate extremes of work hardening capacity typical of construction, marine, and pressure vessel grade steels. The high work hardening steel is A78 Grade B. A78 is a C–Mn construction grade steel made to an old ASTM standard which was discontinued in 1946; it is similar in composition and properties to ASTM A36. A78 has a work hardening capacity typical of many low strength steels found throughout our aging infrastructure (e.g. storage tanks, pipelines, bridges, and commercial ships). Conversely, the higher strength steel (Supralism 690) has limited capacity to work harden. This is characteristic of many of the newer generation steels which are finding applications in high pressure pipelines, offshore structures, naval combatants, and other critical applications. Two SE(B) geometries, one shallow crack (a/W=0.1) and one deep crack (a/W=0.5), are modelled using each material. The yield strength, ultimate strength, and n values (determined using eqns. (12) and (13)) for each steel are summarized in Table 3.

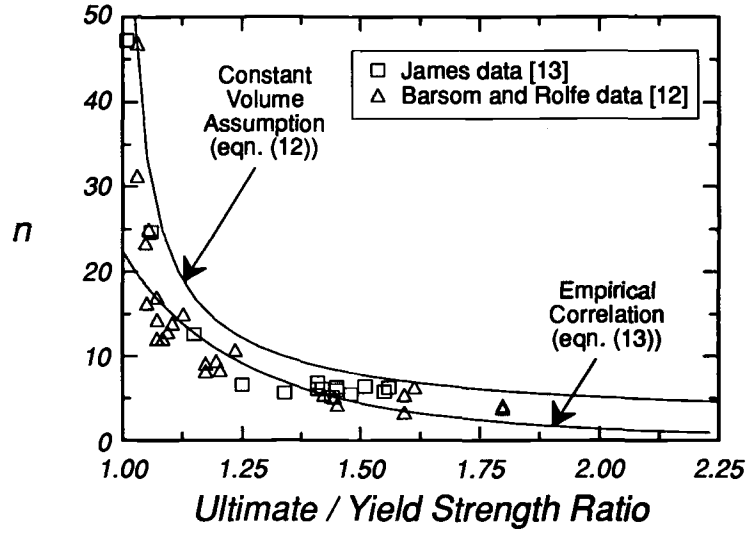


Figure 10: The variation of n with the ratio of ultimate to yield strength.

Table 3: Summary of tensile data and calculated n values for the two steels modelled using incremental plasticity.

Property	ASTM A78 Grade B	Supralism 690
Work Hardening Capacity	High	Low
Yield Strength [MPa I ksi]	193 I 28	758 I 110
Ultimate Strength [MPa I ksi]	414 I 60	841 I 122
Flow Strength [MPa I ksi]	303 I 44	800 I 116
Ultimate / Yield Strength Ratio	2.14	1.11
n from constant volume assumption, eqn. (12)	4.8	21.2
n from empirical correlation, eqn. (13)	1.1	14.7

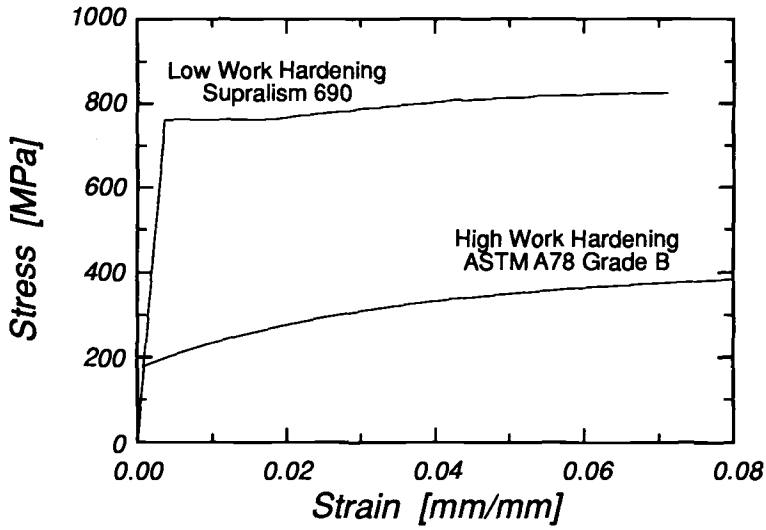


Figure 11: Measured stress–strain curves for two steels used as input to the finite element analysis using an incremental plasticity material model.

Figure 12 presents the variation of CTOD with *CMOD* determined by these finite element analyses along with the variation predicted by eqn. (10) using the n values from Table 3. Table 4 summarizes the $\overline{ERR}$ values for each analysis / n value combination. For the low work hardening steel both conversions between σ_{uts}/σ_{ys} and n produce CTOD estimates of approximately equal accuracy. However, for moderate to highly work hardening materials, the empirical correlation, eqn. (13), clearly under–

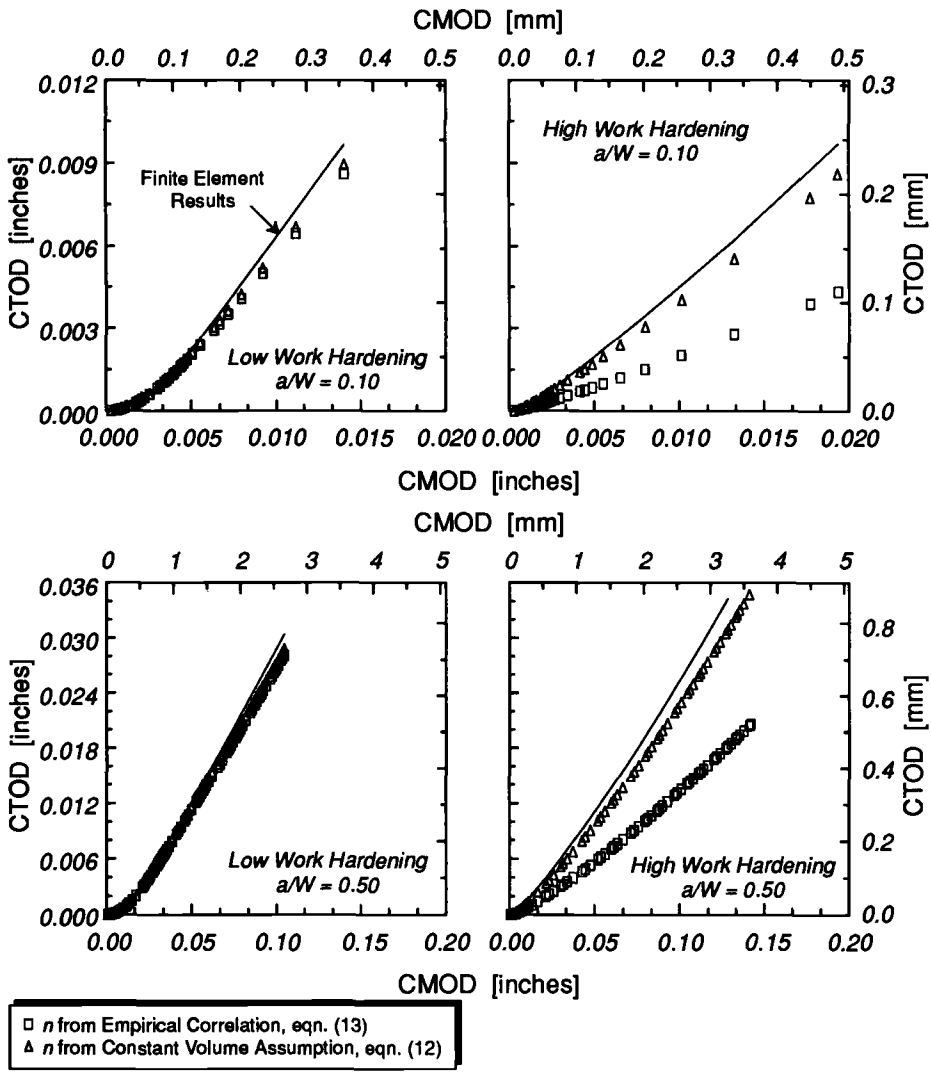


Figure 12: Comparison of the variation of CTOD with *CMOD* predicted by finite element analysis and that predicted by eqn. (10) using two different values for n estimated from the ultimate to yield strength ratio.

estimates the value of n, predicting a value of 1.1. A value of 1 represents a purely elastic response; examination of Figure 11 shows that the stress–strain response of A78 is far from purely elastic. This inadequacy leads to CTOD estimates based on eqn. (10) that are far from accurate for both shallow and deeply cracked specimens ($\overline{ERR}$ = 55% and 47%, respectively) when eqn. (13) is used to estimate n. These analyses indicate that the best CTOD estimation is obtained when a constant volume as-

sumption eqn.(12) is used to estimate the work hardening coefficient from the ratio of the ultimate strength to the yield strength.

Table 4: Summary of RMS error values from the four incremental plasticity analysis of SE(B) specimens.

a/W	Material	Work Hardening Capacity	n	Equation n is determined from[1]	*ERR* [%]
0.10	ASTM A78 Grade B[2]	High	1.1	(13)	55.1
			4.8	(12)	10.7
	Supralism 690[3]	Low	14.7	(13)	8.1
			21.2	(12)	6.1
0.50	ASTM A78 Grade B	High	1.1	(13)	47.4
			4.8	(12)	10.6
	Supralism 690	Low	14.7	(13)	7.4
			21.2	(12)	5.1

Notes: (1) Eqn. (12) is the constant volume assumption while eqn. (13) is the empirical correlation.
(2) A C–Mn construction grade steel made to an old ASTM standard. Similar in composition and properties to ASTM A36.
(3) A proprietary high strength steel manufactured by Fabrique de Fer de Charleroi.

Summary and Conclusions

The following CTOD estimation equation is developed for single edge notch bend specimens based on results from plane–strain finite element analyses:

$$\text{CTOD} = \frac{1}{m\sigma_{flow}}\left[\frac{K^2(1-\nu^2)}{E} + \frac{\eta_{J-C}}{Bb}A_{pl}|_{CMOD}\right]$$

where

$$\eta_{J-C} = 3.785 - 3.101\frac{a}{W} + 2.018\left(\frac{a}{W}\right)^2$$

$$m = 1.221 + 0.793\frac{a}{W} + 2.751\frac{1}{n} - 1.418\frac{a}{Wn}$$

and n is estimated from the σ_{uts}/σ_{ys} ratio determined from a simple tension test:

$$\mathbf{R} = \frac{\sigma_{uts}}{\sigma_{ys}} = \left(\frac{1}{0.002n}\right)^{\frac{1}{n}} \Big/ \exp\left(\frac{1}{n}\right)$$

This equation applies to specimens having crack depths (a/W) between 0.05 and 0.70 and Ramberg–Osgood work hardening exponents (n) between 4 and 50. It's applicability to steels obeying an incremental plasticity model is demonstrated. The equation provides CTOD estimates which are up to five times more accurate than those obtained using the equation recommended by ASTM E1290, which is funda-

mentally in error for moderate to highly work hardening materials. It should be noted that this equation contains no crack growth correction and, consequently, applies only to the determination of initiation toughness values.

References

[1] ASTM Standard Test Method for J_{Ic}, A Measure of Fracture Toughness, E813–89.

[2] ASTM Standard Test Method for Crack–Tip Opening Displacement (CTOD) Fracture Toughness Measurement, E1290–89.

[3] BS 5762: 1979, "Methods for Crack Tip Opening Displacement (*COD*) Testing," British Standards Institution, London, 1979.

[4] Hutchinson, J.W., "Singular Behavior at the End of a Tensile Crack in a Hardening Material," *Journal of Mechanics and Physics of Solids*, Vol. 16, pp. 13–31, 1968.

[5] Rice, J.R., and Rosengren, G.F., "Plane Strain Deformation Near a Crack Tip in a Power–Law Hardening Material," *Journal of Mechanics and Physics of Solids*, Vol. 16, pp. 1–12, 1968.

[6] Sumpter, J.D.G., "Prediction of Critical Crack Size in Plastically Strained Welded Panels," *Nonlinear Fracture Mechanics: Volume II – Elastic–Plastic Fracture, ASTM STP 995*, J.D. Landes, A. Saxena, and J.G. Merkle, eds., American Society for Testing and Materials, pp. 415–432, 1989.

[7] Kirk, M.T., and Dodds, R.H., "An Analytical and Experimental Comparison of J_i Values for Shallow Through and Part Through Surface Cracks," *Engineering Fracture Mechanics*, Vol. 39, No. 3, pp. 535–551, 1991.

[8] Kirk, M.T., and Dodds, R.H., "*J* and *CTOD* Estimation Equations for Shallow Cracks in Single Edge Notch Bend Specimens," *Journal of Testing and Evaluation*, JTEVA, Vol. 21, No. 4, July 1993, pp. 228–238.

[9] Dodds, R.H., and Lopez, L.A., "Software Virtual Machines for Development of finite–element Systems," *International Journal for Engineering with Computers*, Vol. 13, pp. 18–26, 1985.

[10] Li, F.Z., Shih, C.F., and Needleman, A., "A Comparison of Methods for Calculating Energy Release Rates," *Engineering Fracture Mechanics*, Vol. 21, pp. 405–421, 1985.

[11] Shih, C.F., Moran, B., and Nakamura, T., "Energy Release Rate Along a Three–Dimensional Crack Front in a Thermally Stressed Body," *International Journal of Fracture*, Vol. 30, pp. 79–102, 1986.

[12] Dieter, G.E., *Mechanical Metallurgy*, Third Edition, McGraw–Hill Book Co., New York, pp. 289–290, 1986.

[13] Considère, A., *Ann. ponts et chaussées*, Vol. 9, Ser. 6, pp. 574–775, 1885.

[14] Barsom, J.M., and Rolfe, S.T., *Fracture and Fatigue Control in Structures – Applications of Fracture Mechanics*, Prentice Hall, Inc., Englewood Cliffs, New Jersey, 1987.

[15] James, L.A., "Ramberg–Osgood Strain–Hardening Characterization of an ASTM A302–B Steel," Accepted for publication by the *Journal of Pressure Vessel Technology*.

James A. Joyce[1] and Richard E. Link[2]

EFFECTS OF CONSTRAINT ON UPPER SHELF FRACTURE TOUGHNESS

REFERENCE: Joyce, James A. and Link R.E., Effects of Constraint on Upper Shelf Fracture Toughness," Fracture Mechanics: 26th Volume, ASTM STP 1256, Walter G. Reuter, John H. Underwood and James C. Newman, Jr., Eds., American Society for Testing and Materials, Philadelphia, 1995.

ABSTRACT: The upper shelf fracture toughness and tearing resistance of two structural steels, HY-100 and ASTM A533, Gr. B, were determined over a wide range of applied constraint. The constraint conditions were varied by changes in specimen geometry and loading mode. Bend specimens with shallow and deep cracks, compact specimens, and single and double edge notched tension specimens were used in this study. A rotation correction was developed for the single edge notch tension specimen which greatly improved the behavior of the J-R curves determined using this specimen. The experimental results were used to investigate the applicability of the Q and T stress parameters to the correlation of upper shelf initiation toughness, J_{Ic}, and tearing resistance, T_{mat}. The J-Q and J-T stress loci, and corresponding plots of material tearing resistance plotted against Q and T, were developed and compared with the expectations of the O'Dowd and Shih and the Betégon and Hancock analyses. The principle conclusions of this work are that J_{Ic} does not appear to be dependent on T stress or Q while the material tearing resistance, T_{mat}, is dependent on T stress and Q, with the tearing modulus increasing as constraint decreases.

KEYWORDS: fracture toughness, constraint effects, elastic-plastic fracture, upper shelf fracture, J integral, ductile fracture, rotation correction, T stress, Q, J_{Ic}, tearing modulus

[1] Professor of Mechanical Engineering, U.S. Naval Academy, Annapolis, MD 21402-5067 USA

[2] Senior Mechanical Engineer, Naval Surface Warfare Center, Fatigue and Fracture Branch, Annapolis, MD 21402-5067 USA.

Copyright © 1995 by ASTM International www.astm.org

OBJECTIVES

Constraint has been an important consideration in fracture mechanics from the earliest work that was done to develop the 1974 version of the ASTM Standard E399. Stringent thickness and size requirements, expressed in terms of the plastic zone size, were placed on the test samples. These requirements often invalidated the results in practical application sizes. The restrictions have been retained in later revisions, often requiring the engineer to test in his application thickness and to work generally with "invalid" data, using engineering judgement and experience to avoid catastrophic failure of his structure. Similar size requirements have been incorporated into more recent elastic-plastic fracture test standards like ASTM E813 and ASTM E1152, even though experimental data has not shown a clear and direct relationship between specimen size and the resulting initiation toughness or the resistance curve shape.

O'Dowd and Shih[1] have proposed that the difference in crack tip stress fields between the SSY solution and the finite body solution can be quantified in terms of a field quantity that they have called Q. The Q quantity is a function of J, the crack shape and size, the structural geometry, mode of loading and on the level of deformation and can only be calculated from a high resolution elastic-plastic computational analysis. O'Dowd and Shih propose that a J-Q fracture locus can be developed experimentally for a particular material, with higher Q's meaning higher constraint and resulting in lower J measures at cleavage or at ductile crack initiation, or at whatever critical measurement point is to be used. This procedure avoids the need to start with a fracture criterion, which is a serious difficulty if one wishes to apply a toughness scaling approach[2] to the case of ductile crack extension. Examples of a J-Q fracture locus for the case of cleavage have been developed by Kirk, Koppenhoeffer and Shih[3] and also by Sumpter and Forbes[4] and these results seem to support the J-Q concept.

A similar, simpler, but more controversial approach has been suggested by Betégon and Hancock[5] who use the first non-singular term of the elastic crack-tip stress field solution[6] as a measure of elastic-plastic crack tip constraint. This quantity has been called the "T-stress", a notation used by Larsson and Carlsson[7] who studied the effect of this term on the crack tip stress field. This quantity is only dependent on the initial geometry and loading and hence is relatively easy to calculate, and is available in the literature for many geometries. The application of this elastic quantity to elastic-plastic fracture is highly controversial, but published results have shown good correlation[8] and the ease of use is a strong selling point for this parameter.

The objective of this work is to develop some upper shelf, elastic-plastic experimental results to investigate the applicability of the Q and T stress parameters to the correlation of upper shelf initiation toughness and J resistance curves. The first objective was to obtain upper shelf J resistance curves, J_{Ic}, and tearing resistance, T_{mat}, results for a range of applied constraint. The J-Q and J-T stress

loci were developed and compared with the expectations of the O'Dowd and Shih and the Betégon and Hancock analyses. Constraint was varied by changing the crack length and also by changing the mode of loading from bending to predominantly tensile. Test techniques and analysis have been developed as needed for the low constraint fracture test geometries. Two materials have been used in this study, an HY-100 high strength structural steel and an A533B pressure vessel steel. Some of the results for the HY-100 steel have been reported previously[9], but they are repeated again here to demonstrate the consistency of the results found for the two materials.

EXPERIMENTAL DETAILS

Material Description

Two structural steels were tested in this study. The first material was HY-100, a high strength structural steel with tensile mechanical properties and chemistry as shown in Table 1. This material was from a 6.35 cm thick plate and all specimens were oriented so that the crack plane was in the T-L direction as designated by ASTM E399. The second material was an ASTM A533 Grade B pressure vessel steel with the tensile mechanical properties and chemistry also shown in Table 1. The plate for this material was originally 21.5 cm thick, but for these tests all samples were cut from the center 15 cm. All specimens of this material were oriented in the L-T orientation.

Specimen Details

Four distinct test geometries were studied in this work: the standard 1T compact, C(T), specimen; the single edge-notched bend, SE(B), specimen; the single edge-notched tensile, SE(T), specimen that was pin-loaded and the double edge-notched tensile, DE(T), specimen, also pin-loaded. The SE(B) specimens were tested in a standard deep notched configuration with crack length to specimen width ratio, a/W = 0.6, and also in a shallow notched configuration with a/W = 0.15. The SE(T) and DE(T) configurations were tested with a/W ratios from 0.35 to 0.7. Schematic drawings of the SE(T) and DE(T) geometries are shown in Figure 1. All specimens were 25 mm thick and side grooved to a total thickness reduction of 20%. All specimens were side grooved after precracking.

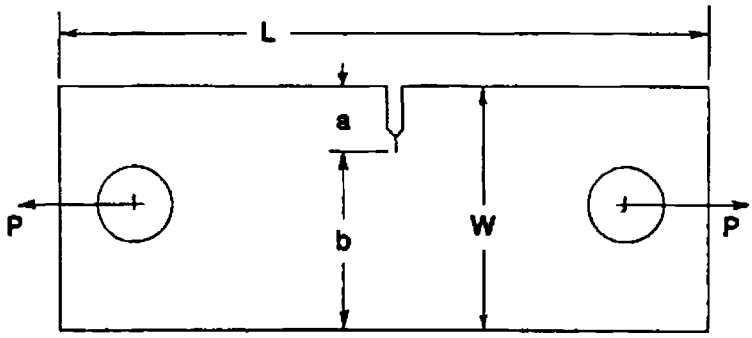
Some non-side grooved specimens of the HY-100 steel were tested and reported in reference 9; however, all specimen results presented here are for specimens which have been side grooved to a total reduction of 20%. Matrices of the test specimens are presented in Table 2 and Table 3 for the two materials tested and reported here. Tests of the HY-100 steel were done at ambient temperature (25°C), while the A533B was tested at approximately 100°C to assure that the fracture mode for all tests was fully ductile throughout.

Specimen Precracking

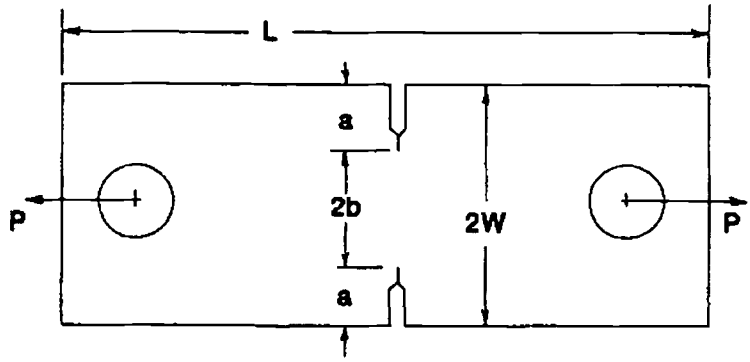
The SE(B) and C(T) specimens were precracked using conventional methods and the SE(T) and DE(T) specimens were precracked in bending using a three or four point bend apparatus. The short cracked HY-100 bend specimens were precracked starting from a wide specimen, with W = 70 mm, and precracked until the crack was about 27 mm long. The specimens were subsequently machined to remove 20 mm of the material at the crack flanks, until a final configuration was obtained with a crack length of about 7 mm in a remaining ligament of 50 mm. The precrack fronts obtained in this fashion for this material were found to be straight and accurate in all cases, but the method was expensive and arduous. The

Table 1 Chemical composition and mechanical properties of steel alloys used in this investigation (All element values in weight percent).

Element	HY-100 (FYO)	A533, Grade B (H13)
Carbon	0.16	0.22
Manganese	0.26	1.48
Phosphorus	0.003	0.012
Sulfur	0.009	0.018
Silicon	0.19	0.25
Nickel	2.78	0.68
Chromium	1.57	-
Molybdenum	0.42	-
Vanadium	0.003	-
0.2% Yield Strength, MPa (ksi)	747 (109)	397 (58)
Ultimate Strength, MPa (ksi)	877 (128)	555 (81)
Elongation in 25 mm (%)	16.5	26
Reduction of Area (%)	57	68



SE(T) Specimen



DE(T) Specimen

Figure 1 Schematic drawings of the SE(T) and DE(T) geometries tested in this investigation.

A533B short crack bend specimens were precracked by starting with a bar of width 50 mm with a short machined notch, 5 mm in depth. Then a single large reverse bending load was applied that was calculated to introduce a compressive plastic zone of 0.5 mm in extent. The specimen was then fatigue precracked as usual. The crack length was monitored using a computer controlled servo-hydraulic test machine, and the short crack compliance equation obtained by Joyce[**10**] until the final precrack length of approximately 7 mm was obtained. These cracks were found to be straight, and the single load reversal method was much simpler than the double machining process used on the HY-100 short cracked bend specimens. This technique has become standard practice, even on large, shallow cracked bend bars.

Table 2 List of HY-100 specimens tested in this investigation.

Specimen Type	a/W	B (mm)	W (mm)	Number of Specimens
SE(B)	0.65	50	50	2
SE(B)	0.6	25	50	2
SE(B)	0.6	12.5	50	2
SE(B)	0.14	50	50	1
SE(B)	0.14	25	50	2
SE(B)	0.11	12.5	50	2
SE(T)	0.35-0.47	25	64	3
SE(T)	0.65	25	64	1
DE(T)	0.6-0.7	25	32	2
All specimens side-grooved to a total thickness reduction of 20%.				

Table 3 List of A533B specimens tested in this investigation.

Specimen Type	a/W	B (mm)	W (mm)	Number of Specimens
C(T)	0.6	25	50	3
SE(B)	0.6	25	50	3
SE(B)	0.15	25	50	3
SE(T)	0.4	25	64	3
SE(T)	0.65	25	64	2
DE(T)	0.7	25	32	3
All specimens side-grooved to a total thickness reduction of 20%.				

The SE(T) specimens were precracked in three point bending, starting with machined notches with a/W = 0.15, and grown to an a/W between 0.35 and 0.65 for testing. The DE(T) specimens were precracked in four point bending, with two rollers spaced closely over the compression side notch. The initial notch depths were kept at a/W = 0.15 in the DE(T) specimens even though deep cracks were desired so that the ligament during precracking was a large as possible. A tightly fitting wedge was pushed into the compression side notch, and this allowed using standard SE(B) compliance equations for monitoring the crack length of the DE(T) specimens during precracking. The specimens were reversed several times to obtain even precracks on both sides. Matching the bend compliances in the two directions seemed to accurately match the lengths of the two cracks. As a final check the specimen was loaded in tension and the outputs of two clip gages mounted across the two cracks were compared. It was generally found that the bending compliance-matched cracks were of equal length and any remaining difference in COD output was usually due to misalignment of the test machine load train.

Test Technique

All tests were conducted using a single specimen, computer interactive, unloading compliance test procedure which allowed monitoring the specimen crack length and the applied J integral during the course of the test. Equations were presented in [9] for the required elastic and plastic components of the J integral and for estimating the crack length or lengths from the experimentally measured crack opening compliance. A simple rotation correction procedure greatly improves accuracy of the crack length estimation in the SE(T) specimen. The rotation correction that is used here is similar to that used in ASTM E1152 for the C(T) specimen, a correction that is, of course, used for the C(T) specimens tested in this work. The SE(T) specimen rotation correction is developed in the next section. The results presented here for the HY-100 alloy SE(T) specimens are altered considerably from that reported previously[9] because the SE(T) specimen rotation correction is used here.

In all cases, crack growth corrected J equations are used here, as developed in [9] which are similar to those required for the deep SE(B) specimens and the C(T) specimens by ASTM E1152. All data was stored on magnetic media for subsequent re-analysis as needed.

The SE(B) specimens were tested with standard bend fixtures which were made much sturdier than usual to accommodate the higher loads typical of short crack specimens. The procedures used for the short crack tests were presented by Joyce[10] which showed clearly that unloading compliance was a viable test technique for SE(B) specimens with a/W as short as 0.1. The compliance equations

are much less sensitive in the short crack region, but the load applied increases with $(W-a)^2$ so that the unloadings become much larger for the short crack specimens, and the crack opening displacement (COD) continues to be adequately large and can be measured with a high resolution digital voltmeter. The combination of high loads and less sensitive unloading compliance makes these test more difficult, but if care is taken, excellent results can be obtained. A flex bar was used to measure the load line displacements for all SE(B) specimens[11] since significant indentations did occur at the rollers for these specimens.

The SE(T) and DE(T) specimens were loaded with oversized tension clevises similar to what is used for standard C(T) specimens. The HY-100 tests were done with clevises that had round holes while the A533B tests were done with clevises that had flat bottomed holes to allow for the loading pin to roll as the specimen rotated during test. It was found that allowing the specimen half to rotate freely, and correcting for the rotation effects was the preferred method for the SE(T) tests. However, it was also found that round bottom holes were preferred for DE(T) specimens, providing an initial alignment that was essential to accurately estimate the crack length of the DE(T) specimen both at the start of test and as crack growth proceeded. For the SE(T) specimens a standard clip gage was installed to measure the crack mouth opening displacement, which was used for crack length estimation, and an LVDT gage was installed on the initial specimen load line to measure the load line extension of the specimen. For the DE(T) specimen, two COD gages were used as well as an LVDT gage on the specimen centerline. In general the average COD displacement was used to estimate the average crack length for the DE(T) specimen. Both COD gage readings were recorded in the data file and can be plotted separately, if desired.

ANALYSIS

J Integral Analysis

The J integral is calculated here by summing the elastic and plastic components, with the components calculated separately. The elastic component of J, J_{el}, is calculated from:

$$J_{el} = \frac{K^2}{E'} \tag{1}$$

where K is the elastic stress intensity factor for the specimen, $E'=E/(1-\nu^2)$, and E and ν are the elastic modulus and Poisson's ratio, respectively. The plastic component of J, J_{pl}, is calculated using the ASTM Standard E1152 J_{pl} equation:

$$J_{pl(i)} = J_{pl(i-1)} + \frac{\eta_i}{b_i}\left[\frac{A_{pl(i)} - A_{pl(i-1)}}{B_N}\right]\left[1 - \frac{\gamma_i\,(a_i - a_{(i-1)})}{b_i}\right] \tag{2}$$

with:

A_{pli} = area under the load versus plastic load line displacement curve to increment i,

B_N = net specimen thickness at the side groove roots,
η_i = the plastic η factor at crack length a_i
b_i = the incremental remaining ligament
W = the specimen width and

$$\gamma_i = \left[\eta_i - 1 - \frac{b_i}{W}\frac{\eta_i'}{\eta_i}\right] \tag{3}$$

evaluated at the crack length a_i, and:

$$\eta_i' = d\eta_i/d(a_i/W) \tag{4}$$

Formulas for the compliance relationships, K's, η's, and γ's used to obtain the J-R curves for the SE(B), SE(T), and DE(T) specimens were taken from [9].

SE(T) Rotation Correction

A rotation correction can be developed for the SE(T) specimen using the notation of Figure 2. Two separate corrections are needed, one to correct the COD for the effect of rotation, the second to correct the load for the effect of rotation.

The objective of the first correction is to correct the measured displacement $d_{m/2}$ to obtain the correct displacement $d_{c/2}$, as shown in Figure 2. Using the geometry of Figure 2 gives:

$$\frac{d_{c/2} + D}{R_G} = \tan\left(\theta + \tan^{-1}\frac{D}{R_G}\right) \tag{5}$$

and using the standard trigonometry identity for tan(x+y) and eliminating small terms gives:

$$d_{c/2} = R_G\tan\theta \tag{6}$$

where:

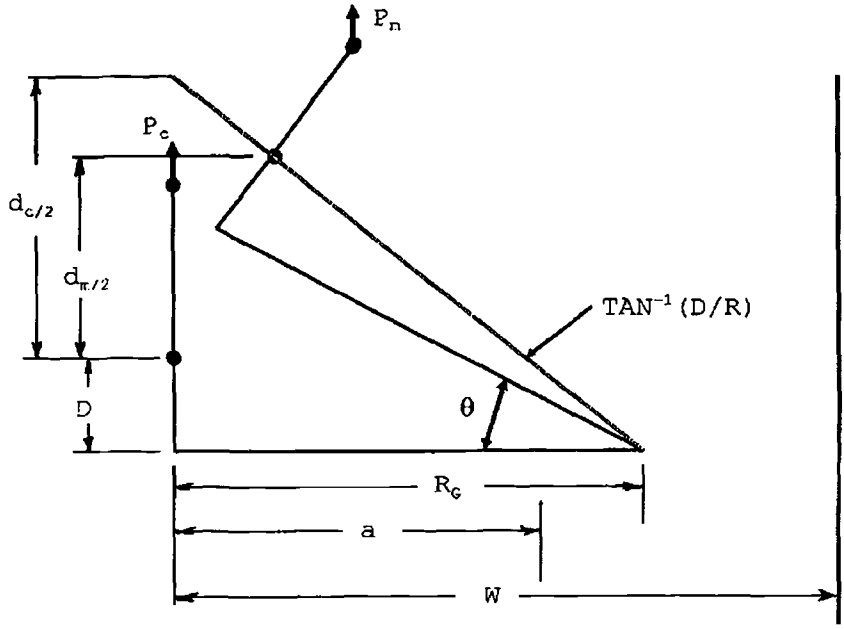


Figure 2 Geometric relationship of variables used in rotation correction of COD.

$$\theta = \sin^{-1}\left[\frac{(d_{m/2} + D)}{(D^2 + R_G^2)^{1/2}}\right] - \tan^{-1}\frac{D}{R_G} \tag{7}$$

Similarly from Figure 2:

$$\frac{d_{m/2} + D}{\sqrt{(D^2 + R_G^2)}} = \sin(\theta + \tan^{-1}\frac{D}{R_G}) \tag{8}$$

and again using the standard identity for sin(x+y) and eliminating small terms gives:

$$d_{m/2} = R_G \sin\theta + D\cos\theta - D \tag{9}$$

and the desired displacement correction factor can then be written as:

$$\frac{d_{c/2}}{d_{m/2}} = \frac{R_G \tan\theta}{R_G \sin\theta + D\cos\theta - D} \tag{10}$$

or as:

$$\frac{d_{c/2}}{d_{m/2}} = \frac{1}{(\cos\theta - \frac{D\tan\theta}{2R_G})} \tag{11}$$

The load rotation correction is obtained by requiring:

$$P_c R_L = P_m R_m \tag{12}$$

where P_m is the measured load and P_c is the corrected load.

From Figure 3,

$$R_m = R_L\cos\theta - H^*\sin\theta \tag{13}$$

Substituting and reducing gives:

$$\frac{P_c}{P_m} = (\cos\theta - \frac{H^*\sin\theta}{R_L}) \tag{14}$$

Combining these correction factors gives:

$$C_c = \frac{C_m}{(\cos\theta - \frac{D\tan\theta}{2R_G})(\cos\theta - \frac{H^*\sin\theta}{R_L})} \tag{15}$$

This equation was used to correct the measured compliance, C_m, to obtain the corrected compliance, C_c, before calculation of the estimated crack length for the partial unloading.

It was also necessary to apply a rotation correction to the load line compliance so that accurate separation of the measured J into elastic and plastic components was possible. This correction is effectively just the load component of the COD correction of Eq. 15 giving:

$$C_{LLDc} = \frac{C_{LLDm}}{(\cos\theta - \frac{H^*\sin\theta}{R_L})} \tag{16}$$

This equation was used to correct the measured load line compliance, C_{LLDm}, to

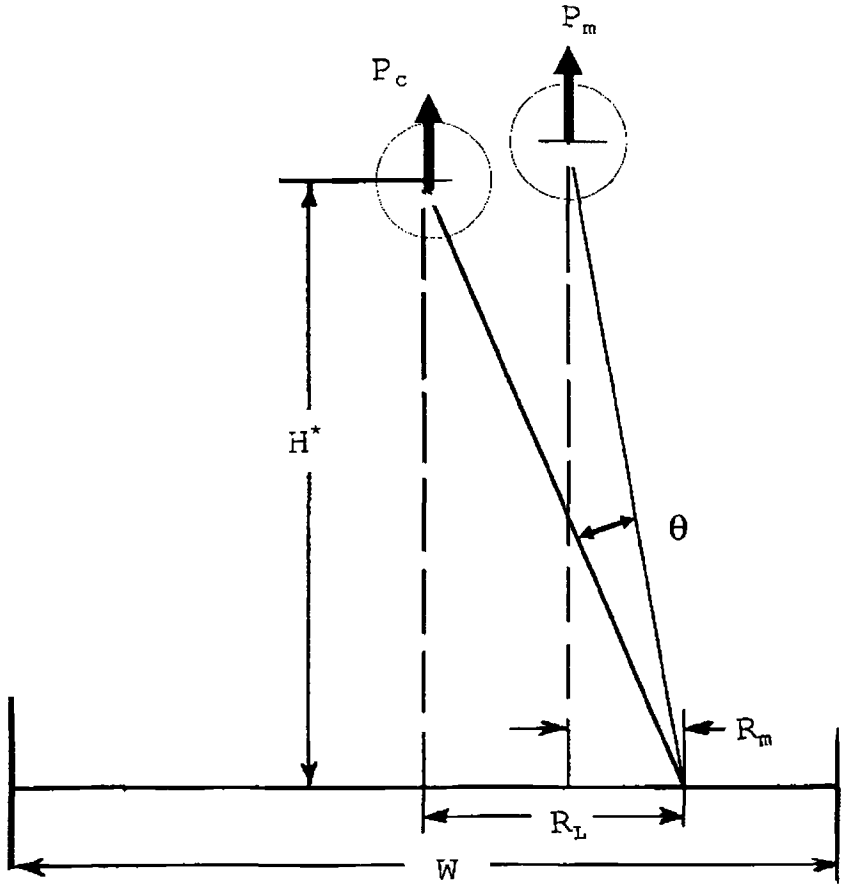


Figure 3 Geometric relationship of variables used to rotation correct the load.

obtain the corrected load line compliance, C_{LLDc}, before calculating the elastic and plastic area components used to calculated the elastic and plastic J components.

To use this analysis it is necessary to assume a position for the center of rotation for the SE(T) specimen. In the standard C(T) analysis of ASTM E1152 the center of rotation is assumed to be at the center of the remaining ligament, and that assumption was also used here, i.e. $R_G = (a + W)/2$ and $R_L = R_G - W/2$.

Constraint Correlations

Recently two quantities have been proposed to quantify the "constraint" present for a given combination of crack geometry, mode of loading, and material toughness. These are the "T-stress" approach[5][12] and the Q parameter of O'Dowd and Shih[1][13]. These two quantities are described and utilized separately in the next two subsections.

T Stress Indexing Parameter

The linear elastic crack tip stress field for a crack along the negative x-axis, with its tip at the origin, has the form:

$$\sigma_{xx} = \frac{K}{\sqrt{2\pi r}} f_{xx}(\theta) + T_o \tag{17}$$

$$\sigma_{yy} = \frac{K}{\sqrt{2\pi r}} f_{yy}(\theta) \tag{18}$$

$$\sigma_{xy} = \frac{K}{\sqrt{2\pi r}} f_{xy}(\theta) \tag{19}$$

where the T_σ term is the only term of order r^0 that exists, and it only affects σ_{xx}. Larsson and Carlsson[7] showed that the sign and magnitude of this term does alter the size and shape of the plastic zone, and recently Betegón and Hancock[5] and Al-Ani and Hancock[12] have suggested that the amplitude of the T_σ term may be an effective constraint indexing parameter, even in the elastic-plastic regime. They show that low constraint geometries like short crack or tensilely loaded geometries have different T_σ values than deep cracked bend geometries, and they suggest that the T_σ difference causes higher apparent toughnesses to be found in such cases.

To assess the effect of T_σ, a biaxiality parameter is used having the form:

$$\beta = T_\sigma \frac{\sqrt{\pi a}}{K} \tag{20}$$

This quantity has been evaluated for various test geometries using finite element and other methods and is available in the literature[14][15][16].

Results for SE(B), SE(T), and DE(T) specimens are shown in Figure 4. For convenience, this data has been used to develop polynomial relationships giving β in terms of a/W:

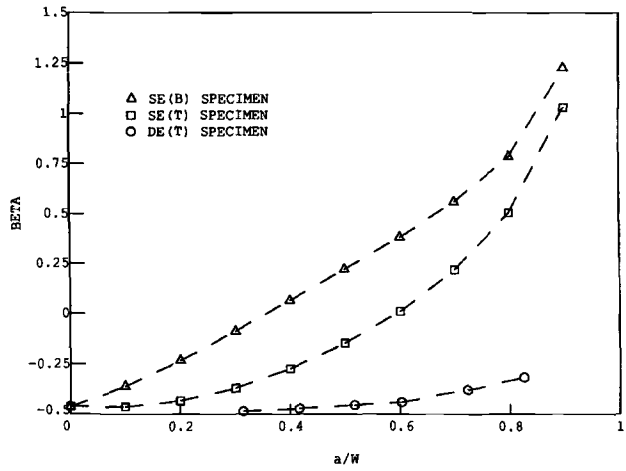


Figure 4 Biaxiality factor, β, for three specimen geometries.

SE(B):

$$\beta = -0.463 + 1.1207\left(\frac{a}{W}\right) - 1.4441\left(\frac{a}{W}\right)^2 + 11.264\left(\frac{a}{W}\right)^3 - 20.950\left(\frac{a}{W}\right)^4 + 12.5\left(\frac{a}{W}\right)^5 \quad (21)$$

SE(T):

$$\beta = -0.463 + 0.1012\left(\frac{a}{W}\right) - 1.6844\left(\frac{a}{W}\right)^2 + 13.344\left(\frac{a}{W}\right)^3 - 21.926\left(\frac{a}{W}\right)^4 + 12.5641\left(\frac{a}{W}\right)^5 \quad (22)$$

DE(T):

$$\beta = -0.5844 + 0.6249\left(\frac{a}{W}\right) - 1.3527\left(\frac{a}{W}\right)^2 + 1.2031\left(\frac{a}{W}\right)^3 \quad (23)$$

Using these relationships the value of β for each test geometry in this study has been calculated as shown in Table 4 and Table 5. Using the relationships for K as a function of load and a/W, the T_σ value at the crack initiation (J_{Ic}) point has also been evaluated for each specimen tested. These results will be discussed in subsequent sections.

The Q Indexing Parameter

The Q parameter has been proposed by O'Dowd and Shih[1][13] as an extension of the T_σ concept to deformation plasticity. They take the second term of the stress fields around the crack tip in a power law hardening material and propose that its intensity can be represented by a Q parameter, and that this parameter can be used to index the relative constraint of a test geometry. The authors basically relate the "true" finite body stress components in front of the crack to those of the small scale yielding (SSY), infinite body case in the form:

$$\sigma_{xx} = \sigma_{xx}|_{SSY} + Q\sigma_o \tag{24}$$

$$\sigma_{yy} = \sigma_{yy}|_{SSY} + Q\sigma_o \tag{25}$$

$$\sigma_{xy} = \sigma_{xy}|_{SSY} \tag{26}$$

where σ_o is the power law material yield stress and Q is a dimensionless parameter found by O'Dowd and Shih to be between 0.2 and -2., in front of the crack. Q must be evaluated using precise finite element techniques so that the differences between the true stress field and the SSY stress field can be accurately determined. Results for Q for the SE(B) geometry from [13] for the case of n = 10 are shown in Figure 5, and used to estimate Q values for the SE(B) specimens tested in this program.

Q values for the SE(T) and DE(T) specimens have been obtained from analysis provided by Dodds[3] as shown in Figure 6 for two SE(T) and one DE(T) geometry.

[3]Private communication, R.H. Dodds, Jr. 1993.

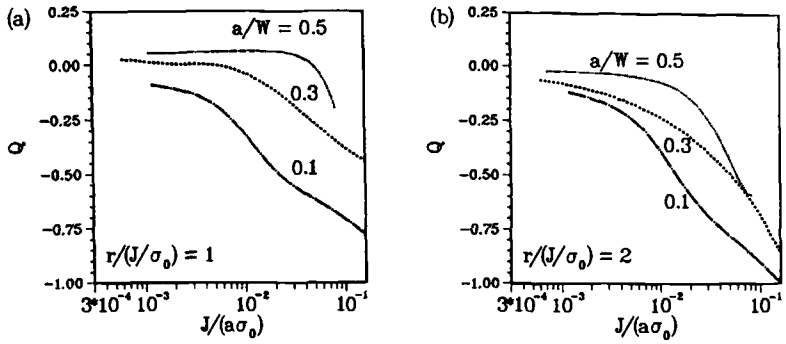


Figure 5 The Q constraint factor for SE(B) specimens with short and deep cracks, n=10[13].

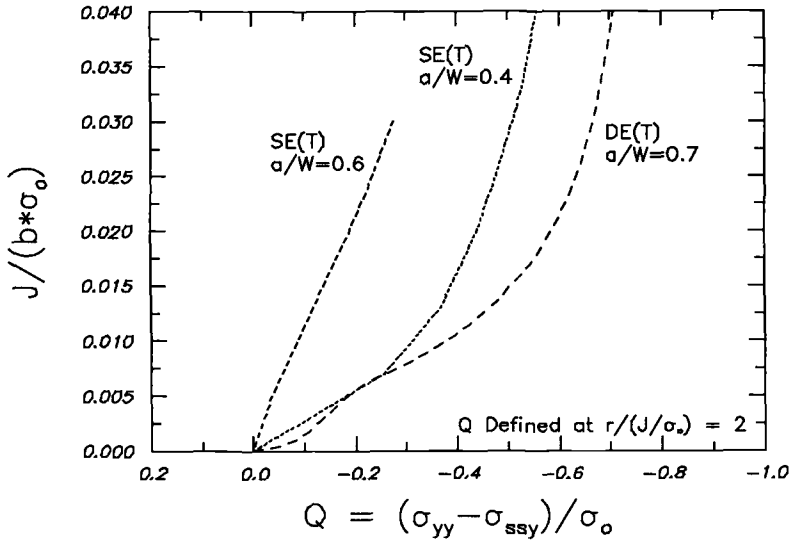


Figure 6 The Q constraint parameter for the DE(T) and SE(T) specimen with n=10 (R.H. Dodds, Private Communication).

Calculation of J_{Ic}

In order to compare J_{Ic} across a range of specimen types, special care had to be taken in its evaluation. The J_{Ic} value calculated is dramatically affected by the initial crack length, a_0, used to calculate the crack extension, Δa, during the test. The ASTM Task Group E8.08.03 has proposed a method to utilize the initial test data to determine a best a_o for use in calculating Δa and hence in J_{Ic} calculations[4]. The proposed method involves fitting a straight line of slope $2\sigma_Y$ to the initial J - Δa data, and choosing the best fit line to the data in the interval $0.2J_Q \leq J \leq 0.6J_Q$. Since the choice of a_o affects the subsequent J_Q value, an iterative process is necessary to obtain the final best fit a_o, J_Q, and hence a J_{Ic} value from a particular experimental data set. The proposed method also adds the requirement that at least three data pairs exist in the region $0.2J_Q \leq J \leq 0.6J_Q$ so relatively dense data is required for a_o and J_{Ic} evaluation.

This method was initially used in this program, but it was found that the method disqualified some specimens due to a lack of data in the region $0.2J_Q \leq J \leq 0.6J_Q$. In place of the above ASTM method an alternative method was developed that was not so dependent on the early data on the J-R curve. In this method the relationship:

$$a_i = a_o + AJ_i^2 + BJ_i^3 \tag{27}$$

was fit to the a_i - J_i data of each set from the minimum a_i to a_i + 2.5 mm of crack growth, as shown in Figure 7. A least squares procedure was used to evaluate the coefficients a_o, A, and B, and the a_o parameter was the desired, best-fit, initial crack length which was then used to calculate the Δa_i quantities for the J-R curve. This method worked well on all specimens analyzed here and in all cases adequate data was available for the fit, no iteration was needed, and the least squares technique gave a unique and fully defined average crack length for each specimen, while the proposed ASTM method gives only a range from which each investigator could choose a somewhat different result based on the details of his iteration procedure.

---

[4] "New Standard Method for J-Integral Characterization of Fracture Toughness," Draft Standard of ASTM Subcommittee E08.08, March 1993, American Society for Testing and Materials, Philadelphia, PA.

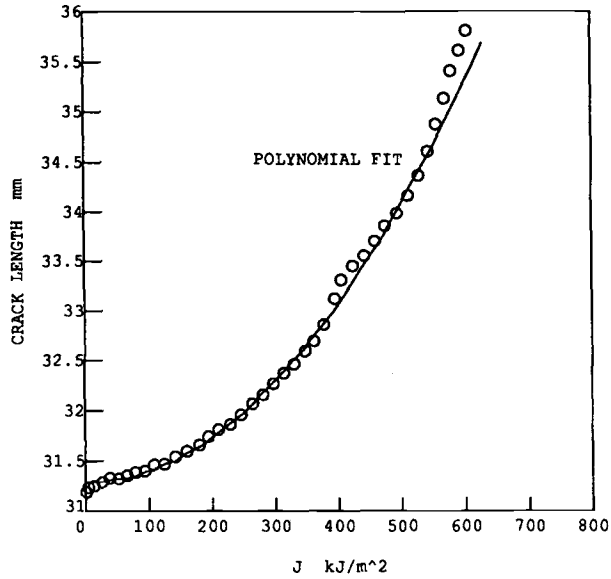


Figure 7 Polynomial fit of crack length versus J for determining the best-fit initial crack length, a_o.

DISCUSSION

The Rotation Correction

The SE(T) specimens were a new geometry and problems were encountered in developing test procedures for this geometry. One obstinate problem encountered in testing this geometry was the initial hook, or "crack backup" observed in the J-R curve obtained from these specimens as shown in Figure 8. The early compliance measurements show a clear increase in specimen stiffness as the load is increased, both in the elastic and the elastic-plastic regimes. This problem was initially assumed to result from the round hole clevises that were used for the first tests of HY-100 (FYO). New clevises with flat bottomed holes were machined and hardened to allow a free rotation of the specimen halves during the test; however, this change did not improve the results. It was then that a rotation correction was proposed as a possible solution. The rotation correction was developed, as described previously, in a fashion similar to that used in ASTM E1152 for the C(T) specimen.

The effect of the rotation correction was to remove the initial crack backup while increasing J and Δa slightly. The most dramatic effect is at the start of the J-R curve where the apparent initial stiffening of the specimen is corrected to show

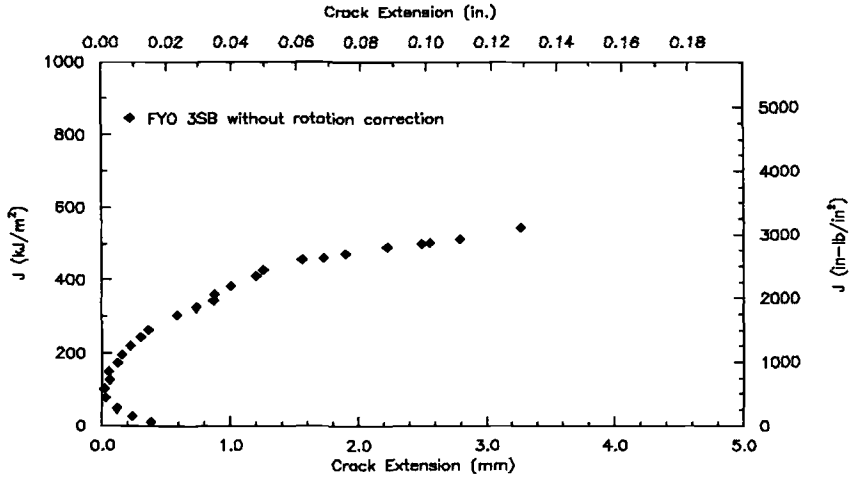


Figure 8 J-R curve from an SE(T) specimen exhibiting "crack backup" in the early portion of the test.

an improved resistance curve, especially in the initial portion, which improved the consistency of the calculated J_{Ic} results. A comparison of a rotation corrected SE(T) specimen J-R curve and the corresponding uncorrected J-R curve is shown in Figure 9.

The resistance curve slope, T_{mat}, measured at 1 mm of crack growth, was not found to be changed markedly by the application of the rotation correction, being beyond where most of the effects of the rotation correction was felt.

J_{Ic} and T_{mat}

J_{Ic} was calculated for all specimens included in this study using the polynomial
relationship - least squares fit approach described above to determine the initial crack length, a_0. The results for both materials are shown in Table 4 and Table 5 and plotted as a function of specimen type in Figure 10 and Figure 11. J_{Ic} does not appear, from these plots, to be very sensitive to the specimen type, at least compared to the large variability demonstrated by each specimen type taken individually.

The material tearing resistance, T_{mat}, introduced by Paris, et al.[17] was also evaluated for these specimens:

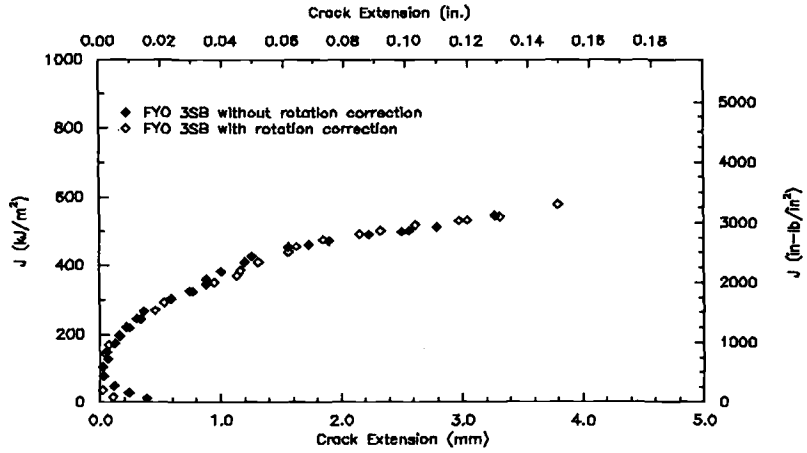


Figure 9 Comparison of J-R curves for an HY-100 SE(T) specimen with and without rotation correction.

$$T_{mat} = \frac{\sigma_y^2}{E}\frac{dJ}{da} \tag{28}$$

where σ_y is the material yield stress and dJ/da is evaluated by fitting a two parameter power law, as used to evaluated J_{Ic}, to the J-R curve data in the standard ASTM E813 exclusion zone, and then evaluating dJ/da at a crack extension of 1 mm (0.04 in). The measured T_{mat} values obtained from this set of specimens are shown in Table 4 and Table 5 and plotted as a function of specimen type in Figure 12 and Figure 13. The tearing resistance varies for each material by a factor of about 2.5 and appears to be dependent on the specimen type.

In the following sections these results for J_{Ic} and T_{mat} will be correlated with the T_σ and Q constraint parameters.

J-R Curves

Figure 14 and Figure 15 show the measured J-R curves for the baseline, deep notched SE(B) and C(T) specimens of each material. The variability shown in these figures is assumed to be due to material variability, and is typical of what is usually found for structural steels. The dashed bounding lines shown in the figures

Table 4 Fracture toughness and constraint quantities for HY-100 specimens.

Specimen ID	Type	a/W	J_{Ic} (kJ/m^2)	T_{mat} (1 mm)	β	T_σ @ J_{Ic} MPa	Q @ J_{Ic}
FYO 1	SE(B)	0.66	111.7	25.2	0.476	229.	-0.1
FYO 3	SE(B)	0.66	137.8	31.2	0.476	255.	-0.1
FYO 21	SE(B)	0.14	177.2	49.9	-0.311	-410.	-0.8
FYO 26	SE(B)	0.13	163.7	35.6	-0.322	-425.	-0.8
FYO 27	SE(B)	0.14	173.7	48.0	-0.311	-406.	-0.8
FYO 150	SE(B)	0.61	145.1	21.3	0.395	226.	-0.1
FYO 151	SE(B)	0.61	129.7	26.6	0.395	213.	-0.1
FYO 158	SE(B)	0.60	140.5	23.8	0.381	216.	-0.1
FYO 159	SE(B)	0.62	179.9	24.2	0.411	259.	-0.1
FYO 160	SE(B)	0.11	120.1	38.2	-0.345	-423.	-0.8
FYO 161	SE(B)	0.11	113.9	40.9	-0.345	-412.	-0.8
FYO 2SB	SE(T)	0.40	148.0	59.0	-0.270	-182.	-0.25
FYO 3SB	SE(T)	0.47	217.0	60.0	-0.183	-138.	-0.30
FYO 4SA	SE(T)	0.65	227.5	41.0	-0.101	-65.9	-0.11
FYO 10SA	SE(T)	0.35	187.6	68.0	-0.325	-259.	-0.31
FYO 11SB	DE(T)	0.68	88.4	31.0	-0.407	-217.	-0.43
FYO 12SA	DE(T)	0.61	107.1	39.2	-0.433	-268.	-0.40

Table 5 Fracture toughness and constraint quantities for A533B specimens.

Specimen ID	Type	a/W	J_{Ic} kJ/m^2	T_{mat} (1 mm)	β	T_σ @ J_{Ic} MPa	Q @ J_{Ic}
CT3	C(T)	0.60	244.4	122.4	0.573	428	-0.1
CT9	C(T)	0.60	265.0	125.3	0.573	446	-0.1
CT10	C(T)	0.60	239.2	112.1	0.573	423	-0.1
DB1	SE(B)	0.62	240.3	149.9	0.411	300	-0.1
DB2	SE(B)	0.62	308.5	142.9	0.411	339	-0.1
DB3	SE(B)	0.62	323.8	160.5	0.411	348	-0.1
SB1	SE(B)	0.15	306.3	238.2	-0.299	-498	-0.8
SB2	SE(B)	0.15	228.7	260.8	-0.299	-431	-0.8
SB3	SE(B)	0.15	333.0	239.2	-0.299	-520	-0.8
SEN1	SE(T)	0.41	145.5	228.7	-0.271	-172	-0.30
SEN2	SE(T)	0.38	159.5	289.8	-0.315	-220	-0.30
SEN4	SE(T)	0.66	305.2	229.1	0.009	6.7	-0.22
SEN10	SE(T)	0.62	231.8	178.6	-0.009	5.8	-0.20
SE5D	DE(T)	0.70	164.6	301.1	-0.397	-285	-0.70
SE6D	DE(T)	0.70	182.1	257.3	-0.397	-300	-0.71
SE7D	DE(T)	0.68	189.8	253.3	-0.407	-311	-0.72
SE8D	DE(T)	0.70	226.6	255.0	-0.392	-335	-0.76

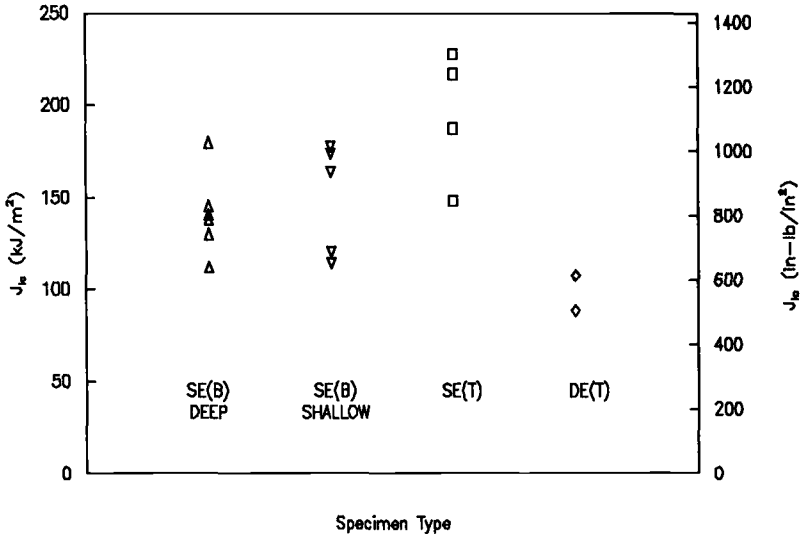


Figure 10 J_{Ic} fracture toughness of HY-100 as a function of specimen type.

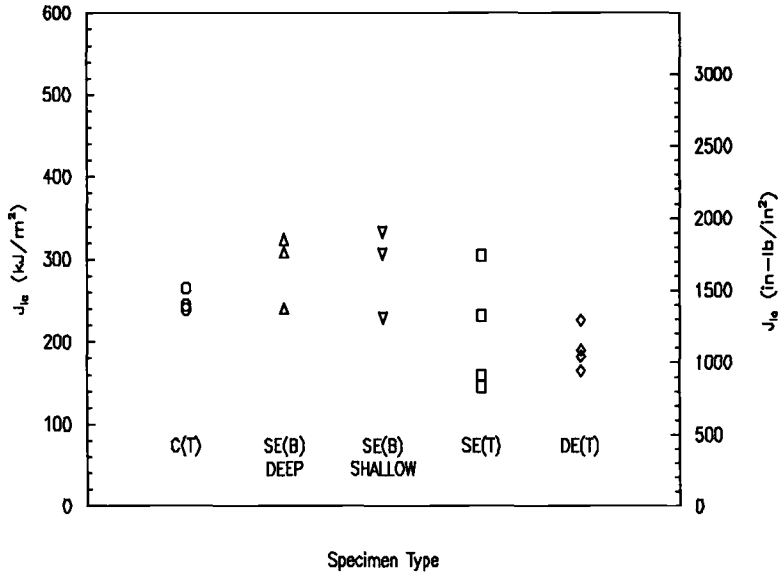


Figure 11 J_{Ic} fracture toughness of A533B as a function of specimen type.

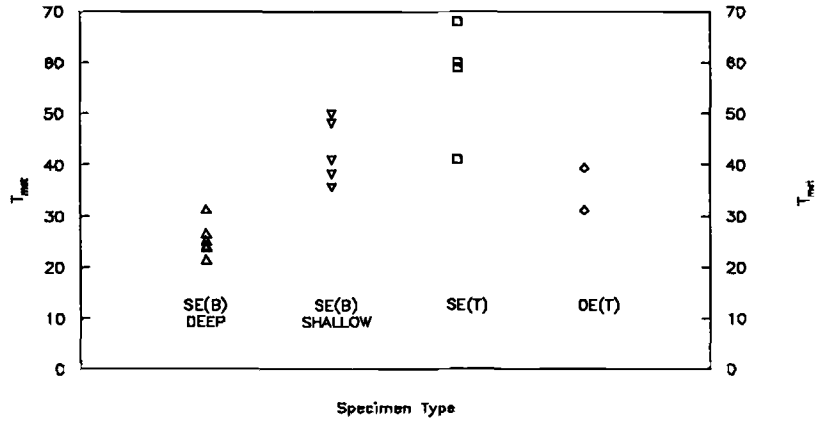


Figure 12 Tearing resistance of HY-100 as a function of specimen type.

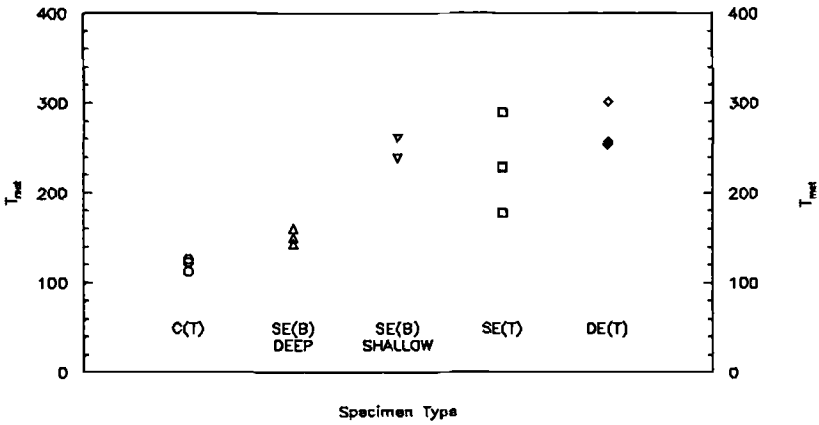


Figure 13 Tearing resistance of A533B as a function of specimen type.

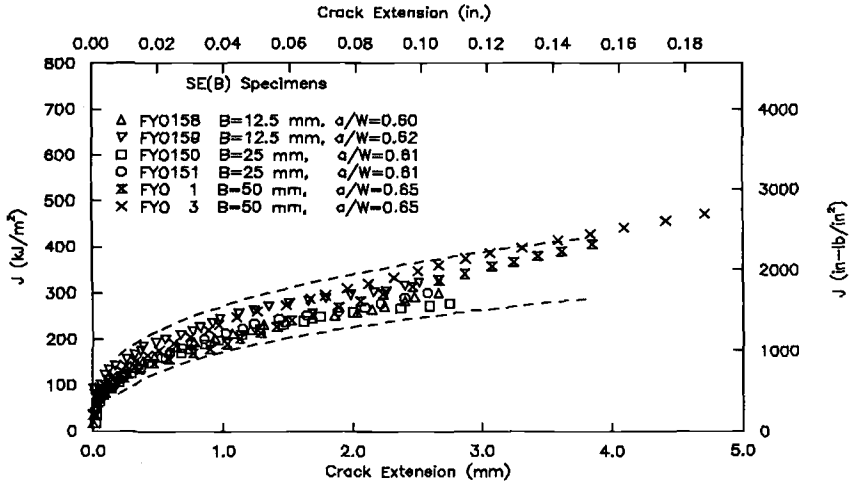


Figure 14 Baseline J-R curves for HY-100 from deep-cracked SE(B) specimens.

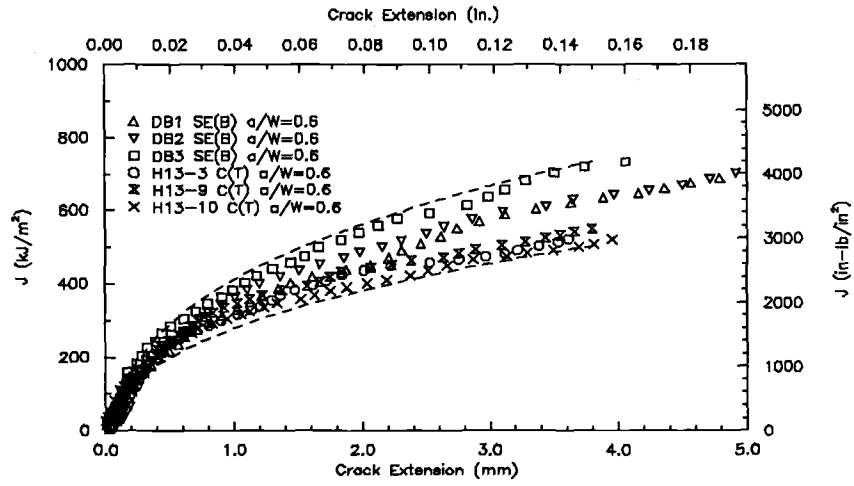


Figure 15 Baseline J-R curves for A533B from deep-cracked SE(B) specimens.

will be used on subsequent plots for comparison of the baseline results and results from the non-standard specimens. Comparisons of these baseline J-R curves with the J-R curves of the short cracked SE(B), SE(T), and DE(T) specimens for both materials are shown in Figure 16 through Figure 21. An immediate observation that can be made from these figures is that short cracks and tensile loading seem to have little effect on the J_{Ic} value, but a measurable effect on the slope of the J-R curve, or T_{mat} values, with higher slopes being found for all of the short crack and tensilely loaded specimens in comparison with the standard, deeply notched geometries.

CONSTRAINT CORRELATIONS

T_σ Correlation

The T_σ quantity was calculated for each specimen from the applicable K, a/W, and β at J_{Ic} and is tabulated in Table 4 and Table 5. Figure 22 and Figure 23 show plots of J_{Ic} versus T_σ for each material. The short and deep SE(B) specimens, and the C(T) specimens for the A533B alloy are considered to be the best experimental results obtained in this study. The dashed lines are drawn to encompass the results of these geometries. These geometries demonstrate J_{Ic} results that appear to be insensitive to the applied T_σ for both materials. The tensiley loaded SE(T) and DE(T) specimens are in general agreement. The HY-100 tensilely loaded specimens show considerable scatter, with the SE(T) specimens being high relative to the SE(B) results and the DE(T) specimens being low. It is quite possible that improvements in test technique that have been incorporated in the more recent A533B tests in part explain the reduction in scatter shown by the A533B tensile results, in comparison with the earlier HY-100 results.

Figure 24 and Figure 25 show plots of T_{mat} versus T_σ for each material, and now a clear trend of material tearing resistance versus constraint is apparent in the data, with the tearing resistance being more than doubled when measured with the low constraint short crack SE(B) specimen, in comparison to the standard, high constraint, deeply notched bend or compact specimens. The dashed lines are again drawn to bound the deeply cracked C(T) and SE(B) results at high constraint, and the shallow cracked SE(B) results at low constraint. The HY-100 material again shows much more scatter in T_{mat} values than does the A533B material. This might be due, in part, to the much smaller T_{mat} values obtained from the HY-100 material, as well as from basic improvements in the SE(T) and DE(T) test methods between the HY-100 tests and the A533B tests. The appearance of these results is improved by the lower scatter for each specimen type demonstrated by the T_{mat} parameter, in comparison with the J_{Ic} parameter.

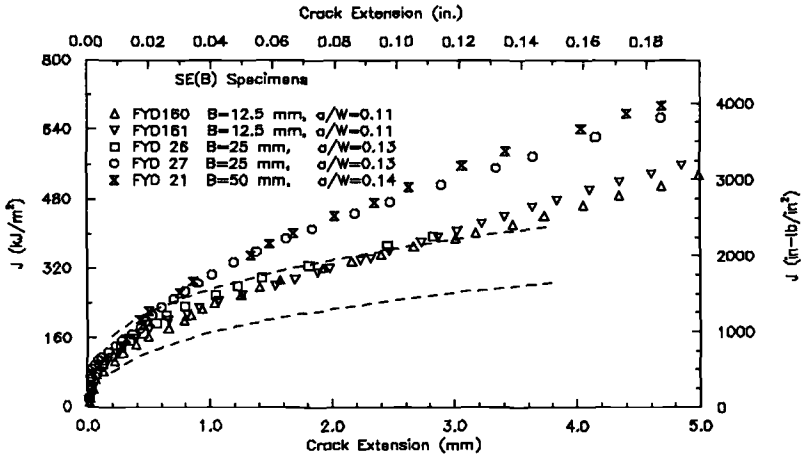


Figure 16 J-R curves for HY-100 from short-cracked SE(B) specimens.

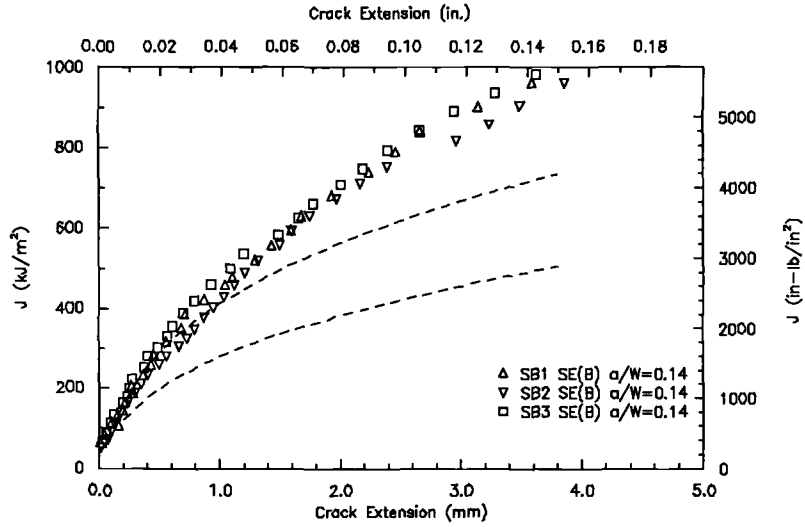


Figure 17 J-R curves for A533B from short-cracked SE(B) specimens.

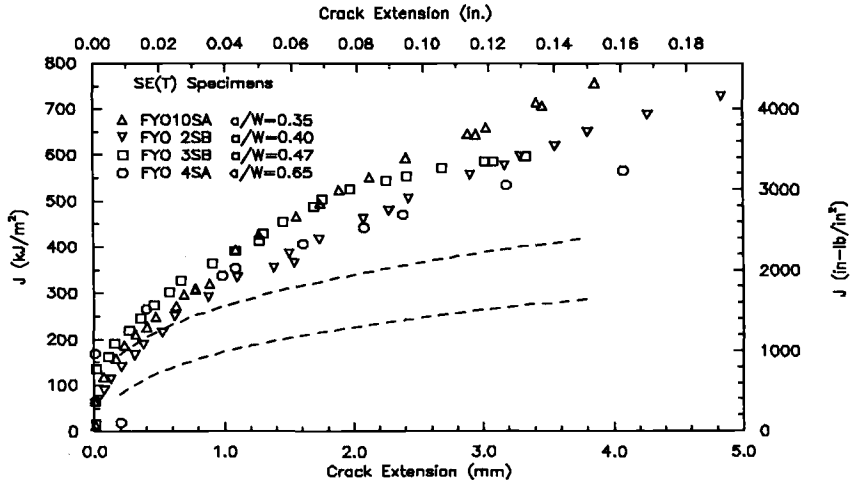


Figure 18 J-R curves for HY-100 from SE(T) specimens.

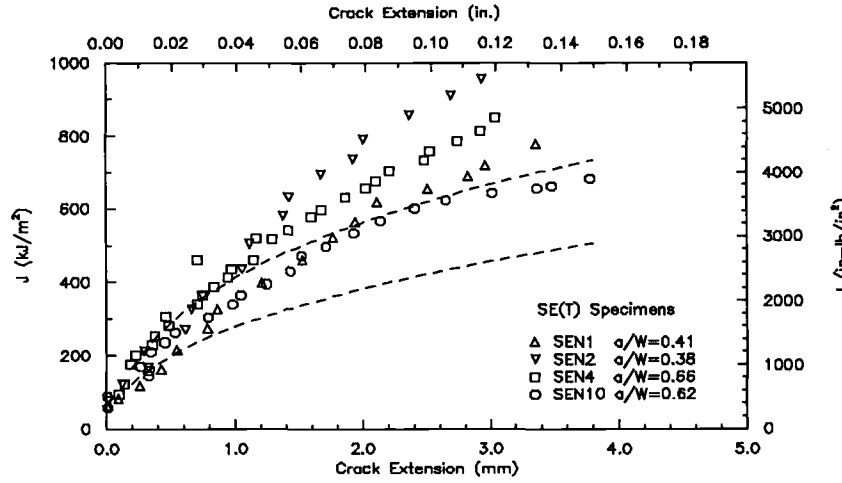


Figure 19 J-R curves for A533B from SE(T) specimens.

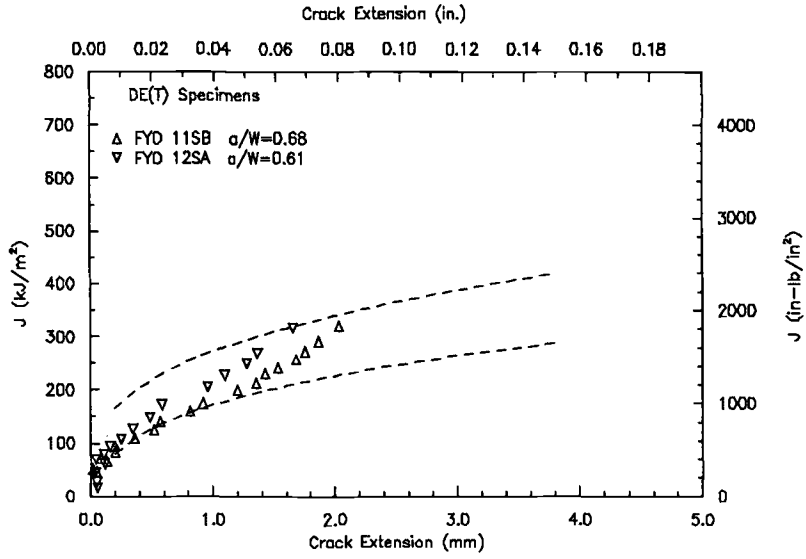


Figure 20 J-R curves for HY-100 from DE(T) specimens.

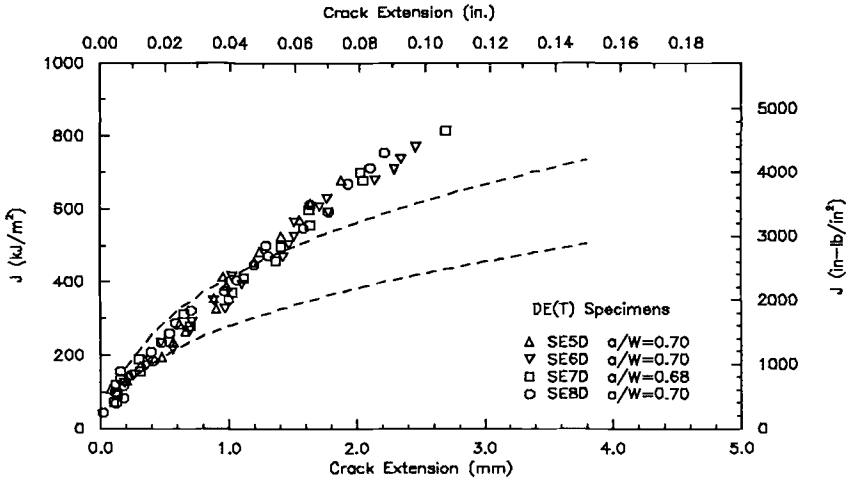


Figure 21 J-R curves for A533B from DE(T) specimens.

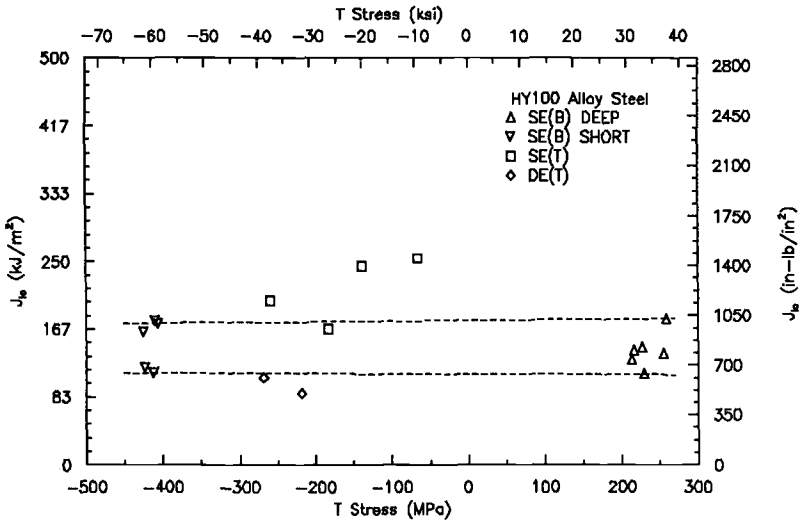


Figure 22 Fracture toughness, J_{Ic}, as a function of T_σ for the HY-100 specimens.

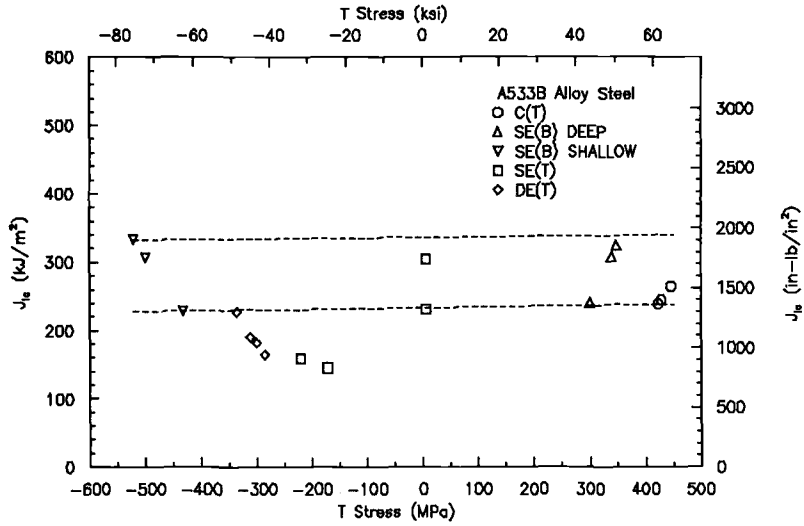


Figure 23 The fracture toughness, J_{Ic}, as a function of T_σ for the A533B specimens.

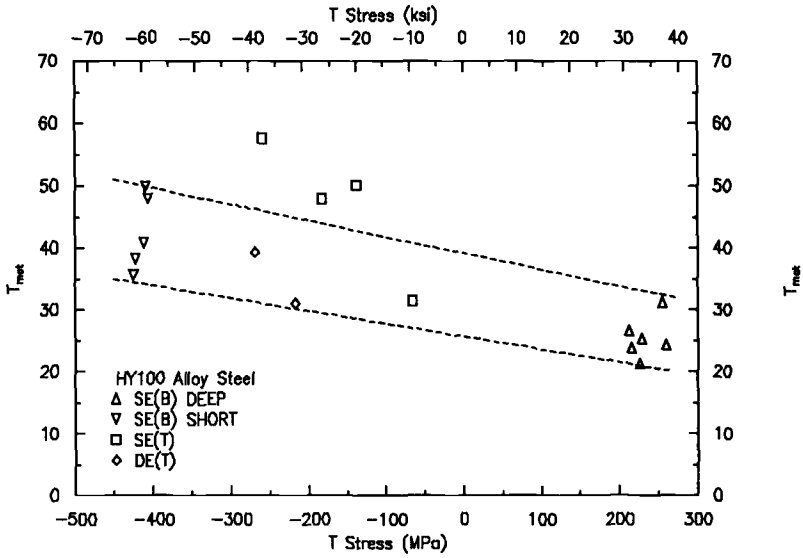


Figure 24 Tearing modulus, T_{mat}, as a function of T_σ for the HY-100 specimens.

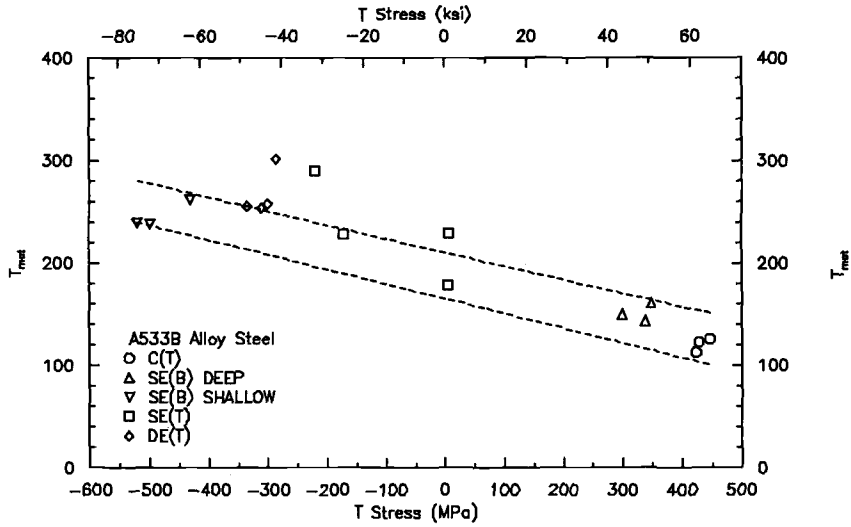


Figure 25 Tearing modulus, T_{mat}, as a function of T_σ for the A533B specimens.

Q Correlation

The Q quantity was evaluated for each specimen from the applicable analysis using Figs. 8-10, and the J_{Ic} and a/W and is tabulated in Table 4 and Table 5 for each specimen tested. Figure 26 and Figure 27 show plots of J_{Ic} versus Q at J_{Ic} for all specimens of each material. As above, neither material shows dependence of J_{Ic} on Q, at least, any that can be separated from the material and test variability. The HY-100 shows much more scatter than is shown by the A533B material. Overall it seems that J_{Ic} is not strongly affected by constraint, as measured by Q, in these specimen geometries.

Figure 28 and Figure 29 show plots of T_{mat} versus Q (at J_{Ic}) for each material. A clear trend is now shown, with higher constraint resulting in lower tearing resistance in these materials. For both materials there appears to be a clear increase in T_{mat} with decreasing Q as Q changes from 0 to -0.8.

SUMMARY

For these materials, at least, the J_{Ic} toughness parameter is relatively insensitive to constraint as characterized by T_σ or Q, while the tearing resistance is elevated by reduced constraint as measured by either T_σ or Q. Thus the J-Q fracture locus is inconsequential for fully ductile behavior, but the T_{mat} - Q locus is an important curve to measure the extent of toughness enhancement that would be expected under conditions of low constraint.

The best results for a low constraint specimen geometry are obtained from the short crack bend specimen geometry. This specimen is now relatively easy to test in the laboratory and has a low constraint in terms of Q or T_σ, especially if the a/W is less than 0.15.

CONCLUSIONS

The following conclusions are drawn from this work:

1) A rotation correction is essential for obtaining an accurate J_{Ic} or J-R curve from a SE(T) specimen of the type used in this work. The rotation correction developed here greatly improved the appearance of the SE(T) J-R curves.
2) J_{Ic} does not seem to be dependent on constraint, as applied in this study, at least as characterized by T_σ or Q.
3) The material tearing resistance, as characterized by T_{mat}, is strongly affected by constraint, with T_{mat} increasing rapidly with decreasing constraint. This is true whether constraint is measured with T_σ or Q.
4) The best low constraint test specimen geometry is the short crack bend

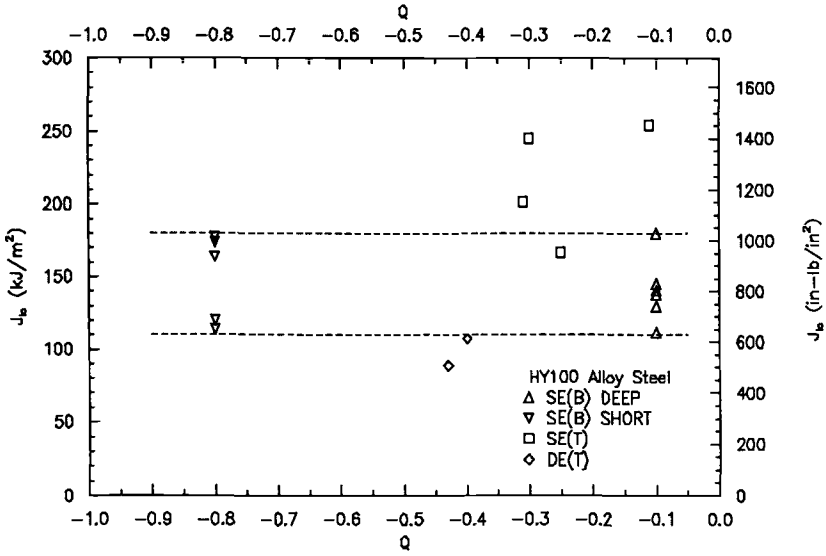


Figure 26 Fracture toughness, J_{Ic}, as a function of Q for HY-100 specimens.

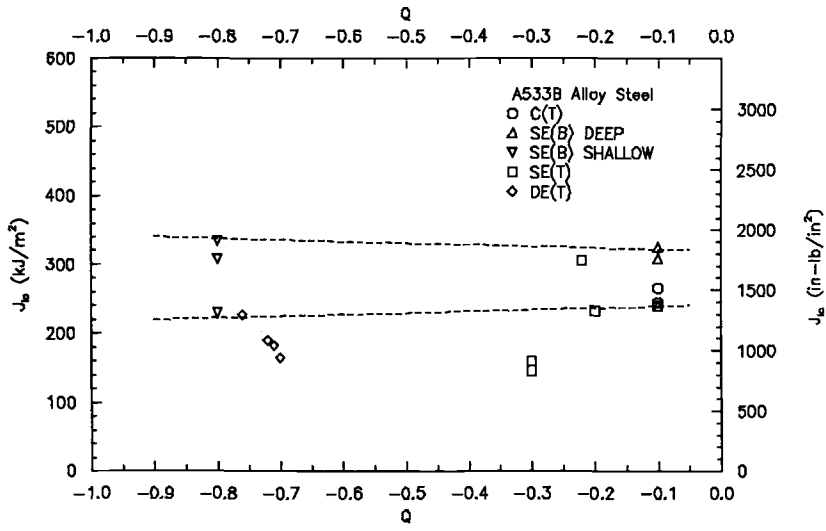


Figure 27 Fracture toughness, J_{Ic}, as a function of Q for the A533B specimens.

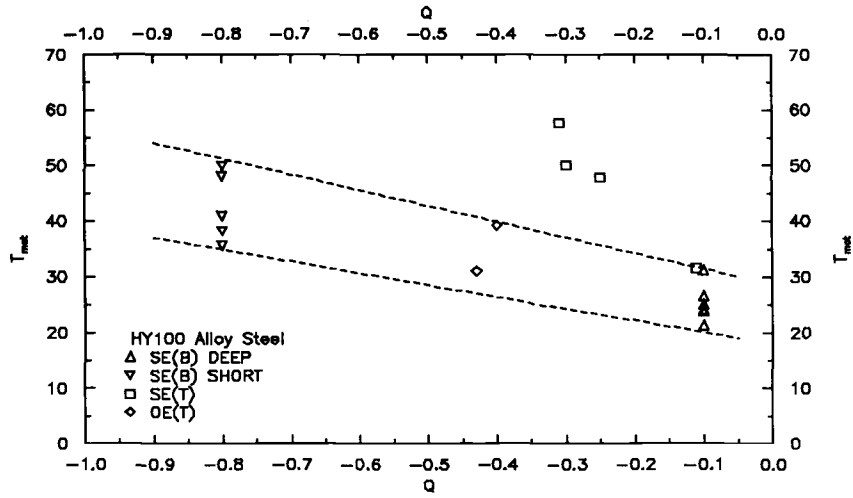


Figure 28 Tearing modulus, T_{mat}, as a function of Q for the HY-100 specimens.

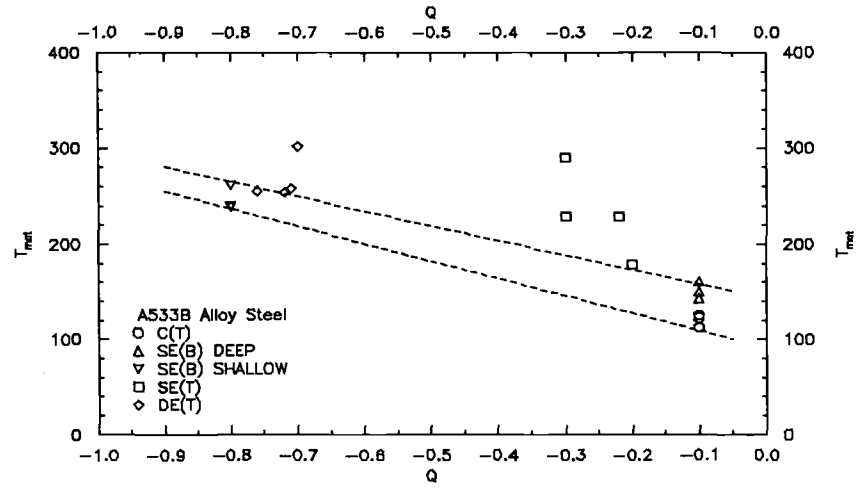


Figure 29 Tearing modulus, T_{mat}, as a function of Q for the A533B specimens.

specimen. Techniques have been developed which make it relatively easy to prepare and to test short crack bend specimens with a/W as small as 0.1.

ACKNOWLEDGEMENTS

This work was performed at the U.S. Naval Academy under the program "Elastic-Plastic Fracture Evaluation of LWR Alloys," R. E. Link of the Naval Surface Warfare Center, Annapolis, MD, Program Manager. The program is sponsored by the Office of Nuclear Regulatory Research of the U.S. Nuclear Regulatory Commission (NRC). The technical monitor for the NRC was Dr. Shah Malik. The authors would like to acknowledge the help of Mr. Wayne Farmer and Mr. John Hein of the U.S. Naval Academy for technical assistance with several aspects of this project, and also the Technical Support Department of the U.S. Naval Academy Engineering and Weapons Division for specimen and fixture machining.

REFERENCES

[1] O'Dowd, N.P. and Shih, C.F., "Family of Crack-Tip Fields Characterized by a Triaxiality Parameter - I. Structure of Fields," *Journal of Mechanics and Physics of Solids*, Vol. 39, pp. 989-1015, 1991.

[2] Anderson, T.L. and Dodds, R.H., Jr., "Specimen Size Requirements for Fracture Toughness Testing in the Transition Region," *Journal of Testing and Evaluation*, JTEVA, Vol. 19, No. 2, March 1991, pp. 123-134.

[3] Kirk, M. T., Koppenhoefer, K. C., and Shih, C. F., "Effect of Constraint on Specimen Dimensions Needed to Obtain Structurally Relevant Toughness Measures." *Constraint Effects in Fracture, ASTM STP 1171*, E. M. Hackett, et al., Eds., American Society for Testing and Materials, Philadelphia, 1993, pp. 79-103.

[4] Sumpter, J. D. G. and Forbes, A.T., "Constraint Based Analysis of Shallow Cracks in Mild Steel", *Proceedings of TWI/EWI International Conference on Shallow Crack Fracture Mechanics, Toughness Tests and Applications*, Cambridge, UK, 1992.

[5] Betegón, C. and Hancock, J. W., "Two-Parameter Characterization of Elastic-Plastic Crack-Tip Fields", *Journal of Applied Mechanics*, Vol. 58, 1991, pp. 104-110.

[6] Williams, M. L., "On the Stress Distribution at the Base of a Stationary Crack", *Journal of Applied Mechanics*, Vol. 24, 1957, pp. 109-114.

[7] Larrson, S.G. and Carlsson, A.J., "Influence of Non-Singular Stress Terms and Specimen Geometry on Small-Scale Yielding at Crack tips in an Elastic-Plastic Material," *Journal of Mechanics and Physics of Solids*, Vol. 21, 1973, pp. 263-278.

[8] Sumpter, J.D.G., "An Experimental Investigation of the T-Stress Approach," *Constraint Effects in Fracture, ASTM STP 1171*, Hackett, E.M., et al. Eds, American Society for Testing and Materials, Philadelphia, 1993, pp. 492-502.

[9] Joyce, J.A., Hackett, E.M. and Roe, C., "Comparison of J_{Ic} and J-R Curves for Short Crack and Tensilely Loaded Specimen Geometries of a High Strength Structural Steel," NUREG/CR-5879, U.S. Nuclear Regulatory Commission, Washington D.C., 1992.

[10] Joyce, J.A., "J-Resistance Curve Testing of Short Crack Bend Specimens Using Unloading Compliance," *Fracture Mechanics: Twenty-Second Symposium (Volume I), ASTM STP 1131*, H.A. Ernst, A. Saxena, and D.L. McDowell, Eds., American Society for Testing and Materials, Philadelphia, 1992, pp. 904-924.

[11] Hackett, E.M and Joyce, J.A., "Dynamic J-R Curve Testing of a High Strength Steel Using the Key Curve and Multi-Specimen Techniques," *Fracture Mechanics, ASTM STP 905*, American Society for Testing and Materials, Philadelphia, 1986, pp. 741-774.

[12] Al-Ani, A. M. and Hancock, J. W., "J-Dominance in Short Cracks in Tension and Bending", *Journal of Mechanics and Physics of Solids*, Vol. 39, 1991, pp. 23-43.

[13] O'Dowd, N.P., and Shih, C.F., "Family of Crack-Tip Fields Characterized by a Triaxiality Parameter: Part II - Fracture Applications," *Journal of the Mechanics and Physics of Solids*, Vol. 40, 1992, pp. 939-963.

[14] Leevers, P. S. and Radon, J. C., "Inherent Stress Biaxiality in Various Fracture Specimen Geometries", *International Journal of Fracture*, Vol. 19, 1982, pp. 311-325.

[15] Kfouri, A.P., "Some Evaluations of the Elastic T-term using Eshelby's Method in *International Journal of Fracture*, Vol. 30, 1986, pp. 301-315.

[16] Sham, T. L., "The Determination of the Elastic T-Term Using Higher Order Weight Functions", *International Journal of Fracture*, Vol. 48, 1991, pp. 81-102.

[17] Paris, P.C., Tada, H., Zahoor, A. and Ernst, H., "The Theory of Instability of the Tearing Mode of Elastic-Plastic Crack Growth," *Elastic-Plastic Fracture, ASTM STP 668*, J.D. Landes, et al., Eds., American Society for Testing and Materials, Philadelphia, 1979, pp. 5-36.

David K.M. Shum[1]

EFFECTS OF 3-D TRANSVERSE CONSTRAINT ON THE EVOLUTION OF IN-PLANE Q-STRESS

REFERENCE: Shum, D.K.M., **"Effects of 3-D Transverse Constraint on the Evolution of In-Plane Q-Stress,"** Fracture Mechanics: 26th volume, ASTM STP 1256, Walter G. Reuter, John H. Underwood, and James C. Newman, Jr., Eds., American Society for Testing and Materials, Philadelphia, 1995.

ABSTRACT: This study examines the limits of validity of the $Q \approx 0$ assumption under monotonic loading along the crack front in the "high constraint" 2-in.- and 4-in.-thick 4T-planform CT specimen geometries. Preliminary results indicate that progressive deviation of the in-plane crack-tip fields from $Q \approx 0$ occurs with increasing load, along the crack front up to the symmetry plane of the geometries. The nature of the in-plane deviation can be described using J-Q theory. Significantly, no indication of possible 3-D transverse loss-of-constraint effects on the crack-tip fields is manifested in a 2-D plane strain analysis of the 4T-planform geometry. Uniformity of J or K values along the crack front does not imply either the existence of single-parameter-dominant conditions or the absence of substantial 3-D variations in the in-plane crack-tip fields. Preliminary results also suggest that current K_{Ic}-related size requirements in ASTM-E399 might be sufficient to preclude the onset of significant 3-D transverse Q-stress effects for the 4-in.-thick geometry. However, significant deviation from J-dominant conditions could occur within the existing J_{Ic}- and J_R-related size requirements in ASTM-E813 and ASTM-E1152 for both geometries.

KEYWORDS: J-Q theory, crack-tip constraint, fracture toughness, crack-tip fields, small-scale yielding, CT, warm prestress

INTRODUCTION

Background and Objectives

It is a common assumption that the in-plane crack-tip fields along much of the crack front in "high constraint" specimens, such as "thick-section" compact (CT) specimens with nominal flaw-depth to width ratio a/W ~0.5, can be adequately described within a two-dimensional (2-D) plane strain single-parameter (K or J) dominance framework. In the context of J-Q theory, the assumption of single-parameter dominance of crack-tip fields is associated with a crack-tip constraint state characterized by $Q \approx 0$ [1].

[1]Research Associate, Saint-Gobain/Norton Industrial Ceramics Corporation, Goddard Road, Northboro, MA, USA 01532-1545.

Copyright© 1995 by ASTM International www.astm.org

The objective of this study is to examine the limits of validity of the $Q \approx 0$ assumption for the "high constraint" 2-in.- and 4-in.-thick 4T-planform CT specimens under monotonic loading conditions. The goal is to quantify the "capacity" of these specimen geometries with respect to the determination of values of the crack-driving force and, hence, fracture toughness that is consistent with the $Q \approx 0$ crack-tip constraint state.

The results of this study are applicable to the interpretation of "conventional" isothermal fracture-mechanics data that involve monotonic loading, and to a refined description of the preload and final-fracture phases of fracture-mechanics specimens subjected to non-monotonic load paths such as warm prestress (WPS) loading conditions [2,3].

Reference Datasets

The specimen geometry under consideration is the *plane-sided* 4T-planform CT specimen with a/W ~0.5. A WPS-enhanced fracture toughness dataset for unirradiated reactor pressure vessel (RPV)-grade A533B steel obtained using this specimen geometry has been identified [4]. The WPS data, herein referred to as the MEA dataset, involve 2-in.-thick (50.8 mm) 4T-planform CT specimens with a/W = 0.5. The WPS cycle corresponds to load-unload-cool-fracture (type-II WPS) [2,3]. The preload was carried out at 177°C (351°F) with K_{WPS} ~200 MPa$\sqrt{m}$ (182 ksi$\sqrt{in}$). Fracture occurred at -95°C (-139°F) with K_c ~170 MPa$\sqrt{m}$ (155 ksi$\sqrt{in}$). In the absence of prior WPS, the toughness at -95°C is K_{Ic} ~70 MPa$\sqrt{m}$ (64 ksi$\sqrt{in}$).

Analysis has also been carried out for a 4-in.-thick (101.6 mm) 4T-planform CT specimen with the same a/W ratio. Motivation for considering the 4-in.-thick geometry is two folds. Firstly, comparison of analysis results based on the 2-in.- and 4-in.-thick models will highlight potential thickness effects associated with the 4T-planform CT geometry. Secondly, a fracture toughness dataset without prior WPS, herein referred to as the ML dataset, for unirradiated A533B steel based on both 2-in.- and 4-in.-thick 4T-planform CT specimen geometries has also been identified [5]. (It is emphasized that aside from the nominal A533B designation, no relation exists between the MEA and the ML steels). In the case of the ML dataset, crack initiation took place at 0°C (32°F) with K_c ~219 MPa$\sqrt{m}$ (199 ksi$\sqrt{in}$) for the 2-in.-thick specimen and K_c ~191 MPa$\sqrt{m}$ (174 ksi$\sqrt{in}$) for the 4-in.-thick specimen.

FINITE ELEMENT ANALYSIS FORMULATION

This study considers 2-D plane strain and 3-D finite element models of the 4T-planform CT specimen geometry with a flaw-depth to width ratio a/W = 0.56. All finite element models are obtained using the mesh-generation program ORMGEN [6]. Preliminary results indicate that the applied load (P)-K relation is sensitive to the a/W ratio. For a fixed value of the applied load the value of K for a/W = 0.56 can be substantially larger than that for a/W = 0.5. This finding is in accord with known differences of 22% in K for a fixed value of P for these two a/W ratios from LEFM calculations. While the P-K relation is sensitive to the a/W ratio, analysis results indicate that the level of constraint associated with a given value of K, expressed in terms of the Q-stress parameter, is nearly identical for a/W = 0.5 and 0.56 over the range of

loadings considered. Consequently, the difference in a/W ratio between the analysis (0.56) and the data (0.5) is not significant with respect to the applicability of the constraint-related conclusions to be presented.

Finite Element Models

From symmetry considerations, only one-half of the 4T-planform CT geometry is modeled in the 2-D analysis. The crack-tip region is modeled alternately with two crack-tip mesh arrangements using collapsed elements as indicated in Figs. 1 (a,b). The "coarse" arrangement indicated in Fig. 1(a) permits the application of higher values of the mode I stress intensity factor (K) than the "refined" arrangement indicated in Fig. 1(b) without incurring numerical convergence difficulties. The refined crack-tip arrangement provides improved resolution of the near-tip crack-tip fields at a given value of K relative to the coarse arrangement. The 2-D finite element model with a refined crack-tip region is made up of 475, 8-node plane strain isoparametric elements for a total of 1535 nodes. The integration order of these elements is 2x2.

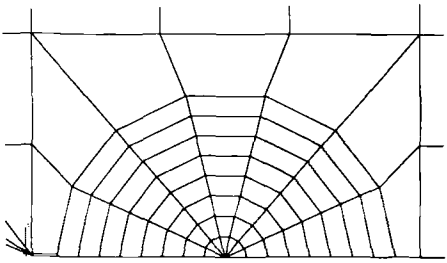
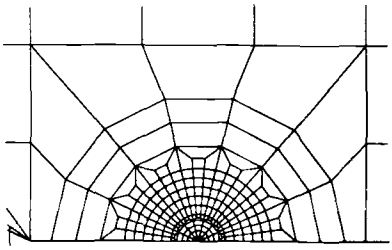


FIG. 1--(a) Coarse crack-tip model.



(b) Refined crack-tip model.

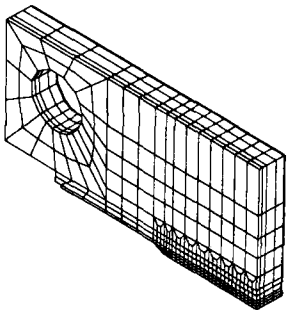
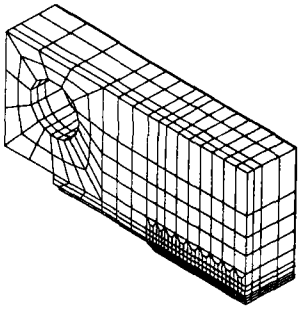


FIG. 2--(a) 2-in.-thick 3-D model.



(b) 4-in.-thick 3-D model.

The 3-D 4T-planform CT models for the 2-in.- and 4-in- thick specimen geometries are indicated in Figs. 2 (a,b), respectively. These models are obtained by projecting the 2-D finite element mesh along the thickness direction of the specimen. From symmetry considerations only one-quarter of the 3-D geometries are modeled. Similar to the 2-D model, analysis results have been obtained for each of the 3-D models using both the coarse and refined crack-tip mesh arrangement. Each of the 3-D models with a coarse crack-tip region is made up of 1640, 20-

node isoparametric elements for a total of 8394 nodes. The integration order of these elements is 2x2x2.

The 2-D models are constructed to permit interpretation of the results based on current application of the J-Q methodology in a manner to be discussed shortly. On the other hand, the potential influence of 3-D specimen-thickness effects on the crack-tip fields can only be examined via 3-D models of the 4T-planform CT geometry.

Material Properties

Uniaxial stress-strain data are not available for either the MEA or the ML dataset. In view of the scoping nature of the present investigation, uniaxial tensile stress-strain data for unirradiated A533B steel, taken from a steel plate designated as HSST plate-13A, are used to construct the reference stress-strain curve in the analyses [7]. Specifically, the analysis stress-strain curve corresponds to that for the plate-13A material at 0°C (32°F) "shifted up" by 50 MPa (7 ksi). The elevation in stresses is incorporated to reflect the slightly higher yield and ultimate stresses for the unirradiated A533B steel associated with the ML dataset. The analysis stress-plastic strain curve is indicated in Fig. 3. The material properties are as follows: Young's Modulus (E) = 207 GPa (30,000 ksi), Poisson's ratio (v) = 0.3, initial yield stress (σ_0) = 483 MPa (70 ksi) and ultimate stress (σ_u) = 701 MPa (102 ksi).

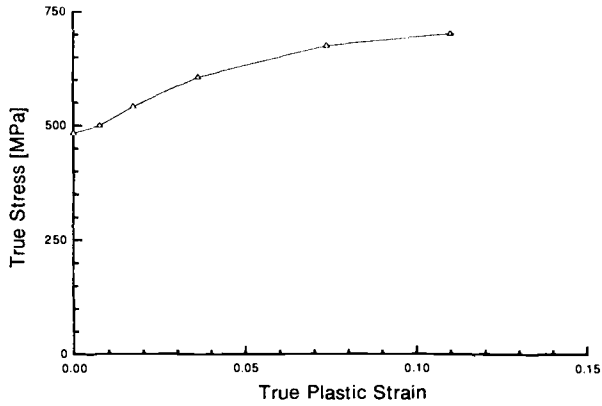


FIG. 3--Uniaxial true stress-true plastic strain curve.

Loading Conditions and Analysis Assumptions

Various analysis techniques to subject the CT specimen geometry to mode I loading have been considered [2]. In the case of the 2-D models, it is concluded that mode I loading of the specimen is best accomplished through application of distributed pressure loads on the upper-surface of the pin-hole of the specimen. In the case of the 3-D models, loading is accomplished by imposing uniform displacement boundary conditions along the upper-surface of the pin-hole of the specimen. Analysis results are obtained using the finite element code ABAQUS [8]. Analysis results to be presented are obtained based on a rate-independent, large-deformation, elastic-plastic, J_2 (isotropic-hardening) incremental plasticity formulation as implemented in ABAQUS. Additional

calculations based on small-deformation theory have been performed for the 2-D models for comparison and validation purposes and will be discussed shortly.

FINITE ELEMENT ANALYSIS RESULTS

The 2-D and 3-D results to be presented are preliminary in nature in that the finite element models are not sufficiently refined to yield accurate near-tip stress and strain results over distances less than ~10X the crack-tip-opening displacement (CTOD) ahead of the crack tip. However, the results do appear to be sufficiently detailed over distances >10xCTOD to permit comparison and interpretation on both qualitative and quantitative levels. Over distances >10xCTOD, analysis results should not be sensitive to whether large- or small-deformation theory is employed and this expectation is confirmed based on comparison of 2-D results presented in Ref. [2]. Aside from differences with respect to (1) the range of K values investigated and (2) the resolution of the crack-tip fields, analysis results based on the coarse and refined crack-tip meshes are compatible for similar values of K. Consequently, no attempt is made to identify the crack-tip mesh used to generate the results to be presented.

Another reason behind the preliminary nature of the present results is that, as discussed in Ref. [2], it appears that the finite element models indicated in Figs. 1 and 2 underestimate the calculated crack-tip constraint, expressed in terms of deviation of the crack-tip fields from the associated small-scale yielding (SSY) distribution discussed below, for a given value of K as compared to that determined from a more refined model that employs a blunted-notch, boundary-layer-type crack-tip mesh. Preliminary indications are that the underestimate of crack-tip constraint is associated with the focused crack-tip mesh and/or global mesh arrangement. For the purpose of ascertaining the *relative* importance of in-plane (2-D) vs out-of-plane (3-D) effects on the crack-tip fields and crack-tip constraint, however, it is believed that comparison of the 2-D and 3-D results using the present models is both qualitatively and quantitatively meaningful.

Plane Strain Near-Tip Crack-Tip Fields

In Fig. 4, distribution of the opening-mode stress component (σ) along the crack plane directly ahead of the crack front are indicated for the 2-D plane strain model at various stages of loading expressed in terms of the applied value of K (determined from the associated J-integral value based on plane strain assumptions). The opening-mode stress is normalized with respect to the yield stress (σ_0). Distances ahead of the crack tip are normalized with respect to J/σ_0 where J is the value of the J-integral evaluated within ABAQUS. Recall that the finite element results are not accurate for distances $r < 10$xCTOD ahead of the crack tip. Based on the approximate relation $J/\sigma_0 \approx 2$xCTOD, the $r < 10$xCTOD limitation is approximately equivalent to $r < 5\ J/\sigma_0$. Accordingly, in Fig. 4 and subsequent figures, the distributions are not shown for $r < 3\ J/\sigma_0$.

Also indicated in Fig. 4 is the distribution of σ associated with the so-called K-dominant small-scale-yielding (SSY) conditions. The concept of SSY is discussed in Ref. [2]. Briefly, plane strain fracture toughness is identified with the magnitude of K at the onset of crack initiation under K-dominant SSY conditions. A significant feature of

the 4T-planform CT results is that, over the range of loading considered and for $r/(J/\sigma_0) > 5$, the plane strain distributions of σ ahead of the crack tip are essentially identical to those associated with the K-dominant SSY condition.

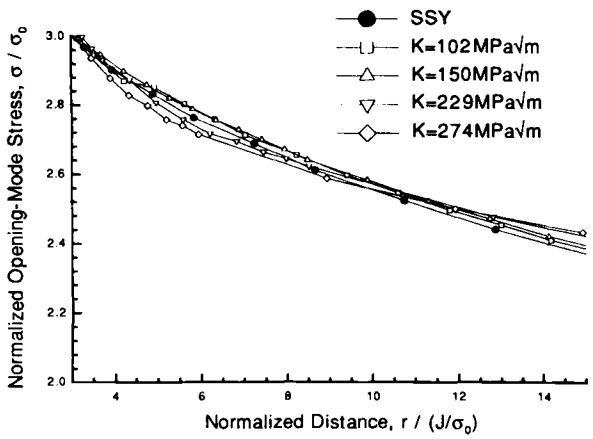


FIG. 4--Distributions of σ/σ_0 along the crack plane directly ahead of the crack tip for the 2-D plane strain model. Also indicated is the SSY distribution.

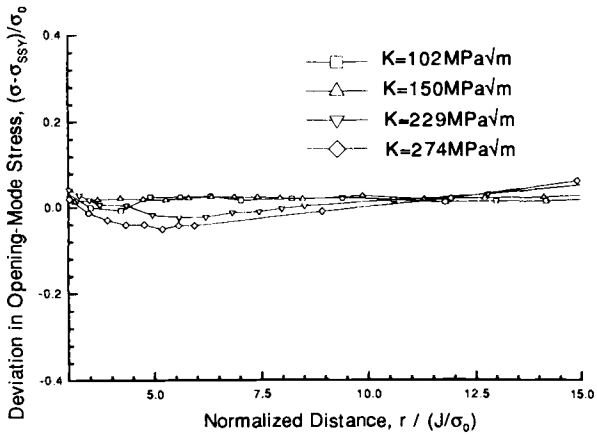


FIG. 5--Deviations of the 2-D plane strain results from the SSY distribution in terms of σ/σ_0.

Deviations (differences) of the 2-D plane strain results from those under SSY conditions are made explicit in Fig. 5. In Fig. 5, these deviations are expressed in terms of differences in σ between the 2-D and the SSY distributions. An alternate representation of these deviations in terms of differences in the mean (hydrostatic) stress σ_m can be found in Ref. [2]. Results shown in Fig. 5 and similar plots to

be presented will be used to provide quantitative measures of crack-tip constraint in a manner to be explained shortly.

Distribution of Crack-Driving Force Along 3-D Crack Front

In Fig. 6, distribution of the crack-driving force along the crack front for the 2-in.-thick 4T-planform CT model is indicated at various stages of loading. Crack-front location is expressed in terms of the normalized crack-front coordinate (η), where (η = 0) corresponds to the symmetry-plane location and (η = 1) corresponds to the specimen's free-surface. The crack-driving force is expressed in the normalized form $\sqrt{(J/J_0)}$, where J is the value of the J-integral at a given crack-front location and J_0 is the value of the J-integral at η = 0. The various stages of loading is expressed in terms of K_0, where K_0 is the value of K at η = 0 determined from J_0 based on the plane strain relation between K and J. In Fig. 7, distribution of the crack-driving force along the crack-front for the 4-in.-thick model is indicated at various stages of loading in a manner completely analogous to the 2-in.-thick results.

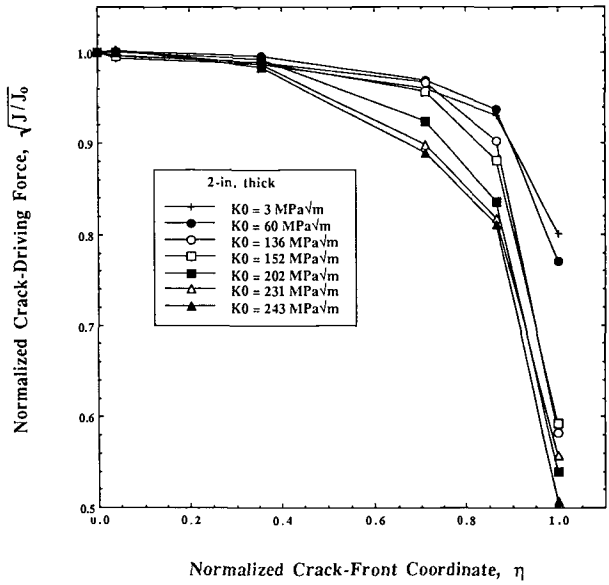


FIG. 6--Distribution of $\sqrt{(J/J_0)}$ along the crack front for the 2-in.-thick model as a function of symmetry-plane value K_0.

Near-Tip Crack-Tip Fields for 2-in.-Thick Model

In Fig. 8, distributions of σ along the crack plane directly ahead of the crack front are indicated at a stage of loading characterized by $K_0 \approx 100$ MPa$\sqrt{m}$ (J/σ_0 = 91 μm) for the 2-in.-thick model. Distributions are presented for four crack-front locations η = 0, 0.35, 0.71 and 0.88. In Fig. 9, deviations of the 3-D results from SSY conditions are quantified in terms of the differences in σ between the 3-D and SSY distributions. In Figs. 10 and 11, 3-D results for the 2-in.-thick

model at a stage of loading characterized by $K_0 \approx 200$ MPa$\sqrt{m}$ ($J/\sigma_0 = 364$ μm) are indicated.

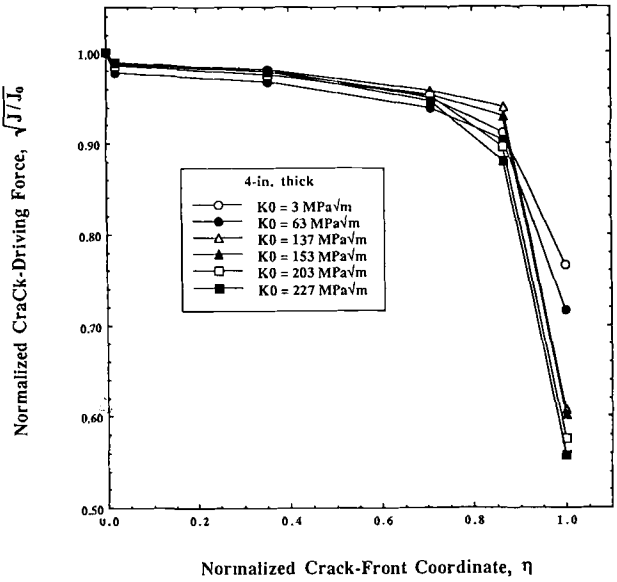


FIG. 7--Distribution of $\sqrt{(J/J_0)}$ along the crack front for the 4-in.-thick model as a function of symmetry-plane value K_0.

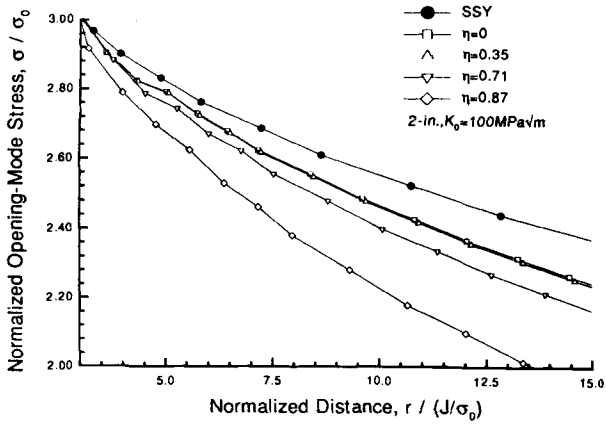


FIG. 8--Distributions of σ/σ_0 along the crack plane directly ahead of the crack tip for the 2-in.-thick model at $K_0 = 100$ MPa$\sqrt{m}$.

Near-Tip Crack-Tip Fields for 4-in.-Thick Model

In Figs. 12 to 15, results similar to those in Figs. 8 to 11 are indicated for the 4-in.-thick 4T-planform CT model at two stages of loading characterized by $K_0 \approx 100$ and 200 MPa$\sqrt{m}$.

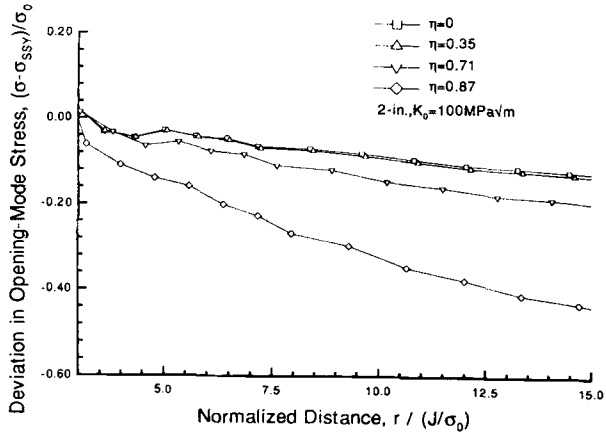


FIG. 9--Deviations of the 3-D results from the SSY distribution in terms of σ/σ_0 at K_0 = 100 MPa√m for the 2-in.-thick model.

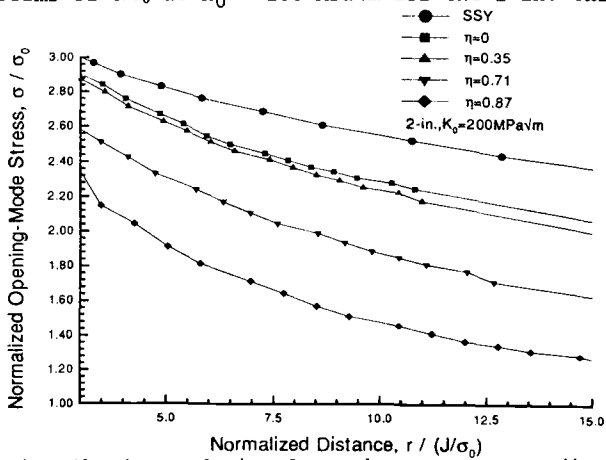


FIG. 10--Distributions of σ/σ_0 along the crack plane directly ahead of the crack tip for the 2-in.-thick model at K_0 = 200 MPa√m.

CRACK-TIP CONSTRAINT IN TERMS OF Q AND Q_m

As discussed in Ref. [1], the magnitude of the Q-stress parameter is defined as the difference in the opening-mode stress component (σ) between the full-field (FF) [e.g. finite element model of the 4T-planform CT geometry] and the SSY distribution at a distance of 2 J/σ_0 ahead of the crack tip along the crack plane. Both the FF and the SSY analyses are performed under plane strain assumptions. Full-field solutions for the various 4T-planform CT models are not available at 2 J/σ_0 due to insufficient mesh refinement. Instead, deviation of the various 2-D and 3-D full-field solutions from the plane strain SSY distribution in terms of σ has been quantified over the range of distances indicated in previous figures. For the purpose of this study, then, a *formal* definition of the Q-stress parameter is employed based on

the difference in σ at a distance of 5 J/σ_0 ahead of the crack tip along the crack plane. Additionally, a formal definition of the Q-gradient parameter Q' based on $5 \leq r/(J/\sigma_0) \leq 10$ is adopted to provide an alternate measure of the approximate validity of the J-Q annular approach.

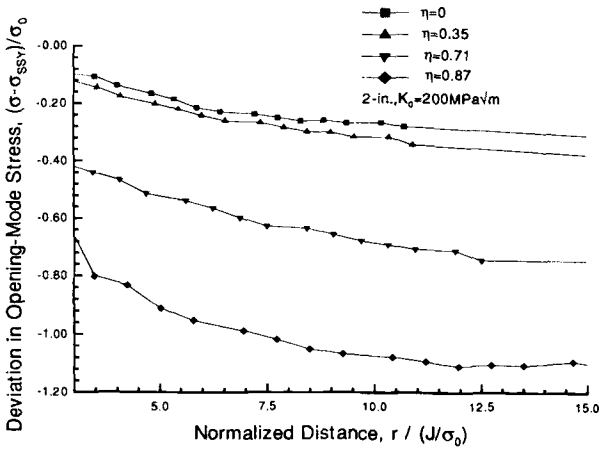


FIG. 11--Deviations of the 3-D results from the SSY distribution in terms of σ/σ_0 at K_Q = 200 MPa$\sqrt{m}$ for the 2-in.-thick model.

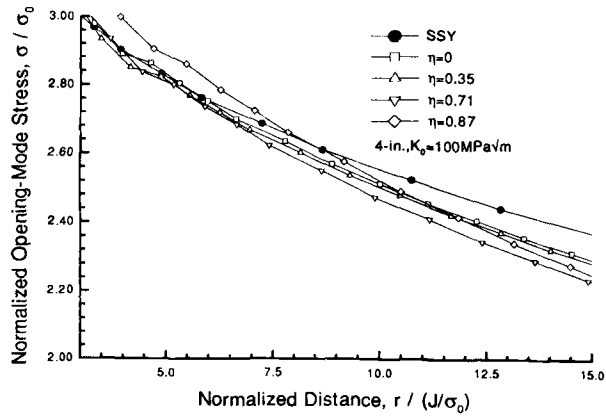


FIG. 12--Distributions of σ/σ_0 along the crack plane directly ahead of the crack tip for the 4-in.-thick model at K_Q = 100 MPa$\sqrt{m}$.

Characterization of crack-tip constraint based on Q and Q' are motivated primarily by considerations of cleavage crack initiation. Cleavage fracture is often the fracture mode associated with the final reload-cycle in small-specimen WPS experiments. However, the initial WPS preload-cycles in these experiments are often carried out over the upper-transition or the upper-shelf temperature regime. Consequently, the mean (hydrostatic) stress σ_m would appear to be a more appropriate measure of crack-tip constraint under these conditions. The constraint

parameters Q_m and Q_m' based on σ_m are also defined in Ref. [1] and the associated analysis results discussed in Refs. [2,3].

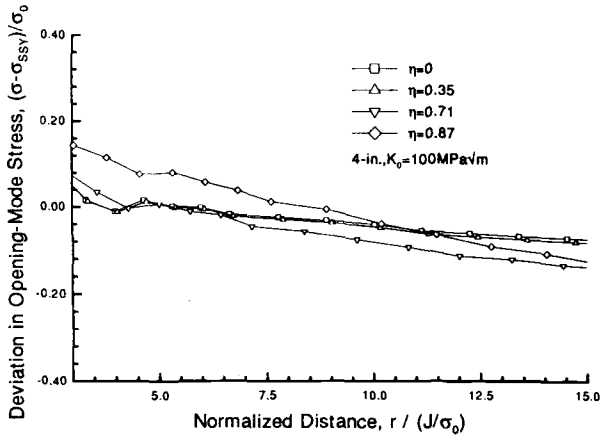


FIG. 13--Deviations of the 3-D results from the SSY distribution in terms of σ/σ_0 at K_0 = 100 MPa$\sqrt{m}$ for the 4-in.-thick model.

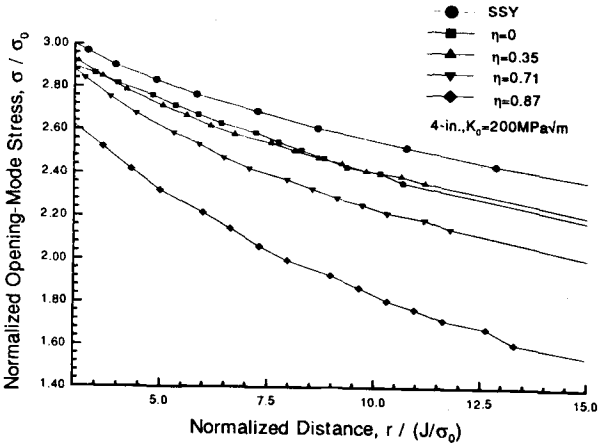


FIG. 14--Distributions of σ/σ_0 along the crack plane directly ahead of the crack tip for the 4-in.-thick model at K_0 = 200 MPa$\sqrt{m}$.

INTERPRETATION BASED ON 2-D CRACK-TIP FIELDS

For fracture mechanics applications where both the geometry and the applied load are 2-D in nature and "sufficient" section-thickness is believed to exist, it is common practice to examine the crack-tip fields using 2-D plane strain assumptions. Within the context of this 2-D approach, constraint effects on the crack-tip fields and fracture toughness are examined under the premise that the essential features of these constraint effects are "in-plane" in nature. Fracture mechanics applications that have incorporated the above 2-D viewpoint and the J-Q

approach include analysis of plane-sided deep- and shallow-flaw three-point-bend specimens and single-edge-notched-tension specimens [9-11].

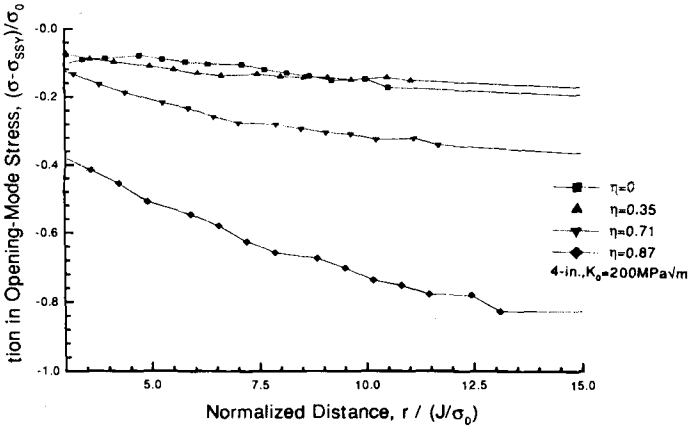


FIG. 15--Deviations of the 3-D results from the SSY distribution in terms of σ/σ_0 at K_0 = 200 MPa$\sqrt{m}$ for the 4-in.-thick model.

The present cases of 2-in.- and 4-in.-thick plane-sided 4T-planform CT specimen geometries are often assumed to fall within a 2-D viewpoint and the 2-D plane strain analysis results have been obtained for this reason. Within the context of the 2-D viewpoint, the interpretation of the results indicated in Figs. 4 and 5 is that the 4T-planform CT specimen geometry is well able to maintain a $Q \approx 0$ ($Q' < 0.1$) constraint state over a range of crack-tip loading up to 274 MPa$\sqrt{m}$. Similar conclusions are reached based on Q_m and Q_m' as discussed in Ref. [2], as there exist minimal differences between (Q,Q') and (Q_m,Q_m').

The WPS preload for the MEA dataset was carried out with K_{WPS} ~200 MPa$\sqrt{m}$. Crack initiation for the non-WPS 2-in.- and 4-in.-thick ML specimens was reported to occur at K = 219 MPa$\sqrt{m}$ and 191 MPa$\sqrt{m}$, respectively. Recall that in the context of J-Q theory, a K-dominant SSY stress state is associated with a state of crack-tip constraint characterized by $Q \approx 0$ (or $Q_m \approx 0$). Consequently, on the basis of the results in Figs. 4 and 5, one would (erroneously, as revealed by the 3-D results to be discussed shortly) conclude that a single-parameter approach based only on K (or J) is appropriate for correlating the loading histories of these specimens up to the values indicated.

INTERPRETATION BASED ON 3-D CRACK-TIP FIELDS

Results in Figs. 8 and 9 indicate that deviation from K-dominant SSY conditions occurred along a substantial portion of the crack front for the 2-in.-thick 4T-planform CT specimen by ~100 MPa$\sqrt{m}$. From Figs. 10 and 11, it is further observed that the extent of the deviation from SSY conditions increased substantially with increase in load as characterized by K_0 from ~100 MPa$\sqrt{m}$ to ~200 MPa$\sqrt{m}$. Results in Figs. 12 to 15 indicate that the extent of the deviation from SSY conditions is much less for the 4-in.-thick specimen as compared to the 2-in.-thick

specimen for the same value of K_Q. Conditions of K-dominance in the 4-in.-thick 4T-planform CT specimen are maintained at ~100 MPa$\sqrt{m}$. However, significant deviation from SSY conditions is observed by ~200 MPa$\sqrt{m}$.

Results in Figs. 8 to 15 are significant since it is commonly assumed that the in-plane crack-tip fields along much of the crack front in "thick-section", "high-constraint" specimens such as the 2-in.- and 4-in.-thick 4T-planform CT specimens with a/W ~0.5 are of the K-dominant type and, therefore, are assumed to be well approximated using 2-D plane strain analysis models. Indeed, one would have arrived at this conclusion based on the 2-D plane strain results presented in Figs. 4 and 5. However, the 3-D results clearly indicate the presence of 3-D effects on crack-tip constraint. Furthermore, depending on the applied load as characterized by K_Q, the loss of SSY-constraint can occur even at the symmetry plane of the specimens. Significantly, no indication of possible 3-D loss of constraint effects on crack-tip fields of the type indicated in Figs. 8 to 15 is manifested in a 2-D plane strain analysis of the specimen geometry in the form of Q-stress-like in-plane effects.

From Figs. 6 and 7, it is observed that essential uniformity of J-integral values along the crack front for both the 2-in.- and 4-in.-thick 4T-planform CT specimens is maintained up to $K_Q \approx 200$ MPa$\sqrt{m}$. Evidently, then, uniformity of J-integral (or equivalently K) values along the crack front does not imply either the existence of single-parameter-dominant conditions or the absence of substantial 3-D variations in the in-plane crack-tip fields. This is a also significant result since it is commonly believed that uniformity of J-integral values along the crack front is indicative of 2-D plane-strain-like in-plane crack-tip fields under single-parameter-dominant conditions.

The results in Figs. 8 to 15 indicate that, along the crack front, the deviation of in-plane crack-tip fields from the reference SSY distribution can be characterized in a Q-like or Q_m-like manner. Indeed, these results quantify the essential J-Q and J-Q_m annular nature of the 3-D variation since $Q' < 0.1$ and $Q_m' < 0.1$ along the crack front. It is noted that the magnitude of the constraint-loss, relative to SSY conditions, is load-dependent and is generally slightly larger based on Q than Q_m. Nevertheless, it would appear that while the conventional 2-D J-Q and J-Q_m viewpoints formulated based on 2-D plane strain assumptions are inappropriate for much of the analysis conditions examined here, a 3-D J-Q and J-Q_m interpretation provides a very accurate description of the 3-D crack-tip fields as they exist in the specimen geometries considered.

Finally, based on the observed elevation of numerically calculated crack-tip constraint using the 2-D blunted-notch vs the focused crack-tip models as discussed in Ref. [2], it is anticipated that refinement of the 3-D analyses presented above using blunted-notch models would similarly elevate the calculated crack-tip constraint. However, the significant observation of 3-D loss of constraint effects that are absent from a 2-D plane strain analysis can reasonably be expected to hold for the blunted-notch 2-D and 3-D models.

3-D J-Q Methodology

In anticipation of the need to develop a 3-D J-Q methodology, one of the challenges is expected to be the development of an appropriate definition for a single Q-like parameter for use under 3-D conditions. A number of candidate *effective* 3-D Q-stress constraint parameters (Q^{eff}) are defined by the following relations:

$$Q^{eff} = Q^{3D} \text{ at a specified crack-front location.} \tag{1}$$

$$Q^{eff} = \frac{1}{\ell}\int_0^{\ell} Q^{3D}\, d\eta \quad , \; 0 < \ell \leq L \tag{2}$$

$$Q^{eff} = \frac{1}{\ell}\int_0^{\ell} F\left(Q^{3D}\right) d\eta \quad , \; 0 < \ell \leq L \tag{3}$$

The above three relations represent different approaches to account for the "point-wise" nature of the 3-D crack-tip constraint state with respect to crack-front location. The appropriate form for Q^{eff} may depend on the micromechanics that govern fracture in a specific fracture application. For example, Eqn. (1) is appropriate for situations in which the crack-front variation of constraint is relatively strong, and a clear correlation between the point-wise value of crack-tip constraint (Q^{3D}) and the initiation event can be established. Eqn. (2) represents a crack-front-average definition of Q^{eff}, and is appropriate for situations in which the crack-front variation of constraint is relatively week, and a clear correlation between the point-wise value of Q^{3D} and the initiation event cannot be established. The averaging indicated in Eqn. (2) can take place over some portion of the crack-front ($0 < \ell \leq L$) up to the limiting case of the total length of the crack front (L). Eqn. (3) represents a *family* of definitions based on Eqn. (2), where the introduction of a general weighting function $F(Q^{3D})$ permits the definition of Q^{eff} to be tailored to take into account micromechanical details of the fracture process.

IMPLICATIONS TOWARD EXPERIMENTAL EVALUATION OF FRACTURE TOUGHNESS

Currently, experimental evaluation of fracture toughness under monotonic-loading conditions in terms of K_{Ic} and J_{Ic} is performed in accordance with ASTM standards. These standards stipulate "size requirements" that, along with other requirements, permit the determination of so-called "valid" fracture toughness values. While not explicitly stated in the standards, an implication associated with the satisfaction of size requirements is that the resultant fracture toughness values correspond to "high constraint" K- or J-dominant conditions. Analysis results obtained thus far permit a direct evaluation of the sufficiency of these size requirements to ensure K- or J-dominance. For the 2-in.- and 4-in.-thick 4T-planform CT specimens considered here, the applicable size requirements are as follows:

$$\text{E399: } 25\left(\frac{K_{Ic}}{\sigma_0}\right)^2 < B \tag{4}$$

$$\text{E813: } 25\left(\frac{J_{Ic}}{\sigma_{Fl}}\right) < B \text{ or } 25\left(\frac{\left(1-\nu^2\right) K_{Jc}^2}{E\,\sigma_{FL}}\right) < B \qquad (5)$$

In Eqns. (4,5), σ_0 is the yield stress, σ_{FL} is the flow stress based on the average of the yield and ultimate stresses, E is Young's Modulus, v is Poissons' ratio, and B is the specimen thickness. The symbol K_{Jc} in Eqn. (5) represents the fracture toughness J_{Ic} expressed in terms of units appropriate to the stress intensity factor K, and is adopted here to facilitate evaluation of the J_{Ic} size requirement based on the results obtained in this study. For the 2-in.-thick specimen, the maximum values of fracture toughness that are considered valid based on Eqns. (4,5) are K_{Ic} = 69 MPa$\sqrt{m}$ and K_{Jc} = 523 MPa$\sqrt{m}$. Corresponding values for the 4-in.-thick specimen are K_{Ic} = 98 MPa$\sqrt{m}$ and K_{Jc} = 740 MPa$\sqrt{m}$.

With respect to K_{Ic}-related size requirements, a definitive evaluation of the 2-in.-thick geometry is not possible since the smallest value of K_0 discussed herein (see Figs. 8 and 9) is 100 MPa$\sqrt{m}$. However, it is emphasized that significant deviation from SSY conditions has occurred by 100 MPa$\sqrt{m}$. On the other hand, results in Figs. 12 and 13 indicate that the size requirement does ensure K-dominance for the 4-in.-thick geometry.

With respect to J_{Ic}-related size requirements, it is significant to note that for both the 2-in.- and 4-in.-thick specimens, significant deviation from J-dominant SSY conditions occur for values of K_{Jc} much less than the maximum values based on Eqn. (5) (see Figs. 8-15). It is recognized that the introduction of side grooves, a common practice in the case of J_R testing, tends to preserve the uniformity of J values along the crack front. However, following the observations discussed thus far and in particular in relation to results presented in Figs. 6 and 7, the effects of side grooves on the maintenance of crack-tip constraint is not obvious. Consequently, it would appear that the existing size requirements for J_{Ic} (and by implication J_R resistance curve) testing are not sufficiently stringent to ensure that the fracture toughness results correspond to "high constraint" conditions.

Finally, as suggested by a reviewer of this paper, the above approach to ascertain the "validity" of fracture toughness data may shed light on the interpretation of surface crack test results in an essentially linear-elastic material (see Reuter and Epstein, ASTM STP 969 (1987), pp. 597-619).

IMPLICATIONS TOWARD VESSEL FRACTURE-MARGIN ASSESSMENT

Fracture Toughness Under Monotonic Loading

Currently, probabilistic fracture-margin assessment of reactor pressure vessels (RPVs) under pressurized thermal shock (PTS) loading conditions is based in part on a statistical interpretation of the ASME lower-bound toughness curve K_{Ic} for the prediction of crack initiation and re-initiation after crack arrest. Specifically, the lower-bound K_{Ic}

curve was interpreted as the minus two standard deviations (-2σ) toughness curve in the context of the integrated pressurized thermal shock (IPTS) methodology [12]. The scatter in K_{Ic} values with respect to the lower-bound curve is then used to define the *mean-value* toughness curve and to evaluate the magnitude of one standard deviation ($|\sigma|$). On the basis of the above statistical interpretation, the toughness data base is extrapolated to provide a $\pm 3\sigma$ description of the toughness results for use in a probabilistic evaluation of the fracture-margin of RPVs.

A key assumption inherent to the above statistical interpretation of the ASME K_{Ic} toughness data base is the assumption that all data are "high constraint" in nature, and that the scatter is a reflection of material variability and its effect on crack initiation. Present findings on the evolution of 3-D constraint-loss effects with increasing failure load in nominally "high constraint" small-specimen geometries have significant implications toward the fracture-margin assessment of RPVs in the following sense. Present findings suggest the possibility that the existing ASME data base represent toughness measurements obtained under both "high" and "low" constraint conditions as quantified by the J-Q methodology. The likelihood that the reported fracture toughness is "low constraint" in nature increases with increasing values of the toughness. On the other hand, results presented in Chapter 3 of Ref. [2] suggest that for a wide range of PTS analysis conditions, the fracture response of an RPV should be determined from "high constraint" toughness data.

Present findings thus appear to suggest the need to perform a constraint-based re-interpretation of the ASME K_{Ic} toughness data base for the purpose of identifying, if present, the subset of toughness data that can properly be identified as "high constraint" plane strain fracture toughness. It is anticipated that the to-be-determined subset of "high constraint" toughness data, when applied within an IPTS-type methodology, would result in the use of a mean-value toughness curve that is potentially lower in magnitude than that previously assumed. At the same time, the magnitude of one standard deviation ($|\sigma|$) would also be lowered.

In the context of an IPTS-type evaluation, a lower mean-value toughness curve would tend to increase the likelihood of predicting vessel failure. A lower value of $|\sigma|$ would (1) decrease the maximum value of toughness ($+3\sigma$) assumed in the analysis and thus increase the likelihood of predicting vessel failure, and (2) increase the minimum value of toughness (-3σ) and thus decrease the likelihood of predicting vessel failure. The net effects of these competing factors on the overall predicted conditional probability of vessel failure [P(F|E)], relative to an evaluation based on the current interpretation of the ASME toughness data base, cannot be determined without direct evaluation based on a specific PTS analysis scenario.

Finally, it is emphasized that the motivation for the constraint-based re-interpretation of the ASME K_{Ic} toughness data base is the observation of 3-D constraint effects along the crack front for nominally "high" constraint geometries. This type of "constraint correction" is very different than that associated with the so-called "shallow" vs "deep" flaw constraint correction [9-11]. The latter correction is based on crack-depth-related constraint effects that are

evaluated using a common framework of 2-D plane strain assumptions and, therefore, does not take into account 3-D effects as discussed here.

Warm Prestress-Enhanced Fracture Toughness

Results on the 4T-planform CT geometry presented thus far indicate that the preload phase of the WPS loading history for the MEA dataset was performed under conditions of increasing loss of crack-tip constraint. Observations concerning the constraint state during the unloading and reloading phases of the WPS cycle cannot be made since these phases have not been examined via direct calculation. However, since the values of K at preload and final fracture are similar for the MEA dataset, the results obtained thus far do suggest the likelihood that the reported WPS-enhanced toughness results might have been obtained under "low constraint" situations. Therefore, efforts are needed to (1) identify the constraint state associated with final fracture for the MEA dataset through direct evaluation, and (2) determine the applicability of the MEA dataset to vessel WPS scenario based partly on "matching" of their respective constraint states. Preliminary efforts toward establishing the nature of the crack-tip fields under WPS conditions and SSY assumptions are underway [2,3].

CONCLUSIONS

Preliminary results indicate that for the 4T-planform CT geometry progressive deviation in the form of loss of crack-tip constraint, with respect to the in-plane crack-tip fields for 2-D single-parameter dominance conditions, occurs with increasing load. Extent of the loss of constraint varies along the crack front. The loss of single-parameter dominance is observed to occur even at the symmetry plane of the 2-in.- and 4-in.-thick geometries. The nature of the in-plane deviation can be described using J-Q theory. Significantly, no indication of possible 3-D transverse loss-of-constraint effects on the crack-tip fields is manifested in a 2-D plane strain analysis of the 4T-planform CT specimen geometry. Uniformity of J or K values along the crack front does not imply either the existence of single-parameter-dominant conditions or the absence of substantial 3-D variations in the in-plane crack-tip fields.

Preliminary results also suggest that current K_{Ic}-related size requirements in ASTM-E399 might be sufficient to preclude the onset of significant 3-D transverse Q-stress effects for the 4-in.-thick geometry. On the other hand, preliminary results also suggest that significant deviation from J-dominant conditions could occur within the existing J_{Ic}-related, and by implication J_R-related, size requirements in ASTM-E813 and ASTM-E1152 for both geometries. A 3-D J-Q methodology thus appears necessary to provide a more accurate description of the specimen crack-tip fields and fracture toughness under some situations.

ACKNOWLEDGMENT

Analyses described herein were carried out while the author was a member of the Heavy-Section Steel Technology Program at the Oak Ridge National Laboratory. Helpful discussions with J.G. Merkle during the course of manuscript preparation are gratefully acknowledged.

REFERENCES

[1] N. P. O'Dowd, C. F. Shih, *Two-Parameter Fracture Mechanics: Theory and Applications*, USNRC Report NUREG/CR-5958 (CDNSWC/SME-CR-16-92), February 1993.

[2] D. K. M. Shum, *Preliminary Findings on the Inclusion of Warm Prestress Effects in Fracture-Margin Assessment of Reactor Pressure Vessels*, USNRC Report NUREG/CR-5946 (ORNL/TM-12236), to be published.

[3] D. K. M. Shum, "Interpretation of Warm Prestress-Induced Fracture Toughness Based on Crack-Tip Constraint", Fracture Mechanics: 25th volume, ASTM STP 1220, F. Erdogan and Ronald J. Hartranft, Eds., American Society for Testing and Materials, Philadelphia, 1994.

[4] R.B. Stonesifer, E.F. Rybicki and D.E. McCabe, *Warm Prestress Modeling: Comparison of Models and Experimental Results*, USNRC Report NUREG/CR-5208, MEA-2305, 1989.

[5] D.E. McCabe and J.D. Landes, *The Effect of Specimen Plan View Size and Material Thickness on the Transition Temperature Behavior of A533B Steel*, Research Report, Westinghouse R&D Center, November 1980.

[6] B.R. Bass and J.W. Bryson, *ORMGEN-3D: A Finite Element Mesh Generator for 3-Dimensional Crack Geometries*, USNRC Report NUREG/CR-2997, Vol 1 (ORNL/TM-8527/V1), December 1982.

[7] D. J. Naus et al., *Crack-Arrest Behavior in SEN Wide Plates of Quenched and Tempered A533 Grade B Steel Tested Under Nonisothermal Conditions*, USNRC Report NUREG/CR-4930 (ORNL-6388), August 1987.

[8] *ABAQUS User Manual*, Version 4-9-1, Hibbit, Karlsson & Sorensen, Inc., Providence, Rhode Island (1991).

[9] T. J. Theiss, D. K. M. Shum, S. T. Rolfe, *Experimental and Analytical Investigation of the Shallow-Flaw Effect in Reactor Pressure Vessels*, USNRC Report NUREG/CR-5886, ORNL/TM-12115, July 1992.

[10] J. D. G. Sumpter and J. W. Hancock, Shallow Crack Toughness of HY80 Welds: An Analysis based on T stresses, *International Journal of Pressure Vessels and Piping*, Vol. 45, pp. 207-221, 1991.

[11] Kirk, M. T., Koppenhoefer, K. C. and Shih, C. F., Effect of Constraint on Specimen Dimensions Needed to Obtain Structurally Relevant Toughness Measures, *Constraint Effects in Fracture, ASTM STP 1171*, E. M. Hackett, K.-H. Schwalbe, and R. H. Dodds, Eds., American Society for Testing and Materials, Philadelphia, 1993, pp. 79-103.

[12] D. L. Selby et al., *Pressurized Thermal Shock Evaluation of the H. G. Robinson Unit 2 Nuclear Power Plant*, USNRC Report NUREG/CR-4183 (ORNL/TM-9567), Vols. 1 and 2, September 1985.

Constraint Crack Growth

Frank A. McClintock[1], Yun-Jae Kim[2], and David M. Parks[1]

TESTS AND ANALYSES FOR FULLY PLASTIC FRACTURE MECHANICS OF PLANE STRAIN MODE I CRACK GROWTH

REFERENCE: McClintock, F. A., Kim, Y.-J., and Parks, D. M., **"Tests and Analyses for Fully Plastic Fracture Mechanics of Plane Strain Mode I Crack Growth,"** Fracture Mechanics: 26th Volume, ASTM STP 1256, Walter G. Reuter, John H. Underwood, and James C. Newman, Jr., Eds., American Society for Testing and Materials, Philadelphia, 1995.

ABSTRACT: Under monotonic loading, structures should ideally be ductile enough to provide continued resistance during crack growth. Such fully plastic behavior is of interest in design against collisions, tank car accidents, earthquakes, and ship groundings. For fully plastic crack growth in low strength alloys, existing asymptotic solutions for elastic-plastic growing cracks are not applicable because they reach the fracture strain only in regions small compared to the inhomogeneities of the actual fracture process.

For the limiting case of non-hardening fully-plastic plane strain crack growth, in a number of geometries and loadings the near-tip fields are characterized in terms of *three* parameters: an effective angle $2\theta_s$ between a pair of slip planes, and the normal stress σ_s and the increment of displacement δu_s across the planes. This three-parameter characterization is in contrast to the one- or two-parameter (K or J and T or Q) characterization in linear or non-linear elastic fracture mechanics. These θ_s, σ_s, and δu_s parameters are found from the far-field geometries and loadings through slip line fields or least upper bound analyses based on circular arcs. The resulting crack growth, in terms of the crack tip opening angle (CTOA), is a function of θ_s, σ_s, and the material. The geometry of the crack growing between two moving slip planes emanating from its tip reduces this function to the critical fracture shear strain left behind the slip planes, γ_f, as a function of σ_s. $\gamma_f(\sigma_s)$ is found theoretically from a hole initiation and growth model. It is also found from preliminary fully plastic crack growth experiments on unequally grooved specimens with fixed-grip extension or 4-point bending of a 1018 CF steel. At high triaxialities and also after strain aging, cleavage intervened abruptly, even during stable, slow deformation.

KEYWORDS: fracture mechanics, crack growth, Mode I, plane strain, fully plastic, non-hardening, ductile, strain aging, cleavage, CTOA, analysis, experiments

INTRODUCTION

Under monotonic loading, structures should ideally be ductile, in order to provide

[1]Professor Emeritus and Professor, respectively, Massachusetts Institute of Technology, Cambridge, MA 02139-4307.

[2]Institute of Materials Research, GKSS Research Centre, 21502-Geesthacht, Germany.

Copyright© 1995 by ASTM International www.astm.org

both a warning before initial crack growth and continued resistance during crack growth. Such fully plastic behavior is of interest in design against collisions, tank car accidents, earthquakes, and ship groundings, for example. Before considering the mechanics of crack growth in fully plastic structures, we briefly review the criteria for initial and early crack growth in elastic and plastic structures.

For brittle structures in tensile (Mode I) loading across a crack, only a criterion for initial growth is needed, because the crack is immediately unstable. The criterion is based on the discovery in the 1950's that there can be an annular region around the crack tip, large compared to either a plastic zone or to the microstructural fracture process zone, and small compared to the distance to the next nearest boundary, in which there is plane strain and the stress and strain are uniquely defined in terms of a single parameter, the stress intensity factor K_I (e.g. [*1*]). For a given material, at a critical value K_{Ic} the crack begins to grow unstably (e.g. [*2*], [*3*]). (At lower values of K_I, the growth is negligible unless loading is repeated thousands of times, as in fatigue.) The value of the applied K_I is determined from the far-field geometry and loading [*4*], [*5*]. Thus for a brittle structure (one with a crack tip plastic zone small compared to any characteristic dimension of the part or of the crack itself), unstable crack growth occurs under the local condition

$$K_I(\text{geometry and loading}) \geq K_{Ic}(\text{material}) \quad . \tag{1}$$

For more extensive plastic flow around a crack in a structure, an analogous criterion was found in the 1960's for power-law strain hardening material in which the equivalent stress $\bar{\sigma}$ is given in terms of the equivalent strain $\bar{\varepsilon}$ in terms of the flow stress at unit strain σ_1 and a strain hardening exponent n:

$$\bar{\sigma} = \sigma_1 \bar{\varepsilon}^n \quad . \tag{2}$$

With a sufficiently high strain hardening exponent n, there may be an annular region around the crack tip in which the stress and strain fields are uniquely defined in terms of a coefficient J, such that crack growth begins under the local condition

$$J(\text{geometry, loading, } \sigma_1, n) \geq J_c(\text{material}) \quad . \tag{3}$$

For the left-hand function, see [*6*], [*7*]. Data for J_c are scattered. With further increase in J, but with subsequent crack growth small compared to the annular region in which the stress and strain are characterized by J, the crack growth Δa is controlled by

$$\Delta a = \Delta a[J(\text{geometry, loading, } \sigma_1, n), \text{material}] \quad . \tag{4}$$

For initial growth, the singular expansions giving the first-order coefficients K and J have been extended to higher stress levels (toward general yield) by including second-order coefficients T or Q (e.g. [*8*], [*9*]), but the difficulties with finite crack growth remain. For crack growth large compared to the annular region in which the original J-field was dominant, the J-concept is no longer valid because it would have to be based on the current crack tip, and would not include the prior history which has left inhomogeneous strain, strain-hardening, and residual stress. In other words, for large crack growth the J-concept is based on non-linear (rubber) elasticity, not plasticity. In Fig. 1 the ranges of validity of the K and J representations of crack initiation and early growth are contrasted with the range of fully plastic crack growth that is of interest here.

Asymptotic solutions have been found for elastic-plastic growing cracks and are useful for high-strength alloys. For the low strength alloys of interest here ($\varepsilon_f/\varepsilon_y \approx 50$), the regions in which such ratios of fracture strain to yield strain exist turn out to be of sub-atomic size ([*10*], [*11*] pp 81-84). Thus outside the fracture process zone, where the

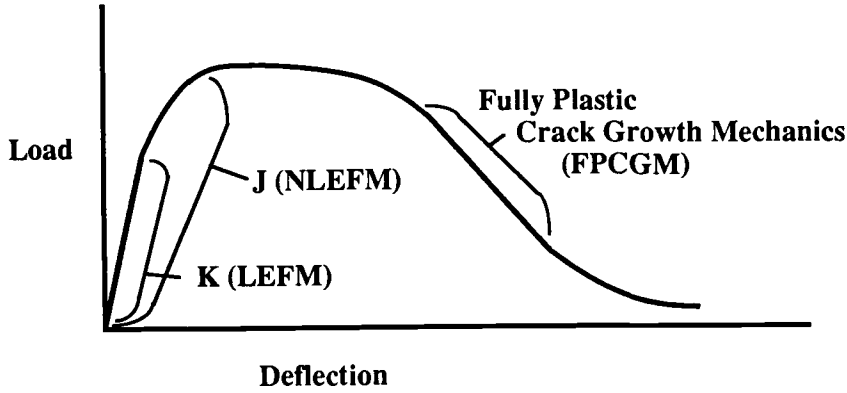


FIG. 1--Typical ranges of validity of linear and non-linear elastic fracture mechanics and of the fully plastic crack growth mechanics considered here.

material can be considered homogeneous, elastic strains are negligible and the rigid-plastic approximation applies, at least near the crack.

For fully plastic flow in the limiting case of a vanishingly small strain hardening exponent n, the governing equations become hyperbolic. Unique singular solutions do not exist, and the effects of far-field loading and geometry penetrate all the way to the crack tip in a number of different ways (e.g. [*12*]). With elastic strains negligible, the fields of strain increments and stress for growing cracks are the same as for stationary cracks. The plastic strains are then found by superposition of the increments for successive crack tip positions, as illustrated in Fig. 2 for two slip lines at a crack tip. Thus the known slip line fields for stationary cracks can be applied to growing cracks.

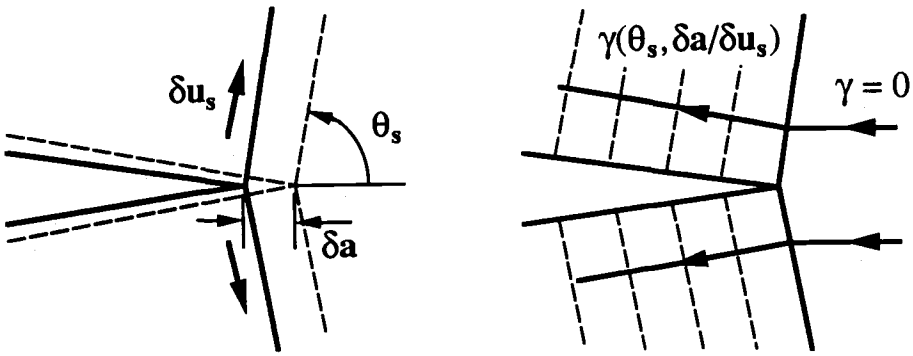


FIG. 2--The superposition of displacement increments at successive tip positions (Fig. 2a) leaves behind a zone of shear strain (Fig. 2b).

The distortion of non-hardening fields by strain hardening is less in growing than in stationary cracks, because the advance of the fields through the material smoothes discontinuous displacement fields into continuous ones. For instance the incremental displacement discontinuity of Fig. 2a is reduced to the strain discontinuity of Fig. 2b. Even in annealed aluminum, with a ratio of tensile to yield strength of 2.5, the deformation field around a growing crack (shear bands either side of a rigid wedge in front of the crack) shows a strong resemblance to the non-hardening field ([*13*], p 378).

Here we review the extension of fracture mechanics to the limiting case of non-hardening, plane-strain Mode I crack growth. It turns out that in this case, many of the infinite variety of non-hardening stress and strain fields can be usefully approximated by just three parameters, which for growing cracks can be reduced to shear strain left behind a pair of slip planes as a function of normal stress across those planes. (For unsymmetrical fields, see [*14*].) This provides a guide for the design of crack-growth-resistant structures of common low-strength alloys. Compliance of the surroundings usually prevents the design of crack-growth-resistant structures of high strength alloys.

NEAR-TIP FIELD CHARACTERIZATION FROM SLIP-LINE FIELDS

Fields of stress and displacement increments for cracked structures of rigid-plastic, non-hardening materials have been found for a variety of geometries and loadings (see [*12*], [*15*]). At the crack tip, a number of the Mode I (opening) fields consist simply of a pair of slip lines surrounded by rigid regions. An example is the single-face-cracked specimen under bending of Fig. 3a. Other Mode I fields consist of a pair of deforming fans surrounded by regions with less concentrated plastic flow, such as the doubly cracked specimen under tension of Fig. 3b. To simplify such problems, regard the deformation in the fan at the crack tip as being concentrated on discrete (dotted) slip lines between rigid regions. (Note that although the deformations in the fan are similar to those in discrete slip lines, the rotations are different, as follows. In the fans of Fig. 3b the circumferential displacements tend to string the holes out circumferentially, whereas at the crack tips the dotted slip lines tend to string the holes out radially. For the small values of 1.5 to 2 generally found for the ratio of hole radius at macro-fracture to that at hole formation, this effect is likely to be negligible.)

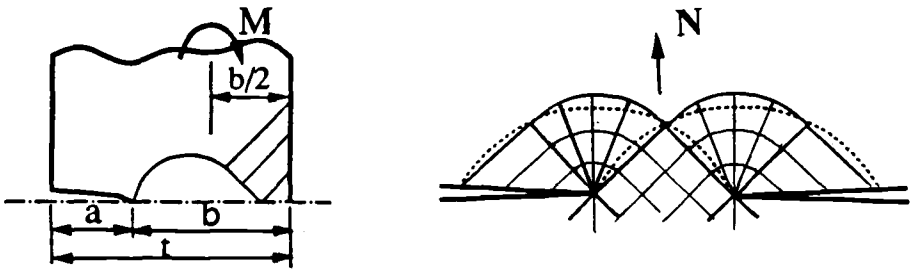


FIG. 3--Slip line fields (a) for a deep, single-face-cracked plate under pure bending, and (b) a symmetric doubly face-cracked plate in tension.

In summary, near-tip fields are here characterized by just three parameters: the slip line angle θ_s, and the normal stress σ_s and shear displacement δu_s across the slip line. The three parameters θ_s, σ_s, and δu_s describe a local field (as does K) as a function of loading and geometry:

$$\begin{Bmatrix} \theta_s \\ \sigma_s \\ \delta u_s \end{Bmatrix} = \{ f(far\text{-}field\ geometry, loadings, and\ their\ increments) \} \quad . \tag{5}$$

These variables, along with the material properties, set the crack growth increment δa.

Alternatively, one may think of the kinematically determined shear strain γ_k for a given slip angle and crack growth rate per unit slip line displacement, $\delta a/\delta u_s$, as being determined by the shear strain γ_f on the crack flanks required for crack growth in a given material with a given normal stress σ_s across the slip plane:

$$\gamma_k\left(\theta_s, \frac{\delta a}{\delta u_s}\right) = \gamma_f(\sigma_s, material) \quad . \tag{6}$$

This is the analogue for fully plastic crack growth of Eqs 1, 3, and 4 for crack initiation and early growth in the linear and non-linear regimes. (Kinematics also allows expressing $\delta a/\delta u_s$ in terms of the crack tip opening angle, CTOA).

Examples of Eq 5 will now be considered, particularly for the unequally face-grooved plates in tension and bending, for which experiments are reported here.

Tension of Unequally Face-Grooved Plates

The slip line field of Fig. 4 and the stress and displacement fields were given in [*12*] pp 141-143, along with the required plate width and shoulder thicknesses for the validity of the plane strain field. For the back half-angle $\omega = 90°$, the specimen corresponds to a single-face-cracked plate (the single edge-notched (SEN) specimen). For $\omega = 0°$, the specimen corresponds to the symmetrical, double-face-grooved plate (the double edge-notched (DEN) specimen). The crack tip parameters for these cases are given in the first block of Table 1 under SLF, which is all that need be considered now. For $\omega > 0°$, the slip plane angle θ_s is constant at 45° and the slip displacement per unit far-field displacement, $\delta u_s/\delta u$, is constant at $1/\sin 45° = \sqrt{2}$. The normal stress across the slip line rises linearly from $\sigma_s/2k = 0.5$ toward $0.5 + \pi/2$ as ω drops from 90° toward 0°. This increase in σ_s should decrease the crack growth shear strain γ_f of Eq 6, increase the crack advance per unit displacement, and decrease the crack tip opening angle, as shown later.

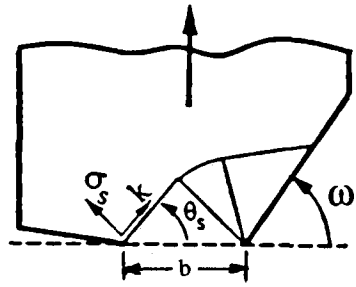


FIG. 4--Slip line field for unequally face-grooved plates in tension.

At $\omega = 0°$ the field for unequally grooved tension becomes symmetrical, with a unique stress distribution but a non-unique strain distribution. The Neimark distribution, with linearly varying displacements along the deforming flanks, seems most consistent

with strain-hardening. (e.g. [*12*] pp 123-126). All the non-unique strain fields involve fans above and below the crack tip, and the mean normal stress varies throughout the fans. A single slip plane, chosen as a lumped parameter model, will be discussed later.

TABLE 1--*Crack tip parameters for non-hardening plane strain crack growth.*
Angles and displacements are relative to planes of symmetry
Method: SLF: by slip line field; LUB (with entries indented): by least upper bound arc

Unequally Grooved Tension						
Method	Half back-angle ω °	Loading for width w $N/2kwb$[1]	Slip plane at crack tip: Angle θ_s °	Normal stress $\sigma_s/2k$	Displ. discont. $\delta u_s/\delta u$	
SLF	90	1	45	0.5	1.414	Single face groove
LUB_{arc}	90	1	45	0.5	1.414	"
LUB_{block}	90	1	45	0.5	1.414	"
SLF	75	1.262	45	0.762	1.414	"
SLF	60	1.524	45	1.024	1.414	"
SLF	45	1.785	45	1.285	1.414	"
LUB_{arc}	45	1.845	56.2	1.510	1.885	"
LUB_{block}	45	1.829	41.8	unkn	1.500	"
SLF	30	2.047	45	1.547	1.414	"
SLF	15	2.309	45	1.809	1.414	"
SLF	0	2.571	45-135	2.071-0.5	(fans)	Equal face grooves
$LUB_{2\ arcs}$	0	2.760	66.8	2.546	1.088 at each tip	"
LUB_{block}	0	2.828	35.3, 90	unkn	0.866, 1 on two lines at each tip	

Transverse Shear					
Method	ω	V/kwb	θ_s	$\sigma_s/2k$	$\delta u_s/\delta v$
SLF		0.978	±8.2	±0.14	0.62
LUB_{arc}		1	0	0	1

Unequally Grooved Bending						
Method	ω	$M/(kwb^2/2)$	θ_s	$\sigma_s/2k$	$\delta u_s/b\delta\theta$	
SLF	90	1.261	72.0	1.541	0.389	Single face groove
(Fig. 6a)	82.8	1.311	70.8	1.388	0.443	"
(Fig. 6b)	75.6	1.345	72.1	1.289	0.486	"
"	60	1.372	68.8	1.225	0.522	"
"	45	1.379	67.2	1.176	0.539	"
(single arc)	30-0	1.380	66.8	1.165	0.544	Equal face grooves
LUB_{arc}	0-90	1.380	66.8	1.165	0.544	Single and equal

Transverse Shear of Singly Face-Grooved Plates

More insight into the variety of non-hardening crack tip fields can be found by considering transverse shear, shown in Fig. 5 [*16*]. As listed in Table 1, the

[1] For visual clarity, here and elsewhere multiplication precedes division (/), so $N/2kwb = N/(2kwb)$.

discontinuous displacements across the outer slip lines account for only 62% of the far-field displacement, with the remaining 38% uniformly distributed through the fan. Here again, a single slip plane would give a lumped parameter model, but the direction of crack growth would be biased by the tensile stresses on one side of the fan. Further modeling is needed.

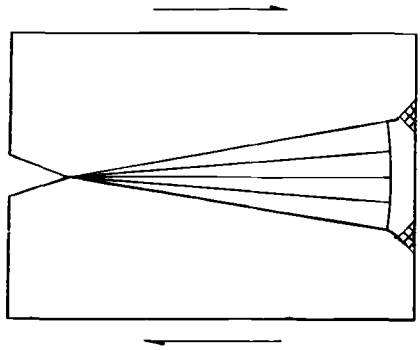


FIG. 5--Slip line field for transverse shear of a single-face-grooved plate.

Bending of Unequally Face-Grooved Plates

For this geometry and loading, the fields of Fig. 6 were developed by Kim [*11*] pp 106-110, 135-139 from the single (Fig. 1) and double face-grooved ones, both from Green (e.g. [*12*] pp 145-151). As shown in Table 1, although the limit moment increases with decreasing back flank half-angle ω, the normal stress $\sigma_s/2k$ decreases. The range of values of $\sigma_s/2k$ is much less than that for tension. The slip angle is nearly constant at $\theta_s = 70°$, compared to the 45° of tension. Thus bending and tension tests can each provide an effect of normal stress, with the slip line angle being different between them.

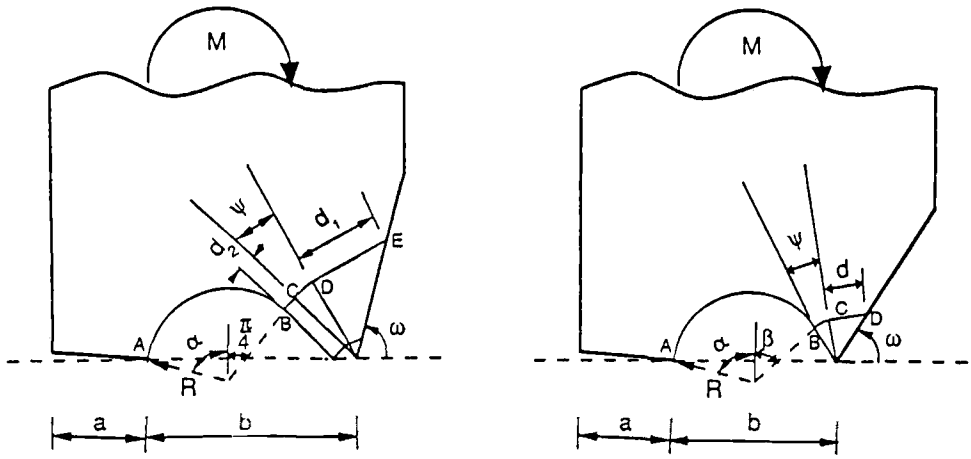


FIG. 6--Slip line fields for unequally face-grooved plates in bending. See Fig. 3a for $\omega = 90°$. a) $\omega > 75.6°$. b) $75.6° \geq \omega > 30°$. For $30° \geq \omega \geq 0°$, region d vanishes and the field consists of a single arc with $\alpha = \beta = 66.8°$.

NEAR-TIP FIELD CHARACTERIZATION FROM LEAST UPPER BOUND ARCS

Since slip line fields are not always available, and sometimes involve fans rather than only a pair of slip lines, we here find approximate values of the near-tip crack growth parameters θ_s, σ_s, and δu_s in terms of far-field geometry and loading (Eq 5) for such cases. As an example of the method we take the single-face-cracked plate under combined bending and tension (Fig. 7a). To gain further insight into the validity of the method, we then apply it to cases in which the slip line fields are known.

Finding the Slip Line Angle θ_s and Displacement δu_s, illustrated with a single-face-cracked plate under combined bending and tension

When a slip line field is not available, the least upper bound (LUB) field for a circular arc provides a rigorous bound to the limit load. It also provides a plausible deformation field (although in non-hardening plasticity even a complete solution may not give a unique field). For instance on the net section of Fig. 7a, for a given shear V (= 0) and tension N, upper bounds to the moment M can be found from the work of rotation due to sliding along the arc. The least of these moments is the LUB for arc sliding. It is found by minimizing M with respect to the two arc parameters α and β of Fig. 7a ([*17*] or [*11*] pp 38-40, 66-69). The deformation field that goes with the LUB gives plausible values of θ_s and δu_s, the more so the closer the LUB is to the actual moment.

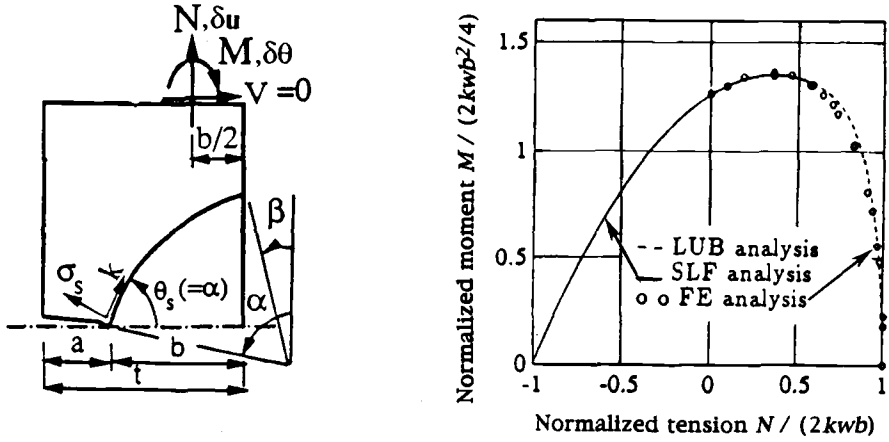


FIG. 7--(a) Circular arc for an upper bound in a deep, single-face-cracked specimen under combined bending and large tension, and
(b) Limit loads from slip line field, least upper bound arc, and finite element analyses.

The accuracy of the LUB for arc sliding is shown in Fig. 7b, including that part where slip line fields are known from Shiratori and Dodd [*18*]. Figure 7b also includes the finite element (FE) results of Lee and Parks [*19*]. Selected points from Fig. 7b are presented in Table 2. For predominant bending ($0 \le N/(2kwb) < 0.551$), the FE results are consistent with the SLF solutions. At $N/(2kwb) = 0.551$, the SLF field is simply two symmetrical arcs intersecting the back surface at 45°, as found from the LUB analysis. These may not be exact solutions, because it is generally found (e.g. [*20*]) that arcs approaching a free surface connect with it through a small, triangular, constant state region. Nonetheless, the FE results indicate that the SLF and LUB bounds are very close.

At $N/(2kwb) = 1$, the SLF is two straight 45° slip lines, and the SLF and LUB results are exact. At intermediate points, $(0.551 \le N/(2kwb) \le 1.0)$, the LUB locus is no more than 3% beyond the FE results. (The slope of the yield locus, which sets the ratio of extension to bending through the associated flow rule, is not as good a fit, but it, like the limit moment, is not a crack growth parameter *per se*).

Now compare the crack growth parameters directly. θ_s (= α in Fig. 7), from [*17*] or [*11*] pp 37-39, 67-68, is shown in Fig. 8 as well as in Table 2. The FE results run at most 4° above the LUB results, and indeed the LUB shape in Fig. 8 is more plausible.

TABLE 2--*Crack tip parameters for a single-face-cracked plate under combined bending and tension.* (LUB entries are indented.)

Method	Loading		Arc angle	Parameters		
	$M/(kwb^2/2)$	$N/2kwb$	β	$\theta_s(=\alpha)$	$\sigma_s/2k$	$\delta u_s/\delta u$
SLF	0	1	--	45	0.5	1.414
LUB	"	"	45	"	"	"
FE	0.728	0.938	--	64	0.91	not available
LUB	"	0.943	24	59	0.89	1.587
FE	1.216	0.700	--	69	1.32	not available
LUB	"	0.743	-19	70	1.39	3.298
SLF	1.322	0.551	--	72	1.47	8.198
LUB	"	"	-45	"	"	"

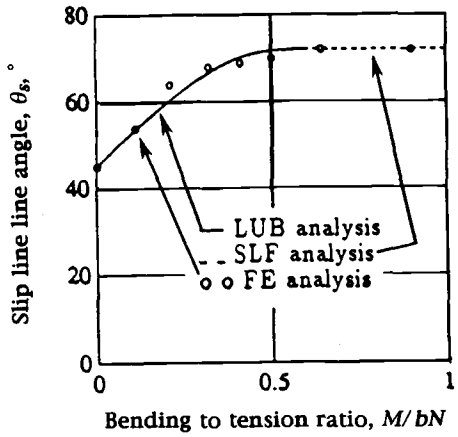


FIG. 8--Near tip slip angle θ_s for a deep, single-face-cracked plate under combined bending and tension.

Next find the geometrical parameter δu_s in terms of the far field increments of rotation $\delta\theta$ and of displacement across the center of the ligament, δu (Fig. 7a):

$$\delta u_s \left(= \frac{\delta CTOD/2}{\sin\theta_s} \right) = \frac{1}{\sin\theta_s}\left[\delta u + \frac{b}{2}\delta\theta\right] \quad . \tag{7}$$

Note that $\delta\theta$ and δu are related through the net section yield locus and the associated flow rule. To report the results for the LUB arc model in Table 2, note from Fig. 7a that

$$\delta u_s = R\delta\theta, \text{ where } R = b/(\sin\alpha - \sin\beta) \text{ and } \delta u = (R\sin\beta + b/2)\delta\theta \ . \quad (8)$$

The resulting values of $\delta u_s/\delta u$ agree with the SLF results in the known limiting cases.

Finding the Mean Normal Stress σ_s, illustrated with a single-face-cracked plate under combined bending and tension

The last crack growth parameter is the normal stress on the slip line at the crack tip, $\sigma_s/2k$, here normalized in terms of the plane strain yield strength, $2k$. In the absence of a complete (exact) solution, an estimate of $\sigma_s/2k$ might be sought from a greatest lower bound stress field, satisfying only equilibrium, the yield condition, and traction boundary conditions. In practice, such bounds are difficult to find, so we use a new method of approximating $\sigma_s/2k$ from the least upper bound for circular arcs.

Consider rigid-body rotation across a circular arc extending from a crack tip across a net section ligament of extent b in a plate with shear strength k (Fig. 9), subject to general loading with three components V, N, and M. Suppose that two loading components are specified and that the circular arc for the LUB to the unspecified loading component has been found. Along the arc, the shear component of traction is k and ϕ is the counter-clockwise angle from a reference point ($_r$). Then the following theorem holds, as proven by Kim ([*17*] or [*11*] pp 24-27 and 52-59):

Assume that the normal component of traction on the LUB arc, $\sigma(\phi)$, satisfies the first Hencky equation of equilibrium, with the unknown reference stress σ_r at $\phi = 0$:

$$\sigma(\phi) = \sigma_r + 2k\phi \ . \quad (9)$$

Then if σ_r is chosen to satisfy force equilibrium in any other than the chordal direction (the 1-direction in Fig. 9), the tractions on the LUB arc satisfy all components of global equilibrium.

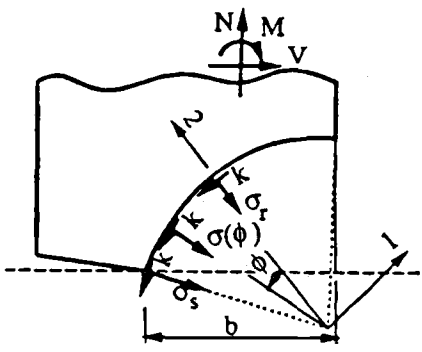


FIG. 9--Tractions on a circular arc subject to rigid-body rotation in a single-face-cracked plate.

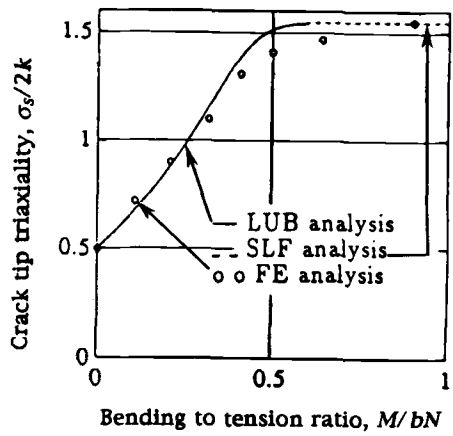


FIG. 10--Near tip slip plane normal stress $\sigma_s/2k$ for deep, single-face-cracked plates under combined bending and tension.

The normal stress across the LUB arc at the crack tip, σ_s, can then be approximated from the Hencky equation (9) with the determined reference stress σ_r. Therefore the LUB arc provides an approximation not only to the limit load, but also to the stress at a crack tip, consistent with global equilibrium.

The resulting values of $\sigma_s/2k$ for the single-face-cracked specimen are shown in Fig. 10 for various ratios of bending moment to tensile load, along with the FE values and the SLF values where known. Some cases were also given in Table 2. The LUB values are exact at the ends of the range $0.551 \leq N/(2kwb) \leq 1$. The FE results are in agreement at $N/2kwb = 1$ ($M/bN = 0$) and well into the SLF range ($M/bN = 0.9$ or $(M/0.5kwb^2)$ / $(N/2kwb) = 3.6$). At intermediate points they range from 4% above to 7% below the LUB results. It is not known to what extent this difference is due to FE or LUB approximations, or to the SLF not being exact where the curved arcs meet the back surface at $N/2kwb = 0.551$, as discussed above.

Altogether, for the single-face-cracked plate under combined tension and bending, the LUB arc method gives crack tip parameters within 5%. (The accuracy of δu_s is not known directly, but can be judged from Eq 7 and the accuracy of θ_s.) The accuracy is well within that needed in view of strain hardening and the anisotropy of fracture.

Unequally Grooved Plates under Tension or Bending

Now consider the accuracy of the LUB arc parameters for cases in which the slip line fields are more completely known: the unequally grooved specimens of Table 1, under either tension or bending. Note that applied load boundary conditions are considered here; applied end motions would require very different fields.

Under tension, for a back half-angle $\omega = 90°$ the LUB arc parameters are exact, as mentioned above. With decreasing ω the LUB slip angle θ_s increases toward 66.8° as $\omega \rightarrow 0°$. At $\omega = 0°$, the SLF becomes symmetrical and the slip line expands into fans from 45° to 135° above and below each crack tip (see Fig. 3b). A set of LUB arcs gives a lumped-parameter model of those fans. At the same time, from $\omega = 90°$ to $\omega = 0°$, the LUB normal stress σ_s rises about 25% more rapidly than the actual SLF normal stress. The LUB displacement u_s rises by a factor of 1.4 over the same range, until symmetry is reached at $\omega = 0°$. Space does not allow presenting the analysis, and only the intermediate value for $\omega = 45°$ could be included in Table 1, under LUB_{arc}.

A better model for asymmetrically grooved plates under tension, and one which evolves more gracefully into the symmetrical case, would be block sliding in which the fan of Fig. 4 is condensed into a single slip line. Not only is the agreement better at $\omega =$ 45°, but the symmetrical limit gives two slip lines above and below each tip, a less discrete model of the symmetrical fans of the SLF. Again space precludes development.

Under bending, the LUB arcs give parameters that are all constant with ω, while the actual SLF's show a 25% decrease in σ_s and a 40% decrease in δu_s. This poor result seems typical of fields that involve an arc in series with a constant-state region.

In conclusion, the LUB arc analysis seems practical for combined bending and tension of single-face-cracked specimens and for unequally grooved tensile specimens, but must be used with judgment in other cases. In some of these, particularly with symmetrically grooved tension, one will have to face the fact that even three parameters are insufficient to describe the stress and strain fields around a fully plastic, growing crack tip.

CRACK GROWTH CRITERION

With the local field characterized by θ_s, σ_s, and δu_s, we turn to the response of the material by crack growth δa. It turns out to be convenient to regroup these variables in terms of first the crack tip opening angle and then the accompanying shear strain in the

flanks of the growing crack. Finally we relate the kinematically required shear strain to the critical flank strain for crack growth under the given normal stress σ_s, giving form to Eq 6.

The Kinematic Shear Strain for Crack Growth

Figure 11 shows the crack growth relative to the shoulders as the result of sliding on first the upper and then the lower slip plane, followed by cracking. The total crack growth can be expressed in terms of the crack tip opening angle CTOA through the tangent of CTOA/2:

$$\delta a = \frac{\delta u_s \sin\theta_s}{\tan(CTOA/2)} \quad . \tag{10}$$

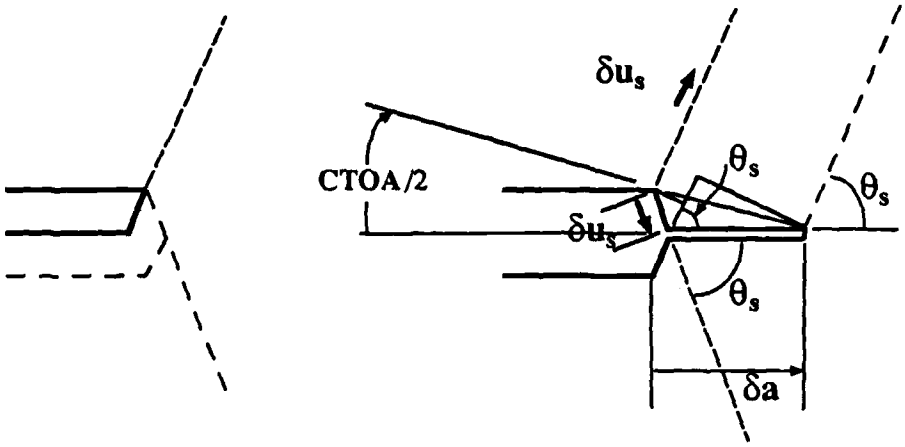


FIG. 11--Stages in sliding off and crack advance at a crack tip with two slip planes.

Thus the crack growth characteristic has been reduced to a geometrical variable, the CTOA. The CTOA in turn depends on two crack tip parameters and material properties: CTOA(θ_s, σ_s, material). It is possible, however, to further simplify the relation in terms of the shear strain produced by $\delta a/\delta u_s$. As shown also in Fig. 11, the shear strain is the slip displacement δu_s per unit distance between the discrete bands, where the distance can be found by projecting δu_s and δa onto the normal to the slip lines:

$$\begin{aligned}\gamma_k &= \frac{\delta u_s}{\delta u_s \sin(\pi - 2\theta_s) + (\delta a - \delta u_s \cos\theta_s)\sin\theta_s} \\ &= \frac{1}{\sin\theta_s(\cos\theta_s + \delta a/\delta u_s)} \quad .\end{aligned} \tag{11}$$

(The corresponding analysis for two unsymmetrical slip planes was given in [*21*].)

Alternatively, eliminating $\delta a/\delta u_s$ in Eq 11 with Eq 10 gives

$$\gamma_k = \frac{1}{\sin\theta_s\left[\cos\theta_s + \dfrac{\sin\theta_s}{\tan(CTOA/2)}\right]} \tag{12}$$

Next consider how fracture sets a limit to γ_k. This limit of the strain on the flank of the crack will be called the critical flank shear strain, γ_f.

Critical Flank Shear Strain for Crack Growth

For typically rough fracture surfaces of alloys of aluminum and low strength steel, observations with a 100-200x stereomicroscope show that the fracture surface deviates from a plane by between a few and scores of hole nucleus spacings (up to hundreds of μm). These deviations are usually out of phase over comparable distances along the crack front, although in some cases they correlate into a regular zig-zag advance. A montage of sections normal to a crack tip by Reuter (see [*10*] or [*11*] p 121) confirms the deviations. A decohering zone behind the crack tip can be used to model the average tractions due to interactions between the out-of-phase deviations. It turns out that with rigid flanks behind the crack tip, as in the cases considered here, the decohering zone does not affect the slip line field ahead of the crack, but only transmits some added load. At the tip, it is plausible to model the crack as growing by a combination of sliding off and cracking on first one slip plane and then the other. Equations 10-12 turn out to be independent of whether the micro-fractures are along the slip lines, or parallel to the macro-crack, as in Fig. 11. Make the leap of faith that the amount of cracking by hole growth will adjust itself so that the average strain in the flank (the widening shear band) is the same as the fracture strain in a uniform shear band under the normal stress σ_s, independent of the slip angle θ_s. Then an expression for the critical flank shear strain as a crack growth parameter will depend only on the normal stress σ_s and the material.

The micromechanisms for crack growth, such as hole nucleation, growth, and linkage by localization or fine cracking, suggest that the fracture strain in a shear band is the sum of strains to initiate holes at inclusions, γ_i, plus the shear strain γ_g to grow the holes from their initial radii R_0 to their radii at impending fracture, R_f. R_f may be less than the hole spacing because of the onset of localized flow in shear bands between the holes (e.g. [*22*], [*23*]) or irregular fine cracks ([*24*], [*25*], [*26*]). In any event, the subsequent strain to shear band fracture is small and neglected here. The expression for shear strain for a given hole growth ratio R_f/R_0 in a power-law strain hardening material with exponent n from [*27*] then gives the hole growth strain γ_g. This is added to γ_i to get the critical flank shear strain γ_f, which is equated to the kinematically determined strain γ_k of Eq 12:

$$\gamma_f\left(\frac{\sigma_s}{2k},\ material\right) = \gamma_i(\sigma_s/2k) + 2\frac{(1-n)\ln\left(R_f/R_0\right)}{\sinh\left[(1-n)\sigma_s/k\right]} = \gamma_k \ . \tag{13}$$

For clean, coherent particles the condition for hole nucleation, $\gamma_i(\sigma_s/2k)$, has been taken to be that the sum of the flow strength plus the mean normal stress reaches a critical value [*28*]. When this criterion is combined with power-law hardening for the flow strength, the result is a far too strong dependence of the initiation strain on the normal stress: either initiation occurs at negligible strains, or at impossibly high strains. Thus for the commercial alloys of interest here, where holes keep forming with increasing stress, $\gamma_f(\sigma_s/2k)$ of Eq 13 must be left in its general form, to be found empirically for each material by equating it to the kinematically determined shear strain of Eqs 11 or 12.

PRELIMINARY EXPERIMENTS

The objectives of the preliminary experiments reported here were to determine the feasibility of simple tests, to test the correlation between bending and tension, and to find the approximate dependence of the critical shear strain on the mean normal stress, all as a basis for further work.

For interpreting these preliminary tests, we neglect the loss in limit load and retarded crack advance due to finite width, shoulder deformation, strain hardening, initial blunting, the effect of finite crack opening angles on the slip line field, and thinning, thickening, or cracking from the back side.

Analysis of Experiments

Determining crack tip parameters θ_s and $\sigma_s/2k$ and the limit loads --In tension, the field is part of the classical Hencky field of Fig. 3b, and is shown in Fig. 4. The angle of the slip line at the crack tip is $\theta_s = 45°$. The mean normal stress on the slip line, σ_s, normalized in terms of the yield strength in shear k, is given in terms of the back flank half-angle ω by:

$$\frac{\sigma_s}{2k} = \frac{1}{2} + \left(\frac{\pi}{2} - \omega\right) . \tag{14}$$

Neglecting edge and root radius effects (see [*12*] pp 119-127 and 141-155) gives the limit load N_L in terms of the specimen width w and ligament thickness b:

$$\frac{N_L}{2kwb} = 1 + \left(\frac{\pi}{2} - \omega\right) . \tag{15}$$

In bending, the corresponding local parameters and arc radius R for the fields of Fig. 6 are given in Table 3 (see [*10*], [*11*] pp 106-110 and 135-139):

TABLE 3--*Local parameters, limit moments, and arc radii for bending.*

Back half-angle, ω, °	≤30	45	60	75	75.6	90
Crack tip slip angle, $\theta_s = \alpha$, °	66.8	67.2	68.8	72.0	72.0	72.0
Crack tip triaxiality, $\sigma_s/2k$	1.17	1.18	1.22	1.29	1.29	1.54
Limit moment factor, $F_M = M_L/(2kwb^2/4)$	1.380	1.379	1.372	1.348	1.347	1.261
$R/b = \delta u_s/b\delta\theta$,	0.544	0.539	0.521	0.489	0.488	0.437
Back face arc angle β, ° (Fig. 7)	66.8	59.5	52.4	45.3	45	45

Determining the fracture shear strain--Three sources of data were used here to determine γ_f: direct measurement of the crack surface angles after fracture, the load drop per unit extension, and the change in back half-angle.

First, the *difference between the average angles of the two fracture surfaces* in tensile specimens gives the CTOA. Then γ_f is found using Eq 12. In bending, for the ductile alloy tested here, the specimen bend angle was of the order of the CTOA, so the surface was curved and detailed measurements would have to be analyzed.

Second, the *load drop per unit applied deformation* gives an indication of the loss of ligament per unit far field displacement, which can in turn be related to the displacements u_s on the slip lines. Then the shear strain can be found from Eq 11. Furthermore, it is the load drop per unit crack extension that is of interest to the structural engineer in determining the load-shedding of a part as it cracks, and thus the overall

stability of the structure. The goal, as in linear elastic fracture mechanics, is to develop tests to measure the behavior of the material at the crack tip so that a wide variety of structural engineering calculations can be carrried out with a minimum number of experiments.

In tension, consider the record of load versus applied testing machine displacement of Fig. 12. The initial finite slope on the rising part of the curve is due to the compliance of the testing machine, grips, and shoulders of the specimen. For fully plastic deformation, virtually none of the compliance is due to elastic deformation in the net section, as shown by the fact that the unloading curves have sharp transitions and are very nearly parallel to the loading curve. This is further shown by the fact that the elastic yield strain, of the order of 0.003, times the net section ligament of 7 mm was only 0.02 mm. At the top of the curve, observations with a 10x Brinell microscope showed that any blunting before crack initiation was at most 0.1 mm. Thus most of the rounding at the top of the curve was due to rounding of the stress-strain curve plus an early transient in crack growth. As the crack grew, the load fell, but the rate of drop never quite reached a steady state. Rather, it steepened until it equalled the slope of the loading curve, at which point the system became unstable. (This illustrates an advantage of plotting the load versus the applied testing machine displacement during the test, as in Fig. 12. The approach of the load trace to vertical serves as a warning of system instability. One can then reduce the applied deformation rate or unload the specimen before final fracture, as was done in some of the tests reported later in Table 4.)

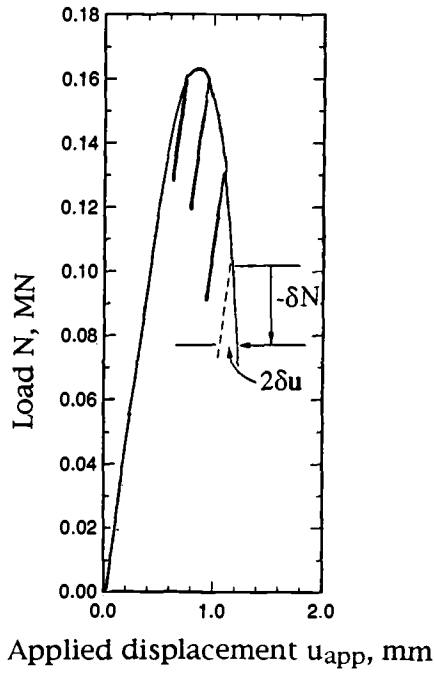


FIG. 12--Finding the load drop ratio $\delta N/\delta u$ from a plot of load versus applied deformation.

As the load drops under increasing applied extension, the incremental end-to-end extension across the net section, $2\delta u$, consists not only of the incremental applied extension, but also of the elastic recovery from the compliance of the machine, grips, and specimen shoulders, as shown in Fig. 12. Assuming that the load drop is due entirely to the loss of ligament, which is the negative of the crack growth δa, allows differentiation of the logarithm of Eq 15 to relate the load drop to the crack growth:

$$\frac{\delta N}{N} = \frac{\delta b}{b} = -\frac{\delta a}{b} \quad . \tag{16}$$

For tension the sliding on one slip plane per unit far field half-displacement δu is $\delta u_s/\delta u = 1/\sin\theta_s = \sqrt{2}$. Then assuming that the original dimensions still nearly hold at the maximum load, as was observed here, allows expressing the crack growth rate per unit sliding as

$$\frac{\delta a}{\delta u_s} = \left(\frac{-\delta N}{\delta(2u)}\right)\left(\frac{2\delta u}{\delta u_s}\right)\left(\frac{b}{N}\right) = \left(\frac{-\delta N}{\delta(2u)}\right)(2\sin\theta_s)\left(\frac{b_0}{N_{\max}}\right) \quad . \tag{17}$$

The corresponding critical flank shear strain γ_f can now be found by equating it to γ_k from Eq 11.

In bending, a similar analysis holds. The limit moment can be given in terms of a constraint factor F_M from Table 3.

$$M = F_M 2kwb^2/4 \quad . \tag{18}$$

For a given specimen with small bend angles, F_M is constant, so that logarithmic differentiation gives

$$\frac{\delta b}{b} = \frac{1}{2}\frac{\delta M}{M} \quad . \tag{19}$$

For 4-point bending let $\delta u_{app} = \Delta L\ \delta\theta$ so that $M = (P/2)\Delta L$ and note that $\delta a = -\delta b$. Further, from Fig. 6, $\delta u_s = R\delta\theta$, where R/b is found as a function of ω in Table 3. Then

$$\frac{\delta a}{\delta u_s} = \left(\frac{b}{2}\right)\left(\frac{1}{R\delta\theta}\right)\frac{-\delta M}{M} = \frac{1}{R/b}\frac{\Delta L}{2}\frac{\left(-\delta P/\delta u_{app}\right)}{P} \quad . \tag{20}$$

As in tension, the corresponding critical flank shear strain can now be found from Eq 11.

The third method of determining the critical flank shear strain in the band generated by the growing crack in tensile testing is the *change in back face half-angle* where the shear band intersects the back surface. Figure 13 shows a shear band of thickness s breaking through to a back face at 45°. For a shear displacement across the band of $s\gamma$, the new angle of the back face relative to the shear band is $\tan^{-1}(s/[s+s\gamma])$, instead of $\pi/4$. Thus the change in back face half-angle, $\delta\omega$, can be expressed in terms of the shear strain, or the shear found in terms of $\delta\omega$:

$$\delta\omega = \frac{\pi}{4} - \tan^{-1}\left(\frac{1}{1+\gamma}\right) \quad \text{or} \quad \gamma = \cot\left(\frac{\pi}{4} - \delta\omega\right) - 1 \quad . \tag{21}$$

In bending, to find the flank shear strain from the change in back face angle would be complicated by closure at the root of the groove on the compression side (see Fig. 6).

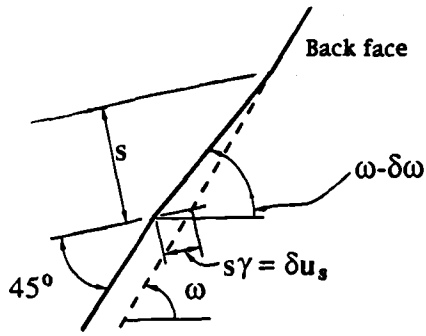


Fig. 13--Finding the strain in a shear band from the change in the back face half-angle.

Specimen Design and Material

Specimens were machined from 25 mm thick bars of 1018 CF steel. Originally 76 mm wide bars were chosen for tension, with reasonable allowance for shoulder and width effects within the limitations of an MTS 410 double-acting servo-hydraulic load frame with 50 ton (0.445 MN) capacity. It was later found that the hydraulic grips only had a rating of 0.311 MN, so the width was reduced to 51 mm in the central 25 mm of the specimen length. Face grooves were milled with 45° included angles and approximately 0.05 mm root radii, as viewed with a 10x Brinell microscope. Back half-angles were milled to $\omega = 45°$, 60°, and 75°, leaving a 7.1 mm ligament in the center of the bar. To ensure plane strain condition and rigid shoulders, the ratio of total thickness to ligament, t/b, for a back flank half-angle of ω should be [*12*] Eq 146 p 143

$$\frac{t}{b} = \left(1 + \frac{1}{\sqrt{3}}\right)\left(2e^{\pi/2-\omega} - 1\right) , \tag{22}$$

where the first factor, $(1 + 1/\sqrt{3})$, is needed to assure plane strain. Here that factor may not be required for plane strain because of the reduction in width from 76 to 51 mm in the central 25 mm of the length. For $\omega = 45°$ ($\pi/4$ radians) the ligament could be as large as 7.5 mm. Indeed, no shoulder deformation could be observed on backlighting a straight edge held against the specimen.

The tensile bars were 610 mm long, with 457 mm between grips. This length was originally chosen for a testing machine with 203 mm long grips. By hindsight, the total extra length between grips of 315 mm contributed a compliance of $\Delta L/AE$ = 315 mm / (76 mm × 25.4 mm × 207,000 N/mm^2) = 0.79 mm/MN, compared to the total system compliance from the initial slope of Fig. 12 of 4.3 mm/MN.

The bending specimens were cut 305 mm long from bars 51 mm wide. The loading rolls were 25 mm in diameter, with the central pair 51 mm apart and the moment arms to the outer rolls ΔL = 86 mm each. The tests were carried out on an Instron 1125 servo-mechanical testing machine of 20,000 lb (88.9 kN) capacity. System stiffness was several times that needed for stability.

Three hardness tests on the central two-thirds of sections of each of the two widths of bar gave 53 ± 1 HRA for the 76 mm wide tensile bars and 52±1 HRA for the 51 mm wide bending bars. Readings on, or within a few mm of, the surfaces of both bars were 55±1 HRA. From hardness conversion charts, the central readings correspond to 178-185 HK or tensile strengths TS of 560-570 MN/m^2.

Results and Discussion

As shown in Table 4, the tension and bending specimens were chosen with ranges of back half-angles ω that would give overlapping values of mean normal stress, $\sigma_s/2k$.

Limit loads--The maximum loads shown in Table 4 were compared to the limit loads and moments calculated from the constraint factors $F_N \equiv N/(2kwb)$ and $F_M \equiv M_L/(2kwb^2/4)$ of Table 1, from the above tensile strengths TS, and from $k = TS/\sqrt{3}$. The maximum loads were typically 40% below the limit loads for both tension and bending. Thus crack initiation began in the elastic-plastic regime. This is consistent with the visual observations at 10x during the tests that no more than 0.1 mm of crack tip opening occurred before crack initiation. This crack initiation in the elastic-plastic regime does not invalidate the crack growth results, for which initial transients were ignored and the strains were clearly fully plastic at the scale of the ligaments.

Load-extension data in tension--A curve for the lowest triaxiality (mean normal stress/plane strain yield strength), $\sigma_s/2k = 0.76$, is shown in Fig. 12. The specimen was occasionally partly unloaded to allow looking for cracks and to try molding with dental rubber to record any cracks. As shown in the first block of data in Table 4, the maximum load was 164 kN, there was no cleavage, and system instability finally occurred at 63 kN. A specimen with the next higher triaxiality, $\sigma_s/2k = 1.02$, showed similar behavior, as summarized in the second column of the first data block in Table 4. At $\sigma_s/2k = 1.29$, however, abrupt cleavage occurred just as the load extension curve was leveling off.

These tests were replicated, as shown in the second data block of Table 4. To allow a more detailed examination of a crack, the second $\sigma_s/2k = 0.76$ specimen was unloaded at about 3/4 of its maximum load. 36 days later the specimen was re-loaded with the intent of getting further ductile crack growth, but the load-extension curve was linear to 132 kN, 6 kN above the load at prior unloading, at which time cleavage fracture occurred with no warning. Similar behavior was found with $\sigma_s/2k = 1.02$, as indicated in the second column of the second data block of Table 4. At $\sigma_s/2k = 1.29$, cleavage occurred on monotonic loading, this time with only a very slight drop in load.

The above results show that it is possible to simulate, in slow loading of specimens subject to analysis, not only cleavage fracture but also the residual stress- or strain-aging embrittlement that has in the past been reported primarily, if not only, in welds [29].

The last row in each block of load-drop data gives the critical flank shear strain for crack growth, γ_f. This was determined rather arbitrarily at 2/3 of the peak testing machine load P_{max}, (= N_{max} in tension), since a steady-state giving a linear decrease in load with extension was never quite reached.

Fracture surface data in tension--The fracture surfaces were irregular over a scale of a millimetre in the crack growth direction, and over a scale of several millimetres along the crack front, with variations of the order of ±5° compared to crack opening angles of 15-30°. Sometimes all the CTOA was on one side of the plane of symmetry.

TABLE 4--*Critical flank shear strain γ_f as a function of normal stress $\sigma_s/2k$.*

Notes: Critical flank shear strains γ_f are underlined.
Successive data blocks correspond to further specimens with the same $\sigma_s/2k$.
clv denotes less than 1/2 mm of cracking by hole growth before cleavage, except 1mm of initial hole growth where noted.
ihgc denotes initial hole growth cracking.
γ_f from testing machine load drop was found at $(2/3)P_{max}$, unless prior fracture or instability.

Slip plane normal stress, $\sigma_s/2k$	(0.5)	0.76	1.02	1.18	1.29	1.55
Back face half-angle, ω, °:						
Tension	(90)	75	60		45	30 (fans)
Bending				45	75	90

Source of critical flank strain for crack growth, γ_f:					
Load drop in tension					
P_{max}, kN	164	149		234	
P_{clv}, kN	--	--		234	
P_{unst}, kN	63	102			
γ_f, Eqs 17, 11, or *clv*	0.13	0.09		*clv*	
P_{max}, kN	166	186		228	
P_{unl}, kN	126	164			
P_{clv}, kN	132	173		227	
γ_f or *clv*	0.14	See text		*clv*	
aged	*clv*	*clv*			
CTOA from fracture surface angles (for tension from Eq 12)					
γ_f or *clv*	0.26	0.26			
γ_f or *clv*	0.19	--			
Back face angle change, $\delta\omega$ (for tension from Eq 21)					
2 ends, 1st spec. γ_f or *clv*	0.19	0.11			
	0.28	0.19			
γ_f or *clv*, aged	*clv*	*clv*			
Load drop in bending					
P_{max}, kN			16.4	17.2	14.8
P_{clv}, kN			--	17.2	13.5
γ_f, Eqs 20, 11, or *clv*			0.27	*clv*	1 mm *ihgc*
P_{max}, kN			16.7		not
P_{clv}, kN			10.9		avail.
γ_f or *clv*			0.24		*clv*
P_{max}, kN			14.7	not	
P_{clv}, kN			14.0	avail.	
γ_f or *clv*			*clv*	1 mm *ihgc*	

The result was that the critical flank shear strains given in Table 4 are only good to 20-30%. For the second specimen at $\sigma_s/2k = 1.02$, the critical flank shear strain was omitted because it was evaluated where the specimen was unloaded, at 85% of the maximum load. Thus the initially flatter slope made the apparent flank strain too high ($\gamma_f = 0.27$).

Back face angle change in tension---The range of values for each specimen is indicative of the high uncertainty in these measurements, but they are useful as a rough check. As mentioned above, the second specimen at each $\sigma_s/2k$ has a very short region of slope change on the back surface due to the cleavage on reloading, so useful results could not be obtained.

Load-deflection data in bending--For the lowest $\sigma_s/2k$ in bending, 1.18, the crack growth mechanism was by hole growth over the first 1.5 mm, with a regular zig-zag pattern having a wavelength of perhaps 0.5 mm. Whether this was due to the higher slip angle than for tension is an unanswered question, as is the cause of zig-zag growth itself. Subsequently the first specimen cracked along the bending slip line arcs, whereas the second cleaved, just below $(2/3)P_{max}$. At higher $\sigma_s/2k$ the specimens cleaved after less than 0.5 mm of hole growth cracking, except for first at $\sigma_s/2k = 1.55$ which showed an initial 1 mm of hole growth cracking. Specimens in the last block of those in bending were from the 76 mm bar cut down to 51 mm for bending, rather than from the 51 mm bars. There are insufficient data to judge any difference in cleavage tendency of the two widths of bars.

In summary, the critical flank shear strain for crack growth may be higher in bending than in tension, but further work is needed.

General discussion of crack growth shear strains--Cleavage prevented any precise testing of the micro-mechanical theory that led to Eq 13, but there appears to be less dependence on normal stress than that equation or the limited data in the literature predict. The critical flank shear strains here are relatively high compared to the reported value at $\sigma_s/2k = 0.5$ of 0.27 for cold-finished steel and 0.35 for normalized 1018 steel [*21*]. Fully plastic crack initiation and early growth tests (to 400μm) have been run on ASTM A710 Grade A steel with a wide range of crack tip triaxiality: three point bending, compact tension, and a center cracked panel (CCP) test [*30*]. (Their CCP test specimens did not meet plane strain requirements, so the resulting crack tip triaxiality would be somewhat lower than that for single-face-cracked specimens in tension.) Their results showed a four-fold decrease in CTOA (∂CTOD/∂a), as $\sigma_s/2k$ (from slip line analysis) increased from 0.5 to 1.55. Symmetrical wedge-opening tests with $\sigma_s/2k = 2.18$ gave a critical flank shear strain of only 0.02 for a hot rolled steel [*31*], but these specimens had fans either side of the growing crack, in contrast to the pairs of slip lines analyzed here.

As a test of Eq 13, the initiation strain γ_i was neglected and the critical hole growth ratio R_f/R_0 was calculated from the critical flank strain and the slip line normal stress, with the strain-hardening exponent rather arbitrarily taken as $n = 0.1$. The load drop data in tension, with $\sigma_s/2k = 0.76$ and 1.02, gave R_f/R_0 constant at 1.14-1.165. The change in back face half-angle gave $R_f/R_0 = 1.2$-1.3 at $\sigma_s/2k = 0.76$ and 1.2-1.4 at $\sigma_s/2k = 1.02$, tolerably constant with stress but different from the load drop values. The surface angle data did not provide a correlation, since the flank strains were the same at both triaxialities. The bending data for hole growth cracking did not cover a range of stresses.

If further tests bear out the suspicion that there is less effect of triaxiality on critical flank shear strains than on strains for crack formation in smooth specimens, one possible reason may be the loss of triaxiality in front of a zig-zagging crack. For instance Carson found a reduction of normal stress from $k(1 + \pi)$ to $k(1 + 3\pi/4)$ on the most critical slip line at the tip of a 45° dog-leg (see his slip line field in [*32*]).

CONCLUSIONS

1. For designing possibly cracked structures in which crack growth must remain ductile under accidental overloads, we present a practical theory for fully plastic, plane strain crack growth. It first appears that the one or two parameter local characterization of the crack tip that is used in linear or nonlinear elastic fracture mechanics must be extended to three parameters for the near tip fields of a growing crack in fully plastic, plane strain conditions: the slip line angle θ_s and the normal stress σ_s and shear displacement δu_s across the slip line. However kinematic considerations for non-hardening slip line fields transform the resulting function for crack growth per unit slip line displacement into a criterion that involves a kinematically required crack flank shear strain as a function of slip line angle and crack tip opening angle (Eq 12). For crack growth, this kinematically required flank shear strain must be equal to a material-dependent critical flank shear strain that is a function of the ratio of mean normal stress on the slip plane to the plane strain yield strength, $\sigma_s/2k$. A tentative theoretical basis for this function is given in Eq 13.

Experimental results are given in Table 4, where the critical flank shear strain is found from i) the crack tip opening angle, ii) the load drop due to crack growth per unit extension or bending of the specimen, or iii) the drawing-in of the back face. The mean normal stress is found for the geometry and loading condition either from slip line field analysis or from least upper bound analysis based on circular arcs, that requires only a programmable calculator. Thus a fracture criterion for fully plastic crack growth has been developed that is analogous, for example, to the K_I (geometry and loading) = K_{Ic}(material) of linear elastic fracture mechanics.

2. Preliminary tests of the theory, carried out on unequally grooved tensile and bending specimens of 1018 CF steel, led to a number of conclusions, as follows.

a) In unequally grooved bars of 51 mm width, 25 mm thickness, and a 7.1 mm ligament, cleavage fracture occurred on slow loading at room temperature with a ratio of slip plane normal stress to plane strain flow strength of greater than about $\sigma_s/2k = 1.2$. Thus these specimens provide a way of testing for cleavage fracture under static design conditions.

b) Unloading deformed tensile specimens after peak load with $\sigma_s/2k = 0.76$ and 1.02 and aging for 36 days at room temperature raised the flow strength by 5% and introduced immediate cleavage fracture. This demonstrates quantitative testing of the embrittlement sometimes encountered in practice with residual stress and strain aging around cracks, especially in welded structures.

c) For this material, the above cleavage limited the range of $\sigma_s/2k$ available for studying its effect on fully plastic cracking by the hole growth mechanism, so the analysis and experimental measurements of the stress-dependence of the shear strain for crack growth remain tentative.

d) The critical flank shear strains for $\sigma_s/2k = 0.76$ are of the order of 0.1 to 0.3. They may be higher in bending. Also in bending, with a crack tip slip plane angle of θ_s = 70° rather than the 45° of tension, there is more tendency for zig-zag crack growth.

RECOMMENDATIONS

1. The analysis and test procedure require a number of further developments.

a) Extend the study to other materials, especially hot-rolled or normalized steel.

b) Use fractography or microtopography to quantify surface features.

c) Analyze back face deformation and cracking, and their effects on the ligament and load reduction. For bending, analyze finite deformations for their effects in curving the fracture surface and in modifying slip line fields and loads.

d) Correct for effects of finite width, and possibly reduce them by side grooving, especially in tension.

e) To initiate the crack with less loss in ligament and less change in the flank angles, re-sharpen the grooves by occasional unloading or load reversal.

2. The work suggests a number of extensions.

a) Experimentally determine crack direction in mixed-mode situations, such as joints and welds, where the crack tip slip planes are asymmetrical or there is only one.

b) Develop an analysis for crack growth with multiple slip planes, as in a fan.

c) Study the possibility of theorems for crack-tip slip-plane stress with block sliding, perhaps involving combinations of straight lines and arcs.

d) See whether a correlation for initial growth of a crack can be based on the critical displacement across a slip line and stress on it.

e) Develop the mechanics of zig-zag cracking.

ACKNOWLEDGMENTS

This work was supported by the Office of Basic Energy Sciences, Department of Energy, under Grant DE-FG02-85ER13331 to M.I.T. and Contract DE-AS07-761D01670 with the Idaho National Energy Laboratory. We are indebted to Sally H. Chang for carrying out the experiments as an undergraduate thesis, and to Suryaprakash Ganti and SungHwan Jung for help with the figures and manuscript.

REFERENCES

[1] Kanninen, M. F. and Popelar, C. H., *Advanced Fracture Mechanics*, Oxford University Press, New York, 1985.

[2] Matthews, W. T., "Plane Strain Fracture Toughness (K_{Ic}) Data Handbook for Metals", Report AMMRC MS 73-6, AD 773-673, Watertown, MA.

[3] Hudson, C. M. and Seward, S. K., "Compendium of Sources of Fracture Toughness and Fatigue Crack Growth Data for Metallic Alloys", *International Journal of Fracture*, Vol. 14, 1978, pp R151-R184. See also "... for Metallic Materials, Part II", Vol. 20, 1982, pp R59-R117.

[4] Tada, H., Paris, P. C., and Irwin, G. R., *The Stress Analysis of Cracks Handbook*, Paris Productions Inc., Saint Louis, MO, 1985.

[5] Murakami, Y., et al., Eds., *Stress Intensity Factors Handbook*, Pergamon Press, Oxford, 1987.

[6] Kumar, V., German, M. D., Shih, C. F., "An Engineering Approach for Elastic-Plastic Fracture Analysis" NP-1931 Research Project 1237-1, Corporate Research and Development, General Electric Company, Schenectady, NY, for Electric Power Research Institute, EPRI Report numbers as above, Palo Alto, CA, 1981.

[7] Zahoor, A., *Ductile Fracture Handbook*, 3 Vols., Reports NP-6301-D, N14-1, Electric Power Research Institute, Palo Alto, CA 1989

[8] Parks, D. M., "Advances in Characterization of Elastic-Plastic Crack-Tip Fields", in *Topics in Fracture and Fatigue*, A. S. Argon, Ed., Springer-Verlag, Berlin, 1992, pp 59-98.

[9] O'Dowd, N. P., and Shih, C. F., "Family of Crack-Tip Fields Characterized by a Triaxiality Parameter - II. Fracture Applications", *Journal of the Mechanics and Physics of Solids*, Vol. 40, 1992, pp 939-963.

[10] McClintock, F. A., Kim, Y.-J., and Parks, D .M., "A Criterion for Fully Plastic, Plane Strain Crack Growth", *International Journal of Fracture*, in press, 1995.

[11] Kim, Y.-J., "Modeling Fully Plastic Plane Strain Crack Growth", Ph.D. Thesis, Department of Mechanical Engineering, Massachusetts Institute of Technology, Cambridge, MA, 1993.

[12] McClintock, F. A., "Plasticity Aspects of Fracture", in *Fracture*, Vol. 3, H. Liebowitz, Ed., Academic Press, New York, 1971, pp 47-225.

[13] McClintock, F. A., and Argon, A. S., *Mechanical Behavior of Materials*, Addison Wesley, 1966, reprinted by Tech Books, Fairfax, VA 1993.

[14] McClintock, F .A., "Reduced Crack Growth Ductility Due to Asymmetric Configurations", *International Journal of Fracture*, Vol. 42, 1990, pp 357-370.

[15] Hundy, B. B., "Plane Plasticity", *Metallurgia*, Vol. 49, 1956, pp 109-118.

[16] McClintock, F. A. and Clerico, M., "The Transverse Shearing of Single-Grooved Specimens", *Journal of the Mechanics and Physics of Solids*, Vol. 28, 1980, pp 1-16.

[17] Kim, Y.-J., McClintock, F. A., and Parks, D. M., "Global Equilibrium of Least Upper Bound Circular Arcs and its Application to Fracture Mechanics", in manuscript.

[18] Shiratori, M. and Dodd, B. "Effect of Deep Wedge-Shaped Notches of Small Flank Angle on Plastic Failure", *International Journal of Mechanical Sciences*, Vol. 22, 1980, pp 127-131.

[19] Lee, H. and Parks, D. M. "Fully Plastic Analyses of Plane Strain Single Edge Cracked Specimens Subject to Combined Tension and Bending", *International Journal of Fracture*, Vol. 63, 1993, pp 329-349.

[20] Ewing, D. J. F., "Calculations on the bending of rigid/plastic notched bars" *Journal of the Mechanics and Physics of Solids*, Vol. 16, 1968, pp 205-213.

[21] Kardomateas, G. A. and McClintock, F. A., "Shear Band Characterization of Mixed Mode I and II Fully Plastic Crack Growth", *International Journal of Fracture*, Vol. 40, 1989, pp 1-12.

[22] Needleman, A. and Tvergaard, V., "An Analysis of Ductile Rupture Modes at a Crack Tip", *Journal of the Mechanics and Physics of Solids*, Vol. 35, 1987, pp 151-183.

[23] Hancock, J. W. and Cowling, M. J., "Role of State of Stress in Crack-Tip Failure Processes", *Metal Science*, Vol. 14, August-September 1980, pp 293-304.

[24] Neimark, J. E. "The Fully Plastic, Plane-Strain Tension of a Notched Bar", *Journal of Applied Mechanics*, Vol. 35, 1968, pp 111-116.

[25] McClintock, F. A., "On the Mechanics of Fracture from Inclusions", in *Ductility*, H. W. Paxton, Ed., American Society for Metals, Metals Park, Ohio, 1968, pp 255-277.

[26] McClintock, F. A. and Zheng, Z. M., "Ductile fracture before localized necking in a strip under tension", *International Journal of Fracture* Vol. 64, 1993, pp 191-200.

[27] McClintock, F. A., Kaplan, S. M., and Berg, C. A., "Ductile Fracture by Hole Growth in Shear Bands", *International Journal of Fracture Mechanics*, Vol. 2, 1966, pp 614-627.

[28] Argon, A. S., "Formation of Cavities from Nondeformable Second-Phase Particles in Low Temperature Ductile Fracture", *Journal of Engineering Materials and Technology, Transactions of the American Society of Mechanical Engineers*, Vol. 98, 1976, pp 60-68.

[29] Dawes, M. G. "Significance of Locally Intensified Strain Ageing to the Fracture Toughness of Welded Steel Structures", *Fracture Mechanics: 26th Volume, ASTM STP 1256*, Walter G. Reuter, John H. Underwood, and James C. Newman, Eds., American Society for Testing and Materials, Philadelphia, 1995.

[30] Hancock, J. W., Reuter, W. G., and Parks, D. M., "Constraint and Toughness Parameterized by *T*", in *Constraint Effects in Fracture, ASTM STP 1171*, E. M. Hackett, K.-H. Schwalbe, and R. H. Dodds, Eds., American Society for Testing and Materials, Philadelphia, 1993, pp 21-40.

[31] McClintock, F. A. and Wineman, S. J., "A Wedge Test for Quantifying Fully Plastic Fracture," *International Journal of Fracture*, Vol. 33, 1987, pp 285-295.

[32] McClintock, F. A., "Fracture Mechanics for Corrosion Fatigue," in *Corrosion Fatigue, NACE-2*, A. J. McEvily and R. W. Staehle, Eds., National Association of Corrosion Engineers, Houston, 1972, pp 289-302.

D.S. Dawicke[1] , J.C. Newman, Jr.[2], and C.A. Bigelow[3]

THREE-DIMENSIONAL CTOA AND CONSTRAINT EFFECTS DURING STABLE TEARING IN A THIN-SHEET MATERIAL

REFERENCE: Dawicke, D. S., Newman, J. C., Jr., and Bigelow, C. A., "Three-Dimensional CTOA and Constraint Effects During Stable Tearing in a Thin-Sheet Material", Fracture Mechanics: 26th Volume, ASTM STP 1256, Walter G. Reuter, John H. Underwood, and James C. Newman, Jr., Eds, American Society for Testing and Materials, Philadelphia, 1995.

ABSTRACT: A small strain theory, three-dimensional elastic-plastic finite element analysis was used to simulate fracture in thin sheet 2024-T3 aluminum alloy in the T-L orientation. Both straight and tunneled cracks were modeled. The tunneled crack front shapes as a function of applied stress were obtained from the fracture surface of tested specimens. The stable crack growth behavior was measured at the specimen surface as a function of applied stress. The fracture simulation modeled the crack tunneling and extension as a function of applied stress. The results indicated that the global constraint factor, α_g, initially dropped during stable crack growth. After peak applied stress was achieved, α_g began to increase slightly. The effect of crack front shape on α_g was small, but the crack front shape did greatly influence the local constraint and through-thickness crack-tip opening angle (CTOA) behavior. The surface values of CTOA for the tunneled crack front model agreed well with experimental measurements, showing the same initial decrease from high values during the initial 3mm of crack growth at the specimen's surface. At the same time, the interior CTOA values increased from low angles. After the initial stable tearing region, the CTOA was constant through the thickness. The three-dimensional analysis appears to confirm the potential of CTOA as a two-dimensional fracture criterion.

KEYWORDS: Fracture, constraint, stable crack growth, CTOA, crack tunneling, thin sheet, elastic-plastic, finite-element and experimental data

NOMENCLATURE

b Uncracked ligament length, mm
B Sheet thickness, mm

[1] Senior Scientist, Analytical Services and Materials, Inc., Hampton, VA 23666
[2] Senior Scientist, NASA Langley Research Center, Hampton, VA 23665
[3] Senior Scientist, FAA Technical Center, Atlantic City, NJ 08405

Copyright© 1995 by ASTM International www.astm.org

ν Poisson's ratio
E Elastic modulus, MPa
a Half crack length, mm
S Applied stress, MPa
Δa_s Crack growth at the specimen's surface, mm
x,y,z, Cartesian coordinates, mm
u,v,w Displacements in the x, y, and z directions, mm
σ_{ii} Normal stress in the i direction, MPa
σ_0 Flow stress (average of yield and ultimate), MPa
α_g Global constraint factor
A_i Projected area of element i on the crack plane, mm^2
A_m Total projected area of all yielded elements on the crack plane, mm^2
K Stress-intensity factor, MPa $\sqrt{m}$
K_n Normalized stress-intensity factor, MPa $\sqrt{m}$
ψ_c Critical crack-tip opening angle, degree
v_i v-displacement at location of ψ_c measurement, mm
x_i Distance from crack-tip to location of ψ_c measurement, mm
w Half width of specimen, mm

INTRODUCTION

The prediction of residual strength in an aircraft fuselage structure requires a fracture criterion that can account for large amounts of stable tearing in thin-sheet material. One criterion that has been proposed is the crack-tip opening angle (CTOA) [1-6]. This criterion states that stable crack growth will occur when the local angle made by the upper crack surface, crack-tip, and lower crack surface reaches a critical value. Experimental studies have shown that at the surface, initial CTOA values are high, but quickly decrease and maintain a constant value after a small amount of stable crack growth [7-9]. Reuter and Lloyd [10] have shown experimentally that for a surface crack, CTOA is not constant around the crack perimeter. Two-dimensional numerical studies that neglect the initial transient and through-thickness variation in CTOA behavior have shown that this criterion can successfully be used to predict residual strength for a number of different specimen configurations [8, 11-13].

The early stage of stable tearing where the measured surface CTOA is not constant has prompted concerns about the local crack-tip stress fields and the constraint in thin sheet materials. Hom and McMeeking [14] analyzed stationary, straight, through-thickness notches in thin sheets using a large deformation theory, three-dimensional elastic-plastic finite element analysis. Newman et al [8, 15-16] analyzed stationary, straight and tunneled cracks, using a small strain theory, three-dimensional elastic-plastic finite element analysis. Both found that considerable constraint develops even in thin materials where significantly higher stresses develop in the interior than on the surface.

In addition to constraint variations and the large CTOA values during early stages of crack growth, significant changes in crack front shape also occur. Sutton, Dawicke, and Newman [17] have shown that for 2024-T3 aluminum alloy in the T-L orientation (load applied perpendicular to the rolling direction with the crack parallel to the rolling direction), stable crack growth will initiate in the interior. The crack will continue to grow stably at a higher rate in the interior than at the surface until the crack length has

grown about 3mm at the surface. By this time, the crack front has developed a deeply tunneled shape that extends in a self-similar manner [17]. Shear lips did not form in this orientation.

Thus, the initial stage of fracture in thin sheet aluminum appears to be dominated by variations in constraint, crack front shape, and CTOA. Furthermore, even in the steady state region, where the surface measurements of CTOA are constant, the crack front shape can be severely tunneled. These issues raise concerns over the validity of using surface measurements of CTOA as a fracture criterion in a two-dimensional analysis.

The objective of this paper is to numerically examine the initial transient stage of fracture in thin-sheet materials as well as the effect of crack tunneling on the steady state region. A three-dimensional, elastic-plastic finite-element simulation of stable crack growth in thin sheet 2024-T3 aluminum alloy in the T-L orientation will be presented. The analyses considered both straight and tunneled crack fronts. Experimental data used in the numerical simulations were taken from Ref. 17. Comparisons are made between the critical crack-tip opening angle (CTOA), global constraint factor, and through-thickness stresses for the tunneled and straight crack fronts.

CRACK CONFIGURATION AND MATERIAL PROPERTIES

A middle crack tension, M(T), specimen 76.2mm wide by 2.3mm thick (initial a/w=0.33 and a/B=5.56) was analyzed. The material was 2024-T3 aluminum alloy in the T-L orientation. The modulus of elasticity (E) was 71,400 MPa and Poisson's ratio (v) was 0.3. In the analyses, a multi-linear representation of the uniaxial stress-strain curve, given in Table 1, was used. The stable tearing behavior was obtained from fracture tests where the applied stress (S) was recorded as a function of crack growth at the specimen surface (Δa_s) [17], as shown in Fig. 1. An average of the applied stress against crack extension at the specimen surface data is given in Table 2.

Table 1--Multi-linear representation of the uniaxial stress-strain curve for 2024-T3 aluminum alloy in the T-L orientation [17]

σ (MPa)	ε
303	0.00425
355	0.015
403	0.04
448	0.1
476	0.16
476	0.2

Deeply tunneled crack fronts were observed to develop during stable tearing tests of M(T) specimens [17]. The tunneled crack front shapes were obtained from fracture tests where the specimens were allowed to stably tear for a predetermined amount of crack growth at the specimen surface. Then, the specimens were fatigue cycled at a high stress ratio until failure. These changes in loading produced both macroscopic and microscopic changes in the fracture surface, creating a distinct interface between the

stable tearing and fatigue crack growth regions. Each boundary represents the crack front shape at a specific time during the stable tearing process.

The shape of the crack front changed significantly during the early stages of stable tearing, as shown in Fig. 2. Prior to stable tearing, the crack front shape was slightly tunneled due to the fatigue cycling used to generate a sharp crack-tip. During the initial stages of stable tearing, the crack grew faster in the interior. By the time the crack growth at the specimen surface reached 0.25mm, the growth in the interior was about 1mm. The crack front shape stabilized after about 3mm of crack growth at the specimen surface. The stabilized shape was deeply tunneled, also shown in Fig. 2. Also, it was observed that the fracture surfaces were macroscopically perpendicular to the direction of loading (i.e., shear lips did not form) [17].

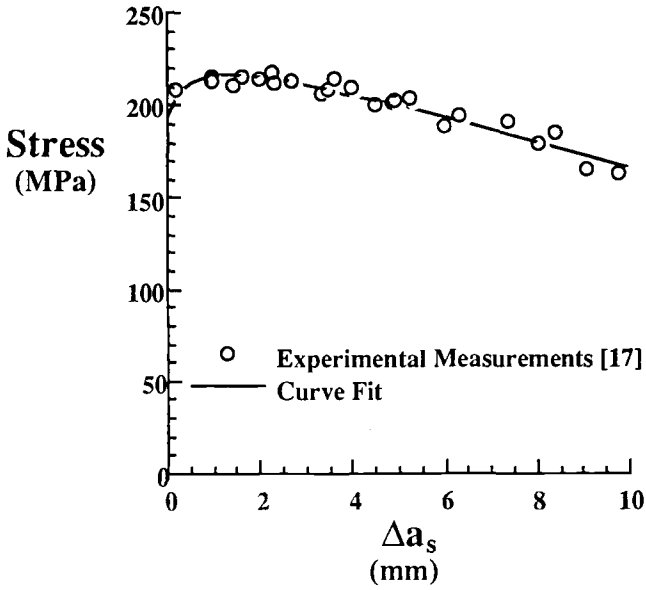


FIG. 1--Experimental measurements of stress against crack growth at the surface and the multi-linear curve fit for 2024-T3 aluminum alloy in the T-L orientation

The crack front shapes given in Fig. 2 were digitized and fit with polynomial expressions to describe the crack front shape as a function of through-thickness position. Additional crack front profiles were generated from the polynomial curve fits to describe the approximate crack front shape at each 0.25mm increment of crack growth at the specimen surface, as shown in Fig. 3.

FINITE ELEMENT ANALYSES

A three-dimensional, elastic-plastic finite element analysis code, ZIP3D [18] was used for the fracture simulation. The program uses 8-noded, hexahedral elements, the von Mises yield criterion, isotropic hardening, small-strain deformation theory, and Drucker's associated flow rule. The elastic-plastic analysis is based on the initial-stress

method and the incremental theory of plasticity [18]. The finite-element formulation and solution method are given in Ref. 19.

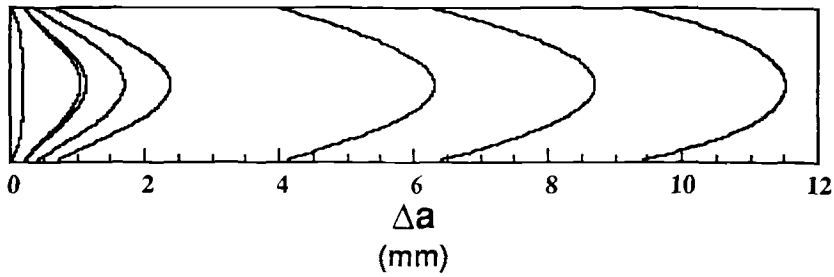


FIG. 2--Crack front profiles during stable tearing for 2024-T3 in the T-L orientation [17].

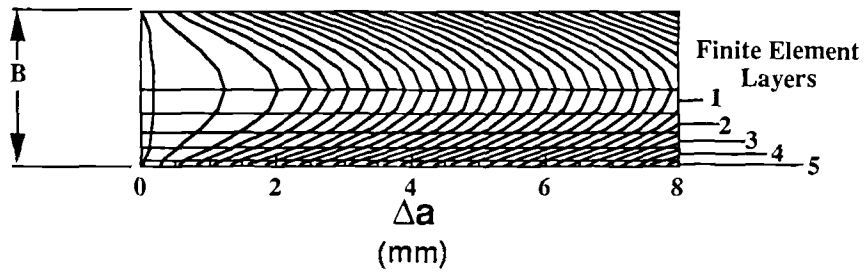


FIG. 3--Crack front profiles at even increments of crack growth at the specimen surface, generated from polynomial curve fits to the measurements given in Fig. 2.

Two different finite element models were created; one with straight, and one with tunneled crack front shapes. Symmetry conditions required that only one eighth of the M(T) specimens be modeled. Both models used five layers of elements through the half thickness (B/2=1.143mm) and had 7398 nodes and 5650 elements. The thicknesses of the layers 1 through 5 (with the layer adjacent to the mid-plane denoted as layer 1) were 0.125, 0.125, 0.125, 0.075, and 0.05 of B, respectively. The crack plane elements of the straight crack front mesh were 0.25mm in the y-direction and the x-direction, as shown in Fig. 4. The crack plane elements of the tunneled crack front mesh were 0.25mm in the y-direction and in the x-direction at the surface, but the length of the x-direction elements in the interior were greater to reflect the extent of tunneling present. This is illustrated in Fig. 3, where a view of the crack plane (x-z plane at y = 0) is shown.

Normally, the nodes along the crack line and ahead of the crack-tip are fixed, while those behind are free. This analysis uses springs along the crack line to change boundary conditions associated with crack growth. The spring stiffness is set equal to zero for nodes behind the crack tip and assigned an extremely large value for nodes ahead of the crack tip. A nodal-release procedure [20] is employed for crack growth. Stable crack growth was simulated by allowing the crack to grow when the applied stress reached a predetermined level. These predetermined stress levels were obtained from the fracture test results reported in Ref. 17 and shown in Fig. 1. In these tests, the crack length at the surface and the applied stress were measured during stable tearing. The

curve fit shown in Fig. 1 was evaluated to give the stress required for crack growth (critical stress) for each of the discrete crack lengths (measured at the surface) used in the finite element model. These values are listed in Table 2. In the finite element simulation, the entire crack front was allowed to advance one node when the applied stress reached the critical value corresponding to the current crack length at the surface.

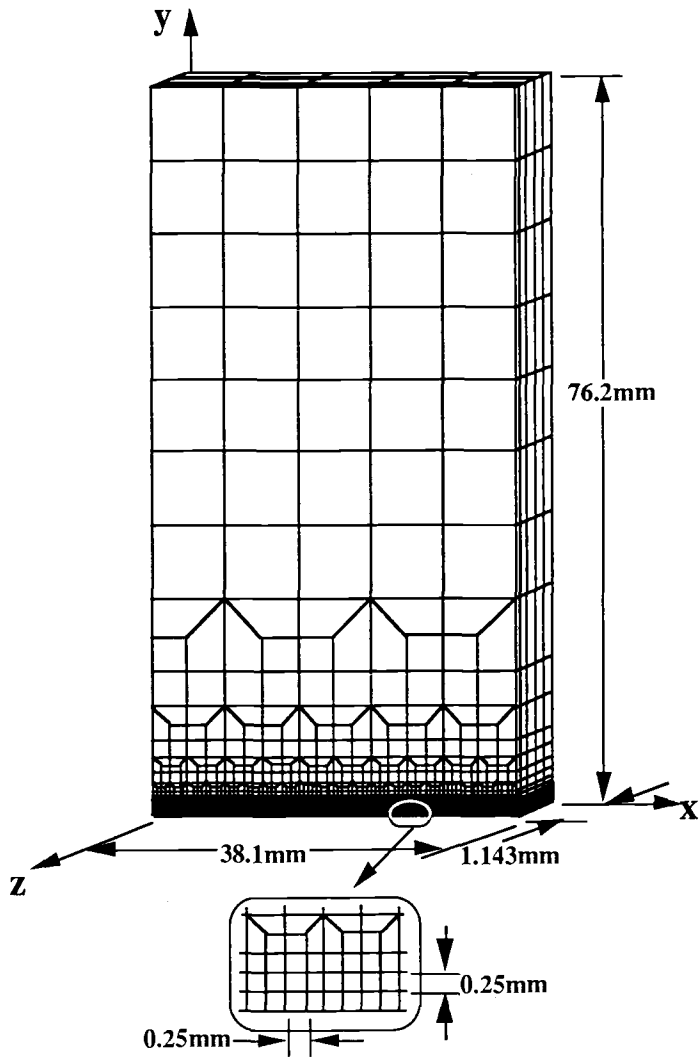


FIG. 4--Finite element mesh model of 1/8th of the M(T) specimen.

RESULTS AND DISCUSSION

Elastic-plastic finite element analyses were conducted to simulate fracture in the M(T) specimens. Two models were examined; in the first, a straight through-thickness crack front was modeled and in the second, a tunneled through-thickness crack front was modeled. Loading was simulated with uniform tractions in the y-axes along the y=76.2mm surface of the models. The material stress-strain curve, applied stress-crack growth behavior at the specimen surface, and crack front profile shapes were obtained from experimental measurements [17]. The finite element analyses used this information to define the fracture behavior and generate the local crack-tip stresses, the global constraint factor, local crack-opening displacements, and through-thickness crack-tip opening angle (CTOA) values.

Table 2--Stable crack growth data for 2024-T3 aluminum alloy in the T-L orientation [17]

Δa_s (mm)	S (MPa)
0.00	193.0
0.25	206.3
0.50	212.0
0.75	214.5
1.00	216.0
1.25	216.5
1.50	216.3
1.75	215.8
2.00	215.2
2.25	214.4
2.50	213.7
2.75	212.3
3.00	211.0
3.25	209.5
3.50	208.2
3.75	206.5
4.00	203.6
4.25	202.5
4.50	201.2
4.75	199.8
10.0	165.0

Local Crack-Tip Stresses

The stresses ahead of the crack tip in the direction of loading (σ_{yy}) were obtained from the finite element analyses of the straight and tunneled crack fronts. The reported σ_{yy} stresses are at the applied stress level required for crack growth, but before the crack front was allowed to grow. Due to the singularity at the crack tip and the approximations inherent in the small strain finite element analysis, the stresses in the crack-tip element were ignored. However, the stresses in the other elements should be reasonably accurate.

The σ_{yy} stresses, normalized by the flow stress (σ_0), on the crack plane ahead of the crack-tip in the straight crack front analysis are shown in Figs. 5a and 5b for the surface and mid-plane elements, respectively. Prior to crack growth, the trends of the σ_{yy} stresses agree with the large deformation theory finite element results of Hom and McMeeking [14]. Their analysis found that, for a blunt notch in a thin sheet, the σ_{yy} stresses at the mid-plane were greater than those at the surface with normalized peak stresses (σ_{yy}/σ_0) of about 2.0 at the mid-plane and 1.2 at the surface. The present results exhibited similar behavior with normalized peak stresses of 1.3 at the surface and 2.0 at the mid-plane.

The σ_{yy} stresses, normalized by the flow stress (σ_0), on the crack plane ahead of the crack tip in the tunneled crack front analysis are shown in Figs. 6a and 6b for the surface and mid-plane elements, respectively. For the tunneled crack front, the trends of the normalized σ_{yy} stresses at the mid-plane as a function of distance from the crack tip agree with the straight crack results for the mid-plane. However, the surface results are different for the two crack front shapes. After crack growth, the normalized stresses ahead of the crack-tip in the tunneled crack front model decrease from a value around 2, reach a minimum of about 1 and increase to a second peak before decreasing once again.

The differences in the normalized σ_{yy} stresses along the crack plane in the tunneled and straight crack front finite element analyses are further illustrated in the contour plots of Figure 7. These plots show lines of constant σ_{yy}/σ_0 stress in the steady-state region of crack growth (just prior to the 10th increment of crack growth) for an area extending from the crack front to about 3mm ahead of the crack front. Also superimposed on these plots are the finite element sdizes along the crack plane. The high σ_{yy}/σ_0 stress gradients occur over a minimum of 5 elements, which, though not sufficient to capture the magnitude stresses at the crack front, should be sufficient to capture the behavioral trends and the stress magnitude several elements ahead of the crack front. The finite element results indicate that the wedge formed at the surface of the tunneled crack front significantly increases the near surface stresses. The stresses along the mid-plane of the tunneled crack front are also greater than those at a similar position in the straight crack front analysis.

Global Constraint Factor

The global constraint factor (α_g) was defined by Newman, Bigelow, and Shivakumar [15] to be the average normal-stress-to-flow-stress ratio for elements in the plastic zone.

$$\alpha_g = \frac{1}{A_T} \sum_{m=1}^{M} \left(\frac{\sigma_{yy}}{\sigma_o}\right)_m A_m \qquad (1)$$

where, A_m is the projected area on the uncracked ligament of a yielded element m, A_T is the total projected area for all elements that have yielded, and M is the total number of yielded elements. Newman et al [16] found the global constraint factor to be nearly independent of specimen type for crack length to thickness (a/B) and uncracked ligament to thickness ratios (b/B) greater than 4. An equation expressing the global constraint as a function of the stress-intensity factor was obtained from elastic-plastic finite element

analyses of stationary, straight through-thickness cracks in an elastic-perfectly plastic material [16] as

$$\alpha_g = 1.15 + 1.25\, e^{-0.85\, K_n^{1.5}} \tag{2}$$

$$K_n = \frac{K}{\sigma_0 \sqrt{B}} \tag{3}$$

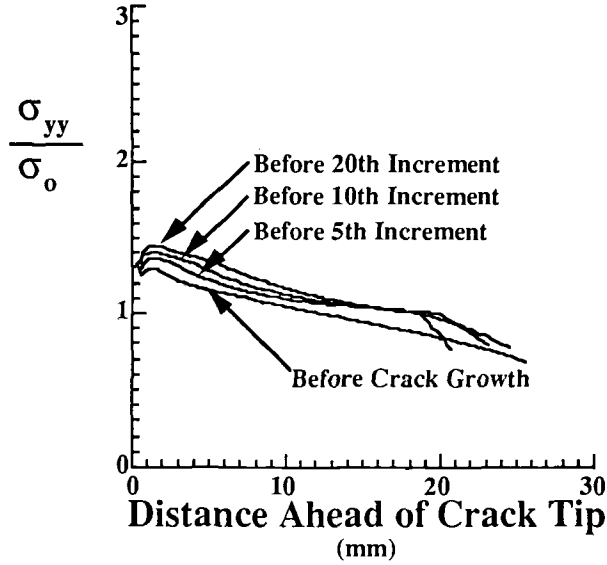
$$K = S \sqrt{\pi a \sec\left(\frac{\pi a}{2w}\right)} \tag{4}$$

Using Eqn. 1, the global constraint factor for the straight and tunneled crack analyses are plotted in Fig. 8 as a function of the normalized stress-intensity factor. For the tunneled crack, the stress-intensity factor was calculated, using Eqn. 4, neglecting the crack front curvature and using the surface crack length measurement (Note that by using the surface crack length, the average stress intensity factor of the tunneled crack would be about 10% less than that obtained using the crack length at maximum depth. This surface crack representation was used throughout the paper to be consistent with experimental measurements, where only the surface value is known.). Initially, α_g for the tunneled crack is slightly greater than that of the straight crack for the same normalized stress-intensity factor. As the stress-intensity factor increases, α_g levels off at 1.3 for both the crack front shapes. This value is higher than that calculated from Eqn. 2, however, the present analysis simulates a material that strain hardens rather than an elastic-perfectly plastic material. As the crack begins to grow, the global constraint factor drops until the maximum stress is reached. A slight increase in α_g was observed after the peak stress was reached.

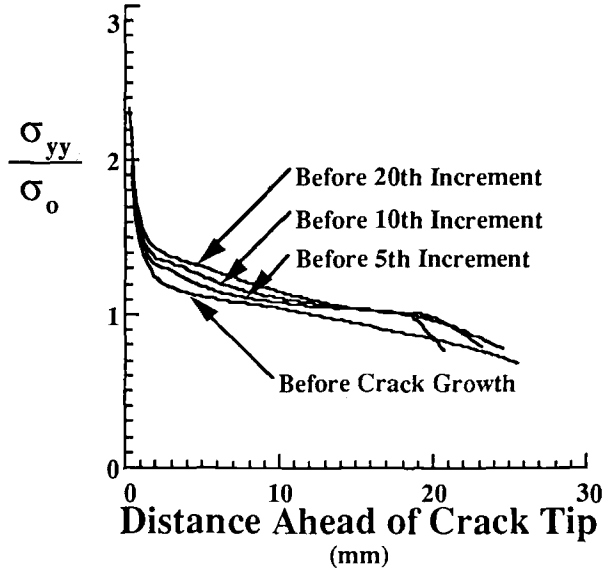
Crack Surface Displacements and CTOA

During the finite element simulation, the displacements of the nodes behind the crack tip on the crack plane were recorded at several stress levels and prior to each increment of crack growth. The displacements in the direction of loading (v) were used to calculate the crack-tip opening angle (CTOA). CTOA was calculated in the same manner as Dawicke and Sutton [9] using surface measurements. CTOA is defined to be the angle (ψ_c) made by a point on the upper crack surface, the crack tip, and a point on the lower crack surface directly below the one on the upper surface. The locations of the points on the upper and lower crack surfaces were 1mm behind the crack-tip if the amount of stable tearing exceeded 1mm, or at the node ahead of the original crack front if the total amount of stable tearing was less than 1mm. This is illustrated in Fig. 9 for displacements obtained from the finite element analysis. This definition was used to prevent anomalous CTOA values that would result from the blunted region formed at the original crack-tip. In terms of the finite element results, ψ_c is determined from the v-displacement at a distance 1mm behind the crack-tip (or at the node immediately ahead of the original crack tip if $\Delta a < 1$mm) and the x-distance from the crack-tip to the point of v-displacement measurement.

$$\psi_c = 2 \tan^{-1}\left(\frac{v_i}{x_i}\right) \tag{3}$$

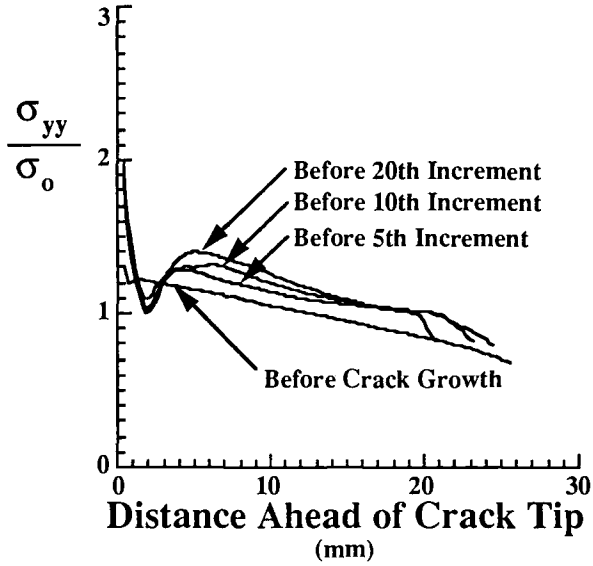


a. Surface (z/B=0.5)

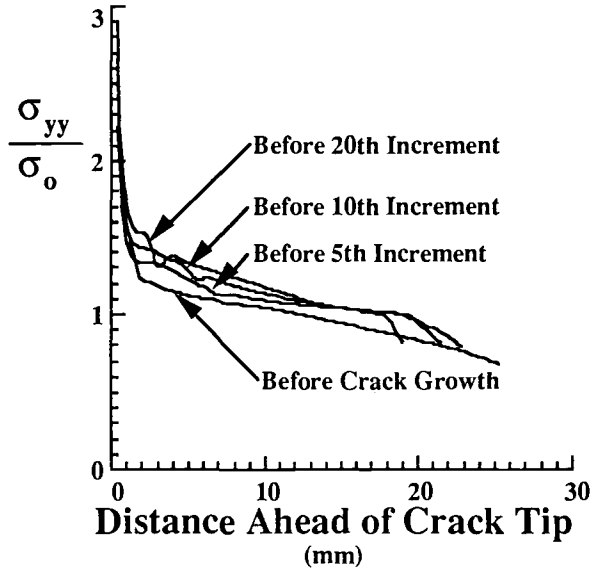


b. Mid-plane (z/B=0)

FIG. 5--Normalized σ_{yy} stresses at the second element ahead of the crack-tip from the elastic-plastic finite element analysis of the M(T) specimen with a straight crack front.

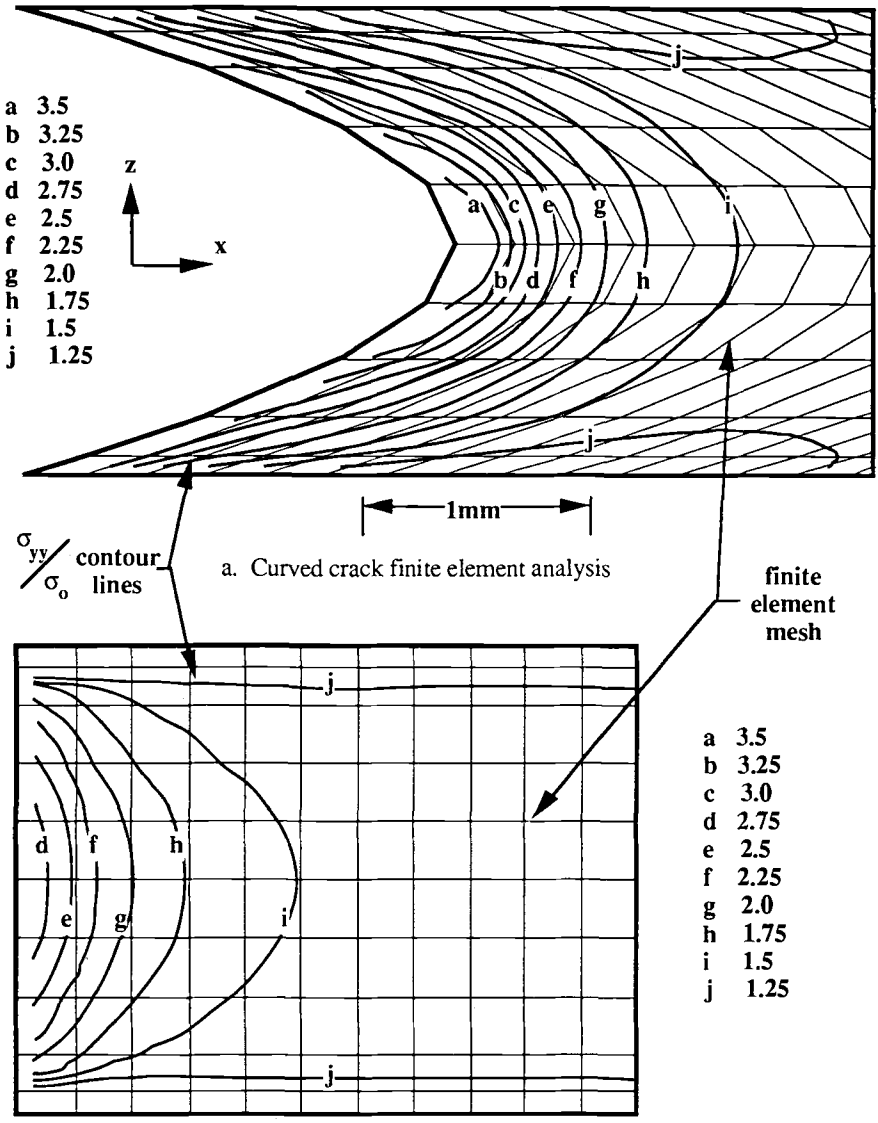


a. Surface (z/B=0.5)



b. Mid-plane (z/B=0)

FIG. 6--Normalized σ_{yy} stresses (after the first element ahead of the crack-tip) from the elastic-plastic finite element analysis of the M(T) specimen with a tunneled crack front.



b. Straight crack finite element analysis

FIG. 7--Contour plots of σ_{yy}/σ_o ahead of the crack front before the 10th increment of crack growth and the mesh pattern along the crack plane.

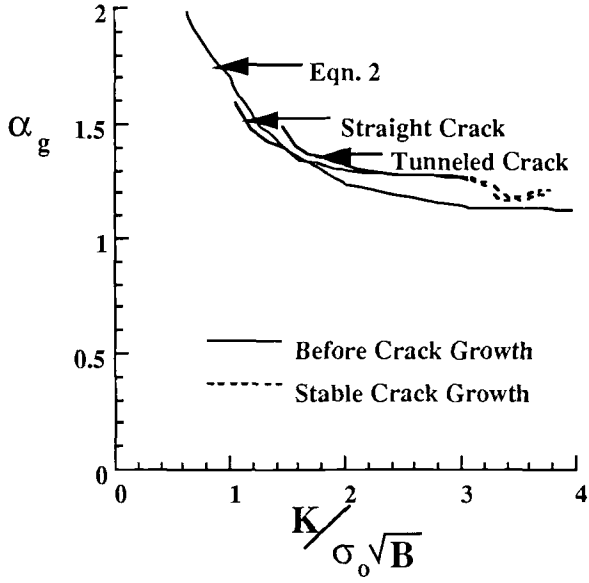
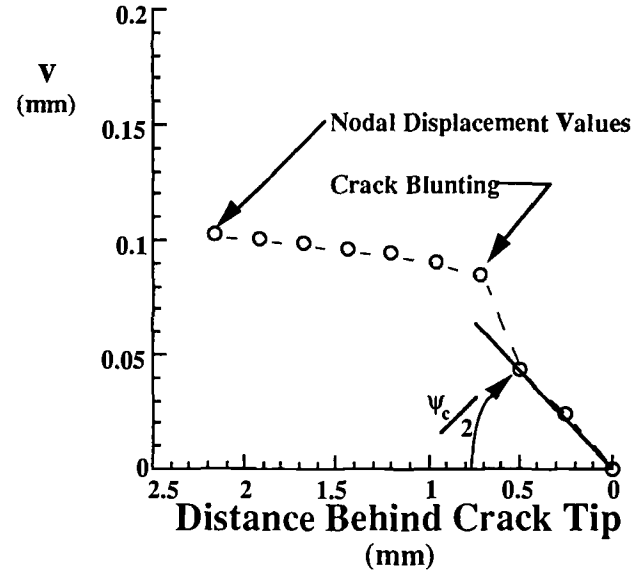
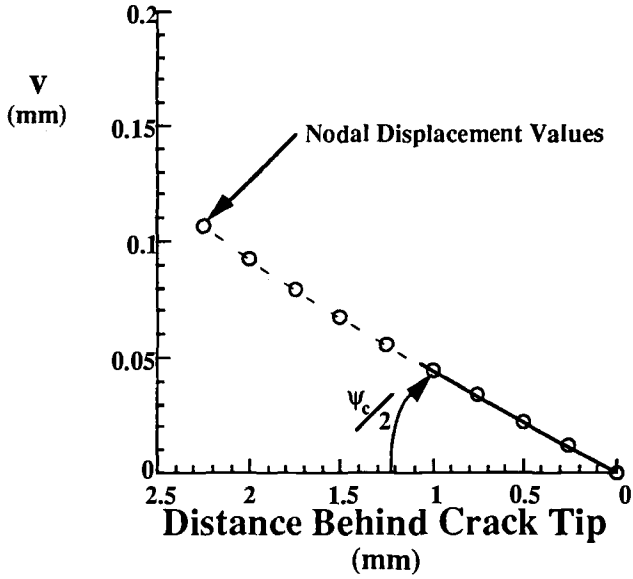


FIG. 8--Global constraint factor, α_g, as a function of the normalized applied stress-intensity factor.

The CTOA was calculated just prior to each increment of crack growth (except the first) for both the tunneled crack front and the straight crack front models, as shown in Figs. 10a and 10b, respectively. CTOA values were calculated at the surface (z/B=0.5), the mid-plane (z/B=0), and at different through-thickness locations (z/B=0.125, 0.25, 0.375, and 0.45). The tunneled crack front simulation exhibited a considerable variation in CTOA through-thickness during the initial 3mm of crack growth at the specimen's surface. The surface CTOA values agreed with the experimental surface measurements, with an initial angle of 10° at a crack growth at the specimen's surface of 0.5mm. The calculated CTOA values decreased through-the-thickness to a value of about 4° at the mid-plane. After 3mm of crack growth at the specimen's surface, all through-thickness calculations of CTOA approached the average CTOA (4.7°) that was experimentally measured at the surface. The straight crack simulation showed very little variation in CTOA through-the-thickness. Initially, the calculated CTOA value was between 5° and 6° (with the lower value at the surface). As the simulation grew the crack, the calculated CTOA values decreased slightly to between 4° and 5°.

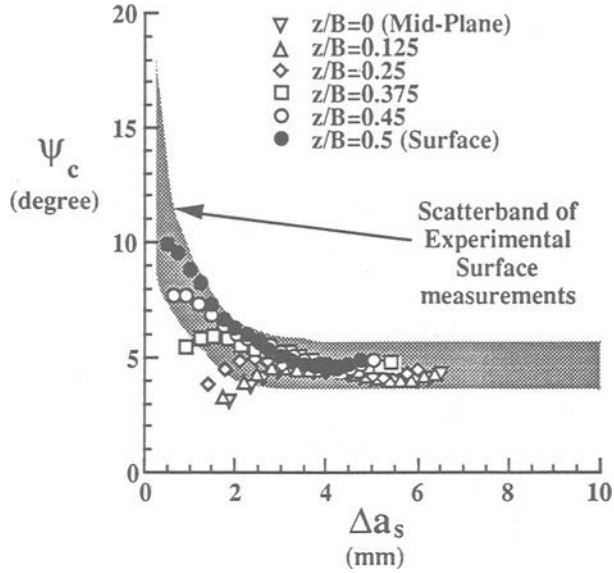


a. 0.75mm of crack growth, ψ_c measured 0.5mm behind crack-tip

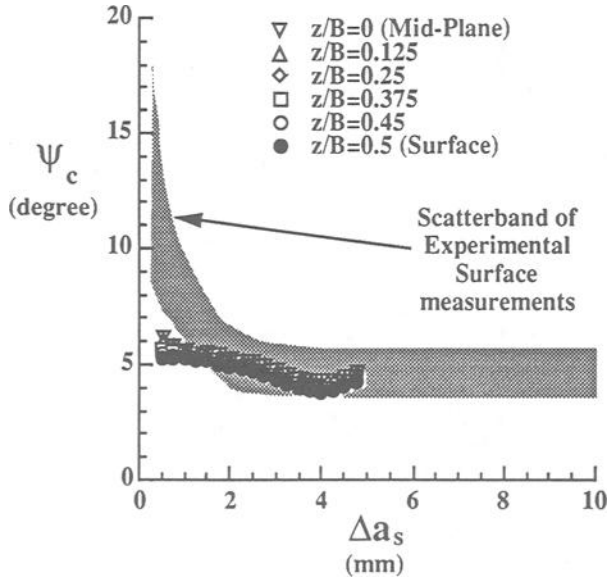


b. 3mm of crack growth, ψ_c measured 1mm behind crack-tip

FIG. 9--Crack opening displacements at the surface for a tunneled crack front indicating the location of CTOA measurement.

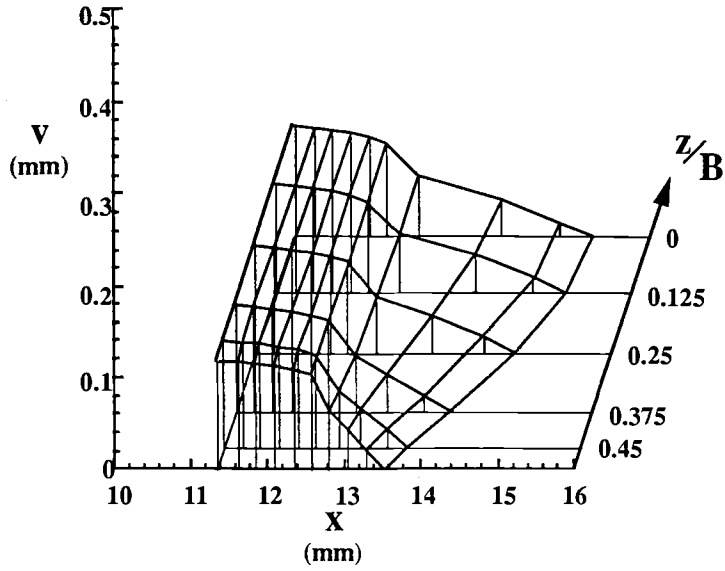


a. finite element results for tunneled crack front

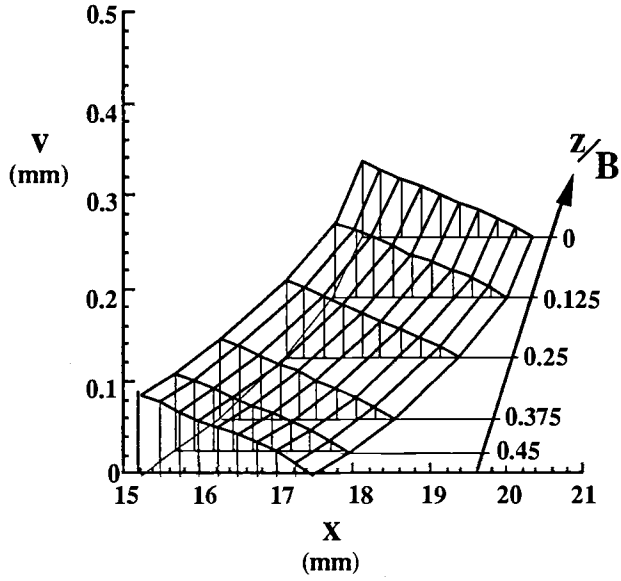


b. finite element results for straight crack front

FIG. 10--Experimental surface crack-tip opening angle measurements [17] and finite element results for a 2024-T3 aluminum alloy in the T-L orientation.



a. $\Delta a_s = 0.75$mm



b. $\Delta a_s = 4.75$mm

FIG. 11--Through-the-thickness crack opening displacement profiles for a tunneled crack front at two stages of crack growth.

To further illustrate the through-thickness variation in CTOA for the tunneled crack front, the crack opening displacement was plotted as a function of crack length and position through-the-thickness, as shown in Figures 11a and 11b for crack growth at the specimen surface of 0.75mm and 4.75mm, respectively. The crack opening displacements shown in Figure 11 are just prior to the next increment of crack growth. In Figure 11a, the crack has grown three nodes past the original crack-tip. The large initial tunneling in the interior is evident, as is the severe blunting of the original crack front and the variation in CTOA through-the-thickness. The first two elements along the mid-plane are significantly larger (in the crack growth direction) than those at the surface due to the severe tunneling during the early stages of stable tearing. However, after the second increment of crack growth, the crack growth at the mid-plane becomes closer to that at the surface, yet the differences in CTOA remain large (see Figure 10a). In Figure 11b, the crack has reached a "steady-state" condition, where the crack front profile (imposed condition) and the CTOA (calculated result) are constant through-the-thickness.

A convergence study was not performed to assess the effect of element size on the through-the-thickness CTOA behavior. However, the element size used in this study was small enough to provide accurate predictions of stable tearing and local crack opening displacements in earlier two-dimensional predictions [8-9, 11-13]. The CTOA was determined four elements (except for the second and third increments of crack growth where two and three elements were used, respectively) away from the crack front. Additional layers through-the-thickness and smaller elements would give more accurate results, but the trends shown in this analysis would probably not change.

The tunneled crack front finite element simulation indicates that CTOA may be a fracture criterion for thin-sheet materials that can be incorporated into a two-dimensional analysis. The three-dimensional analyses indicate that after steady-state conditions have been achieved, the CTOA measured at the surface is representative of what is happening in the interior. In the transient region the surface CTOA measurements are higher than in the interior and the average CTOA through-the-thickness is close to the steady-state CTOA. In a two-dimensional fracture simulation, using the constant steady-state CTOA during the transient region may be an adequate approximation, especially if the amount of stable tearing is large compared to the transient region. Earlier two-dimensional, elastic-plastic finite element analyses, using the measured steady-state CTOA value as a fracture criterion, have successfully predicted fracture behavior of single and multiple cracks in 2.3mm thick by 300mm wide sheets of 2024-T3 [21].

CONCLUSIONS

A small strain theory, three-dimensional elastic-plastic finite element analysis was used to simulate fracture in thin sheet 2024-T3 aluminum alloy in the T-L orientation. Both straight and tunneled crack fronts were modeled. The tunneled crack front shapes were obtained from experimental measurements. The stable crack growth behavior was measured at the specimen surface as a function of applied stress. The fracture simulation modeled the crack tunneling and extension as a function of applied stress. The results indicate that:

(1) The global constraint factor, α_g, dropped at the onset of stable crack growth. After peak stress was achieved, α_g began to increase. The effect of crack front shape on α_g was small.

(2) The crack front shape did influence both the local constraint and through-the-thickness CTOA behavior. Failure to account for these crack shapes in any three-dimensional simulations or predictions may give inaccurate results.

(a) Local constraint differences: Prior to crack growth, the local σ_{yy} stresses ahead of the crack-tip were higher at the mid-plane and lower at the surface in the tunneled crack model than they were in the straight crack model. In the straight crack model, both the surface and mid-plane σ_{yy} stresses increased slightly with crack growth. In the tunneled crack model, the local stresses dropped during the initial crack growth. During the rest of the initial transient region ($\Delta a_s < 3$mm), the mid-plane stresses increased sharply and the surface stress only slightly increased. After the initial transient region, the mid-plane stresses in the tunneled crack model were greater than and the surface stresses were less than those of the straight crack model.

(b) CTOA differences: Results from the tunneled crack front model indicated that during the initial transient region ($\Delta a_s < 3$mm) the CTOA at the mid-plane was less than 4° and increased with crack growth. The initial CTOA at the surface was about 10° and decreased with crack growth, which agreed with experimental surface CTOA measurements. At other through-thickness locations, the CTOA values fell between the surface and mid-plane values. After the transient region, the experimentally measured through-the-thickness CTOA was nearly constant, at a value of 4.7°. For the straight crack front model, the CTOA was constant thought-the-thickness and the initial surface CTOA values did not agree with the experimental measurements.

(3) The three-dimensional analysis appears to confirm the potential of CTOA as a two-dimensional fracture criterion. In the initial transient region, the high angles measured at the surface do not reflect the behavior in the interior and an average value would be close to the steady state surface measurements. In the steady state crack growth region, the CTOA appears to be constant though-the-thickness.

REFERENCES

[1] Wells, A. A., "Unstable Crack Propagation in Metals: Cleavage and Fast Fracture," in Proceedings of the Cranfield Crack Propagation Symposium, Vol. 1, 1961, pp. 210-230.

[2] Wells, A.A., "Application of Fracture Mechanics at and Beyond General Yielding," British Welding Journal, Vol. 11, 1961, pp. 563-570.

[3] Wells, A.A., "Notched Bar Tests, Fracture Mechanics and Brittle Strengths of Welded Structures," British Welding Journal, Vol. 12, 1963, pp. 2-13.

[4] Anderson, H., "Finite Element Representation of Stable Crack Growth," Journal of Mechanics and Physics of Solids, Vol. 21, 1973, pp. 337-356.

[5] de Koning, A. U., "A Contribution to the Analysis of Quasi Static Crack Growth in Steel Materials," in Fracture 1977, Proceedings of the 4th International Conference on Fracture, Vol. 3, pp. 25-31.

[6] Kanninen, M. F., "The Analysis of Stable Crack Growth in Type 304 Stainless Steel," in Proceedings of the International Conference of Fracture 1980, pp. 1759-1768.

[7] Demofonti, G. and Rizzi, L., "Experimental Evaluation of CTOA in Controlling Unstable Ductile Fracture Propagation," ESIS Pub. 9, 1991, pp. 693-703.

[8] Newman, J. C., Jr., Dawicke, D. S., and Bigelow, C. A., "Finite-Element Analysis and Measurement of CTOA During Stable Tearing in a Thin-Sheet Aluminum Alloy," Durability of Metal Aircraft Structures, S. N. Atluri, C. E. Harris, A. Hoggard, M. Miller, and S. G. Sampath, Eds., 1992, pp. 167-186.

[9] Dawicke, D. S. and Sutton, M. A., "Crack-Tip Opening Angle Measurements and Crack Tunneling Under Stable Tearing in Thin Sheet 2024-T3 Aluminum Alloy", NASA CR-191523, September 1993.

[10] Reuter, W. G. and Lloyd, W. R., "Measurements of CTOD and CTOA Around Surface-Crack Perimeters and Relationships Between Elastic and Elastic-Plastic CTOD Values," Surface-Crack Growth: Models, Experiments, and Structures, ASTM STP 1060, W. G. Reuter, J. H. Underwood, and J. C. Newman, Jr., Eds., American Society for Testing and Materials, Philadelphia, 1990, pp. 152-176.

[11] Newman, J. C., Jr., Dawicke, D. S., Sutton, M. A., and Bigelow, C. A., "A Fracture Criterion for Widespread Cracking in Thin-Sheet Aluminum Alloys," Durability and Structural Integrity of Airframes, Volume I, A. F. Blom, Ed., 1993, pp. 443-467.

[12] Dawicke, D. S., Sutton, M. A., Newman, J. C., Jr., and Bigelow, C. A., "Measurement and Analysis of Critical CTOA for an Aluminum Alloy Sheet," NASA TM-109024, 1993.

[13] Dawicke, D. S., Newman, J. C., Jr., Sutton, M. A., and Amstutz, B. E., "Stable Tearing Behavior of a Thin-Sheet Material with Multiple Cracks," NASA TM-109131, 1994.

[14] Hom, C. L. and McMeeking, R. M., "Large Crack Tip Opening in Thin, Elastic-Plastic Sheets," International Journal of Fracture, Vol. 45, 1990, pp. 103-122.

[15] Newman, J. C., Jr., Bigelow, C. A., and Shivakumar, K. N., "Three-Dimensional Elastic-Plastic Finite-Element Analyses of Constraint Variations in Cracked Bodies," Engineering Fracture Mechanics, Vol. 46, No. 1, 1993, pp. 1-13.

[16] Newman, J. C., Jr., Crews, J. H., Jr., Bigelow, C. A., and Dawicke, D. S., "Variations of a Global Constraint Factor in Cracked Bodies Under Tension and Bending Loads," Constraint Effects in Fracture: Theory and Applications, ASTM STP 1244, Mark Kirk and Ad Bakker, Eds., American Society of Testing and Materials, Philadelphia, 1994.

[17] Sutton, M. A., Dawicke, D. S., and Newman, J. C., Jr., "Orientation Effects on the Measurement and Analysis of Critical CTOA in an Aluminum Alloy Sheet," Fracture Mechanics: 26th Volume, ASTM STP 1256, Walter G. Reuter, John H. Underwood, and James C. Newman, Jr., Eds, American Society for Testing and Materials, Philadelphia, 1995.

[18] Shivakumar, K. N. and Newman, J. C., Jr., "ZIP3D - An Elastic and Elastic-Plastic Finite-Element Analysis Program for Cracked Bodies," NASA TM 102753, 1990.

[19] Zienkiewicz, O. C., Valliappan, S., and King, I. P., "Elasto-Plastic Solutions of Engineering Problems, Initial Stress, Finite-Element Approach," International Journal of Numerical Methods in Engineering, Vol. 1, 1969, pp. 75-100.

[20] Chermahini, R. G., Shivakumar, K. N., and Newman, J. C., Jr., "Three-Dimensional Finite-Element Simulation of Fatigue Crack Growth and Closure," Mechanics of Fatigue Crack Closure, ASTM STP 982, J. C. Newman, Jr., and W. Elber, eds., 1988, pp. 398-413.

[21] Dawicke, D.S., Newman, J.C., Jr., Sutton, M.A., and Amstutz, B.E., "Influence of Crack History on the Stable Tearing Behavior of a Thin-Sheet Material with Multiple Cracks", FAA/NASA International Symposium on Advanced Structural Integrity Methods for Airframe Durability and Damage Tolerance, May 1994.

M. A. Sutton[1], D. S. Dawicke[2], and J. C. Newman, Jr.[3]

ORIENTATION EFFECTS ON THE MEASUREMENT AND ANALYSIS OF CRITICAL CTOA IN AN ALUMINUM ALLOY SHEET

REFERENCE: Sutton, M. A., Dawicke, D. S., and Newman, J. C., Jr., "Orientation Effects on the Measurement and Analysis of Critical CTOA in an Aluminum Alloy Sheet", Fracture Mechanics: 26th Volume, ASTM STP 1256, Walter G. Reuter, John H. Underwood, and James C. Newman, Jr., Eds, American Society for Testing and Materials, Philadelphia, 1995.

ABSTRACT: Fracture tests were conducted on 76.2mm wide, 2.3mm thick middle crack tension (M(T)) specimens machined from 2024-T3 aluminum sheet. The specimens were tested in the T-L orientation and comparisons were made to similar tests conducted in the L-T orientation. Measurement of critical crack tip opening angle (CTOA), applied stress, and crack front shape were made as a function of crack extension. A two-dimensional, elastic-plastic finite element analysis was used to simulate the fracture behavior for both orientations. The results indicate that the T-L orientation had a 10% lower stress at fracture than similar tests conducted in the L-T orientation. Correspondingly, the critical CTOA in the T-L tests reached a constant value of 4.7° after 2-3mm of crack extension and the L-T tests reached a value of 6°. The fracture surface of the T-L specimens were observed to remain flat, while those of the L-T specimens transitioned to a 45° slant fracture after about 2-3mm of crack extension. The tunneling behavior of the two orientations also differed; the T-L specimens reached a deeply tunneled stabilized crack front shape, while the L-T specimens were observed to have only a small amount of tunneling once the crack began to grow on the 45° slant. The two-dimensional, elastic-plastic finite element analysis was able to simulate the fracture behavior for both the T-L and L-T orientations.

KEYWORDS: Fracture, stable crack growth, CTOA, thin sheet, rolling orientation, and experimental data

NOMENCLATURE

ΔS	Applied stress range, MPa
R	Stress ratio
w	Specimen width, mm

[1] Professor, Department of Mechanical Engineering, University of South Carolina, Columbia, SC 29208
[2] Senior Scientist, Analytical Services and Materials, Inc., Hampton, VA 23666
3 Senior Scientist, NASA Langley Research Center, Hampton, VA 23665

Copyright© 1995 by ASTM International www.astm.org

a	Half crack length, mm
d	Distance behind crack tip for CTOA measurement, mm
ψ_c	Critical crack tip opening angle, degree
δ_C	Critical crack opening displacement, mm
Δa	Crack extension, mm
Δa_s	Surface crack extension, mm
Δa_i	Mid-plane crack extension, mm
B	Sheet thickness, mm

INTRODUCTION

The aging of the commercial transport aircraft fleet has brought greater awareness of the deleterious effects of fatigue damage developing in pressurized fuselage structures. Analysis tools are needed to assess the influence of fatigue cracks on structural integrity and define inspection intervals. One of the objectives of the NASA Aircraft Structural Integrity Program [1] is to develop the methodology necessary to predict residual strength of cracked pressurized aircraft fuselage structures. The approach taken is to develop a local fracture criterion that can be used with shell-code finite element analyses. The fracture criterion should be able to predict large amounts of stable crack growth under conditions of large-scale yielding in thin sheet materials.

One local fracture criterion is the crack tip opening angle (CTOA) [2-6]. This criterion postulates that a crack will undergo stable crack growth when the angle made by the upper and lower crack surfaces (at a fixed distance behind the crack tip) and the crack tip, reaches a critical value. The critical CTOA criterion has been experimentally verified and successfully used to predict residual strength in laboratory specimens of 2024-T3 in the L-T orientation (i.e., the load was applied in the longitudinal or rolling direction and the crack was in the transverse direction or perpendicular to the longitudinal direction) [7-9]. However, this material has been shown to have anisotropic fracture properties, with the T-L orientation (i.e., the load was applied in the transverse and the crack was in the longitudinal direction) having about a 10% lower fracture toughness than the L-T orientation [10]. Moreover, in a pressurized aircraft fuselage structure, the maximum hoop stress would result in a preference for cracks developing lengthwise along the fuselage (T-L orientation). As these cracks grow towards circumferential tear straps, they will either "flap", (a process where the cracked fuselage would peel open in a small local region and lead to safe decompression) or run through the tear strap. If flapping does occur, the crack will then be growing in the L-T orientation. Thus, in order to predict the residual strength of cracks in 2024-T3 aluminum alloy fuselage structures, both the L-T and T-L properties must be known.

The objective of this study was to examine stable tearing behavior in the T-L orientation of 2024-T3 aluminum alloy. Fracture tests were conducted with measurements made of load, crack extension, and critical CTOA. The critical CTOA criterion and an elastic-plastic finite element analysis were used to predict stable crack growth observed in the tests. Also, the macroscopic fracture surface behavior was examined through comparisons of the stable tearing crack tunneling behavior.

EXPERIMENTAL PROCEDURE

Fracture tests were conducted on 2.3mm thick 2024-T3 aluminum alloy. The yield stress and ultimate strength of the material in the L-T orientation were 345 and 490 MPa, respectively. The yield stress and ultimate strength of the material in the T-L orientation were 303 and 476 MPa, respectively. The multi-linear representations of the uniaxial stress-strain curve for both orientations are given in Table 1 and plotted in Fig. 1. The tests were conducted on 76.2mm wide middle crack tension, M(T), specimens. Measurements were made of the critical CTOA and crack-tip strain fields.

TABLE 1--Multi-linear representation of the uniaxial stress-strain curve for 2024-T3

L-T Orientation		T-L Orientation		
σ (MPa)	ε	σ (MPa)	ε	
345	0.00483	303	0.00425	
390	0.015	355	0.015	E = 71,400 MPa
430	0.04	403	0.04	
470	0.1	448	0.1	ν = 0.3
490	0.16	476	0.16	
490	0.2	476	0.2	

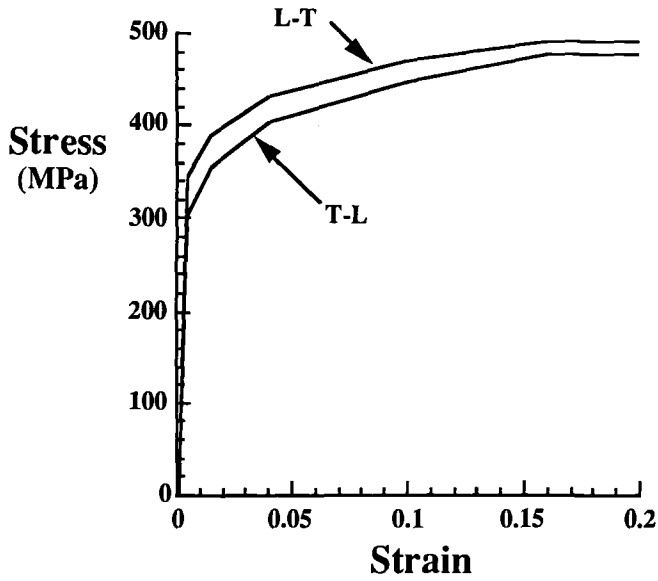


FIG. 1--Multi-linear stress-strain curve for 2024-T3 in the L-T and T-L orientations.

Fracture Tests

The M(T) crack configuration is shown in Fig. 2. All of the specimens were cracked in the T-L orientation (i.e., the load was applied in the transverse or perpendicular to the rolling direction and the crack was in the longitudinal direction or rolling direction). The specimens were fatigue cycled under constant amplitude loading (ΔS = 34.5 MPa and R = 0.02) until the total crack length was 25.4mm (a/w = 0.33). The stable tearing tests were conducted using displacement control, with a constant loading rate of 0.002mm/sec. During each test, measurements of load, crack length, and surface CTOA were made.

In some of the tests, the cracks were stably grown to pre-selected crack lengths. The specimens were then fatigue cycled until failure to mark the stable crack growth region. The maximum applied fatigue stress was 50-80% of the observed maximum applied stress during stable tearing and the stress ratio was R=0.8.

Measurement Techniques

The critical CTOA during stable tearing was measured by direct observation of the surface using both the digital image correlation (DIC) and the optical microscopy (OM) technique. The OM technique uses a video camera and a long focal length microscope to image the tearing crack. The CTOA is calculated directly from points located on the upper and lower crack surfaces (between 0.5mm and 1.5mm behind the crack tip) and the crack tip. Similarly, the DIC technique [11-15] measures the CTOA based on displacements of referenced surface regions located near the upper and lower crack surfaces and the crack tip. This technique uses a computer controlled video camera and lens system to digitize images of the specimen surface. To make measurements, the specimen surface was coated with a high contrast random pattern. A small region, or subset, is identified in a reference image and the relative displacement of that same subset in a subsequent image is calculated. Additional details of the DIC and OM CTOA techniques are given in References 7 and 8.

FINITE ELEMENT ANALYSIS

The elastic-plastic finite element code ZIP2D [16] was used to simulate the stable tearing behavior in the fracture tests. The program uses 3-noded, constant strain triangular elements and a critical CTOA criterion to extend the crack The elastic-plastic analysis employs the initial-stress concept [17] based on incremental flow theory and small strain assumptions. A multi-linear representation of the uniaxial stress-strain curve for 2024-T3, with the data given in Table 1, was used in the analysis with a von Mises yield criterion.

Finite Element Code and Meshes

The element size along the line of crack extension was 0.48mm. One half of the specimen was modeled, with the axes of symmetry along the crack line. The finite element model consisted of 821 nodes and 1447 constant strain triangular elements, as shown in Fig. 3. Normally, the nodes along the crack line and ahead of the crack tip are fixed, while those behind are free. This analysis uses fictitious springs along the crack line to change boundary conditions associated with crack extension. The stiffness of the springs are set equal to zero for the nodes behind the crack tip and assigned extremely large values for the nodes ahead of the crack tip. Monotonic loading (under displacement control) was applied to the model. Crack growth by stable tearing was

governed by the critical CTOA criterion. References 8 and 9 contain the details of the elastic-plastic finite element analysis used in this work.

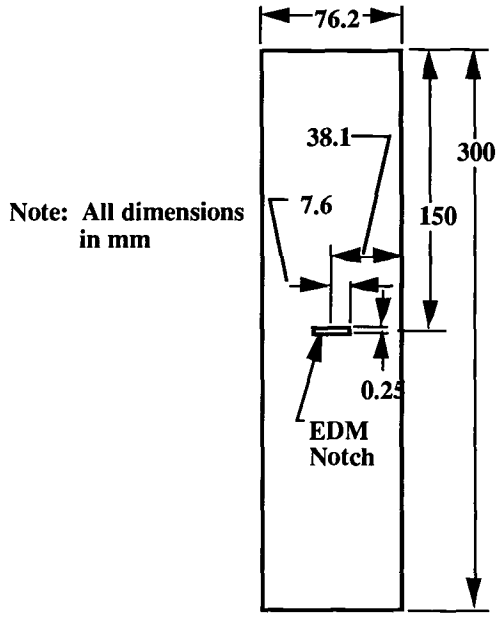


FIG. 2--M(T) specimen configuration.

Critical CTOA Criterion

The critical CTOA, ψ_c, criterion is equivalent to a critical crack tip opening displacement (CTOD) , δ_c, value at a specified distance, d, behind the crack tip equal to one element length and is given by:

$$\psi_c = 2 \tan^{-1}\left(\frac{\delta_c}{2/d}\right) \quad (1)$$

The crack-tip node was released and the crack advanced to the next node whenever the CTOA equaled or exceeded a preset critical value (ψ_c) during incremental loading. This process was repeated until the crack reached the desired length. The critical CTOA value (ψ_c) was determined experimentally from surface measurements made using both the OM and DIC techniques.

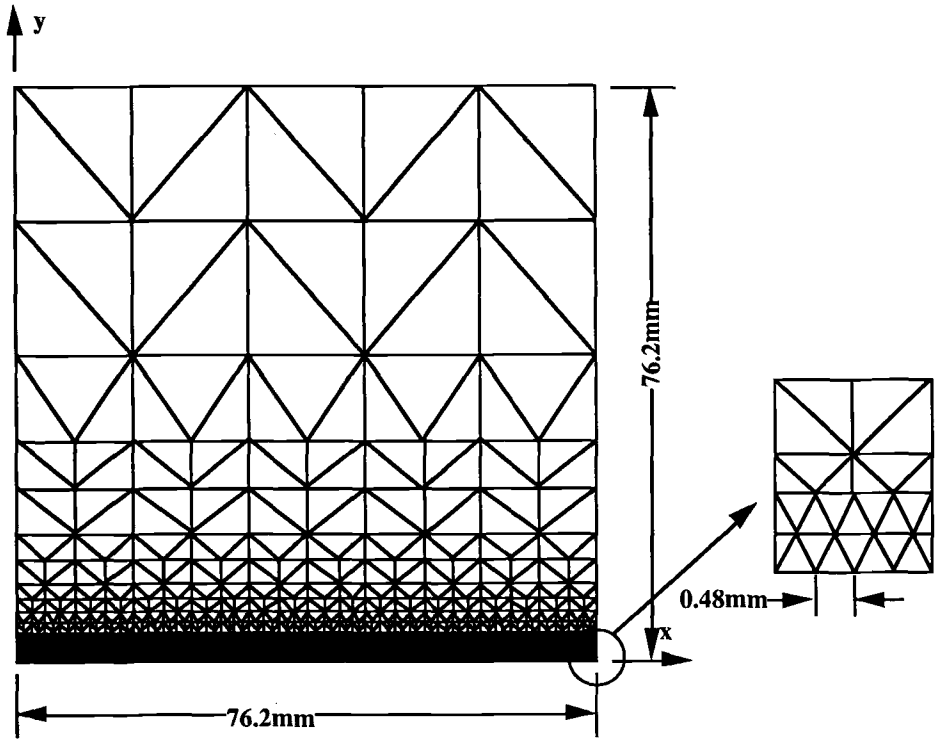


FIG. 3--Finite element model of 1/2 of the M(T) specimen.

RESULTS AND DISCUSSION

Fracture tests were conducted on 2024-T3 aluminum alloy M(T) specimens in the T-L orientation, with comparisons made to similar tests conducted on specimens in the L-T orientation [7]. Surface crack growth measurements were made using an optical microscope. Surface CTOA measurements for tearing cracks were made using the OM and DIC methods. The extent of crack tunneling during stable tearing was determined through metallographic analysis of fracture surfaces subjected to a loading history that marked the crack front. The load against crack extension behavior was simulated using an elastic-plastic, two-dimensional finite element analysis.

Critical CTOA Measurements

The critical CTOA measurements for the M(T) tests are shown in Fig. 4. Also included in this figure is a scatterband that represents the measurements made on similar tests conducted in the L-T orientation. The initial CTOA values, in both the L-T and T-L tests, were high and decreased rapidly during the first 2.5mm of stable crack extension. After this initial transient period, the CTOA measurements in both tests stabilized within scatterbands of about ±1°.

Each data point shown in Fig. 4 corresponds to one image captured while the crack was growing. For each image, 5 to 10 CTOA measurements were made at distances of 0.5-1.5mm behind the crack tip. These measurements were then averaged to give the CTOA for a specific amount of crack extension. The scatter in the data was due to a combination of experimental error and material variability. The experimental error was mainly associated with difficulties in accurately locating the crack tip. The camera systems used were able to resolve the crack tip to within 0.03mm, resulting in an error of about ±0.3°. The material variability resulted primarily from the meandering of the crack path during stable tearing. At a macroscopic level (1x magnification), the crack path appears very straight (This is especially true for the T-L orientation and the L-T orientation after the first 2mm of crack extension.). However, at a microscopic level (100x magnification or greater) the crack path appears quite torturous, with variations in crack trajectory, perpendicular to the direction of nominal crack growth, as much as 0.5mm. Due to these variations in crack trajectory, it was not uncommon to see CTOA measurements vary as much as ±1° for stable crack growth in consecutive images, however, the measurements appeared to oscillate about the average CTOA value.

The average CTOA value in the stabilized region ($\Delta a > 2$mm) in the T-L tests was 4.7° with a standard deviation of 0.4° compared to an average CTOA of 6° and a standard deviation of 0.6° for the L-T tests. The distributions of the CTOA measurements are shown in Fig. 5 for both the L-T and T-L orientations. The distributions clearly indicate significant differences between the angles measured for the L-T and T-L orientations.

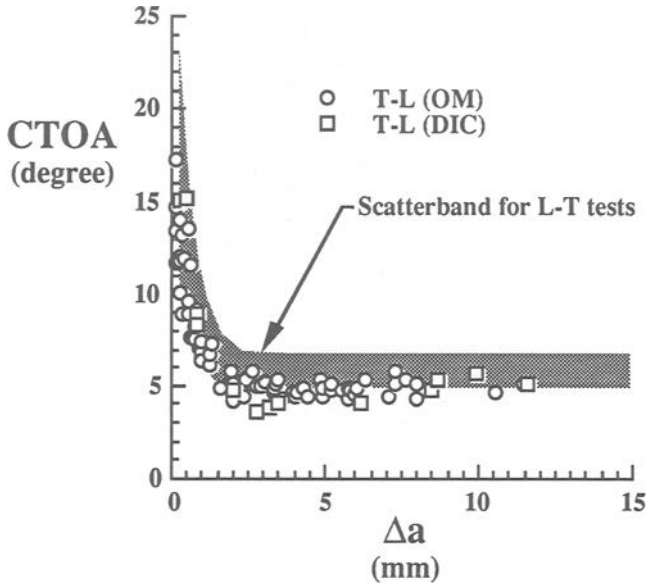


FIG. 4--Critical CTOA measurements for the M(T) specimens in the T-L orientation (precracked at a stress range of $\Delta S = 34.5$ MPa) and the scatterband for similar M(T) L-T tests [7].

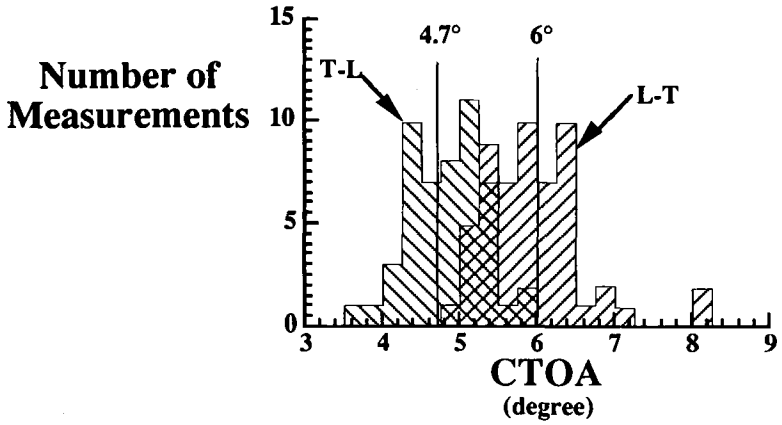


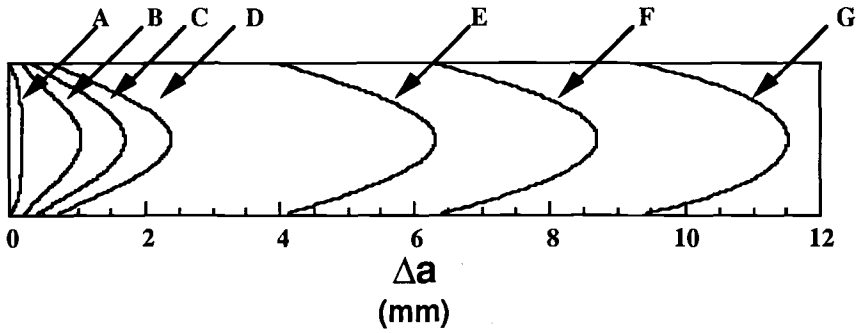
FIG. 5--Distribution of the measured CTOA values for the L-T and T-L orientations.

Crack Tunneling Measurements

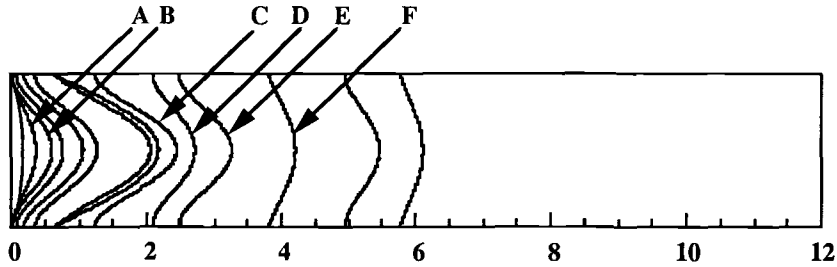
A fractographic analysis of fracture surfaces was performed to quantify the crack tunneling behavior present during stable crack growth. As described in Reference 7, a distinct change in the macroscopic appearance of the fracture surface occurs when the loading changes from fatigue cycling to stable tearing. To facilitate the marking of the tunneled crack front, some specimens were fatigue precracked, loaded for a limited amount of stable crack growth, then fatigue cycled at a high stress level (high R) until failure. The stable tearing regions and the fatigue precrack regions have sharply different appearances, with a distinct interface between them. This interface denotes the shape of the crack front just prior to stable tearing. Also, a second distinct interface occurs when the loading is changed from stable tearing to high-R fatigue cycling, marking the shape of the crack front after the stable tearing. The interfaces between the different regions were digitized for several fracture tests.

Sequences of crack front profiles from specimens tested in both the T-L and L-T orientation, with increasing amounts of stable crack extension, are shown in Figs. 6a and 6b, respectively. The crack fronts shown in Fig. 6 represent trends in through-thickness crack extension rather than the progression of a single crack front, since each came from a different fracture test.

In the T-L tests, the cracks grew, on the average, about 0.1 mm more in the interior than on the surface during fatigue cycling, as indicated by profile A in Fig. 6a. The second crack front (profile B) showed that stable tearing progressed faster and probably began in the specimen interior. This crack front revealed about 0.25mm of surface crack extension, but the interior grew about 1mm. The next two crack fronts (profiles C and D) indicate that the extent of tunneling (defined as the difference between the interior crack length and the surface crack length) increased with surface crack extension. The extent of tunneling stabilized at about 2mm, after about 2mm of surface crack extension (profiles E, F, and G). The fracture surface remained macroscopically flat during the entire fracture process.



a. T-L orientation



b. L-T orientation [7]

FIG. 6--Crack front profiles after stable tearing for specimens tested in the T-L and L-T orientations.

In the L-T tests [7], the stable crack growth began in the interior, similar to the T-L test, as seen by profiles A and B shown in Fig. 6b. However, between 1-4mm of surface crack extension the crack front began to straighten (profiles C, D, E, and F), with the surface nearly catching up to the interior. This reduction in the extent of tunneling corresponded to the onset of 45° slant crack growth [7].

The extent of tunneling that developed during stable tearing is shown in Fig. 7, where the normalized extent of tunneling (the difference between the interior crack length and the surface crack length (a_i - a_s) divided by the thickness (B)) is plotted as a function of the surface crack extension (Δa_s). The tunneling in the L-T tests peaked at about 70% of the thickness after about 0.8 mm of surface crack growth and dropped off to about 20% of the thickness for longer crack extensions. Initially the tunneling behavior in the T-L tests was identical to that in the L-T tests, but after about 1mm of surface crack extension the tunneling in the T-L tests continued to increase, peaking at about 110% of the thickness.

Metallographic evaluation of both the T-L and L-T fracture surfaces did not show any significant differences; both demonstrated classical dimpled rupture profiles through the thickness and along the crack front. However, metallographic evaluations of

the as-tested rolled sheet confirms that the grain structure is elongated in the rolling direction, though it is not totally clear how this variation contributes to observed crack growth differences.

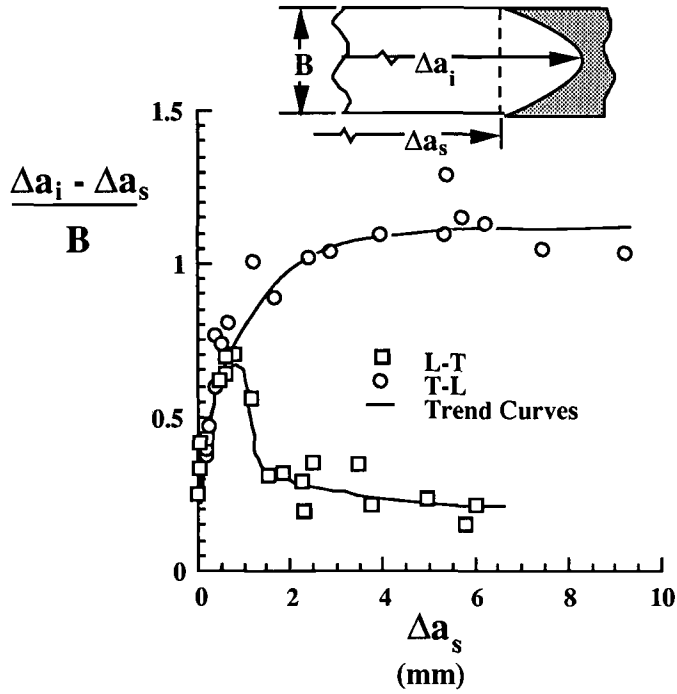


FIG. 7--Extent of crack tunneling for specimens tested in the T-L and L-T orientations.

Stable Crack Growth Measurements and Simulations

The load against surface crack extension measurements and the finite element simulations are shown in Fig. 8 for specimens tested in the T-L and L-T orientation. The peak stresses in the L-T tests were about 10% greater than that observed in the T-L tests. The finite element analyses used the stress-strain curves given in Table 1 and the critical CTOA values measured in the fracture tests to simulate the stable tearing behavior. The critical CTOA values were 6° and 4.7° for the L-T and T-L simulations, respectively. As seen in Fig. 8, the finite element simulations of peak stress were about 2% less than the peak stresses observed in the tests. The finite element analyses overestimated the amount of initial crack extension, but after reaching peak stress the analyses agreed well with the experimental measurements.

The two-dimensional finite element analysis assumes that the crack front is straight and flat through-the-thickness. The experimental results shown above indicate that for the L-T specimen, the crack front attains a nearly straight crack front (after tunneling during the first 1mm of surface crack growth), but grows on a 45° slant. The T-L crack front remains flat, but developes and maintains a deeply tunneled shape. The finite element analysis neglects these effects and using only the stress-strain curve and the measured

CTOA predicts the stress at failure and crack growth after the initial transient region. In the initial transient region, the finite element analysis overpredicts the crack extension measurements made at the surface, but a through-thickness average crack length measurement (considering the tunneling) would increase the measured crack extension values, resulting in better agreement between the finite element predictions and the experimental measurements.

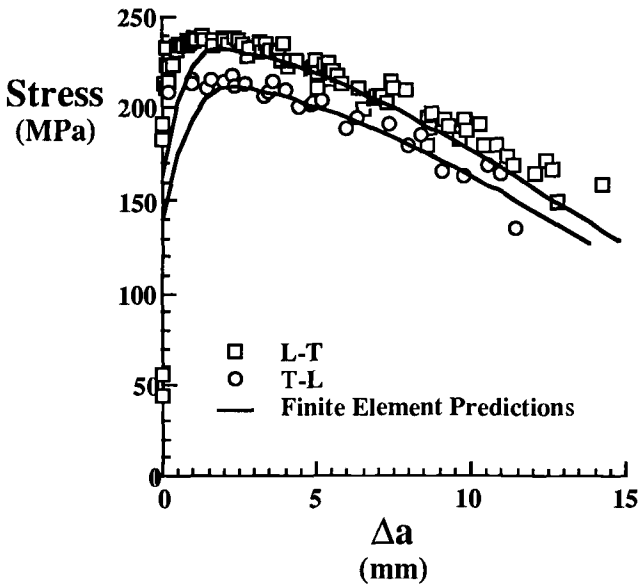


FIG. 8--Stress against surface crack extension measurements and finite element predictions for tests conducted on specimens in the L-T and T-L orientation.

CONCLUDING REMARKS

Fracture tests were conducted on M(T) specimens machined from 2024-T3 sheet aluminum in the T-L orientation and comparisons were made with similar tests conducted on specimens in the L-T orientation. Using two independent experimental methods, CTOA was determined for 10mm of crack growth. Results indicated that:

1. The CTOA trends were similar for both orientations; initially large CTOA values were measured, followed by a rapid decrease to a constant CTOA value for $\Delta a > 2.5$mm.
   a. For the T-L orientation, the constant CTOA was about 4.7°.
   b. For the L-T orientation, the constant CTOA was about 6°.

2. A substantial difference was observed between the T-L and L-T crack growth processes.
   a. The T-L fracture surface remained flat and exhibited significant tunneling (a difference in crack length between the surface crack and interior of about 2mm).

b. The L-T fracture was on a 45° slant after about 2-3mm of surface crack extension and initially exhibited significant tunneling, but as the stable tearing transitioned from flat-to-slant, the tunneling decreased.

3. The tests conducted in the T-L orientation had a peak fracture stress that was 10% less than that observed in the L-T tests.

4. The two-dimensional, elastic-plastic finite element analysis was able to simulate the peak fracture stress for both the T-L and L-T orientations.

5. The two-dimensional, elastic-plastic finite element analysis overpredicted crack growth during the first 2mm of crack extension, where the surface CTOA and the amount of crack tunneling are changing.

REFERENCES

[1] Harris, C. E., "NASA Aircraft Structural Integrity Program", NASA TM 102637, April 1990.

[2] Anderson, H., "Finite Element Representation of Stable Crack Growth," Journal of Mechanics and Physics of Solids, Vol. 21, 1973, pp. 337-356.

[3] de Koning, A. U., "A Contribution to the Analysis of Quasi Static Crack Growth in Steel Materials," in Fracture 1977, Proceedings of the 4th International Conference on Fracture, Vol. 3, pp. 25-31.

[4] Wells, A. A., "Unstable Crack Propagation in Metals: Cleavage and Fast Fracture," in Proceedings of the Cranfield Crack Propagation Symposium, Vol. 1, 1961, pp. 210-230.

[5] Wells, A. A., "Application of Fracture Mechanics at and Beyond General Yielding," British Welding Journal, Vol. 11, 1961, pp. 563-570.

[6] Wells, A. A., "Notched Bar Tests, Fracture Mechanics and Brittle Strengths of Welded Structures," British Welding Journal, Vol. 12, 1963, pp. 2-13.

[7] Dawicke, D. S. and Sutton, M. A., "Crack-Tip-Opening Angle Measurements and Crack Tunneling Under Stable Tearing in Thin Sheet 2024-T3 Aluminum Alloy", NASA-CR-191523, September 1993, also accepted for publication in Experimental Mechanics.

[8] Dawicke, D. S., Sutton, M. A., Newman, J. C., Jr., and Bigelow, C. A., "Measurement and Analysis of Critical CTOA for an Aluminum Alloy Sheet", NASA-TM-109024, September 1993, also accepted for publication in Fracture Mechanics: Twenty-Fifth National Symposium, ASTM STP 1220.

[9] Newman, J. C., Jr., Dawicke, D. S., and Bigelow, C. A., "Finite-Element Analysis and Measurement of CTOA During Stable Tearing in a Thin-Sheet Aluminum Alloy," Proceedings from the International Workshop on Structural Integrity of Aging Airplanes, April 1992, pp. 167-186.

[10] Grover, H. J., Hyler, W. S., and Howell, F. M., "Axial-Load Fatigue Properties of 245-T and 755-T Aluminum Alloy as Determined in Several Locations," NACA-TN-2928, 1953.

[11] Sutton, M.A., Bruck, H.A., Chae, T.L., and Turner, J.L., "Experimental Investigations of Three-Dimensional Effects Near a Crack Tip Using Computer Vision," International Journal of Fracture, Vol. 53, 1991, pp. 201-228.

[12] Sutton, M.A., Bruck, H.A., and McNeill, S.R., "Determination of Deformations Using Digital Correlation with the Newton Raphson Method for Partial Differential Correction," Experimental Mechanics, Vol. 29 (3), 1989, pp. 261-267.

[13] Sutton, M.A., Turner, J.L., Chae, T.L., and Bruck, H.A., "Development of a Computer Vision Methodology for the Analysis of Surface Deformation in Magnified Image," ASTM STP 1094, MICON 90. 1990, pp. 109-132.

[14] Sutton, M.A., Turner, J.L., Bruck, H.A., and Chae, T.L., "Full-Field Representation of the Discretely Sampled Surface Deformation for Displacement and Strain Analysis," Experimental Mechanics, Vol. 31 (2), 1991, pp. 168-177.

[15] Sutton, M.A. and McNeill, S.R., "The Effects of Subpixel Image Restoration on Digital Correlation Error Estimates," Optical Engineering, Vol. 27 (3), 1988, pp. 163-175.

[16] Newman, J. C., Jr., "Finite-Element Analysis of Fatigue Crack Propagation--Including the Effects of Crack Closure," Ph.D. Thesis, VPI & State University, Blacksburg, VA, May 1974.

[17] Zienkiewicz, O. C., Valliappan, S., and King, I. P., "Elasto-Plastic Solutions of Engineering Problems, Initial Stress, Finite Element Approach," International Journal of Numerical Methods in Engineering, Vol. 1, 1969, pp. 75-100.

Byron E. Amstutz[1], Michael A. Sutton[2], David S. Dawicke[3] and James C. Newman[4]

AN EXPERIMENTAL STUDY OF CTOD FOR MODE I/MODE II STABLE CRACK GROWTH IN THIN 2024-T3 ALUMINUM SPECIMENS

REFERENCE: Amstutz, B. E., Sutton, M. A., Dawicke, D. S., and Newman, J. C., **"An Experimental Study of CTOD for Mode I/Mode II Stable Crack Growth in Thin 2024-T3 Aluminum Specimens,"** Fracture Mechanics: 26th Volume, ASTM STP 1256, Walter G. Reuter, John H. Underwood, and James C. Newman, Jr., Eds., American Society for Testing and Materials, Philadelphia, 1995.

ABSTRACT: An experimental study of crack tip opening displacement (CTOD) for Mode I/Mode II stable crack growth in thin sheet 2024-T3 aluminum has been conducted. To perform the experiments, an Arcan specimen and fixture was modified so that (1) slippage in the grips was eliminated, (2) large rotations of the fixture components were achievable and (3) bending stresses were minimized. Defining Θ to be the angle between the Mode I loading direction (perpendicular to the crack line) and the direction of applied loading, experimental results indicate that (a) for large amounts of crack extension, $a \geq 10$ mm, the value of CTOD at 1 mm behind the crack tip appears to approach a constant value of 0.1 mm for all modes of loading, (b) the direction of crack extension varied with applied mixed mode loading, (c) Mode I crack extension is predominant for $0° \leq \Theta \leq 60°$, (d) Mode II crack extension is predominant for $75° \leq \Theta \leq 90°$ and (e) a transition zone exists for angles Θ near 75°.

KEYWORDS: Mode I/II, stable crack growth, cracks, CTOD, aluminum alloy, fracture

[1] Graduate Student, Mechanical Engineering Department, University of South Carolina, Columbia, SC 29208

[2] Professor, Mechanical Engineering Department, University of South Carolina, Columbia, SC 29208

[3] Senior Research Scientist, AS&M, Hampton, VA 23666

[4] Senior Research Scientist, NASA-Langley Research Center, Hampton, VA 23681

Copyright © 1995 by ASTM International www.astm.org

INTRODUCTION

Aging of the commercial aircraft fleet, particularly the increased potential for multi-site damage, has heightened the need for methods to predict the residual strength of aircraft components[1,2]. In an effort to develop an experimentally verifiable methodology for stable crack extension predictions, a variety of fracture criteria have been investigated. However, since stable crack extension occurs in most aircraft fuselage structures prior to collapse, primary emphasis has been placed on deformation-based fracture criteria. This is consistent with the work of Orowan[3] who noted that although a stress-based fracture criterion for ductile fracture is unlikely to be useful, a deformation-based fracture criterion is more plausible.

Early work for Mode I crack extension by Wells[4-6], Rice[7], Kanninen[8,9] and Shih[10] gave credence to the use of crack-tip-opening-displacement (CTOD) or crack-tip-opening-angle (CTOA) as a plausible fracture parameter for ductile materials. Recent work by Newman, et. al.[11-13] has shown that, under Mode I loading, stable crack extension in thin sheets and plates can be accurately predicted using a critical CTOA or, equivalently, a critical CTOD. Recent work by Dawicke, et. al.[14,15] has confirmed the validity of a CTOA or CTOD criterion for thin aluminum alloy sheets and indicated that initial crack extension of about the sheet thickness is strongly affected by local three-dimensional transient effects. After about one thickness of stable crack extension, the critical CTOA, strain fields and crack tunnelling behavior (the difference between crack extension on the surface and in the center of the specimen) tend to stabilize and are relatively invariant during additional crack extension. Dawicke, et. al.[16] recently demonstrated that a critical CTOA/CTOD can be used to predict the residual strength of thin aluminum sheets exhibiting multi-site damage.

Though stable crack extension under nominally Mode I conditions has received considerable attention, it should be noted that in an aircraft fuselage the presence of stiffeners, rivets and other constraining members may introduce a state of stress in the crack tip region that is not purely Mode I. Even if stiffeners are not present, internal pressure will induce "crack pillowing", which is interpreted as a combination of Mode I/Mode III in the crack tip region.

Relative to Mode I/Mode II stable crack extension, some work has been done using energy concepts, with the primary emphasis on the J-integral and its effectiveness as a fracture parameter in mixed mode initiation and crack extension. Cotterell, Lee and Mai[17] used a staggered, deep edge notched tension specimen originally suggested by Hill[18] to perform mixed mode, stable crack extension experiments. They separated the J-integral into Mode I (J_{Ip}) and Mode II (J_{IIp}) components. From their work, they concluded that J_{Ip} and J_{IIp} are strong functions of the mode of loading. In addition, recent work by Tohgo, et. al.[19] led to the development of a single edge cracked bending specimen with the crack offset into a region of non-zero shear force. Though their work on the aluminum alloy 6061-T651 concentrated primarily on the initiation phase for cracks, their work clearly indicated that the total J integral during crack growth is a strong function of the mode of loading, being largest for the pure shear case.

In the present paper, experimental measurements of CTOD in aluminum 2024-T3 during stable crack growth utilizing a modified Arcan fixture under nominally Mode

I and Mode II loading conditions are presented. Results for mixed mode loading are compared to Mode I results.

EXPERIMENTAL APPROACH

Test Fixture and Specimen Geometry

As described previously, there are several methods one may adopt to obtain a mixed mode loading condition. In this work, the Arcan[20] test fixture (originally used to obtain mixed mode loading for specimens undergoing predominantly elastic deformations) was adopted. Figure 1 shows the dimensions of the modified Arcan fixture. To ensure that the Arcan fixture could accommodate the large-scale deformations anticipated during stable crack extension, several baseline tests of the Arcan fixture with uncracked specimens were completed. Strain gage rosettes were mounted on each side of the specimen in the test section and the specimen loaded beyond yielding to quantify the effect of out-of-plane bending. Results from these tests indicated that several modifications to the original fixture and specimen geometry were necessary. The modifications included (a) enlarging the slots between the two halves of the fixture to 15.9 mm to allow for larger rotations, (b) addition of symmetric, 2.4 mm diameter, hardened drill-rod inserts placed in grooves in the grip region to reduce slippage and increase grip fixity, (c) machining of several precision spacers for the grip region to allow specimens from 1 mm to 2.5 mm in thickness (B) to be tested without introducing bending, (d) increasing the specimen notch radius to enlarge the size of the "test section" and (e) use of specimens that had an additional 25 mm end tab on each end to simplify the fatigue precracking process (the end tabs were removed from the specimens by machining prior to mixed mode testing).

Material and Crack Geometry

All tests were performed on B = 2.3 mm thick, bare 2024-T3 aluminum alloy sheet material in the L-T orientation (Mode I fatigue precracking load was applied in the rolling or longitudinal direction, with the crack perpendicular to the rolling direction). Figure 2 shows a typical fatigue precracked specimen. Figure 3 shows the dimensions on the modified Arcan specimen. Each specimen was initially notched on one side using a jeweler's saw. The notched specimen was fatigue precracked under Mode I at a nominal stress level ($\Delta S = P/(2.67WB) \approx 18$ MPa; $S_{min}/S_{max} \approx 0.1$) to initiate a sharp fatigue crack at the notch tip. The total length of the sawcut and fatigue crack is $a \approx 6.4$ mm; initial a/w for all cases was 1/6.

Test Procedure

A total of four different Mode I/Mode II configurations were tested using the modified Arcan fixture (see Figure 1), with data being obtained for $\Theta = 15°$ (predominantly tension with some shear), 45° (equal amounts of tension and shear), 75° (predominantly shear with some tension) and 90° (pure shear). Mode I ($\Theta = 0°$) tests were not performed with the Arcan fixture since several Mode I tests were completed

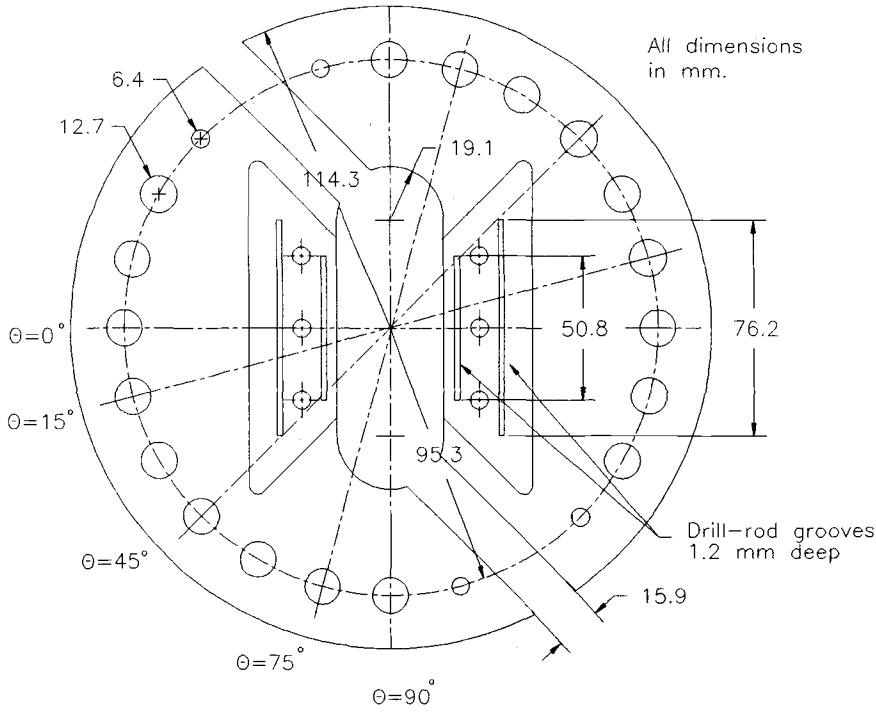


Figure 1 -- Schematic of modified Arcan fixture showing loading angles

previously[14,15] using compact tension (C(T)) and middle crack tension (M(T)) specimen geometries and a large amount of CTOD data has been obtained for these cases. For both C(T) and M(T) specimens, the Mode I CTOD during stable crack extension is roughly constant at 0.1 mm for large amounts of crack extension ($\Delta a \geq 10$ mm), with a scatter band of $\pm$ 0.02 mm.

Each test was performed using crosshead displacement control, with both the load and grip point displacements monitored. After fatigue precracking, and prior to mounting the specimen in the Arcan fixture, one side of the specimen was lightly spray painted with white acrylic paint. A black powder was misted onto the painted surface and baked in place on the surface in a random pattern. The baking was performed at approximately 100° C and lasted for 25 minutes. A test specimen with random pattern is shown in Figure 4. At several load values during the test, the random pattern was digitally recorded by a charge-coupled device (CCD) digital camera system. These images were later analyzed by a digital image correlation technique[14-16] to obtain CTOD at a specific location behind the current crack tip.

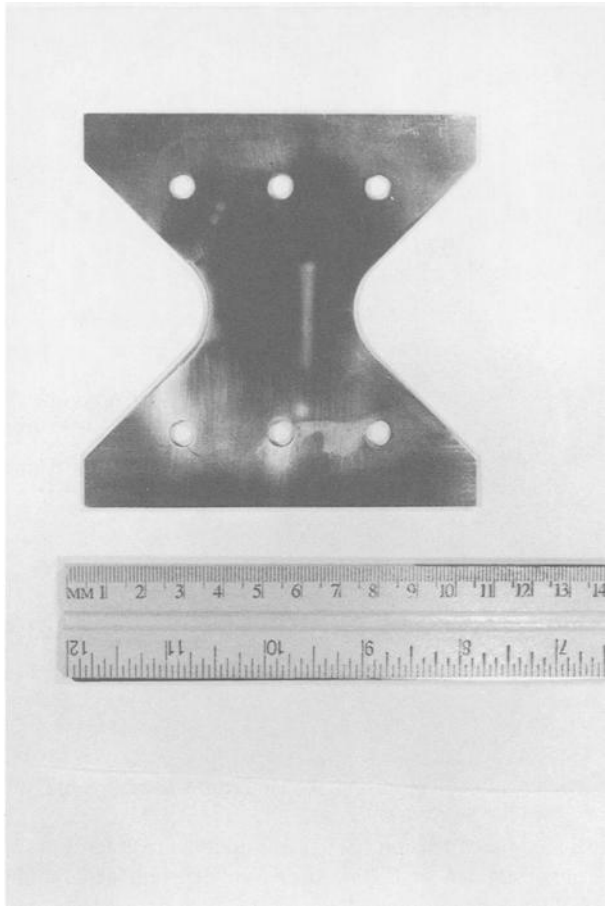


Figure 2 -- Arcan specimen with fatigue precrack

For Θ = 15°, 75° and 90°, single specimen fracture tests were conducted. Each test continued until (a) the two components of the modified Arcan fixtures incurred large rotations and made contact or (b) the crack passed the centerline of the specimen (the component of stable tearing in the direction of the initial fatigue precrack was approximately 14 mm). In most cases, termination of the test occurred for 14 mm $\leq \Delta a \leq$ 20 mm, with the crack passing the centerline of the specimen. For Θ = 45°, the fracture tests continued until the crack grew beyond the test section and approached the Arcan fixture; this occurred for $\Delta a \approx$ 14 mm.

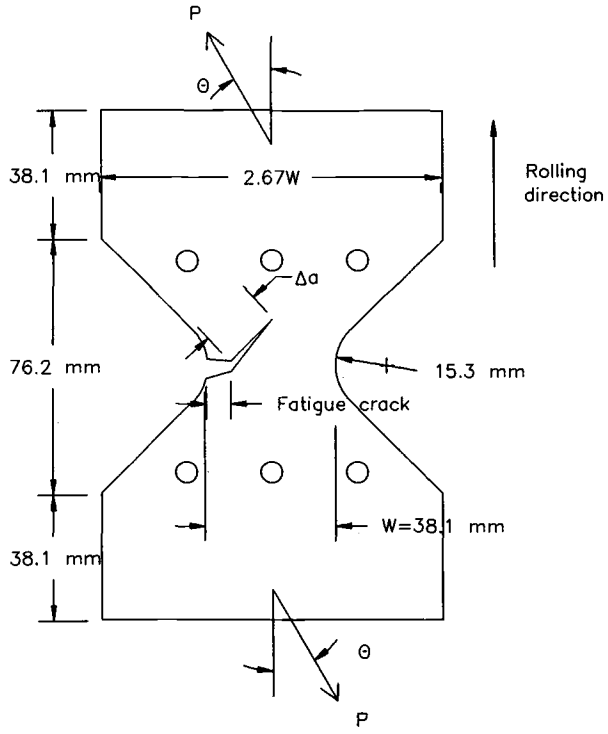


Figure 3 -- Arcan specimen showing loading angle and crack orientation

Image Analysis to Determine CTOD

Images were analyzed using digital image correlation procedures outlined previously[14] for Mode I. In short, a small subset of an "undeformed" image is correlated with a "deformed" image. This correlation yields the displacement of the subset between two different images. Typical transverse magnification (ratio of pixels in an image to length on the specimen in mm) used in this work was 95 pixels/mm and the region imaged was approximately 5 mm x 5 mm. In this work, the relative displacements from three pairs of subsets were computed. Each pair of points contained one position below and one position above the crack line, with the position above the crack line defined as the reference. The relative displacements from the three pairs of subsets were averaged to determine CTOD at the specified distance behind the crack tip. For $\Delta a < 1$ mm, the positions of the subsets were just behind the original crack tip. These subsets were used to obtain CTOD until $\Delta a = 1$ mm. For $\Delta a > 1$ mm, the subsets were located approximately 1 mm behind the current crack tip. Figure 5a shows a schematic of the measured CTOD. The displacement vector can be expressed in equation form:

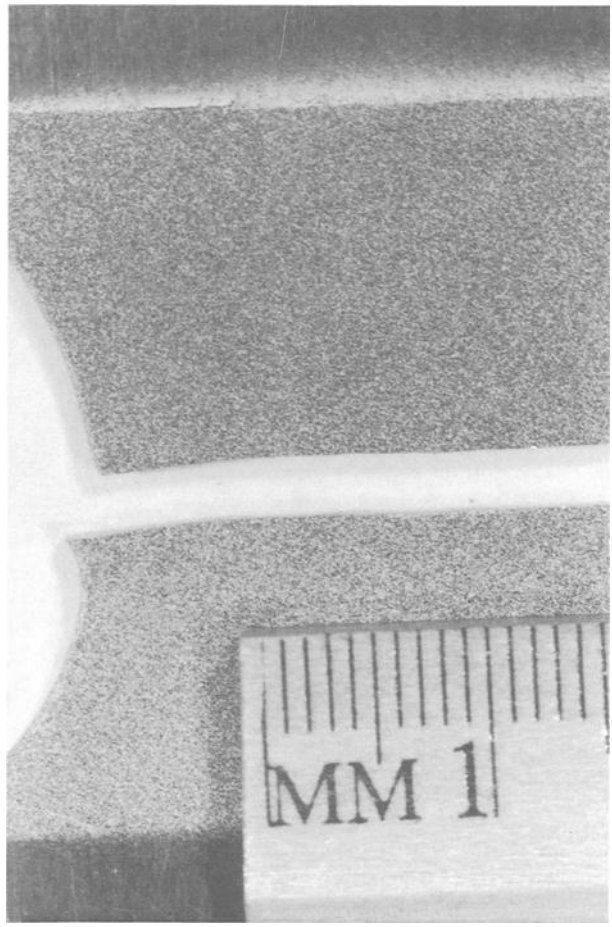


Figure 4 -- Random speckle pattern on test specimen

$$\left(CTOD_{\parallel},\ CTOD_{\perp} \right)_i = \left(\left(d_{\parallel}(B) - d_{\parallel}(A)\right), \left(d_{\perp}(B) - d_{\perp}(A)\right) \right)_i \qquad (1)$$

$$CTOD_i = \sqrt{\left(CTOD_{\perp_i}\right)^2 + \left(CTOD_{\parallel_i}\right)^2} \qquad (2)$$

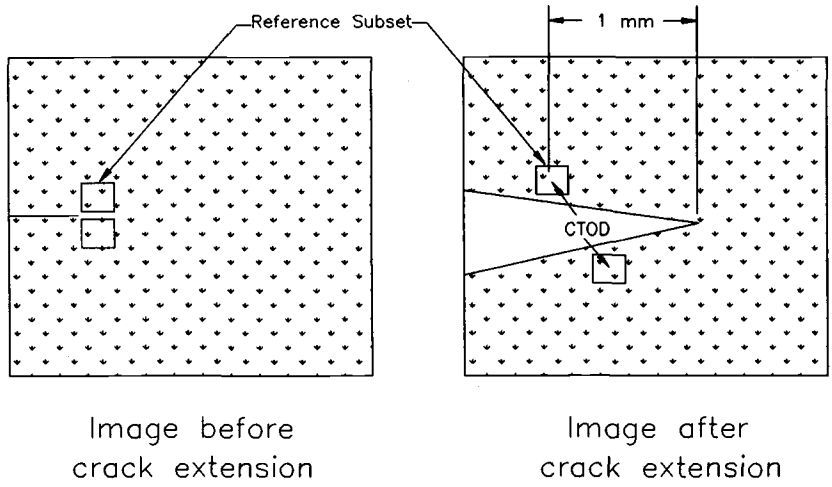


Figure 5a -- Schematic showing measured CTOD

$$CTOD = \frac{\sum_{i=1}^{i=N} CTOD_i}{N} \quad (3)$$

where:

B	=	subset below the crack line and behind the current crack tip
A	=	subset above the crack line and behind the current crack tip
$d_{\parallel}$	=	displacement parallel to the local crack extension direction
$d_{\perp}$	=	displacement perpendicular to the local crack extension direction
i	=	i^{th} pair of subsets
N	=	number of pairs of subsets used to estimate CTOD

The value for CTOD is obtained using both the perpendicular (Mode I) and parallel (Mode II) components of the relative displacement vector. Figure 5b defines the directions for positive displacement as well as two definitions of crack extension angle: a local angle, Ψ_l, and a global angle, Ψ_g. To determine Ψ_g, the current crack tip location and the original crack tip location are used to define a position vector, $\mathbf{r_g}$. To define Ψ_l, the current crack tip location in the preceding image and the preceding crack tip location in the preceding image are used to define a position vector, $\mathbf{r_l}$. These angles can be mathematically defined:

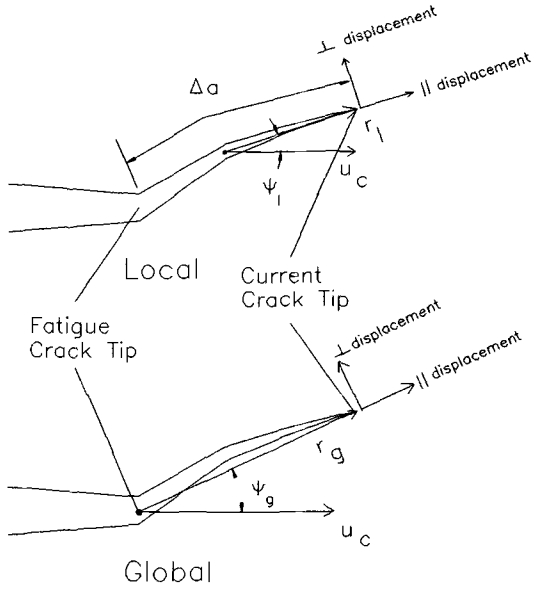


Figure 5b -- Definition of local and global angles of crack extension direction

$$\Psi_g = \arccos(\underline{u}_g \cdot \underline{u}_c) \quad (4)$$

$$\Psi_l = \arccos(\underline{u}_l \cdot \underline{u}_c) \quad (5)$$

where:

$\underline{u}_g$ = unit vector in the direction of $\underline{r}_g$
$\underline{u}_l$ = unit vector in the direction of $\underline{r}_l$
$\underline{u}_c$ = unit vector in the direction of the initial crack line

RESULTS AND DISCUSSION

Prior to discussing the results, it is conjectured that microstructural variability had an influence on the experimental CTOD data, increasing scatter and altering the relative displacements during fracture. For example, a few data points with large local angles were observed. Careful macroscopic inspection of the images indicated that the observed large angles coincided with a significant deviation in crack path, presumably around a microstructural feature. However, detailed microscopic studies were not performed to identify the local feature. Furthermore, crack kinking also changes the effective crack extension grain orientation and the fracture behavior of the Al 2024-T3[21].

Figure 6 presents the load-crack extension data for Θ = 15°, 45°, 75° and 90°.

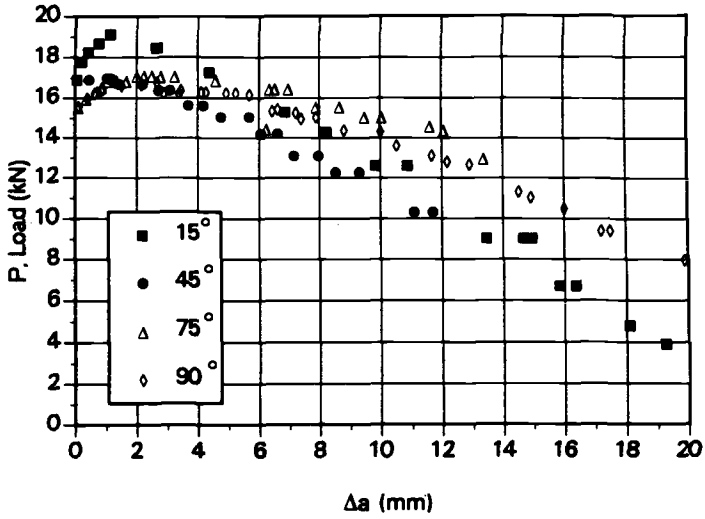


Figure 6 -- Load against crack extension for Arcan specimens

Initiation of crack extension requires slightly higher loadings for crack extension under predominantly Mode I loading. However, a crossover occurs at about 4 mm of crack extension and continued crack extension under predominantly Mode II loading requires slightly higher loads than for the Mode I case. The fact that large amounts of stable crack extension under Mode II dominant conditions requires larger loading is consistent with the observations of previous researchers[17,19]. One possible explanation for the initially higher loadings could be two competing slip planes for the tensile dominated case. The tensile component of the load tends to cause ductile failure along a through-thickness plane that is oriented at 45° to the applied load, whereas the shear component of the load tends to cause ductile failure along planes that are parallel to the shear load. The interaction of these two different slip planes may cause the initially higher loads.

Figure 7 presents both the local and global angles for the crack extension direction for Θ = 15°, 45°, 75° and 90°. The data indicates that the crack tended to grow in the direction of initial crack extension. Ψ_l and Ψ_g agreed closely in all cases for up to 15 mm of crack extension. After 15 mm of crack extension, crack curvature was observed in the 15° case; this is reflected in the observed differences between Ψ_l and Ψ_g. The change in crack direction after substantial crack extension is most likely due to a change in the stress/strain field in the crack tip region, introducing changes in the specimen configuration. Detailed finite element analyses and experimental strain measurements in the crack tip vicinity will be required to assist in understanding the fracture process.

Figure 8 presents plots of $d_\perp$ and $d_\parallel$ for Θ = 15°, 45°, 75° and 90°, where Ψ_l was used to decompose the relative displacement into components. Because the local angle changes as the crack grows, the perpendicular and parallel displacements are in the same directions relative to the crack tip. Similar trends were observed by using Ψ_g. Figure 8 demonstrates that for $0° \leq \Theta \leq 45°$, the local relative displacements are

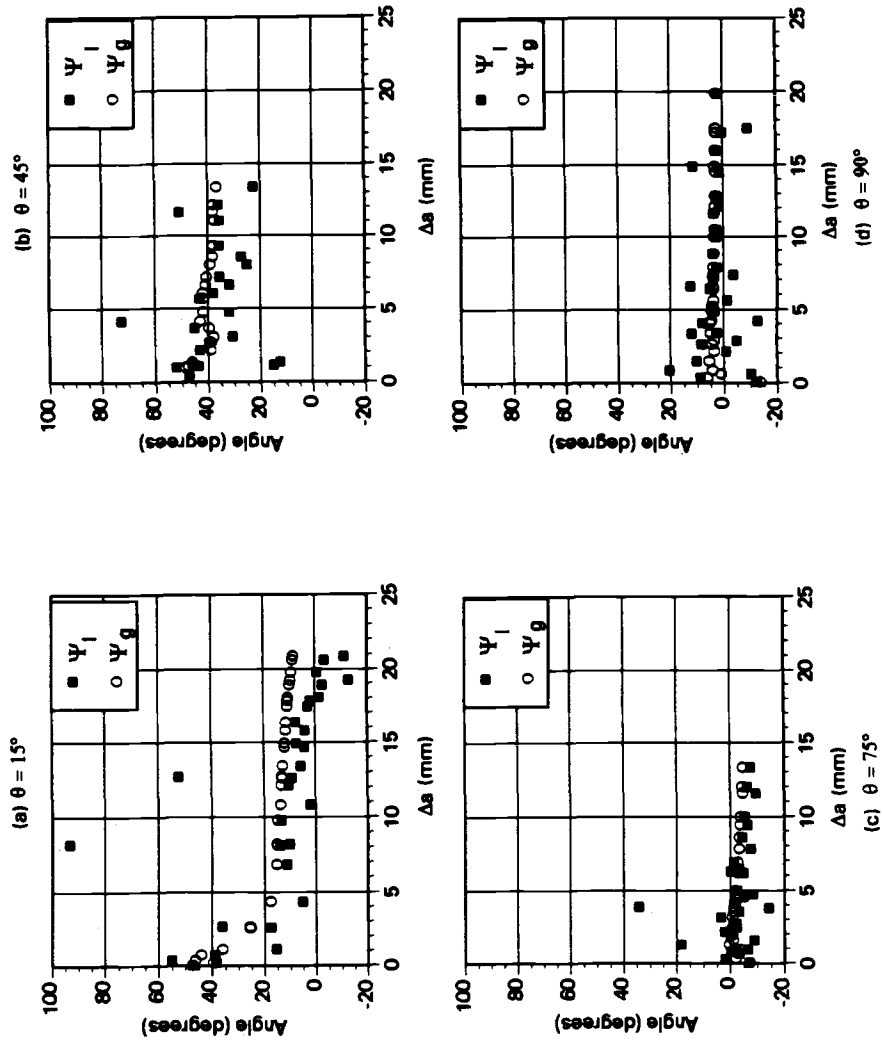


Figure 7 -- Ψ_I and Ψ_θ against Δa for various modes of applied loading

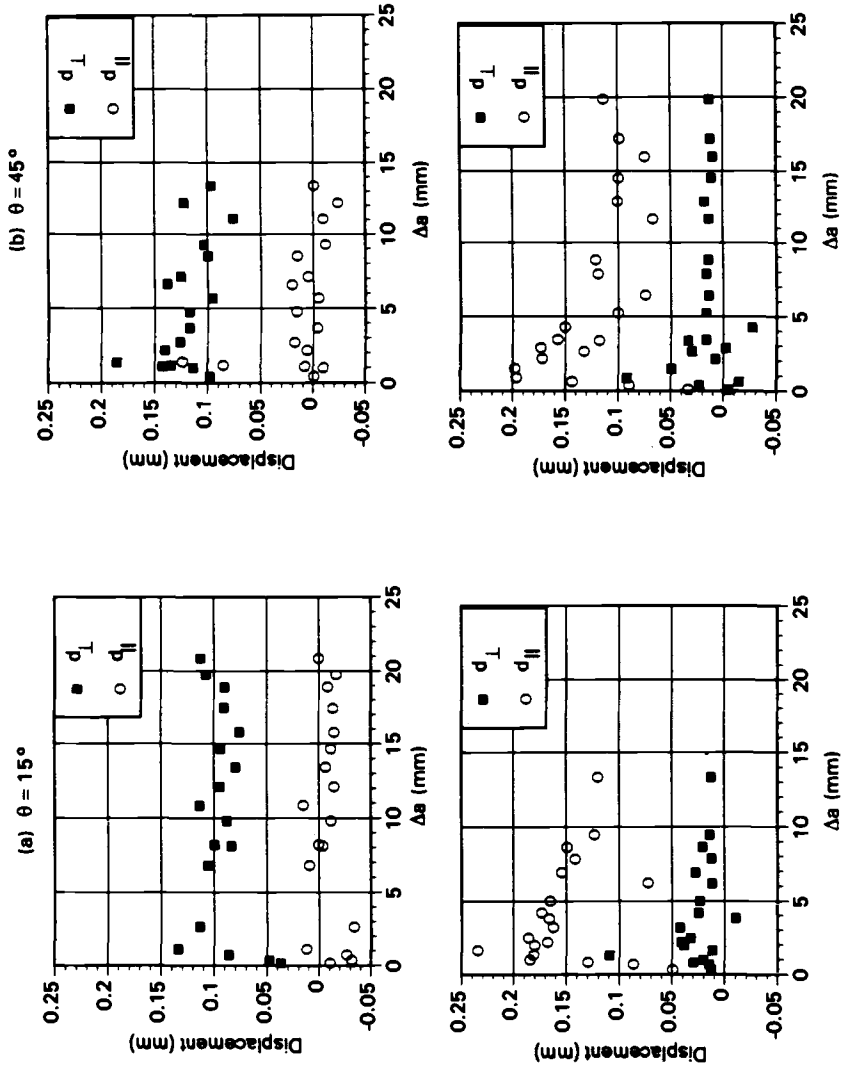


Figure 8 -- $d_{\perp}$ and $d_{\parallel}$ against Δa for various modes of applied loading for local angles

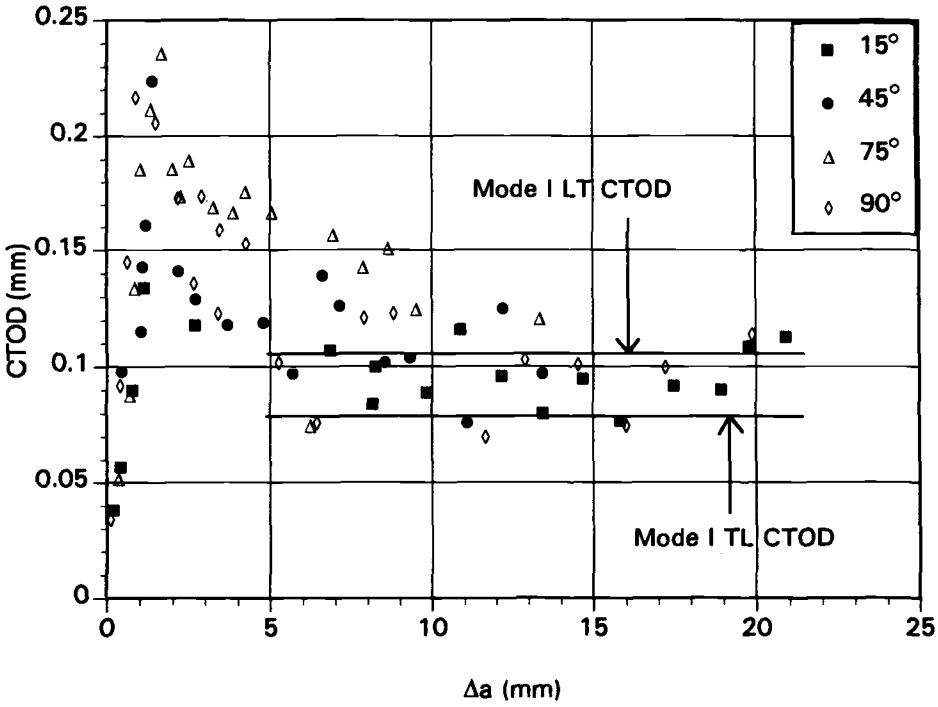


Figure 9 -- CTOD against Δa for Mode I and mixed mode loading

perpendicular to the crack line, indicating Mode I dominated crack extension. However, for $75° \leq \Theta \leq 90°$, the local relative displacements are parallel to the crack line, indicating Mode II dominated crack extension. The results indicate that for mixed mode loading from $60° < \Theta < 90°$, there is a transition in the local relative crack tip displacements between Mode I and Mode II. Additional tests are needed to further define the transition zone. It is noted that, occasionally, very small negative perpendicular relative displacements are measured in the shear dominated experiments. These measurements are an artifact of the measurement method used to convert the subset displacements into CTOD. Since small, but finite, subsets are used to estimate the displacements on the crack line, the subsets will undergo large shear deformations and, potentially, compressive loads due to the interaction of the uneven crack surfaces as the crack faces slide past each other. These effects result in a small negative displacement.

Figure 9 presents CTOD data obtained for $\Theta = 15°$, 45°, 75° and 90°; the CTOD data was generated using Eqs. (1) - (3). In addition, horizontal lines representing the average CTOD value obtained from several Mode I C(T) and M(T) tests ($\Theta = 0°$) for both the LT and TL grain orientation are included in Figure 9[21]. Figure 9 suggests that (a) regardless of the type of global mixed mode loading, for $\Delta a > 10$ mm, all CTOD values approach a constant value of 0.1 mm which is approximately equal to the CTOD

value obtained from Mode I loading and (b) during the early stages of crack growth, a common transient behavior is observed for all mixed modes of loading--initially low values for CTOD, rising to a maximum CTOD for $\Delta a \approx 2$ mm and a decrease towards a constant value for larger Δa values. Most of the data falls between the CTOD lines for Mode I TL and LT crack growth, with the 0.02 mm scatter band for Mode I data enclosing the majority of the mixed mode results. Macroscopic inspection of the fracture surfaces has shown that crack extension changed from a flat growth condition to slant fracture for both $\Theta = 15°$ and 45°. This transition was complete after approximately 2 mm of crack extension. The mixed mode transient behavior in CTOD is quite similar to the roughly 2.3 mm transition observed in Mode I tests. Since a CTOA criterion at a fixed distance behind the crack tip is equivalent to a CTOD criterion, the similarity in these trends is expected. Only $\Theta = 75°$ requires more than 6 mm of crack growth to reach a constant CTOD value.

CONCLUSIONS

An experimental study of crack-tip-opening-displacement (CTOD) for Mode I/Mode II stable crack growth in thin sheet 2024-T3 aluminum has been conducted. A modified Arcan fixture was developed to ensure grip fixity, allow for larger specimen rotations and minimize bending stresses. Results from the experiments indicate that:

- The value of the CTOD approaches a constant value of 0.1 mm for all modes of loading for larger amounts of crack growth ($\Delta a > 10$ mm).
- The global angle, Ψ_g, of crack extension was constant until the crack crossed the specimen centerline.
- From $0° \leq \Theta \leq 45°$, crack extension was Mode I dominated.
- From $75° \leq \Theta \leq 90°$, crack extension was Mode II dominated.
- There is a transition between Mode I dominated crack extension and Mode II dominated crack extension for angles Θ near 75°.

ACKNOWLEDGMENTS

The support of NASA and Dr. C. E. Harris through NASA NAG-1-1489 is deeply appreciated. In addition, the authors wish to thank Mr. Edward Phillips, Dr. Robert Piascik and Mr. Richard Everett at NASA Langley Research Center for their technical advice and support. Also, the technical support and advice of Dr. Stephen R. McNeill and Mr. Jeffrey Helm at the University of South Carolina are gratefully acknowledged.

REFERENCES

1. Maclin, J.R., "Commercial Airplane Perspective on Multi Site Damage",

International Conference on Aging Aircraft and Structural Airworthiness (1991).
2. Harris, C.E., "NASA Aircraft Structural Integrity Program", NASA TM-102637 (1990).
3. Orowan, E., "Fracture and Strength of Solids", Report of Progress in Physics, 12, pp 185-233 (1949).
4. Wells, A.A., "Unstable Crack Propagation in Metals: Cleavage and Fast Fracture", Proceedings of the Cranfield Crack Propagation Symposium, 1, pp 210-230 (1961).
5. Wells, A.A., "Application of Fracture Mechanics at and Beyond General Yielding", British Welding Journal, 11, pp 563-570 (1961).
6. Wells, A.A., "Notched Bar Tests, Fracture Mechanics and Brittle Strengths of Welded Structures", British Welding Journal, 11, pp 2-13 (1963).
7. Rice, J.R. and Sorensen, E.P., "Continuing Crack-Tip Deformation and Fracture for Plane Strain Crack Growth in Elastic-Plastic Solids", Journal of Mechanics and Physics of Solids, 26, pp 163-186 (1978).
8. Kanninen, M.F., "The Analysis of Stable Crack Growth in Type 304 Stainless Steel", Proceedings of International Conference on Fracture, pp 1759-1768 (1980).
9. Kanninen, M.F., Popelar, C.H. and Broek, D., "A Critical Survey on the Application of Plastic Fracture Mechanics to Nuclear Pressure Vessels and Piping", Nuclear Engineering and Design, 67, pp 27-55 (1981).
10. Shih, C.F., "Studies on Crack Initiation and Stable Crack Growth", ASTM STP 668, pp 65 (1979).
11. Newman, J.C., "Finite Element Analysis of Crack Growth Under Monotonic and Cyclic Loading", ASTM STP 637, pp 56-80 (1977).
12. Newman, J.C., Dawicke, D.S. and Bigelow, C.A., "Finite Element Analyses and Fracture Simulation in Thin Sheet Aluminum Alloy", NASA TM-107662 (1992).
13. Newman, J.C., Dawicke, D.S., Sutton, M.A. and Bigelow, C.A., "A Fracture Criterion for Widespread Cracking in Thin-Sheet Aluminum Alloys", 17th Symposium of International Committee on Aeronautical Fatigue in Stockholm (1993).
14. Dawicke, D.S. and Sutton, M.A., "Crack Tip Opening Angle Measurements and Crack Tunneling Under Stable Tearing in Thin Sheet 2024-T3 Aluminum Alloy", NASA CR 191523 and to be published in Experimental Mechanics.
15. Dawicke, D.S., Sutton, M.A., Newman, J.C. and Bigelow, C.A., "Measurement and Analysis of Critical CTOA for an Aluminum Alloy Sheet", 25th National Symposium for ASTM (1993).
16. Dawicke, D.S., Newman, J.C., Sutton, M.A., and Amstutz, B. E., "The Influence of Crack History on the Stable Tearing Behavior of Thin-Sheet Materials with Multiple Cracks", to be published in Proceedings of FAA/NASA Symposium on Advanced Structural Integrity Methods for Airframe Durability and Damage Tolerance (1994).
17. Cotterell, B, Lee, E. and Mai, Y.W., "Mixed Mode Plane Stress Ductile Fracture", International Journal of Fracture, 20, pp 243-250 (1982).
18. Hill, R., "A New Method for Determining the Yield Criterion and Plastic Potential of Ductile Metals", Journal of Mechanics and Physics of Solids, 1, pp

271-276 (1953).

19. Tohgo, K. and Ishii, H., "Elastic Plastic Fracture Toughness Test Under Mixed Mode I-II Loading", Engineering Fracture Mechanics, 41(4), pp 529-540 (1992).
20. Arcan, M., Hashin, Z. and Voloshin, A., "A Method to Produce Uniform Plane-Stress States with Applications to Fiber-reinforced Materials", Experimental Mechanics, 18, pp 141-146 (1978).
21. Sutton, M. A., Dawicke, D. S., Newman, J. C., Jr. "Stable Tearing of This-Sheet 2024-T3 Aluminum Alloy in the L-T and T-L Orientations", Fracture Mechanics: 26th Volume, ASTM STP 1256, Walter G. Reuter, John H. Underwood and James C. Newman, Jr., Eds, American Society for Testing and Materials, Philadelphia, 1994.

Kenneth K. Yoon[1], Leonard B. Gross[1], C. Scott Wade[2] and W. Alan VanDerSluys[2]

EVALUATION OF DISK-SHAPED COMPACT SPECIMEN FOR DETERMINING J-R CURVES

REFERENCE: Yoon, K. K., Gross, L. B., Wade, C. S., and VanDerSluys, W. A., "**Evaluation of Disk-Shaped Specimen for Determining J-R Curves**," Fracture Mechanics: 26th Volume, ASTM STP 1256, Walter G. Reuter, John H. Underwood, and James C. Newman, Jr., Eds., American Society of Testing and Materials, Philadelphia, 1995.

ABSTRACT: A set of equations are developed for a disk-shaped compact (DC(T)) specimen to be used in conjunction with ASTM E 1152-87 standard which is for determining J-R curves using rectangular compact specimens. A slightly different disk-shaped tension specimen design (BWDC(T)) is used by B&W Owners Group in their Integrated Reactor Vessel Material Surveillance Program [1] (IRVSP). This specimen is analyzed by a finite element method to investigate whether the standard DC(T) compliance relationship is appropriate for use. Validation tests using both square C(T) and DC(T) specimens were performed and the resulting J-R curves are compared. It is concluded that using this procedure both C(T) and BWDC(T) specimens yield similar J-R curves.

KEY WORDS: fracture toughness, J-integral testing, disk-shaped specimen, disk-shaped compact specimen

The ASTM standard test method for determining J-R curves was revised in 1987 and the new standard was issued as E 1152-87. This standard is for testing rectangular compact tension and bend specimens. Disk-shaped tension (DC(T)) specimens have been used for determining J-R curves for many years. However, E 1152 does not include DC(T)s. The only reference in the ASTM standards relevant to DC(T) is a stress intensity factor equation found in ASTM E 399-83. Futato wrote a test procedure for DC(T)s in Babcock & Wilcox in 1984 based on the works of Newman [2] and Underwood [3]. A validation test was conducted to demonstrate that DC(T) specimen testing produces closely comparable J-R curves to those from standard C(T) testing in 1993.

[1]Advisory Engineers, B&W Nuclear Technologies, Lynchburg, VA 24506-0935.

[2]Section Manager and Scientist, respectively, Babcock & Wilcox, Alliance Research Center, 1562 Beeson St., Alliance, OH 44601.

Copyright© 1995 by ASTM International www.astm.org

This paper presents (1) a set of equations for disk-shaped tension specimen testing in the same format of E 1152-87, (2) a finite element analysis of a disk-shaped specimen to determine compliance of a slightly different disk-shaped tension specimen used in the B&W Owners Group IRVSP, and (3) the results of a validation testing to compare DC(T) with standard C(T) specimens for identical weld metal and the data analysis by the proposed equations and by current E-1152. The resulting J-R curves are compared.

DETERMINATION OF J-R CURVES USING STANDARD DISK-SHAPED COMPACT SPECIMEN

ASTM E 1152 can be directly used for disk-shaped specimen testing with some modifications to the following three equations, i.e., stress intensity factor, compliance, and crack length equations, to account for geometric differences in the specimen designs. The plastic component of J is assumed to be the same as the C(T) specimen and this assumption will be verified experimentally in a later section of the paper.

1. Stress Intensity Factor Equation

The equation for stress intensity factor for the standard C(T) specimen is given in equations 4 and 5 in E 1152 and shown below:

$$K_{(i)} = \frac{P}{(BB_N W)^{1/2}} f(a_i/W) \tag{1}$$

$$f(a/W) = \frac{[2+ a/W]\,[d_0 + d_1(a/W) + d_2(a/W)^2 + d_3(a/W)^3 + d_4(a/W)^4]}{(1 - a/W)^{3/2}} \tag{2}$$

where a - crack depth
W - specimen width
B - specimen thickness
B_N - specimen net thickness

All the coefficients for the C(T) specimen from E 1152 and those for the DC(T) from E 399 are listed in Table 1.

2. Compliance Equation

For test methods that do not utilize the elastic compliance techniques, the compliance, C_i, can be determined from a/W using the following compliance equation (equation 9 of E 1152): $C_i = (V_{LL}/P)_i$

and

TABLE 1--Coefficients for f(a/W) Equation

Coefficient	C(T)	DC(T)
d_o	0.886	0.677
d_1	4.64	4.277
d_2	-13.32	-10.317
d_3	14.72	10.184
d_4	- 5.60	-3.635

$$\frac{B_E E V_{LL}}{P} = \left[\frac{1 + a/W}{1 - a/W}\right]^2 \left[b_o + b_1(a/W) + b_2(a/W)^2 + b_3(a/W)^3 + b_4 (a/W)^4 + b_5(a/W)^5\right] \quad (3)$$

where $B_E = B - (B-B_N)^2/B$ - specimen effective thickness
E - Young's modulus
V_{LL} - load-line displacement
P - load

The coefficients in the above compliance equation are given in Table 2.

TABLE 2--Coefficients for Compliance Equation

Coefficient	C(T)	DC(T)
b_0	2.163	2.0462
b_1	12.219	9.6496
b_2	-20.065	-13.7346
b_3	-0.9925	6.1748
b_4	20.609	0
b_5	-9.9314	0

A slightly different form of equation (3) was derived by Underwood [3] based on the data generated by Newman using a boundary collocation technique. Table 3 shows the Underwood/Newman data points and the calibration equation. To be compatible with E 1152, these data were refit in this paper and the resulting coefficients are listed in Table 2. These data points and a curve predicted by equation (3) were plotted in Figure 1, which shows excellent agreement in the range of a/W from 0.2 to 0.8.

3. Crack Length Equation

E 1152 provides the following equation for crack length as a function of load-line displacement [4] (equation 16 of E 1152):

TABLE 3--Stress Intensity Factor and Displacement for Disk-Shaped Specimen [3]

a/W	Yk[1]	$KB^{1/2}/P$	Yd[2]	$V_{LL}EB/P$
0.2000	2.9518	4.1252	4.9950	7.8046
0.2500	3.1475	4.8460	5.7848	10.2842
0.3000	3.2967	5.6291	6.5551	13.3777
0.3500	3.4082	6.5036	7.3067	17.2938
0.4000	3.4903	7.5098	8.0405	22.3347
0.4500	3.5508	8.7053	8.7575	28.9505
0.5000	3.5969	10.1735	9.4588	37.8350
0.5500	3.6347	12.0406	10.1451	50.0992
0.6000	3.6694	14.5046	10.8175	67.6095
0.6500	3.7050	17.8931	11.4770	93.6896
0.7000	3.7440	22.7855	12.1244	134.7157
0.7500	3.7877	30.3016	12.7608	204.1725

[1] $Yk = (KBW^{1/2}/P)\ (1 - a/W)^{3/2}$

[2] $Yd = (V_{LL}EB/P)\ (1 - a/W)^2$
$= 1.62 + 17.80\ (a/W) - 4.88\ (a/W)^2 + 1.27\ (a/W)^3$

$$a/W = g_o + g_1(U_{LL}) + g_2(U_{LL})^2 + g_3(U_{LL})^3 + g_4(U_{LL})^4 + g_5(U_{LL})^5 \quad (4)$$

where the coefficients are given in Table 4 and V_{LL}/P is elastic compliance on an unloading/reloading sequence.

The load-line compliance calibration equation for the DC(T) specimen was developed using the compliance data from Reference 3. Equation (4) with the coefficients listed in Table 4 is used to calculate crack length.

Using the new sets of coefficients listed in Tables 1, 2 and 4, E 1152 can be directly used to determine J-R curves for DC(T) specimens. It is assumed that the plastic component of J for DC(T) specimens is the same as that of C(T) specimens. Validity of this assumption is verified by a comparison of J-R curves from the validation tests in the later part of this paper.

TABLE 4--Coefficients for Crack Length Equation

Coefficients	C(T)	DC(T)
g_0	1.000196	.9982
g_1	-4.06319	-3.881
g_2	11.242	0.1871
g_3	-106.043	20.371
g_4	464.335	-45.213
g_5	-650.677	44.527

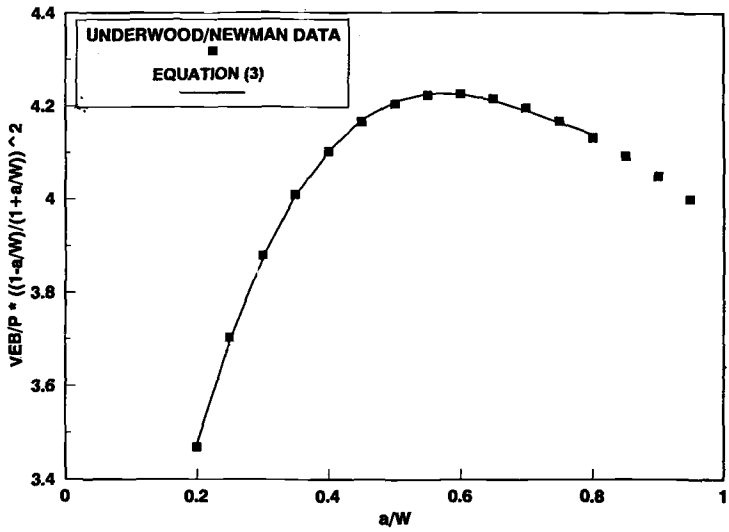


FIG. 1-- Compliance Equation vs. Underwood/Newman Data

COMPARISON BETWEEN STANDARD DC(T) AND BWDC(T) SPECIMENS

In the B&W Owners Group IRVSP, disk-shaped specimens close to 2 inches in diameter were fabricated from various weld metals to monitor fracture toughness changes with increased neutron radiation. The geometry of this disk-shaped specimen (BWDC(T)) differs slightly from the standard DC(T) specimen used in Reference 3 as shown in Figure 2. A finite element analysis was performed using the ABAQUS computer code to investigate how much deviation this modified DC(T) will have. Figure 2 shows the design for the "standard" DC(T) specimen used by Newman and the BWDC(T) specimen used by the B&W Owners Group. Since the thickness of the BWDC(T) specimen is 0.936 inches (23.77 mm), the specimen is referred to

as a "0.936T DC(T)" specimen or simply "BWDC(T)" in this paper. The purpose of this analysis was to verify by finite element analysis the appropriateness of using the compliance relationships for the standard DC(T) to the BWDC(T) specimen. Although the BWDC(T) specimen has a large crack mouth opening to accommodate a displacement gage at the load-line, the two specimens are actually quite similar, as the comparison of parametric ratios in Table 5 shows:

TABLE 5--Dimensional Parametric Ratio

Parametric Ratios	DC(T)	BWDC(T)
L/W	0.325	0.334
D/W	1.350	1.332
d/W	0.275	0.276
R/W	0.125	0.125

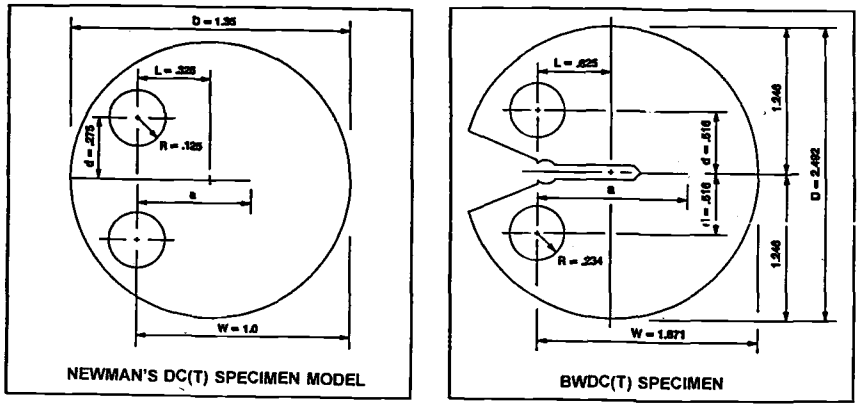


FIG. 2-- Disk-shaped Specimens

Finite Element Analysis of BWDC(T) Specimen

ABAQUS was used to model the BWDC(T) specimen shown in Fig. 2. Fig. 3 is a plot of the symmetric two-dimensional plane stress model. A Young's modulus of 189,260 MPa (27,450 ksi) and Poisson's ratio of 0.3 were used. The model was used in a linear elastic finite element analysis to determine applied loads, load-line displacements and stress intensity factors corresponding to various crack length extensions. Loads were applied indirectly by imposing vertical displacements at the center of the loading spider and obtaining load point reaction forces from the solution. The center of the loading spider was held fixed in the horizontal direction. Crack length, in terms of a/W, was varied from 0.617 to 0.845 by specifying zero vertical

displacement along the remaining ligament. Boundary conditions for the initial crack length, a/W = 0.617, are shown in Fig. 3. Load-line results of the finite element analysis, presented in Table 6, are based on the effective thickness, B_E, of 22.76 mm (0.896 in.).

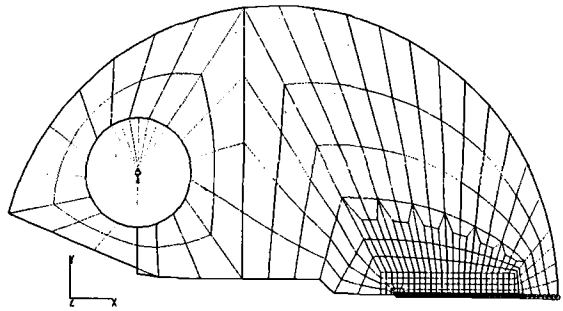


FIG. 3-- Finite Element Model of BWDC(T) Specimen

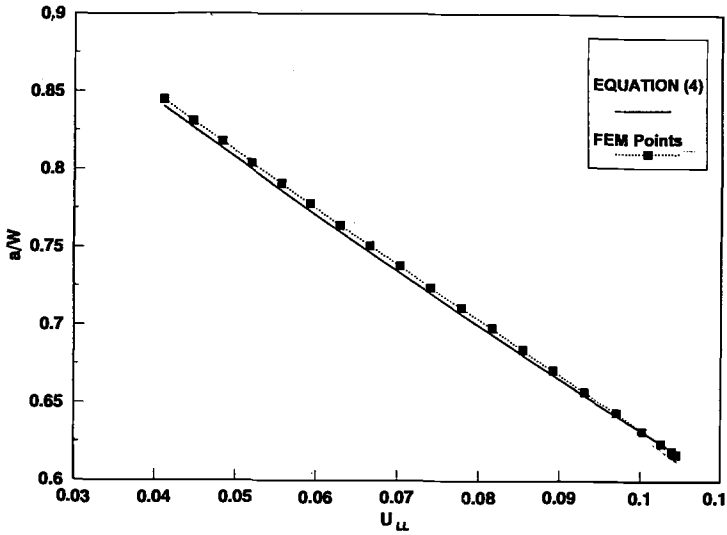


FIG. 4-- a/W vs. Load-line Displacement

Compliance relationships are presented graphically in Figures 4 and 5, for both DC(T) and BWDC(T) specimens. In Figure 4, the curves for a/W differ by less than 1% between the two specimen geometries, while in Figure 5, the curves for compliance show a maximum difference of only 6% at the greatest crack length (a/W = 0.845). Figures 4 and 5 confirm that

TABLE 6--Finite Element Results for BWDC(T) Specimen

Crack Depth a/W	Compliance	Displace. U_{LL}	K ksi$\sqrt{in}$	K MPa$\sqrt{m}$
0.617	73.46	0.1045	23.4	25.7
0.632	80.59	0.1002	89.7	98.5
0.671	104.21	0.0892	132.4	145.5
0.711	140.48	0.0778	144.3	158.6
0.751	196.41	0.0666	157.4	173.0
0.791	288.78	0.0556	181.8	199.8
0.831	456.51	0.0447	210.1	230.9
0.845	543.73	0.0411	217.5	239.0

the polynomial compliance expressions for a standard DC(T) specimen may be used for the BWDC(T) specimen with little loss in accuracy. A normalized curve for stress intensity factor is shown on Figure 6, where $KB_E\sqrt{W}/P$ is plotted against the normalized crack length, a/W. This plot shows that the stress intensity factor equation for DC(T) predicts approximately 2% higher than the finite element analysis results for BWDC(T) so it is concluded the test procedure for the DC(T) specimens can also be used for the modified design used by B&W Owners Group.

VALIDATION BY J-TESTS

BWDC(T) specimen compliance has been shown to be very close to that of DC(T) specimens. Therefore, BWDC(T) is a valid specimen design to generate J-R curves. To conclusively demonstrate the specimen's validity, a comparative test program was performed. Standard rectangular C(T) and BWDC(T) specimens were fabricated from the same material, stress-relief annealed to the same temperatures and times, and tested in the same facility. The results of these tests are presented below.

Test Specimens

The specimens were fabricated from weld metal WF-209-1. WF-209-1 is a Babcock & Wilcox designation for a particular run of deposited weld metal using a copper-coated Mn-Mo-Ni steel consumable wire and Linde 80 (neutral) flux. This material is typical of the reactor vessel weld materials of interest to the B&W Owners Group. The material was stress-relief annealed at 607 $\pm$ 14 C(1125 $\pm$ 25 F) for 30 and 40 hours. The standard specimens, 1T C(T), have an a/W ratio of approximately 0.55 after fatigue precracking. All standard specimens were

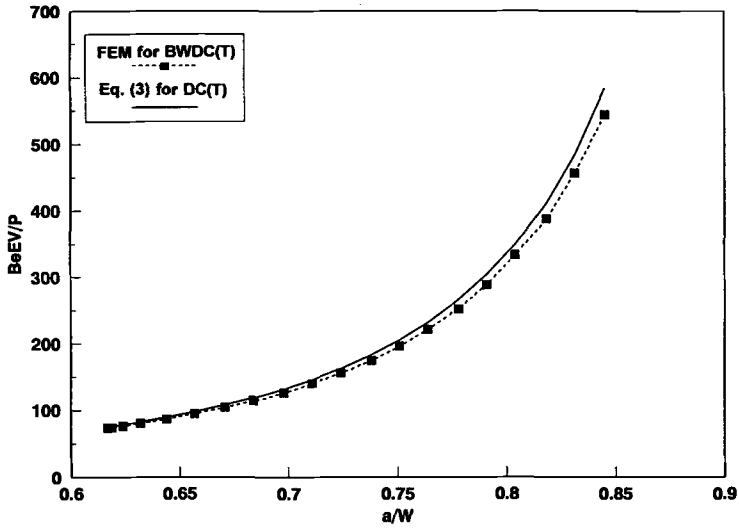


FIG. 5-- DC(T) Compliance Equation vs. BWDC(T) Finite Element Points

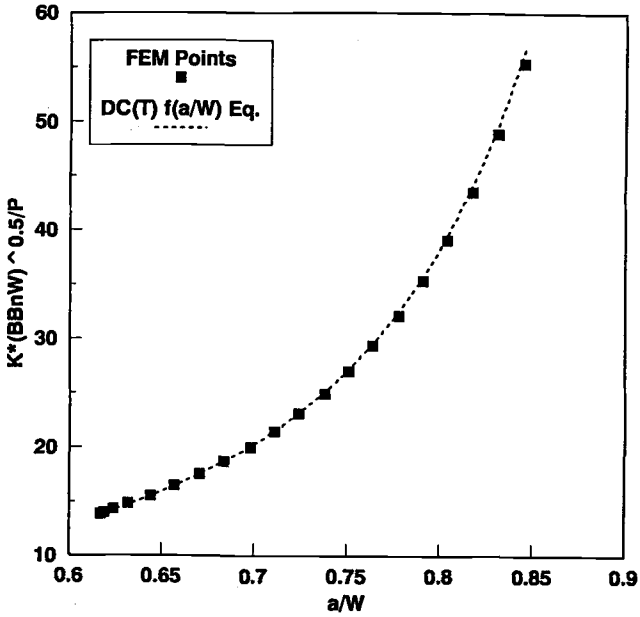


FIG. 6-- Normalized Stress Intensity Factor vs. Crack Size (a/W)

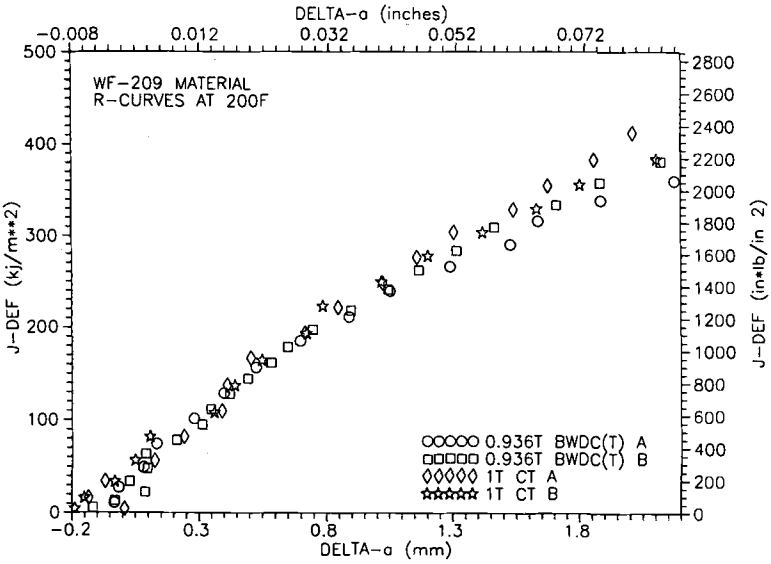


FIG. 7--J-R Curves for WF-209-1 at 200F

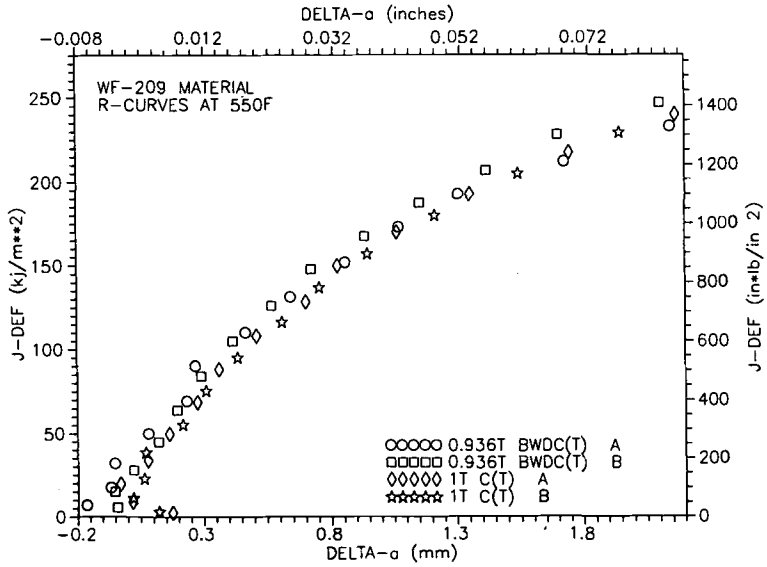


FIG. 8--J-R Curves for WF-209-1 at 550F

precracked and side-grooved to a depth of 20% (10% on each side). The BWDC(T) specimens (0.936T) have an a/W ratio of approximately 0.53 after fatigue precracking. All round specimens were precracked and side-grooved to a depth of 20% (10% on each side).

Test Results

J-R curves were obtained by testing round and standard compact fracture specimens of WF-209-1 weld metal that was stress-relieved for 30 and 40 hours. Specimens were tested at two temperatures, 93 C (200 F) and 288 C (550 F). The J-R curves plotted in Figure 7 represent testing done at 200F and show J values exceeding 2000 lb-in/in^2 at crack extension of 0.8 inch. In this figure there is approximately 9% difference between the two J-R curves of the same type of specimens and between the J-R curves of the two types of specimens. The J-R curves of the C(T) specemens are above the BWDC(T) specimens. There is a silimalr result shown in Figure 8 with the data from the 550F testing. In this case in the early portion of the J-R curve the C(T) results are below the BWDC(T) results. The C(T) results go above the BWDC(T) results at a J level of about 1500 lb-in/in^2. These deviations are within the expected variance between J-R curves developed in duplicate tests. The interlaboratory test results cited in E1152 and E813 showed a 10% variation in J values for C(T) specimens. There is little apparent difference that can be attributed to specimen type. From these J-R curves, it is evident that both specimen tests analyzed according to E 1152 and the currently proposed equations in this paper resulted in closely comparable J-R curves.

CONCLUSIONS

1. Three sets of coefficients for compliance, crack length and stress intensity factor equations are provided. These enable direct use of ASTM E 1152 for disk-shaped tension specimens to determine J-R curves. It is recommended that these sets be added to E 1152 for disk-shaped specimen testing.
2. A finite element analysis was used to investigate whether compliance relationships derived for the standard ASTM DC(T) specimen are appropriate for use with the BWDC(T) specimen. It was shown that compliances for the standard specimen are within 6% of those for the BWDC(T) specimen. This confirms that the compliance equations for a standard DC(T) specimen may be used to reduce fracture toughness data for the BWDC(T) specimen with little loss in accuracy.
3. J-R curves were obtained by testing round and standard compact fracture specimens of WF-209-1 weld metal that was stress-relieved for 30 and 40 hours. Specimens were tested at two temperatures, 200 F and 550 F. The J-R curves are very close, within a scatter band typical of the J-test for a material; there is little apparent difference that can be attributed to specimen type.

ACKNOWLEDGEMENT

The authors acknowledge the support provided by the B&W Owners Group for this work. The finite element analysis was performed by D. E. Killian, B&W Nuclear Technologies.

REFERENCES

[1] A. L. Lowe, Jr., K. E. Moore, and J. D. Aadland, "Integrated Reactor Vessel Materials Surveillance Program for Babcock & Wilcox 177-FA Plants," ASTM STP-870, American Society of Testing Materials, Philadelphia, PA, 1985, p.931-950.

[2] J. C. Newman, Jr., "Stress Intensity Factors and Crack Opening Displacements for Disk-Shaped Specimens," International Journal of Fracture, Vol. 17, No. 6, December 1981, pp 567-578.

[3] J. H. Underwood, J. C. Newman, Jr., and R. R. Sealey, "A Proposed Standard Round Compact Specimen for Plane Strain Fracture Toughness Testing," J. of Testing and Evaluation, Nov. 1980, pp308-313.

[4] A. Saxena and S. J. Hudak, "Review and Extension of Compliance Information for Common Crack Growth Specimens," International Journal of Fracture, Vol. 14, No. 5, pp 453-468, 1978.

Dennis M. Lambert[1] and Hugo A. Ernst[2]

CONSTRAINT EFFECTS OBSERVED IN CRACK INITIATION STRETCH

REFERENCE: Lambert, D. M., and Ernst, H. A., "**Constraint Effects Observed in Crack Initiation Stretch,**" Fracture Mechanics: 26th Volume, ASTM STP 1256, Walter G. Reuter, John H. Underwood, and James C. Newman, Jr., Eds., American Society for Testing and Materials, Philadelphia, 1995.

ABSTRACT: The current paper characterizes constraint in fracture: J-modified resistance (J_MR) curves were developed for two tough structural materials, 6061-T651 (aluminum) and IN718-STA1 (nickel-base superalloy). A wide variety of configurations was tested to consider load configurations from bending to tension including three specimen types (compact tension, center-crack tension, and single-edge notched tension), and a range of ligament lengths and thicknesses, as well as side-grooved and smooth-sided ligaments.

The J_MR curves exhibited an inflection point after some crack extension, and the data were excluded beyond the inflection. Qualified J_MR curves for the two materials showed similar behavior, but R-curves were identical for equal ligament length-to-thickness ratio, R_L, for the aluminum alloy, with increasing slope for increasing R_L, while for the nickel, the resistance curves aligned for equal ligament thickness, B, and the slope increased for decreasing B.

Displacements at the original crack tip (δ_5) were recorded throughout the test for several specimens. δ_5-versus-crack extension curves were developed, and data were excluded beyond the inflection point (as with the J_MR curves). The data collapsed into two distinct curves, thought to represent the surface, plane stress effect and the central, plane strain effect. This was observed for both materials.

A technique called *profiling* is presented for the aluminum alloy only, where the crack face displacements are recorded at the final point of the test as a function of the position throughout the crack cavity, along with an effort to extract the observations in a usable form. Displacements were consistent throughout the cross-section at and behind the original crack tip. In the region where the crack grew, this displacement was developed by a combination of stretch and crack growth. The stretch required to initiate crack extension was a function of the depth beneath the surface into the cross-section.

KEYWORDS: elastic-plastic fracture mechanics, J-integral, modified J-integral, J-resistance curves, crack tip opening displacement, crack face separation profiles.

[1]Postdoctoral Fellow and [2]Professor, G.W. Woodruff School of Mechanical Engineering, The Georgia Institute of Technology, Atlanta, GA 30332-0405.

Copyright© 1995 by ASTM International www.astm.org

INTRODUCTION

Fracture behavior is a vital concern of the aerospace industry. A dramatic loss of strength occurs when compared to elastic and plastic deformation, and the failure can be catastrophic in nature. Energy-related parameters such as K, G, J, and J_M [1 - 4] have been developed to predict fracture by assuming simplified material behavior, and each parameter works well, as long as the defining assumptions are met. Developing plasticity produces a change of constraint, and as a result the assumptions are violated, and the parameter becomes ineffective. The material fracture resistance at the surface differs from that at the center of a cross-section due to the variation of constraint through the thickness. *Constraint* is a measure of the degree of triaxiality of the stress field. One goal of fracture mechanics is to incorporate constraint into fracture prediction, and many parameters have been devised to describe the prevailing level of constraint in the fracture process [5].

A substantial effort has been expended by many, e.g., Hellmann and Schwalbe [6] and Ernst, et al [7], to develop a fracture parameter using relevant displacements. As an example, δ_5 [6] is a displacement parameter, measured over a 5-mm gage length at the original crack tip, that shows some promise. One complaint raised about the use of δ_5 after crack growth initiation is that the growing crack moves increasingly further from the location where δ_5 is measured, and the measurement becomes less and less sensitive. Saxena [8] has suggested that with some growth, δ_5 becomes more and more a measure of the compliance of the specimen, a quantity related to the crack length.

The actual profile of the loaded crack might provide a useful improvement to the δ_5 parameter, since the measurement comes from the current configuration and is thought to be a natural extension of the idea of the δ_5 measurement.

The purpose of this investigation was to develop experimental evidence of the varying fracture behavior of the two materials, with varying constraint, the degree of triaxiality of the stress field, and the current paper presents experimental data developed for two tough materials used for structural applications: 6061-T651, aluminum alloy, and IN718-STA1, nickel-base superalloy. The focus is on the characterization of the plasticity and crack growth in the cross-section of the deforming body.

TESTING DETAILS

Two materials were selected, and these were 6061-T651, an aluminum alloy, and IN718-STA1, a nickel-base super alloy. Both are tough materials, exhibiting a large degree of plasticity before final failure. The composition of the aluminum alloy was, as follows: magnesium - 1%, silicon - 0.6%, copper - 0.25%, chromium - 0.2%, and aluminum - balance, while the nickel alloy had the following composition: chromium - 19%, iron - 17%, niobium - 5%, molybdenum - 3%, titanium - 0.8%, aluminum - 0.6%, and nickel - balance. The aluminum alloy expresses elastic perfectly plastic mechanical behavior, and the nickel alloy is often used for designs where the temperature is elevated.

TABLE 1: Mechanical Properties of the Selected Materials

PROPERTY	AL6061-T651	IN718-STA1
Young's Modulus, E	64.83 GPa	210.3 GPa
Poisson's Ratio (from literature), ν	.33	.29
Yield Strength at 0.5% Offset, $\sigma_{0.5}$	304.1 MPa	1,214 MPa
Ultimate Tensile Strength, σ_{UTS}	325.5 MPa	1,400 MPa
Flow Stress, $\sigma_o = (\sigma_{0.5} + \sigma_{UTS})/2$	315.2 MPa	1,303 MPa
Reference Strain, $\epsilon_o = \sigma_o/E$	.00486	.00622
Hardening Coefficient, α	.0113	.0164
Hardening Exponent, n	19.6	12.3

The tensile test results for the two materials appear in table 1, above, with α, σ_o, n, and ϵ_o arising from a fit of the tensile data to the Ramberg-Osgood equation, as follows:

$$\epsilon = \frac{\sigma}{E} + \alpha \left(\frac{\sigma}{\sigma_o}\right)^n \qquad (1)$$

The purpose of this investigation was to develop experimental evidence of the varying fracture behavior of the two materials, with varying constraint, the degree of triaxiality of the stress field. To assess this, constraint effect, a variety of different configurations were tested, and these variations included the specimen type, the initial remaining ligament lengths and thicknesses, and the use of both smooth-sided and side-grooved conditions. The specific test matrices are included below in tables 2 and 3, along with a summary of these details, to follow. Three specimen types were chosen to provide a range of the loading configuration from mostly bending (compact tension or *CT* specimens) to pure tension (center-crack tension or *CCT* specimens) and include some data from an intermediate configuration (single-edge notched tension or *SENT* specimens). The range of the ligament dimensions provided initial lengths from 6.4- to 25.4-mm and thicknesses from 3.2- to 21.6-mm, and a range of the ligament length-to-thickness proportion from 0.5 to 4. These ranges of ligament shape were thought to be a broad enough range of the variables to provide the desired deviation of prevailing constraint. Some specimens were side-grooved, because this promotes plane strain condition by removing the surface plane stress layer [9].

TABLE 2: 6061-T651 Planar Specimens

REF.	TYPE	W[a] (mm)	B (mm)	a_o/W	SG[c]
#55@	CCT	25.4	3.18	0.5	0
#54	CCT	25.4	6.35	0.5	0
#D6@	CCT	25.4	12.7	0.5	0
#B9@	CCT	25.4	21.6	0.5	0
#C0	CCT	25.4	21.6	0.6	20%
#29	SENT	50.8	12.7	.75	0
#C1	SENT	50.8	21.6	.75	0
#53	CT	25.4	6.35	.75	0
#66	CT	50.8	6.35	.75	0
#51@	CT	50.8	6.35	0.5	0
#E0	CT	25.4	12.7	.75	0
#D8	CT	25.4	12.7	0.6	20%
#81	CT	50.8	12.7	.75	0
#82@,83,84@, E2@[b]	CT	50.8	12.7	0.5	0
#08@,E3*	CT	50.8	12.7	0.6	20%
#C8	CT	50.8	21.6	.75	0
#C9@,D1*	CT	50.8	21.6	0.5	0
#D0	CT	50.8	21.6	0.5	20%

Notes: a. W≡load-line to the back face for CCT and CT, W≡total width for SENT, b. multiple-specimen test was run using four specimens of the same configuration, c. Side-grooving: 20% of the total thickness (10% per side). *duplicated configurations, †crack popped into ligament. *@ profiled* specimens.

Test procedures came primarily from ASTM Test Standards E1152-87 and E647-91 [10,11]. The initial and the final crack lengths were measured and the intermediate lengths were derived from unloading compliance measurements outlined in those specifications. The change of curvature of the crack front as the crack evolved obliged the use of a curvature correction as outlined in [11]. The needed formulae for the SENT configuration were derived from data appearing in the EPRI Handbook [12]. Here, J-modified is presented, instead of the J-integral. With the CT and the SENT configurations, the formula for J_M is, as follows [4]:

$$J_M = G + \int_0^{v_{pl}} \frac{\eta P}{Bb} dv_{pl} \qquad (2)$$

The terms in equation 2 include the linear elastic component of the crack driving force, $G = K^2/E'$, where E' is Young's modulus for plane stress or $E' = E/(1-\nu^2)$ for plane strain; B and b are the ligament thickness and length, respectively, and P is the load and v_{pl} is the plastic component of the displacement; η appears in [10] for CT specimens and a formula for η was developed from data appearing in [12] for the SENT configuration and is, as follows:

$$\eta_{SENT} = 0.0092 + \frac{0.9592}{a/W} \tag{3}$$

For this equation, a is the crack length measured from the face of the specimen, and W is the total width of the specimen.

TABLE 3: IN718-STA1 Planar Specimens

REF.	TYPE	W (mm)	B (mm)	a/W	SG
#24	CCT	25.4	6.35	0.5	0
#25	CCT	25.4	6.35	0.6	20%
#12	CT	25.4	6.35	.75	0
#13	CT	50.8	6.35	.75	0
#85	CT	50.8	6.35	0.6	0
#86,87,88,14	CT	25.4	6.35	0.5	0
#D2	CT	25.4	6.35	0.6	20%†
#D4	CT	25.4	12.7	0.6	20%†
#D9	CT	25.4	12.7	.75	0
#17	CT	50.8	12.7	.875	0
#93,95*	CT	50.8	12.7	.75	0
#94	CT	50.8	12.7	0.6	0
#A5	CT	50.8	20.3	0.5	0
#A7,A8*	CT	50.8	20.3	0.5	20%

Notes: see notes from Table 2 for information regarding symbols

The J-modified formula for the CCT configuration is, as follows:

$$J_M = G + \int_0^{v_{pl}} \frac{P}{Bb}\, dv_{pl} + \int_0^{P} \frac{v_{pl}}{Bb}\, dP - \int_{a_o}^{a_f} \frac{v_{pl}}{b} \left[\frac{dJ_{Mpl}}{dv_{pl}}\right] da \qquad (4)$$

For the CCT configuration, $\eta = 1$ and $\eta_c = -1$, and these have been incorporated in equation 4.

The crack opening displacement (δ_5) was measured throughout the test at the original crack tip location using a gage length of 5-mm. A linear relationship between J_M and δ_5 has been suggested:

$$\delta_5 \approx d_n \frac{J_M}{\sigma_o} \qquad (5)$$

In equation 5, d_n is the constant of proportionality between J_M and δ_5 ($0.5 \leq d_n \leq 1.2$).

R-CURVE ANALYSIS

J_M-Resistance Curves

The data developed from CT specimens appear in figure 1. Because of the presence of an inflection point in some of the data and a large apparent scatter of the overall group, an investigation was made of potential disqualifying criteria. The candidates were based on the onset of plasticity-dominated behavior. At the point where plasticity saturates the ligament, fracture mechanics methodologies are expected to become ineffective in predicting the behavior. A detailed discussion is beyond the scope of this presentation, however it will be noted that various candidate parameters showed reasonable correlation with each other and also with the J_MR-curve inflection points. The data were consequently disqualified beyond the inflection point as being unrepresentative of fracture mechanics behavior. The qualified CT specimen data appear in figure 2.

Several observations can be made for the qualified aluminum fracture resistance curves: (a) although some variation still exists for similar curves, the correlation of the data has improved; (b) the basis that provides similar fracture resistance for the aluminum specimens is the initial ligament length-to-thickness ratio, R_L; (c) in figure 2a, the aluminum specimens with $R_L = 2$ and $R_L = 4$ are very close, and this is thought to be *plane stress* fracture; (d) also in figure 2a, the side-grooved and the $R_L = 1/2$ curves are indistinguishable, suggesting that the $R_L = 1/2$ data are *plane strain* fracture.

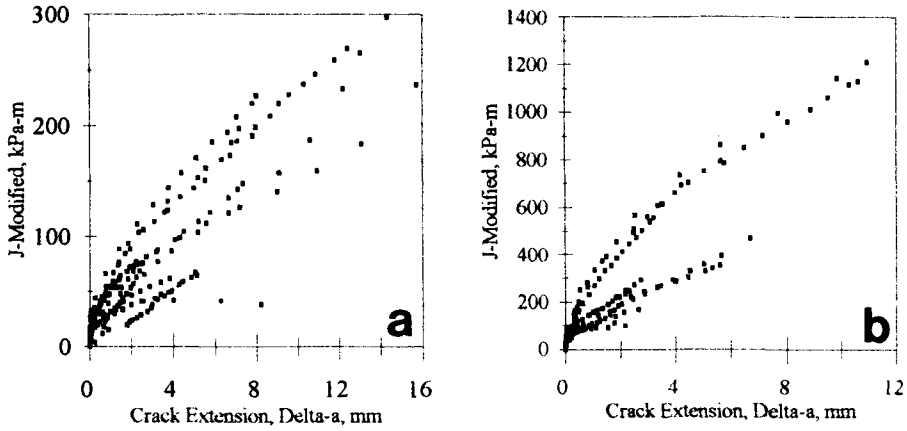


Figure 1: $J_M R$ behavior of a variety of 6061-T651, aluminum, and IN718-STA1, nickel, compact tension fracture specimens (ligament dimensions were varied): (a) aluminum, (b) nickel.

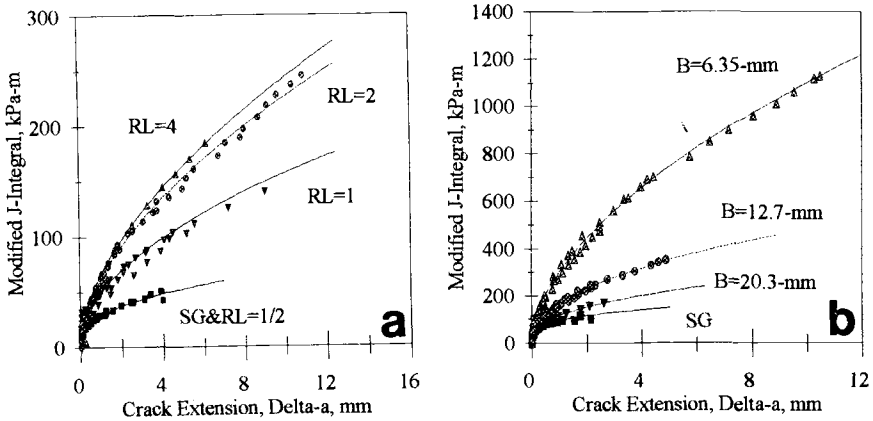


Figure 2: Results of using the inflection point of the $J_M R$-curve as a validity limiting criterion, also showing results of regression analyses of the qualified data fit to a power-law form (a) aluminum alloy and (b) nickel alloy.

Similar observations can be made for the qualified nickel fracture resistance curves: (a) the basis that provides similar fracture resistance character for the nickel specimens is the ligament thickness (from visual observation); (b) in figure 2b, the thickness B = 20.3-mm data do not agree completely with the side-grooved data and are only near to plane strain behavior, suggesting they do not reach plane strain conditions.

The qualified CCT data appear in figures 3a and 3b. The CCT results follow the blunting line to a much higher level of J_M than the CT results with little corresponding crack growth, but the trend of the CCT data are identical to that of the CT data, ranking according to the R_L value for the aluminum and B for the nickel. The aluminum SENT results (no data are shown) followed the blunting line to a higher level than the CT, but when the data diverge from the blunting, the SENT resistance curves quickly blend with the CT resistance curves of the same R_L value.

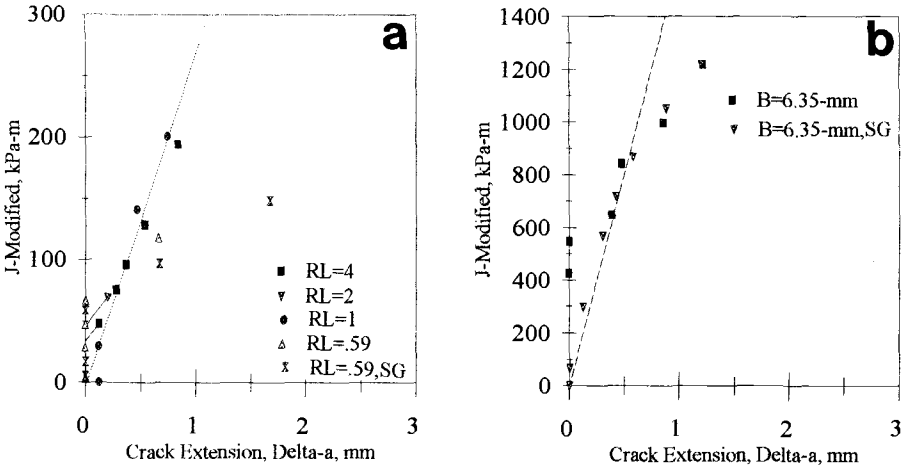


Figure 3: Qualified J_MR-curves for center-crack tension specimens comparing different ligament thicknesses: (a) aluminum alloy and (b) nickel alloy.

δ_5R-Curves

One alternative to using J or J_M as a fracture parameter is the use of the crack-tip opening displacement, δ_5. A substantial effort to develop this technique has been expended by many, e.g., Hellmann and Schwalbe [6] and Ernst [7]. A linear correspondence between J_M and δ_5 is suggested (equation 5). Data were recorded for a variety of specimens for both materials, and an inflection point similar to that observed with the J_MR-curves occurred at approximately the same point in the test. The data beyond the inflection point were excluded and the resulting δ_5R-curves are presented in figure 4. The qualified data can be observed to fall into one distinct behavior group for each of the materials with relatively good correlation within these groups. A second,

almost horizontal, response can be seen in figure 4a: this behavior was evident for all of the side-grooved and the thickest of the specimens for both materials. The application of the exclusion criterion removed all but one set of data. This flat response is thought to be the expression of plane strain conditions, whereas the other "steeper" response arises from plane stress conditions.

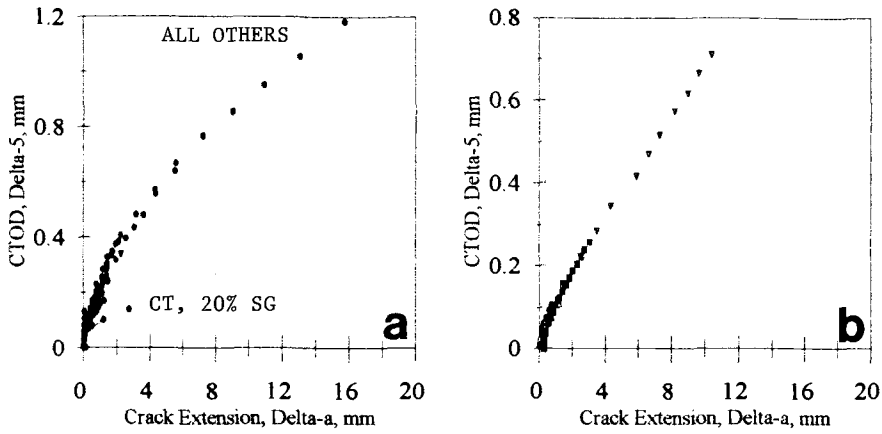


Figure 4: Qualified δ_5R-curves for (a) aluminum CT, CCT, and SENT specimens and (b) nickel CT and CCT specimens.

PROFILES

The crack tip opening displacement, δ_5, is used as a fracture parameter. As the crack grows, δ_5 is measured progressively further behind the advancing crack tip, and the measurement is expected to lose sensitivity. It was thought that the actual shape of the loaded crack might provide a useful improvement to the δ_5 parameter, since the measurement comes from the current configuration. Several of the aluminum specimens (table 2) were wedged at the final displacement of the test and were then sectioned to allow the measurement of the crack face profiles as a function of the position within the cracked ligament. The *profiles* are the Cartesian "xy" plots of the crack shapes that were exposed by sectioning at different levels (z-position) through the thickness with the origin set at the midpoint between the load points.

Procedures

The specimens selected for profiling were mounted in a cold-set epoxy resin, commonly used in metallography. This served to immobilize the crack faces and to minimize rounding of the crack edge that reduces the profile definition. To infuse the epoxy into the depths of the crack, specimens were placed into a mold in a sealed chamber, and a vacuum was drawn briefly to remove air bubbles from the crack gap. The CCT specimens were cut down to approximately a 25-mm-by-50-mm size to fit the mold.

In the course of the crack extension for both materials tested, a necked region is formed at the free surfaces at the tip of the initial fatigue precrack. In the case of the nickel specimens, this neck was continually reformed as the crack extended, while for the aluminum, the necked region was only associated with the first step of crack extension. The selected specimens (table 2) were polished to produce a well-defined profile at the root of the neck formed. Once this surface profile was recorded, the specimen was ground between 0.64- and 0.89-mm to expose the next surface to be profiled, and the procedures were repeated. Sectioning was repeated for each specimen from the surface to the mid-thickness.

A measuring device combining a microscope, a video camera, and a computer with a digitizer tablet was used to record the crack profile (Zydas Corporation "VIDAS21" software). The data output from the profiling procedure were converted from pixel position information into actual crack profiles. Once the coordinates of each point were established in this way, the crack face displacement was determined by subtracting the y-coordinate of the lower crack surface from that of the upper crack surface at the same x-coordinate location.

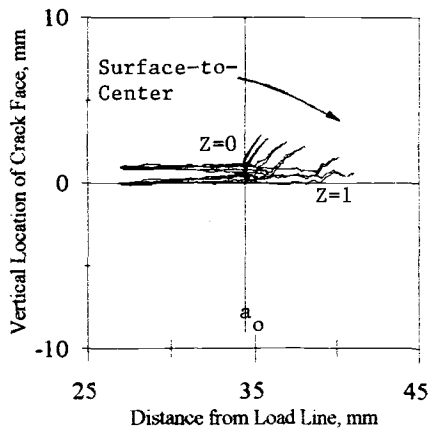


Figure 5: Example crack profiles, characterizing a CT specimen. by a series of cross-sections taken from surface-to-center.

Results

Figure 5 shows the change of the advancing crack shape typical of all profiled specimens as a function of the section depth. The fraction of depth below the surface is indicated by Z, where Z = 2z/B, with z being the actual depth below the surface, and with B being the specimen thickness. Thus, Z = 0 at the surface and Z = 1 at the center plane. The crack grows in the horizontal direction, with the dimensions referenced to the load line. The initial location, the tip of the fatigue-sharpened precrack, is indicated by "a_o". The crack profile is sharply angled beyond the fatigue precrack in the surface profile. This angled crack shape is associated with shear. The profiles become straighter and longer for progressively deeper sections.

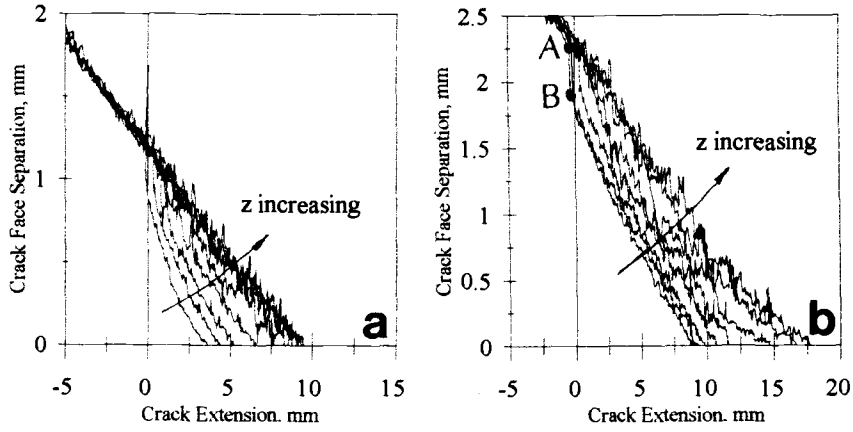


Figure 6: Separation profiles for two CT specimens (a) specimen #81; (b) specimen #E2 (see table 2 for details of specimen configurations)

Figures 6a and 6b show two full sets of the crack face separation profiles for different specimens. The precrack regions are to the left of zero in the figures. The horizontal axis gives the crack extension from the initial *average* crack tip location. At the left side of the graph the curves exhibit the displacement associated with the tip of the fatigue precrack at the final position of the test. This displacement is the same throughout the cross-section, regardless of the depth into the thickness and was within five-percent of the final value of δ_5 for all of the profiled specimens.

It can be seen in figures 6a and 6b that the angle is relatively constant near the crack tips of each cross-section for each specimen. This suggests that once the plasticity has developed sufficiently in a given cross-section, the displacement criterion associated with crack extension is constant through the cross-section.

The initial crack tip was at the origin when the test was started. As the displacement was applied, the initial crack tip blunted, and eventually, the crack began to grow. The surface cross-section plots show a substantial stretching or blunting (a vertical excursion in the profiles with little horizontal excursion) before the crack begins to grow. The crack has grown to the right while the points behind the evolving crack tip have displaced upwards. The blunting of one of the surface plots is labelled "AB" in figure 6b. For deeper sections, the stretch is progressively less, while the crack is longer. At the center of the specimen (top curves in figures 6a and 6b), no discrete stretch zone is obvious.

Once the initial stretching has occurred, all of the profiles develop approximately the same slope. It should be noted that a few of the surface profiles appeared to be identical. This trend was also true of some of the center profiles: a set of "transition profiles" can be seen to blend smoothly from the stretch-and-fracture behavior of the surface to that of the center. The profiles are taken at relatively even increments of thickness, and the profiles seem to be equally spaced through the transition. This was not the case for the CCT specimen profiles which blunted equally for all but the centermost profile. The behavior of the CCT profiles could be best described as a uniform surface effect that occurs for all but the innermost sections.

Calibration Profiles

The deviation of the growing crack profile from that of a non-growing crack with the current crack length was determined. Profiles are derived from the final values present at the final point of the test. It was assumed that the total displacement, δ_{tot}, could be decomposed, as follows:

$$\delta_{tot} = \delta_{el} + \delta_{pl} - \delta_{st} \tag{6}$$

This fits the entire displacement along the crack faces to a *calibration* displacement evaluated as the sum of elastic plus plastic displacement components that are found in the literature [13 - 15]. The last term in equation 6 is the remainder after removing the first two and represents an effect of the crack growth. The total displacement is less than the calibration displacement in the region of crack growth, and has been devised as a positive value subtracted from the calibration value. It will be shown that $\delta_{st} = \delta_{st}(r,z)$, a function of the position in the crack growth direction and the depth into the thickness, z.

The elastic displacement was characterized by Williams [13], and near the crack tip it was estimated to be linearly related to the square root of the distance from the crack front.

$$\delta_{el} = \delta_{el}(r) = \frac{4K}{E'}\sqrt{\frac{2}{\pi}}\sqrt{r} \tag{7}$$

In equation 7, δ_{el} is the elastic displacement of the crack faces at a distance r from the crack tip, and K is the stress intensity.

Hutchinson [14] and Rice and Rosengren [15] provided a similar characterization for fracture of fully-plastic materials (this is the so-called HRR field solution):

$$\delta_{pl} = \delta_{pl}(r) = C_e(J)^{n/n+1}(r)^{1/n+1} \propto (r)^m \tag{8}$$

$$with \quad m = 1/(n+1) \tag{9}$$

δ_{pl} is the plastic displacement and n is the hardening exponent from the Ramberg-Osgood relation where $\epsilon \propto \sigma^n$. The HRR field solution suggests a fit as shown in the middle expression of equation 8, but because of the difficulty of assessing J in a given section and then noting the presence of concave-upward precrack regions for many of the profiles, a power-law fit to the precrack region was adopted, as shown on the far right in equation 8. The concave-upward shape was thought to be an accumulation of beam deflection-type displacements added to the HRR displacements. Although the suggested beam deflection effect was not considered, adding of higher-order terms to the calibration function might be warranted, however the results presented here are consistent and physically reasonable. The chosen form for δ_{pl} is this:

$$\delta_{pl} = C_{pl}(r_{sh})^m \tag{10}$$

The constants C_{pl} and m come from a linear regression analysis of the natural logarithms of δ_{pl} and r_{sh} data taken from the precrack region. The position r relative to the crack tip in the profile was shifted to r_{sh}, which is referenced to the crack tip at the deepest point. The need for such a shift became obvious in looking at the profiles from a short crack growth specimen (#82): no other scheme was successful in capturing the profiles of this specimen. Other alternatives considered included shifting r by a constant or else a smoothly varying function of the depth into the thickness. These last two would imply that some plasticity zone precedes the crack tip at each point, similar to Irwin's [1] insertion of the plastic zone effect into the LEFM "K-solution" as an adjustment, but this procedure did not work well.

For CCT specimens, the actual crack face displacements were much smaller in the precrack region than those of the calibration profiles due to the elastic displacement component (equation 7). The final loads of the CCT specimens were dramatically higher than those of the CT specimens, and the possibility of relaxation of some of the elastic displacements upon wedging and load removal is thought to be the cause of the discrepancies.

Stretch Analysis

The calibration profile is that which would be expected to develop with no crack growth and the crack at the length observed at the end of the test. The deviation of the actual separation profiles from the calibration profiles is a result of the growth of the crack as the load-line displacement is applied. For surface sections, the difference is quite pronounced, but for center sections, the deviation is insignificant.

The deviation of the profile data from the calibration profile is referred to as *stretch*. Fig. 7a and b show a series of stretch profiles developed by 2 specimens at different section-depths. Some of the stretch occurs prior to crack growth, and then crack extension begins. Once the crack begins to extend at the section, the stretch *may* continue to increase, but this increase may be a result of the use of improper calibration functions.

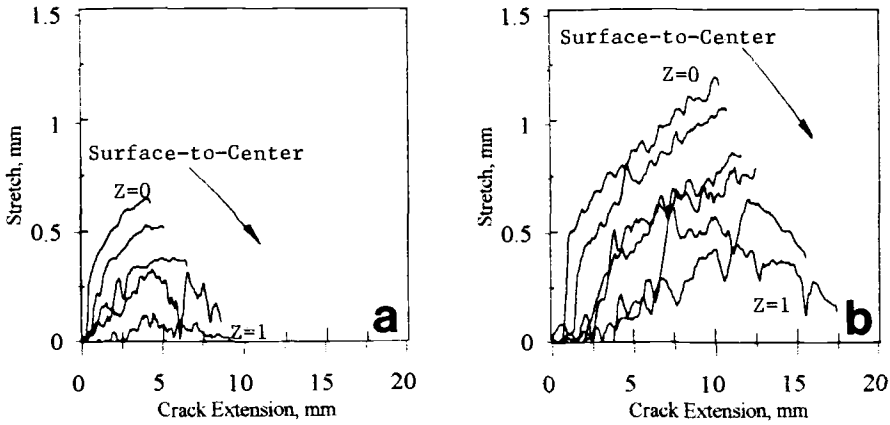


Figure 7: Characterization of stretch as a function of depth into the specimen thickness (a) Stretch "resistance" for specimen #81; (b) stretch "resistance" for specimen #E2.

Figure 8 shows a comparison of the surface stretch characteristics for all of the specimens profiled. For all of the specimens shown, the stretch at the point where the crack begins to grow, or *initiation stretch*, is approximately the same. Again, the slope following initiation could be representative of different stretch-versus-crack extension characteristics for the different configurations but is more likely due to the choice of inaccurate calibration functions.

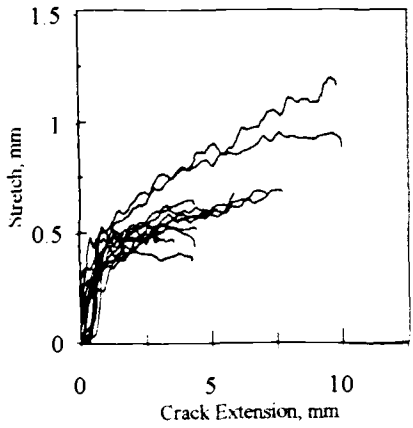


Figure 8: Surface stretch resistance comparison.

Initiation Stretch

The profiling effort in this investigation was an attempt to extend the measurement methodology to incorporate the current crack tip position. the stretch, δ_{st}, is the deviation from the bulk material behavior, estimated by the calibration displacement and has been fitted to a form, as follows:

$$\delta_{st} - \delta_{ref}) = C_{st}(\chi)^p \qquad (11)$$

The values of δ_{ref} and C_{st} come from a linear regression analysis of δ_{st}-versus-$(\chi)^p$, with χ being the crack extension in the profile in question: $\chi = a_f(z) - a_o(z)$. The value of C_{st} is somewhat intuitive, but that of δ_{ref} is not obvious: the regression analysis produced better correlation with δ_{ref} than if the regression was forced through $\delta_{ref} = 0$. The exponent of χ is $p = 1/(n+1) = 0.043 \approx 0$. This corresponds to displacements associated with power-law plasticity [12]. The early part of the stretch curves seemed to be almost vertical, exhibiting blunting, and then the stretch profile became approximately constant. Thus, imposing the exponent of p seemed reasonable. Two behaviors were observed: (a) the values of C_{st} were relatively constant for the surface profiles across all of the data, and the center profiles produced a different, constant C_{st} , and (b) the values of δ_{ref} seemed to be increasingly negative for the progressively deeper profiles. Since the value of $p \approx 0$ for this material, the form of the stretch fit gives

$$\delta_{st} = \delta_{ref} + C_{st}(\chi)^p \approx \delta_{ref} + \zeta C_{st} = \delta_i \qquad (12)$$

A factor of ζ has been inserted to produce the value of the second term in the middle expression in equation 12 at the knee of the curve. This approximation arises from the exponent p being near zero, producing relative insensitivity of δ_{st} with respect to χ above some nominal value of χ. The value of the sum, δ_i, monotonically decreases for most of the compact tension specimens with increasing z ≡ depth of section, and is approximately constant for the center-crack tension specimens. Apparently, the ligament of the CCT specimens must be more uniformly deformed throughout the whole of the fracture process, only exhibiting a small initiation stretch; and at least for this material, the initiation stretch, δ_i, appears to be a function of the depth beneath the surface, designated s. A strict definition of s is necessary at this point: the first profile was taken in each case at the root of the necked region formed on the side of the specimen. This was assigned a value of z = 0-mm. Because of the necking phenomenon, the z = 0 surface is somewhat below the original surface, and thus, s was defined as z plus the neck-root depth. Figure 9a shows the initiation stretch, δ_i-versus-s for all of the profiles. The lines connect adjacent profiles in each specimen. The initiation stretch decreases as s increases, but the correlation between specimens is not apparent. No obvious explanation exists for the CCT specimen results with $R_L \equiv b_o/B = 1$ in figure 9a.

Various forms were considered to establish the behavior of δ_i-versus-s, and clearly the best correlation was with a parameter $\kappa \equiv sB/b_o$, and this is plotted in figure 9b. Except for the behavior of the CT specimen with $R_L = 4$, all of the behavior seems to be along the same curve within experimental error. For each specimen, a surface zone exists, and as the depth below the surface increases, the surface effect makes a transformation into the uniform subsurface behavior. In the case of the two specimens with $R_L = 4$, the surface effect is thought to have permeated the whole thickness, and the entire cross-section degenerates into a surface effect defined by the calibration profile up to the point of initiation of crack growth.

SUMMARY

The current paper presents experimental data developed for two tough materials used for structural applications: 6061-T651, aluminum alloy, and IN718-STA1, nickel-base super alloy. The focus is on the characterization of the plasticity and crack growth in the cross-section of the deforming body.

J-modified resistance curves (J_MR-curves), arising from a wide variety of configurations, have been included. Cracks were grown to approximately 40-percent of the initial remaining ligament, and the J_MR-curves were observed to pass through an inflection point. This inflection is thought to arise from the onset of plasticity-dominated behavior, and the data beyond this point were excluded. For either material, R-curves

derived from compact tension specimens were found to be identical, based on some ligament characteristic, however the basis was different for the two materials: for the aluminum alloy, the R-curves were identical when the ligament length-to-thickness ratio was the same, and the slope increased as the ratio increased, while for the nickel alloy, the R-curves were the same based on the thickness of the ligament. In the case of the nickel, the slope of the R-curves increased with decreasing ligament thickness.

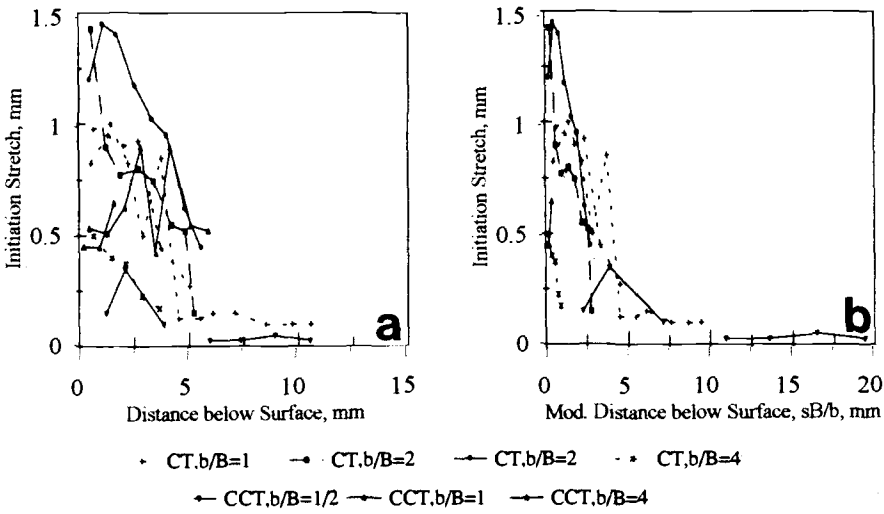


Figure 9: (a) Initiation stretch-versus-depth and (b) initiation stretch-versus-modified depth.

Results of crack displacement measurements have also been included: specifically, the crack opening displacement measured at the tip of the original crack (δ_5) and crack face displacement *profiles* developed throughout the whole of the crack cavity. The δ_5-versus-crack extension curves (δ_5R-curves) were subjected to disqualification beyond an observed inflection, and two distinct behaviors persisted for each of the materials. These are thought to be associated with the surface, plane stress behavior and the central, plane strain behavior. Plane strain was observed in the side-grooved configurations, as well as the thickest ligaments, and produced a large crack growth for a small δ_5 displacement relative to the plane stress.

Profiling was thought to be a natural extension of the idea of δ_5 measurement. The profiles show the current configuration (at the final displacement in the test) and agree with the δ_5 data taken at the initial crack tip locations.

A total calibration displacement of δ_{tot}, derived as the sum of a linear elastic displacement plus a fitted estimate of the nonlinear displacement, was developed for the profile data, and the actual profile displacements were subtracted from δ_{tot} to give the deviation, referred to as the *stretch* displacement. This exhibited an initial stretch prior to

the crack growth. After initiation, the crack face separation profiles appear to be parallel. The principal difference is in the amount of initiation stretch, and this is found to vary smoothly as a function of the depth beneath the ligament surface from a maximum at the surface to a negligible value at some nominal depth.

CONCLUSIONS

The results suggest that given a method to evaluate the constraint along an arbitrary crack front and given the boundary conditions, the calibration displacement of each point could be determined, and an estimate of the stretch and crack growth characteristics of the point might be easily determined by using the profiling results of a planar crack growth analysis as presented, above.

The two materials tested exhibited fracture resistance characteristics with a differing basis for comparison: for the aluminum alloy, 6061-T651, the resulting J_MR-curves aligned according to the ligament length-to-thickness ratio ($R_L = b_o/B$), while the nickel alloy, IN718-STA1, showed like behavior for common thicknesses.

Two distinct δ_5R-curves were generated for the two materials, and the lower of these is thought to be plane strain behavior, while the upper curve is thought to be plane stress behavior. The displacement measured at the surface (δ_5) was the same as the displacements observed inside the cross-section at the original crack tip. This common displacement is developed in a different manner depending on the depth into the thickness considered: the value of δ_i, the initiation stretch, was the deviation from the total calibration function and seemed to be a function of the depth beneath the surface, although an alternate functionality that included the ligament proportions and the depth beneath the surface was also suggested. At some depth, the stretch prior to initiation is negligible. This is thought to be the plane strain condition.

The crack angle was approximately constant throughout the ligament cross-section after crack growth initiates. This was seen as parallel crack face separation profiles in figures 6a and 6b, and suggests that once the plasticity has been able to sufficiently in any cross-section, crack growth is initiated and will proceed in a common fashion.

ACKNOWLEDGEMENTS

The authors would like to acknowledge NASA Marshall Space Flight Center for providing funding, materials, and prepared specimens through Grant NGT-50641, via the Graduate Student Researcher's Program.

BIBLIOGRAPHY

[1] Irwin, G.R., "The Onset of Fast Crack Propagation in High Strength Steel and Aluminum Alloys," *Sagamore Research Conference Proceedings, Vol. 2* (1956), pp. 289-305.

[2] Griffith, A.A., "The Theory of Rupture," *Proceedings, 1st Conference on Applied Mechanics* (1924), pp. 55-63.

[3] Rice, J.R., "A Path-Independent Integral and the Approximate Analysis of Strain Concentrations by Notches and Cracks," *Journal of Applied Mechanics* (1968), pp. 379-86.

[4] Ernst, H.A., "Further Developments on the Modified J-Integral," *ASTM STP 995* (1989), pp. 306-19.

[5] *Constraint Effects in Fracture, ASTM STP 1171*, E.M. Hackett, K.-H. Schwalbe, and R.H. Dodds, Jr., eds., American Society for Testing and Materials, Philadelphia, PA (1993), 507 pages.

[6] Hellmann, D., and Schwalbe, K.-H., "Geometry and Size Effects on JR- and δR-Curves Under Plane Stress Conditions," *ASTM STP 833* (1984), pp. 577-605.

[7] Ernst, H.A., Schwalbe, K.-H., Hellmann, D., and McCabe, D.E., "Modified J, J_M-Resistance Curves Under Plane Stress, *International Journal of Fracture, Vol. 37* (1988), pp. 83-100.

[8] Saxena, A., private conversation, April 20, 1994.

[9] Dodds, R.H., and Kirk, M.T., "An Analytical and Experimental Comparison of J_i Values for Shallow Through and Part Through Surface Cracks," Interim Report (N61533-88-C-0035) to David Taylor Research Center (July 1990).

[10] ASTM E1152-87, "Standard Test Method for Determining JR-Curves," *1989 Annual Book of ASTM Standards, Vol. 03.01* (1989), pp. 814-24.

[11] ASTM E647-91, "Standard Test Method for Measurement of Fatigue Crack Growth Rates," *1992 Annual Book of ASTM Standards (1992) Volume 03.01.*

[12] *An Engineering Approach for Elastic-Plastic Fracture Analysis*, Electric Power Research Institute Report NP-1931, Research Project 1237-1, prepared by General Electric Company (July 1981).

[13] Williams, M.L., "Stress Singularities Resulting from Various Boundary Conditions in Angular Corners of Plates in Extension," *Journal of Applied Mechanics, Transactions of the ASME, Vol. 74* (1952), p 526.

[14] Hutchinson, J.W., "Plastic Stress and Strain Fields at a Crack Tip," *Journal of the Mechanics and Physics of Solids, Vol. 16* (1968), pp. 337-47.

[15] Rice, J.R., and Rosengren, G.F., "Plane Strain Deformation Near a Crack Tip in a Power-Law Hardening Material," *Journal of the Mechanics and Physics of Solids, Vol. 16* (1968), pp. 1-12.

W. Randolph Lloyd[a] and Robert S. Piascik[b]

THREE-DIMENSIONAL CRACK GROWTH ASSESSMENT BY MICROTOPOGRAPHIC EXAMINATION

REFERENCE: Lloyd, W. R., and Piascik, R. S., **"Three-Dimensional Crack Growth Assessment by Microtopographic Examination,"** Fracture Mechanics: 26th Volume, ASTM STP 1256, Walter G. Reuter, John H. Underwood, and James C. Newman, Jr., Eds., American Society for Testing and Materials, Philadelphia, 1995.

ABSTRACT: The initial stage of the stable tearing process in two 2.3 mm sheet 2024-T3 aluminum alloy M(T) specimens are analyzed using fracture surface microtopography reconstruction techniques. The local crack tip opening angles (CTOA) in the interior of the specimens are determined relative to both crack extension and through-thickness position. The microtopographic analysis of cracks grown in the L-T and T-L orientations reveal that interior CTOA is comparable to those measured on the surface using standard optical analysis methods. Similar to surface CTOA results, interior (mid-thickness) CTOA exhibit a transient behavior; CTOA transitions from high angles, at near crack initiation, to a lower steady-state value of 5 deg. and 4.2 deg. for L-T and T-L, respectively, at crack lengths greater than 1.5 mm. Fracture surface topographic projection maps are used to study the evolution of crack front tunneling during the initial stage of the fracture process. Stable tearing initiates at mid-thickness followed by a crack front tunneling process to a depth of approximately 2 mm. A brief discussion of the basis of the fracture process reconstruction method is provided and comments on the general utility of microtopographic fracture surface examination for general assessment of elastic-plastic and fully-plastic fracture processes are made.

KEYWORDS: fracture surface microtopography, CTOA, crack tunneling, ductile fracture, stable tearing, fracture process reconstruction, 2024-T3 aluminum sheet.

[a] Engineering Research Specialist, E-mail: qrl@inel.gov, Idaho National Engineering Laboratory, P.O. Box 1625, Mail Stop 2218, Idaho Falls, ID 83415-2218 USA

[b] Senior Scientist, NASA - Langley Research Center, Mechanics & Materials Branch. MS 188E, Hampton, VA 23681-0001 USA.

Copyright© 1995 by ASTM International www.astm.org

INTRODUCTION

Advanced methodologies are being developed for the prediction of residual strength of aircraft fuselage structures. Crack tip opening angle (CTOA) has been proposed as a local fracture criterion for thin sheet aluminum [1]. Prior to incorporating this fracture criterion into advanced shell-code finite element analyses for fuselage skin, detailed characterization of CTOA during stable tearing is required.

Background

Optical microscopy and digital image correlation techniques have been used to characterize the critical CTOA at the outer surface as a function of stable tearing crack length (Δa_s, subscript s denotes an outer surface measurement) in 2024-T3 sheet [2, 3]. Results of tests conducted in the transverse-longitudinal (T-L) orientation in Figure 1 show that CTOA exhibits a transient behavior during the initial stage of stable tearing. CTOA decreases from 17 deg., at small surface crack lengths Δa_s, to a steady state level of 4.7 deg. for $\Delta a_s > 2$ mm. A similar transient behavior and a steady state CTOA of 6.0 deg. was observed for longitudinal-transverse (L-T) crack growth in 2024-T3 sheet.

Fractographic studies were also conducted to characterize the tunneling behavior during stable tearing in the T-L and L-T orientations [2,3]. Many tests were conducted to generate a series of specimens, each having a different amount of ductile tearing. The fracture surface of each specimen was characterized using scanning electron microscopy (SEM), revealing the crack front geometry at different crack lengths. From this extensive study, it was shown that the crack front geometry varies during the initial onset of crack growth ($\Delta a_s < 2$ mm); cracks initiate near mid-thickness and typically obtain a stable tunneled geometry at Δa_s of nearly 2 mm.[a]

Prior studies have used outer surface measurement techniques to characterize CTOA and laborious SEM based fractographic methods to characterize crack front tunneling behavior. From these studies, no experimental data was available concerning the through-thickness variation of CTOA. The objective of this work is to

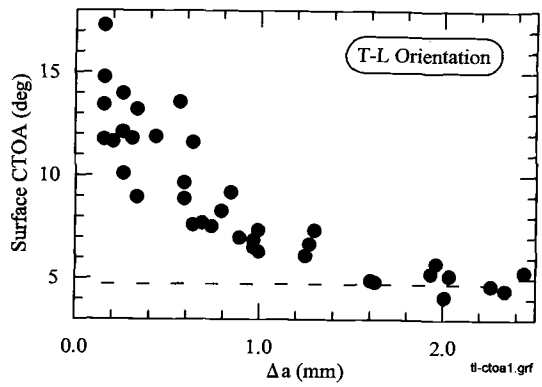


Figure 1 -- CTOA versus crack extension as measured on the surface of 2024-T3 M(T) specimens having T-L orientation.

[a] tunneling - crack extends more in the central area of the specimen thickness (mid-thickness) than at the surfaces, producing a curved crack front.

develop an understanding of through-thickness CTOA behavior and to show that crack front geometry characterization can be performed using microtopographic-based reconstruction techniques.

EXPERIMENTAL PROCEDURE

Specimen Geometry and Crack Growth

Fracture tests were conducted on two 2024-T3 alloy middle crack tension [M(T)] specimens, 76.2 mm wide (2W) and 2.23 mm thick (t), shown in Figure 2. Tests were performed using a servohydraulic test machine and fixed-end-wedge-type grip loading conditions. Each specimen (one T-L, one L-T orientation) was fatigue precracked at a

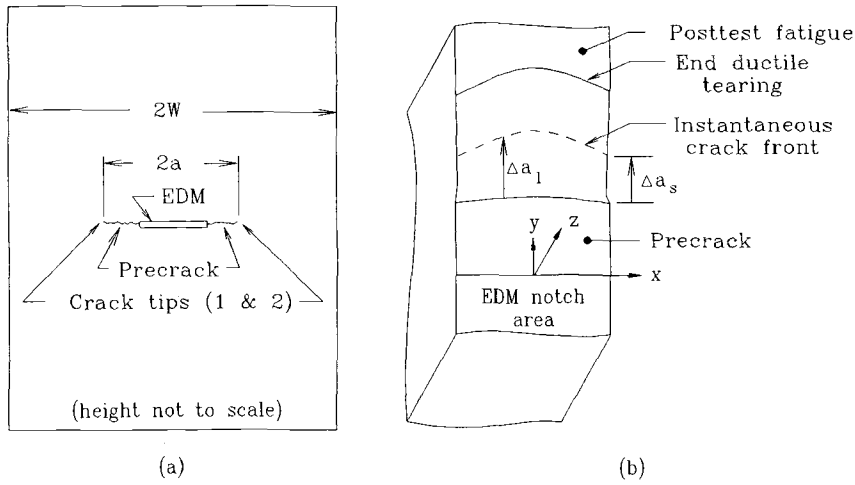


Figure 2 -- Geometry of the M(T) specimen and typical fracture surface details.

constant stress amplitude of 34.5 MPa and a stress ratio, R (= S_{max}/S_{min}), of 0.2 until a total crack length (a) of 25.4 mm (a/W = 0.33) was achieved. Following the initial fatigue crack growth, the stable tearing test was conducted using displacement control. Stable tearing of the T-L specimen was stopped at $\Delta a_s \approx 0.50$ mm with a maximum applied stress of 211 MPa. The end of the stable tearing crack growth region was marked with additional fatigue cycling (posttest fatigue) under load control (σ_{max} = 168 MPa, R = 0.8; posttest fatigue crack as shown in Figure 2). The high R fatigue crack growth was continued until the specimen was broken, exposing a uniquely marked fracture surface that clearly outlined the stable crack growth region. The L-T specimen was prepared and tested in a similar manner to the T-L specimen. Displacement controlled stable tearing of the L-T specimen was stopped after $\Delta a_s \approx 1.6$ mm (see Figure 2) at a maximum stress of

235 MPa. The extent of stable tearing was then marked by posttest fatigue cycles at σ_{max} = 200 MPa with R = 0.8.

Fracture Surface Topographic Data Collection

Fracture surface data (topographic height data) were collected by both the Idaho National Engineering Laboratory (INEL) and NASA Langley Research Center (NASA LaRC) using independent methods described below. INEL performed microtopography analysis on the L-T specimen and NASA LaRC analyzed the T-L specimen. Various computer programs were used to analyze the height data and generate the fracture process characterization, including crack tip opening displacement (CTOD), CTOA, and instantaneous extension (crack front shapes) as a function of through-

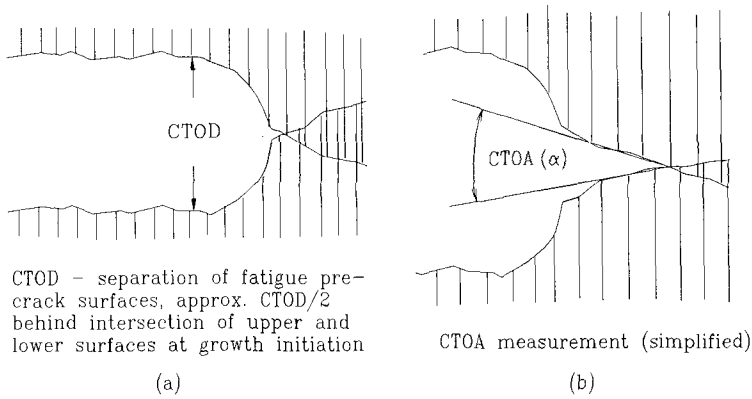


Figure 3 -- A schematic representation of the crack profile showing CTOD at initiation and CTOA for some amount of ductile tearing.

thickness position. These parameters are illustrated schematically in Figures 2 and 3. Note that CTOD is defined as the separation of the precrack surfaces when initiation of growth from the blunted crack tip is detected. This is essentially equivalent to the common definition of the intersection of lines of a 90 deg. included angle with the opening profile, with the vertex of the lines at the center of the blunted crack tip. CTOA is shown in simplified form in Figure 3.

INEL System -- The INEL-developed system (MICTOP) uses optical triangulation to measure relative surface heights on the fracture surfaces. These data are further processed using various commercial software packages to provide the CTOD, CTOA, and crack front shape distributions.

System hardware was assembled from commercially available components. Computer-controlled X-Y stages[a] were used for specimen positioning below the height

[a] Parker-Daedal Motion Control Systems

measuring head.[a] These stages allow spatial resolutions of 5-10 μm over a 100 x 150 mm range. A height measuring sensor head system (point range sensor, or PRS) collects fracture surface height data using a focused laser diode beam spot, fixed optical elements, a 24 x 512 CCD array, and optical triangulation algorithms coded in firmware. Various PRS heads are available with height resolutions from less than 1 to over 25 μm, with measurement ranges about 450 times the measurement sensitivity. Height measurements are accurate down to surface features as small as 5 μm diameter. Verification trials on calibration samples have been performed to determine the data accuracy of the MICTOP system. They showed typical fracture surface height measurement repeatability within ±1.5 to 2.5 μm. The height data obtained with the system is manipulated using both commercially-available software packages (sorting and graphing) and software developed specifically for fracture process analysis (surface height inversion, axis flips, and data filtering). Analysis of the data allow for the determination of CTOD, CTOA, and instantaneous crack front position in the plane of the crack.

NASA LaRC System -- A confocal scanning laser microscope[b] was used for all topographic measurements. The laser-based system is capable of performing accurate non-contact profilometry on fracture surfaces. The computer based topographic system is capable of a measurement resolution of 0.5 μm and a repeatability of 0.05 μm in the x, y and z directions.

The system uses a commercially available software[c] that controls microscope scanning functions over selected areas (x, y translations). The software processes the digital topographic (height -z) data. Several routines can be used to smooth the laser determined height measurements by averaging anomalous data (spikes) produced by specularly reflecting surfaces at steep angles. An iterative procedure is used to construct a three dimensional fracture surface topographic map representative of the true fracture surface. Repeated matching (registration) of the paired (upper and lower) fracture surfaces, and three-dimensional constructions of conjugate fracture surfaces is performed by comparing microstructural features in selected regions with SEM fractographic characterizations. Once the exact digital reconstruction is accomplished, further analysis is performed using various techniques, i.e., area projection mapping and profile section views. These reconstructions of the fracture surface provide through-thickness CTOA distributions and crack front geometry characterizations detailed in the RESULTS section.

Fracture Process Reconstruction by Topographic Data Analysis

The reconstruction process relies on the irreversible plasticity that occurred during the fracture process to "lock in" the details for later retrieval. In theory, some irreversible deformation occurs in all fracture events. However, from a practical aspect, moderate

---

[a] Cyberoptics Corp. PRS system.

[b] Nikon Inc. / Lasertec Model 1LM21w .

[c] see Kobayashi and Shockey [4,5].

amounts of plastic deformation during fracture are required to be able to extract a usable reconstruction of the process.

The reconstruction technique is represented in Figure 4. Shown in Figure 4a are the upper and lower surface profiles prior to collapsing the conjugate surfaces. The **initial**

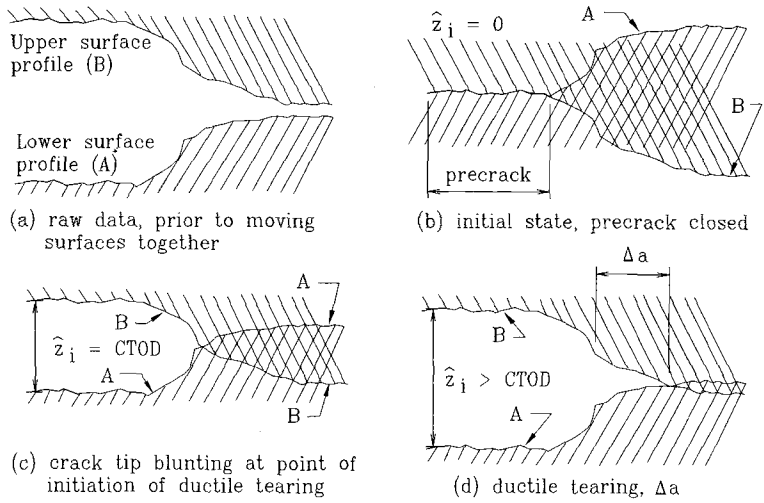


Figure 4 -- A representation of the fracture process reconstruction technique.

state, shown in Figure 4b, is defined by making a zero separation between the fatigue precrack surfaces. By incrementally separating the two surfaces in a direction parallel to the global loading vector, the kinematics of the fracture process are revealed. Any **instantaneous state** (Figures 4c and 4d) is then described by the global opening increment, $\hat{z}_i$, equal to the separation of the fatigue precrack surface. For the present case of symmetric Mode I loading of a symmetric geometry, $\hat{z}_i$ completely defines the instantaneous state. The local crack opening is then available as a function of position, $z_i(x_j, y_j)$. Positive opening values are seen in areas where the crack surfaces have separated, e.g. the white areas shown in the fracture surface projections in Figure 5 and open portions of Figure 4. The loci of $z_i(x, y) = 0$ indicate the instantaneous crack front position (crack border, boundary between white and black in Figure 5). Areas of negative height difference (crosshatch regions in Figure 4, black regions in Figure 5) are still connected. The negative height difference (virtual material overlap) is a result of the plastic deformation that occurs during the fracture process, after the indicated state. The resultant three-dimensional data set then contains all information about the kinematics of the fracture process.

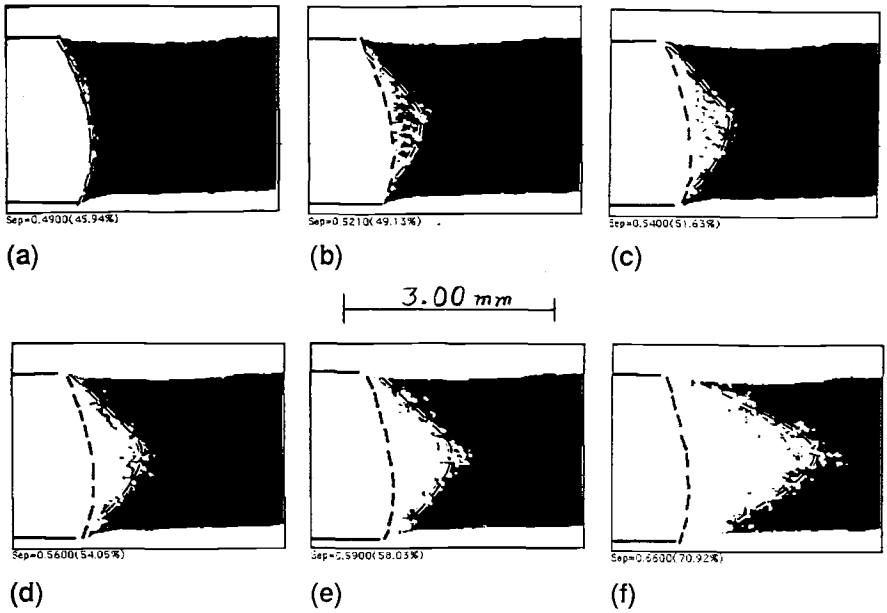


Figure 5 -- Fracture surface projection (plan view) of T-L fracture surface showing the initial fatigue crack front in (a) and the progression of the stable tearing crack front in (b)-(f).

RESULTS

Crack Front Shape Evolution (Tunneling)

T-L Orientation -- The micrograph in Figure 6 shows the stable tearing flat fracture surface of the T-L orientation. The small arrows in Figure 6a signify the direction of crack propagation and mark the border between the transgranular fatigue precrack and ductile tearing. The dashed line in Figure 6a outlines the tunneled stable tearing region and marks the transition from ductile fracture to high R transgranular fatigue crack growth which is easily seen at a higher magnification. The distance L noted in Figure 6a marks the ductile tearing crack length (Δa_s = 0.48 mm) at the outside surface of the specimen. The ductile tearing crack extension at mid-thickness (Δa_{mid}) was found to be approximately 2.0 mm.

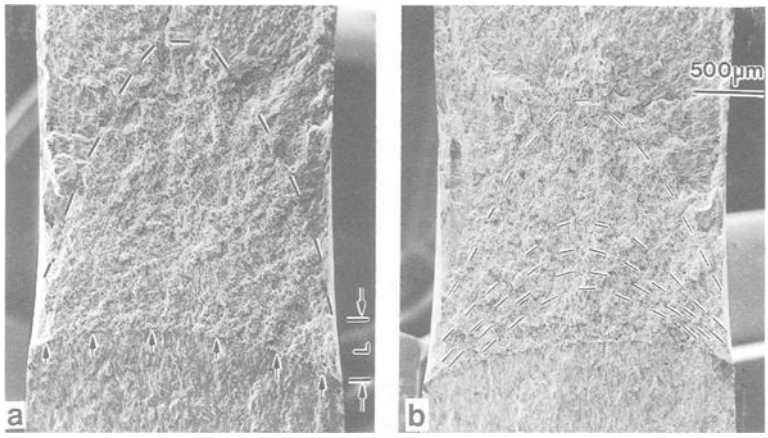


Figure 6 -- SEM micrographs of conjugate fracture surfaces of a T-L specimen, showing precrack boundary and extent of ductile tearing (a) and positions of instantaneous crack front position during stable tearing (b).

The dashed lines in Figure 6b mark the instantaneous crack front profile positions as determined from the microtopography reconstruction shown in Figures 5b-5f. The fracture surface area projection plots, illustrated in Figure 5, were constructed from conjugate fracture surface height difference maps generated from the T-L specimen height data. The projection maps were then produced by separating (digitally) the two conjugate surfaces until the region of crack growth (surface separation) was observed, similar to that depicted in Figure 3. The sequence of six projection plots in Figure 5 are for increasing fracture surface separations, i.e., increased crack opening displacement (COD, $\hat{z}_i$), and show the crack growth associated with the increments of COD. The images illustrate the evolution of tunneled crack front geometry for an crack advancing in the longitudinal direction. The first evidence of ductile crack extension from the fatigue precrack is noted in the middle half of the specimen thickness. The crack propagates with an increasingly curved front as illustrated by the increase in white regions in Figures 5b-5f. The crack front profiles shown in Figure 5 are identical to those produced by the fractographic method [2,3]. The isolated black regions (islands) observed in the fracture projection map (Figure 5) could result from a combination of the following, (1) connected ligaments of highly strained material in the wake of the advancing crack, (2) near vertical surfaces produce limited laser reflection, resulting in anomalous height measurement, i.e. no data, and (3) areas where spatial (x and/or y) registration of the mating surfaces is not maintained[a]. Macroscopic measurements were performed here to obtain the general crack

[a] e.g., due to asymmetric lateral deformation associated with the slant fracture zones, where separation distance is not being assessed between true mating surface locations (erroneous separation values).

front tunneling behavior during stable tearing. Further research, at higher magnification, will be required to resolve the black islands observed in Figure 5.

L-T Orientation -- The L-T orientation exhibited a high degree of slant fracture as shown by the three-dimensional topographic map in Figure 7. The large shear lips formed along both sides of the specimen and grew increasingly larger during the stable tearing process. Microtopography analysis of this specimen revealed an increase in lateral (x-direction) misalignment with increased crack length (y-direction) or as the shear lips grow larger. This suggests some component of Mode III (antisymmetric shear) deformation associated with large amounts of slant fracture. This made accurate registration of the two surfaces in the deep slant fracture region (near surface, moderate crack extension) extremely difficult. A systematic approach to solve this registration problem is being developed. Accurate microtopography results were obtained over the entire flat fracture region of this specimen where lateral misalignment was not observed.

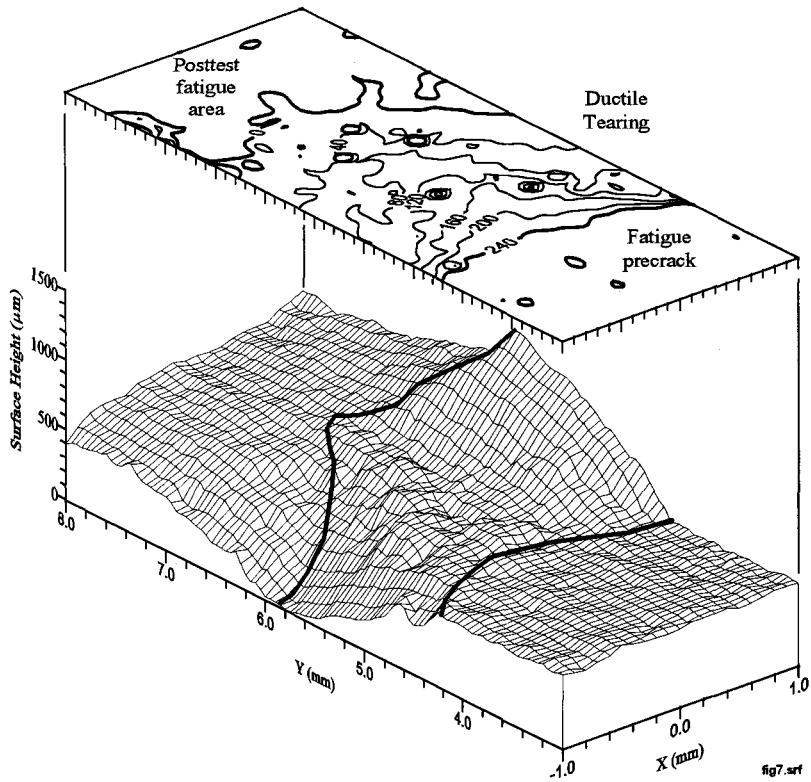


Figure 7 -- Surface net plot of L-T fracture surface with precrack boundary and ductile crack growth extent shown (lower), and contour plot of crack opening separation showing instantaneous crack front positions (upper).

The top projection in Figure 7 is a detailed elevation (contour) map showing the instantaneous crack front profile position at various amounts of crack opening. The contour lines represent surface separation ($\hat{z}_i$) intervals of 40 μm. By tracing a constant separation distance contour, the crack front is outlined for a given crack opening. The 200 μm, 180 μm, and 160 μm contour lines exhibit a tunneling profile for the region of crack growth dominated by flat fracture. At longer stable tearing crack lengths (Δa_{mid} = 1.5 mm to 2.5 mm corresponding to Y= 5.6 mm to 6.6 mm, respectively), the contour lines exhibit less overall curvature, suggesting less crack front tunneling with the onset of 45 deg slant crack growth. These results are consistent with fractographic observations of stable tearing crack profiles for the L-T orientation [2,3].

Crack Tip Opening Angle

The principle focus of this work is to measure the internal CTOA (away from exterior surfaces) as a function of through-thickness position during the initial stages of ductile crack extension. CTOA can be visualized by viewing profile sections through the two conjugate fracture surfaces as depicted in Figure 3. Both INEL and NASA LaRC methods for determining CTOA are similar; both use an averaging technique over a length scale range of "y" behind the chosen crack tip position. Care must be exercised in selecting the length scale. If chosen too small, the analysis of CTOA (a macro-scale parameter) will be excessively influenced by local strains, resulting in anomalous fluctuations in the measured CTOA. Unusually large length scales may obscure true variations in the CTOA, since a straight line fit (one slope angle) is being used during the analyses. The analysis length scale must be chosen based on some knowledge of the fracture process, and the intended use of the CTOA values to be determined.

T-L Orientation -- A profile section view of the crack at mid-thickness (x = 0) is shown in Figure 8. It should be noted that the vertical axis in Figure 8 has been expanded by a

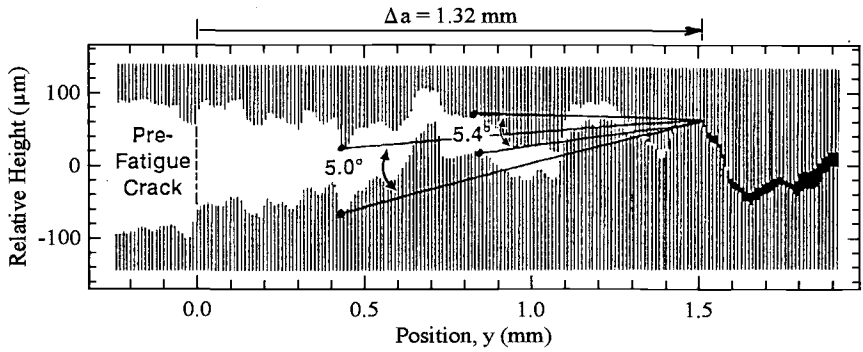


Figure 8 -- Crack opening profile of T-L specimen at mid-thickness, after 1.3 mm of ductile crack extension. End of precrack/start of ductile tearing (dash line) and two measurements of CTOA (solid lines) are shown.

factor of 2 relative to the horizontal axis. The illustrated state shown in Figure 8 corresponds to a local Δa_{mid} = 1.32 mm with two CTOA measurements of 5.0 and 5.4 deg shown. The solid lines shown extend from the measurement position on the fracture surfaces behind the crack tip, to the instantaneous tip position. For a given Δa, an average CTOA was determined by averaging a minimum of seven such measurements, over a distance of 0.5 mm to 1.5 mm (1 mm length scale) behind the instantaneous crack tip position. This method is identical to that used by others for surface CTOA measurements [2,3].

CTOA measured in this way and corresponding Δa results are plotted versus through-thickness position (x) for the T-L specimen orientation in Figure 9. Figure 9a shows the through-thickness tunneled crack front behavior and the corresponding CTOA results for Δa_s = 0.48 mm. Here, CTOA ranges form 8.2 deg. and 9.1 deg. at the outer surfaces, x = 1.12 mm and -1.12 mm, respectively, to 4.2 deg at the interior (x = -0.17 mm). The microtopography results (8.2 deg. and 9.1 deg.) compare well with an optical surface CTOA measurement of 8.8 deg performed on this specimen at Δa_s = 0.48 mm. It should be noted that surface optical measurements of CTOA were performed here using procedures identical to those reported elsewhere [2]. Knowing that interior crack front shape and CTOA behavior is nearly symmetrical about the mid-thickness, later microtopography analysis (Figure 9b) were only performed on half-thickness. Figure 9b shows that microtopography based measurements of CTOA at Δa_s = 0.39 mm. CTOA varies from 4.6 deg. at x = 0 mm to 13.6 deg. near the surface. (Optical measurement at Δa_s = 0.39 mm revealed a surface CTOA of 13.6 deg.). A comparison

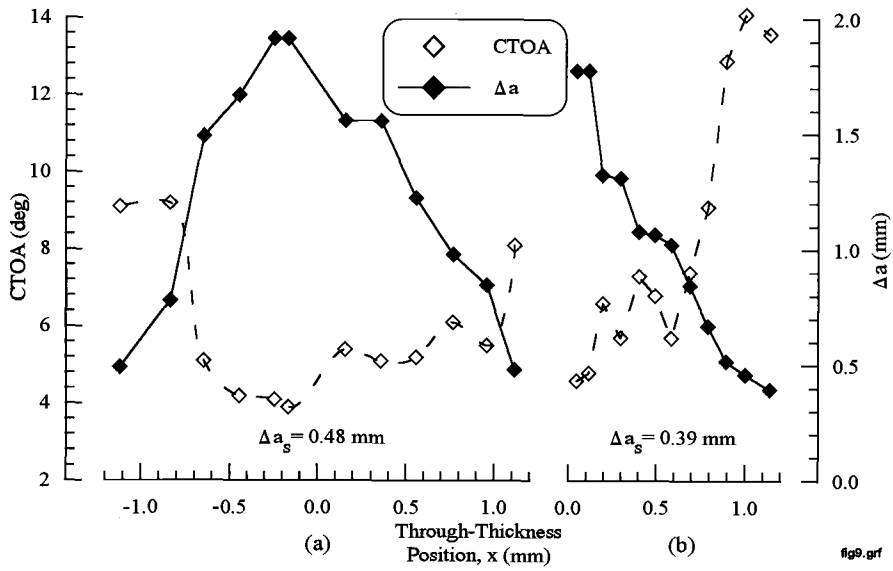


Figure 9 -- Through-thickness variation of CTOA and corresponding Δa (crack front shape) for T-L orientation at (a) Δa_s = 0.48 and (b) Δa_s = 0.39 mm.

of the results in Figs. 9a and 9b suggests that both interior and surface CTOA increases with shorter Δa. A plot of CTOA versus Δa in Figure 10 shows this transient behavior during the initial phase of stable tearing from a single L-T specimen. The triangle data points in Figure 10 represent microtopography-based CTOA data at mid-thickness and the squres are optical measurement of CTOA at the surface. The Δa values correspond to the instantaneous values at the data position. These data suggest that CTOA decreases to a constant level at longer Δa , similar to that shown in Figure 1. These results also show that mid-thickness CTOA possibly reaches a steady state value very near to that obtained from the surface measurements (4.7 deg. shown in Figure 1).variations in the CTOA, since a straight line fit (one slope angle) is being used during the analyses. The analysis length scale must be chosen based on some knowledge of the fracture process, and the intended use of the CTOA values to be determined.

T-L Orientation -- A profile section view of the crack at mid-thickness (x = 0) is shown in Figure 8. It should be noted that the vertical axis in Figure 8 has been expanded by a factor of 2 relative to the horizontal axis. The illustrated state shown in Figure 8 corresponds to a local Δa_{mid} = 1.32 mm with two local measurements of 5.0 and 5.4 deg shown. For a given Δa, an average CTOA was determined by averaging a minimum of seven local measurements, similar to those shown in Figure 8, over a distance of 0.5 mm to 1.5 mm (1 mm length scale) behind the instantaneous crack tip position. The indicated lines extend from the measurement position on the fracture surfaces behind the crack tip, to the instantaneous tip position. This method is identical to that used by others for surface CTOA measurements [2,3].

L-T Orientation -- For the L-T orientation, local CTOA is determined by performing a least squares linear regression on the fracture surface separation data. Any through-thickness position (any "x" scan line) can be selected. Interpolation to intermediate points is also possible, but accuracy may suffer depending on the character of the fracture surface. Selecting a position "y" determines the local instantaneous crack extension. A suitable length scale over which the regression analysis is performed is chosen, as described earlier.

Figure 11 shows an orthographic view of the crack opening (full separation distance), Δz, versus position (x and y) for crack tip #1 of the L-T specimen.

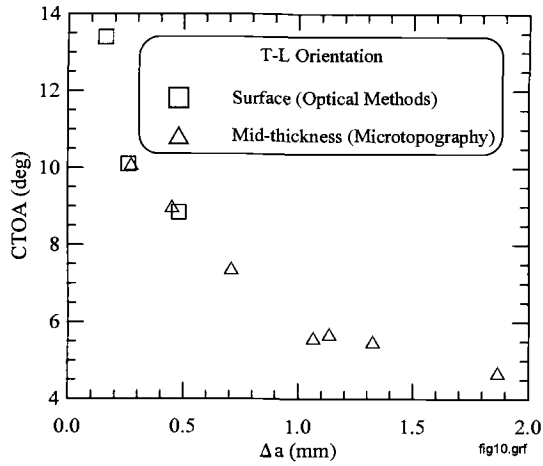


Figure 10 -- CTOA versus Δa showing transient behavior of CTOA during initial crack growth.

This may be viewed as an idealized opening profile, since it does not reveal the z variations due to slant fracture or general vertical "wandering" of the crack plane. The actual crack profile at mid-thickness (x = 0) is shown in Figure 12, where the position, y = 0, corresponds to the beginning of the fatigue precrack, not the beginning of ductile crack extension. The fatigue precrack, identifiable by a mean opening angle of 0, ends at position, y = 4.3 mm. This is shown in Figure 13, that represents the same mid-thickness data. The tip blunting zone (or stretch zone; characterized by a large local opening angle based on a small length scale) extends (locally) between 0.05 and 0.10 mm (data resolution limited), to 4.4 mm. This is followed by ductile fracture to y ≈ 6.8 mm (Δa_{local} = 2.4 mm). The damage zone makes the exact extent hard to determine. The posttest fatigue crack (mean opening angle of 0) extends from that point forward.

In the stable tearing region, y = 4.4 to 6.8 mm, the CTOA varies from 7.0 to 4.5 deg, respectively, depending on the chosen length scale and crack extension amount (reference position). Using a length scale of about 1 mm yields two zones of essentially constant CTOA of about 6 deg. and 5 deg., each over about 1 mm of crack extension. The apparent transition from 6 deg. to 5 deg. occurs between y = 5.4 and 5.8 mm. Whether there is a gradual transition, a localized transition, or no transition is a bit subjective, and is strongly dependent on the length scale used for analysis. Similar data were obtained from the same specimen at mid-thickness of the other crack tip (#2) and yielded a mean CTOA of 5.2 deg.

The significance of the length scale issue can be seen by viewing the local height

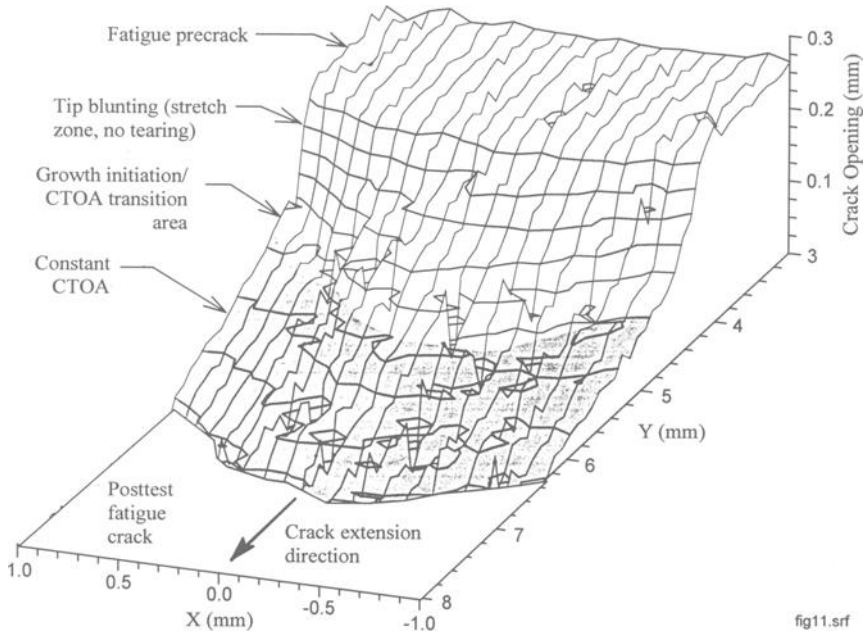


Figure 11 -- Surface separation distribution of L-T specimen showing: fatigue precrack; tip blunting; initiation/CTOD transition area; and zone of constant CTOA.

variation (roughness) of the opening profile shown in Figure 12. About half of this amplitude (≈10 μm) is due to local fracture process (dimple rupture), and does not relate to systematic data error (noise). The MICTOP system noise level has been examined using calibration specimens and elastic fatigue cracked surfaces. Deviations were found to be less than ±5 μm. Much of the locally (<0.1 mm) jagged nature of the opening is due to the actual fracture process, a combination of local shear (sliding off) and local void growth and coalescence (dimple rupture). This 0.1 mm process size scale is smaller than the 0.5 to 1.0 mm (or larger) size scale where the CTOA is considered a useful fracture characterization parameter.

These results from mid-thickness correlate with the outer surface data presented in Dawicke and Sutton [2] for the steady-state condition beyond about 1 mm of local crack extension. However, the larger CTOA at the onset of stable tearing crack extension was not seen at mid-thickness. This is likely the result of higher constraint at the mid-thickness position, that restricts the plastic deformation prior to and immediately after crack initiation. This type of behavior has been seen in many other ductile fracture specimens investigated at INEL.

The tunneling profiles, shown in Figure 7, obtained from the single specimen MICTOP analysis are almost identical to those shown by Dawicke and Sutton [2] that were obtained from multiple specimens stopped at various extents of ductile tearing crack extension. This comparison shows the value of the microtopography technique, with its ability to determine the whole three-dimensional fracture process from a single test specimen.

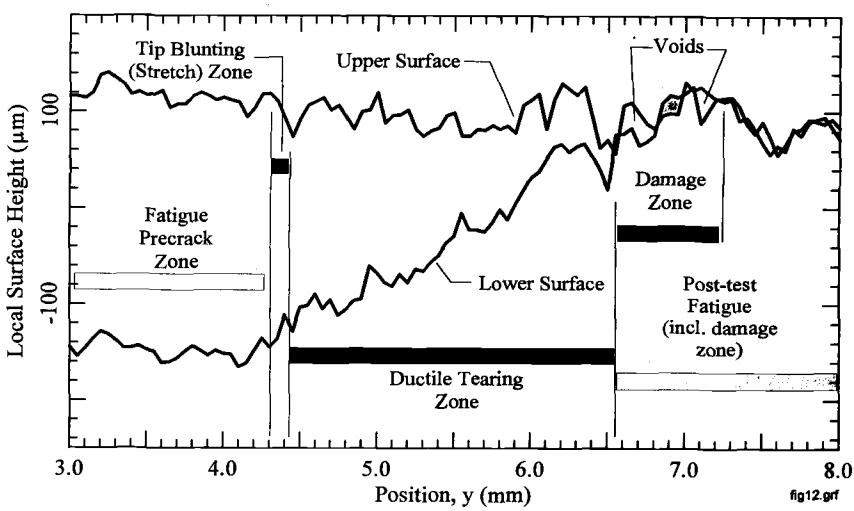


Figure 12 -- Actual crack opening profile (surface height scale expanded 8x) of L-T specimen at mid-thickness showing process areas and surface roughness.

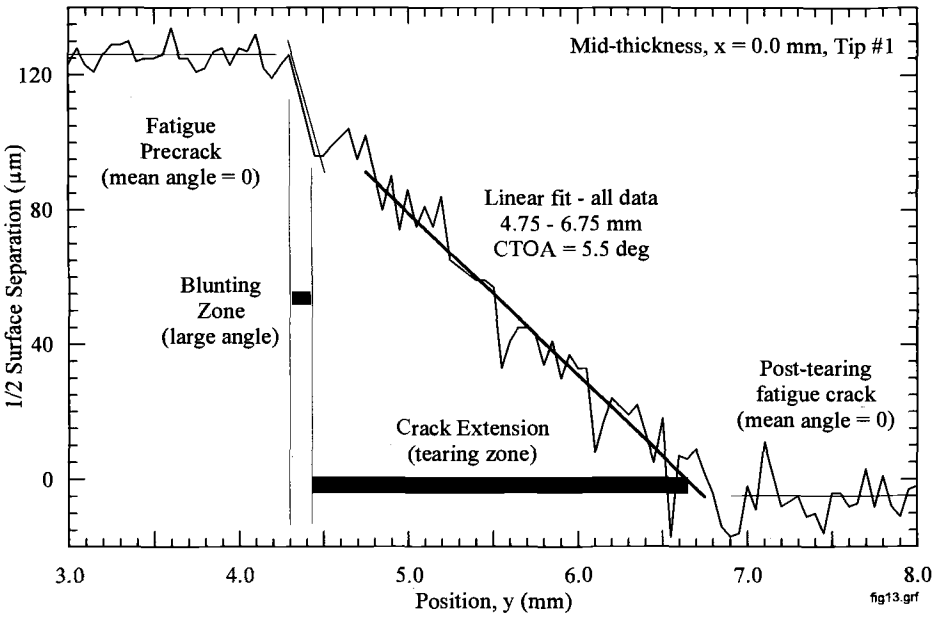


Figure 13 -- Surface separation of an L-T specimen (same as shown in Fig. 12) revealing "idealized" profile. Various fracture process zones are indicated.

CONCLUSIONS

M(T) fracture specimens from 2024-T3 aluminum sheet material in both T-L and L-T orientations were studied. The through-thickness characteristics of early stage stable tearing ($\Delta a < 2$ mm) have been investigated using two independent microtopographic examination and analysis systems. From the results presented, the following conclusions may be made:

1. For $\Delta a \leq 2$ mm, the crack tip opening angle:
   (a) exhibits a transient behavior with elevated values at initiation, with larger initial values at the surface than in the specimen interior;
   (b) decreases along the tunneled crack front (with increasing Δa and increasing distance from the free surface), reaching a minimum at near mid-thickness; and
   (c) approaches a steady state, constant single value across the entire crack front.

2. Microtopographic data collection and fracture process reconstruction show that near-surface CTOA are comparable to optical microscopy-based and digital image

correlation-based surface CTOA measurements, thus validating the previous surface CTOA measurements by an independent method.

3. Microtopographic fracture surface analysis is capable of characterizing the kinematic evolution of ductile crack extension in single specimens. This obviously saves time and requires less material, while providing a more complete description of the ductile fracture process.

REFERENCES

1. Newman, J.C., Jr., Dawicke, D.S., Sutton, M.A. and Bigelow, C.A., *Proceedings: ICAF 17th Symposium*, Stockholm, Sweden, June 9-11, 1993.

2. Dawicke, D.S. and Sutton, M.A., Crack-Tip-Opening Angle Measurements and Crack Tunneling Under Stable Tearing in Thin Sheet 2024-T3 Aluminum Alloy, **NASA CR-191523**, 1993.

3. Sutton, M.A., Dawicke, D.S., and Newman, J.C., Jr., "Orientation Effects On The Measurement And Analysis Of Critical CTOA In An Aluminum Alloy Sheet", *Fracture Mechanics: 26th Volume, ASTM STP 1256*, Walter G. Reuter, John H. Underwood, and James C. Newman, Jr., Eds., American Society for Testing and Materials, Philadelphia, 1995.

4. Kobayashi, T. and Shockey, D.A., *J. of Adv. Mat'ls. and Proc.*, **140**(5), pp. 28-34, 1991.

Weldments

Christophe Eripret,[1] *Christian Franco,*[2] *and Philippe Gilles*[2]

On the Effect of Mismatching on Structural Resistance of Welds

REFERENCE: Eripret, C., Franco, C., and Gilles, P., **"On the Effect of Mismatching on Structural Resistance of Welds,"** *Fracture Mechanics: 26th Volume, ASTM STP 1256,* Walter G. Reuter, John H. Underwood, and James C. Newman, Jr., Eds., American Society for Testing and Materials, Philadelphia, 1995.

ABSTRACT: The usual fracture mechanics based concepts available to assess structural integrity have been developed for homogeneous structures. When considering cracks in welds, these methods assume that cracks are located in a material of uniform properties and neglect any difference of strain carrying capacity due to mismatching effects. The French Cracked Weld Research Programme (FCWRP, conducted by CEA, EDF, and FRAMATOME) has been in progress for the last three years to investigate how the effects of weld metal mismatch may affect structural resistance of welded structures. This paper gives an overview of the conclusions and results drawn from this program.

KEYWORDS: fracture mechanics, welds, mismatch, structural integrity, constraint effect, ductile tearing

Investigating structural resistance of piping welds is of major importance for nuclear or offshore industry. Cracks are more likely to appear in welds, due to manufacturing processes (hot or cold cracking, homogeneity defect) or welding technology (sensitivity of stainless steels to integranular corrosion, for instance). In order to ensure structural integrity of welded components, recommendations are made but they may be difficult to satisfy: tensile properties or toughness properties of welds are sometimes lower than those of the parent material. Although, these mechanical properties heterogenity of parent material, weld metal, and heat affected zone (HAZ) are generally not considered in current fracture mechanics-based assessment procedures. The integrity assessment methods have been developed for homogeneous structures, and they assume that any present or postulated crack is located in a material of uniform tensile and toughness properties. What are called the mismatch effects are not accounted for, which may lead to overconservatism or nonconservatism, in some circumstances, for integrity assessment procedures as well as for fracture mechanics testing.

This paper presents results and conclusions drawn from an important numerical program, which involved numerous and various detailed finite element analyses performed to investigate the significance of mismatch effects on structural resistance of welds. Mismatch is hereafter defined as the ratio of weld metal yield strength to base metal yield strength. Particular attention has been devoted to differences of mechanical behavior observed between welded structures and corresponding homogeneous structures (made up with parent material or weld metal). Mismatch effects on plasticity development pattern, limit load

[1]Mechanical engineer, Fracture Mechanics, Electricité de France (EDF), Research and Development Branch, Les Renardières, 77250 Ecuelles, France.

[2]Mechanical engineer and expert, respectively, Fracture Mechanics, FRAMATOME, Tour Fiat, Cedex 16, 92084 Paris-La-Défense, France.

Copyright © 1995 by ASTM International www.astm.org

analysis, and fracture resistance were focused to derive modifications of existing testing and assessment procedures.

The first part of this work is devoted to general considerations on plasticity development patterns in matched and mismatched structures. The second part gives estimation formulae for calculating limit load of mismatched structures based on a very simple slip line theory. The third part discusses the validity of the ASTM E 813-88 procedure to estimate toughness properties in mismatched structures. The fourth and fifth parts discuss the finite element analyses results obtained by the current ongoing program. The last and sixth part presents some comments about constraint effects in mismatched structures.

In the present paper, we shall only consider cracks located in the center of the weld metal. Studies on HAZ cracks are still under progress.

Comparison of Plasticity Development Pattern in Mismatched Welds and Homogeneous Structures

Integrity analyses for assessing the significance of cracks in mismatched welds postulate that the crack is located in a fictitious material of uniform tensile and toughness properties. For this homogeneous material, tensile properties of the weld metal are often considered when the crack is located in the middle of the weld seam.

For instance, in the case of overmatched welds [*1*] containing large cracks, it is assumed that this homogeneous material has the same mechanical properties as the weld metal. The stress is concentrated at the crack tip because of the large size of the crack, so yielding mainly occurs in the crack tip area. Plasticity is contained, and it can be reasonably assumed that the parent material has no influence on the welded structure resistance. However, for medium or shorter cracks in overmatched welds [*1,2*], another plastic zone may appear at the fusion line in the base metal right above the crack tip (Fig. 1). As long as loading is increasing, these two plastic zones grow until they join together, which may generate local unloading of the crack tip zone. In that case, it is not easy to determine which mechanical and toughness properties must be used for safety analyses, and one often chooses the lowest yield stress and the lowest toughness value of parent and weld metal. Lastly, when considering shallow cracks in very overmatched welds, it can be observed that plasticity only develops in the softer base metal. Because of its lower yield strength, the base metal acts

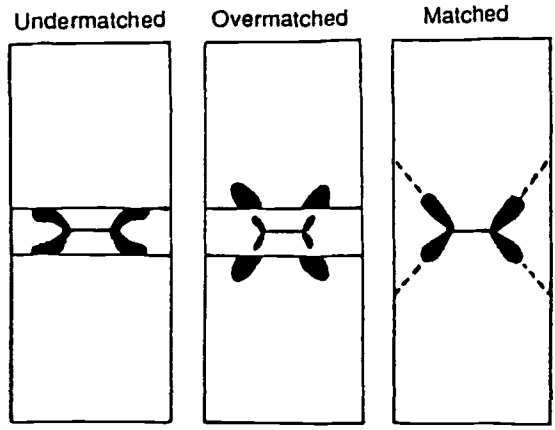


FIG. 1—*Comparison of plastic zone development pattern in an homogeneous center cracked pannel (CCP) and in mismatched CCP specimen.*

like a "fuse" and prevents plasticity from developing in the harder weld metal. Therefore, a crack located in the center of the weld may not be dangerous.

These different configurations and the parameters that control plasticity extension deserve to be investigated to better understand crack initiation in a welded component and to improve the accuracy of integrity assessment methods.

On the contrary, when considering undermatched welds [*3*], plasticity is concentrated mainly in the weld metal. The larger yield strength of the parent material prevents plasticity from spreading out of the weld, which may weaken the weld resistance to fracture. In that case, it can be expected that the weld metal toughness would be lower than that measured on a homogeneous specimen made entirely of weld metal due to the extreme concentration of plasticity in the weld metal [*4*]. The structural resistance of a strongly undermatched weld is very different from the structural resistance of a homogeneous structure. As far as the limit load of a welded structure is concerned, the development of the plastic zone will violate the classical slip line theory (Fig. 1) [*4*], and other types of stresses and strains concentration will play an important role. For instance, when considering short cracks in welds, a great mismatch may generate a strain singularity at the interface between base and weld metal due to differences of strain carrying capacities. Consequently, both limit load and structural resistance to fracture are affected.

Consequences for Limit Load Analyses

On the basis of the general trends presented previously, some conclusions can be drawn in connection with the structural behavior of mismatched welds. First, two different types of stresses/strains singularity must be considered when looking at the extension of plasticity in an heterogeneous structure. The first stress singularity is well-known and comes from the presence of the crack. The second one is a so-called "thorn singularity" and is due to the compatibility shear stresses at the interface between base and weld metal. Both have important consequences on the limit load of the welded structure, and two different regimes of plastic zone extension have been highlighted depending on which stress singularity is predominant.

As far as the crack tip area stress singularity is concerned, the important parameter that should be accounted for is the size of the plastic zone with regard to the weld seam width. Let us consider as a first step the center cracked panel configuration. Roughly, considering that the plastic zone at the crack tip as well as the slip-line network develop like in an homogeneous structure (Fig. 2), we can derive the expression of the limit load under plane strain conditions by separating the contribution of each material (that is, the weld metal (WM) until the plastic zone reaches the interface, and the base metal (BM) afterwards)

$$P(\text{inhomogeneous}) = 4/\sqrt{3}\,\sigma_y(\text{WM})\,h + 4/\sqrt{3}\,\sigma_y(\text{BM})\,(W\text{-}a\text{-}h) \tag{1}$$

As far as the interface stress singularity is concerned, the mechanical parameter that controls the plastic zone extension in the structure is the limit load of the uncracked base metal, which corresponds to the load at which large-scale yielding of the specimen arms will be obtained (gross scale yielding in the base metal). The expression of that limit load can be given by the following expression under plane strain conditions

$$P(\text{uncracked BM}) = 4/\sqrt{3}\,\sigma_y(\text{BM})\,W \tag{2}$$

Thus, different plasticity extension to that already described may be provided, whether the limit load of the uncracked base metal is larger or lower than the limit load of the cracked

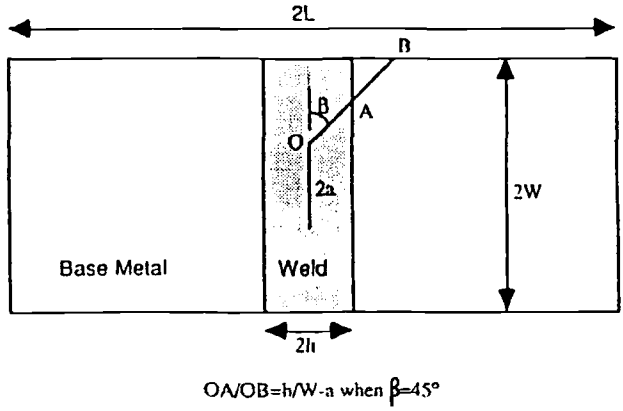


FIG. 2—*Slip-line model for plasticity development in an overmatched CCP specimen.*

mismatched structure. Those two different regimes of plasticity extension are featured on Fig. 3. They are obtained depending on the mismatch ratio and weld seam dimensions: if

$$\frac{\sigma_y(\mathrm{WM})h + \sigma_y(\mathrm{BM})(W\text{-}a\text{-}h)}{\sigma_y(\mathrm{BM})W} \geq 1 \tag{3a}$$

plasticity will follow feature (*a*)

(shallow crack configuration, that is, two plastic zones are developing at the same time in the structure)

if

$$\frac{\sigma_y(\mathrm{WM})h + \sigma_y(\mathrm{BM})(W\text{-}a\text{-}h)}{\sigma_y(\mathrm{BM})W} \leq 1 \tag{3b}$$

plasticity will follow feature (*b*)

(deep crack configuration, that is, one main plastic zone is developing like in homogeneous structures)

The former feature corresponds to a "shallow crack" plasticity extension, while the latter corresponds to a "deep crack" plasticity extension. The frontier between shallow and deep cracks is more difficult than ever to be given for mismatched structure. For homogeneous monomaterial structures, it is generally considered that shallow cracks are those which exhibits a different plasticity development pattern: this condition depends on specimen configuration and loading nature (that is, bending or tension). It depends also on the mismatch ratio for mismatched welds, which is quite obvious. Nevertheless, a geometrical parameter defined as the ratio of weld width upon ligament size, $h/(W\text{-}a)$, appears to play a very important role. This last parameter characterizes the role that the base metal will play on the overall behavior of the inhomogeneous structure.

In a second step, let us consider an overmatched three-point bend specimen. In that case, bending instead of tension makes for different plasticity and constraint. The global plasticity

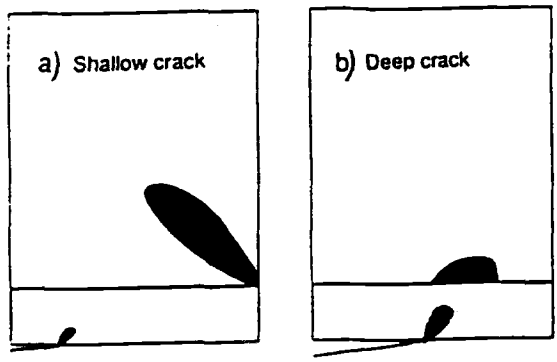


FIG. 3—*Different plasticity development pattern in a CCP specimen, corresponding to the shallow crack and deep crack configurations.*

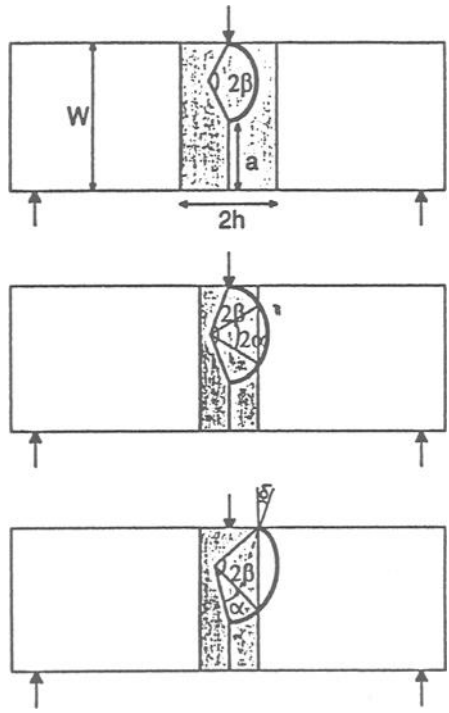


FIG. 4—*Slip-line model for plasticity development in an overmatched SENB specimen.*

development pattern in the cracked structure is always controlled by the same ratio of the limit load for the inhomogeneous cracked structure versus limit load for the uncracked base metal. The so-called mismatch effects will appear as soon as plasticity can no longer develop in a homogeneous structure, that is, when the plastic zone reaches the interface between base and weld metal. As presented in Ref *5*, let us consider that a circular slip line

model, as evidenced for homogeneous SENB specimens, is still valid to model plasticity development in the inhomogeneous cracked beam (Fig. 4). In that case, it has been shown that an upper bound estimate of the limit load could be given by

$$P(\text{inhomogeneous}) = (\beta - \alpha)/\beta\, P(\text{BM}) + \alpha/\beta\, P(\text{WM}) \tag{4}$$

where α represents the angular extent of the slip line mechanism outside of the weld seam, as indicated in Fig. 4. Its expression can be given by

$$\alpha = \text{Arc}\cos(\cos\beta + 2h/(W\text{-}a)\sin\beta) \tag{5}$$

The relevant values of β should minimize the dissipated energy, and have been solved numerically in Ref *5*.

By using this expression, it is possible to know whether the strain singularity that developed in the softer base metal will control plasticity development in the structure, or, on the opposite, if the stress and strain crack tip singularity will control the plastic zone extension. Therefore, we can distinguish two different features of plasticity development pattern:

if

$$\frac{\dfrac{\beta - \alpha}{\beta} P(\text{BM}) + \dfrac{\alpha}{\beta} P(\text{WM})}{P(\text{uncracked BM})} \geq 1 \tag{6a}$$

plasticity will follow feature (*c*)

(shallow crack configuration, that is, two plastic zones appear in the same time in the structure)

if

$$\frac{\dfrac{\beta - \alpha}{\beta} P(\text{BM}) + \dfrac{\alpha}{\beta} P(\text{WM})}{P(\text{uncracked BM})} \leq 1 \tag{6b}$$

plasticity will follow feature (*d*)

(deep crack configuration, that is, one main plastic zone is developing like in homogeneous structures)

Here again, feature (*c*) corresponds to a "shallow crack" plasticity extension, while feature (*d*) corresponds to a "deep crack" plasticity extension. It may be noticed that the frontier between shallow and deep cracks defined previously for bending is different than that for tension.

In the case of shallow crack configuration, the expression of limit load of the mismatched structure is affected by the fact that the assumed circular slip line does not come back into the weld metal (Fig. 5). A slightly different expression of the limit load can be proposed, always assuming a circular slip line development (Fig. 4), but which minimizes the role played by the weld metal. This second estimation formula can be given by

$$P(\text{inhomogeneous}) = (2\beta - \alpha)/2\beta\, P(\text{BM}) + \alpha/2\beta\, P(\text{WM}) \tag{7}$$

where

$$\alpha = \beta + \delta - \text{Arc cos}\,(\beta + \delta + 2h \sin\beta/(h^2 + (W\text{-}a)^2)^{1/2}) \tag{8}$$

and

$$\delta = \text{Arc tan}\,(h/W\text{-}a) \tag{9}$$

In the case of overmatching, this expression leads to lower limit load estimates than that proposed previously. Those values are in better agreement with plasticity extension pattern observed in experiments or modeled by finite element analyses (Fig. 5).

Thus we can roughly assume, on the basis of the simple slip line theory, that the global behavior of the mismatched SENB specimens is not affected by mismatch effects if the ratio $h/(W\text{-}a)$ is greater than 0.329, or merely ⅓. This condition ensures that plasticity will

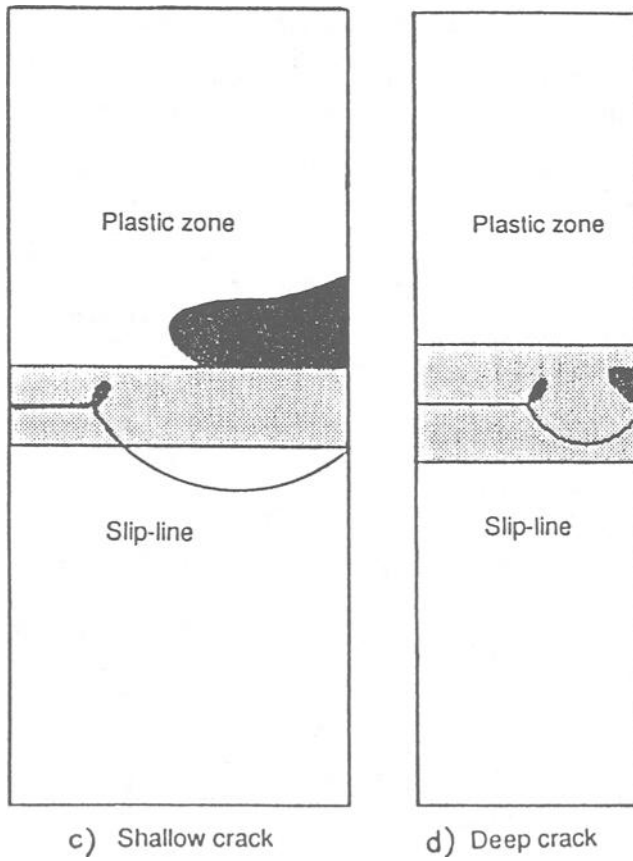


FIG. 5—*Equivalent strain isovalues in an overmatched SENB specimen obtained through finite element analyses.*

develop in the weld metal identically to what happens in a homogeneous weld metal specimen.

However, the frontier between short or deep cracks is somewhat different for tensile loading. On the basis of a straight 45° slip-line theory, we can draw the line for short cracks for $h/(W\text{-}a)$ values lower than 1, corresponding to a domain where plasticity extends out of the weld metal. Compared to bending loading, the plasticity development pattern for tensile loading gets the mismatching effects magnified. For the same crack size a/W, mismatching effects will be greater in a CCP specimen than in a SENB specimen. That means that the frontier between short cracks and deep cracks is related to the nature of loading.

Evolution of the Crack Driving Force J

Firstly, the computed J-value obtained for mismatched welds is plotted versus load and compared to the J-evolution that was calculated for homogeneous specimens. Two materials (marked A and B) have been considered in order to constitute the homogeneous and bimaterial specimens. Material B yield strength is about 3 times higher than that of material A. It can be seen on Fig. 6 that J-evolution for the overmatched weld (A-B-A) is quite different from that calculated for homogeneous specimens, while the undermatched weld (B-A-B) crack driving force is closer to that of material A. In fact, J-evolution for the mismatched weld is similar to that of the weld metal at low loads (that is, much lower than the limit load), until the plastic zone remains contained around the crack tip. When plasticity goes on developing, two different cases must be considered.

The first case corresponds to shallow cracks (that is, for a/W ratios less than or equal to 0.25). In that case, the stress and strain singularity at the crack tip seems to be less important than the strain concentration observed at the interface between base metal and weld metal. Large shear stresses are generated along the fusion line, due to differences of tensile properties of the materials involved. The weld metal which exhibits a higher yield strength prevents the softer and yielded base metal from necking. This point confirms the effect pointed out in Ref 2. These compatibility shear stresses weaken the structural resistance of the welded specimen and generate a strong triaxial stress state at the interface on both sides of the specimen. This phenomenon can be attributed to the difference of strain at a given

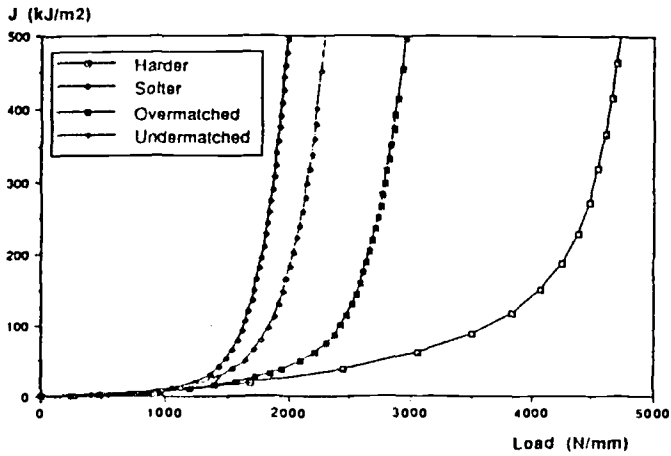


FIG. 6—*Evolution of the crack driving force in homogeneous and mismatched structures (SENB, 200% overmatching, 50% undermatching,* a/W = *0.25).*

stress, which generates another type of stress and strain singularity, so-called "thorn singularity," different from that observed at the crack tip, but which may be influent more on structural resistance for very high mismatch ratios and shallow cracks.

In terms of crack driving force, it has been observed that the deeper the crack, the closer evolution of the crack driving force to that of the homogeneous weld metal specimen. The mismatch effects on crack driving force can be described properly through a limit load analysis. For deep cracks contained in a large weld seam, plasticity will develop in the weld metal. Consequently, the limit load of the bimaterial specimen is rather identical to that of the homogeneous weld metal specimen. On the opposite side, as soon as the geometrical parameter $h/W\text{-}a$ decreases, the plastic zone spreads out of the weld into the softer base metal. Then, the limit load of the bimaterial specimen is lower than that of the homogeneous harder weld metal specimen (Fig. 6).

Accuracy of J-Estimation Procedures Based on the Area Under Load-Displacement Curve

For each specimen configuration we investigated, the crack driving force J was calculated numerically along different closed contours as well as evaluated through the standard ASTM E 813-88 procedure for SENB specimens, and through a procedure developed in Ref *6* for CCP specimen. Those two estimation schemes derive a global energetic J value from the load-load line displacement curve

$$J = J_{el} + J_{pl}, \text{where } J_{pl} = \frac{\eta_{pl} * A}{b * B} \tag{10}$$

where η_{pl} is equal to 1 for CCP specimens, A is corresponding to the plastic area under the load-load line displacement curve, b is the ligament, and B is the net thickness of the specimen.

A comparison between the calculated J-contour integral value and the energetic J-value (noted J-ASTM) derived from the load-load line displacement curve is plotted for SENB configuration in Fig. 7. The J-ASTM is not really a J-integral value but rather the amount of energy provided to the specimen, that includes the energy for crack initiation and propagation, but also the plastic strain energy which is dissipated in the structure, and in the present case in the base metal. This plastic strain energy does not propagate the crack and must not be included in the toughness value derived from the test. It may be concluded from those results that great care is needed when using an experimental assessment procedure based on the area under the load-load line displacement to determine toughness properties of strongly mismatched welded components. This experimental procedure is relevant to homogeneous structure testing, involving plastic zone extension limited to the crack tip area, but may not be adapted for mismatched welds.

Those estimation procedures include a certain amount of plastic strain energy dissipated in the softer base metal, which does not play any role in crack initiation. This energetic quantity can be considered as an "apparent toughness" of the structure, that is measured experimentally but which does not represent the real loading which the crack tip is subjected to [*4*]. Nevertheless, for deep cracks (that is, $h/(W\text{-}a)$ greater than 0.5), and for mismatch ratio ranging from 1 to 0.5, the standard ASTM E 813-88 procedure would provide good estimates of the crack driving force J if the potential energy is calculated from the area over the bimaterial load-versus load line displacement curve, and considering for mechanical properties the yield stress and Young's modulus of the weld metal [*4*].

When considering undermatched welds for which yielding is even more concentrated in

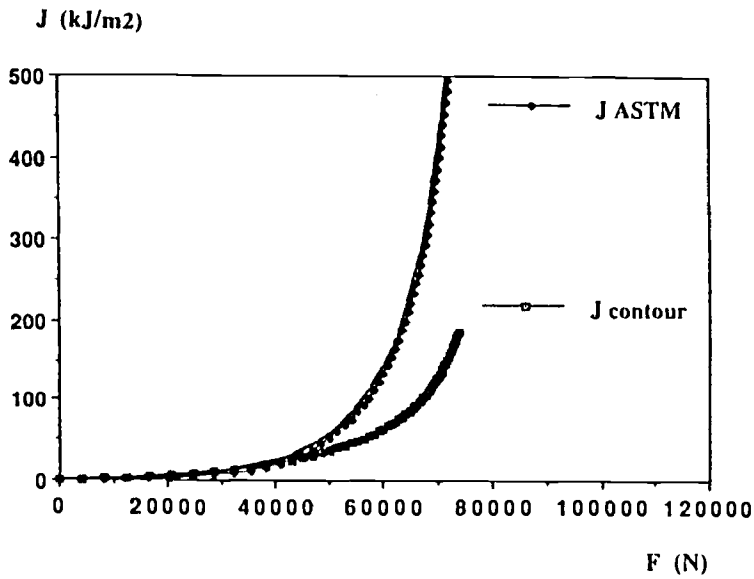


FIG. 7—*Comparison of calculated J-contour integral and estimated J-value (SENB, 200% overmatching,* a/W = *0.25).*

the crack tip area than in homogeneous structures. The important mismatch ratio prevents the plastic zone from extending out of the weld metal. Thus, as soon as the plastic wings achieves the fusion line, plasticity keeps on developing along the interface between parent material and weld metal. Therefore, the estimation procedure, which uses the area under the load-load line displacement and does not account for this concentration of plastic strain in the weld metal, underestimates the applied J-value. Moreover, the larger the crack size is, the more important is the underestimation. Nevertheless, for deep cracks (that is, $h/(W-a)$ greater than 0.5), and for mismatch ratio ranging from 1 to 0.5, the standard ASTM E 813-88 procedure would provide good estimates of the crack driving force J if the potential energy is calculated from the area under the bimaterial load-versus load line displacement curve, and considering for mechanical properties the yield stress and Young's modulus of the weld metal [*4*].

A New J-Estimation Scheme for Mismatched Structures: The Aramis Method

On the basis of those results, a new J-estimation scheme has been developed, trying to predict the global response of a welded structure (load versus load line displacement) as well as J-evolution at the tip of a crack located in the weld metal. Following the theoretical background exposed in Ref *8*, we tried to investigate the structural behavior of the overmatched CCP specimens through a limit load analysis, considering that the global response of the inhomogeneous component could be obtained by superimposing the global response of the uncracked structure and the contribution of the crack. The terms corresponding to the uncracked structure response are function of mechanical properties of both

materials, while those corresponding to the contribution of the crack are only function of the weld metal properties.

When applying this new estimation scheme to the flawed welded bodies, we assume, as in the engineering approach proposed by Kumar, German, and Shih [*8*], that the crack driving force J, the remote displacement corresponding to the applied load P, and lastly the crack tip opening displacement (CTOD) can be obtained by combining the elastic and fully plastic solutions. However, the difference with the original engineering approach consists of considering the contribution of both materials in the structure response, and introducing different limit loads that account for the extension of plasticity in each of the materials involved in the welded joint.

Thus, we also consider that the different materials involved can be characterized by a Ramberg-Osgood stress-strain relation that exhibits the linear elastic and the fully plastic terms.

For a given load, we assume that the remote displacement is given by

$$\Delta = \Delta^{e}_{nc} + \Delta^{pl}_{nc} + \Delta^{e}_{c} + \Delta^{pl}_{c} \tag{11}$$

where Δ^{e}_{nc} represents the elastic part of the remote displacement of the uncracked body, Δ^{pl}_{nc} represents the plastic part of the remote displacement of the uncracked body, Δ^{e}_{c} represents the elastic part of the remote displacement due to the presence of the crack, and Δ^{pl}_{c} represents the plastic part of the remote displacement due to the presence of the crack. The only difference with the standard EPRI estimation scheme developed for homogeneous structures is the use of the limit load of the mismatched structures, considering consequently the role played by each material to the overall response of the heterogeneous cracked body.

The limit load values of the inhomogeneous structures have been accurately estimated from the finite element analyses of overmatched CCP and SENB specimens in Ref *4*. The estimation formulae presented previously proved to provide good estimates, which differs from those obtained through finite element analyses by less than 5%.

As far as J-evolution as a function of applied load is concerned, we consider that the crack driving force J is controlled by the limit load of the inhomogeneous cracked body, which refers to the plasticity development pattern presented previously. However, one important point is that the J-evolution rate seems to be controlled by the weld metal properties (namely, hardening exponent of the weld metal) in all cases but where mismatch ratio is so high that plasticity develops like in a shallow crack configuration. In those exceptional cases, J is driven by the weld metal properties until the plastic zone developed at the crack tip reaches the interface between base and weld metal. However, as soon as the two plastic zones join together (the plastic zone spreads from weld metal into the base metal) it is the base metal properties that control J-evolution. This effect has been noticed when observing the evolution of the J plastic term, J_{p1}, as function of applied load.

Introducing those values into the expressions of the new estimation scheme described previously, reasonable estimates of remote displacement and J can be obtained. A comparison between finite element results and the estimation scheme predictions will be illustrated hereafter. It can be noticed on few examples (Figs. 8 to 10) that the agreement is quite good and it can be concluded that the engineering method developed in Refs *4* and *7* can be extended to welded structures as soon as the interaction between base metal and weld metal is known. In particular, it is necessary to study how plasticity extends from the crack tip to the structure, and to determine the corresponding values of the limit load of the heterogeneous structure.

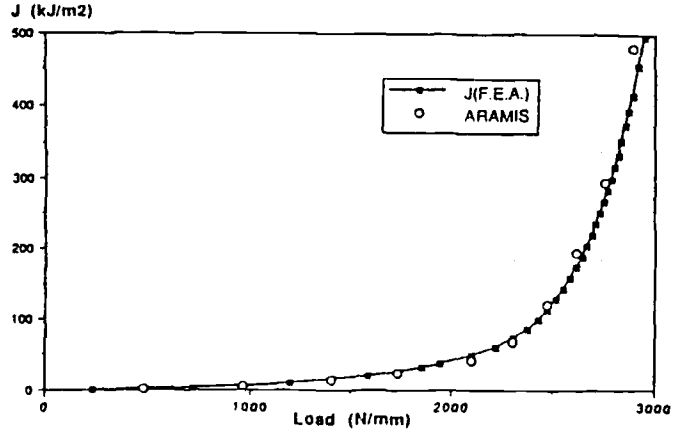


FIG. 8—*Comparison of J-evolution obtained by FEA and predicted by the ARAMIS method (SENB, 200% overmatching, a/W = 0.25).*

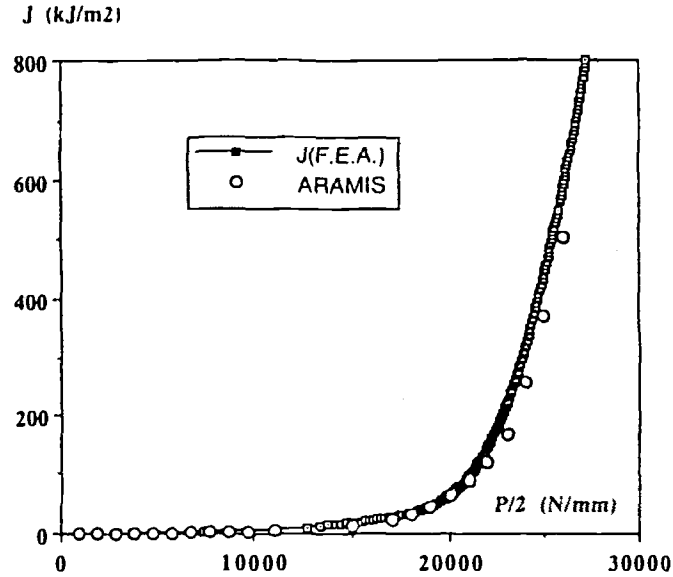


FIG. 9—*Comparison of J-evolution obtained by FEA and predicted by the ARAMIS method (CCP, 200% overmatching, a/W = 0.25).*

Consequences for Integrity Assessment Analyses

An important point that should be mentioned is the influence of the crack size on the structure response, and especially on the development of plasticity. As referenced in Ref *4*, the apparent toughness, as may be measured for an overmatched weld containing a deep crack, should be more or less identical to the toughness of the weld metal. In that case, the singularity arising from the presence of the crack in the overmatched weld is sufficient to generate a contained plastic zone ahead of the crack, while the base metal parts of the

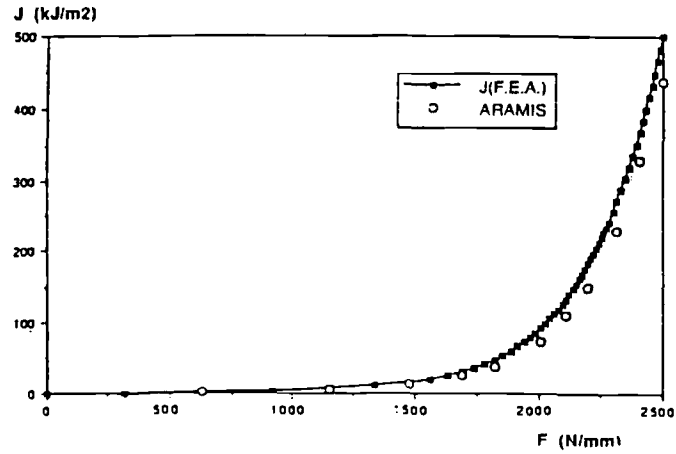


FIG. 10—*Comparison of J-evolution obtained by FEA and predicted by the ARAMIS method (SENB, 200% overmatching,* a/W = *0.5).*

specimen remain quasi elastic. The linear elastic fracture mechanics conditions are satisfied and the global as well as local response of the welded structure is controlled by the tensile and toughness properties of the weld metal.

On the contrary, when considering a medium or a shallow crack in an overmatched weld, the influence of the base metal increases as the ratio *a/w* is decreasing. Then, it is necessary to cope with interactions between the plastic zone developed at the crack tip and the other one that appears at the interface between the base metal and the weld right above the crack tip. When this second plastic zone appears in the base metal, it may produce an unloading of the crack tip zone which may finally lead to an increase of the bimaterial structural resistance compared to the homogeneous weld metal plate.

When considering an undermatched weld containing either a deep or a shallow crack, the influence of the base metal leads to plastic strain concentration in the softer material, that is, in the weld metal. The larger yield strength of the base metal prevents the plastic zone developed at the crack tip from spreading out of the weld, which generates an over localization of the strain compared to what occurs for a homogeneous structure entirely made of weld metal. Thus, the structural resistance of an undermatched welded specimen may be lower than that of the homogeneous weld metal plate.

As far as fracture assessment models application is concerned, important results have been obtained. When performing structural integrity assessment of inhomogeneous structures, tensile and toughness properties must be retained to input into fracture assessment models. However, it is difficult to determine whether adopting the parent material tensile properties is more relevant assuming that the material that contains the flaw controls effectively the structural resistance. The latter option is generally accepted.

On the basis of the present work, some conclusions can be drawn:

1. For mismatched welds, adopting the softer material tensile properties is always conservative.
2. Using the weld metal tensile properties for safety analyses of overmatched welds can lead to nonconservatism and unsafe assessments.

3. Using the weld metal tensile properties for safety analyses of undermatched welds can lead to overconservatism and excessive safety margins.
4. The shallower the crack, the greater the influence of the base metal on the fracture resistance of mismatched welds. Shallow cracks increase the mismatching effects.

Application of Two-Parameter Approach and Local Approach to Fracture of Welded Specimens

A detailed investigation of crack initiation in homogeneous and in mismatched structures has been conducted recently. Only the conclusions of this work are given here. Details can be obtained in Ref *9*.

In this work, we investigated "geometry effects" and the influence of mismatch between base and weld metal tensile properties on ductile crack initiation. The two-parameter models J-Q and J-T and the local criterion based on the critical cavity growth rate have been applied to various specimen configurations (17 homogeneous specimens, 8 overmatched weld specimens, and 6 undermatched ones).

From a theoretical point of view, all these criteria combine crack-tip deformation and stress triaxiality parameters. However the local approach differs from the two-parameter models on three important points. First, the local criterion describes explicitly the ductile fracture mechanism and therefore makes a difference between brittle and ductile fracture, in opposition to the purely mechanic J-T and J-Q models. Second, the local criterion specifies the physical meaning of "local" by introducing a critical size characteristic of the cracked material for the estimation of the cavity growth rate. Third, the local criterion measures the loss of constraint effect as a function of not only the crack-tip stress triaxiality but also the local equivalent plastic strain.

In a first step, the performance of three criteria have been compared on homogeneous cracked specimens. The predictions of "size effects" on toughness are qualitatively equivalent. However the validity of the two-parameter approach seems to be limited to initiation loads lower than the yield strength limit load relative to the cracked bimaterial structure. The local criterion does not present such a limitation and gives constraint corrections of toughness which are much lower than those obtained through the two-parameter models. This result has to be considered with some care, since the critical size parameter of the local criterion was fixed in this study to an arbitrary value.

For the bimaterial overmatched or undermatched specimens, the following conclusions have been reached:

1. All the approaches give the same trends for the considered specimens in which the crack lies on the centerline of the mismatched joint. That is the "geometry effects" are not modified by the mismatch, in spite of its high value. For load levels much higher than the limit load, it is expected that the overmatch tends to amplify the constraint correction on toughness, the reverse being true for the undermatched cases,
2. The T-stress model is the easier to apply but gives nonsense results when investigating mismatching configurations: mismatching effects appear only in plastic regime, where the elastic or small-scale yielding reference field is no more valid. Moreover, for homogeneous structures, this approach predicts very high constraint effects, which may be unconservative and is only applicable when the load does not exceed the limit load,
3. The Q-stress model present an improvement in comparison with the T-stress model, but its application is also limited to bimaterial structures where crack initiation takes place at a load inferior to the limit load of the mismatched cracked structure,
4. The local approach do not have the same limitations and remains valid beyond the limit

load in large scale yielding. This approach demonstrates the absence of mismatch effect on the toughness locus even for high mismatch values and for welded specimens having a crack on the centerline of "sufficiently" wide joint to get a deep crack configuration. The validity domain of this fixed by a "mismatch" load, the level of which depends on geometry parameters of the cracked weld joint: crack length, ligament size, and weld height. For the cases examined in this study the "mismatch" load is about 10% lower or up to 20% (even 50% for a mismatch value of 2) higher than the limit load. The R/R_o local criterion seems to give a lower bound of the toughness correction factor, while the two-parameter approach unreasonably magnifies the geometry effects.

Conclusion

This paper gathers the results of the French Cracked Weld Research Programme on the effect of mismatch on fracture resistance of welded structures. Elastic plastic finite element analyses have been carried out for different specimen geometries in order to characterize the effects of mismatching on plasticity development and its consequences on toughness measurement. First, for shallow cracks, some problems may result in using the standard test methods and the associated J-estimation formula recommended by ASTM. The values determined through experiments correspond to what can be called an "apparent toughness" but which may not exactly correspond to the resistance of the structure to ductile tearing. These testing procedures should be used cautiously when considering welded components. On the other hand, the softer material tensile and toughness properties should be used in the integrity assessment analyses to provide safe assessments, but this may lead, in some cases, to excessive safety margins. Last, it is necessary to perform tests considering various configurations in order to better understand the behavior of mismatched welds and to improve structural integrity assessment methods for welded engineering structures. Performing those tests is under progress.

References

[1] Smith, E., "Comments on the Problem of Crack Extension from a Defect in a Weld," *Pressure Vessel and Piping Conference,* Vol. 215, 23–27 June, 1991, San Diego, pp. 67–71.

[2] Eripret, C. and Hornet, P., "Prediction of Overmatching Effects on the Fracture Behaviour of Stainless Steel Cracked Welds," *Shallow Cracks Fracture Mechanics Conference,* Cambridge, 23–24 Sept. 1992.

[3] Hao, S., "Plane Strain Slip Line Solutions for Undermatched Welds," *Mismatch '93 Conference,* Lüneburg, 26–28 May 1993.

[4] Eripret, C. and Hornet, P., "Prediction of Mismatching Effects on Fracture of Stainless Steel Cracked Welds," *Mismatch '93 Conference,* Lüneburg, 26–28 May 1993.

[5] Joch, J., Ainsworth, R. A., and Hyde, T. H., "Limit Load and J-Estimates for Idealised Problems of Deeply-Cracked Welded Joints in Plane Strain Bending and Tension," University of Nottingham, Department of Mechanical Engineering, Internal Report.

[6] Roos, E., Eisele, U., and Silcher, H., "A Procedure for the Experimental Assessment of the J-Integral by Means of Specimens of Different Geometries," *International Journal of Pressure Vessel and Piping,* Vol. 23, 1986, pp. 81–93.

[7] Gilles, P. and Franco, C., "A New J-Estimation Scheme for Cracks in Mismatching Welds," *Mismatch '93 Conference,* Lüneburg, 26–28 May 1993.

[8] Kumar, V., German, M. D., and Shih, C. F., "An Engineering Approach for Elastic Plastic Fracture Analysis," EPRI Technical Report NP 1931, Research Project 1237-I, July 1981.

[9] Franco, C., Gilles, P., Eripret, C., and Nallet, S., "Constraint Effects in Cracked Welded Specimens," *2nd Conference on Constraint Effect on Fracture, ASTM STP 1244* American Society for Testing and Materials, Philadelphia, 1994.

Patrick Hornet, Mustafa Koçak, Su Hao, Alfred Cornec and Karl-Heinz Schwalbe

CTOD (δ_5) ESTIMATE OF MIS-MATCHED JOINTS USING THE ETM-MM PROCEDURE

REFERENCE: Hornet, P., Kocak, M., Hao, S., Cornec, A., and Schwalbe, K.-H., **"CTOD (δ_5) Estimate of Mis-Match Joints Using the ETM-MM Procedure,"** Fracture Mechanics: 26th Volume, ASTM STP 1256, Walter G. Reuter, John H. Underwood, and James C. Newman, Jr., Eds., American Society for Testing and Materials, Philadelphia, 1995.

ABSTRACT: Defect assessment analyses of engineering structures require information on the elastic-plastic crack driving force. The Engineering Treatment Model (ETM) has been developed at the GKSS Research Center to estimate the crack tip opening displacement CTOD (δ_5) and the J-integral for homogeneous specimens. When the plasticity properties of base and weld metals are different, which is referred to as weld strength mis-match, the defect assessment procedures need to be modified accordingly. Therefore, the ETM has recently been extended (ETM-MM) to predict the CTOD for tension loaded wide plates with transverse strength **mis-matched** welds containing through thickness cracks parallel to the weld / base metal interface, in the middle of the weld by finite element calculations and analytical considerations.

This paper presents the comparison between the estimates of the ETM-MM procedure and the experimental results of as-welded (AW) and stress relieved (SR) highly overmatched weld CCT specimens. The ETM-MM predictions have been obtained using the yield stress (σ_0) and strain hardening exponent (n) data approximated from the true (σ_0^t, n^t) and the engineering (σ_0^e, n^e) stress-strain curves of the base and eight overmatched weld metals. The ETM-MM procedure generally provides very good estimates; however, it always yields conservative estimates of the CTOD (δ_5) for all eight CCT panels with the use σ_0^e and n^e data. On the other hand, the use of σ_0^t and n^t values provides a better agreement with the experimental results for a large range of CTOD (δ_5) cases.

KEYWORDS: Weld, Strength Mis-match, CTOD(δ_5), Engineering Treatment Model (ETM), Wide plates, Limit load, Defect assessment.

GKSS Research Center Geesthacht, Institute of Materials Research
D - 21502 Geesthacht, F.R.GERMANY

Copyright by ASTM Int'l (all rights reserved); Wed Dec 23 19:26:25 EST 2015
Downloaded/printed by
Copyright 1995 by ASTM International www.astm.org
University of Washington (University of Washington) pursuant to License Agreement. No further reproductions authorized.

Fitness for purpose assessments of flawed engineering structures require information on the crack driving force parameters. These crack driving force parameters, crack tip opening displacement (CTOD) or J-integral, depend on the material's mechanical properties, the type of loading and the test piece geometry for homogeneous specimens. Most fracture assessment procedures such as design curves [1], BS PD 6493 [2-3] and R6-rev 6 option 2 [4] were designed to obtain conservative predictions, without aiming at estimating the crack driving force. In contrast, simple engineering methods such as describing in the EPRI handbook [5] and the Engineering Treatment Model (ETM) [6] allow a quick estimate of the crack driving force for an engineering structure. The ETM procedure considers a material with a piece-wise power law hardening stress-strain curve. In practice, however, the material stress-strain curves are not of this type and hence the mechanical properties data to be used must be approximated by using either engineering or true stress-strain curves. The method used to approximate the material deformation law may have a significant influence on the crack driving force estimate and must be examined in particular for strength mis-matched weld configurations.

The failure behaviour of a welded structure associated with a defect in the weld zone will certainly be influenced by the difference of the yield strength levels of the weld metal (σ_{YW}), heat affected zone (HAZ) and base metal (σ_{YB}). Therefore, currently used defect assessment procedures (CTOD and J- Design Curves, R6 Method) originally developed for homogeneous materials can not be applied in a straightforward manner to strength mis-matched weld configurations [7-9]. If the plasticity properties of base and weld metals are different (overmatching, $\sigma_{YW}>\sigma_{YB}$ or undermatching, $\sigma_{YW}< \sigma_{YB}$), which is referred to as weld strength mis-match, the defect assessment procedures need to be modified. For mis-matched welds, the relationships defined between crack driving force and applied strain differ from those of a homogeneous plate material. In this direction, extensive research has recently been conducted on the development of a new simple estimation scheme for strength mis-matched welded structures [10-18], and this topic has specifically been addressed during the recent International Symposium *MIS-MATCH'93* [7-9, 11-12, 16-17].

The ETM has been extended by Schwalbe et al [14-18] to tension loaded wide plates with transverse strength mis-matched welds containing through thickness cracks in the middle of the weld metal by analytical considerations combined with a large parametric study using finite element calculations. The ETM for mis-matched welds (ETM-MM) not only includes the mechanical properties of the base and the weld metal (σ_{YB}, σ_{YW}, n_B, n_W) but also the geometrical parameters (a/W, H/(W-a) and H/B) of the welded specimen or component, since the geometry (width of the weld, 2H and size of the uncracked ligament, W-a) of the defective mis-matched weld joint significantly influences the deformation and fracture behaviour of the specimens. Here, the degree of strength mis-match is defined by the ratio of weld metal yield strength to the base metal one, $M= \sigma_{YW}/\sigma_{YB}$.

Since the ETM-MM procedure is not yet firmly established, a programme to validate this procedure by comparing its predictions with various sets of experimental results and FE analyses is underway. Comparisons with undermatched (UM) weld wide-plates have already been presented in [19]. This paper compares the estimates of the ETM-MM procedure with the experimental results obtained from highly overmatched (OM) center cracked tensile panels containing through thickness cracks with a/W ratio of 0.5 at the middle of the eight different shielded metal arc weld metals (SMAW).

EXPERIMENTAL PROCEDURE

The details of the multipass V-groove butt-weld preparation are already reported elsewhere [20]. The ferritic weld metals contained four different levels of total nitrogen (83, 113, 153, 213 ppm) and through thickness cracked CCT specimens were tested in the as-welded (AW) and stress relieved (SR, at 580°C/2h) conditions. The mechanical properties of the base and eight different weld metals are shown in Table 1. The strength mis-match factor, M, varied between 1.6 and 2.0, depending on the total nitrogen content and condition of the weld joints. The 17 mm thick and 150 mm wide CCT panels shown in Figure 1 have been fatigue pre-cracked to obtain through thickness weld metal cracks with the a/W ratio 0.5. These eight panels have been tested in tension at room temperature. The experimental approach was to measure the crack tip opening displacement, CTOD(δ_5) with GKSS made clip-on gauges at the original fatigue crack tip over a gauge length of 5 mm [21], the crack mouth opening displacement (CMOD), the crack growth using the DC-potential drop method [22] and the overall elongation as a function of the applied load.

ENGINEERING TREATMENT MODEL (ETM)

The ETM and its extension to strength mis-matched welds (ETM-MM) have been developed by Schwalbe et al and details of these procedures have been published in [6, 14-18]. In this section brief outlines of this model will be given.

Homogeneous Case [6]

For homogeneous materials with stress-strain curves as follow :

if $\sigma \le \sigma_Y$ then $e = \sigma_Y / E$ (1a)

if $\sigma \ge \sigma_Y$ then $\left(\frac{e}{e_Y}\right) = \left(\frac{\sigma}{\sigma_Y}\right)^{1/n}$ (1b)

The following equations have been given for a CCT panel in plane stress and they can easily be extended to many engineering components. For homogeneous CCT specimens, the CTOD (δ_5) can be estimated by the following formulas for different loading stages.

Stage 1: $F < F_Y$

$$\delta_5 = \frac{K_{eff}^2}{E\sigma_Y} \tag{2a}$$

where $$K_{eff}^2 = \pi a_{eff} f^2(a_{eff}/W)\left(\frac{F}{2WB}\right)^2$$

$$a_{eff} = a + \frac{K^2}{2\pi\sigma_Y^2}$$

$$f(a/W) = (1 - 0.025(a/W)^2 + 0.06(a/W)^4) / \sqrt{\cos\left(\frac{\pi a}{2W}\right)}$$

Stage 2 : $F > F_Y$

$$\delta_5 = \delta_Y \left(\frac{F}{F_Y} \right)^{1/n} \tag{2b}$$

where δ_Y is determined from equation (2a) for $F = F_Y$

The yield load of the homogeneous panel is determined (plane stress) as:

$$F_Y = 2B\sigma_Y(W - a)$$

The basic ETM procedure [6] requires use of the strain hardening exponent, n determined from the engineering stress-strain curve of the material. However, it is of interest to define the sensitivity of this model with respect to the method of determination of the yield stress and strain hardening exponent. This aim is part of the current verification programme of the ETM and ETM-MM procedures at GKSS Research Center.

Overmatched Weld Case and the use of ETM-MM

The stress-strain curves of the base and weld metals are assumed to follow a law as described in eqn. (1) and are characterised by the parameters E, σ_{YB}, n_B and σ_{YW}, n_W respectively. The entire deformation mechanism of the over- or under-matched specimens and hence the description of the yield loads differ significantly from those for homogeneous base metal specimen analysis as described above. The degree of influence of strength mis-match on the limit load depends on the mis-match level (M), weld height (2H) and crack size (a/W, H/(W-a)).

Following a procedure similar to that for homogeneous specimens, the formulation analogous to basic ETM, eqn. (2) takes the form, for overmatched CCT panels in plane stress as proposed by Hao, Cornec and Schwalbe [17 , 18]:

Stage 1 : $F < F_{YOM}$

Identical with equation (2a) of Stage 1 for homogeneous specimens using :

$$\sigma_Y = \sigma_{YW} \tag{3a}$$

and

$$a_{eff} = a + \left(1 + (\frac{\sigma_{YW}}{\sigma_{YB}} - 1)\frac{a}{H} \right) \frac{K^2}{2\pi\sigma_{YW}^2} \tag{3b}$$

Stage 2 : $F > F_{YOM}$

$$\delta_5 = \delta_{5OM} \left(\frac{F}{F_{YOM}} \right)^{1/n_M} \tag{3c}$$

where δ_{5OM} is determined from equations (2a) and (3b) for $F = F_{YOM}$

F_{YOM} and n_M depend on the mode of the plastic zone development at the uncracked ligament (W-a) of the specimen [17, 18]. For overmatched specimens, the plastic deformation mechanism is expected to cross the weld/base metal interface (mis-match boundary), then penetrating into the base metal. For such a condition, the following definition of the limit load, F_{YOM}, and strain hardening exponent for mis-matched configuration, n_M, developed by Hao et al [17, 18] as a function of the mis-match factor (M) and weld geometry can be used:

$$F_{YOM} = 2B(1.54H\sigma_{YW} + (W - a - 1.54H)\sigma_{YB}) \quad (5a)$$

and

$$n_M = (1.54Hn_W + (W - a - 1.54H)n_B)/(W - a) \quad (5b)$$

The expressions 5a and 5b provide closed form formulations for limit load and strain hardening exponents for mismatched CCT configurations, respectively. Both expressions contain the effects of strength differences between base and weld metals as well as the geometrical dimensions of the cracked weld zone. Obviously, the use of both expressions in the structural analysis of mismatched welds should significantly increase the accuracy of the predictions. In this context, no other defect assessment procedure than the ETM-MM considers the use of such newly developed expressions (5a and 5b). Further details of both ETM and ETM-MM procedures are given in references [6] and [14-18]. The purpose of this paper is to verify these solutions by using a new set of experimental results obtained from highly overmatched CCT panels containing long cracks. Furthermore, the sensitivity of the analysis to the type of stress-strain curves (engineering or true stress-strain curves) used was also investigated.

RESULTS AND DISCUSSIONS

Stress-Strain Curves

The strain hardening exponent, n, is defined as the slope of the stress-strain curve in a logarithmic scale and σ_Y is defined by the intersection between this line and the elastic part. Figure 2 presents the method used to approximate the stress strain curves schematically. This way of approximation naturally does not fit perfectly to the experimental data as shown in Figure 3, but it has the advantage of being simple and independent of the user. In order to improve this fit and hence the later crack driving force estimates, further work is in progress. The values of σ_0^e, n^e, σ_0^t, n^t, obtained by this method are given in Table 2 for the base metal and the eight different welds.

ETM-MM for Overmatched Specimens

For each panel the analysis was carried out using the actual crack length as predicted by the DCPD method. According to the equations presented above, Figure 4 shows the comparison between experimental results and the ETM-MM estimates using engineering and true stress-strain data for all four welded panels in the as-welded condition (AW). In these analyses, the residual stress level was not taken into account due to the extensive plasticity of the specimens before failure. The experimental and predicted load vs CTOD (δ_5) results show very good agreement with each other. Generally, for all four cases, the ETM-MM procedure provides very good and in most cases conservative predictions regardless of the type of stress-strain approximation used to obtain input data for the

analysis. However, the level of conservatism increases when using the engineering stress-strain curve. These comparisons suggest that ETM-MM can satisfactorily be used as originally suggested with the engineering stress strain curve to obtain the yield stress and strain hardening exponent to yield conservative estimate of the crack driving force. Similar conclusions have already been suggested for highly undermatched welded CCT panels in [19]. Nevertheless, the use of the true stress strain curve significantly improves the predictions of the ETM-MM for a large range of deformation. For all the panels in AW conditions, the agreement between the experimental results and the estimates using the true stress strain curve is very good which indicates that the ETM-MM is able to give an estimate of the CTOD (δ_5) when knowing the resistance curve of the overmatched weld metal.

Figure 5 presents the comparison between the estimate of the ETM-MM and the experimental results of the four panels in stress relieved (SR) condition. Again, the use of the engineering stress-strain curve systematically provides a conservative estimate of the crack driving force as defined in this study as CTOD (δ_5). Similarly, the estimate obtained using the true stress-strain curve fits better with the experimental results, with little non conservatism in some part of the experiment. This non conservatism is probably due to the use of higher values of strain hardening exponent (n^t) compared to the n^e values as shown in Table 2.

Obviously, the load vs. CTOD (δ_5) results are showing that the prediction of the load for a given CTOD level is very good for both cases, as shown in Figures 4 and 5. However, it is of interest to plot the direct comparison between the estimated CTOD (δ_5) and the experimental values as shown in Figure 6. As an example, this figure presents the results of two CCT panels (AW-1 and SR-1). In both cases, the use of the engineering stress-strain curve gives good estimates of the crack driving force for CTOD lower than 1 mm which corresponds to a crack growth of about 1mm. For the AW condition, the use of the true stress-strain curve allows estimating of the experimental CTOD with an error lower than 5% till a CTOD of 5mm, Fig. 6a. For the stress relieved condition, the ETM-MM estimates the experimental CTOD with an error of about 20% on the non conservative side when the true stress strain curve is used. It should be kept in mind that a deformation quantity - the CTOD (δ_5) - has been estimated from the applied load under fully plastic conditions.

This ETM-MM validation study (as well as numerous others conducted earlier [6,7,15-19]) shows clearly that the CTOD (δ_5) can be directly measured and estimated as a crack driving force parameter using the simple ETM-MM formalisms. A complete defect assessment procedure for wide plates containing strength mis-matched welds can be proposed in a procedural form including modified limit load and strain-hardening exponent for mis-matched configurations in the formalisms of the ETM-MM. It should be noted that presently no other defect assessment procedure has yet put forward any model to include the strength mis-match effect on the defect assessment procedure to avoid any under estimation of the crack driving force or critical defect size.

CONCLUSIONS

The estimates of the Engineering Treatment Model for Mis-Matched configurations (ETM-MM) have been compared with experimental results of highly overmatched (60-80 %) multipass butt-welded CCT specimens with long cracks (a/W=0.5) located in the middle of the weld. The following conclusions can be drawn from this verification study of the ETM-MM procedure:

- The Engineering Treatment Model for mis-matched configurations (ETM-MM) gives generally very good estimates for all eight tested welds in AW or SR conditions.
- For the specimens in as-welded (AW) condition, the ETM-MM estimates the experimental CTOD (δ_5) with an error lower than 5%, when the true stress-strain curve is used. However, for the stress relieved (SR) specimens, the ETM-MM slightly underestimates the experimental CTOD (δ_5), if the true stress-strain curve is used.
- For the eight highly overmatched cases examined, the use of σ_0^e and n^e provides more conservative predictions of the CTOD (δ_5) than the use of σ_0^t, n^t. The results suggest that ETM-MM can be used with the engineering stress strain curve as originally suggested to obtain conservative estimates. If some cases require less conservatism, the true stress-strain data can be used as an input data of the ETM-MM procedure.
- The CTOD (δ_5) can be directly measured on the CCT panels and estimated as a crack driving force parameter using the simple ETM-MM procedure.

Acknowledgements: Sincere thanks are extended to Dr. G.M. Evans, Oerlikon Welding Ltd., Zurich for providing the welded panels and Dr. B. Petrovski for conducting the CCT tests.

NOTATION

a : current half crack length
a_0 : half crack length before initiation of crack growth
b : ligament length : b=W-a
B : specimen thickness
e : strain
e_Y : yield strain
e_{YB} : base metal yield strain
e_{YW} : weld metal yield strain
E : Young's modulus
F : applied load
F_Y : net section yield load
F_{YOM} : yield load of the overmatched weld joint
H : half height of the weld
K : stress intensity factor
M : mismatch ratio , $M= \sigma_{YW} / \sigma_{YB}$
$R_{P0.2}$: 0.2% proof stress
R_m : ultimate tensile strength
R_e : stress at elasticity limit
n_W : strain hardening exponent for weld metal
n_B : strain hardening exponent for base metal
n_M : strain hardening exponent of the mis-match specimen
n^e : strain hardening exponent approximated from engineering stress-strain curve
n^t : strain hardening exponent approximated from true stress-strain curve
W : half width of the specimen
δ_5 : CTOD measured with GKSS made δ_5 clip-on gages at the original fatigue crack tip over a gauge length of 5 mm
δ_{5OM} : δ_5 predicted using equations (2a) and (3b) for $F= F_{YOM}$
σ : stress
σ_0^e : yield stress approximated from engineering stress-strain curve
σ_0^t : yield stress approximated from true stress-strain curve
σ_Y : yield strength
σ_{YB} : base metal yield strength
σ_{YW} : weld metal yield strength

REFERENCES

[1] Turner, C. E., "Further developments of a J-based design curve and its relationship to other procedures", Elastic-Plastic Fracture: 2nd Symp., Vol. II, Fracture Resistance Curves and Engineering Applications, ASTM STP 803, C.F. Shih and J.P. Gudas, Eds. ASTM, 1983, pp. II-80-II-102.

[2] British Standards Institution PD6493:1980, "Guidance on some methods for the derivation of acceptance levels for defects in fusion welded joints".

[3] British Standards Institution PD6493:1991, "Guidance on methods for assessing the acceptability of flaws in fusion welded structures".

[4] Milne, I., Ainsworth, R. A., Dowling, A. R. and Steward, A. T., "Assessment of the integrity of structures containing defects", CEGB report R/HR6-Rev. 3, May 1986.

[5] Kumar, V., German, M. D. and Shih, C. F., "An engineering approach for elastic-plastic fracture analysis", EPRI report NP1931, 1981.

[6] Schwalbe, K.-H. and Cornec, A., "The Engineering Treatment Model (ETM) and its practical application", Fatigue Fract. Engn. Mater. Struct.,Vol. 14, No. 4, pp. 405-412, 1991.

[7] Hornet, P., Koçak, M., Cornec, A., Petrovski, B., and Schwalbe, K.-H. "Effect of weld metal mis-matching on crack driving force", Mis-Matching of Welds, ESIS 17, (Edited by K.-H. Schwalbe and M. Koçak) 1994, Mech. Eng. Publications, London.

[8] Petrovski, B. and Koçak, M., "Evaluation of fracture behaviour of strength mismatched steel weld joints with surface cracked tensile panels and SENB specimens", Mis-Matching of Welds, ESIS 17, (Edited by K.-H. Schwalbe and M. Koçak) 1994, Mech. Eng. Publications, London, pp. 511-538.

[9] Kirk, M. T. and Dodds, R. H. Jr., "Effect of weld strength mismatch on elastic-plastic fracture parameters for small tension loaded cracks", Mis-Matching of Welds, ESIS 17, (Edited by K.-H. Schwalbe and M. Koçak) 1994, Mech. Eng. Publications, London, pp. 369-386.

[10] Zhang, J. X., Shi, Y. W. and Tu, M. J., "Studies on the fracture mechanics parameters of weldment with mechanical heterogeneity", Engineering Fracture Mechanics, Vol. 34, No 5/6, pp 1041-1050, 1989.

[11] Eripret, C., Hornet, P., "Prediction of overmatching effects on fracture of stainless steel cracked welds", Mis-Matching of Welds, ESIS 17, (Edited by K.-H. Schwalbe and M. Koçak) 1994, Mech. Eng. Publications, London, pp. 685-708.

[12] Gilles, P. and Franco, C., "A new estimation scheme for cracks in mismatching welds : the A.R.A.M.I.S. method", Mis-Matching of Welds, ESIS 17, (Edited by K.-H. Schwalbe and M. Koçak) 1994, Mech. Eng. Publications, London.

[13] Franco, C., Gilles, P. and Eripret, C., "Application of the simplified J-estimation scheme A.R.A.M.I.S. to mismatching welds in C. C. P." To appear in proceedings of the Pressure Vessel and Piping conference, Denver, July 25-29, 1993.

(14] Schwalbe, K.-H., "Effect of weld metal matching on toughness requirements: some simple analytical considerations using the engineering treatment model (ETM)", Int. Journal of Fracture, Vol. 56, 1992, pp. 257-277.

[15) Schwalbe, K.-H., "Welded joints with non-matching weld metal-Crack driving force considerations on the basis of the engineering treatment model (ETM)", Int. Journal of Fracture, Vol. 62: pp. 1-24, 1993.

[16] Schwalbe, K.-H., Hao, S. and Cornec, A., "ETM-MM - The engineering treatment model for mismatched welded joints", Mis-Matching of Welds, ESIS 17, (Edited by K.-H. Schwalbe and M. Koçak) 1994, Mech. Eng. Publications, London, pp. 539-560.

[17] Hao, S., Cornec, A. and Schwalbe K.-H., "On the crack driving force and constraint state in a mismatched welded plate under tension", Mis-Matching of Welds, ESIS 17, (Edited by K.-H. Schwalbe and M. Koçak) 1994, Mech. Eng. Publications, London, pp. 561-571.

[18] Hao, S., Cornec, A. and Schwalbe K.-H., "On the crack driving force and fracture resistance of mismatched weldments", 10th European Conf. on Fracture, Berlin, FRG, September 1994, (Edited by K.-H. Schwalbe and C. Berger), Vol. II, pp. 1117-1124.

[19] Hornet, P., Koçak, M., Hao S., Petrovski, B., Cornec, A., and Schwalbe K.-H., "CTOD(δ_5) estimate of tension loaded wide plates using the ETM, DVM-Arbeitskreis "Bruchvorgänge", September 1994, Magdeburg, F.R.G.

[20] Koçak, M., Petrovski, B., Achar, D. R. G., and Evans, G. M., "Fracture mechanics and wide-plate tests for analysis of nitrogen and strain aging effects on weld metal fracture properties", 12th Int. Conf. on Offshore Mechanics and Artic Engineering (OMAE' 93), 20-24 June 1993, Glasgow, Scotland.

[21] Schwalbe, K.-H., "Introduction of δ_5 as an operational definition of the CTOD and its practical use", ASTM National Symp. on Fracture Mechanics, Idaho Falls, USA, June 1994.

[22] Schwalbe, K.-H., Hellmann, D., "Application of the electrical potential method to crack length measurements using Johnson's formula", Journal of Testing and Evaluation, Vol. 9, No. 3, pp. 218-221, May 1981.

Table 1: Mechanical properties of the welds and base metal

Material	$R_{P0.2}$ [MPa]	$e_{0.2}$	R_m^e [MPa]	e_m^e	R_m^t [MPa]	e_m^t	M
BM	246	0.32	394.35	21.806	480.34	19.726	–
AW-1	433	0.44	511.50	16.364	595.20	15.155	1.760
AW-2	440	0.42	514.43	14.56	589.33	13.593	1.788
AW-3	442	0.41	537.83	17.142	630.02	15.821	1.796
AW-4	450	0.42	548.25	15.541	633.45	14.446	1.829
SR-1	401	0.39	485.30	16.478	565.27	15.253	1.630
SR-2	400	0.39	486.85	17.028	569.75	15.724	1.626
SR-3	413	0.40	505.08	15.638	584.06	14.530	1.678
SR-4	433	0.41	507.07	14.295	579.56	13.362	1.760

M= $R_{P0.2}$ weld metal / $R_{P0.2}$ base metal.

$R_{P0.2}$ of BM represents σ_{YB}, other $R_{P0.2}$ values represent individual σ_{YW}.

Table 2: Results of the approximation of the engineering and true stress-strain curves as presented in Figure 2.

Material	σ_0^e [MPa]	n^e	σ_0^t [MPa]	n^t
BM	217	0.112	203	0.162
AW-1	418	0.046	403	0.090
AW-2	427	0.044	414	0.084
AW-3	427	0.053	413	0.097
AW-4	433	0.055	420	0.097
SR-1	386	0.051	373	0.094
SR-2	385	0.052	372	0.096
SR-3	397	0.055	384	0.097
SR-4	420	0.045	408	0.084

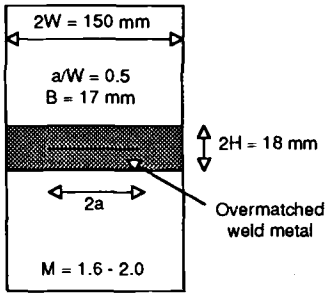


Figure 1 : Schematic is showing the CCT panels with transverse overmatched weld.

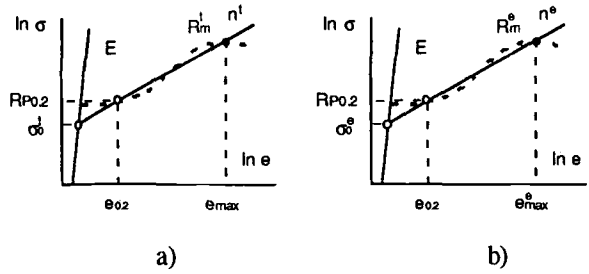


Figure 2 : Approximation of the stress-strain curve for the application of the ETM.
a) True stress-strain curve, b) Engineering stress-strain curve

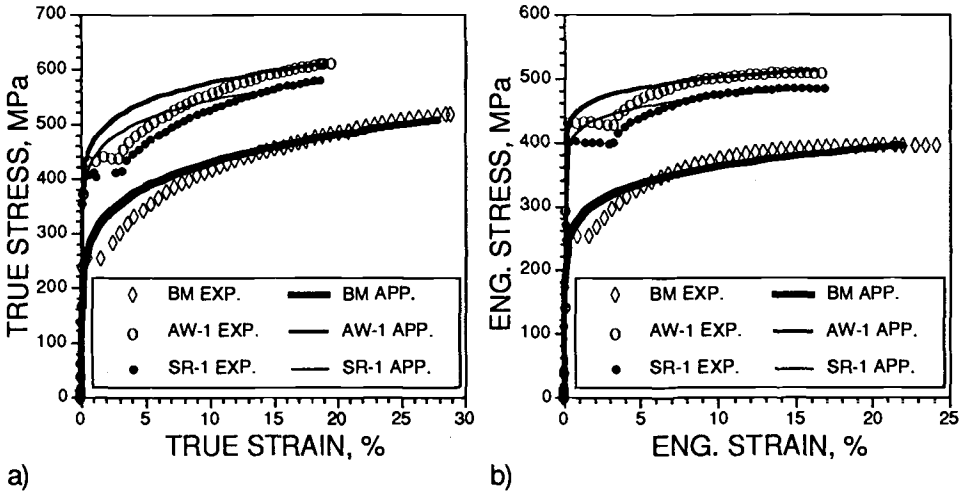


Figure 3 : Comparison between the experimental and the approximate stress-strain curves.
a) True stress-strain curve, b) Engineering stress-strain curve

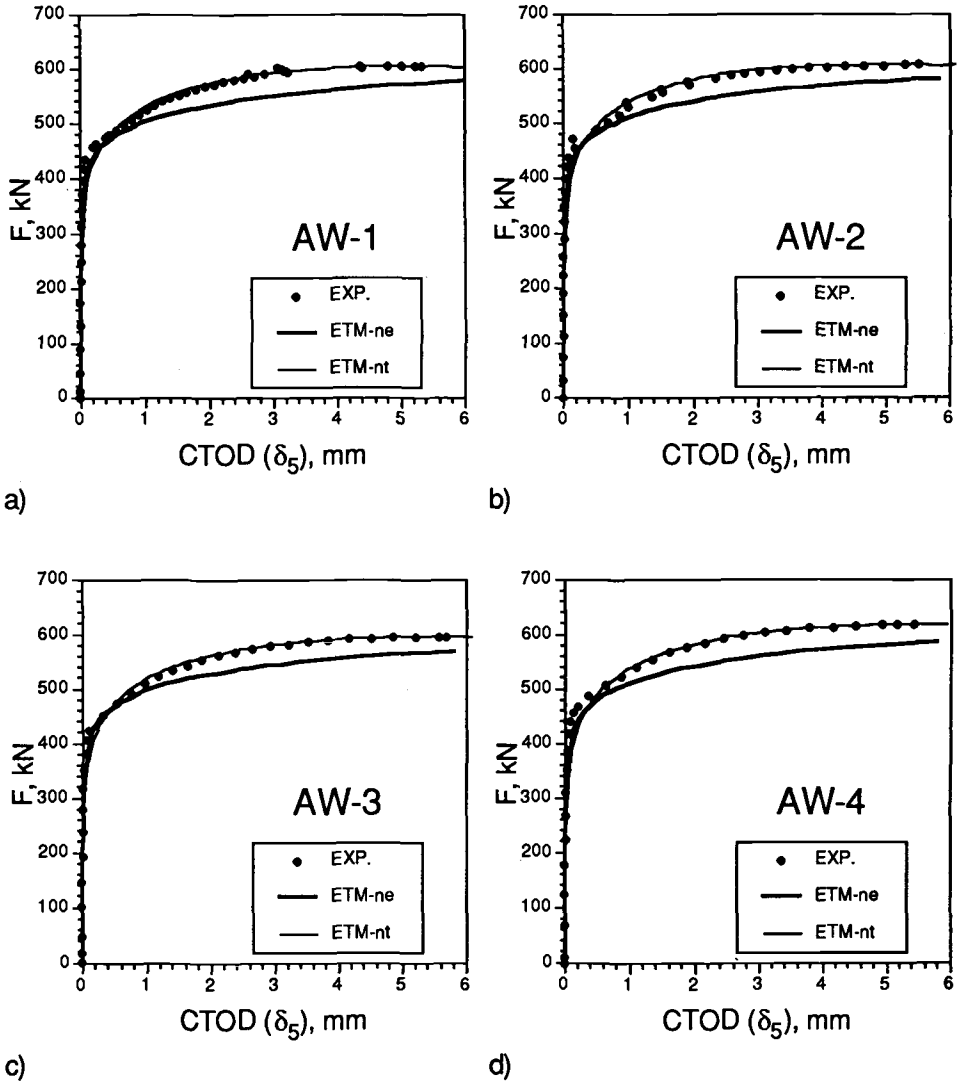


Figure 4 : Comparison between the experimental results of the tested panels and the estimates of the Engineering Treatment Model for the overmatched panels in **as-welded condition**:
a) weld nr. 1, b) weld nr. 2, c) weld nr. 3, d) weld nr. 4

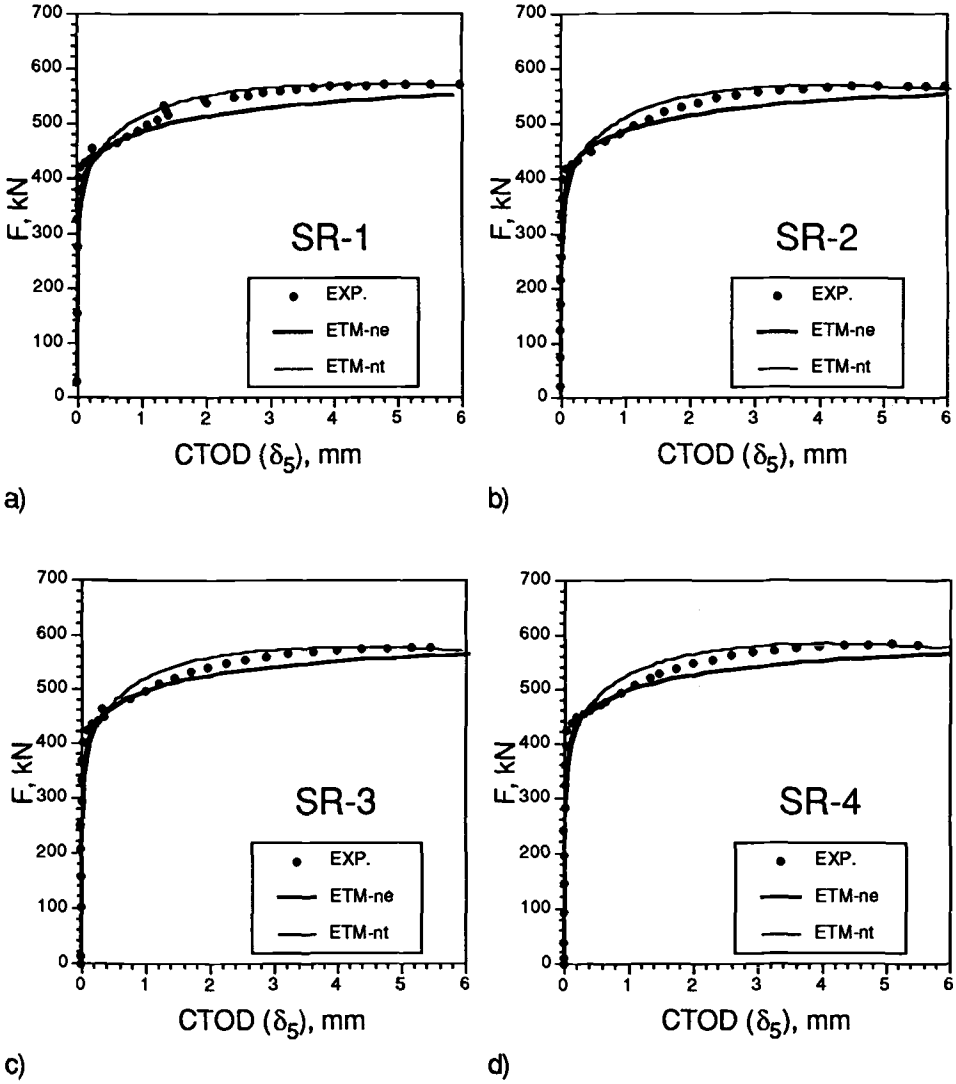
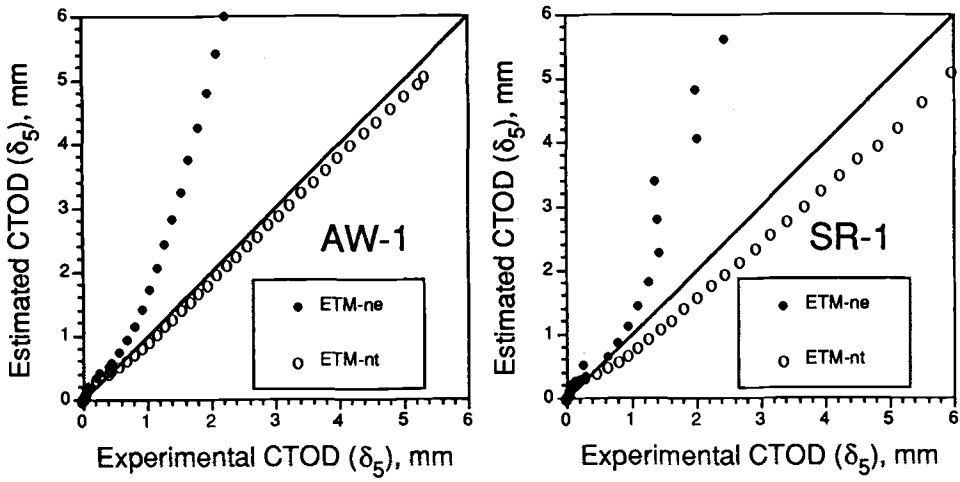


Figure 5 : Comparison between the experimental results of the tested panels and the estimates of the Engineering Treatment Model for the overmatched panels in **stress relieved(SR) condition**: a) weld nr. 1, b) weld nr. 2, c) weld nr. 3, d) weld nr. 4



a) b)

Figure 6 : Comparison between the experimentally measured CTOD(δ5) and the estimated one for the weld nr. 1: a) as-welded condition, b) stress relieved condition.

Michael G Dawes[1]

SIGNIFICANCE OF LOCALLY INTENSIFIED STRAIN AGEING TO THE FRACTURE TOUGHNESS OF WELDED STEEL STRUCTURES

REFERENCE: Dawes, M. G., "**Significance of Locally Intensified Strain Ageing to the Fracture Toughness of Welded Steel Structures,**" *Fracture Mechanics: 26th Volume, ASTM STP 1256,* Walter G. Reuter, John H. Underwood, and James C. Newman, Jr., Eds., American Society for Testing and Materials, Philadelphia, 1995.

ABSTRACT: A review of past studies shows that tests on specimens notched after welding can give overestimates of the fracture toughness that occurs at the tips of flaws present during welding. This situation results from locally intensified straining and ageing embrittlement (LISAE), which has been shown to trigger low stress brittle fractures in both notched and welded wide plate tension tests, and welded structures in service. Although the relative susceptibilities of steels to strain ageing embrittlement are sometimes assessed by testing bulk strained and aged samples, the results of such tests may be optimistic. A summary is given of work to develop a fracture toughness test method for LISAE. The new test will give increased confidence and accuracy in fracture assessments, be of use in selecting tough materials, and aid the development of materials that are resistant to LISAE.

KEYWORDS: Strain ageing embrittlement, LISAE, toughness, brittle fracture, base metal, weld metal, weld heat-affected zone, fracture mechanics, test methods.

Considerations of the fracture toughness of welded joints in steels generally focus on the visually obvious weld metal and transformed weld heat-affected-zones (HAZs), for which there are now a number of published fracture mechanics toughness testing procedures [1-3]. However, the regions of lowest toughness in welded steel joints can be associated with phenomena that are undetectable at the highest magnifications associated

[1] Principal Consultant - Fracture Testing, TWI (formerly The Welding Institute), Abington Hall, Abington, Cambridge, CB1 6AL, UK.

Copyright © 1995 by ASTM International www.astm.org

with light microscopes. One such phenomenon is strain ageing embrittlement [4–7]. This occurs when thermally activated carbon and nitrogen atoms diffuse to dislocations, and effectively lock them, restricting further plastic deformation and ductility. Strain ageing embrittlement can occur during welding, in any region of a welded joint, including the base metal in the sub-critical HAZ several millimetres away from the visibly transformed HAZ. Strain ageing embrittlement in welds can also occur by straining and subsequent ageing during fabrication and service.

When the welds are free of macroscopic flaws, embrittlement may be associated with **bulk strain ageing**, which may be assessed by conventional fracture toughness tests on specimens that have been notched and fatigue precracked after welding, or after subsequent straining and ageing [8]. Bulk strain ageing embrittlement may be contrasted with the potentially more serious, and often overlooked, **locally intensified strain ageing embrittlement**, LISAE; which is associated with the tips of flaws that occur during or following welding and ageing [9–12], as described later.

This paper reviews the phenomenon of LISAE, early instances where LISAE has been associated with low stress brittle fractures, early test methods for LISAE in base metals, recently observed situations where LISAE has occurred, and current work to develop a fracture mechanics toughness test method for LISAE.

EARLY BRITTLE FRACTURES

The more than 2500 now legendary brittle fractures in welded steel ships, and other brittle fractures in non-ship structures prior to 1954, were reviewed in Welding Research Council Bulletins by Acker [13] and Shank [14], respectively. They showed that most of the early brittle fractures involved cleavage at nominal applied stresses of less than half yield, and fracture initiation in weld regions. In about 10% of the ship failures these 'low stress brittle fractures' were associated with calm seas and essentially static loading. One of the most dramatic of these involved the T2 tanker S. S. Schenectady [15]. This was a new ship docked in calm water on January 16, 1943. The air temperature at 14:30 hours in the afternoon was 3°C, and by 23:00 hours in the evening it had dropped to −5°C; when the ship suddenly fractured almost in half leaving the bows and stern resting on the bottom of the dock, and the fractured mid-ship area raised above the waterline. While ships are generally subjected to dynamic loading, most non-ship structures are subjected to slowly applied or static loading. Therefore it is not surprising that most brittle fractures in non-ship structures have been associated with static loading.

Research on brittle fracture of welded structures over more than 60 years has now confirmed that fracture initiation is invariably associated with flawed welds and/or severe stress concentrations, highly restrained geometries, weld repairs and low toughness in the weld regions. Also, the driving forces for crack extension are clearly associated with the combination of the applied, residual and thermal stresses; the latter being generally low (< 20 MPa) when associated with changes in air temperature. It now seems obvious that thick sections, high yield strengths, low temperatures and dynamic loading all increase the risk of brittle fracture initiation, and that a steel base metal having a Charpy V-notch

impact energy of less than 20 J at the operating temperature will have a low resistance to brittle crack propagation.

EARLY FRACTURE TESTS

Although early investigators were aware of many of the factors contributing to brittle fractures in welded steel structures, they were often puzzled by their inability to reproduce low stress brittle fractures in the laboratory, e.g. under the same conditions of static loading and temperature as the in-service failures they were investigating. Typically, tests on welded plates prepared with sharp notches or cracks after welding, failed at applied stresses greater than yield.

In May 1949 T. W. Greene published a very significant paper in the Welding Journal [16]. He described what were believed to be the **first laboratory tests** to demonstrate **low stress brittle fractures** under **slowly applied loading**, at the **ambient temperatures** for ships.

Greene [16] tested welded plates approximately 900 x 900 x 20 mm thick in slowly applied three point bending. Series of plates were prepared with welded over, but not completely melted out, solidification cracks in weld metal, and welded over jewellers sawcut notches in the weld preparation edges. The latter plates had one notch tip in the weld metal and one tip in the base metal. Low stress brittle fractures occurred in all as-welded plates tested at temperatures in the range -29°C to -7°C. One plate, which had been cooled to -32°C, was warming-up to the test temperature of -29°C when it fractured with no applied bending!

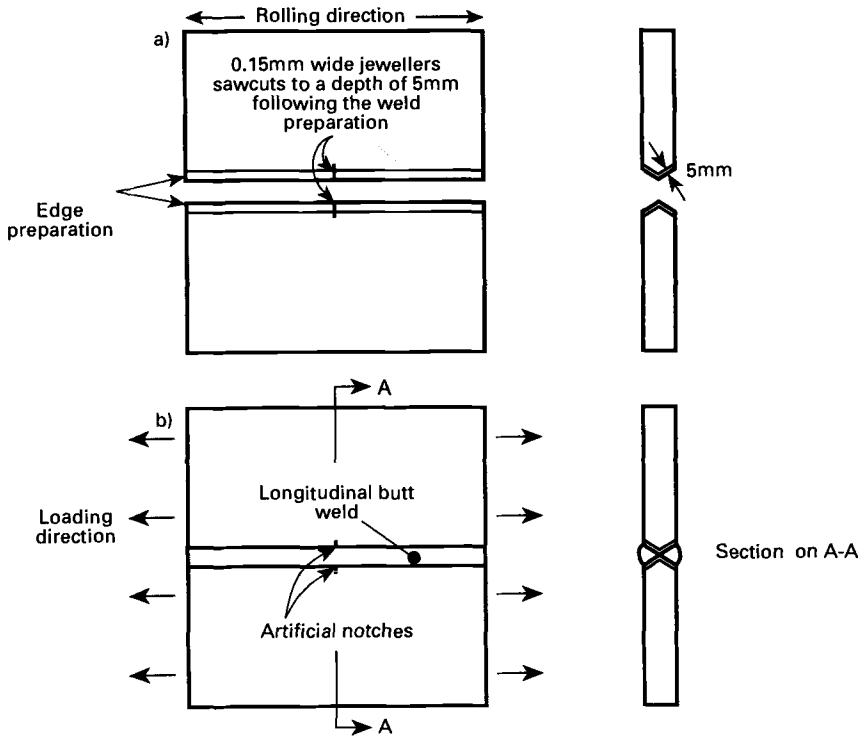
A very important lesson learned from the work of Greene [16] was that **notches or cracks introduced after welding can result in higher fracture resistance compared to notches and cracks introduced before or during welding.**

Significantly, in 1952 two oil storage tanks at Fawley in England failed by brittle fracture during hydrostatic acceptance tests [17]. Fracture in one tank initiated at a welded-over sawcut where a weld probe sample had been removed and replaced. The fracture in the other tank initiated at a welded-over (partially repaired) pre-existing crack!

Greene's work [16] was followed and confirmed by Wells [18] and others [19], all of whom developed notched and welded wide plate tension tests. Figure 1 illustrates the preparation and general form of the Wells wide plate test [18]; the results of which have provided a basis for existing UK design standards for low temperature pressure vessels and storage tanks [20].

All the aforementioned investigators [16-20] were able to demonstrate substantial improvements in wide plate fracture resistance following thermal stress relief treatments. These improvements were derived from the removal of both the residual welding stresses, and the LISAE at the welded over notch tips. The LISAE at the welded over notch tips

was demonstrated by Burdekin [9]. By welding over notches of different depths in a 25 mm thick steel plate, and then extracting identical geometry 10 mm square section bend specimens with the same notch tips from the plate, Burdekin [9] was able to both relax the residual welding stresses, and use the bend specimens to establish the crack tip opening displacement (CTOD) fracture toughness associated with each welded over notch depth. Burdekin [9] found that the base metal fracture toughness was reduced most by welding over a 5 mm deep notch, which was also the notch depth used in the Wells wide plate test (Fig.1). He also showed that the LISAE could be removed by a 600°C 'stress relief' heat treatment. Further confirmation of LISAE at the tips of welded over notches was provided by Burdekin [10] and others [11,12].



❶ Take initial plate, 900x900mm x full plate thickness
❷ Flame cut in half
❸ Flame cut weld preparation for longitudinal butt weld
❹ Cut artificial notches in plate edges prepared for welding
❺ Align plates so that the sawcut notches are co-planar
❻ Make longitudinal butt weld to complete the specimen

Fig.1. Notched and welded wide plate brittle fracture test specimen
a) preparation, b) final form

Figure 2 illustrates the locally intensified straining that occurs at a welded over notch tip. This illustration was obtained by welding over a 0.15 mm wide notch in a high nitrogen steel, which was subsequently aged, sectioned, polished and etched to reveal the strain patterns [12]. Other studies indicated that the strains at welded over notch tips can exceed 30% [21]. Also, thin-foil transmission electron microscopy has been used to study the increases in dislocation density that occur close to a welded over notch tip. These studies revealed bowed and pinned dislocations that were believed to be typical of those associated with dynamic strain ageing [12,22].

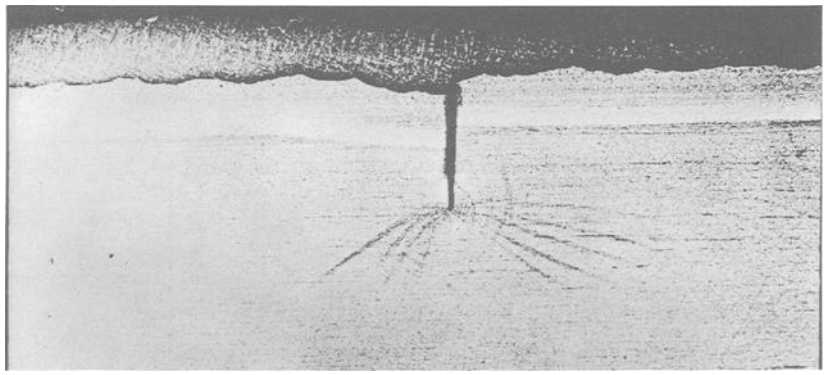


Fig.2. Locally intensified straining at a welded over notch tip [Ref 12]

Burdekin [10] conducted further CTOD tests on 10 mm square section specimens extracted from a 25 mm thick plate with and without welded over 5 mm deep notches. As shown in Fig.3, he demonstrated that LISAE raised the ductile/brittle transition for one particular steel by 80°C.

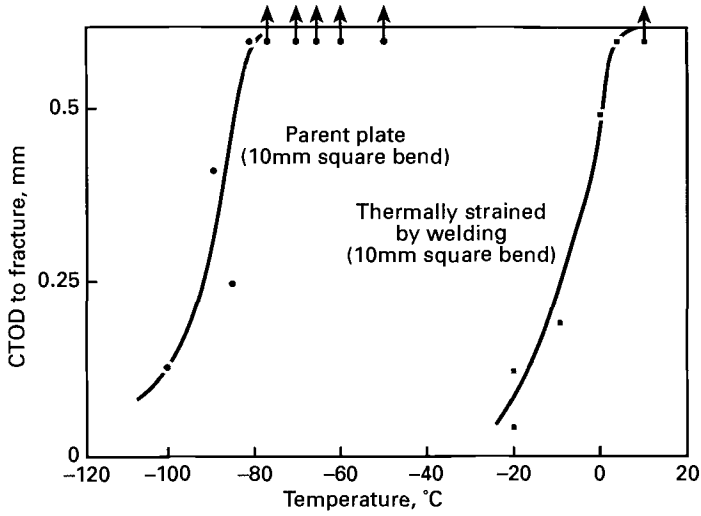


Fig.3. Effect of thermal straining by welding on the fracture toughness of a susceptible steel [Ref 10]

Thus, wide plate [16,18–20] and CTOD tests [9–12] drew attention to the dangers of LISAE in the early rimming, semi–killed and silicon–killed steels, and encouraged the use of the more resistant fully–killed aluminium treated and normalised steels [12].

RECENT EXPERIENCE

The use of LISAE resistant steels, has led to the development of alternative designs of welded wide plate tests [23,24], and fracture mechanics tests on welded joints using specimens that are generally notched after welding into specified regions of a weld [1–3], e.g. the weld metal or the grain coarsened region of the visibly transformed weld HAZ.

The question now has to be asked, 'can we forget about LISAE?'. The answer to this question is surely 'no'; for three main reasons. Firstly, there are many old as–welded structures in service that are fabricated from LISAE susceptible steels, and these will be sensitive to weld repairs. Secondly, many existing weld metals are known to be susceptible to bulk strain ageing embrittlement [7,8], and therefore LISAE also. Thirdly, it would seem unwise to assume that all modern steels and rolling processes will give immunity from LISAE.

There have been two relatively recent examples where LISAE contributed to catastrophic brittle fractures in more than 25 year old steels. These are the failures of the Exxon Port Jerome pressure vessel in 1981, following weld repairs [22], and the Ashland oil tank failure in 1988, after the tank had been rebuilt at a different site [25]. In both instances it was not possible to explain the failures using the results of fracture mechanics toughness tests on specimens notched and precracked after welding. However, fracture mechanics tests on specimens containing welded over notches to induce LISAE showed a dramatic drop in fracture toughness, which then made both catastrophic failures explicable in terms of fracture mechanics analyses.

Figure 4 illustrates some different welded joint situations that have resulted in unpublished low stress brittle fractures in weld metals in as–welded structures in the last 20 years. All involved weld flaws, which acted to intensify the strains during welding. Lack of weld penetration was observed to be an especially potent cause of weld metal failures.

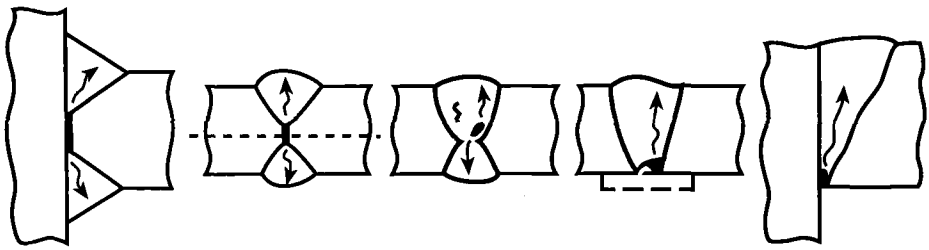


Fig.4. Details associated with brittle fractures in weld metals

Existing steel weld metals have relatively high nitrogen contents compared to modern base metal steels, which has resulted in concern over their susceptibility to bulk strain ageing embrittlement. This is generally assessed [7,8] by compressing a weld to induce 5–10% plastic strain, ageing it at 250°C, and then extracting, notching and testing the fracture toughness specimens in the conventional way (Fig.5), i.e. after welding. Although such treatments may provide useful comparative information, they are clearly arbitrary, and may give misleading overestimates of the fracture toughness associated with LISAE, which as mentioned earlier, can involve notch tip strains greater than 30%.

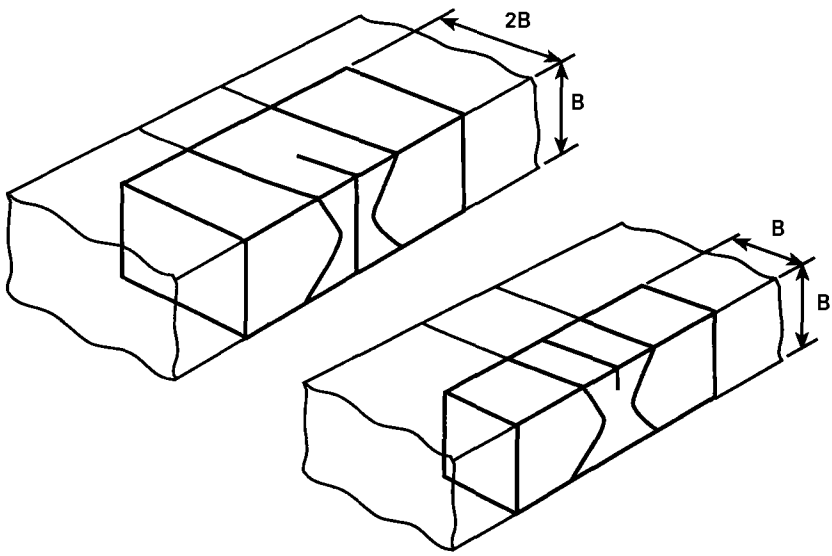


Fig.5. Conventional specimen orientations for fracture toughness tests on weld metals

The above concern for weld metals, concern over failures in old base metal steels [22,25], and even a concern that some modern steels may be susceptible, clearly justifies work to develop fracture mechanics toughness test methods for LISAE.

TEST METHOD FOR LISAE

The proposed test method is based on full thickness square section single edge notched bend specimens (Fig.5). These are prepared and tested in general accordance with the ASTM E-1290 [26], BS 7448 [27], and the draft ISO [28] crack tip opening displacement (CTOD) and J fracture toughness test methods.

Initial development work is concentrated on a LISAE test method for weld metals, as these are presently considered to be of most concern. Commonly used gas shielded metal arc and submerged arc welds are being investigated, and results are being compared for specimens that have been notched either before or after the completion of welding.

Figure 6 illustrates the welding sequence and preparation for four series of comparative bend tests on each weld metal, as follows:

Series STD – Standard specimens with fatigue cracked through thickness notches (Fig.6a).

Series BSA – Specimens given a common bulk straining and ageing treatment, followed by notching and fatigue cracking as above (Fig.6a).

Series LOP – Specimens having surface notches formed by lack of weld penetration (Fig.6b).

Series WOF – Specimens having surface notches formed by welding over flaws (Fig.6b).

Comparing Figs 4 and 6, it can be seen that the Series LOP and WOF simulate the planar flaws that have been associated with brittle fractures in weld metals. Therefore one of these two series probably represents the most appropriate design for a standard LISAE test method for weld metals. The most appropriate design will be determined by the lowest fracture toughness results in the ongoing tests, which include weld metals known to be susceptible to strain ageing embrittlement.

Future work to develop a fracture toughness test for LISAE in base metals is expected to involve welding over notch tips in base metal.

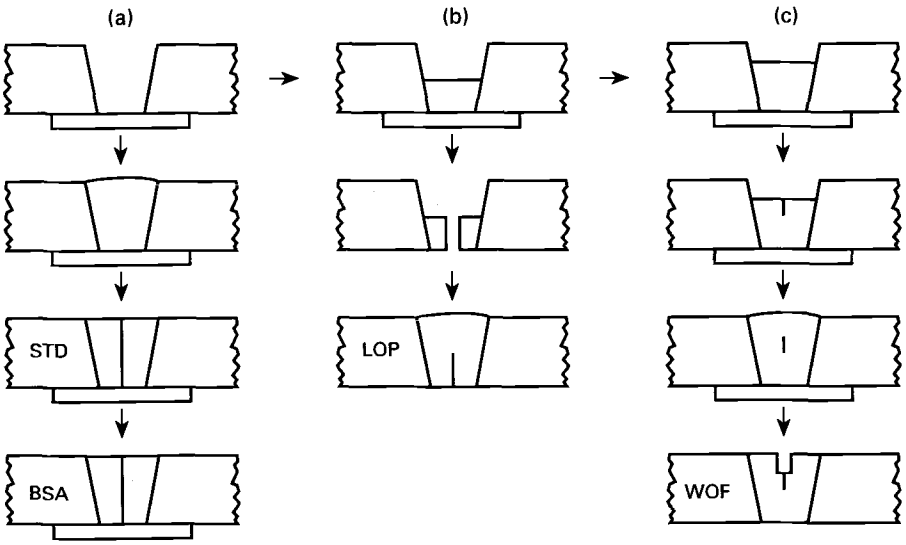


Fig.6. Welding and preparation of specimens for LISAE studies

CONCLUSIONS

1. Locally intensified strain ageing embrittlement (LISAE) in steels is a very potent cause of low stress brittle fractures, and is generally associated with as-welded structures, weld repairs, the older steels, and both old and new weld metals.

2. Fracture toughness tests on steels subjected to bulk straining (5–10%) may grossly overestimate the toughness associated with LISAE.

3. There is an urgent need for a fracture mechanics toughness test methods for LISAE, especially for weld metals.

4. A new test method for LISAE will:
   - Give increased confidence and accuracy in fracture assessments.
   - Be of use in the selection of materials that are resistant to LISAE.
   - Help manufacturers to develop materials that are resistant to LISAE.

ACKNOWLEDGEMENTS

The author is pleased to acknowledge the encouragement and helpful suggestions of his colleagues, and also the financial support of the Industrial Members of TWI in preparing this paper.

REFERENCES

[1] Dawes, M. G., Pisarski, H. G. and Squirrell, S. J., "Fracture mechanics tests on welded joints," ASTM STP 995, Vol. II, 1989, pp 191–213.

[2] Toyoda, M., "Significance of procedure/evaluation of CTOD test of weldments," IIW Doc. X-1192-89, 1989.

[3] API RP 2Z Second edition 1992, "Recommended practice for preproduction qualification for steel plates for offshore structures," API, 1992.

[4] Mylonas, C. and Rockey, K. C., "Exhaustion of ductility by hot straining – An explanation of fracture initiation close to welds," Welding Journal, Vol. 40, No. 7, Research Supplement, 1961, pp 306s–310s.

[5] Baird, J. D., "Strain ageing of steel – a critical review," Iron and Steel, 1963, pp 186–192, 326–334, 386–374, 400–405, 450–457.

[6] Baird, J. D., "The effects of strain ageing due to interstitial solutes on the mechanical properties of welds," Metallurgical Reviews, Vol. 5, February 1971, pp 1–18.

[7] Achar, D. R. G. and Kocak, M., "Nitrogen and strain ageing effects on steel weld metal microstructure and fracture toughness behaviour – A literature review," IIW Doc. II-A-878-93, 1993.

[8] Kocak, M., Petrovski, B., Achar, D. R. G. and Evans, G. M., "Fracture mechanics and wide-plate tests for analysis of nitrogen and strain ageing effects on weld metal fracture properties," IIW Doc. X-1285-93, 1993.

[9] Burdekin, F. M., "Effects of thermal straining during welding on the fracture toughness of a mild steel," British Welding Journal, Vol. 14, No. 2, 1967, pp 81-83.

[10] Burdekin, F. M., "The practical application of fracture tests to prevent service failures," Welding Journal, Vol. 33, No. 3, Research Supplement, 1968, pp 129s-139s.

[11] Dawes, M. G., "Thermal cycles and straining effects in a multipass butt weld," British Welding Journal, Vol. 15, No. 11, 1968, pp 563-570.

[12] Dolby, R. E. and Saunders, G. G., "Sub-critical HAZ fracture toughness of C:Mn steels," Metal Construction and British Welding Journal, Vol. 4, No. 5, 1972, pp 185-190.

[13] Acker, H. G., "Review of welded ship failures," Welding Research Council Bulletin, No. 19, November 1954.

[14] Shank, M. E., "Brittle failure in carbon plate steel structures other than ships," Welding Research Council Bulletin, No. 17, January 1954.

[15] "Final Report of a Board of Investigation to Inquire into the design and methods of construction of welded steel merchant vessels," Washington D.C.; Government Printing Office, 15 July 1946.

[16] Greene, T. W., "Evaluation of effect of residual stress," Welding Journal, Vol. 28, No. 5, Research Supplement, 1949, pp 193s-204s.

[17] Feely, F. J. and Northup, M. S., "Failure of two oil storage tanks, Fawley, England," Standard Oil Development Company, Esso Engineering Department, November 1952 (Presented at an API Meeting, Chicago, 11 November 1952).

[18] Wells, A. A., "The brittle fracture strengths of welded steel plates," Transactions of Institute of Navel Architects, Vol. 98, 1956, pp 296-326.

[19] Hall, W. J., Kihara, H., Soete, W. and Wells, A. A., "Brittle fracture of welded plate," Published by Prentice-Hall, Inc/Englewood Cliffs, New Jersey, 1967.

[20] Woodley, C. C., Burdekin, F. M. and Wells, A. A., "Mild steel for pressure equipment at subzero temperatures," British Welding Journal, Vol. 11, No. 3, 1964, pp 123–136.

[21] Burdekin, F. M., Dawes, M. G., Archer, G.L., Bonomo, F. and Egan, G.R.,'Selection of weldments to avoid fracture initiation', British Welding Journal, Vol. 15, No 12, 1968, pp 590–600.

[22] Merrick, R. D. and Ciuffreda, A. R., "Brittle fracture of a pressure vessel – study results and recommendations," API 48th Midyear Refining Meeting, Session on Unexpected Material Failures – Refinery Performance Impaired, Los Angeles, May 1983.

[23] Dawes, M. G., "Fracture control in high yield strength weldments," Welding Journal, Vol. 53, No. 9, Research Supplement, 1974, pp 369s–379s.

[24] Pisarski, H. G., "Philosophy of welded wide plate testing for brittle fracture assessment," The Fracture Mechanics of Welds, EGF Publication 2 (Edited by J. G. Blauel and K–H. Schwalbe), 1987, Mechanical Engineering Publications, London, pp 191–208.

[25] Mesloh, R. E.,Marschall, C. W., Buchheit, R. D., Kiefner, J. F., Maxey, W. A., Talbert, S. G., Gruber, H. T., Miele, C. R., and Galliher, R. D., "Failure investigation of Ashland Oil Tank No. 1338 at Floreffe, Pennsylvania," Battelle Report, June 1988.

[26] ASTM E1290–93, "Standard test method for crack tip opening displacement (CTOD) fracture toughness measurement," ASTM, Philadelphia, 1993

[27] BS 7448:Part 1:1991, "Fracture mechanics toughness tests, Part 1. Method for the determination of K_{Ic}, critical CTOD and critical J values of metallic materials," BSI, London, 1991.

[28] ISO/TC164/SC4 Committee, "6th draft unified test method for the determination of quasistatic fracture toughness," ISO, 1993.

Wolfram Baer[1] and Gerhard Pusch[2]

INVESTIGATION OF FRACTURE MECHANICAL BEHAVIOUR OF NODULAR CAST IRON AND WELDED JOINTS WITH PARENT-MATERIAL-LIKE WELD METAL

REFERENCE: Baer, W., and Pusch. G., "**Investigation of Fracture Mechanical Behaviour of Nodular Cast Iron and Welded Joints with Parent-Material-Like Weld Metal,**" Fracture Mechanics: 26th Volume, ASTM STP 1256, Walter G. Reuter, John H. Underwood, and James C. Newman, Jr., Eds., American Society for Testing and Materials, Philadelphia, 1995

ABSTRACT: The focus of the investigations was the determination of fracture mechanical characteristics and crack resistance curves of the J-Integral and CTOD concept by application of the partial unloading compliance technique and D.C. potential drop technique (four point bend) under static load.

The results show a close correlation between crack initiation values as well as crack resistance curves and graphite morphology parameters determined by means of quantitative microstructural analysis where the influence of the matrix (distance of graphite particles) dominates the crack resistance and fracture performance of ferritic nodular cast iron under consideration of the notch effect of graphite particles.

SEM in-situ tensile tests showed that due to a beneficial shielding effect of the strength overmatching parent-material-like weld metal (mis-match ratio M=1.21), cracks positioned directly in the plane of the fusion line did not deviate into the weld metal in spite of its lower toughness compared to that of the parent material. They also showed an unsymetrical formation of damage in front of the crack tip.

KEYWORDS: fracture mechanics, crack resistance curves, nodular cast iron, quantitative graphite morphology parameters, welded joints, mis-matching, in-situ tensile test, ductile damage

Taking into account the increasing application of welded castings [1], the determination of fracture mechanical characteristics of ductile cast iron materials and their

[1]PhD-Student and [2]Professor, Freiberg University of Mining and Technology, Institute of Materials Engineering, D-09599 Freiberg/Sachsen, G.-Zeuner-Straße 5, Germany

Copyright © 1995 by ASTM International www.astm.org

welded joints is the basis for an assessment of the influence of the graphite morphology (size, shape, distance of the particles) and different microstructural components in the weld area as a function of the applied stress. Furthermore, this is a prerequisite for fracture mechanical safety analysis of castings containing cracks or crack-type stress concentration spots.

The correlation between crack or flaw size, applied stress and fracture toughness (defined as material resistance to crack initiation or crack propagation depending on the stress mode), which can be derived by means of fracture mechanical concepts, together with conventional criteria of fracture safety permits an assessment of components which is more adequate to the applied stress. This must be taken into consideration, particularly in the case of the safety assessment of potential fracture-endangered castings and their welded joints.

The characterization of the overall performance of a welded joint requires that the effect of non-matching weld metal (overmatching, undermatching) on the toughness behaviour and the fracture mechanical parameters is considered. A lot of research work has been carried out in this field in recent years [2-4].

When discussing the beneficial or detrimental effect of non-matching weld metal (shielding effect of overmatching weld metal, concentration effect of undermatching weld metal) it is important to note that the behaviour of a crack depends not only on the mismatch ratio but also on the hardening behaviour of both components, the weld metal and the parent material. The combined action of the different plastic and toughness properties of weld metal, heat affected zone (HAZ) and parent material makes difficult the quantification of the global behaviour of a welded joint containing a crack-like flaw [5].

Compared to steels, nodular cast iron materials do also exhibit the typical stages of ductile damage during stable crack initiation (crack opening, stretching, debonding of graphite particles from the matrix, growth of holes around the graphite particles, tearing of metal bridges) [6].

This paper focuses on the characterization of the toughness behaviour of nodular cast iron materials of the type GGG-40 and welded joints of these materials by the application and adaptation of experimental methods and concepts of elastic-plastic fracture mechanics (J - Integral, CTOD), which are commonly used for the assessment of steels with special emphasis on the influence of graphite morphology.

EXPERIMENTAL METHOD

Investigated Materials

The materials studied are ferritic nodular cast iron GGG-40 with varying graphite morphology and welded joints of these materials with parent-material-like weld metal (i.e. the weld metal is similar to the parent material, with a ferritic matrix and graphite nodules). In addition, two types of ferritic cast iron GGV-30 with vermicular graphite shape were examined (Table 1).

TABLE 1--Mechanical properties and graphite morphology parameters of the investigated materials

Material	σ_U MPa	$\sigma_{0.2}$ MPa	A %	f	λ µm	ø µm	d µm
GGV-30/4	295	240	5	0.32	37	12	-
GGV-30/6	325	255	8	0.44	51	17	-
GGG-40/1AZ	416	277	24	0.85	54	23	35
GGG-40/2AZ	393	259	26	0.84	58	21	30
GGG-40/4AZ	381	265	21	0.65	93	48	59
Welded Joint with Parent-Material-like Weld Metal							
GGG-40/3AZ	387	278	25	0.70	102	54	50
GGG-40/3GW	369	248	19	0.55	96	49	47
GGG-40/3SG	433	300	19	0.71	20	8	22

The notation is as follows: "/3AZ" - /3...internal numbering, AZ...original state without welding procedure, GW...parent material after welding procedure and post weld heat treatment, SG...weld metal, σ_U...ultimate tensile strength, $\sigma_{0.2}$...0.2 proof stress, A...elongation at rupture.

A detailed characterization of the graphite morphology (Table 1) was carried out by means of a quantitative microstructural analysis with the following parameters: f (shape parameter that approximately describes the notch effect of the particle, $f \leq 1$, f=1 spherical shape, f<1 deviation from spherical shape), λ (mean distance of graphite particles), ø (mean diameter of particles), d (ferrite grain size).

Welding Procedure

The welded joints generated by the application of an optimized welding and in-situ heat treatment technology (Table 2) are characterised by 21% strength-overmatching of the parent-material-like weld metal (mis-match ratio M=1.21, $M=\sigma_{0.2}$ of the weld metal devided by $\sigma_{0.2}$ of the parent material) and a ferritic matrix in the weld metal and the parent material (Table 1). The deposited weld metal contains clearly smaller graphite particles due to relatively fast solidification and the great number of nuclei for graphite formation. During the post weld heat treatment the graphite nodules restrain the ferrite grain growth.

The result of the applied temperature-time regime during the welding and heat treatment procedure is that there are neither brittle structural components nor microstructural gradients in the heat affected zone so that the fusion line directly divides weld metal and parent material.

TABLE 2--Welding technology of ferritic nodular cast iron GGG-40 with parent-material-like weld metal [7]

welding method:	manual metal-arc welding, D.C., electrode = plus pole
weld metal:	parent-material-like rod electrode GRICAST 55
welding seam preparation:	single-bevel butt weld, 45°-angle, plate thickness = 14 mm, root split = 2 mm, 2° roof pass (TIG-tacked)
backing:	shaped copper bar
welding parameters:	preheating temperature 650 - 700 °C, maintained by heating mats, 5 layers
post weld heat treatment:	920°C/180min (in-situ, i.e. without intermediate cooling from the welding heat: heating and maintaining of temperature by heating mats), cooling: $t_{8/5}$-time = 190 min

Fracture Mechanics

The determination of fracture mechanical characteristics of the original state and the welded joints by application of the J-Integral and CTOD concepts was carried out on 20% sidegrooved SENB specimens (a/W=0.5, thickness B=10 mm, width W=20 mm), under static load and 4-pt bend according to the ESIS Procedure for Determining the Fracture Behaviour of Materials (P2-92) [8]. Computer aided testing and analysis of the crack resistance curves (J-R and δ-R curves) were performed by the partial unloading compliance technique. By means of an additional device that is directly fixed to the specimen, the load-line displacement for the determination of the compliance and J Integral values was measured in the plane of crack propagation (Fig. 1). The J_i^{BL} and δ_i^{BL} physical crack initiation values were determined at the point of intersection of the calculated J-R and δ-R curves with the analytical blunting line and the technical crack initiation values $J_{0.2}$ and $\delta_{0.2}$ at a value of $\Delta a = 0.2$ mm of stable crack growth.

Simultaneously, the D.C. potential drop technique was applied for experimental determination of stable crack initiation and provided J_i^{EP} and δ_i^{EP} crack initiation values.

An analysis of the registered potential - deflection curves showed that it was possible to reproducibly and relatively unambiguously determine the point of stable crack initiation even in the case of a combination of the D.C. potential drop technique with the partial unloading compliance technique.

Stretch Zone Measurement

A new method for stretch zone measurement with a laser instrumented device for the measurement of surface roughness by the profile method [9] was practised as an alternative to the SEM technique and adapted to the analysis of ferritic nodular cast iron.

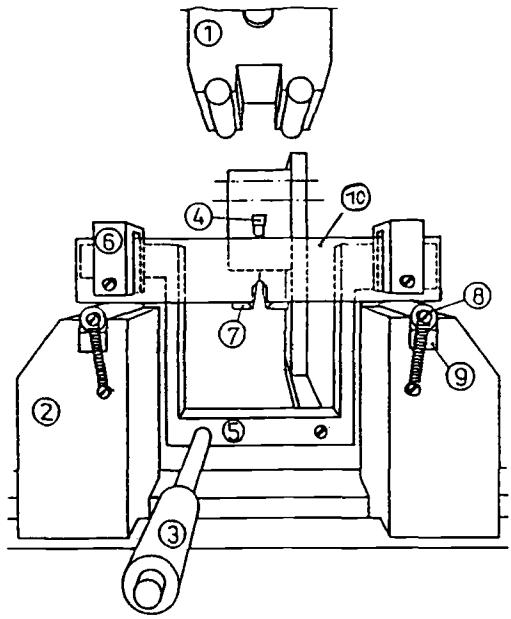


FIG. 1--Scheme of used test device for the registration of deflection for J-R and δ-R curve analysis (4-pt bend):
1-Bending plunger, 2-Support, 3-Balance load, 4-Transducer for load point displacement, 5-Fixation frame, 6-Fixation bow, 7-Knife edges for fixation of CTOD clip-on transducer, 8-Support rollers, 9-Support plates, 10-SENB specimen

The fracture surface is scanned in 70 profiles across the specimen thickness with a resolution of 1 micron horizontal and 0.1 microns vertical. With the help of special analyzing software the profile data can be processed and it is possible to determine the critical values of stretch zone width (SZB_c) and height (SZH_c) at the same time (Fig. 2). The combination of the 2-dimensional profiles provides a 3-dimensional outline of the fracture surface (Fig. 3). This method offers handling and time advantages and was justified by comparative measurements with SEM.

With the analysis of nodular cast iron arises a number of material-specific difficulties such as the relatively strong roughness of the fatigue crack surface due to the graphite particles, non-uniform stretch zone formation across the specimen thickness, and a possible local terrace-shaped image of the stretch zone. Additional information such as the fatigue crack length was found to be useful for a better reproducible determination of stretch zone parameters.

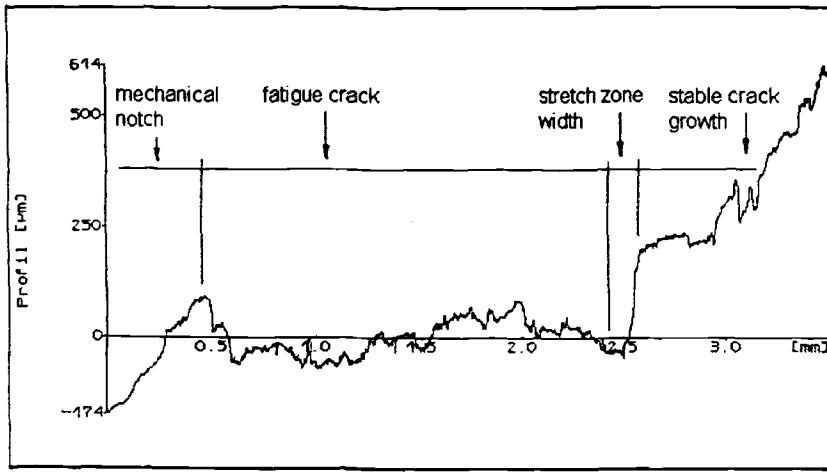


FIG. 2--Single profile for analysis of fracture surface topography

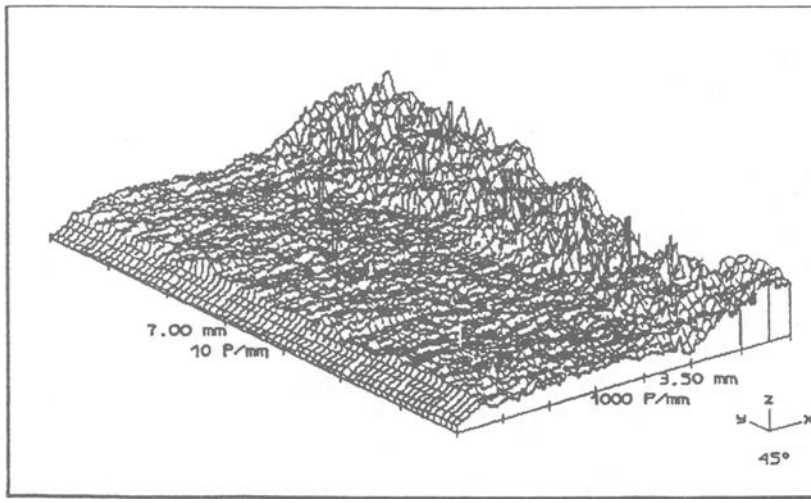


FIG. 3--Three-dimensional image of a GGG-40 SENB specimen fracture surface

In-situ Tensile Tests

SEM in-situ tensile tests were performed with the use of specimens with different crack positions in the weld (Fig. 4), to examine and document on video the damage processes in front of the crack tip (crack opening, stretching, debonding of graphite particles from the matrix, growth of holes around the graphite particles, tearing of metal bridges) during crack initiation and propagation, and to investigate the influence of weld metal mismatching on the toughness behaviour of GGG-40 welds.

The surfaces of the specimens were in polished condition so that it had additionally been possible to analyse the formation of the plastic zone and the different deformation behaviour of weld metal and parent material by measuring the distribution of lateral deformation by means of a laser instrumented surface roughness measurement system.

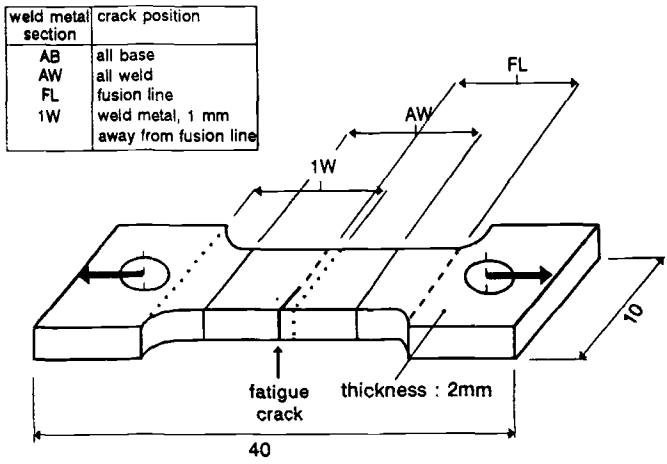


FIG. 4--Scheme of the used SEM in-situ tensile specimens

The subject of the investigations was not only the influence of different crack positions in the weld but also different notch acuity. Each set of specimens (Fig. 4) was tested with three different notch radii: 150; 85 and 0 (fatigue crack) microns, respectively. The influence of notch acuity will be the subject of a future paper. This paper concentrates on first results of the influence of the crack position.

RESULTS AND DISCUSSION

The following analysis mainly concentrates on the results of the J Integral concept because the CTOD concept provided widely adequate correlations.

The J-R crack resistance curves (Fig. 5) reflect the increasing crack growth resistance of ferritic nodular cast iron with rising distance of the graphite particles, as well as the detrimental influence of the higher notch effect of the vermicular graphite. In the investigated welded joints of GGG-40/3AZ, the weld metal showed a clearly lower crack initiation toughness defined by the physical and technical crack initiation values (Table 3). A comparison of strength values of the original state, parent material and

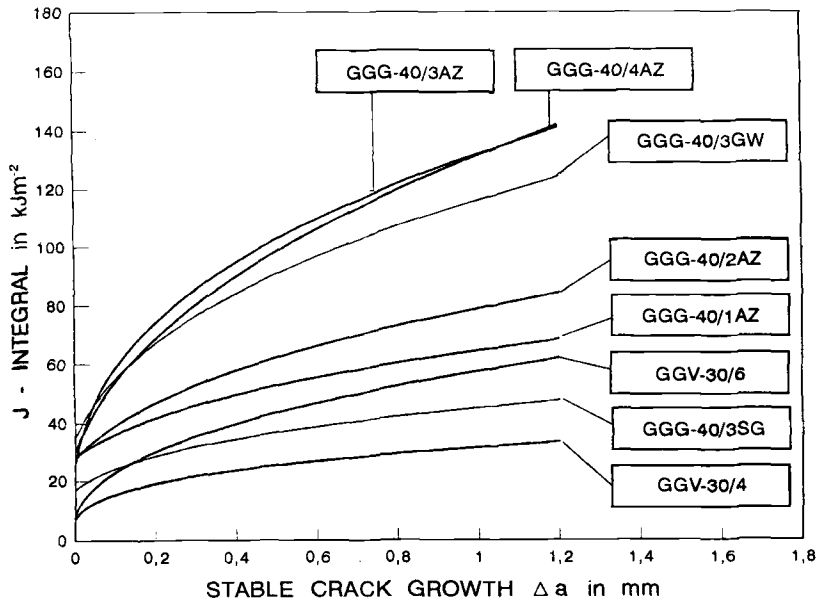


FIG. 5--Crack resistance curves of the investigated ferritic nodular cast iron materials and welded joints

weld metal shows their increase for the weld metal depending on the microstructure, whereas the deformation characteristics remain nearly constant. The hardening behaviour of the weld metal (hardening exponent n = 0.16) nearly equals that of the parent material (hardening exponent n = 0.17).

Obviously, there is no correlation between the values of the critical stretch zone width and the graphite morphology parameters. The crack initiation toughness values J_i^{SZBc} based on the critical stretch zone width SZB_c are clearly lower than the technical values $J_{0.2}$ and show good agreement with the other physical crack initiation values J_i^{BL}.

The experimental determination of physical crack initiation characteristics by use of the D.C. potential drop technique is possible at a justifiable cost and offers the advantage, especially with the evaluation of welded joints, that the influence of a possible crack deviation (e.g. from the HAZ into the weld metal) is eliminated by the restriction of the amount of stable crack growth. For the investigated materials these J_i^{EP} values fit in between the J_i^{BL};J_i^{SZBc} and $J_{0.2}$ values but tend to correspond to the physical crack initiation values.

The crack initiation and propagation resistance of ferritic ductile cast iron is dominated by the ductile matrix. The strength overmatching of the weld metal is accompanied by lower crack initiation and propagation toughness which is due to the small size of the graphite particles in spite of the beneficial effect of a small ferrite grain size

TABLE 3--Fracture mechanical characteristics and critical Stretch Zone Width

Material	J_i^{BL} kJm^{-2}	J_i^{EP} kJm^{-2}	J_i^{SZBc} kJm^{-2}	$J_{0.2}$ kJm^{-2}	SZB_c µm
GGV-30/4	8	15	-	19	-
GGV-30/6	11	20	13	28	23
GGG-40/1AZ	23	28	25	41	21
GGG-40/2AZ	30	34	30	47	21
GGG-40/4AZ	35	52	36	68	23
Welded Joint with Parent-Material-like Weld Metal					
GGG-40/3AZ	40	56	40	75	25
GGG-40/3GW	42	36	41	68	24
GGG-40/3SG	18	21	20	30	17

on toughness. A smaller mean distance between the graphite particles correlates with its smaller size. This and the direct proportionality between the critical crack tip opening δ and the size of particles resulting from theoretical models are also considered to be the reason for the loss of toughness with decreasing particle size. Concerning the shape of graphite particles, it should be noticed that a deviation from the spherical shape represented by the shape factor also leads to a decrease of crack initiation toughness due to the additional increase of the notch effect (Fig. 6).

The slight loss of crack propagation resistance (slope of R-curve) of the parent material GGG-40/3GW after the welding procedure compared to that of the original state GGG-40/3AZ may be due to the slightly smaller shape factor of graphite particles as a result of the segregate graphite formation during post weld heat treatment. It seems to be very unlikely that this effect could also be the reason for the relatively great difference between J_i^{EP} of GGG-40/3AZ and GGG-40/3GW rather than a random experimental error.

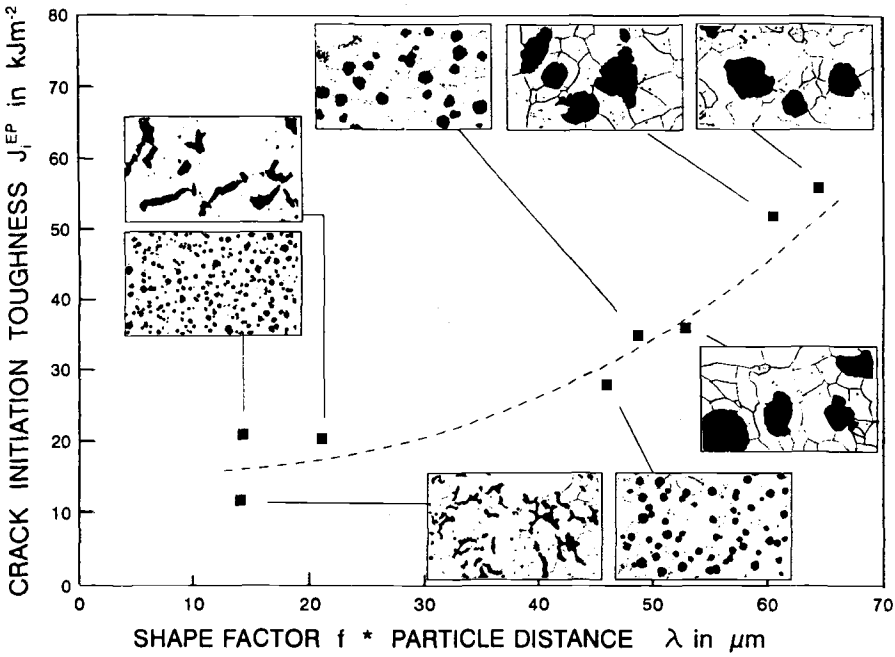


FIG. 6--Correlation between crack initiation values of the investigated ferritic nodular cast iron materials and graphite morphology parameters

The SEM in-situ tensile tests showed adequate mechanisms of damage for the material with both large and small graphite particles (parent material and weld metal, respectively). The stages of crack opening, stretching, debonding of graphite particles from the matrix, growth of holes around the graphite particles, tearing of metal bridges were observed in front of the crack tip (Fig. 7a and 7b). Figure 7a) shows a blunted crack tip on the upper margin and graphite particles (black spots) surrounded by holes due to intensive plastic deformation. Partly, the holes have already coalesced and form microscopical cracks. The black spot on the right margin marks an intersected hole of a graphite particle under the surface. Measurements of the size of the holes around the graphite particles normalized by the particle size provided values of up to 40% of local plastic strain. This formation of damage characterizes a strong energy dissipative process because not all the newly formed microscopical cracks do necessarily coalesce with the main crack, and the formation of holes has been detected in a range up to several millimeters aside the plane of crack propagation.

Two mechanisms of debonding of the matrix from nearly nodular shaped graphite particles have been observed and first occur as early as during the elastic deformation of the specimen. Either the matrix debonds directly from the nodule's surface or the

debonding occurs on the interface between primary and segregate graphite (Fig. 7b). Graphite particles with highly irregular shape, for instance vermicular graphite, may also break through.

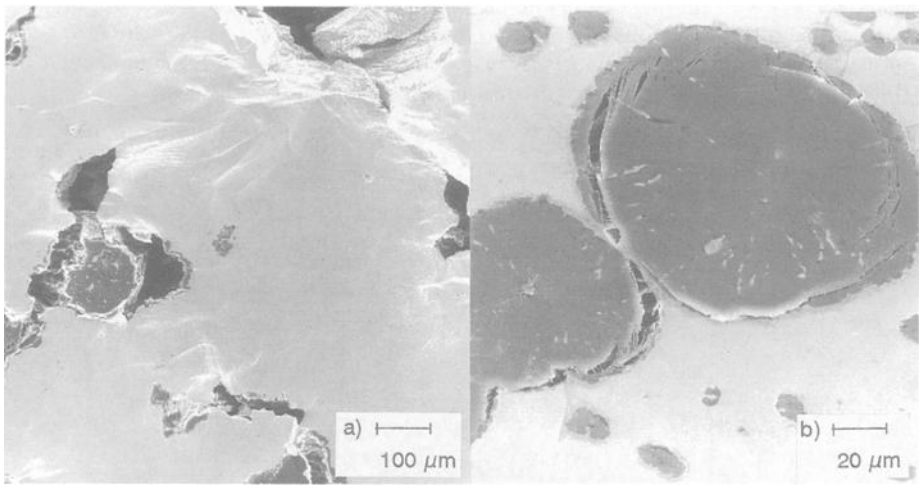


FIG. 7a) and b)--Local damage of nodular cast iron

Figures 8a) and 8b) illustrate that the crack originally positioned on the fusion line exactly follows this line when gradually extending from one large graphite particle to

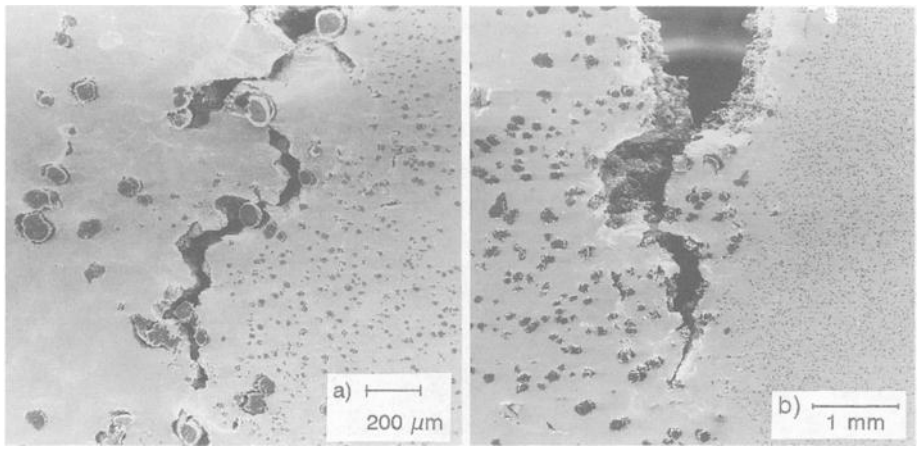


FIG. 8a) and b)--Crack line of an in-situ tensile specimen with a crack positioned on the fusion line

the next and does not deviate into the weld metal in spite of its lower toughness (Table 3). This can be explained as a result of a shielding effect of the 21 per cent strength-overmatching weld metal.

The process of blunting and growth of holes is repeated during crack propagation, in which the crack is not initiated before the damage reaches a critical value over a characteristic length that sometimes seems to be greater than the mean particle distance.

An analysis of the specimen surfaces was performed after the tests. Figure 9 shows the image of an FL-specimen (Fig. 4) with weld metal left and parent material right.

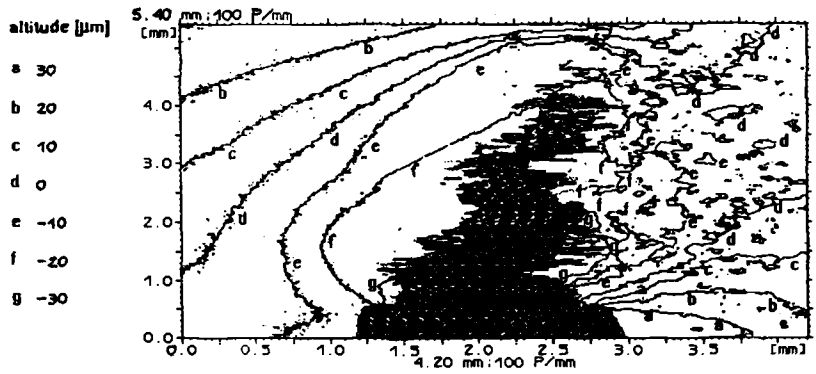


FIG. 9--Image of asymmetric distribution of lateral deformation of an FL-specimen

The spacing of the contours underlines the asymmetric distribution of lateral deformation. Furthermore, the area of damage in the parent material is significantly greater than in the weld metal, which is characterized by the open shape of the contours towards the right edge. In comparison to Figure 9, Figure 10 illustrates the symmetric de-

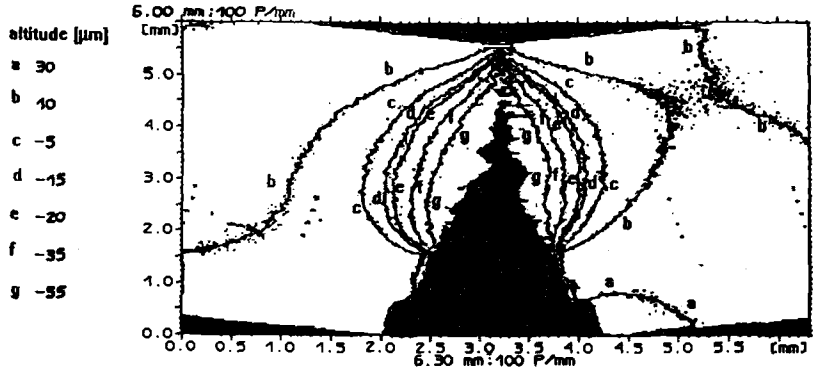


FIG. 10--Image of the symmetric distribution of lateral deformation of an AW-specimen

formation behaviour of an AW-specimen (Fig. 4).

With the SEM in-situ tensile tests, after the end of crack tip blunting the degree of crack tip opening displacement δ_{crack} was measured at the point of stable crack initiation (Table 4). Provided that

$$\delta_{crack} = 2 * SZH_C \quad (1)$$

and

$$SZH_C = 2 * SZB_C \quad (2)$$

where

SZH_C = critical stretch zone height, μm, and
SZB_C = critical stretch zone width, μm,

holds for nodular cast iron materials [10], the crack initiation toughness values J_i^{SZBcis} were calculated by substituting SZB_{cis} in the relevant R-curve equation.

TABLE 4--Crack initiation data calculated from critical stretched zone values of AB- and AW-specimens

Specimen (see Fig. 4)	δ_{crack} , μm	Critical stretch zone width SZB_{cis} , μm	J_i^{SZBcis} , kJm^{-2}
AB	198	50	46
AW	61	15	19

SZB_{cis} ... critical stretch zone width of in-situ tensile specimens
J_i^{SZBcis} ... crack initiation toughness for $\Delta a = SZB_{cis}$

In spite of the totally different sample size and geometry, the crack initiation toughness values J_i^{SZBcis} show good agreement with the J_i^{SZBc} values of the SENB specimens (Table 3).

CONCLUSIONS

Fracture mechanical investigations of ferritic nodular cast iron materials with different graphite morphology and their welded joints with parent-material-like weld metal draw attention to the significant correlation between graphite morphology and both crack initiation and crack growth resistance. The crack initiation toughness values increase with a greater mean graphite particle distance and a greater shape factor.

SEM in-situ tensile investigations of the influence of strength mis-matching on the toughness behaviour of the welded joints showed that due to a shielding effect of the overmatching weld metal the loss of toughness of the weld metal is not necessarily

critical for the global behaviour of a welded joint containing a crack-like flaw. Furthermore, the examinations of damage formation on the graphite particles in front of a crack tip underline the ductile damage mechanism of the investigated materials.

The proportion in size of the graphite particles in nodular cast iron compared to inclusions in steels reduce the experimental difficulties of observation and analysis of ductile damage processes. Therefore, ferritic nodular cast iron materials seem to be especially suitable for the application of damage mechanics regarding the aspect of permanent comparison of models and calculations with experimental data.

The object of further investigations will be the application of micromechanical models of ductile damage to ferritic nodular cast iron materials for failure prediction.

ACKNOWLEDGEMENT

The financial support of this investigation by the Deutsche Forschungsgemeinschaft (German Science Foundation) is gratefully acknowledged.

REFERENCES

[1] Proceedings of the Fifth Conference "Sicherung der Güte von Schweißungen an Gußstücken", April 2-3, 1992, DVS-Berichte Vol. 149, Dt. Verlag für Schweißtechnik, DVS-Verlag, 1992

[2] Koçak, M. and Schwalbe, K.-H.: Fracture Mechanics of Weldments: Microstructural, Experimental and Mechanical Aspects, Proc. of the 9th Biennial European Conf. on Fracture - ECF 9, 21-25 September, 1992, Varna, Bulgaria, Vol. II, pp. 717-747

[3] Dexter, R. J. and Denys, R.: Behaviour of Line Pipe with Overmatched/Undermatched Girth Weld or Softened HAZ, Proc. of the 8th Biennial Joint Technical Meeting on Line Pipe Research, Paris, May 14-17, 1991, Vol. II, paper no. 23

[4] Toyoda, M. and Satoh, K.: Fracture toughness of welds: The incidence of mechanical heterogenity in the correlation of toughness parameters, Welding in the world, Vol. 22, 1984, No. 3/4, pp. 76-86

[5] Schwalbe, K.-H.: Effect of weld metal mis-match on toughness requirements: Some simple analytical considerations using the Engineering Treatment Model (ETM), International Journal of Fracture, 56, 1992, pp. 257-277

[6] Pusch, G., Baer, W. and Rehmer, B., "Gefüge und Bruch duktiler Gußeisenwerkstoffe", Conference "Gefüge und Bruch", Bochum, March 17-19, 1993

[7] Pusch, G., Baer, W. und Michael, A.: Beitrag zur Optimierung artgleicher Schweißverbindungen des ferritischen Gußeisenwerkstoffes GGG-40, Gießerei , 80 (1993) 7, pp. 227-231

[8] European Structural Itegrity Society: ESIS Procedure for Determining the Fracture Behaviour of Materials ESIS P2-92, ESIS Office, Delft University of Technology, The Netherlands, January 1992

[9] Louis, H. "Stretchzonen-Bestimmung mit Hilfe eines modifizierten Tastschnittverfahrens", research report Lo 223/8-2, Universität Hannover, 1991

[10] Pusch, G. and Baer, W., Ermittlung fließbruchmechanischer Kennwerte für ferritische Gußeisenwerkstoffe und ihre Schweißverbindungen, research report Pu 104/1-3, TU Bergakademie Freiberg, 1994

Mustafa Koçak , Patrick Hornet , Alfred Cornec and Karl-Heinz Schwalbe

FRACTURE TOUGHNESS TESTING OF BI-MATERIAL JOINTS WITH HIGH STRENGTH MIS-MATCH

REFERENCE: Kocak, M., Hornet, P. Cornec, A., and Schwalbe, K.-H, "**Fracture Toughness Testing of Bi-Material Joints with High Strength Mis-Match,**" Fracture Mechanics: 26th Volume, ASTM STP 1256, Walter G. Reuter, John H. Underwood, and James C. Newman, Jr., Eds., American Society for Testing and Materials, Philadelphia, 1995.

ABSTRACT : This paper deals with the influence of strength mis-match on CTOD (δ_5) R-curves obtained from homogeneous and electron beam (EB) welded bimaterial CT and SENB specimens of two aluminium alloys. The R-curves of metal-metal bimaterial specimens are compared with the R-curves of each alloy to determine the effect of strength mismatch on the locally measured CTOD (δ_5) fracture toughness properties. The homogeneous specimens of two different aluminium alloys, namely 2024-FC and 2024-T351 with yield strengths of 80 and 360 MPa respectively, as well as EB welded bi-material 5 mm thick CT and SENB specimens (a/W=0.15 and 0.5) have been tested at room temperature. The local CTOD (δ_5) fracture toughness measurements on such composite specimen configurations produced generally strength mis-match and geometry independent R-curves.

KEYWORDS: bimaterial, strength mis-match, R-curves, CTOD (δ_5), shallow crack, metal-metal interface, electron beam weld, Al-alloys.

The different regions of conventional weld or bi-material joints exhibit significantly different mechanical properties. All fusion welding processes produce a heat affected zone (HAZ), which results in material properties different from those of base and weld deposit. Additionally, there are many structural components containing dissimilar (bimaterial) weld joints with a high degree of strength mis-match and such joints are the most susceptible regions for defects and/or cracks. The failure behaviour of a welded structure associated with a defect in the weld zone will certainly be influenced by the differences of the strength levels of the weld metal (σ_{YW}), heat affected zone (HAZ) and base metal (σ_{YB}). The strength mis-match has usually been defined by the mis-match factor, M, $M = \sigma_{YW}/\sigma_{YB}$.

GKSS Research Center Geesthacht, Institute of Materials Research
D - 21502 Geesthacht, F. R. Germany

Copyright © 1995 by ASTM International www.astm.org

The bi-material joints

The study of complex stress/strain fields around interface cracks and the application of elastic-plastic fracture mechanics parameters under various loading modes are of great interest for the strength and fracture toughness analysis of bi-material joints. It has been well documented that the fracture resistance of a bimaterial interface crack strongly depends on mode mixity (crack growth occurs under mixed mode conditions) [10-14]. Therefore, interfacial fracture toughness has usually been characterized for various mixed mode loading conditions or phase angles (ψ) [15-16]. The phase angle or mode of mixity gives the ratio of the normal to shear stress ahead of the crack, when ε = 0. In terms of K_I and K_{II} definitions, the phase angle can be defined as; $\tan(\psi) = K_{II} / K_I$. An increase of toughness has been observed by Tvergaard and Hutchinson [11] with increasing proportion of mode II to mode I due to the development of plastic deformation outside of the fracture process zone. The studies of Shih and Asaro [12-14] on bimaterial cracks in elastic-plastic materials show that the stress state and extent of plasticity are determined mainly by the lower strength (weaker) material.

Specimen geometry

The strength mismatch effect on fracture toughness properties, however, does not only depend on the tensile properties of the materials involved, the specimen's dimensions and the crack size, but also on the loading mode (bending or tension) and the position of the crack (distance and orientation to the interface) [17-19]. Failure of the structural components (under residual and/or applied stresses) containing bimaterial interfaces may occur either along the interface or within one of the constituents (material A or B) depending on the toughness of each constituent, toughness of the interface, specimen geometry and type of loading. It is generally believed that for deeply weld metal cracked (a/W=0.5) mis-matched bend specimens, standard CTOD and J-integral procedures can be used if the weld width (2H) is greater than the uncracked ligament (W-a) of the bend specimen. However, the limit of the applicability of present toughness testing procedures with respect to the degree of mis-match levels and weld widths needs to be established. The application of J-integral to a crack in the EB weld metal of finite size (approx. 2mm) or at a bi-material interface relies on an existing stress field at the crack tip comparable to the known stress and displacement field of homogeneous materials. However, a bi-material interface influences the crack tip stress field and crack tip plasticity development and hence global plastic deformation behaviour of the specimen substantially. Therefore, the problem of measuring a meaningful J-integral value on a bimaterial specimen is very hard to solve, since it is not easy to distinguish the contributions of both sides of the crack tip or bulk material parts of the specimens to the remotely measured load line displacement (V_{LL}) normally used in J estimate.

A study conducted by the authors provided some information on the J R-curve behaviour of the SENB specimens with shallow and deep cracks located in the highly mismatched middle strip (weld metal). It was concluded that the local CTOD (δ_5) measurements on such complex specimen configurations provided mis-match and geometry independent R-curves, whereas, standard J estimation scheme and some modified J formulations (for mis-matched and shallow cracked configurations) still showed the effects of strength mis-match on the R-curves significantly [20].

This paper presents the results of an experimental study on the influence of strength mis-match on the CTOD (δ_5) R-curves obtained from deep and shallow cracked bend specimens. The present study covers the CTOD (δ_5) R-curves for cracks

For example, for cracked girth welded pipes, there are no currently available reliable estimation techniques to evaluate the structural performance of such pipes. Predictions are usually made using base metal stress-strain data and cracked weld metal resistance curves. Obviously, such a procedure can lead to conservative or non-conservative predictions depending on the strength mis-match ratio, M and relative weld joint size with respect to the uncracked ligament of the specimen on which R-curves are determined. Therefore, the effect of weld strength mis-match on elastic-plastic fracture parameters (CTOD & J-integral), crack resistance curves and hence on the standard fracture toughness test procedures should be determined since these procedures are frequently used to determine the fracture toughness properties of welded joints. It is apparent, however, that both standardized parameters determined by standard test procedures can not fully quantify the fracture toughness of such bimaterial joints due to heterogeneous deformation patterns at the vicinity of the crack tip.

Therefore, the commonly used standard procedures to evaluate fracture toughness (J or CTOD) of homogeneous specimens [1-4] cannot be extended in a straightforward manner to strength mis-matched weld or bimaterial configurations. In fact, the experimental way to calculate the J-integral from the area under the load-load line displacement curve ($F\text{-}V_{LL}$) cannot be generally applied to inhomogeneous fracture mechanics specimens [5-8]. Also, in the case of a specimen with a crack located in the middle of the highly overmatched weld, remote plasticity may develop in the base metal and hence the standard J-integral estimated can be significantly overestimated [6-7]. The CTOD inferred from remotely measured crack mouth opening displacement (CMOD) can also provide toughness properties influenced by the strength mis-match of the weld metal. The CMOD measurements made on part of the crack faces must bear some relation to crack tip displacements even in the bimaterial and mis-matched cases, but the nearer the displacement measurements made to the crack tip itself, the more reliable they are likely to be.

The local CTOD (δ_5)

The use of local CTOD (δ_5) measurements on a 5 mm gauge length perpendicular to the crack at its tip, as developed by Schwalbe et al [9] at the GKSS research center, is a useful method of conducting measurements to indicate crack tip opening behaviour in fracture toughness tests. Therefore, the use of this locally measured CTOD (δ_5) for weld metal, HAZ and bi-material interface fracture toughness testing can be considered as a meaningful method. This technique provides local measurement without the need to infer from remotely measured quantities, like the J-integral or the standardised CTOD. This is of particular importance when the specimen is mechanically inhomogeneous, as it is the case for mis-matched welds and bi-material interfaces, since an interface crack or the HAZ of mis-matched joint exhibit a CTOD which is composed of the contributions from both sides of the crack joints. For highly mismatched weld and bimaterial configurations, CMOD measurements can also be considered as a remote quantity to measure crack tip deformation due to the asymmetric crack tip opening and/or remote plasticity at the lower strength part of the test pieces. This effect can be particularly extreme on shallow cracked specimens. Therefore, it would be ideal, if the critical crack tip characterising parameter can be **locally quantified or measured** on mis-matched or bi-material joints and not be inferred from remotely measured quantities, like J-Integral and standardised CTOD.

located at the interface (EB weld zone) of bimaterial joints and highly strength mis-matched weld specimens with cracks located in the middle of the weld zone.

EXPERIMENTAL PROCEDURE

Two aluminium alloys, Al 2024-FC (Material **A**) and Al 2024-T351(Material **B**) with very different yield strengths (80 MPa and 360 MPa respectively) have been welded by the electron beam (EB) process to obtain highly strength mis-matched bimaterial joints. The engineering stress strain curves of both alloys are given in Figure 1. The combination of both materials provides a dissimilar joint in which one of the component remains elastic while the other undergoes fully plastic deformation. Standard round tensile, compact tension (CT) and single edge cracked bend (SENB) specimens were extracted from these welded plates of 5 mm thickness.

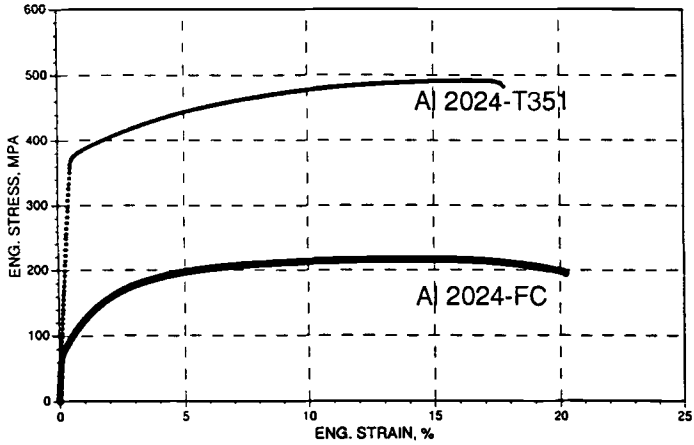


FIG. 1--The stress - strain curves of the two aluminium alloys.

The undermatching (**UM**) weld joint (**B-A-B** configuration) was simulated by EB welding the lower strength material **A** strip of 8 mm width (2H) with the higher strength material **B** blocks as shown in Figure 2. For overmatched (**OM**) specimens (**A-B-A** configuration), a strip of higher strength material **B** with identical width was welded to simulate the weld metal, whereas material A served as a base metal. By using these combinations, 5 mm thick SENB specimens with a high degree of mis-matching; M=0.22 and M=4.5 were obtained for undermatching and overmatching cases, respectively. Such an experimental matrix enabled us to conduct fracture toughnesss tests on homogeneous specimens (**A** and **B**) to compare with UM and OM specimens as shown in Figure 2. For bimaterial specimens (**A-B** configuration), the cracks were located at the EB weld region (2mm wide) and hence specimens were treated as an interface crack parellel to the boundary dividing the two materials, Figure 2.

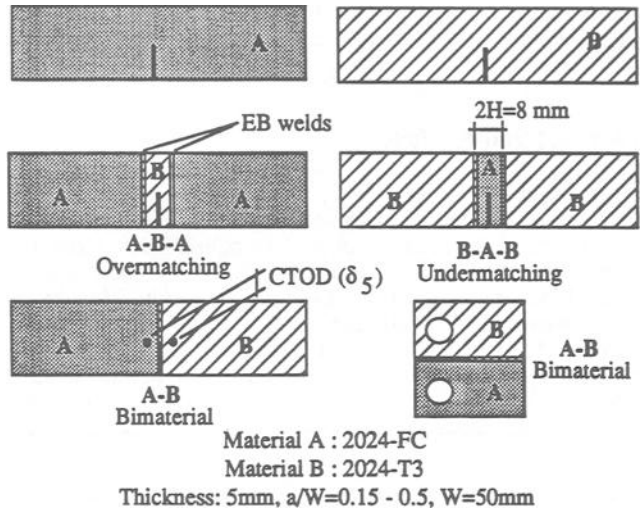


FIG.2--The SENB and CT specimen configurations used in this study. The SENB specimens were tested using shallow (a/W=0.15) and deep cracks (a/W=0.5).

Homogeneous, UM, OM and bimaterial SENB specimens (B=5 mm, W=50 mm) were fatigue pre-cracked to obtain shallow (a/W=0.15) and deep cracks (a/W=0.5) and were tested at room temperature. The experimental approach used was to measure the crack tip opening displacement, CTOD (δ_5) with GKSS made δ_5 clip-on gauges at the original fatigue crack tip over a gauge length of 5 mm, [9], the crack mouth opening displacement (CMOD) and the crack propagation using the DC-potential drop method [21] as a function of the applied load. In addition to the homogeneous round tensile specimens (d=5mm) of both alloys, bimaterial round tensile specimens have also been tested with a gauge length of 25 mm. On these bimetallic specimens, an elongation of each material part was measured separately by two different clips to determine the contribution of each material to the fracture strain.

RESULTS AND DISCUSSION

Mechanical Properties

Figure 3 shows the Vickers hardness profile across the bimaterial electron beam weld joint. The hardness differences between both Al-alloys and EB weld region (and σ-ε curves of both materials, Fig. 1) indicate the extreme heterogeneity of the bimaterial joint. According to the hardness distribution, the weld region represents a zone of mixture of both Al-alloys due to the equal dilution of both materials. The hardness value of this zone is about 110 Hv which is about an average value of both sides (70 and 140 Hv for A and B materials respectively). Hence, it can be assumed that the EB weld zone has the average tensile strength properties of both Al-alloys.

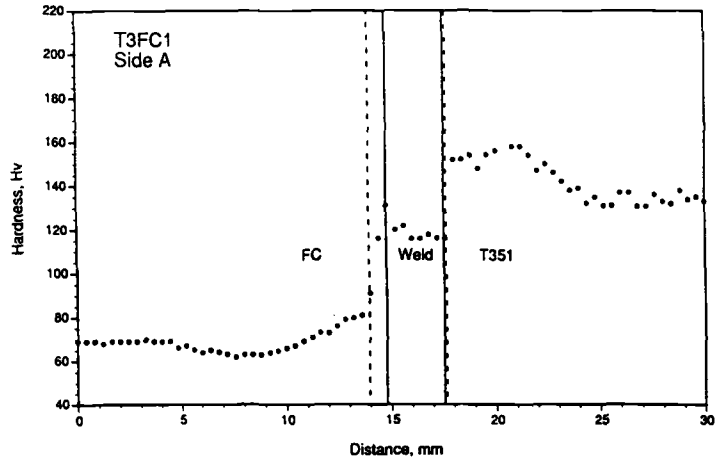


FIG. 3--The hardness distribution across the EB weld joint (A - B configuration) of two aluminium alloys.

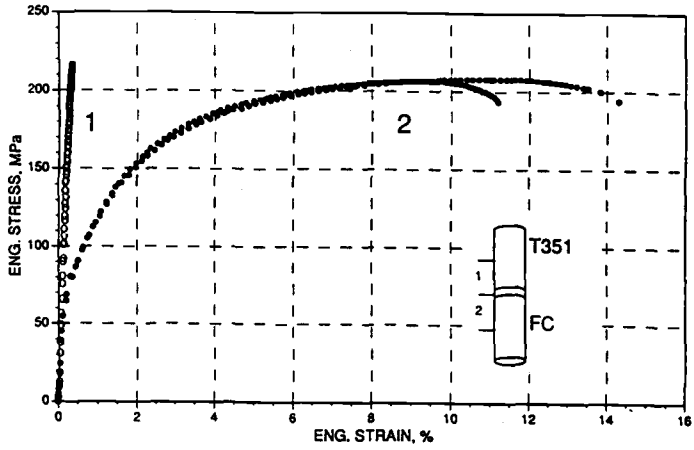
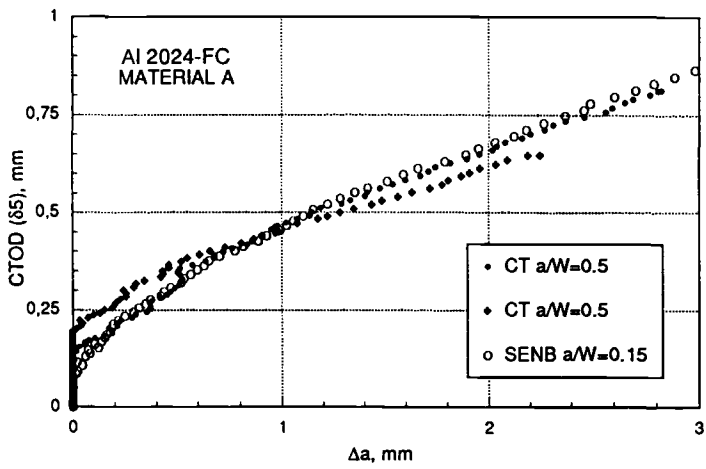


FIG. 4--The stress - strain curves obtained from round tensile specimens extracted from the EB welded joint. Three clip gauges were used to obtain strain levels of both constituents of bimaterial joint. Curves 1 and 2 for material B and A respectively (Gauge length of 8 mm for clip 1 and 2).

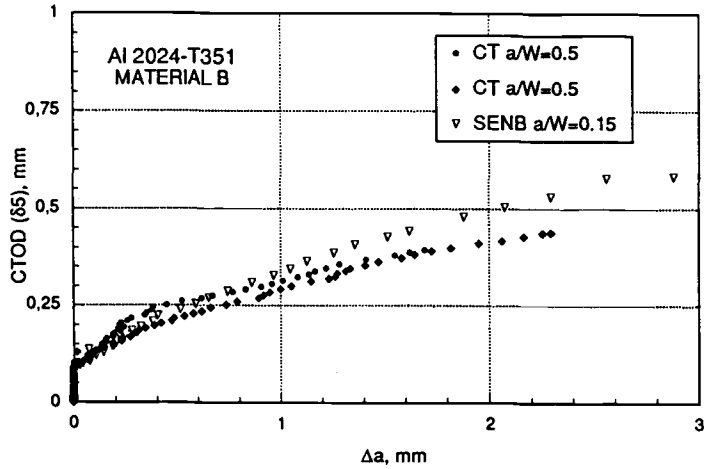
Figure 4 presents the stress-strain curves obtained from two bimaterial round tensile specimens. Here the elastic properties of the constituents (materials A, B and EB weld zone) of the bimaterial specimen are the same, while one material has a substantially larger yield strength than the other which remains elastic for the whole loading range. Therefore, material A (lower yield strength) deforms and breaks without any plastic deformation of the higher yield strength material B. The comparison between Figures 1 and 4 shows that when combined with B, material A has a lower straining capacity. The presence of the stronger material creates shear stresses at the interface which may cause an increase of the stress level in the material A side. Development of plasticty concentration at the bimaterial interface (due to the disparity in strength which exist between the two zones) has also been observed in [7] for short cracked overmatched CCT specimens. It is apparent that the presence of higher strength (overmatched) material has a negative influence on the plastic straining capacity of the neighbouring undermatched material.

CTOD (δ_5) R-Curves

The CTOD (δ_5) resistance curves of materials A and B obtained from CT and shallow cracked (a/W=0.15) SENB specimens are shown in Figure 5. No dependence of the R-curves of both materials on the crack size can be seen in these plots when shallow cracked SENB results are compared with the two deep notched CT specimen R-curves. Nevertheless, a reasonable scatter for the CTOD (δ_5) resistance curves can be observed for two similar CT specimens made of the same material (Fig. 5a and 5b). By comparing the CTOD (δ_5) resistance curves of the two materials (Figs. 5a and 5b), the material A provides higher resistance curves than the material B (for 1mm crack growth, the CTOD (δ_5) is about 0.5mm for material A and 0.3mm for material B). The amount of stable crack growth (Δa) measured during the tests by using DC potential drop (DCPD) method and measured from the fracture surfaces of the tested CT and SENB specimens were compared. The differences between the fracture surface and the potential drop values are found to be less than 20%.



a)



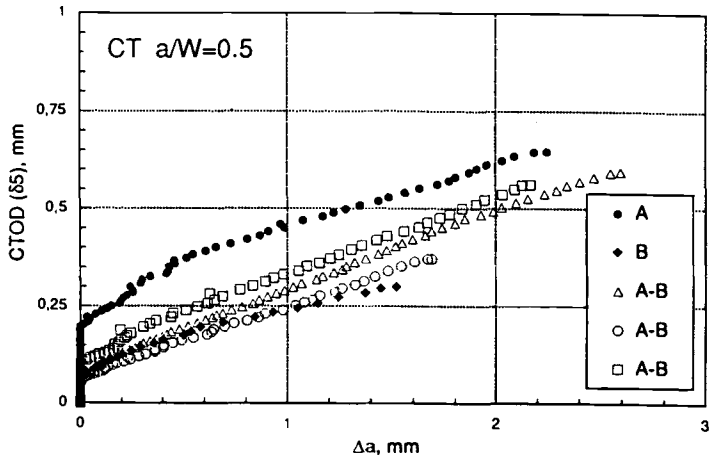
b)

FIG. 5--The geometry independent CTOD(δ_5) R-curves obtained from homogeneous deep notched CT and shallow cracked SENB specimens for: a) lower strength material A, b) higher strength material B.

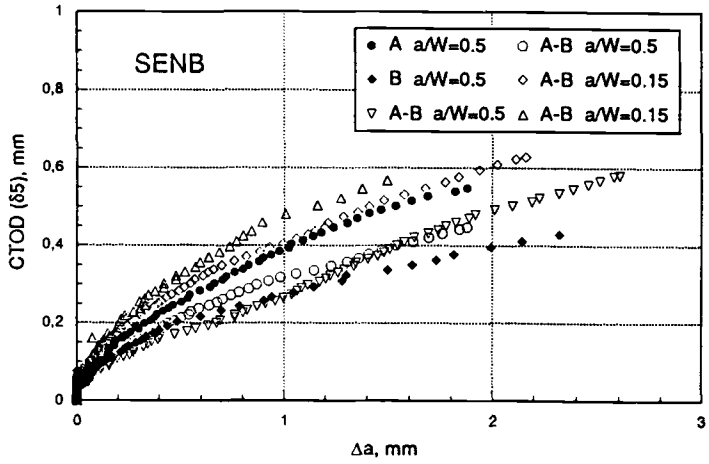
Figure 6a presents the comparison between CTOD (δ_5) R-curves obtained from homogenous and three bimaterial (A-B configuration) CT specimens. For sake of clarity, in this figure only one of each homogeneous specimen results (Fig. 5) are replotted. For bimaterial A-B specimens, the crack initiation always occured within the EB weld zone. As expected, with increasing deformation extensive plastic zone development occured at the lower yield strength side (material A) of the specimen and the crack deviated into the softer (but tougher) material A. However, the bimaterial R-curves, as seen in Fig. 6a, are basically developed (nearer to the higher strength material B R-curve) between the R-curves of the two homogeneous materials. Apparenly, crack deviation into the softer material A did not produce similarly higher R curves as the homogenous bulk specimen A. Hence, these three bimaterial specimens produced resistance curves nearer to that of material B due to the additional constraint induced by high strength mis-match. These results indicate that the crack path (i.e extent of plasticity) mainly determined by the softer material, nevertheless, the R-curves of this material were found to be lower than its "original R-curves" obtained from homogeneous bulk specimen.

Due to very high strength mismatch at the vicinity of the crack tip of the bimaterial specimens, extensive plastic zone development at the lower strength side of the specimens should be expected. Such an asymmetric deformation causes a crack path deviation into the lower strength (but tougher) material A side. However, these bimaterial specimens did not produce R-curves similar to the bulk homogeneous R-curve of the material A. The localization of the plasticity (asymmetric) at the lower strength side apparently exhausts the crack resistance capacity of material A drastically. In a bulk (homogenous) specimen the plasticity develops at the crack tip in commonly known symmetrical shape which spreads the damaged zone at both sides of

the crack tip. It can be concluded that the presence of higher strength (elastic) material causes a drop of toughness of the mating softer (plastic) material when determined by testing of the deep notched bimaterial bend specimens.



a)



b)

FIG. 6--The CTOD(δ_5) R-curves obtained from a) homogeneous and three bimaterial (**A** - **B**) deep notched CT specimens, b) homogeneous and bimaterial (**A** - **B**) deep notched and shallow cracked SENB specimens

In Fig. 6b, the CTOD (δ_5) R-curves of homogeneous as well as shallow and deep cracked bimaterial SENB specimens are plotted. For deep notched bimaterial specimens, the tendency of the R-curves is similar to the CT specimens results shown in Fig. 6a. The R-curves of these two specimens again show lower bound nature by being similar to the R-curve of material B. However, for bimaterial shallow cracked specimens, the situation is rather different. The two R-curves obtained from shallow cracked bimaterial specimens are even higher than the one obtained from the tougher material (material A). Some crack path deviation (not as clear as in the deep notched specimens) into the softer side was also observed on these specimens.

The plasticity development in the shallow cracked bimaterial specimens is not necesarily confined at the crack tip and into the ligament (W-a). In fact, much extensive spread of plasticity can be expected even towards the front face of the specimen at the softer side. Furthermore, the development of different degrees of mixed-mode condition (modification of the ratio of mode II to mode I) at the shallow crack tip compared to the deep notched bimaterial specimen plays an important role for the fracture of interfacial cracks, as underlined in [15-16].

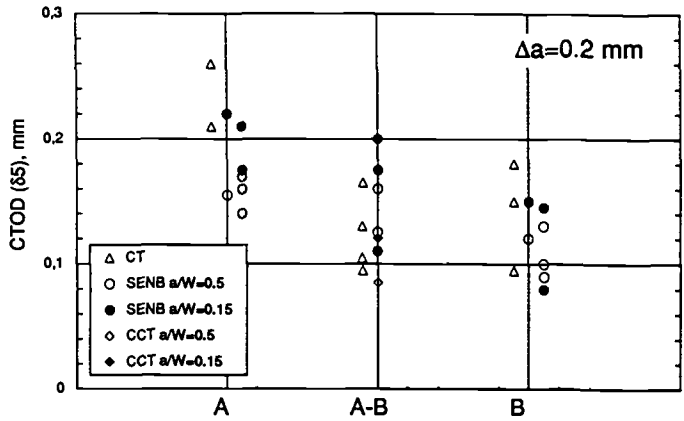


FIG. 7--The CTOD(δ_5) values for initiation of ductile tearing ($\Delta a = 0.2$ mm) for homogeneous specimens of material A and B as well as bimaterial (A-B) specimens for various configurations showing the intermediate toughness level obtained from bimaterial A-B specimens.

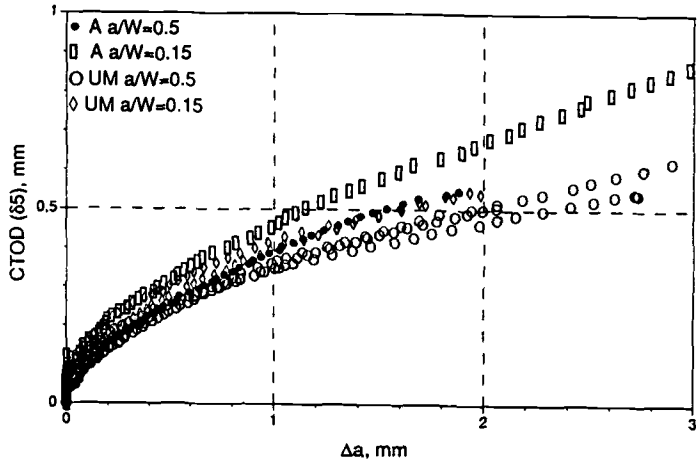
The values of the CTOD (δ_5) at the onset of ductile tearing (defined as a CTOD-value at the crack growth, $\Delta a = 0.2$ mm) are plotted in Figure 7 for different geometries of the bimaterial and homogeneous specimens. In this plot the results of center cracked tensile (CCT) bimaterial specimens are also included. The R-curves of the CCT specimens are not covered in this manuscript due to the limit on the length of the paper. The initiation of the ductile tearing values, critical CTOD (δ_5), for interfacial cracks are between the values obtained from material A and material B on

bulk homogeneous specimens. Even for the shallow cracked SENB specimens (solid symbols), the same trend can be seen within some scatter band. At initiation of the ductile tearing, the size of the plastic zone is of course limited and hence the role of the mode II component can be negligible compared to the crack growth stage. When the load level increases, the extent of plastic deformation at the crack tip increases and the shear stress component due to the bimaterial nature of the crack plane (interface discontinuity) became higher which produces predominatly tilted (shear) fracture appearance. The development of such fracture mode may affect the fracture behaviour of the specimen and may cause an increase of fracture toughness.

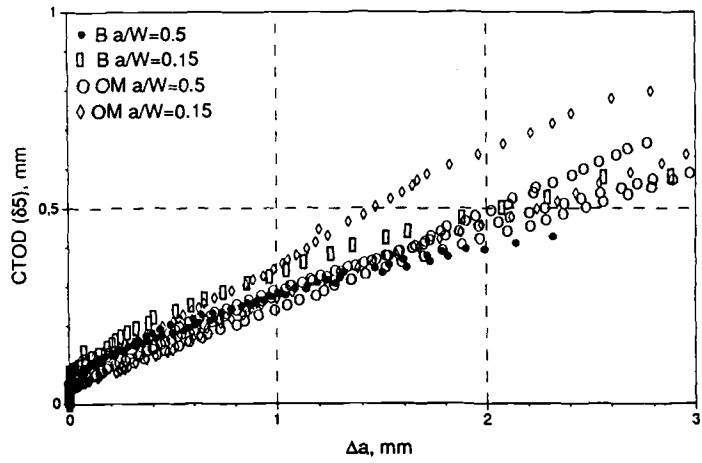
Figure 8 presents the CTOD(δ_5) R-curves of all shallow and deep cracked specimens (a/W=0.15 and a/W=0.5) of homogeneous and strength mis-matched (A-B-A and B-A-B configurations) specimens. The mis-matched specimens are compared with respective homogeneous specimens made by the material where the crack was located. Therefore, the R-curves obtained from undermatching specimens (UM) are compared with the R-curves of material-**A** (Fig. 8a) and similarly, the ones obtained for overmatching (OM) case with the results of material-**B** (Fig. 8b).

Only a slight dependence of the R-curves of the homogeneous specimens on the crack size can be seen in these plots, with the short crack leading to a somewhat higher crack growth resistance curve. The comparison between the mis-matched and the homogeneous specimen results clearly shows that even such an extremely high over- and undermatching have little influence on the CTOD(δ_5) R-curves due to local nature of the δ_5-clip measurements which does not include any remote deformation to the crack tip plasticity. The presence of bimaterial boundaries at the vicinity of the crack tip plastic deformation zone will inevitably interact with the crack tip plastic zone development and cause a discontinuity. For such cases, any measure of global or remote deformation (such as CMOD and VLL) of the specimen should not be used to define the crack tip plasticity since there will be no unique correlation between local crack tip and global deformations. Using the crack tip opening displacement (CTOD) measured locally by the δ_5-clip, the resistance curve of a cracked inhomogeneous structure appear to be only depend on the material where the crack is located. However, it should be noted that the strength mis-match can exert additional constraint effects at crack tip which can lead to different constraint condition for a given specimen configuration.

Under such conditions, some metallic materials (sensitive to the variation of the constraint at ductile regime) may show different crack growth resistance curves. However, for these materials, the R-curves are relatively insensitive (only slightly higher slope measured for the shallow cracked specimens) to constraint change with varying a/W ratio of the SENB specimens. The experimental results generated in this study show also no strength mismatch effects on the R-curves of the A-B-A (overmatching) and B-A-B (undermatching) specimens as shown in Fig. 8.



a)



b)

FIG. 8--The CTOD (δ_5) resistance curves of the SENB specimens contained shallow and deep cracks showing unique R-curves independent of crack size and strength mis-matching;
a) crack is located in material-**A**, b) crack is located in material-**B**.

During the Mis-match'93 conference [22], it has been concluded that the strength mis-match effect on fracture toughness can be small if the width of the weld metal (2H) is greater than the uncracked ligament (W-a) of the bend type specimen. However, decreasing weld metal width for a given uncracked ligament size increases the interaction of the weld metal plasticity with the surrounding base plate and hence an effect of mis-match on standard CTOD or J R-curves can be expected, since one measures the applied displacement remotely. On the contrary, the CTOD(δ_5) R-curve of the very small weld metal regions ($2H/(W-a)<<1$) shows, as presented in Figure 8, identical R-curves to the homogeneous (all weld metal, A and B) specimens without any effect of surrounding base plate, although one may expect that by decreasing the a/W and 2H/(W-a) ratios, the effect of mis-matching on CTOD should increase. However, this can occur if one obtains the CTOD or J from remote displacement measurements such as V_{LL} and CMOD.

The Figures 7 and 8 have significant implications for fracture toughness testing procedures of strength mis-matched welds and bimaterial compounds. The CTOD(δ_5) technique has a unique capacity to provide material resistance curve independent of both crack size and strength mis-match of any degree due to its local nature. This technique offers the best way (to our knowledge) to determine experimentally the crack driving force. The standardized CTOD and J R-curve determination procedures are not applicable to the mismatched and bimaterial specimens with high degree of strength mismatch. This limitation however, does not apply to the CTOD(δ_5) technique due to its local nature of CTOD measurement at the original fatigue crack tip.

CONCLUSIONS

The CTOD(δ_5) technique was used to determine the R-curves of two aluminum alloys by using homogeneous and highly overmatched, undermatched EB weld joints and bimaterial specimens (CT and SENB) with shallow and deep notches (a/W=0.15 and 0.5). The following conclusions can be drawn from this experimental study:

- For testing of bimaterial specimens which contain elastic and plastic components using standard (a/W=0.5), bend-type specimen (CT or SENB), simple and direct CTOD(δ_5) technique provides similar R-curves for different geometries.

- For testing of bimaterial specimens which contain elastic and plastic components simple and direct CTOD(δ_5) technique provides similar CTOD values at the initiation of ductile tearing (Δa=0.2 mm) for various specimen geometries.

- The CTOD(δ_5) R-curves obtained from shallow cracked and deep notched bimaterial (A-B) specimens with interfacial cracks produced different tendencies compared to the homogeneous bulk specimens. The presence of higher strength (elastic) material caused a drop of toughness of the mating softer (plastic) material when determined by testing of the deep notched bimaterial bend specimens. However, a similar conclusion can not be made for shallow cracked bimaterial specimens.

- Commonly known limits (2H > (W-a) and degree of mismatch (about 50%)) for application of standard CTOD or J-estimation procedures for mis-matched welds (A-B-A) seem not to apply to the CTOD(δ_5) technique, since the undermatching and overmatching SENB specimens considered in this study give similar R-curves as the respective homogeneous specimens. This fact is probably due to the local nature of displacement measurement at the original fatigue crack tip of the CTOD(δ_5).

REFERENCES

[1] ASTM E1152-87, "Standard Test Method for determining J-R-curves"

[2] ASTM E1290-89, "Standard Test Method for Crack Tip Opening Displacement Fracture Toughness Measurement"

[3] ASTM E813-89, "Standard Test Method for J_{IC}, a Measure of Fracture Toughness"

[4] ESIS P1-92, "ESIS recommendations for determinig the fracture resistance of ductile materials", January 1992

[5] Koçak, M., Saarenheimo, A., Petrovski, B., Talja, H. and Schwalbe K.-H., "Analysis of fracture behaviour of mismatched welds on tensile panels : experimental and numerical study", Mis-Matching of Welds, ESIS 17, (Ed. by K.-H. Schwalbe and M. Koçak) 1994, Mech. Eng. Pub., London, pp. 461-483.

[6] Eripret, C., Hornet, P., "Prediction of overmatching effects on fracture of stainless steel cracked welds", Proc. of the Int. Conf. on shallow crack fracture mechanics, toughness tests and applications, TWI, Cambridge, U.K, 23-24 Sept. 1992.

[7] Eripret, C., Hornet, P., "Prediction of overmatching effects on fracture of stainless steel cracked welds", Mis-Matching of Welds, ESIS 17, (Ed. by K.-H. Schwalbe and M. Koçak) 1994, Mech. Eng. Publications, London, pp.685-708.

[8] Hornet, P., Koçak, M., Cornec, A., Petrovski, B., and Schwalbe, K.-H. "Effect of weld metal mis-matching on crack driving force", Mis-Matching of Welds, ESIS 17, (Edited by K.-H. Schwalbe and M. Koçak) 1994, Mech. Eng. Publications, London, pp. 589-607.

[9] Schwalbe, K.-H., "Introduction of $\delta 5$ as an operational definition of the CTOD and its practical use", ASTM National Symposium on Fracture Mechanics, Idaho Falls, June 1994.

[10] Graham, S. M., Reuter, W. G., Lloyd, W.R. and Epstein, J. S., "The Validity of standard test methods for characterizing weld fracture", Transactions of the ASME, Vol. 114, pp. 16-21, Febuary 1992

[11] Tvergaard and Hutchinson, "The influence of plasticity on mixed mode interface toughness", J. Mech. Phys. Solids, Vol. 41, No. 6, pp. 1119-1135, 1993.

[12] Shih, C. F. and Asaro, R. J., "Elastic-plastic analysis of cracks on bimaterial interfaces : Part I - small scale yielding.", Journal of Applied Mechanics, Vol. 55, pp. 299-316, June 1988.

[13] Shih, C. F. and Asaro, R. J., "Elastic-plastic analysis of cracks on bimaterial interfaces : Part II - Structure of small scale yielding.fields", Journal of Applied Mechanics, Vol. 56, pp. 763-779, December 1989.

[14] Shih, C. F., Asaro, R. J. and O'Dowd, N. P., "Cracks on bimaterial interfaces : plasticity aspect", Scripta Metall. Conf. on Bonding, Structural and Mech. properties, New York, 1990.

[15] Suo, Z. and Hutchinson, J. W., "Sandwich test specimens for measuring interface crack toughness", Mat. Sci. and Eng., A107, pp. 135-143, 1989.
[16] O'Dowd, N. P., Shih, C. F. and Stout M. G., "Test geometries for measuring interfacial fracture toughness", Int. Journal Solids Structures, Vol. 29, No. 5, pp. 571-589, 1992.
[17] Tschegg, E. K., Kirchner, H. O. K. and Koçak, M., "Interfacial and subinterfacial cracks in the copper-ferrite system", Engineering Fracture Mechanics, Vol. 39, pp. 739-750, 1991.
[18] Tschegg, E. K., Kirchner, H. O. K., Koçak, M. and Zelezny, M. F. "Subinterfacial Fracture in Bimaterial Joints", Mis-Matching of Welds, ESIS 17, (Ed. by K.-H. Schwalbe and M. Koçak) 1994, Mech. Eng. Pub., London, pp. 291-305.
[19] Tschegg, E. K., Zelezny, M. F., Kirchner, H. O. K. and Schwalbe, K.-H. "Elastic-Plastic Behavior around Subinterfacial Cracks", Mis-Matching of Welds, ESIS 17, (Edited by K.-H. Schwalbe and M. Koçak) 1994, Mech. Eng. Pub., London, pp.307-317.
[20] Hornet, P., Koçak, M., Cornec, A. and Schwalbe, K.-H. "Fracture of Bi-Material Joints : Effect of Strength Mis-Match on Crack Resistance Curves.", 10th European Conference on Fracture, ECF 10 - Structural Integrity, Experiments, Models, Applications, Berlin, FRG, September 1994, pp. 1125-1138.
[21] Schwalbe, K.-H., Hellmann, D., "Application of the electrical potential method to crack length measurements using Johnson's formula", Journal of Testing and Evaluation, Vol. 9, No. 3, pp. 218-221, May 1981.
[22] Burdekin, F. M., Koçak, M., Schwalbe, K.-H. and Denys, R., "Significance of strength mis-match in welds - summary of a round table discussion", Mis-Matching of Welds, ESIS 17, (Edited by K.-H. Schwalbe and M. Koçak) 1994, Mech. Eng. Pub., London, pp.103-111.

Table 1 : Tensile properties of the two aluminum alloys.

Material	E-modulus [MPa]	Yield stress [MPa]	Ultimate stress [MPa]	Elongation at fracture [%]
A (Al 2024-FC)	70300	80	190	19
B (Al 2024-T351)	70300	360	560	15

D. M. Parks, S. Ganti, and F. A. McClintock[1]
J. S. Epstein, L. R. Lloyd, and W. G. Reuter[2]

Experiments and Analyses on Undermatched Interleaf Specimens in Bending

REFERENCE: Parks, D. M., Ganti, S., McClintock, F. A., Epstein, J. S., Lloyd, L. R., and Reuter, W. G., **"Experiments and Analyses on Undermatched Interleaf Specimens in Bending,"** Fracture Mechanics: 26th Volume, ASTM STP 1256, Walter G. Reuter, John H. Underwood, and James C. Newman, Jr., Eds., American Society for Testing and Materials, Philadelphia, 1995.

ABSTRACT: Model weldment fracture specimens have been fabricated, tested, and analyzed using finite elements. The specimens consist of an interleaf of commercially pure titanium diffusion-bonded to a harder alloy titanium. A deep edge crack is introduced symmetrically into the interleaf, and the specimens are loaded in pure bending. Variation of the thickness ($2h$) of the soft interleaf layer provides insight into effects of weld geometry in strongly undermatched weldments tested in plane strain bending. Ductile crack growth (beyond blunting) initiated at loads giving $J \doteq 95\,kJ/m^2$ in all specimens. In the thickest interleaf geometries, stable tearing was obtained, but in the thinnest interleaf ($2h \doteq 3\,mm$), crack initiation resulted in a massive pop-in of $5.4\,mm$ across an initial ligament of $12\,mm$. Finite element studies show that the thinnest interleaf geometry had slightly higher peak stress triaxiality at the beginning of cracking, and that the highest triaxiality extended over a larger region than in the thicker interleaf specimens loaded to the same initiation J-values. More importantly, the blockage of plastic straining above and below the crack tip in the $3\,mm$ interleaf specimen forced higher values of plastic strain to spread forward into the $\pm 45^o$ sector of highest stress triaxiality directly ahead of the crack tip. The higher strains, in conjunction with the slightly higher stress triaxiality, led to the unstable pop-in initiation.

KEY WORDS: undermatched weldment, strength mismatch, commercially pure titanium, crack-tip constraint, fracture mechanics, finite element analysis, interleaf specimen.

[1]Professor, Research Assistant, and Professor Emeritus, respectively, Department of Mechanical Engineering, Massachusetts Institute of Technology, Cambridge, MA 02139, USA.
[2]Idaho National Engineering Laboratory, Idaho Falls, ID 83415, USA.

Copyright© 1995 by ASTM International www.astm.org

INTRODUCTION

Self-similar crack tip fields are defined by various singularity measures like K_I and J within the K-dominant and J-dominant regimes [1, 2, 3]. Measures of stress triaxiality such as T and Q can improve the description of the crack tip fields [4]. The ability of one- or two-parameter descriptions to characterize elastic-plastic crack tip fields uniquely becomes problematic when the scale of crack tip deformation, as measured by J/σ_0 or crack-tip opening displacement ($CTOD$) becomes sufficiently large compared to characteristic in-plane dimensions (e.g., crack length, remaining ligament, etc.) of the cracked specimen or component. In such cases, even two-parameter descriptions of the crack tip fields fail to capture essential features of the crack tip stress and deformation fields which are responsible for driving the fracture micromechanisms. Here we investigate another situation which can limit the applicability of two-parameter fracture mechanics descriptions, namely, a crack lying within a strip of one material which is bonded to an external region having different mechanical properties. The distance from the crack tip to the bi-material bond becomes an additional in-plane dimension which must be compared with the scale of crack-tip deformation.

The situation is particularly serious for a crack situated within a thin weld or interleaf region which is of lower strength than its surroundings, because the constrained plastic deformation of the interleaf can lead to very high levels of crack tip stress triaxiality while simultaneously amplifying plastic strain in crack tip regions of highest stress. Welds pose further complications because of metallurgical and mechanical heterogeneities like the heat affected zone, compositional and microstructural gradients, residual stresses, etc. The mismatch in strength between a weld metal and its baseplate ($M = \sigma_y^{wm}/\sigma_y^{bm}$) is termed under-matching ($M < 1$) or over-matching ($M > 1$), respectively, if the weld metal yield strength is lower or higher than the base material.

The effects of mismatch on fracture toughness of weld specimens have received considerable attention in recent years [5, 6, 7, 8]. Kirk et al. [7] use an equivalent J-value to study the effects of under- and over-matched welds in plane strain three-point bending. They define an equivalent J for a finite body to express the fields in a self-similar fashion. The equivalent J_{ssy} is defined as the J to which the infinite body must be loaded to achieve the same stressed volume as in the finite body [9, 7]. They find the assumption that J_{ssy} of the weld specimen equals J_{ssy} for a homogeneous weld material is valid up to 20 percent mismatch if the distance from the crack tip to weld interface exceeds $5\,mm$ [7]. For higher levels of overmatch or for decreasing weld widths, the value of J_{ssy} departs significantly from the assumption. They also note the importance of absolute width of the weld, in addition to a dimensionless parameter like h/a, for small edge cracks in tension. In a related study, Varias et al. [10] observed a similar dependence of J on the width of the soft metallic interlayer between rigid ceramic plates.

For center-cracked tension specimens, Hao et al. [6] provide slip-line fields and closed form limit load expressions for a crack in a soft middle strip. They provide a minimum

Material	E (GPa)	Poisson's ratio	ϵ_0 (%)	σ_0 (MPa)	α	n	J_{IC} (kJ/m^2)
CP-Ti	112.3	0.24	0.33	366	0.60	11.0	110.0
6Al-4V-Ti	115.1	0.28	0.72	896	0.35	31.8	62.7

Table 1: Mechanical Properties of CP-Ti and 6Al-4V-Ti

weld width to ligament ratio, above which there is no effect of the weld interface. Neglecting the influence of the base metal, Schwalbe [8] has studied the effect of mismatch using the Engineering Treatment Model (ETM). When the weld width becomes sufficiently small compared to that of the ligament, interaction effects take over very early in the deformation and affect the stress and strain fields significantly. Cray et al. [5] study the influence of under- and over-matched double V-groove welds in tension and bending. They show the dependence of J on mismatch level, loading and geometry of the specimen. At fully developed plasticity, the mean stress levels in undermatched ligaments increase due to constraint effects, hence raising the load carrying capacity.

In this investigation, we study, both computationally and experimentally, deep edge cracks located symmetrically within severely undermatched (mismatch ratio, $M < 0.5$) interleaf specimens subjected to pure bending. Effects of interleaf thickness on deformation and fracture are investigated in model weldments formed by diffusion-bonding titanium alloys of similar elastic and thermal expansion properties, thereby minimizing the effects of residual stress. Specimens were tested to fracture, and were instrumented for surface observation using Moire interferometry. Plane strain and three-dimensional finite element analyses were performed, and several comparisons were made between computations and experimental data. At the beginning of crack extension (beyond the blunting line), the crack tip stress and plastic strain in the thinnest interleaf specimen were both considerably higher than in specimens of larger interleaf thickness. This difference manifested itself in large pop-in bursts of cracking, as contrasted with stable ductile tearing in the thickest specimens. A complete description of the observed fracture behavior would seem to require implementation of local fracture criteria (e.g., a Gurson-type model).

MATERIALS, GEOMETRY, AND FINITE ELEMENT MODELS

Material System

The interleaf material chosen for this study is commercially pure titanium (CP-Ti), diffusion-bonded to 6Al-4V titanium (6Al-4V-Ti). The uniaxial tensile stress/strain response for the two materials, shown in Fig. 1, was approximated by the Ramberg-Osgood form

$$\frac{\epsilon}{\epsilon_0} = \frac{\sigma}{\sigma_0} + \alpha\{\frac{\sigma}{\sigma_0}\}^n \tag{1}$$

where σ is the applied or equivalent stress, the subscript "0" denotes the yield state. Table 1 contains the specific mechanical properties for the two materials, averaged over several results. One advantage of this approach to a "model" weld system is

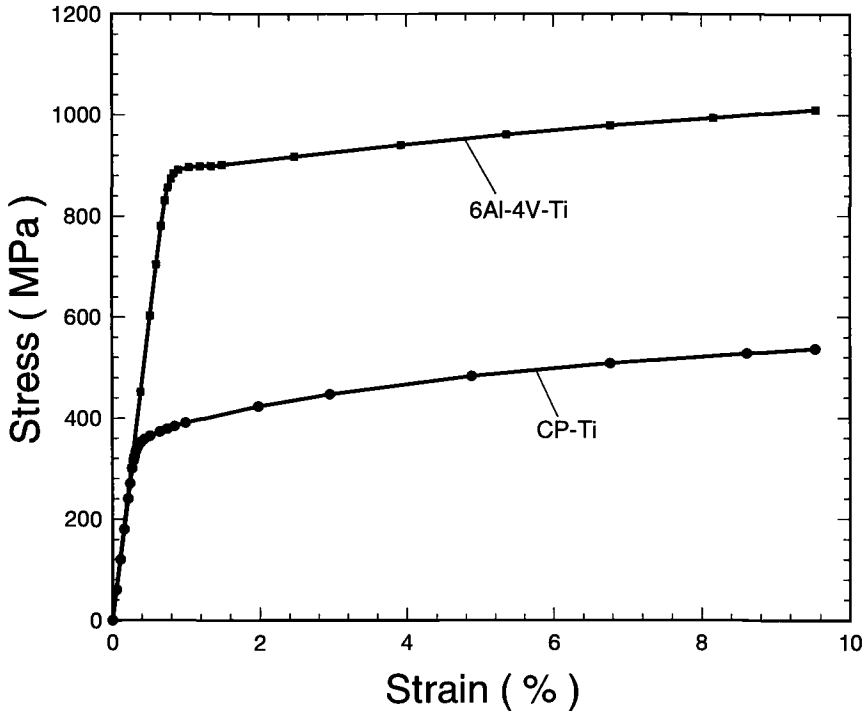


Figure 1: Experimental true stress–true strain response for CP-Ti and 6Al-4V-Ti in uniaxial tension.

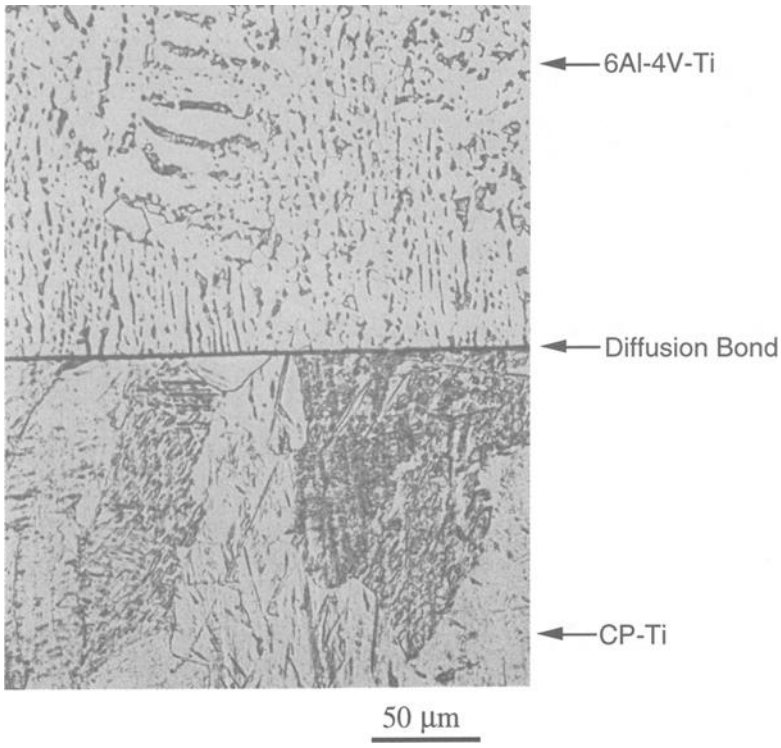


Figure 2: Micrograph of the diffusion bonded joint obtained using Kroll's reagent showing a sharp interface with no visible diffusion of materials across it.

that the elastic moduli and coefficients of thermal expansion of the two materials are nearly identical, thus minimizing complications due to residual bonding stresses. However, the great difference in yield strength causes the CP-Ti interleaf to yield while the 6Al-4V-Ti remains essentially elastic.

The diffusion bonding process begins with $50\,mm$ diameter blanks that are $50\,mm$ long and machined to produce parallel faces. The blanks are polished with a $1\,\mu m$ diamond paste, acid-etched to remove oxides, and then inserted into a $178\,kN$ capacity hot press. They were held at $870°C$ and a nominal pressure of $3.44\,MPa$ for 1 hour, then furnace-cooled to room temperature. This diffusion bonding process produces a sharp interface. The CP-Ti interleaf thicknesses used were $2h = 12.5$, 6.4, and $3.2\,mm$. Figure 2 shows a micrograph of the bond line region using Kroll's etch. The large α- grains are evident in the CP-Ti, as well as the long α- structure interdispersed with the darker β phases in the 6Al-4V-Ti. The bond is well-defined, with no visual evidence of diffusion across it.



Figure 3: Metallographic section of CP-Ti showing the morphology of Fe-Ti stringers.

As all fractures took place within the CP-Ti material, further consideration of its compositon and microstructure is warranted. The alloy was Grade 2 unalloyed titanium. Weight percent composition limits for this material include [11] $C < 0.10$, $H < 0.015$, $Fe < 0.30$, $N < 0.03$, $O < 0.25$, each other element < 0.05, total other elements < 0.30, balance Ti. Figure 3 shows a metallographic section of the CP-Ti. A prominent microstructural feature is long, thin "stringer-like" precipitates of a few microns thickness, several tens of microns in length, and tens of microns in spacing. X-ray intensity analysis of the precipitates shows them to be Fe-rich; presumably they are an iron/titanium intermetallic phase. Within one α- grain, the orientation of the precipitates is coordinated, as shown in the figure, but orientation varies from grain to grain. The largest of the precipitates is of order $200\,\mu m$ in length, with a spacing of order $100\,\mu m$. Fractographic evidence (to be discussed further below) suggests that these precipitates play a central role in the fracture process, nucleating cavities which grow to coalescence in association with interparticle ligament tearing.

Wide-angle x-ray scattering was performed to determine if any preferential crystal-

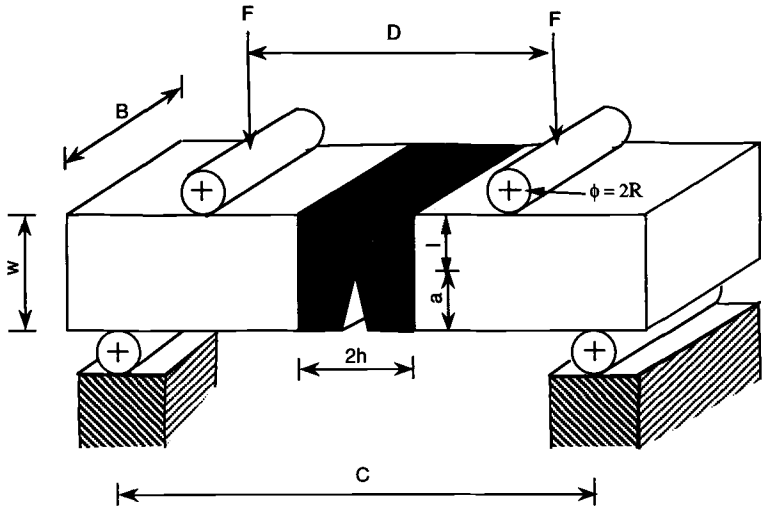


Figure 4: Schematic of the interleaf specimen loaded in four point bending.

lographic texture was present in the CP-Ti; no statistically significant texture could be detected.

Specimen Geometry

The interleaf specimen geometry and loading is shown schematically in Fig. 4. Values of the specimen dimensions in mm, including crack length a, thickness B, width W, and interleaf thickness $2h$, are given in Table 2. The crack was introduced into the interleaf through an EDM notch, and fatigue-cracked to the final dimension under bending.

As indicated in Fig. 4, loading was in four-point bending. For the $6\,mm$ and $12\,mm$ interleaf specimens, the minor span was $D = 50\,mm$ and major span was $C = 135\,mm$; for the $3\,mm$ thick interleaf specimen, $C = 120\,mm$ and $D = 25\,mm$ was used. The four rollers had diameter $2R = 12.7\,mm$. The total load applied to the specimen during bending, $2F$, was monitored in the load cell and converted into the mid-span bending moment by $M = F \cdot (C - D)/2$. Cross-head motion Δ was converted into relative rotation of the end-sections via $\theta = 4\Delta/(C - D)$.

The load vs. crack mouth opening displacement ($CMOD$) and load-line displacement

Specimen Name	$2h$	a	W	B	a/W	h/l
3mm	3.2	16.9	28.9	25.8	0.58	0.13
6mm	6.3	15.0	25.4	25.1	0.59	0.30
12mm	12.8	15.7	25.4	25.4	0.62	0.66

Table 2: Dimensions (in mm) of specimens tested.

Δ were measured directly, while the X- and Y- displacement fields on the lateral surfaces of the specimens were recorded by interferometry [12] using 600 $1/mm$ crossed gratings with multiplication factor of 2 (0.8 μm per fringe order).

Finite Element Models

Although the similar elastic constants of the two materials make the structure nearly elastically homogeneous, the substantially lower yield strength of the CP-Ti will intensify plastic deformation and constraint-induced stress variation within the interleaf region. Accordingly, each interleaf specimen was meshed with a fine grid within the interleaf domain. To accomodate the finite strains near the singularity, the crack tip was modelled as a blunted opening with 17 nodes along a circular arc whose radius was 1/1000 of any other significant dimension in the specimen [3]; in practice, the smallest such dimension was interleaf half-thickness h.

Both plane strain and three-dimensional finite element analyses were performed. To resolve the strong field variations in the radial direction near the crack tip, a nearly converging radial mesh was generated in a circular region around the crack tip. Eight-noded elements with reduced integration (ABAQUS [13] element type CPE8R) were used for the plane strain analyses, while 8-noded bricks with selectively reduced integration (ABAQUS element type C3D8) were used in the three-dimensional analyses. In the 3-D analyses, 5 layers of bricks having one-fourth the in-plane mesh density shown in Fig. 5 were "stacked" along the crack-front in the Z-direction.

Symmetry of the specimen and loading necessitates modeling of only half the plane strain specimen (one-fourth of the 3-D model). Since the distance between the inner rollers is comparable to the width of the specimen ($D/W \simeq 1$ to 2), the presence of rollers had to be taken into account in the finite element modeling. Symmetry boundary conditions were imposed on the ligament (and mid-plane in the 3-D run), and the loading was displacement-controlled with displacement specified on the inner cylinder. All the contacts were modelled as frictionless. The outer roller was stationary. Both loading rollers were treated as rigid, and specimen/roller contact was allowed to develop (ABAQUS element type IRS22 in plane strain) with increasing load.

The constitutive model used in the finite strain formulation was finite strain J_2 flow theory, with isotropic hypoelasticity. The true stress/strain curve obtained from the experimental engineering stress-strain data of each material was curve-fit with the power law form of eq. (1) using material constants in Table 1, and extrapolated to a plastic strain of 0.6. The resulting flow stress vs. true plastic strain curve was multi-linearized as input into the ABAQUS finite element program along with the elastic

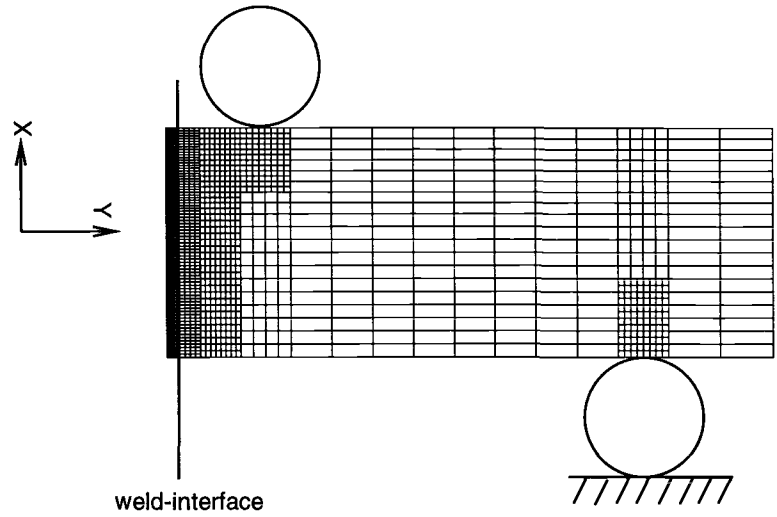


Figure 5: Finite Element Mesh used in the plane strain analysis for $2h = 3\,mm$.

properties, using the parameter σ_0 for each material as the initial yield strength.

RESULTS

Load-Deformation

Testing took place in two phases. First, under contained yielding, the crack tip asymptotic fields were investigated using Moire interferometry. The specimens were then reloaded to obtain crack growth J_R-curves for each interleaf thickness. Figure 6 shows the normalized applied moment versus bend angle relations for the $3\,mm$ and $6\,mm$ interleaf specimens. Both the experimental and simulated curves are shown. The thin $3\,mm$ interleaf specimen ($h/l = 0.13$) shows significantly elevated load-carrying capacity, owing to the constraint imposed on ligament plasticity by the elastic surroundings. In contrast, the plastic zone in the $6\,mm$ thick interface specimen is nearly uninfluenced by the hard regions in this geometry of $h/l = 0.30$ (see also discussion below). The plane strain finite element solution for $2h = 3\,mm$ is closer to the experimental curve than it is for $2h = 6\,mm$, showing the predominance of plane strain effects in thin soft interleafs. In the latter case, the plane strain overestimate of specimen load is reduced in the 3-D finite element analysis.

Evidently, in the limit of vanishing interleaf thickness, the moment/rotation response approaches that appropriate to the plastic properties of the 6Al-4V-Ti material, while for sufficiently large values of h/l, the response will be that of a homogeneous CP-Ti

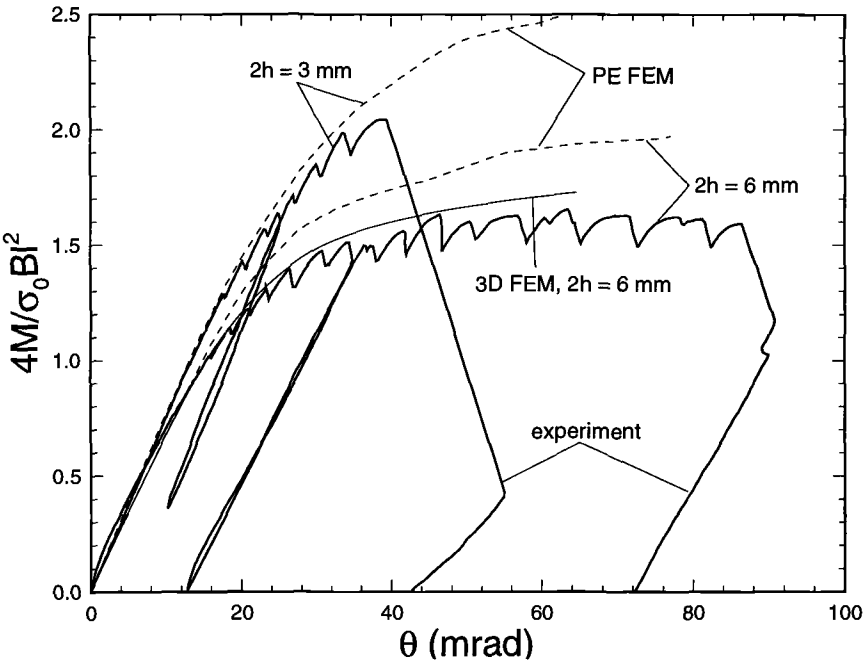


Figure 6: Normalized moment *vs* bend angle for $2h = 3$ and $6\,mm$ - Experiment and Plane Strain (PE) FEM solution. A 3D FEM solution is also shown for the $2h = 6\,mm$ case.

specimen. Figure 7(a) shows the monotonic effect of changing interleaf thickness at fixed $a = 16.9\,mm$ and $W = 28.9\,mm$. The homogeneous CP-Ti moment/rotation curve coincides with that of the $2h = 6\,mm$ interleaf specimen, with the homogeneous 6Al-4V-Ti curve providing an upper bound.

For a deep edge-cracked bend specimen, the nonhardening slipline solution of Green and Hundy [14] extends above the crack plane a distance of approximately $0.37l$. For h/l-values significantly smaller than this, we expect the harder end pieces to alter fully-plastic flow in the ligament, but plastic flow can take place in interleafs of substantially larger h/l in essentially the same way as in homogeneous bend specimens. This is consistent with the results of Fig. 7(a).

J-Integral

The J-integral was evaluated using the virtual crack extension (VCE) [15] domain integral method provided in ABAQUS. The path-dependence of J in elastic-plastic finite deformation finite element solutions shows a monotonic increase with increasing distance from the tip, reaching a saturation at distances larger than a few multiples of J/σ_0 [3]. Because of the highly refined mesh, a large number of contours were taken to reach the remote (constant) value for J. Figure 7(b) shows the J_{VCE} vs. rotation curves for the specimens analyzed in Fig. 7(a). The increased load-carrying capacity of the $3\,mm$ interleaf specimen provides higher J-values at fixed deformation, as compared to thicker interleafs. The J–response of the interleaf with $2h = 6\,mm$ essentially coincides with that of the homogeneous CP-Ti specimen.

The final loading of the $3\,mm$ specimen terminated with an abrupt pop-in extension as indicated in Fig. 6, while the $12\,mm$ specimen showed extensive stable ductile tearing. The $6\,mm$ interleaf showed both stable ductile tearing and, subsequently, a less-pronounced pop-in. The experimental load-deflection curves, with small unloadings to monitor crack growth, were converted into the experimental J_R curves shown in Fig. 8, Δa being calculated from the compliance measurements.

In general, the procedures used for determining J from experimental load/displacement curves in homogeneous bodies do not apply to interleaf geometries [9]. However, in the specimens used here, the standard procedures are believed to be accurate, for the following reasons. Finite element J-integral evaluations were made for each of the actual specimen geometries, and comparisons were made between J-values as determined from the domain integral method and those based on the (homogeneous) deep-cracked formula

$$J_{M\theta} = \frac{2}{Bl}\int_0^\theta M\,\mathrm{d}\theta. \tag{2}$$

For $2h = 6\,mm$ and $12\,mm$, the overall moment/rotation curves coincided with the homogeneous case (see Fig. 7(a)), and the two methods of J-determination were identical for these specimens. For the $2h = 3\,mm$ interleaf, the moment/rotation curve showed only small nonlinearity up to pop-in (Fig. 6); thus the compliance-based estimate of J was dominated by the ($\sim$ homogeneous) elasticity of the specimen, so eq.(2) again gave good results up to the point of pop-in. At higher computed loads in the $3\,mm$ specimen, eq. (2) underestimated the actual J-values.

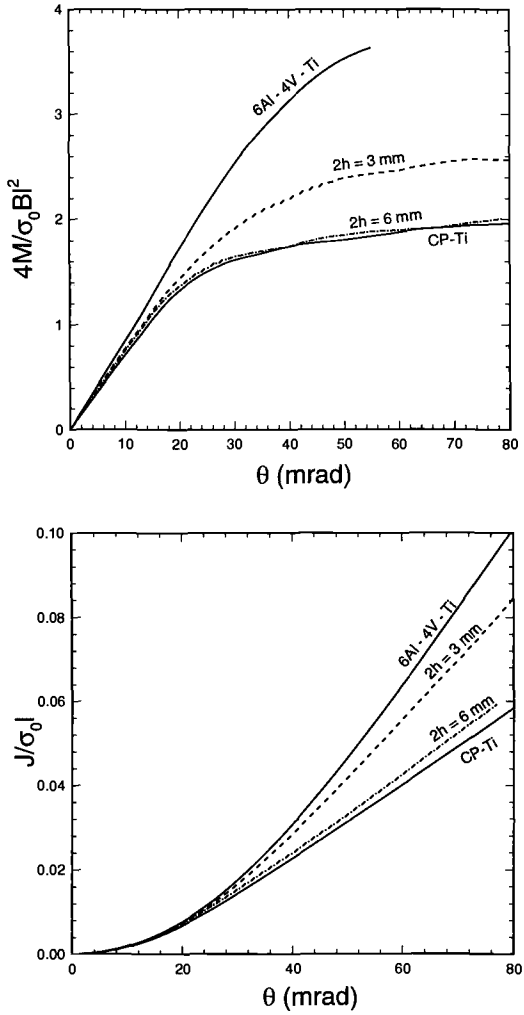


Figure 7: (a) Simulated plane strain Moment *vs* bend angle curves for specimens with varying interleaf thickness, keeping the other geometrical parameters unchanged ($a = 16.9\,mm$; $w = 28.9\,mm$). (b) Simulated J_{VCE} *vs* bend angle for specimens with varying thickness for the geometries of 7(a) above.

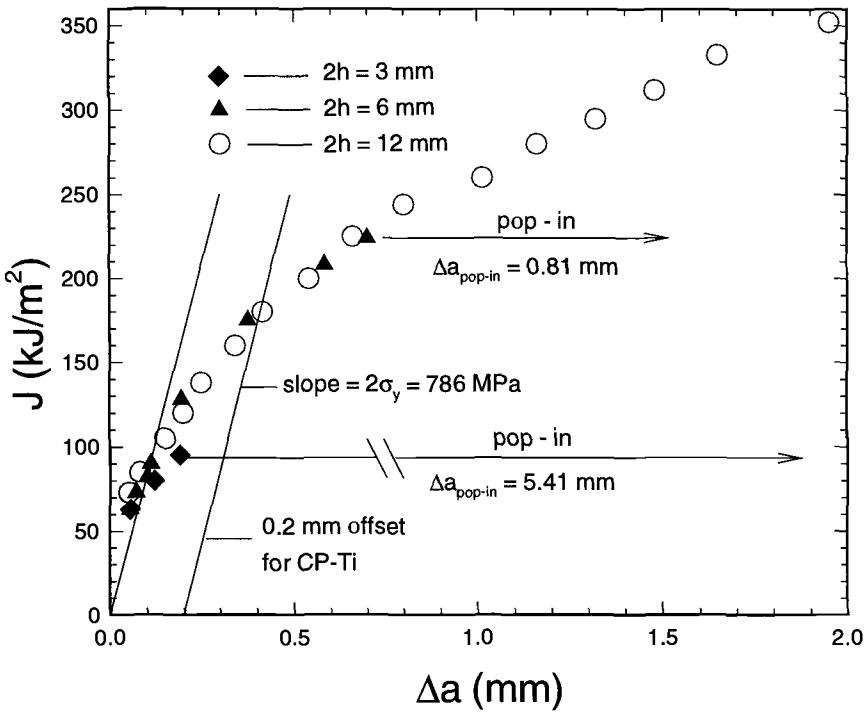


Figure 8: Experimental J_R-curves for $2h = 3, 6$ and $12\,mm$ specimens showing the deviation from the blunting lines and the pop-ins. Here σ_y is the average of the proportional limit ($300\,MPa$) and ultimate stress ($486\,MPa$) for the CP-Ti.

Returning to Fig. 8, all specimens showed deviation from the blunting line $\Delta a = J/2\sigma_0$ at an applied J-level of $\sim 95\,kJ/m^2$. For the thicker interleaf specimens, this point marked the beginning of stable tearing. The R-curves for these specimens crossed the $0.2\,mm$ offset crack growth line at $J = 175\,kJ/m^2$. The $6\,mm$ interleaf showed a pop-in growth of $\Delta a_{\text{pop-in}} = 0.81\,mm$, commencing at $J \doteq 230\,kJ/m^2$. Interestingly, the $3\,mm$ interleaf showed no stable tearing, but instead exhibited a pop-in of $\Delta a_{\text{pop-in}} = 5.41\,mm$ at $J = 95\,kJ/m^2$. The highly constrained interleaf specimens seem to reduce the constraint imposed by the rigid base material by means of an unstable $\Delta a_{\text{pop-in}}$ sufficient for a full Green and Hundy field of lower constraint to exist (see also Discussion).

Displacement fields near the crack tip

Figure 9 shows the unloaded u_X-displacement field for the $3\,mm$ interleaf. This figure shows clearly the effect of the 6Al-4V-Ti ends in constraining the crack tip plastic zone. There is a caustic region in the interleaf specimens, where the lens did not collect fringe information due to the intense out-of-plane deformation.

Fringes of u_X- and u_Y-displacement contours similar to that shown in Fig. 9 were digitized for subsequent data reduction. Figures 10(a) and 10(b) show the near-tip radial distribution of displacement at various angles, Φ, from the crack extension plane for the $3\,mm$ interleaf specimen. The experimental points are in an unloaded condition after previous loading to $4M/\sigma_0 Bl^2 = 1.23$ ($J = 21.0\,kJ/m^2$), while the plane strain finite element results are in the loaded configuration (at the same loading). The agreement between the finite element and experimental displacement fields is very good, especially if allowance is made for elastic unloading. Figures 11(a) and 11(b) show corresponding displacement fields for the $6\,mm$ specimen loaded to $4M/\sigma_0 Bl^2 = 1.29$ ($J = 38.4\,kJ/m^2$). The plane strain displacement fields are not in as good quantitative agreement with the experimental results for the thicker interleaf, but they are in good qualitative agreement. The surface displacement fields of the three-dimensional finite element solution were in better agreement, but the results of Figs. 10 and 11, as do those of Fig. 6, demonstrate that the plane strain models capture essential features of the near-tip fields. In the next section, we investigate the plane strain near-tip finite element fields in detail.

Stress and strain distributions near the crack tip

The experimental results show a marked influence of interleaf thickness on the crack extension behavior of the CP-Ti; presumably this reflects corresponding differences in the crack-tip stress and deformation fields. Figure 12 shows the computed distribution of equivalent plastic strain, $\bar{\epsilon}$, in homogeneous CP-Ti and in two interleaf specimens, when each is loaded to $J = 95\,kJ/m^2$, the beginning of deviation from the blunting line (Fig. 8). The different ligament lengths correspond to the specimens tested. As can be seen, plasticity in the $3\,mm$ specimen has been severely blocked, while that in the $6\,mm$ specimen has just "grazed" the surrounding hard layers.

Figure 13(a) shows the circumferential variation of normalized hydrostatic stress, $\sigma_{kk}/3$, at radii 2 and 3 times J/σ_0, for the $3\,mm$ specimen and for the identical

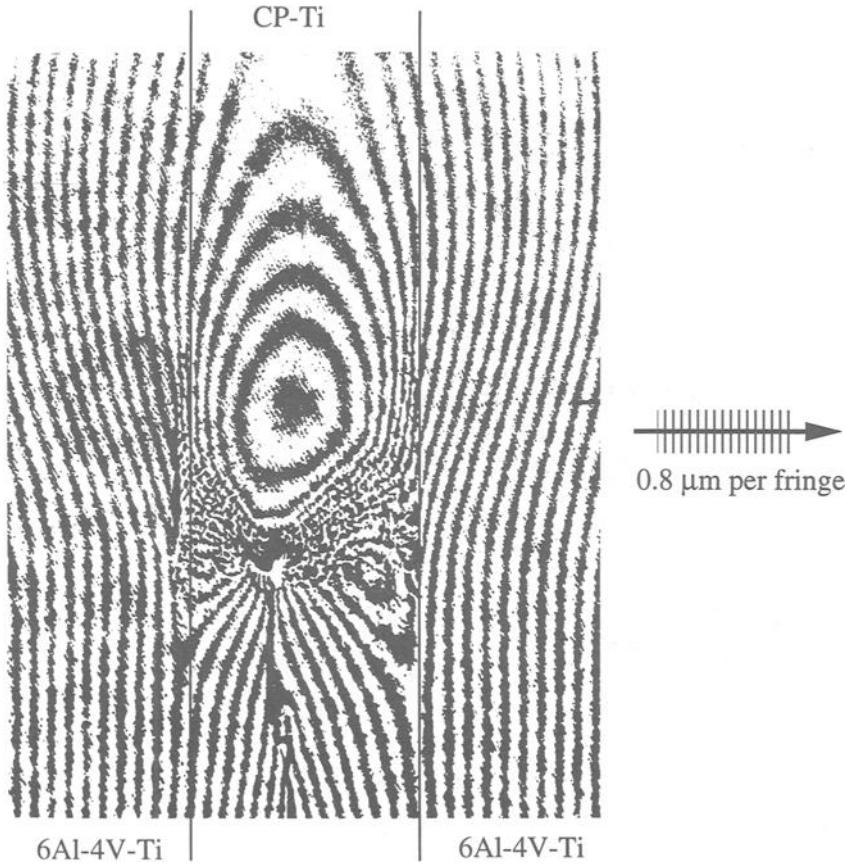


Figure 9: Moire fringe pattern of the displacement field for the $2h = 3\,mm$ specimen near the crack tip. Photo is taken in the unloaded configuration, after initial loading to $4M/\sigma_0 Bl^2 = 1.6$.

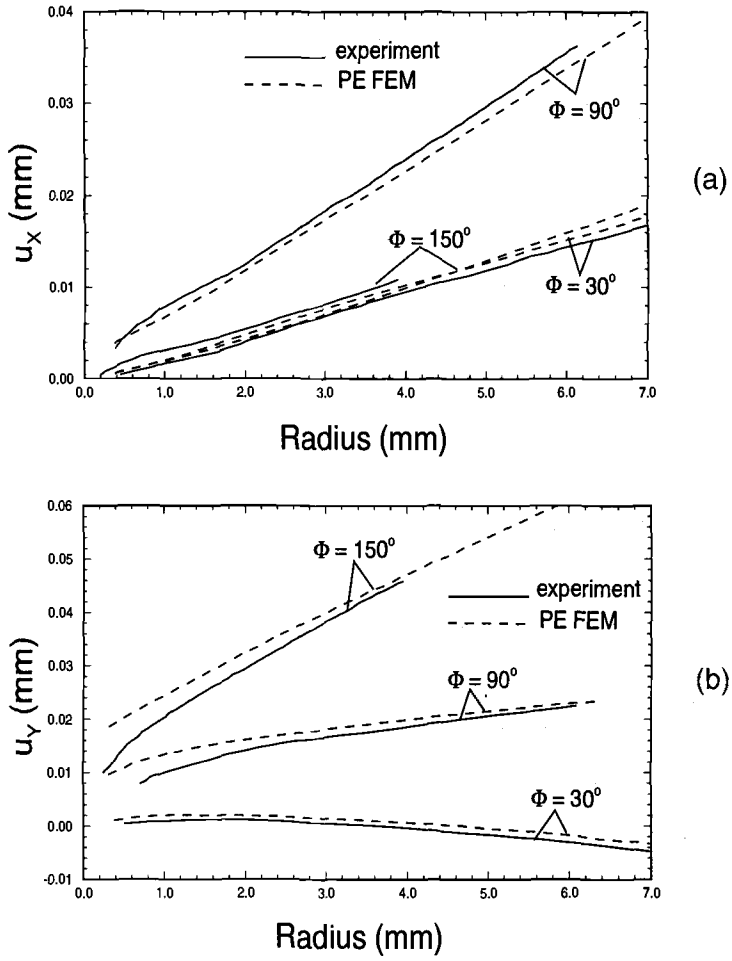


Figure 10: Comparison of the displacement fields obtained from the Moire fringe data, in the unloaded configuration, and PE FEM simulation, in the loaded condition, for $2h = 3\,mm$ after loading to $4M/\sigma_0 Bl^2 = 1.23$. (a) u_X–displacement (b) u_Y–displacement.

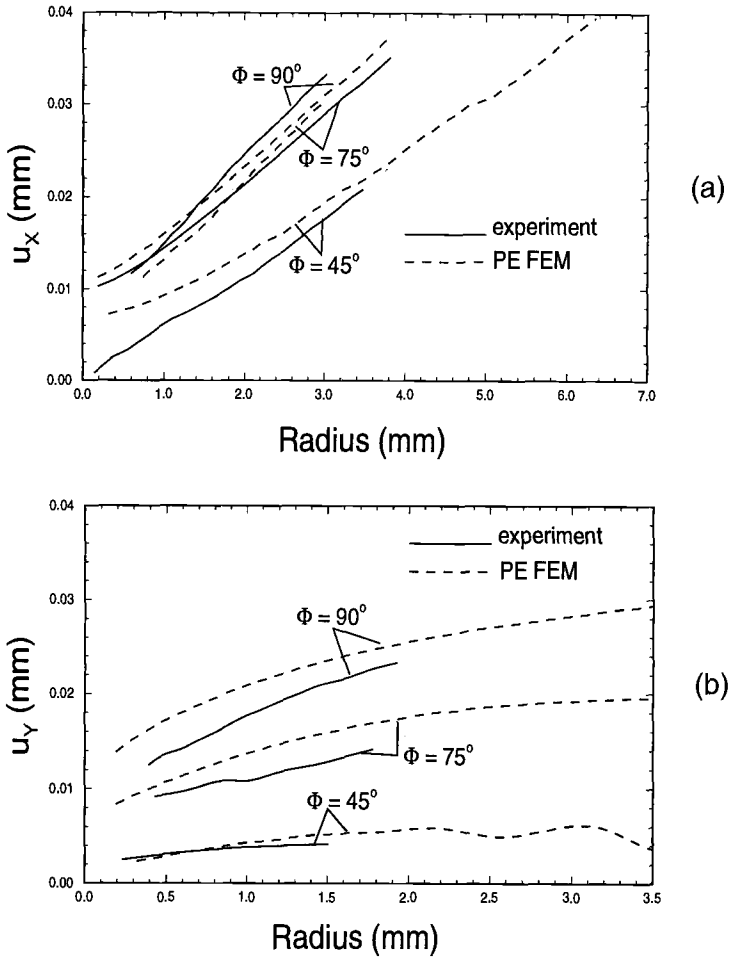


Figure 11: Comparison of the displacement fields obtained from the Moire fringe data, in the unloaded configuration, and PE FEM simulation, in the loaded condition, for $2h = 6\,mm$ after loading to $4M/\sigma_0 Bl^2 = 1.29$. (a) u_X–displacement (b) u_Y–displacement.

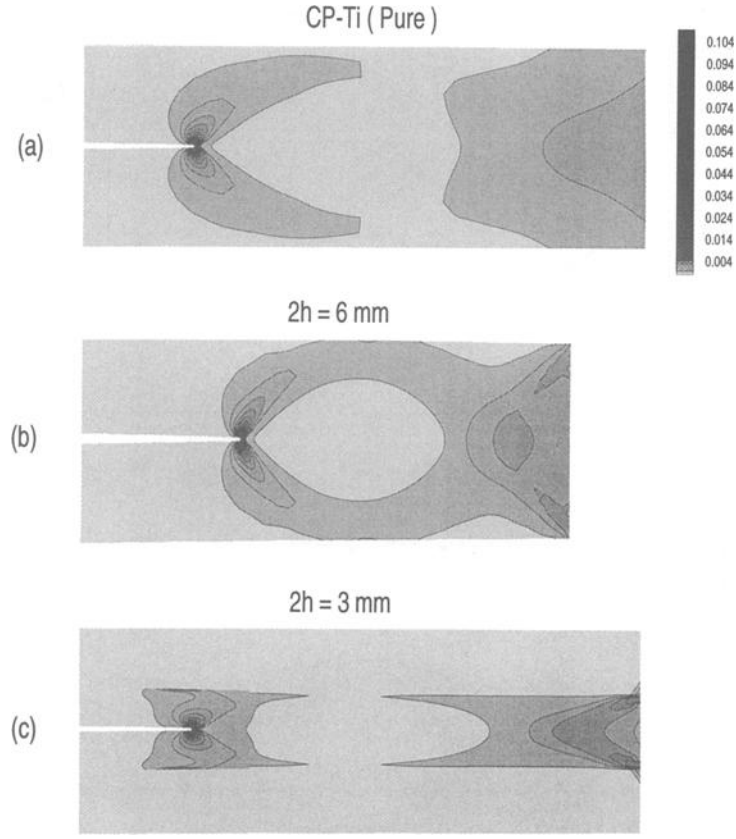


Figure 12: Distribution of the equivalent plastic strain in the softer metal for $2h = 3,6\,mm$ and CP-Ti at $J = 95\,kJ/m^2$.

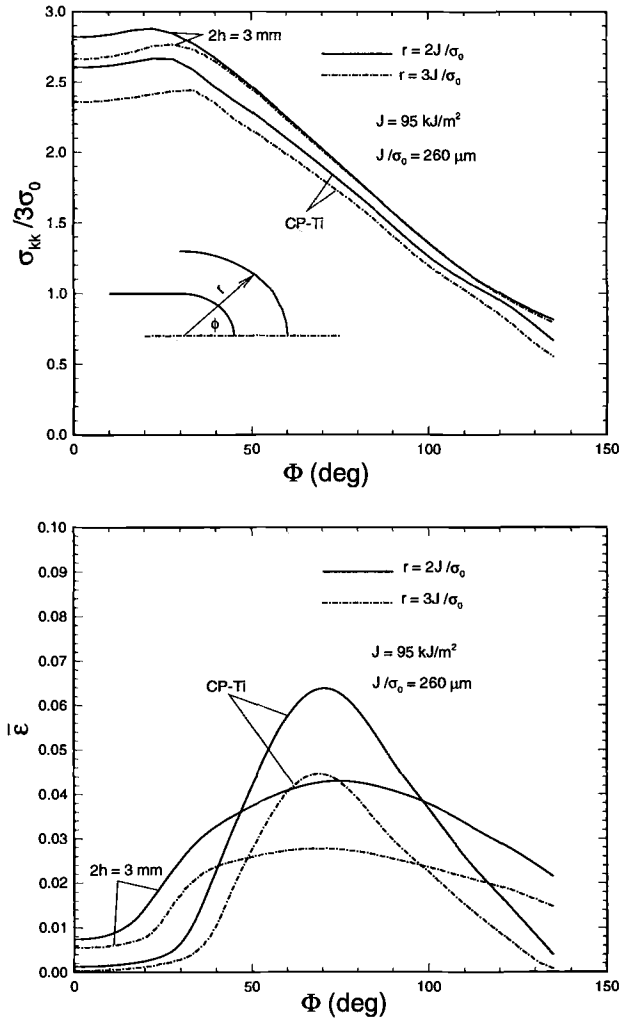


Figure 13: (a) Circumferential variation of normalized hydrostatic stress for $2h = 3\,mm$ and homogenous interleaf specimen, CP-Ti, each loaded in bending to $J = 95\,kJ/m^2$. (b) Circumferential variation of cumulative plastic strain for $2h = 3\,mm$ and CP-Ti at $J = 95\,kJ/m^2$.

homogeneous CP-Ti specimen, both loaded to $J = 95\,kJ/m^2$. The higher stress triaxiality in the $3\,mm$ specimen is evident. Figure 13(b) shows the corresponding circumferential variations of $\bar{\epsilon}$. The strain distribution in the homogeneous material shows the familiar peak near $\Phi = 70^o$ typical of the Green and Hundy field, with intensity of deformation dropping rapidly at angular locations $\Phi < 45^o$ and $\Phi > 135^o$. In contrast, the strain fields of the $3\,mm$ interleaf specimen show reduced peak values near $\Phi = 70^o$, and a broader distribution of strain extends into the regions $\Phi < 45^o$ and $\Phi > 135^o$. This trend is consistent with the "blocked" plastic strain field of Fig. 12(c). In particular, much greater strain has been forced into the region of highest stress triaxiality ahead of the crack tip. To the extent that both stress triaxiality *and* plastic strain determine ductile fracture mechanisms [19, 20, 21], it is easy to appreciate that crack growth ductility in the $3\,mm$ interleaf specimen will be reduced.

Figure 14(a) shows the radial variation of normalized hydrostatic stress along the plane $\Phi = 0$ for two interleaf specimens and a homogeneous CP-Ti specimen loaded to $J = 95\,kJ/m^2$. The peak triaxiality in the $3\,mm$ specimen is not only higher than in the others but also decays more slowly with distance beyond the peak. Figure 14(b) dramatically illustrates the increased plastic strain ahead of the crack tip in the $3\,mm$ interleaf specimen at $J = 95\,kJ/m^2$.

Finally, Figure 15 summarizes near-tip contour values of $\sigma_{kk}/3\sigma_0$ and $\bar{\epsilon}$ for the $3\,mm$ and $6\,mm$ interleaf specimens at $J = 95\,kJ/m^2$. The material regions shown are identical for all four figures. The fields in both specimens are sufficient to generate crack extension, but in the $3\,mm$ specimen, it is unstable. The challenge is to develop models which can predict both types of growth.

DISCUSSION

The importance of the local stress triaxiality in interpreting plane strain crack growth, in conjunction with a measure of crack-tip deformation intensity such as $CTOD$ or J/σ_0, has recently been emphasized by several authors [16, 17, 4, 18]. One of the most popular approaches is based on the so-called $J - Q$ description of local stress triaxiality. Within a forward fan of angular extent $|\Phi| \leq 45^o$, O'Dowd and Shih [16, 17] suggest that the local stress fields can be expressed as

$$\sigma_{ij}(r, \Phi) = \sigma_{ij}^{REF}(r/(J/\sigma_0), \Phi) + Q\sigma_0\,\delta_{ij}, \tag{3}$$

where δ_{ij} is the Kronecker delta, σ_{ij}^{REF} is a reference similarity stress field with spatial dependence only on distance from the tip, r, normalized by J/σ_0. The reference field may be chosen as either the HRR field [1, 2] or the small-scale yielding (SSY) boundary layer solution. The fields are described by the two loading parameters J and Q, where the deviation from the reference stress field is evidently a hydrostatic stress of magnitude $Q\sigma_0$. Since plastic deformation is insensitive to hydrostatic stress, there is a *lack of variation of plastic strain fields* implicit in such a two-parameter description; i.e., a corresponding formula for strains would be

$$\epsilon_{ij}(r, \Phi) = \epsilon_{ij}^{REF}(r/(J/\sigma_0), \Phi). \tag{4}$$

As shown in Figs. 13–15, the strain fields at crack extension fail to scale solely with

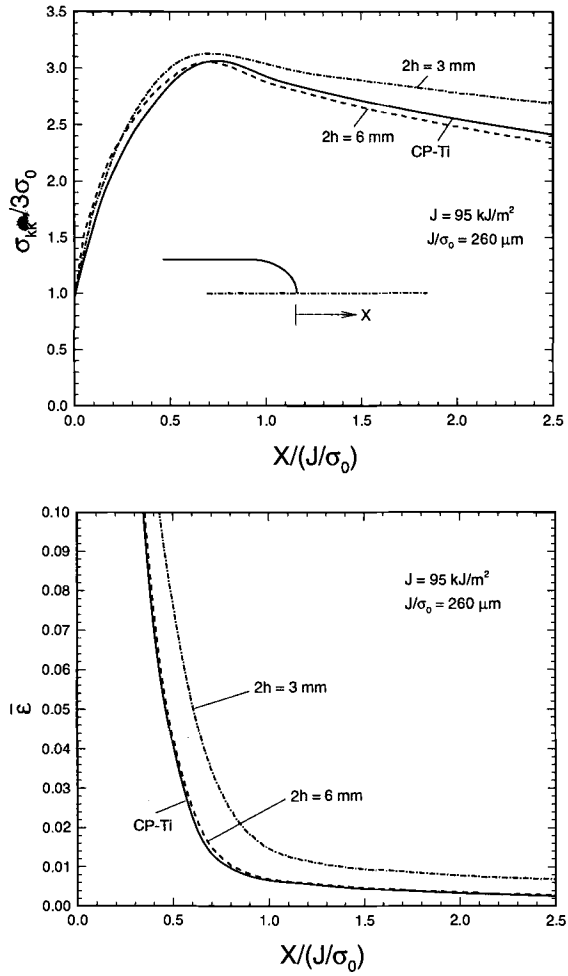


Figure 14: Variation of crack-tip hydrostatic stress and plastic strain fields on the ligament for $2h = 3,6\,mm$ and CP-Ti specimens loaded to $J = 95\,kJ/m^2$. (a) Hydrostatic stress. (b) Cumulative equivalent plastic strain.

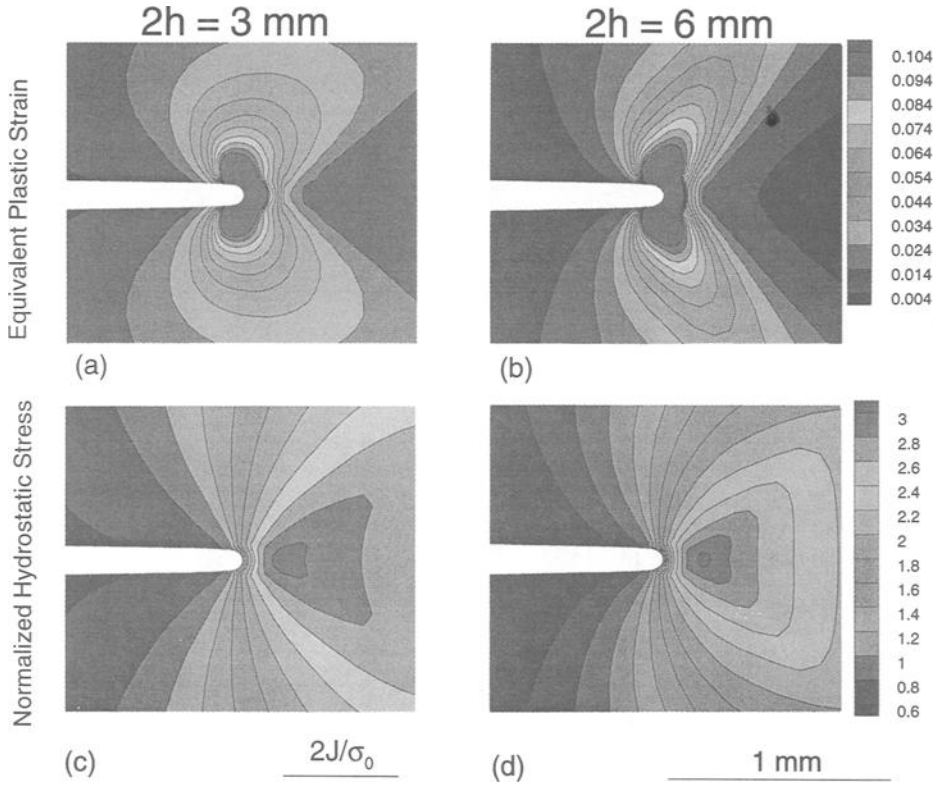


Figure 15: Normalized hydrostatic stress, $\sigma_{kk}/3\sigma_0$, and equivalent plastic strain distributions near the crack tip for $2h = 3$ and $6\,mm$ at $J = 95\,kJ/m^2$.

J (as implied by eq. (4)). This clearly emphasizes the need for attention to limits of applicability of one- or two-parameter fracture mechanics characterizations.

In the present $3\,mm$ specimen, the strain fields were well described by eq. (4) up to loads giving $J \simeq 35\,kJ/m^2$, at which point the plastic zone began to be strongly influenced by the hard surrounding layers. Re-phrasing limits on imposed deformation relative to specimen dimensions, we require

$$J \leq \frac{\sigma_0 h}{m}, \tag{5}$$

where h is half-thickness of the interleaf (minimum characteristic in-plane dimension) and $m \doteq 15$, as assuring that the strain fields are in agreement with eq. (4). This restriction is analogous to that proposed by McMeeking and Parks [3], but for a fundamentally different reason. In the former case, they considered deviation in stress triaxiality from SSY fields; in the present case the principal deviation is in the strain field.

The fracture surfaces of the $3\,mm$ and the $6\,mm$ interleaf specimens were examined in a scanning electron microscope. Figure 16(a) shows the surface of the $3\,mm$ specimen near mid-plane. The direction of crack extenson is from bottom to top of the photo. Several elongated "splits" are evident, oriented with their long directions in the crack extension direction. Higher magnification study of these cavities showed them to be formed from an iron-rich particle, presumably one of the intermetallic inclusions shown in Fig. 3. Also shown in the lower right corner of Fig. 16(a) is a region within the fracture plane which was nucleated by one of these inclusions. Figure 16(b) shows the central portion of the $6\,mm$ specimen fracture surface at the same magnification ($100\times$). There are fewer of the elongated splits, but their lateral opening is greater, as compared to Fig. 16(a). Roughly, this is consistent with the crack tip analyses and experimental results. Presuming the nucleation of cavities at the inclusions to be stress-controlled, the higher stress triaxiality of the $3\,mm$ specimen should tend to nucleate a larger number density of cavities, but the larger crack tip strains associated with stable crack extension in the $6\,mm$ specimen (tearing vs. pop-in) would tend to cause larger opening per cavity, as in Fig. 16(b).

It is interesting to note that the pop-in of magnitude $5.4\,mm$ which occurred in the $3\,mm$ thick interleaf specimens left a remaining ligament of $l_{\text{residual}} = 6.6\,mm$, corresponding to $h/l_{\text{residual}} = 0.24$. In the $6\,mm$ specimen, pop-in following stable ductile cracking arrested with a ligament length of $l_{\text{residual}} = 8.86\,mm$, or $h/l_{\text{residual}} = 0.36$. These values are sufficiently close to the transitional value of $h/l = 0.3$ which resulted in reduced crack-plane strain levels, that one might be tempted to speculate that the pop-in extension continued until plasticity in the remaining ligament was free of the constraint of the hard layers.

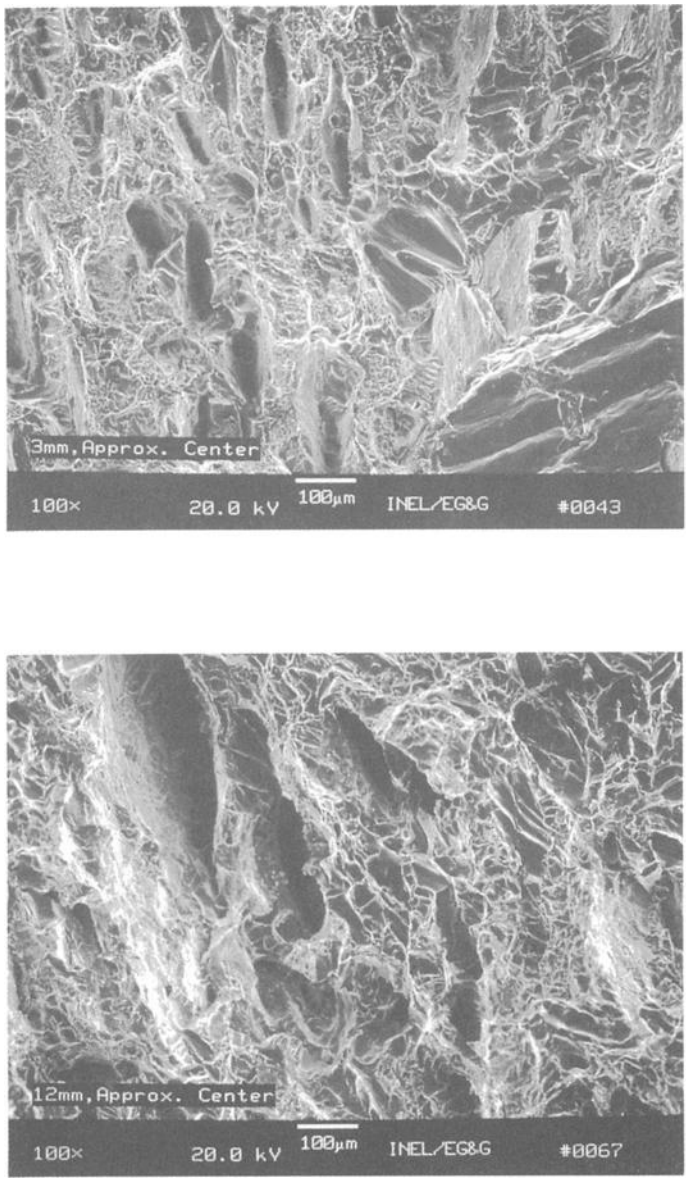


Figure 16: SEM micrographs of the fracture surfaces near the crack tip at center specimen, showing cavity formation near the Fe-Ti stringers, along with other features, for (a) $2h = 3\,mm$ (b) $2h = 6\,mm$.

ACKNOWLEDGMENTS

This work was supported by the Office of Basic Energy Sciences, Department of Energy, under Grant $\#DE-FG02-85ER13331$. Computations were performed on Hewlett Packard workstations obtained under the DOE grant and under NSF Grant $\#DDM-8914161$. The ABAQUS finite element program was made available under academic license from Hibbitt, Karlsson, and Sorensen, Inc., Pawtucket, RI.

REFERENCES

[1] Hutchinson, J. W., "Singular Behavior at the End of a Tensile Crack in a Hardening Material," *Journal of the Mechanics and Physics of Solids*, Vol. 16, 1968, pp. 13–31.

[2] Rice, J. R. and Rosengren, G. F., "Plane Strain Deformation Near a Crack Tip In a Power-Law Hardening Material," *Journal of the Mechanics and Physics of Solids*, Vol. 16, 1968, pp. 1-12.

[3] McMeeking, R. M. and Parks, D. M., "On Criteria for J-Dominance of Crack-Tip Fields in Large-Scale Yielding," in *Elastic-Plastic Fracture*, ASTM STP 668, ASTM, 1979, pp. 175–194.

[4] Parks, D. M., "Advances in Characterization of Elastic-Plastic Crack-Tip Fields," in *Topics in Fracture and Fatigue*, McClintock Festschrift, Ed. Argon, A. S., Springer Verlag, New York, 1992, pp. 58–98.

[5] Cray, M. J., Luxmoore, A. R. and Sumpter, J. D. G., "The Effect of Weld Metal Strength Mismatch on J and $CTOD$," in *Defect Assessment in Components-Fundamentals and Applications*, Eds., Blauel, J. G. and Schwalbe, K. H., Mechanical Engineering Publications, London, 1991, pp. 893–907.

[6] Hao, S., Cornec, A. and Schwalbe, K. H., "Plastic Stress-Strain Fields and Limit Loads of a Crack in an Undermatched Weldment", in *Series of Reports of Mismatch Problems, No.3, Mismatch 93*, Eds. Schwalbe, K. H., Kocak, M., Mechanical Engineering Publications, London, 1993, pp. 893–907.

[7] Kirk, M. T. and Dodds, R. H., Jr., "The Influence of Weld Strength Mismatch on Crack Tip Constraint in Single Edge Notch Bend Specimens," *International Journal of Fracture*, Vol. 63, 1993, pp. 297–316.

[8] Schwalbe, K. H., "Welded Joints with Non-Matching Weld Metal Crack Driving Force Consideration on the Basis of Engineering Treatment Model," *International Journal of Fracture*, Vol. 62, 1993, pp. 1–24.

[9] Dodds, R. H., Jr., Shih, C. F. and Anderson, T. L., "Continuum and Micromechanics Treatment of Constraint in Fracture," *International Journal of Fracture*, Vol. 64, 1993, pp. 101–133.

[10] Varias, A. G., Suo, Z., and Shih, C. F., "Ductile Failure of a Constrained Metal Foil," *Journal of the Mechanics and Physics of Solids*, Vol. 39, 1991, pp. 963–986.

[11] *Metals Handbook, Vol. 3*, ASM, Metals Parks, Ohio, Ninth Edition, 1980, pp. 372–406.

[12] Post, D., "Moire Interferometry," Chapter. 7, *Handbook on Experimental Mechanics*, ed. Kobayashi, A., Second Edition, VCH, NY, 1987.

[13] Hibbitt, Karlsson and Sorensen, Inc., *ABAQUS User's Manual*, version 5.2, 1992, Hibbitt, Karlsson and Sorensen, Inc., Pawtucket, RI.

[14] Green, A. P. and Hundy, B. B., "Initial Plastic Yielding in Notch Bend Tests," *Journal of the Mechanics and Physics of Solids*, Vol. 4, 1956, pp. 128–144.

[15] Parks, D. M., "The Virtual Crack Extension Method for Nonlinear Material Behavior," *Computer Methods in Applied Mechanics and Engineering*, Vol. 12, 1977, pp. 353–364.

[16] O'Dowd, N. P. and Shih, C. F., "Family of Crack Tip Fields Characterized by a Triaxiality Parameter- I. Structure of Fields," *Journal of the Mechanics and Physics of Solids*, Vol. 39, No. 8, 1991, pp. 989–1015.

[17] O'Dowd, N. P. and Shih, C. F., "Family of Crack Tip Fields Characterized by a Triaxiality Parameter- II. Fracture Applications," *Journal of the Mechanics and Physics of Solids*, Vol. 40, No. 5, 1991, pp. 939–963.

[18] Betegón, C., and Hancock, J. W., "Two-Parameter Characterization of Elastic-Plastic Crack-Tip Fields," *Journal of Applied Mechanics*, Vol. 58, 1991, pp. 104–110.

[19] McClintock, F. A., "A Criterion for Ductile Fracture by the Growth of Holes," *Journal of Applied Mechanics*, Vol. 35, 1968, pp. 363–371.

[20] McClintock, F. A., "Plasticity Aspects of Fracture," in *Fracture*, Vol. 3, ed., Leibowitz, H., Academic Press, New York, 1971, pp. 47–225.

[21] Rice, J. R. and Tracey, D. M., "On the Ductile Enlargement of Voids in Triaxial Stress Fields," *Journal of the Mechanics and Physics of Solids*, Vol. 17, 1968, pp. 201–217.

Ludvik Hodulak[1] and Dieter Siegele[1]

FRACTURE BEHAVIOUR OF SUBCLAD CRACKS

REFERENCE: Hodulak, L. and Siegele D., **"Fracture Behaviour of Subclad Cracks"**, Fracture Mechanics: 26th Volume, ASTM STP 1256, Walter G. Reuter, John H. Underwood, and James C. Newman, Jr., Eds., American Society for Testing and Materials, Philadelphia, 1995.

ABSTRACT: An approximate calculation method for stress-intensity factors at the deepest point of finite-length subclad cracks accounting for plastic deformation of the cladding was reported elsewhere. An extension of this method for the part of the crack front near to interface and for infinitely long cracks is described in the first part of this paper. The second part of the paper deals with some applications of this calculation method.

KEYWORDS: safety assessment, thermal shock, stress-intensity factor, cladding, simplified methods

INTRODUCTION

To prove the safety of nuclear installations detailed analyses are done for components like pressure vessels and piping under service and emergency conditions [2]. Small defects are assumed especially in welds under the cladding as schematically shown in Fig. 1. Three-dimensional elastic-plastic finite-element calculations are necessary to obtain the crack-tip loading in terms of J or the stress-intensity factor (SIF) as a function of time during transient loadings like start-up or emergency cooling. To reduce the calculation expenses a combination of 3D elastic-plastic FE calculations for components with cracks and simplified analytical calculations using a modified weight function method was proposed in [1]. This approach has been demonstrated on the example of subclad circumferential cracks in a cylindrical wall (internal radius 2039 mm, wall thickness with cladding 200 mm) of a reactor pressure vessel under different transients. The finite-element calculations have been done for cracks shaped as rectan-

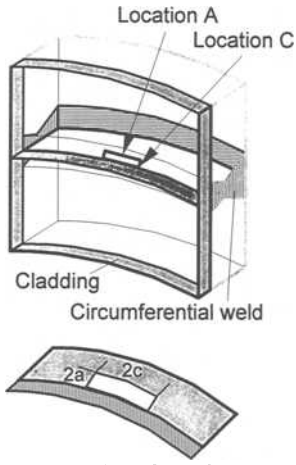


Fig 1. Subclad crack

[1]Fraunhofer-Institut für Werkstoffmechanik, Wöhlerstr. 11, D-79110 Freiburg, Germany

Copyright © 1995 by ASTM International www.astm.org

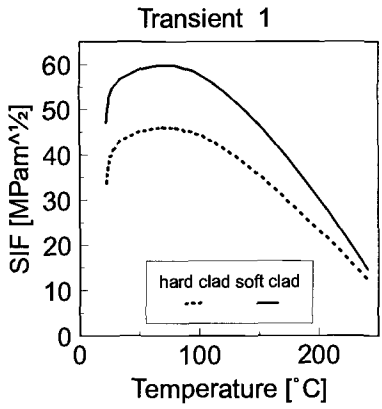


Fig 2. Stress-intensity factor for subclad crack (2a = 4 mm, 2c = 50 mm) obtained from FE calculations

gular segments; this is a conservative model for real cracks. For the applications, however, where not a safe but a best estimate is required, semielliptical subclad cracks were investigated using the simplified method.

The following situation is considered, where the yield stress of the cladding is lower than that of the base material and the base material behaves elastically, while the cladding may yield under loading. The assessment of fracture conditions can be focused on the part of the crack front in the base material because of the high toughness of the cladding. For this part of the crack front the SIF may still be used as the fracture governing parameter, but its value cannot be calculated by linear-elastic methods. Significant increase of the SIF due to yielding of the cladding is demonstrated in Fig. 2, where the SIF at the apex (location A in Fig. 1) of a 4 mm-deep and 50 mm-long crack under cladding (thickness 8 mm) as obtained by 3D elastic-plastic FE calculations is plotted versus the crack-tip temperature during a thermal shock loading ($\Delta T \approx 250°$ C, stripe cooling). The SIF for the realistic "soft" cladding (thickness 6 + 2 mm, yield stress of the clad material and fusion zone at 110°C is 355 and 421 MPa, respectively) is higher than for the hard cladding, which does not yield.

In the simplified method [1] for the SIF estimation, subclad cracks are considered as surface cracks with crack closing stresses prescribed for the part of the crack in the cladding. The calculation procedure has to be calibrated by the results of a limited number of finite-element calculations. Then, the SIF can be easily calculated on personal computers using stress transients as input. This method will be called "analytical", though it involves numerical calculations and can be regarded as a model based interpolation between finite-element solutions.

Based on additional finite-element calculations for subclad cracks of finite and infinite lengths, the analytical method described in [1] has been modified and extended for a larger range of crack geometries and for SIFs in the length direction of finite-length cracks.

FINITE-ELEMENT CALCULATIONS

Three-dimensional elastic-plastic finite element calculations have been performed for a cladded reactor pressure vessel loaded by internal pressure and different thermal shock transients. For the calculations a 45 degree model of the vessel was used and the cladding

modeled by two layers, an internal layer of pure austenite and a transition zone between the austenite and the weld material.

In order to get the input data for the analytical SIF calculation, the temperature and stress distribution within the pressure vessel was calculated with a homogeneous uncracked model. The calculations were done with the programs ADINA [3] and ADINA-T [4]. Fig. 3 shows as an example the distribution of axial stresses for transient 2 (thermal shock due to an assumed 120 cm^2-leak in a hot leg) across the wall thickness for different times. For this transient the stresses in the weld material remain elastic whereas in the cladding plastic deformations occur.

Three-dimensional analyses of the pressure vessel with different rectangular-shaped subclad cracks were performed and the J-integral was calculated at different positions of the crack front[5]. The SIF values derived from the J-integral were used to fit the analytical results. The finite element mesh of the vessel with a rectangular crack of the depth of 30 mm and the length of 50 mm (half model) is plotted in Fig. 4. Fig. 5 shows the J-integral values at the crack positions A (in thickness direction), B, C and D (in length direction). For this crack geometry the J-integral (and SIF) dominates in the length direction. Calculations of other crack geometries show that for smaller ratios of crack depths to length (a/c < 0.32) the maximum J-value is shifted to position A in thickness direction.

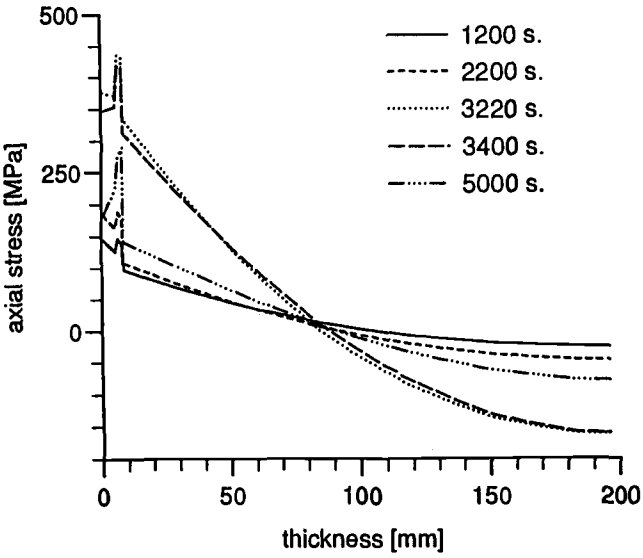


Fig. 3. Axial stresses for transient 2 (elastic-plastic calculation).

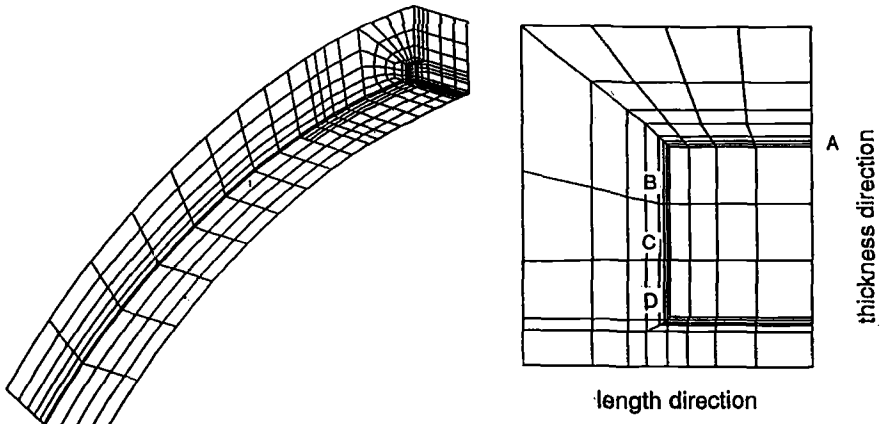


Fig. 4. FE mesh for subclad crack (2a = 30 mm, 2c = 50 mm) and an explosion of the mesh (crack plane).

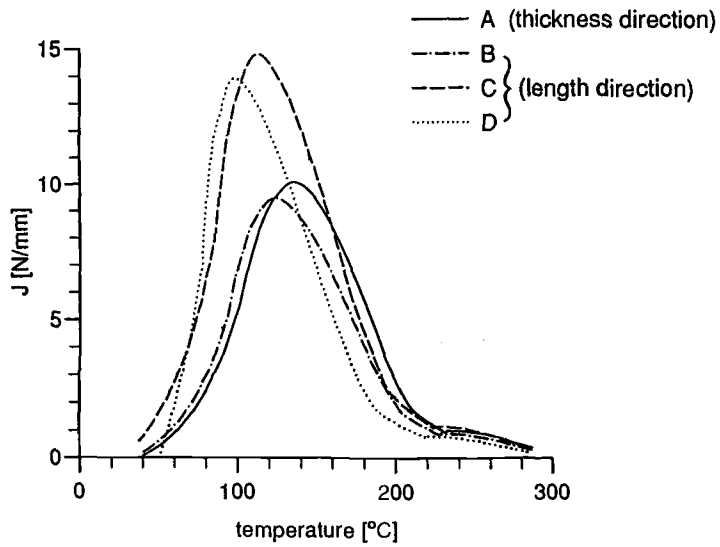


Fig. 5. J Integral on different locations (see Fig. 4) of the crack front in thickness and length direction (crack 30 x 50 mm^2).

ANALYTICAL MODEL FOR SUBCLAD CRACKS

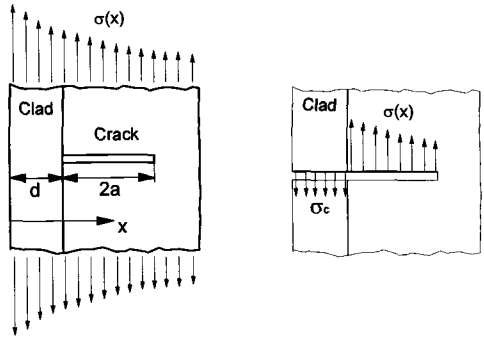


Fig. 6. A model for subclad crack

For the calculation of the SIF at the deepest point of a subclad crack with depth 2a and length 2c under the cladding with thickness d, the embedded crack is modelled as an infinitely long surface crack with a depth of $a_m = 2a + d$ and the part of the crack in the cladding is subjected to the stress σ_c (see Fig. 6) which simulates the effect of the intact cladding on the SIF.

The stress intensity factor K_o is calculated as

$$K_o = \sqrt{\frac{2t}{\pi}} \int_0^{\frac{a_m}{t}} \frac{R_i + x}{R_i + a_m} \frac{\sigma(x)\, m\left(\frac{x}{t}, \frac{a_m}{t}\right)}{\sqrt{\frac{a_m}{t} - \frac{x}{t}}} d\left(\frac{x}{t}\right) \tag{1}$$

where $m(x/t, a_m/t)$ are weight functions from [6], t is wall thickness, R_i is internal radius, and $\sigma(x)$ are the "undisturbed" stresses over the wall thickness for $x \geq d$, and

$$\sigma(x) = \sigma_c \text{ for } x < d. \tag{2}$$

For finite-length cracks, the influence of the finite crack length on the SIF at the deepest point of the crack is taken in account by the shape factor Q

$$K_a = \frac{K_o}{\sqrt{Q}}, \qquad Q = 1 + 1.464\left(\frac{a}{c}\right)^{1.65} \tag{3}$$

in the same way as in [7] for embedded elliptical cracks in bodies under uniform tension.

To obtain the SIF for the apex of rectangular cracks, the relation

$$K_{a,rectangle} = K_a \cdot (1 + 0.24a/c) \tag{4}$$

is used. This relation was originally based on a linear approximation of data from [8]; to achieve a better agreement with FE results, the value of the coefficient was adjusted from 0.19 to 0.24.

The crack closure stress σ_c is calculated from stresses over the embedded crack by the relation

$$\sigma_{c,elastic} = -\sigma_m \; a/d \cdot F \tag{5}$$

where the coefficient F is to be found by fitting the analytical results to corresponding finite-element results for linear-elastic conditions, i.e. at low load levels. The stress σ_m at the center of the crack is used instead of the average value of stresses $\sigma(x)$ over the embedded crack for simplicity. By fitting the SIF for the 4 x 50 mm^2 crack, F = 1.08 has been obtained, which also works well for larger cracks. For very deep cracks, however, some dependence of this parameter on a/d and a/t has to be expected.

Although the computed average stress in the cladding is increasing with increasing load, the effective closing force is decreasing, due to the finite plastic deformation. Therefore, it is assumed that for elastic-plastic conditions the average stress in the cladding (the sum of the average value σ_p of stresses $\sigma(x)$ over the cladding thickness obtained from an elastic-plastic calculation for the pressure vessel without crack and of the closure stress $\sigma_{c,elastic\text{-}plastic}$) cannot exceed a reference stress σ_r,

$$\begin{aligned} \sigma_{c,elastic\text{-}plastic} &= \sigma_{c,elastic} \quad \text{for} \quad \sigma_p - \sigma_{c,elastic} \le \sigma_r \\ \sigma_{c,elastic\text{-}plastic} &= \sigma_p - \sigma_r \quad \text{for} \quad \sigma_p - \sigma_{c,elastic} > \sigma_r \end{aligned} \tag{6}$$

hence the closure stress may decrease with increasing external loads and simulate the effect of the yielded cladding on the SIF.

The reference stress is supposed to be approximately equal to the flow stress of the cladding. By fitting the maximum SIF to finite element results for the crack 4x50 mm^2, a reference stress σ_r = 435 MPa has been obtained. For an arbitrary crack shape the "plastic" component of the SIF(component resulting from decreasing closure stress according to Eq. 6) is multiplied by the factors $M(2a/c)/M(4/25)$ and $\sqrt{Q(4/25)/Q(2a/c)}$, where $M = K/\left(\sigma\sqrt{\pi a/Q}\right)$ is the stress-intensity magnification factor. The use of the crack aspect ratio 2a/c instead of a/c reflects the fact that at fully yielded cladding the embedded crack appears as a surface crack.

A comparison with available FE results for relatively short cracks (2c = 50 mm, 2a equal to 4, 8, 16, and 30 mm) under transient 2 shows that this model works reasonably well (Fig. 7).

For very long cracks, however, the SIFs are overestimated, i.e. the reference stress should be higher. Therefore, for the increase of the reference stress with increasing crack size, a strain hardening model is used.

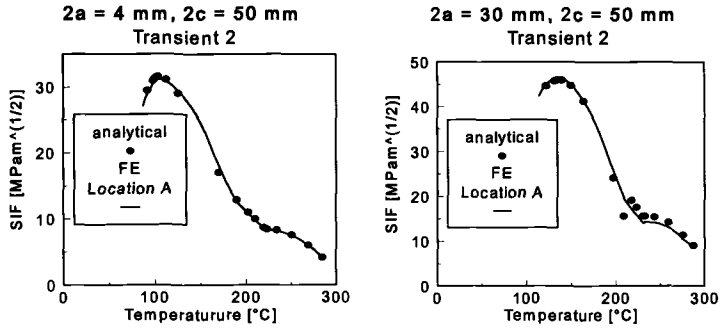


Fig. 7. SIF for the depth direction of rectangular subclad cracks.

Assuming a potential form of the stress-strain curve, the crack-size dependent reference stress $\sigma_r(a,a/c)$ is calculated as

$$\sigma_r(a, a/c) = \sigma_r \cdot \left(\delta(a, a/c) / \delta(4, 0.08)\right)^{1/n} \tag{7}$$

where $\delta(a, a/c)$ is the crack-mouth opening displacement of a surface crack.

For n the value 10 is chosen. The δ is estimated under the assumption $\delta \propto M(a, a/c, a/t)^2$, where $M(a, a/c, a/t)$ is the stress-intensity magnification factor for surface cracks. For finite-length cracks, values of $M(a, a/c, a/t)$ are calculated using formulae from [7].

For cracks of infinite length, M is evaluated for a/c = 0.1 and δ is divided by 0.7, accounting for the fact that δ is not constant for finite-length cracks along the length direction (and its mean value is lower than its maximum by about 30 %), while δ is constant for cracks of infinite length.

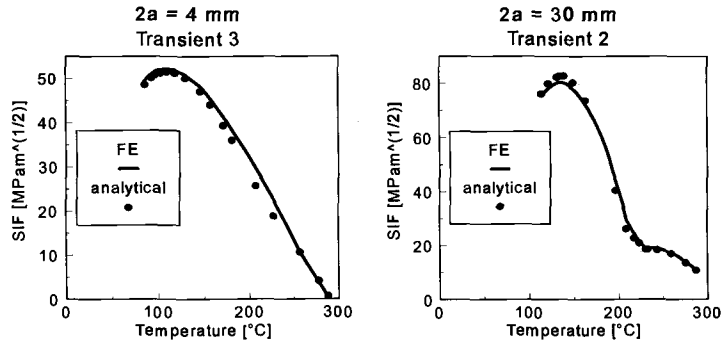


Fig. 8. SIF for infinite long subclad cracks

A comparison of SIFs for infinitely long cracks calculated by FE and the analytical method in Figs. 8 shows good agreement. Transient 3 is a severe axisymmetrical thermal shock.

SIF for the length direction of finite-length cracks

Stress-intensity factors K_c for length direction of rectangular cracks are calculated from stress-intensity factors K for depth direction (Eq. 3) as

$$K_c = K_a \sqrt{a/c} F_{er} \sigma_i / \sigma_m \tag{8}$$

where σ_i is the stress at the interface between the base material and the cladding, σ_m is the mean stress over the crack depth, and F_{er} is a factor for conversion from elliptical to rectangular crack shape

$$F_{er} = 1 + 0.19 c/a \tag{9}$$

Eq. 8 is obtained by extrapolation of data from [7].

For the crack front in the length direction (Fig. 9) analytical values agree well with FE results for the location with the highest SIF values (location C in Fig 3). For the crack with the depth 2a = 4 mm, the analytical calculation overestimates the SIF; a possible reason is the extrapolation of the factor F_{er} by Eq. 8 far beyond available data.

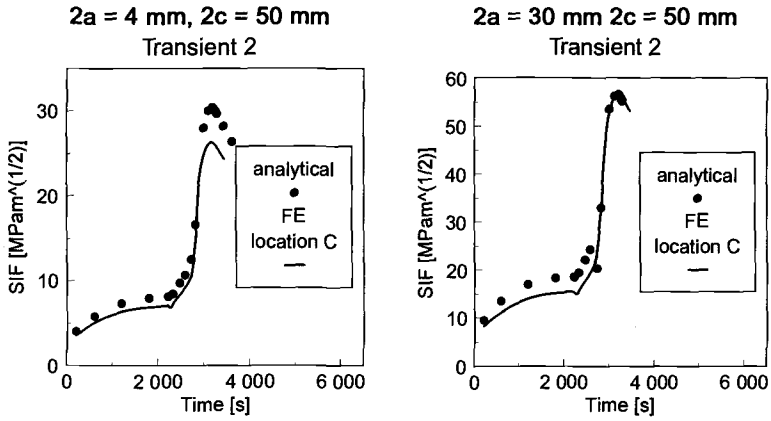


Fig. 9. SIF for the length direction of rectangular subclad cracks

The method for calculation of SIFs described here can also be used for other geometry and material conditions, like different tensile properties and thicknesses of the cladding, but a new calibration of the calculation procedure by finite-element results for several crack sizes and/or transients may be necessary.

APPLICATION

The calculation method developed for nuclear pressure vessels is used here in pre- and post-test calculations for tests on cladded components. These tests have been done at low temperatures to simulate material embrittlement.

Cleavage fracture of large-scale bending specimens DD2 and DSR3

In this example post-test calculations have been done for experiments on specimens DD2 and DSR3 [9] with subclad cracks. Large-scale specimens made of ferritic steel A508 Cl 3 with stainless steel cladding (yield stress of the cladding 346 MPa at -170°C), containing artificial semielliptical subclad defects have been tested in 4-point bending (spans s_1 = 1450 mm, s_2 = 450 mm) at a temperature of about -170°C to obtain crack instability by cleavage fracture [9]. The geometry and loading data for experiments DD2 and DSR3 reported in [9] are given in Table 1.

Table 1. Input data for post-test calculations

Specimen	Specimen Thickness B [mm]	Specimen Width W [mm]	Clad Thickness d [mm]	Crack Depth [mm]	Crack Length 2c [mm]	Bending Stress at Fracture [MPa]
DD2	125.2	145	6	4.5	48	587
DSR3	124.6	145	4.5	13	40	463

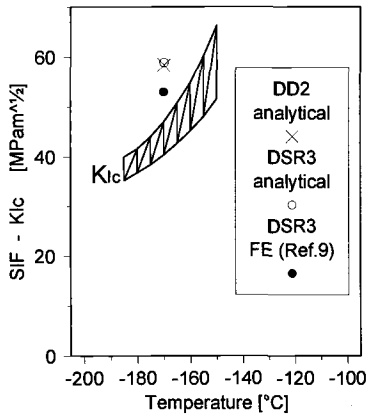


Fig 10. Comparison of the SIF for fracture load with fracture toughness K_{Ic}

The linear stress distribution over the plate thickness was used for calculations of the SIF, although the cladding would yield. This simplification may slightly increase the SIF. The stress at the plate surface σ_b has been calculated from the maximum load P_{max}

$$\sigma_b = 3(s_2 - s_1)P_{max}/(2BW^2). \qquad (10)$$

SIFs in the thickness direction at the deepest point of the crack front are compared with the fracture toughness K_{Ic} of the base material at temperature T $\approx$ -170 °C in Fig. 10. For the specimen DSR3, the SIF from a 3D elastic-plastic FE calculation [9] is included in Fig. 10 for comparison.

For DSR3 the SIF calculated analytically is higher than the corresponding FE-value, which demonstrates once more the conservativism of the approach.

Other elastic-plastic FE calculations for these experiments reported in [9] are only two-dimensional. Their results are compared with analytical results in Table 2. For the infinitely long cracks the accuracy of the analytical method is better than 10 %.

Table 2. SIF for crack depth direction at fracture load and the difference Δ between analytical and FE results.

Specimen	SIF [MPam$^{1/2}$]					
	2D (infinite crack length)			3D (finite crack length)		
	FE	analyt.	Δ [%]	FE	analyt.	Δ [%]
DD2	61	62.7	2.8	----	58.4	----
DSR3	80	86.9	8.6	53	58.9	11.1

Spinning cylinder experiment NESC1

In this example pre-test calculations have been done for the experiment NESC1 of a spinning cylinder with axial subclad cracks subjected to thermal shock. The experiment is being designed and will be conducted and analysed in the framework of the international project NESC (Network for Evaluating Steel Component). The aim of the present calculation is to assess the possibility of a cleavage fracture initiated from hypothetical cracks in an axial weld of a composite cylinder.

For this assessment, "Version 3" of the input data specification has been used:

- a cylinder with internal diameter 1150 mm, length 1300 mm, and thickness 150 mm including 4 mm-cladding
- rotational speed 2500 rpm, thermal shock 320 → 5°C
- yield stress 510 MPa and 210 MPa for the base material and the cladding, respectively

The reference stress for the analytical method was decreased from 435 MPa to 257 MPa (proportionally to different yield stresses in NESC1 experiment and in the calibration of the calculation method: $\sigma_r = 435 \cdot 210/355$).

For the example of a semielliptical subclad crack (depth 40 mm, length 240 mm), for which FE results are available (Brochard, J., Minutes of the 4th NESC TG3 meeting, Appendix IV, Lyon, February 2-3, 1994), the performance of the method has been tested. Fig. 11 shows good agreement between analytical and elastic-plastic FE results for both, the crack apex and the crack front near the interface (12° and 20° from interface). The appreciable effect of the yielding of the cladding on the SIF at the crack apex is shown by the comparison of linear-elastic and elastic-plastic FE results in Fig. 11.

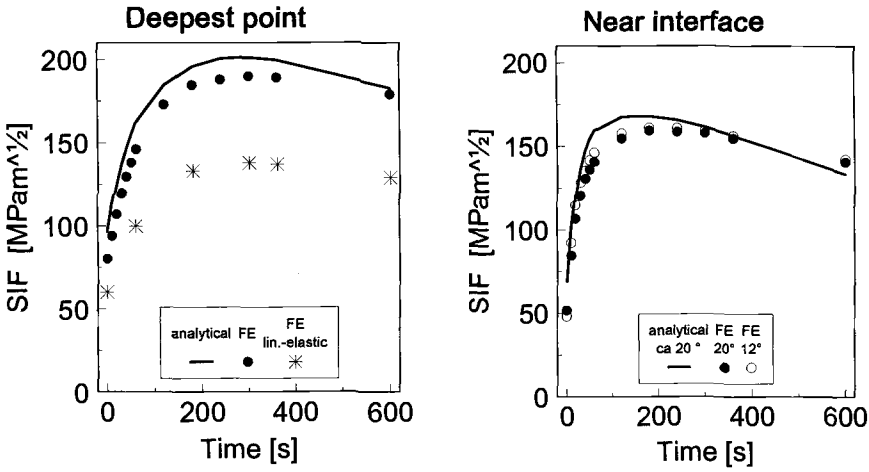


Fig. 11 A comparison of analytical and FE results for the semielliptical subclad crack 40x240 mm^2 (NESC1).

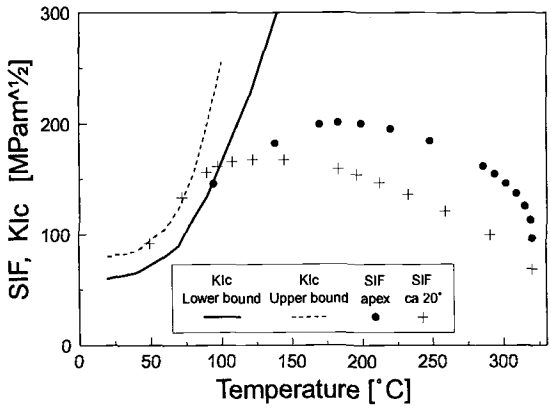


Fig. 12 Assessment of cleavage fracture for an axial semielliptical subclad crack 40x240 mm^2 in a spinning cylinder under thermal shock (NESC1).

In Fig. 12 the SIF for the semielliptical subclad crack 40x240 mm^2 obtained with the analytical method is plotted together with the preliminary fracture toughness scatter band. Although the SIF for the length direction exceeds the fracture toughness at low temperatures, the crack will not initiate because of the warm prestressing effect (WPS). Hence, for the assessment of the safety against crack initiation under thermal shock loading, it is sufficient to show, that the maximum of the SIF lies on the right hand side of the fracture toughness lower bound.

For assumed extended subclad cracks in an axial weld of the spinning cylinder, the maximum values of the SIF for crack depth up to 40 mm are plotted in Fig. 13. Using the preliminary fracture toughness data K_{Ic}, the graph shows significant safety margins against crack initiation.

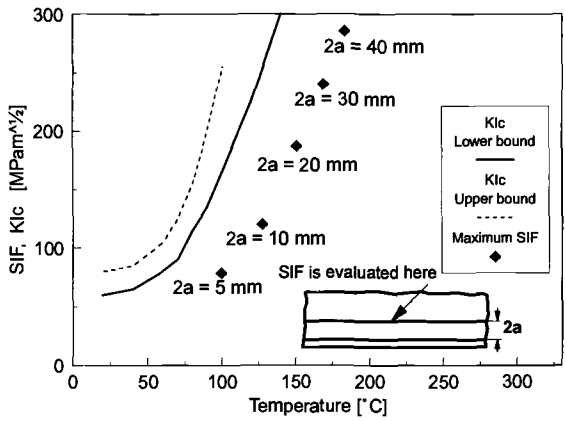


Fig. 13 Initiation assessment for extended axial subclad cracks of different depths 2a.

CONCLUDING REMARKS

The calculation method for the SIF at the deepest point of cracks under yielded cladding [1] has been modified to cover a larger range of crack geometries (crack sizes and crack aspect ratio), and to involve estimates of the SIF near the interface. The method may be used for other cases after its calibration with a limited number of finite-element results. This combination of analytical and finite-element methods appreciably reduces the calculation effort, but still maintains accurate results.

The application of the method for other geometry and loading conditions than those used in the calibration of the calculation method still yielded good engineering estimates.

ACKNOWLEDGEMENTS

The authors wish to express their appreciation to the PreussenElektra AG, Hannover for the permission to publish results obtained in contract work done for them and the GRS, Köln for providing the FE input data of the spinning cylinder problem..

REFERENCES

[1] Hodulak, L. and Siegele, D., "Calculation of Stress Intensity Factors for Cracks Under Thermal Shock Transients", to be published in Fracture Mechanics: 25th Volume, ASTM STP 1220, ASTM, Philadelphia, 1994.

[2] Nagel, G., Blauel, J.G., and Schmitt, W., "A Multibarrier Safety Concept for the Reactor Pressure Vessel of the Stade Power Plant", to be published in Nuclear Engineering and Design.

[3] ADINA, A Finite Element Program for Automatic Incremental Nonlinear Analysis, Report ARD 87-2, ADINA R&D, Inc., Watertown, MA, 1987.

[4] ADINA-T, A Finite Element Program for Automatic Incremental Nonlinear Analysis of Temperatures, Report ARD 87-2, ADINA R&D, Inc., Watertown, MA, 1987.

[5] D. Siegele, "3D-crack propagation using ADINA.", Computers & Structures Vol. 32, No. 3/4, pp 639-645, 1989.

[6] Labbens, R., Pellisier-Tanon, A. and Heliot, J., "Practical Method for Calculating Stress-Intensity Factors Through Weight Functions", ASTM STP 590, pp. 368-384, 1976.

[7] Newman, J.C. and Raju, I.S., "Stress-Intensity Factor Equations for Cracks in Three-Dimensional Finite Bodies", ASTM STP 791, 1983, pp. I-238 - I-265.

[8] Isida, M., Yoshida, T., and Noguchi, H., "A rectangular crack in an infinite solid, a semi-infinite solid and a finite-thickness plate subjected to tension", International Journal of Fracture 52, pp. 79-90, 1991.

[9] Moinereau, D., Debruyne, G., Bethmont, M., and Rousselier, G., "Cleavage Fracture of Specimens Containing an Underclad Crack", ASME Pressure Vessels and Piping Conference, New Orleans, June 21-25, 1992.

Janis A. Keeney[1] and John W. Bryson[1]

STRESS-INTENSITY-FACTOR INFLUENCE COEFFICIENTS FOR SEMIELLIPTICAL INNER-SURFACE FLAWS IN CLAD PRESSURE VESSELS

REFERENCE: Keeney, J. A. and Bryson, J. W., "**Stress-Intensity-Factor Influence Coefficients for Semielliptical Inner-Surface Flaws in Clad Pressure Vessels**," Fracture Mechanics: 26th Volume, ASTM STP 1256, Walter G. Reuter, John H. Underwood, and James C. Newman, Jr., Eds., American Society for Testing and Materials, Philadelphia, 1995.

ABSTRACT: A problem of particular interest in pressure vessel technology is the calculation of accurate stress-intensity factors for semielliptical surface cracks in cylinders. Computing costs for direct solution techniques can be prohibitive when applied to three-dimensional (3-D) geometries with time-varying boundary conditions such as those associated with pressurized thermal shock. An alternative superposition technique requires the calculation of a set of influence coefficients for a given 3-D crack model that can be superimposed to obtain mode-I stress-intensity factors. This paper presents stress-intensity-factor influence coefficients (SIFICs) for axially and circumferentially oriented finite-length semielliptical inner-surface flaws with aspect ratios [total crack length (2c) to crack depth (a)] of 2, 6, and 10 for clad cylinders having an internal radius (R_i) to wall thickness (t) ratio of 10. SIFICs are computed for flaw depths in the range of $0.01 \leq a/t \leq 0.5$ and two cladding thicknesses. The incorporation of this SIFIC data base in fracture mechanics codes will facilitate the generation of fracture mechanics solutions for a wide range of flaw geometries as may be required in structural integrity assessments of pressurized-water and boiling-water reactors.

KEYWORDS: stress-intensity-factor influence coefficient, pressurized thermal shock, finite-length flaw, reactor pressure vessel, superposition

Several techniques have been employed by analysts to calculate accurate stress-intensity factors for semielliptical surface cracks in cylinders. Solution techniques that have been applied to this problem include direct three-dimensional (3-D) calculations using a

[1]Engineers, Oak Ridge National Laboratory, P. O. Box 2009, Oak Ridge, TN 37831-8056.

Copyright © 1995 by ASTM International www.astm.org

finite-element method [1,2]. However, computing costs for this direct approach can be prohibitive when applied to 3-D geometries with time-varying boundary conditions such as those associated with pressurized thermal shock. Several investigators [3-5] have focused on an alternative superposition technique that requires calculation of a set of influence coefficients for a given 3-D crack model. In this technique, the crack surface of a specified geometry is subjected to four stress distributions in the radial direction: uniform, linear, quadratic, and cubic. Stress-intensity-factor influence coefficients (SIFICs) obtained from these solutions are then superimposed to obtain mode-I stress-intensity factors for other stress distributions, such as those due to internal pressure or thermal shock. Considerable economy can be achieved in this approach because the only direct 3-D solutions required are those used to calculate the influence coefficients.

The Heavy-Section Steel Technology Program at the Oak Ridge National Laboratory currently has the objective of developing a data base of validated SIFICs for a wide range of axially and circumferentially oriented finite-length semielliptical inner-surface flaw geometries for a range of clad-vessel geometries. The incorporation of this SIFIC data base into fracture mechanics codes such as FAVOR [6] will facilitate the generation of fracture mechanics solutions for a wide range of flaw geometries as may be required in structural integrity assessments of pressurized-water and boiling-water reactors.

In this paper, SIFICs are presented for axially and circumferentially oriented finite-length semielliptical inner-surface flaws with aspect ratios [total crack length (2c) to crack depth (a)] of 2, 6, and 10 for clad cylinders having an internal radius (R_i) to wall thickness (t) ratio of 10. The SIFICs are computed for flaw depths in the range of $0.01 \le a/t \le 0.5$, with particular emphasis on shallow flaws ($a/t \le 0.1$) and cladding. SIFICs are computed for two cladding thicknesses (t = 3.96 and 6.35 mm). This paper first outlines the technique for computing the SIFICs. Next, results from the application of the superposition technique are compared with direct 3-D finite-element solutions. Finally, the calculated SIFICs are compared with results obtained by other investigators for $a/t \ge 0.2$ (SIFICs for shallow flaws from other sources were not available for comparison).

SUPERPOSITION TECHNIQUE

The stress-intensity factor (K_I) is calculated by a superposition technique proposed by Bueckner [7]. Instead of calculating K_I for the cracked structure using the actual loads, the calculation is performed with a distributed pressure applied to the crack surfaces only. This pressure is opposite in sign, but equal in magnitude and distribution, to the stresses along the crack line that are calculated for the uncracked structure with the actual loads applied. For an arbitrary stress distribution and the case of a 3-D semielliptical flaw, the truncated stress distribution is approximated with a third-order polynomial as indicated by Eq. (1):

$$\sigma(a') = C_0 + C_1(a'/a) + C_2(a'/a)^2 + C_3(a'/a)^3 , \qquad (1)$$

where $\sigma(a')$ is the stress normal to the crack plane at radial position a', and a' and a are defined in Fig. 1. The K_I values are calculated for each of the individual terms (stress distributions) in Eq. (1) and are then added to obtain the total K_I value as indicated by Eq. (2):

$$K_I(a) = \sum_{j=0}^{3} K_{Ij}(a) = \sum_{j=0}^{3} C_j \sqrt{\pi a} K_j^*(a) , \qquad (2)$$

$$K_j^*(a) = K_{Ij}'(a) / (C_j'\sqrt{\pi a}) \ . \tag{3}$$

Values of $K_{Ij}'(a)/C_j'$ are calculated for each of the normalized stress distributions corresponding to each term in Eq. (1) (uniform, linear, quadratic, and cubic), using the 3-D finite-element analysis and an arbitrary value of C_j', such as unity. The quantity $K_j^*(a)$ is referred to as the influence coefficient and, as indicated by Eq. (3), is dimensionless. Once the influence coefficients are obtained, they can be used with any values of C_j to obtain corresponding values of $K_I(a)$. For 3-D flaws, $K_j^*(a)$ values can be calculated for several points along the crack front, in which case $K_j^*(a)$ in Eq. (2) becomes $K_j^*(a,\phi)$, where ϕ is the elliptical angle denoting the point on the crack front.

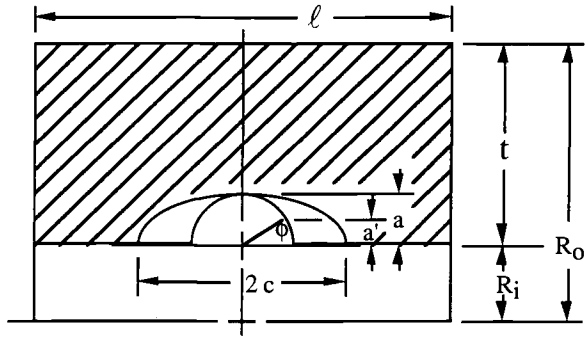


FIG. 1--Axially oriented semielliptical flaw on inner surface of cylinder.

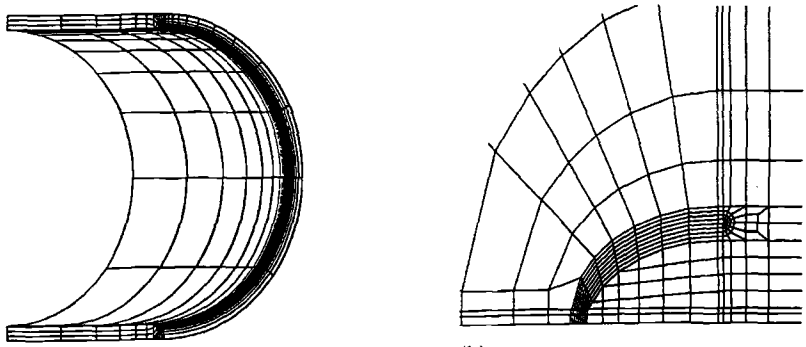
The presence of a thin layer of stainless steel cladding on the inner surface of reactor pressure vessels has a significant effect on the K_I values for inner-surface flaws because of very high thermal stresses generated in the cladding during a thermal transient. When using coefficients for 3-D flaws, it is necessary to represent the stress distribution in the uncracked cylinder with a third-order polynomial, and thus the discontinuity in the thermal stress at the clad-base material interface presents a problem. To accommodate the stress discontinuity associated with the cladding [5], influence coefficients were calculated for the cladding stresses alone; the corresponding K_I value can then be superimposed on the K_I value due to the stresses in the base material. This is accomplished by first calculating a K_I value for a continuous-function stress distribution obtained by a linear extrapolation of the stress distribution in the base material into the cladding. Then a K_I value is calculated for a stress distribution in the cladding which is obtained by subtracting the extrapolated distribution from the actual distribution in the cladding, which is also assumed to be linear. The total K_I value is simply the sum of the two. Because the stress distribution in the cladding is essentially linear, only a first-order polynomial is used for the cladding coefficients.

CALCULATION OF SIFICs (K_j^*)

For the present study, K_j^* values were computed using the ABAQUS [8] finite-element code. ABAQUS is a nuclear-quality-assurance certified (NQA-1) code that

employs a domain integral method for the computation of the J-integral. A 3-D finite-element model was generated for each crack depth and aspect ratio. The analysis matrix included a crack depth range from 2.16 mm to 108.0 mm (crack depth/vessel thickness ratio of 0.01 to 0.5) and three different aspect ratios (2c/a) of 2, 6, and 10. A total of 39 finite-element models and over 200 analyses were required to generate the K_j^* values.

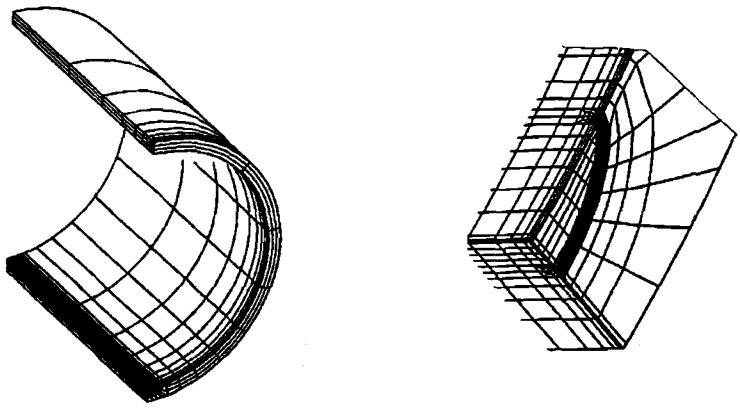
The 3-D finite-element models were generated with the ORMGEN [9] mesh generating program. A typical finite-element mesh for an axial, inner-surface, semielliptical flaw is shown in Fig. 2 (2c/a = 6 and a/t = 0.2). The vessel in Fig. 2 has a t = 216 mm (including cladding), R_i = 2184 mm, and ℓ = 4699 mm.



(a) (b)

FIG. 2--Finite-element model for an axial inner-surface flaw having R_i/t = 10, a/t = 0.2, and 2c/a = 6: (a) complete model, and (b) crack-tip region.

This model has 10792 nodes and 2255 twenty-noded isoparametric elements (reduced 2 x 2 x 2 integration). The mesh refinement was increased (more nodes and elements) near the crack tip for models with shallower flaws. From symmetry conditions, only one-fourth of the vessel is included in the finite-element model. Figure 3 shows the finite-element mesh for a circumferential flaw (2c/a = 6 and a/t = 0.3).



(a) (b)

FIG. 3--Finite-element model for a circumferential inner-surface flaw having R_i/t = 10, a/t = 0.3, and 2c/a = 6: (a) complete model, and (b) crack-tip region.

In the process of calculating the SIFICs, careful attention was paid to using adequately converged finite-element meshes and an appropriate cylinder length. The number of elements in the circumferential and axial directions and around the crack front was increased, one at a time, to the point where addition of one element changed the value of K_I by less than one percent. The resultant converged meshes for a 180°, half-length segment of the cylinder had ~30,000 degrees of freedom. The minimum length of the cylinder to negate end effects was estimated from the cylinder radial dimensions [10] to be ≈ 3353 mm. From previous studies [5], the appropriate length for a cylinder with a 6:1, inner-surface, semielliptical flaw (a/t = 0.2) was 1.4 times the estimated value, so a cylinder length of 4699 mm was used in these analyses. A second analysis was performed on a cylinder in which the length of the cylinder was doubled. The K_I values around the crack front changed less than one percent.

The adequacy of using SIFICs was investigated by calculating K_I values by both the superposition (as implemented in the FAVOR code) and direct ABAQUS finite-element techniques. The first comparison was for the 6:1 axial semielliptical flaw with a/t = 0.075 and the thermal loading through the vessel wall as indicated in Fig. 4 (a). Representative material properties for these analyses (Table 1) were obtained from the NRC-EPRI cosponsored PTS Benchmarking Exercise [11]. The results of this comparison analysis indicate a maximum difference of ≈ 2 % along the crack front [Fig. 4 (b)]. The second comparison was for a 10:1 axial semi-elliptical flaw with a/t = 0.5 and the same loading. The results, given in Fig. 4 (b), show good agreement.

TABLE 1--Material properties for cylinder analyses.

Material Property	Base	Clad
Thermal Conductivity (k), W/m•K	41.54	17.31
Specific Heat (c_p), J/kg•K	502.4	502.4
Density (ρ), kg/m^3	7833	7833
Young's Modulus (E), GPa	193.05	186.16
Coeff. of Thermal Exp. (α), /°C	1.449E-05	1.638E-05
Poisson's Ratio (ν)	0.30	0.30
Fluid-film heat transfer coefficient (h) = 1816 W/m^2•K		

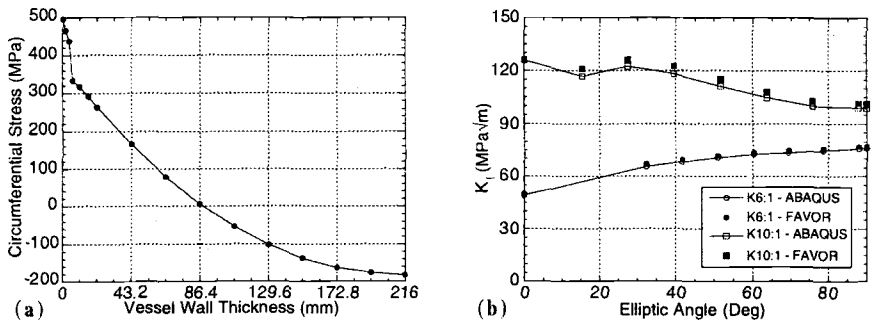


FIG. 4--(a)Thermal-stress profile in clad cylinder used to calculate K_I, and (b) comparison of K_I values calculated by superposition and direct finite-element techniques for axially oriented 6:1 and 10:1 flaws (a/t = 0.075 and 0.5, respectively) for severe thermal transient.

Two analyses were performed on a clad cylinder having $R_i/t = 10$ and $a/t = 0.1$ with uniform and quadratic loading so a comparison of SIFICs could be made for vessels with the same R_i/t and a/t ratios but different t. The SIFICs around the crack front had less than 0.02 % difference between the analyses of the two cylinders (t = 216 mm and 108 mm).

At the outset of the present study, it was anticipated that SIFICs for shallow circumferential flaws ($a/t \leq 0.1$) would be essentially identical to those computed for shallow axial flaws. This anticipated result was arrived at by examining SIFICs computed and reported [12,13] previously for 2-D flaws. Figure 5 shows the maximum thermally induced value of K_I (with respect to time) as a function of crack depth for both long axial flaws and continuous circumferential flaws for a reference calculational model used in the NRC-EPRI cosponsored PTS Benchmarking Exercise [11]. It can be seen that the two

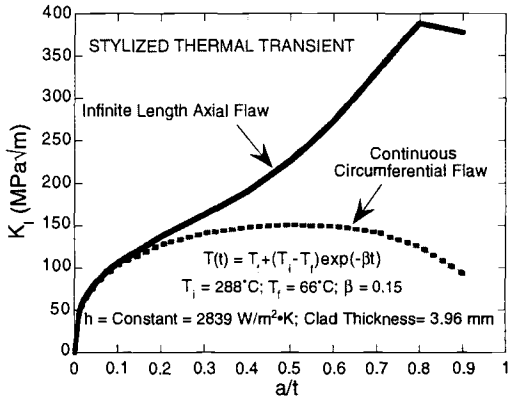


FIG. 5--Variation of maximum K_I (with respect to time) as a function of crack depth for inner-surface long axial flaws and continuous circumferential flaws for the stylized thermal transient reference calculational model.

flaw geometries give essentially identical results for $a/t \leq 0.1$, however, significant differences can be observed for deeper flaws. It could be expected that finite axial and circumferential flaws would show no differences for shallow flaws and less difference than that shown in Fig. 5 for deeper flaws due to the increased constraint provided by the 3-D geometry.

These expected results were indeed realized in the present study as can be observed in Fig. 6. Variations of the SIFICs at the deepest point on the crack front are shown as a function of a/t ratios for 2c/a = 10. It can be observed that there are essentially no differences between calculated SIFICs for circumferential and axial semielliptical inner-surface flaws having an $a/t \leq 0.3$. Small differences (~5%) can be observed for flaw geometries having an a/t = 0.5 and 2c/a = 10. This difference is less for 2c/a of 2 and 6. Calculations for shallow flaws indicated no differences between SIFIC for finite axial and circumferential flaws.

Tables 2–10 give the results of this study in terms of non-dimensionalized K_j^* values for axially and circumferentially oriented, inner-surface flaws in a cylinder, with surface length-to-depth ratios of 2:1, 6:1, and 10:1, and with t = 216 mm (including the cladding), R_i = 2184 mm, and ℓ = 4699 mm. Also, there are coefficients for two cladding thicknesses (t_{cl}), 6.35 mm and 3.96 mm. K_j^* values are obtained by computing K from J using a plane-strain relation, where K is the stress-intensity factor per unit stress applied to

the crack face and then dividing by $\sqrt{\pi a}$. While English units were utilized to compute the K_j^* values, the K_j^* values, which are nondimensionalized, in the tables are appropriate for any consistent set of units (English, SI, etc.).

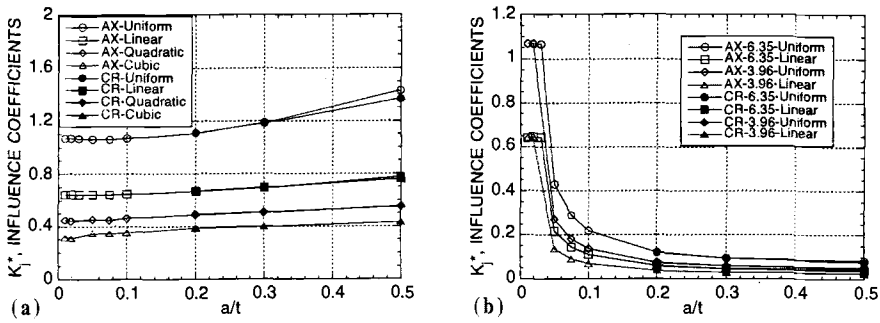


FIG. 6--Influence coefficients for semielliptical inner-surface flaws (2c/a = 10) at $\phi = 90°$: (a) four reference loads applied over crack face, and (b) uniform and linear load applied over portion of crack face within cladding.

TABLE 2--Influence coefficients for inside axial surface crack: a/t = 0.01.

Aspect Ratio	Elliptic Angle	K0 Uniform	K1 Linear	K2 Quadratic	K3 Cubic	K0 t_{cl}=6.35	K1 t_{cl}=6.35	K0 t_{cl}=3.96	K1 t_{cl}=3.96
2:1	0.00	0.764	0.153	0.061	0.034	0.764	0.153	0.764	0.153
	2.37	0.754	0.165	0.062	0.032	0.754	0.165	0.754	0.165
	16.6	0.690	0.192	0.079	0.040	0.690	0.192	0.690	0.192
	30.8	0.669	0.264	0.127	0.069	0.669	0.264	0.669	0.264
	45.0	0.660	0.335	0.196	0.124	0.660	0.335	0.660	0.335
	59.2	0.653	0.393	0.269	0.198	0.653	0.393	0.653	0.393
	73.4	0.651	0.434	0.329	0.268	0.651	0.434	0.651	0.434
	87.6	0.649	0.463	0.366	0.310	0.649	0.463	0.649	0.463
	90.0	0.649	0.468	0.372	0.317	0.649	0.468	0.649	0.468
6:1	0.00	0.670	0.134	0.048	0.024	0.670	0.134	0.670	0.134
	2.37	0.667	0.134	0.043	0.019	0.667	0.134	0.667	0.134
	16.6	0.654	0.170	0.055	0.009	0.654	0.170	0.654	0.170
	30.8	0.741	0.269	0.109	0.029	0.741	0.269	0.741	0.269
	45.0	0.827	0.381	0.199	0.100	0.827	0.381	0.827	0.381
	59.2	0.893	0.481	0.302	0.197	0.893	0.481	0.893	0.481
	73.4	0.938	0.559	0.389	0.290	0.938	0.559	0.938	0.559
	87.6	0.970	0.594	0.435	0.341	0.970	0.594	0.970	0.594
	90.0	0.975	0.601	0.443	0.350	0.975	0.601	0.975	0.601
10:1	0.00	0.515	0.090	0.020	0.006	0.515	0.090	0.515	0.090
	2.37	0.529	0.094	0.010	0.005	0.529	0.094	0.529	0.094
	16.6	0.610	0.146	0.033	0.005	0.610	0.146	0.610	0.146
	30.8	0.762	0.258	0.060	0.019	0.762	0.258	0.762	0.258
	45.0	0.889	0.389	0.171	0.066	0.889	0.389	0.889	0.389
	59.2	0.979	0.507	0.290	0.136	0.979	0.507	0.979	0.507
	73.4	1.033	0.593	0.389	0.249	1.033	0.593	1.033	0.593
	87.6	1.064	0.635	0.439	0.307	1.064	0.635	1.064	0.635
	90.0	1.069	0.642	0.447	0.316	1.069	0.642	1.069	0.642

TABLE 3--Influence coefficients for inside axial surface crack: a/t = 0.0184.

Aspect Ratio	Elliptic Angle	K0 Uniform	K1 Linear	K2 Quadratic	K3 Cubic	K0 t_{cl}=6.35	K1 t_{cl}=6.35	K0 t_{cl}=3.96	K1 t_{cl}=3.96
2:1	0.00	0.777	0.155	0.061	0.034	0.777	0.155	0.777	0.155
	2.37	0.767	0.167	0.062	0.032	0.767	0.167	0.767	0.167
	16.6	0.700	0.194	0.079	0.040	0.700	0.194	0.700	0.194
	30.8	0.677	0.266	0.127	0.069	0.677	0.266	0.677	0.266
	45.0	0.667	0.338	0.196	0.125	0.667	0.338	0.667	0.338
	59.2	0.660	0.397	0.270	0.198	0.660	0.397	0.660	0.397
	73.4	0.657	0.438	0.330	0.267	0.657	0.438	0.657	0.438
	87.6	0.654	0.467	0.366	0.310	0.654	0.467	0.654	0.467
	90.0	0.653	0.472	0.373	0.317	0.653	0.472	0.653	0.472
6:1	0.00	0.653	0.128	0.043	0.021	0.653	0.128	0.653	0.128
	2.37	0.654	0.128	0.038	0.016	0.654	0.128	0.654	0.128
	16.6	0.654	0.168	0.045	0.021	0.654	0.168	0.654	0.168
	30.8	0.758	0.271	0.099	0.026	0.758	0.271	0.758	0.271
	45.0	0.852	0.387	0.192	0.085	0.852	0.387	0.852	0.387
	59.2	0.920	0.492	0.298	0.187	0.920	0.492	0.920	0.492
	73.4	0.963	0.569	0.387	0.283	0.963	0.569	0.963	0.569
	87.6	0.994	0.609	0.434	0.335	0.994	0.609	0.994	0.609
	90.0	0.999	0.616	0.442	0.344	0.999	0.616	0.999	0.616
10:1	0.00	0.525	0.092	0.019	0.007	0.525	0.092	0.525	0.092
	2.37	0.538	0.096	0.009	0.005	0.538	0.096	0.538	0.096
	16.6	0.621	0.149	0.039	0.005	0.621	0.149	0.621	0.149
	30.8	0.777	0.262	0.050	0.022	0.777	0.262	0.777	0.262
	45.0	0.899	0.392	0.164	0.075	0.899	0.392	0.899	0.392
	59.2	0.982	0.509	0.283	0.127	0.982	0.509	0.982	0.509
	73.4	1.033	0.595	0.383	0.242	1.033	0.595	1.033	0.595
	87.6	1.063	0.637	0.433	0.300	1.063	0.637	1.063	0.637
	90.0	1.068	0.644	0.441	0.310	1.068	0.644	1.068	0.644

TABLE 4--Influence coefficients for inside axial surface crack: a/t = 0.05.

Aspect Ratio	Elliptic Angle	K0 Uniform	K1 Linear	K2 Quadratic	K3 Cubic	K0 t_{cl}=6.35	K1 t_{cl}=6.35	K0 t_{cl}=3.96	K1 t_{cl}=3.96
2:1	0.00	0.701	0.133	0.045	0.022	0.596	0.171	0.598	0.212
	31.0	0.681	0.276	0.131	0.070	0.615	0.278	0.238	0.119
	40.5	0.670	0.323	0.178	0.108	0.386	0.208	0.175	0.090
	50.0	0.663	0.367	0.231	0.158	0.268	0.147	0.146	0.075
	59.4	0.659	0.404	0.282	0.212	0.226	0.124	0.129	0.067
	68.9	0.654	0.432	0.325	0.263	0.206	0.112	0.119	0.062
	78.4	0.653	0.451	0.355	0.301	0.194	0.105	0.114	0.059
	87.9	0.651	0.472	0.379	0.327	0.186	0.101	0.108	0.056
	90.0	0.651	0.476	0.384	0.333	0.184	0.100	0.107	0.056
6:1	0.00	0.513	0.100	0.027	0.010	0.479	0.186	0.444	0.177
	31.0	0.764	0.275	0.100	0.022	0.700	0.346	0.336	0.166
	40.5	0.823	0.352	0.162	0.072	0.528	0.270	0.292	0.147
	50.0	0.875	0.429	0.235	0.137	0.445	0.232	0.271	0.137
	59.4	0.915	0.497	0.310	0.210	0.417	0.215	0.259	0.130
	68.9	0.944	0.551	0.375	0.279	0.400	0.205	0.251	0.126
	78.4	0.964	0.589	0.423	0.334	0.391	0.199	0.247	0.124
	87.9	0.984	0.611	0.449	0.363	0.384	0.195	0.243	0.122
	90.0	0.989	0.616	0.454	0.369	0.382	0.194	0.242	0.122
10:1	0.00	0.424	0.075	0.012	0.008	0.373	0.163	0.323	0.147
	31.0	0.781	0.261	0.044	0.016	0.713	0.345	0.372	0.182
	40.5	0.868	0.350	0.126	0.056	0.578	0.300	0.333	0.167
	50.0	0.932	0.437	0.211	0.082	0.501	0.258	0.309	0.155
	59.4	0.981	0.514	0.294	0.172	0.471	0.240	0.293	0.147
	68.9	1.017	0.575	0.367	0.251	0.450	0.229	0.283	0.142
	78.4	1.040	0.617	0.419	0.311	0.440	0.222	0.278	0.139
	87.9	1.057	0.639	0.446	0.341	0.431	0.217	0.272	0.136
	90.0	1.061	0.644	0.452	0.347	0.430	0.216	0.271	0.136

TABLE 5--Influence coefficients for inside axial surface crack: a/t = 0.075.

Aspect Ratio	Elliptic Angle	K0 Uniform	K1 Linear	K2 Quadratic	K3 Cubic	K0 t_{cl}=6.35	K1 t_{cl}=6.35	K0 t_{cl}=3.96	K1 t_{cl}=3.96
2:1	0.00	0.697	0.134	0.045	0.022	0.604	0.210	0.511	0.204
	32.3	0.683	0.284	0.137	0.075	0.250	0.127	0.138	0.063
	41.6	0.673	0.331	0.185	0.114	0.187	0.096	0.108	0.054
	50.9	0.666	0.373	0.236	0.163	0.157	0.081	0.092	0.047
	60.1	0.662	0.409	0.286	0.217	0.139	0.073	0.083	0.042
	69.4	0.657	0.436	0.327	0.266	0.129	0.067	0.076	0.039
	78.6	0.656	0.454	0.356	0.303	0.123	0.064	0.073	0.037
	87.9	0.654	0.474	0.379	0.328	0.118	0.061	0.070	0.036
	90.0	0.654	0.478	0.384	0.334	0.116	0.060	0.069	0.035
6:1	0.00	0.499	0.099	0.026	0.009	0.436	0.171	0.357	0.162
	32.3	0.772	0.285	0.102	0.018	0.356	0.177	0.208	0.099
	41.6	0.829	0.360	0.164	0.073	0.311	0.157	0.188	0.093
	50.9	0.878	0.434	0.237	0.138	0.289	0.146	0.177	0.089
	60.1	0.916	0.499	0.309	0.210	0.276	0.139	0.170	0.085
	69.4	0.943	0.551	0.372	0.278	0.268	0.135	0.166	0.083
	78.6	0.963	0.587	0.418	0.330	0.264	0.133	0.163	0.082
	87.9	0.982	0.609	0.443	0.358	0.266	0.134	0.165	0.082
	90.0	0.986	0.614	0.448	0.365	0.267	0.134	0.165	0.082
10:1	0.00	0.368	0.077	0.011	0.010	0.312	0.141	0.231	0.127
	32.3	0.796	0.276	0.049	0.025	0.394	0.195	0.234	0.112
	41.6	0.878	0.363	0.131	0.053	0.353	0.178	0.216	0.107
	50.9	0.939	0.447	0.215	0.089	0.328	0.165	0.203	0.101
	60.1	0.985	0.520	0.296	0.176	0.312	0.157	0.194	0.097
	69.4	1.018	0.578	0.365	0.252	0.302	0.152	0.188	0.094
	78.6	1.039	0.618	0.415	0.310	0.296	0.149	0.184	0.092
	87.9	1.056	0.639	0.441	0.339	0.291	0.146	0.181	0.090
	90.0	1.060	0.644	0.447	0.345	0.289	0.145	0.180	0.090

TABLE 6--Influence coefficients for inside axial surface crack: a/t = 0.1.

Aspect Ratio	Elliptic Angle	K0 Uniform	K1 Linear	K2 Quadratic	K3 Cubic	K0 t_{cl}=6.35	K1 t_{cl}=6.35	K0 t_{cl}=3.96	K1 t_{cl}=3.96
2:1	0.00	0.715	0.133	0.046	0.023	0.576	0.217	0.486	0.211
	27.2	0.687	0.256	0.116	0.060	0.206	0.102	0.116	0.052
	37.3	0.676	0.308	0.164	0.095	0.146	0.074	0.087	0.042
	47.4	0.669	0.357	0.220	0.145	0.119	0.061	0.072	0.036
	57.5	0.663	0.399	0.275	0.203	0.104	0.053	0.063	0.032
	67.7	0.659	0.431	0.323	0.258	0.095	0.049	0.057	0.029
	77.8	0.657	0.452	0.357	0.301	0.090	0.046	0.055	0.028
	87.9	0.655	0.474	0.383	0.329	0.086	0.044	0.052	0.026
	90.0	0.655	0.479	0.388	0.335	0.085	0.043	0.051	0.026
6:1	0.00	0.553	0.095	0.027	0.011	0.457	0.179	0.380	0.170
	27.2	0.741	0.242	0.084	0.011	0.278	0.137	0.164	0.079
	37.3	0.811	0.324	0.144	0.053	0.240	0.120	0.147	0.073
	47.4	0.869	0.407	0.220	0.118	0.221	0.111	0.136	0.068
	57.5	0.915	0.483	0.299	0.194	0.210	0.105	0.130	0.065
	67.7	0.948	0.544	0.371	0.270	0.203	0.102	0.126	0.063
	77.8	0.971	0.586	0.424	0.330	0.199	0.100	0.124	0.062
	87.9	0.991	0.610	0.453	0.362	0.196	0.098	0.122	0.061
	90.0	0.996	0.615	0.459	0.369	0.195	0.098	0.121	0.061
10:1	0.00	0.417	0.071	0.013	0.006	0.352	0.156	0.286	0.144
	27.2	0.752	0.228	0.041	0.017	0.310	0.151	0.186	0.089
	37.3	0.849	0.321	0.116	0.057	0.274	0.137	0.169	0.084
	47.4	0.922	0.415	0.202	0.067	0.252	0.126	0.157	0.078
	57.5	0.979	0.500	0.290	0.162	0.239	0.119	0.149	0.074
	67.7	1.020	0.569	0.370	0.247	0.230	0.115	0.143	0.072
	77.8	1.046	0.616	0.428	0.313	0.225	0.113	0.140	0.070
	87.9	1.065	0.640	0.457	0.346	0.220	0.110	0.137	0.069
	90.0	1.068	0.645	0.463	0.353	0.219	0.110	0.137	0.068

TABLE 7--Influence coefficients for inside axial surface crack: a/t = 0.2.

Aspect Ratio	Elliptic Angle	K0 Uniform	K1 Linear	K2 Quadratic	K3 Cubic	K0 t_{cl}=6.35	K1 t_{cl}=6.35	K0 t_{cl}=3.96	K1 t_{cl}=3.96
2:1	0.00	0.723	0.127	0.046	0.025	0.471	0.204	0.391	0.195
	19.8	0.695	0.214	0.089	0.044	0.130	0.063	0.071	0.031
	31.1	0.679	0.273	0.133	0.073	0.080	0.039	0.048	0.023
	42.5	0.671	0.332	0.192	0.120	0.061	0.031	0.038	0.019
	53.8	0.665	0.383	0.255	0.182	0.052	0.026	0.032	0.016
	65.2	0.660	0.423	0.312	0.245	0.047	0.023	0.029	0.014
	76.5	0.658	0.450	0.354	0.296	0.044	0.022	0.027	0.014
	87.9	0.656	0.475	0.384	0.329	0.041	0.021	0.025	0.013
	90.0	0.656	0.479	0.389	0.335	0.040	0.020	0.025	0.013
6:1	0.00	0.625	0.101	0.034	0.017	0.423	0.189	0.354	0.179
	19.8	0.699	0.194	0.066	0.019	0.157	0.074	0.093	0.043
	31.1	0.781	0.280	0.118	0.045	0.127	0.063	0.079	0.039
	42.5	0.856	0.375	0.195	0.101	0.116	0.058	0.072	0.036
	53.8	0.915	0.464	0.283	0.180	0.110	0.055	0.069	0.034
	65.2	0.958	0.538	0.366	0.265	0.106	0.053	0.066	0.033
	76.5	0.986	0.590	0.430	0.336	0.104	0.052	0.065	0.032
	87.9	1.010	0.619	0.464	0.373	0.102	0.051	0.064	0.032
	90.0	1.014	0.624	0.470	0.380	0.102	0.051	0.063	0.032
10:1	0.00	0.506	0.077	0.022	0.009	0.368	0.180	0.314	0.164
	19.8	0.694	0.183	0.050	0.025	0.174	0.078	0.106	0.050
	31.1	0.815	0.280	0.107	0.011	0.149	0.073	0.093	0.046
	42.5	0.915	0.387	0.190	0.083	0.137	0.068	0.085	0.043
	53.8	0.991	0.488	0.287	0.170	0.130	0.065	0.081	0.040
	65.2	1.045	0.572	0.379	0.263	0.125	0.062	0.078	0.039
	76.5	1.080	0.631	0.449	0.340	0.122	0.061	0.077	0.038
	87.9	1.103	0.660	0.483	0.378	0.120	0.060	0.075	0.037
	90.0	1.107	0.666	0.490	0.385	0.120	0.060	0.075	0.037

TABLE 8--Influence coefficients for inside axial surface crack: a/t = 0.3.

Aspect Ratio	Elliptic Angle	K0 Uniform	K1 Linear	K2 Quadratic	K3 Cubic	K0 t_{cl}=6.35	K1 t_{cl}=6.35	K0 t_{cl}=3.96	K1 t_{cl}=3.96
2:1	0.00	0.723	0.127	0.048	0.026	0.404	0.188	0.334	0.176
	17.4	0.708	0.203	0.083	0.042	0.102	0.049	0.056	0.025
	29.1	0.690	0.264	0.126	0.068	0.058	0.028	0.034	0.016
	40.9	0.680	0.326	0.185	0.114	0.043	0.021	0.026	0.013
	52.6	0.673	0.381	0.251	0.177	0.036	0.018	0.022	0.011
	64.4	0.668	0.423	0.310	0.242	0.032	0.016	0.020	0.010
	76.1	0.665	0.452	0.355	0.297	0.030	0.015	0.018	0.009
	87.9	0.662	0.478	0.385	0.331	0.028	0.014	0.017	0.009
	90.0	0.662	0.482	0.391	0.337	0.027	0.014	0.017	0.009
6:1	0.00	0.665	0.112	0.041	0.022	0.380	0.181	0.315	0.167
	17.4	0.715	0.190	0.068	0.027	0.117	0.054	0.069	0.032
	29.1	0.804	0.277	0.118	0.051	0.093	0.045	0.057	0.028
	40.9	0.886	0.376	0.194	0.104	0.085	0.042	0.053	0.026
	52.6	0.951	0.470	0.284	0.182	0.081	0.040	0.050	0.025
	64.4	0.998	0.549	0.372	0.270	0.078	0.039	0.049	0.024
	76.1	1.028	0.605	0.439	0.345	0.077	0.038	0.048	0.024
	87.9	1.053	0.635	0.475	0.384	0.075	0.038	0.047	0.024
	90.0	1.058	0.640	0.481	0.391	0.075	0.037	0.047	0.023
10:1	0.00	0.562	0.085	0.029	0.014	0.344	0.168	0.290	0.153
	17.4	0.707	0.176	0.052	0.016	0.128	0.059	0.078	0.037
	29.1	0.848	0.276	0.104	0.016	0.110	0.054	0.068	0.034
	40.9	0.962	0.389	0.188	0.082	0.102	0.051	0.064	0.032
	52.6	1.051	0.498	0.288	0.169	0.098	0.049	0.062	0.031
	64.4	1.115	0.590	0.385	0.265	0.096	0.048	0.060	0.030
	76.1	1.157	0.653	0.460	0.346	0.095	0.047	0.060	0.030
	87.9	1.183	0.685	0.496	0.387	0.094	0.047	0.059	0.029
	90.0	1.187	0.691	0.503	0.394	0.094	0.047	0.059	0.029

TABLE 9--Influence coefficients for inside axial surface crack: a/t = 0.5.

Aspect Ratio	Elliptic Angle	K0 Uniform	K1 Linear	K2 Quadratic	K3 Cubic	K0 t_{cl}=6.35	K1 t_{cl}=6.35	K0 t_{cl}=3.96	K1 t_{cl}=3.96
2:1	0.00	0.736	0.132	0.053	0.029	0.327	0.162	0.272	0.150
	15.4	0.746	0.203	0.083	0.043	0.079	0.037	0.045	0.020
	27.5	0.719	0.263	0.124	0.067	0.042	0.020	0.025	0.012
	39.6	0.704	0.327	0.183	0.112	0.029	0.014	0.018	0.009
	51.7	0.693	0.383	0.249	0.175	0.023	0.012	0.015	0.007
	63.7	0.685	0.426	0.311	0.242	0.021	0.010	0.013	0.006
	75.8	0.681	0.456	0.357	0.299	0.019	0.009	0.012	0.006
	87.9	0.676	0.483	0.389	0.334	0.018	0.009	0.011	0.006
	90.0	0.676	0.488	0.395	0.340	0.017	0.009	0.011	0.005
6:1	0.00	0.758	0.142	0.059	0.033	0.322	0.163	0.268	0.149
	15.4	0.814	0.213	0.083	0.040	0.091	0.041	0.054	0.025
	27.5	0.908	0.302	0.132	0.065	0.070	0.034	0.043	0.021
	39.6	0.998	0.405	0.208	0.116	0.065	0.032	0.040	0.020
	51.7	1.069	0.504	0.300	0.195	0.062	0.031	0.039	0.019
	63.7	1.120	0.588	0.392	0.285	0.061	0.030	0.038	0.019
	75.8	1.153	0.647	0.463	0.363	0.060	0.030	0.038	0.019
	87.9	1.182	0.679	0.500	0.404	0.059	0.029	0.037	0.018
	90.0	1.187	0.685	0.506	0.411	0.059	0.029	0.037	0.018
10:1	0.00	0.666	0.119	0.049	0.028	0.302	0.156	0.254	0.140
	15.4	0.822	0.208	0.077	0.033	0.097	0.044	0.060	0.028
	27.5	0.995	0.316	0.131	0.056	0.086	0.042	0.054	0.027
	39.6	1.138	0.440	0.216	0.112	0.083	0.041	0.052	0.026
	51.7	1.251	0.560	0.321	0.198	0.083	0.041	0.052	0.026
	63.7	1.335	0.662	0.425	0.298	0.083	0.041	0.052	0.026
	75.8	1.390	0.734	0.506	0.383	0.083	0.041	0.052	0.026
	87.9	1.423	0.770	0.546	0.427	0.083	0.041	0.052	0.026
	90.0	1.429	0.776	0.553	0.434	0.083	0.041	0.052	0.026

TABLE 10--Influence coefficients for inside circumferential surface crack: a/t = 0.5.

Aspect Ratio	Elliptic Angle	K0 Uniform	K1 Linear	K2 Quadratic	K3 Cubic	K0 t_{cl}=6.35	K1 t_{cl}=6.35	K0 t_{cl}=3.96	K1 t_{cl}=3.96
2:1	0.00	0.741	0.134	0.054	0.030	0.324	0.162	0.269	0.151
	15.4	0.750	0.205	0.084	0.044	0.079	0.038	0.045	0.020
	27.5	0.721	0.264	0.124	0.067	0.042	0.020	0.025	0.012
	39.6	0.706	0.328	0.183	0.112	0.029	0.014	0.018	0.009
	51.7	0.698	0.384	0.250	0.175	0.024	0.012	0.015	0.007
	63.7	0.692	0.430	0.312	0.243	0.021	0.010	0.013	0.007
	75.8	0.686	0.461	0.360	0.301	0.019	0.010	0.012	0.006
	87.9	0.682	0.488	0.392	0.336	0.020	0.010	0.012	0.006
	90.0	0.682	0.493	0.398	0.343	0.020	0.009	0.013	0.006
6:1	0.00	0.727	0.132	0.053	0.030	0.315	0.161	0.262	0.147
	15.4	0.786	0.205	0.079	0.037	0.087	0.039	0.052	0.024
	27.5	0.882	0.295	0.128	0.062	0.067	0.032	0.041	0.020
	39.6	0.974	0.398	0.205	0.114	0.062	0.031	0.038	0.019
	51.7	1.049	0.499	0.298	0.193	0.060	0.030	0.037	0.019
	63.7	1.103	0.584	0.390	0.284	0.058	0.029	0.036	0.018
	75.8	1.138	0.644	0.462	0.362	0.057	0.029	0.036	0.018
	87.9	1.166	0.676	0.499	0.403	0.058	0.029	0.036	0.018
	90.0	1.171	0.682	0.506	0.410	0.058	0.029	0.036	0.018
10:1	0.00	0.616	0.101	0.040	0.023	0.291	0.152	0.247	0.138
	15.4	0.770	0.195	0.071	0.028	0.090	0.039	0.055	0.026
	27.5	0.936	0.301	0.125	0.053	0.078	0.038	0.049	0.024
	39.6	1.076	0.424	0.211	0.109	0.075	0.037	0.047	0.024
	51.7	1.190	0.544	0.315	0.196	0.075	0.037	0.047	0.023
	63.7	1.275	0.647	0.420	0.295	0.075	0.037	0.047	0.023
	75.8	1.330	0.719	0.501	0.381	0.075	0.037	0.047	0.023
	87.9	1.363	0.755	0.542	0.425	0.075	0.037	0.047	0.024
	90.0	1.368	0.762	0.549	0.433	0.075	0.037	0.047	0.024

COMPARISON WITH OTHER INVESTIGATORS

A comparison of some of the 3-D influence coefficients generated in this study with similar coefficients obtained by other investigators [3,4] is shown in Figs. 7–9. To compare the coefficients with those obtained from Raju and Newman [3], the influence coefficients in Figs. 7 and 8 represent K_j^* values multiplied by $\sqrt{Q}$, where the shape factor (Q) is the square of the complete elliptic integral of the second kind. The shape factor for an elliptical crack is approximated by the following equation:

$$Q = 1 + 1.464\,(a/c)^{1.65} \quad . \tag{4}$$

As indicated in Figs. 7 and 8, the coefficients being compared pertain to axially oriented, inner-surface flaws in a long cylinder with a/t = 0.2 and 0.5 and aspect ratios of 2:1 and 10:1.

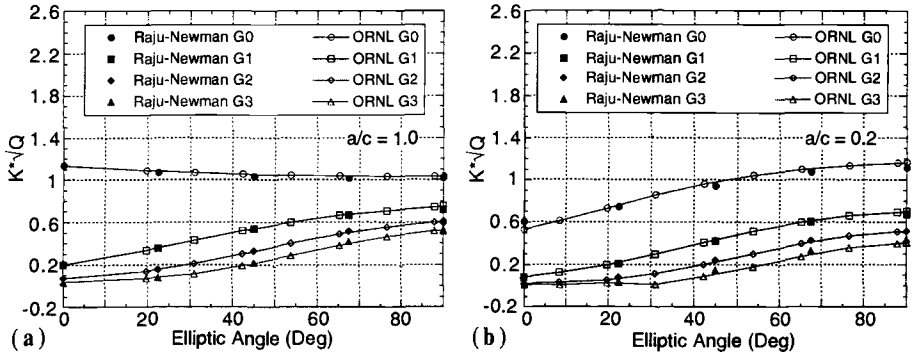


FIG. 7--Influence coefficients for axially oriented semielliptical flaws (a/t = 0.2) on inner surface of cylinder: (a) 2:1 aspect ratio; (b) 10:1 aspect ratio

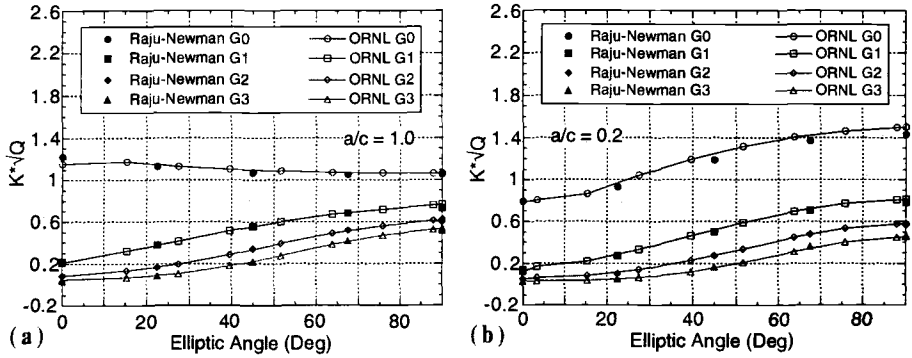


FIG. 8--Influence coefficients for axially oriented semielliptical flaws (a/t = 0.5) on inner surface of cylinder: (a) 2:1 aspect ratio; (b) 10:1 aspect ratio.

The coefficients in Fig. 9 (Ref. 4) are K_j^* values for an aspect ratio of 6:1 and a/t = 0.5. The results of all the comparisons indicate good agreement. The other investigators [3,4] did not publish SIFICs for the shallower flaw depths so a comparison could not be made for a/t ratios less than 0.2.

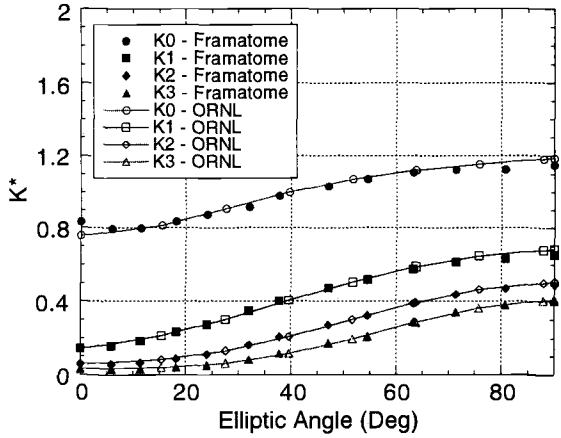


FIG. 9--Influence coefficients for an axially oriented semielliptical flaw with a/t = 0.5 and 6:1 aspect ratio.

SUMMARY AND CONCLUSIONS

The results of the present study show that there are essentially no differences in SIFICs for finite inner-surface axial and finite inner-surface circumferential flaws having flaw depths ($0.01 \le a/t \le 0.5$) and flaw aspect ratios ($2c/a = 2, 6, 10$). This important finding implies that SIFICs for axial flaws can be used for circumferential flaws as deep as halfway through the vessel wall with very little error provided that $2c/a \le 10$. As might be expected, the greatest difference (~5%) between the two is obtained for flaw geometries with an $a/t = 0.5$ and $2c/a = 10$. For implementation into fracture mechanics codes, it is recommended that SIFICs calculated for axial flaws be used for circumferential flaws having an $a/t < 0.5$ and $2c/a \le 10$. The SIFICs given in Table 10 should be utilized for circumferential flaws having an $a/t = 0.5$.

ACKNOWLEDGMENTS

Research sponsored by the Office of Nuclear Regulatory Research, U.S. Nuclear Regulatory Commission under Interagency Agreement 1886-8011-9B with the U.S. Department of Energy under Contract DE-AC05-84OR21400 with Martin Marietta Energy Systems, Inc.

The submitted manuscript has been authored by a contractor of the U.S. Government No. DE-AC05-84OR21400. Accordingly, the U.S. Government retains a nonexclusive, royalty-free license to publish or reproduce the published form of this contribution, or allow others to do so, for U.S. Government purposes.

REFERENCES

[1] DeLorenzi, H. G., "3-D Elastic-Plastic Fracture Analysis with ADINA," *Computers and Structures* , Vol. 13, 1981, pp. 613–621.

[2] Bass, B. R. and Bryson, J. W., "Applications of Energy Release Rate Techniques to Part-Through Cracks in Experimental Pressure Vessels," *J. Pressure Vessel Tech.*, Vol. 104, November 1982, pp. 308–316.

[3] Raju, I. S. and Newman, J. C., Jr., "Stress-Intensity Factor Influence Coefficients For Internal and External Surface Cracks in Cylindrical Vessels," *Aspects of Fracture Mechanics in Pressure Vessels and Piping, ASME Pub. PVP* , Vol. 58, American Society of Mechanical Engineers, 1982, pp. 37-48.

[4] Lance,C., Robisson, F., and Pellissier-Tanon, A., "Influence of Cladding on the Values of K_I for Emerging Defects in the Vessel Beltline," Framatome (1981), ORNL-TR-4960, Oak Ridge National Laboratory, Oak Ridge, TN, February 1983.

[5] Ball, D. G., Bass, B. R., Bryson, J. W., Cheverton, R. D., and Drake, J. B., "Stress-Intensity-Factor Influence Coefficients for Surface Flaws in Pressure Vessels," USNRC Report NUREG/CR-3723 (ORNL/CSD/TM-216), U. S. Nuclear Regulatory Commission, Washington DC, February 1985.

[6] Dickson, T. L., "FAVOR: A New Fracture Mechanics Code for Reactor Pressure Vessels Subjected to Pressurized Thermal Shock," *Pressure Vessel Integrity, ASME Pub. PVP,* Vol. 250, American Society of Mechanical Engineers, 1993, pp. 3-10.

[7] Bueckner, H. F., "A Novel Principle for the Computation of Stress Intensity Factors," *Z. angew. Math. Mech.*,Vol. 50, 1970, pp. 529–546.

[8] *ABAQUS Theory Manual, Version 5.2*, Hibbit, Karlson and Sorensen, Inc., Providence, RI, 1992.

[9] Bass, B. R. and Bryson, J. W., "Applications of Energy Release Rate Techniques to Part-Through Cracks in Plates and Cylinders, Volume 1, ORMGEN-3D: A Finite Element Mesh Generator for 3-Dimensional Crack Geometries," USNRC Report NUREG/CR-2997/V1 (ORNL/TM-8527), December 1982.

[10] Timoshenko, S., *Theory of Plates and Shells*, McGraw-Hill, New York, 1940.

[11] Bishop, B. A., Dickson, T. L., and Simonen, F. A., "Benchmarking of Probabilistic Fracture Mechanics Analyses of Reactor Vessels Subjected to Pressurized Thermal Shock (PTS) Loading," Electric Power Research Institute, Research Project 2975-5, Final Report, July 1993.

[12] Cheverton, R. D., "Thermal Shock Studies Associated with Injection of Emergency Core Coolant Following a Loss-of-Coolant Accident in PWRs, " *Nuclear Safety,* Vol. 19, No. 1, January-February 1978.

[13] Bryson, J. W. and Dickson, T. L., "Stress-Intensity-Factor Influence Coefficients for Axial and Circumferential Flaws in Reactor Pressure Vessels, "*Pressure Vessel Integrity, ASME Pub. PVP-*, Vol. 250, American Society of Mechanical Engineers, 1993, pp. 77-87.

Engineered Materials

Y.MUTOH[1]

EVALUATION AND SIGNIFICANCE OF FRACTURE TOUGHNESS IN CERAMIC MATERIALS

REFERENCE: Mutoh, Y., **"Evaluation and Significance of Fracture Toughness in Ceramic Materials,"** Fracture Mechanics: 26th Volume, ASTM STP 1256, Walter G. Reuter, John H. Underwood, and James C. Newman, Jr., Eds., American Society for Testing and Materials, Philadelphia, 1995.

ABSTRACT: Fracture toughness tests of several ceramic materials were carried out according to the various test methods, that is the Bridge indentation(BI,SEPB), Fatigue precrack(FP), Controlled surface flaw(CSF), Chevron notch(CN) and Indentation fracture(IF) methods. Mutual comparison of the test results was made to discuss the validity and applicability of the each test method. Significance of the apparent fracture toughness with stable crack growth was discussed. The intrinsic fracture toughness can be obtained by the CSF method, in which a small surface crack is used. At high temperatures, since nonlinear deformation due to softening of glass phase and stable crack growth occur, nonlinear fracture mechanics approach should be applied. J_{Ic}-value is successfully evaluated according to the R-curve method.

KEYWORDS: fracture toughness, test method, ceramics, stable crack growth, high temperature, R-curve

It is considered that a combination of pre-existing flaw size and fracture toughness determines fracture strength of ceramic materials. Therefore, the basic material parameter for referring fracture and strength properties of materials

[1]Professor, Department of Mechanical Engineering, Nagaoka University of Technology, Nagaoka-shi 940-21, Japan

Copyright© 1995 by ASTM International www.astm.org

may be the fracture toughness rather than the fracture strength for a brittle material such as ceramics. Many test methods for evaluating fracture toughness of ceramic materials have been proposed. Some problems on the test methods proposed have been pointed out: fracture toughness values obtained by various test methods are not consistent [1,2], and applicability of the test method is dependent on material [1]. A test method for evaluating fracture toughness of ceramic materials is not always well established at this moment. Furthermore, although ceramic materials are candidate materials for high temperature structural components, a test method for evaluating high temperature fracture toughness has not yet been developed.

In the present paper, applicability and problems of each fracture toughness test method are discussed based on the fracture toughness test results of several ceramic materials. Some ceramic materials exhibit stable crack growth before unstable fracture in fracture toughness tests. Significance of apparent high fracture toughness due to the increasing R-curve with stable crack growth is also discussed from the view point of structural design. Furthermore, the test method for evaluating high temperature fracture toughness is discussed based on fracture toughness test results at elevated temperatures.

METHODS FOR EVALUATING FRACTURE TOUGHNESS

Many test methods exist for evaluating fracture toughness proposed. Several typical test methods, that is the SEPB (Single edge precracked beam) method [3] (based on the BI (Bridge indentation) method [4]), the FP (Fatigue precrack) method [1,5], the CSF (Controlled surface flaw) method [6], the CN (Chevron notch) method [7,8], and the IF (Indentation fracture) method [9,10] are outlined in this section. Details of these test methods have been reported in Ref.[1]. Subsequently, mutual comparison of the test results according to these test methods for several ceramic materials are made to understand problems and applicability of the each test method.

BI(SEPB) method: The SEPB method[3] is basically after the BI method proposed by Sadahiro and Takatsu [4]. A specimen between the grooved lower anvil and the upper punch is pressed to initiate a through-thickness brittle sharp precrack, as shown in Fig. 1. Crack-starter flaws on the center line of the specimen are introduced by the indentation method. The precrack length can be controlled by adjusting the groove width of the lower anvil.

FP method: A fatigue precrack is introduced at the tip of the BI precrack. The value of K_{fmax} for fatigue precracking is controlled to be lower than $0.6K_{IC}$ according to the ASTM Standard E399, while in the BI(SEPB) method the K-value at precracking is almost equal to K_{IC} or K_a values.

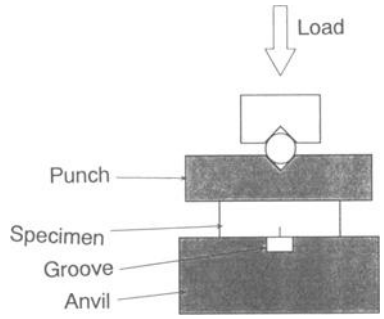


FIG. 1--The BI method (The SEPB method).

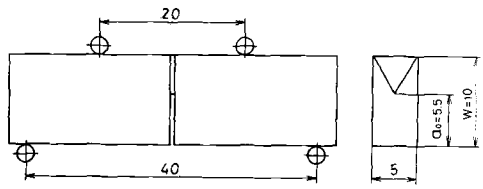


FIG. 2--Chevron notch specimen in the CN method(unit:mm).

CSF method: A surface precrack is introduced in the center of the specimen by the indentation method. Since a residual compressive stress is induced around the surface precrack, it is of importance to remove it by a surface grinding or annealing techniques. After fracture toughness test, the geometry and sizes of the surface precrack are measured on the fracture surface to calculate a fracture toughness value using the Newman-Raju equation [11].

CN method: A chevron notch is machined into a specimen, as shown in Fig. 2. The narrow notch is required to induce slow crack growth from the notch tip. Unstable fracture occurs at a certain stable crack extension, which is dependent only on the specimen geometry. The fracture toughness can be estimated using the measured fracture load according to the method proposed Munz et al [8]. The following two requirements should be satisfied: ① slow crack growth occurs before unstable fracture, and ② a resistance curve for slow crack growth is flat. (An increasing R-curve gives a different unstable fracture point from the minimum compliance point of the specimen.)

TABLE 1--Composition of original powder materials (wt%).

	Si_3N_4	SiC	ZrO_2	Al_2O_3	TiB_2	AlN	Y_2O_3	B_4C
Si_3N_4-A	88	---	---	---	---	4	8	---
Si_3N_4-B	93	---	---	2	---	---	5	---
SiC	---	97	---	---	---	---	---	---
TiB_2	---	---	---	---	80	---	---	20
ZrO_2	---	---	95	---	---	---	5	---
Al_2O_3	---	---	---	99.5	---	---	---	---

TABLE 2--Mechanical properties of the materials used.

	E(GPa)	σ_f(MPa)	Hv(GPa)	ρ(Mg/m^3)
Si_3N_4-A	320	912	15.6	3.27
Si_3N_4-B	318	1120	15.1	3.25
SiC	402	490	24.5	3.13
ZrO_2	206	845	12.6	6.07
Al_2O_3	343	294	15.7	3.90
TiB_2	530	834	28.0	4.60

IF method: A fracture toughness value is evaluated using the measured length of indented flaw and the indentation load according to the semi-empirical equation proposed in [12,13,14,15]. The K_{IC}-estimating equations proposed depend on the geometry of indented flaw, such as the median crack, the Palmqvist crack, etc. The specimen surface needs to be finely polished to remove residual stress and to aid in measuring the crack length.

The test methods mentioned above were applied to several ceramic materials; compositions and mechanical properties are listed in Tables 1 and 2, respectively. Dimensions of the specimens for the BI(SEPB), FP and CN methods are $5\times10\times55$ (mm). The precrack length to width ratios a/W for BI(SEPB) and FP specimens are in the range of 0.4~0.6 and the span length of three-point bending is 40mm. In the FP method, a fatigue precrack was introduced at a K_{fmax} level less than $0.6K_{IC}$ for Si_3N_4, ZrO_2 and Al_2O_3. For SiC and TiB_2, since the threshold value for crack growth K_{th} was higher than $0.6K_{IC}$[16], a fatigue precrack was introduced at $K_{fmax} = 0.8K_{IC}$. From Ref.[16], where the same materials were used, the ratios of K_{th} and K_{IC} were as follows; Si_3N_4-A: 0.39, Si_3N_4-B: 0.44, SiC: 0.63, ZrO_2: 0.26, Al_2O_3: 0.49 and TiB_2: 0.74.Dimensions of

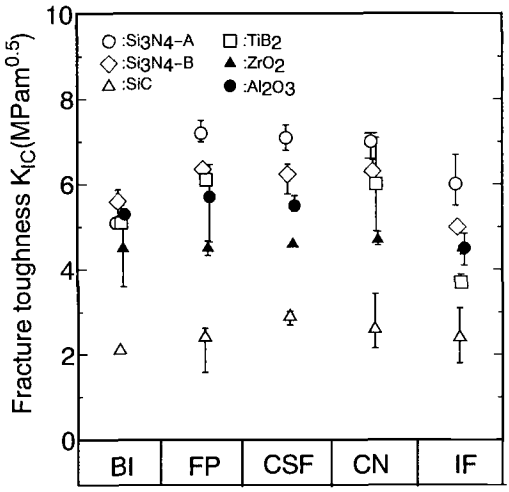


FIG. 3--K_{IC}-values obtained by various test methods.

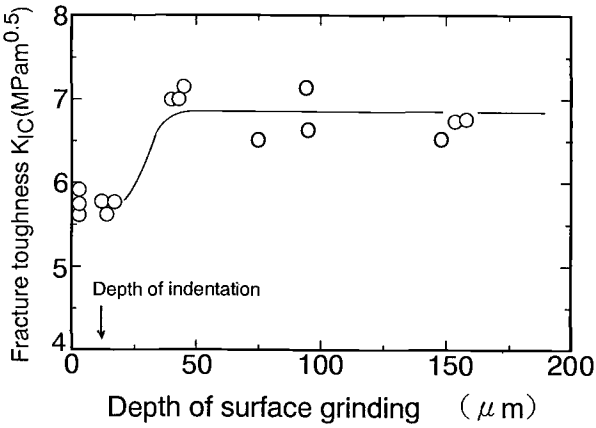


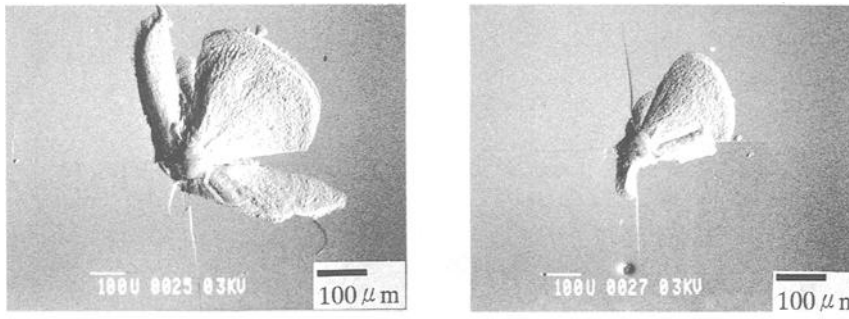
FIG. 4--Relationship between ground depth and K_{IC} (Si_3N_4-A).

the CSF specimen are 4×3×35(mm) and the span length for three-point bending is 30mm.

Figure 3 shows the test results. The data points represent the average values of 3~5 specimens. No significant stable crack growth was observed for the BI(SEPB), FP, CSF and CN methods in all the materials used. The fracture toughness values obtained according to the FP, CSF and CN methods almost coincide with each other. The fracture toughness value by the BI(SEPB) method tends to be lower than those obtained by the FP, CSF and CN methods, except for some materials, such as ZrO_2. The lower K_{Ic} value obtained by the BI(SEPB) method will be caused by the microcracking at the tip of the precrack[17], which results from the introduction of the precrack at a K-level as high as K_{Ic}.

Based on the fatigue crack growth test results of ceramic materials, stress shielding effect due to bridging and interfriction by asperity contact is developed during crack extension [16]. The stress shielding effect increases apparent K-value. Therefore, in the FP method, a short fatigue-precrack less than 2mm is desirable to avoid the stress shielding effect on K_{Ic}-value based on the experience of fatigue crack growth tests.

In the CSF method, the annealing used for removing residual stress induced by the indentation often gives crack healing. Surface grinding and subsequent polishing is recommended for removing residual stress. Figure 4 shows the relationship between grinding depth and K_{Ic}-value for Si_3N_4-A. The residual stress can be removed by grinding up to 4 times of the indentation depth. Similar results for grinding depth to remove residual stress have been reported[6].



(a) Si_3N_4 (b) TiB_2

FIG. 5--Decohesion of indented surface layer in the IF method.

The fracture toughness value obtained by the IF method is not in good agreement with those obtained by the other fracture mechanics-based methods. It is better to understand that the K_{Ic}-value obtained by the IF method gives a reference value of fracture toughness similar to the case of the Charpy impact energy in metallic materials. Another problem with the IF method is found in some materials, such as SiC and TiB_2, where decohesion of indented surface layer occurs, as shown in Fig. 5.

SIGNIFICANCE OF FRACTURE TOUGHNESS WITH STABLE CRACK GROWTH

The relationship between fracture toughness and grain size for Si_3N_4 is shown in Fig. 6. The materials used were basically the same as Si_3N_4-B, but the sintering conditions were varied The fracture toughness values obtained by the FP and SEPB methods increase with increasing grain size, while those obtained by the CSF method are almost constant regardless of grain size.

The relationship for alumina is shown in Fig. 7. The alumina specimens with various grain sizes were produced using the same high purity (99.9%) and fine grain (0.23μm) active starting powders under various sintering conditions. The fracture toughness values obtained by the FP method

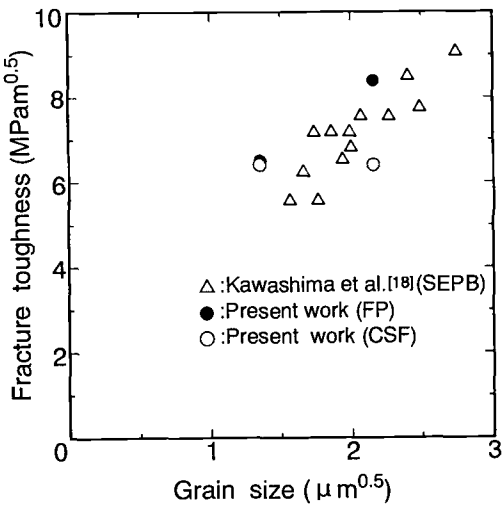


FIG. 6--Relationship between grain size and fracture toughness for Si_3N_4-B.

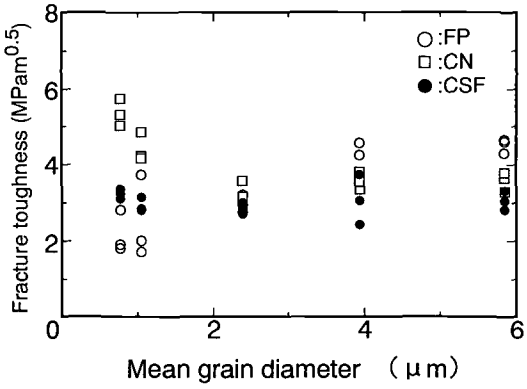


FIG. 7--Relationship between grain diameter and fracture toughness for Alumina.

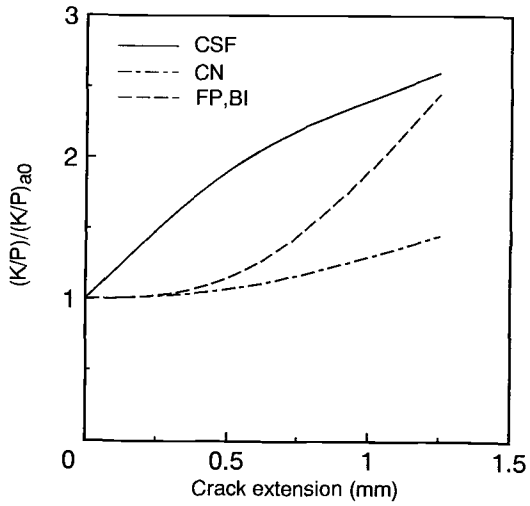


FIG. 8--Variation of K-value with crack extension.

increase with increasing grain size, while those obtained by the CSF method are almost constant regardless of grain size, similar to the case of Si_3N_4. The fracture toughness values obtained by the CN method are significantly high in the small grain size region, where no stable crack growth is observed and then the K_{IC}-values obtained are not valid. A narrower notch is required to initiate slow crack growth for finer grain materials. With increasing grain size, the K_{IC}-value increases in the large grain size region.

The R-curve behavior with stable crack growth in ceramic materials is known. Vekinis-et al. [19] reported that the R-curve behavior, which increases the apparent fracture toughness, is significant in larger grain sizes. From the detailed observations of crack path and fracture surface, the stable crack growth was observed for the specimens with large grain size in the FP and CN methods, while no significant stable crack growth was found in the CSF method. The specimen geometry dependence of stable crack growth can be understood based on the variation of K with crack extension, as shown in Fig. 8. The change in K is not significant for the specimens with a long through-thickness crack (in the BI(SEPB) and FP methods) compared to the specimen with a small surface crack (in the CSF method). From the foregoing discussion, the CSF method may be recommended for evaluating the intrinsic fracture toughness without stable crack growth, and the intrinsic fracture toughness growth is independent of grain size in the range of the present work, as shown in Figs. 6 and 7. Figure 3 indicates that the fracture toughnesses obtained by the CSF method and other methods are higher compared to that obtained by the BI method. Generally

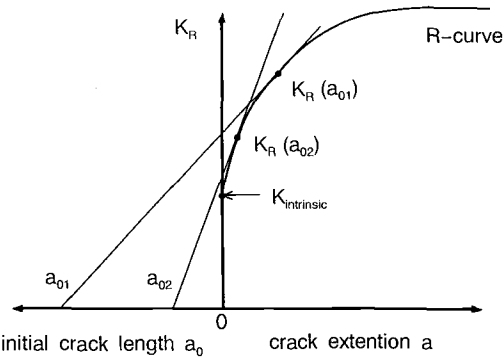


FIG. 9--Schematic illustration of crack resistance curve (R-curve).

material design would be based on a conservative value of a material based parameter. However the lower value of the BI method results from the damage zone formed at the tip of precrack, as discussed before. The CSF method gives a conservative value compared to the other method(FP,CN), as can be seen from Figs.6 and 7.

In material development, since the intrinsic fracture toughness is very hard to improve, the increase in crack extension resistance is attempted to improve the apparent fracture toughness with stable crack growth. As discussed above, the apparent fracture toughness strongly depends on the specimen size and geometry. The relationship between the apparent fracture toughness and crack length is schematically shown in Fig. 9. The apparent fracture toughness decreases and approaches the intrinsic fracture toughness with decreasing crack size. In practical structural ceramic components, large cracks will not be allowed to exist. This means that the intrinsic fracture toughness is acceptable for designing the components rather than the size-dependent apparent fracture toughness with stable crack growth. However, the high crack extension resistance is still effective for fatigue crack growth properties due to the significant stress shielding effect [20].

HIGH TEMPERATURE FRACTURE TOUGHNESS

The relationship between apparent fracture toughness obtained by the FP method and temperature for Si_3N_4-B is shown in Fig. 10. The fracture toughness decreases with

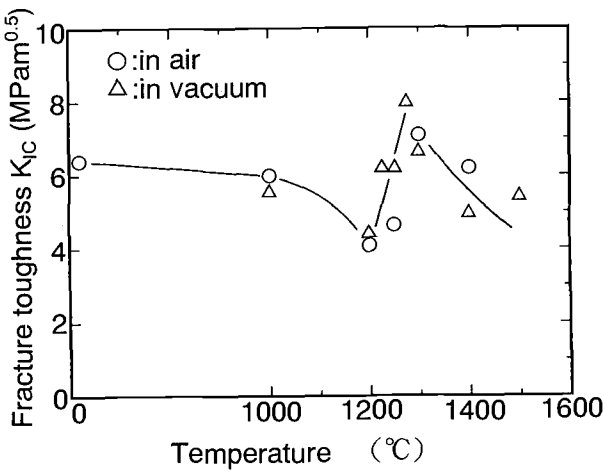


FIG. 10--Temperature dependence of K_{IC} for Si_3N_4-B.

increasing temperature. A brittle-to-ductile transition in fracture mechanism occurs [21] and the fracture toughness increases in the temperature range from 1200℃ to 1275℃. With increasing temperature further, the fracture toughness decreases. At temperatures higher than the transition temperature, stable crack growth with ductile pull-out of Si_3N_4 particles is observed. Similar stable crack growth behavior at elevated temperatures has been reported [22,23].

The relationship between apparent fracture toughness obtained by the FP method and temperature for Sialon is shown in Fig. 11. The grain boundary glass phase of Sialon is significantly less compared to that in Si_3N_4. The composition of the original powder materials of the Sialon are 91wt%Si_3N_4 and 9wt%Al_2O_3. The fracture toughness increases withincreasing temperature up to 1400℃. Above 1400℃, it decreases. A stable crack growth is also observed at temperatures higher than 1200℃. The difference in temperature dependence of fracture toughness between Si_3N_4 and Sialon results mainly from the difference in the amount of grain boundary glass phase [24]: the residual stress induced during sintering process will be significantly higher in Sialon with less grain boundary glass phase compared to Si_3N_4 with certain amount of glass phase which is soft and relaxes residual stress at elevated temperatures. With increasing test temperature, the residual stress in Sialon relaxes and then fracture toughness increases. On the contrary, with increasing temperature, the strength of grain boundary glass phase in Si_3N_4 degrades and then the fracture toughness decreases.

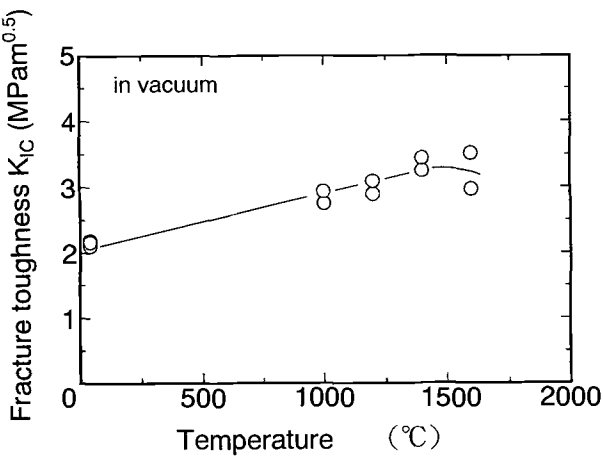


FIG. 11--Temperature dependence of K_{IC} for Sialon.

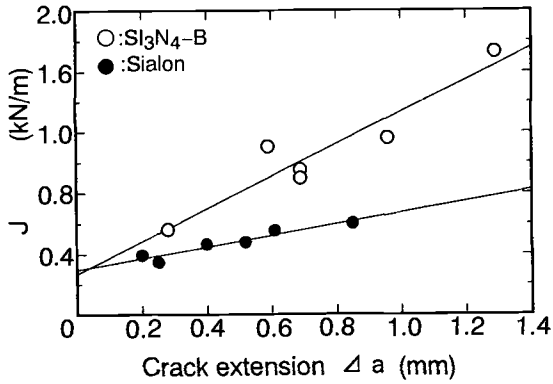


FIG. 12--Crack resistance curves at elevated temperatures for Si_3N_4-B and Sialon.

At elevated temperatures, nonlinear deformation due to softening of glass phase and stable crack growth are observed. Therefore, nonlinear fracture mechanics approach is suitable in this region. The relationships between J and stable crack length for Si_3N_4-B at 1400°C and Sialon at 1600°C are shown in Fig. 12, where a multiple specimen technique was conducted. The multiple specimen technique involved unloading specimens at several different displacement levels. The unloaded specimens were broken at room temperature in a brittle manner to measure the extension of stable crack growth. The increasing resistance curves are found for both the materials. J_{IC}-values can be obtained according to the R-curve method similar to the case of metallic materials (ASTM Standard E813). It should be noted that the R-curve depends on the loading rate due to visco-elastic nature of the glass phase.

SUMMARY

(1) When the unstable fracture occurs directly from the tip of a precrack without stable crack growth, fracture toughness values obtained by the FP, CSF and CN methods coincide, while that obtained by the BI(SEPB) method tends to be lower due to the damage zone formed at the tip of precrack during precracking.

(2) For the materials with large grain size, significant stable crack growth behavior is found for the specimens with large size of crack in the BI(SEPB), FP and CN methods. Apparent fracture toughness values become high due to the crack extension resistance(R-curve behavior). On the other

hand, the intrinsic fracture toughness can be obtained by using the specimen with a small surface crack, such as the CSF method, where the unstable fracture occurs without significant stable crack growth. In structural design, the intrinsic fracture toughness is acceptable because large cracks, which result in stable crack growth, are not allowed to exist in practical ceramic components.

(3) At elevated temperatures, since non-linear deformation due to softening of glass phase and stable crack growth occur, nonlinear fracture mechanics approach should be applied. J_{Ic}-value is successfully evaluated according to the R-curve method.

REFERENCES

[1] Mutoh,Y.,Tanaka,K., and Miyahara,N., "A Method for Evaluating the Fracture Toughness of Ceramics," Trans. Jpn. Soc. Mech. Eng.,vol 55, 1989, pp.2144-2151.

[2] Mussler,B., Swain,M.V., and Claussen,N., "Dependence of Fracture Toughness of Alumina on Grain Size and Test Techniques," J. Am. Ceram. Soc., vol.65, 1982, pp.566-572.

[3] Nose,T., and Fujii,T., "Evaluation of Fracture Toughness for Ceramic Materials by a Single-Edge-Precracked-Beam Method," J. Am. Ceram. Soc., vol.71, 1988, pp.328-333.

[4] Sadahiro,T., and Takatsu,S., "A New Precracking Method for Fracture Toughness Testing of Cemented Carbides,"Modern Develop. in Podwer Metall., vol.12-14, 1981, pp.561-572.

[5] Miyahara,N., Mutoh,Y., Tanaka,K., and Takahashi,M., "Fracture Toughness Evaluation of Five Structural Ceramic Materials by Various Testing Methods," Trans. Jpn. Soc. Mech. Eng., vol.57, 1991, pp.1326-1333.

[6] Petrovic,J.I., and Jacobson,L.A., "Controlled Surface Flaws in Hot-Pressed SiC," J. Am. Ceram. Soc., vol.59, 1976, pp.34-39.

[7] Bluhm,J.I., "Slice Synthesis of a Three-Dimensional Work-of-Fracture Specimen," Eng. Fract. Mech., vol.7, 1975, pp.593-604.

[8] Munz,D., Bubsey,R.T., and Shannon,J.L., "Fracture Toughness Determination of Al_2O_3 Using Four-point-Bend Specimens with Straight-Through and Chevron Notches," J. Am. Ceram. Soc., vol.63, 1980, pp.300-305..

[9] Palmqvist,S., "Method att bestamma segheten hos sproda material, sarskilt hard-metaller," Jernkontorets Ann., vol.141, 1957, pp.300-307.

[10] Lawn,B.R., and Swain,M.V., "Microfracture Beneath Point Indentations in Brittle Solids," J. Mater. Sci., vol.10, 1975, pp.113-122.

[11] Newman,J.C., and Raju,I.S., "An Empirical Stress-Intensity Factor Equation for the Surface Crack," Eng. Fract. Mech., vol.15, 1981, pp.185-192.

[12] Lawn,B.R., and Fuller,E.R., "Equilibrium Penny-Like Cracks in Indentation Fracture," J. Mater. Sci., vol.10, 1976, pp.2016-2024.

[13] Antis,G.R., Chantikul,P., Lawn,B.R., and Marshall,D.B., "A Critical Evaluation of Indentation Techniques for Measuring Fracture Toughness: I, Direct Crack Measurements, " J. Am. Ceram. Soc., vol.64, 1981, pp.533-538.

[14] Niihara,K., Morena,R., and Hasselman,D.P.H., "Evaluation of K_{IC} of Brittle Solids by the Indentation Method with Low Crack-to-Indent Ratios," J. Mater. Sci. Lett., vol.1, 1982, pp.13-16.

[15] Tanaka,K., "Elastic/Plastic Indentation Hardness and Indentation Fracture Toughness: The Inclusion Core Model," J. Mater. Sci., vol.22, 1987, pp.1501-1508.

[16] Mutoh,Y., Takahashi,M., and Takeuchi,M., "Fatigue Crack Growth in Several Ceramic Materials," Fatigue Fract. Engng. Mater. Struct., vol.16, 1993, pp.875-890.

[17] Nishida,T., and Mutoh,Y., "Fracture Toughness Tests of Sintered and Melted High Speed Steels," Proc. ICM-6, kyoto, Pergamon Press, vol.3, 1991, pp.563-568.

[18] Kawashima,K., Okamoto,H., Yamamoto,H., and Kitamura,A., "Grain Size Dependence of the Fracture Toughness of Silicon Nitride Ceramics," J. Ceram. Soc. Jpn., vol.99 1991, pp.320-323.

[19] Vekinis,G.,Ashby,M.F., and Beaumont,P.W.R., "R-Curve Behaviour of Al_2O_3 Ceramics," Acta Metall., vol.38, 1990, pp.1151-1162.

[20] Takahashi,M., "Basic Study on Fatigue Crack Growth Behavior of Ceramic Materials," Doctral Thesis, Nagaoka Univ. of Tech., 1993.

[21] Mutoh,Y., Yamaishi,K., Miyahara,N., and Oikawa,T., "Brittle-to-Ductile Transition in Silicon Nitride," Fract. Mech. Ceram., Plenum Press, vol.10, 1992, pp.427-440.

[22] Kohler,N., Ikuhara,Y., Awaji,H., and Funatani,K., "High Temperature Fracture Mechanism of Gass-Pressure Sintered Silicon Nitride," Fract. Mech. Ceram., vol.10, 1992, pp.367-377.

[23] Hansson,T., Swan,A.H., and Warren,R., "High Temperature Fracture of a SiC Whisker Reinforced Alumina in Air and Vacuum, "J. European Ceram.Soc., in press.

[24] Mutoh,Y., Miyahara,N., Yamaishi,K., and Oikawa,T., "High Temperature Fracture Toughness in Silicon Nitride and Sialon," Trans. ASME, J. Eng. Mat. & Tech., vol.115, 1993,pp.268-272.

Frederick W. Brust[1] ,B. S. Majumdar[2], Golam M. Newaz[3]

ANALYSIS OF DAMAGE AND FAILURE IN METAL MATRIX COMPOSITES

REFERENCE: Brust, F. W., Majumdar, B. S., and Newaz, G. M., **"Analysis of Damage and Failure in Metal Matrix Composites,"** Fracture Mechanics: 26th Volume, ASTM STP 1256, Walter G. Reuter, John H. Underwood, and James C. Newman, Jr., Eds., American Society for Testing and Materials, Philadelphia, 1995.

ABSTRACT: This paper presents the results of the analysis of the constitutive response of a model Metal Matrix Composite (MMC) system. The model is described first, followed by some direct comparison of predicted response to corresponding experimental data. An important result discussed here is that when model verification is made, it is important to compare load direction response to the experimental data, but also, comparisons to the out of load direction response must be made, or the model may not be performing as desired. Some discussion of failure predictions using simple models is also made here.

KEYWORDS: metal matrix composite, composite, damage, plasticity, analysis, experiments

INTRODUCTION

Metal/intermetallic matrix composites are currently under intense development for intermediate temperature applications of 400 to 1300 C. Titanium alloy matrix composites, typically reinforced with SiC fibers, are under intensive development for applications in moderate temperature ranges (e. g., 400 to 800 C). What makes titanium matrix composites attractive is their low density and high strength to weight ratios. The strength to weight ratios of titanium reinforced with SiC (SCS-6) fibers are higher than that of Ni-base superalloys. To date, Ti-matrix composites have been utilized in applications such as aircraft wings and rear stabilizers. These composites are also being considered for use in the compressor section of advanced turbine compressors where their high strength to weight ratio is attractive for decreasing mass and improving turbine efficiency. As noted by Dix [1], a one pound decrease in turbine weight decreases airframe weight by approximately seven

[1] Currently at Georgia Institute of Technology, Atlanta, Georgia, 30332.
[2] Universal Energy Systems, Dayton, OH
[3] Wayne State University, Detroit, MI

Copyright © 1995 by ASTM International www.astm.org

pounds.

Before these materials can be used with confidence in engineering structures, an understanding of the constitutive response, damage development and failure process is required. A large volume of research work has appeared in recent years which is concerned with the damage development and failure processes in metal matrix composites (MMC).

A summary of many such analytical/experimental models, and their effectiveness in modeling a number of different MMC systems, has been presented by Bigelow, Johnson, and Naik [2]. They concluded that such models can be quite effective in predicting the constitutive and damage response of MMC systems. For example, Sherwood and Boyle [3] used the Bodner constitutive model with an axisymmetric assumption to examine the global constitutive response of a Titanium Aluminide MMC. Sherwood, Quimby, and Doore [4] also recently used a three-dimensional model to examine [0], [90], and [0/90]s systems with reasonable comparison with experimental data. Nimmer et al [5], and Gunawardena, Jansson, and Leckie [6] effectively used finite element micromechanics models to study the constitutive response of SiC/Ti-15-3, SiC/Ti-6-4, and an aluminum alloy matrix reinforced by alumina fibers. Reference [6] also showed that classical damage mechanics' theory can be used to predict crack nucleation sites. Arnold and Kruch [7] have recently examined three multiaxial isothermal continuum damage models and their applicabilty to MMC systems. These models, which are of the Chaboche type, are somewhat cumbersome to obtain material constants, but they offer promise for future applications.

References [2-7] were studies which coupled micromechanics analysis and experimental results. The synergism of such combined experimental/analytical approaches is very effective for studying the damage evolution in MMC systems. However, interesting insight can be obtained from purely micromechanics studies. Jones, Boyd, and Allen [8] used a Miller viscoplastic constitutive law and a plane strain model to examine the response of a 304SS/SiC system subjected to different applied strain rates. Despite the fact that their interface failure model relied on a maximum shear failure criterion, which resulted in initial fiber/matrix debonding at sites 45 degrees from the load direction (debonding is typically observed perpendicular to the load direction), they found the stress strain response to increase as applied strain rate increased. Byrom and Allen [9] also used a Bodner-Partom model, plane strain assumption, and a perfect interface bond condition to investigate processing induced residual stress effects on the response of aTi-15-3/SiC system. Gosz, Moran, and Achenbach [10] assumed a hexagonal periodic array, an interface element, and included cracks explicitly and predicted crack growth directions in a brittle matrix composite system. This study, while inappropriate for ductile matrix composites, provided mixed mode crack tip stress intensity factors for microcracks approaching second phase particles, and postulated a crack growth direction criterion which may also extend to ductile materials.

Investigations of the crack growth behavior of MMC systems have also been made by many researchers, including Bahei-El-Din, Dvorak and Wu [11] and Mital, Caruso and Chamis [12]. Detailed studies of the interface zone between the fiber/matrix interface have also recently been made by Naik, Johnson and Dicus [13]. The strength and behavior of the interface region in MMC's is a complex problem which has an important effect on composite performance; the stronger the bond, the better the performance. Needleman [14-15] has proposed a potential to model interface constitutive response and failure (debonding). This model can be used as a phenomenologically based interface failure model with the free

parameters interpreted as material properties which are unique for a given material system, and temperature. This model was modified by Brust, Newaz, Mohan, and Majumdar [16] to permit adequate performance when processing induced residual stresses are present. Tvergaard [17] has also modified this model and has studied the response of chopped fiber MMC systems. Many other interface models have been used also, but we believe that those of the type in References [14-17] have the most practical utility.

Castelli et al. [17] studied the thermomechanical fatigue (TMF) behavior of a 9-ply unidirectional SCS-6/ Ti-15-3 laminate over a temperature range of 93 C to 538 C. They observed that the TMF loading greatly reduced cyclic fatigue lives when compared with isothermal and in-phase nonisothermal data. Under out-of-phase TMF loading matrix dominated failures were observed. For the same composite, Gabb et al. [18] found that both in-phase and out-of-phase TMF lives were reduced compared to isothermal fatigue lives at 300 C and 550 C. For Ti-24Al-11Nb/SCS-6 composites, Russ et al. [19] also observed that out-of-phase TMF tests led to matrix dominated failures while other loading histories (in-phase and isothermal) suggested fiber dominated failures. These results demonstrated the potentially severe problems encountered when metal matrix and intermetallic composites are subjected to TMF. Micromechanics models have been somewhat successful in modeling TMF effects (Miramadi et al. [20], and Newaz, Majumdar and Brust [21]), but much more work is required to fully understand the phenomena of TMF behavior of MMC's, especially under out-of-phase TMF loading.

Here we do not provide an exhaustive literature review of micromechanics methods and experimental investigations for MMC systems. The above papers, many of which are very recent, provide large reviews of other studies. The general conclusion from these studies confirms that micromechanics models, separately or combined with a substructuring approach, can provide reasonable assessments of time-independent and time dependent response of MMC systems. Here we further use miromechanics models, combined with experimental results, to develop a further understanding of the MMC constitutive, damage development, and failure process. Particular emphasis is focused on processing residual stresses and their effects on the failure process for a model unidirectional 90 and 0-degree Ti-15-3/SCS-6 MMC system. In particular, it is established that an accurate micromechanics model must be capable of predicting the response out of the loading plane, in addition to the in-plane response.

EXPERIMENTS: SUMMARY OF OBSERVATIONS

The experimental approach taken is described in detail in References [21-26]. The material tested was an eight-ply unidirectional Ti-15-3/SCS6 composite, approximately 1.99 mm thick, fabricated by Textron (serial number 890556), using a Hot Isostatic Press (HIP) consolidation technique. The SCS6 fiber is approximately 0.14 mm in diameter, and contain alternating outer layers of Carbon and non-stoichiometric SiC, which protect the fiber during handling. The fibers are connected to each other with thin molybdenum ribbons to allow adequate fiber spacing during fabrication. As will be shown later, these ribbons appear to degrade the performance of the composite. The Ti-15-3 (Ti-15 wt% V-3 wt% Cr-3 wt% Al-

3 wt% Sn) alloy is a metastable b.c.c. B-Ti alloy, the b.c.c. phase being stabilized by V. The thickness of the fabricated 8-ply unidirectional system is about 1.99 mm and the fiber volume fraction is approximately 0.34.

Specimens were prepared with two different orientations: 0 and 90 -degrees, and were loaded uniaxially to failure. The $[0]_8$ specimens were loaded in a direction parallel to the fibers; the $[90]_8$ specimens were loaded perpendicular to the fibers (see Figure 1). The 90-degree load cases permitted easy fiber/matrix debonding to occur. All specimens were tested in the as-fabricated condition which involved cooling from the HIP pressure of approximately 85 Mpa and temperature of 815 C to room temperature; no heat treatment was performed prior to testing. The longitudinal (load direction), width and thickness strains were monitored throughout the displacement controlled tests with both strain gauges and extensometers, and these measurements represent global or average response over a fixed gauge length as illustrated in Figure 1. Specimens were sectioned and examined using both SEM and TEM to track damage, fiber/matrix debonding, slip band formation, etc. at different points during the loading process. See References [21-26] for more details.

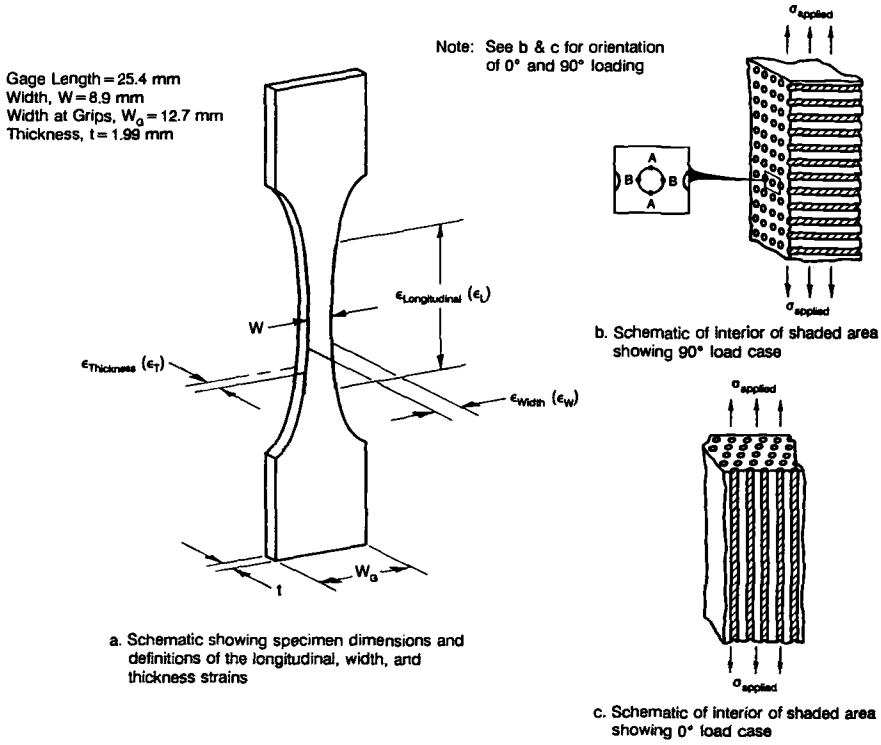


FIG. 1 *Specimen dimensions and definitions.*

Observations of 90-degree tests. As the specimen is loaded, the onset of minimal plastic slip bands can be detected at the top and bottom of the fibers at an applied strain level of about 0.002, i.e., at points A in the inset of Figure 1(b). (Recall that this represents an average applied global strain over a large gauge length, as illustrated in Figure 1.) Partial fiber-matrix debonding, again at the top and bottom of the fibers, begins to occur at a strain of 0.003 to 0.005. Slip bands and reaction zone microcracks begin to form around 90-degrees from the load direction (near points B, Figure lb), and simultaneous nucleation of slip bands at those locations at applied strains of about 0.006. Extensive fiber/matrix debonding followed by extensive matrix plasticity occurs at strain levels slightly greater than 0.006. At 0.009 applied strain, intense shear bands develop between the fibers. Finally, failure occurs by shear crack nucleation and propagation throughout the matrix at strain levels approaching 0.17.

Observations of 0-degree tests. The appearance of slip bands at the fiber/matrix reaction zone microcracks (perpendicular to the load direction) begins at an applied strain of about 0.004 to 0.005. At 0.006 applied strain, slip bands nucleate at grain boundaries and this event triggers the onset of extensive matrix plastic deformation. Also at about 0.006 applied strain, localized fiber/matrix debonding within the fiber coating layers occurs. This may be influenced by the reaction zone microcracks, which continue to appear. Extensive slip bands form in the matrix at about 0.008 strain. Failure occurs by fiber failure at greater than 0.01 applied strain. The elastic brittle fibers fail at fiber stress levels significantly lower than that expected based on a critical stress failure, and rule of mixture predictions. The fiber failures are initiated by fracture of the Mo-ribbon, which are present to align the fibers during fabrication.

THE MICROMECHANICS MODEL

Prediction of the constitutive response and damage development described above is attempted using a micromechanics model with periodic boundary conditions. The model assumptions are quite similar to the models described in many of the references with several important differences. The model is discussed first before presenting predicted results and comparing those to experimental data. It is important to remark that the model was developed while the experiments were being performed. As such, experimental results drove the model development, while at times model predictions drove the experimental directions. The synergistic direct interaction between analysis and experiment proved most effective in gaining an understanding on the MMC failure processes.

Model Details. Figure 2 illustrates the model geometric assumptions. Figure 2a shows the eight ply unidirectional system that was tested. As seen, we envision a perfectly ordered system, with each ply perfectly ordered above and below the others through the thickness of the composite. This is, of course, not seen in real systems, where imperfections render such ordering rather rare. However, References [21-26] show that with this system, the arrangement is reasonably well ordered (see some of the micrographs in Reference [22]). The type of arrangement that is assumed for developing the unit cell micromechanics model

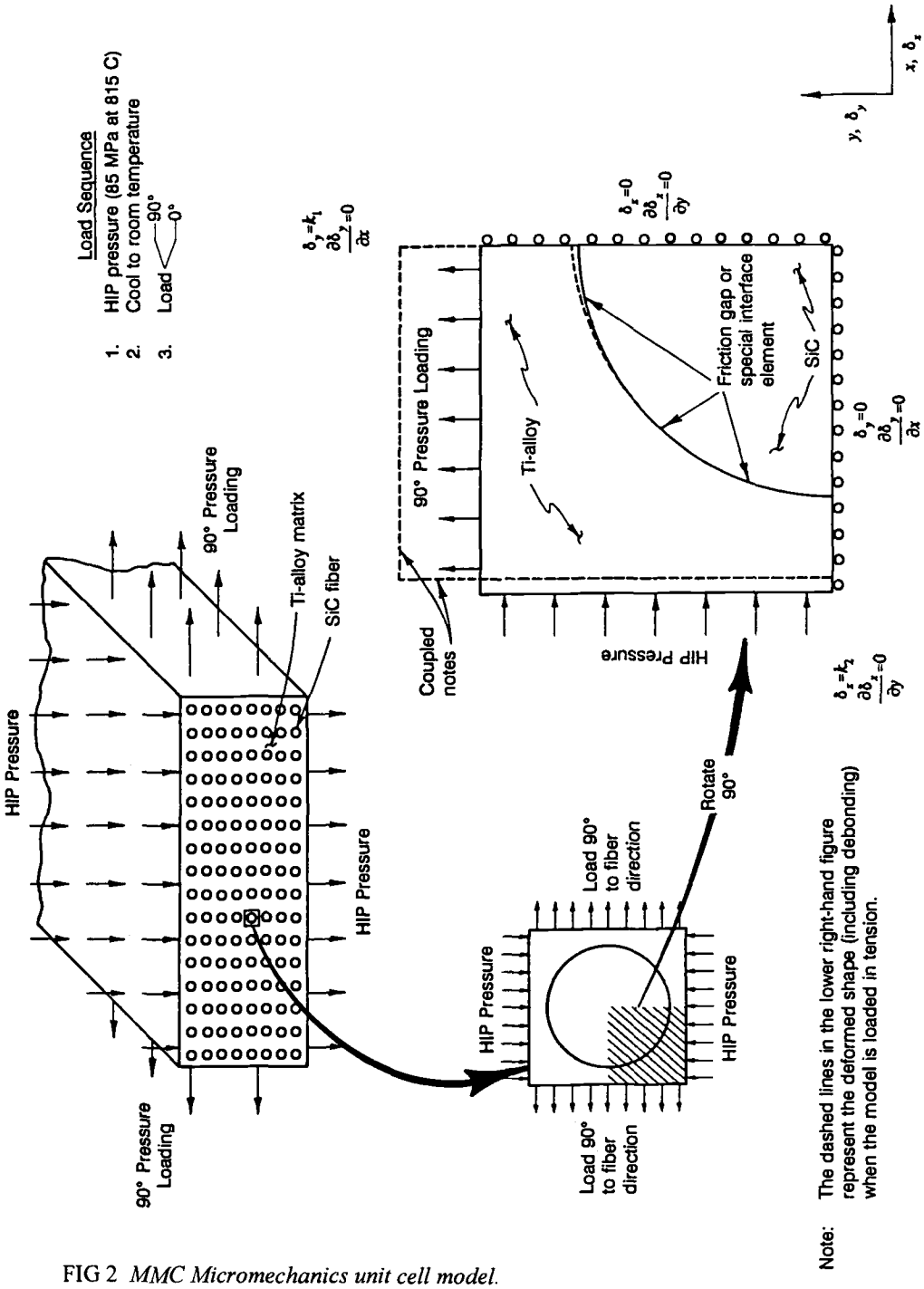


FIG 2 *MMC Micromechanics unit cell model.*

can affect the predicted results. However, our experience has shown that the type of arrangement chosen here performs quite well when comparisons are made to experimental data. This may be because these systems are rather thin (only 8-ply).

Figure 2b illustrates the symmetric unit cell which is considered in the model, i.e., the fiber and surrounding matrix are assumed to be extracted from the center region of the plies, at mid thickness. A one-fourth model of this cell is considered in constructing the micromechanics model.

Figure 2c shows the geometric boundary conditions imposed on the model. The right side and bottom of the cell are symmetry planes (signified by the rollers in Figure 2c). The top and left side of the cell have their nodal points coupled so that they can only deform together, producing periodic boundary conditions. The dashed lines in Figure 2c illustrate a typical deformed shape for tensile loading. Note from the schematic of the deformed shape from Figure 2c the potential for fiber matrix interface failure is included in the model.

The periodic boundary conditions are imposed by coupling the deformation of each node along the boundary of interest so that a constant displacement, and zero slope results. The constants result naturally from the solution procedure, and are not rigidly imposed.

Out-of-plane, i.e., in the z-direction, generalized plane strain boundary conditions are imposed, without rotation. This means that, in the z-direction, the displacement is constant. If we denote by w, the displacement in the z-direction, this may be expressed mathematically as:

Out of Plane

$$w = k_3;\ \partial w/\partial (x, y, z) = 0 \qquad (1)$$

i.e., the derivative of w is zero with respect to all coordinates. Again, k_3 is not an imposed constant, but rather naturally results from the solution procedure.

In addition to these conditions, the interfaces between the fibers and the matrix are assumed to either be a perfect bond, or have an interface which can fail. This latter condition is imposed in two separate ways. (i) If the bond is very weak, then contact with friction conditions are imposed using gap elements. With these conditions, interpenetration between the fibers and the matrix is always prevented. Moreover, if the interface is in contact, then sliding friction is permitted which permits interface shear stresses. If the normal stress between the fiber and the matrix is tensile, then separation occurs. (ii) The second type of interface is imposed using a user written special interface element. This element performs in a similar manner as the friction-gap elements when the normal stress between the fiber and matrix is compressive. However, when the normal stress becomes tensile, an interface strength is permitted until a critical stress or displacement is reached, after which, the interface fails. The details of the interface element are to be discussed elsewhere. However, since the interface element is very similar to that discussed by Needleman and co-workers (References [27-31]), the interested reader should consult those references. The potential used to represent this interface element is written such that if compressive stresses develop, the element becomes very stiff so that interpenetration between the fiber and the matrix

cannot occur. If the interface stress is tensile, then a bond strength keeps the fiber and matrix basically in tact until a critical stress and displacement occurs, after which the interface element stiffness becomes small; i.e., failure occurs. Both normal and shear interfaces are accounted for. We use this as a phenomonological failure law, and as such, the material constants are determined by modeling an experiment. This element is quite flexible in that by the proper choice of constants, a brittle or highly ductile interface failure may be modeled. For the application considered here, a brittle interface failure condition was chosen.

The out-of-plane boundary conditions impose generalized plane strain, without rotation, as seen in Equation 1. For out of plane loading, i.e., what we refer to in Figure 1c as the 0-degree load case, the loads are applied to the out of plane node, and as such, the out of plane deformation is entirely consistent with the in-plane assumptions at the coupled node lines. These assumptions of planes remaining plane after deformation appears to be consistent with experimental observations. In the experiments, if one observes the surface of the deformed specimen, it appears to be smooth and straight. These assumptions would not be valid if a wavy pattern was observed on the surface during and after deformation.

Material Model. The SiC fiber was modeled as an isotropic elastic material. Due to the fiber fabrication process, it is likely that fibers have an oriented microstructure, and hence, orthotropic elastic properties. However, since such properties are very difficult to obtain on fibers in the radial direction, the elastic properties as determined in the long direction are used, and isotropy is assumed. The Ti-15-3 material is modeled using classical plasticity theory with isotropic hardening. Temperature dependent material properties are used for both the fiber and the matrix. The elastic properties of the fiber and matrix are listed in Tables 1a and 1b, respectively.

Temperature (C)	**Elastic Modulus (GPa)**	**Poisson's Ratio (ν)**	**Mean Coef. of Thermal Expan. (α)(mm/mm-C)**
25	400	0.19	2.2E-06
300	400	0.19	2.2E-06
550	400	0.19	2.2E-06
700	400	0.19	4.5E-06
815	400	0.19	4.9E-06

TABLE 1(a) *Elastic properties of SCS-6 fiber.*

Temperature (C)	Elastic Modulus (GPa)	Poisson's Ratio *(v)*	Mean Coef. of Thermal Expan. (α) (mm/mm-C)
25	90	0.32	8.1E-06
300	80	0.32	9.3E-06
550	75	0.32	1.0E-05
700	70	0.32	1.05E-05
815	6.0	0.32	1.09E-05

TABLE 1(b) *Elastic properties of Ti-15-3 matrix.*

A Ramberg-Osgood equation was fit to the data for different temperatures to model the elastic-plastic response of the matrix in the form:

$$\epsilon_p = (\alpha \cdot \epsilon_o) \cdot (\sigma/\sigma_o)^n \qquad (2)$$

In equation (1), $\epsilon_o = \sigma_o/E$, where σ_o is the yield stress at temperature, and E is the temperature dependent elastic modulus listed in Table 1b. The material properties are listed in Table 2.

Temperature (C)	α	n[1]	σ_o[1] (Mpa)
25	0.01	50 (13.4)	725 (689)
300	0.0254	10.2	593
550	0.039	7.3	400
700	0.044	6.2	210
815	0.0478	5.36	64.3

TABLE 2 *Plastic constants for Ti-15-3 Matrix material.*

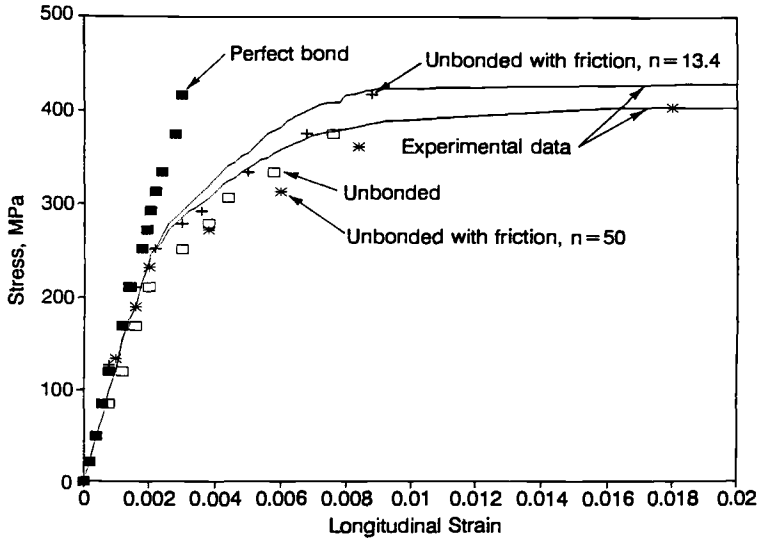
[1] At 25 C two sets of Ramberg - Osgood constants were used which represented the range of extremes. For most analyses n=50 and σ_o = 725 were used. However, for some analyses, the values in the parenthesis are used.

Fabrication Model. Properly including the effects of processing induced residual stresses in the micro-mechanics model can have an important effect on the predicted response. As illustrated in the load sequence in Figure 2, two steps are involved in the processing model: modeling the Hot Isostatic Press (HIP) process, and then cooling to room temperature. As schematically illustrated in Figure 2a, a HIP pressure is assumed to be applied to the thin composite at near the consolidation temperature, where the matrix begins to attain observable stiffness. The actual fabrication process involves the large deformation flow behavior of very soft matrix material as it is pressed around the rather rigid fibers. This complex process is neglected, assuming that the matrix material behaves as a fluid (with no memory of deformation history), until the neat packing arrangement shown in Figure 2a is attained. The pressure is only applied to the top flat area of the thin composite sheet, assuming that curling of the edges occurs in these thin materials (see also Figure 2b). However, it has been observed that including the pressure on all faces does not have a large influence on the resulting predictions. Note that hydrostatic pressure applied to all edges in a two-phase composite will result in matrix plasticity. After the HIP pressure is applied, the system is cooled to room temperature while the pressure is linearly reduced to zero. The system is then loaded, or heated to the temperature of interest, and then loaded.

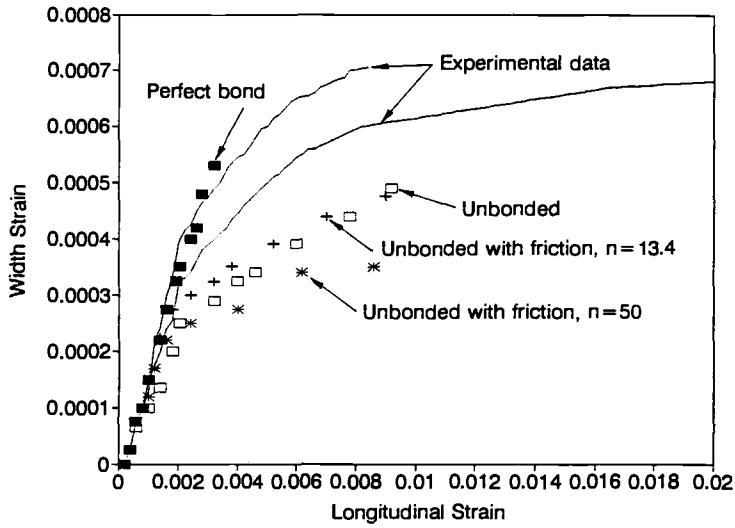
While it is clear that this processing model does not truly model the complex fabrication process, it appears to provide adequate results. It will be seen that neglecting this step results in predictions of *off load axis response* that are inadequate compared to experimental data.

ANALYSIS RESULTS

90-Degree Load Case. The results for the load application 90-degrees to the fiber direction, applied in tension, are presented first (see Figure 1b). Figure 3a shows the prediction of the applied nominal stress plotted as a function of nominal longitudinal strain. This is the case where no HIP pressure was included in the analysis, i.e., step 1 of the load sequence provided in Figure 2 is not included here. The solid squares represent the case where the fiber and matrix are assumed to be perfectly bonded. It is seen that the perfect bond case compares well with the experimental data up until a strain of about 0.2 percent, after which, the comparison is poor. The knee in the curve at a strain of 0.2 percent is predicted rather well for the three other analysis cases shown here. Two of the cases shown include the possibility of frictional sliding between the fiber and matrix during debonding. For these cases, the coefficient of sliding friction used was 0.5, which was taken from a handbook for the case of a metal/ceramic interface sliding. For these two cases (labeled unbonded with friction in Figure 3), two different room temperature Ramberg-Osgood power coefficients of n = 13.4 and 50 (Table 2) were used. It is seen that, with the higher n value, the experimental data is better predicted for large strains. In Figure 3a, for strains greater than about 0.01, the experimental curves flatten out as the plasticity in the matrix material extends across the entire ligament. This suggests that the nearly elastic-perfect plastic coefficient of n = 50 may represent the material response best, and is emphasized in most of the following figures. The open squares in Figure 3a represent the case of frictionless sliding

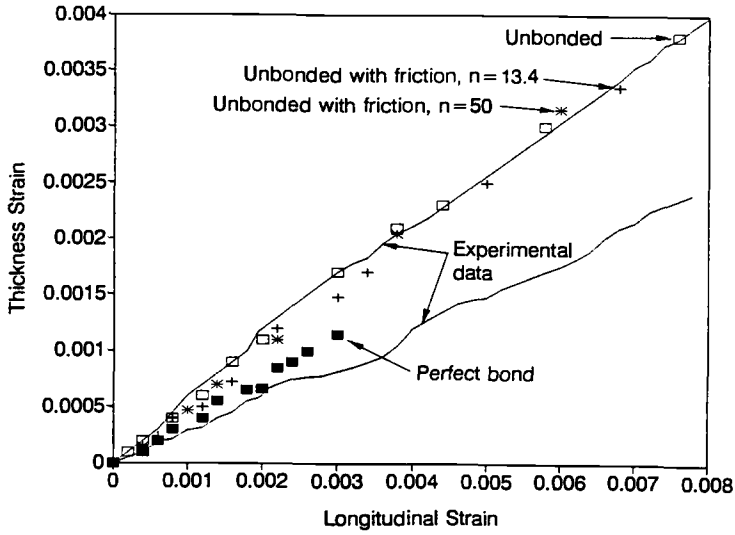


(a) *Stress versus longitudinal strain (ϵ_l).*



(b) *Width direction strain (ϵ_w) versus applied longitudinal strain (ϵ_l).*

FIG. 3 *Predicted response compared to experimental results. Two sets of experimental data (lines) and four sets of analysis results are presented. No HIP pressure was included, i.e., Step 1 of the load sequence illustrated in Fig. 2 was not performed. n=13 and n=50 represent the room temperature Ramberg-Osgood exponents used for the four analyses.*



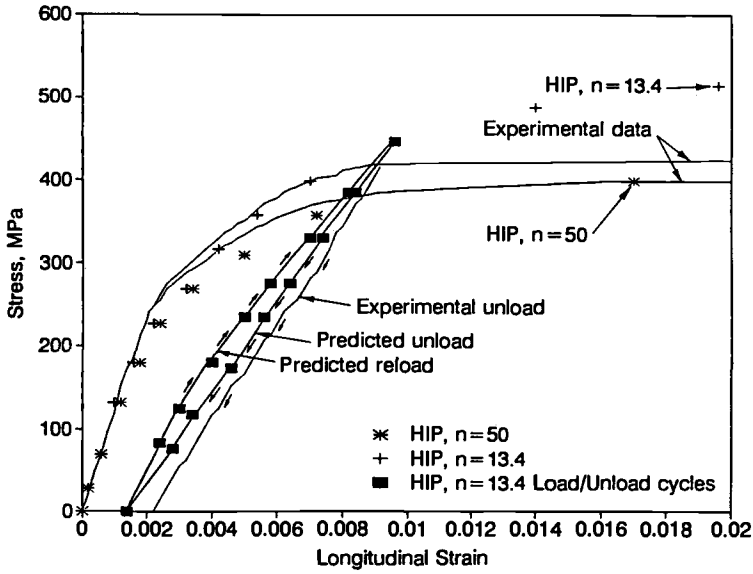
(c) *Thickness direction strain (ϵ_T) versus longitudinal strain (ϵ_l).*

along the fiber/matrix interface after debonding for the n = 50 case. Most analysis results shown in the following include frictional sliding.

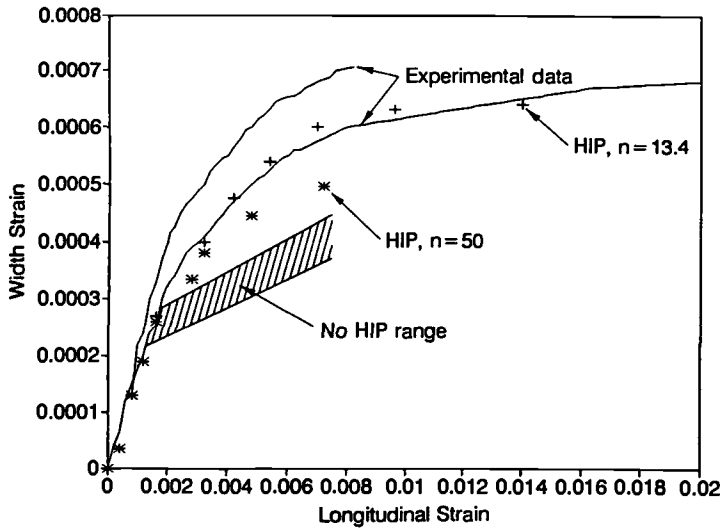
Figures 3b and 3c compare predicted and experimental off load axis strains. Both the width strain, and thickness strain are defined in Figure 1. Figure 3b shows that the predicted strains under predict the experimental response for all cases where fiber matrix debonding is included. Again, this is the case where the HIP pressure was not included in the analysis, and the fabrication stresses were estimated by cooling from 815 C to room temperature only. The thickness direction strains (Figure 3c) compare well with the experimental data regardless of the model used.

Figure 4a shows comparisons (analogous to those in Figure 3a) for the case where the analysis model includes the modeling of the HIP pressure as Step 1 in the analysis (see Step 1 of Figure 2 load sequence). It is seen that good comparison results, as was also seen in Figure 3a where the HIP pressure was ignored. Also shown in Figure 4a are predicted results when an unload/load sequence is modeled. Note that at zero applied stress upon unloading, a residual composite offset plastic strain state occurs.

However, Figure 4b clearly shows that comparisons of width direction strains to the experimental data are much better when the HIP process is included in the analysis. The HIP pressure modeling causes some plasticity to occur at the high temperature of application, since the material is weak and can flow plastically rather easily. This causes an 'oriented' initial plastic strain state. When the fabrication process is modeled only by cooling to room temperature, the initial stress and strain state is symmetric. The effect of an initial plastic strain state which is oriented appears to be important in predicting off axis constitutive response of the MMC system, and is used from here on. Figure 4c also shows the thickness direction strains when the HIP process is included as part of the fabrication process.

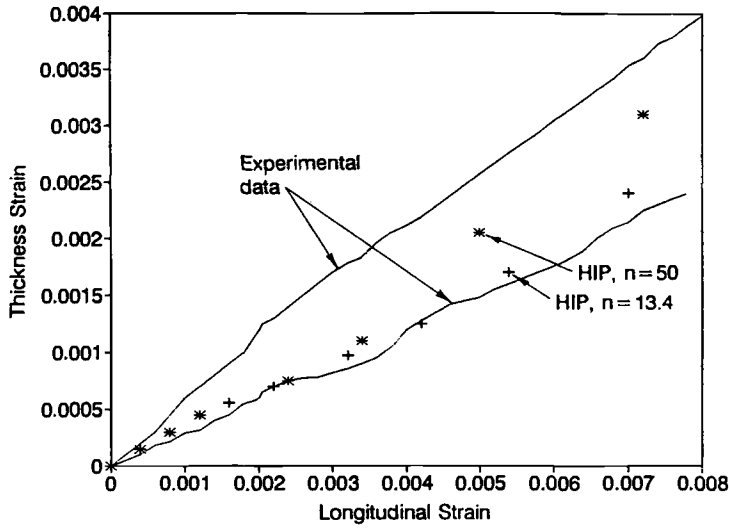


(a) *Stress versus longitudinal strain (ϵ_l). A predicted and experimental unload/reload comparison is also included - Notice the residual strain after unloading.*



(b) *Width direction strain (ϵ_w) versus applied longitudinal strain (ϵ_l).*

FIG. 4 *Predicted response compared to experimental results. Two sets of experimental data (lines) and two sets of analysis results are presented. The HIP pressure was included, i.e., Step 1 of the load sequence illustrated in Fig. 2 was performed. n=13 and n=50 represent the room temperature Ramberg-Osgood exponents used for the analyses.*



(c) *Thickness direction strain (ϵ_T) versus longitudinal strain (ϵ_l).*

Fiber/Matrix Interface Stresses. It is useful to observe the stresses that develop along the fiber and matrix interface resulting from both the fabrication induced residual stresses, and during the loading phase. Figure 5 shows the predicted residual stresses that develop along the interface caused by fabrication. As seen in Figure 2, fabrication stresses are modeled by first applying a HIP pressure at temperature, then cooling to room temperature while reducing the HIP pressure to zero. The stresses are plotted as a function of angle as illustrated in the inset of Figure 5. Stresses in the fiber and in the matrix at the interface are plotted. Note that both σ_R and $\sigma_{R\theta}$ are equivalent at this interface. From Figure 5 it is seen that some slight differences in the normal and shear stress are observed along this interface. However, these differences are small, and indicate the solution accuracy. The hoop (σ_R) and out-of-plane (σ_z) stresses are positive in the matrix, and compressive in the fiber. Note also that the stresses are not symmetric about the 45-degree (0.78-Radian) line, as occurs when the fabrication stresses are modeled by only cooling to room temperature. The corresponding plastic strain state from fabrication is likewise not symmetric about this plane. Note also that the radial (σ_R) stresses reach a maximum at an angle of about 45-degrees.

Figure 6 shows the corresponding residual stresses along the interface as the unit cell model is loaded perpendicular to the fiber direction. Figure 6a shows the interface stresses at an applied load that is about 86 percent of the maximum load. Note that the radial stresses are zero beyond an angle of about 0.6 radians indicating that fiber/matrix debonding occurs there. Also, the hoop stresses are large and tensile up to an angle of about 45-degrees. Figure 6b illustrates the interface stresses at an applied load of 412 Mpa, which is very close to the failure load. Note that the radial stresses are zero everywhere along the interface. Near $\theta = 0$, the interface is not debonded. Rather, the matrix at the interface has experienced so much plasticity, and the corresponding tangent modulus is so low, that the resulting

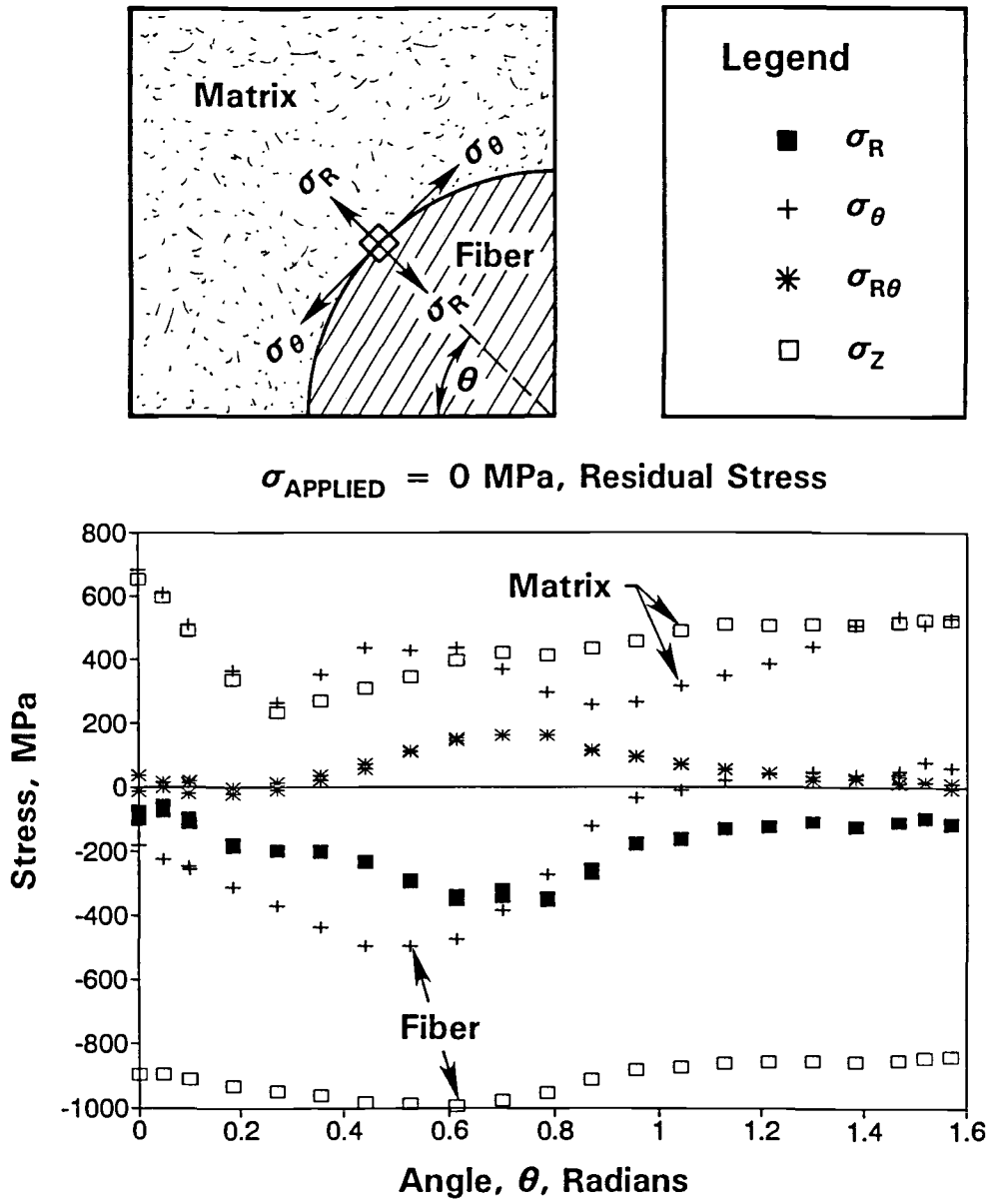
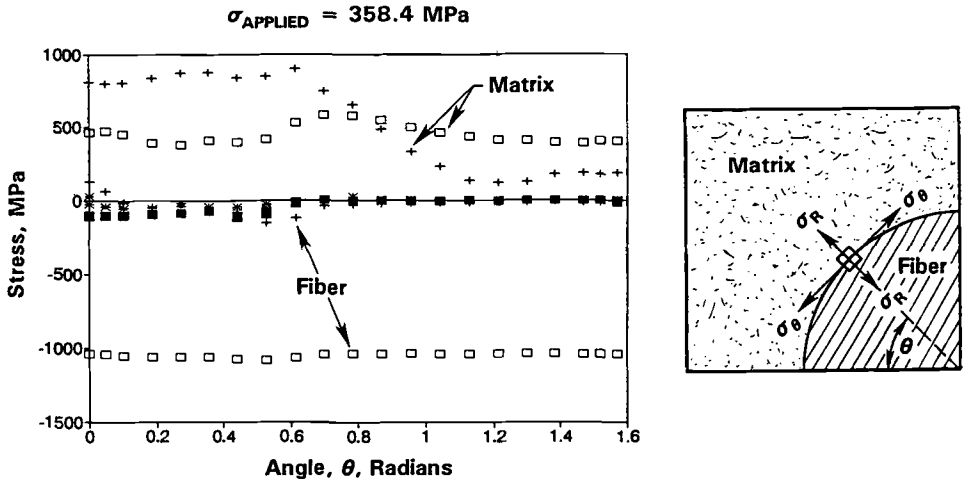
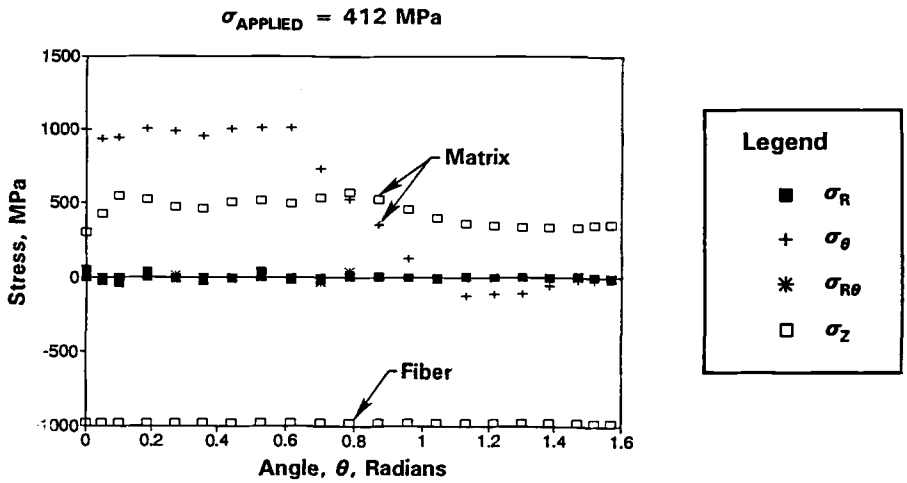


FIG 5 *Residual stresses after modeling fabrication, before loading. The stresses are at the fiber/matrix interface, slightly in the fiber, or slightly in the matrix, as noted.*



(a) *Applied stress = 358.4 MPa, about 86 % of the failure load.*



(b) *Applied stress = 412 MPa, very close to the failure load.*

FIG 6 *Fiber/matrix interface stresses. The location is in the fiber or matrix, as indicated.*

contact stresses are negligible. Note also, that the only active stress in the fiber near failure is σ_z. As will be seen in the next subsection, cracks initiate at an angle of about 22-degrees (0.44-Radian).

Failure for the 90-Degree Load Case. To predict the point of failure in this system caused by crack nucleation and growth, a phenomenological classical damage mechanics approach was used. The damage law, which is a modification of Lemaitre's [30] model by Tai and Yang (Reference [31]) is written as:

$$D = \int_0^{\epsilon_p} (\sigma^* \, d\epsilon_p)/\epsilon_0^p \tag{3}$$

where,

$$\sigma^* = 2/3 \, (1 + \nu) + 3 \, (1 - 2\nu) \, (\sigma_m/\sigma)) \tag{4}$$

with υ Poisson's ratio, σ_m is 1/3 the trace of the stress tensor, and σ is the classical Von Mises equivalent stress. The only material constant needed is the uniaxial plastic strain at failure; $\epsilon^P{}_0$, at temperature. D = 0 with no damage, and D = 1 at local failure. D is integrated throughout the strain history, including processing. This parameter predicts failure rapidly at regions of high constraint (i.e., high σ_m), and predicts failure conditions much slower at conditions of low constraint. This type of classical local approach appears to perform quite well in composite materials where a dominant crack is not present. However, for monolithic materials with a dominant crack present, performance is poor because damage localizes at the crack tip and failure predictions depend on the mesh size near the crack tip.

Figure 7a provides contour plots of this damage parameter as predicted for the load case which was ninety degrees to the fiber direction. The load at this point is 403 Mpa, which is very close to the failure load of 414 Mpa. Here it is seen that two zones of failure are predicted; one which begins at the fiber matrix interface (at θ = 22-degrees using the coordinate system in the insert of Figure 5), and one in the lower left corner, between fibers. As more load is applied, these two failure zones meet, and failure is predicted at about 412 Mpa. Figure 7b shows a micrograph of sliplines developing at this interface, prior to crack nucleation. It is seen that this simple damage model predicts both the maximum load magnitude, and crack nucleation location rather well for this case. Note that the slip zones develop at about 22 degrees from the horizontal (Fig. 7b) and D=1 (Fig. 7a) at near this same location. Other damage models such as the early model of Hancock and Mackenzie [32] predict similar behavior, except the magnitude of the failure load is different. (Here, the Reference [32] model predicted failure at about 400 Mpa.)

O-Degree Load Case. The second case considered is for the load applied in the fiber direction; see Figure 1. Recall that for this case, the load is applied *in the generalized plane strain direction,* and only extension is permitted, i.e., no rotation. Figure 8a provides a comparison of predicted stress versus load direction strain compared to experiment. Two

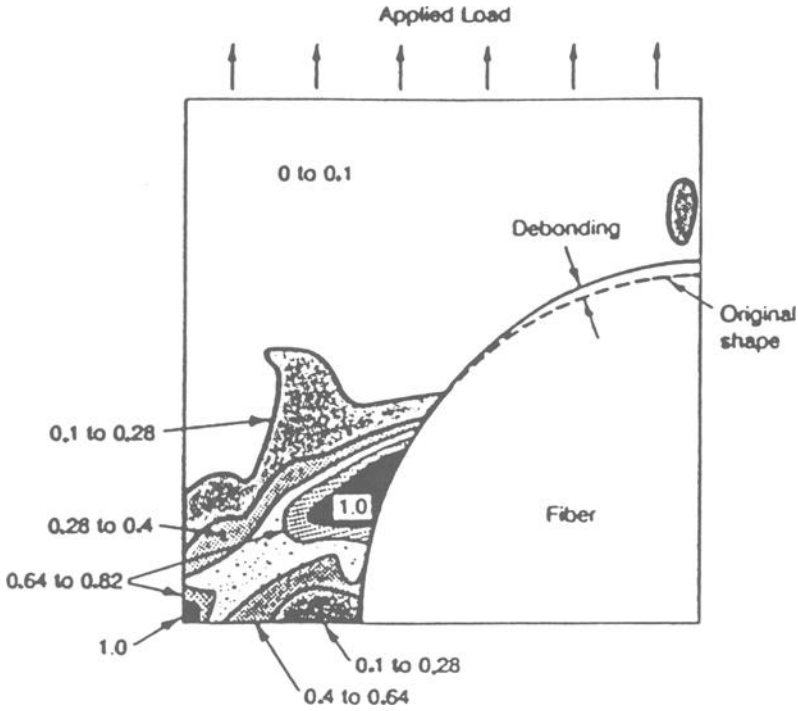


FIG 7a *Predicted damage contour plots for tensile load case. D = 1 represents failure, D = 0, no damage. Applied stress = 403.2 MPa. Experimental applied failure stress was 414 MPa.*

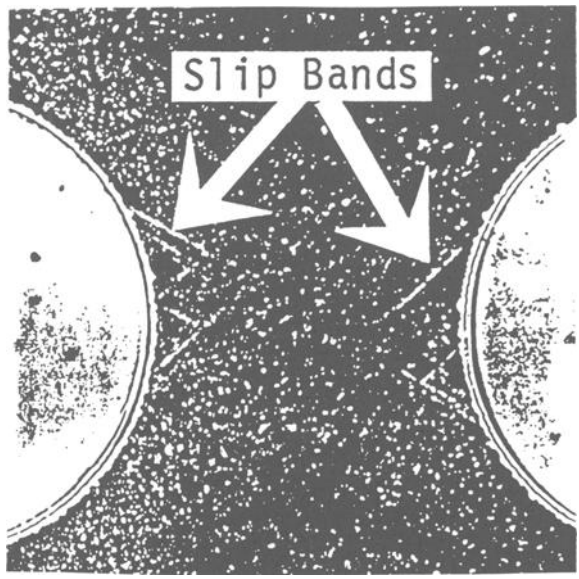


FIG 7b *Micrograph of slip bands forming between fibers prior to failure.*

analysis cases are shown for the two Ramberg-Osgood power law constants listed in Table 2 (n = 13.4 and n = 50). Again, slightly better comparison is seen for the n=50 case. Both the experiment and the analysis results show an initial linear response followed by a slow change to another constant slope. This second slope is that after net section plasticity of the matrix material occurs. Both the initial slope, E_1 = 177 Gpa, and the final slope, E_2 = 133 Gpa are accurately predicted using rule of mixture formulas. For the latter slope, the plastic modulus is used for this purpose.

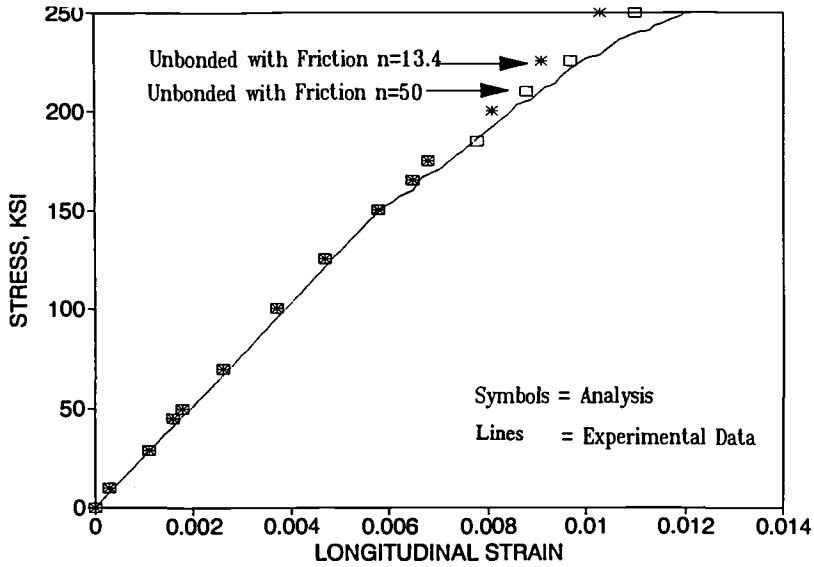
Figure 8b shows the comparison of the width direction strain (again refer back to Figure 1 for clarity) versus the longitudinal strain. Again, a good prediction as compared to experimental data is seen to develop from the model. Although not shown here, the effect of neglecting the HIP pressure as part of the fabrication modeling effort is less important here as compared to the 90-degree load case.

Figure 9 shows the stress state along the fiber/matrix interface at a load of about 1551 Mpa, which is about 90 percent of the failure load. The original stress state due to fabrication is again shown in Figure 5. Here, it is seen that the fiber stress in the fiber direction at this interface is a nearly constant value of 3000 Mpa. The tensile strength of free fibers is about 3000 to 3500 Mpa.

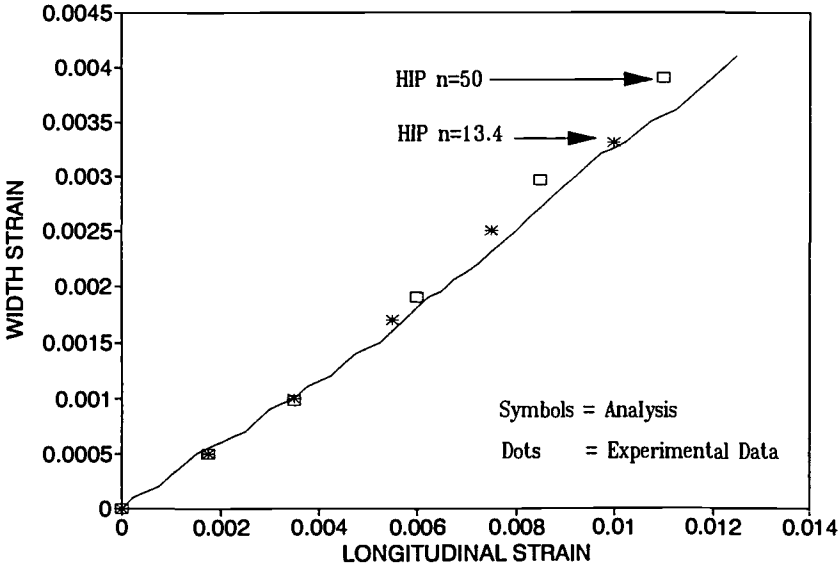
At an applied load of 1720 Mpa, the damage as evaluated using Equation (3) was about 0.3 everywhere in the matrix. The corresponding fiber stress at this load level is about 3500 Mpa. Fiber failure was then modeled by slowly reducing the stiffness in the fiber to a small value. After this, the load is transferred to the matrix. The damage after fiber failure is then greater than 1 everywhere in the matrix, indicating that sudden failure occurs after the fiber fails. This was indeed observed experimentally. Figure 10 shows the development of slip lines for the 0-degree load case. Reaction zone microcracks do develop before the catastrophic failure of this composite. However, these cracks are small, and do not extend across the matrix cross section until fiber failure occurs.

CONCLUSIONS

Here we have shown that micromechanics finite element models with periodic boundary conditions can be successfully used to predict the experimental constitutive response and failure response of unidirectiond MMC systems. Modeling the HIP pressure as a part of the fabrication model is important in order to insure that off axis strain predictions are accurate. Simple local failure models can also be used to predict both the failure loads, and the crack nucleation and failure origination sites. For this system tested at room temperature, the fiber/matrix interface strength was found to be quite weak for this system. However, at higher temperature, the interface appears to exhibit some strength, even though the radial residual contact stresses are smaller compared to room temperature. For this case, the use of the interface element, discussed briefly here, is important. This observation was reported in Reference [16].The results of the material response at higher temperature, including creep response, will be presented shortly in a related publication.



(a) *Predicted stress versus strain compared with experiment.*



(b) *Predicted width (ϵ_w) strain versus longitudinal (ϵ_l) strain compared with experiment.*

FIG 8 *0 - degree load case. Prediction compared with experiment.*

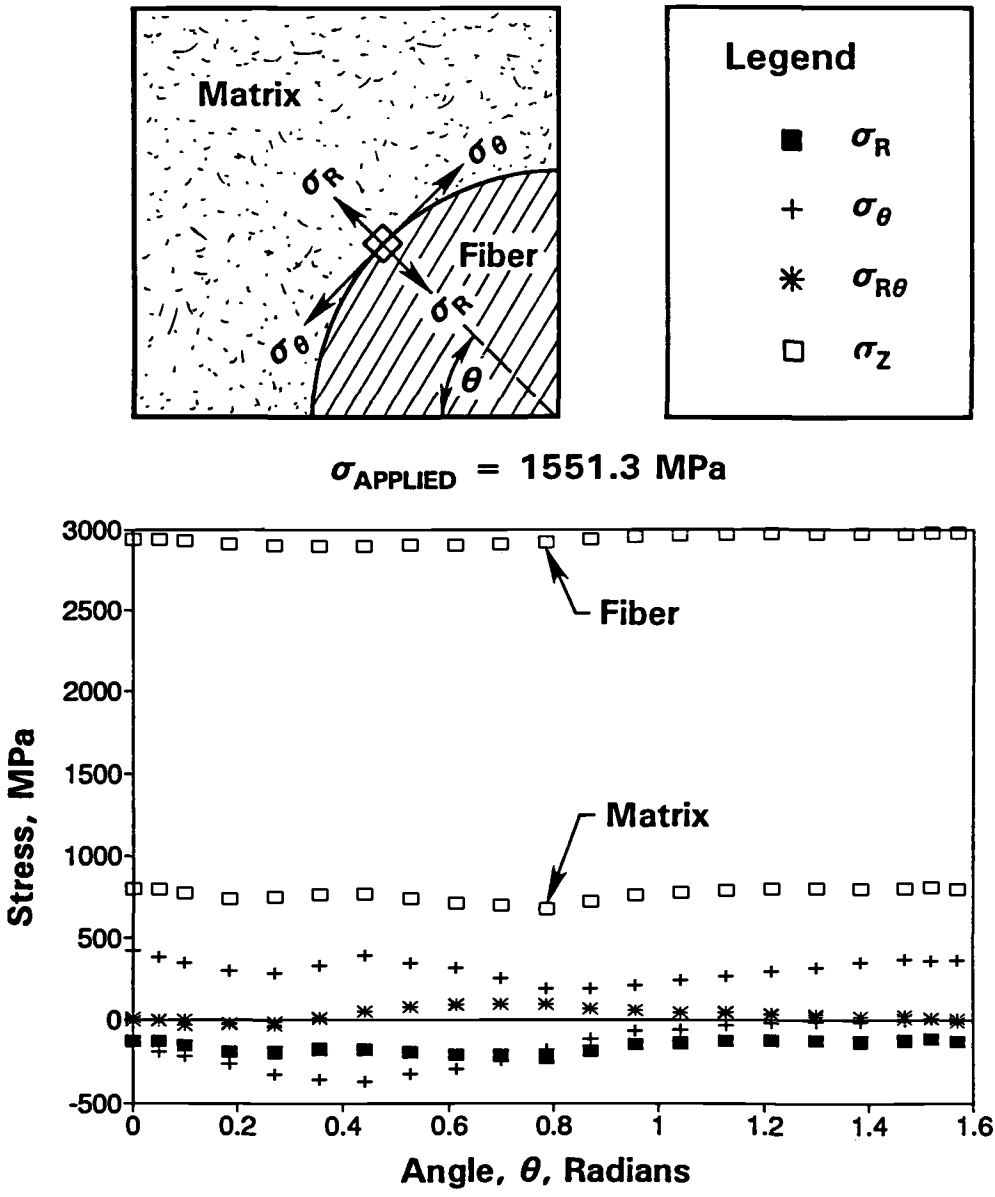


FIG 9 *Fiber/matrix interface stresses for 0-degree load case. Applied load of 1551.3 MPa is about 90% of the failure load.*

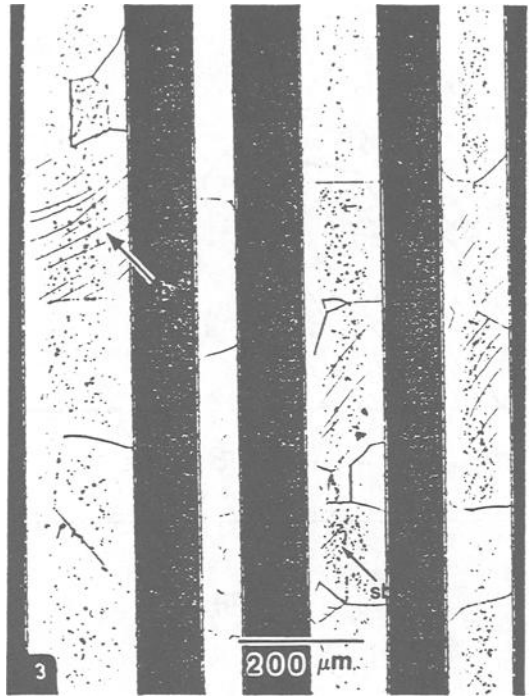


FIG. 10 *Optical micrographs of polished and etched 0-degree load specimen; longitudinal cross section. The loading axis was parallel to the fibers. Slip bands are indicated by arrows.*

REFERENCES

[1] Dix, D., "Keynote Address of 1988 Turbine Technology Symposium - A Focus on the Future", Turbine Engine Division, Aero-Propulsion Laboratory, Wright Research and Devopment Center, P. 6, September, 1988.

[2] Bigelow, C. A., Johnson, W. S., and Naik, R. A., "A Comparison of Various Micromechanics Models for Metal Matrix Composites," Mechanics of Composite Materials, ed. J. N. Reddy and J. L. Telpy, 1989.

[3] Sherwood, J. A., and Boyle, M. J., "Investigation of the Thermomechanical Response of a Titanium Aluminide Metal Matrix Composite Using a Viscoplastic Constitutive Theory," Air Force Contractor Report, Grant No. F33615-88-C-5402, 1990.

[4] Sherwood, J. A., Quimby, H. M., and Doore, R. J., "Non-linear Micromechanics Analysis Predictions of the Behavior of Titanium-Aluminum Matrix Composites", ASME AD-Vol. 27, ed. A. Nagar, pp. 59-64, November 1992.

[5] Nimmer, R. P., Bankert, R. J., Russell, E. S., and Smith, G. A., "Micromechanical Modeling of Fiber-Matrix Interface Effects in SiC/Ti Metal Matrix Composites," presented at the ASM Materials Conference Week, Indianapolis, Indiana, October 2-5, 1989.

[6] Gunawardena, S. R., Jansson, S., and Leckie, F. A., "Transverse Ductility of Metal Matrix Composites," AD-Vol. 22/AMD-Vol. 122, Failure Mechanisms in High Temperature Composite Materials, ASME, New York, 1991.

[7] Arnold, S. M., and Kruch, S., "Differential Continuum Damage Mechanics Models for Creep and Fatigue of Unidirectional Metal Matrix Composites," NASA Technical Memorandum 105213, 1991.

[8] Jones, R. H., Boyd, J. G., and Allen, D. H., "Micromechanical Analyis of Inelastic Composites Including the Effects of Matrix Viscoplasticity and Evolving Damage," Center For Mechanics of Composites, CMC Report No. 91-14, Texas A&M University, November, 1991.

[9] Byrom, T. G., and Allen, D. H., "Effects of Processing Induced Residual Stresses on Damage Dependent Micromechanics of Metal Matrix Composites", ASME AMD - Vol. 150/AD- Vol. 32, Damage Mechanics in Composites, Ed. D. H. Allen and D.C. Lagoudas, pp. 233-253, 1992.

[10] Gosz, M., Moran, B., and Achenbach, J. D., "Matrix Cracking in Transversely Loaded Fiber Composites with Compliant Iterphases," AMD-Vol. 150/AD - Vol. 32, Damage Mechanics in Composites, Ed. D. H. Allen and D. C. Lagoudas, 1992.

[11] Bahei-El-Din, Y. A., Dvorak, G. J., and Wu, J., "Fracture of Fibrous Metal Matrix Composites - II. Modeling and Numerical Analysis", Engineering Fracture Mechanics, Vol. 34, No. 1, pp. 105-123, 1989.

[12] Mital, S. K., Caruso, J. J., and Chamis, C. C., "Metal Matrix Composites Microfracture: Computational Simulation," NASA Technical Memorandum 103153, 1990.

[13] Naik, R. A., Johnson, W. S., and Dicus, D. L., "Micromechanical Thermal Analysis of Interphase Region in a Titanium Aluminide MMC," presented at the Ti-Al MMC Composites Workshop, Orlando, Florida, May 16-18, 1990.

[14] Needleman, A., "A Continuum Model for Void Nucleation by Inclusion Debonding," Journal of Applied Mechanics, Vol. 54, pp. 525-531, 1987.

[15] Needleman, A. and Tvergaard, V., " An Analysis of Ductile Rupture Modes at a Crack Tip," J. Mech. Phys. Solids, Vol. 35, pp. 151-183, 1987.

[16] Brust, F. W., Newaz, G. M., and Majumdar, B. S., "Damage Development in Metal Matrix Composites Including Plasticity And Creep Effects," Presented at ICF-8, Kiev, Ukraine, June 1993. Also to appear in Material Science Journal.

[17] Castelli, M. G., Bartolotta, P. A., and Ellis, J. R., "Thermomechanical Fatigue Testing of High Temperature Composites: Thermomechanical Fatigue Behavior of SiC *(SCS-6)/Ti-15-3,"* Composite Materials: Testing and Design (Tenth Volume, ASTM STP 1120, American Society for Testing and Materials, Philadelphia, 1991.

[18] Gabb, T. P., Gayda, J., and MacKay, R. A., "Isothermal and Nonisothermal Fatigue Behavior of a Metal Matrix Composites," Journal of Composite Materials, Vol. 24, pp. 667-686.

[19] Russ, S. M., Nicholas, T., Bates, M. and Mall, S., "Thermomechanical Fatigue of SCS-6/Ti-24AL-11NB Metal Matrix Composites," AD-Vol. 22/AMD-Vol. 122, Failure Mechanisms in High Temperature Composite Materials, ASME, New York, 1991.

[20] Mirdamadi, M., Johnson, W. S., Bahei-El-Din, Y. A., and Castelli, M. G., "Analysis of Thermomechanical Fatigue of Unidirectional Titanium Metal Matrix Composites," NASA Technical Memorandum 104105, 1991.

[21] Newaz, G., Majumdar, B., and Brust, F. W., "Thermo-Cycling Response of Quasi-Isotropic Metal Matrix Composites," Journal of Engineering Materials and Technology, Vol. 114, pp. 156-161, April, 1992.

[22] Majumdar, B. S., and Newaz, G. M., "Inelastic Deformation in Metal Matrix Composites: Plasticity and Damage Mechanisms," Philosophical Magazine, Vol. 66, No. 2, pp. 187-2 12, London, 1992.

[23] Majumdar, B. S. and Newaz, G. M., "Thermomechanical Fatigue of a Quasiisotropic Metal Matrix Composite," Composite Materials: Fatigue and Fracture, ASTM STP 1110, Ed. T. K. O'Brien, 1991.

[24] Brust, F. W., Majumdar, B., and Newaz, G. M., "Constitutive Response Analysis of Metal Matrix Composites Via the Unit Cell Model", presented at the 11th ASTM Symposium on Composite Materials: Testing and Design, Pittsburgh, Pennsylvania, May 4-8, 1992.

[25] Newaz, G. M., and Majumdar, B. S., "Deformation and Failure Mechanisms in Metal Matrix Composites", Failure Mechanisms in High Temperature Composites, AD-Vol. 22, presented at the ASME Winter Annual Meeting, Atlanta, Georgia, December, 1991.

[26] Majumdar, B. S., Newaz, G. M., Brust, F. W., and Ellis, J. R., "Deformation Mechanisms In A Ti-Alloy/SiC Metal Matrix Cornposite", Proc. of the VII World Conference on Titanium, San Diego, June, 1992.

[27] Needleman, A., "A Continuum Model for Void Nucleation by Inclusion Debonding", Journal of Applied Mechanics, Vol. 54, pp. 525-531, 1987.

[28] Needleman, A., "An Analysis of Tensile Decohesion Along An Interface," J. Mech. of Phys. Solids, Vol. 38, 1990.

[29] Povirk, G., Needleman, A., and Nutt, S. R., Material Science Engg., A132, pp. 31-38, 1991.

[30] Tai, W. H., and Yang, B. X., "A New Damage Mechanics Criterion For Ductile Fracture," Engineering Fracture Mechanics, Vol. 27, No. 4, pp. 371-378, 1987.

[31] Hancock, J. W., and MacKenzie, A. C., "On The Mechanisms of Ductile Failure in High-Strength Steel Subjected to Multi-Axial Stress States", J. Mech. Phys. Solids, Vol. 24, pp. 147-169, 1976.

John H. Underwood,[1] Mark T. Kortschot,[2] W. Randolph Lloyd,[3]
Harvey L. Eidinoff,[4] Dale A. Wilson,[5] and Noel Ashbaugh[6]

TRANSLAMINAR FRACTURE TOUGHNESS TEST METHODS AND RESULTS FROM INTERLABORATORY TESTS OF CARBON/EPOXY LAMINATES

REFERENCE: Underwood, J. H., Kortschot, M. T., Lloyd, W. R., Eidinoff, H. L., Wilson, D. A. and Ashbaugh, N., "**Translaminar Fracture Toughness Test Methods and Results from Interlaboratory Tests of Carbon/Epoxy Laminates,**" Fracture Mechanics: 26th Volume, ASTM STP 1256, Walter G. Reuter, John H. Underwood and James C. Newman, Jr., Eds., American Society for Testing and Materials, Philadelphia, 1995.

ABSTRACT: Fracture tests were performed with carbon/polymer laminates and analyzed for the purpose of developing translaminar fracture toughness test and analysis procedures. Notched specimens were tested of two types of symmetrical layups - quasi-isotropic [0/45/90] and [0/90]; two carbon fiber/epoxy materials - a relatively brittle T300 fiber/976 epoxy and a tougher AS4 fiber/977-2 epoxy; two laminate thicknesses - 2 mm and 4 mm; and three specimen configurations - the standard three-point bend and compact configurations, and an extended compact specimen with arm-height to specimen-width ratio of 1.9. Stress and displacement expressions were obtained for the extended compact specimen, including those for stress intensity factor, K, and crack mouth opening displacement, V, in terms of relative notch length, a/W, and for a/W in terms of V. Relationships for the bending stresses that control self-similar and off-axis cracking for the extended compact specimen were derived.

Damage was characterized in the tests, including that associated with arm breakage in the standard compact specimen and load-point damage in the bend

[1] Research Engineer, Army Armament RD&E Center, Watervliet, NY, 12189
[2] Professor of Chemical Engineering & Applied Chemistry, University of Toronto, Toronto, Canada, M5S 1A4
[3] Engineering Specialist, Idaho National Engineering Laboratory, Idaho Falls, ID, 83415
[4] Group Manager of Structural Mechanics, Northrup-Grumman Corp., Bethpage, NY, 11714
[5] Professor of Mechanical Engineering, Tennessee Technological University., Cookeville, TN, 38505
[6] Senior Engineer, University of Dayton Research Institute, Dayton, OH, 45469

Copyright© 1995 by ASTM International www.astm.org

specimen. Two types of notch-tip damage were characterized using radiography, that which extends perpendicular to the notch in predominantly 0° fiber layups, and that which occurs ahead of the notch in quasi-isotropic and 90° fiber layups.

The applied K at maximum load, K_{max} , determined in a way that took account of the effective crack growth up to the maximum load point, was used as a measure of fracture toughness. For deviations from the linear P-V plot corresponding to $\Delta a/W \leq 0.04$, K_{max} gave consistent measurements of fracture toughness. This criterion also excluded tests with damage of the type that violates the basic concept of fracture toughness measurement. Plots of K_{max} vs $\Delta a/W$ showed increasing resistance to crack growth for quasi-isotropic layups and constant resistance to crack growth for predominantly 90° fiber layups.

KEYWORDS: fracture toughness, laminated composites, carbon/epoxy, notch-tip damage, X-ray radiography, translaminar fracture, specimen configuration

INTRODUCTION

The definitive research on the development of translaminar fracture toughness test methods for carbon/epoxy laminates is the work of Harris and Morris [1,2]. They performed load versus crack opening displacement experiments, notch-tip damage characterization and finite element K analysis for a wide variety of notched, carbon/epoxy, cross-ply specimens. They observed consistent values of fracture toughness and similar types of damage in center-notched, compact, and three-point bend specimens of varying thickness. Their work addressed the translaminar fracture behavior of laminates with through-thickness defects, as opposed to the more common concern with interlaminar fracture of composite laminates. Interlaminar fracture toughness has received considerably more attention, because of the inherent weakness of delamination compared with thru-thickness fracture of a cross-ply laminate. The work of O'Brien et al [3] describes one part of the extensive development of interlaminar fracture toughness test methods.

There are, however, situations in which through-thickness translaminar fracture is of concern with laminates. Battlefield damage to composite structures can be through-thickness, as can inadvertent projectile impact with commercial aircraft structures. The use of laminates with too few cross plies is another situation in which translaminar fracture is important. Recent work by some of the current authors and others has addressed the development of translaminar fracture toughness tests, using the work of Harris and Morris [1,2] as a guide. Center-notched panels of two carbon/polymer laminates [4] gave consistent values of fracture toughness in tests with a relatively brittle matrix or with a significant portion of cross-ply fibers. For a tougher matrix or with predominantly 0° fibers, splitting perpendicular to the notch line caused a significant increase in the apparent fracture toughness. Load versus deflection plots and radiographs of notch-tip damage in compact specimens of a quasi-isotropic carbon/epoxy laminate [5] gave similar results to those of reference [4]. For some tests limited notch-tip damage and consistent fracture toughness values were

observed. For other tests splitting and extensive damage in a direction perpendicular to the notch and increased apparent toughness values were observed.

The objectives of the work here are to identify a specimen configuration and data analysis methods that produce consistent measurements of fracture toughness for carbon/polymer laminates for a wide range of material and layup conditions. Each of the three specimen configurations that has been used for fracture toughness tests of laminates has its problems. The center-notched panel requires a relatively high load for a given applied K value and a large amount of material. The compact specimen has an inherent weakness in its loading arms, which, as shown in the results here, can be a problem for predominantly 0° fiber laminates. The three-point bend specimen has a loading point in close proximity to the notch tip, which, as shown here, can cause a problem. Regarding data analysis methods, the X-ray characterization of notch-tip damage has been shown to be crucial to the understanding the test results, but radiographs are too complex to be made part of a routine test and analysis method. What is needed is a method of analyzing the load-deflection data from the test that gives some of the same damage information without the complexity of radiography. The thorough analysis of several series of load-deflection tests and the associated notch-tip damage from radiographs will be used to identify test configurations and data analysis methods that give simple yet consistent fracture toughness measurements.

PARTICIPANTS AND TEST PLAN

The overall plan of test and analysis was developed as part of the technical committee meetings of ASTM Committee E8 on Fatigue and Fracture. A number of university, government and industry laboratories were interested in the topic of

TABLE 1 -- Laboratory participants

LABORATORY	PARTICIPATION
Lab 1; Army Armament RD&E Center	- fracture tests / analysis - coordination of tests
Lab 2; University of Toronto	- fracture tests - damage characterization
Lab 3; Idaho National Engineering Laboratory	- fracture tests - damage characterization
Lab 4; Grumman Aerospace	- fracture tests
Lab 5; Tennessee Technological University	- fracture tests
Lab 6; University of Dayton Research Institute	- damage characterization

translaminar fracture toughness of laminates. The laboratories that could devote the time and resources at the time the tests began are shown in Table 1. These laboratories performed the various tests and analyses described here in a cooperative program, with administrative support from ASTM Committee E8. The two main tasks were performing the fracture tests and analysis and characterizing the notch-tip damage that accompanies fracture.

Materials

The materials tested were T300 carbon fiber/976 epoxy and AS4 carbon fiber/977-2 toughened epoxy, each in two symmetrical [0/45/90] and [0/90] lay-ups, as shown in Table 2. The [0/45/90] lay-ups were selected because of the common usage of quasi-isotropic laminates in composite structures. The $[0_2/90]$ and $[90_2/0]$ lay-ups were selected to investigate the problems that can arise in fracture testing of materials with considerable orthotropy. The laminates were made in the form of a 0.45 m by 0.50 m plate with thickness that varied by up to ±6% from the mean values in Table 2. The mean values were used for all calculations.

TABLE 2 -- Test conditions and elastic modulus results

material / thickness	Calculated Elastic Modulus, E; GPa: 3-point bend	standard compact	extended compact
	( ) - number of tests performed		
T300/976 LAMINATES			
$[0/+45/90/-45]_{4s}$; 2.1 mm:	54 (2)	57 (2)	55 (2)
$[90/-45/0/+45]_{4s}$; 2.1 mm:	47 (2)	55 (4)	59 (2)
$[0/0/90]_{6s}$; 2.4 mm:	47 (1)	37 (2)	45 (2)
$[90/90/0]_{6s}$; 2.4 mm:	33 (2)	32 (2)	34 (2)
AS4/977-2 LAMINATES			
$[0/+45/90/-45]_{4s}$; 4.2 mm:	52 (2)	60 (2)	53 (2)
$[90/-45/0/+45]_{4s}$; 4.2 mm:	55 (6)	58 (12)	56 (2)
$[0/0/90]_{6s}$; 4.8 mm:	45 (2)	30 (5)	44 (2)
$[90/90/0]_{6s}$; 4.8 mm:	32 (3)	29 (3)	34 (2)

Specimens

The initial plan was to use the compact and three-point bend specimens for the tests, the same configurations (except for thickness) as those used for many other fracture tests, such as in ASTM Test Method for Plane-Strain Fracture Toughness of Metallic Materials (E 399). These configurations are shown in Fig. 1. Also shown is

the typical notch detail that was used, including the 0.3 mm notch width and the integral knife edges that were machined at the crack mouth. Both of these features are important for consistent results. Notch widths much larger than 0.3 mm would be expected to cause increases in apparent toughness [1, 4]. And non-integral knife edges can introduce errors in the measured crack-mouth displacement and an improper interpretation of test results.

As the work progressed, problems arose with the compact and three-point bend specimens, as will be discussed later. This led to the use of a third specimen configuration, called the extended compact, see Fig. 1[d]. This type of specimen was used by Richardson and Goree [6] in fracture testing and failure modeling of aluminum, using a half-height of the loading arms relative to specimen width, H/W, of 1.2. Recently, Piascik and Newman [7] calculated values of applied stress intensity factor, K, and crack-mouth displacement, V, for an extended compact specimen with H/ W = 1.9, the configuration chosen for use here. Note that, in addition to the different H/W compared with the standard compact specimen, the extended compact has different definitions of W and a, the notch length. W is the full width of the specimen and a is measured from the edge of the specimen. A summary of the number of tests performed with each type of specimen is given in Table 2.

K AND DISPLACEMENT EXPRESSIONS

Accurate, wide range expressions for elastic K and V in terms of load, P, and specimen dimensions and a/W in terms of P and V are needed for analysis of the P versus V plots. For the standard compact and bend specimens this information is readily available, since it is commonly used in various fracture tests. For the extended compact specimen, basic elastic stress analysis results [7] are used here to develop new expressions. It is recognized that the K and V expressions should account for the anisotropic nature of laminates. This was considered to be beyond the scope of this work and is the subject of a continuing effort.

Three-Point Bend Specimen

The dimensionless applied stress intensity factor, $KBW^{1/2}/P$, is [8]

$$KBW^{1/2}/P = [3\,\alpha^{1/2}\,S/W]\,[1.99 - \alpha(1-\alpha)(2.15 - 3.93\,\alpha + 2.7\,\alpha^2) / 2(1+2\alpha)(1-\alpha)^{3/2}]$$

$$\text{for } 0 \le \alpha \le 1 \text{ and } S/W = 4 \qquad (1)$$

where B is thickness, S is span, and α = a/W, relative notch depth. The dimensionless elastic crack-mouth displacement, VEB/P, is [9]

$$VEB/P = [6\,\alpha\,S/W]\,[0.76 - 2.28\,\alpha + 3.87\,\alpha^2 - 2.04\,\alpha^3 + 0.66/(1-\alpha)^2]$$

$$\text{for } 0 \le \alpha \le 1 \text{ and } S/W = 4 \qquad (2)$$

where E is elastic modulus. The inverse of Eq. (2), giving α in terms of VEB/P [10], is

$$\alpha = 0.999748 - 3.9504\ u + 2.9821\ u^2 - 3.21408\ u^3 + 51.51564\ u^4 - 113.031\ u^5$$

$$\text{for } u = 1/[(VEB/P)^{1/2} + 1] \quad \text{and} \quad 0.2 \le \alpha \le 1 \ . \tag{3}$$

Standard Compact Specimen

The $KBW^{1/2}/P$ expression is [8]

$$KBW^{1/2}/P = [2+\alpha]\,[0.886 + 4.64\,\alpha - 13.32\,\alpha^2 + 14.72\alpha^3 - 5.6\,\alpha^4] \,/\, [1-\alpha]^{3/2}$$

$$\text{for } 0.2 \le \alpha \le 1 \ . \tag{4}$$

The VEB/P expression is [11]

$$VEB/P = [1+\alpha]^2\ [2.163 + 12.219\,\alpha - 20.065\,\alpha^2 - 0.9925\,\alpha^3 + 20.609\,\alpha^4 - 9.9314\,\alpha^5] \,/\, [1-\alpha]^2$$

$$\text{for } 0.2 \le \alpha \le 1 \ . \tag{5}$$

The α expression is [12]

$$\alpha = 1.000196 - 4.06319\ u + 11.242\ u^2 - 106.043\ u^3 + 464.335\ u^4 - 650.677\ u^5$$

$$\text{for } u = 1/[(VEB/P)^{1/2} + 1] \quad \text{and} \quad 0.2 \le \alpha \le 1 \ . \tag{6}$$

Extended Compact Specimen

Recent numerical results [7] provide the basis for K and displacement expressions for the extended compact specimen. The results, for the configuration shown in Fig. 1 (d) are summarized in Table 3. These results were used here to obtain expressions in the same form as Eqs. 1-6, above, using regression analysis and also fitting to the shallow and deep crack limit solutions as in recent work [13]. The resulting K expression is

$$KBW^{1/2}/P = \alpha^{1/2}\,[1.4+\alpha]\,[3.97 - 10.88\,\alpha + 26.25\,\alpha^2 - 38.9\,\alpha^3 + 30.15\,\alpha^4 - 9.27\,\alpha^5] \,/\, [1-\alpha]^{3/2}$$

$$\text{for } 0 \le \alpha \le 1 \ . \tag{7}$$

Equation (7) fits the numerical results and the limits within 0.4 %, except for the numerical results at the two extremes (a/W = 0 and 0.92), which are 0.9% below and

0.7% above the values from Eq. (7), respectively. The VEB/P expression is

$$VEB/P = [15.52\,\alpha - 26.38\,\alpha^2 + 49.70\,\alpha^3 - 40.74\,\alpha^4 + 14.44\,\alpha^5] / [1-\alpha]^2$$

$$\text{for } 0 \le \alpha \le 1 \ , \qquad (8)$$

which fits the numerical results and the limits within 0.3 %, except for a/W = 0.92 where the numerical result is 0.7 % above the value from Eq. (8) . The inverse of Eq. (8) is

$$\alpha = 1.0004 - 3.5495\,u + 6.0988\,u^2 - 16.0075\,u^3 + 32.3436\,u^4 - 22.2843\,u^5$$

$$\text{for } u = 1/[(VEB/P)^{1/2} + 1] \quad \text{and} \quad 0.15 \le \alpha \le 1 \ . \qquad (9)$$

Equation (9) fits the numerical results and the deep crack limit within 0.04 % over the range $0.15 \le \alpha \le 1$.

TABLE 3 -- K and displacement results for extended compact specimen [7]

a/W	$KBW^{1/2}/P$	VEB/P	a/W	$KBW^{1/2}/P$	VEB/P
0.100	1.721	1.664	0.600	10.25	40.30
0.150	2.155	2.622	0.650	12.88	57.58
0.200	2.586	3.750	0.700	16.67	85.51
0.250	3.049	5.127	0.725	19.24	106.2
0.300	3.571	6.853	0.750	22.48	134.1
0.350	4.178	9.072	0.775	26.66	172.6
0.400	4.904	11.99	0.800	32.21	227.6
0.450	5.792	15.91	0.825	39.84	309.7
0.500	6.907	21.33	0.840	45.95	379.5
0.550	8.343	29.02	0.920	136.4	1743.

The numerical results for $KBW^{1/2}/P$ and VEB/P are compared with Eqs. (7) and (8) in Fig. 2. Note that functions of a/W derived from the shallow and deep crack K and V limits have been used in the plot, in order to obtain finite values over the entire range of a/W. It is clear that the numerical results and the fitted expressions are well behaved and properly approach the known, exact limits.

Notch-Tip Stresses

The notch-tip splitting and damage that extends off the axis of the notch, discussed earlier, occurs in compact specimen tests of other materials [14]. In Ref [14] calculations of the nominal bending stress in two directions at the notch tip were made which showed why off-axis splitting occurred in standard compact specimens and did not occur in bend specimens. These calculations are summarized as follows.

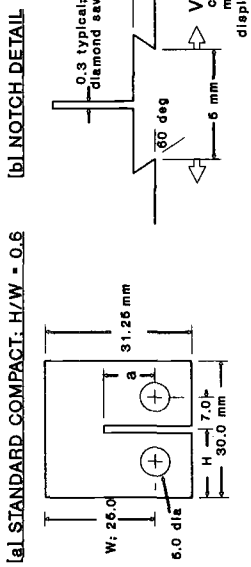


FIG. 1 - *Specimen configurations*

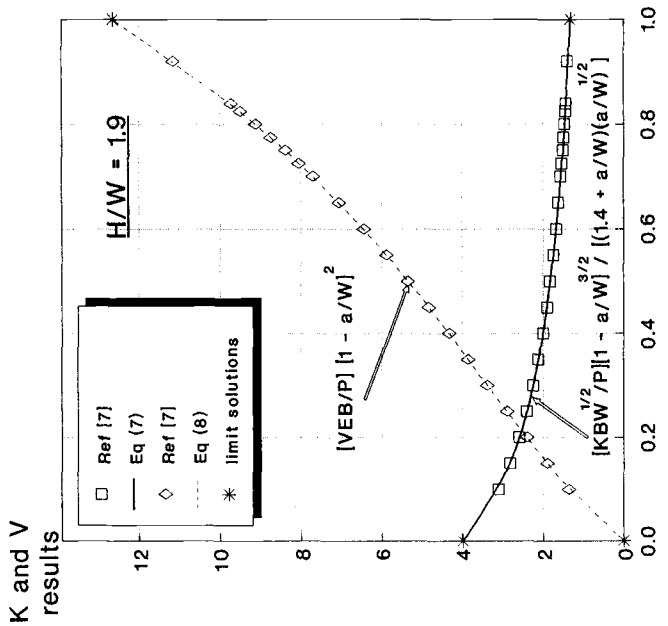


FIG. 2 - *Stress intensity and displacement results for the extended compact specimen.*

For the standard compact specimen

$$S_Y W^{1/2}/K = 3(1+\alpha) / f_C (1-\alpha)^2 \quad (10)$$

$$S_X W^{1/2}/K = 16.67 \alpha / f_C \quad (11)$$

where S_Y and S_X are the nominal, notch-tip bending stresses that control self-similar and off-axis cracking, respectively, and $f_C = KBW^{1/2}/P$ for the compact specimen. For the bend specimen

$$S_Y W^{1/2}/K = 1.5 / f_B \ (1-\alpha)^2 \quad (12)$$

$$S_X W^{1/2}/K = 0.375 / f_B \quad (13)$$

where $f_B = KBW^{1/2}/P$ for the bend specimen.

Similar calculations were made here for the extended compact specimen, as follows, referring also to Fig. 3. The expression

$$S_Y = 6 M / B (W-a)^2 \quad (14)$$

gives the y-direction nominal bending stress that drives self-similar cracking from the notch, where the applied moment, M, is

$$M = P [a - 0.2 W + (W-a)/2] \ . \quad (15)$$

Combining Eqs. (14), (15) and (7) gives

$$S_Y W^{1/2}/K = 3(0.6 + \alpha) / f_E (1-\alpha)^2 \quad (16)$$

where, as before, $f_E = KBW^{1/2}/P$, from Eq. (7) in this case. For the x-direction bending stress that drives off-axis cracking

$$S_X = 6 M / B H^2 \quad \text{and} \quad (17)$$

$$M = 6 P (a - 0.2 W) \quad (18)$$

and the result is

$$S_X W^{1/2}/K = 16.67 (\alpha - 0.2) / f_E \quad (19)$$

Equations (10-13), (16) and (19) are plotted in Fig. 3. They compare the bending stresses that control self-similar and off-axis cracking for the three specimen configurations. The plot of $SW^{1/2}/K$ provides a dimensionless comparison of these important bending stresses at any given applied K level and for a range of a/W. For the standard compact specimen at relatively small a/W the off-axis bending stress approaches the same magnitude as that for self-similar cracking. This explains the off-

axis cracking problems with this specimen. Note that this problem is not expected for the extended compact specimen, nor for the three-point bend specimen. The large dimensions of these specimen configurations in the direction perpendicular to the notch reduces the bending stress, S_X (also referred to as the T-stress), that drives off-axis cracking, so that this type of cracking does not occur.

RESULTS AND DISCUSSION

Load-Displacement and Modulus

Load versus crack-mouth-displacement tests were performed for each of the twenty four test conditions summarized in Table 2, that is, for each of the three specimen configurations and the eight laminates. Figures 4 and 5 show the measured loads and displacements for the AS4/977-2 material in [0/0/90] layup and the T300/976 material in [90/-45/0/+45] layup, respectively. The types of load-displacement behavior shown in Fig. 4 and 5 are the two general types noted in the tests, a predominantly nonlinear P-V plot with an early and significant deviation from initial linearity, and a predominantly linear plot with just a few nearly linear unloading and reloading segments. The nonlinear plots were typically from specimens with more 0° fibers and those made of the AS4/977-2 material. Note in Fig. 4 that the extremely nonlinear P-V plot from a [0/0/90] standard compact specimen was associated with a splitting failure of the specimen arm in a direction perpendicular to the notch axis.

For all tests an accurate measurement of the initial linear slope was possible. Using the slope, the initial notch depths and Eqs. (2), (5) and (8), calculations of elastic modulus were made and listed in Table 2. In general the measured modulus was in the expected range [1]. Also of interest are the differences in measured modulus for certain combinations of specimen configuration and layup. Note the relatively low E values for the [0/0/90] standard compact tests. The low E may be an indication of an imminent splitting-type of arm failure, discussed above, since it occurred with the same combination of configuration and layup. Note one other relatively low E value, that for the [90/-45/0/+45] T300/976 three-point bend tests. This low E value is believed to be due to the type of damage that occurs ahead of the notch in the three-point bend specimen, discussed next.

Notch-Tip Damage

A potential problem with the close proximity of the middle load point and the notch tip in the three-point bend specimen was noted during testing. Damage could be seen by the unaided eye around the load point. To investigate this further, specimens were unloaded just after the maximum load had been attained and inspected for notch-tip and load point damage using an ultrasonic test method. A through-transmission attenuation method was used that scanned the unloaded specimens. Figure 6 shows results for two layups of the AS4/977-2 material. The [90/90/0] specimen shows a quite well developed notch-tip damage zone and no evidence of damage at the load point, whereas the [90/-45/0/+45] specimen, with a smaller notch-tip damage zone,

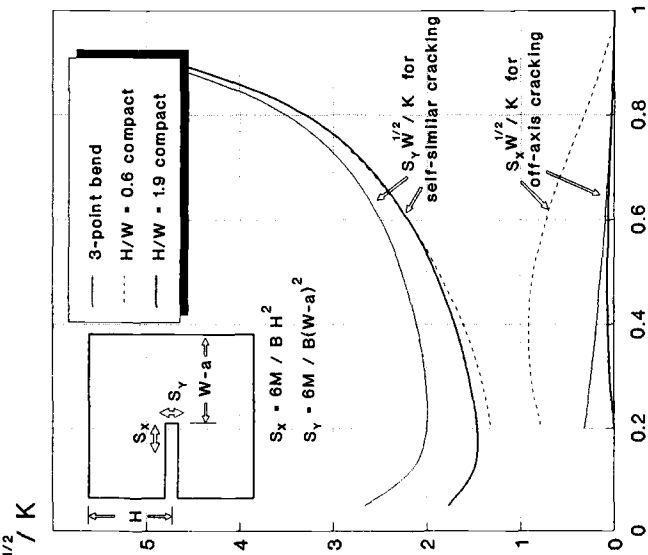


FIG. 3 - *Stresses controlling off-axis and self-similar cracking in bend, compact and extended compact specimens.*

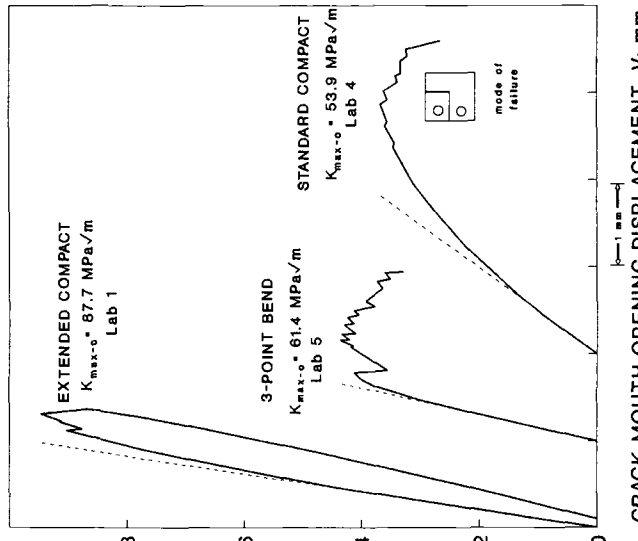


FIG. 4 - *Load vs V for bend, compact and extended compact specimens; AS4/977-2 with [0/0/90] layup*

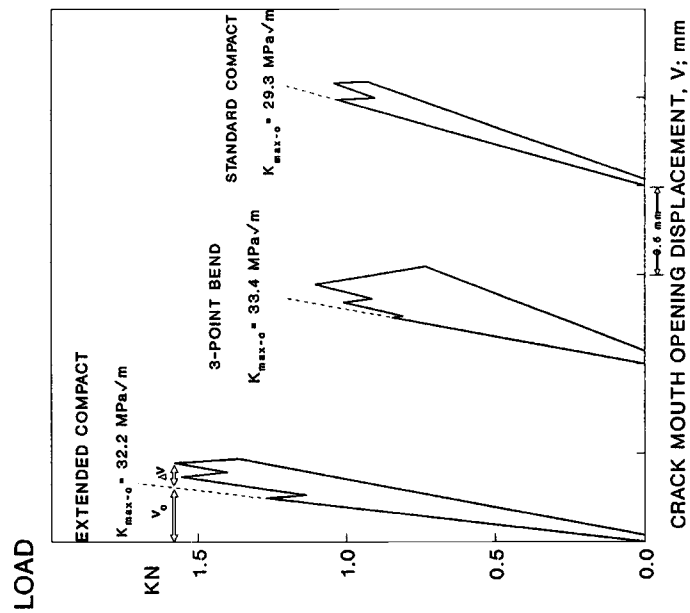


FIG. 5 - *Load vs V for bend, compact and extended compact specimens; T300/976 with [90/-45/0/45] layup*

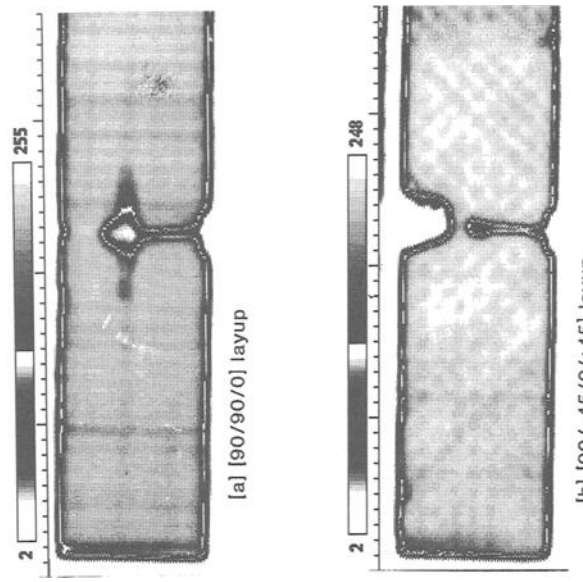


FIG. 6 - *Ultrasonic attenuation in notch-tip and load-point damage zones for AS4/977-2 laminates*

shows considerable load-point damage. It is clear that, for some layups, the three-point bend specimen is inadvisable for use in fracture toughness testing.

The arm failure problem with the standard compact specimen and the load-point problem with the three-point bend specimen led to the interest in the extended compact specimen. Characterization of the notch-tip damage zone development and any significant load-point damage with the extended compact specimen was performed using the X-ray infiltration method [15]. Specimens of each of the eight material and layup combinations in Table 2 were unloaded just after maximum load had been attained and inspected by radiography. Selected results are shown in Figs. 7 and 8. The only damage noted in all samples was associated with the notch. No damage was observed at the holes. However, had a layup been tested with more than a 2:1 ratio of 0° to 90° fibers, hole pullout might have been experienced.

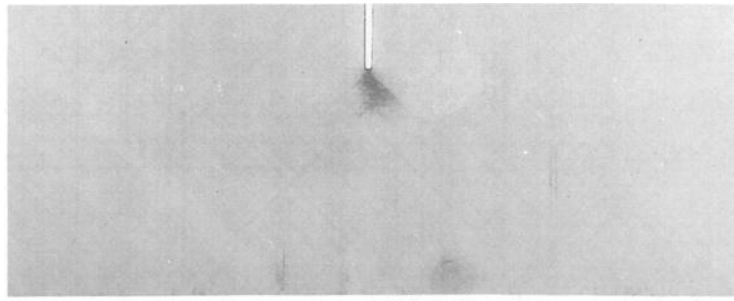
The AS4/977-2 results in Fig. 7 are interpreted as: a damage zone extends primarily ahead of the notch tip for the [90/-45/0/+45] layup (with very similar results for the [0/+45/90/-45] layup, not shown); a zone extends perpendicular to the notch by splitting along the 0° fibers for the [0/0/90] layup; an intense zone and effective crack growth occur directly ahead of the notch and lesser damage extends perpendicular to the notch for the [90/90/0] layup.

The T300/976 results in Fig. 8 are similar in general nature to those in Fig. 7, but with larger damage zones and more effective crack growth because the more brittle T300/976 material sustained more damage before the unloading could be accomplished. The [90/-45/0/+45] layup zone extends primarily ahead of the notch, as with the other material, but an intense damage zone and effective cracking directly ahead of the notch can also be seen. The [0/0/90] zone extends perpendicular to the notch, as with the other material , but intense damage directly ahead of the notch can also be seen. The [90/90/0] damage zone is dominated by intense damage directly ahead of the notch, with significant damage perpendicular to the notch occurring in only two locations. These locations are believed to correspond to specific linear segments of the P-V curve, of the type shown in Fig. 5.

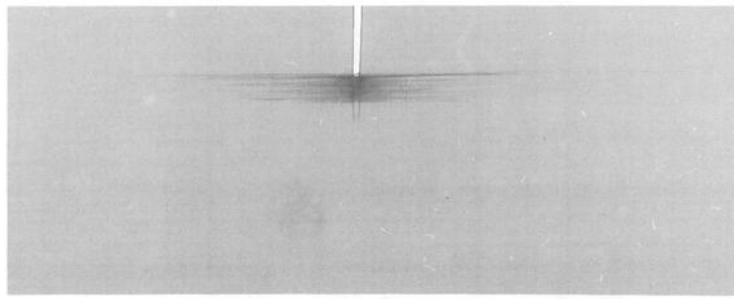
In summary, the infiltration radiographs showed damage extending ahead of the notch and, for layups with a significant portion of 0° fibers, damage extending perpendicular to the notch. As the damage zone grows, an area of intense damage directly ahead of the notch occurs that is associated with effective through-thickness crack growth ahead of the notch. The extension of damage ahead of the notch tip was measured from the radiographs for fifteen extended compact specimens (the unloading of one specimen was not quick enough). Comparison of these measurements of effective crack growth with calculations of crack growth based on the P-V plots is presented next.

Calculated Crack Growth

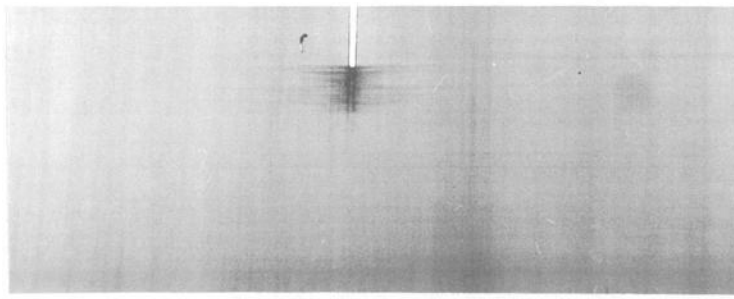
Calculations of crack growth were made from the unloading slope of the P-v plots, using Eqs. (3), (6) and (9) and the E values determined from the loading slope. These calculations are compared in Fig. 9 with the measured full extent of the damage zone from radiographs taken after unloading, such as those in Figs. 7 an 8. In prior work [5] with standard compact specimens of the same AS4/977-2 [0/+45/90/-45]



[a] [90/-45/0/+45] layup

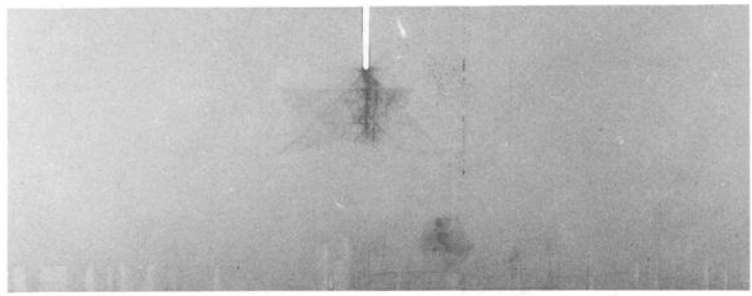


[b] [0/0/90] layup

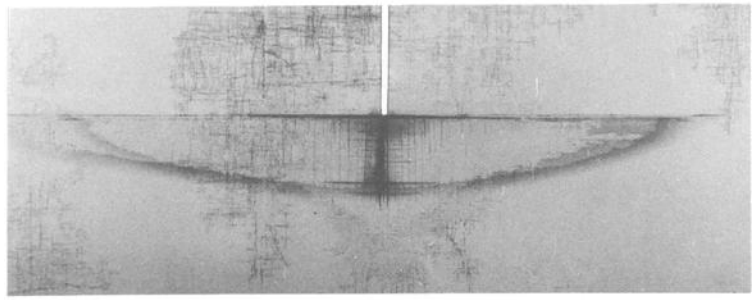


[c] [90/90/0] layup

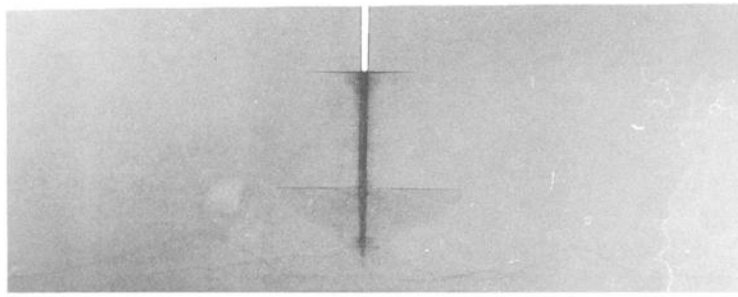
FIG. 7 - Infiltration radiographs of damage in AS4/977-2 laminates.



[a] [90/-45/0/+45] layup



[b] [0/0/90] layup



[c] [90/90/0] layup

FIG. 8 - Infiltration radiographs of damage in T300/976 laminates.

laminate used here, the unloading slope calculation of crack growth was found to correspond to about 80% of the full extent of the radiographic damage zone. In Fig. 9 the regression line indicates that unloading slope crack growth averages 76% of the full extent of the radiographic damage zone. Thus, the results for extended compact specimens of two materials and various layups show a similar close relationship between unloading-slope crack growth and damage zone, as was the case in the prior work.

Additional crack growth calculations were made just beyond the P_{max} point in the test, based on the additional increment of crack-mouth-displacement, ΔV , beyond the initial linear P-V plot, V_o , see Figure 5. The calculation was made by modifying Eq. 9 with a different expression for u, as follows

$$u_{max} = 1 / [(V_o\, EB/P_{max} + \Delta V\, EB/P_{max})^{1/2} + 1] \quad . \tag{20}$$

where u_{max} corresponds to the total relative notch-plus-crack length at P_{max} *including* the crack growth associated with ΔV. Combining Eq. (20) with (9) (or with the appropriate expressions for the other specimen configurations) gives a method to calculate elastic crack growth at P_{max} . For P-V plots such as those in Fig. 5, with displacements that are predominantly elastic, this calculation is appropriate. For plots such as those in Fig. 4 , comparison of results may indicate whether or not it is appropriate. A comparison of crack growth calculated using ΔV (Eq. 20) with that using the unloading slope just after P_{max} (Eqs. 3,6,9) is shown in Fig. 10, for all tests for which both calculations were possible. The two calculations are in good agreement, as shown by the regression line lying close to the dashed line that indicates perfect agreement. Since the crack growth calculated from the ΔV value at P_{max} does not require an unloading at a specific point, it is the more useful determination of crack growth in assessments of fracture toughness, discussed next.

Fracture Toughness

Two calculations of the applied K value at the maximum load point were made, as prospective fracture toughness determinations from the tests, designated $K_{max\text{-}o}$ and K_{max} . The calculations were made using Eqs. (1), (4) and (7) as appropriate and using α_o , the a/W of the machined notch, and α_v , the a/W of the notch plus the crack growth calculated using Eq. (20). Table 4 summarizes the calculations for the specimens of Fig. 5. Note that K_{max} , which includes the ΔV calculation of crack growth, is considerably higher than $K_{max\text{-}o}$, 37 % higher for the extended compact specimen. The summary of all the $K_{max\text{-}o}$ and K_{max} results may indicate which is the better measure of fracture toughness.

Figures 11 and 12 show the mean values of $K_{max\text{-}o}$ and K_{max} for the test conditions listed in Table 2. An example of the variability of the results are eight AS4/977-2 [90/+45/0/-45] tests (from two labs) that gave mean and standard error $K_{max\text{-}o}$ values of 56.6 and 2.9 MPa$\sqrt{m}$ and mean and strandard error K_{max} values of 61.3 and 4.0 MPa$\sqrt{m}$. The largest difference between $K_{max\text{-}o}$ and K_{max} for both material types was noted for standard compact specimens with the [0/0/90] layup. This is attributed to the arm breakage problem which occurred with this specimen-layup

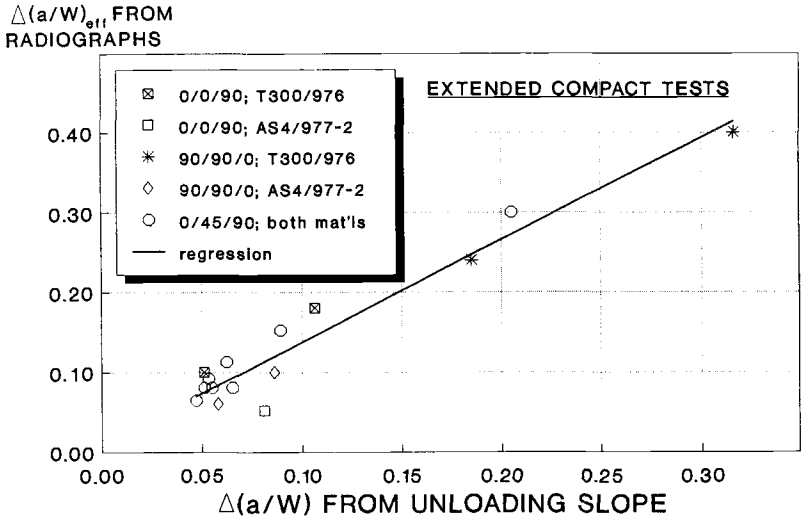


FIG. 9 - *Effective crack growth from radiograph damage versus calculated crack growth from unloading slope.*

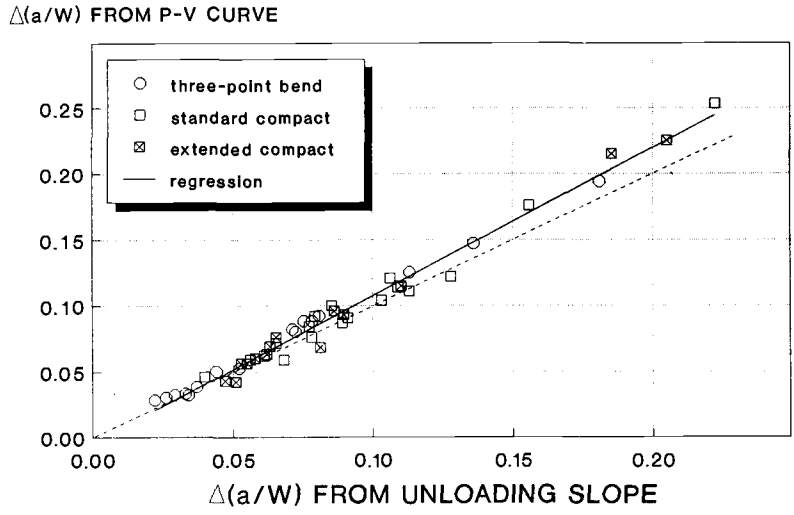


FIG. 10 - *Crack growth calculated from P-V curve compared with crack growth calculated from unloading slope*

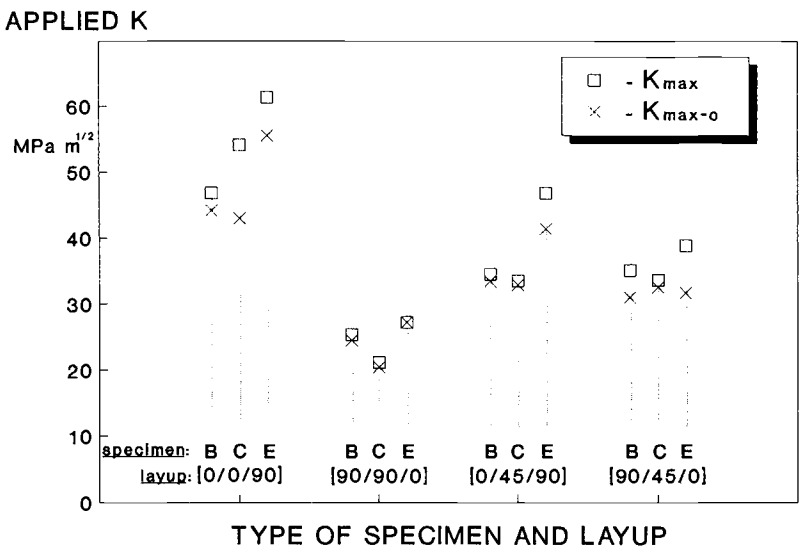


FIG. 11 - *Mean applied K values at maximum load for T300/976 laminates*

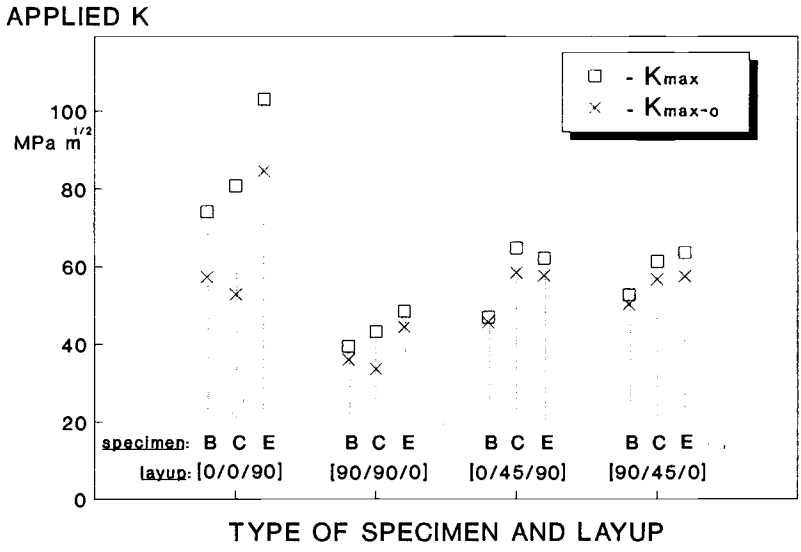


FIG. 12 - *Mean applied K values at maximum load for AS4/977-2 laminates*

TABLE 4 -- Typical spread sheet calculations for T300/976 [90/-45/0/45] layup specimens shown in Fig. 5

	α_o -- test	P_{max} KN test	K_{max-o} MPa$\sqrt{m}$ Eq 1,4,7	ΔV mm test	α_v -- Eq 20	K_{max} MPa$\sqrt{m}$ Eq 1,4,7
Three-Point Bend	0.480	1.10	33.4	0.11	0.531	39.3
Standard Compact	0.490	1.05	29.3	0.09	0.527	32.9
Extended Compact	0.508	1.58	32.2	0.15	0.575	44.1

combination. In general the more brittle T300/976 material showed less difference between K_{max-o} and K_{max} than the AS4/977-2 material; this is consistent with less crack growth at P_{max} for the more brittle material. For the extended compact results, which are not affected by either arm breakage or load-point damage, the value of K_{max} averages 12 % above K_{max-o} . Particularly the last two observations suggest that the difference between K_{max-o} and K_{max} is real and is due to an increasing crack growth resistance curve for at least some of the material and layup combinations of these tests. A similar observation was made in the prior work [5].

Additional evidence of increasing crack growth resistance behavior can be seen in Fig. 13, a plot of K_{max} versus calculated crack growth at maximum load (using Eq. 20). Note that each point on the plot is a separate test, so that taken together the results for a given material and layup combination describe the general crack growth resistance for that type of laminate. Three definitive types of behavior were noted (with specimens of each of the three configurations) and illustrated using linear regression lines. For the AS4/977-2 material in [0/+45/90/-45] and [90/-45/0/+45] layups a relatively steeply rising K-R curve was seen, whereas for the T300/976 material in [0/+45/90/-45] and [90/-45/0/+45] layups a less steeply rising K-R curve was seen. For the AS4/977-2 material in [90/90/0] layup a nearly horizontal K-R curve was noted. These three types of behavior are rationalized as follows: the AS4 0/45/90 layups, having a tough matrix and quasi-isotropic properties, has significant fiber bridging and thus a steeply rising K-R curve; the T300 0/45/90 layups, although quasi-isotropic, have a less tough matrix and thus less bridging and a less steeply rising K-R curve; the AS4 90/90/0 layup is dominated by the 90° fibers aligned with the crack growth direction which prevent fiber bridging and any rising K-R curve behavior.

One other set of results is plotted in Fig. 13, those for the AS4 0/0/90 layup tests. No trend of these results was considered because of the problems with the bend and compact specimens discussed earlier. These problems may have caused low K_{max} values for the AS4 0/0/90 bend and standard compact tests (indicated with B and C in the plot), compared with the extended compact tests. Other T300 test results were so closely grouped that no significant K-R curve trends were apparent.

The consistent trends of K-R behavior noted in Fig. 13 were determined from

elastic calculations of crack growth based on the ΔV of the P-V plot. This suggests that a series of $\Delta a/W$ versus $\Delta V/V_o$ curves can be drawn for different specimen configurations and starting crack lengths, as shown in Fig. 14. The curves were calculated using Eq. (20) with Eqs. (3) and (9), by assuming values of $\Delta V/V_o$ and calculating the $\Delta a/W$ that would have caused those values of $\Delta V/V_o$. The plots of Fig. 14 can be used with the summary of K_{max} versus $\Delta a/W$ results in Fig. 13 to propose a simple criterion for determining fracture toughness from a P-V plot of a carbon/epoxy specimen. From Fig.13 the preponderance of results have $\Delta a/W$ values of 0 to 0.04; for the extended compact specimen this corresponds to $\Delta V/V_o$ of 0 to 0.3. This is proposed as the basis of fracture toughness determination for these types of carbon/epoxy laminates, as follows. The extended compact specimen is used with a starting a/W between 0.5 and 0.6; P versus v is recorded and K_{max} is calculated from Eqs. (7), (9) and (20); K_{max} gives a measure of fracture toughness provided that $\Delta V/V_o \leq 0.3$. This determination of fracture toughness would give consistent results for the tests here. It would also exclude the tests affected by whole-specimen and notch-tip damage uncharacteristic of the self-similar crack growth that must dominate a determination of fracture toughness. The $\Delta V/V_o \leq 0.3$ criterion would exclude tests with: the arm-breakage damage of the standard compact specimen; the load-point damage of the bend specimen; and the damage extending perpendicular to the notch for all tests of layups with a significant portion of 0° fibers.

SUMMARY

Fracture tests were performed with carbon/polymer laminates and analyzed for the purpose of developing translaminar fracture toughness test and analysis procedures. Notched specimens were tested of two types of symmetrical layups - quasi-isotropic [0/45/90] and [0/90]; two carbon fiber/epoxy materials - a relatively brittle T300 fiber/976 epoxy and a tougher AS4 fiber/977-2 epoxy; two laminate thicknesses - 2 mm and 4 mm; and three specimen configurations - the standard three-point bend and compact configurations used for many types of fracture tests, and an extended compact specimen with arm-height to specimen-width ratio of 1.9, compared to 0.6 for the standard compact specimen. Plots of load versus crack mouth opening displacement were obtained and analyzed to determine the progression of crack growth and damage during the test.

Wide range stress and displacement expressions were obtained for the extended compact specimen. Expressions for applied stress intensity factor, K, and crack mouth opening displacement, v, in terms of relative notch length, a/W, and for a/W in terms of v were developed from recent numerical results. Relationships for the nominal bending stresses that control both self-similar and off-axis cracking for the extended compact specimen were derived and used to explain the types of cracking observed.

Damage that was unrelated to crack growth from the notch tip was characterized in the tests, including: the damage associated with the arm breakage problem with the standard compact specimen; and the load-point damage with the three-point bend specimen. Notch-tip damage of two types was characterized using radiography: damage that extends primarily perpendicular to the notch in

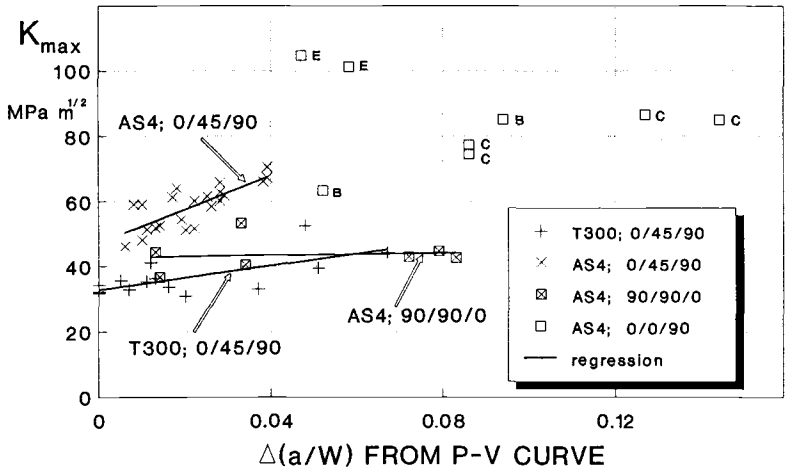


FIG. 13 - *Correspondence of applied K and calculated crack growth at point of maximum load*

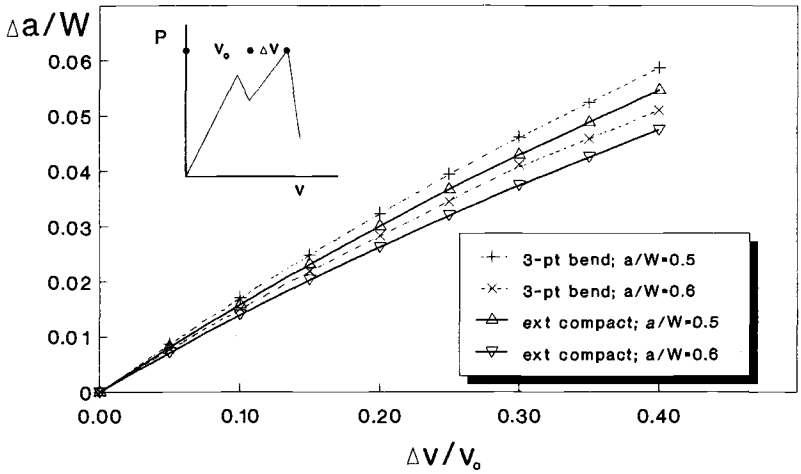


FIG. 14 - *Calculated crack growth corresponding to relative change in crack-mouth-opening displacement*

predominantly 0° fiber layups, associated with high toughness: and damage that extends primarily ahead of the notch in quasi-isotropic and predominantly 90° fiber layups, associated with lower toughness. Elastic calculations of crack extension from the notch tip averaged 76 % of the extent of radiographic notch-tip damage zone.

The applied K at maximum load, K_{max} , including the effect of the crack growth up to the maximum load point, was used as a measure of fracture toughness. Imminent arm breakage with the standard compact specimen and load-point damage with the bend specimen adversely affected the measurement of K_{max} , causing significant decreases. Plots of K_{max} versus crack growth unaffected by adverse damage showed an increasing resistance to crack growth for quasi-isotropic layups and a constant resistance to crack growth for predominantly 90° fiber layups. The K_{max} from the extended compact specimen, including the effect of crack growth, was proposed as a measurement of translaminar fracture toughness for carbon/epoxy laminates. For deviations from the linear P-v plot corresponding to $\Delta a/W \leq 0.04$, the K_{max} values gave consistent measurements of fracture toughness. This criterion also excluded tests with damage of the type that violates the concept of fracture toughness measurement.

ACKNOWLEDGEMENT

We are pleased to acknowledge the help of D. Crayon of the Army Armament RD&E Center in the performance of much of the testing in this program, and of J. C. Newman, Jr. of NASA Langley Research Center for reading the manuscript and providing the K and displacement results of Fig. 2.

REFERENCES

[1] Harris, C. E. and Morris, D. H., "Fracture Behavior of Thick Laminated Graphite/Epoxy Composites," NASA CR-3784, National Aeronautics and Space Administration, Washington, March 1984.

[2] Harris, C. E. and Morris, D. H., "A Comparison of the Fracture Behavior of Thick Laminated Composites Utilizing Compact Tension, Three-Point Bend and Center-Cracked Tension Specimens," Fracture Mechanics: Seventeenth Volume, ASTM STP 905, American Society for Testing and Materials, Philadelphia, 1986, pp. 124-135.

[3] O'Brien, T. K., Johnston, N. J., Raju, I. S., Morris, D. J. and Simonds, R. A., "Comparisons of Various Configurations of the Edge Delamination Test for Interlaminar Fracture Toughness," Toughened Composites, ASTM STP 937, N. J. Johnston, Ed., American Society for Testing and Materials, Philadelphia 1987, pp. 199-221.

[4] Underwood, J. H., Burch, I. A. and Bandyopadhyay, S., "Effects of Notch Geometry and Moisture on Fracture Strength of Carbon/Epoxy and Carbon/Bismaleimide Laminates," Composite Materials: Fatigue and Fracture

(Third Volume), ASTM STP 1110, T. K. O'Brien, Ed., American Society for Testing and Materials, Philadelphia, 1991, pp. 667-685.

[5] Underwood, J. H. and Kortschot, M. T., "Notch-Tip Damage and Translaminar Fracture toughness Measurements from Carbon/Epoxy Laminates," Proceedings of 2nd International Conference on Deformation and Fracture of Composites, The Institute of Materials, London, 1993.

[6] Richardson, D. E. and Goree, J. G., "Experimental Verification of a New Two-Parameter Fracture Model," Fracture Mechanics: Twenty-Third Symposium, ASTM STP 1189, Ravinder Chona, Ed., American Society for Testing and Materials, Philadelphia, 1993, pp. 738-750.

[7] Piascik, R. S. and Newman, J. C., Jr., NASA Langley Research Center, International Journal of Fracture , to be published.

[8] Srawley, J. E., "Wide Range Stress Intensity Factor Expressions for ASTM E399 Standard Fracture Toughness Specimens," International Journal of Fracture Mechanics, Vol 12, June 1976, p.475.

[9] Tada, H., Paris, P.C. and Irwin, G.R., The Stress Analysis of Cracks Handbook, Paris Productions, St. Louis, MO, 1985, pp. 2.16 - 2.18.

[10] Wu, S. X., "Crack Length Calculation Formula for Three-Point Bend Specimens," International Journal of Fracture, Vol 24, 1984, pp. R33 - R35.

[11] Andrews, W. R., Clark, G. A., Paris, P. C., Schmidt, D. W., "Single Specimen Tests for J_{Ic} Determination," Mechanics of Crack Growth, ASTM STP 590, American Society for Testing and Materials, Philadelphia, 1976, pp. 27-32.

[12] Saxena, A. and Hudak, S. J., Jr., "Review and Extension of Compliance Information for Common Crack Growth Specimens," International Journal of Fracture, Vol 14, 1978, pp. 453-468.

[13] Underwood, J. H., "Stress Intensity Factor and Load-Line Displacement Expressions for the Round Bar Bend Specimen," International Journal of Fracture, Vol 62, 1993, pp. R49-R55.

[14] Troiano, E., Underwood, J. H., Abbott, R. T., Kapusta, A. A. and Leighton, D.E., "Fracture Response of Whisker Reinforced SiC/Aluminum Metal Matrix Composite," Proceeding of ASME Winter Annual Meeting, American Society of Mechanical Engineers, New York, 1993.

[15] Kortschot, M. T. and Beaumont, P. W. R., "Damage Mechanics of Composite Materials: I - Measurements of Damage and Strength," Composites Science and Technology, Vol. 39, pp. 289 - 301, 1990.

Mark J. Hoffman[1], Shuichi Wakayama[2], Yiu-Wing Mai[3], Teruo Kishi[4], and Masanori Kawahara[2]

CYCLIC FATIGUE MECHANISMS IN PARTIALLY STABILISED ZIRCONIA

REFERENCE: Hoffman, M.J., Wakayama, S., Mai, Y-W., Kishi, T.,and Kawahara, M.,"**Cyclic Fatigue Mechanisms in Partially Stabilised Zirconia**", Fracture Mechanics: 26th Volume, ASTM STP 1256, Walter G. Reuter, John H. Underwood, and James C. Newman, Jr., Eds., American Society for Testing and Materials, Philadelphia, 1995.

ABSTRACT: Cyclic fatigue crack growth rate and crack resistance curve testing were undertaken on 6 different grades of Mg-PSZ. The width of the transformation zone at the flanks of the cracks was determined using Raman spectroscopy and, combined with R-curve toughening values, used to ascertain the level of crack-tip shielding during cyclic fatigue crack growth and hence the crack-tip stress intensity factor amplitude. By normalising the crack-tip stress intensity factor amplitude with the intrinsic toughness of the material, it was found that the cyclic fatigue threshold stress intensity factor was independent of the extent of crack-tip shielding and a function of the stress intensity factor at the crack tip. *In situ* SEM observations of cyclic fatigue revealed crack bridging by uncracked ligaments and the precipitate phase. Under cyclic loading the precipitate bridges were postulated to undergo frictional degradation at the precipitate/matrix interface with the degree of degradation determined by the cyclic amplitude. Acoustic emission testing revealed acoustic emissions at three distinct levels during the loading cycle: firstly, near the maximum applied stress intensity factor caused by crack propagation; secondly, at the mid-range of the applied stress intensity factor attributed to crack closure near the crack tip, presumably as a result of transformation induced dilation; and thirdly, intermittently near the base of the loading cycle as a result of fracture surface contact due to surface roughness at a significant distance behind the crack tip. Crack closure near the crack tip due to dilation is proposed to significantly reduce the crack tip stress intensity factor amplitude and hence the degree of cyclic fatigue.

KEYWORDS: zirconia, fatigue, crack closure, transformation toughening, cyclic fatigue, crack bridging, fatigue mechanism, acoustic emission

[1]Research Associate, TH Darmstadt, FG Nichtmetallisch-Anorganische Werkstoffe, Hilpertstrasse 31, Building D, 64295 Darmstadt, Germany.

[2]Associate Professor and Professor, respectively, Department of Mechanical Engineering, Tokyo Metropolitan University, 1-1 Minami-Ohsawa, Hachioji-shi, Tokyo 192-03, Japan.

[3]Professor, Centre for Advanced Materials Technology, Department of Mechanical and Mechatronic Engineering, University of Sydney, NSW 2006, Australia.

[4]Director, RCAST, The University of Tokyo, 4-6-1 Komaba, Meguro-ku, Tokyo 153, Japan.

Copyright© 1995 by ASTM International www.astm.org

INTRODUCTION

The degradation of structural ceramics under cyclic loads is a recently recognised, but well acknowledged, phenomenon. Due to the limited crack-tip plasticity of structural ceramics and their expected linear elastic stress-strain behaviour, analogous to their traditional ceramic counterparts, structural ceramics were initially believed not to suffer cyclic fatigue degradation[1,2]. Subsequent extensive studies of alumina[3-6], silicon nitride[7] and zirconia[8-14] have clearly ascertained the existence of enhanced crack growth rates and reduced fatigue thresholds and strengths in samples loaded under cyclic versus static loads. Some mechanism of cyclic fatigue degradation is therefore present and, in most cases, overshadows the effects of environmental or static fatigue.

The direction undertaken in the design of structural ceramics has been to reduce the flaw sensitivity of ceramic materials during strength testing. This has been accomplished by instilling into the materials various hysteretic processes which cause the material to toughen with crack extension, essentially by 'shielding' the crack tip, resulting in crack resistance or R-curve behaviour. These toughening mechanisms include crack bridging by grains, fibres or ductile particles, crack deflection, crack branching and phase transformation toughening.

The material used in this study, magnesia partially stabilised zirconia(Mg-PSZ), utilises phase transformation toughening to improve toughness. In phase transformation toughening zirconia ceramics a metastable tetragonal phase undergoes an essentially irreversible stress induced transformation to a monoclinic phase which is accompanied by a 4% dilation and ~16% shear strain in the unconstrained condition. In PSZ the tetragonal phase exists in the form of platelets(avg. dia. ~180nm, aspect ratio 4.5:1) which are distributed orthogonally within a cubic phase matrix. Transformation dilation results in compressive residual stresses while shear strains are relieved by twinning within the precipitates[15]. Extended sub-eutectoid ageing has been shown to lead to the development of a delta phase around the precipitates[16] which effectively prestresses the precipitates, lowering the applied stress required for phase transformation. Another transformation-toughening zirconia ceramic, tetragonal zirconia polycrystal(TZP), consists almost totally of fine tetragonal grains, occasionally interspersed with cubic grains. Young's Modulus has been determined to be 207 MPa and, under flexural loading stress-strain behaviour was observed to be linear to 350 MPa followed by slight non-linearity observed up to 450 MPa [13].

The mechanisms of cyclic fatigue may be divided into two categories; *extrinsic* fatigue mechanisms involve degradation of the crack-tip shielding mechanism causing greater stresses at the crack tip while *intrinsic* fatigue mechanisms involve a reduction of the intrinsic toughness of the material, through some crack-tip process, independent of the toughening mechanism.

In the case of a grain bridging toughening ceramic, alumina, extensive theoretical modelling[5,17,18] combined with *in situ* SEM observation[6] clearly identified an intrinsic mechanism for cyclic fatigue degradation. Toughening is caused by grains bridging the crack and 'shielding' the crack tip. Under cyclic loads however the coefficient of friction between the bridging grains and the 'matrix' is reduced through abrasion at the interface resulting in 'easier' interface sliding and reduced crack-tip shielding.

In the case of phase transformation toughening zirconia ceramics, however, clear identification of the mechanism of cyclic fatigue is yet to be made. A study undertaken on Y-TZP rods loaded in cyclic tension[19] observed increased compliance, accumulated plastic strain and the development of a hysteretic stress versus plastic strain loop. These phenomena were attributed to accumulated microcracking and internal friction under cyclic load. Failure was then claimed to occur through the coalescence of microcracks, initiating from an inherent processing flaw.

Microcracking has been observed around transformed precipitates in both tangential and radial directions in TEM studies of PSZ materials[15,20]. Tangential microcracks are presumably the result of tangential residual stresses arising from phase transformation while the radial microcracks are associated with strains arising from the twinning process.

An *in situ* SEM study of Mg-PSZ[21] observed the formation of slip lines ahead of the crack tip during cyclic loading at room temperature. Subsequent cycling resulted in the failure of these slip lines with crack propagation occurring along them in a process similar to cyclic fatigue crack propagation in metals. A strain mapping technique simultaneously provided evidence of a crack-tip blunting and sharpening process again in similitude with cyclic fatigue in metals. Interestingly, similar tests at elevated temperatures(450 and 650°C), where phase transformation and subsequent crack-tip plasticity processes are very limited, showed no 'metal-like' crack propagation features.

The same study also observed striation markings on the fracture surface which were claimed to result from the crack-tip blunting/sharpening process. Similar markings observed by other authors[22] were claimed to be the result of alternating critical/subcritical crack growth just prior to failure.

Experimental evidence appears to indicate, unlike crack bridging structural ceramics, that the mechanism of cyclic fatigue in PSZ is intrinsic in nature. Cyclic fatigue has been observed to occur in both as-fired and overaged condition PSZ materials where the level of phase transformation is very limited[9]. The very limited crack-tip plasticity occurring in zirconia ceramics, combined with the fact that crack opening displacements(CODs) are so small as to make impossible their direct observation, would appear to preclude a plasticity associated fatigue mechanism as occurs in metals and polymers.

In this study it is seen that cyclic fatigue threshold is governed by the extent of phase transformation. Microstructural features affecting transformation toughening, and hence cyclic fatigue thresholds, are also considered. When the effects of phase transformation are accounted for it is seen that the mechanism of cyclic fatigue is independent of the extent of crack-tip shielding and is affected by the intrinsic toughness of the material, K_0. SEM observations have shown that the precipitate phase acts to bridge the crack tip, significantly affecting K_0, and that repeated cycling at the crack tip abrades these bridges reducing the critical crack-tip stress intensity factor for crack propagation, K_{tip}^c. Acoustic emission(AE) observations have shown the existence of crack-tip closure under cyclic fatigue which is shown to reduce the crack-tip stress intensity factor amplitude, ΔK_{tip}, and hence the extent of abrasive cyclic fatigue degradation.

EXPERIMENTAL METHODS

In this work a number of different tests were undertaken using two distinct CT sample configurations. Initially cyclic crack growth rate tests and R-curve measurements were made using 6 variations of PSZ. The width of the phase transformation zone was measured after each test using Raman spectroscopy providing 12 maps of the transformation zones.

The second series of tests involved *in situ* cyclic fatigue testing inside an SEM using a material similar to one of the variations used in the initial testing. Here, as well as observing the crack tip during cycling, acoustic emission testing was done to study crack closure.

Materials

Twelve PSZ samples, stabilised with 9mol% MgO and two each of 32, 50 and 100μm grain size, were obtained in 50x50x3mm plates*. Half the

*Manufacturer: Nilcra Ceramics, Clayton, Victoria, Australia

samples were of a strength optimised MS Grade while half the samples had undergone subeutectoid ageing to improve toughness to a TS Grade. All samples were manufactured in a compact tension(CT) configuration of the same dimensions as the plates received from the manufacturer and both sides polished to a 1μm finish.In this paper the nomenclature used to describe a particular sample will consist of the grain size followed by the heat treatment condition e.g. 32TS is the TS Grade 32μm grain size sample. Crack growth rate tests, crack resistance curves and transformation zone width measurements were made on all 12 samples.

For the *in situ* SEM fatigue testing and AE measurements a material similar to the 32TS material was used, being manufactured from the same base powder and heat treatment cycles, but at a different time. The samples used in this testing were of the CT configuration recommended in ASTM E399-83 with specimen width, W=25.5mm but with a thickness, B=2.9mm. A smaller value of B is possible due to the very limited plasticity in the material. Samples were coated with a 100Å thick PdPt coating following polishing to 1μm.

Crack Growth Rate Tests, Transformation Zone Width Measurements and Crack Resistance Curve Tests

Crack growth rate testing was undertaken under tension-tension loading at a stress ratio, R, of 0.1 and frequency of 25Hz. Crack lengths were monitored by the change in electrical potential of a NiCr Krak® gauge which had been evaporated onto the surface of the sample. Potential drop was measured only at the peak of the load cycle so as to ensure reconnection of the fracture surface, due to possible crack closure, did not affect measurements. As the samples were not of standard ASTM configuration applied stress intensity factors were determined by interpolating between values previously determined for non-standard specimens [23]. The applied stress intensity factor amplitude, ΔK, was decreased with crack extension at such a rate so as to limit the effects of loading history upon crack growth rates[9]. Testing was stopped when crack growth rates, da/dN, fell below 10^{-10}m/cycle when crack growth could be assumed dormant as recommended by ASTM E647-86a [24].

Transformation zone widths were measured using Raman spectroscopy as a phase characterisation technique. This provides far better resolution than more commonly used X-ray diffraction techniques. Phase transformation occurs around cracks as a result of phase transformation at the crack tip. With crack propagation, crack-tip transformation zones move into the crack wake providing crack tip shielding which is essentially proportional to the width of the transformation zone, H. The profile of the extent of phase transformation was determined as the fraction of tetragonal phase that had undergone transformation to monoclinic phase, F_m, according to:

$$F_m = \frac{f_m}{f_m + f_t} \tag{1}$$

where f_m and f_t are the fractions of monoclinic and tetragonal phase respectively, their calibration spectra being previously determined[25,26]. A 2-D detector was used allowing the Raman spectra of sectional volumes across the transformed zone, perpendicular to the crack, to be obtained at a resolution of 20~47μm across the crack, depending upon zone width. Horizontal translations of the detector were made at steps of 260~400μm depending upon crack length and values for F_m stored on computer disc for later analysis.

Crack resistance curve measurements were made using the same samples following annealing in an inert He environment at 800°C to revert the transformed monoclinic phase to the metastable tetragonal phase, hence providing a sharp crack essentially free of damage. The

sample was then loaded under displacement control and load versus crack length recorded on a chart recorder which was subsequently converted to a K versus crack extension, Δa, plot.

Following the determination of the crack resistance curve, another series of Raman spectroscopy measurements were made to determine the extent of phase transformation around a critically propagated crack.

Determination of Phase Contents using Neutron Diffraction

Following R-curve testing the phase contents of all samples were determined. In addition, samples of identical material that were either unused or failed during testing prior to heat treatment were examined for phase content to determine the effect of the annealing process. Neutron diffraction was used to monitor the bulk phase content of each sample. Traditionally X-ray diffraction has been used to determine phase contents. However, X-rays have very low penetration and as such results are affected by surface finish. Neutrons on the other hand are capable of penetrating several centimetres below the surface.

Neutron diffraction step patterns were recorded using the high resolution powder diffractometer at the Australian Nuclear Science and Technology Organisation's HIFAR research reactor. The diffractometer is equipped with 8 neutron detectors, spaced 6° apart, recording 8 diffraction patterns simultaneously, which are then averaged. All patterns were recorded at room temperature, using a 0.1500nm neutron wavelength, over a 2θ range of 10~150°. The neutron patterns were analysed by a computer program which applied the Reitveld method for quantitative phase analysis [27,28].

In Situ Cyclic Fatigue Crack Growth Observations

All testing was undertaken using an externally located Instron SH2150 hydraulic servopulser and controller with crosshead inside an Hitachi S-2500CX SEM. Applied stress intensity factors were calculated according to ASTM E399-83 [29]. Cracks were initiated under displacement control using cyclic tension loading at a maximum stress intensity factor, K_{max}, of 10.4MPa$\sqrt{m}$ and R=0.05-0.2. The PdPt coating was then removed using 1μm polishing fluid and the sample etched in 46%HF solution for 6.5mins. The effect of the etching process was to remove the cubic phase matrix on the surface to allow observation of microstructural features such as grain boundaries and precipitates.

The sample was then recoated and returned to the SEM chamber. A cyclic load was applied under load control and the crack grown at a variety of crack growth rates at ΔK values of 8.1-10.4MPa$\sqrt{m}$, at R=0.05-0.2, and frequencies of 0.1-0.4Hz. Observations were recorded using a VCR and testing regularly interrupted to enable still photographs to be taken. The majority of photographs were taken at stress intensity factors equal to the maximum stress intensity factor during cycling, K_{max}, to enable observation at maximum crack opening. No environmental crack growth would be expected to occur, as all testing was undertaken in vacuum.

Following fatigue testing inside the SEM a crack opening wedge was placed in the crack mouth and the sample observed in a high resolution field emission SEM of the Leica 360FE type. The sample was then quickly broken under monotonic load and the fracture surface observed to examine the fracture surface differences as a result of cyclic versus monotonic crack growth.

Acoustic Emission(AE) Measurements during Cyclic Loading

A piezo-electric AE sensor was attached on the side of the CT sample adjacent to the crack-tip. The sensor was located on the fixed side of the load train so as to reduce the possibility of frictional acoustic noise affecting the data. All testing was undertaken inside the SEM in the same manner as the previously described *in situ* observations

to allow simultaneous observation of the crack tip. The signal was carried outside the SEM chamber via an electromagnetically shielded cable, through a 60dB pre-amplifier and into a PAC:LOCAN AE system where data was recorded on a computer floppy disk. The load signal from the Instron controller was recorded simultaneously with AE events every 40ms or 20 times per cycle at 2.5Hz, the cycling frequency during the majority of tests. Any AE events occurring between these 40ms intervals were superimposed on top of the regular data. Various applied loads were used and the frequency reduced in a number of tests to ensure there were no frequency effects within the data recording system. AE signals ranged in amplitude from the preset threshold level of 46dB to ~70dB.

EXPERIMENTAL RESULTS

Cyclic Fatigue Crack Growth Rate Tests

Results of the first series of cyclic fatigue tests can be seen in Fig. 1. A number of features are immediately apparent with the first being that the MS Grade materials exhibit lower cyclic fatigue thresholds than the TS Grade materials. This is to be expected; cyclic fatigue threshold values in PSZ generally scale with toughness both in crack growth measurements[9] and strength testing[30] and, the toughness optimised TS Grade materials are generally tougher than the strength optimised MS Grade ones. Consistent with other ceramic materials the curves are very steep with a large Paris law($da/dN=A\Delta K^n$) crack growth exponent, n>30. Because of the steepness of these curves it is not possible to accurately determine a specific value for n. Stable cyclic fatigue crack growth, therefore, occurs over a very narrow region of stress intensity factor amplitudes.

The effect of grain size, however, is somewhat difficult to ascertain; while the 32μm grain size materials exhibited higher crack growth rates in both the MS and TS Grade materials, the 50 and 100μm materials exhibited similar behaviour.

As has been previously observed in other structural ceramic materials[31], the crack growth pattern was not uniform in most cases. In both the 50 and 100μm materials crack growth tended to occur in a stepwise discontinuous fashion with the crack making intermittent jumps and then arresting at irregular intervals. These jumps tended to scale with the grain diameter and were especially pronounced in the MS-Grade materials. In the 32μm materials, however, crack growth appeared to be stable and continuous to within the resolution of the crack length measurement(~2μm). As the resolution of crack length measurement was significantly greater than the grain size, it can be assumed that these 'jumps' were not completely grain size dependent.

Crack Resistance Curves

Fig. 2 shows the crack resistance curves for all the materials used in the crack growth measurements. Initiating the crack growth from a sharp notch devoid of surrounding phase transformation provides a far better indication of toughening or crack-tip shielding in the initial stages of crack extension than has previously been published, where blunt notches [32] or transformed cracks [9] were used. While the presence of some, as yet undefined, fatigue degradation may affect the initiation point this is not believed to be significant, considering the dominant effect of phase transformation toughening in the material.

All curves appear to rise initially from their intrinsic toughness values at a similar rate. The TS-Grade materials, not unexpectedly, however exhibit higher plateau values than the MS-Grade materials with the 100TS sample reaching a peak toughness well in excess of that previously reported for Mg-PSZ materials. The TS material's R-curve plateaux appear also to scale with grain size whereas the MS material's do not. As described later, this is not believed to be significant as crack growth is transgrannular. In almost all cases the curves rose to a

peak value and fell somewhat before reaching a steady state value. This feature is consistent with theoretical predictions for the effects of phase transformation toughening [33,34], but has not previously been shown experimentally.

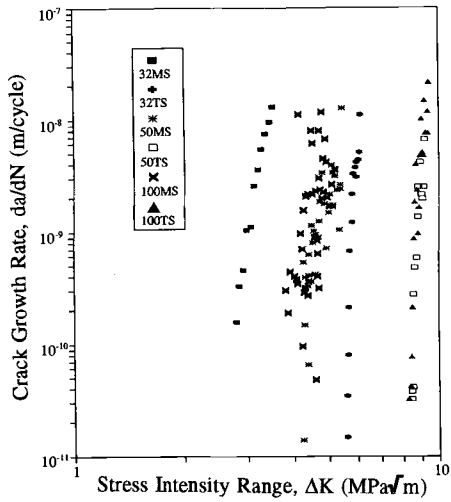


FIG. 1--Cyclic fatigue crack growth rates, da/dN, as a function of applied stress intensity factor amplitude, ΔK.

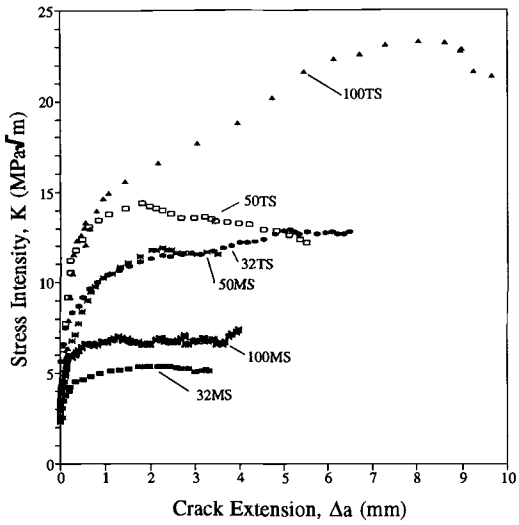


FIG. 2--Crack resistance curves of different Mg-PSZ materials tested in cyclic fatigue crack growth rate testing following annealing at 800°C.

Transformation Zone Measurements

The extent of transformation around the cracks was plotted onto contour maps. A sample of the contour maps can be seen in Fig. 3 which shows the transformation around the crack in the 100TS sample following R-curve testing. The contours represent F_m as outlined in Eq(1). It can clearly be seen that the extent of phase transformation decreases as one moves away from the crack tip and flanks. The effect of the annealing process can also be clearly seen in Fig. 3. Here, the region to the left of the zone, which had previously been transformed following cyclic fatigue crack growth, shows negligible levels of phase transformation. It can therefore be seen that the annealing process reversed the stress induced phase transformation that occurred near the crack during cyclic fatigue crack propagation.

From the Raman spectroscopy contour maps it is possible to measure the width of the transformed zones. The boundary of the transformed zone was deemed to be where F_m becomes equal to the background level. The half zone width, H, was determined by measuring across the zone and halving. It was found that H was essentially constant with crack extension for both forms of crack propagation but that, in most cases, the zone widths following R-curve testing were approximately twice those obtained in cyclic fatigue crack growth experiments. Table 1 shows the results of the zone width measurements.

TABLE 1--Transformation zone widths as determined using Raman spectroscopy

Sample	Half Zone Width, H(mm)	
	Fatigue Crack	R-curve
32MS	...	0.48
50MS	0.43	0.70
100MS	0.37	0.60
32TS	0.92	1.07
50TS	0.86	2.20
100TS	0.78	2.12

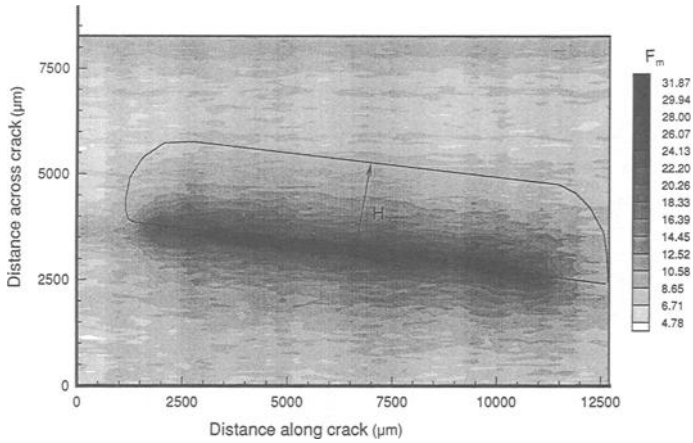


FIG. 3--Sample contour map of Raman spectroscopy results of 100TS sample following R-curve testing showing the half-width, H, of the transformation zone.

Phase Contents

Results of neutron diffraction tests are given in Table 2. It can

be seen that the annealing process has had negligible effect upon the phase contents validating comparisons between the cyclic fatigue and R-curve tests. Also of note is the fact that, while the tetragonal phase contents are similar in the MS and TS-Grade materials, the delta phase contents are higher in the tougher TS-Grade materials. This confirms previous reports[16] that the formation of a delta phase during subeutectoid ageing enhances toughness by prestressing the tetragonal precipitates.

TABLE 2--Results of phase analysis using neutron diffraction of materials used in cyclic fatigue(unannealed) and R-curve(annealed)

Sample		Phase Analysis			
		% cubic	% tetragonal	% monoclinic	%delta
32MS	Unannealed	...	...	...	...
	Annealed	54.8	45.5	0.0	0.0
50MS	Unannealed	27.0	53.6	4.6	14.8
	Annealed	27.2	55.8	2.0	15.1
100MS	Unannealed	24.6	57.2	0.0	18.2
	Annealed	22.7	57.8	2.7	16.9
32TS	Unannealed	12.2	50.0	16.9	20.9
	Annealed	9.3	50.6	17.3	22.9
50TS	Unannealed	11.5	57.7	8.6	22.2
	Annealed	10.6	55.6	7.9	25.9
100TS	Unannealed	9.4	60.9	7.8	21.9
	Annealed	10.9	59.5	6.9	22.6

In situ SEM Observations

Discontinuous crack growth was again a feature of cyclic fatigue crack growth and in fact more so due to the small crack extensions over which the crack length was measured. During *in situ* testing crack extensions are comparable to the microstructure of the material and are hence significantly affected by it. Crack bridging by uncracked ligaments and the precipitate phase was observed to occur during *in situ* SEM observations.

As noted in previous work[35] uncracked bridging ligaments were seen to form by a process demonstrated in Fig. 4. Initially a small crack forms ahead of the main crack, slightly out of plane(Fig. 4a), forming a bridging ligament. Simultaneously the crack growth rate significantly decreases. With subsequent cycling the bridging ligament breaks over a small number of cycles, frequently over one cycle, and the crack tip jumps forward(Fig. 4b). As these bridging ligaments are of no more than grain size dimensions while the sample is 2.7mm thick, they are clearly not a through thickness feature. The broken ligament results in a crack face perpendicular to the crack plane which may be a source of friction. It should be noted however that crack tip 'jumps' do not necessarily correspond with an observed bridging ligament failure on the surface of the sample. This indicates the presence of bridging ligaments in the bulk of the sample which cannot be seen in observations of the crack profile.

Fig. 5 shows an etched surface and provides an explanation for the processes which lead to bridging ligament formation. The crack progresses down from the top of the figure and encounters a grain boundary. While crack growth is essentially transgrannular, the crack moves along the grain boundary for ~3μm before moving into the next grain. Approximately 4μm in the crack propagation direction can be seen a small cluster of large precipitates. These form during manufacture, usually close to grain boundaries, as a result of MgO concentrations. During the cooling cycle these large precipitates transform to the monoclinic phase, with dilation, resulting in tangential residual stresses around them[36]. When the stress field surrounding the crack tip approaches these regions of residual stress the combined stresses

result in the formation of a crack ahead of the crack tip and a subsequent bridging ligament.

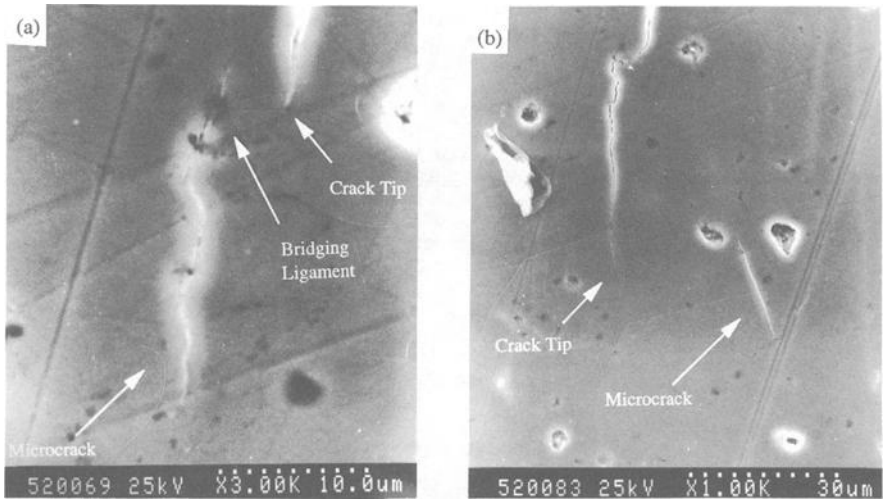


FIG. 4--(a)Crack bridging ligament formed by formation of out of plane crack ahead of crack tip and (b)ligament breaks with subsequent cycling leading to an appearance of crack deflection. Note new out of plane crack preceding new crack bridging ligament. Crack is propagating from top to bottom of the figure.

Crack bridging by the precipitate phase in PSZ has been postulated in theoretical work[37] but has never been considered to significantly affect crack growth behaviour. *In situ* observations of an etched sample surface however clearly show bridging by the precipitate phase near the crack tip. Fig. 6 shows an FESEM micrograph of the crack profile at a region close to the crack between two pores. Higher magnification images of the same region may be seen in Fig. 7. The dimple like surface is caused by the coating placed on the sample for SEM observation. It can be seen that the crack progresses through the matrix material with the precipitates forming crack bridges in a manner similar to small fibres or particulates in a composite material. No evidence can be seen of precipitate cleavage. It is estimated from *in situ* crack profile observations that precipitates act as bridges for a distance of approximately 1.5μm behind the crack tip.

Comparisons of cyclically and monotonically formed fracture surfaces show a number of significant differences which can be clearly seen in Fig. 8. The crack front is slightly diagonal across the specimen as indicated with the crack moving from right to left of the figure. To the right of the crack front can be seen a darker region where crack propagation was under cyclic loading. To the left can be seen a lighter region where the sample was broken under fast fracture. The appearance of the light colour is a result of charging of the higher and sharper peaks of the sample. Under cyclic loading these peaks are 'smoothed off' by abrasion resulting from contact of the fracture surfaces.

Different conclusions about abrasion of the fracture surface may be made however by observations at a higher magnification which allow resolution of the precipitates. Fig. 9a shows the fracture surface following fast fracture. Some precipitates can be seen sitting proud of the matrix material but essentially it is a smooth surface. In Fig. 9b there is, as result of cyclic loading, a very different rougher fracture surface. There are no precipitates sitting proud of the fracture surface

though many can be seen nestled in the matrix material which has been broken away from them as a result of abrasion by debris and a rough contact surface.

Therefore it can be seen that under cyclic loading high sharp peaks on the fracture surface are smoothed out by abrasion but that the same abrasive processes wear away the matrix material surrounding the precipitates on the fracture surface. At no stage were fatigue striations on the fracture surface or any other form of plasticity associated crack growth phenomena observed.

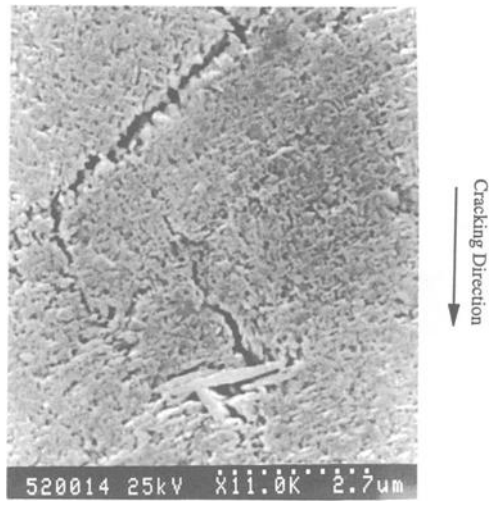


FIG. 5--Etched sample showing clump of large precipitates leading to formation of bridging ligament.

AE Testing During Cyclic Loading

In AE testing crack growth rates were monitored by setting applied cycling stress intensity factors to K_{max}=9.8MPa$\sqrt{m}$, ΔK=8.8MPa$\sqrt{m}$ and the AE noise threshold to 46dB. This resulted in three distinct AE bands as seen in Fig. 10; the first, close to the peak of the cycle, are emissions resulting from crack propagation, the second band of emissions in the 5-7MPa$\sqrt{m}$ region are a result of crack-tip closure while the third band of intermittent emissions at ~1.5MPa$\sqrt{m}$ are a possible indication of another region of crack closure. Reductions of K_{max} and ΔK resulted in a lower crack growth rate and subsequently fewer crack propagation emissions near K_{max}. However the other two AE bands remained.

A further test was undertaken to confirm the causes of the various acoustic emissions observed. Results can be seen in Fig. 11. Initially a low K_{max} and ΔK were used (as indicated by the dashed lines) and virtually no acoustic emission hits were recorded. K_{max} was then increased to just above where the mid-range AE hits had previously been observed while K_{min} remained the same. Two bands of emissions were then noticed; one at 6~7MPa$\sqrt{m}$ and another close to K_{min}. No clear evidence of crack propagation had been made up to this stage. K_{max} was then increased to a level where crack propagation was known to occur and K_{min} increased above the level for crack closure. No crack closure emissions were observed but a number of crack propagation emissions could be seen near

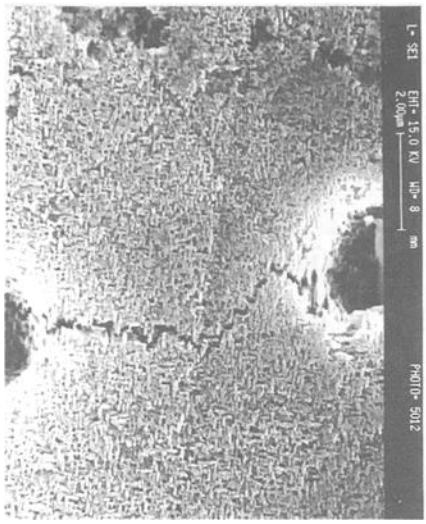


FIG. 6--Crack in etched material between two pores. Crack mouth wedged open.

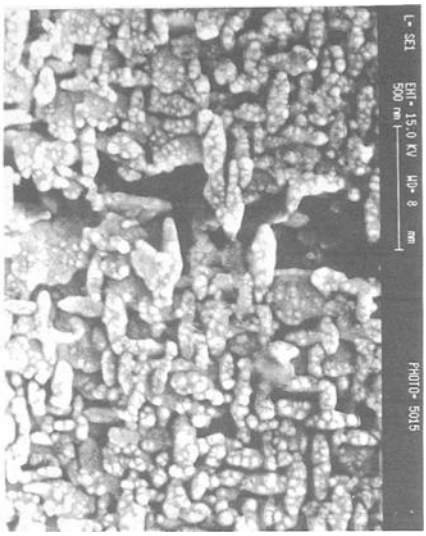


FIG. 7--Fracture profile following fatigue cracking as observed using high resolution FESEM showing bridging by precipitates.

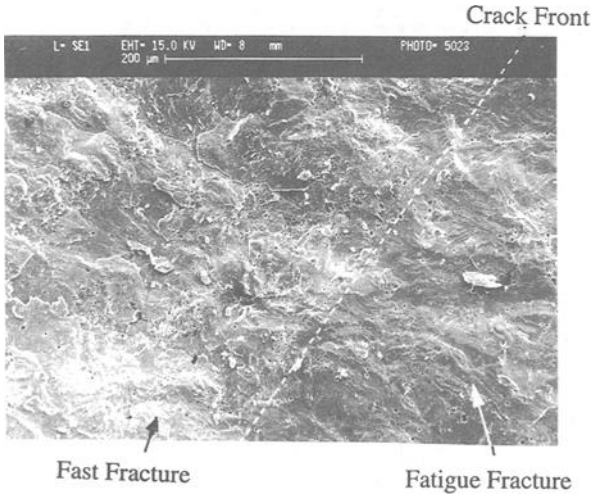


FIG. 8--Fracture surface showing different surface textures as a result of fatigue cracking and critical fracture.

K_{max}. K_{min} was then reduced to its initial level and three bands of emissions could now be seen; the number of crack propagation emissions

was significantly increased due to increased ΔK, the mid-range emissions could again be seen as could the emissions near K_{min}.

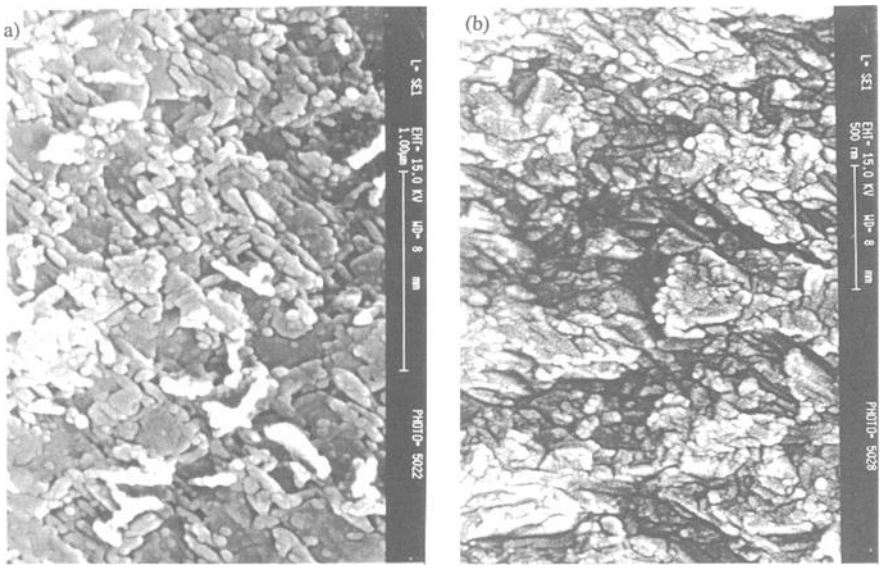


FIG. 9--Fracture surface as observed by high resolution FESEM following (a)cracking under monotonic loading showing precipitates sitting proud of the fracture surface following pullout from the matrix and (b)cyclic fatigue fracture showing precipitates nestled within matrix material which has been abraded away.

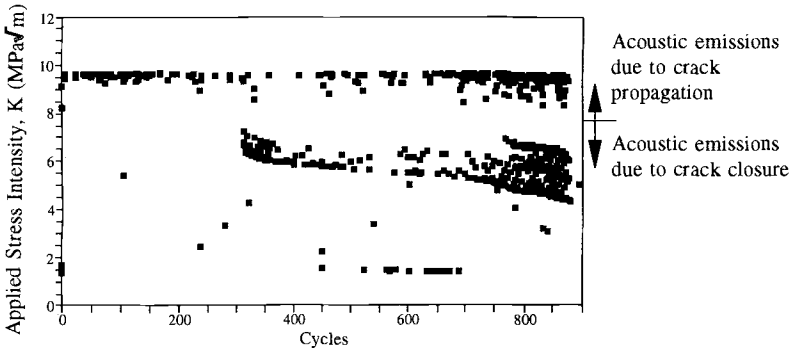


FIG. 10--Applied stress intensity factors at which AEs occurred. AE_{th}=46dB.

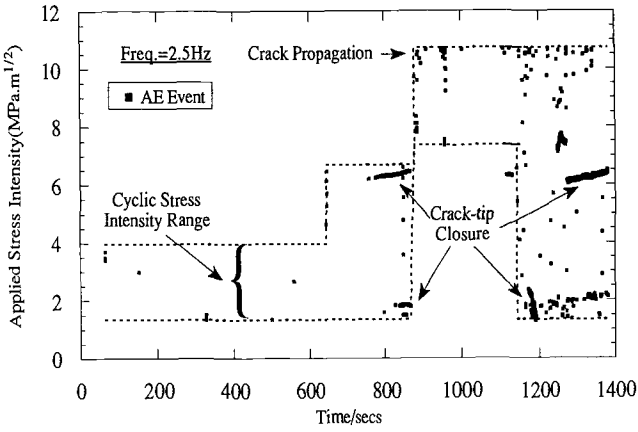


FIG. 11--Applied stress intensity factors at which acoustic emissions occurred during cyclic loading at various values of K_{max} and K_{min} as indicated by dashed lines.

ANALYSIS AND DISCUSSION

Determination of Fatigue Mechanism as Intrinsic

Observation of the R-curve(Fig. 2) data reveals that there are significant variations in the crack-tip shielding properties of the materials tested. This is also to be expected from the variation in transformation zones widths observed using Raman spectroscopy(Table 1). Fatigue crack growth is a function of the crack-tip stress intensity factor amplitude, ΔK_{tip}, where:

$$\Delta K_{tip} = \Delta K_a + K_s \tag{2}$$

ΔK_a is the applied stress intensity factor amplitude and K_s is the crack-tip shielding effect due to phase transformation and is hence negative. K_s may be expressed as [38] :

$$K_s = \frac{E}{3\sqrt{(2\pi)}(1-\nu)} \iint_A e^T \nu R^{-3/2} \cos\frac{3}{2}\Phi \, dA \tag{3}$$

where E is Young's modulus(207GPa), ν is Poissons ratio(0.31), e^T is the transformation strain(4%) and v is the volume fraction of transformable(tetragonal) phase. R transcribes the boundary of the transformed zone at the crack tip as a function of Φ [38]. i.e.:

$$R(\Phi) = \frac{2}{9\pi}(1+\nu)^2 \left(\frac{K}{\sigma_m^c}\right)^2 \cos^2(\Phi/2) \tag{4}$$

where σ_m^c is the critical hydrostatic transformation stress and K is the stress intensity factor at the crack tip. For $\Delta a=0$, K is equal to the applied stress intensity factor, K_a, however once a wake zone develops K becomes equal to K_{tip}. The transformation zone half height, H, can be

determined for crack propagation at constant K_{tip} by equating Eq(4) to give:

$$H = \frac{\sqrt{3}(1+\nu)^2}{12\pi}\left(\frac{K_{tip}}{\sigma_m^c}\right)^2 \quad (5)$$

During R-curve testing equilibrium crack growth is maintained with K_{tip} equal to the intrinsic toughness of the material K_0. A constant width transformation zone, as observed in the Raman spectroscopy experiments, is therefore formed and by substitution into Eq(5); the ratio (K_0/σ_m^c) may be obtained. Noting that during R-curve testing:

$$K_R(=K_a) = K_0 + K_s \quad (6)$$

a theoretical R-curve may be generated by equating K_s according to Eq(3). K_0 and σ_m^c, as seen in Table 3, were then determined by fitting the theoretical results to the experimental R-curve data.

TABLE 3--Values of K_0 and σ_m^c determined from R-curve testing and used in calculating crack-tip shielding.

Material	K_0, MPa$\sqrt{m}$	σ_m^c, MPa
50MS	2	20.5
100MS	2	25.0
32TS	4	34.3
50TS	4	40.0
100TS	5	30.5

The values of σ_m^c shown in Table 3 are somewhat lower than expected and vary from sample to sample. This may be explained by considering the calculated values of σ_m^c in conjunction with the delta phase content. The effect of the delta phase is to effectively prestress the tetragonal precipitates. This will result in variations in the observed critical transformation stress. Direct correlations between H and σ_m^c cannot be made, however, due to the concurrent effects of K_0. It can be seen in Fig. 12, however, that increases in delta phase content raises the cyclic fatigue threshold via increased phase transformation toughening as evidenced by wider transformation zones.

As stress induced phase transformation is essentially irreversible, the extent of transformation around a crack grown under cyclic loading will be a function of the maximum crack-tip stress intensity factor, $K_{tip(max)}$, which, as seen in the AE testing, is the critical crack-tip stress intensity factor at which crack propagation occurs. For the cyclic loading case Eq(2) becomes:

$$K_{tip(max)} = K_a(\sigma_{max}, a+\Delta a) + K_s(K_{tip(max)}, \Delta a) \quad (7)$$

where σ_{max} is the maximum applied stress and K_s is as shown in Eq(3). Eq(7) may be solved iteratively for $K_{tip(max)}$ and K_s determined. K_{tip} may then be calculated at any stage in the loading cycle allowing determination of ΔK_{tip}. However, while crack growth testing was undertaken at decreasing ΔK, the transformation zones around the cracks are, within the resolution of the Raman spectroscopy measuring system, essentially constant in width. This is due to (a)the steep crack growth curves and (b)the discontinuous crack growth pattern. As σ_m^c is already known, Eq(5) may be used to determine $K_{tip(max)}$. As ΔK_s is known from testing, K_s may be ascertained using Eq(2) and ΔK_{tip} determined.

Previous work[9] showed that crack closure in PSZ occurred and that the applied stress intensity factor at which crack closure occurs, $K_{cl} \sim K_s$. As:

$$K_{tip(min)} = K_{cl} - K_s \quad (8)$$

then $K_{tip(min)}$~0 and ΔK_{tip}~$K_{tip(max)}$[†]. Crack growth rates can now be determined as a function of the crack-tip stress intensity amplitude. Normalising ΔK_{tip} with the intrinsic toughness, K_0(Table 3), as seen in Fig. 13 confirms that the mechanism of cyclic fatigue is independent of the extent of toughening and is a function of the intrinsic toughness of the material.

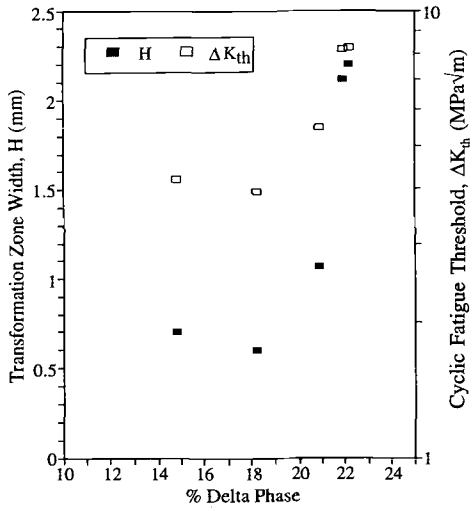


FIG. 12--Effects of delta phase content upon transformation zone width, H, and cyclic fatigue threshold stress intensity factor, ΔK_{th}.

At this stage we introduce K_{tip}^c which is the critical stress intensity factor *at the crack tip*. During R-curve testing K_{tip}^c is equal to the intrinsic toughness, K_0. The effect of an intrinsic fatigue mechanism is to reduce K_{tip}^c to some value less than K_0. In this case K_{tip}^c=0.6~0.9K_0 as may be seen in Fig. 13 where crack growth occurs in the region of $\Delta K_{tip}/K_0$=0.6~0.9. The level of crack-tip shielding in the 32MS sample could not be calculated due to the absence of Raman spectroscopy data for this sample due to premature heat treatment of the sample.

Identification of a Cyclic Fatigue Mechanism

In situ observations of the crack-tip reveal that the precipitates within the material act as small bridges near the crack tip in a manner similar to a small fibre bridging material. Observations reveal also that the crack progresses either parallel to, or perpendicularly to(Fig.14a&b), the major axis of the precipitate depending upon the orientation of the precipitate in relation to the approaching crack. While stress concentrations are highest at the ends of the precipitates, strains are greatest in the centre. Obviously, when crack propagation is parallel to the precipitate there will be no bridging effect.

It has been shown that the cause of toughening in bridging materials is the frictional resistance to pullout of the bridging elements [5,39]. There are a number of reasons to expect a significant degree of friction between the precipitates and the matrix material.

[†] Traditionally in fatigue literature ΔK_{eff} is used when expressing the effects of crack closure. However, in this case, due to the added factor of crack-tip shielding, ΔK_{tip} is used to avoid confusion with other fatigue processes.

First, when phase transformation occurs the precipitates undergo dilation while the matrix material remains unchanged. Therefore a significant compressive force exists at the matrix/precipitate interface which would raise the friction force at the interface, as shown schematically in Fig. 14a. Second, transmission electron microscopy(TEM) studies [15] have shown that the shear stresses associated with phase transformation are relieved by twinning within the precipitates. This process results in a corrugated surface on the precipitate as shown in Fig. 14b which would raise the coefficient of friction at the interface. Coincidentally, twinning also results in microcracking at the matrix/precipitate interface. This is possibly the reason why precipitates 'pullout' in the first place rather than cleaving at the crack tip. Should precipitate cleavage occur the level of increased toughening would be significantly reduced.

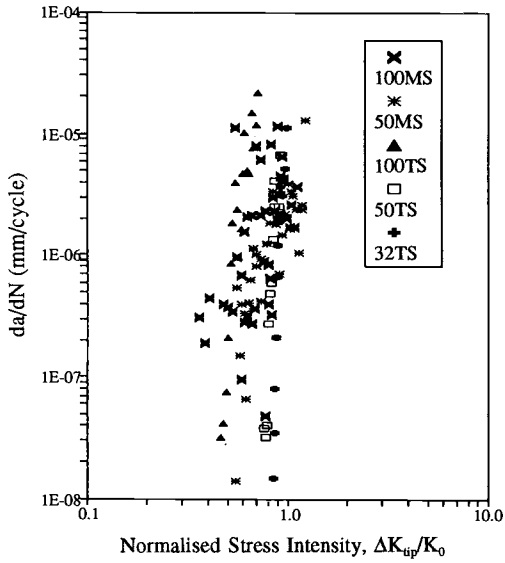


FIG. 13--Cyclic fatigue crack growth rates, da/dN, as a function of normalised crack-tip stress intensity factor amplitude, $\Delta K_{tip}/K_0$.

This bridging process theoretically results in R-curve behaviour near the crack tip[40]. The length of the bridging zone of precipitate bridges is <5μm. However the transformation toughening R-curve plateaus at a crack length of 2 to 4mm as seen in Fig. 2 effectively overwhelming in rising R-curve effects in the precipitate bridging R-curve. To all intents and purposes, therefore, the intrinsic toughness, K_0, can be considered to be the plateau of the precipitate bridging R-curve.

During cyclic loading repeated abrasion appears to occur at the matrix/precipitate interface. This is confirmed by comparing Figures 9a and 9b. Fig. 9a was taken following fracture under monotonic load and shows precipitates penetrating above an essentially smooth surface of what appears to be matrix material. In Fig. 9b the matrix material has been removed under cyclic load and the penetrating precipitates broken away, presumably as a result of significant abrasion. The effect of this abrasion is therefore to reduce the friction coefficient at the matrix/precipitate interface and/or to totally remove the bridging precipitates hence, lowering K_{tip}^c to less than K_0.

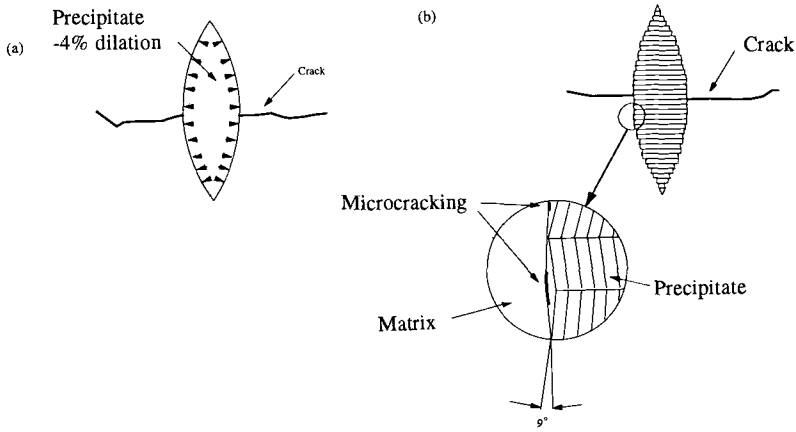


FIG. 14--Schematic diagram showing factors affecting matrix/precipitate interfacial friction. (a)precipitate dilation and (b)corrugated precipitate surface following twinning.

Cyclic fatigue is therefore caused by frictional processes at the crack tip and is subsequently dependent upon ΔK_{tip}, is intrinsic in nature, and is dependent upon K_o in full agreement with the crack growth data.

Factors Affecting ΔK_{tip}

As cyclic fatigue is dependent upon ΔK_{tip}, crack-tip closure would therefore be expected to affect crack growth rates. Crack-tip closure involves the contact of the fracture surfaces at a stress intensity factor greater than K_{min}. Any increase in K_{min} results in a reduction in ΔK_{tip}. This results in less abrasion at the crack tip and hence less reduction in K_{tip}^c. The AE data appears to reveal fracture surface contact at two levels; one close to K_{min} and another at about the mid-range of the loading cycle.

The region of crack-tip closure near K_{min} was intermittent and at times appeared to decrease with crack propagation. This is most likely the result of contact some distance behind the crack tip as a result of fracture surface roughness or asperities falling between the fracture surfaces and explains the 'smoother' fracture surface in Fig. 8 following cyclic fatigue crack growth. As K_{cl} here is close to K_{min} limited reduction in ΔK_{tip} occurs.

The crack closure at the midrange of the loading cycle is likely to be caused by dilation of the material around the crack flanks and this was confirmed by observation of the crack profile. This mid-range crack closure is significant because: (a)it occurs near the crack tip where frictional degradation is occurring and (b)it significantly reduces ΔK_{tip} and hence the amount of frictional degradation.

The actual crack-tip stress intensity amplitude factor of the sample examined during AE testing may be determined. The material used was of a similar microstructure and showed similar toughness values to the 32TS material used in crack growth rate testing. Crack tip shielding may therefore be considered similar to the 32TS material with K_s=2.3MPa$\sqrt{m}$ as was determined using Eq(3).

The crack-tip stress intensity factor amplitude may be expressed as:

$$\Delta K_{tip} = K_{tip(max)} - K_{tip(min)} \quad (9)$$

with:

$$K_{tip(max)} = K_a - K_s \quad (10)$$

and $K_{tip(min)}$ expressed as in Eq(8). Considering, for example, the case shown in Fig 10: $K_{tip(max)}$ is therefore reduced from 10.8MPa$\sqrt{m}$ to 8.5MPa$\sqrt{m}$ as per Eq(10) and $K_{tip(min)}$ becomes equal to K_{cl}(=6.5MPa$\sqrt{m}$) less K_s(=2.3MPa$\sqrt{m}$) which equals 4.2MPa$\sqrt{m}$. Hence ΔK_{tip}=4.3MPa$\sqrt{m}$, as per Eq(9), compared with the applied stress intensity factor amplitude, ΔK, of 9.4MPa$\sqrt{m}$. The combined effects of crack-tip shielding and crack-tip closure upon ΔK_{tip} are hence remarkable.

Analysis has been made of the effect of uncracked ligament bridging upon overall crack growth rates [41] using an analysis developed for a similar phenomenon in Al/SiC_p [42]. It was found that uncracked bridging ligaments have limited effect, essentially due to their infrequency and the low level of plasticity in PSZ. They are, however, an explanation for the discontinuous crack growth behaviour observed; the formation of a bridging ligament near the crack tip causes a reduction in K_{tip}, and consequently crack growth rate, due to added crack-tip shielding. However on cleavage of the ligament K_{tip} rises rapidly causing a jump forward in the crack tip followed by arrest to normal crack growth rates.

CONCLUSIONS

The analysis of cyclic fatigue crack growth rates and comparisons with microstructural contents, and *in situ* SEM observations combined with AE testing have allowed a number of significant conclusions to be made regarding cyclic fatigue in transformation toughening PSZ:

(1) The cyclic fatigue thresholds of PSZ materials' increase with the materials ability to undergo phase transformation toughening. The delta phase around precipitates acts to prestress them, therefore lowering the activation energy for phase transformation. Hence a lower applied stress is necessary to cause phase transformation resulting in wider transformation zones and greater crack-tip shielding.

(2) The mechanism of cyclic fatigue is intrinsic in nature. Near the crack tip bridging by the precipitates occurs raising the intrinsic toughness. During cyclic loading, however, frictional degradation of the precipitate/matrix interface occurs, reducing the toughening effect of the precipitate bridges and, hence, lowering the critical crack-tip stress intensity factor for crack propagation, K_{tip}^c, below the intrinsic toughness. Increases in intrinsic toughness do, however, result in increases in K_{tip}^c.

(3) As cyclic fatigue involves a crack-tip frictional degradation process, it is dependent upon crack-tip stress intensity factor amplitude, ΔK_{tip}. ΔK_{tip} is reduced by lowering $K_{tip(max)}$ through crack-tip shielding and raising $K_{tip(min)}$ through crack-tip closure. Near tip crack-tip closure appears to be caused by phase transformation associated dilation, as is crack-tip shielding.

(4) Uncracked bridging ligaments have minimal effect upon overall crack growth rates. They are however a plausible explanation for the discontinuous nature of cyclic fatigue crack growth in PSZ.

High fatigue crack growth exponents, as indicated by steep fatigue curves, combined with the discontinuous nature of crack growth in PSZ restrict the ability to make accurate lifetime predictions for structural design situations. It would therefore appear prudent that in the case of PSZ that stress intensity factors, below the cyclic fatigue threshold, of $0.5K_0$ be used in engineering design. This would ensure security of maintaining structural integrity independent of the loading cycle.

ACKNOWLEDGMENTS

The authors would like to thank the Australian Research Council (ARC), the DITAC New Materials Technology and Manufacturing Programme and ICI Advanced Ceramics Ltd for supply of materials and continued financial support of the work. M.J.H. was supported by the ARC with an APRA (Industry) and in Japan by the Iketani Science and Technology Foundation. Thanks to J.C. Healy for helpful advice, R.H.J. Hannink for assistance with the FESEM observations and J. Argyriou and C. Howard for assistance with the neutron diffraction phase analysis. Crack growth testing, R-curve testing and Raman spectroscopy were undertaken at Lawrence Berkeley Laboratory, Berkeley, USA through the generous assistance of R.O. Ritchie and R. Dauskardt.

REFERENCES

[1] Evans, A. G., "Fatigue in Ceramics" International Journal of Fracture, Vol. 16, 1980, pp 485-98.

[2] Evans, A. G. and Fuller, E. G., "Crack Propagation in Ceramic Materials Under Cyclic Loading Conditions" Metallurgical Transactions, Vol. 50, 1974, pp 27-33.

[3] Fett, T., Martin, G. and Munz, D., "Determination of da/dN-ΔK Curves for Small Cracks in Alumina in Alternating Bend Tests" Journal of Materials Science, Vol. 26, 1991, pp 3320-8.

[4] Guiu, F., Reece, M. J. and Vaughan, D. A. J., "Cyclic Fatigue of Ceramics" Journal of Materials Science, Vol. 26, 1991, pp 3275-3286.

[5] Lathabai, S., Mai, Y. W. and Lawn, B. R., "Cyclic Fatigue Behaviour of an Alumina Ceramic with Crack Resistance Characteristics" Journal of the American Ceramic Society, Vol. 75, No. 4, 1989, pp 848-53.

[6] Lathabai, S., Rodel, J. and Lawn, B. R., "Cyclic Fatigue from Frictional Degradation at Bridging Grains in Alumina" Journal of the American Ceramic Society, Vol. 74, No. 6, 1991, pp 1340-1348.

[7] Masuda, M. T., Soma, T., Matsui, M. and Oda, I., "Cyclic Fatigue of Sintered Silicon Nitride" Journal of the European Ceramic Society, Vol. 6, 1990, pp 253-258.

[8] Dauskardt, R. H., Carter, W. C., Viers, D. K. and Ritchie, R. O., "Transient Subcritical Crack-Growth Behaviour in Transformation-Toughened Ceramics" Acta Metallurgica et Materiala, Vol. 38, No. 11, 1990, pp 2327-2336.

[9] Dauskardt, R. H., Marshall, D. B. and Ritchie, R. O., "Cyclic Fatigue Crack Propagation in Magnesia-Partially-Stabilised Zirconia Ceramics" Journal of the American Ceramic Society, Vol. 73, No. 4, 1990, pp 893-903.

[10] Duan, K., Cotterell, B. and Mai, Y. W., "Crack Growth in Zirconia Bearing Ceramics under Cyclic Load", Vol. Fracture Mechanics of Ceramics, No. 9, Nagoya, Japan, R.C.Bradt, D. P. H. Hasselman, D. Munz, M. Sakai &. V. Ya Shevchenko Eds., Plenum Press, New York, USA, 1992B.pp 507-516.

[11] Grathwohl, G. and Liu, T., "Crack Resistance and Fatigue of Transforming Ceramics: I, Materials in the ZrO_2-Y_2O_3-Al_2O_3 System" Journal of the American Ceramic Society, Vol. 74, No. 2, 1991, pp 318-325.

[12] Grathwohl, G. and Liu, T., "Crack Resistance and Fatigue of Transforming Ceramics: II, CeO2-Stabilised Tetragonal ZrO_2" Journal of the American Ceramic Society, Vol. 74, No. 2, 1991, pp 3028-3024.

[13] Hoffman, M. J., Lentz, W., Swain, M. V. and Mai, Y. W., "Cyclic Fatigue Crack Propagation in Partially Stabilised Zirconia with Crack-Resistance Curve Characteristics" Journal of the European Ceramic Society, Vol. 11, 1993, pp 445-453.

[14] Liu, T. and Mai, Y. W., "Cyclic Fatigue Crack Propagation of 9Ce-TZP Ceramics with Different Grain Size" Journal of the

American Ceramic Society, Vol. 76, No. 10, 1993, pp 2601-2606.
[15] Muddle, B. C. and Hannink, R. H. J., "Crystallography of the Tetragonal to Monoclinic Transformation in MgO-Partially-Stabilised Zirconia" Journal of the American Ceramic Society, Vol. 69, No. 7, 1986, pp 547-555.
[16] Hannink, R. H. J., Howard, C. J., Kisi, E. H. and Swain, M. V., "Relationship Between Fracture Toughness and Phase Assemblage in Mg-PSZ", Fourth International Conference on the Science and Technology of Zirconia, Los Angeles, CA, 1989.
[17] Hu, X. Z., Mai, Y. W. and Lathabai, S., "Compliance Analysis of a Bridged Crack Under Monotonic and Cyclic Loading" Journal of the European Ceramic Society, Vol. 9, 1992, pp 213-217.
[18] Dauskardt, R. H., "A Frictional Wear Mechanism for Fatigue- Crack Growth in Grain Bridging Ceramics" Acta Metallurgica and Materiala, Vol. 41, No. 9, 1993, pp 2765-2781.
[19] Liu, S. Y. and Chen, I. W., "Fatigue of Yttria-Stabilised Zirconia: I, Fatigue Damage, Fracture Origins and Lifetime Prediction" Journal of the American Ceramic Society, Vol. 74, No. 6, 1991, pp 1197-1205.
[20] Heuer, A. H., Ruhle, M. and Marshall, D. B., "On the Thermoelastic Martensitic Transformation in Tetragonal Zirconia" Journal of the American Ceramic Society, Vol. 73, No. 4, 1990, pp 1084-1093.
[21] Davidson, D., Campbell, J. B. and Lankford, J., "Fatigue Crack Growth through Partially Stabilised Zirconia at Ambient and Elevated Temperatures" Acta Metallurgica et Materiala, Vol. 39, 1991, pp 1319-1330.
[22] Liu, S. Y. and Chen, I. W., "Fatigue of Yttria-Stabilised Zirconia: II, Crack Propagation, Fatigue Striations and Short-Crack Behaviour" Journal of the American Ceramic Society, Vol. 74, No. 6, 1991, pp 1206-1216.
[23] Sih, G. H., Handbook of Stress Intensity Factors Lehigh University Press, Bethlehem, USA, 1991, pp 1.5.1-1.
[24] ASTM Standard E647-86a, "Standard Test Method for Measurement of Fatigue Crack Growth Rates", 1987 ASTM Annual Book of Standards, American Society for Testing and Materials, Philadelphia, PA, USA, 1987, pp 899-926.
[25] Viers, D. K., Ager, J. W., Loucks, E. T. and Rosenblatt, G. M., "Mapping Materials Properties with Raman Spectroscopy Utilising a Two-Dimensional Detector" Applied Optics, Vol. 29, 1990, pp 4969-80.
[26] Viers, D. K., Ager, J. W., Loucks, E. T. and Rosenblatt, G. M., "Materials Characterisation by Imaging Raman Spectroscopy" Ceramics Transactions, Vol. 19, 1991, pp 1043-50.
[27] Howard, C. J., Hill, R. J. and Reichert, B. E., "Structures of ZrO2 Polymorphs at Room Temperature by High Resolution Neutron Powder Diffraction" Acta Crystallographica, Vol. B40, 1988, pp 116-120.
[28] Howard, C. J. and Hill, R. J., "The polymorphs of zirconia- phase abundance and crystal structure by Reitveld analysis of neutron and x-ray diffraction data" Journal of Materials Science, Vol. 26, 1991, pp 127-134.
[29] ASTM Standard E399-83, "Standard Test Method for Plane-Strain Fracture Toughness of Metallic Materials", 1983 ASTM Annual Book of Standards, American Society for Testing and Materials, Philadelphia, PA, USA, 1983, pp 488-512.
[30] Swain, M. V. and Zelizko, V., Comparison of Static and Cyclic Fatigue in Mg-PSZ Alloys Eds.Somiya, S., Yamamoto, H., Yanagida, H., Science and Technology of Zirconia III **24B** Journal of the American Ceramic Society, Westerville, OH, 1988. pp 595- 606
[31] Mai, Y. W., Hu, X., Duan, K. and Cotterell, B., "Crack- Resistance Curve and Cyclic Fatigue in Ceramic Materials", Vol. Fracture Mechanics of Ceramics, No. 9, Nagoya, Japan, R.C.Bradt, D. P. H. Hasselman, D. Munz, M. Sakai &. V. Ya Shevchenko Eds., Plenum Press, New York, USA, 1992.pp 387-422.

[32] Lutz, E. H. and Swain, M. V., "Interrelation Between Flaw Resistance, R-Curve Behaviour and Thermal Shock Strength Degradation in Ceramics" Journal of the American Ceramic Society, Vol. 74, No. 11, 1991, pp 2859-2868.

[33] Stump, D. M. and Budiansky, B., "Finite Cracks in Transformation-Toughened Ceramics" Acta Metallurgica et Materiala, Vol. 37, No. 12, 1989, pp 3297-3304.

[34] Stump, D. M. and Budiansky, B., "Crack Growth Resistance in Transformation-Toughened Ceramics" International Journal of Solids and Structures, Vol. 25, No. 6, 1989, pp 635-646.

[35] Hoffman, M. J., Dauskardt, R. H. and Ritchie, R. O., "Mechanics and Mechanisms of Cyclic Fatigue Crack-Propagation in Transformation-Toughened Zirconia Ceramics", Proceedings of Zirconia V, Melbourne, Australia, S.P.S.Badwal, M. J. Bannister &. R. H. J. Hannink Eds., 1992.

[36] Green, D. J., Hannink, R. H. J. and Swain, M. V., Transformation Toughening of Ceramics, CRC Press, Florida, USA, 1989.

[37] Jorgensen, M. H. and Karihaloo, B. L., "Cyclic fatigue of ZTC - Micromechanical modelling" Mechanics of Materials, Vol. 14, 1993, pp 291-299.

[38] Budiansky, B., Hutchinson, J. W. and Lambropoulos, "Continuum Theory of Dilatant Transformation Toughening in Ceramics", International Journal of Solids and Structures, Vol. 19, 1983, pp 337-355.

[39] Cotterell, B. and Mai, Y. W., "Modelling Crack Growth in Fibre-Reinforced Cementitious Materials" Material Forum, Vol. 11, 1988, pp 341-351.

[40] Hu, X. Z. and Mai, Y. W., "Crack-Bridging Analysis for Alumina Ceramics Under Monotonic and Cyclic Loading" Journal of the American Ceramic Society, Vol. 75, No. 4, 1992, pp 848-853.

[41] Hoffman, M. J., PhD Thesis: Cyclic Fatigue in Transformation-Toughened Zirconia Ceramics University of Sydney, Sydney, Australia, 1994.

[42] Shang, J. K. and Ritchie, R. O., "Crack Bridging by Uncracked Ligaments during Fatigue-Crack Growth in SiC-Reinforced Aluminium-Alloy Composites" Metallurgical Transactions A, Vol. 20A, 1989, pp 897-907.

Jennifer A. Cordes[1], *Rahmi Yazici*[2]

PREDICTING CRACK GROWTH IN CONTINUOUS-FIBER COMPOSITE MATERIALS

REFERENCE: Cordes, J. A., and Yazici, R., **"Predicting Crack Growth in Continuous-Fiber Composite Materials,"** Fracture Mechanics: 26th Volume, ASTM STP 1256, Walter G. Reuter, John H. Underwood, and James C. Newman, Jr., Eds., American Society for Testing and Materials, Philadelphia, 1995.

ABSTRACT: Pre-notched composite lamina with unidirectional fibers were studied experimentally and using finite element analysis. Experiments were conducted on notched graphite/aluminum and glass/epoxy panels and the results were compared to a finite element method. Under remote tensile loading, cracks in the graphite/aluminum panels propagated perpendicular to the applied load without stable crack growth. In the glass/epoxy panels, crack propagation was initially stable and parallel to the fibers. A nonlinear damage zone method (DZM) was used to predict the crack growth directions, estimate damages, model stable and unstable crack growths, and predict the loads at failure. For both materials, the predicted loads at failure were within 20% of experimental loads.

KEY WORDS: Composite materials, stable crack growth, damage zone model, finite element analysis, fracture

This paper describes an experimental and numerical study of notched, continuously-reinforced composite panels. Samples were loaded in remote tension using applied displacements at the panel edges. The resulting crack growth directions, the load versus displacement behaviors, and the panel damages were recorded and used to assess the accuracy of a fracture criterion for composite materials. Electron-microscopy was used to quantify the crack tip damage zones and to evaluate the fracture surfaces. Cracks in the glass/epoxy (Gl/Ep) samples progressed in a stable fashion parallel to the fibers, shearing the matrix from the fiber. The graphite/aluminum (Gr/Al) panels failed by unstable crack growth perpendicular to the applied tensile load leaving little fiber pullout in the wake of the crack.

Failure prediction for notched composite panels is complicated by the micro-mechanics of damage at the crack tip. As represented in Figure 1, crack tip damage can include fiber fracture, fiber/matrix debonding, and matrix yielding. The nature of these

[1]Assistant Professor, Stevens Institute of Technology, Hoboken, New Jersey

[2]Research Professor, Stevens Institute of Technology, Hoboken, New Jersey

Copyright © 1995 by ASTM International www.astm.org

micro-mechanical failures determines the overall nature of the failures in the lamina. If matrix/fiber debonding strength is relatively weak, then stable and unstable crack growth occurring along the fibers is likely. If the matrix /fiber bonds are relatively strong, crack growth perpendicular to the tensile load is likely.

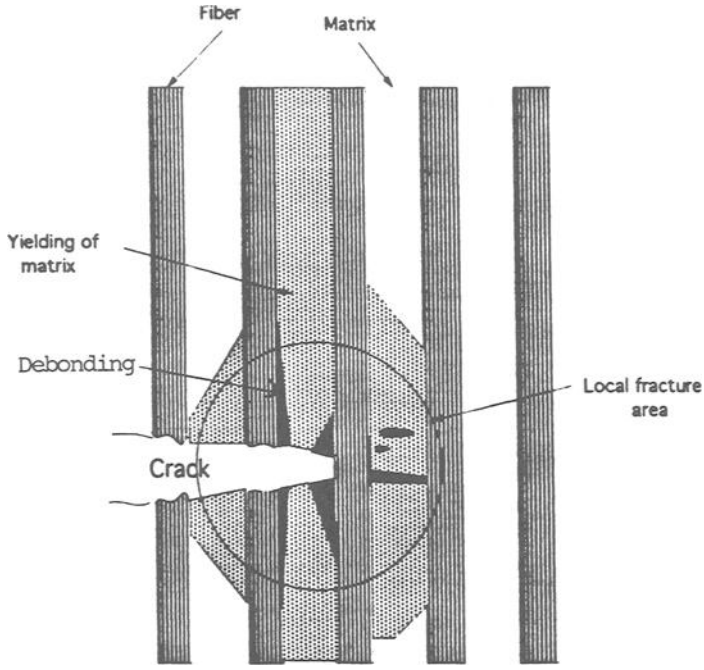


Figure 1. Representation of Local Damage Near a Crack Tip

For some composite materials, the stress/strain diagrams in directions parallel to the fibers are nearly linear while the shear-stress versus shear-strain diagrams are nonlinear, indicating progressive damage in the matrix or along the fiber/matrix interface in the shear mode. Examples of materials which display nonlinear behavior in shear include boron/epoxy [1], boron/aluminum [2], glass/epoxy, alumina/aluminum [3], graphite/epoxy [4], and silicon/titanium [5]. The usual criteria for predicting failure in homogeneous orthotropic materials, Hill criterion and Tsai-Wu criterion, do not include provisions for the nonlinear shear-stress behavior which may effect crack growth direction and the amount of load that can be sustained before final failure.

This paper uses a damage zone method (DZM) to predict the overall nature of failure and the failure load for continuous-fiber composites. This criterion is phenomenological rather than theoretical. The method predicts the direction of crack growth from the crack tip stress ratios, uses cohesive stresses to incorporate nonlinear material behavior, and uses relative displacements at the crack tip as the criterion for

predicting crack growth. For the glass/epoxy examples, cohesive stresses parallel to the fiber simulated the nonlinear behavior in shear. The critical parameter for predicting fracture failure was the crack tip sliding displacement (CTSD) which was determined experimentally. As shown in Figure 2a, the CTSD parameter represents the relative slip in the shear direction near the crack tip. For the aluminum/graphite panels, cohesive stresses were inserted in the original crack direction to simulate the material damage. The critical fracture parameter was the crack tip opening displacement (CTOD), shown in Figure 2b.

Background

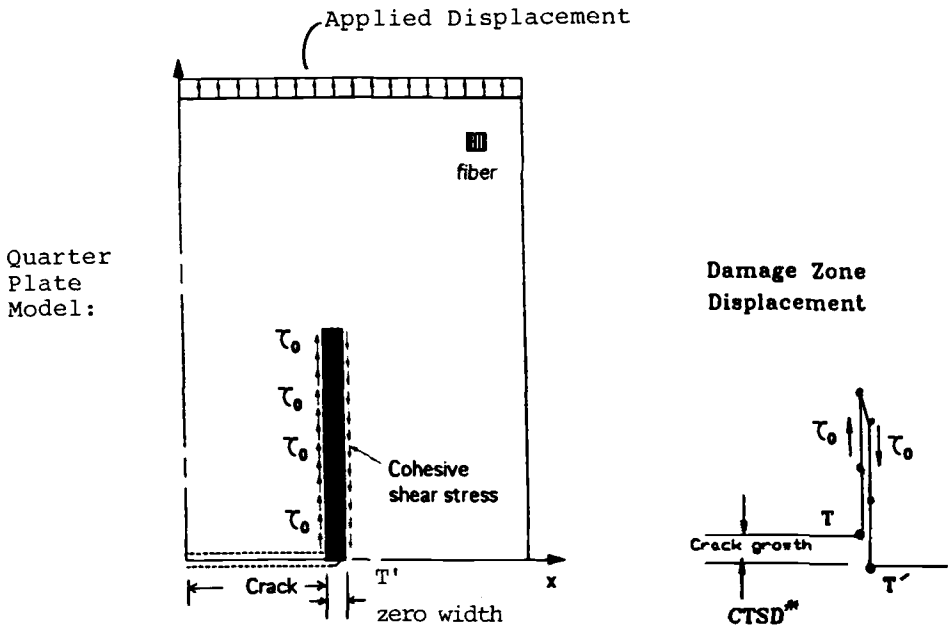
Crack Growth Direction in Unidirectional Composites

As summarized in Table 1, crack growth in uni-directionally reinforced composites generally occurs perpendicular to the load or along the fibers.

TABLE 1: Crack Growth Direction in Pre-cracked Continuous-fiber Composites

Material	Fiber Direction w/to load	Original Crack w/to load	Crack Growth w/to fiber	Ref
Glass/Epoxy	0 degrees	90 degrees	parallel to fiber	
Graphite/Epoxy	0 degrees	90 degrees	parallel to fiber	[6]
Graphite/Epoxy	-30 degrees	90 degrees	parallel to fiber	[6]
Graphite/Epoxy	-15 degrees	90 degrees	parallel to fiber	[6]
Graphite/Epoxy	-15 degrees	75 degrees	parallel to load	[6]
Graphite/Epoxy	0 degrees	90 degrees	perpend. to fiber	[7]
Graphite/Epoxy	-30 degrees	90 degrees	parallel to fiber	[8]
Graphite/Epoxy	-15 degrees	90 degrees	parallel to fiber	[8]
Graphite/Epoxy	-15 degrees	75 degrees	parallel to fiber	[8]
Alumina/Aluminum	0 degrees	90 degrees	parallel to fiber	[9]
Alumina/Magnesium	0 degrees	90 degrees	parallel to fiber	[9]
Boron/Aluminum	0 degrees	90 degrees	parallel to fiber	[10]
Boron/Aluminum	0 degrees	90 degrees	parallel to fiber	[11]
Graphite/Aluminum	0 degrees	60 degrees	perpendicular to load	
Graphite/Aluminum	0 degrees	90 degrees	perpendicular to load	
SiC/Titanium	0 degrees	90 degrees	perpendicular to load	[12]
SiC/Aluminum	0 degrees	90 degrees	parallel to fiber	[9]
Carbon/Carbon	0 degrees	90 degrees	perpendicular load	[13]

a. Crack Growth Parallel to Fiber



b. Crack Growth Perpendicular to Fiber

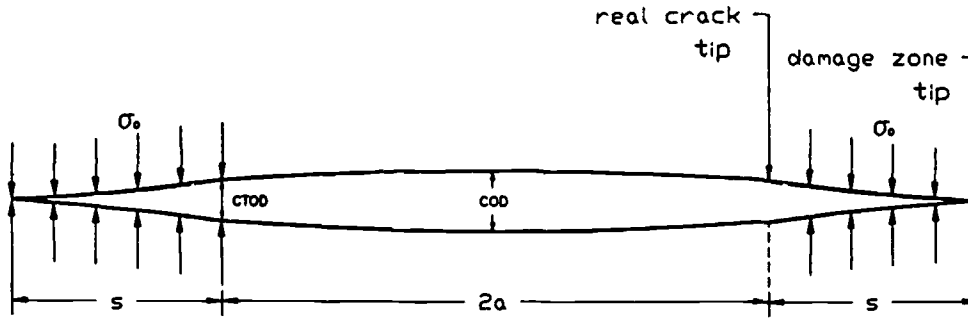


Figure 2. Damage Zone Assumptions

With the exception of one of the graphite/epoxy examples [6], cracks propagated either parallel to the fiber or perpendicular to the applied load. For each composite type, differences in the crack growth direction resulted from differences in fiber volumes, bond strengths, and constituent material properties. Pre-cracked lamina such as glass/epoxy and boron/aluminum [11], displayed large damage zones perpendicular to the fiber prior to crack growth. For the carbon/carbon [13] composite and for the SiC/titanium composite [12], the crack progressed in a self-similar fashion, while fibers debonded from the matrix and remained in the wake of the advancing crack.

Crack Growth Theories from Isotropic Materials, Applied to Composite Materials

Several workers on composite materials investigated the feasibility of using mixed-mode fracture criteria developed for isotropic to evaluate composite materials. In mixed-mode fracture of isotropic materials, stresses near the crack tip act in tension to open the surfaces (Mode I) and in shear to slide the surfaces relative to one another (Mode II). Tensile stresses and shear stresses also act at the crack tip in composite materials.

Ellyin and Kadi [6] reviewed four crack growth direction criteria and concluded that Sih's [14] maximum strain energy criterion was the best predictor for graphite/epoxy. In a similar fashion, Gregory and Herakovich [8] reviewed three isotropic failure criteria and concluded that a different criterion, the normal stress criterion, was the best predictor of crack growth direction in graphite/epoxy.

The likelihood of crack growth is determined using a fracture parameter and a mixed mode fracture criteria. Methods to separate K_I and K_{II} [15,16] or J_I and J_{II} [17] assume that the lamina behaves as an orthotropic and homogeneous material. The strain energy release rate G_c for linear material and the critical J-integral value for nonlinear material behavior are then used to predict fracture under mixed-mode loading:

$$G_c = G_I + G_{II} \quad \text{or} \quad J_c = J_I + J_{II} \tag{1}$$

For graphite/epoxy, G_c and the calculated G_I/G_{II} ratio were found to be a function of crack angle rather than a material parameter [4]. Binienda and Reddy [18] studied crack growth in graphite/epoxy with various angles with respect to the fiber direction. G_c and G_{II} at failure increased as the angle of the crack decreased with respect to the tensile direction while G_I increased only slightly. The implication was that G_{Ic} may be a more accurate prediction of fracture failure than G_c for an angle-cracked composite laminae.

For self-similar crack-growth perpendicular to the applied load, cohesive zone models have been successful in predicting unstable crack growth in composite materials. These models are based on the work of Dugdale [19] and Barrenblatt [20] for isotropic materials. Hillerborg, Modee'r and Peterson used cohesive tension stresses, G_{Ic} and a critical crack tip opening displacement parameter to predict unstable crack growth in

concrete [21]. Bäcklund and Arronson used cohesive tensile stresses successfully to model nonlinear damage and predict self-similar crack growth in glass/epoxy and graphite/epoxy laminae with cracks and notches [7,22].

Failure Criteria Specifically for Composite Materials

Several researchers have developed fracture failure criteria that consider the heterogeniety of the composite and apply exclusively to uni-directionally reinforced materials. The shear-lag models used by Nairn [23] and others [24,25] assume that tensile stresses are carried by the fibers and shear stresses are carried by the matrix and interface. Crack growth is assumed to occur either parallel to the fibers or though the fibers, consistent with the crack growth directions found in the literature and repeated in Table 1. Crack growth direction predictions are based on strain energy release rate ratios and the critical strain energy release rate is the fracture parameter. The critical strain energy release rate includes a parameter associated with the heterogeneous failure mechanism at the crack tip. The method is analytic and has been used to determine crack-tip stress concentrations for a number of specific geometries.

A finite element method was used by Dvorak, Bahei-el-din, and others [10,26] to predict the onset of fracture in boron/aluminum composites. The panel was modeled using elastic-orthotropic elements surrounding a deforming shear region parallel to the fibers. The local fracture criterion was based on the maximum principal stress to off axis strength ratio. The accuracy of the finite element stress analysis, critical to the stress-based fracture criterion was enhanced by superposing an analytic solution near the crack tip. The method did not include stable crack growth.

Failure Criterion in this Paper

In an effort to develop a generalized fracture method for uni-directional composite materials, aspects of the damage zone concept for Mode I and the shear failure methods from the shear-lag theory and Dvorak were used for the finite element criterion described in this paper. Geometries can be consistent with plane stress or plane strain assumption and can have angle cracks or notches. The use of shear cohesive stresses of zero width and a CTSD parameter were not found in the literature for composite materials. The CTSD parameter was previously used by Cordes et. al. for predicting mixed-mode [27] and Mode II failure [28] in aluminum samples. Neither experimental nor numerical studies of fracture in Gr/Al were found in the literature.

Crack Growth Direction Criterion

Crack growth was assumed to be either parallel to the fiber or perpendicular to the applied tensile load. The ratio of the stress at the crack tip to the material strength were used to predict the crack growth direction as follows:

$\tau_{12}/\tau_o > \sigma_{22}/\sigma_o$ shear damage, damage zone parallel to fiber (2a)
$\tau_{12}/\tau_o < \sigma_{22}/\sigma_o$ tensile damage, damage zone perpendicular to fiber (2b)

where $\tau 12$ is the shear stress at the crack tip, τ_o is the shear strength of the matrix, σ_{22} is the tensile stress at the crack tip, and σ_o is the tensile strength of the composite parallel to the fiber direction. The direction of crack growth was determined before the damage zone direction was inserted into the model.

Fracture Parameters and Fracture Failure Criteria

In this paper, two crack tip opening displacements serve as the critical fracture parameter. If crack growth parallel to the fiber is predicted, a crack tip sliding displacement (CTSD) is used as a fracture parameter and failure along the fiber direction is modeled. If crack growth is predicted to be perpendicular to the fiber, a crack tip opening displacement (CTOD) parameter is used and self-similar crack growth is modeled. Summarizing:

$CTSD \geq CTSD^*$ crack growth parallel to fiber, shear failure (3a)
$CTOD \geq CTOD^*$ crack growth perpendicular to load, tensile failure (3b)

This criteria is equivalent to a J-integral (or strain energy release rate) criteria:

$$J_{II} = \int_0^{CTSD^*} \tau_o \, d\delta \quad \text{shear failure, damage zone parallel to fiber} \qquad (4a)$$

$$J_I = \int_0^{CTOD^*} \sigma_o \, d\delta \quad \text{tensile failure, damage zone perpendicular to fiber} \qquad (4b)$$

Modeling the Damage Zone

The cohesive stress or damage zones provide mechanisms for modeling nonlinear material behavior which may be the result of debonding, micro-cracks, fiber breakage, and yielding in the matrix. Effects of manufacturing voids are neglected and perfect bonding before loading is assumed. For damage parallel to fibers, some sliding of surfaces relative to one another was noted. However the normal forces were very small and the effects of friction were neglected.

For both models, cohesive stress zones were modeled using duplicate grid point pairs were inserted into the model in the direction of crack growth as determined by the stress criterion shown in equations (2a) and (2b). Figure 3 shows a finite element mesh with duplicate grid point pairs in the direction of crack growth, parallel to the fiber. Initially, all grid point pairs were constrained to have the same displacement. The panel models were loaded incrementally by increasing the displacements at the panel edges. At a

grid point pair where the stress component reached yield strength (τ_o = yield in shear) or failure strength (σ_o= strength in tension), the displacement constraint between the grid point pair was removed and a cohesive stress was inserted between the grid points. For crack growth along the fibers, cohesive stresses acted parallel to the fibers and imposed a constant shear stress between grid point pairs:

$$\tau_o = \text{yield in shear, constant} \tag{5a}$$

For self similar crack growth, cohesive stresses acted in tension between duplicate grid point pairs. The cohesive force remained at a constant value:

$$\sigma o = \text{ultimate strength in tension, constant} \tag{5b}$$

Cohesive stresses remained at the constant value until the critical crack tip displacement at a grid point pair, given in equation (3) was reached. After the critical displacement was reached, the cohesive stress was removed creating a free surface and simulating crack growth of one finite element in length.

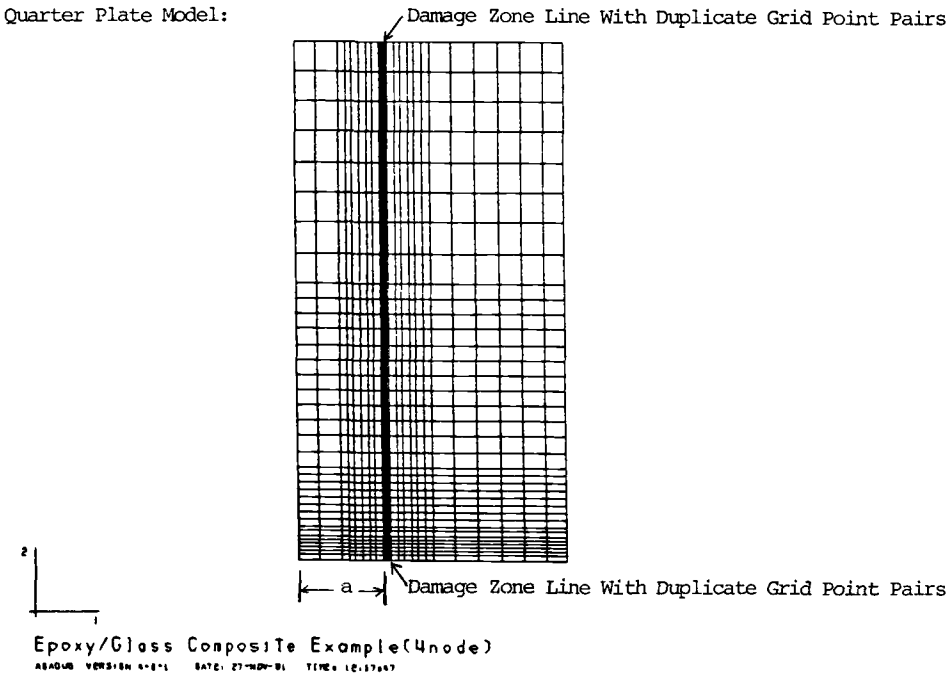


Figure 3. Finite Element Mesh, Glass/Epoxy Panel

Finite Element Package Requirements

DZM can be used to evaluate the fracture behavior of a precracked lamina using a general-purpose finite element package that includes the following:

- plane stress or plane strain elements
- nonlinear spring elements, required in some packages to model constant spring force values
- nonlinear solution methods
- linear-elastic orthotropic material model
- interface and slide elements to prevent overlap of the crack surfaces

Special crack tip elements and special material yield models are not required for the analysis. All yield-type effects are incorporated into the damage zone and modeled as cohesive stresses having a magnitude equal to the lamina strength. Effects of friction along crack and damage surfaces were neglected.

Experiments on Composite Panels

Materials

Two technologically important composite materials were chosen for validation of DZM: E-glass reinforced epoxy (Gl/Ep) and graphite reinforced 6061-T6 aluminum (Gr/Al). Both materials have critical applications in aerospace and other technologies due to properties such as high specific strength and rigidity. These two materials were chosen for analysis because of their differing crack propagation behavior.

The composites consist of unidirectional, continuous fibers with fiber volume percent of 40% and 53% for Gr/Al and Gl/Ep respectively. Table 2 summarizes the material properties, determined experimentally except as noted. The Gr/Al coupons were cut from 300 mm by 300 mm by .4125 mm thick sheets supplied by DWA Composites Corporation. The matrix was 6061-T6 aluminum and the fibers were continuous Pitch-75 graphite.

The glass/epoxy composites were purchased from 3M as prepreg tapes. Glass/epoxy samples were cured [29] to reach the material properties shown in Table 2. Gl/Ep samples were 0.6 mm thick and 50.0 mm with center notches were cut by a jeweller's saw following curing. A crack-tip diameter of 0.175 mm was achieved. Notched Gr/Al samples were fabricated using an electic-arc spark cut and a 1.75 mm crack tip diameter was achieved. Sample preparation adhered to ASTM E-338-81 (Sharp Notch Tension Testing [30] and ASTM D-3552-82 [31].

Table 2. Material Properties

Property	E-Glass/Epoxy	Graphite/Aluminum
Longitudinal Tensile Strength	800. MPa	402. MPa
Longitudinal Elastic Modulus, E11	4.1E4 MPa	2.25E5 MPa
Transverse Tensile Strength	15. MPa	43. MPa
Transverse Elastic Modulus, E22	8.7E3 MPa	2.24E4 MPa
Shear Modulus, G12 (literature)	4.5E3 MPa	2.23E4 MPa
Poisson's Ratio, v12	.29	.3

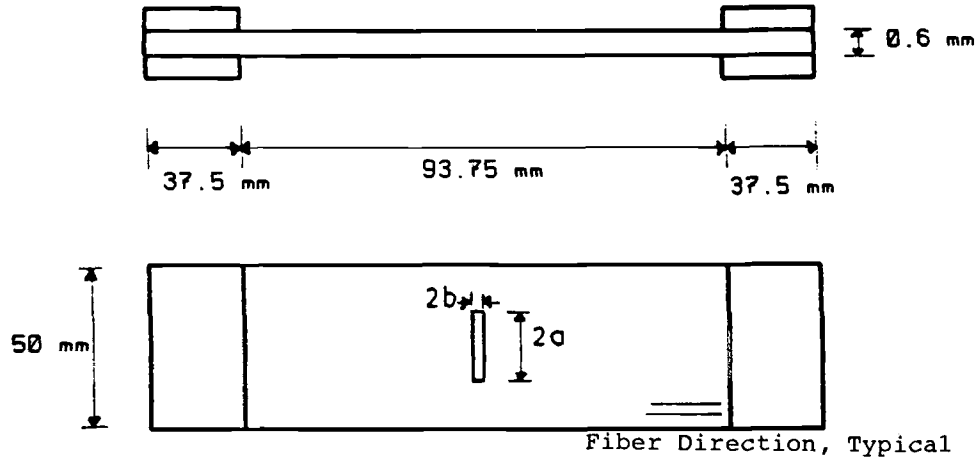
Fracture Tests

Uniaxial tensile loads were applied quasi-statically to the notched panel geometries shown in Figure 4. A range of crack-length to width ratios were studied for both materials. The failure loads, the direction of crack growth, and the crack opening displacement at the center of the crack (COD) was recorded. For the Gr/Al material, samples with notch angles of 30 degrees were also tested to determine the crack growth direction.

In the Gl/Ep composites, crack propagation was parallel to the fibers and to the applied displacement direction. When the panels were subjected to continuous loading that increased incrementally, stable crack growth occurred parallel to the fibers. The "parallel" crack propagation consisted of interfacial debonding along the fiber and trans-matrix failure. In some regions, trans-fiber fracture was also observed on the fracture surface. Microstructural investigation revealed that along the crack path, the crack growth was predominately along the fiber matrix interface. Figures 5 and 6 show typical outward (ligament side) and inward (pre-notch side) surfaces. Nearest the outward panel edge, the matrix was sheared from the remaining fiber. On the inward fracture side, the ruts where the fibers have been separated are shown. There was no detectable extension of the crack perpendicular to the applied load and in the direction of the original crack. A typical fracture surface at the crack front is shown in Figure 7. The white patch in the middle of the micrograph is the bundle-rich, pre-cut crack front. Although there was no detectable extension of the crack perpendicular to the applied load, there was a small amount of trans-fiber fracture which occurred along the crack path. An example of trans-fiber fracture is shown in Figure 8.

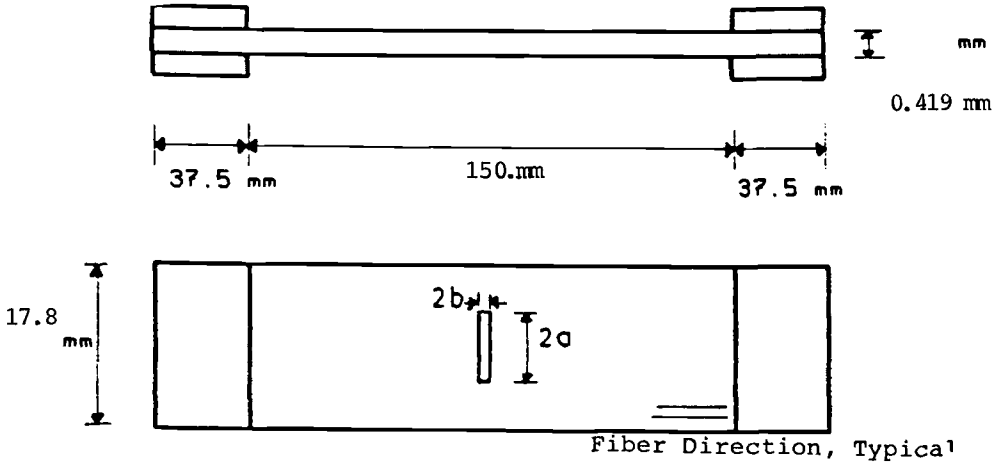
Figure 9 shows the edge-on view of the fracture surface in a Gr/Al sample. Unstable crack growth occurred perpendicular to the applied load, in the original direction of the crack, and through the fibers. Deviation form this crack growth direction was limited to small regions of fiber-bundle pullout which were approximately 100 μm in length. An example of the fiber-bundle pullout is shown in Figure 10. The micro-plastic

a. Glass/Epoxy Panels



2b = 0.175 mm
2a = 10.2 mm, 17.45 mm, 24.85 mm

b. Graphite/Aluminum Panels



2b = 0.175 mm
2a = 3.4 mm, 5.34 mm, 5.94 mm, 6.48 mm

Figure 4. Panel Geometries

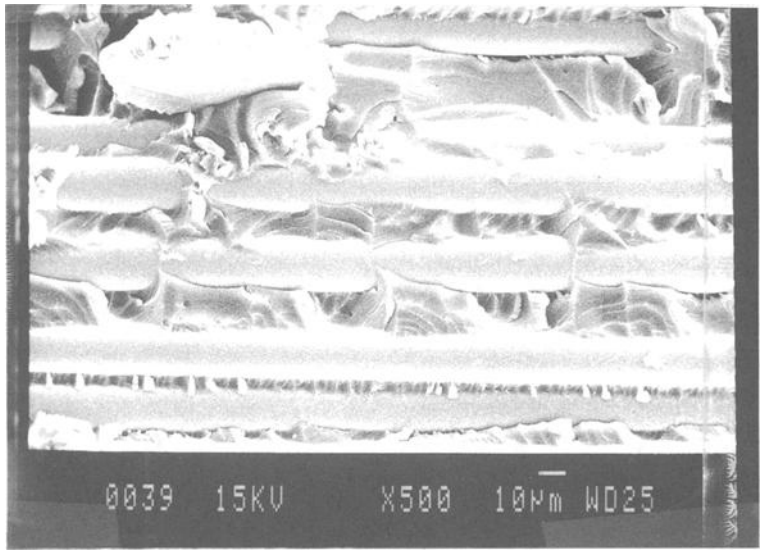


Figure 5. Outward Fracture Surface of Glass/Epoxy Panel
(Note, fiber adhering to ligament side)



Figure 6. Inward Fracture Surface of Glass/Epoxy Panel
(Note, fiber debonded from matrix on crack side)

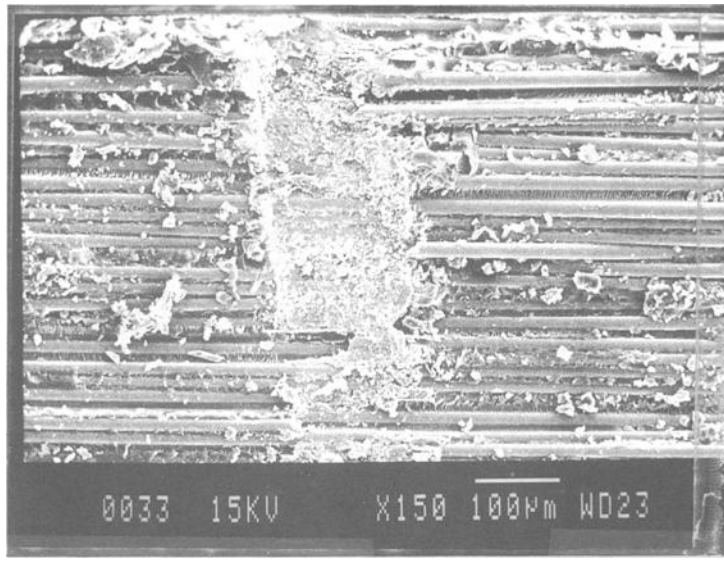


Figure 7. Edge-on View of Fracture Surface, Glass/Epoxy Panel

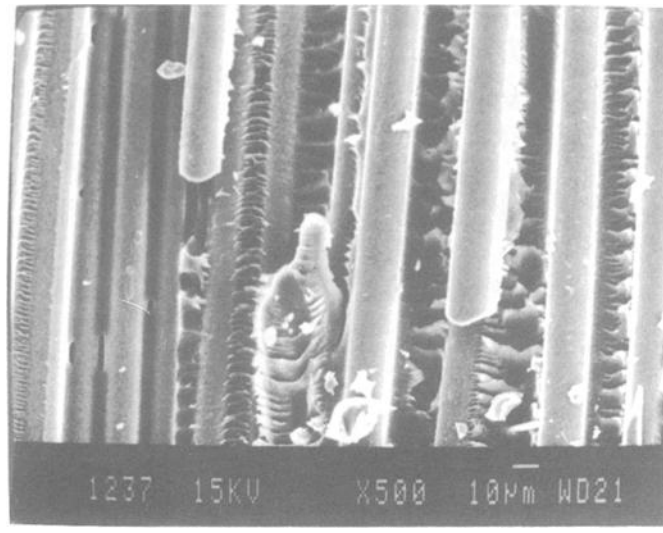


Figure 8. Trans-fiber Fracture in Glass/Epoxy Panel

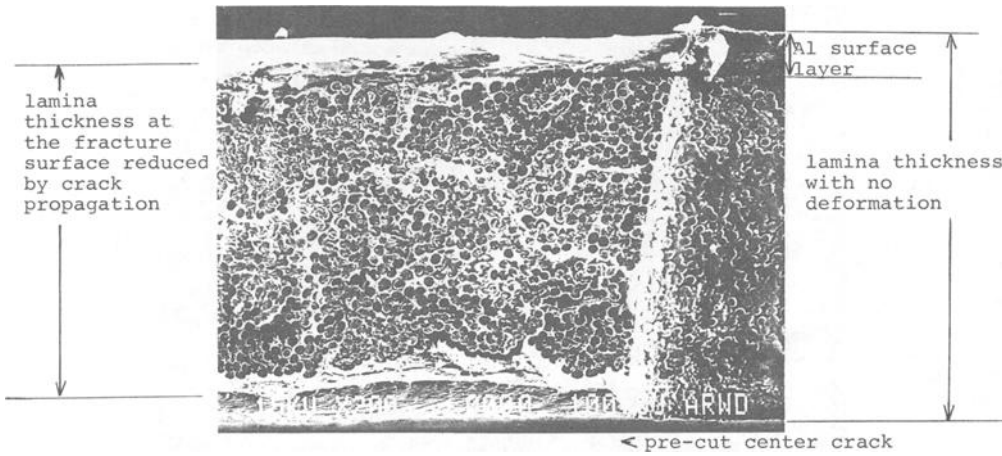


Fig. 9 Edge-on view of fracture surface of Gr/Al lamina

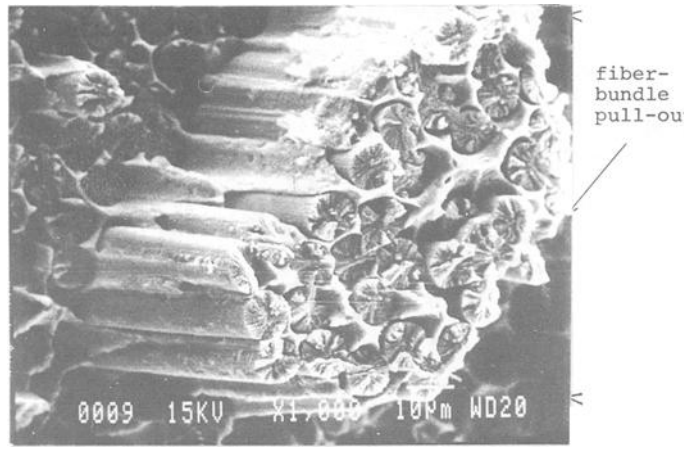


Fig.10 Typical fiber-bundle pull-out on fracture surface of Gr/Al lamina

zone length was 100 μm -150 μm in the direction parallel to the fibers. At this micro-plastic zone, the reduction in cross section was approximately 15%. Most of this plasticity, however, took place in the thin, protective aluminum layers on the top and bottom surfaces of the laminae. The reduction in cross section in the fiber reinforced region was about 5%. Micro-plasticity in the fiberous bulk areas was confined to the matrix regions between the fibers.

Example Application of the Fracture Criterion, Gl/Ep and Gr/Al Panels

Glass /Epoxy Panels

The finite element mesh used in the crack tip region is shown in Figure 3. The smallest element in the analysis was 0.635 mm. One quarter of the plate was modeled for the analysis. The plate was modeled as a linear-elastic, orthotropic material. All material nonlinearities are confined to the damage zone.

An initial linear analysis was completed to determine the likely direction of crack growth. Near the crack tip the following normalized stress ratios were calculated from the linear analysis:

$$\tau_{12}/\tau_o = 1.; \qquad \sigma_{22}/\sigma_o = .71$$

Since the shear stress ratio exceeded the tensile stress ratio, the damage zone was assumed to be parallel to the fiber direction. This assumption was consistent with experimental results.

The critical crack sliding displacement (CTSD) parameter served as the critical fracture parameter. This parameter was determined using the DZM for the notched panel with a crack length-to-width ratio 2a/w=0.349. The critical CTSD* was estimated to be 0.13 mm, by matching the applied force at initial, stable fracture.

Analysis Steps, Glass/Epoxy

The finite element mesh in Figure 3 had a line of duplicate grid point pairs. In ABAQUS, the general-purpose finite element package used for the analysis, the displacements of the duplicate pairs were constrained to be the same using multi-point-constraints. In the first step of the analysis, the applied displacement resulting in the shear stress at the crack tip reaching the shear strength, 15. MPa, was determined.

For the second analysis step, the constraint at the crack tip was removed and a spring was inserted between the crack tip grid points. The nonlinear spring simulated the cohesive shear stress which was assumed to be constant and equal to the shear strength 15. MPa. Subsequently, the applied load causing damage at the next grid point pairs was determined. The process of stepwise model change and increase in the load was repeated

until the damage zone extended up to the panel edge (simulating yield-type damage) or the CTSD* value was reached between all duplicate grid point pairs.

Results of Glass/Epoxy Analysis

Figures 11, 12, and 13 present the results. The model predicted an applied load within 17.% of the experimental load. The applied force versus the crack opening displacement (COD) parallel to the load and at the center of the crack followed the nonlinear behavior in the experiments.

In the experiments, the length of stable crack growth varied from 6.45 mm to 18.5 mm for the three different crack-length-to-width ratios. In each case, the critical CTSD* was reached before the stress parallel to the crack exceeded the composite material strength, indicating crack growth through the damage zone (and parallel to the fiber direction). However, the amount of stable crack growth predicted by the DZM was less than the experimental crack growth. This difference probably results from the variation in material uniformity in the actual sample and the estimate of the shear strength (stiffer than the sample). In addition, damage outside the cohesive stress zone was not included, in part due to the lack of an appropriate damage criteria in the general purpose finite element package ABAQUS [32]. The predicted nonlinear relationship between the applied load and the amount of stable crack growth is similar to the experimental behavior. In all cases final lamina failure was by crack growth parallel to the fiber.

Aluminum/Graphite Panels

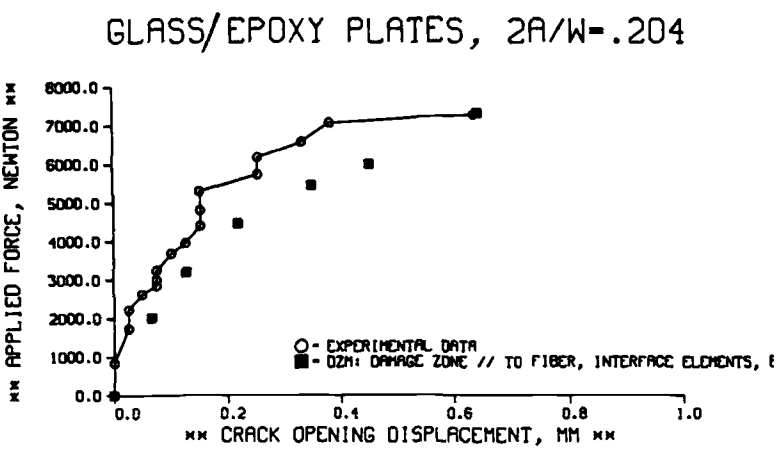
The DZM was used to predict the applied load at failure in the aluminum/graphite samples. The mesh consisted of 4-node, plane stress elements. The minimum element size was 0.18 mm or about 0.02% of the plate ligament. Outside of the damage zone, the composite was modeled as a linear elastic, orthotropic material.

The direction of the damage zone and subsequent unstable crack growth was predicted based on the stress to strength ratios, shown in equation (2). For a linear analysis of the crack aluminum/graphite plate with no singularity elements, normalized stress ratios were found to be:

$$\tau_{12}/\tau_o = 0.36; \qquad \sigma_{22}/\sigma_o = 1.$$

Since the tensile stress ratio exceeded the shear stress ratio, the damage zone was inserted perpendicular to the fiber direction. The cohesive tensile stresses were used to model the damage zone. The cohesive was a constant value σ_o= 400 MPa until the critical crack tip opening displacement was reached.

The following critical crack tip opening displacement (CTOD*) was estimated from Kc and the assumed cohesive stress relation. ASTM standard E561 for isotropic materials was used to estimate the fracture toughness Kc:



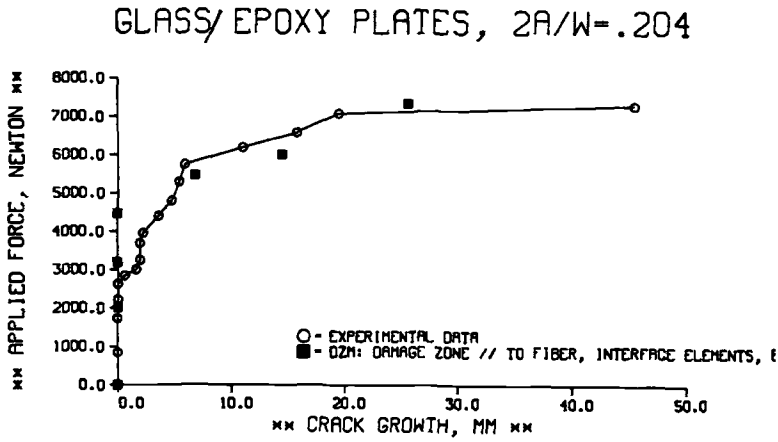
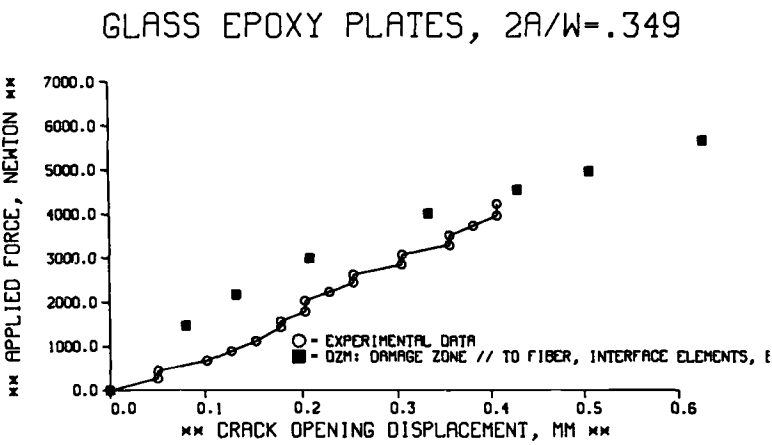


Figure 11. Results, Glass/Epoxy Panel, 2a/w=0.204



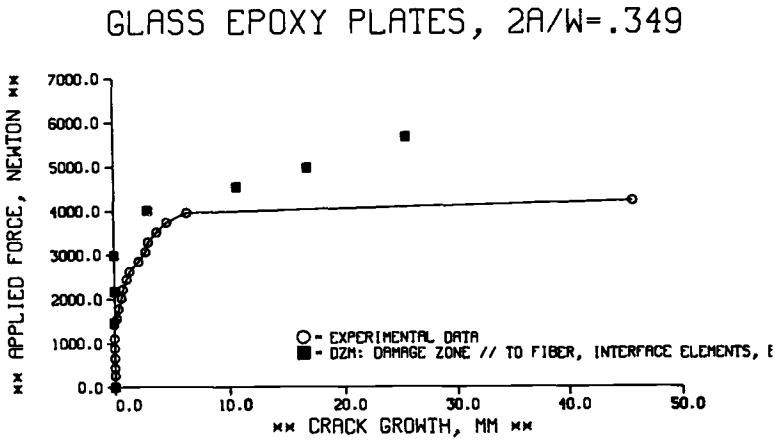
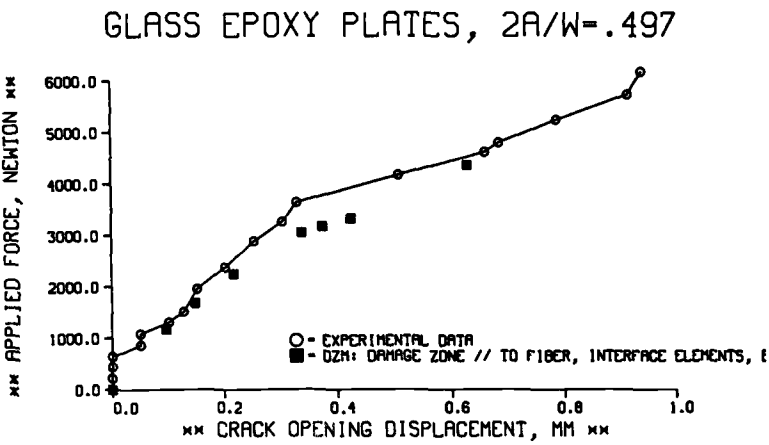


Figure 12. Results, Glass/Epoxy Panel, 2a/w = 0.349



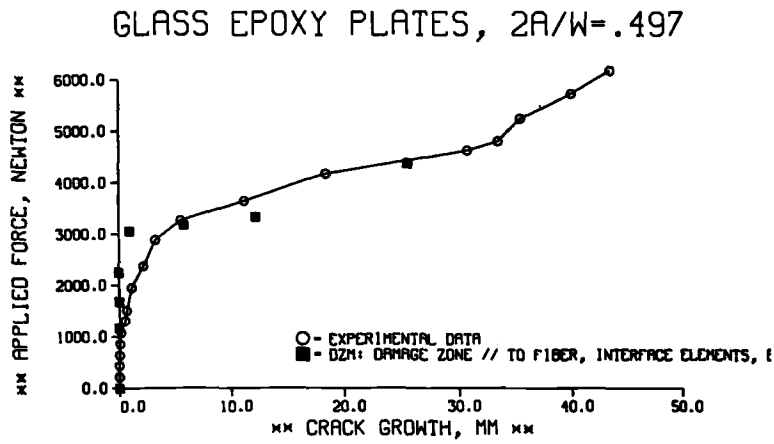


Figure 13. Results, Glass/Epoxy Panels, 2a/w = 0.0497

$$Kc = \sigma_f \sqrt{\pi a} \sqrt{1 + \frac{\pi * \pi * a * a}{2*W*W}}$$

is the σ_f = applied stress at fracture, a is the half crack length, and W is the plate width. The critical value as averaged from three tests with crack length-to-width ratios (2a/W) between 0.3 and 0.4 was:

$$Kc = 12.5 \text{ MPa } \sqrt{m} \quad = 11{,}378. \text{ psi} \sqrt{\text{inch}}$$

Comparative values were not found in the literature or supplied by the manufacturer.

The critical CTOD* value was determined:

$$Jc = Gc = Kc^2/E_{11} \qquad CTOD^* = Gc/(2*\sigma_o)$$

Results of Graphite/Aluminum Analysis

The load at fracture versus initial crack length is shown if Figure 14. Maximum difference in predicted failure loads was -8.8% for the smallest crack size. Applied force versus crack opening displacement for a crack length to width ratio of 0.363 is shown in Figure 15.

Discussion and Future Work

As in previous work on self-similar crack growth in composite materials, predictions for the Gr/Al composite were accurate. Use of the method for evaluating the angled notches in the Gr/Al is in progress. Since the damage is both parallel and perpendicular to the fibers, methods for incorporating the actual stress-strain diagrams in the surrounding materials should be investigated. Modeling of the surrounding material as elastic/plastic orthotropic would lead to higher failure load predictions. Incorporation of linear stress-strain behavior parallel and perpendicular to the loading direction cannot be conveniently accomplished using general-purpose finite element programs with the usual material models. Special damage elements will need to be developed.

The Gl/Ep analysis would also benefit from use of a nonlinear orthotropic material model surrounding the damage zone. In addition, since crack growth propagated in a stable fashion, curve-type parameter, similar to the R-curves used in isotropic material analysis, might improve the overall accuracy of the solution.

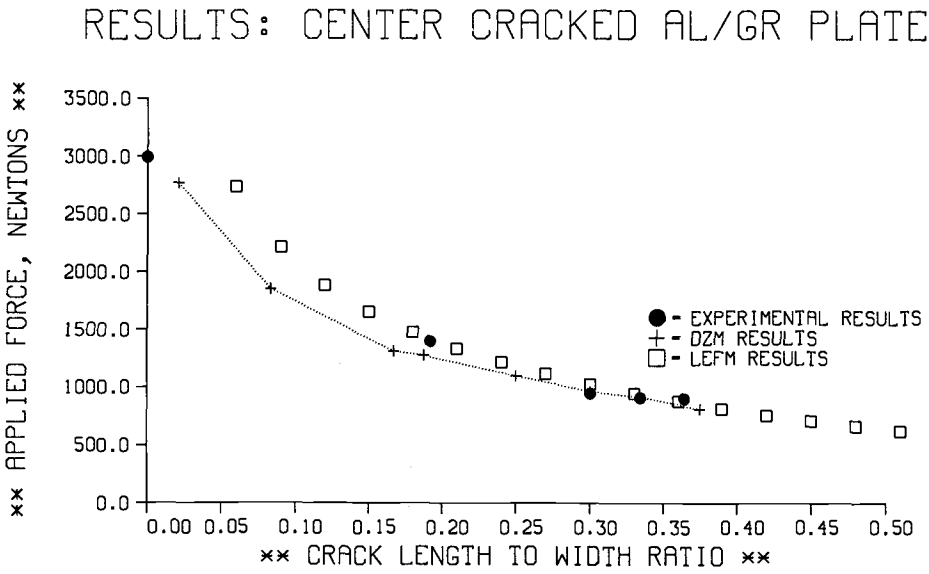


Figure 14. Results, Graphite/Aluminum Panels

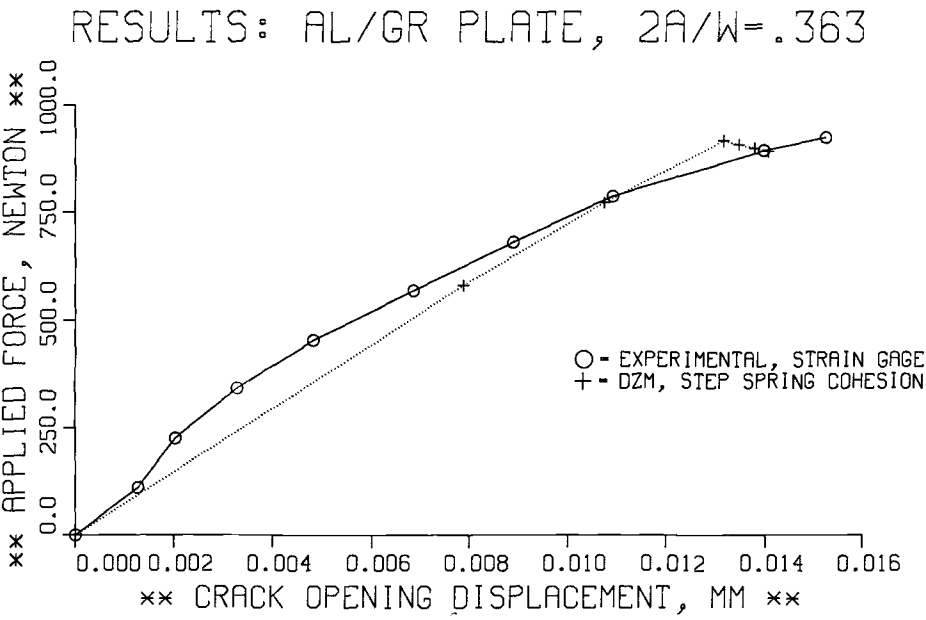


Figure 15. Results, Aluminum/Graphite Panel, 2a/w = 0.363

References

[1] Hahn, H.T., and Tsai, S.W., "Nonlinear Elastic Behavior of Unidirectional Composite Laminae," Journal of Composite Materials, Vol. 7, 1973, pp. 102-116.

[2] Pindera, M.J., Herakovich, C.T., Becker, W., Aboudi, J., "Nonlinear Response of Unidirectional Boron/Aluminum", Journal of Composite Materials, Vol. 24, pp. 2-17, 1990.

[3] Jansson, S., "Mechanical Characterization and Modeling of Non-linear Deformation and Fracture of a Fiber Reinforced Metal Matrix Composite," Mechanics of Materials, Vol. 12, 1991, pp. 47-62.

[4] Sun, C.T. and Chen, J.L., "A Simple Flow Rule for Characterizing Nonlinear Behavior of Fiber Composites", Journal of Composite Materials, Vol. 23, 1989, pp. 308-325.

[5] Sun, C.T., Chen, J.L., Sha, G.T., Koop, W.E., "Mechanical Characterization of SCS-6/Ti-6-4 Metal Matrix Composite," Journal of Composite Materials, Vol. 24, 1990, pp. 1029-1058.

[6] Ellyin, F., and El Kadi, H.E, "Predicting Crack Growth Direction in Unidirectional Composite Laminae," Engineering Fracture Mechanics, Vol. 36, 1990, pp. 27-37.

[7] Aronsson, C-G. and J. Backlund, "Tensile Fracture of Laminates with Cracks", Journal of Composite Materials, Vol. 20, 1986, pp. 287-307.

[8] Gregory, M.A. and Herakovich, C.T., "Predicting Crack Growth Direction in Unidirectional Composites", Journal of Composite Materials, Vol. 20, 1986, pp. 67-85.

[9] Tsangarakis, N., Nunes, J. and Slepetz, J., "Fracture Toughness Testing of Metal Matrix Composites," Engineering Fracture Mechanics, Vol. 30, 1988, pp. 565-577.

[10] Dvorak, G.J., Bahei-el-din, Y.A., and Bank, L.C., "Fracture of Fibrous Metal Matrix Composites- I. Experimental Results", Engineering Fracture Mechanics, Vol. 34, 1989, pp. 87-104.

[11] Awerbuch, J. and Hahn, H.T., "Crack-tip Damage and Fracture Toughness of Boron/Aluminum Composites", Journal of Composite Materials, Vol. 13, 1979, pp. 82-107.

[12] Ghosn, L.J., Kantzos, P., and Telesman, J., "Modeling of Crack Bridging in a Unidirectional Metal Matrix Composite," International Journal of Fracture, Vol. 54, 1992, pp. 345-357.

[13] Miyajima, T., and Sakai, M., "The Fracture Toughness for First Matrix Cracking in Unidirectionally Reinforced Carbon/Carbon Composites," Journal of Material Research, Vol. 6, 1991, pp. 2312-2317.

[14] G.C. Sih and Chen, E.P., "Fracture Analysis of Unidirectional Composites," Journal of Composite Materials, Vol. 7, 1973,

pp. 230-244, 1973.

[15] Cheong, S.K. and C.S. Hong, C.S., "Analysis of Cracks Emanating from a Circular Hole in an Orthotropic Plate under Mixed Mode Deformation", Engineering Fracture Mechanics, Vol. 31, 1988, pp. 237-248.

[16] Yum, Y.J. and Hong, C.S., "Stress Intensity Factors in Finite Orthotropic Plates with a Crack under Mixed-mode Deformation", International Journal of Fracture, 47, 1991, pp. 53-67.

[17] Chu, S.J., and Hong, C.S., "Application of the JK Integral to Mixed Mode Crack Problems for Anisotropic Composite Laminates", Engineering Fracture Mechanics, Vol. 35, 1990, pp. 1093-1103.

[18] Binienda, W.K., Reddy, E.S., "Mixed-Mode Fracture in Unidirectional Graphite Epoxy Composite Laminates with Central Notch," Journal of Reinforced Plastics and Composites, Vol. 2, 1992, pp. 324-338.

[19] Dugdale, D.S., "Yielding of Steel Sheets Containing Slits", Journal of Mechanics, Physics, and Solids, Vol. 8, 1960, pp. 100-104.

[20] Barenblatt, G.I., "The Mathematical Theory of Equilibrium Cracks in Brittle Fracture", Advances in Applied Mechanics 7, (Edited by H.L. Dryden and T. von Karman), Academic, NY, 1962.

[21] Hillerborg, A., Modéer, M. and Petersson, P-E, "Analysis of Crack Formation and Crack Growth in Concrete by Means of Fracture Mechanics and Finite Elements", Cement and Concrete, Vol. 6, 1976, pp. 773-782.

[22] C-G Aronsson and J. Backlund, "Tensile Fracture of Laminates with Holes," Journal of Composite Materials, 20, 1986, pp. 287-307.

[23] Nairn, J.A., "Fracture Mechanics of Unidirectional Composites Using the Shear-Lag Model Ipp. Theory", Journal of Composite Materials, Vol. 22, 1988, pp. 589-600.

[24] Kobelev, V. V., "Microstructural Model of a Fibrous Composite Fracture", Mechanics, Structures, and Machines, Vol. 20, 1992, pp. 1-16.

[25] Dharani, L.R., Recker, R.L., "Growth of Longitudinal Matrix Damage in Unidirectional Composites," Engineering Fracture Mechanics, Vol. 38, 1991, pp. 185-195.

[26] Bahei-el-din, Y.A., Dvorak, G.J., and Wu, J-F, "Fracture of Fibrous Metal Matrix composites II. Modeling and Numerical Analysis," Engineering Fracture Mechanics, Vol. 34, 1989, pp. 105-123.

[27] Cordes, J., Yazici, R., Seo, M., "Mixed Mode Fracture in Plastically Deforming Materials," Journal of Pressure Vessel Technology, ASME, 1993, pp. 348-352.

[28] Cordes, J., and Yazici, R. "Elastic-Plastic Mode II Fracture in

an Aluminum Beam," accepted for publication, Fracture Mechanics: 24 Symposium, ASTM STP 1207, edited by J.D. Landes and D.E. McCabe, American Society for Materials Testing, Philadelphia, 1994.

[29] Cordes, J., "A Fracture Critical Failure Criterion for Composite Materials", Phase II report, Castle Point Research Technologies, P.O. Box 5136, Hoboken, New Jersey 07030, 1992.

[30] ASTM E-338-81: "Sharp Notch Tension Testing", Annual Book of ASTM Standards, p. 620, 1987.

[31] ASTM ED-3355-74, "Fiber Content of Unidirectional Fiber/Polymer Composites", ASTM Standards and Literature Reference for Composite Materials, 1987, p. 94.

[32] ABAQUS, Version 5.2, Hibbitt, Karlsson, and Sorensen, Inc., 100 Medway Street, Providence, Rhode Island, 02906, USA, 1992.

Hamid R. Daghyani,[1] Lin Ye[1], Yiu-Wing Mai[1]

Constraint Effect on Fracture Behaviour of Adhesive Joints With Different Bond Thickness

REFERENCES: Daghyani, H. R., Ye, L., and Mai, Y.-W., "**Constraint Effect on Fracture Behaviour of Adhesive Joints with Different Bond Thickness**," Fracture Mechanics: 26th Volume, ASTM STP 1256, Walter G. Reuter, John H. Underwood, and James C. Newman, Jr., Eds., American Society for Testing and Materials, Philadelphia, 1995.

ABSTRACT: The main aims of this work are to investigate the constraint effect of adherends on the fracture behaviour of adhesive joints and to study the fracture properties of aluminium-adhesive joints using a rubber-modified epoxy resin (G_{Ic} = 2.76 kJ/m^2) as an adhesive material. Compact tension (CT) adhesive joints were manufactured for a wide range of bond thickness and fracture tests were conducted. The fracture energy was found to increase, though not monotonically, towards the fracture energy of the bulk adhesive as the bond thickness was increased. The constraint and stress triaxiality at the crack tip in the adhesive joints were also characterised for various bond thickness using elastic-plastic finite element method. It was found that as the adhesive bond thickness was increased, the stress triaxiality near the crack tip was relieved by the intensive deformation of the adhesive. Furthermore, the relationship between J-integral and crack-tip opening displacement (CTOD) was dependent on the constraint around the crack tip. Scanning electron microscopy (SEM) was used to examine the fracture surface morphology. Brittle fracture mechanisms were observed for thin bonds ($0.04 < t < 0.5$ mm) but tough fracture mechanisms were identified for thick bonds ($t > 1$ mm). The fracture energy of adhesive joints was proportional to the size of the crack tip plastic zone and the transfer of the bulk adhesive fracture toughness was governed by the constraint at the crack tip. Results from this work would improve integrity assessment of engineering adhesive joints.

KEY WORDS: fracture energy, constraint, adhesive joints, bond thickness, finite element analysis, J-Q theory, crack-tip opening displacement

Adhesive joints are widely used in aerospace and civil engineering structures with both economic and technical benefits in the last few decades. Many efforts have been

[1]Graduate Student, Lecturer and Professor, respectively, Centre for Advanced Materials Technology, Department of Mechanical and Mechatronic Engineering, The University of Sydney, Sydney, NSW 2006, Australia.

Copyright © 1995 by ASTM International www.astm.org

made to investigate crack propagation in adhesive joints. Several studies were concerned with the effect of bond thickness on fracture energy. However, no simple relationship was found between these two parameters. In fact the fracture energy of adhesive joints is dependent on the bond thickness, material properties of the adhesives and adherends, as well as testing procedures and methods of analysing the results [1-12]. The size of the plastic zone formed at the crack tip and/or morphology of the adhesive fracture surface have been found to affect the relationship between the fracture energy and the bond thickness of adhesive joints [4-6,13]. The constraint of the adherend influences both the stress and strain fields at the crack tip and controls the plastic zone size. Therefore, the fracture energy of the adhesive joints is dependent on the crack tip constraint.

In the present study, CT adhesive joints with a rubber-modified epoxy adhesive were used to investigate the fracture behaviour of the adhesive joints with various bond thickness. The constraint effects on stress distribution, plastic zone shape, stress triaxiality as well as the relationship between J-integral and crack-tip opening displacement (CTOD) were investigated using elastic-plastic finite element method. The morphology of fracture surfaces of the specimens were studied using scanning electron microscopy (SEM).

Experimental Study

The adhesive material was a diglycidyl ether of bisphenol A (DGEBA) epoxy resin (Araldite® GY260, supplied by Ciba-Geigy, Australia) modified with rubber (2% of CTBN, 1300 X 13, BF. Goodrich). Curing agent was piperidine, in a ratio of 5:100 wt% mixed with the pure resin. The rubber-modified epoxy was prepared first by adding the CTBN rubber to the DGEBA epoxy resin by hand-mixing for about 5-10 minutes, and degassed in a vacuum oven (-80 kPa) at 60°C. Piperidine was then added to the mixture with minimum air entrapment. The adherends were prepared from 6061 aluminium alloy. Fig. 1 illustrates a typical CT adhesive joint used in this study. The bond surfaces of the adherends were first ground using a 400 grit paper, degreased

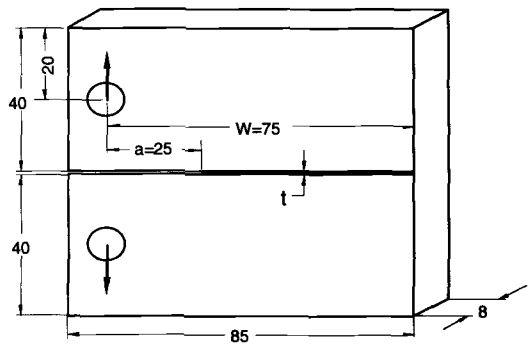


FIG. 1--Schematic of typical CT adhesive joints (t is bond thickness). All dimensions in mm.

with acetone, and then cleaned in an alkaline solution. The surfaces were etched by the P2 etching procedure with sulfo-ferric solution and finally dried in clean air [14]. Pre-cracks (a/w = 1/3) were introduced at the centre of bond line by a teflon film of 20 μm thickness. The assembled specimen frames were then preheated in an oven for 15 minutes at 120°C and the prepared resin was cast into the bond line. The CT adhesive joints were finally cured at 120°C for 16 h. After curing, the edges of bondlines were polished to produce a smooth surface. All the fracture toughness tests were conducted using an Instron 4302 machine at ambient temperature with a crosshead speed of 0.3 mm/min. The fracture surfaces of the specimens were first stained with osmium tetroxide (OsO_4) to enhance contrast and then coated with a thin layer of platinum to increase surface conductivity. A JEOL 35C scanning electron microscope (SEM) with an accelerating voltage of 15 kV was applied for the fractographic studies.

Finite Element Modelling

Large deformation and elastic-plastic finite element models (FEM) were developed to estimate J-integral values, crack-tip opening displacement (CTOD) and plastic zone shapes around the crack tip of the CT adhesive joints with different bond thickness. All finite element analyses (FEA) were carried out assuming linear-elastic behaviour for the aluminium adherends and elastic-plastic behaviour for the adhesive material. The recent work of Richardson et al. [15], comparing two and three dimensional FEA revealed that the adhesive remains in plane strain over most of the specimen adherend thickness. They showed that the two-dimensional FEA provides adequate requirement to evaluate the stress state and the fracture analysis of the adhesive joints. Although the stress-strain response of adhesives is triaxial stress dependent, this is difficult to describe using the model in FEA. Therefore, the nonlinearity of the adhesive material was described by the uniaxial stress-strain curves obtained from the experiments according to ASTM-D638M standard, which was simplified to the piecewise curve for the FEM analysis (Fig. 2). Some typical properties of the adhesive are: Young's modulus (E) = 3.15 GPa, ultimate strength (σ_u) = 81 MPa and Poisson's ratio (ν) = 0.35. Similar properties for the 6061 aluminium alloy are: E = 71 GPa, σ_u = 126 MPa and ν = 0.30.

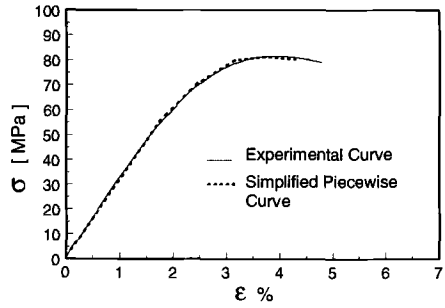


FIG. 2--Uniaxial tensile stress-strain and simplified piecewise curves of bulk adhesive material.

The two-dimensional finite element models consisted of eight-noded quadrilateral plane strain elements. Coarse meshes were considered for the adherend and fine meshes were used around the crack tip region for the adhesive material. The plastic zones for different bond thickness were evaluated from the model with singular elements around a sharp crack tip, while the model with a finite radius crack tip (R = 0.01 mm) was developed to evaluate the J-CTOD relationship using large strain theory of plasticity. Figs. 3a, b, and c illustrate the mesh configurations around the sharp and finite radius crack tips. The J-estimation of the finite element models was evaluated using the interrelationship the stress and strain fields around the sharp and finite radius crack tips based on the Rice [16] J-contour integration theory. The results were then compared to the J-estimation evaluated by the virtual crack extension (VCE) method in FEA [20] and good agreement was obtained. The CTOD was determined from the deformed crack opening profile. i.e, the vertical displacement of point A in Fig. 3c [17,18]. A typical finite element model involved 937 elements with 3016 nodes. The finite element analyses (FEA) were carried out by ABAQUS [19] and ADINA [20] softwares.

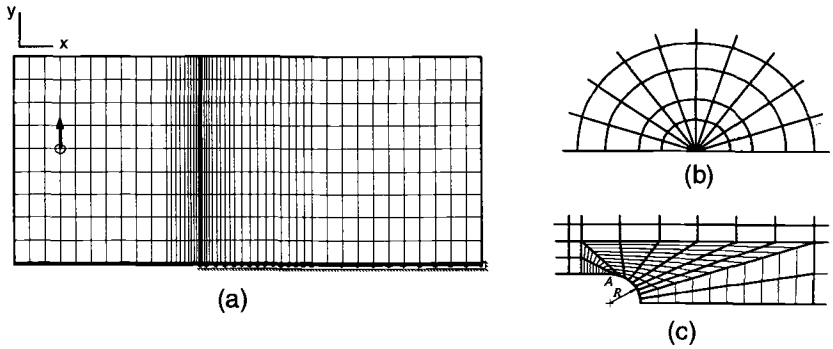


FIG. 3--(a) A typical finite element model of CT adhesive joint, (b) mesh configurations around a sharp crack tip, and (c) mesh configurations around a crack tip of finite radius.

Results and Discussions

Fracture properties of rubber-modified epoxy

The GY260 epoxy resin used in this study exhibited a high fracture toughness (1.76 kJ/m^2) compared to the normal epoxy systems [21]. However, by adding only 2% rubber to the pure GY260 epoxy resin the fracture toughness was considerably increased (2.76 kJ/m^2). Further increase in rubber content did not provide any more toughness enhancement. Scanning electron microscopy (SEM) from the fracture surfaces of specimens exhibited no rubber particle cavitation. Instead the fracture morphology of the bulk adhesive material revealed that shear yielding was the major energy dissipation mechanism [20].

Effect of bond thickness on fracture energy

Fig. 4a shows the variation of P_C with the bond thickness, t, obtained from the experiments. The critical (fracture) load, P_C, of the CT adhesive joints with an identical starter crack lengths (a = 25 mm) was used to evaluate the fracture energy, J_C. In FEA, because of the nonlinear response of the adhesive, the applied load was increased incrementally up to P_C to estimate J_C. Fig. 4b illustrates the variation of J_C as a function of t. The fracture behaviour varied according to the bond thickness. For $t < 1$ mm as shown in Fig.4, the relationship between J_C and t is similar to that between P_C and t. For larger bond thickness, J_C approaches a plateau (685 J/m^2) value in the range $1 < t < 4$ mm. However, J_C increases sharply when $t > 4$ mm. These results indicate that by increasing the bond thickness, the constraint effect from the adherends is reduced, hence enhancing the fracture energy of the adhesive joints.

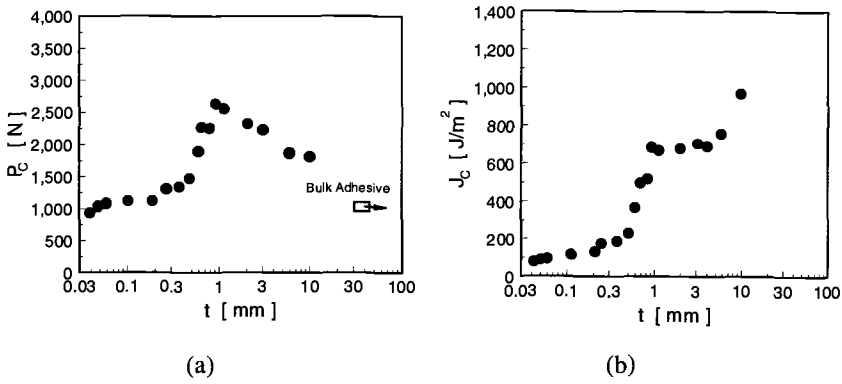


FIG. 4--Variation of (a) P_C and (b) J_C as a function of bond thickness (t).

Fracture morphology

The fracture surfaces of the CT adhesive joints clearly showed cohesive failure for all bond thickness. When $0.04 < t < 0.06$ mm, the crack propagated mainly through the centre line of the adhesive layer. However, in some areas it proceeded along the plane adjacent to the adhesive/adherend interface (Fig. 5b). For $0.06 < t < 0.5$ mm, the pre-crack could initiate in a direction about 45° to its plane until the crack reached the adhesive/adherend interface and jumped back and proceeded along the mid-plane of the adhesive layer. Figs. 5a and b illustrate the fracture surfaces of CT adhesive joints when $t = 0.05$ mm and $t = 0.2$ mm. High magnification photographs indicated that the adherend was coated with the adhesive resin which meant that failure was cohesive.

As the bond thickness was increased, the constraint imposed by the adherends decreased and large deformation around the crack tip became obvious. Fig. 6a shows

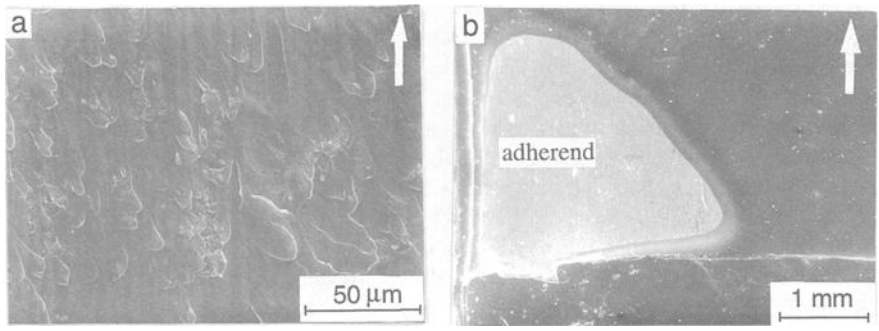


FIG. 5--Fracture surfaces of CT adhesive joints. (a) t = 0.05 mm, and (b) t = 0.2 mm. (Arrow indicates crack growth direction).

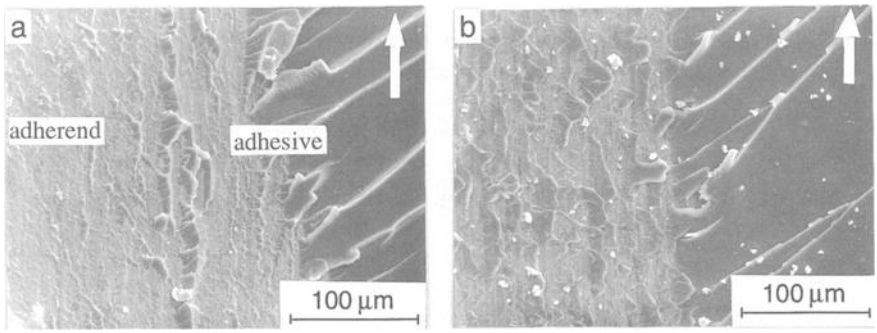


FIG. 6--Fracture morphology near the adhesive/adherend interface. (a) t = 1 mm, and (b) t = 2 mm. (Arrow indicates crack growth direction).

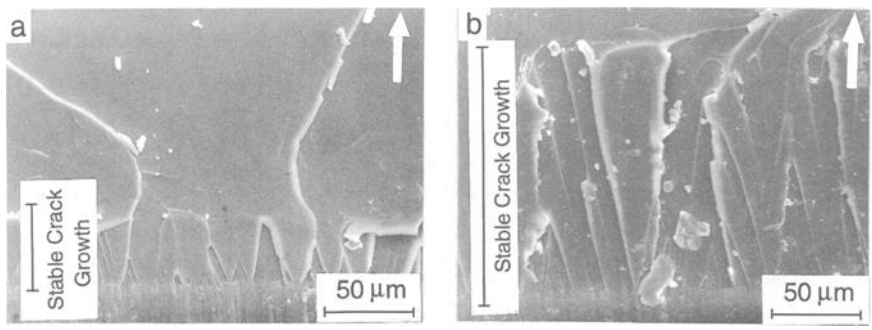


FIG. 7--Mechanisms of plastic deformation in stable crack growth region. (a) t = 10 mm, and (b) bulk adhesive material. (Arrow indicates crack growth direction).

the fracture morphology near the adhesive/adherend interface when t = 1 mm. There was substantially more plastic deformation at this bond thickness. When $1 < t < 4$ mm, J_C reached a plateau. Fig. 6b illustrates the fracture morphology near the adhesive/adherend interface when t = 2 mm. This is similar to that for t = 1 mm and they have similar fracture energies. For $t > 4$ mm, J_C increases sharply towards the fracture energy of the bulk adhesive material (J_C = 2.76 kJ/m^2) [21]. Fig. 7 shows the plastic deformation in the stable crack growth region [22] formed ahead of the pre-crack. This indicates that for large bond thickness ($t > 6$ mm) the crack extended steadily prior to reaching P_C. Obviously this region in the joint with t = 10 mm (Fig. 7a) was much shorter than that in the bulk adhesive material (Fig 7b). Therefore, the constraint from the adherends still limits the plastic deformation even for the joint with large bond thickness, and consequently the fracture energy was lower than that of the bulk adhesive.

Stress distributions in adhesive joints

Fig. 8 shows the distributions of normal stresses σ_{xx} and σ_{yy} ahead of a sharp crack tip (X denotes the ligament length from the crack tip) for a typical CT adhesive joint with t = 0.2 mm subjected to the critical load, P_C. Both σ_{xx} and σ_{yy} represent a high stress state within the singular region. Along the ligament length up to about 20 mm from the crack tip, σ_{yy} is tensile, and then becomes compressive. Fig. 8b gives the distribution of the hydrostatic tensile stress ahead of the crack tip, which has a similar distribution to σ_{yy}.

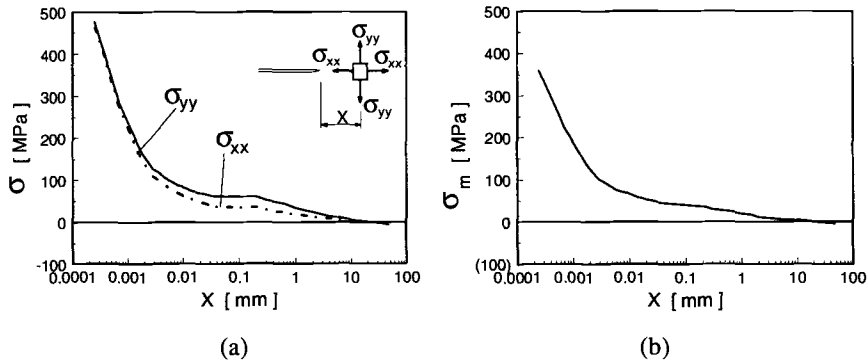


FIG. 8--Stress distributions ahead of a sharp crack at t = 0.2 mm. (a) σ_{xx} and σ_{yy}, and (b) hydrostatics stress, σ_m.

The effect of adhesive bond thickness on the crack tip stress distribution was evaluated at a constant load (120 N/mm). Fig. 9 shows σ_{yy} normalised by the 0.2% offset yield stress, σ_o, for the bulk adhesive and the joints with different bond thickness in a log-log plot. From comparisons of various curves of σ_{yy}, the bulk specimen has the highest value. This is attributed to the higher stiffness (Young's

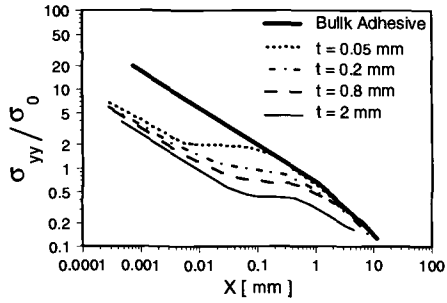


FIG. 9--σ_{yy} distribution ahead of a sharp crack tip for bulk adhesive and adhesive joints with different bond thickness.

modulus) of the adherends than that of the bulk adhesive [13,23] (E = 71 GPa. and at t = 0.2 mm in the distance between 0.01 to 0.1 mm ahead of the crack tip. Further increase in the bond thickness from t = 0.2 mm to 2 mm reduces σ_{yy} more. However σ_{yy} approaches the same value at about 10 mm from the crack tip for both the bulk adhesive and the adhesive joints with various adhesive bond thickness. In the region ahead of the crack tip ($0 < X < 2 \times 10^{-3}$ mm) [13,23], σ_{yy} has the expected slope (-1/2) associated with crack singularities for various t, though the singular region for the bulk adhesive extends to 0.3 mm ahead of the crack tip. For the adhesive joint with t = 0.05 mm, σ_{yy} shows a plateau between X = 0.01 and 0.1 mm. For larger bond thickness, similar observations can be seen but they occur at a distance further from the crack tip. These features of stress (σ_{yy}) distribution in the CT adhesive joints are similar to those of the DCB adhesive joints as reported by other investigators [13,23].

J-Q theory and constraint effect

The stress distributions ahead of the crack tip for a power-hardening material are characterised in terms of the J-integral by Hutchinson [24], Rice and Rosengren [16], and called the HRR solution. The stress σ_{ij} and strain ε_{ij} fields are given by :

$$\sigma_{ij} = \sigma_o \left(\frac{E J}{\alpha \sigma_o^2 I_n r}\right)^{\frac{1}{n+1}} \sigma_{ij}(\theta, n) \qquad (1)$$

$$\epsilon_{ij} = \frac{\alpha \sigma_o}{E} \left(\frac{E J}{\alpha \sigma_o^2 I_n r}\right)^{\frac{n}{n+1}} \epsilon_{ij}(\theta, n) \qquad (2)$$

where θ and r are the polar coordinates, α a material constant, n a hardening parameter, σ_0 the yield stress, I_n an integration constant and J is the amplitude of the HRR singularity defined by the path independent J-integral [16]. The HRR solution is based on the constraint around the crack tip in an infinite plane strain medium

which results in a high triaxial stress state that is too high to be realised for any finite size specimen of real elastic-plastic material. The results of the finite element analysis [17,18] have shown that the triaxiality near the crack tip of finite size specimens is clearly lower than that of the HRR solution. O'Dowd and Shih [25,26] have introduced a two-parameter theory, J and Q, to characterise a full range of high and low triaxial stress states near the crack tip, where J sets the size scale of the process zone over which large stresses and strains develop, while Q scales the near crack tip stress state relative to a reference stress state (i.e. the HRR field) with a high triaxiality. The Q field is defined by :

$$Q = \frac{\sigma_{\theta\theta} - \sigma_{\theta\theta}|_{HRR}}{\sigma_o} \tag{3}$$

where $\sigma_{\theta\theta}$ is the actual angular stress and $\sigma_{\theta\theta}|_{HRR}$ the corresponding HRR stress component. This field is defined within the sector $|\theta| < \pi/2$ and $J/\sigma_o < r < 5J/\sigma_o$. However, for definition, Q is evaluated at $r = 2J/\sigma_o$ and $\theta = 0.0$ [26]. In fact Q is a measurement of the stress triaxiality near the crack tip, or the constraint relative to a reference stress state with a high triaxiality.

In this work, the Ramberg-Osgood power-law idealisation is used to describe the nonlinear and strain hardening behaviour of the adhesive material in uniaxial deformation given by:

$$\epsilon = \frac{\sigma}{E}\left[1 + \alpha\left(\frac{\sigma}{\sigma_o}\right)^{n-1}\right] \tag{4}$$

Fig. 10 shows the distributions of σ_{yy}, normalised by σ_o as a function of the normalised distance, $X\sigma_o/J$, from the crack tip, evaluated by FEA for a sharp crack tip when the fracture loads are applied in FEM for different bond thickness. As

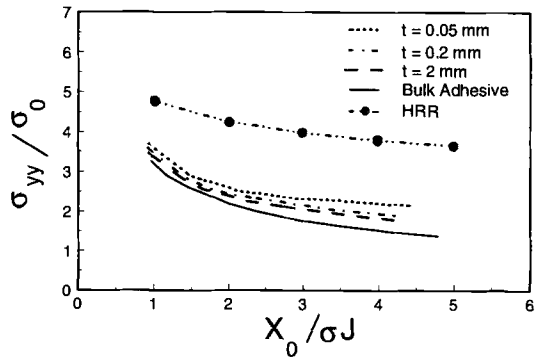


FIG. 10--Normalised σ_{yy} distribution ahead of the crack tip in bulk adhesive and adhesive joints with different t and HRR stress field.

mentioned previously, σ_0 is triaxial stress dependent. It is difficult to evaluate the precise σ_0 of the adhesive of different bond thickness. Thus, σ_0 of the bulk adhesive was used as a reference stress to normalise the other stress states. The difference between the stress state of the HRR field and those in the CT adhesive joints indicates that the triaxiality or crack tip constraint in the joints are much lower than that in the HRR field [25,26]. Furthermore, for small adhesive thickness (t = 0.05 mm), the stress state is clearly influenced by the constraint of the aluminium adherends and involves a higher degree of stress triaxiality compared to that in the bulk adhesive. With increasing bond thickness, the constraint is reduced towards that of the bulk adhesive material. The stress triaxiality as characterised by Q is shown in Fig. 11 for the adhesive joints with different bond thickness. The considerable difference in the triaxiality between stress states of the adhesive joints and the HRR field confirms that the high constraint effect defined by the HRR stress field is effectively relieved for finite size geometries [27].

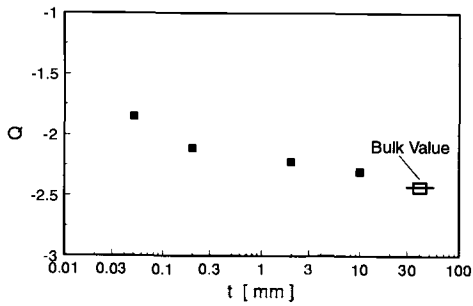


FIG. 11--Q value as a function of adhesive bond thickness.

Constraint effect on plastic zone size

The stress distributions in the adhesive joints are strongly affected by the adherends, i.e. the constraint from the adherends controls the stress state and deformation field, thereby influences the energy absorption of the adhesive material around the crack tip. Fig. 12 shows the plastic zone configurations in the bulk adhesive and the CT adhesive joints with different bond thickness when P_C was applied in the FEM. The plastic zones are evaluated using the critical load and Von-Mises criterion based on a 0.2% effective plastic strain. For small adhesive thickness (t < 0.2 mm) a plastic zone has occurred around the crack tip. For larger bond thickness (t > 0.2 mm), the adherends still influence the deformation of the adhesive material and the constraint from both adherends and adhesive has restricted the growth of the plastic zone, which is still much smaller than that in the bulk adhesive. Fig. 13 displays the variation of the critical plastic zone height, h_c, as a function of t. Comparisons of Figs. 4b and 13 shows that the relationship between h_c and t resembles that between J_C and t. This indicates that the plastic zone height is related to the fracture energy.

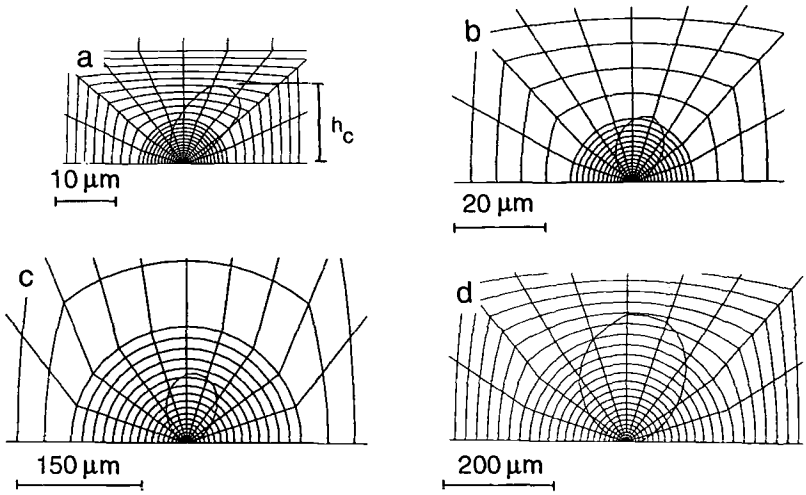


FIG. 12--Plastic zone shapes in bulk adhesive and adhesive joints with different bond thickness. (a) t = 0.05 mm, (b) t = 0.2 mm, (c) t = 2. mm, and (d) bulk adhesive.

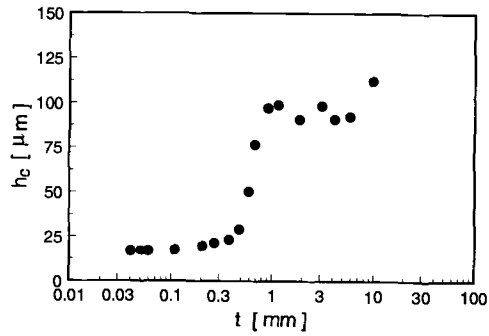


FIG. 13--Variation of critical plastic zone height versus bond thickness.

J-CTOD relationship and constraint effects

For elastic-plastic materials, a unique relationship exists between J and CTOD which is given by [28,29]:

$$J = m\,\sigma_o\,CTOD \tag{5}$$

where m is a dimensionless constant which is an indication of constraint and depends on the stress state and material properties. The difference in Q value on the stress state around the crack tip in the adhesive joints indicates that the relationship between J and

CTOD might be different for various bond thickness.

To evaluate the constraint effects of the adherends on J-CTOD relationship, using the model with a crack tip of finite radius in FEM, J and the corresponding CTOD are evaluated at different load levels for various bond thickness. A straight line J-CTOD relationship for each bond thickness is established in Fig. 14. From the slope of each line and a constant yield stress of the adhesive material (i.e. σ_0 = 0.2% offset yield stress), m can be evaluated for different bond thickness. The variation of m as a function of bond thickness, t, is shown in Fig. 15. The results indicate that the constraint of adherends has restricted the crack tip deformation for the small adhesive bond thickness ($t < 0.2$ mm) and therefore, higher values of m are obtained, while for larger bond thickness ($t > 0.2$ mm), m is reduced asymptotically towards the value of the bulk adhesive. A high constraint imposed by adherends, therefore, produces a small crack-tip opening displacement and vice versa.

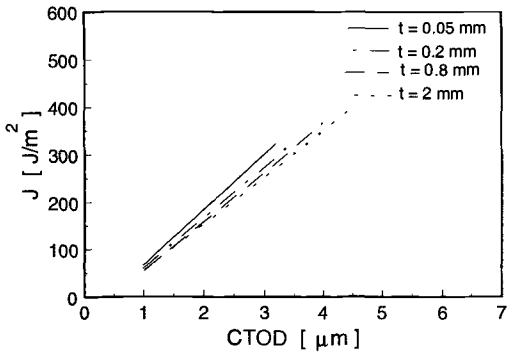


FIG. 14--Linear regression between J-CTOD for different bond thickness.

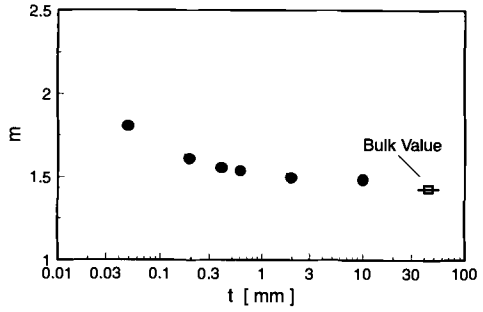


FIG. 15--Variation of m as a function of adhesive bond thickness.

Relationship between fracture energy and constraint parameters

It has been argued that the fracture energy in the adhesive joints is directly related to the stress and strain fields around the crack tip. From the discussion in the previous sections, it can be seen that either parameter Q or m describes the degree of constraint, the higher the value of Q or m, the higher the constraint at the crack tip. Thus, from Figs. 11 and 15, the constraint imposed by the adherends in the adhesive joints is clearly reduced as the bond thickness is increased. Consequently, intensive deformation and plastic flow would be promoted, which result in an increase of fracture energy towards the value of the bulk adhesive. Therefore, the fracture energy of the adhesive joint is highly dependent on the constraint around the crack tip. The higher the constraint is, the lower the fracture energy.

CONCLUSIONS

The fracture behaviour of compact tension (CT) aluminium-adhesive joints of different bond thickness with rubber-modified epoxy resin as the adhesive material was investigated using fractography and elastic-plastic finite element analysis (FEA). The critical J-integral, J_C, evaluated by FEA, depends on the bond thickness, t, of the adhesive joints. For $0.04 < t < 0.5$ mm, J_C increases gradually from 75 J/m^2 to 225 J/m^2 as t is increased. However, for $0.5 < t < 1$ mm, J_C rises sharply from 225 J/m^2 to 685 J/m^2. In the range of $0.5 < t < 4$ mm, J_C is invariant but for $t > 4$ mm, J_C increases gradually towards the fracture energy of the bulk adhesive material (J_C = 2.6 kJ/m^2).

The stress triaxiality near the crack tip in the bulk adhesive and the adhesive joints with different bond thickness was characterised and compared to the HRR stress field based on the J-Q theory. The results confirm that the high triaxiality of the HRR stress field is relieved by the extensive deformation of the adhesive around the crack tip of the finite size CT specimens. The relationship between the J-integral and crack tip opening displacement (CTOD) in the adhesive joints has been investigated. The results reveal that this relationship depends on the constraint at the crack tip which in turn depends on the bond thickness. It is also shown that the crack tip constraint controls the fracture energy, CTOD and plastic zone height of the adhesive material. Further, the critical plastic zone height is proportional to the fracture energy.

SEM micrographs show that the fracture is fully cohesive and brittle fracture mechanisms prevail for thin bond thickness with high constraint ($0.04 < t < 0.5$ mm), and tough fracture mechanisms dominate for larger t. In summary, based on the results obtained in this work, the following conclusions can be made:

(1) As the bond thickness is increased, the constraint and/or stress triaxiality at the crack tip is reduced, which increases the crack tip plastic zone size.

(2) When the constraint at the crack tip is reduced, the fracture energy of the adhesive

joint is significantly increased towards that of the bulk adhesive material.

(3) The J-CTOD relationship is dependent on the constraint at crack tip. At the same level of J, a high constraint produces a small crack-tip opening displacement, which indicates that the deformation of the material around the crack tip is suppressed.

(4) There is a direct relationship between the fracture energy of adhesive joints and the plastic deformation zone formed at the crack tip which is controlled by the bond thickness.

ACKNOWLEDGMENTS

Thanks are due to Dr. S. X. Wu for his assistance in finite element analysis. H. R. Daghyani was supported by a scholarship from the Ministry of Culture and Higher Education of Iran (MCHE).

REFERENCES

[1] Mostovoy, S. and Ripling, E. J., "Effect of Joint Geometry on The Toughness of Epoxy Adhesives," Journal of Applied Polymer Science, 15, 1971, pp. 661-673.

[2] Mostovoy, S., Ripling, E. J. and Bersch, C. F., "Fracture Toughness of Adhesive Joints," Journal of Adhesion, Vol. 3, 1971, pp. 125-144.

[3] Kinloch, A. J. and Shaw, S. J., "The Fracture Resistance of a Toughened Epoxy Adhesive," Journal of Adhesion, Vol. 12, 1981, pp. 59-77.

[4] Hunston, D. L. and Bascom, W. D., "Failure Behaviour of Rubber-Toughened Epoxies in Bulk, Adhesives and Composites Geometries," in ACS, Advances in Chemistry Series, No. 208: Rubber-Modified Thermoset Resins (eds. C. K. Riew and J. K. Gillham), Amer. Chem. Soc., 1984, pp. 83-99.

[5] Chai, H., "Bond Thickness Effect in Adhesive Joints and Its Significance for Mode-I Interlaminar Fracture of Composites," 7th Sym p. on Composite Materials: Testing and Design (Seventh Conference), STP 893, J. M. Whitney, Ed., American Society for Testing and Materials, Philadelphia, 1986, pp. 209 231.

[6] Chai, H., "On The Correlation Between The Mode-I Failure of Adhesive Joints and Laminated Composites," Engineering Fracture Mechanics, Vol. 20, No. 3, 1986, pp. 413-431.

[7] Mall, S. and Ramamurthy, G., "Effect of Bond Thickness on Fracture and Fatigue Strength of Adhesively Bonded Composite Joint," International Journal of Adhesion and Adhesives, Vol. 9, No. 1, 1989, pp. 33-37.

[8] Hamoush, S.A. and Ahmad, S. H., "Fracture Energy Rate of Adhesive Joints," International Journal of Adhesion and Adhesives, Vol. 9, No. 3, 1989, pp. 171-178.

[9] Schmueser, D. W. and Johnson, M. L., "Effect of Bond Thickness on Mixed Mode Debonding of Adhesive Joints to Electroprimed Steel Surface," Journal of

Adhesion, Vol. 32, 1990, pp. 171-191.
[10] Fernuld, G. and Spelt, J. K., "Failure Load Prediction of Structural Adhesive Joints," International Journal of Adhesion and Adhesives, Vol. 11, No. 4, 1991, pp. 213-220.
[11] Fernuld, G. and Spelt, J. K., ibid, Vol. 11, No. 4, 1991, pp. 221-227.
[12] Schupp, D. A. and Gerberich, W. W., "Effect of Film Thickness on The Work of Fracture Between Adhesives and Glass", Journal of Adhesion, Vol. 35, 1991, pp. 269- 283.
[13] Crews, J. H., Jr., Shivakumar, K. N. and Raju, I. S., "Factors Influencing Elastic Stresses in Double Cantilever Beam Specimens," Adhesive Bonded Joints: Testing And Design, STP 981, W.S. Johnson Ed., American Society for Testing and Materials, Philadelphia, 1988, pp. 119-132.
[14] Wegman, R. F., in Surface Preparation Techniques for Adhesive Bonding, Noyes Pub., 1989, pp. 9-27.
[15] Richardson, G., Crocombe, A. D. and Smith, P. A, (1993), "A Comparison of Two- and Three-Dimensional Finite Element Analyses of Adhesive Joints," International Journal of Adhesion and Adhesives, Vol. 13, 1993, pp. 193-200.
[16] Rice, J. R. and Rosengren, G. F., "Plane Strain Deformation Near a Crack Tip in a Power-Law Hardening Material," Journal of Mechanics and Physics of Solids, 1968, Vol. 16, pp.1-12.
[17] McMeeking, R. M., "Finite Deformation Analysis of Crack-Tip Opening in Elastic-Plastic Materials and Implication for Fracture," Journal of Mechanics and Physics of Solids, Vol. 25, 1977, pp. 357-381.
[18] McMeeking, R. M. and Parks, D. M., "On Criteria for J-Dominance of Crack-Tip Fields In Large-Scale Yielding on Elastic-Plastic Fracture," in Elastic-Plastic Fracture, STP 668, J. D. Landes, J. A. Begley, and G. A. Clarke, Eds., American Society for Testing and Materials, 1979, pp. 175-194.
[19] Habbit, Karlsson and Sorensen, "ABAQUS User's Manual," Pawtucket, RI, USA., 1989.
[20] ADINA R & D, Inc., USA., 1992.
[21] Daghyani, H.R., Ye, L., Mai, Y.-W. and Wu, J. S., "Fracture Behaviour of a Rubber-Modified Tough Epoxy System,"Journal of Material Science Letters, 13, 1994, 1330-1333.
[22] Yamini, S. and Young, R. J., "The Mechanical Properties of Epoxy Resins," Journal of Material Science, 15 1980, pp. 1823-1831.
[23] Wang, S. S., Mandell, J. F. and McGarry, F. J., "An Analysis of The Crack Tip Stress Field in DCB Adhesive Fracture Specimens," International Journal of Fracture, Vol. 14, No. 1, 1978, pp. 39-58.
[24] Hutchinson, J. W., "Singular Behaviour at the End of a Tensile Crack in a Hardening Material," Journal of Mechanics and Physics of Solids, Vol. 16, 1968, pp. 13-31.
[25] O'Dowd, N. P. and Shih, C. F., "Family of Crack-Tip Fields Characterised by a Triaxiality Parameter-I, Structure of Fields," Journal of Mechanics and Physics of Solids, Vol. 39, 1991, pp. 989-1015.
[26] O'Dowd, N.P. and Shih, C. F., to appear in ASTM STP for the US 24th National Symposium on Fracture Mechanics, American Society for Testing and Materials,

Philadelphia, 1994

[27] Anderson, T. L., "Crack Tip Parameters for Large Scale Yielding and Low Constraint Configurations," International Journal of Fracture, Vol. 41, 1989, pp. 79-104.

[28] Shih, C. F., "Relationships Between the J-Integral and the Crack Tip Opening Displacement for Stationary and Extending Cracks," Journal of Mechanics and Physics of Solids, Vol. 29, 1981, pp. 305-326.

[29] Anderson, T. L., in Fracture Mechanics, fundamental and Applications, CRC Press, 1991, p. 156.

Yingyuan Yang[1] and Dietrich Munz[2]

REDUCTION OF THE STRESSES IN A JOINT OF DISSIMILAR MATERIALS USING GRADED MATERIALS AS INTERLAYER

REFERENCE: Yang, Y.Y. and Munz, D., **"Reduction of the Stresses in a Joint of Dissimilar Materials Using Graded Materials as Interlayer,"** Fracture Mechanics: 26th Volume, ASTM STP 1256, Walter G. Reuter, John H. Underwood, and James C. Newman, Jr., Eds., American Society for Testing and Materials, Philadelphia, 1995.

ABSTRACT: If two dissimilar materials are joined at high temperature, very high residual stresses develop near the free edge of the interface during cooling to room temperature. In most cases, the stresses are singular for elastic material behaviour. One method to avoid the stress singularities is to introduce a graded interfacial zone with a continuous change of all material properties between the two joined components. In this paper the distribution of the stresses in FGM has been calculated by FEM. The interlayer has continuous material properties, which means that the graded interlayer has not been treated as N layers. The value of the peak stress and the location of the peak stress in the joint have been investigated.

KEYWORDS: functionally graded material, FEM, peak stress, location of the peak stress, joint, interlayer

If two dissimilar materials are joined at high temperature, very high residual stresses develop near the free edge of the interface during cooling to room temperature. In most cases, the stresses are singular for elastic material behaviour [1, 2]. These stresses may cause failure directly after cooling or after little mechanical loading. In order to reduce the residual stresses, an interlayer can be introduced between the two materials [3]. By adapting the properties of the interlayer to those of the joined components and by varying the thickness of the interlayer the residual stresses can be greatly reduced compared to those occuring when two materials were joined directly. However, due to the discontinuity of the material properties at the interfaces (see Fig.1, the interface between materials 1 and 2, and between materials 2 and 3), in most cases, there are still stress singularities near the free edge of the interface [4]. The stress singularity gets only weaker by introduction of a favorable interlayer.

Another way of reducing the residual stresses is the application of a graded interfacial zone with a continuous change of all material properties. In the last five years many investigations have been made about the graded materials, which are called Functionally Graded Material (FGM). These investigations have concentrated on the following aspects: (a) manufacturing of FGM [5]; (b) design of FGM [6]; (c) describing the stress distribution in FGM [7]; (d) stress field at the tip of the crack in FGM [8], etc. Up to now only the finite element method (FEM) has been used to calculate the stress distribution in FGM [7, 9]. In those papers the FGM was treated as N-layers laminate

[1] Dr.- Ing., University of Karlsruhe, Institute for Reliability and Failure Analysis

[2] Professor, University of Karlsruhe, Institute for Reliability and Failure Analysis and Nuclear Research Center Karlsruhe, IMF II, D-76021 Karlsruhe, Germany

Copyright © 1995 by ASTM International www.astm.org

which means that each layer has different material properties, but the material properties in each layer remain constant. Then, in each layer, the theory of elasticity for homogeneous material can be used and the stress analysis is the same as in homogeneous material.

Graded materials can be manufactured either by layers or by a continuous variation of the properties. In a N-layers laminate, theoretically, there is always a jump of the stresses at the interface of the two layers due to the discontinuous material properties at the interface. If N is large the jump is negligible. If N is not large the jump is obvious and at the free edge of the interface stress singularities may exist for elastic material behaviour. The significance of the stress singularity requires a special discussion (see reference [1]). In this paper the distribution of the stress has been calculated by ABAQUS-code. By using the subroutine UMAT it is possible to apply an arbitrary function in the graded interlayer, where the interlayer has continuous material properties. Its advantage is that an arbitrary mesh can be used, not always a N-layers mesh, so that the mesh is fine in a higher stress zone and coarse in a low stress zone. One example is given in Fig.2. If in reality the graded part is made of N layers and N is large enough the principle results about an optimized function form of the material properties should be the same as for a continuous distribution of material properties. In the FE-calculation four edges element with 8 nodes has been used and the smallest element has the edge length $10^{-5} \times L$.

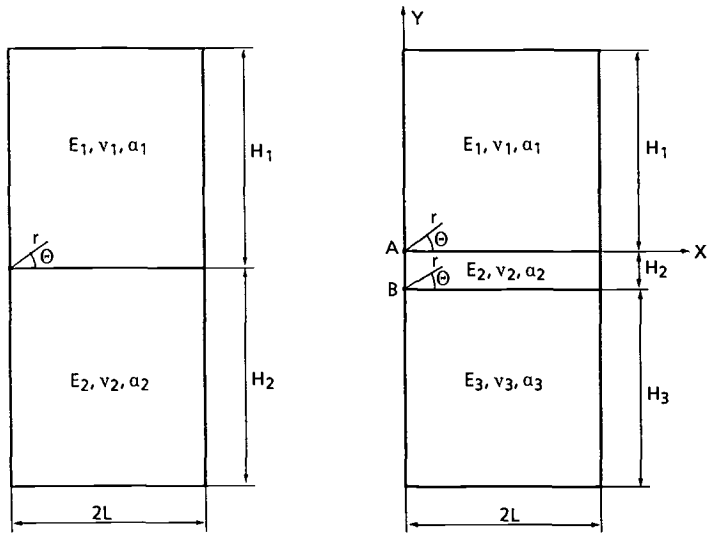


Fig.1---Geometries considered.

For the joint shown in Fig.1b material 2 is a graded interlayer, i.e. the Young's modulus E, the Poisson's ratio ν, and the thermal expansion coefficient α depend on the coordinate y (e.g. $E_2 = f(y)$, $\nu_2 = g(y)$ and $\alpha = h(y)$). Different criteria can be applied to an optimized graded interlayer (e.g. minimum tensile or shear stress at the interface, minimum principal stress in material 1). From the stress analysis of the FEM it is known that under this thermal loading the peak stress $\sigma_y|_{max}$ occurs always along the free edge. In this study, the maximum stress σ_y along the free edge is taken as a criterion. The relationship between the peak stress (designated $\sigma_y|_{max}$) and the ratio H_2/H_1 (for $H_1 = H_3$) and the form of the functions f, g and h is investigated. The functions f, g and h may be a polynomial function , a exponential function or a sinusoidal function. Many dif-

ferent functions (more than 120) have been studied to find the conditions for minimising the peak stress. The location of $\sigma_y|_{max}$ (described as $y|_{\sigma_y|_{max}}$) is also presented as a function of H_2/H_1 and the form of f, g and h. To avoid delamination a location of the peak stress away from the interface is favorable. The conditions under which $\sigma_y|_{max}$ does not occur at the interface are also provised.

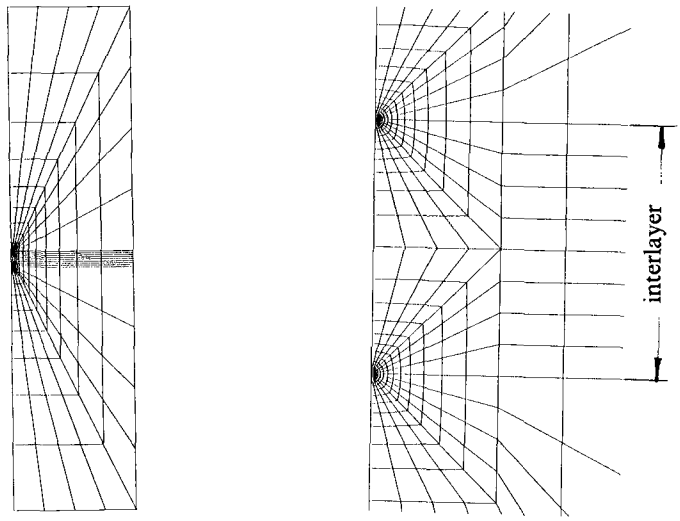


Fig.2---The mesh for a joint with interlayer.

STRESS SINGULARITY AT THE INTERFACE OF THE JOINT

In this paper perfect bonding at the interface and isotropic elastic behaviour are considered. Therefore, for most material combinations stress singularities exist. Dependent on the yield strength of the materials and the loading plasiticity may occur in one or both materials, which can reduce the elastically calculated stresses. However, the main trends of the stress distribution in a joint can be evaluated from pure elastic calculation. The plasticity effect is not considered in this paper. The stresses near the free edge of the interface in a dissimilar materials joint can be analytically described as [10, 11]

$$\sigma_{ij}(r,\theta) = \sum_{k=1}^{N} \frac{K_k}{(r/L)^{\omega_k}} f_{ijk}(\theta) + \sigma_0 f_{ij0}(\theta). \tag{1}$$

In Eq.(1) L is a characteristic length of the joint, ω_k is the stress exponent, $f_{ijk}(\theta)$ are the angular functions, $\sigma_0 f_{ij0}(\theta)$ is the regular stress term, and K_k is called stress intensity factor. All the quantities $\omega_k, f_{ijk}(\theta)$, and $\sigma_0 f_{ij0}(\theta)$ can be calculated analytically [11, 12]. Only the stress intensity factor K must be determined by a numerical method, for instance, the finite element method [13].

If the stress exponent ω is positive, a stress singularity exists, i.e. if r = 0, the stresses are infinity. It is obvious that in reality no infinity stress occurs. Due to microcracking or plastic deformation the stress remains finite and a small process zone develops near the singular point. Nevertheless Eq.(1) characterizes the stress state as the corresponding relation in linear elastic fracture mechanics for a crack. For the joint shown in Fig.1 with the angles $\theta_1 = 90°$ and $\theta_2 = -90°$ at the free edge one singular term is sufficient to

describe the singular stress field (i.e. N = 1). For this joint some empirical relations between the K-factor and the stress exponent ω have been found [10, 14]. For general material combinations Eq.(1) can describe the stresses in the range of $r/L < 0.01$ very well.

As an example Fig.3 shows the distribution of the stress exponents for plane strain versus the material properties $(E_1^* - E_2^*)/(E_1^* + E_2^*)$ for given ν_1 and ν_2 (where $E_i^* = E_i/(\nu_i(1+\nu_i))$). It can be seen that for most material combinations, though the difference of the two materials is not large, $\omega \neq 0$ and $\omega > 0$. The stress distribution of a joint ($E_1 = 400$ GPa, $\nu_1 = 0.24$, $\alpha_1 = 4.5 \times 10^{-6}/K$, and $E_2 = 114$ GPa, $\nu_2 = 0.33$, $\alpha_2 = 8.5 \times 10^{-6}/K$, $\Delta T = -100K$ and $H_1/L = H_2/L = 2$) is shown in Fig.4. The temperature change of 100K was chosen arbitrary, because the stresses are proportional to ΔT ($\Delta T = T_1 - T_0$, T_1 is the end temperature and T_0 is the initial temperature). The stresses from the FEM (entered as points) and those from Eq.(1) (entered as line) are compared. It can been seen that they are in good agreement up to $r/L < 0.01$ (Fig.4a) and the stress singularity occurs at the interface (Fig.4b).

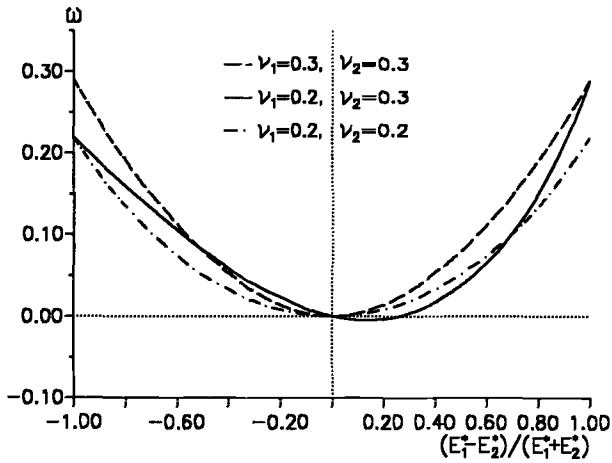


Fig.3---Distribution of the stress exponent ω for $\theta_1 = 90°$ and $\theta_2 = -90°$.

BASIC EQUATIONS FOR FGM

Neglecting the effect of body forces, the equilibrium equations of an elastic material for a two-dimensional problem are given by

$$\frac{\partial \sigma_{ij}}{\partial x_j} = 0 \tag{2}$$

where i,j = 1,2; x_i are the Cartesian coordinates and σ_{ij} are the stress components in a Cartesian system. The usual convention of summing over a repeated Latin suffix is adopted here. The stresses can be obtained from a stress function Φ in a Cartesian system by

$$\sigma_x = \frac{\partial^2 \phi}{\partial y^2}, \qquad \sigma_y = \frac{\partial^2 \phi}{\partial x^2}, \qquad \tau_{xy} = -\frac{\partial^2 \phi}{\partial x \partial y} \tag{4}$$

and the equilibrium equations are satisfied automatically where $x_1 = x$ and $x_2 = y$. As the proper solution of the problem the strain compatibility condition must be satisfied as well, it reads

$$\frac{\partial^2 \varepsilon_x}{\partial y^2} + \frac{\partial^2 \varepsilon_y}{\partial x^2} = 2\frac{\partial^2 \varepsilon_{xy}}{\partial x \partial y} \tag{5}$$

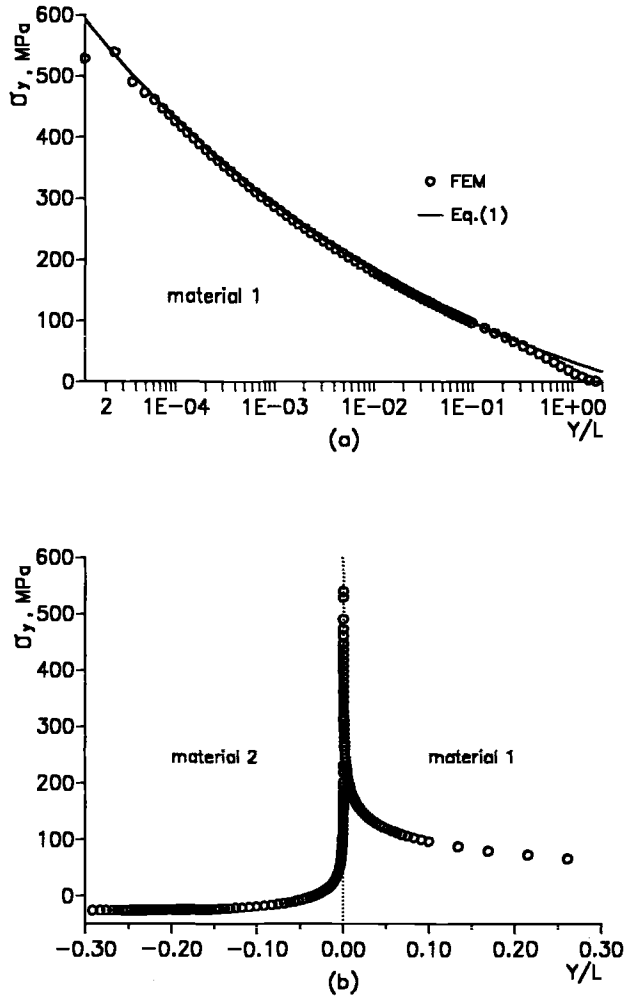


Fig.4---The stress σ_y along the free edge (x = 0, coordinates see Fig.1) for a joint without interlayer, (a) in material 1; (b) near the interface between material 1 and 2.

In graded material the relations between the stresses and the strains including the thermal strain are

$$\varepsilon_x = \frac{1}{E(x,y)}[\sigma_x - \nu(x,y)\sigma_y] + \alpha(x,y)\Delta T$$

$$\varepsilon_y = \frac{1}{E(x,y)}[\sigma_y - \nu(x,y)\sigma_x] + \alpha(x,y)\Delta T$$

$$\varepsilon_{xy} = \frac{1}{2G(x,y)}\tau_{xy} \tag{6}$$

where ΔT is the homogeneous temperature change in the joint and $G = E/(2(1+\nu))$.

In FGM the material properties are a function of the coordinates, that is E = E(x,y), $\nu = \nu(x,y)$ and $\alpha = \alpha(x,y)$. Introducing Eq.(4) into Eq.(6) and in the compatibility condition Eq.(5) gives

$$\nabla^4\Phi + F\left(\frac{\partial E(x,y)}{\partial x}, \frac{\partial E(x,y)}{\partial y}, \frac{\partial \nu(x,y)}{\partial x}, \frac{\partial \nu(x,y)}{\partial y}, \frac{\partial \alpha(x,y)}{\partial x}, \frac{\partial \alpha(x,y)}{\partial y}, \frac{\partial \Phi(x,y)}{\partial x}, \frac{\partial \Phi(x,y)}{\partial y}, \ldots\right) = 0 \tag{7}$$

where F(...) means that the second term is a function of the first and the higher-order differentiation of E(x,y), $\nu(x,y)$, $\alpha(x,y)$ and $\Phi(x,y)$. The function F is very complicated and, therefore, it is generally very difficult to find an analytical solution of Eq.(7). From Eq.(7) it can be seen that the stress function Φ is no longer a biharmonic function. For thermal loading (homogeneous change of temperature in the joint) there is yet no analytical solution for the stress distribution in FGM. In the next section the stress distribution in a joint with graded interlayer has be obtained by the FEM. Our FE-calculations for a joint with a graded interlayer have shown that the mesh size has a negligible effect on the value of the peak stress, but it has a small effect on the location of the peak stress, especially for a very small thickness of the interlayer.

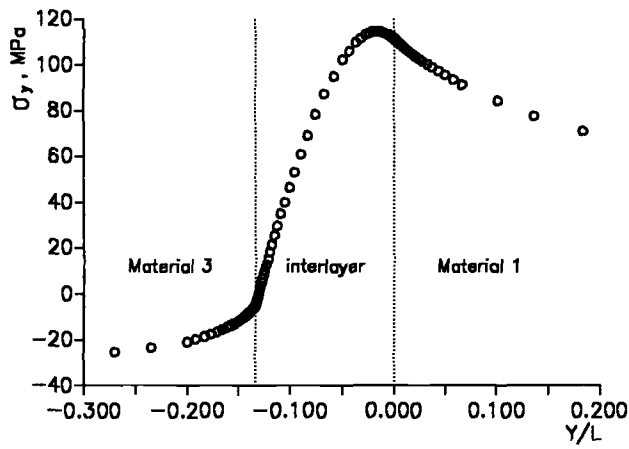


Fig.5--- σ_y along the free edge (near the interfaces) for a joint with a graded interlayer.

RESULTS OF FEM CALCULATIONS AND DISCUSSION

In this section the joint shown in Fig.1 with the geometry $H_1/L = H_3/L = 2$ (only the ratio H_2/H_1 varies) is considered and the material properties in the interlayer vary only in y-direction (coordinates see Fig.1). The results are valid for plane strain and the temperature difference is $\Delta T = -100K$. In all calculations the properties of materials 1 and 3 are

$$E_1 = 400 \text{ GPa}, \quad \nu_1 = 0.24, \quad \alpha_1 = 4.5 \times 10^{-6}/K$$

$$E_3 = 114 \text{ GPa}, \quad \nu_3 = 0.33, \quad \alpha_3 = 8.5 \times 10^{-6}/K$$

and $E_2|_{y=0} = E_1$ and $E_2|_{y=-H_2} = E_3$ (there is always $E_1 > E_3$). Material 1 is SiC and material 2 is Ti. As a first example, the transition between materials 1 and 3 was

$$E_2 = E_1 + (E_3 - E_1)\left(\frac{y}{H_2}\right)^2, \quad \nu_2 = \nu_1 + (\nu_3 - \nu_1)\left(\frac{y}{H_2}\right)^2, \quad \alpha_2 = \alpha_1 + (\alpha_3 - \alpha_1)\left(\frac{y}{H_2}\right)^2 \tag{8}$$

and $H_2/H_1 = 1/15$ was chosen. The stress distribution of σ_y along the free edge near the interfaces is shown in Fig.5. It can be seen that the stress singularity has vanished (compared to Fig.4b) and the maximum stress does not occur at the interface. The value and the location of the peak stress depend on the transition function form of the Young's modulus E, the Poisson's ratio ν and the thermal expansion coefficient α in the interlayer. It is the aim of the following calculations to find the rules under which $\sigma_y|_{max}$ does not occur at the interface and the peak stress $\sigma_y|_{max}$ is small.

In all further calculations the same function forms have been chosen for E_2, ν_2 and α_2. Because the polynomial, the exponential and the sinusoidal function are the simple and usually used functions, to obtain a wide variety of function forms the following combinations have been used

$$E_2 = E_1 + (E_3 - E_1)\left|\frac{y}{H_2}\right|^n \tag{9}$$

$$E_2 = E_1\left(\frac{E_3}{E_1}\right)^{\left|\frac{y}{H_2}\right|^n} \tag{10}$$

$$E_2 = E_1 + (E_3 - E_1)\sin^n\left|\frac{\pi}{2}\frac{y}{H_2}\right| \tag{11}$$

$$E_2 = E_3 + (E_1 - E_3)\left(\frac{y + H_2}{H_2}\right)^n \tag{12}$$

$$E_2 = E_3\left(\frac{E_1}{E_3}\right)^{\left(\frac{y+H_2}{H_2}\right)^n} \tag{13}$$

$$E_2 = E_3 + (E_1 - E_3)\sin^n\left(\frac{\pi}{2}\frac{y + H_2}{H_2}\right) \tag{14}$$

$$E_2 = E_1 + A\frac{y}{H_2} + B\left(\frac{y}{H_2}\right)^2 + C\left(\frac{y}{H_2}\right)^3 + D\left(\frac{y}{H_2}\right)^4 \tag{15}$$

$$E_2 = E_1 + A\frac{y}{H_2} + B\left(\frac{y}{H_2}\right)^2 + C\left(\frac{y}{H_2}\right)^3 + D\left(\frac{y}{H_2}\right)^4 + F\sin^n\left(\frac{\pi}{2}\frac{y}{H_2}\right) \tag{16}$$

$$E_2 = A + B\frac{y}{H_2} + C\left(\frac{y}{H_2}\right)^2 + D\left(\frac{y}{H_2}\right)^3 + F\left(\frac{y}{H_2}\right)^4 + a\left(\frac{E_3}{E_1}\right)^{\left|\frac{y}{H_2}\right|^n} \tag{17}$$

Different values of $\partial E_2/\partial y\,|_{y=0}$, $\partial E_2/\partial y\,|_{y=-H_2}$, $\partial^2 E_2/\partial y^2\,|_{y=0}$ and $\partial^2 E_2/\partial y^2\,|_{y=-H_2}$ can be obtained by varying the coefficients a, A, B, C, D, F and the exponential n. They can be positive, negative, small, large or zero.

For some of these relations the variation of the Young's modulus with y/H_2 is shown in Fig.6. It can be seen that the transition from material 1 to the interlayer or from material 3 to the interlayer is smooth for some functions, whereas for others the transition is neither smooth from material 1 to interlayer nor from material 3 to the interlayer.

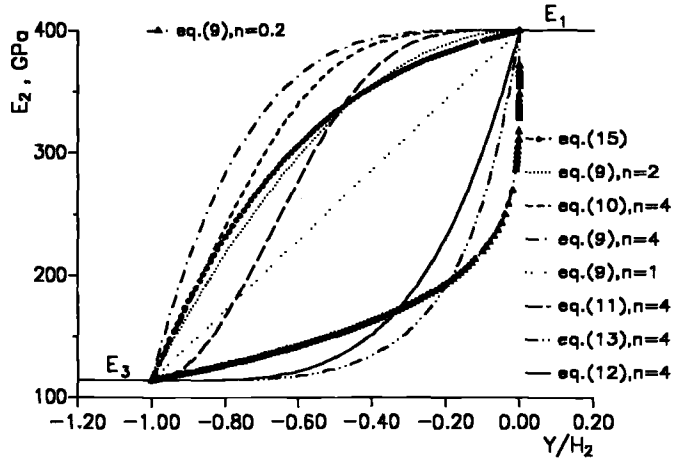


Fig.6---Typical curves of the $E_2(y)$ functions considered.

The Effect of the Thickness of the Interlayer on the Peak Stress

The thickness of the interlayer H_2 varies from $H_2/H_1 = 0.002$ to $H_2/H_1 = 0.2$. For the functions shown in Fig.6 and different ratios H_2/H_1 the peak stresses $\sigma_y\,|_{max}$ and the location of the peak stress $y_{\sigma_y|max}$ have been calculated by FEM. The peak stresses $\sigma_y\,|_{max}$ are plotted in Fig.7 versus H_2/H_1. These results can be described by the relation

$$\sigma_y\,|_{max} = A + B\,\lg(H_2/H_1) + C\,\lg^2(H_2/H_1) \qquad (H_2/H_1 \le 1) \tag{18}$$

For $H_2/H_1 > 0.1$ $\sigma_y\,|_{max}$ decreases nearly linearly with increasing interlayer thickness, it is similar to the previous results shown in [9]. For very small H_2/H_1 $\sigma_y\,|_{max}$ decreases not linearly with increasing interlayer thickness. The location of the peak stress $y_{\sigma_y|max}$ is given in Fig.8. The fluctuation in Fig.8 for small value of H_2/H_1 is due to the effect of the FEM mesh size.

From the results shown in Figs.6-8 it can be supposed with some likelihood that: (i) the peak stresses are low, if there is a smooth transition from material 1 (with the larger

Young's modulus) to the interlayer; (ii) the peak stresses are high, if there is a sharp transition in the material properties from material 1 to the interlayer; (iii) the location of the peak stress ($y_{\sigma_y|max}/H_2$) is independent of the thickness of the interlayer; if $\partial E_2/\partial y|_{y=0}$ is above a critical value, the peak stress occurs always at the interface between the material 1 and the interlayer. These suppositions will be studied further in next section.

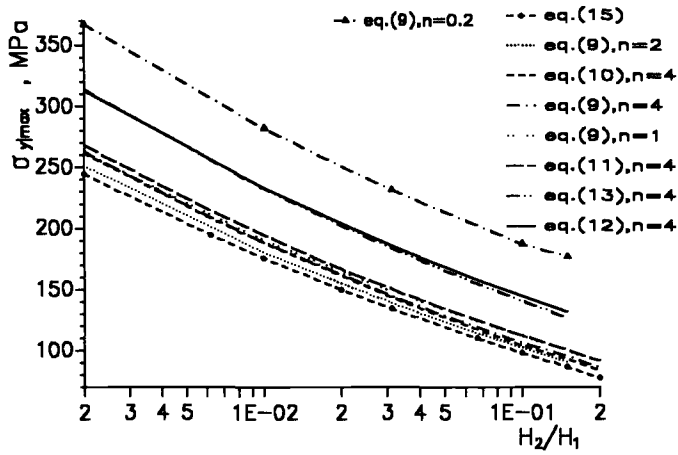


Fig.7---The peak stress $\sigma_y|_{max}$ versus H_2/H_1 for the functions shown in Fig.6.

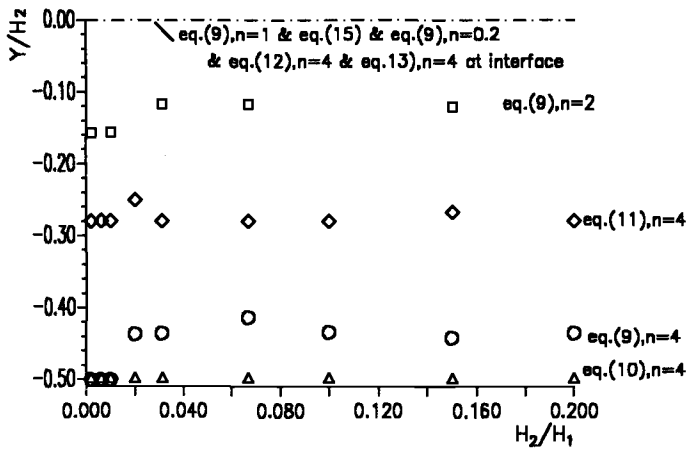


Fig.8---The location $y_{\sigma_y|max}/H_2$ versus H_2/H_1 for the functions shown in Fig.6.

The Effect of the Exponent of the Transition Function on the Peak Stress

For a given ratio H_2/H_1 and material 1 and material 3 the value of n in Eqs.(9) and (10) was varied from 0.2 to 7. The effect of n on the peak stress $\sigma_y|_{max}$ and the location $y_{\sigma_y|max}$ is shown in Figs.9 and 10. For the ratio H_2/H_1 = 0.002 and H_2/H_1 = 0.1 the peak stress $\sigma_y|_{max}$ is plotted versus lg(n) in Fig.9(a) and Fig.10(a), and the location of the peak stress $y_{\sigma_y|max}$ is plotted versus lg(n) in Fig.9(b) and Fig.10(b). For H_2/H_1 = 0.002, the values of $y_{\sigma_y|max}$, according to Eq.(9) and Eq.(10), are identical. In Figs.9 and 10 the solid lines represent the results from the fitted empirical form Eq.(19), the circles describe the

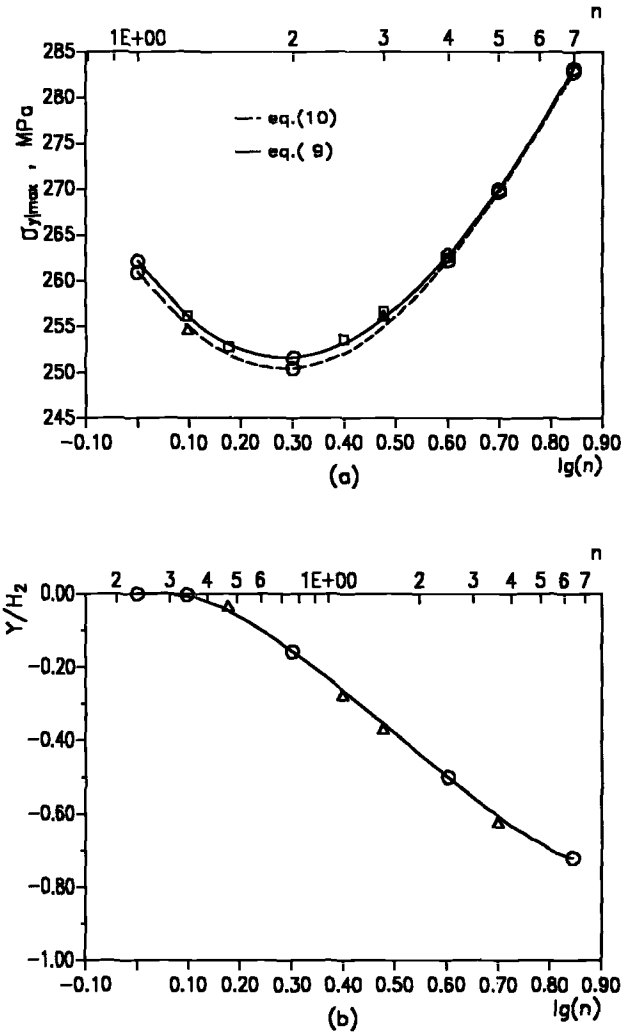


Fig.9---H_2/H_1 = 0.002; (a) $\sigma_y|_{max}$ versus lg(n); (b) $y_{\sigma_y|max}$ / H_2 versus lg(n).

points which are used to fit the curve, and the triangles or squares are the points used to test the accuracy of the fitted form. It can be seen that between $\sigma_y|_{max}$ and lg(n) and between $y_{\sigma_y|max}/H_2$ and lg(n) a unique relation exists and they can be fitted by means of a fourth order polynomial of lg(n) like

$$\sigma_y|_{max} = A + B\,\lg(n) + C\,\lg^2(n) + D\,\lg^3(n) + E\,\lg^4(n) \tag{19a}$$

$$\frac{y|_{\sigma_y|max}}{H_2} = a + b\,\lg(n) + c\,\lg^2(n) + d\,\lg^3(n) + e\,\lg^4(n) \tag{19b}$$

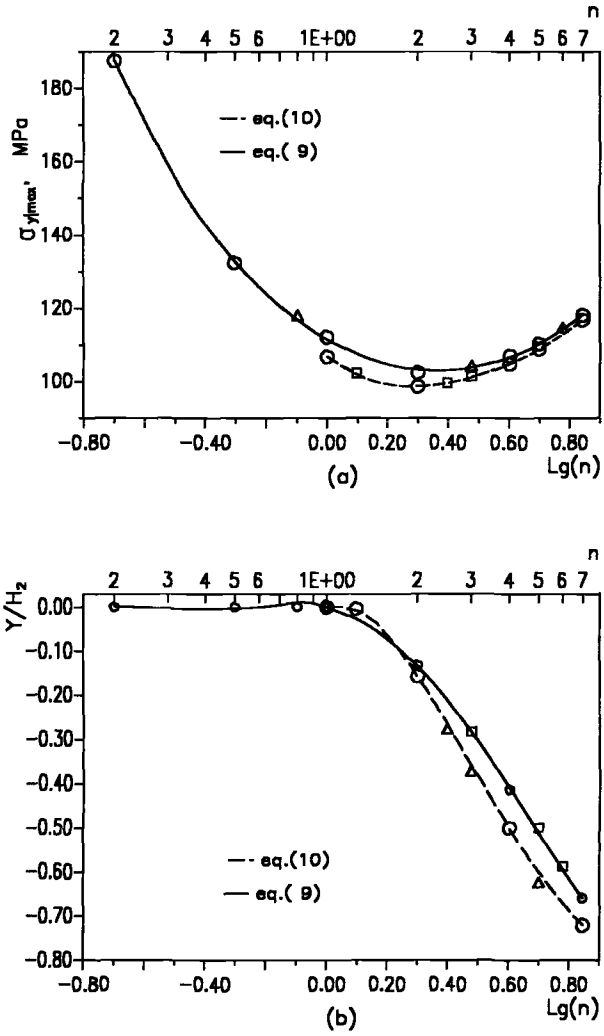


Fig.10---H_2/H_1 = 0.1; (a) $\sigma_y|_{max}$ versus lg(n); (b) $y_{\sigma_y|max}$ / H_2 versus lg(n).

Therefore by five FEM calculations for five different values of n the peak stress $\sigma_y|_{max}$ and $y_{\sigma_y|max}$ for another arbitrary n can be obtained using Eq.(19) without any additional FEM calculations. From Eq.(19) we can find the minimum value of $\sigma_y|_{max}$. For the examples shown in Figs.9 and 10 the minimum $\sigma_y|_{max}$ occurs at about n=2. In [9] a similar result has been shown, i.e. there is a minimum value of $\sigma_y|_{max}$ relate to a exponent n. For $y_{\sigma_y|max}$, in the range shown in Figs.9 and 10, applies: the higher n is, the larger is the value of $|y_{\sigma_y|max}|/H_2$ which means that the peak stress occurs away from the interface between the material 1 and the interlayer, and it is in the interlayer.

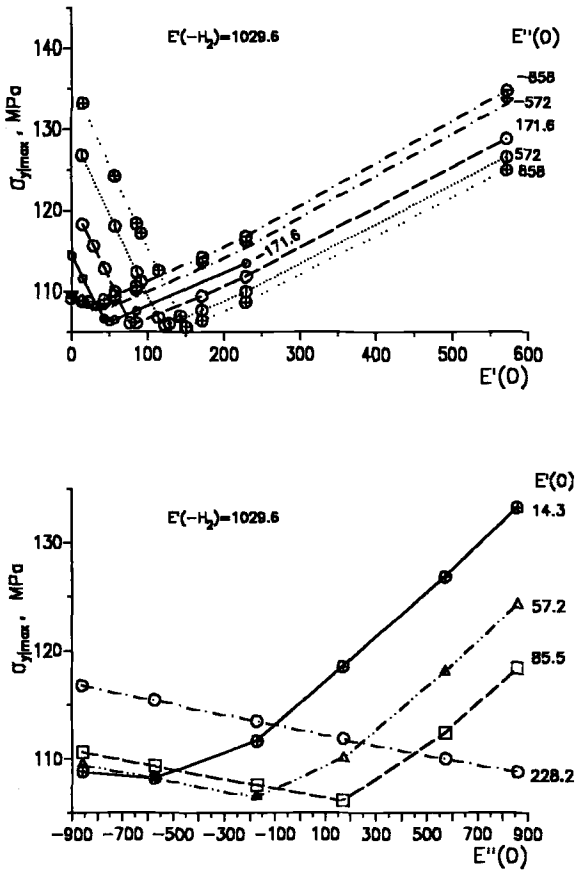


Fig.11---(cont.)

The Effect of the Transition Function Form in FGM on the Peak Stress

To find the rules for minimising the peak stress and the peak stress occuring away from the interface many different functions have been chosen which are given in Eqs.(9)-(17) with different coefficients a, A, B, C, D, F and n so that $\partial E_2/\partial y|_{y=0}$, $\partial E_2/\partial y|_{y=-H_2}$,

$\partial^2 E_2/\partial y^2|_{y=0}$ and $\partial^2 E_2/\partial y^2|_{y=-H_2}$ can be positive, negative, small, large or zero. Their $\sigma_y|_{max}$ and $y_{\sigma_y|max}$ values have been calculated by means of FEM.

For $H_2/H_1 = 1/15$ and the given materials 1 and 3 (with always $E_2|_{y=0} = E_1$, $E_2|_{y=-H_2} = E_3$ and $E_1 > E_3$), as example the results of $\sigma_y|_{max}$, $y_{\sigma_y|max}$, $\partial E_2/\partial y|_{y=0}$, $\partial E_2/\partial y|_{y=-H_2}$, $\partial^2 E_2/\partial y^2|_{y=0}$ and $\partial^2 E_2/\partial y^2|_{y=-H_2}$ are given in Figs.11 and 12, in which $E'(-H_2)$ is $\partial E_2/\partial y|_{y=-H_2}$ and $E''(0)$ is $\partial^2 E_2/\partial y^2|_{y=0}$. It is shown that the relation between $\sigma_y|_{max}$, $y_{\sigma_y|max}$, $\partial E_2/\partial y|_{y=0}$, $\partial E_2/\partial y|_{y=-H_2}$, $\partial^2 E_2/\partial y^2|_{y=0}$ and $\partial^2 E_2/\partial y^2|_{y=-H_2}$ is very complicated. However, it is clear that if $\partial E_2/\partial y|_{y=0}$ is small (smaller than $(E_1 - E_3)/5$), $\partial E_2/\partial y|_{y=-H_2}$ is very large, $\partial^2 E_2/\partial y^2|_{y=0} < 0$ and its absolute value is very large the peak stress is small and the peak stress occurs away from the interface. A general rule will be developed and reported in another paper.

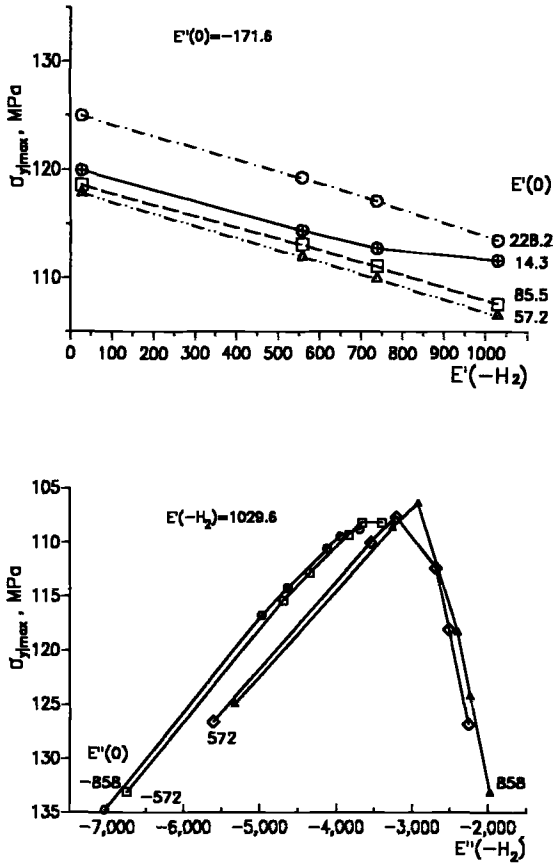


Fig.11---Relation between the peak stress and the differentiation of E(y).

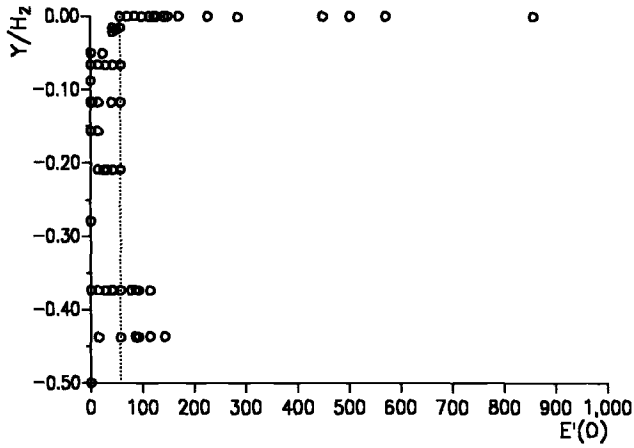


Fig.12---Relation between the location of peak stress $y_{\sigma_y|max}$ / H_2 and $\partial E_2/\partial y\,|_{y=0}$.

CONCLUSIONS

The stresses in a joint with an FGM interlayer are analyzed by means of the FEM. The peak stress $\sigma_y\,|_{max}$ and the location of peak stress $y_{\sigma_y|max}$ are investigated. The following conclusions are received:

(a) If $\partial E_2/\partial y\,|_{y=0}$ is small (smaller than $(E_1 - E_3)/5$), $\partial E_2/\partial y\,|_{y=-H_2}$ is very large, $\partial^2 E_2/\partial y^2\,|_{y=0} < 0$ and its absolute value is very large the peak stress is small and the peak stress occurs away from the interface.

(b) The peak stress increases with decreasing thickness of the interlayer H_2/H_1 and the location of the peak stress ($y_{\sigma_y|max}$ /H_2) is independent of the thickness of the interlayer.

(c) The mesh size of FEM has a negligible effect on the value of $\sigma_y\,|_{max}$, but it has a small effect on the location of the peak stress ($y_{\sigma_y|max}$), especially for a very small thickness of the interlayer.

REFERENCES

[1] Munz, D. and Yang, Y.Y., "Stresses in Ceramic-Metal Joints under Mechanical and Thermal Loading," Proc. of Mis-matching of Welds, ESIS 17, Mechanical Engineering Publications, London, 1994.

[2] Mizuno, K., Miyazawa, K. and Suga, T., "Characterization of Thermal Stress in Ceramic/Metal-Joint," J. of the Faculty of Eng., the Uni. of Tokyo (B), Vol.XXXIX, No.4, 1988, pp 401-412.

[3] Suganuma, K., Okamoto, T., Koizumi, M. and Shimada, M., "Effect of Interlayers in Ceramic-Metal Joints with Thermal Expansion Mismatches", Comm. J. Am. Cer. Soc., Vol.70, 1984, pp C256-C257.

[4] Munz, D., Sckuhr, M. and Yang, Y.Y., "Thermal Stresses in Ceramic-Metal Joints with an Interlayer", J. of Am. Cer. Soc., to appear.

[5] Nagano, T. and Wakai, F., "Fabrication of Zirconia-Alumina Functionally Gradient Material by Superplastic Diffusion Bonding," J. of Mater. Sci., Vol.28, 1993, pp 5793-5799.

[6] Hirano, T., Teraki, J. and Yamada, T., "On the Design of Functionally Gradient Materials," Proc. of the First Intern. Symp. FGM, Sendai, 1990.

[7] Arai, Y., Kobayashi, H. and Tamura, M., "Analysis on Residual Stress and Deformation of Functionally Gradient Material and It's Optimum Design," Proc. of the First Intern. Symp. FGM, Sendai, 1990.

[8] Erdogan, F., "Fracture Problems in FGMs and Applications to Graded Interfaces and Coatings," Proc. of the First Intern. Symp. FGM, Sendai, 1990.

[9] Williamson, R.L., Rabin, B.H. and Drake, J.T., "Finite Element Analysis of Thermal residual Stresses at Graded Ceramic-Metal Interface. Part I. Model Description and Geometrical Effects," J. Appl. Phys., Vol.74, 1993, pp 1310-1320.

[10] Munz, D. and Yang, Y.Y., "Stress Singularity at the Interface in Bonded Dissimilar Materials under Mechanical and Thermal Loading", ASME J. Appl. Mech., Vol. 59, 1992, pp 857-861.

[11] Yang, Y.Y., "Spannungssingularitäten in Zweistoffverbunden bei mechanischer und thermischer Belastung," Bericht VDI, Reihe 18 Nr.113, 1992, VDI Verlag, Düsseldorf (in German).

[12] Munz, D. and Yang, Y.Y., "Stresses near thr Free Edge of the Interface in Ceramic to Metal Joints", J. of the Euro. Cer. Soc., Vol.13, 1994, pp453-460.

[13] Munz, D. and Yang, Y.Y., "Stresses near the Edge of Bonded Dissimilar Materials Described by Two Stress Intensity Factors", Int. J. Fract., Vol.60, 1993, pp 169-177.

[14] Tilscher, M., Munz, D. and Yang, Y.Y. "The Stress Intensity Factor in Bonded Quarter Planes after a Change in Temperature", J. of Adhesion, 1994, in print.

Yiu-Wing Mai,[1] Herman He,[1] Roy Leung,[1] and Rajinder S. Seth[2]

IN-PLANE FRACTURE TOUGHNESS MEASUREMENT OF PAPER

REFERENCE: Mai, Y-W., He, H., Leung, R., and Seth, R.S., "**In-Plane Fracture Toughness Measurement of Paper**," Fracture Mechanics: 26th Volume, ASTM STP 1256, Walter G. Reuter, John H. Underwood, and James C. Newman, Jr., Eds., American Society for Testing and Materials, Philadelphia, 1995.

ABSTRACT: Paper sheet material has a high toughness and a low yield stress so that linear elastic fracture mechanics is inappropriate to measure its fracture resistance. Experiments have been conducted on single edge-notched tension SE(T) specimens using the J-integral analysis but there are difficulties in identifying the crack initiation, and the J_c value at 0.2 mm crack growth as required by ASTM E813-89 depends on the slope of the J_R-curve which may be affected by specimen size and geometry effects. To overcome these problems the essential fracture work concept is applied to paper and an experimental technique developed to evaluate the specific fracture energy using deeply double-edge notched tension DE(T) specimens containing different ligament lengths. With this technique the fracture resistance of papers from hardwood and softwood pulps, the effects of level of bonding and recycling can be compared. It is recommended that the essential fracture work method be used for quality control of paper by the pulp and paper industry.

KEY WORDS: paper sheets, recycling, fracture, toughness, essential work, test method

Fracture toughness is an important service parameter for most end uses of paper in which stresses are applied in the plane of the sheet. However, the resistance to fracture is currently measured by the out-of-plane Elmendorf [1] or Brecht-Imset [2] tear tests. Some papers, like newsprints, are brittle but many papers such as handsheets of beaten softwood kraft pulps are ductile, Fig. 1. For brittle papers their

[1]Professor, research assistant and student, respectively, Centre for Advanced Materials Technology, Department of Mechanical and Mechatronic Engineering, University of Sydney, Sydney, NSW 2006, Australia.

[2]Research scientist, Pulp and Paper Research Institute of Canada, 3800 Wesbrook Mall, Vancouver, BC, Canada V6S 2L9.

Copyright © 1995 by ASTM International www.astm.org

fracture resistances can be easily measured with linear elastic fracture mechanics parameters like the potential energy release rate G_c or the critical stress intensity factor K_c [3]. For the ductile papers with large fracture resistance to yield stress ratios, the crack tip plastic zone size is large enough to make all linear elastic fracture mechanics characterisation methods invalid [4]. There have been a few attempts [5,6] to measure in-plane fracture toughness of ductile paper sheets using the multiple-specimens and single-specimen techniques of the J-integral [7,8], as well as the non-linear elastic energy release rate $\tilde{G}$ method of Liebowitz and Eftis [9]. But it is not clear that they have provided results independent of specimen size and crack geometry. There are obvious difficulties trying to identify incipient crack initiation in a fibrous sheet material like paper and to determine the corresponding J_c value.

In the present study the use of the J-integral technique according to the ASTM E813-89 standard [10] will be followed to examine the fracture resistance behaviour with crack extension in terms of a J_R-Δa curve. These results are then compared to those obtained using an essential fracture work technique developed particularly for thin sheets. The theoretical basis of essential fracture work method is outlined in the paper but a more detailed treatment has been previously given in references [10-15].

ESSENTIAL FRACTURE WORK METHOD

As shown in Fig. 2, in a deeply double-edge notched tension DE(T) specimen of a ductile sheet material, the ligament L will be fully yielded prior to crack initiation upon loading. The fracture propagation along the ligament gives a total fracture work W_f which consists of two components: the work to form the outer plastic zone W_p which is specimen geometry dependent and the work to tear the ligament W_e which is dissipated in the fracture process zone. Because W_e scales with the ligament size L and W_p scales with the ligament squared L^2, a straight line relationship between W_f/tL (where t is sheet thickness) and L is expected, i.e.

$$W_f/(Lt) \quad w_f = w_e + \beta w_p L \tag{1}$$

where β is the shape factor of the outer plastic zone, w_p the plastic work per unit volume and w_e the specific essential fracture work. By extrapolating the w_f versus L plot to zero ligament yields w_e. It has been shown [12] that, for a given sheet thickness, the specific essential fracture work is a material constant independent of specimen size and geometry effects and it has been identified as equal to J_c for crack propagation [13,14,16-18]. This method has been extensively used to measure the fracture resistance of metallic and polymeric sheet materials [11-14,16-20] and will be employed in this study for different grades of paper sheets. It is expected that this method will provide a simple and effective measurement of the quality of paper.

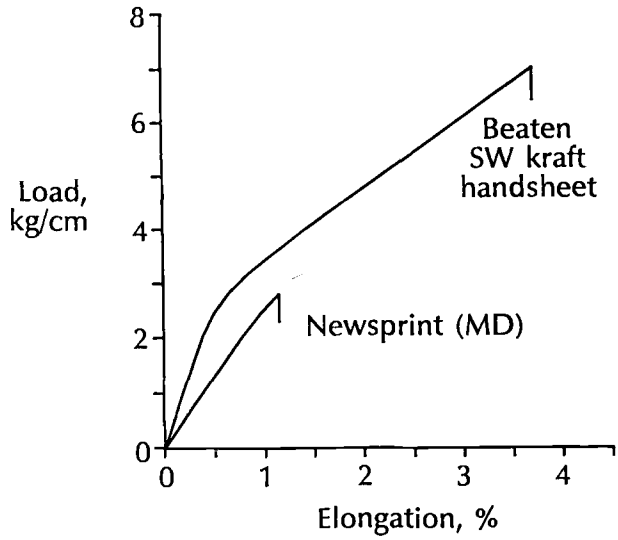


FIG. 1--Load-elongation curves for brittle and tough papers.

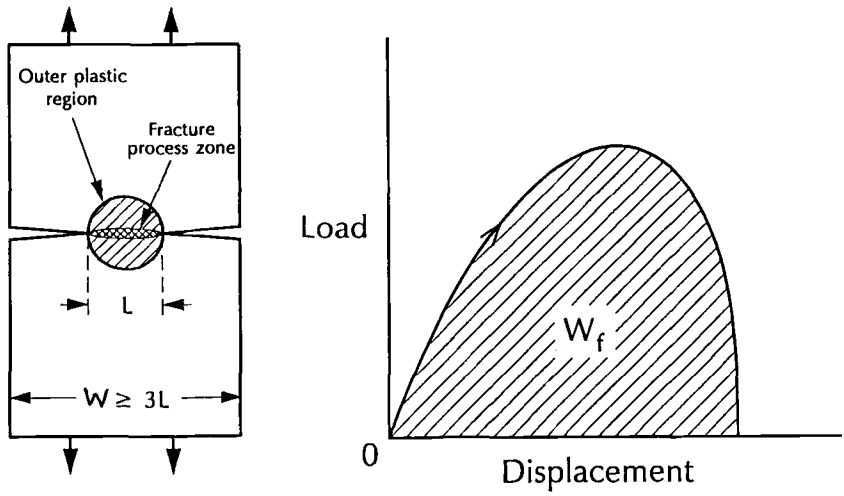


FIG. 2--DE(T) specimen and load-displacement curve for essential fracture work measurement.

EXPERIMENTAL WORK

Materials and Specimen Preparation

The copying papers were obtained from those used for photocopiers and the de-inked recycled and non-de-inked recycled copying papers were supplied by Associated Pulp and Paper Mills (APPM) and Australian Paper Manufacturers (APM), respectively. Handsheets of lightly beaten and well beaten softwood bleached kraft pulp were provided for testing by Pulp and Paper Research Institute of Canada, Vancouver Laboratory. The level of bonding was determined by the amount of beating of the pulp before papermaking. The physical and mechanical properties of these paper sheets are given in Table 1. All mechanical properties were obtained from tension tests according to ASTM E345-81 for metal foils as there is no similar standard for paper sheets.

TABLE 1--Description and mechanical properties of test materials.

Material	Grammage (g/m^2)	Thickness (μm)	Tensile strength (MPa)	Yield strength$^+$ (MPa)	Young's modulus (GPa)	Elongation to break (%)
Copying paper MD	80	95	57.2	29.8	5.96	0.84
Copying paper CD	80	95	27.5	14.2	2.75	1.57
Copying paper, de-inked and recycled MD	80	105	32.9	17.7	3.50	0.80
Copying paper, non-de-inked and recycled MD	80	120	33.5	18.9	3.50	0.75
Handsheets of lightly beaten* SW BK pulp	65.7	105	34.4	19.9	3.64	3.06
Handsheets of well beaten** SW BK pulp	70	94	77.9	39.7	5.83	3.55

MD: machine direction; CD: cross direction; SW: softwood; BK: bleached kraft; $^+$0.2% offset; *500 revolutions in PFI mill; **6000 revolutions in PFI mill; PFI: Papirindustriens Forskningsinstitutt (The Norwegian Pulp and Paper Research Institute).

Fracture Testing

For the J_R-Δa curve evaluation multiple specimens of the single edge notch tension SE(T) geometry were used. Two sizes of SE(T) were used: one with a width

W of 50 mm and the other 200 mm. The initial crack size a_o to width W ratio was maintained at 0.5. Each specimen was loaded in an Instron testing machine with a crosshead rate of 0.5 mm/min at ambient temperature (23°C) and humidity (50% R.H.) until a small crack extension was seen. Crack growth was measured after unloading at each crack extension with an optical profilometer at a magnification of $\times 100$. The area U under the load-displacement curve was measured and used to calculate J_R for the given Δa, i.e.

$$J_R = \eta U/[t(W - a)] \tag{2}$$

where η, which depends on the specimen size and geometry, may be obtained from ASTM E813-89 [10] and Wu et al. [21]. Different specimens were used to obtain different amount of crack growth. J_R-Δa curves were then plotted for the two specimen sizes and J_c determined according to the procedures specified by ASTM E813-89 [10].

For the essential fracture work tests, deeply double edge notch tension DE(T) specimens were used. Three specimen sizes with widths W = 50, 100 and 200 mm allowed a wide range of ligaments between 6 and 45 mm to be obtained. Like the SE(T) geometry all the DE(T) specimens were cut with surgical blades in the machine direction (MD) so that the crack propagated along the cross direction (CD) for the copying paper sheets. All tests were also conducted in the same Instron testing machine at the same ambient conditions. The results for each ligament length were repeated five times and plotted according to Eq 1 to obtain the specific essential fracture work w_e.

Observation of Plastic Zone in DE(T) Specimens

To reveal the shape of the outer plastic zone a light blue colour copying paper was used. Initially, the DE(T) sample with a given ligament size was soaked in melted wax and pressure applied on both sides. Several wax coatings were required to obtain good effects. Upon stretching by an external load the opacity of the ligament region was enhanced by the presence of the wax coating. Figure 3a shows the circular outer plastic zone for a ligament of 26 mm immediately after the crack had initiated. Plastic yielding of the ligament prior to cracking was confirmed. Figure 3b shows the crack tips and the outer plastic zone moments before complete fracture of the same ligament. Notice that the two crack tips eventually joined but the fracture path was quite tortuous and not always straight. Nonetheless, the physical basis of the derivation of Eq 1 for paper sheets was substantiated.

RESULTS AND DISCUSSION

J_R-Δa Crack Growth Resistance Curve

The J_R-Δa crack resistance data for the two sizes of SE(T) specimens, W = 50 and 200 mm, shown in Fig. 4 seem to agree with each other. By adopting the ASTM E813-89 procedures the exclusion lines for Δa = 0.15 and 1.5 mm were drawn

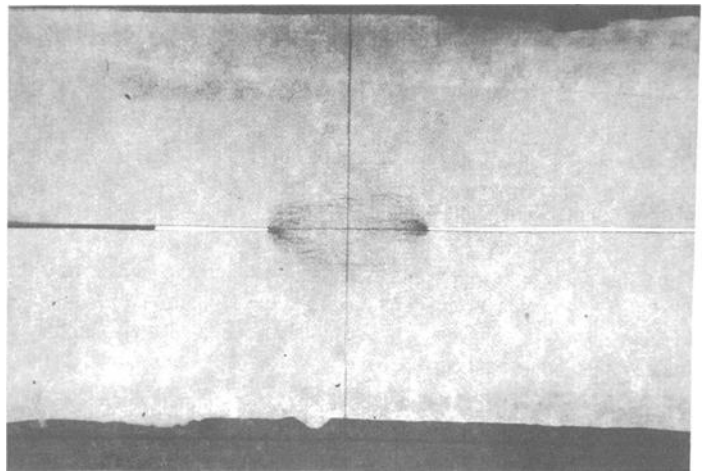


FIG. 3(a)--Outer plastic zone shape in DE(T) specimen at tear initiation (L = 22.6 mm).

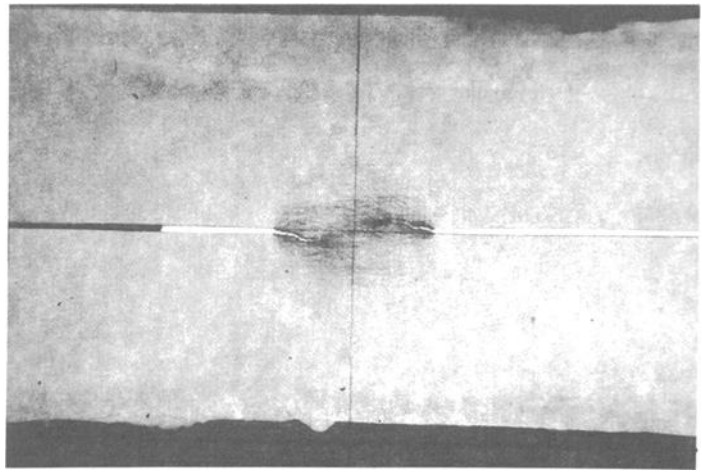


FIG. 3(b)--Outer plastic zone shape in DE(T) specimen with tortuous crack growth (L = 22.6 mm).

parallel to the blunting line. Data points within these two lines were then fitted to a power law equation through the origin. J_c was then determined from the J_R-Δa curve at $\Delta a = 0.2$ mm and this gave a value of $J_c = 8.80$ kJ/m^2 for the copying paper sheets. If a least squares straight line were fitted to these data points its intersection with the blunting line would give a J_c value at crack initiation of about 8 kJ/m^2. The difference is small and is probably caused by a crack growth of 0.2 mm.

The effect of specimen size is negligible in the region between the two exclusion lines. However, outside the 1.5 mm exclusion line, the data points for the smaller size samples seem to lie above those of the larger size samples for similar crack growths. Size effect can be important in this region and larger crack growths of the J_R-Δa curve. Similarly, specimen geometries will also affect the shape of the J_R-Δa curve but this effect has not been studied.

Essential Fracture Work Results

The experimental essential fracture work data for the three sizes of DE(T) specimens are plotted against ligament length in Fig. 5. Quite clearly, these results obey the linear straight line relationship of Eq 1. Extrapolation of the data to zero ligament gives the specific essential fracture work of $w_e = 8.37$ kJ/m^2 for the copying paper sheets. This value compares quite favorably with $J_c = 8.80$ kJ/m^2 defined at 0.2 mm crack extension and 8 kJ/m^2 at crack initiation (according to ASTM E813-81). Certainly, J_c at 0.2 mm crack growth overestimates the specific essential fracture work w_e which is a fundamental material property independent of specimen size. This overestimation can be considerable if the J_R-Δa curve has a steep gradient. It is therefore inappropriate to compare w_e with J_c ($\Delta a = 0.2$ mm) according to ASTM E813-89 but comparison with J_c ($\Delta a = 0$ mm) is not permissible by this new standard. In view of these difficulties the best method to measure the in-plane fracture resistance of paper sheets seems to be the essential fracture work technique given herein. It is relatively simple and easy to adopt in an industrial environment for quality control test of paper. It has a sound theoretical basis and is preferred to the J-integral method. In the following section the specific essential fracture works for a range of paper sheets are determined in order to evaluate its effectiveness in differentiating influences of hardwood and softwood pulps, level of bonding caused by beating of the pulps and recycling.

Effects of Recycling, Level of Bonding and Pulping on Specific Essential Fracture Work

For high quality recycled office and photocopy papers, waste papers are largely collected from printing operations and only black and white copying paper and computer print-out paper are selected. Some recycled papers are de-inked in which case the ink from the pulp is first removed by chemically dissolving or loosening the ink particles and then mechanically washed to remove the ink. Other recycled papers are non-de-inked. The essential fracture work data shown in Fig. 6 suggest that de-inking or not has little effect on the specific fracture work. The specific essential fracture work w_e, however, is about 4.50 kJ/m^2 which is half that of the copying

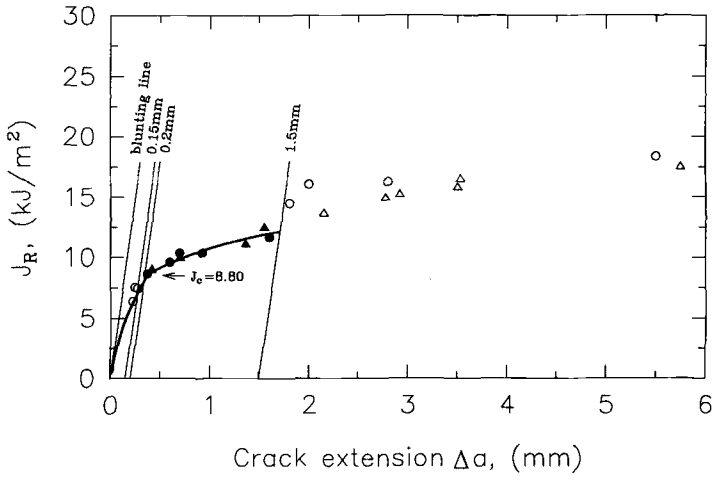


FIG. 4--J_R-Δa plot for W = 50 mm (○ ●) and 200 mm (Δ ▲) specimens.

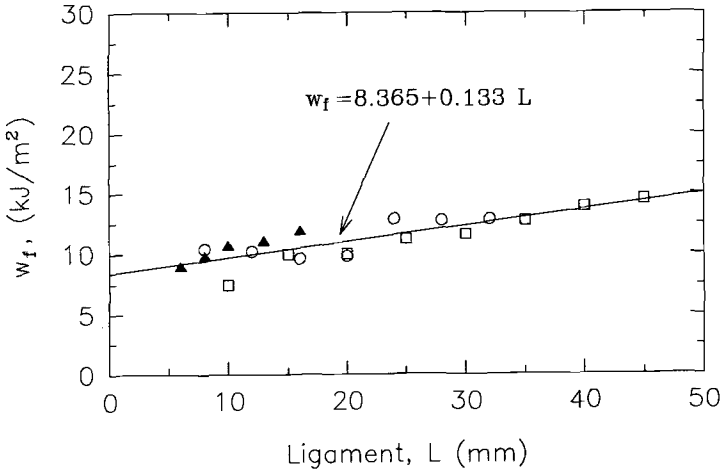


FIG. 5--Total specific work of fracture (w_f) against ligament length (L) for W = 50 mm (▲), 100 mm (○), 200 mm (□) DE(T) specimens.

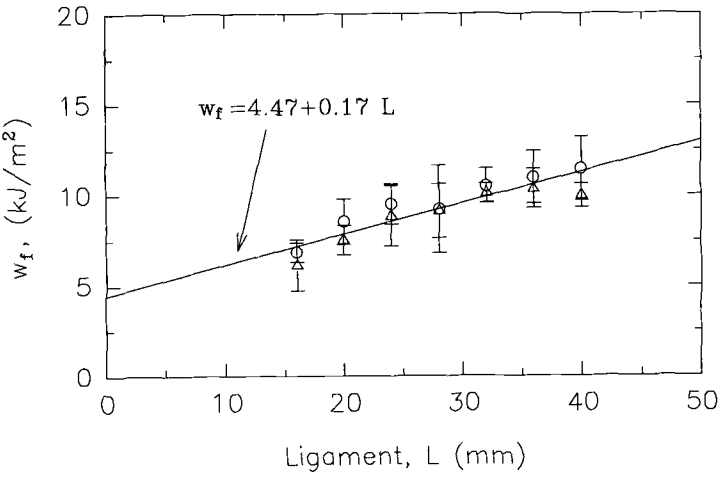


FIG. 6--Total specific work of fracture (w_f) against ligament length (L) for non-de-inked (○) and de-inked (Δ) copying papers.

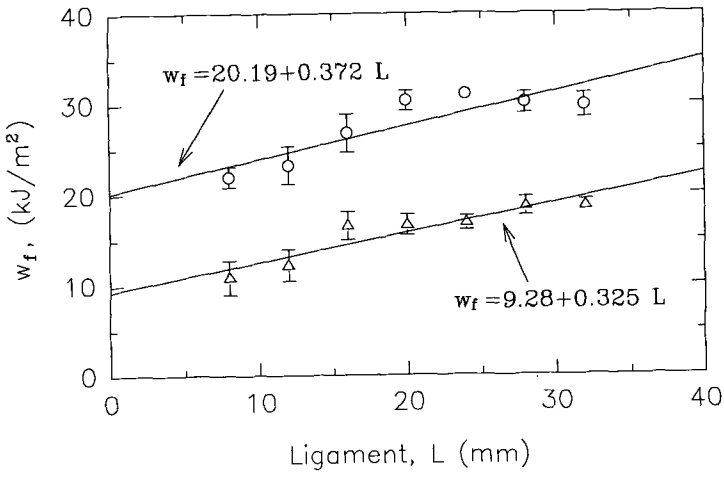


FIG. 7--Total specific work of fracture (w_f) against ligament length (L) for well-beaten (○) and lightly beaten (Δ) handsheets.

paper given in Fig. 5. As expected recycling does reduce the fracture resistance of paper sheets caused by degradation of their bonding potential. This is also supported by the decreased tensile properties of the recycled and copying papers shown in Table 1.

Figure 7 shows the fracture results for the handsheets of lightly and well beaten softwood bleached kraft pulps. The specific essential fracture work for the well beaten handsheets (w_e = 20.2 kJ/m^2) is about twice that of the lightly beaten handsheets (w_e = 9.28 kJ/m^2). The difference in w_e is dependent on the level of bonding due to the beating of the pulp before sheetmaking. The lightly beaten handsheets have tensile strengths only half the well beaten sheets and during the fracture experiments the fibres pull out rather than break.

TABLE 2--Specific essential and non-essential fracture works for different paper sheets.

	w_e(kJ/m^2)	βw_p(kJ/m^3)	Ew_e/σ_o^2(mm)	t(μm)
Copying paper MD	8.37	133	56.2	95
De-inked and non de-inked recycled papers MD	4.48	170	50.1	105-120
Handsheets of lightly beaten SW BK pulp	9.28	325	85.3	105
Handsheets of well beaten SW BK pulp	20.2	372	74.7	94
Handsheets of lightly beaten HW BK pulp	5.85	21.4	72.7	112
Handsheets of well beaten HW BK pulp	21.3	253	83.8	83
Handsheets of well beaten SW BS pulp	11.9	223	46.6	82
Softwood TMP	6.54	2	63.6	178

HW: hardwood; BS: bleached sulphite; TMP: thermomechanical pulp

Experimental work carried out at the Vancouver Laboratory of the Pulp and Paper Research Institute of Canada on other paper sheets shows that the specific essential fracture work is a most useful material property to differentiate the quality of papers as may be affected by hardwood or softwood pulps, method of pulping, and amount of beating [22]. These results together with those of the present work are shown in Table 2. Clearly, the specific essential fracture work w_e is strongly affected by the level of bonding; well beaten handsheets are always tougher than unbeaten or lightly beaten handsheets for the same pulp but there is little difference between hardwood and softwood handsheets for the same amount of beating received.

However, papers from thermomechanical pulps give the lowest specific essential fracture work. In Table 2 w_p represents the amount of plastic work per unit volume dissipated in the outer plastic zone (Fig. 2) and $\beta \approx \pi^2/4$ for a circular shape factor (Fig. 3). The parameter Ew_e/σ_o^2, where σ_o is the 0.2% offset yield stress and E is Young's modulus, is a relative measurement of the ductility of materials [23]. The size requirements for valid toughness evaluation are proportional to the magnitude of this parameter. For many brittle polymers this is about 0.4 mm, ceramics is approximately 0.03 mm, and for many high strength steels and aluminium alloys this is in the order of 2-3 mm. Therefore, papers have very large Ew_e/σ_o^2 values of 50-80 mm and with laboratory-sized specimens, linear elastic fracture mechanics parameters G_c and K_c do not apply. The present approach based on the essential work of fracture technique is hence useful to determine the in-plane specific fracture resistance and to differentiate the quality of papers as may be affected by the type and treatment of pulps and recycling processes. It should be seriously considered by the pulp and paper industry as a standard method for in-plane fracture toughness measurement.

CONCLUDING REMARKS

Because of their high fracture toughness to yield strength ratios the in-plane tearing resistance of papers cannot be characterised by conventional parameters G_c or K_c using laboratory-sized samples. The specific essential fracture work w_e is shown to be a material property and can be unambiguously determined using DE(T) samples. Experiments show that w_e is a sensitive function of the processing variables of papermaking including the type of pulps, hardwood or softwood and kraft or sulphite processes, as well as the level of bonding and its deterioration caused by recycling.

ACKNOWLEDGEMENTS

The authors wish to thank Associated Pulp and Paper Mills (APPM) and Australian Paper Manufacturers (APM) for their assistance in providing the recycled copying papers.

REFERENCES

[1] TAPPI Test Method T414 om-88 and CPPA Technical Section Standard D-9, "Internal Tearing Resistance of Paper," 1977.

[2] DIN Standard 53 115, "Testing of Paper: Tear Growth Test According to Brecht-Imset," 1977.

[3] Seth, R. S. and Page, D. H., "Fracture Resistance of Paper," Journal of Materials Science, Vol. 9, 1974, pp. 1745-1749.

[4] Mai Y-W., "On the Tear Resistance of Paper," Appita, Vol. 36, 1983, pp. 461-465.

[5] Yuhara, T. and Kortschot, M. T., "A Simplified Determination of the J-integral for Paper," Journal of Materials Science, Vol. 28, 1993, pp. 3571-

3580.

[6] Westerlind, B. S., Carlsson, L. A., and Andersson, Y. M., "Fracture Toughness of Liner Board Evaluated by the J-integral," Journal of Materials Science, Vol. 26, 1991, pp. 2630-2636.

[7] Begley, J. A. and Landes, J. D., "The J-integral as a Fracture Criterion," in Fracture Toughness, ASTM STP 514, American Society for Testing and Materials, Philadelphia, Pa., 1972, pp. 1-20.

[8] Rice, J. R., Paris, P. C., and Merkle, J. G., "Some Further Results of J-integral Analysis and Estimates," in Progress in Flaw Growth and Fracture Toughness Testing, ASTM STP 536, American Society for Testing and Materials, Philadelphia, Pa, 1973, pp. 231-245.

[9] Liebowitz, H. and Eftis, J., "On Nonlinear Effects in Fracture Mechanics," Engineering Fracture Mechanics, Vol. 3, 1971, pp. 267-281.

[10] ASTM Standard E813-89, "Standard Test Method for J_{IC}, a Measure of Fracture Toughness".

[11] Cotterell, B. and Reddell, J. K. "The Essential Work of Plane Stress Ductile Fracture," International Journal of Fracture, Vol. 13, 1977, pp. 267-277.

[12] Mai, Y-W and Cotterell, B., "Effect of Specimen Geometry on the Essential Work of Plane Stress Ductile Fracture," Engineering Fracture Mechanics, Vol. 21, 1985, pp. 123-128.

[13] Mai, Y-W. and Cotterell, B., "On the Essential Work of Ductile Fracture in Polymers," International Journal of Fracture, Vol. 32, 1986, pp. 105-125.

[14] Mai, Y-W. and Powell, P., "Essential Work of Fracture and J-integral Measurements for Ductile Polymers," Journal of Polymer Science B (Polymer Physics), Vol. 29, 1991, pp. 785-793.

[15] Mai, Y-W., "On the Plane-Stress Essential Fracture Work in Plastic Failure of Ductile Materials," International Journal of Mechanical Sciences, Vol. 35, 1993, pp. 995-1005.

[16] Paton, C. A. and Hashemi, S., "Plane Stress Essential Work of Ductile Fracture for Polycarbonate," Journal of Materials Science, Vol. 27, 1992, pp. 2279-2290.

[17] Wnuk, M. P. and Reed, D. T., "Essential Work of Fracture (w_e) Versus Energy Dissipation Rate (J_e) in Plane Stress Ductile Fracture," International Journal of Fracture, Vol. 31, 1986, pp. 161-171.

[18] Wu, J-S., Mai, Y-W., and Cotterell, B., "Fracture Toughness and Fracture Mechanisms of PBT/PC/IM Blend: Part I Fracture Properties," Journal of Materials Science, Vol. 28, 1993, pp. 3373-3384.

[19] Hashemi, S. and O'Brien, D., "The Essential Work of Plane Stress Ductile Fracture of PEEK Thermoplastic," Journal of Materials Science, Vol. 28, 1993, pp. 3977-3982.

[20] Mai, Y-W., Cotterell, B., Horlyck, R. and Vigna, G., "The Essential Work of Plane Stress Ductile Fracture of Linear Polyethylenes," Polymer Engineering and Science, Vol. 27, 1987, pp. 804-809.

[21] Wu, S-X., Mai, Y-W., and Cotterell, B., "Plastic $\acute{\eta}$-Factor of Fracture Specimen with Deep and Shallow Cracks," International Journal of Fracture, Vol. 45, 1990, pp. 1-18.

[22] Seth, R. S., Robertson, A. G., Mai, Y-W. and Hoffman, J. D., "Plane Stress Fracture Toughness of Paper," Tappi Journal, Vol. 76, No. 2, 1993, pp. 109-116.

[23] Atkins, A. G. and Mai, Y-W., Elastic and Plastic Fracture: Metals, Polymers, Ceramics, Composites, Biological Materials, Ellis Horwood/John Wiley, Chichester, 1985.

Subcritical Crack Growth

Raghu V Prakash[1] *and Basant K. Parida*[1]

Fatigue Crack Growth Behavior of Al-Li Alloy 1441

REFERENCE: Prakash, R. V., and Parida, B. K., **"Fatigue Crack Growth Behavior of Al-Li Alloy 1441,"** Fracture Mechanics: 26th Volume, ASTM STP 1256, Walter G. Reuter, John H. Underwood, and James C. Newman, Jr., Eds., American Society for Testing and Materials, Philadelphia, 1995.

ABSTRACT : Fatigue crack growth behavior of Al-Li alloy 1441 having a marginally lower lithium content, compared to 80xx and 20xx series Al-Li alloys is presented in this paper. This investigation was conducted on single edge tension - SE(T) - specimens, under constant amplitude as well as under MiniLCA flight spectrum loading with the specific objective of determining the effects of stress ratio, orientation, thickness and cladding. Three thicknesses were considered: 1.2 mm(clad and unclad), 2.0 mm(clad and unclad) and 8.0 mm unclad. Constant amplitude fatigue tests were conducted at stress ratios of -0.3, 0.1 and 0.7. Testing was performed under ambient conditions and along three orientations, namely L-T, T-L and L+45 degrees. Crack growth characteristics of this alloy are compared with that of BS:L73 (2014-T4 equivalent) for assessing the possibility of replacing BS:L73.

Significant effect of stress ratio on crack growth rate was observed in all thicknesses. However, in case of 1.2 and 2.0 mm thick sheets, the effect was minimal at intermediate-crack growth regime. The orientation of the specimen does not adversely affect the fatigue crack growth behavior of 8.0 mm and 2.0 mm thick specimens. However, for 1.2 mm unclad sheet crack growth resistance in L-T direction was found to be superior to that along T-L direction. In majority of test cases considered, no significant effect was observed on crack growth rate due to thickness or cladding. Crack growth characteristics of Al-Li alloy 1441 and Al-Cu alloy BS:L73 under constant amplitude as well as MiniLCA spectrum loading are similar in the low and intermediate-crack growth rate regime. Based on these observations, it is felt that this Al-Li alloy has the potential for future aerospace applications.

KEY WORDS : Al-Li alloy, fatigue crack growth, constant amplitude loading, flight spectrum loading, stress ratio, orientation, thickness, cladding effects, anisotropy.

1. Scientists, Structural Integrity Division, National Aerospace Laboratories, Bangalore 560 017, India.

Copyright © 1995 by ASTM International www.astm.org

INTRODUCTION

The need for further improvement in the performance of aerospace vehicles has provided impetus towards development of a new generation of advanced light- weight materials. Use of conventional aluminum alloys in aircraft construction is expected to diminish in future, due to progressively increased usage of composite materials for lighter airframes. Prospective aerospace materials include a variety of new metallic materials, metal-matrix composites and fiber reinforced-resin matrix composites. The development of aluminum- lithium alloys has been motivated by prospective weight savings due to decreased density and increased stiffness as compared to conventional aluminum alloys[*1-2*]. Some of the Al-Li alloys like 2090, 2091, 8090 and 8091 have been shown to possess certain superior mechanical properties compared to that of 20xx and 70xx series Al-alloys. However, the improvements in elastic modulus and density are normally accompanied by a significant decrease in ductility, especially in the short transverse direction. Anisotropy with regard to mechanical/fracture properties is another drawback of this class of materials [*3-5*]. This has constrained most aerospace designers to avoid its use in damage-tolerant airframes so far.

In an attempt to overcome this problem, a new Al-Li alloy designated 1441, having a marginally lower Lithium content and higher Copper content was jointly developed by the Defence Metallurgical Research Laboratory (India) and Russian agency, VIAM. The objective of this investigation was to determine the strength and fatigue characteristics of this alloy so as to assess its suitability for aerospace applications.

MATERIAL AND EXPERIMENTAL PROCEDURE

Aluminum-Lithium alloy 1441 was received in sheet form, in three different thicknesses, viz.: 1.2 mm, 2.0 mm and 8.0 mm. Nominal chemical composition of the alloy in percent weight is given in Table 1. Chemical composition of Al-Li alloy 2090 and 8090 is also presented in this table for comparison. The base sheets/plates of alloy 1441 were stress relieved at 400-450 deg. C for three to four hours and then air-cooled. The sheets/plates were solution treated at 530 deg. C for 20 minutes in case of 1.2 and 2.0 mm thick sheets, and for 45 minutes for 8.0 mm thick plates. Stretching of 1-2 % for thin sheets and 2-3 % for thick plates was done within 1 hour after quenching followed by age-hardening at 170 deg. C for 24 hours in an air-circulation furnace. The resultant sheet/plate was in peak-aged (T11) condition. The microstructure of 8 mm thick plate was found to be partially recrystallized, while that of 1.2 mm sheet was equi-axed and completely recrystallized. The 2.0 mm thick sheet was also recrystallized, but the grains were rather lamellar. Average grain size was of the order of 20-25 micrometer, considering width in case of lamellar grains. Some of the thin (1.2 and 2.0 mm) sheets were cladded. Cladding thickness was about 0.05 mm on both sides of the sheet. Figure 1 shows the microstructure of the as received material along three planes for 8.0 mm thick plate. The specimens used for the tensile strength determination were as per ASTM Standard, E-8M with a nominal width of 12.5 mm. Static strength values of the new material obtained along longitudinal(LT), transverse(TL) are listed in Table 2. This Table also includes data from literature [*6*] for commonly used Al-Cu alloy, 2024-T3 for comparison.

TABLE 1--Chemical Composition of Al-Li alloys (by % weight)

Alloy	Li	Cu	Mg	Zr	Fe	Si	Al
1441	1.85	1.8	1.0	0.09	0.10	0.05	Balance
8090	2.2-2.7	1.0-1.6	0.6-1.3	0.04-0.16	0.3	0.2	Balance
2090	1.9-2.6	2-4-3.0	0.25	0.08-0.5	0.12	0.1	Balance

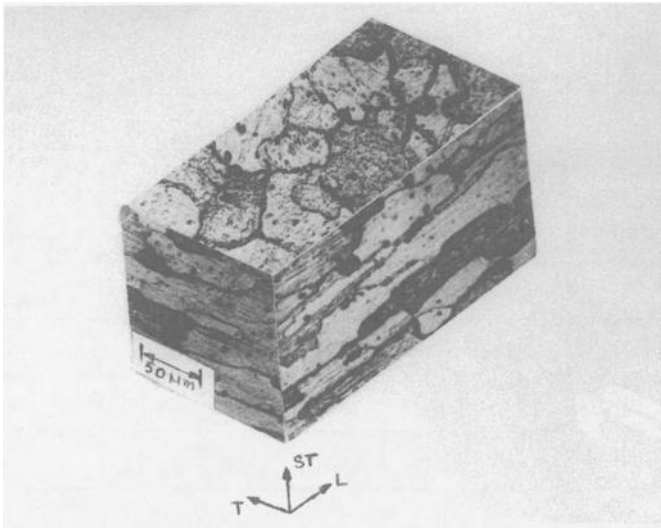


FIG.1--Optical Microstructure of Al-Li alloy 1441 - 8 mm thick plate - Unclad.

Single edge tension - SE(T) - specimens with the following dimensions were used for crack growth testing: 180 mm long and 45 mm wide for 1.2 mm and 2.0 mm thicknesses; 230 mm long and 75 mm wide for 8.0 mm thickness. All specimen-notches were machined by wire EDM process to a depth of 3.0 mm and a notch-root radius of 0.125 mm. Testing was conducted on INSTRON 1341/1342 model servo-hydraulic load frames. The specimens were gripped hydraulically and tested under fixed-displacement conditions. Anti-buckling guides were used for testing 1.2 and 2.0 mm thick specimens. Crack growth tests were conducted under room-temperature, laboratory air conditions. In-house developed micro-processor-based test controller [*7*] connected to a central MicroVAX II host computer system was used for test automation. Specially developed application software was used for FCP test control, including reproduction of a fighter aircraft load spectrum on test specimens, data acquisition. This software also permitted interactive processing of test results[*8*].

During the test, crack length was estimated on-line, by unloading compliance, with the help of a crack mouth opening displacement (CMOD) gage. Compliance based crack length estimates were cross-checked by optical measurements at frequent intervals.

TABLE 2--Mechanical Properties of Al-Li alloy 1441 compared with other Aluminum Alloys

Material	Orientation	0.2% P.S (MPa)	UTS (MPa)	% Elongn.	Density, g/cm^3	K_c $MPam^{1/2}$	Remarks
1441-T11*	LT	440	495	7.0	2.57	31-37	2 mm(Unclad)
1441-T11*	TL	430	485	6.2	2.57	29-40	2 mm (Unclad)
1441-T11*	LT	405	465	7.1	2.57	31-37	1.2mm(Unclad)
1441-T11*	TL	395	450	6.5	2.57	29-40	1.2mm(Unclad)
8090-T81*	LT	341	445	7.0	2.55	30-40	1.6mm(Alcan)
2091-T8X	LT	331	442	15.0	2.58	-	1.7mm [6]
2024-T3	LT	381	502	18.0	2.77	95	1.6mm [6]
BS:L73*	LT	360	421	19.0	2.79	70	2 mm

* Tensile test data generated at N.A.L., Bangalore

Fatigue crack growth studies were made under constant amplitude loading as well as under a fighter aircraft spectrum loading. Constant amplitude tests were conducted at three different stress ratios, R = -0.3, 0.1 and 0.7. Incidentally, stress ratio of -0.3 corresponds to that of the extreme(most severe) load cycle of a fighter aircraft load spectrum. Stress ratio of 0.7 ideally represents the behavior of a fully open crack. Spectrum load fatigue crack growth tests were conducted under Mini-LCA load sequence, which is a derivative of a typical fighter aircraft design (wing-under surface) load spectrum [9]. The Mini-LCA load sequence was obtained by eliminating small-amplitude load cycles that do not contribute to the fatigue damage. A block of random load sequence, representing an approximate 150 hours of flight, was repetitively applied on the specimens, till failure.

Generally, two specimens were tested, but in some cases more than two specimens were tested for each set of parameters to confirm the observed crack growth behavior. Fatigue crack growth rate was determined using incremental polynomial technique. Growth rates

were computed as mm/cycle for constant amplitude loading and as mm/hour of service load spectrum used. Figures showing spectrum load fatigue crack growth rate in this paper have been plotted as mm/flight, assuming that duration of one flight corresponds to one hour. Further, constant amplitude crack growth rates are plotted against stress intensity range, while spectrum load crack growth rates are plotted against reference stress intensity, K_{ref}, i.e. stress intensity computed for a stress level, compatible with 9g- manoeuver. Similarly, in case of constant amplitude loading with negative stress ratio, growth rates have been shown against maximum stress intensity, K_{max} (stress intensity variation under compressive part of the cycle has been neglected).

RESULTS AND DISCUSSION

From Table 2, it is seen that alloy 1441 has the highest value of 0.2% proof stress among all the materials compared. The ultimate tensile strength of alloy 1441 is also superior to that of 8090-T81 and 2091-T8X and is very close to that of the Al-alloy 2024-T3. Percentage elongation of alloy 1441 is same as that of alloy 8090-T81, but is substantially lower than the other two alloys, namely, 2091-T8X and 2024-T3. Fracture toughness for the thin sheet material ranged between 31.0-37 $MPam^{1/2}$ in LT orientation and 29-40 $MPam^{1/2}$ in TL orientation. It is well known that Al-Li alloys generally promote crack deflection, display relatively lower fatigue crack growth rates and markedly anisotropic effects[*10-14*]. However, 1441 was found to exhibit lower growth rates and very little anisotropy for the entire range of orientations and thicknesses tested in this investigation.

Effect of Stress Ratio

Figures 2 through 4 display the effect of stress ratio on fatigue crack growth rate of Al-Li alloy 1441 under constant amplitude loading along all three orientations and for all three thicknesses considered. For the sake of brevity, sample plots for 2 mm thick sheet along L+45 orientation and for 1.2 mm thick sheet along TL orientation are shown as Fig. 3 and 4. It is seen that the fatigue crack growth rate(FCGR) for 8.0 mm thick plate stock at stress ratios of -0.3 and 0.1 is almost identical(Fig.2a), while that at a stress ratio of 0.7 it is distinctly different and higher at any given stress intensity. This implies that R=0.7 represents a state of crack growth for a fully open crack, whereas crack closure may be responsible for relatively lower crack growth rates for R= -0.3 and 0.1. It may further be observed that FCGR at different stress ratios for 8 mm thick plates along TL and L+45 degrees orientation show similar trends(Fig.2b and Fig.2c) as observed along LT orientation(Fig.2a). In the case of 1.2 mm and 2.0 mm thick sheets, similar effects of stress ratio have been observed along all three orientations.

It may further be observed that the influence of stress ratio on fatigue crack propagation rate is appreciable at lower stress intensity ranges, while at higher ΔK, the effect is less pronounced. The reason for this may be ascribed to appearance of rough fracture surfaces at lower ΔK (Fig.5) and associated roughness induced crack closure.

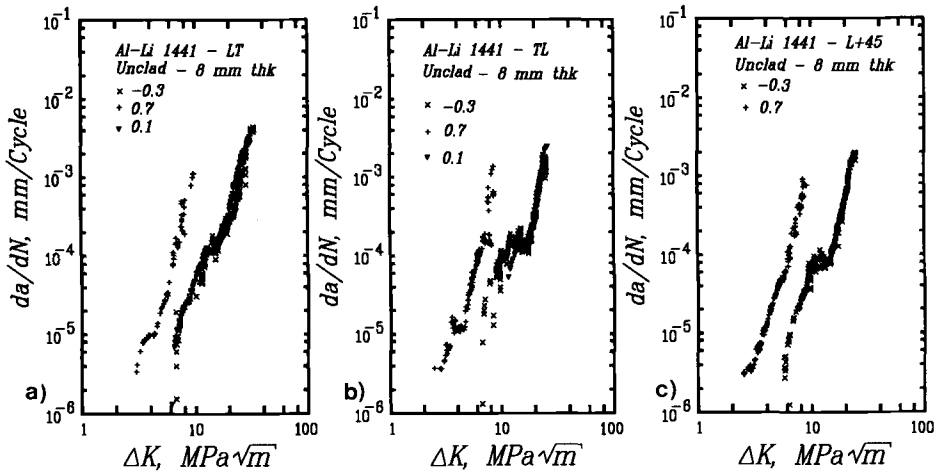


FIG. 2--Effect of stress ratio on fatigue crack growth rate - Al-Li alloy 1441 - 8 mm thick - a) LT orientation, b) TL orientation - c) L+45 orientation.

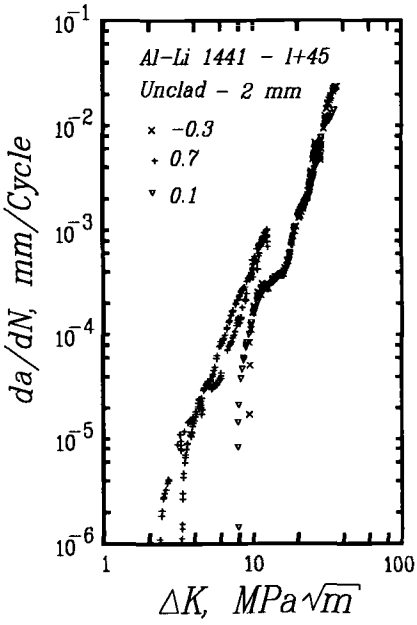


FIG. 3--Stress ratio effect on FCGR-1441 Al-Li alloy-2 mm thick-Unclad-L+45

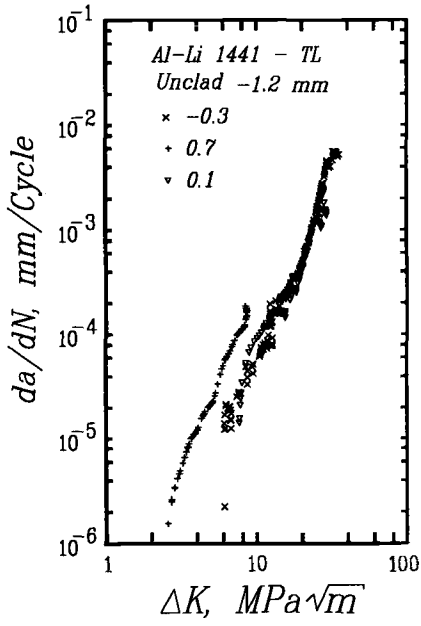


FIG.4--Stress ratio effect on FCGR-1441 Al-Li alloy-1.2 mm thick-Unclad-TL

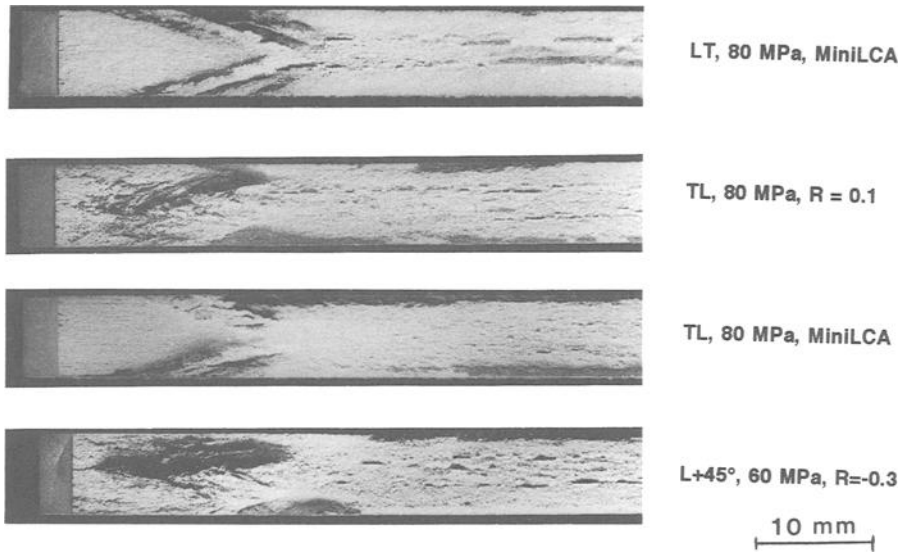


FIG.5--Optical micrograph of fracture surfaces-8 mm thick-SE(T) specimens.

To summarize, stress ratio effect is similar for all thicknesses and orientations considered. Fatigue crack growth rate curves for R=-0.3 and 0.1 are almost identical, but are distinctly different from those obtained at a stress ratio of 0.7.

Effect of Orientation

Figures 6a and 6b show the effect of orientation on fatigue crack growth rate under constant amplitude loading for 8 mm thick plate at stress ratios of -0.3 and 0.7 respectively. At R=-0.3, crack growth rates along all three orientations appear to be similar over the entire range. However, in the mid- stress intensity range, one can observe some scatter in the data for LT, TL and L+45 orientations with transverse direction(TL) growth rates indicating similarity in a mean trend between longitudinal(LT) and 45-degree plane-growth rates(Fig.6a). Observed jumps in the FCGR-curve for TL orientation may be ascribed to pronounced roughness in fracture surfaces (Fig.5). The crack growth behavior along all three orientations for R=0.7 is seen to be identical (Fig.6b), which implies that in the absence of closure of any kind, fatigue crack growth rate is free of orientation effects or anisotropy.

Figure 6c shows the effect of orientation under flight spectrum load for 8 mm thick plate material. From this figure it can be seen that the crack growth rate curves are almost similar for all three orientations considered. For 2.0 mm thick unclad sheet, rate of fatigue crack propagation along the three orientations for a stress ratio of 0.7 is shown in Fig.7 and it is seen that there is no discernible orientation effect. Figure 8 shows effects of orientation

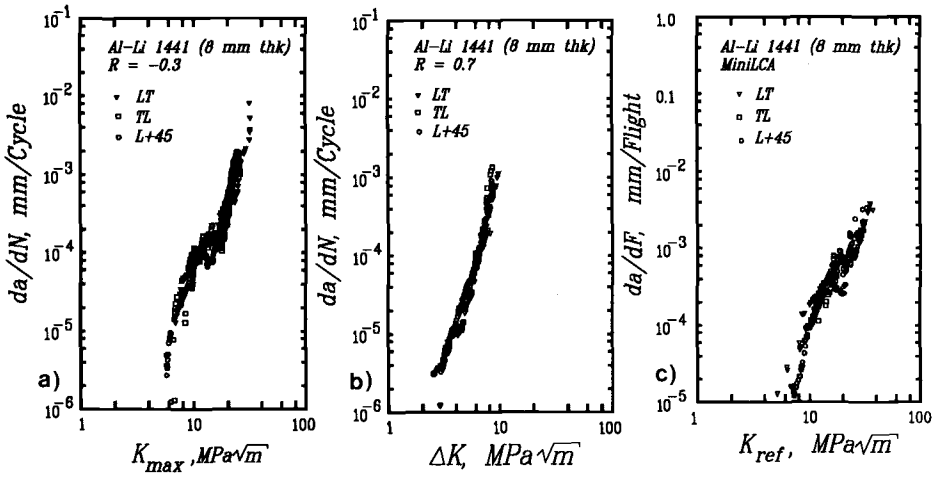


FIG. 6--Orientation effect-Al-Li alloy 1441- 8 mm thick - a) stress ratio: -0.3, b) stress ratio: 0.7, c) MiniLCA spectrum.

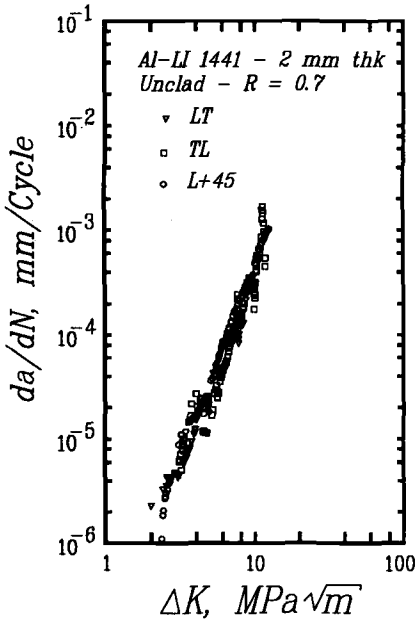


FIG.7--Orientation effect-2 mm thick - stress ratio: 0.7.

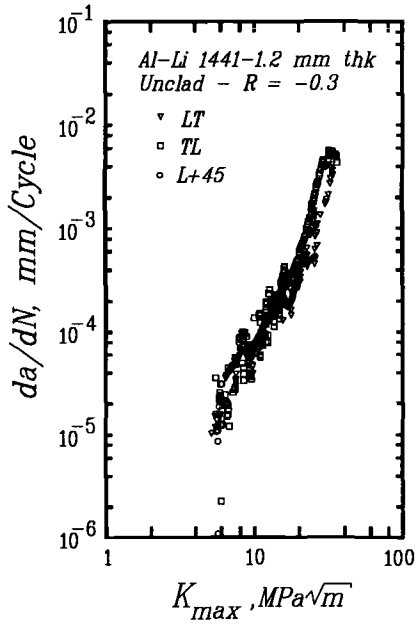


FIG. 8--Orientation effect-1.2 mm thick-stress ratio: -0.3.

on FCGR in an unclad sheet of 1.2 mm thickness for R=-0.3 and it is seen that crack growth rates are identical, thereby exhibiting no orientation effects. In contrast, fatigue crack growth behavior of most commercially available Al-Li alloys show appreciable orientation effects or anisotrophy [*15*].

In summary, absence of any pronounced orientation effects on the fatigue crack growth rate of alloy 1441 sheets of different thicknesses and under varied stress ratios, including flight spectrum loading, is unusual for an Al-Li alloy.

Effect of Thickness

Figure 9 presents the effect of specimen thickness on fatigue crack growth rate of alloy 1441. Crack growth rate curve for all three thicknesses is similar for specimens tested at R =-0.3 (Fig. 9a). This is in contrast to the general expectation of increasing crack growth rates for increasing thicknesses. The observed trend in 1441 alloy could be due to roughness induced closure which is significant in higher thicknesses. However, this trend was not observed for tests conducted at R=0.7 (Fig. 9b and 9c), where the fracture surfaces are smooth. Fatigue crack propagation curves under Mini-LCA flight load spectrum for 2.0 mm and 8.0 mm thick sheets suggest negligible influence of specimen thickness on crack propagation rates at low and high stress intensity ranges(Fig.9d).

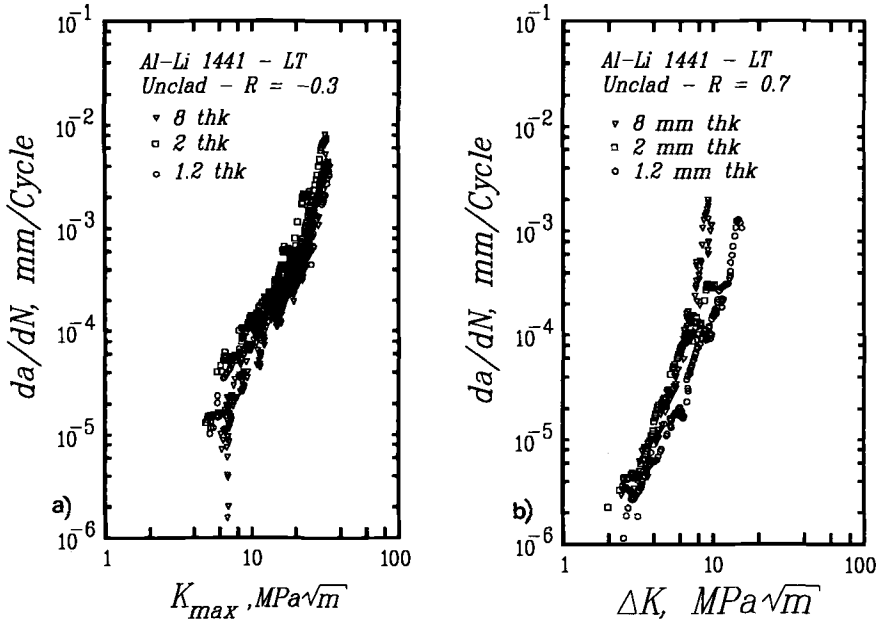


FIG. 9--Thickness effect-Al-Li alloy 1441-a) LT orientation, R = -0.3, b) LT orientation, R = 0.7.

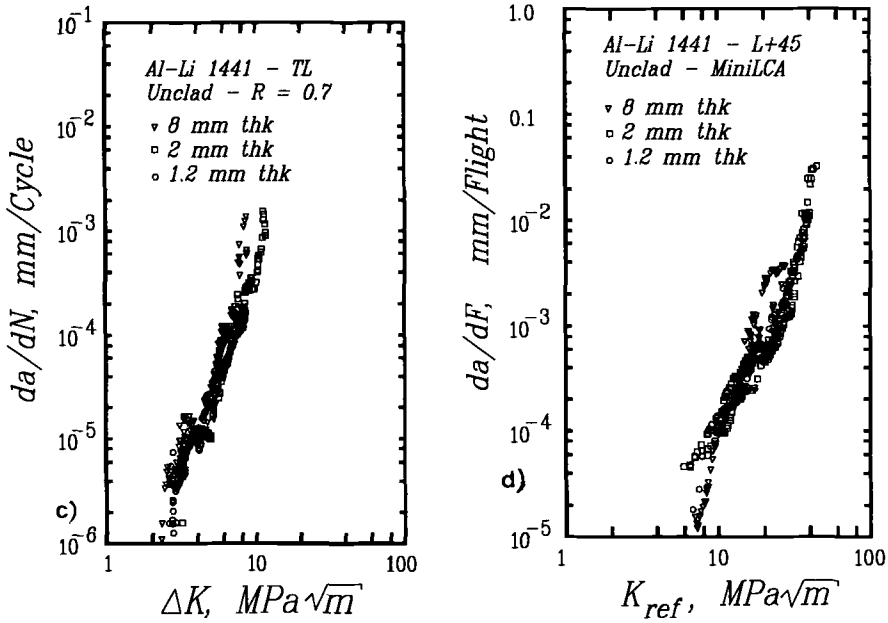


FIG. 9--Effect of thickness- Al-Li alloy 1441- c) TL orientation, R = 0.7, d) L+45 Orientation, MiniLCA Spectrum.

From the above observations, it may be concluded that specimen thickness, over the interval studied, does not significantly affect the fatigue crack propagation rates in this new alloy.

Effect of Cladding

Influence of cladding on fatigue crack growth rate of Al-Li alloy,1441 sheets of different thicknesses and orientations are shown in figure 10. It is observed that cladding does not materially affect the fatigue crack growth rates of 1.2 mm and 2.0 mm thickness sheets along LT, TL and L+45 degree orientations. However, in the case of 1.2 mm thick sheets, unclad material showed a slightly lower crack growth rate at higher stress intensity ranges for all stress ratios considered(Fig.10c and Fig.10d).

In summary, cladding does not significantly affect the fatigue crack growth rate in Al-Li alloy, 1441.

Comparison of FCGR of Al-Li alloy- 1441 with Al-Cu alloy-BS:L73

Fatigue crack growth rate data of Al-Li alloy 1441 and Al-Cu alloy BS:L73 (2014-T4 equivalent) were compared for assessing the possibility of replacing L73 with 1441 in fighter aircraft structures. Crack growth rate tests were conducted on L73 sheets of 2 mm and 3 mm thickness in lab air conditions, under constant amplitude and MiniLCA spectrum loading. Figure 11a presents the crack growth rate comparison between 1441 and BS:L73

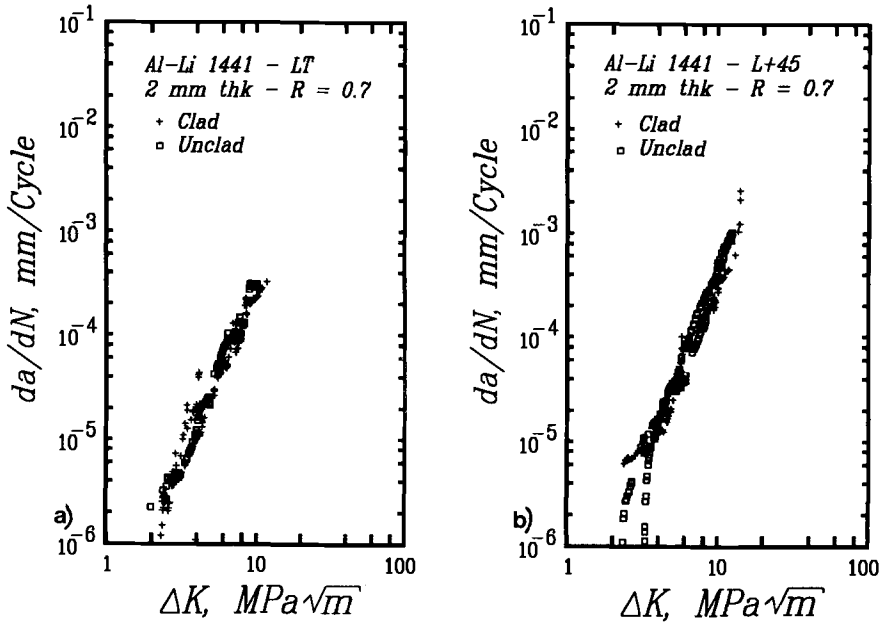


FIG. 10--Effect of cladding on FCGR - Al-Li alloy 1441 - a) 2 mm thickness, LT orientation, R = 0.7, b) 2 mm thickness, L+45 orientation, R = 0.7.

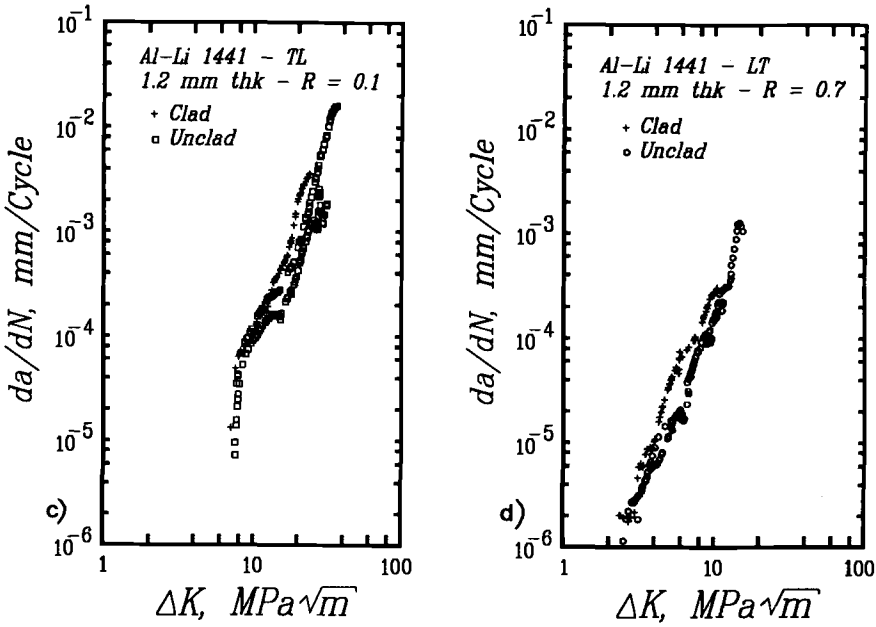


FIG. 10--Effect of cladding on FCGR - Al-Li alloy 1441 - c) 1.2 mm thick, TL orientation, R = 0.1, d) 1.2 mm thick, LT orientation, R = 0.7.

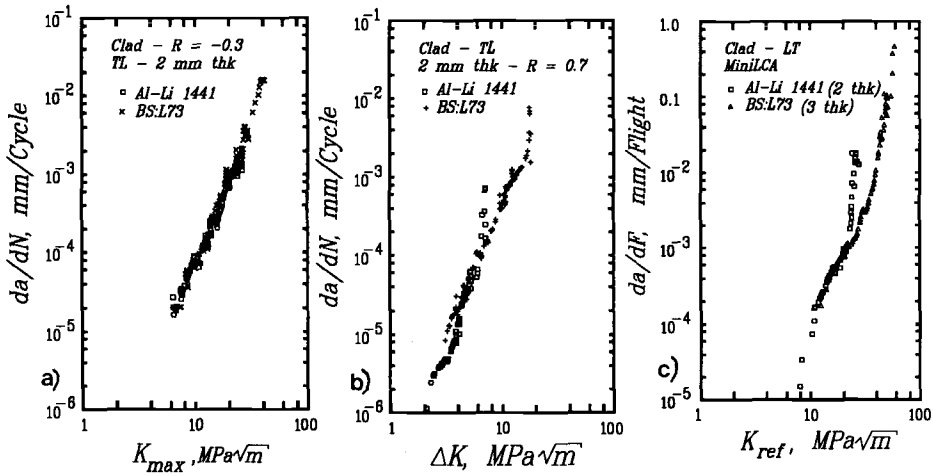


FIG. 11--Comparison of FCGR of Al-Li 1441 with that of BS:L73 - a) R = -0.3, b) R = 0.7, c) MiniLCAspectrum.

evaluated in the TL orientation at a stress ratio of -0.3. It may be observed that both the materials offer almost identical resistance to crack growth over the entire stress intensity range. However, at a stress ratio of 0.7 (Fig.11b), it can be seen that 1441 exhibits a slower crack growth rate as compared to BS:L73, in the intermediate region. It may be mentioned here that based on a comparative fatigue crack growth studies of Al-Li sheet alloys, Wanhill et al.[*1,6,15*] have observed that under constant amplitude loading, alloy 8090-T81 was superior to 2091-T8X and 2024-T3 in overall fatigue crack growth performance. From the present test results, it can be said that Al-Li alloy 1441-T11 exhibits good fatigue crack growth resistance under constant amplitude loading as compared to many other Al-Li and Al-alloys.

Figure 11c compares crack growth rates of 1441 and L73 along LT orientation under MiniLCA aircraft spectrum loading. It is observed that fatigue crack growth rate, expressed as mm/flight is almost identical in the lower stress intensity range, but at higher stress intensity range, BS:L73 offers better resistance to crack growth than Al-Li alloy 1441. This is due to the higher K_c value for BS:L73, as opposed to 1441. Also, MiniLCA load spectrum employed here had large number of high-amplitude loading cycles. The trend in fatigue crack growth may have been different, had we considered a transport aircraft loading spectrum like TWIST, where majority of loading cycles are of smaller magnitude. Incidentally, evaluating the fatigue behavior of Al-Li alloy 1441 under transport aircraft spectrum loading was beyond the scope of this study. However, work is in progress to assess the material behavior in the presence of hot/corrosive environments and also to improve the fracture toughness of this alloy.

CONCLUSIONS

Based on this experimental study pertaining to static and fatigue crack propagation property evaluation of Al-Li alloy- 1441, it may be said that this alloy possesses many desirable features like lower density, high strength, negligible anisotropy and good fatigue crack growth resistance to qualify as a damage-tolerant material. The study indicates insignificant influence of specimen thickness and cladding on the fatigue crack growth properties of this material. These promising features make this new Al-Li alloy-1441 a candidate material for airframe applications in future. However, more work is needed to improve the fracture toughness property of this alloy by suitable alloy/heat-treatment modifications. Also, it is necessary to evaluate the short crack growth behavior and its long crack growth behavior under other spetra, before any firm conclusion can be made as to whether this alloy can replace the conventional aluminium alloys in damage-tolerant aerospace structures.

Acknowledgment

This work was funded by the Aeronautical Development Agency. The authors acknowledge the helpful discussions with Dr. R. Sunder. Mr. M.J. Williams, Mr. Selvamani Babu and Technicians of Comat System Solutions assisted during experimentation.

References

[1] Wanhill, R. J. H.,"Fatigue Crack Growth in Damage Tolerant Al-Li Sheet Alloys", NLR TP 90107U, NLR, The Netherlands, 1990

[2] Gregson, P. J. and Flower, H. M.,"Microstructural Control of Toughness in Aluminium-Lithium Alloys, Acta Metallurgica, Vol. 33, 1985, pp. 527-537

[3] Miller, W. S., White, J. and Lloyd, D. J.,"The Metallurgy of Al-Li Based Alloys", Aluminum Alloys- Their Physical and Mechanical Properties", Vol.III, Eds. E.A.Starke,Jr and T.H.Sanders,Jr., EMAS Publications, 1986, pp.1799-1836

[4] Harris, S. J., Noble, B. and Dodd, A.,"The Effect of Texture on the Tensile and Fatigue Properties of 8090 Plate Alloys", Proceedings of the Fifth International Aluminum-Lithium Conference, Williamsburg, Virginia, Eds. T.H. Sanders,Jr. and E. A. Starke, Jr., 1989, pp.1061-1074

[5] Nicholas, D. J. and Martin, J. W.,"Microstructural Effects on Small Crack Growth in Aluminum-Lithium Alloys", Proceedings of the Fifth International Aluminum-Lithium Conference, Williamsburg, Virginia, Eds. T.H.Sanders, Jr. and E.A.Starke,Jr., 1989, pp.1003-1012

[6] Wanhill, R. J. H., Schra, L. and Hart, W. G. J. 't," Fracture and Fatigue Evaluation of Damage Tolerant Al-Li Alloys for Aerospace Applications", NLR TP 90132 U, NLR, The Netherlands, 1990.

[7] Sunder, R. and Venkatesh, C. S.,"Dedicated Microprocessor Based Controller for Fatigue Testing", Applications of Automation Technology to Fatigue and Fracture Testing, ASTM STP 1092, A.A. Braun, N.E. Ashbaugh and F.M. Smith, Eds., American Society for Testing and Materials, Philadelphia, 1990, pp. 68-82

[8] Sunder, R.,"Automated Fatigue and Fracture Laboratory with Multiple Load Frames and Single Host Computer System", Applications of Automation Technology to Fatigue and Fracture Testing, ASTM STP 1092, A.A. Braun, N.E. Ashbaugh and F.M. Smith, Eds., American Society for Testing and Materials, Philadelphia, 1990, pp. 232-249

[9] Sunder, R.,"Contribution of Individual Load Cycles to Crack Growth under Aircraft Spectrum Loading",in Advances in Fatigue Lifetime Predictive Techniques, ASTM STP 1122, Eds: M.R. Mitchell and R.W. Landgraf, ASTM, Pa, 1992, pp. 176-190.

[10] Blankenship, Jr., C.P., Roven, H.J., and Starke, Jr., E.A., " The Fracture and Fatigue behavior of Al-Li-X Alloys", FATIGUE 90, Vol II, Eds: H. Kitagawa and T. Tanaka, MCEP, Birmingham, 1990, pp 937-955.

[11] Henkener, J.A., Scheumann, T.D., and Grandt, Jr. A.F., " Fatigue Crack Growth Behavior of a Peak AgedAl-2.6 Li- 0.09 Zr Alloy", FATIGUE 90, Vol II, Eds: H. Kitagawa and T. Tanaka, MCEP, Birmingham, 1990, pp. 957-962.

[12] Stanzl-Tschegg, S. E., Konig, J. and Tschegg, E. K.,"Near Threshold Fatigue Crack Growth of Al-Li Alloys", FATIGUE 93, Vol. I, Eds: J. P. Bailon and J. I. Dickson, EMAS, U.K., 1993, pp. 519-524

[13] Venkateswara Rao, K. T., Bucci, R. J. and Ritchie, R. O.,"On the Micromechanisms of Fatigue Crack Propagation in Aluminum-Lithium Alloys: Sheet vs. Plate Material", FATIGUE 90, Vol. II, Eds: H. Kitagawa and T. Tanaka, MCEP, Birmingham, 1990, pp. 963-970.

[14] Peel, C.J., Evans, B., and Mc Darmaid, D., " Current Status of UK Light Weight Lithium-Containing Aluminium Alloys, Proc. of the 3rd Int. Conference on Al-Li Alloys, Eds: C. Becker, P.J. Gregson, S.J. Harris, and C.J. Peel, Inst. of Metals, London, 1986, pp. 26-36.

[15] Wanhill, R. J. H., 't Hart, W. G. J. and Schra, L.,"Flight Simulation and Constant Amplitude Fatigue Crack Growth in Aluminium-Lithium Sheet and Plate", NLR TP 91104 U, NLR, The Netherlands, 1991

David C. Maxwell[1] and Theodore Nicholas[2]

FATIGUE CRACK GROWTH BEHAVIOR OF TI-1100 AT ELEVATED TEMPERATURE

REFERENCE: Maxwell, D. C. and Nicholas, T., **"Fatigue Crack Growth Behavior of Ti-1100 at Elevated Temperature,"** Fracture Mechanics: 26th Volume, ASTM STP 1256, Walter G. Reuter, John H. Underwood, and James C. Newman, Jr., Eds., American Society for Testing and Materials, Philadelphia, 1995.

ABSTRACT: Effects of temperature, frequency, and cycles with superimposed hold times are evaluated in Ti-1100 in order to study the complex creep-fatigue-environment interactions in this material. Crack growth rate tests conducted at a cyclic loading frequency of 1.0 Hz show that raising the temperature from 593 to 650°C has only a slightly detrimental effect on crack growth rate, although these temperatures produce growth rates significantly higher than at room temperature. From constant ΔK tests, the effects of temperature at constant frequency show a minimum crack growth rate at 250°C. From the minimum crack growth rate at 250°C, the crack growth rate increases linearly with temperature. Increases in frequency at constant temperatures of 593 and 650°C produce a continuous decrease in growth rate in going from 0.001 to 1.0 Hz, although the behavior is primarily cycle dependent in this region. Tests at 1.0 Hz with superimposed hold times from 1 to 1000 s are used to evaluate creep-fatigue-environment interactions. Hold times at maximum load are found to initially decrease and then increase the cyclic crack growth rate with increasing duration. This is attributed to crack-tip blunting during short hold times and environmental degradation at long hold times. Hold times at minimum load show no change in growth rates, indicating that there is no net environmental degradation to the bulk material beyond that experienced during the baseline 1 Hz cycling.

KEYWORDS: frequency, temperature, hold times, crack growth rate, ΔK, environment, Titanium, threshold

[1]Materials Test Specialist, University of Dayton Research Institute, Dayton, OH 45469-0128.
[2]Senior Scientist, Air Force Wright Laboratory, Materials Directorate, Wright-Patterson AFB, OH 45433-7817 USA.

Copyright © 1995 by ASTM International www.astm.org

INTRODUCTION

Advanced aerospace applications demand high strength, lightweight, damage-tolerant materials which are capable of surviving in high temperature environments. In an attempt to reduce weight, high temperature titanium and titanium aluminide intermetallics have been evaluated as possible candidates for such applications. Titanium alloys show great potential as replacements for conventional nickel-base superalloys, provided they possess adequate high temperature crack growth damage tolerance as well as room temperature ductility and fracture toughness. Preliminary results on a new, high-temperature titanium alloy, Ti-1100 [1,2], have demonstrated promising crack growth rate characteristics [2,3,4], although the mechanisms governing the behavior appear to be attributed to a complex combination of fatigue, environmental effects, time-dependent creep/stress relaxation, and crack closure [3,5].

Ti-1100 is a β-processed near α titanium alloy developed to operate up to a maximum temperature of 593°C (1100°F). The crack growth behavior of this alloy has been evaluated at room temperature in the near threshold regime [5] as well as at elevated temperatures as a function of frequency [3,4]. To assess the temperature limits of this material, a recent study has found that raising the temperature from 593 to 649°C has little or no influence on the fatigue crack growth rates at a frequency of 100 Hz [3], while an earlier study conducted at 10 Hz also found no significant change in growth rate with the same temperature increase[6]. In parallel investigations, crack closure due to oxide induced asperities, crack tip blunting due to long hold times at maximum load, and environmental degradation due to decrease in frequency have all been shown to influence crack growth behavior at 593°C [4,5]. This study is undertaken to further expand the range of conditions under which the crack growth behavior of Ti-1100 is studied by evaluating the effects of frequency, temperature and creep-fatigue interactions of Ti-1100 at temperatures up to 650°C.

Frequency, temperature, and wave shape are known to have an influence on crack growth rate behavior in nickel-base superalloys, and systematic studies of these effects have led to an understanding of the governing mechanisms in Alloy 718, for example [7]. In applying the same thought processes to high temperature titanium alloys such as Ti-1100, the systematic variations with variables observed in Alloy 718 are not as pronounced, and sometimes different. For example, a systematic increase in growth rate with decrease in frequency is observed in Alloy 718 until the behavior is purely time dependent. At high frequencies, the behavior is purely cycle dependent meaning that growth rate is independent of frequency. Contrast this behavior with what is observed in Ti-1100 where at high frequencies, up to 200 Hz, the growth rate decreases with increase in frequency but never becomes purely cycle dependent [3]. On the other hand, as the frequency decreases below about 1 Hz at 593°C, the growth rate becomes almost constant, implying cycle dependent behavior at low frequency [3,4]. Further, 10 and 30 s hold times superimposed on 1 Hz cycling at either maximum or minimum load have very little effect on growth rate in Ti-1100 at 593°C [3], whereas

similar loading produces substantial changes in growth rate in Alloy 718 [7]. However, addition of a 300 s hold time on 0.05 Hz cycling produces an increase in growth rate in Ti-1100 at 593°C [8]. These apparently confusing if not conflicting results are attributed to a complex combination of mechanisms and factors which include fatigue, environmental degradation (oxidation), creep or relaxation phenomena, crack closure due to asperities, and microstructural instabilities [8].

EXPERIMENTAL

The material used in this study is a beta processed near alpha titanium alloy, Ti-1100, developed by TIMET, Henderson, NV, to provide optimum creep, fatigue, and stability performance up to a maximum temperature of 593°C (1100°F) [1,2]. The nominal composition of this alloy is Ti-6Al-2.8Sn-0.4Mo-0.45Si-0.070$_2$-<0.03Fe. The material was processed from billets which were hot rolled above the beta transus to obtain 12 mm plates which were then aged for 8 hours at 593°C. The resulting microstructure, shown in Fig. 1, consists of a Widmanstätten structure with aligned colonies of α-platelets showing no preferred orientation.

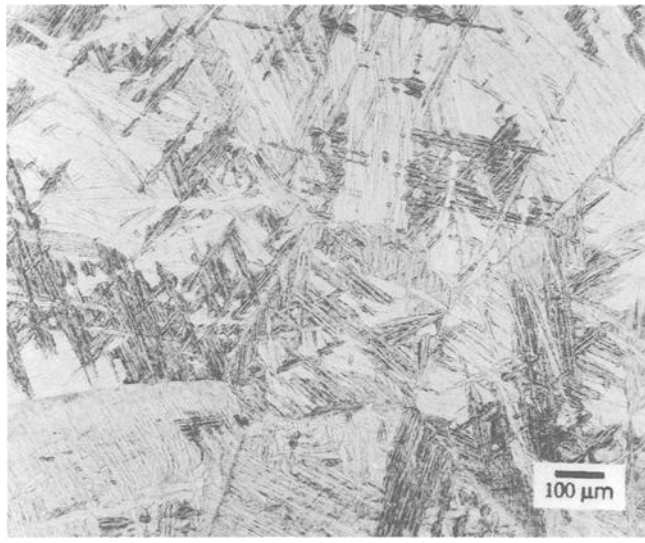


FIG. 1---*Microstructure of Ti-1100*

The prior β-grain size was approximately 500-600 µm. In this study, mini compact tension specimens (B = 5 mm, W = 20 mm) were used for all fatigue crack growth tests. Specimens were electro-discharge machined (EDM) from the plate with the crack growth direction perpendicular to the rolling direction.

Fatigue crack growth tests were conducted under either ΔK-decreasing, constant-load amplitude or constant stress intensity range (ΔK) conditions using a closed-loop computer controlled servohydraulic test machine. All tests were conducted in accordance with ASTM Standard Test Method for Measurement of Fatigue Crack Growth Rates (E 647 88a) [9]. For the constant ΔK tests, the fatigue crack growth rates reported in this paper were determined by fitting a linear equation to the a-versus-N (crack length versus number of cycles) data after steady state growth was established at each experimental test condition. Crack lengths were computed using the front face compliance measurements from an extensometer. This calculated compliance crack length was periodically verified by optical measurements using a traveling microscope. All specimens were precracked under identical conditions, and the final ΔK from precracking was always lower than the initial ΔK for subsequent testing. All tests were conducted in laboratory air and the elevated temperature tests were heated with a clamshell wire-wound resistance furnace.

One set of tests was conducted to establish complete da/dN-ΔK crack growth curves under several different conditions. In these tests, fatigue crack growth rates starting from the near threshold region (less than 10^{-9} m/cycle) to rates greater than approximately 10^{-6} m/cycle were determined at room temperature, 593, and 650°C at a cyclic loading frequency of 1.0 Hz. All tests in this study were conducted at a stress ratio (R) of 0.1. To obtain the complete da/dN-ΔK curve, tests were initiated after precracking under a ΔK-decreasing condition at a load shedding rate of $C = -0.0787$ mm^{-1} until a fatigue crack growth threshold (the asymptotic value of ΔK at which da/dN approaches zero) was established. The cracks were then grown under constant load amplitude until specimen failure occurred.

A second set of tests was conducted in order to obtain discrete values of crack growth rate over a broad range of test conditions at a single value of ΔK. To accomplish this, constant ΔK fatigue crack growth rate tests were conducted at a $\Delta K = 15$ MPa$\sqrt{m}$. The effects of temperature at constant frequency and effects of frequency at constant temperature were investigated in this manner. Fatigue crack growth rate tests were conducted at room temperature and every 100°C from 150 to 650°C and every 50°C from 650 to 800°C at a cyclic loading frequency of 1.0 Hz to determine the effects of temperature. Constant ΔK fatigue crack growth rate tests were conducted at frequencies from 0.001 to 1.0 Hz to investigate the effects of frequency over a range expected to encompass mainly time-dependent as well as mainly cycle-dependent regions of crack growth. These tests were conducted at 593 and 650°C.

Finally, effects of superimposed hold times on fatigue cycling were determined. A baseline fatigue cycle of 1.0 Hz was used. Constant ΔK fatigue crack growth rate tests with superimposed hold times at maximum load ranging from 1 to 1000 seconds were conducted at 593 and 650°C to investigate the combined effects of fatigue, creep, and environmentally assisted crack growth to the overall fatigue crack growth rate.

Additional tests with superimposed hold times at minimum load were conducted to evaluate environment interactions in the absence of creep.

RESULTS AND DISCUSSION

da/dN versus ΔK Behavior

Figure 2 shows the fatigue crack growth rate (FCGR) of Ti-1100 at room temperature, 593, and 650°C at a frequency of 1 Hz.

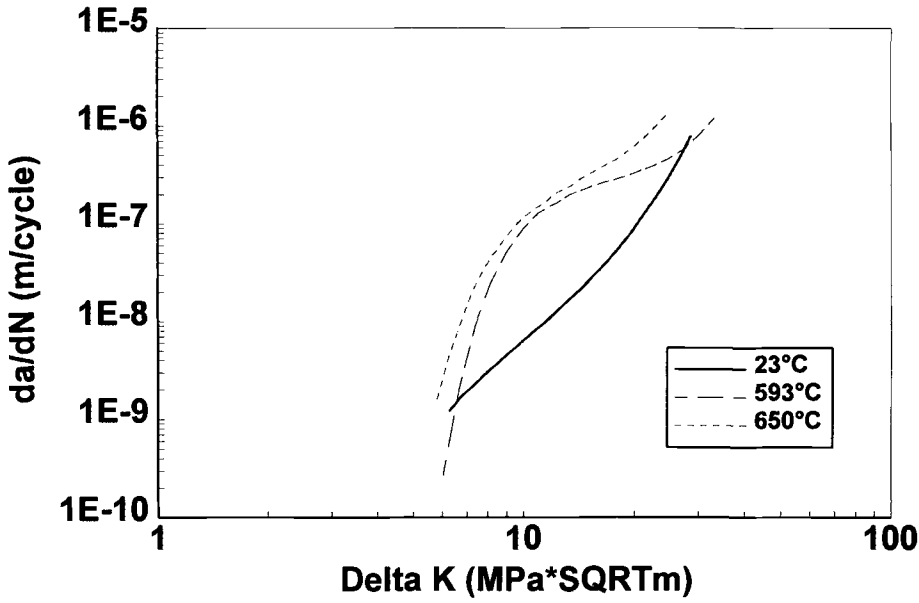


FIG. 2---*Fatigue crack growth behavior of Ti-1100*

The FCGR data are fit with a hyperbolic sine function (sinh). While individual data points are not shown, the sinh fit provides a very good representation of the data points and is used for presentation clarity. The da/dN-ΔK crack growth rate curve at room temperature does not exhibit an apparent ΔK_{th} at the lowest growth rates obtained, about 10^{-9} m/ cycle in the near threshold regime. The threshold ΔK is somewhat below approximately 6 Mpa$\sqrt{m}$, the lowest ΔK reached in the threshold test over a reasonable period of time. Down to this level, any inflection point in the da/dN-ΔK curve is not apparent. No attempt was made to continue the test down to lower growth rates because of the testing time required. On the other hand, the crack growth rate curves at 593 and 650°C are much steeper in the near threshold region and exhibit better defined

inflections in the curve from the threshold region to steady state crack growth. The da/dN-ΔK crack growth rate curves at 593 and 650°C produce a value of ΔK_{th} of approximately 6 MPa$\sqrt{m}$. The ΔK at failure is approximately 30 MPa$\sqrt{m}$ at 593°C, whereas at 650°C it is approximately 25 MPa$\sqrt{m}$. In the steady state growth region, the elevated temperature tests exhibit a growth rate approximately an order of magnitude faster than at room temperature, but the increase from 593 to 650°C shows only a marginal increase in growth rate. While the maximum use temperature of this material is projected to be 593°C (1100°F), the crack growth rates at 650°C under 1 Hz cycling do not seem to be significantly faster and indicate that the use temperature for fatigue may be higher than anticipated. This observation is consistent with the findings of Parida and Nicholas [3] who found no significant difference in growth rates between 593 and 650°C under 100 Hz high frequency cycling and Foerch et al. [6] who also saw no difference at 10 Hz.

Effect of Temperature

Figure 3 shows the FCGR of Ti-1100 as a function of temperature from room temperature to 800°C in laboratory air at a constant ΔK = 15 Mpa$\sqrt{m}$.

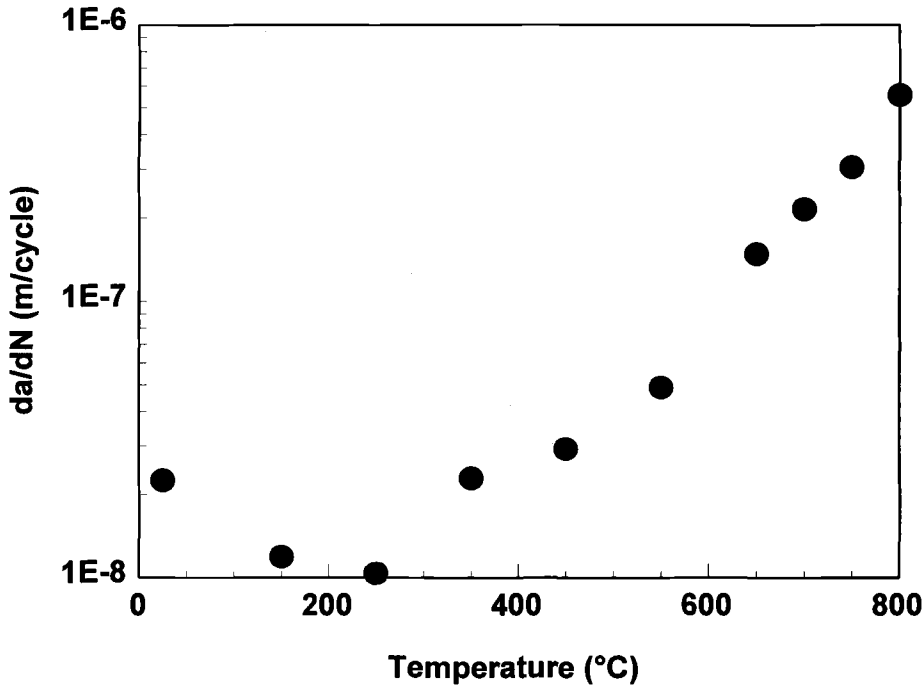


FIG. 3---*Effect of temperature on the fatigue crack growth rate of Ti-1100*

From these results of constant ΔK testing, the growth rate is found to be slightly in excess of $2x10^{-8}$ m/cycle at room temperature and then decreasing to a minimum of $1x10^{-8}$ m/cycle at a temperature of 250°C as temperature is increased. From this minimum, the (log) growth rate increases in an almost linear manner with further increase in temperature up to 800°C. The initial decrease in growth rate with temperature to a minimum, and the subsequent increase with further increase in temperature, is attributed to two competing mechanisms. The decrease in growth rate at low temperatures up to 250°C is attributed to a gradual increase in the ductility of Ti-1100 with increase in temperature [10]. At high temperatures, up to 800°C, environmental effects, in the form of oxidation in the vicinity of the crack tip, are considered to play a dominant role in the crack growth rate behavior. As temperature increases, the rate of environmental degradation is expected to increase resulting in a higher crack growth rate. Similar trends in increase in FCGR rate as a function of temperature have been observed for two titanium aluminides, Ti-24Al-11Nb [11] and Ti-25Al-25Nb [12]. For Ti-1100, comparisons of crack growth rate data in air and vacuum at similar values of ΔK used in this investigation have shown that environmental effects have an important influence on growth rates at temperature in the range from 593 to 650°C [4,6]. Conversely, crack tip oxidation effects are not significant at room temperature. As an example, crack growth rates at 593°C in vacuum are approximately the same as those at room temperature in air in Ti-1100 at a frequency of 10 Hz. For the same test in air at 593°C, the growth rate is higher [6]. The net result of the decrease in growth rate due to ductility increase at low temperatures and the increase in growth rate due to environmental effects at higher temperatures is a minimum in growth rate at an intermediate temperature as shown in Fig. 3.

The results obtained here are in conflict with the concept suggested by Foerch et al. [6] who demonstrate that the parameter $\Delta K^2/\sigma yE$, which is proportional to the CTOD, may be used as the governing parameter for consolidating data at different temperatures. In their case, they were more or less able to consolidate data at 10 Hz at three temperatures, 23, 593, and 650°C. Data for modulus and yield strength as a function of temperature [2,6] show that both quantities decrease in a continuous and smooth manner with increase in temperature over the entire temperature range covered in this investigation. Such a smooth variation in these quantities would preclude the use of CTOD as a correlating parameter if the minimum in growth rate at an intermediate temperature is to be reproduced.

Effect of Frequency

Figure 4 shows FCGR as a function of frequency at 593 and 650°C. The data show that the crack growth rate per cycle decreases as the frequency increases in the range from 0.001 to 1.0 Hz. The data are obtained at ΔK=15 MPa$\sqrt{m}$. Three regions of fatigue crack growth have been defined in nickel-base superalloys, that is, (a) at low frequencies, fully time-dependent crack growth; (b) at high frequencies, fully cycle dependent crack growth; and (c) a region of intermediate frequency exhibiting a mix of

both time- and cycle-dependent behavior [7]. On a log-log plot, the slope of fully time-dependent behavior would be -1 while the slope of fully cycle-dependent behavior would be zero. When the data for Ti-1100 are approximated by a straight line, the slopes of the linear regression are -0.14 and -0.19 for the 593 and 650°C data, respectively, indicating that the fatigue crack growth is in the region of mixed time- and cycle-dependent behavior at both temperatures. This behavior is closer to cycle dependent (slope = 0) than time dependent (slope = -1) although at both temperatures the behavior seems to trend towards more time dependent at the lowest frequency of 0.001 Hz. Both sets of data indicate that Ti-1100 has still not achieved fully cycle-dependent behavior at a frequency as high as 1 Hz.

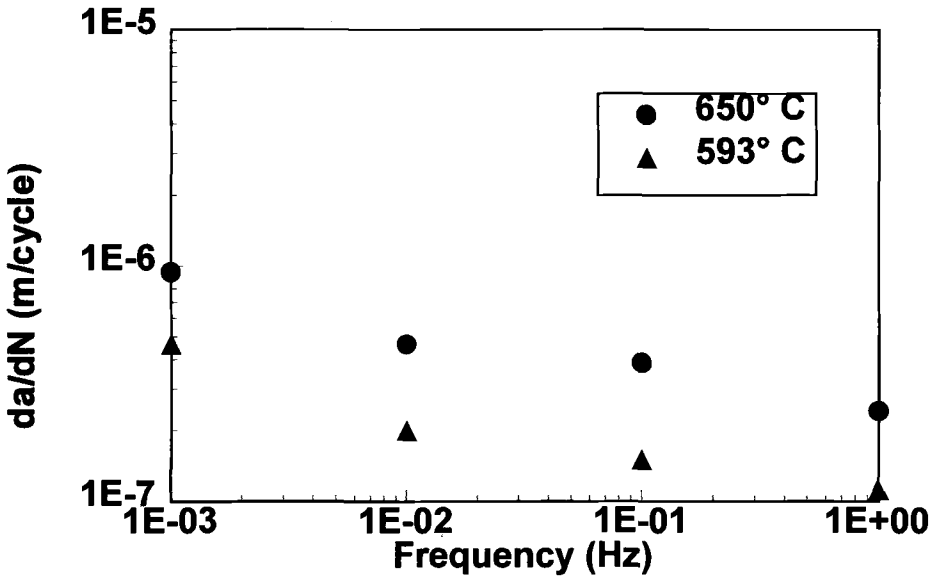


FIG. 4---*Effect of cyclic frequency on the fatigue crack growth rate of Ti-1100*

By comparison with the results obtained here, Parida and Nicholas [3] found that at 593°C the growth rate in this material increases with decrease in frequency from 200 to 1 Hz, but that further decrease in frequency did not alter the growth rate significantly. Their experiments were performed under constant load amplitude cycling and the data are reported for a value of ΔK=20 MPa$\sqrt{m}$ which is somewhat higher than the value of 15 MPa$\sqrt{m}$ used here. The low slope of the fit to the data in Fig. 4 could be interpreted as an insignificant change in growth rate at these frequencies. By contrast, Ghonem and Foerch [4] report that, at the same temperature, growth rates increase with decrease in frequency from 10 to 0.05 Hz at low ΔK, but provide essentially the same rate at values of ΔK in excess of 30 MPa$\sqrt{m}$. Discounting the high frequency data, the original data of Parida and Nicholas [3] could be interpreted as having these same general trends.

Thus, both frequency range and ΔK are important parameters in discussing trends in data with change in frequency.

In the work of Ghonem and Foerch [4], decreasing the frequency at low ΔK from 10 Hz resulted in an increase in the growth rate in air at 593°C. The damaging effect of lower frequencies was attributed less to overall exposure time and more to the duration of the loading part of the cycle. The use of asymmetric wave forms with extended loading times as well as waveforms with hold times at maximum load were considered to cause more extensive creep damage. From the results presented here, the small effect of frequency on growth rate in air appears to be less of an effect of environment and more of one due to creep damage at the crack tip. For environment to play a major role, the growth rate would tend to double when frequency is halved. Clearly this is not the case. Further, it has been observed that oxidation takes place rapidly, effecting even high frequency fatigue up to 30 Hz at these temperatures, whereas creep takes longer and is dominant at low frequencies [6]. At the very lowest frequencies in our tests, however, the creep damage may start to saturate and the environmental effect becomes more important as evidenced by the increase in (negative) slope in Fig. 4 at 0.001 Hz.

Effect of Hold Time

Hold times at maximum load are used to evaluate the creep-fatigue interactions as well as the environmental effect of elevated temperatures at the crack tip. In this type of test, creep effects are maximized since the hold is at maximum load for sustained periods. Additionally, at maximum load the crack is completely open and the crack tip is exposed to the environment during the hold times. Figure 5 shows the influence of superimposed hold times at maximum load on the cyclic crack growth rate (1 Hz) at 593 and 650°C. Crack growth rates are plotted against total cycle time which is the 1 Hz cycle plus the hold time. The data point at 1 s, therefore, represents the 1 Hz cyclic behavior without hold time. At 593 and 650°C, hold times ranging from 1 to 1000 s are shown to first decrease and then increase the crack growth rate per cycle with increasing hold times. Since the only change from one hold time to another is the duration of the cycle, the initial decrease in growth rate with increase in hold time is speculated to be due to additional creep at the crack tip which may result in crack tip blunting or crack branching, although no direct observations of blunting or branching were made in this study. Any environmentally induced effect would result in higher crack growth rates due to increase in cycle time. At longer hold times, it is hypothesized that the crack tip remains blunted and open, and the additional exposure time to the environment results in degradation of the material in the vicinity of the crack tip. This causes an increase in crack growth rate per cycle with increasing hold time. A 100 s hold time produces the lowest growth rate at 593°C while a 10 s hold produces the minimum at 650°C. The higher rate of environmental degradation at 650°C accounts for this difference. It should be noted that no sustained-load creep crack growth during the hold times was observed.

Rosenberger and Ghonem [8] observed no significant creep crack growth for Ti-1100 at 593°C within practical time periods at K levels within the range used here.

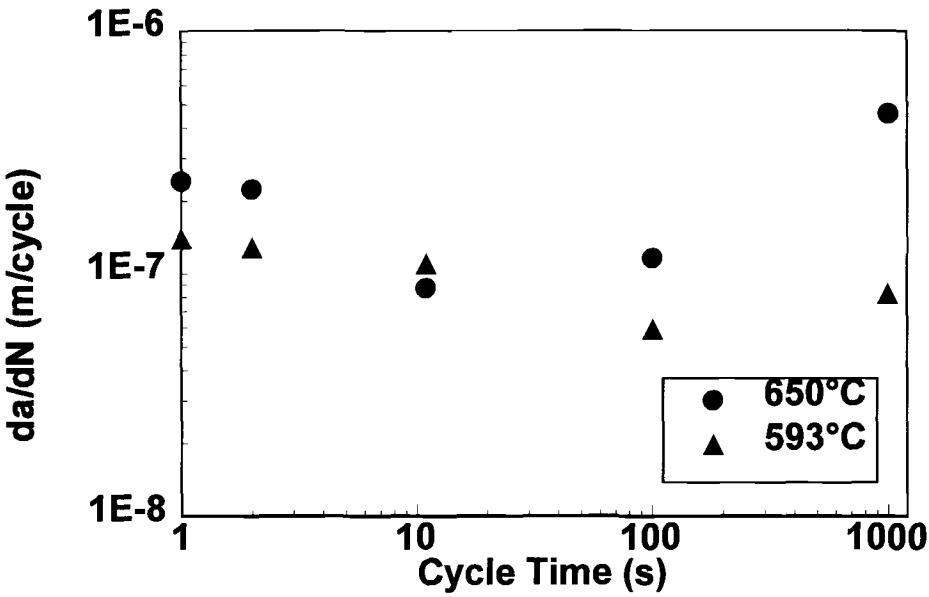


FIG. 5---*Effect of hold times at maximum load on the fatigue crack growth rate of Ti-1100*

Further, Ashbaugh et al. [13] failed to observe creep crack growth in this material at temperatures 590, 650 and 700°C. This implies that the growth rate at long hold times is not due to a summation of creep and fatigue crack growths, but rather that environmental effects degrade the material and make it more susceptible to crack extension with increase in exposure time. Therefore, a prediction of the FCGR under fatigue cycles with superimposed hold times resulting from a linear summation model (based on cyclic- and sustained-load data) cannot be made at this time. Similar results have been observed in Ti-24Al-11Nb and Ti-25Al-25Nb alloys [11,12].

The mechanisms of creep-fatigue interactions in Ti-1100 are discussed in detail by Rosenberger and Ghonem [8]. In their work, hold times were superimposed on a baseline fatigue cycle of 0.05 Hz, whereas a frequency of 1.0 Hz was used in the present work. The nature of creep-fatigue interactions has been observed to be influenced by the frequency of the baseline fatigue cycle in Inconel 718 [7] because the mode of fracture due to the cycle may be different that the mode due to sustained load. In the work of Rosenberger and Ghonem, low frequency cycling or dwell times were characterized by grain boundary cracking producing an intergranular fracture mode. The interaction between creep and fatigue was attributed to the ability of creep to modify the localized deformation at the crack tip, and the addition of hold time increased the growth rate per cycle. In the present case, the fatigue portion of the cycle (1 Hz) produces a quasi-cleavage fracture mode [4]. The change in mode due to hold

times may result in a temporary retardation of growth rate for short hold times as has been observed to happen in Inconel 718 [7].

Figure 6 shows the influence of superimposed hold times at minimum load on the cyclic crack growth rate (1.0 Hz) at 593 and 650°C. Hold times at minimum load are used to show the environmental effect of elevated temperature on the bulk properties of the material. At minimum load the crack may be completely closed so that the crack tip is not exposed to the environment as much as during the hold times at maximum load. Further, creep effects are not expected to be present. The growth rate, plotted as a function of total cycle time, shows that at 593 and 650°C the hold time at minimum load has no effect on the crack growth rate of Ti-1100. At temperatures up to 650°C, there appears to be no net environmental effect on the bulk properties of Ti-1100 over that which occurs during the baseline 1 Hz cycling. Foerch, et al. [6] noted that the effect of oxidation on crack growth occurs very rapidly and, thus, the environmental degradation

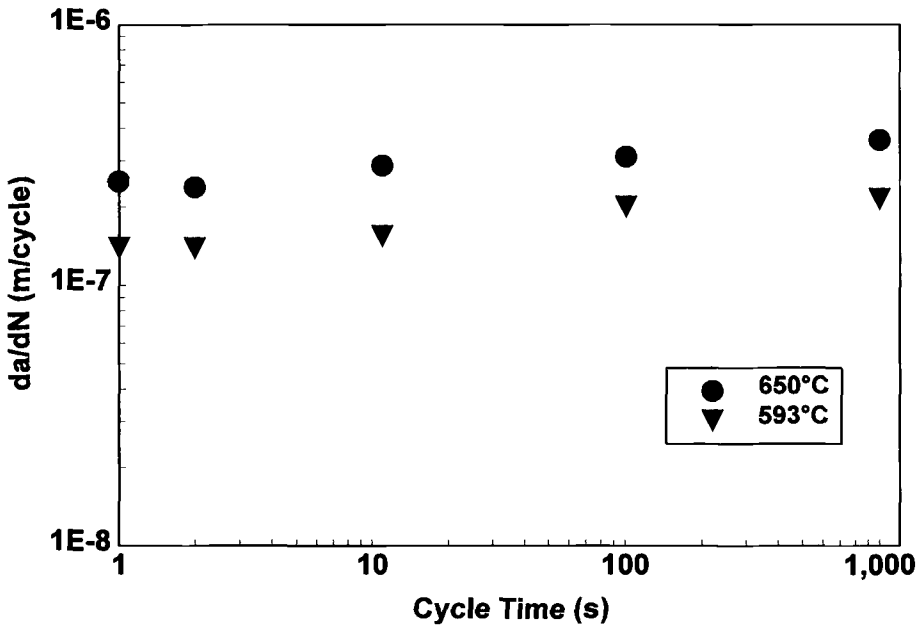


FIG. 6---*Effect of hold times at minimum load on the fatigue crack growth rate of Ti-1100*

may already occur during the baseline cycling. Thus, further exposure, particularly at minimum load, has no significant additional degradation associated with it. The lack of change in growth rate due to added hold times at minimum load is further evidence of the roles creep and environment play in hold times at maximum load where both effects are present. At minimum load, neither effect appears to be significant.

It is of interest to compare the hold time effects observed here with those of prior investigations. In nickel-base superalloys it has been found that hold time additions to fatigue cycling have an effect on growth rate which is dependent on the frequency of the baseline cycling [7]. Similar trends might be expected in Ti-1100, although the governing mechanisms may be different. For example, Ghonem and Foerch [4] observe an increase in growth rate due to the addition of a 300 s hold time to baseline 0.05 Hz cycling at 593°C while Parida and Nicholas [3] find that additions of 10 or 30 s hold times at either maximum or minimum load produce growth rates that are essentially unchanged from the baseline 1 Hz cycling without holds. In the latter reference, at minimum load, branching and microcracking were observed due to the addition of hold times, producing crack closure or a decrease in effective stress intensity range. This produces a decrease in driving force which appears to be offset by the reduced resistance to crack growth from environmental degradation due to oxidation at the crack tip. The complex combinations of environmental degradation, crack closure, and potentially less severe oxidation at the crack tip at minimum load because of a closed crack all appear to contribute to crack growth with superimposed hold times, making interpretation of the data both difficult and speculative.

SUMMARY AND CONCLUDING REMARKS

The results of this study show that Ti-1100, which was designed for a maximum operating temperature of 593°C (1100°F), still has good crack growth rate behavior which does not deteriorate when the temperature is increased from 593 to 650°C. In the near threshold region of fatigue crack growth, where the majority of component life occurs, the FCGR of Ti-1100 at 650°C is approximately an order of magnitude faster than at 593°C. However, when Ti-1100 is compared to two titanium aluminide alloys at 650°C, its FCGR is significantly slower [11,12]. For example, at 650°C and the same values of ΔK and R used here, Ti-24Al-11Nb exhibits growth rates which are approximately an order of magnitude faster than those in Ti-1100 over the frequency range from 0.001 Hz to 1 Hz [11]. A newer orthorhombic + beta titanium aluminide, Ti-25Al-25Nb, has growth rates which fall approximately between those of Ti-24Al-11Nb and Ti-1100 when viewed on a log plot at 650°C, R=0.1, and 1 Hz [12].

The effect of temperature on fatigue crack growth rates of Ti-1100, determined at 1.0 Hz at a constant ΔK of 15 MPa$\sqrt{m}$, shows a minimum growth rate at approximately 250°C and continued increase with increase in temperature above that. Changes in frequency from 0.001 to 1.0 Hz produce fatigue crack growth rates which indicate a combination of cyclic- and time-dependent behavior at both 593 and 650°C, but are primarily cycle dependent up to a frequency of 1.0 Hz.

At 593 and 650°C, the fatigue crack growth rate behavior of Ti-1100 results from a complex combination of creep, fatigue and environment. Hold times at

maximum load are found to initially decrease and then increase the cyclic crack growth rate with increasing duration. During short hold times, the growth rate per cycle decreases, which is attributed to the effects of creep blunting. During longer hold times, the crack tip is held open to the environment for a longer period of time. This appears to degrade material ahead of the crack tip, resulting in higher crack growth rates upon subsequent cycling (a resharpening of the crack tip). Hold times at minimum load show no change in growth rates, indicating that there is no additional contribution of environmental effects due to increased time to the bulk material beyond that experienced during the baseline 1 Hz cycling.

ACKNOWLEDGMENT

This work was supported by the U.S. Air Force under AFOSR Project 2302BW at Wright Laboratory, Materials Directorate, Wright-Patterson Air Force Base, OH.

REFERENCES

1. Bania, P.J., "An Advanced Alloy for Elevated Temperatures," J. Met., **40**, 1988, pp. 20-22.

2. Bania, P.J., "Ti-1100: A New Elevated Temperature Titanium Alloy," 6th World Conf. on Titanium, Part II, Cannes, France, June 6-9, 1988, P. Lacombe, R. Tricot and G. B'eranger, eds., Les Editions de Physique, Les Ulis Cedex, France, 1988, pp. 825-830.

3. Parida, B.K. and Nicholas, T., "Elevated Temperature Fatigue Crack Growth Behavior of Ti-1100," Fatigue Fract. Engng Mater. Struct. **17**, 1994, pp. 551-561.

4. Ghonem, H. and Foerch, R., "Frequency Effects on Fatigue Crack Growth Behavior in a Near-a Titanium Alloy," Mat. Sci. Eng., **A138**, 1991, pp. 69-81.

5. Parida, B.K. and Nicholas, T., "Influence of Crack Closure and Stress Ratio on Near-Threshold Fatigue Crack Growth Behavior in Ti-1100," Cyclic Deformation, Fracture, and Nondestructive Evaluation of Advanced Materials: Second Volume, ASTM STP 1184, M.R. Mitchell and O. Buck, Eds., American Society for Testing and Materials, Philadelphia, 1994, pp. 48-63

6. Foerch, R., Madsen, A. and Ghonem, H., "Environmental Interactions in High-Temperature Fatigue Crack Growth of Ti-11," Met. Trans., **24A**, 1993, pp. 1321-1332..

7. Ghonem, H., Nicholas, T. and Pineau, A., "Elevated Temperature Fatigue Crack Growth in Alloy 718 - Part I: Effects of Mechanical Variables," Fatigue Fract. Engng Mater. Struct., **16**, 1993, pp. 565-576.

8. Rosenberger, A.H. and Ghonem, H., "Influence of Creep-Fatigue Interaction on High Temperature Fatigue Crack Growth Behavior of Ti-1100," Fatigue Fract. Engng Mater. Struct., **17**, 1994, pp. 397-410.

9. "Standard Test Method for Measurement of Fatigue Crack Growth Rates", ASTM Standard: E647-88a, American Society for Testing and Materials, Philadelphia, PA.

10. Peters, M., Bachman, V., Trautman, K.-H., Schurmann, K., Lee, Y.-T., and Ward, C.H., "Room and Elevated Temperature Properties of Ti-1100," Titanium 92, F.H. Froes and I. Caplan, Eds., The Minerals, Metals and Materials Society, 1993, pp. 303-310.

11. Balsone, S.J., Maxwell, D.C., Khobaib, M. and Nicholas, T., "Frequency, Temperature, and Environmental Effects on Fatigue Crack Growth in Ti_3Al," FATIGUE 90, Vol. II, H. Kitagawa and T. Tanaka, Eds., Materials and Components Engineering Publications Ltd, Birmingham UK, 1990, pp. 1173-1178.

12. Balsone, S.J., Maxwell, D.C. and Broderick, T.F., "Fatigue Crack Growth Behavior of Titanium Aluminide Ti-25Al-25Nb," Fracture Mechanics: Twenty Third Symposium, ASTM STP 1189, R. Chona, Ed., American Society for Testing and Materials, Philadelphia, 1993, pp. 551-567.

13. Ashbaugh, N.E., et al., Mechanical Properties for Advanced Engine Materials, Technical Report WL-TR-91-4149, Wright-Patterson Air Force Base, 1992.

Mark J. Viz,[1] Alan T. Zehnder,[1] and John-David Bamford[1]

FATIGUE FRACTURE OF THIN PLATES UNDER TENSILE AND TRANSVERSE SHEAR STRESSES

REFERENCE: Viz, M. J., Zehnder, A. T., and Bamford, J.-D., **"Fatigue Fracture of Thin Plates Under Tensile and Transverse Shear Stresses,"** Fracture Mechanics: 26th Volume, ASTM STP 1256, Walter G. Reuter, John H. Underwood, and James C. Newman, Jr., Eds., American Society for Testing and Materials, Philadelphia, 1995.

ABSTRACT: Crack growth in thin sheets loaded under tension and transverse shear is studied experimentally and the mechanics of such problems are reviewed. A small scale yielding approach is adopted that describes the crack tip fields using a combination of Kirchhoff plate theory and plane stress elasticity. Techniques for calculating the relevant stress intensity factors are presented and validated with results from six test cases. Fatigue crack growth rates are measured using a double-edge notch test specimen configuration loaded in tension and torsion. A geometrically nonlinear finite element computation is used to determine the stress intensity factors as functions of axial load, torque, and crack length.

KEYWORDS: fatigue fracture, aluminum alloys, plate theory, mixed mode fracture, finite element analysis, geometric nonlinearity, aircraft structure

The most general loading of a thin, cracked sheet results in singular crack tip stresses that are a combination of membrane, bending and out-of-plane (transverse) shear components. As shown in Fig. 1, two fracture modes can be identified with membrane stresses, and two fracture modes can be identified with bending and out-of-plane shear stresses. Modelling the near tip stresses of a cracked sheet using plane stress elasticity and Kirchhoff plate theory, four stress intensity factors are required, i.e., the four illustrated in Fig. 1. The standard K_I and K_{II} have their origin in plane stress elasticity while the k_1 and k_2 originate from Kirchhoff plate theory. These stress intensity factors and the mechanics of the problem will be discussed in more detail in the following section.

The utility of the above model for the crack tip stresses lies in the assumption that crack initiation and growth can be correlated with these stress intensity

[1] Graduate Research Assistant, Assistant Professor, and Undergraduate Research Assistant respectively, Department of Theoretical and Applied Mechanics, Cornell University, Ithaca, New York 14853.

Copyright © 1995 by ASTM International www.astm.org

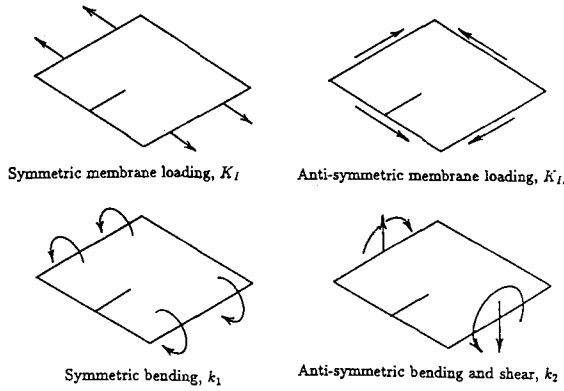


FIG 1 – Membrane, bending and transverse shear fracture modes for a plate with a straight through crack. Stress intensity factors corresponding to each mode are shown.

factors and that there are engineering problems in which such modes occur. One case is the problem of a crack in the skin of a pressurized aircraft fuselage. If the crack lies near a lap joint, as shown in Fig. 2, the side of the crack that is riveted to the stringer is stiffer than the other side, causing one side to bulge relative to the other, resulting in out-of-plane transverse shear and in-plane tension stresses at the crack tip. Analyses of this problem performed at NASA Langley[2] have shown that the relation between the applied loads and the resultant crack tip stress field is a nonlinear one; thus, a proper modelling of this problem requires a geometrically nonlinear analysis.

The importance of the transverse shear stresses relative to the tension stresses can be assessed by computing the tension stress intensity factor, K_I, and the transverse shear stress intensity factor, k_2, for a crack lying at different positions near a lap joint. Computations of the stress intensity factors for cracks lying along a lap joint, and at the $\frac{1}{4}$ and $\frac{1}{2}$ bay positions in a pressurized fuselage were performed by Britt[2]. The results, presented in Fig. 3 in terms of k_2 versus K_I, show that for the crack nearest to the lap joint ("crack along stringer" in Fig. 3) the value of k_2 is comparable to K_I and may therefore be a factor in crack growth. The other two stress intensity factors, K_{II} and k_1, are negligible for the crack along the lap joint. Although this may not be true in all cases, this paper focuses on fracture under a combination of K_I and k_2 modes only, since the primary application of the current research is to the lap joint problem. Whether k_2 does or does not contribute to crack growth is one of the principal subjects of the research described in this paper. An extensive literature search revealed no

[2] Britt, V.O., personal communication, NASA Langley Research Center, (1993).

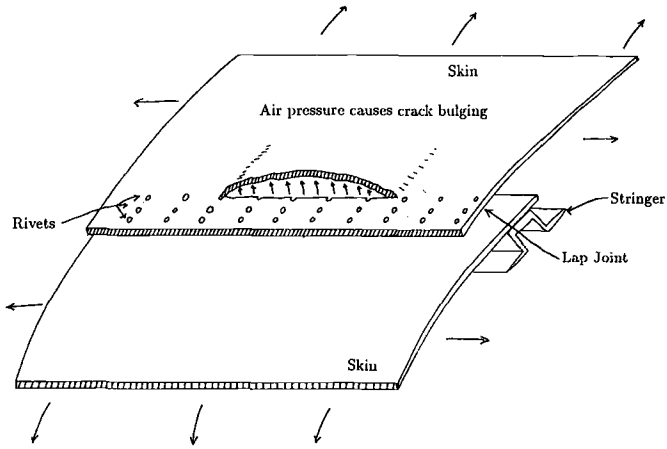


FIG 2 – Crack near a lap joint in the skin of a pressurized fuselage.

data on fracture in thin sheets under tension and transverse shearing, thus a series of experiments have been performed and are described here.

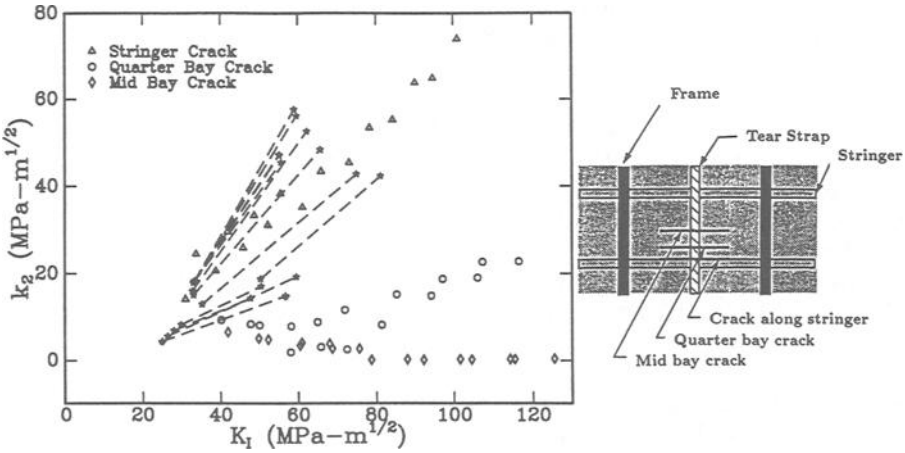


FIG 3 – K_I and k_2 computed for cracks lying at three positions in a fuselage (points), and range of stress intensity factors for which tests have been performed.

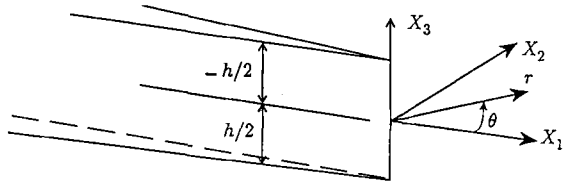


FIG 4 – Coordinate system for a through crack in a plate.

MECHANICS

Under the assumption that the crack tip stresses involve a coupling of the membrane and bending fracture modes, and that the bending part of the problem can be described using Kirchhoff plate theory, the stress field on a plane ahead of the crack ($\theta = 0$ in the coordinate system of Fig. 4) is [1-3]

$$\begin{aligned}
\sigma_{22} &= \frac{K_I}{\sqrt{2\pi r}} + \frac{k_1}{\sqrt{2r}}\frac{2x_3}{h}, \\
\sigma_{12} &= \frac{K_{II}}{\sqrt{2\pi r}} + \frac{k_2}{\sqrt{2r}}\left(\frac{1+\nu}{3+\nu}\right)\frac{2x_3}{h}, \\
\sigma_{23} &= \frac{-k_2 h}{2(2r)^{3/2}(3+\nu)}\left[1 - \left(\frac{2x_3}{h}\right)^2\right],
\end{aligned} \tag{1}$$

where ν is the Poisson ratio and h is the plate thickness. Note the absence of $1/\sqrt{\pi}$ in the k_1, k_2 terms. This makes the definitions of k_1 and k_2 correspond to those introduced by Sih, et al.[3], and adopted by handbooks of stress intensity factors[4].

The in-plane stress components, σ_{12} and σ_{22}, each have a constant and linearly varying through the thickness term corresponding to membrane and bending loads, respectively. The out-of-plane stress component, σ_{23}, varies parabolically through the thickness of the plate and has an $r^{-3/2}$ singularity. However, Eq. 1 does not reflect that the stress intensity factors are nonlinear functions of the applied loading. For example, in an uncracked finite plate an applied transverse shear load will generate not only a resultant transverse shear stress but also a significant membrane stress as the overall plate deflection exceeds the limits of Kirchhoff plate theory. Now if a crack were present in this plate, it would experience both a k_2 and a K_I mode which are not obtainable from a linear superposition of the applied loading. Given any general plate loading (such as those shown on the right in Fig. 5) the coupling of the four fracture modes to the applied load disallows a linear superposition approach whereby it is assumed that the tensile load causes the K_I mode, the in-plane shear load causes the K_{II} mode and so on. Rather, Eq. 1 relies on the approach that the mode coupling is properly accounted for in the geometrically nonlinear finite element analyses used to compute the four stress intensity factors for a given plate loading and crack length, and as such, the mode coupling is quantified through many systematic finite element analyses (see Figs. 7 and 8).

Other models of the crack tip stress state can be constructed using either the three dimensional theory of elasticity or the higher order Reissner plate theory[5]. The plate theory idealization is chosen because three dimensional analysis of cracked plates necessitates numerous degrees of freedom; this necessity quickly becomes prohibitive for engineering problems of pressurized shells. Simmonds and Duva[6] have shown that the energy release rate calculated by either the Reissner or Kirchhoff theories is the same in the limit of a thin plate; thus, correlation of fracture using either plate theory is equivalent. Hui and Zehnder[7] argue for using the Kirchhoff theory since it is simpler that the Reissner theory, and the differences between the two theories occur only in a region around the crack tip comparable in size to the plate thickness. In this region plastic deformation and deviation of the crack surface from the planar surface of Fig. 4 will cause the stress field to deviate from both the Reissner theory result and from the results for a three dimensional elastic analysis of a straight through crack as well. In the spirit of small scale yielding it is proposed that a combination of plane stress elasticity and Kirchhoff plate theories be used to model the crack tip stress fields and to correlate crack growth.

Research into fracture in the context of plate theory began with Williams' asymptotic analysis[2] of the Kirchhoff theory crack tip stresses. This was followed by solutions for stress intensity factors[3,8], stress fields for Reissner plate theory[9] and stress intensity factor solutions for Reissner theory[10-13]. Much of this and related work is summarized in [14] and a more complete list of references can be found in [7].

To determine stress intensity factors by using the finite element method, energy based methods are often preferred. Energy based methods use results of a finite element analysis to compute either the total or the components of the crack tip energy release rate. Stress intensity factors are then computed using the well known relations between them and the energy release rate. Unfortunately, the relation for Kirchhoff plate theory cracks is not so well known. It was first computed two years ago by Hui and Zehnder[7]. For completeness the derivation of their result is outlined here. The corresponding plane stress results are not discussed in detail. Their derivation can be found in any text on fracture mechanics.

The stress field near the tip of a through crack in a thin elastic plate in bending was first obtained by Williams[2] in the context of Kirchhoff plate theory using an eigenfunction approach to solve the biharmonic equation. With respect to the coordinate system shown in Fig. 4 the out-of-plane (x_3 direction) crack displacement field is [2,3]

$$w = \frac{(2r)^{3/2}(1-\nu^2)}{2Eh(3+\nu)}\left\{k_1\left[\frac{1}{3}\frac{(7+\nu)}{(1-\nu)}\cos(3\theta/2) - \cos(\theta/2)\right] + k_2\left[\frac{1}{3}\frac{(5+3\nu)}{(1-\nu)}\sin(3\theta/2) - \sin(\theta/2)\right]\right\} \tag{2}$$

where (r, θ, x_3) is a polar cylindrical coordinate system with its origin located at

the crack tip. The stress fields are

$$\begin{pmatrix}\sigma_{rr}\\ \sigma_{r\theta}\\ \sigma_{\theta\theta}\end{pmatrix} = \frac{k_1}{\sqrt{2r}}\frac{x_3}{2h}\begin{pmatrix}(3+5\nu)\cos(\theta/2)-(7+\nu)\cos(3\theta/2)\\ (1-\nu)\sin(\theta/2)-(7+\nu)\sin(3\theta/2)\\ (5+3\nu)\cos(\theta/2)+(7+\nu)\cos(3\theta/2)\end{pmatrix} + \frac{k_2}{\sqrt{2r}}\frac{x_3}{2h}\begin{pmatrix}(3-5\nu)\sin(\theta/2)+(5+3\nu)\sin(3\theta/2)\\ (1-\nu)\cos(\theta/2)-(5+3\nu)\cos(3\theta/2)\\ -2(5+3\nu)\cos(\theta/2)\sin(\theta)\end{pmatrix}, \tag{3a}$$

$$\begin{pmatrix}\sigma_{r3}\\ \sigma_{\theta 3}\end{pmatrix} = \frac{\left[1-\left(\frac{2x_3}{h}\right)^2\right]h/2}{(2r)^{3/2}}\begin{pmatrix}k_1\cos(\theta/2)-k_2\sin(\theta/2)\\ -k_1\sin(\theta/2)-k_2\cos(\theta/2)\end{pmatrix}, \tag{3b}$$

and

$$\sigma_{33} = 0. \tag{3c}$$

where E is the elastic modulus. The two stress intensity factors, k_1 and k_2, are referred to as Kirchhoff theory stress intensity factors and have the usual units of force/length$^{3/2}$.

The in-plane stress components, σ_{rr}, $\sigma_{\theta\theta}$, $\sigma_{r\theta}$, have an $r^{-1/2}$ singularity, which is the same as predicted by elasticity theory, and the out-of-plane shear stresses, σ_{r3} and $\sigma_{\theta 3}$, have an $r^{-3/2}$ singularity. Unlike the elasticity theory results, the angular variation of the stress fields depends on the Poisson ratio, ν. The discrepancy between the plate theory results and elasticity theory results arises from the inability of the Kirchhoff plate theory to satisfy completely the stress free boundary conditions along the crack face.

The energy released during crack growth is equal to the work done by the tractions acting over the area of crack extension. For a linearly elastic plate, the energy release rate, G, for self-similar extension of a through crack as shown in Fig. 4 is[15,16]

$$G = \lim_{\Delta L\to 0}\frac{1}{2h\Delta L}\int_0^{\Delta L}\int_{-h/2}^{+h/2}\sigma_{2i}(x_1,\theta=0)\Delta u_i(\Delta L - x_1,\theta=\pi)dx_3dx_1, \tag{4}$$

where Δu_i are the components of relative crack tip displacement for a crack extension of ΔL with summation over $i = 1,2,3$.

Substituting the stress and displacement fields from Eqs. 2,3 into Eq. 4, components of the energy release rate corresponding to the symmetric and antisymmetric parts of the stress field are related to the Kirchhoff theory stress intensity factors[7] by

$$\begin{aligned} G_4 &= \frac{k_1^2\pi}{3E}\left(\frac{1+\nu}{3+\nu}\right),\\ G_3+G_5 &= \frac{k_2^2\pi}{3E}\left(\frac{1+\nu}{3+\nu}\right). \end{aligned} \tag{5}$$

Components of the energy release rate corresponding to the membrane loadings are related to the plane stress, stress intensity factors by[16]

$$G_1 = \frac{K_I^2}{E},$$
$$G_2 = \frac{K_{II}^2}{E}. \tag{6}$$

For a general loading the total energy release rate is the sum of the above, i.e.,

$$G = G_1 + G_2 + G_3 + G_4 + G_5. \tag{7}$$

The numbering of the components of G is chosen to correspond to the numbering of the degrees of freedom in the finite element program used for the computations in the following section. If the separate terms of the energy release rate can be found from finite element or other analyses, then the above expressions can be used to compute all four stress intensity factors.

NUMERICAL PROCEDURES

Numerical techniques for computing the four stress intensity factors are necessary since no coherent theory has been developed that faithfully models the complex coupling of the four fracture modes in a geometrically nonlinear regime. Using the finite element method, many such techniques have been developed and verified allowing G or the individual components of G to be computed without the use of special crack tip elements.

Three methods were used to compute the individual G_i terms: virtual crack extension, nodal release and the modified crack closure integral. These techniques are not new in the field of numerical fracture mechanics, and documentation of their use is extensive.

The virtual crack extension (VCE) method[17-20] is essentially a discrete computation of the J integral. As such the VCE method can provide accurate results for the total energy release rate, G, but cannot compute the components of G discussed previously. The nodal release (NR) method[21] computes the components of G on a nodal degree of freedom basis such that each G_i component is related to one of the four fracture modes shown in Fig. 1. The advantage of the NR method as compared to the VCE method is the capability to compute all of the G_i terms: for a completely arbitrary loading, all four stress intensity factors can be found. Yet there is a disadvantage inherent to the NR technique; it requires two separate analyses to be completed, the first to find the nodal forces ahead of the crack tip and the second to obtain the displacements at the corresponding nodes after these nodes originally ahead of the crack tip have been "released."

To validate the proposed method for the computation of K_I, K_{II}, k_1 and k_2, six test analyses (linear) of finite cracks in infinite plates were conducted.

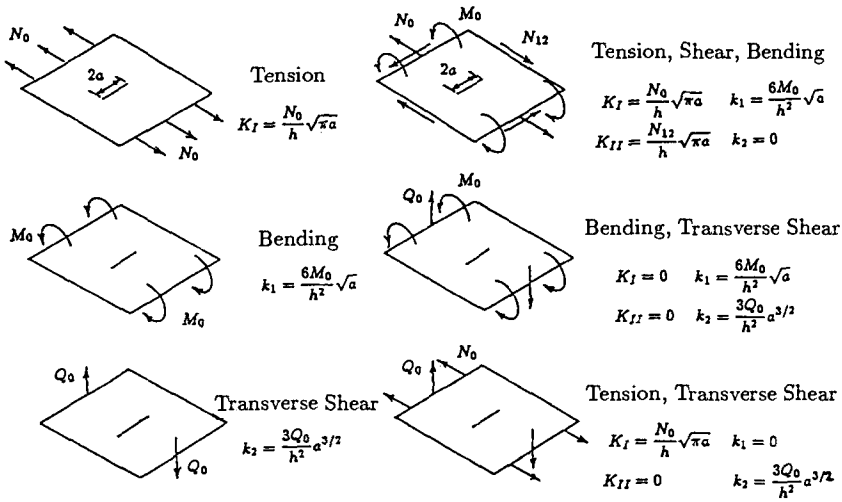
Fig. 5 shows these sample problems along with their theoretical solutions taken from Sih, et al.[3] and Zehnder and Hui[7,8]. Three of these test cases involve only a single mode; thus, the VCE technique is appropriate to compute the single stress intensity factor in each of these problems. The other three test cases involve loadings which generate mixed modes at the crack tip. For these cases, the NR method is necessary to be able to compute the individual $G_i s$ and hence the relevant stress intensity factors.

The computations of Fig. 5 as well as the test specimen calibrations discussed later were performed using the STAGS (STructural Analysis of General Shells) code[22]. The problems were modeled as a thin, flat plate of nondimensionalized width 11.0 by length 10.0 by 0.090 thick containing a centrally located straight crack of length $L = 1.0$ oriented parallel to the 11.0 dimension. No special crack tip elements were used; rather, a four-noded, six degree-of-freedom per node, flat plate element (element 410 in the STAGS library[23]) was used for the entire mesh. All elements were rectangular. In the region of near-tip refinement, which extends a distance $\frac{L}{2}$ above and below the crack line and $\frac{L}{4}$ behind and $\frac{L}{2}$ ahead of the crack tip (where L is the crack length), the elements were square. The standard element size in this region of refinement was $\frac{L}{64}$.

The results of these sample computations are given in Fig. 5. For the three single mode cases the VCE results were all within 3.6% difference from the theoretical solutions. For the three mixed mode cases the NR results were all within 1.3% difference from the theoretical solutions. Based on these results the accuracy of these two methods for obtaining the four relevant stress intensity factors is established.

However, for the series of computations which needed to be performed to provide a stress intensity factor calibration for the particular test specimen configuration used in the fatigue tests, both of the above methods had significant drawbacks. The VCE method could not be used since the actual test specimen loading generates a mixed mode deformation state near the crack tip. The NR method requires two analyses for each data point, thus doubling the already large number of analyses. Consequently, a third method, the modified crack closure integral (MCCI) method[24,25], was used. This method approximates the displacement field over a crack advance of ΔL by using the displacement field behind the crack of length L, thus requiring only a single analysis per stress intensity factor calculation. The results already given which relate components of the energy release rate on a nodal degree of freedom basis to the four stress intensity factors can be applied to the MCCI method.

The accuracy of the MCCI method was investigated by Potyondy[26]. Analyzing four models of a flat, centrally cracked plate loaded to produce single mode crack tip deformations individually, each stress intensity factor could be computed to within 1.0% of the published theoretical value using square crack tip elements, in the limit of mesh refinement. Even for the coarsest mesh analyzed (with a tip element dimension to crack length ratio of 0.25) all stress intensity factors were computed to within 6.0% of the theoretical values. Since the tip element dimen-



Norm. Theoretical Values	k_1 (6.0)	k_2 (3.0)	K_I (1.7725)	K_{II} (1.7725)
Loading:				
Tension (VCE)[1]	-	-	1.754 (1.0%)	-
Bending (VCE)	5.954 (0.8%)	-	-	-
Transverse Shear (VCE)	-	2.891 (3.6%)	-	-
Tension, Shear & Bending (NR)[2]	5.965 (0.6%)	-	1.765 (0.4%)	1.763 (0.5%)
Bending & Transverse Shear (NR)	5.997 (0.1%)	2.967 (1.1%)	-	-
Tension & Transverse Shear (NR)	-	2.963 (1.3%)	1.760 (0.7%)	-

[1]VCE...virtual crack extension technique
[2]NR...nodal release technique

FIG 5 – Six test cases for validation of the stress intensity factor computation techniques: finite length crack in an infinite plate.

sion to crack length ratios used for the calibration plots shown in Figs. 7 and 8 ranged from 0.0125 to 0.0625, the latter ratio being of the same order as Potyondy's most refined mesh, the accuracy of the values in Figs. 7 and 8 are assumed to be within a few percent of the true values.

EXPERIMENTAL PROCEDURE

To determine the fatigue crack growth rate as a function of the two stress intensity factors K_I and k_2, double-edge cracked sheets were tested under constant amplitude cyclic axial and torsional loading. Although axial-torsional fatigue testing of sheets is not a standard test, to the extent possible, the tests were performed in accordance with the ASTM Standard Test Method for Measurement of Fatigue Crack Growth Rates (E647).

The test specimen dimensions and geometry are shown in Fig. 6a. They were machined from the same stock of 2.29mm thick 2024-T3 aluminum alloy sheets used by Hudson[27]. On each side of the test specimen a 6.35mm long, 0.18mm wide starter notch was foil cut using electric discharge machining. The samples were diamond polished to a 3.0 μm finish.

The sample is gripped by mounting it between a massive steel fixture and a steel face plate as shown in Fig. 6c. The assembly is clamped together with 9.0mm diameter bolts tightened to just below their stripping load. By overdrilling the holes in the test specimen to 12.7mm diameter, bearing loading on the plate from the bolts is prevented. Two channels were cut into the fixtures and face plates into which were inserted 1.5mm diameter steel rods, as shown in Fig. 6. When the assembly is clamped together the steel rods indent into the sample ensuring no slip between the sample and grip and providing a known grip line.

The tests were performed using an axial-torsional servo-hydraulic testing machine operating in load and torque control. A 0.51mm long precrack was grown from each starter notch by applying a cyclic axial load at 6Hz with $\Delta K_I \approx 5.5$ $MPa\sqrt{m}$, $R = 0.7$, where $R \equiv P_{min}/P_{max}$, P being the axial tensile load. Typically 100,000 cycles were required for precracking.

Testing was performed at $R = 0.7$ (for both axial and torsional loads) with the axial and torsional loads in phase and constant throughout a given test. The axial loads ranged from 2.0kN to 45.0kN, and the torques from 11.0Nm to 110.0Nm. A thin sheet has a relatively low torsional stiffness, thus the sample undergoes large rotations (on the order of 20° for a torque of 110.0Nm) severely limiting the testing frequency compared to a typical axial loading test. All of the tests were performed at 1Hz where the loads could be controlled to better than 1.0%.

Crack lengths were measured approximately every 0.50mm of crack growth using two travelling microscopes, one for each crack, mounted to the testing frame. As a result of the limitation of having only two microscopes, crack length measurements were taken on only one side of the plate for each crack; therefore there are only two sets of crack length data for each test. When setting up the test the microscopes were rotated to be normal to the plane of the center of the

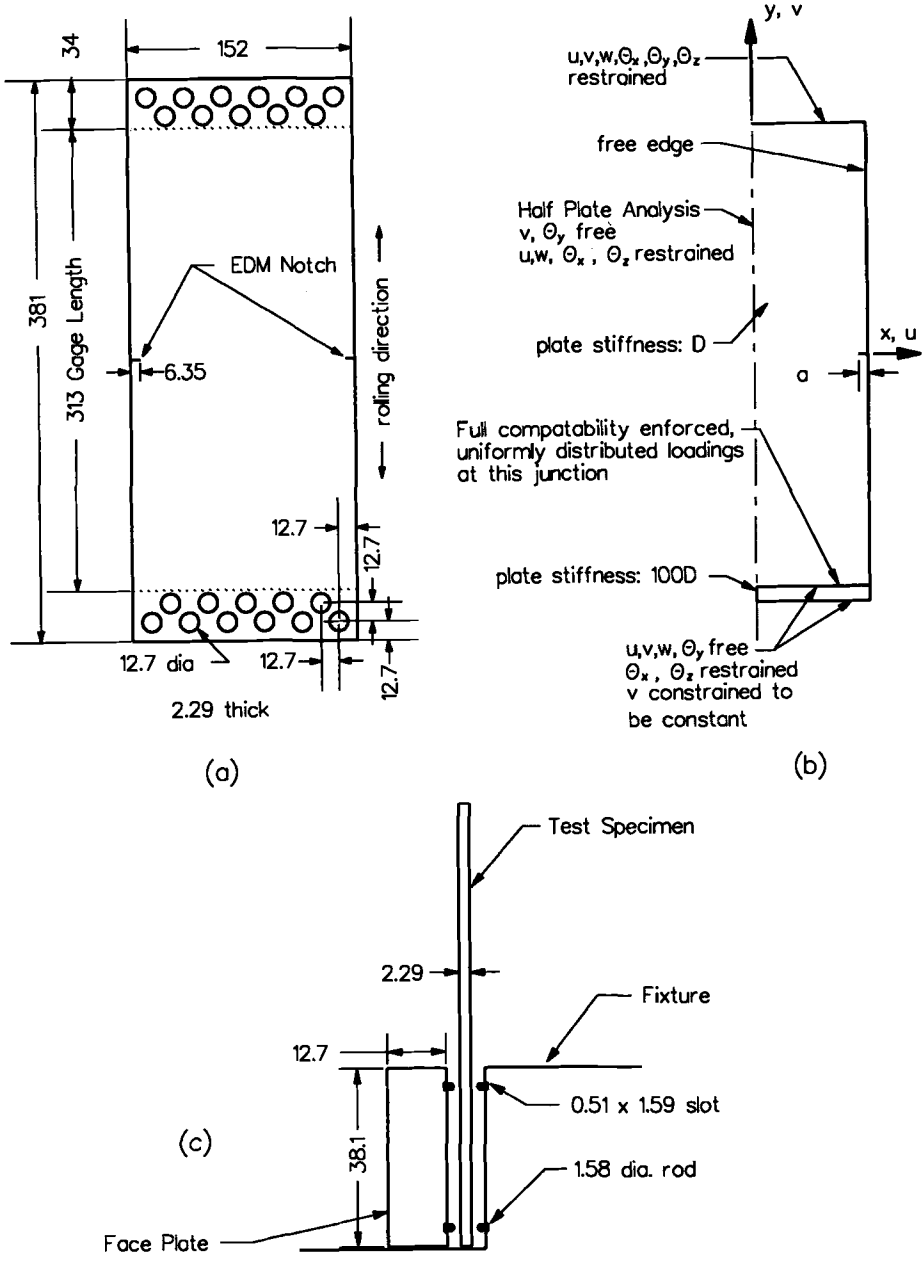


FIG 6 – (a) Test specimen configuration. (b) Boundary conditions used in finite element model. (c) Detail of specimen gripping fixture. All dimensions in mm.

specimen when the mean torque was applied. This initial microscope rotation was maintained throughout the test. The sample was illuminated with flourescent light reflected from white card stock. With this setup crack length was measured to an accuracy of ± 0.05mm.

TEST SPECIMEN CALIBRATION

Correlation of fatigue crack growth rates requires a specimen calibration whereby the K_I and k_2 can be determined from knowledge of P, the net axial load on the specimen, T, the net torque on the specimen, and a, the current crack length. The means used to calculate the stress intensity factors from the results of a finite element calculation were described in a previous section. Using a half-plate model (see Fig. 6b for modelling details and boundary conditions) and the MCCI method to obtain the G_i values, analyses were performed for a grid of P, T values at five discrete crack lengths: 6.35mm, 12.7mm, 19.05mm, 25.4mm and 31.75mm, chosen to span the experimental results which are for crack lengths from 6.0mm to 32.0mm. The K_I calibration "surface" as a function of P, T for three crack lengths, 6.35mm, 19.05mm and 31.75mm is given in Fig. 7. The corresponding k_2 calibration at the same crack lengths is given in Fig. 8.

Although these calibration plots exhibit many interesting features only a few will be discussed here. Notice that for higher torque values K_I becomes less sensitive to increasing axial load (see Fig. 7). This is especially seen for the shortest crack length. Also notice that k_2 at higher torque levels decreases as the axial load is increased (see Fig. 8). This effect is a result of the dependence of the torsional stiffness on the axial tension load in that as the axial load is increased, the torsional stiffness of the plate also increases.

The results of the calibration also show that K_{II} and k_1 are small compared to K_I and k_2, respectively, though they are present. This result is a welcome one, since the crux of this research depends on the fact that the near-tip stress field in the test specimen is essentially the same as the near-tip stress field in the actual cracked aircraft fuselage. Simulations of crack growth in fuselage bays show that indeed the K_{II} and k_1 components are small compared to K_I and k_2, respectively.

FATIGUE CRACK GROWTH RATE DATA

Given the calibration shown in Figs. 7 and 8 an interpolation scheme is used to reduce crack growth data from an actual test. This scheme is in essence quite straightforward. For any given test, two points in "P, T space" are known: the maximum P, T and the minimum P, T. Since all of the testing is done in load and torque control, these two points never change during a given test. Although only three plots each are shown in Figs. 7 and 8, two additional plots for the intermediate crack lengths of 12.7mm and 25.4mm have also been generated, giving K_I and k_2 values for five discrete crack lengths. A typical test however may have crack length data at 60 to 80 points. First, the K_I and k_2 values are interpolated

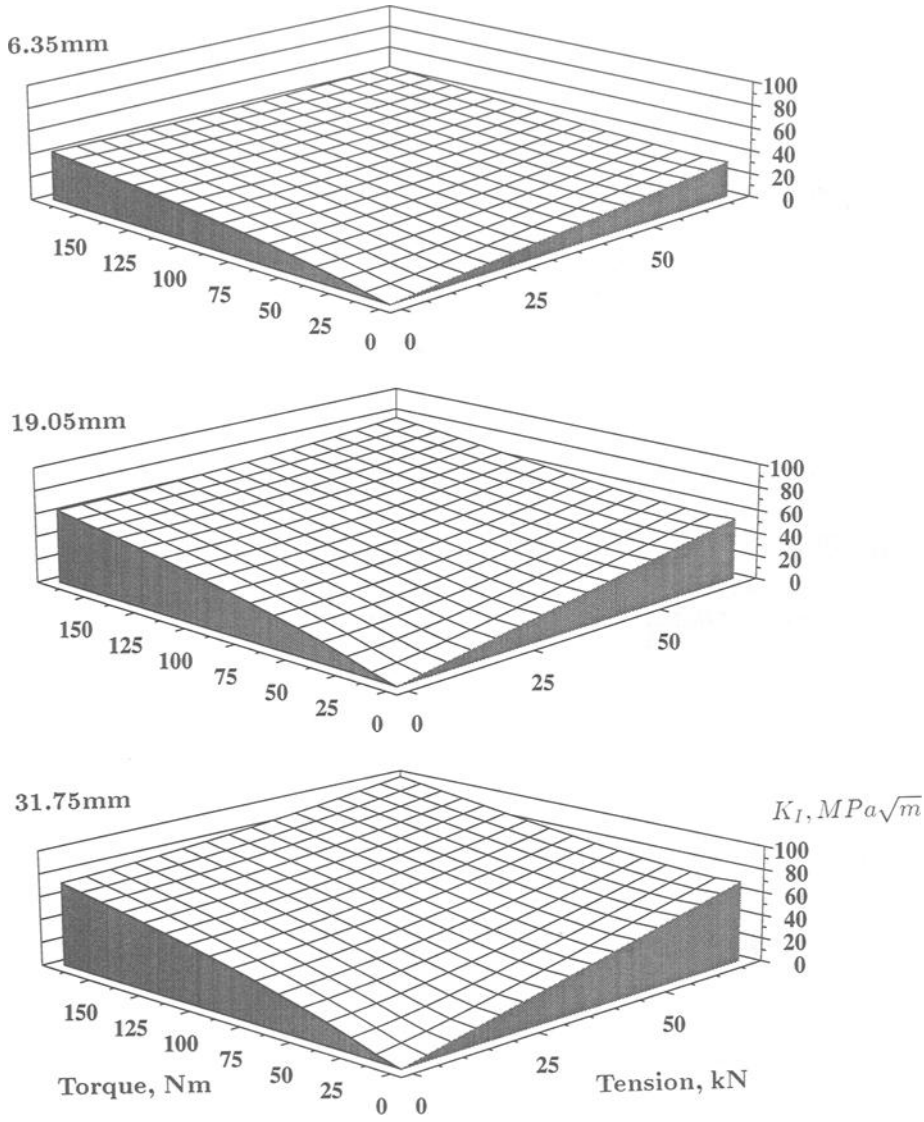


FIG 7 – Stress intensity factor K_I versus axial load and torque for three crack lengths.

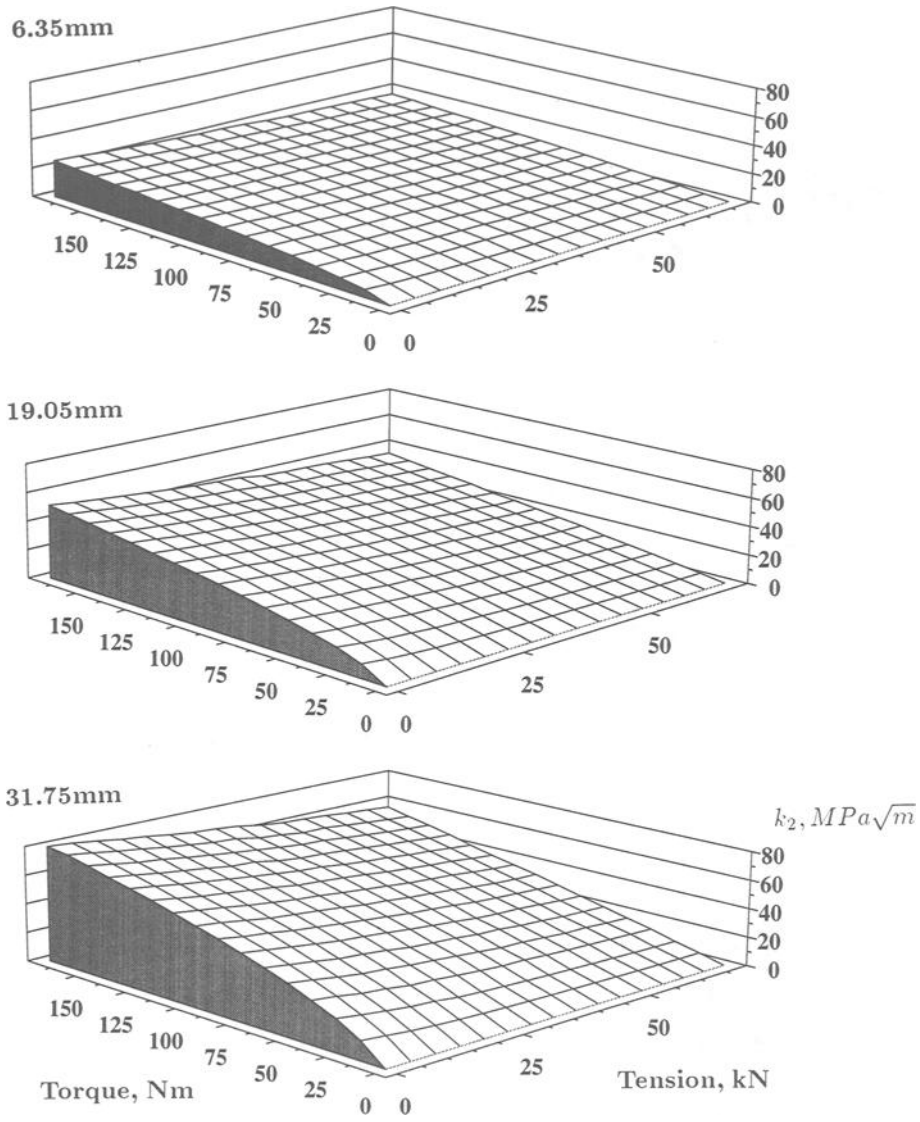


FIG 8 – Stress intensity factor k_2 versus axial load and torque for three crack lengths.

at each of the five crack lengths from actual K_I and k_2 data at the four nearest neighbors to the $(P,T)_{max}$ point and the $(P,T)_{min}$ point. Then, from these interpolated K_I and k_2 values at the five crack lengths a polynomial curve fit is used to generate effective K_I versus a and k_2 versus a functions. Thus knowing the stress intensity factors at each of the crack length data points then allows for the final result of a plot of crack growth rate, $\frac{da}{dN}$, versus ΔK_I or Δk_2.

The a versus N and $\frac{da}{dN}$ versus ΔK_I results from two typical mixed mode fatigue tests are shown in Fig. 9. Test no. 14 was loaded axially from 31.15kN to 44.5kN and torsionally from 78.4Nm to 112.0Nm, whereas test no. 18 had the same torsional load but an axial load reduced by a factor of ten, i.e., from 3.12kN to 4.45kN. The crack growth rate plots corresponding to each of these tests are shown directly underneath their corresponding a versus N plots in Fig. 9. The "A" and "B" distinctions refer to each of the two cracks in a given specimen (recall that these are double- edge notch specimens). The solid and dashed lines in the crack growth rate plots are pure mode I fatigue crack growth rate benchmarks for this material (see Hudson[27] and Newman[3]). The different plotting symbols used in the a versus N plots roughly correspond to regions of crack growth where the rate of growth has maintained a certain trend. These same symbols are then used in the lower plots of crack growth rate versus ΔK_I so that it becomes somewhat easier to follow the growth rate of the crack at increasing ΔK_I.

DISCUSSION

Although the results from only two tests have been presented in Fig. 9, nineteen tests have been completed to date (see Table 1). When the data are presented as in Fig. 9 it becomes clear that there is a significant amount of crack growth rate variability as a function of the torque loads present and even within a single test itself. Referring to tests 14 and 18, the crack growth rates start essentially where they would be in a pure K_I fatigue test, as shown by the Hudson and Newman benchmarks. Then a region of decreasing crack growth rate occurs, followed by a quick acceleration at the end. This changing behavior is believed to be caused by the significant crack surface contact that occurs while the plate is being twisted; the twisting causes the opposing crack faces to be "dragged" across each other.

The phenomenon of crack face contact or rubbing in other than pure K_I fracture testing is common[28-35]. Any local loading or unloading of the crack tip that results from crack face contact is not accounted for in the stress intensity factor calibration presented previously. However, if a reasonable model of the traction distribution on the crack faces as a result of crack face contact were developed, the mechanics model described earlier could accommodate such a refinement. Furthermore, a new stress intensity factor calibration (analogous to Figs. 7 and 8) could be computed that would involve the further refinement of crack face

[3] Newman, J.C.Jr., personal communication, NASA Langley Research Center, (1993).

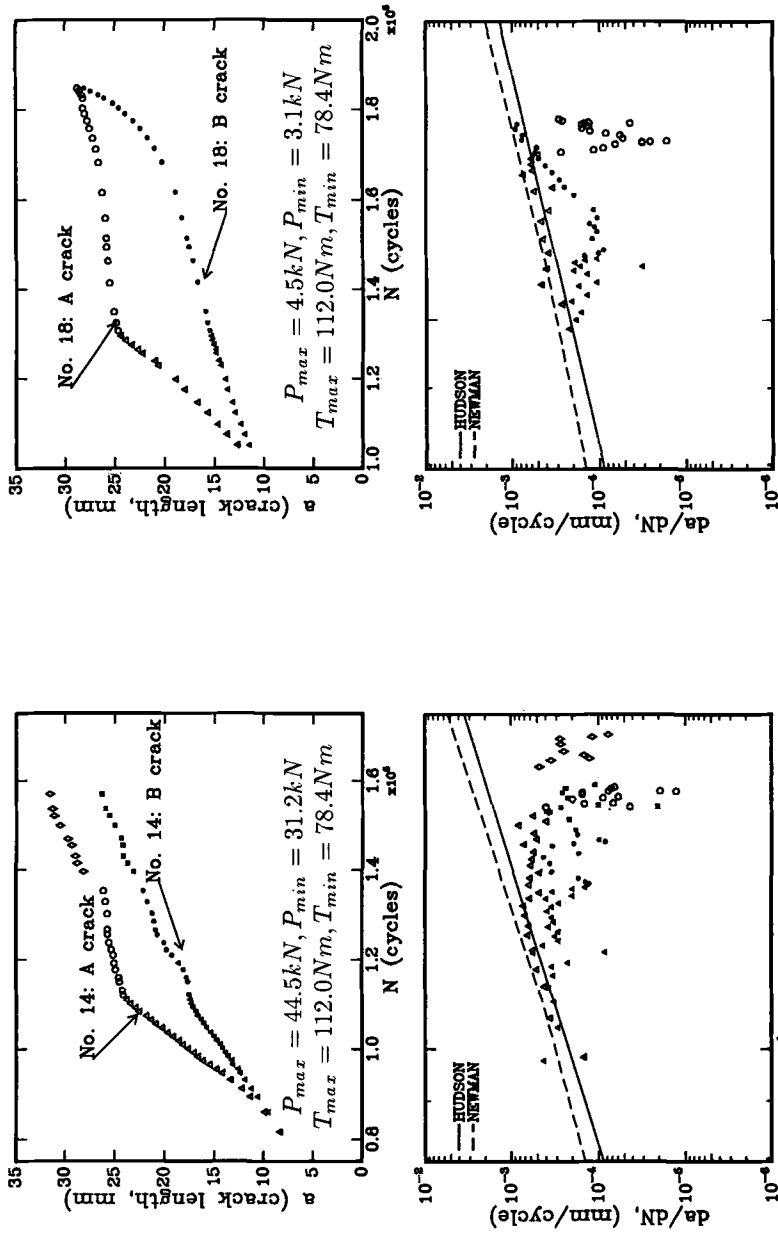


FIG 9 – Crack length, a, versus total cycles, N, and growth rate versus ΔK_I for test no. 14 (*left*) and test no. 18 (*right*).

loading. The authors currently are working on a methodology to incorporate the effect of crack face contact in the stress intensity factor calibrations in both an analytical manner and through the possible development of an empirical correction factor based on the experimental results.

The two cracks in any given specimen rarely grow at the same rate once the torsional loads are applied. The calibration calculations assume that the A and B cracks are the same length. To date a tolerance study has not been completed on how sensitive K_I and k_2 are to slightly different crack lengths.

TABLE 1--Summary of completed fatigue tests.

Specimen	P_{max}[1] (kN)	T_{max}[1] (Nm)	Average Cycles to 12.7mm Crack Growth[2]
2	22.8	0.	134739
6	48.6	36.4	112330
7	48.6	48.5	81170
8	48.6	60.6	52245
9	48.6	72.7	41310
14	44.5	112.0	108434
15	44.5	201.6	30987
16	8.9	112.0	113532
17	6.4	112.0	111470
18	4.5	112.0	140740
19	4.9	112.0	155073
20	8.9	112.0	139212
21	17.8	112.0	148665
22	26.7	112.0	120821
23	35.6	112.0	131615
26	0.	56.0	...[3]
27	0.	56.0	161251
28	44.5	89.6	107866
29	26.7	56.0	180235

[1] Minimum to maximum load ratio for all tests is 0.7.

[2] Result given is the average of the total elapsed cycles for each crack length at the data point nearest to 12.7mm growth.

[3] Specimen 26 buckled before 12.7mm of crack growth occurred.

SUMMARY AND CONCLUSIONS

Although it is still unclear what systematic role, if any, the presence of a k_2 crack tip fracture mode might have on the overall fatigue crack growth rate of a crack in a stiffened fuselage structure, it is clear that characterizing the problem

as one of simple K_I fatigue crack growth resulting from the fuselage hoop stress would greatly underestimate the K_I field at the crack tip. Geometrically nonlinear analyses and resultant stress intensity factor calibrations are necessary to properly describe the crack tip stress field in a cracked fuselage lap joint as well as any test specimen configuration used to examine the fatigue crack growth behavior in such structures. Whether or not the presence of the k_2 mode partially drives the fatigue crack growth or if it is simply the additional K_I supplied by the tearing or bulging aspect of the crack through the geometrically nonlinear effects that drives the crack growth is still not resolved. A fully three dimensional analysis of the near tip region might be necessary to come to a sound resolution of this issue.

Still, a cogent argument has been put forth as to a valid means to characterize the crack tip stress field in a thin plate using Kirchhoff plate theory to describe the bending modes (k_1 and k_2) and plane stress elasticity to describe the membrane modes (K_I and K_{II}). Furthermore, the energy release rate for self-similar growth of a through crack in a thin plate is expressed in terms of these four stress intensity factors and means to calculate these quantities from computed energy release rate terms are presented and validated. The experimental scheme for investigating the influence of the k_2 mode on the fatigue crack growth behavior of 2024-T3 aluminum as configured in a cracked fuselage lap joint is also presented along with some initial findings from the experimentation. Finally, the issues of crack closure and crack surface contact, extant in both the actual cracked aircraft fuselage structure and the test specimen, have been identified as important aspects for further investigation.

ACKNOWLEDGMENTS

This work was supported by NASA Langley Research Center under Award No. NAG-1-1311. The computations were performed using the Central Computing Facility maintained by the Materials Science Center at Cornell, supported by the MRL Program of the National Science Foundation under Award No. DMR-9121654. The authors are grateful to Dr. James Newman of NASA for many discussions on our work and for suggesting the specimen gripping scheme. We are also grateful to Prof. Anthony Ingraffea and Dr. Paul Wawyrzynek of Cornell University and to Dr. Charles Rankin of Lockheed Missiles and Space Company for their many helpful discussions with us on the computational aspects of this work.

REFERENCES

[1] Williams, M.L., "On the Stress Distribution at the Base of a Stationary Crack," *Journal of Applied Mechanics, Vol. 24*, pp. 109-114, (1957).

[2] Williams, M.L., "The Bending Stress Distribution at the Base of a Stationary Crack," *Journal of Applied Mechanics, Vol. 28*, pp. 78-82, (1961).

[3] Sih, G.C., Paris, P.C., and Erdogan, F., "Crack Tip Stress-Intensity Factors for Plane Extension and Plate Bending Problems," *Journal of Applied Mechanics, Vol. 29*, pp. 306-312, (1962).

[4] Murakami, Y., (ed.), *Stress Intensity Factors Handbook - Vol. 2*, Pergammon Press, Elmsford, N.Y., (1987).

[5] Reissner, E., "On Bending of Elastic Plates," *Quarterly of Applied Math, Vol. 5*, pp. 55-68, (1947-48).

[6] Simmonds, J.G., and Duva, J., "Thickness Effects are Minor in the Energy-Release Rate Integral for Bent Plates Containing Elliptic Holes or Cracks," *Journal of Applied Mechanics, Vol 48*, pp. 320-326, (1981).

[7] Hui, C.Y., and Zehnder, A.T., "A Theory for the Fracture of Thin Plates Subjected to Bending and Twisting Moments," *International Journal of Fracture, Vol. 61*, pp.211-229, (1993).

[8] Zehnder, A.T., and Hui, C.Y., "Stress Intensity Factors for Plate Bending and Shearing Problems," to appear in *Journal of Applied Mechanics*, (1994).

[9] Knowles, J.K., and Wang, N.M., "On the Bending of an Elastic Plate Containing a Crack," *Journal of Mathematics and Physics, Vol. 39*, pp. 223-236, (1960).

[10] Hartranft, R.J., and Sih, G., "Effect of Plate Thickness on the Bending Stress Distribution Around Through Cracks," *Journal of Mathematics and Physics, Vol. 47*, pp. 276-291, (1968).

[11] Wang, N.M., "Twisting of an Elastic Plate Containing a Crack," *International Journal of Fracture Mechanics, Vol. 6*, pp. 367-378, (1970).

[12] Tamate, O., "A Theory of Dislocations in the Plate under Flexure with Applications to Crack Problems," *Technology Reports, Tohoku University, Vol. 40*, pp. 67-88, (1975).

[13] Joseph, P., and Erdogan, F., "Bending of a Thin Reissner Plate with a Through Crack," *Journal of Applied Mechanics, Vol. 58*, pp. 842-846, (1991).

[14] Sih, G.C., (ed.) *Mechanics of Fracture 3, Plates and Shells with Cracks*, Noordhoff International Publishing, Leyden, (1977).

[15] Irwin, G.R., "Analysis of Stresses and Strains Near the End of a Crack Traversing a Plate," *Journal of Applied Mechanics, Vol. 24*, pp. 361-364, (1957).

[16] Rice, J.R., "Mathematical Analysis in the Mechanics of Fracture," in *Fracture, Vol. 2*, Liebowitz, ed., Academic Press, (1968).

[17] Parks, D.M., "A Stiffness Derivative Finite Element Technique for Determination of Elastic Crack Tip Stress Intensity Factors," *International Journal of Fracture Mechanics, Vol. 10*, pp. 487-502, (1974).

[18] Hellen, T.K., "On the Method of Virtual Crack Extensions," *International Journal of Numerical Methods in Engineering, Vol. 9*, pp. 187-207, (1975).

[19] deLorenzi, H.G., "Energy Release Rate Calculations by the Finite Element Method," *Engineering Fracture Mechanics, Vol. 21, No. 1*, pp. 129-143, (1985).

[20] Hellen, T.K., and Blackburn, W.S., "Nonlinear Fracture Mechanics and Finite Elements," *Engineering Computation, Vol. 4*, pp. 2-14, (1987).

[21] Ansell, H., "Bulging of Cracked Pressurized Aircraft Structure," *Ph.D. Thesis, No. 138*, Institute of Technology, Dept. of Mechanical Engineering, S-581 Linkoping, Sweden, Report No. LIU-TEK-LIC-1988:11, (1988).

[22] Almroth, B.O., Brogan, F.A., and Stanley, G.M., "Structural Analysis of General Shells," *User Instructions for STAGSC-1, Vol. 2*, Lockheed Missiles and Space Company, Palo Alto Research Park, Report No. LMSC D633873, (1986).

[23] Rankin, C.C., and Brogan, F.A., "The Computational Structural Mechanics Testbed Structural Element Processor ES5: STAGS Shell Element," *NASA CR4358*, Lockheed Missiles and Space Company, Palo Alto Research Park, (1991).

[24] Rybicki, E.F., and Kanninen, M.F., "A Finite Element Calculation of Stress Intensity Factors by a Modified Crack Closure Integral," *Engineering Fracture Mechanics, Vol. 9*, pp. 931-938, (1977).

[25] Viswanath, S., Lakshminarayana, H.V., and Ravindranath, D.D., "A Modified Crack Closure Integral Method for Calculating Stress Intensity Factors for Cracked Plates Subject to Bending Loads," *International Journal of Fracture, Vol. 41*, pp. R45-R50, (1989).

[26] Potyondy, D.O., "A Software Framework for Simulating Curvilinear Crack Growth in Pressurized Thin Shells," *Ph.D. Thesis, Report 93-5*, School of Civil and Environmental Engineering, Cornell University, (1993).

[27] Hudson, C.M., "Effect of Stress Ratio on Fatigue-Crack Growth in 7075-T6 and 2024-T3 Aluminum Alloy Specimens," *NASA TN D5390*, NASA Langley Research Center, (1969).

[28] Schroth, J.G., Hirth, J.P., Hoagland, R.G., and Rosenfield, A.R., "Combined Mode I-Mode III Fracture of a High Strength Low-Alloy Steel," *Metallurgical Transactions A, Vol. 18A, No. 6*, pp. 1061-1072, (1987).

[29] Gross, T.S., "Frictional Effects in Mode III Fatigue Crack Propagation," *Scripta Metallurgica, Vol. 19, No. 10*, pp. 1185-1188, (1985).

[30] Gross, T.S., and Mendelsohn, D., "An Analysis of Frictional Effects on Cylindrical Mode III Fatigue Crack Propagation Specimens," *Fatigue and Fracture of Engineering Materials and Structures, Vol. 11, No. 3*, pp. 167-178, (1988).

[31] Nayeb-Hashemi, H., McClintock, F.A., and Ritchie, R.O., "Effects of Friction and High Torque on Fatigue Crack Propagation in Mode III," *Metallurgical Transactions A, Vol. 13A, No. 12*, pp. 2197-2204, (1982).

[32] Ritchie, R.O., McClintock, F.A., Tschegg, E.K., and Nayeb-Hashemi, H., "Mode III Fatigue Crack Growth Under Combined Torsional and Axial Loading," *Multiaxial Fatigue, ASTM STP 853*, K.J. Miller and M.W. Brown, Eds., American Society for Testing and Materials, Philadelphia, pp. 203-227, (1985).

[33] Tschegg, E.K., Ritchie, R.O., and McClintock, F.A., "On the Influence of Rubbing Fracture Surfaces on Fatigue Crack Propagation in Mode III," *International Journal of Fatigue, Vol. 5, No. 1*, pp. 29-35, (1983).

[34] Tschegg, E.K., and Suresh, S., "Mode III Fracture of 4340 Steel: Effects of Tempering Temperature and Fracture Surface Interference," *Metallurgical Transactions A, Vol. 19A, No. 12*, pp. 3035-3044, (1988).

[35] Plumbridge, W.J., "Fatigue Crack Growth in Plate Specimens under Mode III Loading," *Journal of Materials Science, Vol. 20, No. 3*, pp. 1015-1026, (1985).

Jian Guo Xu[1] and H. W. Liu[2]

THE APPLICATION OF A LOGIC FRAMEWORK FOR FATIGUE CRACK GROWTH ANALYSES TO MICROSTRUCTURAL EFFECTS

REFERENCE: Xu, J. G., and Liu, H. W., **"The Application of a Logic Framework for Fatigue Crack Growth Analyses to Microstructural Effects,"** Fracture Mechanics: 26th Volume, ASTM STP 1256, Walter G. Reuter, John H. Underwood, and James C. Newman, Jr., Eds., American Society for Testing and Materials, Philadelphia, 1995.

ABSTRACT: ΔK has been widely used to correlate da/dN data. The relation between da/dN and ΔK is usually found empirically. However, fatigue crack growth relations can also be derived theoretically. Three fatigue crack growth theories are derived for the state of small scale yielding and plane strain. These three theories constitute a logic framework useful for fatigue crack growth analyses. The application of the logic framework to the analyses of microstructural effects on fatigue crack growth is illustrated.

The fatigue crack growth curve of 7075-T651 aluminum alloy has five distinct regions. A fatigue crack grows by crack-tip shear decohesion forming striations and by brittle fractures of particles followed by localized shear decohesion at these microcracks forming dimples. The logic framework helps to relate the fatigue crack growth behaviors in these five regions to the fractures of inclusions and to the resistance of grain boundaries and dispersoids to shear decohesion.

KEYWORDS: Fatigue crack growth, microstructure, 7075-T651 aluminum alloy, inclusions, dispersoids, crack-tip shear decohesion, striation, dimple.

ΔK has been widely used to correlate da/dN data. The similitude of crack-tip stress fields at a like value of ΔK is the basis for such correlation. The similitude concept can be logically deduced and more specific relations can be derived. In this paper, three fatigue crack growth theories are derived from the nature of the homogeneity of the deformation and fracture properties of the material within a crack growth process zone and from the crack-tip shear decohesion mechanism of fatigue crack growth. These three fatigue crack

[1]Lecturer, Department of Materials Science and Engineering, Zhejiang University, Hangzhou, Zhejiang 310027, China.

[2]Professor Emeritus, Mechanical Engineering, Syracuse University, Syracuse, NY 13244, USA.

Copyright © 1995 by ASTM International www.astm.org

growth theories constitute a logic framework useful to fatigue crack growth analyses. The logic framework is applied to the analyses of microstructural effects on fatigue crack growth in 7075-T651 aluminum alloy.

A fatigue crack grows in the alloy by crack-tip shear slip or shear decohesion forming striations. This is a ductile mode of fatigue crack growth. A fatigue crack can also grow by fractures of brittle particles followed by localized shear decohesion at these newly formed microcracks forming dimples. This is a more brittle mode of fatigue crack growth. The fatigue crack growth curve of the aluminum alloy has five distinct regions and four transition points. The crack growth behaviors in these five regions and at the transition points are identified with specific microstructural entities of the alloy. However, it should be understood at the outset that the deductive reasoning can only point out the more probable reasons for such crack growth behaviors. Systematic empirical studies are needed to substantiate these proposed theories.

A LOGIC FRAMEWORK FOR FATIGUE CRACK GROWTH ANALYSES

In this section, three fatigue crack growth theories will be derived. The derivations of these three theories have been reported earlier [1, 2, 3, 4] and they have been reviewed recently [5]. However, for the sake of completeness in discussing the applications of these theories to the analyses of microstructural effects on fatigue crack growth in the next section, a brief but self-contained review of these theories are given.

The Nature of Material Homogeneity and Fatigue Crack Growth Rate Relations

The linear elastic crack-tip stresses and strains, LECTS, are given below [6, 7].

$$[\sigma_{ij}(r,\theta),\ \varepsilon_{ij}(r,\theta)] = \frac{K}{\sqrt{2\pi r}}\,[\tilde{\sigma}_{ij}(\theta),\ \tilde{\varepsilon}_{ij}(\theta)] \tag{1}$$

where

$\sigma_{ij}(r,\theta)$, $\varepsilon_{ij}(r,\theta)$ = characteristic crack-tip stresses and strains

r, θ = crack-tip polar coordinates

K = stress intensity factor

$\tilde{\sigma}_{ij}(\theta)$, $\tilde{\varepsilon}_{ij}(\theta)$ = known functions of θ.

Equation (1) clearly indicates that K alone is capable of characterizing the entire linear-elastic crack-tip stress and strain fields. However, this equation is valid only within a small region, r_E, near a crack tip. If a cyclic stress of constant amplitude and constant mean stress is applied, the cyclic LECTS are characterized by stress intensity factor range, ΔK, and stress ratio, $R = K_{min}/K_{max}$. In other words, at the same combination of ΔK and R, the cyclic linear-elastic crack-tip stress and strain fields are the same.

Near the tip of a crack in a metallic solid, high stresses cause plastic deformation. The elastic-plastic crack-tip stress and strain fields are characterized by J [8,9]. However, J field is not applicable when unloading takes place. Therefore, J-integral cannot be applied to fatigue crack growth indiscriminately. Furthermore, material inhomogeneity and crystal

anisotropy cause crack-tip stresses and strains to deviate from those calculated by continuum theories. This section will show that even if cyclic plastic deformation takes place, even if a material is inhomogeneous and anisotropic, ΔK and R still characterize the cyclic stresses and cyclic strains in the grains along a crack front. This capability of characterizing crack-tip stress and strain fields is the reason why da/dN correlates so well with ΔK.

Figure 1a shows a cracked plate with a plastic zone, r_p, which is embedded in the region of a characteristic linear-elastic crack-tip field, r_E. The region r_E is taken out as a free body shown in Figure 1b. If r_p is much smaller than r_E, i.e., $r_p << r_E$, the relaxation of the stresses within r_p caused by plastic deformation will not change the stresses on the boundary of r_E. Thus, the boundary stresses on r_E are given by Equation (1) and are prescribed solely by K. The boundary stresses determine uniquely the elastic-plastic stresses and strains within the free body including the region within r_p. The same cyclic boundary stresses on r_E give the same cyclic elastic-plastic stress and strain fields within r_p. This is true if $r_p << r_E$, and r_E is linearly proportional to the size of a specimen. Thus, r_p should be much smaller than all other dimensions of a sample. We conclude that *ΔK and R are capable of characterizing a two-dimensional cyclic crack-tip elastic-plastic stress-strain field if the condition of small scale yielding prevails.*

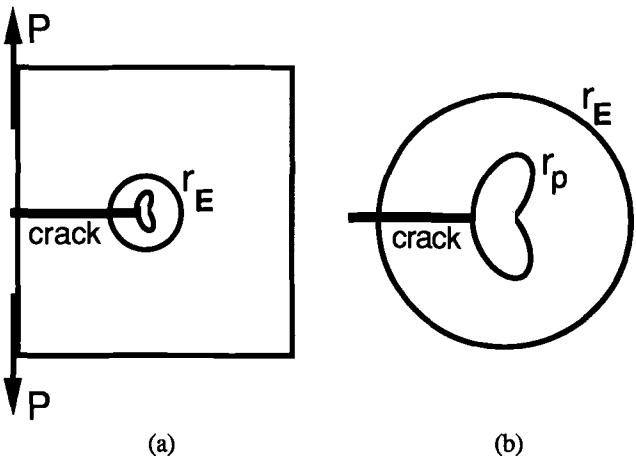


Fig. 1 (a) A cracked sample with a crack-tip plastic zone, r_p. r_E is the crack-tip region within which the linear elastic crack-tip field is valid.

(b) The region of r_E as a free body.

Crack tip stresses in a cracked plate are three dimensional. ΔK, R and plate thickness, B are needed for the characterizing of three dimensional crack-tip stresses and strains. However, if a plate is thick enough, only ΔK and R are necessary for the characterizing of a plain-strain cyclic elastic-plastic crack-tip field. In other words, at the came combination of ΔK and R, the cyclic elastic-plastic crack-tip stresses and strains are the same. Fatigue

crack growth is caused by cyclic stresses and cyclic strains at a crack tip. Same cyclic elastic-plastic crack-tip stresses and strains give the same da/dN. Thus,

$$\frac{da}{dN} = f(\Delta K, R) \tag{2}$$

The functional relation between da/dN and ΔK has to be found empirically. In the derivation of Equation (2), we have tacitly assumed that a material is homogeneous, i.e., the same cyclic crack-tip stresses and strains cause the same crack growth rate.

A fatigue crack grows by shear decohesion or by a combination of shear decohesion and brittle fractures. Figure 2a shows a dimple. The dimple is formed by the fracture of the inclusion followed by local shear decohesion at the microcrack. The successive crack fronts after the inclusion fracture can be traced in the figure. Fatigue striations are shown in Figures 2a and 2b. Striations are formed by cyclic shear decohesion at a crack tip.

In a polycrystal, there are a number of grains along a crack front as illustrated in Figure 3a. The rate of shear decohesion, the rate of brittle fractures of particles, and, thus, the rate of local crack growth vary greatly from grain to grain. However, in a laboratory test, the average growth rate over an entire crack front is measured. Only average growth rates correlate well with ΔK.

When r_p is smaller than grain diameter, the slip process in a crack-tip grain behaves like in a single crystal. Slip in a single crystal takes place in a slip plane in a slip direction, and the driving force of slip in single crystals is resolved shear stress. Thus, shear decohesion in single crystals is highly anisotropic. As r_p increases to enclose a large number of grains, see Figure 3b, the elastic-plastic deformation behavior of the grains within r_p approaches that of a polycrystal. In a polycrystal, extensive shear deformation is localized along shear lines. The slabs between neighboring shear lines are deformed lightly. If the grains in a polycrystal are randomly oriented, the deformation is isotropic, and shear lines coincide with planes of maximum shear stresses. Furthermore, the flow stress of a polycrystal is several times higher than that of a single crystal. Shear decohesion behaviors in single crystals and polycrystals are vastly different. As ΔK increases from a low value, crack-tip shear decohesion process changes from single crystal behavior to polycrystal behavior, and the detailed crack growth process changes accordingly. However, the *same* ΔK and R give the *same* statistical distribution of the cyclic stresses and strains in the grains within a crack growth process zone. The *same* distribution of crack-tip stresses and strains give the *same* average crack growth rate of the grains along a crack front. Thus, da/dN is a function of ΔK and R, i.e. Equation (2). This conclusion is, in essence, the similitude concept.

In the derivation of Equation (2), we have assumed material homogeneity. However, the homogeneity of crack growth behavior assumed in the derivation of Equation (2) is limited to same ΔK level. Thus, we say it is *limited homogeneity*. As ΔK changes, the basic crack growth behavior changes. The derivation also points out that the similitude concept is applicable only in the case of small scale yielding and the crack growth process must be limitedly homogeneous.

If ΔK is high enough and the number of grains in r_p is large enough, the collective deformation behavior of all the grains within r_p remains the same, and the collective shear decohesion process of all the grains along a crack front does not change as the size of r_p increases further. Thus, we say the deformation behavior and the crack growth process are *uniformly homogeneous*. In the case of limited homogeneity, the crack growth process is

closely related to the microstructure of a material and the basic crack growth process changes with ΔK. In the case of uniform homogeneity, the crack growth process remains the same regardless of the level of ΔK and the size of r_p.

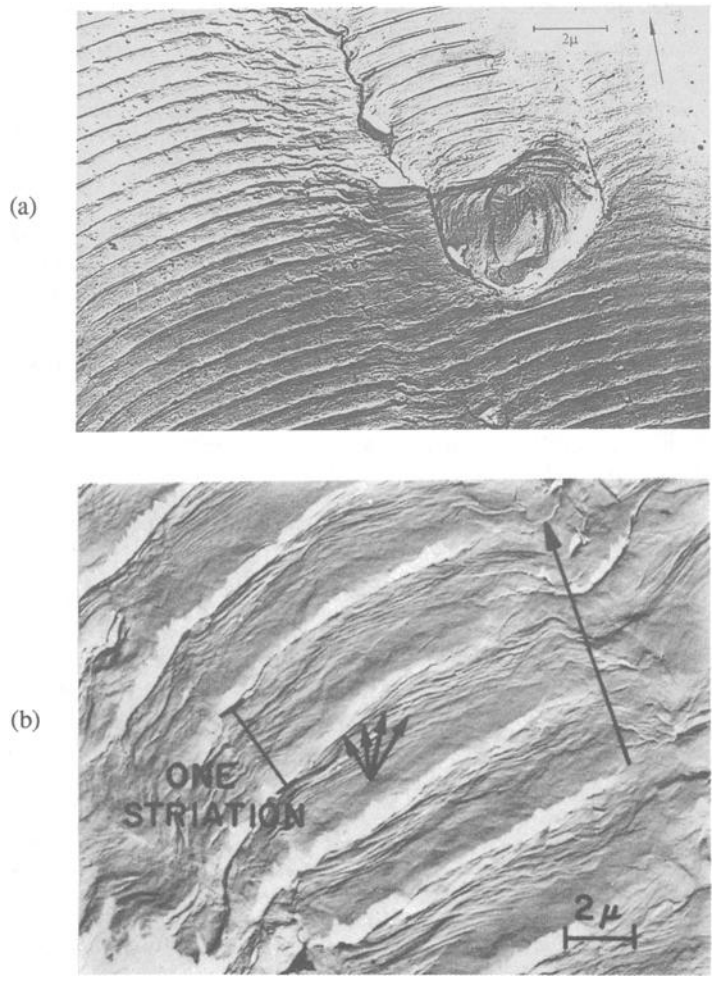


Fig. 2 (a) Striations and a large dimple on a crack surface in a 7075-T651 aluminum alloy. The successive crack fronts near the dimple can be traced.

(b) Striations on a copper crack surface. Several slip steps are within each striation. With the courtesy of C. Laird and the permission of ASTM. [10]

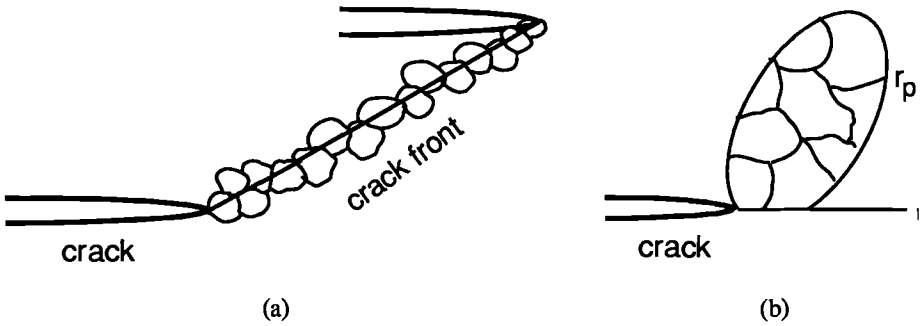


Fig. 3 (a) There are a number of grains along a crack front in a polycrystal.
(b) A large crack-tip plastic zone may enclose a number of grains.

Figure (4) shows two geometrically similar specimens of different sizes. The crack increments, Δa's, are proportional to their respective crack lengths, a's. The same boundary stresses are applied to both specimens. A simple dimensional analysis shows that the stresses and strains at geometrically similar points in these two specimens are identical. Therefore, the cyclic stresses and cyclic strains within these two Δa's must be identical. If r_p is large enough and the materials within r_p is uniformly homogeneous, the sams cyclic stresses and cyclic strains cause the same shear decohesion and micro fracture processes, thus, the same number of cycles, ΔN, are necessary to propagate through these crack increments. As a consequence, the growth rates in these two specimens are linearly proportional to their characteristic lengths, which can be either the diameters of the circular specimens or their corresponding crack lengths.

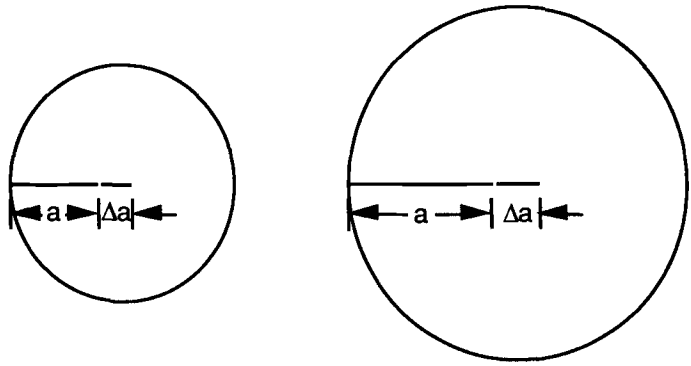


Fig. 4 Two geometrically similar specimens.

Two different samples are loaded to two different ΔK's. If the r_E's of these two samples are proportional to ΔK^2, according to Equation (1), the boundary stresses of these two r_E's

must be identical. If r_p is large enough and the material within r_p is uniformly homogeneous, the crack growth rates of these two samples must be linearly proportional to the characteristic lengths of the r_E's, which are, in turn, proportional to ΔK^2. Thus,

$$\frac{da}{dN} = f(R)\,\Delta K^2 \tag{3}$$

f(R) is an unknown function of R to be determined experimentally.

Plastic deformation was used to illustrate the concept of uniform homogeneity, but the concept is equally applicable to brittle fractures. For example, if the size and spacing of brittle particles are much smaller than striation spacings and if these particles are evenly distributed, the brittle fractures of these particles during a fatigue crack growth process are uniformly homogeneous. If this is true, Equation (3) is applicable even if brittle fractures take place during a crack growth process.

The Unzipping Model of Fatigue Crack Growth

A fatigue crack may grow by a combination of shear decohesion and brittle fractures. If a crack grows by shear decohesion alone and if a crack growth process is uniformly homogeneous, fatigue crack growth rate can be calculated explicitly [2,3,4]. The calculation of fatigue crack growth rate by a finite element model, the unzipping model, will be reviewed briefly in this section.

As K increases, extensive shear deformation takes place along shear lines, and the shear deformation in a slab between two neighboring shear lines is very light. The unzipping model assumes that all shear deformations are localized to shear lines. Figure 5 illustrates the shear decohesion process. Figure 5a shows two sets of mutually perpendicular shear lines at a crack tip. As K increases, one of the two shear lines at the crack tip, α, is activated and shear decohesion takes place. Figure 5b shows the crack-tip profile after the shear decohesion on α. As shear decohesion takes place, the shear stress on α is relaxed and the shear stress on the intersecting shear line b is built up. When the shear stress on b is raised high enough, the decohesion process shifts from α to b. The crack-tip profile after shear decohesions on both α and b is shown in Figure 5c. The crack-tip profile after additional shear decohesions on β and c is shown in Figure 5d. The shear decohesion process alternates between these two sets of shear lines. As shear decohesion takes place on the shear lines, the slab between two neighboring shear lines moves away from the

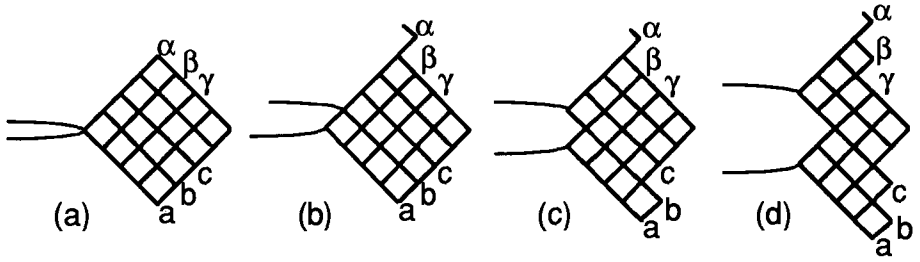


Fig. 5 Crack-tip shear decohesion process

crack tip like the teeth of a zipper during an unzipping process. The alternating shear decohesion process forms shear steps during a fatigue cycle. Several small shear steps within a single striation are clearly visible in Figure 2b.

Figure 6 shows the geometric relation between shear decohesion, crack-tip opening and crack growth. Two shear lines, A and B, are shown. The shear displacements across these shear lines are discontinuous. The discontinuous shear displacement at a crack tip causes shear decohesion, crack-tip opening and crack growth. Only the shear displacement of the shear line at the very tip of a crack, such as A, contributes to crack growth. The shear displacement at a shear line away from a crack tip, such as B, contributes to crack-tip blunting, but not to crack growth. A mechanical model for the calculation of fatigue crack growth rate has to incorporate these two physical features: discontinuous shear displacement and only the shear decohesion at the very tip of a crack contributes to crack growth.

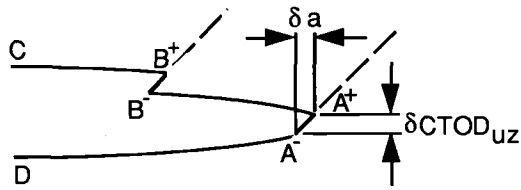


Fig. 6 The geometric relation between $\delta CTOD_{uz}$, δa and crack-tip blunting. Only the shear decohesion of the shear line at the very tip of a crack causes crack growth.

Earlier continuum calculations have shown that CTOD is proportional to K^2 [11,12]. The unzipping model assumes the same general relationship

$$CTOD_{uz} = C\,(1 - \nu^2)\,\frac{K^2}{E\,\sigma_Y} \tag{4}$$

$CTOD_{uz}$ = crack-tip opening displacement due to unzipping process

K = stress intensity factor

ν = Poisson's ratio

E = Young's modulus

σ_Y = yield stress

C = an unknown constant of proportionality.

Differentiating both sides of the equation, we obtain

$$\delta CTOD_{uz} = 2C\,(1 - \nu^2)\frac{K\,\delta K}{E\,\sigma_Y} \tag{5}$$

The constant C is calculated by the finite element unzipping model. First, a load of K is applied, and the crack-tip plastic zone is delineated as shown schematically in Figure 7. A line of shear decohesion, AB, from the crack tip to the boundary of r_p is defined. Then, a small increment δK is applied. During the application of δK, the nodal points along shear line AB are branched. The branched nodal points are allowed to glide along AB, but they are not allowed to move away from the line. During the application of δK, the tangential nodal forces of the branched nodal points are kept constant, and all the elements are allowed to deform according to the elastic-plastic constitutive relation. The calculated value of $\delta CTOD_{uz}$ together with the values of the imposed K and δK are used to evaluate C. Once C is found, Equation (4) can be used to calculate the opening displacement, $CTOD_{uz}$. $CTOD_{uz}$ is related geometrically to crack increment, Δa, as shown in Figure 6. The unzipping model does incorporate the features of discontinuous shear slip at a crack tip and the fact that only the shear slip at a crack tip contributes to crack growth.

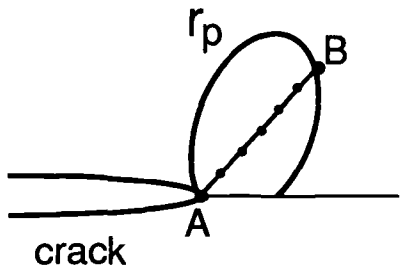


Fig. 7 Crack-tip plastic zone. AB is a shear line. The nodal points along the shear line are shown.

However, Equation (4) is calculated for a static load. The calculated crack increment, Δa, corresponds to the crack growth as K increases from K_{min} to K_{max} during a cyclic load. Thus, the relation between Δa and K of the static calculation becomes the relation between da/dN and ΔK. As K fluctuates between K_{min} and K_{max}, the material within r_p experiences a cyclic stress from σ_{min} to σ_{max}, and the cyclic stress has a positive mean stress. Repeated stress cycles within r_p cause mean stress relaxation. If the mean stress is fully relaxed to zero, the stresses within r_p at K_{max} are close to the cyclic flow stress of a material, thus, σ_Y in Equation (4) should be replaced by cyclic yield stress, $\sigma_{Y(C)}$.

$$\frac{da}{dN} = 0.04\,(1 - \nu^2)\,\frac{\Delta K^2}{E\,\sigma_{Y(C)}} = 0.04\,\frac{\Delta J}{\sigma_{Y(C)}} \tag{6a}$$

If the mean stress is not relaxed at all, the stresses within r_p at K_{max} are close to twice of the cyclic flow stress, thus, σ_Y should be replaced by $2\sigma_{Y(C)}$.

$$\frac{da}{dN} = 0.02\,(1 - \nu^2)\,\frac{\Delta K^2}{E\,\sigma_{Y(C)}} = 0.02\,\frac{\Delta J}{\sigma_{Y(C)}} \tag{6a}$$

ΔJ is the range of the J-integral of a cyclic load. Equations (6a) and (6b) give fatigue crack growth rate explicitly without any adjustable constant. The crack growth rates given by these two equations are limiting cases. Actual crack growth rate is somewhere in between. The calculated and measured crack growth rates agree surprisingly well [4,13].

Summary: In the state of small scale yielding and plane strain, if the material within a fatigue crack growth process zone is limitedly homogeneous, $da/dN = f(\Delta K,R)$; and if the material is uniformly homogeneous, $da/dN = f(R)\ \Delta K^2$. If the material is uniformly homogeneous and if a fatigue crack grows only by shear decohesion, da/dN is given by Equations (6a) and (6b). With each additional condition imposed, the crack growth equation becomes more specific. These three theories constitute a logic framework which is useful to the analyses of microstructural effects on fatigue crack growth.

ANALYSES OF MICROSTRUCTURAL EFFECTS ON FATIGUE CRACK GROWTH IN 7075-T651 ALUMINUM ALLOY

In this section, the logic framework developed in the last section will be used to analyze the microstructural effects on fatigue crack growth in 7075-T651 aluminum alloy. Before going into the analyses of microstructural effects, a brief review of a few general concepts may help to clarify the ensuing discussions. A fatigue crack grows by the mechanisms of shear decohesion, brittle fractures, and a combination of brittle fractures and localized shear decohesion forming dimples. A strong resistance to dislocation motion slows down the growth by shear decohesion. On the other hand, when a major dislocation barrier is overcome or when brittle fractures and dimple formation start to make significant contributions, da/dN increases rapidly with ΔK. Dislocation barriers in an aluminum alloy include solute atoms, precipitates, dispersoids, inclusions and grain boundaries. Inclusions and, perhaps, dispersoids are susceptible to brittle fracture. The relations between the fatigue crack growth behaviors of the aluminum alloy and some of these microstructural entities will be pointed out. Another useful concept established in the last section is that when a crack growth process becomes uniformly homogeneous, da/dN is proportional to ΔK^2.

Experimental Procedures and Results

Fatigue crack growth rates and striation spacings in 7075-T651 aluminum alloy were measured. Compact tension specimens 9.53 mm thick in the L-T orientation were tested. All tests were conducted in laboratory air at the stress ratio R = 0.1 and 0.5.

Commonly, the smallest particles (0.005 - 0.02 μm) are called precipitates; the intermediate size particles (0.02 - 0.5 μm) dispersoids; and the largest particles (1 μm and larger) inclusions or constituent particles [14]. Truckner et al. [15] found that the dispersoids in ingot 7075 aluminum alloy are principally $Al_{12}Mg_2Cr$ compound and the compositions of constituent particles are compounds of aluminum, copper, iron, magnesium and silicon.

Figure 8 shows two fatigue crack growth curves at R = 0.1 and 0.5. Each crack growth curve can be divided into 5 regions. The transition points, $T_{i,j}$, from region i to region j for the curve at R = 0.1 are marked. The five-region crack growth curve profiles are similar to

the ones reported by Robinson and Beevers for a titanium alloy [16] and by Bucci et al. for a laboratory fabricated 7000 series aluminum alloy [17].

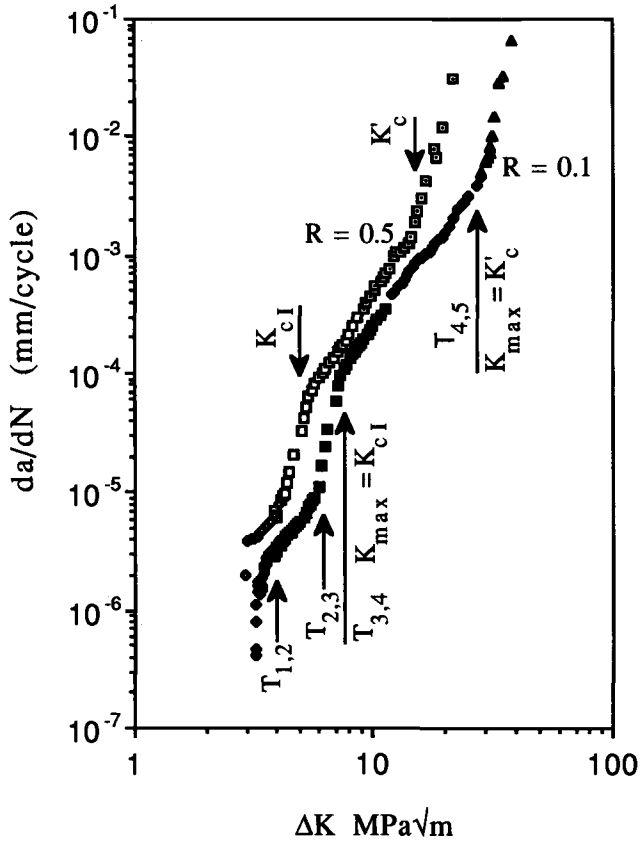


Fig. 8 Fatigue crack growth data. 7075-T651 aluminum alloy. R = 0.1 and 0.5. Each crack growth curve has 5 regions and 4 transition points.

Each striation marks the crack increment during a fatigue cycle. Thus, striation spacing is the local crack growth rate caused by the mechanism of shear decohesion. Fatigue striation spacings were measured in the direction perpendicular to striations. The measured striation spacings in region 4 are shown in Figure 9. Even at a given ΔK, striation spacings vary widely. Only the spacings averaged over a large area of a crack surface correlate well with ΔK. The striation spacing data in Figure 9 were obtained from nearly 200 fractographs.

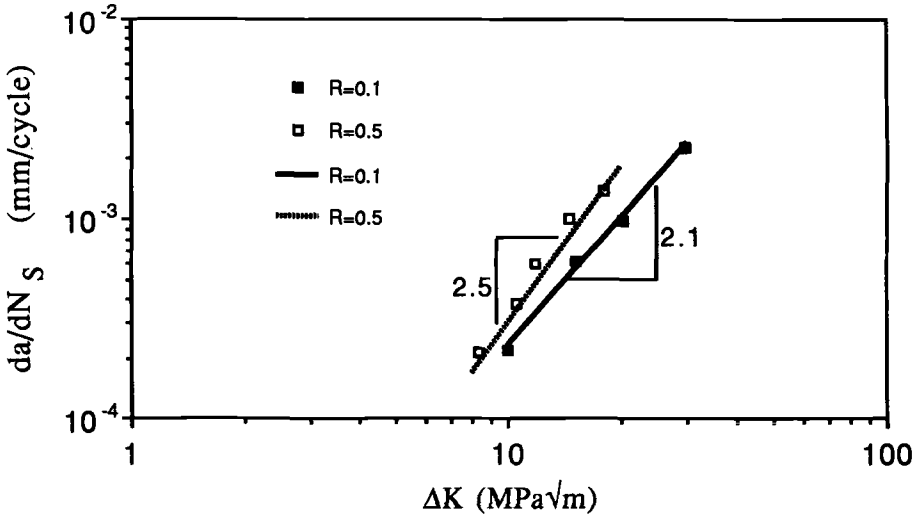


Fig. 9 Striation spacings in region 4. Solid points for R = 0.1. Open points for R = 0.5.

The Effects of Inclusions on da/dN in Regions 4 and 5.

In region 4, a crack grows by both striation growth and dimple growth. The fractographs in Figures 10a and 10b show both striations and dimples at a low and a high ΔK in the region. A dimple is formed by local shear decohesion at a fractured inclusion. The local shear decohesion marks or local striations next to a cracked inclusion can be detected at the lower ΔK in Figure 10a and can be seen clearly at the higher ΔK in Figure 10b. Dimple density, dimple size, and the amount of dimple growth increase rapidly with ΔK. Above $T_{4,5}$, most of the striations are associated with dimples. Away from dimples, there are very few striations. The crack growth mechanism in region 5 follows a sequence of events of void nucleation by inclusion fracture, dimple formation by local shear decohesion, and dimple coalescence. When dimple coalescence becomes the major crack growth mechanism in region 5, da/dN increases rapidly. At a ΔK below region 4, there are hardly any dimples.

In region 4, the measured crack growth rates, Figure 8, are higher than the measured striation spacings, Figure 9. The difference is attributed to dimple growth.

$$\frac{da}{dN_D} = \frac{da}{dN} - \frac{da}{dN_S} \tag{7}$$

where

$\frac{da}{dN_D}$ = rate of dimple growth

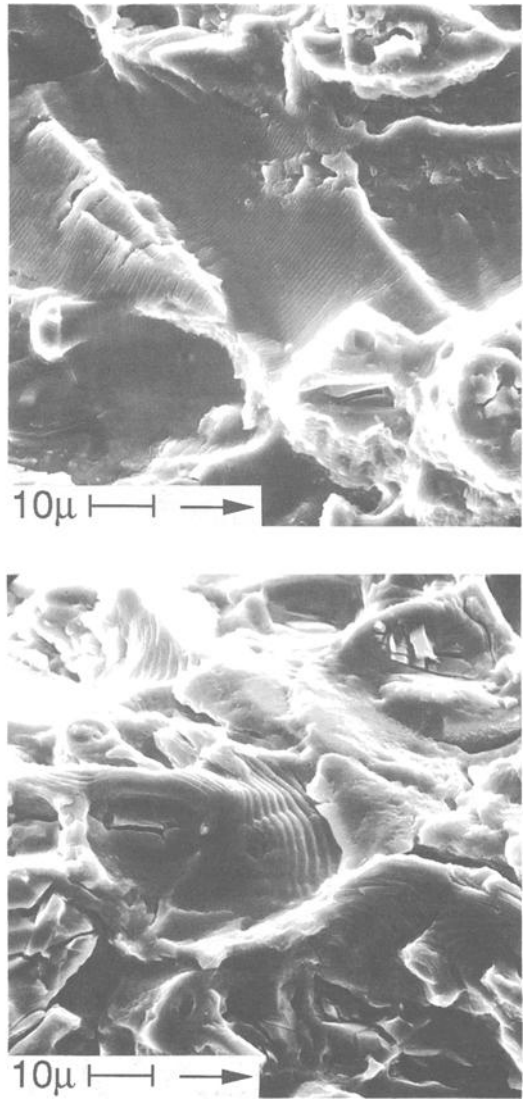


Fig. 10 Fractographs. Cracks grew horizontally from left to right.

(a) $\Delta K = 15.1$ MPa$\sqrt{m}$. da/dN = 8.8×10^{-4} mm/cycle. Lower dimple density.

(b) $\Delta K = 29.5$ MPa$\sqrt{m}$. da/dN = 6.1×10^{-3} nn/cycle. K_{max} very close to K'_c. Larger dimples and higher dimple density.

$\frac{da}{dN}$ = measured crack growth rate

$\frac{da}{dN_S}$ = striation spacing = rate of striation growth

Define a ratio $\alpha = \frac{da}{dN_D} / \frac{da}{dN}$ as the fraction of dimple growth. Figure 11 shows the empirical relation between α and the quantity $[(K_{max} - K_{cI})/K'_c]$. K_{cI} and K'_c are empirical constants. Two lines for R = 0.1 and 0.5 are very close to each other. However, at a given ΔK, the striation spacings and the rate of dimple growth at R = 0.5 are higher than those at R = 0.1. Close to $T_{4,5}$, α is more than 0.8. When ΔK approaches $T_{4,5}$, the amount of striation growth is greatly reduced.

The data in Figure 11 suggest the empirical relation

$$\alpha = \beta \left(\frac{K_{max} - K_{cI}}{K'_c}\right)^m \tag{8a}$$

$$\alpha = 0.81 \left(\frac{K_{max} - 8.4}{31}\right)^{0.57} \quad \text{at } R = 0.1 \tag{8b}$$

and

$$\alpha = 0.70 \left(\frac{K_{max} - 10.0}{30}\right)^{0.72} \quad \text{at } R = 0.5 \tag{8c}$$

K_{max}, K_{cI} and K'_c are in MPa$\sqrt{m}$. When $K_{max} > K_{cI}$, inclusions fracture ahead of a crack tip. When $K_{max} < K_{cI}$, dimples can hardly be found, crack-tip stresses are not strong enough to cause inclusion fractures, and inclusions serve as dislocation barriers, which resist shear decohesion and retard crack growth. Thus, the segment of a crack front at an inclusion lags behind. In either cases of fracturing ahead or lagging behind, the nominal K is not the local K at the instance of the fracture of an inclusion. When an inclusion fractures at the instance when it reaches a crack front as shown in Figure 2a, the nominal K is the local K at the inclusion. This happens when $K_{max} = K_{cI}$, and $\alpha = 0$. Thus, K_{cI} is the micro fracture toughness of the inclusions.

When the local tensile stress at a crack tip is equal to or exceeds the cleavage strength of an inclusion or the debonding strength at an inclusion/matrix interface, micro-fracture takes place. With the Hutchinson-Rice-Rosengren elastic-plastic crack-tip field, the cohesive and debonding strength can be evaluated.

$$\sigma_{Co} \text{ or } \sigma_{Db} = \sigma_Y^{(N-1)/(N+1)} \left(\frac{K_{cI}^2}{D}\right)^{1/(N+1)} \tag{9a}$$

or

$$\sigma_{Co} \text{ or } \sigma_{Db} = \sigma_Y^{(1-n)/(1+n)} \left(\frac{K_{cI}^2}{D}\right)^{n/(1+n)} \tag{9b}$$

where

σ_{Co}, σ_{Db} = cohesive strength, debonding strength

D = particle size

n = strain hardening exponent

N = 1/n

σ_Y = yield stress

The quantitative evaluation of K_{cI} provides a methodology to carry the microstructural analysis one step further to cohesive or debonding strength. A more realistic cyclic crack-tip stress field will certainly improve the methodology.

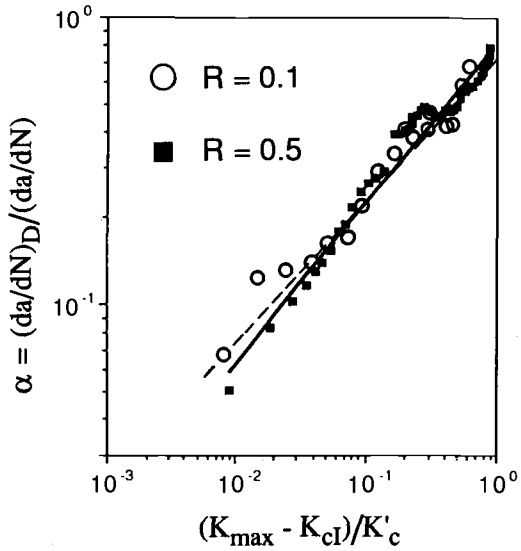


Fig. 11 α - the fraction of crack growth rate caused by inclusion fracture and dimple formation. α as a function of K_{max}.

Striation Spacings in Region 4

The measured striation spacing, $(da/dN)_S$, in Figure 9 is proportional to $\Delta K^{2.1}$ and $\Delta K^{2.6}$ at R = 0.1 and 0.5, respectively. The dependency of $(da/dN)_S$ on ΔK is stronger at R = 0.5. At a high R-value, inclusions are likely to fracture ahead of a crack tip and grow to large dimples. When a dimple merges with a main crack, the local crack front bulges out as shown in Figure 2a. If neighboring dimples are closely spaced along a crack front as illustrated in Figure 12, the local ΔK along the convex crack front lagging behind is higher than nominal ΔK. If dimple density along a crack front is very high, this increased local ΔK gives much wider striation spacings, even if striation spacings are measured away from dimples. The stronger dependency of $(da/dN)_S$ on ΔK at R = 0.5 is caused primarily by the increase in local ΔK due to the interaction of crack-tip field with dimples.

At R = 0.1, the density and the size of dimples are lower and the interaction of crack-tip stress field with dimples is much less than those at R = 0.5. The exponent 2.1 at R = 0.1

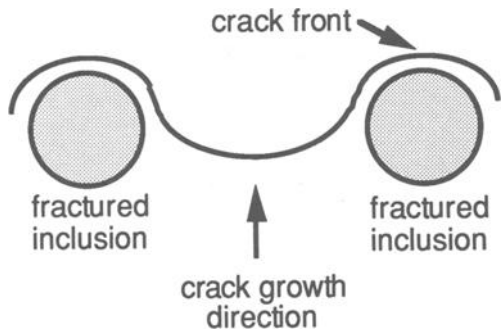


Fig. 12 Schematic diagram showing two dimples and a curved crack front. The segment of the crack front lagging behind has a higher K.

indicates that crack growth process zone is large enough so that the deformation and fracture behaviors within the process zone become uniformly homogeneous.

With ΔK in MPa$\sqrt{m}$, E = 71,000 MPa and $\sigma_{Y(C)}$ = 525 MPa [18], Equations (6a) and (6b) become

$$\frac{da}{dN}\,(\text{mm/cycle}) = 0.26\,\frac{\Delta K^2}{\sigma_{Y(C)}} = 0.96\text{x}10^{-6}\,\Delta K^2\,, \tag{10a}$$

when mean stress is fully relaxed.

$$\frac{da}{dN}\,(\text{mm/cycle}) = 0.133\,\frac{\Delta K^2}{\sigma_{Y(C)}} = 0.48\text{x}10^{-6}\,\Delta K^2\,, \tag{10b}$$

without mean stress relaxation. Equation (10a) gives a higher crack growth rate. At ΔK = 10 MPa$\sqrt{m}$, Equation (10a) gives da/dN = $0.96\text{x}10^{-4}$ mm/cycle. The measured da/dN and striation spacing at the same ΔK at R = 0.1 are 2.2 and $2.1\text{x}10^{-4}$ mm/cycle, which are more than 2.2 times higher than the calculated growth rate. The accuracy of the calculation has not been assessed. However, the difference between the measured and calculated rates is too large to be accounted for by the inaccuracy of the unzipping model alone. Perhaps, the formation of striations is not by the mechanism of shear decohesion alone, the fractures of dispersoids may have also contributed to the crack growth process. Dispersoids are small and evenly distributed, thus, the fracture behavior of the dispersoids is uniformly homogeneous and the slope of the striation spacing curve remains close to two.

Measured striation spacings of a variety of materials are plotted against J/σ_{flow} in Figure 13. The solid lines are calculated with the unzipping model for two values of $\sigma_{Y(C)}$: $\sigma_{Y(C)} = \sigma_{flow}$ and $\sigma_{Y(C)} = \sigma_{flow}/2$. The majority of the measured values fit between these two lines. It is interesting to note that the data of the high strength steels and titanium alloy are close to the upper line, while the data of the low strength steels and copper alloys are close to the lower line. It would be interesting to find out if the larger striation spacings of the high strength materials are partly caused by brittle fractures of their particles. The fact that a high strength material, which is usually more brittle, has a wide striation spacing is consistent with the contention that the fractures of dispersoids may have increased the size

of striation spacings in the 7075-T651 aluminum alloy. It is likely that the crack growths in the ductile steels and copper alloys are caused by shear decohesion alone without brittle fractures of particles.

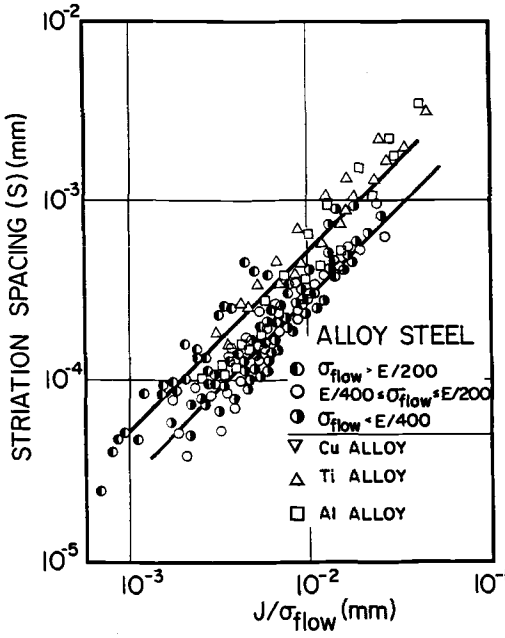


Fig. 13 Striation spacing vs J/σ_{flow}

Direct calculation of fatigue crack growth rate due to cyclic shear decohesion is rather complicated, cyclic stress-strain data needed for the calculation is lacking, and the calculation must be lengthy. Perhaps, a more accurate unzipping fatigue crack growth rate relation can be found empirically by measuring the crack growth rates and striation spacings in ductile materials.

Transition Points $T_{3,4}$ and $T_{2,3}$, and Crack Growth Rate in Region 3

Transition point $T_{3,4}$ coincides with the point at $K_{max} = K_{cI}$ as shown in Figure 8. Below K_{cI}, there are very few dimples. It is tempting to conclude that $T_{3,4}$ is associated with the beginning of the formation of dimples. However, this fails to explain why the crack growth curve changes from a very steep slope in region 3 to a much smaller slope closer to two in region 4. If the rapid decrease in da/dN in region 3 is caused by the resistance of inclusions to dislocation motion, the da/dN in the region must be sensitive to inclusion content. This is contrary to what has been observed by Soudani and Pelloux [19] that below $T_{3,4}$, the amount of inclusions has negligible effect on the crack growth rate in 7075-T651 aluminum alloy.

Yoder et al. analyzed fatigue crack growth behaviors in 7000 series aluminum alloys including the 7075-T651 alloy [20]. They suggested that each transition point is associated with a microstructural length, and $T_{3,4}$ is associated with grain size. The discontinuity between the slip systems of two neighboring grains causes multiple slip and rapid strain hardening. As a consequence, grain boundaries increase resistance to shear decohesion and retard fatigue crack growth. Chen [21] has shown, Figure 14, that as a crack approaches a grain boundary, GB, da/dN decreases five fold. Conversely, as grain boundary resistance to dislocation motion is overcome by a strong stress field, fatigue crack growth rate increases rapidly. When $r_{p(C)}$ approaches the grain size of the alloy at $T_{2,3}$, dislocations start to penetrate grain boundaries in a large scale, and da/dN starts to increase rapidly. When $r_{p(C)}$ approaches 2 to 3 times the grain size, the effect of grain boundary strengthening is fully realized, the cyclic deformation and fracture behaviors of the material within $r_{p(C)}$ become uniformly homogeneous, and the striation spacing in region 4 becomes proportional to ΔK^2. The measured striation spacings in region 4 are much larger than the calculated ones. The discrepancy is possibly caused by the fractures of dispersoids. Thus, it is also possible that the rapid increase in da/dN in region 3 is partly caused by the fractures of dispersoids.

We have suggested that at $T_{3,4}$, $r_{p(C)}$ is 2 to 3 times grain size, and at $T_{2,3}$, $r_{p(C)}$ is nearly equal to grain size. Thus, the ratio of the ΔK's at $T_{3,4}$ and $T_{2,3}$ should be $\sqrt{2}$ to $\sqrt{3}$ or 1.4 to 1.7. $r_{p(C)}$ is approximately given by

$$r_{p(C)} = \frac{1}{6\pi} \frac{\Delta K^2}{\sigma_{Y(C)}{}^2} \tag{11}$$

The data in Figure 8 give the ratios of 1.3 and 1.5 for R = 0.1 and 0.5, respectively.

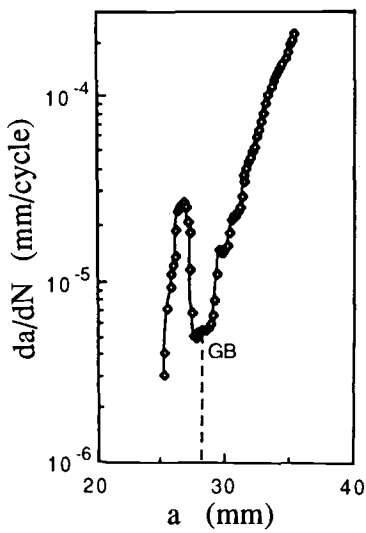


Fig. 14 FCG retardation at grain boundary. Al 7029 alloy. [21]

We have also suggested that both $T_{3,4}$ and $T_{2,3}$ are related to grain size. The grains of the alloy are elongated. The size in the longitudinal direction is 100 to 150 μm, and the size in the transverse direction is approximately 30 μm. For R = 0.1, ΔK at $T_{3,4}$ is 8 MPa$\sqrt{m}$. With $\sigma_{Y(C)}$ = 525 MPa, $r_{p(C)} \approx$ 13 μm. This is the size of $r_{p(C)}$ in the direction of a crack line. In the direction of shear slip, $r_{p(C)}$ is 4 to 5 times bigger. Thus, $r_{p(C)} \approx$ 52 to 65 μm, which is 1.7 to 2.2 times the grain size in the transverse direction. This is less than 2 to 3 times grain size as we have just suggested. However, in view of the crude calculations of $r_{p(C)}$, these estimates are acceptable.

da/dN in Regions 1 and 2 and the Transition Point $T_{1,2}$

Near ΔK_{th}, the crack-tip stress field is weak. Without environmental effects, a crack-tip stress field is not strong enough to fracture particles, thus, a fatigue crack is likely to grow by a mechanism of cyclic plastic deformation. Yoder et al. [20] indicate that, in region 1, $r_{p(C)}$ is close to the spacing between dispersoids and dispersoids are likely the primary dislocation barriers pertinent to the crack growth process. In the region, as the resistance to dislocation motion by dispersoids is overcome, da/dN increases rapidly with ΔK. Perhaps, $r_{p(C)}$ at $T_{1,2}$ is several times dispersoid spacing, and beyond $T_{1,2}$ cyclic shear decohesion behavior becomes uniformly homogeneous. Therefore, da/dN in region 2 is nearly proportional to ΔK^2 as shown by the data in Figure 8.

It is well-known that water vapor accelerates fatigue crack growth in 7075-T651 aluminum alloy. Water vapor reduces the stress necessary to emit dislocations from a crack tip [22,23]. Thus, it reduces ΔK_{th} and increases da/dN. Since a chemical process is usually slow, the environmental effect should be more pronounced in regions 1 and 2. The environmental effect can be incorporated into a mechanical analysis, when the details of the chemical process become known. A more detailed discussion on the effects of water vapor will be given in a forthcoming paper [24].

SUMMARY AND CONCLUSIONS

Three fatigue crack growth theories are deduced for the state of small scale yielding and plane strain.

(1) If a material is limitedly homogeneous, $\frac{da}{dN} = f(\Delta K, R)$ (2)

(2) If a material is uniformly homogeneous, $\frac{da}{dN} = f(R)\ \Delta K^2$ (3)

(3) If a material is uniformly homogeneous and if a crack grows by shear decohesion without any brittle fracture.

$$\frac{da}{dN} = 0.04\ (1 - \nu^2)\ \frac{\Delta K^2}{E\ \sigma_{Y(C)}}$$ Mean stress fully relaxed (6a)

$$\frac{da}{dN} = 0.02\ (1 - \nu^2)\ \frac{\Delta K^2}{E\ \sigma_{Y(C)}}$$ Without mean stress relaxation (6b)

(4) When shear decohesion and micro-fracture behaviors are dependent on the size of crack growth process zone, such behaviors are limitedly homogeneous and are intimately related to the microstructure of a material. When shear decohesion and micro-fracture behaviors are uniformly homogeneous, these behaviors are independent of the size of crack growth process zone and the microstructure of a material.

The deduced theories are used to analyze fatigue crack growth behaviors in 7075-T651 aluminum alloy.

(5) The fatigue crack growth curve of the 7075-T651 aluminum alloy can be divided into five regions with four transition points. Striation growth and dimple growth are the primary crack growth mechanisms of the aluminum alloy.

(6) In region 4, a fatigue crack grows by a combination of striation growth and dimple growth. $r_{p(C)}$ is large enough, so that crack-tip shear decohesion behavior is uniformly homogeneous. Thus, striation spacing in the region is proportional to ΔK^2.

(7) Fatigue crack growth in region 5 follows a sequence of events of brittle inclusion fractures, local shear decohesion forming dimples and dimple coalescence.

(8) In region 3, grain boundary resistance to fatigue crack growth is grossly overcome by crack-tip stresses. Therefore, da/dN increases rapidly with ΔK.

(9) In regions 1 and 2, the crack growth behaviors are related to either dispersoids or the chemical effect of water vapor. In a low ΔK region, dispersoids could be the primary dislocation barriers pertinent to the crack growth process. If this is the case, in region 1, the resistance of dispersoids begins to be overcome, and da/dN increases rapidly with ΔK. As $r_{p(C)}$ in region 2 becomes large enough so that the shear decohesion behavior becomes uniformly homogeneous, da/dN is nearly proportional to ΔK^2. Water vapor accelerate fatigue crack growth rate of 7075-T651 aluminum alloy. The environmental effect should be more pronounced in regions 1 and 2.

It should be pointed out that deductive reasoning can only suggest a probable relation between a crack growth behavior and a specific microstructure entity. Direct experimental evidence is needed to substantiate some of these suggested relations.

ACKNOWLEDGMENT:

Financial support by the NASA Lewis Research Center (Grant No. NAG 3-837) and the Department of Mechanical and Aerospace Engineering of Syracuse University is acknowledged. The authors are also obliged to Dr. R. B. Hanna of the College of Environmental Science and Forestry, SUNY, for his assistance in electron microscopy.

REFERENCES:

[1] H.W. Liu, "An Analysis on Fatigue Crack Propagation", NASA CR-2032, May 1972.

[2] A.S. Kuo, "An experimental and FEM study on crack opening displacement and its application to fatigue crack growth", Ph.D. Dissertation, Solid State Science and Technology, Syracuse University, 1976.

[3] A.S. Kuo and H.W. Liu, Scripta Metallurgica, **10**, 1976, 723.

[4] H.W. Liu, International Journal of Fracture, **39**, 1988, 63-77.

[5] H.W. Liu, Theoretical and Applied Fracture Mechanics, **16**, 1991, 91-108.

[6] M.L. Williams, J. of Applied Mechanics, March 1957, 109.

[7] G.R. Irwin, J. of Applied Mechanics, Sept. 1957, 361.

[8] J. Hutchinson, J. Mechanics and Physics of Solids, **16**, 1968, 13-31.

[9] J.R. Rice and G.F. Rosengren, J. Mech. and Physics of Solids, **16**, 1968, 1-12.

[10] C. Laird, *Fatigue crack propagation*, ASTM STP 415, 1967, 131.

[11] D.S. Dugdale, J. of Mechanics and Physics of Solids, **8**, 1960, 100.

[12] C.F. Shih and M.D. German, Intn. J. of Fracture, **17**, 1981, 27-43.

[13] H.W. Liu and H. Kobayashi, Scripta Metallurgica, **14**, May 1980, 525-530.

[14] D.L. Davidson and J. Lankford, Materials Science and Engineering, 74, 1985, 189.

[15] W.G. Truckner, J.T. Staley, R.J. Bucci and A.B. Thakker, Tech. Rep, AFML-TR-76-169, Air Force Materials Lab., Wright-Patterson Air Force Base, OH, 1976, 24.

[16] J. L. Robinson and C. J. Beevers, Metal Science Journal, **7**, 1973, 153.

[17] R.J. Bucci, A.K. Vasudevan, P.E. Bretz, R.C. Malcolm, Interim Report, July 1, 79 to Aug. 31, 80, to Naval Air Systems Command, Contract No. N00019-79-C-0258, Alcoa Lab. Alcoa Center, PA., 1980.

[18] L. E. Tucker, R. W. Landgraf and W. R. Brose, SAE Report 740279, Automotive Engineering Congress, Feb. 1974.

[19] S. M. El-Soudani and R. M. Pelloux, Met. Trans. **4**, 1973, 519.

[20] G.R. Yoder, L.A. Cooley and T.W. Crooker, Scripta Metallurgica, **16**, 1982, 1021

[21] Qi Chen, "Shear fatigue crack growth analysis in large grain polycrystals", Ph.D. dissertation, Solid State Science and Technology, Syracuse University, 1992.

[22] S. P. Lynch, Acta Metall., **36**, No. 10, 1988, 2639.

[23] H. K. Birnbaum, in Hydrogen Effects on Material Behavior, Edited by N. R. Moody and A. W. Thompson, The Mineral, Metals, & Materials Society,1990, 639.

[24] H. W. Liu, Jian Guo Xu, Wang You Wen, "A Logic Framework for Fatigue Crack Growth Analyses and Its Application to Microstructural Effects", to be published.

Frederick W. Brust[1]

NUMERICAL MODELING AND EXPERIMENTS OF CREEP CRACK GROWTH UNDER CYCLIC LOADING

REFERENCE: Xu, J. G., and Liu, H. W., **"The Application of a Logic Framework for Fatigue Crack Growth Analyses to Microstructural Effects,"** Fracture Mechanics: 26th Volume, ASTM STP 1256, Walter G. Reuter, John H. Underwood, and James C. Newman, Jr., Eds., American Society for Testing and Materials, Philadelphia, 1995.

ABSTRACT: This paper presents a summary of some recent studies of creep crack growth under history dependent load conditions. The effect of a proper constitutive law is illustrated. Moreover, the asymptotic fields are reconsidered under cyclic creep conditions. In addition, several experiments are modeled and the behavior of integral parameters is discussed.

KEYWORDS: creep crack growth, high temperature, T^*-integral, finite element analysis, experiments

The demands for structural systems to perform reliably under severe high temperature operation continues to increase. These demands will continue with the development of advanced power generation methods and in future aerospace applications. Moreover, power generation equipment in the US continues to age and is being used far beyond its intended design life. Because of this, an understanding of the high-temperature creep crack growth process, which is a frequent failure mechanism in these structures, is important.

As noted by Prager [1], the executive director of the Materials Property Council (MPC), historically equipment became obsolete, and was replaced with new designs, before the potential creep fatigue failure time was reached. As a result, experience with creep failures under nominal design conditions has been limited. Some recent failures of high energy steam pipes in fossil power plants (see Lundin, et al. [2]), which were highly publicized and occurred with serious consequences, have clearly illustrated that creep rupture failures must be prevented. From the MPC studies (References [1] to [3]) and field experience it is now known that current engineering methods to predict the life of components that operate in these severe environments are ineffective.

[1] Currently at Georgia Institute of Technology, Atlanta, Georgia, 30332.

Copyright © 1995 by ASTM International www.astm.org

The objective of this paper is to develop a fundamental understanding of the deformation and failure response of cracked bodies which experience history dependent or cyclic loading at high temperature. This effort builds on a previous ongoing work, with some of the results discussed in References [3] to [12]. Peripheral objectives include: (i) The discussion of a computational tool which includes high temperature constitutive laws and special fracture features. (ii) The discussion of an experimental data base for variable load creep crack growth conditions. (iii) Further development and verification of a high temperature history dependent fracture predictive technique.

BACKGROUND

Monotonic Load. The classic empirical approach consists of relating creep crack growth rates (da/dt = å) with some Correlating Parameter (CP) as å = f (CP), as typified in References [13] to [26]. Here the function, f, is generally some simple functional form, such as a power law. Knowing the initial crack (flaw) size, one may estimate the life of the structural component by simply integrating the crack growth rate function with respect to time. A similar method is also used for predicting the life of structural components subject to fatigue and stress corrosion cracking. This approach has dominated the creep crack growth studies up to this point.

Early studies utilized the stress intensity factor, K, as the correlating parameter (reference [13]) which is appropriate under small scale creep conditions. Under large scale creep conditions, the C^*-integral has been used extensively as CP to correlate creep crack growth under large scale steady state creep crack growth conditions as discussed in references [14-21].

Many structural components experience operating conditions in which nonsteady-state creep crack growth occurs. Recognizing this, Saxena [22 to 24] has proposed the C_t parameter, which is an extension of C^* into the transient regime. Reference [24] clearly shows that crack growth rates correlate with C_t for a variety of different conditions for Cr-Mo-V steel. Leung and McDowell [25] provide careful numerical studies of the behavior and performance of C_t for a stationary crack.

Cyclic Load. These efforts represent the philosophy of the experimental/design approach to creep crack growth. When modest cyclic loads are present with creep crack growth, a simple Miner's rule is applied, as summarized in References [17, 26 to 37].

A model suggested by Jaske [17], which is a variation of Manson's [28] partitioning relationships, separates the crack growth into (independent and separate) fatigue and time dependent contributions. The fatigue portion is related to the increment in J-integral (ΔJ), while the time dependent portion relates crack growth rates to the C^*-integral. Koterazawa [29] has recently proposed simply relating crack growth rates, å, to ΔJ. Both of these approaches cannot be considered universally acceptable because (i) ΔJ is based on Dowlings [30] area under the load-displacement curve which cannot be easily determined except in laboratory specimens (i.e. predictions in real components are not easily made), and (ii) both ΔJ and C^* loose their meaning as the strength of the asymptotic crack tip fields when variable loads are applied, as discussed later here.

Logsdon, et al. [31],[32] used a partitioning technique where the creep hold time was included as a variable in the fatigue equation along with the stress intensity factor range. They observed that the hold times could significantly alter creep crack growth rates. However, as noted earlier and discussed in detail in Reference [33], ΔK is expected to correlate creep fatigue crack growth rates only under limited low load situations. Saxena, et al. [34],[35] attempt to characterize the elevated temperature hold times during fatigue conditions by relating average crack growth rates to average values of C_t during the hold times, although the correlations are not entirely convincing. Finally, Liaw, et al. [36],[37] have presented a life prediction methodology for creep fatigue in steam pipes. This method sums up the crack growth which accumulates for each load-hold period over the life. Each increment of crack growth which accumulates during a hold period (t_h) is determined by relating å to C_t and integrating from 0 to t_h. While this technique may be useful for some engineering predictions, it is not general since the history of the load-hold and unload-hold periods (as discussed in the Analysis Section) cannot be accounted for.

These approaches appear to provide adequate design predictions under moderate conditions. Unfortunately, for components which experience severe load conditions, e.g. modern jet and space vehicle engines and modern and aging power plants, these simple approaches appear to be inadequate. Kim, et al. [33] found that integral parameters (to be discussed later) can characterize creep crack growth in severe load history environments of the space shuttle main engine while correlations with other parameters were inadequate. References [4] to [12] have found similar potential for integral creep fracture parameters.

CREEP RESPONSE UNDER CYCLIC LOADING

The creep behavior of a smooth bar and cracked body subjected to history dependent loading are summarized here.

Smooth Bar

Consider the load versus time history, the total creep strain accumulation, and creep strain rate response of a smooth bar which is uniaxially loaded in a history dependent fashion as illustrated in Figure 1. Figure 1a illustrates a uniaxial bar which is loaded, unloaded to negative stress at t_1, and held, reloaded to σ at time = t_2 and held until time = t_3, then finally unloaded and held at negative stress. Figure 1b illustrates the total creep strain which develops as a function of time. Note that after each stress reversal, the creep strain increases rapidly for a period of time. Also shown in Figure 1b are the corresponding strain versus time responses for the constant load case and when assuming classical strain hardening theory of creep. Figure 1c shows the corresponding strain rate versus time response. Note that after each stress reversal, the strain rate increases immediately to a large value. Note also from Figure 1b that the strains predicted using classical strain hardening theory greatly under-predict the response.

If the stress in Figure 1a is reduced after time t_1, but to a non-negative value, this effect is negligible. Hence, it is the stress reversals from positive to negative values and vice-versa

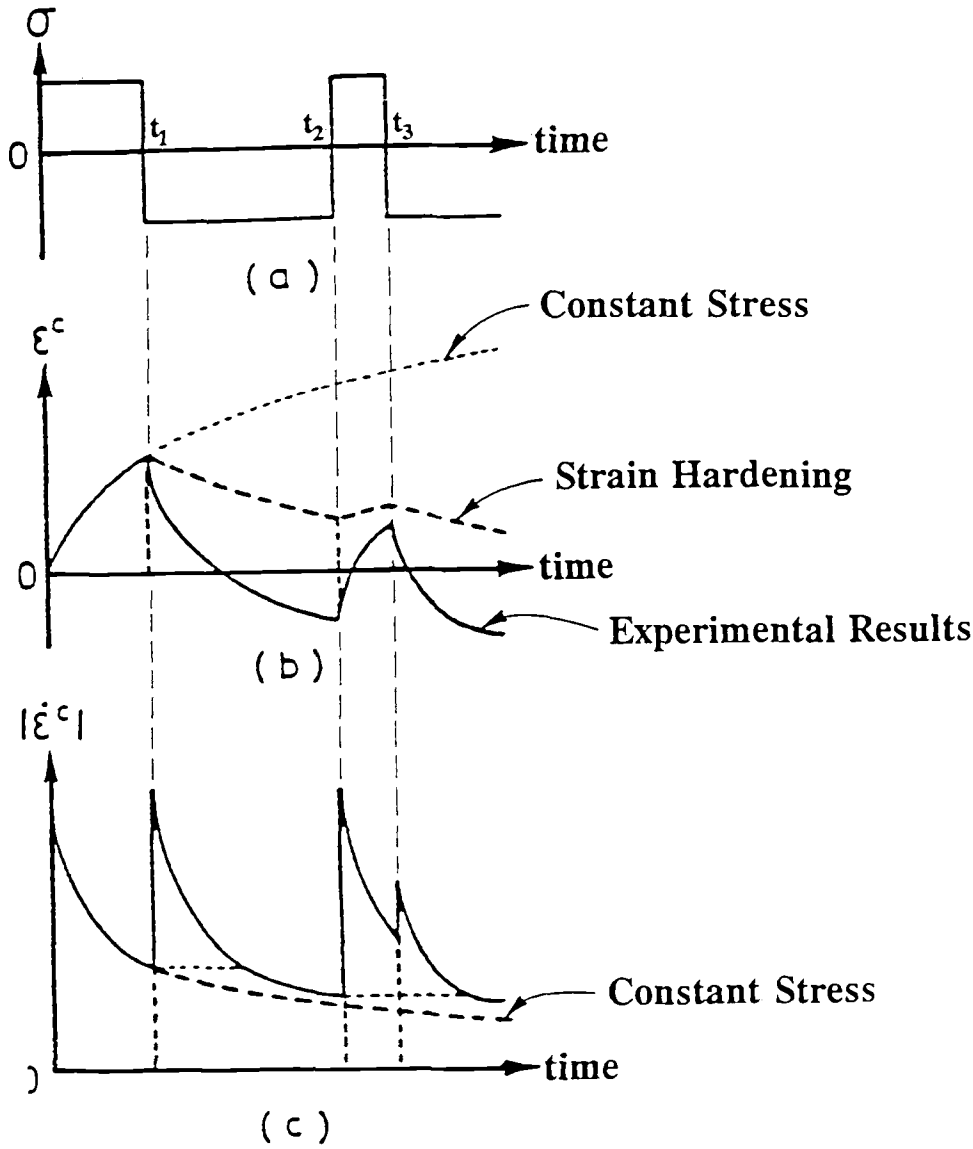


FIG. 1 *Creep response under stress reversals.*

that are important. It is seen next that these stress reversals occur near a crack tip under history dependent loading even if the applied (global) load is not reversed to a negative load.

Creep in a Cracked Body

Consider a cracked body which is loaded and held for a period of time so that a tensile creep zone has developed which emanates from the cracked body. Upon removal of the load,

stress reversal occurs almost immediately at the crack tip because of the localized creep strains previously developed in that region. When the load is completely removed a zone of compressive stresses which can be quite significant in size will develop. Figure 2 illustrates this effect. An experiment was conducted on a compact tension specimen which was subjected to a load spectrum consisting of: (i) load and hold for 24 Hrs., (ii) unload to zero load and hold for 6 minutes (0.1 Hr.), etc. The test lasted for about 30 days. This experiment was modeled in its entirety via the finite element method (see reference [12] for details). Figure 2 represents the compressive stress zones which exist at different periods of time both before and after crack growth, *at the end of the load hold times.* Figure 3 illustrates a blowup of the crack tip zone at time = 677.1 Hr which shows both the finite element mesh refinement, and detailed contour levels. It is seen that the compressive stress zones are quite significant despite the fact that the unload was only to zero load.

There are three important consequences on the creep crack growth process caused by this effect: (i) during the unload hold period, the crack opening displacement *decreases* due to the compressive creep strains which develop at the crack tip; also (ii) the creep strain rates become large and strain hardening or the Norton Creep law significantly underestimate these rates (Figure 1); finally, (iii) after reloading, creep strain rates near the crack tip where stresses again reverse from compressive to tensile, again become quite large. The net result is cyclic stressing near the crack tip which causes large creep strain rates after each unloading or loading sequence. It is clear that neglecting these reversals by using classical creep constitutive theories may be quite non-conservative (Figure 1b).

GENERAL EXPERIMENTAL TRENDS

Several important general conclusions based on experimental results can be made regarding load history dependent creep crack growth (see references [6], [8-9], and [12] :

- During the unload-hold period, load point displacement recovery occurs. This is due to the compressive stresses which develop at the crack tip during unload. This zone of compressive stresses near the crack tip can be quite large, as was seen in Figures 2 and 3, even if the global load is never less than zero. For negative R-ratios, this effect is even more pronounced.

- After reload, the displacement rates increase compared to the rates during the previous loading period. Also the displacement just after reloading is always smaller than the corresponding value just before unloading.

- Load history effects significantly decrease life compared to the constant load tests because of this continual stress changing, and corresponding large creep strain rates, which occur in the crack tip region.

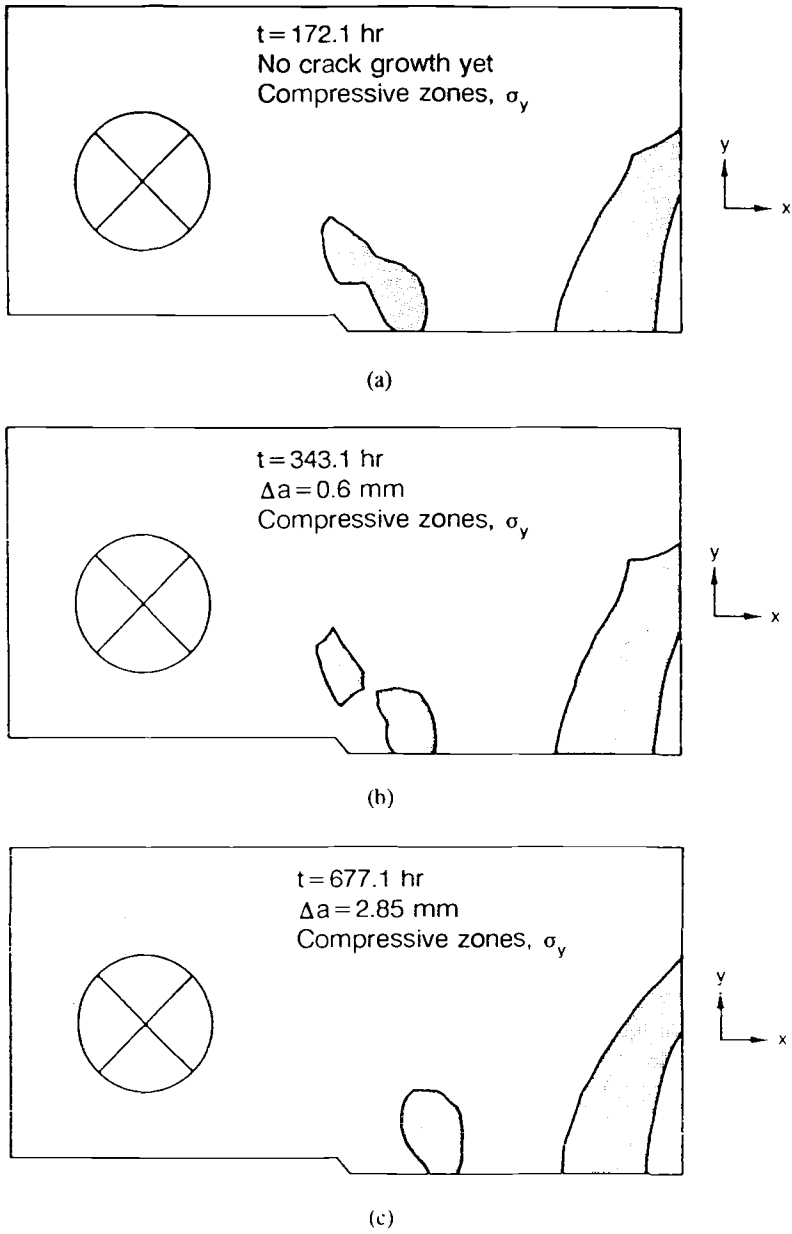


FIG 2 *Compressive stress zones after unloading and holding for 0.1 hours.*

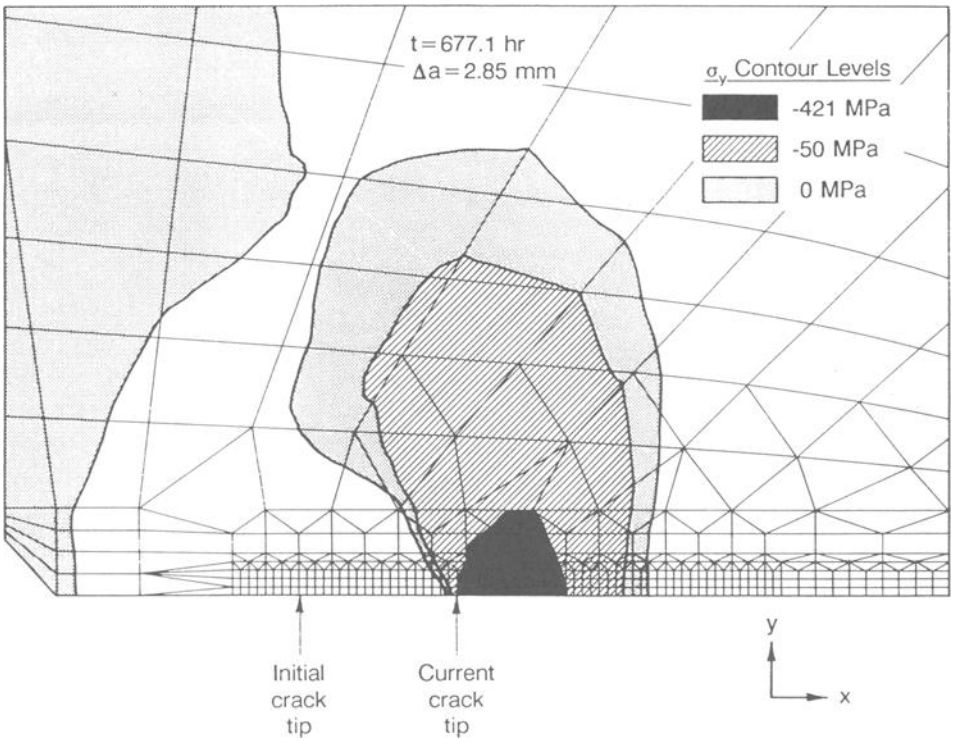


FIG 3 *Contour plots of* σ_y *near the time of 677 hours. The contour levels represent the values at the outermost border of the shade. The size of the elements along the crack growth direction near the tip are 0.15 mm along the side.*

CREEP FRACTURE PARAMETERS

Making a choice as to which fracture parameter(s) to focus on when attempting to characterize history dependent creep crack growth is difficult. We have placed different approaches into three categories: asymptotic approaches, damage or local approaches, and energetic or integral approaches.

Asymptotic approaches, wherein one develops the asymptotic solution to the crack problem for the situation of interest (elastic, plastic, creep, etc.) and fracture criterion is based on the strength of that field, work quite well for monotonically loaded problems [38].

However, for history dependent loading, the asymptotic field changes during each cycle (examination of such fields will be reported in the next section). Such fields are also known to change during crack growth. Moreover, the asymptotic field itself depends strongly on the constitutive law chosen. Hence, it is concluded that asymptotic approaches are impractical for characterizing history dependent fracture.

Local approaches (Reference [39]) are quite useful for predicting crack nucleation for all types of damage, including creep. For crack problems, however, there appears to be a problem. The procedure for both coupled or uncoupled damage theories consists of (i) develop the critical material parameter (scaler or tensor) D_c, (ii) determine a critical length parameter, l_c, i.e. the degree of the finite element refinement near the crack tip, so that experimental behavior is predicted. This same critical dimension is required for all other analyses. Because damage localizes at the crack tip, one finds that predicted results become more and more conservative as the mesh becomes more refined. This is because the finer the mesh, the greater the stress and strain gradients near the crack tip become. The need for this critical length parameter appears to render such methods insufficiently general to extend their use to history dependent creep damage.

Integral parameters have shown promise in several non-linear applications. A number of crack tip parameters expressed in integral forms have appeared in the literature. These include Blackburn [40] (J_B); Kishimoto, Aoki, and Sakata [41] ($\hat{J}$); McClintock [42] (J_M); Watanabe [43] (J_W); Goldman and Hutchinson [44] (C^*); Brust and Atluri [45] (T^*); Cherepanov [46]; and others. If an asymptotic crack tip solution with a free amplitude parameter exists (as for a stationary crack), then it can be shown that the strength of the field can be written in terms of the chosen integral, as long as the integral is of order 0 (1/r).

The physical interpretation of many of these integral parameters is not entirely clear except for the T^*. Brust, Nakagaki, and Gilles [47] showed that the physical interpretation of the T^* integral is that of the energy release rate to a finite sized material volume in the vicinity of the crack tip. (To save space, we eliminate mathematical details of all integrals and their interpretation.) The ability of the T^* integral and other parameters to characterize nonlinear fracture have been documented in References [46,47].

Finally, the NASA Lewis (and their engine subcontractors) have experienced great success in attempting to use integral parameters to characterize high temperature severe load (creep-fatigue) conditions (Kim et al. [33]). The NASA approach is to develop a simple engine fatigue life design procedure by writing the crack growth rate per load cycle as a simple function of the change in integral parameters. This result is a simple extension of classical fatigue life prediction based on the stress intensity factor or J-integral.

FINITE ELEMENT MODELS AND CONSTITUTIVE MODELS

The influence of the constitutive model used to represent time dependent materials on the stress and strain fields in the vicinity of a crack tip have been shown to be significant (see Leung et al. reference [25]), even for constant sustained load. As discussed regarding Figures 1 to 3, upon stress reversal, a temporary increase in strain rate has been observed due to strain softening. Classical time or strain hardening (S-H) creep laws, upon which most

of the current engineering approaches to predicting creep crack growth are based, are incapable of predicting these phenomena. The next section will clearly illustrate this. In the Inoue benchmark problems (reference [48]), a model developed by Murakami and Ohno [49] and a improved by Ohno et al. [50] provided as good or better predictions of complex load response in the creep regime (of the type in figure 1, and more complicated) compared to more than ten different models. The Murakami-Ohno (M-O) law has the advantage of having very simple material property requirements. The mathematical structure, and the complicated effort required to obtain material properties for other recently proposed constitutive models render their use in numerical analyses of the creeping crack problem cumbersome.

The constitutive law used for most of the creep crack growth analyses presented here is based on the concept of a creep hardening surface (CHS) developed by Murakami and Ohno (references [49-50]). This model is quite convenient since the material property requirements consist of only the classical time hardening material constants (A, n, m), and the two Norton law constants, A_1, n_1.

A finite element (FE) algorithm using an implicit scheme has been developed for the Ohno and Murakami constitutive model and discussed in Krishnaswamy et. al. [4,6]. The implicit method used here has the advantage of ensuring convergent and stable solution for large time step sizes, unlike explicit integration schemes. The details of the algorithm have been omitted here and may be found in the cited references. Numerous comparisons using the implicit algorithm are compared to experimental data and to strain hardening theory and are also presented in Krishnaswamy [4] with good results.

The computational model for all analyses consisted of 8-noded isoparametric elements using plane stress or plane strain assumptions. Crack growth was modeled using a node release technique where the nodal forces at both nodes in the particular element the crack is growing through are released simultaneously over a period of time. The integral fracture parameters were calculated using existing element shape functions and nodal averaged field quantities using a direct approach (i.e., a domain integral approach was not used).

CRACK TIP FIELDS FOR CYCLIC CREEP

Asymptotic Solutions to date. Most practical methods for predicting the lives of cracked structural components which operate at temperatures where creep occurs are based on a series of asymptotic solutions using the Norton steady state creep law. For instance, Goldman and Hutchinson [15] used a steady state creep law and showed that the asymptotic solution for a stationary crack is:

$$\sigma_{ij} = C_1 (P_1 / r)^{\frac{1}{n_1+1}} f_{ij}(\theta) \qquad (1)$$

In equation 1, C_1 is a constant which depends on material constants, r and θ are polar coordinates centered at the crack tip (see Figure 3(c)), f_{ij} depend on the angle. P_1 is a rate parameter which depends on geometry of the cracked body, and represents the strength of this field. For primary creep only, Riedel [38] developed the asymptotic solution as:

$$\sigma_{ij} = C(P/r)^{\frac{1}{n+1}} g_{ij}(\theta) \tag{2}$$

In equation 2 the definitions are analogous to equation 1. In both equations, the strength of the singular field depends on the creep hardening exponent , i.e. n_1 (steady state creep), or n (strain hardening creep). P_1 in equation 1 may be identified as the C^*-integral (Goldman and Hutchinson [15]), while P_1 in equation 2 has been defined by Riedel [38] as C^*_h. Riedel and Rice [51], then took the solution of equation 1 (based on steady state creep law), and developed solutions for a creep zone developing in an initially elastic body. The rate parameter which describes the strength of the asymptotic fields was estimated from the elastic field to full scale creep in the body. Since that time, solutions for stationary and growing cracks based on a material law described by primary and secondary creep laws have been developed, many of which are summarized by Riedel [38].

Saxena [23-24] then developed an engineering methodology based on all of these solutions. This approach uses a parameter named C_t, which basically uses the above discussed solutions where they are appropriate, eg. primary creep, or steady state solutions, etc. are utilized to estimate C_t where they are appropriate. This methodology is very nice because C_t may be measured experimentally and estimated analytically.

There are several important points regarding this methodology which must be pointed out: (i) The entire solution methodology is only valid when using the simple constitutive law described above; (ii) C^*, C^*_h, C_t, and other approaches discussed in the introduction are rate parameters, and as such, cannot be used to predict crack nucleation; (iii) All parameters depend explicitly on the material parameters in the constitutive law , for instance:

$$C_t = C_t(n, n_1, \ldots) \tag{3}$$

Hence, if one uses another constitutive law, as is required when variable loads must be considered, these parameters are undefined, and a number of assumptions must be made.

The asymptotic fields upon which the above described engineering approach is based are not valid under history dependent loading. This point is discussed in the next subsection.

Asymptotic Solutions. Consider a standard compact tension specimen with dimensions illustrated in Figure 4. A finite element analysis of this specimen was performed using creep properties of both 9 Cr-Mo Steel at 538 C and 304 stainless steel (SS) at 650 C. A load spectrum was applied that consisted of a load and hold for 24 Hours, unload and hold for 1 Hour, reload and hold for 24 Hours. Both R=0 and R= -0.5 spectrum were used. This spectrum was applied up to 99 total hours. This means that the end of the load-hold periods were 24, 49, 74, and 99 hours while the end of the unload-hold periods were 25, 50, and 75 hours (4 load and 3 unload periods). The material properties are:

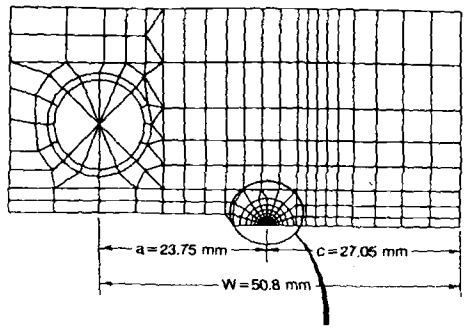


FIG 4(a) *Finite element mesh for 9 Cr-Mo analysis.*

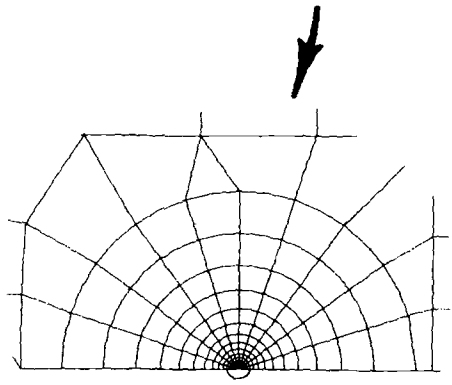


FIG 4(b) *Crack tip mesh blow-up.*

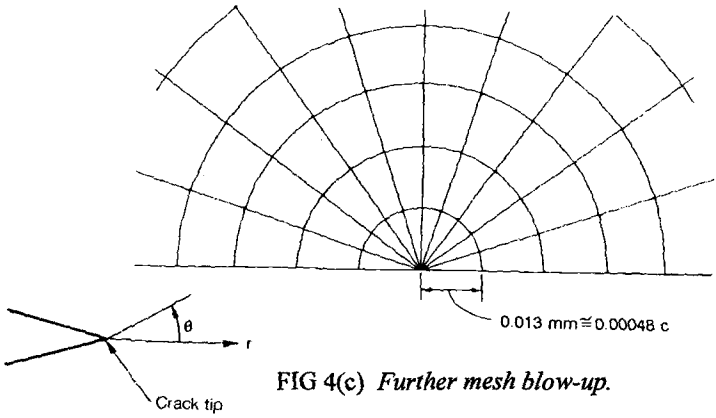


FIG 4(c) *Further mesh blow-up.*

$A = 7.09 \times 10^{-17}$, n = 5.6, m = 0.24 (9 Cr-Mo) (Ref. [8])

$A = 3.10 \times 10^{-19}$, n = 7.2, m = 0.54 (304 SS) (Ref. [49])

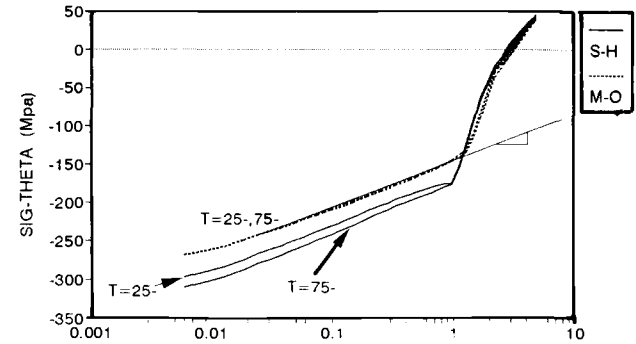
for stress in MPa and time in hours. These same constants are used for a strain hardening law and for the Murakami-Ohno cyclic creep law.

The element size at the crack tip is about 0.00048 c, which is about two and one-half times more refined compared to the mesh used by Shih and German [52] in their studies of HRR field dominance.

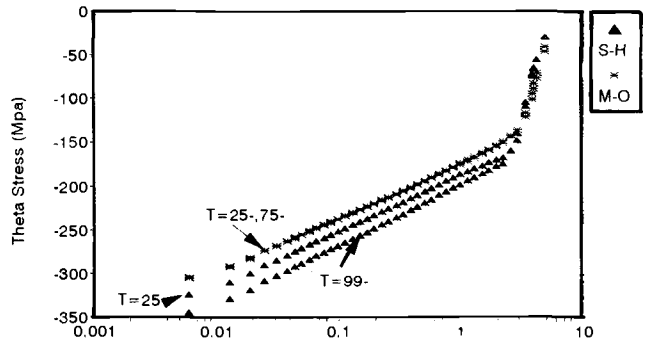
Since the strain rates are quite different depending upon the model which is used after each unload or reload sequence, it is clear that the total accumulated stresses and strains differ also. Figure 5a and 5b show the stresses that develop in the R = 0 and R = -0.5 cases (respectively) for the 304 SS at 650 C at the end of the unload-hold times. (S-H refers to "Strain Hardening" and M-O refers to "Murakami Ohno" constitutive laws in these figures.) Figure 5c similarly shows the stresses at the same times for the R=0 load spectrum for the 9 Cr-Mo case. Figures 5a-c provide plots of σ_θ plotted from the crack tip at the θ=0 line ahead of the crack tip. Note that these figures plot the stress as a function of log(R). In Figure 5a notice the straight line drawn through the Murakami-Ohno results. In fact, for all three cases shown in figure 5, the stresses for the Murakami-Ohno (M-O) cases plot as straight lines, i.e. the singularity appears to be logarithmic. In fact, the results for the Strain-Hardening (S-H) case also appear to have an asymptotic logarithmic relation as a function of distance from the crack tip, R. Also, note in all three figures, that the M-O results appear to converge to one solution, independent of time, while the S-H solution continues to drift away from the M-O solution as time, or cycles, accumulate. One can also observe the size of the compressive zone ahead of the crack tip in these figures. The size of this compressive stress zone is obviously largest for the R= -0.5 case, but note that it not insignificant in size for any of the cases. Recall from the earlier discussion that this zone of compressive stresses, or stress reversal, which occurs despite the fact that the global loads are only zero (for the R=0 cases), is the only source of the differences between the M-O and S-H constitutive laws.

The transition time, as defined by Riedel [51], between small scale creep to the primary creep limit, where creep strains dominate elastic strains is about 24 hours for the 304 SS and less than about two hours for the 9 Cr-Mo steel. These times, which are valid only for monotonic loading and hold, and using a strain hardening creep law, indicate that, for the 304 SS case, transient conditions are still prevalent at the end of the 24 Hr hold periods, and especially, at the end of the one Hr hold periods. Despite this, the stresses are changing very slowly at the end of the one-hour unload period. This was verified by performing another analysis with unload-hold times of 24 hours for the R = 0 case. Basically no differences between the stresses at the end of 1 Hr or 24 Hr hold periods were observed. On the other hand, for the 9 Cr-Mo steel, primary creep conditions dominate at the end of both the load and unload hold times.

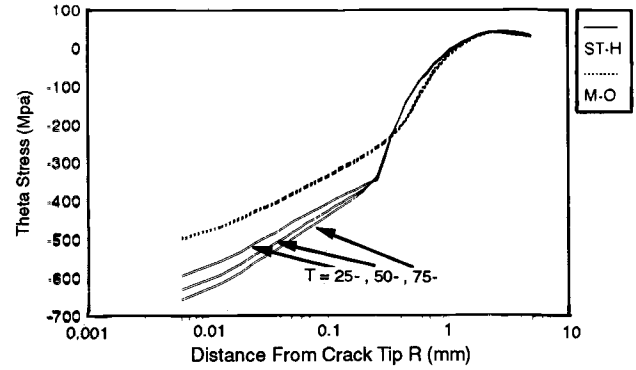
At the end of the load hold times, i.e. time = 24, 49, 74, 99 hours, similar differences occur between the strain hardening and the Murakami-Ohno solutions. However, let us first observe the asymptotic fields for the S-H law. Figure 6 illustrates the σ_θ component of stress



(a) 304SS, R = 0 case.



(b) 304SS R = -0.5 case.



(c) 9Cr-Mo R = 0 case.

FIG 5 σ_θ *stresses plotted as a function of distance from the crack tip for* $\theta = 0$. *See Figure 6 for coordinate definitions. Results are for times of 25 and 75 hours, i. e., after unload-hold sequences.*

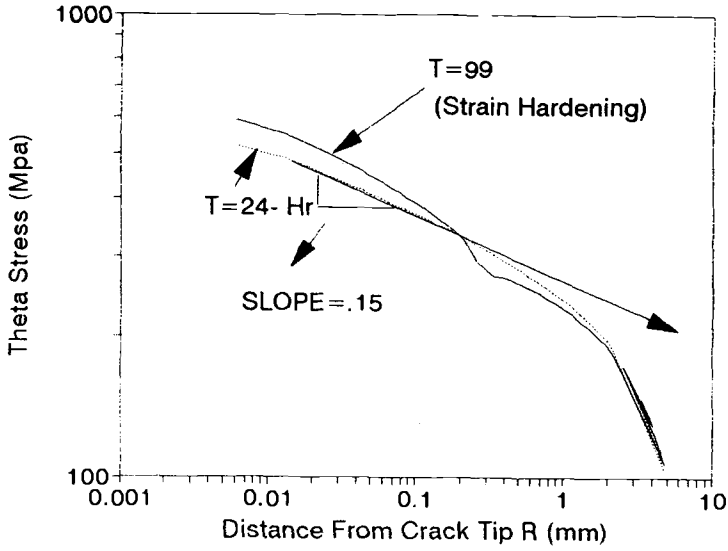


FIG 6 σ_θ *as a function of distance from crack tip for* $\theta = 0$. *Strain hardening solution for 9Cr-Mo steel.*

for $\theta = 0$ degrees as a function of distance from the crack tip. This is for the 9 Cr-Mo steel and the axis scales are logarithmic. The stress approaches the Reidel Strain Hardening field, with a slope of n/(n+1), for n = 5.6. The asymptotic field is realized for a distance of almost .5 mm from the crack tip before any unload cycles are applied at a time of 24 hours. This slope is illustrated with the arrow in figure 6. Similar results are also seen for the 304 SS, although not shown here. Note from figure 6 that the stress field strays from the power law form after the third unload-hold period at time of 99 hours. In fact, it is uncertain that the power law form of the Reidel asymptotic solution characterizes this field at all after unloading occurs. The drift away from this power law form appears to increase as the number of cycles accumulate. This suggests that the asymptotic forms of the equations, and hence, the strength of the singularity changes with variable cycles.

Figure 7a again shows the θ component of stress at an angle of zero, also as a function of distance from the crack tip. Figure 7a shows the stresses at the end of the hold times for 304 SS; R= -0.5 case. Note that these plots show stresses versus log(r). The

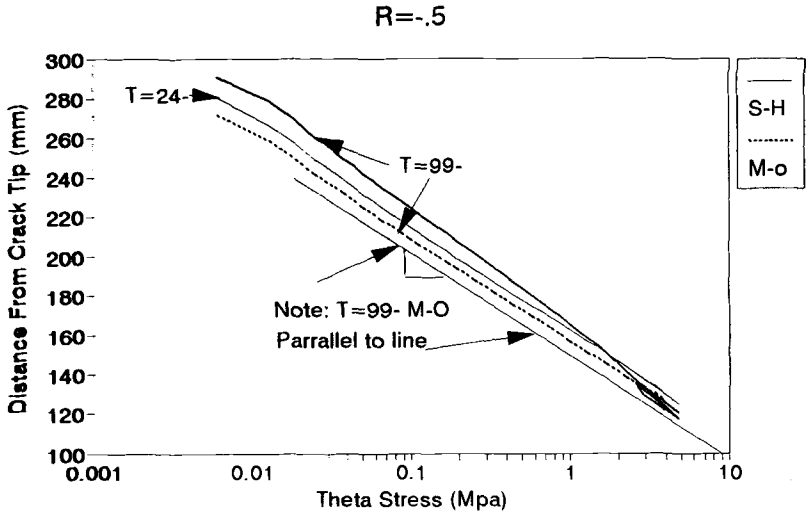


FIG 7(a) σ_θ *stresses for 304 SS, R = -0.5 case, at* $\theta = 0$ *ahead of crack tip.*

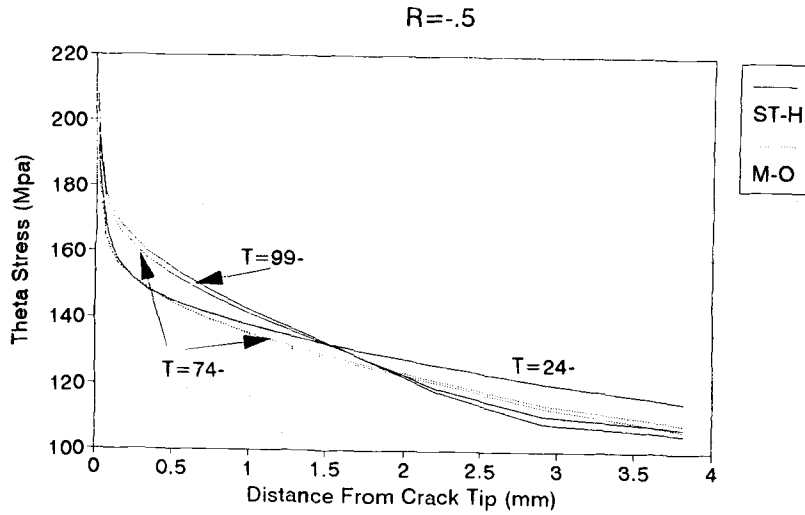


FIG 7(b) σ_θ *stresses for 304SS, R = -0.5 case at* $\theta = 45$ *degrees.*

solution for time = 24 Hr are identical between S-H and M-O solutions, since no unloading has occurred as yet, and the two constitutive laws produce identical results for monotonic loading. Note that after 99 Hr, the S-H and M-O solutions are quite different. The solutions for the Murakami-Ohno case, which has much better capability for modeling stress reversals, appear linear on these plots. While certainly not proven here, it appears that the asymptotic fields are logarithmic in radial coordinate. In fact, this apparent logarithmic singularity appears to dominate over a very large distance, and at least for these cases, doesn't change with cycle. On the other hand, the stress field using a Strain hardening law appears to vary as a function of cycle number. Note also, that the differences between the S-H and M-O solutions increase as the cycle number increases. This was also observed in figure 5 for the compressive stresses. Figure 7b likewise shows differences between the solutions along a radial line which is at $\theta = 45$ degrees. It is clear that the solutions using the different constitutive laws continue to diverge as cycles increase.

The results of this section raise questions regarding the use of the classical approach to creep fracture problems when the cracked structure experiences cyclic loads. The classical approach performs well under constant load conditions. However, under history dependent loading conditions, the asymptotic fields using a strain hardening constitutive law change, perhaps after each load cycle. Classical approaches to creep fatigue life predictions assume that crack growth may be assumed to consist of a fatigue portion, and a creep crack growth portion (see for instance, Jaske [17]), i.e. Miners rule is used. The contributions of fatigue and creep are assumed to be uncoupled. Since the classical approach to creep crack growth correlates crack growth rates with the strength of the asymptotic fields, and the asymptotic fields change with load cycles, one cannot expect this same rate parameter to perform well under these conditions. In other words, using a parameter which is based on the strength of an asymptotic field may not be adequate when the asymptotic fields continually change. Moreover, since these asymptotic fields are developed using constitutive laws which are inadequate under cyclic load conditions, one cannot expect the strength of these fields to have meaning outside their range of validity. With these concepts in mind, we proceed perform analyses of creep crack growth experiments.

FINITE ELEMENT ANALYSES OF CREEP EXPERIMENTS

Two standard compact tension specimens were tested at 650 C. The material was 316 stainless steel. The non-side-grooved specimens had a thickness of 12.7 mm, and a width (from the holes to the specimen edge) of 50.8 mm. One specimen, designated CT-9, had an initial crack size of 27.23 mm. This specimen was subjected to a constant load of 10.271 KN, and held until crack growth and failure occurred. The second specimen, designated CT-10, had an initial crack size of 26.41 mm. This specimen was also loaded to 10.271 KN and held for 2.5 Hr, then unloaded to 0.448 KN, and held for 2 additional in a nearly unloaded state. Finally, the specimen was reloaded and held until additional crack growth and ultimate failure occurred.

Figure 8 illustrates the crack growth versus time history for these tests that, along with the load history, served as input for the analyses. The material constants for 316 SS at

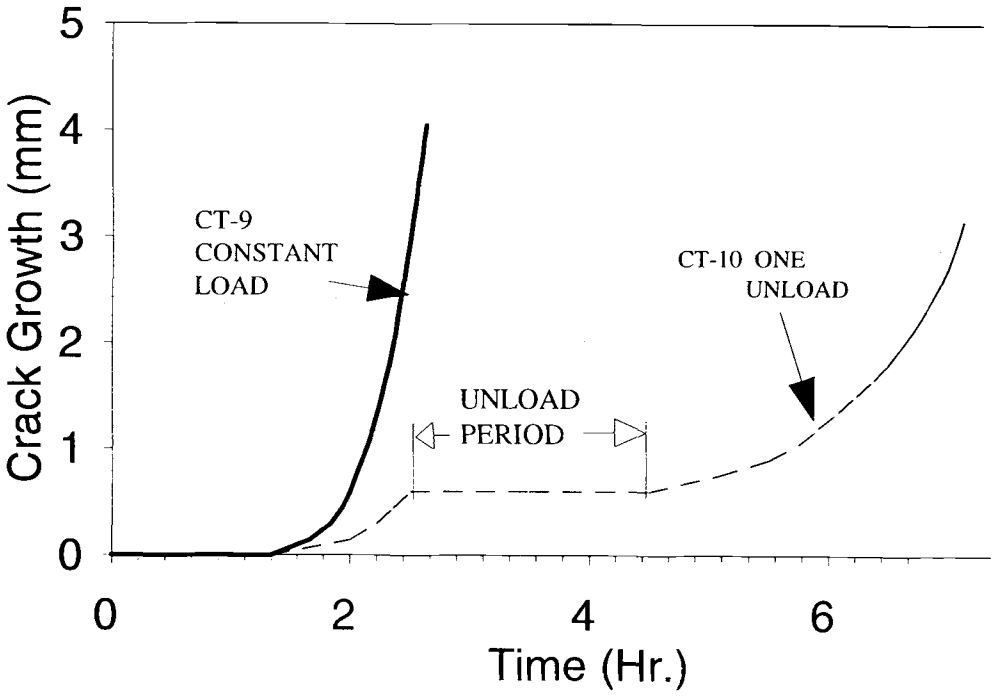


FIG 8 *Crack growth versus time history for 316 SS tests. Used as input to analyses.*

650 for use with the Murakami-Ohno creep constitutive law are: A = 6.393 x 10E-12, n = 4.1, m = 0.23, A_1 = 2.283 x 10E-24, n_1 = 8.96. These constants include the effect of time independent plasticity by including plastic strains over very small times when determining A, n, and m. Figures 9a and 9b compared calculated and experimentally determined displacements for specimens CT-9 and CT-10, respectively. Note that both predictions are quite good, including the unload/reload case of CT-10 in figure 9b.

The T^*-Resistance curve as calculated from the analysis of both tests is illustrated in figure 10. Note that after a short period of crack growth, the resistance curves reach a saturation value. This has been observed for other materials and conditions also (see Reference [12]). The resistance curve decreases from a large value at zero crack growth to the saturation value. This is sometimes, but not always observed. This behavior is likely caused by the crack growth measurements being somewhat inaccurate early on in the test.

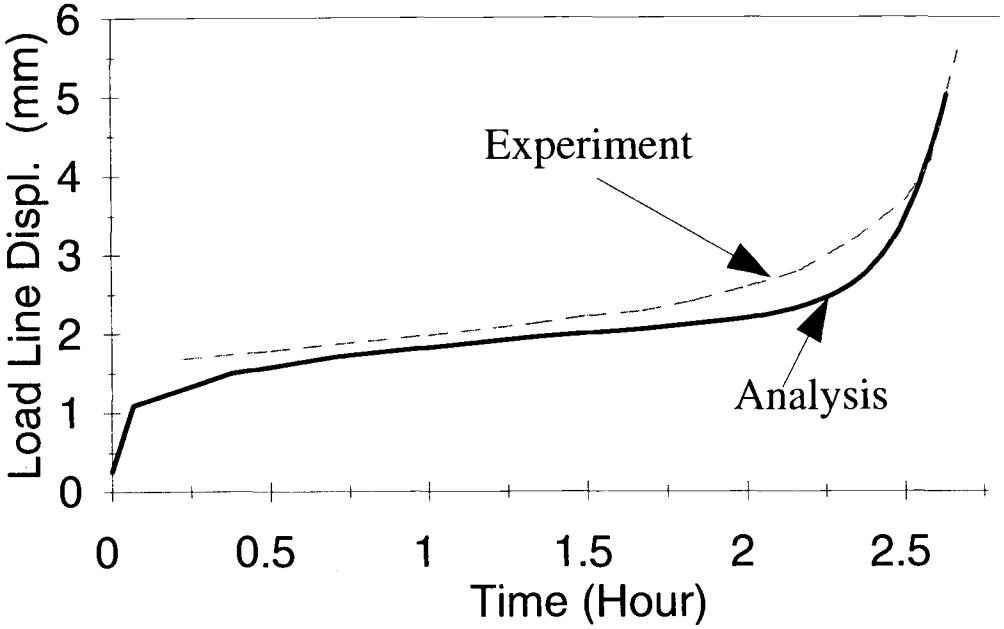


FIG 9(a) *Comparison of displacements for CT-9 test.*

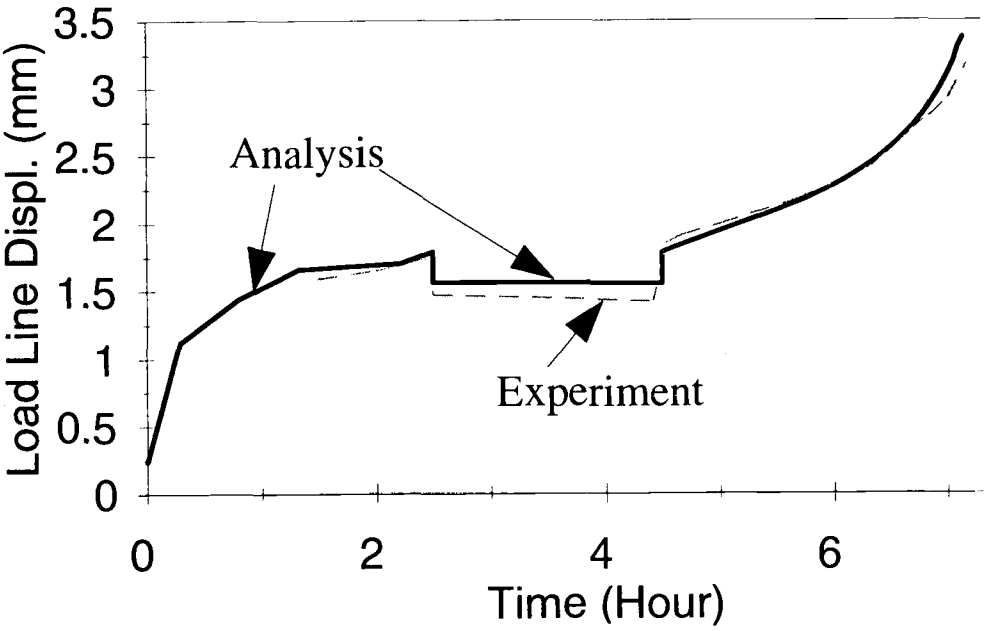


FIG 9(b) *Comparison of displacements for CT-10 test.*

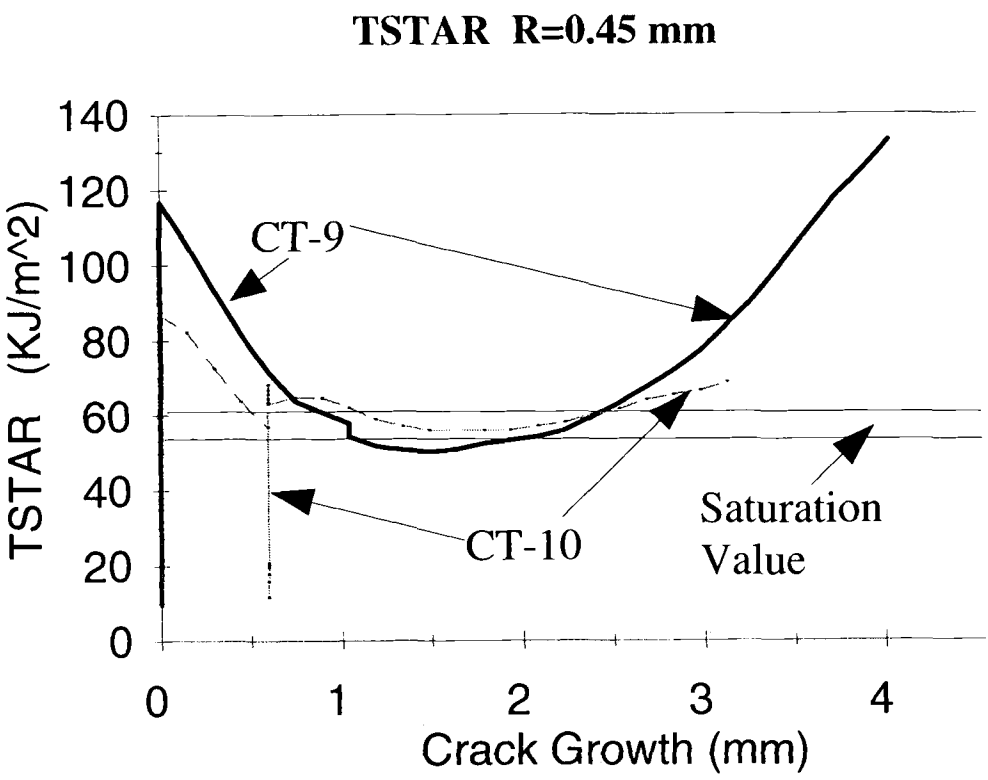


FIG 10 *T^*-resistance curve for CT-9 and CT-10 analyses.*

Finally, Figure 11 shows the J_W and J_M resistance curves. Because of the energetic interpretation of these integrals, they depend somewhat strongly on the crack growth rate. If crack growth actually was modeled to begin earlier than that used in Figure 8, the early portion of this curve decreases significantly. During the latter portion of the test, T^* increases rapidly indicating that failure is approaching, especially for the CT-9 case. The CT-10 case requires more crack growth before failure is expected. Note that the saturation value for both tests is nearly identical. Moreover, note that for the CT-10 case, crack growth after the unload/reload sequence also occurs near the saturation value. This has been observed in previous efforts also indicating that these integral parameters may have the capability for predicting history dependent creep crack growth. In reference [12] an analysis of a 9Cr-Mo test, which experienced more than 25 unload/reload sequences also exhibited this behavior.

CONCLUSIONS

Here it was shown that unload effects can have an important effect on the creep crack growth process. The asymptotic fields upon which all of the currently used cyclic creep fracture predictions are based also break down under cyclic loads. This is important since it raises questions regarding the accuracy of the current engineering approaches that are routinely used to predict cyclic creep crack growth.

The philosophy for predicting cyclic creep crack growth proposed here consists of developing an integral parameter resistance curve, such as that illustrated in Figures 10 and 11, from a constant load test. This is then used to predict the crack growth history for all other load cases in a fashion completely analogous to that used to predict elastic-plastic crack growth and failure based on J-Tearing theory. The fact that the two resistance curves in Figures 10 and 11 are similar despite the fact that they were subjected to different load histories indicate that this approach has potential. Reference [12] discusses this for other load conditions and materials and also provides more details.

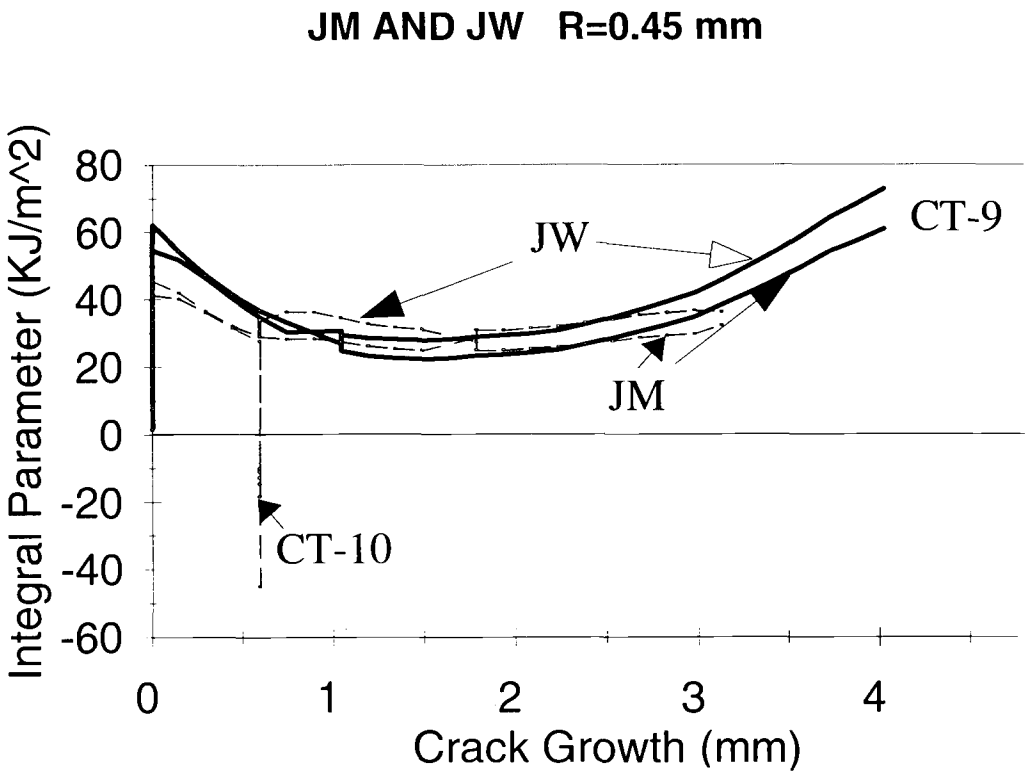


FIG 11 *J_W and J_M resistance curves for CT-9 and CT-10 tests.*

ACKNOWLEDGEMENT

This work was supported by the U.S. Department of Energy, Office of Basic Engineering Sciences, under Grant No. DE-FG02-90ER14135. The author thanks Dr. O. Manley and S. Datta for their support. Also, the author would like to thank Dr. Bhaskar Majumdar for directing the experimental efforts. The author would also like to thank Dr. Prabhat Krishnaswamy for hie efforts in implementing the creep constitutive law.

REFERENCES

[1] Prager, M., "Issues in Life Assessment of Chrome-Moly Welds", PVP-Vol. 2391, MPC-Vol. 33, ASME, 1992.

[2] Lundin, C. D., et. al., "Failure Analysis of a Service-Exposed Hot Reheat Steam Line in a Utility Steam Plant", Excerpt from WRC Bulletin 354, June 1990.

[3] Lundin, C. D., and Wang, Y., "Repair Welding of Service Exposed Cr-Mo Steel Weldments" , Excerpt from WRC Bulletin 348, November, 1989.

[4] Krishnaswamy, P., Brust, F. W., and Ghadiali, N. D., "A Finite Element Algorithm to Study Creep Crack Growth Based on the Creep Hardening Surface", submitted to *Intl J for Num Meth in Eng*. To appear 1995.

[5] Brust, F. W. Krishnaswamy, P., and Majumdar, B. S., "Consideration of History Dependent Damage in Creep Crack Growth", Proceedings of the Tenth Symposium on energy Engineering Sciences, Synergism of Analysis, Modeling, and Experiment, May 11-13, 1992, Argonne, Illinois.

[6] Krishnaswamy, P., Brust, F. W., and Ghadiali, N. D., "Finite Element Analysis of History Dependent Damage in Time Dependent Fracture Mechanics", in *Fatigue, Fracture, and Risk*, 1991 ed. by W. H. Bamford, et al., ASME-PVP Vol. 241, 1992. Also in the *ASME, J of Pressure Vessel Tech*, Vol. 115, November, pp. 339-347, 1993.

[7] Brust, F. W., Krishnaswamy, P., "A Computational Study of the Time Dependent Crack Growth Process", in ASME Applied Mechanics Division Volume (AD-Vol. 27), edited by A. Nagar, et al., November 1992.

[8] Brust, F. W., and Majumdar, B. S., "Load History Effects on Creep Crack Growth", submitted to *Eng Fracture Mech*, to appear 1995.

[9] Brust, F. W., Majumdar, B. S., "Studies of Creep crack Growth Under History-

Dependent Loading", presented at ICF-8, Kiev, Ukraine, June 1993. To appear in Conference Proceedings. Also, to be published in the *Intl J of Material Sci* in 1995.

[10] Brust, F. W., Krishnaswamy, P., and Majumdar, B. S., "Further Studies of History-Dependent Loading in the Creep-Crack Growth Regime", *Fracture Mechanics — Applications and New Materials*, ed. A. Mehta, PVP-Vol. 260, July 1993.

[11] Krishnaswamy, P., Brust, F. W., "Finite Element Modeling of Creep Crack Growth in 316 Stainless and 9 Cr-1 Mo Steels", Proceedings of 22th Intl Invitational Symposium on the Unification of Analytical, Computational Solution Methods, Boston, Massachusetts, August 1993.

[12] Brust, F. W., "Investigations of High Temperature Damage and Crack Growth Under Variable Load Histories", submitted to the *Intl J of Solids and Structure*, in press.

[13] Sadananda, K., and Shahinian, P., "Review of the Fracture Mechanics Approach to Creep Crack Growth in Structural Alloys", *Engineering Fracture Mechanics*, 15, p 327-342, 1981.

[14] Landes, J. D., and Begley, J. A., in *Mechanics of Crack Growth*, ASTM STP 590, American Society for Testing and Materials, p 128-148, 1976.

[15] Goldman, N. L, and Hutchinson, J. W., *Intl J Solids and Structures*, **11** (5), p 575-592, 1975.

[16] Saxena, A., ASTM STP 700, American Society for Testing Materials, p 315-351, 1980.

[17] Jaske, C. E., "Topical Report on Damage Accumulation by Crack Growth Under Creep and Fatigue", Ph.D. Thesis, The Ohio State University, 1984, also Department of Energy Report for Contract No. W-7405-ENG-92-131.

[18] Maas, E., and Pineau, A., *Engineering Fracture Mechanics*, **22**, p 307-325, 1985.

[19] Ohji, K., Ogurta, N., Kudu, S., and Katada, V., in "A Study on Governing Mechanical Parameters of Creep Crack Growth Rate by Using Notched Round Bar Spec. with Proport. Geometry", Proceedings of Japan Congress on Materials Research - Metallic Materials, 1978.

[20] Nikbin, K. M., Webster, G. A., and Turner, C. E., ASTM STP 61, American Society for Testing and Materials, p 47-59, 1976.

[21] Webster, G. A., and Nikbin, K. M., in *Creep in Structures*, Ponter and Hayhurst (eds.), Spring Verlag, 1981.

[22] Saxena, A., in *Fracture Mechanics: Seventeenth Volume*, ASTM STP 905, p 185-201, 1986.

[23] Saxena, A., and Han, J., "Evaluation of Crack Tip Parameters for Characterizing Crack Growth Behavior in Creeping Materials", ASTM Task Group Report E24.08.07/E.24.04.08, 1986.

[24] Saxena, A., "Creep Crack Growth in High Temperature Ductile Materials", *Engineering Fracture Mechanics*, **40** (415), p 721-736, 1991.

[25] Leung, C. P., and McDowell, D. L., "Inclusion of Primary Creep in the Estimation of the C_t Parameter", *Intl J of Fracture*, **46**, p 81-104, 1990.

[26] Suresh, S., "Fatigue of Materials", Cambridge University Press, Cambridge, 1991.

[27] Sadananda, K., "Crack Propagation Under Creep and Fatigue", *Nuclear Engineering and Design*, 83, p 303-323, 1984.

[28] Manson, S. S., "The Challenge to Unify Treatment of High Temperature Fatigue — A Partisan Proposal Based on Strain Range Partitioning", *Fatigue at Elevated Temperatures*, ASTM STP 520, p 744-782, 1973.

[29] Koterazawa, R., "Creep-Fatigue Crack Growth of Metallic Materials at Elevated Temperatures", International Conference on Fracture ICF-8, Kiev, Ukraine, June 1993, to appear in Conference Proceedings.

[30] Dowling, N. E., "Geometry Effects and the J-Integral Approach to Elastic-Plastic Fatigue Crack Growth", ASTM STP 601, p 19-32, 1976.

[31] Logsdon, W. A., et al., "Residual Life Prediction and Retirement for Cause Criteria for SSTG Upper Casings — I Mechanical and Fracture Material Properties Development", *Engineering Fracture Mechanics*, **25** (3), p 259-288, 1986.

[32] Saxena, et al., "Residual Life Prediction and Retirement for cause Criteria for SSTG Upper Casings — II Fracture Mechanics Analysis", *Engineering Fracture Mechanics*, **25** (3), p 289-303, 1986.

[33] Kim, K. S., et al., "Elevated Temperature Crack Growth", Final Report to NASA Lewis Research Center, NASA CR-18191, 1992.

[34] Saxena, A., Han, J., Banerji, K., "Creep Crack Growth Behavior in Power Plant Boiler and Steam Pipe Steels", *J of Pressure Vessel Tech*, **110**, p 137-146, May 1988.

[35] Saxena, et al., "Application of C_t in Characterizing Elevated Temperature Crack Growth During Hold Margin Time", ASME AMD-Vol. 18, ed. S. Mall and T. Nicholas, 1990.

[36] Liaw, P. K., Saxena, A., and Schaefer, J., "Estimating the Remaining Life of Elevated-Temperature Steam Pipes - Part I., Materials Properties", *Engineering Fracture Mechanics*, **32** (5), p 675-708, 1989.

[37] Liaw, P. K., Saxena, A., and Schaefer, J., "Estimating the Remaining Life of Elevated Temperature Steam Pipes - Part II, Fracture Mechanics Analyses", *Engineering fracture Mechanics*, **32** (5), p 709-722, 1989.

[38] H. Reidel, "Fracture At High Temperatures," Springer-Verlag, Berlin, 1987.

[39] J. Lemaitre and J. L. Chaboche, "Mechanics of Solid Materials," Cambridge University Press, 1990.

[40] W. S. Blackburn, "Path Independent Integrals to Predict Onset of Crack Instability In An Elastic Plastic Material," *Int. Journal of Fracture Mech.*, Vol. 8, pp. 343-346, 1972.

[41] K. Kishimoto, S. Aoki, and M. Sakata, "On The Path Independent Integral-J," *Engineering Fracture Mechanics*, Vol. 13, pp. 841-850, 1980.

[42] F. A. McClintock, in *Fracture 3*, Ed. H. Liebowitz, Academic Press, 1971.

[43] K. Watanabe, "The Conservation Law Related To Path Independent Integral And Expression Of Crack Energy Density By Path Independent Integral," Bul. of *JSME*, Vol. 28, No. 235, January 1985.

[44] N. L. Goldman and J. W. Hutchinson, "Fully-Plastic Crack Problems: the Center Cracked Strip Under Plane Strain, *Int. J. of Solids and Struct.* Vol. 11, No. 5, pp. 575-592, 1975.

[45] F. W. Brust and S. N. Atluri, "Studies on Creep Crack Growth Using the T^*-Integral," *Engineering Fracture Mechanics*, Vol. 23, No. 3, pp. 551-574, 1986.

[46] G. P. Cherepanov, "A Remark On The Dynamic Invariant Or Path-Independent Integral," *Int. J. Solids and Structures*, Vol. 25, No. 11, pp. 1267-1269, 1989.

[47] F. W. Brust, M. Nakagaki, and P. Gilles, "Comparison of Elastic-Plastic Fracture Mechanics Techniques," ASTM STP 1074, pp. 448-469, 1990.

[48] T. Inoue, et al., "Evaluation of Inelastic Constitutive Models Under Plasticity-Creep Interaction Condition", *Nuclear Engineering and Design*, Vol. 126, pp. 1-11, 1991.

[49] S. Murakami and N. Ohno, "A Constitutive Equation of Creep Based On The Concept Of A Creep Hardening Surface," *Int. J. of Solids and Structures*, Vol. 18, No. 67, pp. 597-609, 1982.

[50] S. Murakami and N. Ohno, "A Constitutive Equation of Creep Based On The Concept Of A Creep Hardening Surface," *Int. J. of Solids and Structures*, Vol. 18, No. 67, pp. 597-609, 1982.

[51] Riedel, H. and Rice, J. R., "Tensile Cracks in Creeping Solids", *Fracture Mechanics: Twelfth Conference*, ASTM STP 700, American Society for Testing and Materials, Philadelphia, PA, p 112-130, 1980.

[52] Shih, C. F., and German, M. D., "Requirements For a One Parameter Characterization or Crack Tip Fields By the HRR Singularity", *International Journal of Fracture,* Vol. 17, No. 1, February, 1981.

Thomas W. Webb [1] and Dale A. Meyn [2]

INTERMITTENT ENVIRONMENT-ASSISTED CRACK GROWTH DURING SLOW CONSTANT EXTENSION RATE TESTING

REFERENCE: Webb, T. W. and Meyn, D. A., **"Intermittent Environment-Assisted Crack Growth During Slow Constant Extension Rate Testing,"** Fracture Mechanics 26th Volume, ASTM STP 1256, W. G. Reuter, J. H. Underwood, and J. C. Newman, Jr., Eds., American Society for Testing and Materials, Philadelphia, 1995.

ABSTRACT: The slow constant extension rate (CER) test using fatigue precracked fracture specimens offers advantages over the conventional static (fixed displacement and constant load) tests. It generally requires fewer specimens and shorter test times to determine the threshold for crack initiation. However, apparent anomalies in the subcritical crack growth kinetics have been observed, which complicate the interpretation of the CER test measurements. Oscillations in the crack velocity occur resulting in macroscopic intermittent crack growth and periodic fluctuations in the applied load. An analysis of the CER test applied to environment-assisted cracking (EAC) is made and a phenomenological model is proposed to describe the mechanics of macroscopic intermittent crack growth. As a result of the analysis, the oscillations in the crack velocity are found to depend on the elastic behavior of the specimen and loading system and the aggressiveness and activity of the environment at the crack tip.

KEYWORDS: constant extension rate test, environment-assisted cracking, intermittent or discontinuous crack growth, crack growth resistance curves

The slow constant extension rate (CER) test using fatigue precracked fracture specimens (also known as the rising load test, rising displacement test or slow strain rate test) is becoming increasingly more popular as a test method for investigating environment-assisted cracking (EAC) behavior of materials using linear elastic fracture mechanics as well as elastic-plastic fracture mechanics [1-5]. The accepted method for determining the threshold for crack initiation below which no EAC occurs involves the use of conventional static tests such as the constant load and fixed displacement tests and linear elastic fracture mechanics. However, a difficult aspect of the conventional static tests is the determination of an adequate test duration for meaningful threshold measurements. Limitations of the static tests are that long test durations are usually necessary (e.g., 10,000 hours for low strength steels and 1,000 hours for titanium) and multiple specimens and experiments are required to determine the threshold for crack initiation accurately. The slow CER test

[1] NRC Research Associate, Code 6312, Environmental Fracture and Failure Analysis Section, Naval Research Laboratory, Washington, D. C. 20375-5000.

[2] Metallurgist, Code 6312, Environmental Fracture and Failure Analysis Section, Naval Research Laboratory, Washington, D. C. 20375-5000.

Copyright © 1995 by ASTM International www.astm.org

method overcomes these limitations and difficulties since incubation times for crack initiation are significantly reduced and fewer specimens and experiments are required.

Although the slow CER test method offers certain advantages over the conventional static tests, a shortcoming of the slow CER test method is that there are considerable uncertainties and inaccuracies in the determination procedure for subcritical crack initiation during rising load test conditions [6]. Also, since the threshold for crack initiation is loading rate dependent, a difficult aspect with the test method is the determination of the appropriate loading rate which provides a minimum and conservative value for the threshold for crack initiation [7] . In addition, apparent anomalies in the crack growth kinetics are frequently observed in EAC studies using the slow CER test method, which complicate the interpretation of the CER test measurements. For example, Meyn and coworkers [8-10] and Young [11] observed large oscillations in the crack tip velocity resulting in macroscopic intermittent crack growth and periodic fluctuations in the applied load in their EAC studies of several titanium alloys using the CER test method. Therefore, for the slow CER test method to become a replacement to the conventional static tests, the difficulties associated with determining crack initiation should be resolved and the origin of the large oscillations in the crack velocity determined.

The origin of the oscillations in the crack velocity and the possible role that crack tip mechanics plays in macroscopic intermittent crack growth are the main interests of this paper. It is important to realize, however, that macroscopic intermittent crack growth differs from the microscopic intermittent crack growth observed with regularity in EAC [12, 13]. In the macroscopic case, the crack growth increments are larger than the size of the crack tip plastic zone with relatively long waiting periods between crack jumps. This cracking behavior probably does not depend, for example, on the time for diffusion of hydrogen to a region several micrometers ahead of the crack tip and formation of an embrittled process zone, which subsequently ruptures causing the crack to jump forward and arrest when the crack encounters unembrittled material. The parameters involved with macroscopic intermittent crack growth occur over a larger length and longer time scales and include not only the local fracture processes in the crack tip process zone, but also various nonlocal processes (e.g., transport of the active component of the environment to the crack tip) and the elastic behavior of the loading system.

Macroscopic intermittent EAC is similar to intermittent cracking observed in CER tests of polymeric materials in inert environments commonly called stick-slip fracture [14, 15]. In this case, intermittent cracking has been associated with an attempt to impose a crack velocity within an unstable negative slope region of a non-monotonic fracture energy (resistance to cracking) vs crack velocity curve where steady continuous cracking cannot be observed. A mathematical formulation of the stick-slip fracture problem presented by Webb and Aifantis [16] showed that rather than obtaining a stable steady state crack velocity for a constant applied extension rate, the crack velocity oscillates following a limit cycle in the energy release rate G (or stress intensity factor K) vs. crack velocity plane determined by the elastic behavior of the loading system and fracture energy vs. crack velocity relationship.

The aim of this paper is to provide a mathematical formulation for modeling macroscopic intermittent EAC using linear elastic fracture mechanics and EAC theories. The basic equations for the slow CER test applied to EAC are outlined and a governing differential equation for macroscopic intermittent crack growth is derived for several crack growth kinetic laws. In this first attempt, the crack growth kinetic laws are phenomenological in nature and it is assumed that the mechanisms responsible for macroscopic intermittent EAC are manifested in the form of an unstable negative slope region in the crack growth kinetic curve below some threshold or critical crack velocity. The various crack growth kinetic laws and their associated mechanisms were evaluated for their applicability to macroscopic intermittent EAC by comparing the solution of the differential equation derived for each crack growth kinetic law with experimental observations [8-10].

CONSTANT EXTENSION RATE TEST

The basic equations for the slow CER test applied to EAC are given in this section. For simplicity, it is assumed that the linear elastic fracture mechanics approach to EAC is applicable and the assumption of small-scale yielding is valid. Therefore, the stress intensity factor K or energy release rate G is the appropriate mechanical crack tip driving force for initiation and subsequent propagation of EAC.

The stress intensity factor for compact fracture specimens of thickness B and width W can be expressed in the familiar form

$$K = \frac{P}{B\sqrt{W}} f(a/W), \tag{1}$$

where P is the applied load and f(a/W) is a polynomial function of the crack length to width ratio a/W. For most fracture geometries, f(a/W) is a monotonically increasing function, such that, for a given load the stress intensity factor increases for increasing a/W. The crack length is the effective crack length augmented for the effects of plastic deformation at the crack tip and is commonly assumed to be in the form

$$a = a_p + \frac{\alpha}{2\pi}\frac{K^2}{\sigma_Y^2}, \tag{2}$$

where a_p is the physical crack length and the second term in Eq 2 is the plastic zone adjustment where σ_Y denotes the yield strength and α is assumed to be 1 for plane stress and 1/3 for plane strain. The energy release rate for an linear elastic body with a Young's modulus E and Poisson's ratio ν is related to the stress intensity factor and the specimen compliance C(a/W) by

$$G = \frac{K^2}{\tilde{E}} = \frac{P^2}{2B} C'(a/W), \tag{3}$$

where the prime designates differentiation with respect to a/W and $\tilde{E} = E$ for plane stress and $\tilde{E} = E/(1 - \nu^2)$ for plane strain. The slow CER test is a displacement control test and the load applied through a loading machine with a compliance C_m is related to the total displacement δ by the expression

$$\delta = [C_m + C(a/W)]\, P\,. \tag{4}$$

Introducing Eq 4 into Eq 3, the energy release rate can be alternatively written as a function of the total displacement and crack length in the form

$$G = \hat{G}(\delta, a). \tag{5}$$

The time derivative of the energy release rate $\dot{G}$ is

$$\dot{G} = \left(\frac{\partial \hat{G}}{\partial \delta}\right)_a \dot{\delta} + \left(\frac{\partial \hat{G}}{\partial a}\right)_\delta v \tag{6}$$

where $\dot{\delta}$ is constant for a CER test and $v = \dot{a}$ denotes the crack velocity. The subscript associated with the partial derivatives denote the independent variable held fixed. Using Eqs 1, 3 and 4, the time derivative of the energy release rate can be written explicitly as

$$\dot{G} = \frac{4f^2(a/W)G}{BW^2\tilde{E}(C_m + C(a/W))}\left[\sqrt{\frac{W^3\tilde{E}}{4f(a/W)G}}\,\dot{\delta} - \left\{1 - \frac{f'(a/W)BW\tilde{E}}{2f^3(a/W)}(C_m + C(a/W))\right\}v\right], \quad (7)$$

which upon comparison of Eqs 6 and 7 implies that

$$\left(\frac{\partial\hat{G}}{\partial\delta}\right)_a = \frac{2f^{3/2}(a/W)\sqrt{G}}{B\sqrt{W\tilde{E}}(C_m + C(a/W))} \quad (8)$$

and

$$\left(\frac{\partial\hat{G}}{\partial a}\right)_\delta = -\frac{4f^2(a/W)G}{BW^2\tilde{E}(C_m + C(a/W))}\left\{1 - \frac{f'(a/W)BW\tilde{E}}{2f^3(a/W)}(C_m + C(a/W))\right\}. \quad (9)$$

The term $(\partial\hat{G}/\partial\delta)_a$ is always positive and the term $(\partial\hat{G}/\partial a)_\delta$ may be positive or negative depending on the crack length and loading machine compliance. It turns out that for most slow CER tests using precracked fracture specimens that the term $(\partial\hat{G}/\partial a)_\delta$ is positive for most of the crack growth and becomes negative as a/W approaches unity. The condition for the loading machine and specimen is given by Eq 7 and the experimentally observed relationship for G and v are determined by the intrinsic fracture properties for a given material-environment system expressed in terms of the subcritical crack growth kinetics.

SUBCRITICAL CRACK GROWTH KINETICS

The crack velocity for subcritical crack growth under monotonically increasing loads can be written as the linear superposition of the crack growth rate v_{pl} associated with the plastic deformation development during stable mechanical crack growth Δa_{pl} and the EAC velocity v_{EAC} [17], such that,

$$v = v_{pl} + v_{EAC}. \quad (10)$$

The stable mechanical crack growth Δa_{pl} is associated with the crack growth resistance curve and is on the order of a crack tip opening displacement. A common mathematical expression for the crack growth resistance curve under small-scale yielding is the power law equation

$$G = A(\Delta a_{pl})^m, \quad (11)$$

where A and m are empirical parameters. Differentiating Eq 11 and rearranging the results gives [7]

$$v_{pl} = \frac{1}{mA^{1/m}}\left(\frac{G}{A}\right)^{(1-m)/m}\dot{G}. \quad (12)$$

Generally speaking, during monotonic loading the plastic deformation development during crack growth is important, however, in the case of the slow CER test where there are gradual changes in the energy release rate, the influence of plastic deformation development on the crack velocity can be neglected. Therefore, for simplicity the total crack velocity is approximated by the EAC velocity and the subscript for the EAC velocity will be dropped for convenience.

The EAC velocity is the result of various chemical, electrochemical and physical processes that lead to local degradation and failure of material ahead of the crack tip in the fracture process zone. In general, the EAC velocity can be written as a functional or path-dependent function of the history of G (or K) for all past times [17]. However, the EAC velocity is considered to be invariant with respect to time for a constant mechanical crack tip driving force G when the environmental activity and fracture mechanisms remain constant during the crack growth process. In this case, the functional for the EAC velocity degenerates to a simple function of G

$$v = \hat{v}(G) . \tag{13}$$

The function is equal to zero when $G \leq G_{EAC}$, where G_{EAC} denotes the threshold energy release rate and is related to the threshold stress intensity factor K_{EAC} through Eq 3 ($K_{EAC} = \sqrt{\tilde{E}\, G_{EAC}}$). Typically, Eq 13 is usually written in an empirical power law form

$$v = v_o G^n, \tag{14}$$

where v_o and n are adjustable parameters used to fit experimental data.

In general, three regions are exhibited in the EAC v-G diagram measured using static test methods (constant load and fixed displacement) as shown in Fig. 1. Stages I and III are strongly dependent on G and stage II is weakly dependent on G, but essentially there is a constant or plateau velocity v_{II}. Stage III is primarily due to mechanical overload fracture and stage I (dashed) behavior is typical for materials in aggressive and active environments and can be described using Eqs 13 and 14. However, in some material-environment systems a low velocity stage I region is not observed. Instead, a transition region IIa and a G independent stage II region (solid) are observed. In this case, crack growth appears to be essentially independent of G, except that crack growth starts above a threshold G (i.e., G_{EAC}) and a threshold or critical crack velocity v_c. The G independent stage II region or plateau velocity is usually explained in terms of the EAC velocity being limited by mass transport processes, where the plateau velocity of electrochemical or chemical corrosion cracks is proportional to the concentration of the damaging species (e.g., hydrogen gas, various ions, etc.) at the crack tip. The role of G is to simply provide the mechanical loads necessary to rupture the protective surface oxide film near the crack tip [17]. This behavior is common for titanium alloys in neutral aqueous environments [18] and it will be shown in the next section that oscillatory crack growth may occur when the slow CER test is applied to material-environment systems that exhibit this type of stage IIa-II crack growth kinetics by assuming that a region of instability exists below v_c and above G_{EAC}. It should be mentioned that some materials (e.g., titanium) exhibit time dependent subcritical crack growth called sustained load cracking (SLC) in inert environments, for example, due to internal hydrogen-assisted cracking (HAC) [18]. In this case, the v-G diagram does not exhibit the characteristic stage I and/or stage II cracking and instead the v-G diagram increases monotonically as shown in Fig. 1, where the threshold for SLC is higher than the threshold for EAC.

In the case of stress corrosion cracking (SCC), the oxide film is often penetrated by microtunnels, which cause microcracks to branch from the end of the main crack tip during

crack growth [17]. Crack branching reduces the effective G at the main crack tip and acts to toughen the material relative to the single main crack tip. Crack tip shielding and toughening mechanisms may also occur during EAC (e.g., the formation of microcracks ahead the main crack tip which are mismatched with the plane of the main crack and separated by unfractured ligaments that must be fractured by shear before total separation of the crack surfaces can occur [19, 20]) giving rise to a crack length dependence in the crack growth kinetics. In these situations, the EAC velocity may be written as

$$v = \hat{v}(G, \Delta a), \tag{15}$$

where Δa is the crack growth increment and represents the increase in resistance to crack growth with increasing crack length.

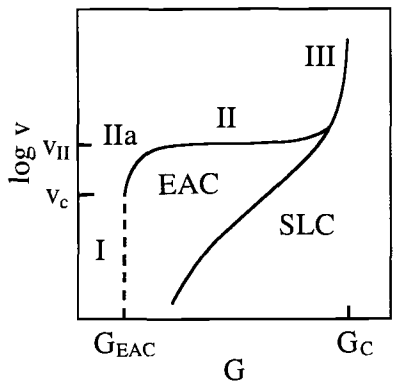


FIG. 1--Schematic of typical subcritical crack growth kinetics.

In some cases the functional dependence of the EAC velocity on prior G can be characterized by writing the EAC velocity as not only a function of G, but also an internal state variable θ,which represents some kind of average of the environmental activity and kinetic processes that evolve during crack growth. The EAC velocity can be expressed as

$$v = \hat{v}(G, \theta), \tag{16}$$

where the evolution equation for the state variable is assumed to depend on G and the current value of the state variable θ in the form

$$\dot{\theta} = g(G, \theta). \tag{17}$$

From experiments it is known that with a sudden change of G applied to a stationary crack or a crack growing at a steady state velocity that the crack will attain steady state crack velocity $v_s(G)$ again only after an incubation and nonsteady crack growth period τ [21-23]. It is believed that this time period depends on the various kinetic processes to cause EAC, which are assumed to depend on G and v. This behavior can be expressed as

$$\dot{v} = \left(\frac{\partial \hat{v}}{\partial \theta}\right)_G \dot{\theta} = -\frac{(v - v_s(G))}{\tau(G,v)} \tag{18}$$

since $dv = (\partial\hat{v}/\partial\theta)_G d\theta$ for G = constant. Substituting Eq 18 back into the time derivative of Eq 16, the equation for nonsteady crack growth is given by

$$\tau(G,v)\,\dot{v} + v = v_s(G) + B(G,v)\,\dot{G}, \tag{19}$$

where $B(G, v) = \tau(G, v)(\partial\hat{v}/\partial G)_\theta$. If $(\partial\hat{v}/\partial G)_\theta = nv/G$ then Eq 19 reduces to a steady state power-law form for the crack velocity given by Eq 14. For the special case of constant G, Eq 19 reduces to [24]

$$\tau(G,v)\,\dot{v} + v = v_s(G), \tag{20}$$

which can be used to describe nonsteady crack growth as a result of step changes in G.

INTERMITTENT CRACK GROWTH

In this section, the governing equations for the slow CER test are derived for the various crack growth kinetic laws proposed in the previous section. The necessary condition for intermittent crack growth is determined and the oscillatory crack growth behavior is constructed from the governing equations. Based on these solutions, the various crack growth kinetic laws and associated mechanisms were evaluated for their applicability to macroscopic intermittent EAC.

Constant Environmental Activity/Fracture Mechanisms

The first crack growth kinetic law considered is the case where the environmental activity and fracture mechanisms do not change during crack growth (Eq 13). For convenience Eq 13 is inverted and rewritten as

$$G = \gamma(v), \tag{21}$$

where $\gamma(v)$ is the fracture energy and represents the resistance to EAC. This equation for the material-environment characteristics together with the condition for the loading machine and specimen determine the energy release rate and crack velocity as a function of time. It follows that the time derivative of Eq 21 is

$$\dot{G} = \frac{\partial\gamma}{\partial v}\,\dot{v} \tag{22}$$

and combining Eq 22 and Eq 6 results in

$$\frac{\partial\gamma}{\partial v}\,\dot{v} - \left(\frac{\partial\hat{G}}{\partial a}\right)_\delta v - \left(\frac{\partial\hat{G}}{\partial\delta}\right)_a \dot{\delta} = 0. \tag{23}$$

The solution of this differential equation provides the crack velocity and subsequently the crack growth as a function of time. The energy release rate is determined from the EAC characteristics (Eq 21) and the applied load P can be determined from

$$P = \frac{B\sqrt{W\tilde{E}G}}{f(a/W)} \tag{24}$$

using Eqs 1 and 3.

The crack velocity is constant or steady state when $\dot{v} = 0$ and from Eq 23 the steady state crack velocity v_s is

$$v = v_s = -\frac{\left(\partial\hat{G}/\partial\delta\right)_a}{\left(\partial\hat{G}/\partial a\right)_\delta}\dot{\delta} \; . \tag{25}$$

which only makes sense for the case where $\left(\partial\hat{G}/\partial a\right)_\delta < 0$ (i.e., positive steady state crack velocity). According to Eq 22 this steady state crack velocity also satisfies the condition for G constant (i.e., $\dot{G} = 0$). The steady state velocity (Eq 25) is proportional to the loading rate and the stability of the steady state crack velocity is examined by introducing a small deviation from the steady state velocity, such that, the crack velocity is in the form

$$v = v_s + \varepsilon e^{\lambda t}, \tag{26}$$

where t denotes time and ε and λ are constants. When λ is negative the small deviation from steady state decays exponentially and the steady state velocity is stable. When λ is positive the small deviation from steady state grows exponentially and the steady state velocity is unstable. Introducing Eq 26 into Eq 23 linearized about the steady state velocity yields

$$\lambda = \frac{\left(\partial\hat{G}/\partial a\right)_\delta}{\partial\gamma(v_s)/\partial v} \; . \tag{27}$$

Since the numerator in Eq 27 is negative, the steady state velocity will be unstable when

$$\partial\gamma(v_s)/\partial v < 0 \tag{28}$$

and is a necessary condition for intermittent cracking to occur.

The assumption made in this paper is that below the threshold or critical crack velocity in the case of stage IIa-II crack growth behavior, a negative slope region or region of instability exists in the v-G (or v-γ) diagram as shown in Fig. 2a. This assumption is supported by the experimentally observed loading rate dependence of the energy release rate for EAC initiation G_i shown schematically in Fig. 2b [18, 25] since the curves in Fig. 2a and Fig. 2b can be related through the relationship between the loading rate and the apparent crack velocity for a monotonically increasing applied load due to crack tip plasticity. Prior to initiation of EAC, the apparent crack velocity is given by

$$v_{app} = \frac{\left(\partial\hat{G}/\partial\delta\right)_a}{\left[2\pi\sigma_Y^2(\bar{E}\alpha)^{-1} - \left(\partial\hat{G}/\partial a\right)_\delta\right]}\dot{\delta} \tag{29}$$

as a result of taking the time derivative of Eq 2 and introducing the results into Eq 6. Eq 29 demonstrates that the apparent crack velocity before crack initiation is proportional to the loading rate and is referred to as the loading curve in the v-G plane [14, 16]. Curve 1 in Fig. 2b is typical of active or aggressive material-environment systems that exhibit stage I EAC and in which the mechanical loading rate has very little influence on crack initiation and curve 2 in Fig. 2b is typical of less active and less aggressive material-environment systems that do not exhibit stage I EAC, such as, titanium alloys in neutral aqueous solutions [18].

It is interesting to note that Eq 2 is typically used to define crack initiation [10] and the apparent crack velocity before crack initiation (Eq 29) is usually omitted from the presentation of experimental results [3]. However, it will be shown that the use of Eq 29 is necessary for the construction of the crack growth kinetics and crack growth resistance curves for EAC under slow CER testing. It should be pointed out that the loading curve, in general, may include other mechanisms (e.g., microcracking, void growth, creep, etc.) along with crack tip plasticity. Also, SLC may occur due to internal HAC in addition to EAC [10]. This makes it difficult to precisely determine the loading curve, which is one reason why it is difficult to accurately define the onset of initiation for EAC in the case of monotonic loading.

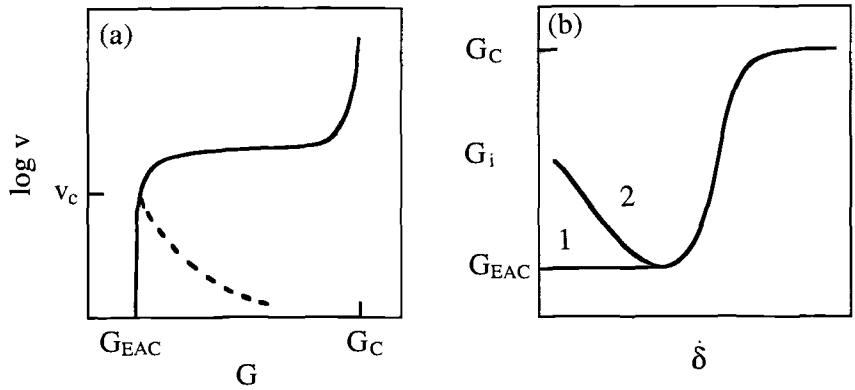


FIG. 2--Schematics showing the relationship between (a) EAC crack growth kinetics and (b) the loading rate effects on crack initiation.

It should be mentioned that even though the assumed v-G curves for the CER test shown schematically in Fig. 2a are similar to the v-G curves shown schematically in Fig. 1 (except for the negative slope region, which is not attainable for steady continuous crack growth in conventional static EAC tests) it is speculated that the curves are probably different. Since the incubation times are significantly reduced for CER tests relative to static conventional tests, this suggests that crack initiation (and propagation) processes are modified by variation of G with time such as occurs in a CER test. For example, the straining that occurs at the surface of the crack tip due to an increase in G and crack tip opening displacement, may aid in the rupture of the oxide film and enhance adsorption and various electrochemical processes. Understanding the mechanisms for crack initiation and the functional dependence of the crack velocity on the history of G is the key to understanding the relationship between static tests and CER tests or even varying extension rate tests, e.g., rising step load test.

As discussed earlier there is a critical apparent crack velocity below which stable crack growth can no longer occur, therefore, Eq 29 implies that there is a threshold or critical loading rate below which stable crack growth will not be possible in a CER test. When the loading rate is less than the critical loading rate the crack velocity follows the loading curve OA (Eq 29) up to the unstable negative slope branch of the v-G diagram in Fig. 3a. According to Eq 28, the crack is unstable at A and from Eq 23 the crack accelerates rapidly ("jumps") to B on the stable branch. The crack velocity outruns the extension rate of the machine ($\dot{\delta} < -\left(\partial\hat{G}/\partial a\right)_{\delta}\left(\partial\hat{G}/\partial\delta\right)_a^{-1}v$) and from Eq 6 $\dot{G}$ is negative. The energy release rate decreases and follows the stable branch to C, however, the crack velocity is still greater than the extension rate of the machine and from Eq 23 the crack

velocity decelerates rapidly ("jumps") to D on the loading curve. The cycle repeats itself as shown in Fig. 3a and gives rise to a sawtooth G vs. Δa curve as shown in Fig. 3b. The maximum value of G would correspond to the intersection of the loading curve with the unstable negative slope branch (point A) and the minimum value of G would correspond to the threshold.

The classical "stick-slip" cycle [14-16] described in Fig. 3a using Eq 21 is inadequate for describing the oscillatory crack velocities observed in slow CER tests by Meyn and coworkers [8-10]. In their experiments, G increases slightly during the crack jumps, whereas, this cycle requires G to decrease during each crack jump. Therefore, the assumption of constant environmental activity and constant fracture mechanisms when using Eq 21 (or Eq 13) is incorrect. It is interesting to note, however, that in their experiments as a/W approaches unity, G decreases during the crack jumps and the oscillatory crack velocity cycle in Fig. 3a may have some application.

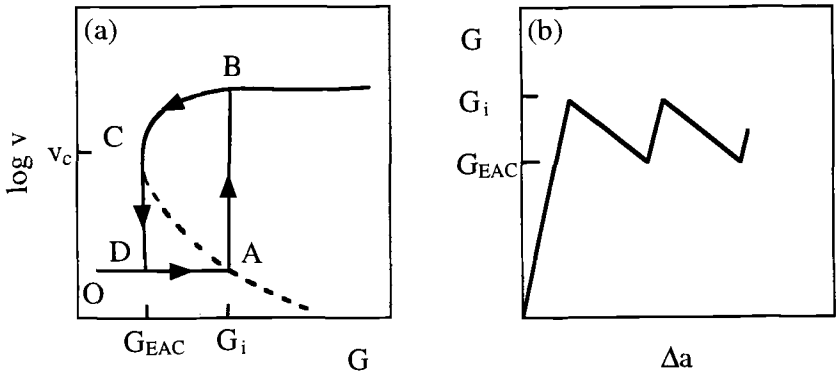


FIG. 3--Schematics of (a) the intermittent crack growth cycle for constant environmental activity/fracture mechanisms and (b) the associated sawtooth G vs. Δa curve.

Crack Tip Shielding and Toughening

The next crack growth kinetic law considered is the case where the fracture mechanisms do not remain constant during crack growth (e.g., as a result of crack branching, formation of restraining ligaments, etc.) and the crack velocity includes the influence of crack tip shielding or toughening (Eq 15). Eq 15 can be inverted and rewritten as

$$G = \gamma(v, \Delta a), \tag{30}$$

where the crack growth increment Δa dependence in Eq 30 represents the various shielding or toughening mechanisms associated with EAC and it follows that $(\partial\gamma/\partial(\Delta a))_v > 0$. Following the same procedure as before, the differential equation for the crack velocity is

$$\left(\frac{\partial \gamma}{\partial v}\right)_{\Delta a} \dot{v} + \left[\left(\frac{\partial \gamma}{\partial(\Delta a)}\right)_v - \left(\frac{\partial \hat{G}}{\partial a}\right)_\delta\right] v - \left(\frac{\partial \hat{G}}{\partial \delta}\right)_a \dot{\delta} = 0 \tag{31}$$

and the steady state crack velocity is given by

$$v = v_s = \frac{\left(\partial \hat{G}/\partial \delta\right)_a}{\left[\left(\partial \gamma/\partial(\Delta a)\right)_v - \left(\partial \hat{G}/\partial a\right)_\delta\right]} \dot{\delta}, \tag{32}$$

which only makes sense for the case where the term in the denominator is positive (i.e., positive steady state crack velocity). This implies that the shielding or toughening term must increase faster than G during crack growth in the case considered here where the term $\left(\partial \hat{G}/\partial a\right)_\delta$ is positive for most of the crack growth [8-10]. A linear stability analysis about v_s using Eq 26 yields

$$\lambda = - \frac{\left[\left(\partial \gamma(v_s, \Delta a)/\partial(\Delta a)\right)_{v = v_s} - \left(\partial \hat{G}/\partial a\right)_\delta\right]}{\left(\partial \gamma(v_s, \Delta a)/\partial v\right)_{\Delta a}} . \tag{33}$$

Since the numerator is assumed positive, the steady state velocity (Eq 32) is unstable when

$$\left(\partial \gamma(v_s, \Delta a)/\partial v\right)_{\Delta a} < 0 \tag{34}$$

and is a necessary condition for intermittent cracking to occur.

As outlined before, when the loading rate is less than the critical loading rate the crack velocity follows the loading curve OA (Eq 29) up to the unstable branch of the v-G diagram in Fig. 4a. According to Eq 34, the crack is unstable at A and from Eq 31 the crack accelerates rapidly ("jumps") to B on the stable branch. Meanwhile, as the crack grows an increment Δa the toughness of the material increases according to Eq 30, which effectively shifts the curve $\gamma(v, \Delta a)$ to the right on the v-G diagram relative to the initial curve $G = \gamma(v, \Delta a = 0)$. Although G increases during the "fast" stage II cracking (from B to C) according to loading machine-specimen condition (Eq 31), the crack decelerates from C to D, because the material toughens at rate faster than the rate G increases. The crack velocity is still too high at D and the crack continues to decelerate rapidly ("jumps") to E on the loading curve. The material continues to toughen with crack growth and cycle repeats itself as shown in Fig. 4a giving rise to a crack growth resistance curve (G vs. Δa curve) as shown in Fig. 4b. A significance of this cycle is that G at crack initiation is greater than the threshold G and therefore, in general, it can be expected that the slow CER test will give a nonconservative value for the "threshold" for crack initiation when intermittent EAC occurs.

This behavior compares well with the experimental results for Ti-15V-3Al-3Cr-3Sn in neutral salt water, air [10] and vacuum[3]. In this case, the influence of the environment on the oscillatory crack velocity behavior appears minor and it is speculated that a toughening or crack tip shielding mechanism may be responsible for the crack arresting even though G increases. However, further CER experiments with this alloy must be performed to determine the role of the environment and the possible role of a crack tip shielding mechanism on intermittent crack growth.

On the otherhand, this scenario does not appear to apply to Ti-6Al-4V in neutral salt water. Preliminary experiments on Ti-6Al-4V in neutral salt water in which the extension was fixed after the first crack jump indicate that an increase in G is not necessary to reinitiate EAC after the first crack arrests[3]. Since only an incubation time (and possibly a crack tip strain rate due to creep) is necessary for initiating the crack, this suggests that

---

[3] Webb, T. W. and Meyn, D. A., unpublished research.

possibly the crack initiates and arrests due to changes in the composition of the solution possibly affecting the repassivation kinetics of the oxide film near the crack tip.

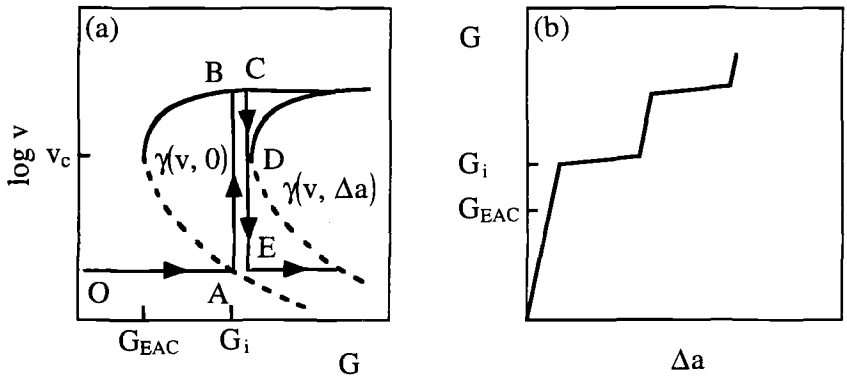


FIG. 4--Schematic of (a) the intermittent crack growth cycle for crack tip shielding and toughening and (b) the associated step-like resistance curve (G vs. Δa).

Varying Environmental Activity

The next crack growth kinetic law considered should include the case where a change of environmental activity occurs during the crack growth process. However, the appropriate functional for the crack velocity (or equivalently the fracture energy) for the particular material-environment system cannot be determined at this time, since the mechanism responsible for initiating and arresting the crack is undetermined. In addition, the procedure for modeling EAC under varying environmental activity conditions is not clear at this point, however, a possible approach may be to adopt the internal state variable approach outlined in the previous section. For example, Eq 16 can be inverted and rewritten as

$$G = \gamma(v, \theta), \tag{35}$$

where the state variable θ would include the influence of various electrochemical and chemical effects at the crack tip. The approach would be to write the appropriate evolution equation for the state variable (similar to the procedure in the previous section, i.e., Eq 18) that would determine the evolution of the environmental activity at the crack tip. However, writing an explicit relationship for the evolution equation for the state variable and deriving the governing equation for intermittent EAC in this case is not possible now without further experiments being conducted under carefully controlled conditions for the crack tip mechanics and environment.

DISCUSSION

The main assumption of this paper was that oscillatory crack velocities occur in material-environment systems that fall somewhere between aggressive and inert. In the aggressive case (Fig. 1, EAC curve, both dashed and solid lines), the loading curve would intersect a positive sloped stage I cracking region during monotonic loading from a slow

CER test in which case continuous cracking would occur. In the inert case (Fig. 1, SLC curve), the loading curve will intersect a positive slope SLC curve again giving rise to continuous cracking. However, in the intermediate case (Fig. 1, EAC curve, solid line only) an extensive positive slope region does not exist and instead a stage IIa and stage II crack growth behavior occurs in which case, the applicable EAC mechanisms are assumed to be manifested in the form of an unstable negative slope region in v-G diagram below a critical crack velocity (Fig. 2a) based on the influence of the loading rate on crack initiation (Fig. 2b).

Our assumption is to some extent supported by the experiments of Meyn and coworkers [8-10], but some inconsistencies are also noted. Intermittent EAC was not observed in the case of Ti-8Al-1Mo-1V and Ti-6Al-4V in an organic solvent (carbon tetrachloride CCl_4 and uninhibited trichloroethane TCE). This behavior is consistent with our assumption since stage I crack growth behavior is observed for both titanium alloys in carbon tetrachloride. However, the behavior of these two alloys in air and neutral salt water is less easily explained. Ti-6Al-4V behaves, insofar as the occurrence of crack jumps (intermittent cracking) is concerned, as if air is an intermediate environment, whereas for Ti-8Al-1Mo-1V it seems inert. Likewise, salt water acts as an aggressive environment for Ti-6Al-4V, but only as an intermediate environment for Ti-8Al-1Mo-1V. In other words the behavior of Ti-6Al-4V is shifted to more active behavior compared with Ti-8Al-1Mo-1V in similar environments. These comments apply to the particular plates of these alloys for which the comparison experiments were conducted, other lots of the same nominal composition might be expected to be more or less active in terms of the intermittent cracking behavior.

Experiments using another plate of Ti-6Al-4V having a different microstructure from that discussed above demonstrated that crack jumps occurring in neutral salt water could be eliminated by increasing the loading rate [10], which is consistent with our hypothesis of a critical crack velocity above which intermittent EAC will not occur during a slow CER test (i.e., $v_s > v_c$). There were also indications that the crack upon initial propagation in air jumps up to stage II with no stage I which supports of the hypothesis that for this alloy air is of intermediate aggressiveness as discussed in the paragraph above. However, more experiments under carefully controlled conditions for the crack tip mechanics and environment are needed to better test the results of this analysis.

Another assumption made in our analysis was that EAC can be described using linear elastic fracture mechanics. In practice, EAC can deviate significantly from the plane strain and small-scale yielding assumption. In this case, the crack tip plasticity must be taken into account and our analysis would have to be extended to elastic-plastic fracture mechanics. In addition, small-scale creep plasticity should be taken into consideration in our analysis, especially with regards to its influence on crack initiation. It is not clear what influence the crack tip plasticity or creep rate has on the oscillatory crack growth behavior.

For simplicity, the analysis presented in the previous section for oscillatory crack growth cycle in the v-G plane assumed that the crack jumps instantaneously between the loading curve and stage II crack velocities. Realistically, the crack accelerates or decelerates over a very short, but finite time interval. However, the equation of motion for the crack (Eqs 21, 30 and 35), for example, predict that with a sudden change in G there is a corresponding sudden change in v. Webb and Aifantis [16] realized this difficulty and modified the traditional equation of motion for the crack to include a crack tip inertia term, which could be considered in a more rigorous analysis of macroscopic intermittent EAC.

CONCLUSION

The equations governing EAC for slow CER tests were derived for different possible crack growth kinetic mechanisms. The existence of macroscopic intermittent EAC was explained by assuming that an unstable negative slope region exists in the v-G diagram

for crack velocities below a critical value. An analysis of the equation for EAC for slow CER tests shows that when the apparent crack velocity due to crack tip blunting and plasticity during monotonic loading is less than this critical crack velocity, oscillations in the crack velocity will occur. The characteristics of these oscillations were shown to depend on the elastic behavior of the loading machine and specimen system and the material-environment function γ. In future studies, experiments will be performed to determine the mechanisms responsible for macroscopic intermittent EAC and theoretical crack tip models will be developed to describe the material-environment function.

Acknowledgment

This work was performed while the first author held a National Research Council-Naval Research Laboratory Research Associateship. Helpful discussions with E. C. Aifantis are gratefully acknowledged.

REFERENCES

[1] Clark, W. G., Jr. and Landes, J. D., "An Evaluation of Rising Load K_{ISCC} Testing," *Stress Corrosion-New Approaches, ASTM STP 610*, H. L. Craig, Jr., Ed., American Society for Testing and Materials, Philadelphia, 1976, pp. 108-127.

[2] Anderson, D. R. and Gudas, J. P., "Stress Corrosion Evaluation of Titanium Alloys Using Ductile Fracture Mechanics Technology," *Environment-Sensitive Fracture: Evaluation and Comparison of Test Methods, ASTM STP 821* , S. W. Dean, E. N. Pugh and G. M. Ugiansky, Eds., American Society for Testing and Materials, Philadelphia, 1984, pp. 98-113.

[3] Abramson, G., Evans, J. T. and Parkins, R. N., "Investigation of Stress Corrosion Crack Growth in Mg Alloys Using J-Integral Estimations," *Metallurgical Transactions A* , Vol. 16A, 1985, pp. 101-108.

[4] Hackett, E. M., Moran, P. J. and Gudas, J. P., "Evaluation of Environmentally Assisted Cracking of a High Strength Steel Using Elastic-Plastic Fracture Mechanics Techniques," *Fracture Mechanics: Seventeenth Volume, ASTM STP 905* , J. H. Underwood, R. Chait, C. W. Smith, D. P. Wilhem, W. A. Andrews and J. C. Newman, Eds., American Society for Testing and Materials, Philadelphia, 1986, pp. 512-541.

[5] Dietzel, W. and Schwalbe, K.- H., "Application of the Rising Displacement Test to SCC Investigations," *Slow Strain Rate Testing for the Evaluation of Environmentally Induced Cracking: Research and Engineering Applications, ASTM STP 1210*, R. D. Kane, Ed., American Society for Testing and Materials, Philadelphia, 1993, pp. 134-148.

[6] Hirano, K., Ishizaki, S., Kobayashi, H. and Nakazawa, H., "Determination of Threshold Stress Corrosion Cracking Characteristics Using Rising Load K_{ISCC} Testing Based on Ultrasonic Method," *Journal of Testing and Evaluation,* JTEVA, Vol. 13, No. 2, March 1985, pp. 162-168.

[7] Mayville, R. A., Warren, T. J. and Hilton, P. D., "Determination of the Loading Rate Needed to Obtain Environmentally Assisted Cracking in Rising Load Tests," *Journal of Testing and Evaluation,* JTEVA, Vol. 17, No. 4, July 1989, pp. 203-211.

[8] Bayles, R. A. and Meyn, D. A., "Stress Corrosion Cracking of a Titanium Alloy in a Hydrogen-Free Environment," *Corrosion Cracking*, V. S. Goel, Ed., American Society of Metals, 1986, pp. 241-248.

[9] Meyn, D. A. and Bayles, R. A., "Fractographic Analysis of Hydrogen-Assisted Cracking in Alpha-Beta Titanium Alloys," *Fractography of Modern Engineering Materials: Composites and Metals, ASTM STP 948*, J. E. Masters and J. J. Au, Eds., American Society for Testing and Materials, Philadelphia, 1987, pp. 400 - 423.

[10] Meyn, D. A. and Pao, P. S., "Slow Strain Rate Testing of Precracked Titanium Alloys in Salt Water and Inert Environments," *Slow Strain Rate Testing for the Evaluation of Environmentally Induced Cracking: Research and Engineering Applications, ASTM STP 1210*, R. D. Kane, Ed., American Society for Testing and Materials, Philadelphia, 1993, pp. 158-169.

[11] Young, L. M.. "Environment-Assisted Cracking in Beta Titanium Alloys," MS Thesis, University of Virginia, Charlottesville, VA, 1993.

[12] Meyn, D. A., "Cleavage in Ti-8Al-1Mo-1V Caused By Hydrogen Gas," *Metallurgical Transactions*, Vol. 3, 1972, pp. 2302-2305.

[13] Nelson, H. G., "A Film-Rupture Model of Hydrogen-Induced, Slow Crack Growth in Acicular Alpha-Beta Titanium," *Metallurgical Transactions A*, Vol. 7A, 1976, pp. 621-627.

[14] Kramer, E. J. and Hart, E. W., "Theory of Slow, Steady State Crack Growth in Polymer Glasses," *Polymer*, Vol. 25, 1984, pp. 1667-1678.

[15] Maugis, D., "Review: Subcritical Crack Growth, Surface Energy, Fracture Toughness, Stick-Slip and Embrittlement," *Journal of Material Science*, Vol. 20, 1985, pp. 3041-3073.

[16] Webb, T. W. and Aifantis, E. C., "Oscillatory Fracture in Polymeric Materials," *International Journal of Solids and Structures* , in press.

[17] Cherepanov, G. P., *Mechanics of Brittle Fracture*, McGraw-Hill, New York, 1979.

[18] Bomberger, H. B., Meyn, D. A. and Fraker, A. C., "Critical Review Environmental Effects on Titanium and its Alloys," *Titanium Science and Technology*, G. Lütjering, U. Zwicker and W. Bunk, Eds., Deutsche Gesellschaft für Metallkunde e. V., Oberusel, West Germany, 1985, pp. 2435-2454.

[19] Gerberich, W. W., "The Micromechanics and Kinetics of Environmentally Induced Fractures," *Fracture Mechanics: Microstructure and Micromechanisms*, S. V. Nair, J. K. Tien, R. C. Bates and O. Buck, Eds., ASM International, 1989, pp. 201-228.

[20] Meletis, E. I. and Aifantis, E. C., "On the Length of Crack Advance During Hydrogen-Assisted Cracking," *Scripta Metallurgica et Materialia*, Vol. 25, 1991, pp. 847-852.

[21] Wei, R. P., Novak, S. R. and Williams, D. P., "Some Important Considerations in the Development of Stress Corrosion Cracking Test Methods," *Materials Research and Standards*, Vol. 12, 1972, pp. 25-30.

[22] Hudak, S. J., Jr. and Wei, R. P., "Consideration of Non-Steady-State Crack Growth in Materials Evaluation and Design," *International Journal of Pressure Vessels and Piping* , Vol. 9, 1981, pp. 63-74.

[23] MacDonald, D. D. and Chung, H. H., "A Study of Transient Crack Growth in AISI 4340 Steel in NaCl Solution," *Corrosion*, Vol. 41, 1985, pp. 151-159.

[24] Aifantis, E. C., "Remarks on Media with Microstructures," *International Journal of Engineering Science*, Vol. 22, 1984, pp. 961-968.

[25] Spiedel, M. O., " Stress Corrosion Cracking and Corrosion Fatigue Fracture Mechanics," *Corrosion in Power Generating Equipment*, M. O. Spiedel and A. Atrens, Eds., Plenum Press, New York, 1984, pp. 85-132.

Dynamic Loading

Pedro M. Vargas[1] *and Robert H. Dodds, Jr.*[2]

Strain Rate and Inertial Effects on Impact Loaded Single–Edge Notch Bend Specimens

REFERENCE: Vargas, P. M., and Dodds, Jr., R. H., **"Strain Rate and Inertial Effects on Impact Loaded Single-Edge Notch Bend Specimens,"** Mechanics: 26th Volume, ASTM STP 1256, Walter G. Reuter, John H. Underwood, and James C. Newman, Jr., Eds., American Society for Testing and Materials, Philadelphia, 1995.

ABSTRACT: Many significant problems in fracture mechanics of ductile metals involve surface breaking defects (cracks) located in structures subjected to short–duration loading caused by impact or blast. When the severity of impact loads is sufficient to produce large inelastic deformations, the assessment of crack–tip conditions must include the effects of plasticity, strain rate and inertia. This work examines the interaction of impact loading, inelastic material deformation and rate sensitivity with the goal of improving the interpretation of ductile fracture toughness values measured under dynamic loading. We focus on shallow and deeply notched bend test specimens, SE(B)s, employed routinely to measure the static fracture toughness of a material. A thorough understanding of the test specimen's dynamic behavior is a prerequisite to the application of measured fracture properties in structural applications.

Three–dimensional, nonlinear dynamic analyses are performed for SE(B) fracture specimens ($a/W = 0.5, 0.15, 0.0725$) subjected to impact loading. Loading rates obtained in conventional drop tower tests (impact load–line velocities of ≈ 6 m/sec) are applied in the analyses. An explicit time integration procedure coupled with an efficient (one–point) element integration scheme is employed to compute the dynamic response of the specimen. Strain–rate sensitivity is introduced via a new, efficient implementation of the Bodner–Partom viscoplastic constitutive model. Material properties for A533B steel (a medium strength pressure vessel steel) are used in the analyses. Static analyses of the SE(B) specimens provide baseline responses for assessment of inertial effects. Similarly, dynamic analyses using a strain–rate insensitive material provide reference responses for the assessment of strain rate effects. Strains at key locations on the specimens and the support reactions (applied load) are extracted from the analyses to assess the accuracy of static formulas commonly used to estimate applied J values. Inertial effects on the applied J are quantified by examining the acceleration component of J evaluated through a domain integral procedure.

KEY WORDS: inertial effects, strain rate sensitivity, impact loading, J, constraint

The interpretation of measured fracture properties for a material under impact loading requires a careful assessment of dynamic effects on specimen response. Impact testing introduces potentially three dynamic effects of interest: 1) stress waves of short duration ($\lesssim 50$ μs) and specimen vibrations at longer times after impact ($\gtrsim 1$ ms), 2) high strain rates at the crack tip, and 3) acceleration of material in the crack–tip region. Direct experimental evaluation of these effects and their individual influence on ductile fracture parameters in shallow and deeply notched SE(B) specimens appears very difficult.

[1] Senior Research Engineer, Exxon Production Research, Houston, Texas, 77252–2189

[2] Professor, Department of Civil Engineering, University of Illinois, Urbana, IL 61801

Copyright © 1995 by ASTM International www.astm.org

In this study, we use 3–D, nonlinear finite element analyses to examine *separately* each of these effects. Quasi–static analyses of the specimens provide reference responses from which inertial effects are assessed. Companion dynamic analyses using two different materials, first a strain–rate independent material and then a strain–rate sensitive material, enable the effects of strain rate alone to be examined.

Strains at key locations on the specimens and the support reactions (or total load), quantities which can be measured during tests, are extracted from the analyses and used in conventional quasi–static methods for J computation (η methods). These estimates for J are compared to those obtained with domain integral computations which use near–tip fields from the nonlinear, dynamic finite–element analyses. A key feature of the analyses involves estimation of the time following impact at which inertial effects diminish sufficiently for the conventional (static) J formulas to apply.

Numerical results are reported here for SE(B) specimens with dimensions $W = B = 50$ mm and a span of 200 mm for which experimental impact results are available [1]. Stress–strain properties for A533B (pressure vessel) steel are adopted in all finite element analyses. Loading rate effects on the uniaxial stress–strain behavior of this material have been studied extensively. The finite element models employed in these analyses have sufficient mesh refinement for accurate evaluation of the J–integrals and Crack Tip Opening Displacement (CTOD) over the crack–front as the loading increases. However, the meshes provide only crude estimates of the strain and stress fields over distances of several CTODs from the tip. Even so, these models require several days of computation on a fast, desktop workstation.

Following a brief discussion of a typical arrangement for impact testing of SE(B) specimens, the three–dimensional finite element models developed for the impact analyses and the constitutive model for viscoplastic effects are described. The remaining sections provide a detailed description and assessment of strain rate and inertial effects on the global specimen response and J–integral values. The paper concludes with a summary of the most significant observations derived from the numerical analyses.

IMPACT TESTING PROCEDURES

Dynamic fracture testing is performed frequently with a drop tower arrangement as illustrated in Fig. 1. Specimens are fabricated with a through–thickness saw cut that is pre–sharpened with fatigue loading. Three–point loading is accomplished with the support arrangement indicated in the figure. Deeply notched specimens ($a/W = 0.5$, where a is the crack depth and W is the total specimen width) with 50 mm square cross–sections and 200 mm span have been successfully tested with a drop weight of 545 Kg with an impact velocity of 6 m/sec. This impact velocity corresponds to a drop height of approximately 1.2 m. The elapsed time from initial impact to specimen fracture is in the range of 0.001–0.006 seconds for ferritic materials with yield strengths of 400–700 MPa. Numerical studies [2,3] have demonstrated that the applied load *vs.* time for deeply notched specimens is predicted accurately using the ordinary static bending formula keyed to longitudinal (bending) strains at the quarter–span locations as indicated on the figure. Two factors enable this accurate correlation of measured strain values with applied load: 1) the soft aluminum wedges minimize elastic rebounding of the drop weight upon impact, and 2) the large a/W ratio confines inelastic deformations to the remaining ligament on the crack plane.

Figure 2 shows the measured displacement–time curve for a typical drop tower test [4,5]. The testing apparatus effectively generates a constant velocity response over two regimes: (1) during the initial elastic and small–scale yielding response and (2) following formation of a full plastic hinge. To provide the final regime of constant velocity loading, the kinetic energy of the tup must eventually overwhelm the internal energy absorbed by the specimen prior to fracture. The nearly constant velocity produces a terminal, linear displacement–time loading of the specimen, i.e., the 2.5 m/sec loading

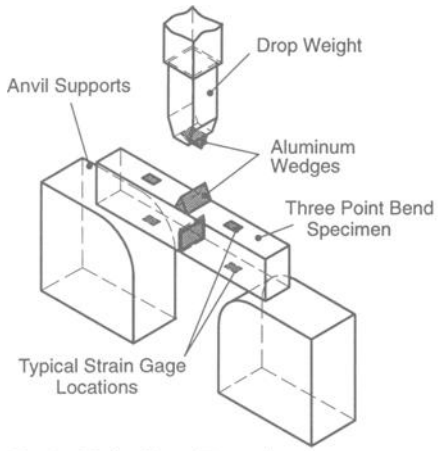


Fig. 1 Typical Drop Tower Arrangement

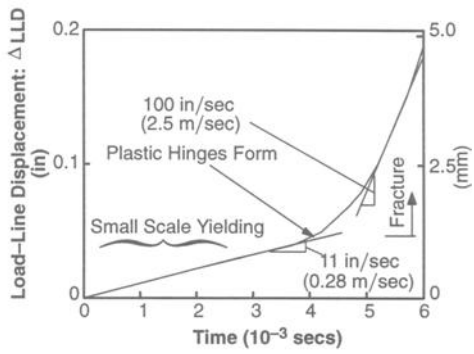


Fig. 2 Load Line Displacement for Drop Tower Test

region shown in Fig. 2. An optical probe attached directly to the specimen is often used to measure the load–line displacement. Even at large deformations, the plastic zone in these specimens is confined to the remaining ligament, leaving a large portion of material remote from the crack plane elastic, with little deformation, which facilitates attachment of the optical light probe.

FINITE ELEMENT MODELS

Figure 3 shows typical finite element models developed in this study. Models with two levels of mesh refinement, denoted *coarse* and *refined*, are shown. Due to symmetry, only one quarter of the specimen is actually modelled (the shaded region). All elements are trilinear hexagonal bricks (8–nodes), using a one point Gauss integration coupled with an effective procedure to control hourglass modes. The figures indicate the number of elements and nodes for each of the finite element models. The anvil supports are modelled by constraining the vertical displacement of the bottom surface nodes 25 mm from the specimen ends.

The Spectrom code [6] is used to compute the dynamic response of the SE(B) specimens subjected to impact loads. This code utilizes an explicit scheme to integrate through time, which makes it ideal for monitoring stress–wave effects. Element formulations accommodate finite–strains and finite–rotations using an Updated Lagrangian approach. The code provides a 4–node shell element and the three–dimensional 8–node brick element. Several nonlinear constitutive models are available in the standard version but not a strain–rate dependent plasticity model. The program runs efficiently on 32–bit workstation environments as well as supercomputers. Numerous modifications and enhancements were implemented to support the SE(B) analyses [7].

The application of time dependent external forces is the preferred method of loading a finite element model. However, the lack of detailed information on the applied loading requires a procedure to generate a loading that, when applied to the finite element model, predicts the displacement history measured in tests. The finite element loading to model the drop tower test is generated by first executing displacement controlled (dynamic) analyses in which the loaded area is uniformly displaced according to a measured displacement history (Fig. 2). The coarse models are used in these analyses. Application of the uniform displacement across the loading area effectively creates a rigid boundary that causes high frequency oscillations. Reactions at the displaced nodes are extracted and smoothed to generate an equivalent external loading history. These external loads are applied to the refined

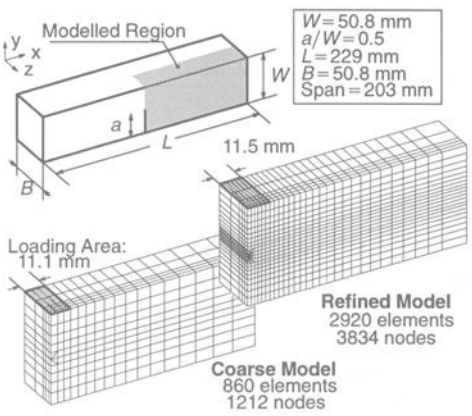


Fig. 3 Finite Element Mesh for Deep Crack Specimen

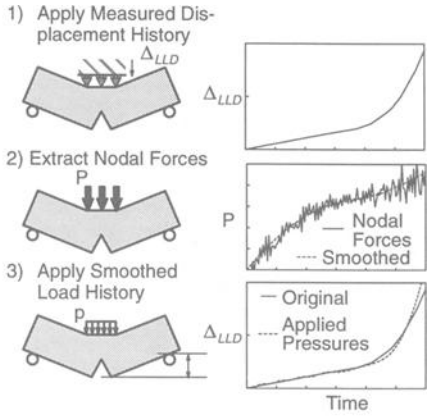


Fig. 4 Methodology to Determine Applied External Loads

models over the loading area as an equivalent (time–dependent) uniform pressure. The computed displacement histories of the specimen under the smoothed loadings are compared for agreement with the measured displacement history, with adjustments in the process until a satisfactory loading is produced. Figure 4 summarizes the steps of this procedure.

MODELING OF VISCOPLASTIC RESPONSE

The Spectrom code was enhanced to include a rate–dependent plasticity model suitable for ductile metals. The selected Bodner–Partom constitutive model belongs to the family of viscoplastic theories of the "unified" approach, which combine both time–independent plasticity and time–dependent phenomena such as creep and stress relaxation into a single state variable [8]. Initially developed from a simple model attributed to Norton [9], the Bodner–Partom material model has since been modified to include isotropic and directional hardening effects [10]. The essential features of the Bodner–Partom model are: 1) the Prandtl–Reuss flow rule, 2) a kinetic equation that relates the strain rate to the stress and the hardening variable, 3) an evolution law for the internal hardening variable, and 4) adiabatic deformation. Vargas and Dodds [7] describe an efficient implementation for the Bodner–Partom material model in Spectrom to support the SE(B) analyses.

Viscoplastic Properties Of A533B Steel

The characterization of viscoplastic properties of a material with the Bodner–Partom material model requires multiple uniaxial tests of the material under widely varying strain rates. The extensive testing and associated expense have limited the number of materials for which constants are available.

Dexter and Chan [11] tested A533B steel to determine properties for the Bodner–Partom material model. Table 1 summarizes the mechanical properties and the Bodner–Partom constants at 50°C used in this study. The corresponding (tensile) stress–strain curves for different strain rates at 50°C are shown in Fig. 5. The yield stress increases significantly with strain rate. In quasi–static analyses and rate–insensitive dynamic analyses, we use the stress–strain curve for a strain rate of 0.001/sec. Other materials similarly characterized for the Bodner–Partom model include: A537 steel, X46 and X70 pipeline steels [12], and B1900+Hf, a nickel based super–alloy [13].

Average Room Temperature Quasi-Static Properties:

Young's Modulus	E = 30,000 ksi (206.9 GPa)
Poisson's Ratio	ν = 0.3
Yield Stress	σ_y = 64.5 ksi (445 MPa)
Ultimate Stress	σ_u = 86.6 ksi (597 MPa)
Elongation	24%
Area Reduction	69%
Density	$\varrho = 7.35 \times 10^{-4}$ lb-sec^2/in^4 (7850 Kg/m^3)

Bodner Partom Constants at 122°F (50°C):

m = 0.441 ksi^{-1} (0.064 MPa^{-1})
n = 1.75
$D_0 = 10^8$ sec^{-1}
Z_0 = 200 ksi (1379 MPa)
Z_1 = 262 ksi (1804 MPa)

Table 1 Mechanical Properties for A533B Steel

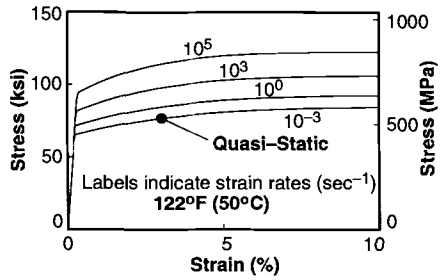


Fig. 5 Stress–Strain Curves for A533B Steel Predicted by Bodner–Partom Model

DYNAMIC EFFECTS IN SE(B) SPECIMENS

Figure 6 shows the vertical displacement histories at mid-span for the deep crack SE(B) ($a/W = 0.5$) specimen. Displacements at two locations on the remaining ligament are indicated. The minimum vertical displacement occurs at the crack tip on the longitudinal centerplane of the specimen; the maximum vertical displacement occurs at nodes on the loaded area at the (outside) free surface. Load–line displacements measured with an optical light probe during the drop tower test are also given. The good agreement between between the finite element analyses and the drop tower test record indicate the success of the load generation scheme described previously. Similar agreement is obtained for the $a/W = 0.15$, 0.0725 specimens.

Times after impact are normalized by the time required for an unbounded dilatational wave to travel the width of the specimen, t_W[2]. Using the elastic properties for A533B steel, the unbounded dilatational wave speed, c_1, is 5.1 $\times$ 10^6 mm/sec. For a specimen width $W = 51$ mm, t_W is then:

$$t_W = \frac{W}{c_1} = 8.5 \times 10^{-6} \text{ sec} \tag{1}$$

The 0.006 sec duration of the analyses corresponds to approximately 700 wave traversals over the specimen width. Spatial diffusion after several traversals significantly diminishes discrete wave effects and they become negligible for most of the specimen response.

The vertical displacement histories shown in Fig. 6 exhibit clear periodic oscillations during the initial 0.003 seconds. Simple elastic vibration in the first dynamic mode produces these oscillations. The first two modes and their frequencies were computed for the finite element models using the POLO–FINITE system [14]. Due to symmetry conditions imposed in the analyses, the first two computed modes correspond to the first and third modes of the full specimen. The periods of the first mode and third mode of the deep crack specimen are 0.62×10^{-3} sec and 0.12×10^{-3} sec, respectively.

Nakamura, et al. [2,3] introduced the concept of a *transition time*, t_T, which defines the point in the response after which inertial effects diminish rapidly. Upon impact of the loading tup, the specimen velocity and the kinetic energy both increase very rapidly. As the specimen begins to deform, the internal energy also increases at a rapid rate. For the range of loading rates, specimen sizes and material flow properties considered here, the total internal energy eventually overtakes the total kinetic energy of the specimen due to extensive plastic deformation. The transition time occurs when the total kinetic energy (T) of the specimen becomes less than the internal energy (U) of the specimen. After the transition time, the kinetic energy continues to increase, but at a much diminished rate relative to the rate of increasing internal energy. Nakamura proposed, and validated, a limit of 2 $\times$ t_T

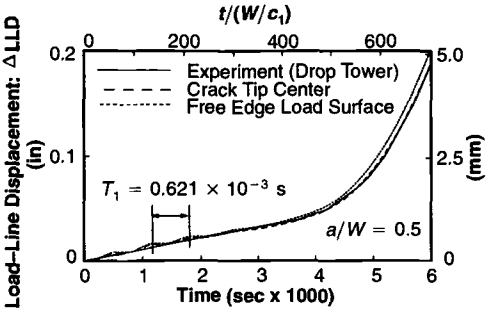


Fig. 6 Mid–Span Displacements for Rate–Sensitive Material, $a/W = 0.5$

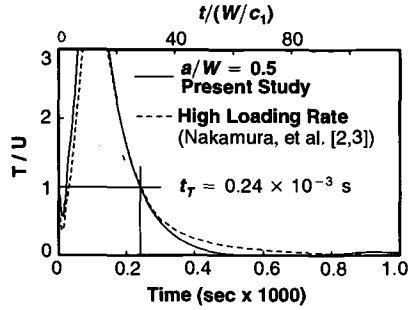


Fig. 7 Energy Ratio of Deep Crack Specimens Under Different Loading Rates

as a time after which the evaluation of the fracture parameters (J–integral) using conventional static formulas based on areas under load–load line displacement curves yields acceptable accuracy.

Figure 7 shows the evolution of the energy ratio after impact for the deep crack specimen. The transition time occurs very early in the response while the specimen remains predominantly linear–elastic. Strain rate effects are negligible during this early stage, and both rate–sensitive and rate–insensitive material models predict identical energy ratios.

Nakamura, et. al [2,3] performed a dynamic finite element analysis of a deep notch SE(B) specimen using a higher loading rate (terminal velocity of 4.7 m/sec compared to 2.5 m/sec here and thickness $B = 25$ mm rather than 50 mm used here). They report the evolution of energy ratio indicated in Fig. 7 with a transition time identical to that found for the deep crack SE(B) specimens of this study. For the present analyses, Fig. 7 shows that the energy ratio decreases very rapidly, approaching zero soon after the transition time of 0.24×10^{-3} seconds, which also corresponds to approximately $28 \times t_W$. Nakamura also reports a similarly normalized transition time of $28 \times t_W$ for a deep crack specimen.

In our study, we conducted dynamic finite element analyses for specimens with a/W ratios of 0.5, 0.15, 0.0725 for a wide–range of loading rates. In all cases, the transition time occurs at approximately 0.4 × the first elastic vibration period of each specimen. A more complete discussion of this issue is given by Vargas and Dodds [7].

J–Integral with Inertia Loading Effects

Extensions of the J–integral to incorporate the effects of dynamic loading for non–growing cracks are developed by including the kinetic energy density of material at the crack tip in the same manner as the strain energy density [2]. Thus,

$$J = \lim_{\Gamma \to 0} \int_{\Gamma} \left((W + T) n_1 - P_{ji} \frac{\partial u_i}{\partial X_1} n_j \right) d\Gamma \tag{2}$$

$$W = |\boldsymbol{F}| \int_0^{\varepsilon_{ij}} \sigma_{ij} \, d\varepsilon_{ij} \; ; \quad \boldsymbol{F} = \frac{\partial \boldsymbol{x}}{\partial \boldsymbol{X}}; \quad \boldsymbol{x} = \boldsymbol{X} + \boldsymbol{u} \tag{3}$$

$$T = \frac{1}{2} \varrho \left(\frac{\partial u_i}{\partial t} \right)^2 \tag{4}$$

where W and T are the strain and kinetic energy densities relative to the undeformed volume at $t=0$, respectively; n_i denotes components of an outward unit vector to the contour, Γ; σ_{ij} and $d\varepsilon_{ij}$ are the Cauchy stresses and differential strains (rate of deformation tensor $\times$ dt), respectively; the (non-symmetric) 1st Piola–Kirchhoff stresses are indicated by P_{ij}; ϱ is the material mass density; u_i are the displacements; t denotes time and X_i denotes coordinates in the undeformed specimen at $t=0$. As indicated in Eqn. 3, $\boldsymbol{F}$ denotes the deformation gradient relative to $t=0$. The positive direction of the contour is shown in Fig. 8. The integral becomes applicable for *arbitrary* material response in the limit as the contour shrinks to a point on the crack front. In three dimensions the contour Γ is defined in a plane perpendicular to the crack front at point s as shown in Fig. 8.

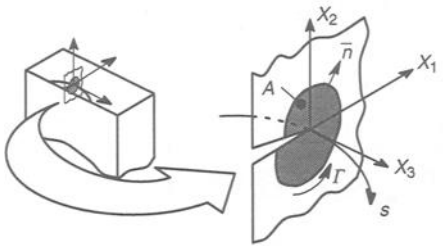


Fig. 8 Local J–integral in 3–D

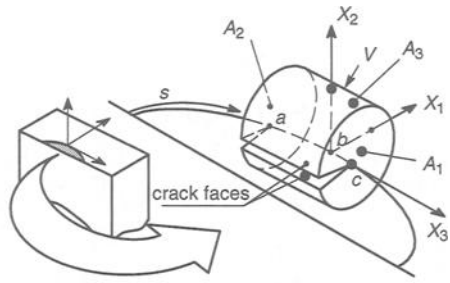


Fig. 9 Finite Volume for Use in Domain Integral Formulation

By using a weight function which may be interpreted as a virtual displacement field, the contour integral is converted into a volume integral in three dimensions [15,16]. The resulting expressions are:

$$\bar{J}_{a-c} = \int_{s_a}^{s_c} \left[J(s)q_t(s)\right] dS = \bar{J}_1 + \bar{J}_2 + \bar{J}_3 \tag{5}$$

$$\bar{J}_1 = \int_{V_0} \left(P_{ji}\frac{\partial u_i}{\partial X_k}\frac{\partial q_k}{\partial X_j} - W\frac{\partial q_k}{\partial X_k} \right) dV_0 \tag{6}$$

$$\bar{J}_2 = -\int_{V_0} \left(\frac{\partial W}{\partial X_k} - P_{ji}\frac{\partial^2 u_i}{\partial X_j \partial X_k} \right) q_k \, dV_0 \tag{7}$$

$$\bar{J}_3 = -\int_{V_0} \left(T\frac{\partial q_k}{\partial X_k} - \varrho\frac{\partial^2 u_i}{\partial t^2}\frac{\partial u_i}{\partial X_k}q_k + \varrho\frac{\partial u_i}{\partial t}\frac{\partial^2 u_i}{\partial t \partial X_k}q_k \right) dV_0 \tag{8}$$

where q_k is the weight function in the k coordinate direction ($q_t(s)$ represents weight function value at point s on the crack front), V_0 represents the volume of the domain surrounding the crack tip (in the $t=0$ configuration), and s denotes position along the crack front segment. Figure 9 shows a typical domain volume defined for an internal segment along a three–dimensional surface crack. Vargas and Dodds [7,17] outline details of computational procedures to evaluate these integrals.

Figures 10 and 11 show the J–values computed using the rate sensitive and rate insensitive material models for the deep notch ($a/W=0.5$) and shallow notch ($a/W=0.0725$) specimens. These thickness average J–values are normalized the flow stress, σ_{fl}, and the remaining ligament, $b=W-a$ (σ_{fl} is the average of the yield and ultimate stresses). Using material property data for A533B steel (see Table 1), σ_{fl} = 520 MPa. The rate sensitive material model produces slightly larger J–values for the deep notch specimen with essentially no difference observed for the shallow notch J–values.

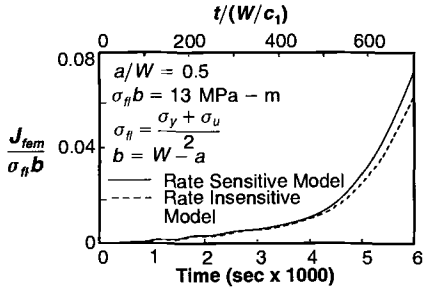


Fig. 10 J_{fem} from Domain Integrals for the Deep Crack SE(B) Specimens

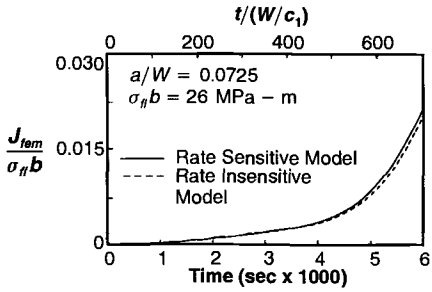


Fig. 11 J_{fem} from Domain Integrals for the Shallow Crack SE(B) Specimens

J Evaluation in Test Specimens

Rice et. al, [18] demonstrated that the J–integral is related closely to the work done by the ligament moment acting through the rotation angle for SE(B) specimens under static loading (see Fig. 12). For deeply notched specimens ($a/W > 0.5$), the J–integral for a SE(B) is given approximately by:

$$J = \frac{2}{bB} \int_0^{\Omega} M \, d\Omega \tag{9}$$

where M is the moment on the remaining ligament at the crack plane and Ω is the relative angle between the specimen ends (see Fig. 12). This definition provides an average value of $J(s)$ across the entire crack front.

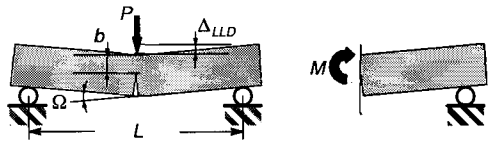


Fig. 12 Idealized 3 Point Bend Specimen

By assuming the two ends of the specimen undergo a simple rigid–body rotation about the crack plane, the angle Ω is related directly to the load–line displacement Δ_{LLD}, $\Omega = \Delta_{LLD}/(L/2)$, where L is the span between supports. From equilibrium, the moment at the specimen center, M, is simply $(PL)/4$. Eqn. 9 can be rewritten as:

$$J = \frac{\eta}{bB} \int_0^{\Delta_{LLD}} P d\Delta_{LLD} \tag{10}$$

where η is the dimensionless parameter ≈ 2 for deep notch SE(B) specimens.

Sumpter [19] separates the external work of the applied load into elastic and plastic components, W_e and W_p and then writes

$$J = J_e + J_p = \frac{\eta_e}{bB} W_e + \frac{\eta_p}{bB} W_p \tag{11}$$

where η_e and η_p are the dimensionless constants that relate the elastic and plastic external work to the fracture driving force. W_p denotes the external work of the applied load acting through the plastic component of the load line displacement. η_p indicates the relative amount of total plastic deforma-

tion that contributes to crack–tip driving force rather than plasticity remote from the crack plane. By using the relationship between the J–integral and stress intensity factor K_I for plane strain, Eqn. 11 is rewritten as:

$$J = J_e + J_p = \frac{K_I^2(1 - \nu^2)}{E} + \frac{\eta_p}{bB} \int_0^{\Delta_{LLD}} P \, d\Delta_p \quad . \tag{12}$$

This form insures compatibility between measured values of J and K_I when the deformation is predominantly linear–elastic.

Because direct measurement of the applied loading may be impractical or very difficult in a dynamic test such as the drop tower, the following indirect methods to infer applied loads are evaluated:

1. Applied loads are evaluated from the support reactions. Experimentalists have proposed to use instrumented supports to measure reactions.
2. Applied loads are evaluated from the quarter–span strains measured on the top and bottom surfaces of the specimen that are calibrated against a static linear–elastic analysis. Because the specimen is statically determinate, the moment at the quarter–span location is one–half the centerplane moment and is equal to the applied load × $L/8$ (neglecting inertial effects). For deep notch specimens, plastic deformation remains confined to the center plane region which leads to a linear–elastic response at the strain gage locations and a linear variation of bending strain over the specimen width. This approach fails when plastic deformation disturbs the through–width, linear strain variation.
3. Applied loads are evaluated from the moment computed at the crack plane using nodal reactions. This moment, which includes inertial effects, is compared to the crack plane moment for a simply supported beam with a statically applied mid–span load. This method predicts a quasi–static, equivalent load needed to achieve the same moment across the ligament that occurs under dynamic loading.

Sumpter [19] obtained values for η_p using 2–dimensional, slip–line solutions for SE(B) specimens with pure moment loading on the crackplane. This approach yields η_p–values of 2.0 for the deep crack specimen and 0.97 for the shallow crack specimen. Figures 13 and 14 show the J–values (denoted J_η) computed using these η_p values and the dynamic finite element, load–load line displacement curves. J_η values are normalized by the full–field domain integral values (denoted J_{fem}) obtained from the dynamic analyses. J_η values computed using the different inferred loads, together with those computed from the (known) applied loads in the analyses, are included in the figures. Deviations of the normalized J–values from unity indicate the relative error incurred in using static formulas for the evaluation of J. Errors in the computation of J approach 10% toward the end of the analysis for the deep crack specimen and 20% for the shallow crack specimen.

The separation of J into elastic and plastic components is somewhat arbitrary. Other separation techniques, such as deformation of the specimen without the crack and the additional deformation that occurs due to the crack, are equally valid [20]. The original derivation by Rice [18] does not assume any separation of the total J. The expression to compute a static J–value without prior separation into J_e and J_p becomes

$$J_{\eta(T)} = \frac{\eta_T}{bB} \int_0^{\Delta_{LLD}} P \, d\Delta_{LLD(T)} \tag{13}$$

where η_T denotes an η factor for the total work on the ligament and Δ_T denotes the total load–line displacement. Static, 3–D finite element analyses of these specimens were performed to obtain estimates for η_T [7]. We find $\eta_T \approx 1.91$ for the deep crack specimen and $\eta_T = 0.82$ for the shallow crack specimen. Figures 15 and 16 compare J–values computed using Eqn. 13 for the deep crack and the shallow crack specimen, respectively, with the full–field domain integral J–values. Relatively large

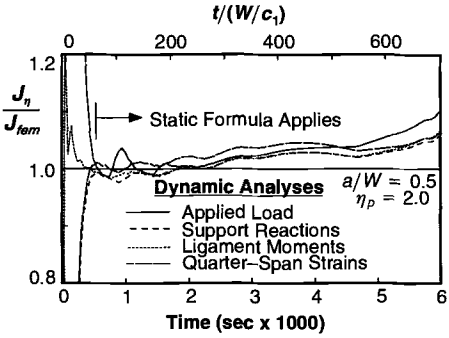


Fig. 13 J_η/J_{fem} for Rate–Sensitive SE(B) $a/W=0.5$, Using Energy Separation

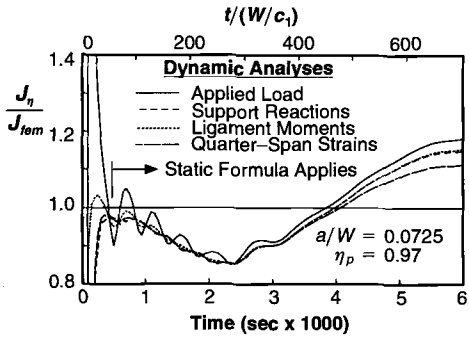


Fig. 14 J_η/J_{fem} for Rate–Sensitive SE(B) $a/W=0.0725$, Using Energy Separation

inertial effects are observed for the initial 0.0006 seconds of the deep crack specimen, and for the initial 0.0004 seconds of the shallow crack specimens. These are approximately 2.5 × the transition time of each specimen. After this time, all three methods to infer the load (for ligament work calculation) produce less than 5% error in J for the deep crack specimen and less than 10% error for the shallow crack specimen. Consequently, J predictions based on a total ligament work rather than a conventional elastic–plastic separation approach are more accurate for a dynamic analysis. Strain–rate sensitivity of the material does not affect the accuracy of J–values obtained using Eqn. 13.

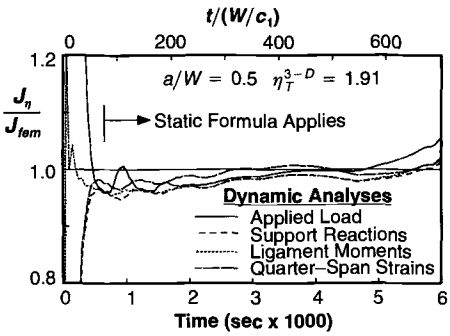


Fig. 15 J_η/J_{fem} for Rate–Sensitive SE(B) $a/W=0.5$, Using Total Energy

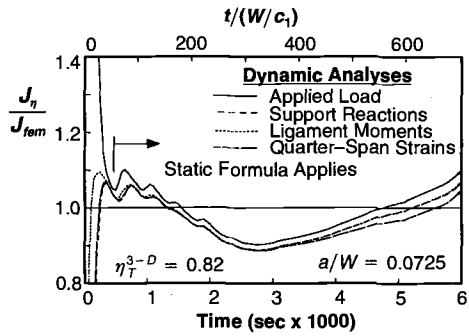


Fig. 16 J_η/J_{fem} for Rate–Sensitive SE(B) $a/W=0.0725$, Using Total Energy

INERTIAL EFFECTS ON J

Equations 6 through 8 describe contributions to the J–integral for dynamic loading. $\bar{J}_1$ and $\bar{J}_2$ are independent of direct inertial effects and their sum is the J–integral for static loading. Inertial effects enter the computation of J directly through $\bar{J}_3$. The first and third terms of Eqn. 8 arise from the kinetic energy and the explicit derivative of the kinetic energy over the integration domain, respectively. These two terms become significant for situations that occur with unstable crack propagation where large velocities and large velocity gradients exist near the crack tip [21]. For the non–propagating cracks investigated in this study, these two terms represent less than 0.1% of $\bar{J}_3$. For the present analyses, the second term in Eqn. 8 (denoted $\bar{J}_{acc}$) dominates the value of $\bar{J}_3$:

$$\bar{J}_{acc} = \int_{V_0} \varrho \frac{\partial^2 u_i}{\partial t^2} \frac{\partial u_i}{\partial \bar{X}_k} q_k \; dV_0 \tag{14}$$

Figure 17 shows the average through thickness value of $\bar{J}_{acc}$ for the deep notch specimen using both a strain–rate sensitive and insensitive material response. $\bar{J}_{acc}$ remains near zero for the initial 0.003 seconds in both cases, after which relatively large oscillations develop. However, the magnitudes of $\bar{J}_{acc}$ are extremely small compared to the total J–integral (see Fig. 10). For all analyses, the contribution of $\bar{J}_{acc}$ to J_{ave} is less than 0.1% over most of the response. Thus for loading rates typical of those in drop tower tests, accurate computation of J–values does not require the $\bar{J}_3$ term. This confirms the quasi–static nature of the experiment with respect to the computation of J and explains the good agreement between J computed with the static equations (Eqns. 12 and 13) and the finite element results from the dynamic analyses described here (Eqn. 5).

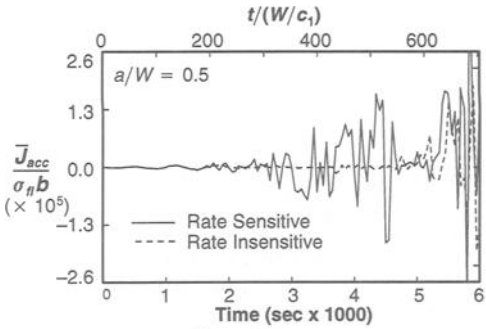


Fig. 17 $\bar{J}_{acc}$ for the SE(B) Specimens

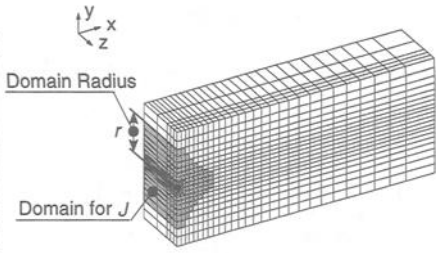


Fig. 18 Large Domain for Deep Crack SE(B) Specimen

Very early in the response ($t < 10^{-4}$ s), when discrete stress waves are still prevalent, $\bar{J}_{acc}$ contributes a significant part of the total J–integral. In particular, for times less than $t < 10^{-4}$ s, $\bar{J}_{acc}$ is *needed* to obtain domain independence of the J–values as shown in Fig. 19. Ten domains, each with an increasingly larger in–plane radius, are defined to examine the domain dependence of the J values. The vertical distance from the crack tip to the domain edge defines the domain radius (size). Figure 18 indicates the largest domain employed with the corresponding domain radius. A unit value of q is specified at every node in the domain interior. The q–value for all other nodes is set to zero.

Figure 19 shows the normalized values of $\bar{J}_1$, (defined in Eqn. 6), $\bar{J}_{acc}$, and the sum $\bar{J}_1 + \bar{J}_{acc}$, as a function of normalized domain radius for the strain–rate sensitive, deep–crack SE(B) analysis. The values of $\bar{J}_{acc}$ and $\bar{J}_1$ correspond to response times of 2–7 $\times$ 10^{-5} secs. The specimen remains predominantly elastic over these response times. The average of all the domains (excluding the domain that contains crack tip elements only) of J_{fem} (Eqn. 5) is used as J_{ave} for the normalization. However, the J–value for the specimen at these response times is *insignificant* (less than 0.03 kPa–m).

$\bar{J}_1$ exhibits a domain dependence at these early response times. At 2 $\times$ 10^{-5} secs $\bar{J}_1$ is negative for the larger domains, and approaches the domain independent value with decreasing domain radius. $\bar{J}_{acc}$ exhibits the opposite behavior, and approaches zero with decreasing domain radius. The sum of these two values is domain independent. At 5 $\times$ 10^{-5} secs, $\bar{J}_1$ alone is equal to the total J–integral for all domains. Small domains defined near the crack tip provide accurate J values using $\bar{J}_1$ alone. Similar path dependence of $\bar{J}_1$ is found by Nikishkov and Atluri [22], and Vargas [23] for thermal loading.

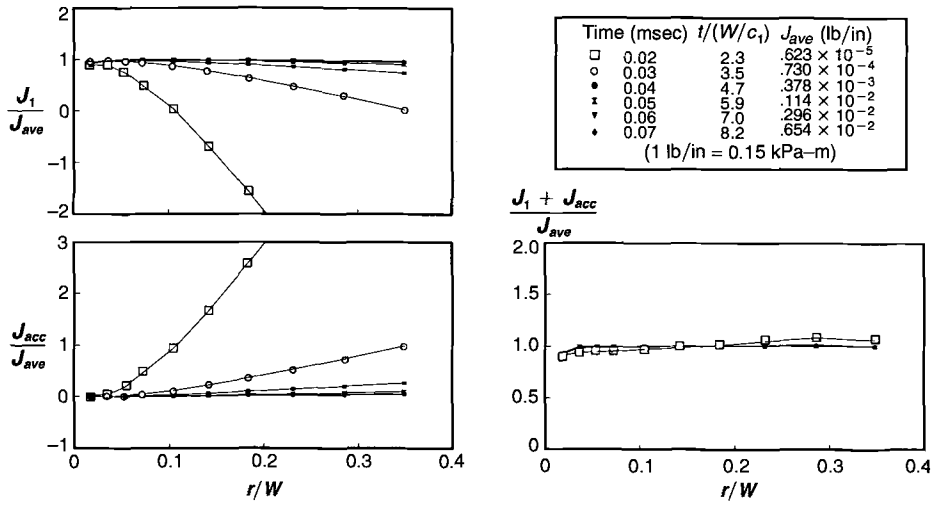


Fig. 19 Domain Radius Dependence of J for the Deep Crack SE(B) Specimen

Effects of Strain–Rate Sensitivity

Figure 20 shows the distribution of strain rates for the three specimens computed using the strain–rate sensitive model ($\dot{\bar{\varepsilon}} = \sqrt{(2/3)\dot{\varepsilon}_{ij}\dot{\varepsilon}_{ij}}$). The visible surfaces include the crack plane, the vertical free surface and the top surface of the specimens. Results for the rate–insensitive analyses are indistinguishable from those in Fig. 20. The identical strain rates are expected since the loading is defined to produce nearly constant velocity response in all specimens.

The strain rate distributions shown in Fig. 20 correspond to two loading regimes of interest: 1) the strain rates from zero to 0.001 seconds after impact, and 2) the strain rates from 0.005 to 0.006 seconds after impact. In these two regimes, the displacement history of the specimens exhibit constant velocity (see Fig. 6): a constant load line velocity of 0.28 m/sec up to 0.004 seconds and a constant terminal velocity of 2.5 m/sec after approximately 0.005 seconds. The load–line velocity at the terminal loading regime is ten times larger than in the initial regime. The strain rates shown in Fig. 20 also reveal the same factor of ten in the strain rates. During the terminal velocity regime, strain rates larger than 50/sec are concentrated in the remaining ligament.

Figure 21 shows the distribution of Mises stress, normalized with respect to the static yield stress of 445 MPa. Results for both rate–sensitive and rate–insensitive analyses are shown in the figures. Rate sensitivity does not affect the Mises stress distributions prior to 0.003 seconds for each of the three specimens—the behavior remains predominantly linear–elastic for all three geometries prior to this time. At 0.004 seconds into the response, all three specimens show full plastic hinge development across the remaining ligament for both material models. (Figure 6 confirms that elastic oscillations of the deep crack specimen cease after this time). The plastic zone for the deep crack specimen is confined to the remaining ligament. For the shallow crack specimen, the plastic zone extends through the depth of the specimen. Once plastic deformation becomes extensive, the rate sensitive material model shows significant increases in the Mises stress levels for all three specimens. The plastic zones developed after initial ligament yielding parallel the formation of high strain rate zones of Fig. 20.

The quasi–static stress–strain curve, shown in Fig. 5 and used in the rate–insensitive dynamic analyses, is also used as the stress–strain curve for the Mises material model in the static analyses.

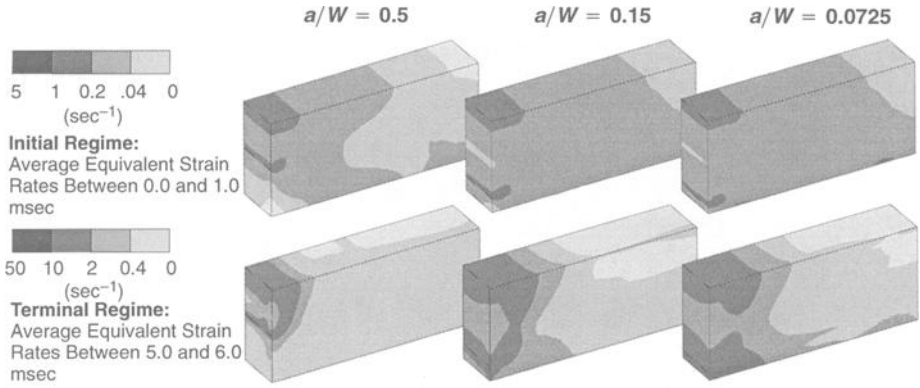


Fig. 20 Strain Rates Shown on Quarter Symmetric Models

Static analyses with this stress–strain curve provide the counterpart for the rate–insensitive dynamic analyses. In addition, static analyses are performed using a stress–strain curve indicative of the strain rates experienced by the specimen. Figure 22 shows the equivalent uniaxial stress–strain history experienced by a typical crack–tip element in the three rate sensitive specimens. The crack–tip element utilized for the stress–strain history in the figure is located on the longitudinal centerplane, directly ahead of the crack tip, i.e., on $\theta = 0$. Also shown in the figure is the equivalent uniaxial stress–strain curve for A533B steel at 50°C, at a strain rate of 50 sec^{-1}. This stress–strain curve closely matches

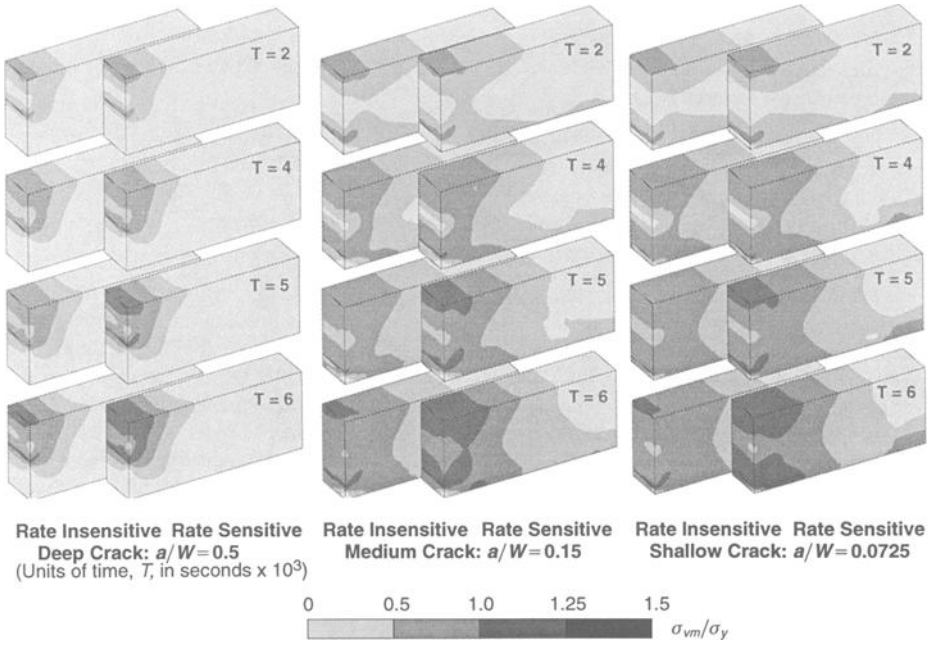


Fig. 21 Mises Equivalent Stresses for the SE(B) Specimens

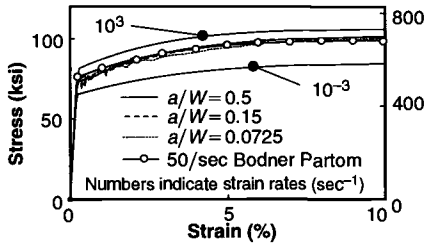


Fig. 22 Elevated Stress–Strain Curves for Static Analyses

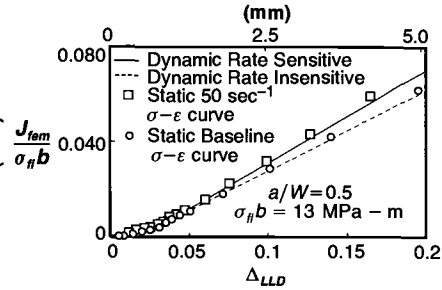


Fig. 23 J_{fem} *vs.* Load–Line Displacement $a/W=0.5$

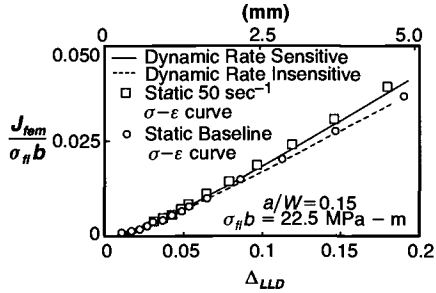


Fig. 24 J_{fem} *vs.* Load–Line Displacement $a/W=0.15$

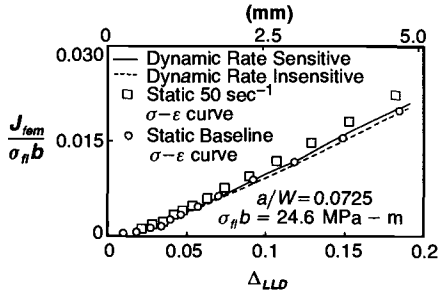


Fig. 25 J_{fem} *vs.* Load–Line Displacement $a/W=0.0725$

the crack–tip stress–strain response shown and is used in a second set of static analyses to simulate the rate sensitive material behavior.

Figures 23 through 25 compare the finite element J–values for the dynamic analysis with J–values for the corresponding static analyses. For a given load–line displacement, the J–values for the static analyses performed with the quasi–static stress–strain curve are nearly identical to those for the rate–insensitive dynamic analyses in all three specimens. *Global* inertia effects on thickness average J–values are thus found to be negligible.

J–values for the second set of static analyses, labelled by the corresponding strain rate of the equivalent Bodner–Partom material model, are also shown in the figures. For the deep crack specimen, these static results closely match the rate–sensitive dynamic analyses. For the medium crack specimen, the static J_{fem} based on the simulated rate sensitivity model exceeds the computed J_{fem} of the dynamic analyses by approximately 4%. For the shallow crack specimen, the static J_{fem} with the simulated rate sensitivity exceeds the computed J_{fem} of the dynamic analyses by nearly 10%. The use of an elevated stress–strain curve in a static analysis predicts the rate–sensitive J–value well for the deep crack specimen. For the shallow crack specimen however, the spatial variation of the strain rates ahead of the crack tip affects the applied J. Consequently, the use of a single, elevated stress–strain curve in a static analysis to predict the applied J is not accurate for the shallow crack specimen.

Figures 26 and 27 show the normalized J distribution across the crack front at the end of the dynamic analyses for the deep crack and the shallow crack specimen, respectively. Also shown on the figures are the static analysis distributions (using the baseline stress–strain curve) at the same, final load–line displacement. The relatively small differences between the three sets of results indicate that J variation across the crack front is independent of both dynamic and strain rate effects.

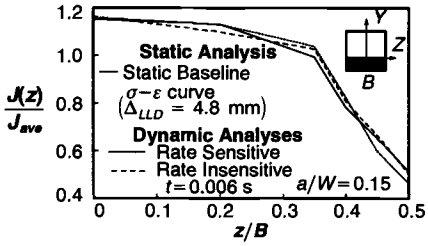


Fig. 26 Crack Front $J(z)/J_{ave}$ Variation at End of Analysis ($a/W=0.5$)

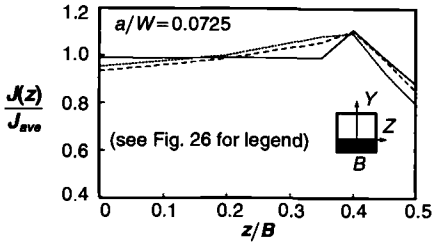


Fig. 27 Crack Front $J(z)/J_{ave}$ Variation at End of Analysis ($a/W=0.0725$)

SUMMARY

Selected results for 3–D, nonlinear dynamic and static analyses have been presented for SE(B) specimens subjected to impact loadings characteristic of those developed in drop tower tests. The static analyses provide reference solutions to assess the relative importance of strain rate and inertial effects in the dynamic analyses. The following items summarize the important observations and conclusions obtained from these analyses:

1) A methodology is presented and verified to load the dynamic models in a manner which predicts load–displacement histories measured experimentally. The method involves two analyses: one in which a displacement response is directly applied to the specimen, and a second analysis in which the nodal reactions from the first analysis are smoothed and then applied as a pressure loading to the detailed model for the specimen. Fracture mechanics parameters are taken only from analyses of the detailed model.

2) The *transition time* at which internal energy exceeds kinetic energy occurs while the specimens remain essentially linear–elastic. The transition time is consistently given by 0.4 × the first period of elastic vibration for each specimen.

3) Three techniques to infer the applied load are evaluated: measured quarter–span strains calibrated to a static analysis, end reactions and ligament moments. All three methods lead to similar predictions of the applied J using η concepts.

4) The static formula to compute J from applied work with η_p values derived from plane–strain models produces errors of 10–20%. Accuracy of the static formula is improved when modified to relate the total energy absorbed by the specimen to J. For response times after approximately 2.5 × the transition time, inertial effects diminish sufficiently for the static formula to apply.

5) Strain rates of up to 50/sec occur near the crack tip in the specimens at the imposed loading rate of 2.5 m/sec. Strain–rate sensitivity of the material increases the applied J and the crack front stresses. Rate sensitive effects for the deep crack specimen can be assessed in a static analysis through the use of an elevated stress–strain curve that corresponds to a strain rate of 50/sec. A similar assessment is not possible for the shallow crack specimen due to the greater spatial variation of the strain rates ahead of the crack tip.

6) The crack–front distribution of J, normalized by the through thickness average J, is independent of strain–rate sensitivity for the SE(B) specimens in this study.

7) The material acceleration component of the J–integral is negligible except very early in the response. At response times less than 10^{-4} s, the acceleration term of the J–integral is necessary to achieve domain independence.

ACKNOWLEDGEMENTS

Partial support for this work was provided by grants from the U.S. Nuclear Regulatory Commission and the Annapolis Detachment of the Naval Surface Warfare Center. Additional support for PMV was provided by a Ford Foundation Doctoral Fellowship awarded through the National Research

Council. Computations were performed on the HP workstation network operated by the Department of Civil Engineering, made possible in part by grants from Hewlett–Packard corporation. Finally, we appreciate the extensive, thoughtful comments of one reviewer which improved the paper.

REFERENCES

[1] Kirk, M. T., Waskey, J. P., and Dodds, R. H.,"Procedure for Drop Tower Testing of Shallow Cracked Single Edge Notched Bend Specimens," David Taylor Research Center, Ship Materials Engineering Department, Research and Development Report, Bethesda, MD DTRC–SME–90/18 (1990).

[2] Nakamura, T., Shih C. F., and Freund L. B., "Three–Dimensional Transient Analysis of a Dynamically Loaded Three–Point–Bend Ductile Fracture Specimen," *Engineering Fracture Mechanics*, Vol. 25, pp. 323–339, (1986).

[3] Nakamura, T., "Effects of Rate–Sensitivity in Dynamically Loaded 3D Fracture Specimen," Proceedings of the 7th International Conference on Fracture (ICF7), Houston, Texas March 20–24, Vol. 1, pp. 795–802 (1989).

[4] Joyce, J. A, and Hackett, E. M., "Application of the Key Curve and Multi–Specimen Techniques to Dynamic J–R Curve Testing of Alloy Steel," U.S. Nuclear Regulation Commission NUREG/CR–4579 (1986).

[5] Kirk, M. T., and Dodds, R. H.,"An Analytical and Experimental Comparison of J_i–values for Shallow Through and Part–Through Surface Cracks," *Engineering Fracture Mechanics*, Vol. 39, No. 3, pp. 535–551 (1991).

[6] Key, Samuel W.,"Spectrom–331, A Finite Element Computer Program for the Large Deformation, Elastic and Inelastic, Transient Dynamic Response of Three Dimensional Solids and Structures," Topical Report RSI–0299, RE/SPEC Inc, P. O. Box 14984, Albuquerque, NM 87191 (1988).

[7] Vargas, P. M., and Dodds. R. H., "Three–Dimensional, Inelastic Response of Single–Edge Notch Bend Specimens Subjected to Impact Loading," *Structural Research Series No.*582, Department of Civil Engineering, University of Illinois at Urbana–Champaign, UILU–ENG–93–2006, Urbana, Illinois (1993).

[8] Bodner, S. R., and Partom, Y., "Constitutive Equations for Elastic–Viscoplastic Strain Hardening Materials," *Journal of Applied Mechanics*, Vol. 42, pp. 385–389 (1975).

[9] Norton, F. H., *Creep of Steel at High Temperature*. Mcgraw–Hill, New York (1929).

[10] Bodner, S. R., and Chan, K. S., "Modeling of Continuum Damage for Application in Elastic–Viscoplastic Constitutive Equations," *Engineering Fracture Mechanics*, Vol. 25, Nos. 5/6, pp. 705–712 (1986).

[11] Dexter, R. J., and Chan, K. S., "Viscoplastic Characterization of A533B Steel at High Strain Rates," *Transactions of the ASME*, Vol. 112 (1990).

[12] Dexter, R. J., Private correspondence. August (1990)

[13] Chan, K. S., Bodner, S. R., and Lindholm, U. S., "Phenomenological Modeling of Hardening and Thermal Recovery in Metals," *Journal of Engineering Materials and Technology*, Vol. 110, pp. 1–8 (1988).

[14] Dodds, R. H., and Lopez, L. A., "Software Virtual Machines for Development of Finite Element Systems," *Engineering Computations*, Vol. 3, pp. 18–26 (1986).

[15] Moran, B., and Shih, C.F., "A General Treatment of Crack Tip Contour Integrals," *International Journal of Fracture*, Vol. 35, pp. 295–310 (1987).

[16] Moran, B., and Shih, C.F., "Crack Tip and Associated Domain Integrals from Momentum and Energy Balance," *Engineering Fracture Mechanics*, Vol. 27, pp. 615–642 (1987).

[17] Dodds, R. H., and Vargas, P. M.,"Numerical Evaluation of Domain and Contour Integrals for Nonlinear Fracture Mechanics: Formulation and Implementation Aspects," *Civil Engineering Studies*, Structural Research Series No. 542, UILU–ENG–88–2006, Department of Civil Engineering, University of Illinois at Urbana–Champaign (1988).

[18] Rice, J. R., Paris, P. C., and Merkle, J. G., "Some Further Results of *J* Integral Analysis and Estimates," *ASTM STP536*, pp. 231–235 (1973).

[19] Sumpter, J. D. G., "J_c Determination for Shallow Notch Welded Bend Specimens," *Fatigue and Fracture of Engineering Materials and Structures*, Vol. 10, No. 6, pp. 479–493 (1987).

[20] Anderson, T. L., *Fracture Mechanics, Fundamentals and Applications*, 1st Edition, CRC Press, Boca Raton, Florida (1991).

[21] Nakamura, T., Shih C. F., and Freund L. B., "Elastic–Plastic Analysis of a Dynamically loaded Circumferentially Notched Round Bar," *Engineering Fracture Mechanics*, Vol. 22 (1985).

[22] Nikishkov, G. P., Atluri, S. N., "An Equivalent Domain Integral Method for Computing Crack–Tip Integral Parameters in Non–Elastic, Thermo–Mechanical Fracture," *Engineering Fracture Mechanics*, Vol. 26, No. 6, pp. 851–867 (1987).

[23] Vargas, P. M., and Dodds, R. H., "Numerical Evaluation of Energy Release Rates," *Structural Materials, Proceedings Structural Congress '89,* Orofino, J. F., Editor, ASCE, pp. 206–215 (1989).

MarjorieAnn E. Natishan[1] and Robert L. Tregoning[2]

EVALUATION OF TEST METHODS FOR DYNAMIC TOUGHNESS CHARACTERIZATION OF DUPLEX STAINLESS STEEL FORGINGS

REFERENCE: Natishan, M. E., and Tregoning, R. L., **"Evaluation of Test Methods for Dynamic Toughness Characterization of Duplex Stainless Steel Forgings,"** Fractures Mechanics: 26th Volume, ASTM STP 1256, Walter G. Reuter, John H. Underwood, and James C. Newman, Jr., Eds., American Society for Testing and Materials, Philadelphia, 1995.

ABSTRACT: Ferralium is a dual-phase stainless steel which consists of roughly equal amounts of ferrite and austenite. Conventional Charpy V-notch impact tests were performed on specimens taken from several locations in three orientations from a forged Ferralium plate to quantify the materials dynamic fracture performance. The Charpy tests were compared with 2.54 cm thick (1T) single edge bend (SE(B)) specimens that were tested in a drop tower to measure dynamic fracture initiation toughness (K_{Id}). SE(B) specimens were removed from three plate locations and tested in a single orientation. Charpy and K_{Id} tests were performed over the entire fracture mode transition temperature range, but the bulk of testing was concentrated at a single temperature -2°C to provide a statistically significant number of tests at a representative point in the ferritic fracture mode transition region. Charpy impact energy varied consistently with both orientation and location within the forged plate even though large scatter was present in the results. This large scatter precluded an accurate assessment of the materials fracture performance within the transition region. The scatter in the drop tower (SE(B)) results was much less and indicated that plate location had a minimal affect on performance. The reduced scatter in the SE(B) specimens is attributed to two factors. First, the microstructure of Ferralium, while macroscopically homogeneous, contains ferritic and austenitic phase sizes that approach the dimensions of the standard Charpy specimen. Second, the Charpy testing technique causes more variation than the standard SE(B) K_{Id} tests within the transition region.

INTRODUCTION

Ferralium 255 is a duplex stainless steel composed of large austenite precipitates within a ferritic matrix. Duplex stainless steels were developed to take advantage of the combination of the desirable properties of each phase instead of being limited to the properties of one phase alone. In this case the ferrite provides strength while the austenite provides good toughness. Both phases exhibit good corrosion resistance since each contains at least 12 weight percent chromium. The properties of a particular dual phase steel are determined by the relative amounts of each of the phases present, which is determined both by the chemistry and the processing history of the steel. It has been found that a microstructure containing approximately 50% austenite in a ferrite matrix provides the best combination of strength, toughness and corrosion resistance in Ferralium 255 [1-3]. This microstructure can be achieved with a composition containing approximately 25 weight percent chromium and 5.5 weight percent nickel with alloy additions for strengthening [4-5].

KEYWORDS: Duplex stainless steel, Ferralium 255, Dynamic fracture toughness, Impact toughness, Fracture safety assessment

[1] Assistant Professor, Mechanical Engineering Department, University of Maryland, College Park, MD 20742-3035

[2] Mechanical Engineer, Fatigue and Fracture Branch, Carderock Division, Naval Surface Warfare Center, Annapolis, MD 21402-5067

Copyright © 1995 by ASTM International www.astm.org

This duplex alloy was chosen for use in submarine components due to its good strength, toughness, corrosion resistance, and resistance to galling. These properties make this alloy ideal for applications in a seawater environment when close mechanical tolerances are required. Its high strength (482 MPa minimum yield strength) makes it less susceptible to galling or wear than other stainless steels, while the dual phase nature of the alloy makes it less susceptible to pitting corrosion, general corrosion and stress corrosion cracking than either ferritic or austenitic single phase stainless steels.

Ferralium 255 has been used in both the cast and wrought (forged) forms in submarine components. Forged components are preferred for the greater control of microstructural homogeneity in large sections. However, it has been found that stress relief heat treatments at temperatures above 345°C are required to maintain close dimensional tolerances of the large Ferralium 255 forgings during machining. Heat treatments above 260 °C are known to degrade the toughness of Ferralium 255 due to precipitation of a chrome-rich ferrite phase within the ferrite matrix [6]. Degradation of weld properties is most severe as larger proportions of ferrite are typically formed during the joining process.

The current requirements for Ferralium 255 submarine components include a minimum yield strength of 482 MPa, a minimum ultimate strength of 689 MPa, and a minimum elongation of 20% over a 50 mm gage length. Also, an average Charpy impact energy of 60 J is required at the lowest anticipated service temperature of -2° C and no single value can fall below 48 J. The relationship between this value and the actual fracture toughness needed to resist fracture under applied service loads is unknown because an empirical correlation between Charpy V-notch energy (CVE) and dynamic fracture toughness (K_{Id}) has never been established. It is possible that material exhibiting CVE values which are less than specified still has sufficient fracture toughness to withstand anticipated service loads, but such performance must be demonstrated.

To date, preliminary testing of a prototype forging, shown in Figure 1, by the producer has characterized tensile behavior and Charpy V-notch (CVN) impact toughness properties of the forged and stress relieved materials. The tensile properties were well above the minimum required yield strength and elongation [7]. However, CVE values ranged from a high of 176 J on the upper circular portion of the forging to a low of 35 J at one end of the forging. Also, CVE values varied widely with location within the forging. This wide variation in CVE value with location was not expected in forged components since

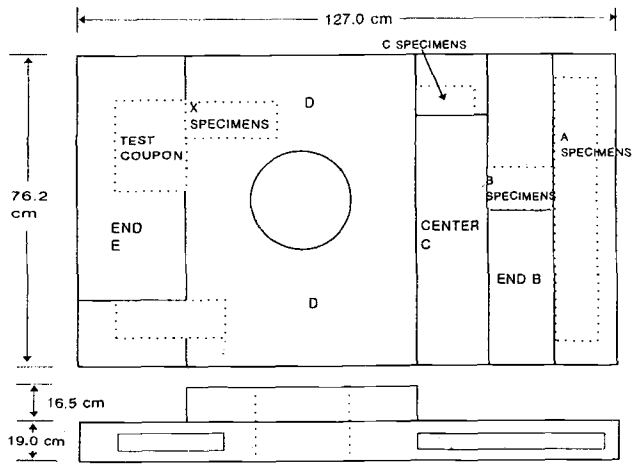


Figure 1: Schematic of Prototype Ferralium 255 Forging

forgings were introduced in an effort to reduce the grain size and increase the homogeneity of phase distribution within the components relative to that of the cast components.

A program was undertaken to establish a fracture toughness requirement for the large, forged, submarine components and to determine whether the Ferralium 255 forgings could meet those requirements. This program included experimental determination of dynamic fracture toughness as well as determination of the critical crack driving force for these components using applied stress information, component geometry and maximum expected flaw size. CVE was also determined for two locations and three orientations to verify the scatter initially reported for the prototype forging by the producer and to determine whether a correlation exists between CVE and K_{Id} which would then allow use of CVE to predict fracture toughness of future Ferralium 255 components. These results are summarized below.

EXPERIMENTAL PROCEDURE AND RESULTS

A number of tests were employed to accurately assess the properties of stress relieved Ferralium and evaluate potential variations resulting from forging location, orientation, and temperature. Initially, static tensile tests were performed to measure strength and ductility differences resulting from specimen location and orientation. Location and orientation were also varied in the CVN tests which are currently used to specify the minimum fracture resistance for Ferralium components. The CVN tests were conducted over a range of temperatures to determine the complete ductile-to-brittle transition behavior. Dynamic tensile specimens were tested to measure the yield stress at the strain rate magnitude and temperatures used in the dynamic fracture tests. Finally, dynamic fracture initiation was evaluated using drop tower testing and procedures developed at CDNSWC, Annapolis.

Static Tensile Tests

The 12.8mm diameter tensile specimens were machined from two locations (forging center, area B and forging edge, area E in Figure 1). All the specimens were machined from material located as close as possible to the mid-thickness (T/2) of the forging and were at least a distance of T/2 from the edge of the forging. At each location, three specimen orientations were tested to measure properties in the forging grain flow direction (L), transverse direction (T) and through-thickness direction (S). Three specimens were tested for each condition at room temperature, 20°C, and the yield strength, σ_{ys}, ultimate tensile strength, σ_{ut}, elongation, EL, and reduction of area, RA, were measured. The tensile testing procedure and analysis were conducted according to the specifications designated in ASTM E-8 [8].

The room temperature, static tensile properties of the stress relieved Ferralium are presented in Table 1. Only the average properties of the three tests from each condition are reported although the tensile test results of each individual test can be found in the Appendix (Table A1). As can be seen in Table 1, the yield and ultimate strength values measured are relatively consistent among all the location/orientation combinations. The elongation and reduction of area results are also similar except that specimens from area E in the S orientation (E-S) exhibited less ductility than all other specimens. The average percent elongation of all specimens except the E-S specimens is 34 with a standard deviation of 5% while the E-S specimen elongation is 15% less than this mean.

Charpy Impact Testing

Standard V-notched Charpy specimens were machined from three separate locations (edge, E, center, B, and side, X, in Figure 1). In all cases, the material for these specimens was located near the mid-thickness (T/2) of the forged plate and at least (T/2) from the edge of the plate. At locations B and E, the impact response from three specimen orientations corresponding to the L-T, T-L, and S-L notch configurations (ASTM E-23 [9]) was measured. These orientations were chosen to provide the maximum property variation due to forging texture. The full transition curve behavior was developed for locations B and E by testing three specimens each at six different temperatures: -73°, -23°, -2°, 20°, 37°,and 82°C. At the final location, X, eight additional specimens were tested at -2°C in the T-L orientation. These tests

provided additional CVE values at the specification testing temperature near the region that the producer found low CVE values.

Location	Orientation	σ_{ys}* (MPa)	σ_{ut} (MPa)	EL (%)	RA (%)
Area B	L	586	786	33	67
	S	572	779	34	59
	T	586	779	32	61
Area E	L	545	765	36	62
	S	545	786	29	54
	T	558	786	35	56

*Minimum Tensile Property Requirements (Room Temp., L & T Oreint.)
σ_{ys} = 482 MPa, σ_{ut} = 689 MPa, EL = 20%

Table 1: Average tensile data for locations B and E of the prototype forging.

All CVN testing and analysis was conducted in accordance with ASTM E-23 [9] although only the CVE was recorded. All CVE results are reported in the Appendix for each specimen while only the average CVE (CVE_a) and the standard deviation (Σ_a) are presented in Table 2 for each unique location, orientation, and temperature test series. CVE_a is plotted as a function of temperature in Figure 2 for each location and orientation while Figures 3, 4, and 5 illustrate the individual CVE data for each separate orientation.

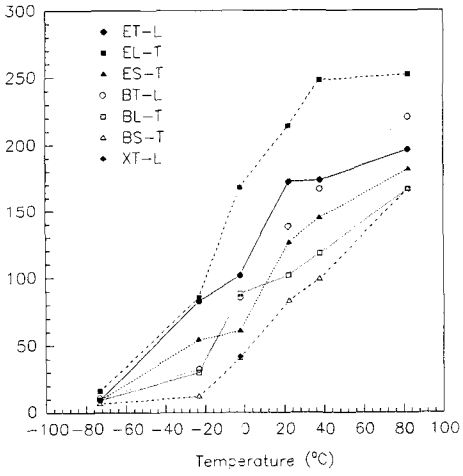


Figure 2: CVE_a for all Testing Configurations

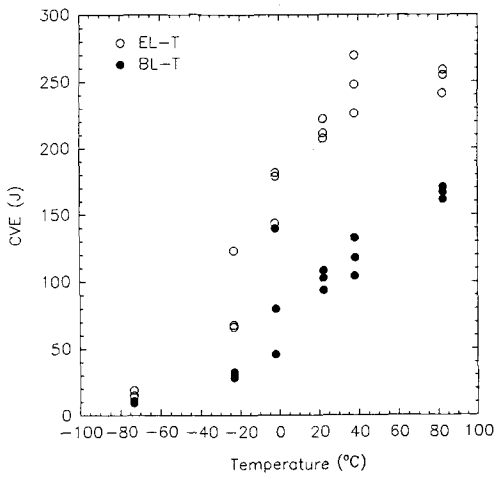


Figure 3: CVE Values for L-T Orientation

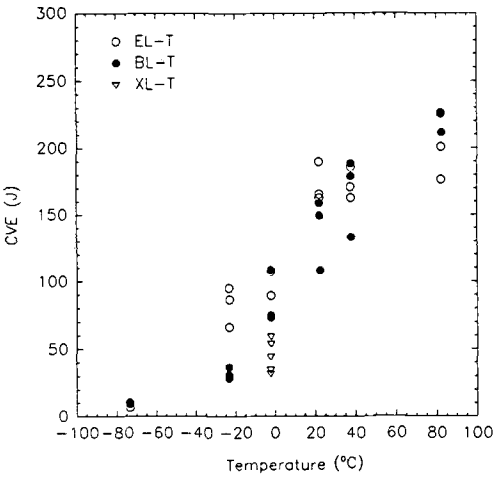


Figure 4: CVE Values for T-L Orientation

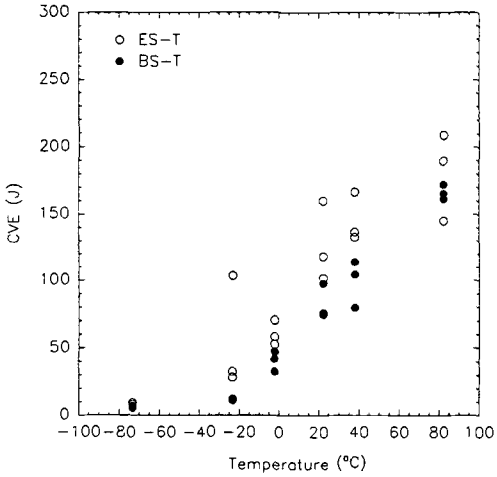


Figure 5: CVE Values for S-T Orientation

Figure 2 and the data in Table 2 shows that the Charpy transition behavior varies with specimen orientation and location. Statistical evaluations performed on each data set confirm that the trends discussed later do exist despite the large scatter evident in the Charpy results. Some of this scatter can be attributed to the ferritic phase which is in transition between -23°C, and room temperature. Indeed, the largest percentage of scatter (represented by the ratio Σ_s/CVE_a) occurs at -2°C for specimens from Area B and at -23°C for the specimens from Area E. Also, the scatter at the lowest and highest temperatures is much less than at the transition temperature. However, at 37°C, when the ferritic response is expected to lie on the upper shelf, the Charpy standard deviation at a single location/orientation combination is still usually at least 10%. Potential reasons for this additional scatter will be enumerated in the discussion section.

Fractography of Impact Specimens

The fracture surfaces of the Charpy impact specimens were characterized using a scanning electron microscope at magnifications ranging between 10X and 2000X in an effort to identify the causes of the large scatter in impact energy observed for these specimens. Fracture mode transition behavior is not observed in austenitic CVN specimens but instead a very gradual decrease in impact energy with decreasing temperature may be observed. However, ferrite tends to exhibit a very pronounced fracture mode transition. Therefore in a duplex alloy composed of a 50-50 mixture of these two phases it was expected that ductile behavior may be observed even at the lowest test temperatures. Instead, almost complete cleavage fracture was observed at the lowest test temperatures with only very small tear ridges connecting cleavage regions, Figure 6a. The microscopic fracture appearance is almost entirely cleavage but the macroscopic appearance includes a large amount of surface relief that is not typical of 100% cleavage fracture. This is most likely due to the cleavage fracture path circumnavigating the austenite grains to remain entirely within the more brittle ferrite matrix. Regions of austenite "pull-out" are apparent in Figure 6b. This fracture appearance suggests that the energy to fracture depends on the continuity of the ferritic matrix in front of the notch in impact specimens. Even though macroscopically the austenite and ferrite are found in a 50/50 ratio, at any point in the forging, this ratio can vary extensively; especially when considering the dimensions of the Charpy impact specimen notch (1 cm) in relation to the dimensions of the forging thickness (18 cm).

Location	Orientation	Temp. (°C)	CVE, (J)*	Σa (J)
Area B	L-T	-73	9	1
		-23	30	3
		-2	88	47
		20	102	8
		37	118	13
		82	167	5
	T-L	-73	11	1
		-23	32	4
		-2	85	20
		20	138	27
		37	167	30
		82	221	8
	S-T	-73	7	1
		-23	12	1
		-2	41	8
		20	83	13
		37	99	18
		82	167	5
Area E	L-T	-73	16	3
		-23	85	32
		2	168	22
		-2	214	8
		37	248	23
		82	252	9
	T-L	-73	9	3
		-23	83	15
		-2	102	11
		20	172	15
		37	173	12
		82	197	18
	S-T	-73	9	1
		-23	54	42
		-2	61	9
		20	126	30
		37	145	19
		82	182	32
Area X	T-L	-2	42	11

*Charpy Requirements (-2°C, T-L orient.) [3]: Ave. for 3 spec. = 60 J, Min. for 1 spec. = 48 J.

Table 2: Average CVE for locations B, E, and X within the prototype forging.



Figure 6: Fractograph of CVN at -73°C; a) Low Mag.; b) High Mag.

At higher temperatures increasing amounts of ductile fracture were observed. Specimens tested at -2 °C showed shear lips and a very small amount of ductility at the notch. The remainder of the specimen exhibited cleavage with the same macroscopically rough surface exhibited by the lower shelf specimens. This indicates that cleavage crack growth is still following a path around the austenite precipitates.

Specimens tested at 82 °C exhibited almost entirely ductile fracture. Small regions of cleavage are visible in Figure 7 (marked with arrows). The macroscopic fracture topography exhibited by these specimens is still quite large. The large macroscopic fracture surface relief is most likely related to the relatively large phase sizes.



Figure 7: Fractograph of CVN at 82 °C

Dynamic Tensile Testing

Dynamic tensile testing was conducted over a range of temperatures (-129°C, -50 °C, -17 °C and 20 °C) to measure the dynamic yield strength, σ_{dys}, at the loading rates and temperatures used in subsequent dynamic fracture toughness tests. This testing was necessary to accurately determine if the dynamic fracture behavior was governed by the single fracture toughness parameter, **K**. The specimen radius at which **K** effectively governs fracture is inversely proportional to σ_{dys}^2 [10] and this radius must be greater than all pertinent specimen length scales to obtain **K**-dominance and a valid $\mathbf{K}_{Id}$ measure during testing. The other reason for conducting these tests was to provide some indication of the strength increase exhibited by Ferralium at high strain rates.

The dynamic tensile testing was performed in a drop tower so that the specimen strain rates would have the same magnitude as expected service loads. The drop tower falling weight generated a compressive stress which was converted into a tensile load using a fixtured rig, Figure 8. Specimen load was measured by strain gages, Figure 8, on the rig which were statically calibrated using a load cell. Specimen strain and strain rate ($\dot{\varepsilon}$) were recorded using a conventional strain gage. The 6.4 mm diameter dynamic tensile specimens were taken from one location (Location C in Figure 1) and the loading axis was always coincident with the L direction in the forging. Only one specimen location and orientation was necessary since the static tensile properties measured earlier varied little as a function of these parameters.

One or two tests were conducted at each temperature and the yield stress was determined using the 0.2% strain offset method. The data is reported in Table 3. At the two lower temperatures, the strain gage glue debonded before the 0.2% yield stress was reached. In these instances, the stress at the time of debonding is the minimum value reported in Table 3 for the dynamic yield stress. This minimum value was used for analyzing the dynamic fracture tests at temperatures near -129 °C while the value at -17 °C was used for tests at temperatures between -17 and -100°C. These lower bound yield stress values obviously yielded conservative conclusions when assessing whether the measured **K** value was a valid $\mathbf{K}_{Id}$ at these low temperatures.

Specimen ID	Temperature (°C)	σ_{dys} (MPa)	$\dot{\varepsilon}$ (10^4 s^{-1})
GVP-26	-129	>1034	1.6
GVP-21	-50	>482	NA
GVP-25	-17	910	1.7
GVP-22	20	807	1.4
GVP-24	20	814	1.2

Table 3: Dynamic tensile behavior from area C specimens in the prototype forging.

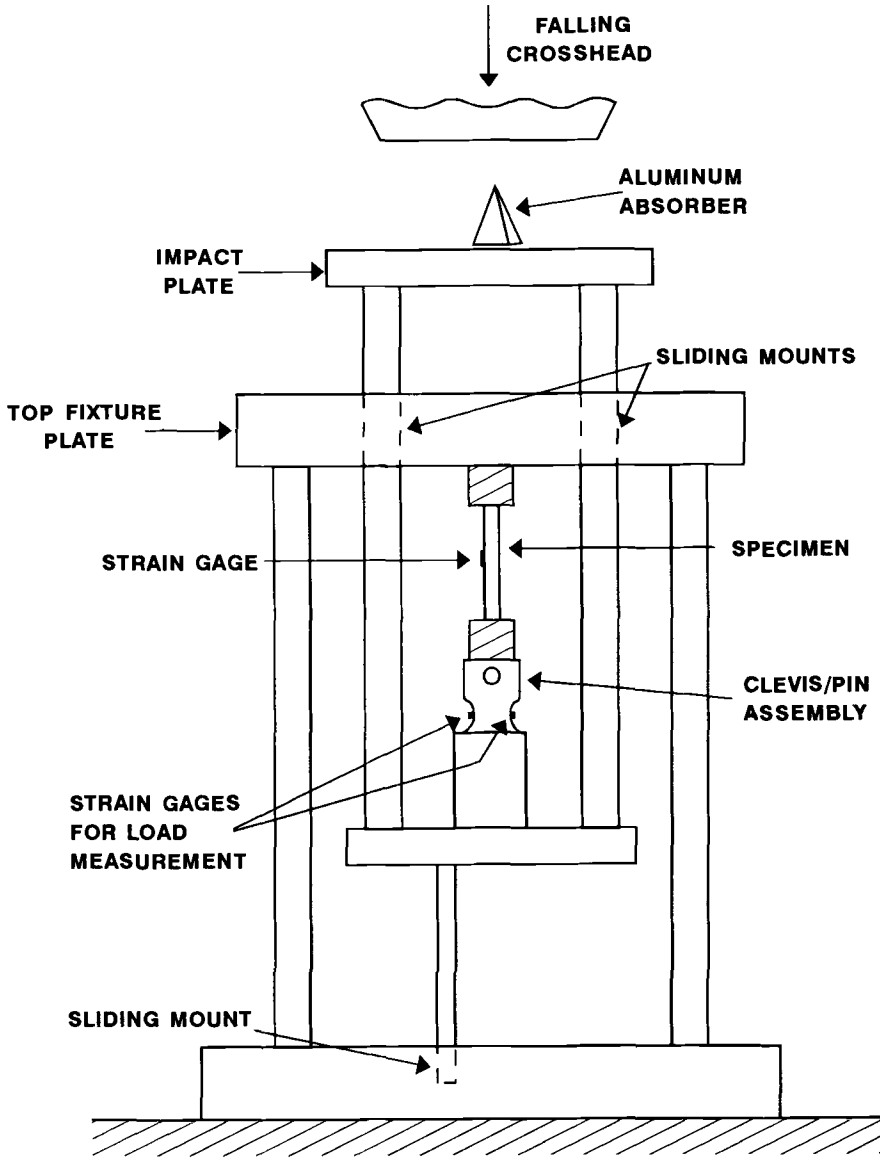


Figure 8: Dynamic Tensile Testing Rig

Significant strain rate and temperature sensitivity was observed in the tensile tests (Table 3). At room temperature, the dynamic yield stress is 40% higher than the quasistatic yield stress and actually is similar to the quasistatic ultimate tensile strength. Lowering the temperature raises the dynamic yield stress even further and at -17°C, σ_{dys} is an additional 12% greater than the room temperature value. Because the strain gages debonded, it is difficult to determine σ_{dys} at the lowest temperatures although increases of 50% of the room temperature strength may be expected at -129°C based on extrapolation of room temperature and -17°C results.

Dynamic Fracture Toughness Testing

Standard 25.4 mm thick, single edge bend (SE(B)) specimens with 2.54 mm side grooves were used for evaluating the dynamic fracture resistance of Ferralium 255 (Figure 9). These specimens were machined from Area A (Figure 1) from the mid-thickness plane and the critical specimen material near the crack tip was located more than T/2 from the plate edges. All specimens were notched and precracked as specified in ASTM E99 [11] to a depth of 12.7 mm so that the a/W ratio was always 0.6. The specimen notch orientation was T-L with respect to the grain flow direction for all specimens. Eighteen specimens were used to measure the K_{Id} transition curve at temperatures of -143°C, -84°C, -50°C, -17°C, -2°C, 20°C and 50°C. Three specimens were tested at each temperature in the steepest region of the transition curve: -17°C, -2°C and 20°C. Two tests were conducted at all other temperatures except at -143°C where only one test was run.

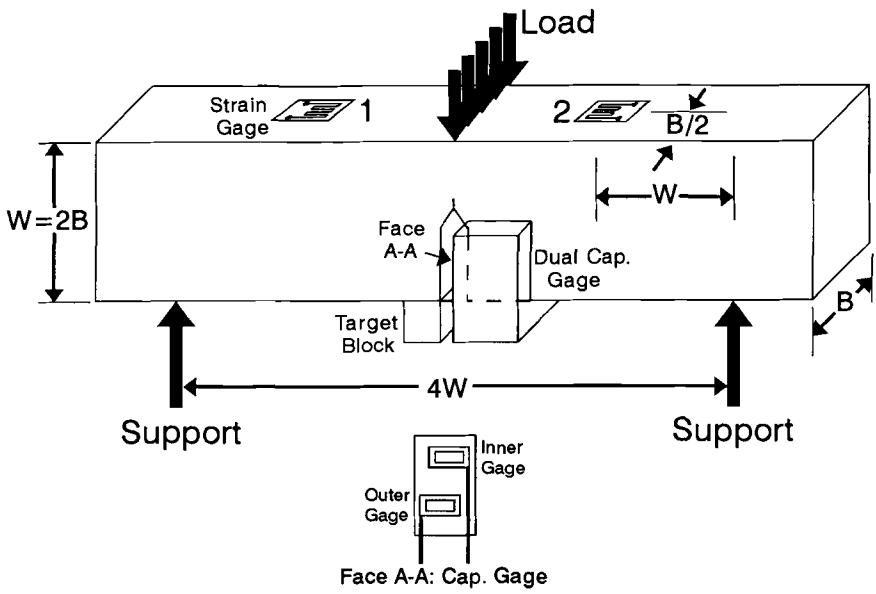


Figure 9: Schematic of Dynamic K_{Id} Specimen

Earlier tests [12] were also conducted at -2°C using three specimens from the test coupon region (Fig. 1) to provide additional data at the minimum service temperature. Information provided by the forging producer indicated that the specimen orientation for these samples was also T-L. However, CDNSWC Charpy results from the test coupon were dramatically different from producers CVE results measured from the adjacent area [12]. This inconsistency raised questions concerning the actual location/orientation of the test coupon. The fracture toughness information from the coupon is still included in this report to provide $\mathbf{K}_{Id}$ information from the opposite end of the forging. The orientation will be reported as specified by the producer.

The dynamic fracture toughness testing was carried out in the drop tower using the experimental setup illustrated in Figure 10. Load (P) was measured by strain gages located at the top and bottom quarter points as shown in Figure 9. These gages were configured in a full bridge and each specimen was elastically calibrated in a static testing machine using a standardized load cell. Specimen strain rate ($\dot{\varepsilon}$) was also measured using these gages to provide a far-field loading rate reference although all tests were found to have similar strain rates, on the order of 1 s^{-1}. Crack mouth opening displacement (CMOD) was measured using the outer gage of a dual capacitance gage (Figure 9).

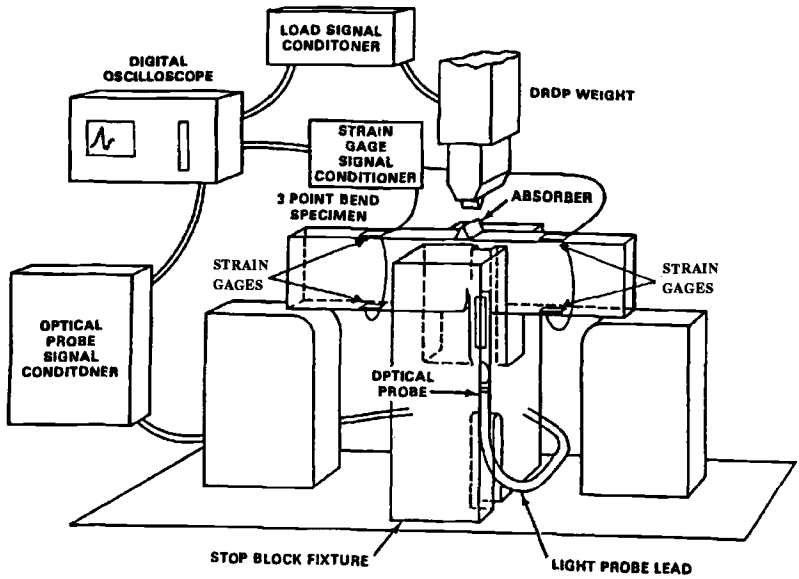


Figure 10: Dynamic Fracture Testing Setup

A typical dynamic P-CMOD response curve is shown in Figure 11. There was no large, sharp drop in the load bearing capability of the test specimen which, if present, typically represents cleavage fracture. The drop was not as gradual as would be expected for ductile, stable crack extension either. Also, the P-CMOD curves were inherently noisier than the quasi-static response because the specimens "ring" at their natural frequency when the load is suddenly applied. The ringing is worse at the low temperatures employed in these tests because the aluminum absorbers, Figure 10, used to smoothly transfer the drop weight loading deform less as the test temperature decreases. The ringing caused some additional uncertainty when the dynamic load at initiation was determined using the analysis specified in ASTM E399 for brittle fracture. Therefore, the dynamic data was analyzed by calculating the total J-integral ($J = J_{elas} + J_{pl}$) and converting this value to an equivalent K at initiation using the standard conversion formula $K^2 = JE/(1-\nu^2)$. The load at initiation P_i was determined when the ratio of the elastic area under the P-CMOD curve, A_{elas}, (Figure 11) to the theoretical elastic area at the same CMOD, A_n, fell below 0.90. This initiation definition is equivalent to the 5% reduced elastic slope method specified in ASTM E399 [11]. The J-integral data evaluation with the area ratio initiation definition naturally averages the dynamic data and led to better precision than with the E399 procedure in these tests.

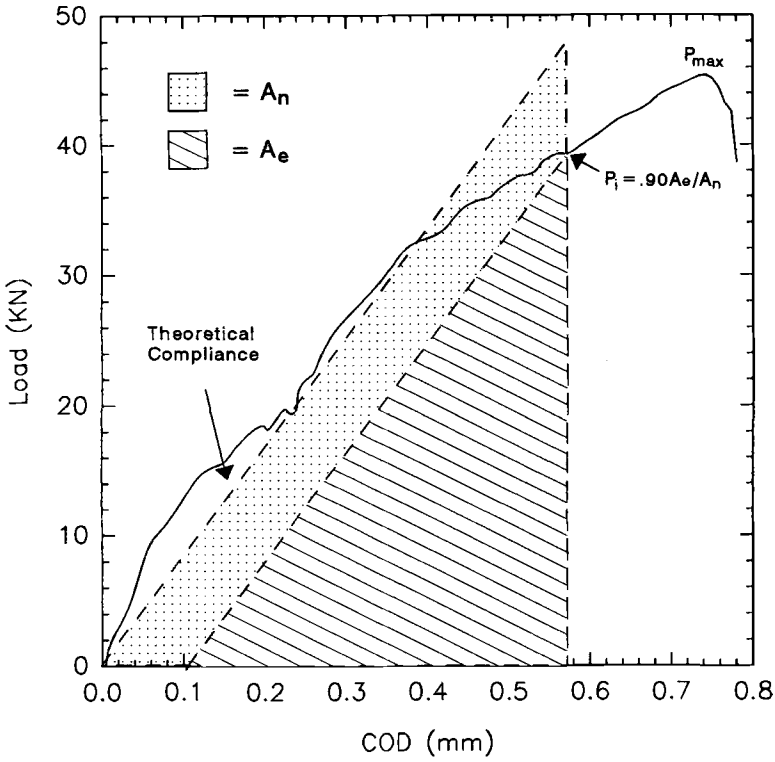


Figure 11: Load-COD Dynamic Response and Analysis Procedure

The average stress intensity factor at initiation calculated using this method ($\mathbf{K}_{J1}$) and the standard deviation among the tests (Σ_K) are reported in Table 4. Once again, the entire data set is included in the Appendix and a graph of the individual test results is presented in Figure 12. The average values of $\mathbf{K}_{J1}$ were typically approximately 5% larger than values calculated using the analysis specified in ASTM E399. However, the standard deviation (Table 4) is typically 50% less than with the ASTM E399 method which proves the usefulness of the smoothing technique.

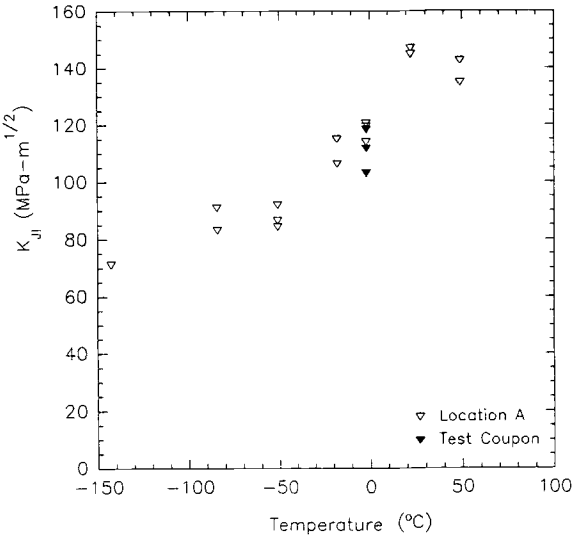


Figure 12: K_{J1} Behavior as a Function of Temperature

The fracture toughness analysis performed is only rigorously accurate when the crack tip deformation and stress fields can be characterized solely by the linear elastic stress intensity factor (K). The specimen size and P-CMOD linearity requirements of ASTM E399 were used to check whether K-dominance was present at crack initiation for each temperature. These results are also included in the K-dominance column of Table 4. A "Y" response means that K-dominance is present during the test and K_{J1} is equivalent to K_{Id} at the given temperature. The "N" and "B" responses mean that the crack tip fields are not K-dominant or are borderline (nearly) K-dominant respectively and K_{J1} is not necessarily equivalent to K_{Id}. However, the borderline tests all passed the linearity requirements and barely exceeded the specimen size requirements so that K_{J1} should not be much different than K_{Id}.

Location	Temp. (° C)	K_{JI} (MPa-$m^{1/2}$)	Σ_K (MPa-$m^{1/2}$)	K-Dominant
Area A	-143	71	NA	Y
	-84	88	5.5	Y
	-50	88	4.4	Y
	-17	110	5.5	B
	-2	119	3.3	B
	20	146	1.1	N
	49	137	5.5	N
Test Coupon	-2	111	7.7	B

Table 4: Average dynamic fracture toughness for Test Coupon and area A Specimens.

Fractography of K_{Id} Specimens:

The fracture surfaces of the dynamic fracture toughness specimens were examined in the scanning electron microscope to characterize the fracture features to compare to those of the CVN specimens. Similar to the fracture behavior observed in the CVN specimens, the fracture mode observed for specimens tested at the lowest temperatures (-143°C) was almost entirely cleavage, Figure 13a. Ductile fracture is expected to be observed within the austenite regions since austenite does not exhibit a transition in fracture mode. Instead, it was apparent that the cleavage fracture remained within the ferrite matrix with the fracture path circumnavigating the austenite precipitates leaving a rough-appearance to the fracture surface topography.

At higher temperatures (-17°C) some ductile fracture was observed, Figure 13b, but the predominant mode remained cleavage. Regions where the fracture path went around austenite precipitates were observed, leaving holes in the fracture surface where the austenite had been (see arrows in Figure 13b).

As test temperatures increased, increasing amounts of ductile fracture were observed. Figure 14a shows part of the fracture surface of a specimen tested at -2°C in which several regions of ductility were observed. Large areas where the fracture path appears to have gone around the austenite are also still readily apparent (note the holes marked by arrows in Figure 14a). Figure 14b shows the fracture surface of a specimen tested at room temperature, where high K_{JI} values were measured. Cleavage is still apparent on the fracture surface but ductile fracture is becoming more dominant. At these temperatures, there was still almost a 50/50 mixture of microvoid coalescence and cleavage. Therefore, higher testing temperatures are required to reach fully ductile fracture.

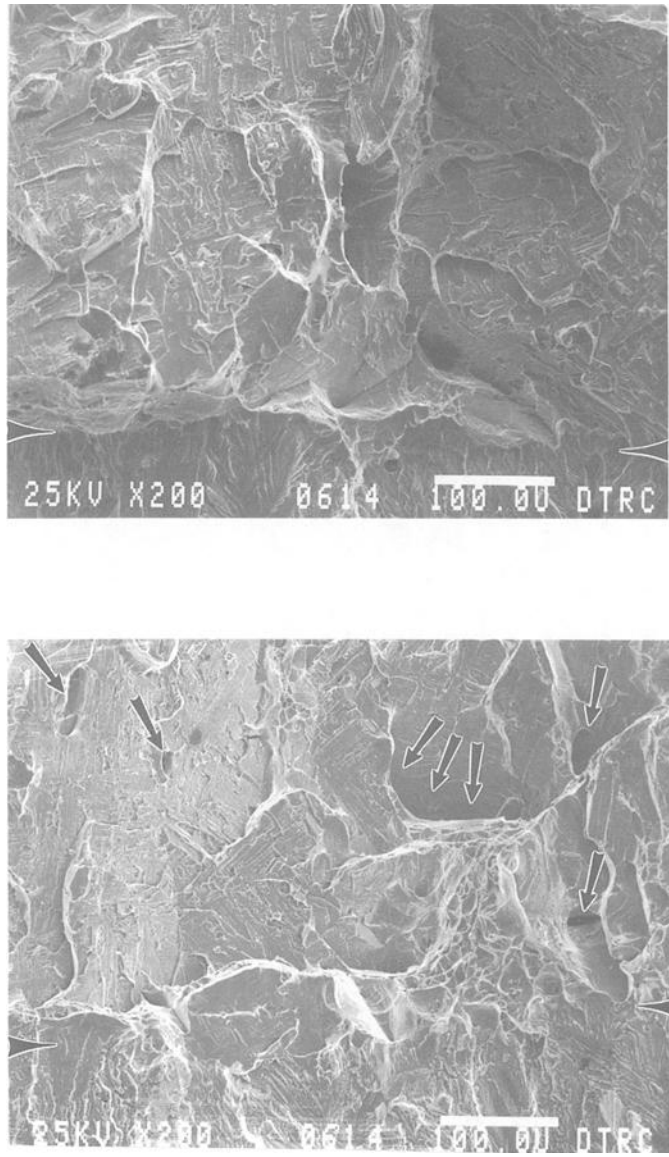


Figure 13: Fractography of SE(B) Specimens; a) -143°C; b) -17°C

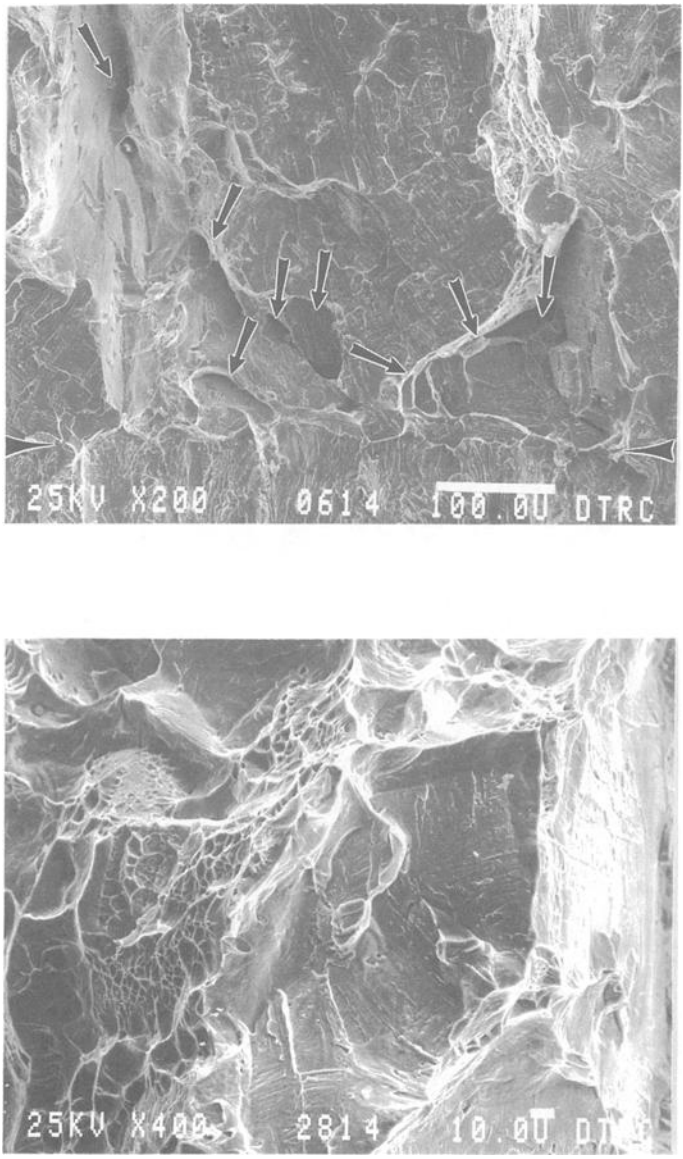


Figure 14: Fractography of SE(B) Specimens; a) -2°C; b) 20°C

DISCUSSION OF EXPERIMENTAL RESULTS

This battery of tests indicates the influence of forging location, orientation, and temperature on the measured mechanical properties. This information can be used to infer variations in other similar Ferralium forgings when testing material from a prolonged end. These relationships are subsequently examined along with the experimental scatter evident in each test. The amount of scatter can be used to judge the reliability of current quality control tests and serve to develop future screening requirements.

Property Variations with Specimen Location

The static tensile specimens were taken near a highly worked area of the forging (Area B) and a lightly worked area (Area E). Therefore, it should be expected that any property variations will be maximized by this choice. There are small, but consistent, differences in σ_{ys} between the two locations as the σ_{ys} from Area B is approximately 5% greater than Area E. These statistical validity of these trends were confirmed using analysis of variance (ANOVA) techniques and a 95% significance level. The ductility measures (EL and RA) also had small, but meaningful variations in the L and T orientations where both measures were greater at location E. This trend is consistent with the lower yield stress determined here. There also appear to be differences in ductility in the S orientation, however the experimental scatter was too large for any definitive conclusions. There was no difference in σ_{ut} with location as should be expected as the forging was stress relieved. However, while the small variations reported do exist, they are not dramatic as a function of location and measurement of tensile properties from a tab or prolonged end should represent tensile properties throughout the forging.

The predominant number of CVN specimens were also extracted from Areas B and E, although several were tested at location X at -2°C in the T-L orientation. One way ANOVA tests were used to ascertain trends from the relatively small number of replicate tests (three) for each unique condition. There are statistically significant (< 5% uncertainty) differences between specimens from locations B and E in the L-T Charpy orientation for nearly every temperature. The S-T orientation also possessed noticeable location variations which can be statistically confirmed except for those cases where the CVE scatter for a group of replicate tests was dramatic (see Table B in the Appendix). The CVE_a values at the more highly worked portion of the forging (location E) in each of these orientations tended to be higher. The CVE_a values in T-L orientation for Areas B and E were not statistically different for nearly every temperature; however, the CVE_a from location X was less than 50% of CVE_a at locations B and E at -2°C. Therefore, the Charpy properties appear to be sensitive to forging location at every orientation.

A limited number of dynamic fracture toughness tests (six) were conducted at two different locations (Area A and the test coupon) in the T-L orientation studied. The average $\mathbf{K}_{JI}$ values for this small matrix were statistically similar even though the SE(B) specimen locations were adjacent to CVE locations E and X respectively where big differences in CVE_a were apparent. The dynamic fracture toughness test is more indicative of the forging's crack initiation behavior which points to one inadequency of using the CVN test to infer behavior in this material.

Property Variations with Specimen Orientation

At location B, none of the tensile properties varied significantly with specimen orientation. There were some small, yet statistically meaningful,variations at location E however, where the plate has been worked more. In the longitudinal direction, σ_{ut} was a few percent less than the other orientations; correspondingly, the ductility measures EL and RA were slightly greater than in the S and T directions. The S orientation had the least ductility of any orientation. These trends are consistent with typical forging behavior. Regardless, as with location differences, these undramatic variations implied that tensile properties were consistent throughout the plate as a result of the stress relief heat treatment. Further, these properties could be inferred from the prolonged end of the forging using specimens taken from any orientation.

The CVE_a values at the lightly worked area B are similar to variations in rolled plate. The L-T

orientation was always greater than values from the S-T direction for every temperature. Along the lower shelf, the L-T and T-L CVE values were similar, but the T-L clearly was the toughest orientation at the upper shelf. Conversely, the S-T orientation was less than the L-T at lower shelf, however these two orientations appeared to converge near upper shelf temperatures. In the more highly worked area E, these trends were different and more definite. The L-T orientation was clearly the toughest of the three over all temperatures tested, while differences between T-L and S-T apparent at location B decreased. In fact, there was not a meaningful statistical separation between the T-L and S-T orientation at area E except at -2°C.

Property Variations with Testing Temperature

The temperature variations of the measured properties had characteristics which were expected for the dual-phased microstructural material. The dynamic tensile behavior (Table 3) was marked by an increase in both σ_{ys} and hardening as the temperature decreased which is characteristics of steel alloys. The dynamic fracture behavior for both the CVE_a and $\mathbf{K}_{JI}$ results consisted of a low toughness region which gradually increased up to approximately -17°C, a region between -17°C and room temperature where the toughness increased at a faster rate, and a final region above roughly 38°C where the toughness increases again at a slower rate. These characteristics are evident in Figure 15 where the $\mathbf{K}_{JI}$ and CVE_a toughness is compared for the T-L orientation between adjacent locations A and B (AT-L and BT-L in Fig. 15) respectively. This behavior resembles the ductile to brittle transition regime in classical ferritic and martensitic steels although no upper shelf is present.

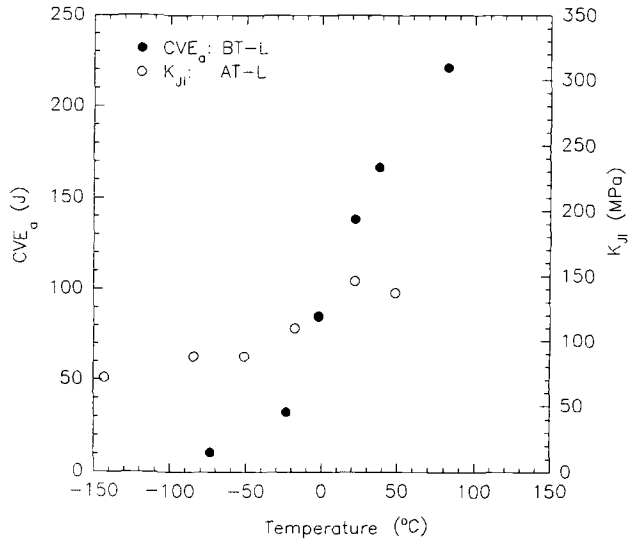


Figure 15: CVE and K_{JI} Behavior at Adjacent Forging Locations

Fractographic examination revealed the characteristic nature of the low, mid, and high temperature failure modes. At low temperatures, the fracture mode of the ferritic matrix was cleavage which was the predominant mode observed on all specimens. Ductile fracture of the austenite was expected, however, it

was not observed because the cleavage crack grew around the regions of ductile austenite (Figures 6 and 13). The result is that little ductile fracture is observed and the cleavage is characterized by a high degree of topographic relief. The fact that the ferritic phase is dominant at lower temperatures could explain the appearance of a lower shelf (Figure 15). At the middle temperatures where toughness increases rapidly with test temperature ductile void growth and coalescence in the austenite is observed (Figure 13b) but entirely ductile fracture is not observed until the highest test temperatures in the CVN specimens and not at all in the $\mathbf{K}_{JI}$ specimens. At higher temperatures, true shelf behavior was not evident due to the presence of the austenite phase.

While the Charpy and dynamic SE(B) fracture toughness temperature relationships were similar, they are not identical. The Charpy specimen has lower constraint as the specimen is smaller and the crack initiates from a notch instead of a true crack. This greater constraint favors cleavage in the SE(B) specimen which is why the steep toughness increases occur at later temperatures than for the Charpy specimen and why fully ductile fracture was not reached in the SE(B) specimens.

Experimental Scatter in the Mechanical Testing

The randomness in the tensile and dynamic fracture toughness testing is representative of the experimental error in the technique and the variability of properties one would expect in a forged plate. The scatter in CVN tests, however, highlights the deficiencies of this test for predicting fracture toughness performance in Ferralium 255. The tensile strength measures (σ_{ys} and σ_{ut}) all had standard deviations which were less than 2% of the mean value in the S and T orientations at both locations. The variation in the L orientation was greater, especially at the lightly worked location B, but it was still always less than 7% of the mean. The ductility measures (EL and RA) had more variation then the strength properties which is characteristic. Although the standard deviation of these properties was always less than 10% of the mean.

The initiation toughness deviation, $\mathbf{K}_{Id}$ (or $\mathbf{K}_{JI}$) was also minimal. At every temperature, the variation was never greater than 7%. This excellent repeatability confirms the robustness of the experimental technique and also indicates that the forging toughness is uniform at (and between) the two locations tested over the entire temperature regime.

The CVN tests possessed acceptable scatter at the lowest (-73°C) and highest temperatures (82°C) ($\Sigma_a < 2$ and $\Sigma_a / CVE_a < 20\%$ respectively) where the ferrite failure mode was either completely brittle or ductile. In the mid-temperature region where CVE_a began to increase, however, the scatter increased dramatically; usually the percent variation with respect to the mean was greater than 10%, and almost a third of the time it was greater than 20%. There was no clear relationship between the amount of scatter and either Charpy specimen orientation or location. Certainly, some of this scatter resulted from the fact that the ferrite phase is in ductile-to-brittle transition over these temperatures. However, scatter from fracture mode changes should also be evident in the fracture toughness results and this was not the case. Obviously, other factors unique to the CVN tests were the predominant reason for the increased scatter.

Some reasons why scatter was typically greater in the CVN test than in the SE(B) test are well known. In transition, the relative amount of ductile and brittle fracture in the fracture path varies among specimens with changes in temperature, crack tip constraint, and location of suitable "cleavage initiation sites." The CVN test results are more sensitive to these variations for a number of reasons. First, this test measures the energy dissipated in the entire fracture process while the SE(B) test determines the response until just past crack initiation ($\mathbf{K}_{Id}$). Second, cracking in the Charpy specimen initiates from a notch, not a well-defined fatigue pre-crack. This causes variability because the crack initiation portion of the CVE will vary greatly with notch geometry, notch tip microstructure, and surface finish, etc. The smaller geometry of the Charpy specimen adds to the variability involved with crack initiation as it inhibits initiation as a cleavage crack. Transition from the ductile, microvoid crack to a fully cleavage crack will increase the randomness.

As mentioned, these well-known differences increased CVE scatter in ferritic and martensitic steels

compared to $\mathbf{K}_{Id}$ measurements on standard, precracked SE(B) specimens. There was another cause for scatter in the CVN tests which is unique to duplex steels. The CVE and fracture toughness depend on the ferrite and austenite concentrations. Nominally the concentration of ferrite/austenite was 50% in this material, although the local concentrations varied significantly (Figure 16). Further, the austenite phase size was often greater than 250 μm or as small as 10 μm. The local phase inhomogeneities and the large microstructural features led to significantly different microstructure which were sampled by the notch tip of the small (10 mm) Charpy specimens. Even for identical concentrations, the bimodal austenite size could result in 20-30 large austenite particles or hundreds of smaller particles at the notch tip. The larger SE(B) specimen thickness (2.5 times greater than the CVN specimen) helped compensate for these local inhomogeneities by sampling more microstructure at the tip. Thus, the fracture toughness measured in the SE(B) represented more of an "averaged" macroscopic quantity than did the CVN specimen.



Figure 16: Microstructure of Prototype Ferralium 255 Forging

FRACTURE INTEGRITY ANALYSIS

One of the finished Ferralium components will predominantly consist of a cylindrical forging as represented by Figure 17. The highest stresses in this component occur at the inner radius under dynamic loading rates. A fracture integrity analysis was performed to model fracture in this region to determine not only if the material tested is suitable for the intended application, but also to identify a suitable material fracture toughness criteria for future Ferralium forgings.

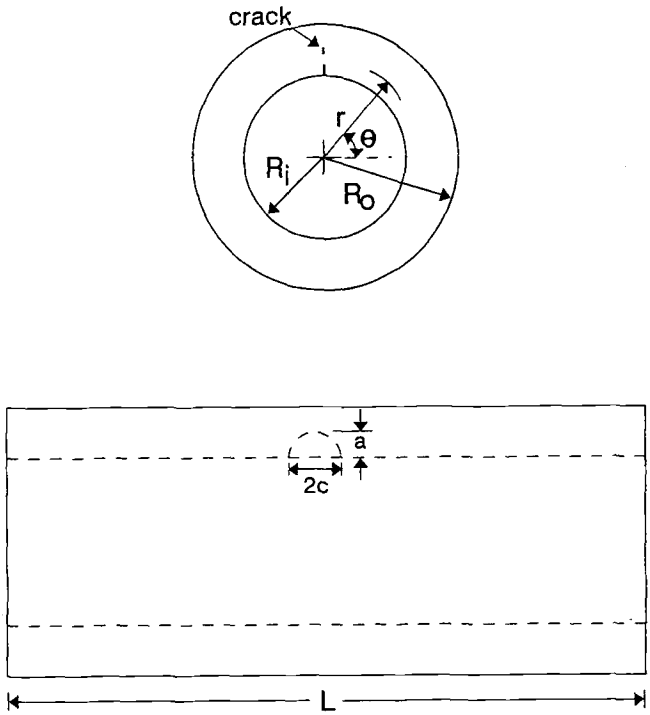


Figure 17: Ferralium 255 Forged Component Geometry

A linear elastic fracture mechanics (LEFM) analysis was conducted because the toughness testing indicated that this assumption was adequate for low temperature component operation. In the analysis, the component geometry was idealized as a long cylindrical tube (see Figure 17) with an inner radius (R_i) of 0.203 m and an outer radius (R_o) of 0.227 m. A "worse-case" surface crack oriented in the θ-r direction and emanating from R_i was assumed. A suitable stress intensity solution for this geometry was found [13] and is presented below:

$$K_I = 1.129 G_o \sigma_{max} \sqrt{a} \qquad (1)$$

In this equation, a is the crack depth of an elliptical surface crack (Figure 17) with a surface length of 2c. Also, G_o is a shape factor and σ_{max} is the maximum tensile or bending stress in the θ-direction at $r=R_i$. Purely tensile loading was assumed for conservativeness along with a semicircular flaw shape (a/c=1). In tensile loading, this shape flaw fails not only under the minimum surface stress (σ_{max}), but it also has the smallest surface area at failure. Hence, it is the flaw which is most difficult to detect. Under these conditions it was assumed that component loading will not exceed the minimum specified static σ_{ys} requirement of 485 MPa during high rate loading applications. This applied loading is consistent with component design requirements and is less than the measured dynamic yield stress by at least 30% at low operating temperatures (see Table 3) so that net section yielding will be avoided with this load.

Equation (1) was used with these assumptions to determine both the required material toughness given an initial flaw size and to find a critical flaw size using the measured Ferralium forging toughness. The first scenario was solved using the current material inspection limits which specify a max allowable flaw depth of 3.18 mm (surface length = 6.35 mm) for this material. For this flaw, G_o was 1.163 [13] and the toughness necessary to withstand fracture (K_{Ir}) was only 38 MPa-$m^{1/2}$. Therefore, the K_{JI}/K_{Ir} ratio is greater than 2.5 for temperatures above -17°C based on the dynamic fracture tests performed here.

For the second scenario, a minimum measured K_{JI} at -2 °C was assumed (100 MPa-$m^{1/2}$) and equation (1) was solved with G_o = 1.348 [13]. The critical flaw depth calculated was 20.3 mm which is over six times greater than the inspection criteria. These results indicate that the Ferralium forging material tested should perform adequately as long as the conditions assumed in the fracture integrity analysis are upheld in practice.

The analysis also suggests that 60 MPa-$m^{1/2}$ would be an adequate minimum fracture toughness criteria at -2 °C . This criteria is 1.5 times greater than the calculated K_{Ir} for the maximum allowable inspection flaw size. The 1.5 safety factor was chosen to build further conservatism into the analysis and to guard against cracks which may remain undetected during inspection. A more refined measure could be determined using more refined modeling and inclusion of plastic zone effects. However, the chosen criteria is well below the toughness values measured for this forging and should be easily met by material producers.

It should be stressed that while the minimum toughness criteria chosen above was easily met at the two locations studied, the current CVE specification (CVE_a = 45 J) was not met at every location. In this case, the CVE specification would lead to rejection of this forging, which appears adequate. Further, an empirical correlation between CVE and K_{Id} to set a new CVE criteria is not recommended due to the dual-phase microstructure and the fact that this material is in transition at the testing temperature. These conditions both lead to unacceptable scatter in the CVE results. It is therefore recommended that a fracture toughness material requirement be utilized along with toughness testing to quantify material acceptability.

CONCLUSIONS

The conclusions of this study are as follow:

1) Charpy impact tests do not provide adequate assurance of fracture toughness and material variability within the forging due to the high amount of scatter caused by fracture mode transition and by the small Charpy specimen size relative to the microstructure of Ferralium 255.

2) The large scatter exhibited by the CVE values are not indicative of the actual fracture toughness of this material. They prohibit definition of a suitable correlation between Charpy impact behavior and dynamic fracture toughness, K_{Id}, and they preclude determining a new minimum or average CVE that would ensure fracture safety of the Ferralium 255 components.

3) Dynamic fracture toughness of the prototype forging was much more uniform which indicates that actual fracture behavior is more consistent throughout the component and suggests that $\mathbf{K}_{Id}$ can be used to set a toughness criteria. A recommended value of 60 MPa-$m^{1/2}$ was chosen for this application.

4) The tensile results also did not exhibit the large scatter and large property variations implied by the CVE results. These tests should be suitable for material qualification at any forging location and orientation.

5) The calculated critical flaw size for this material is 20.3 mm deep by 40.6 mm long for the stress provided at the most critical location in the assumed forging component which is much larger than the inspection criteria for these components.

6) The fracture mode of Ferralium 255 is purely cleavage at low temperatures and is dominated by the ferrite microstructure as failure path deviates around the austenite phase. As temperature increases, the austenite "pull-out" becomes less evident and ductile failure of the austenite region becomes more prevalent until both the ferrite and austenite regions are fully ductile.

APPENDIX

Location	Orientation	σ_{ys} (MPa)	σ_{ut} (MPa)	EL (%)	RA (%)
Area B	L	615	820	32	66
		580	765	32	66
		540	765	34	69
	T	580	770	35	65
		580	770	30	62
		595	785	30	56
	S	575	780	34	56
		565	770	36	61
		565	780	32	60
Area E	L	560	770	35	64
		560	765	36	60
		515	760	36	65
		550	765	38	60
	T	565	780	32	60
		560	785	37	54
		560	785	37	57
		550	780	33	52
	S	530	780	30	55
		560	785	27	52
		545	785	32	57
		540	780	27	52

Table A1: Tensile Results from Locations B and E

Temp. (°C)	Location E			Location B		
	CVE T-L (J)	CVE L-T (J)	CVE S-T (J)	CVE T-L (J)	CVE L-T (J)	CVE S-T (J)
-73	11	15	9	9	11	5
-73	9	19	9	11	9	7
-73	7	14	8	11	9	7
-23	95	66	32	28	28	11
-23	66	68	103	37	30	12
-23	87	123	28	32	33	12
-2	107	144	53	75	80	42
-2	89	182	70	73	140	33
-2	108	179	58	108	46	47
22	165	212	160	108	94	75
22	163	222	118	149	103	98
22	190	207	102	159	108	76
38	163	248	133	133	133	80
38	171	226	167	188	104	104
38	186	270	137	179	118	114
82	212	241	209	226	167	172
82	176	259	190	212	171	161
82	201	255	145	225	161	165

Table A2: CVE Values for Locations B and E

Temp. (°C)	T-L CVE (J)
-2	35
-2	33
-2	54
-2	33
-2	60
-2	35
-2	45
-2	45

Table A3: CVE Values for Location X

Location	Temp. (°C)	$K_{Д}$ (MPa-$m^{1/2}$)
Area A	-143	71
	-84	84
	-84	91
	-51	92
	-51	87
	-51	85
	-18	107
	-18	115
	-18	107
	-2	120
	-2	114
	-2	121
	22	145
	22	147
	22	145
	49	143
	49	135
Test Coupon	-2	119
	-2	112
	-2	103

Table A4: Tensile Results from Locations B and E

REFERENCES

[1] Truman, J.E. and K.R. Pirt, "Properties of a Duplex Stainless Steel and the Effects of Thermal History", "Age Hardening in Duplex Stainless Steel", Duplex Stainless Steels, Conf. Proceedings, Ed. R.A. Lula, ASM, Metals Park, Ohio, 1983, p113.

[2] Kolts, J., "Properties of Ferralium Alloy 255 Duplex Austenitic-Ferritic Stainless Steel for Deep Sour Gas Wells", "Age Hardening in Duplex Stainless Steel", Duplex Stainless Steels, Conf. Proceedings, Ed. R.A. Lula, ASM Metals Park, Ohio, 1983, p233.

[3] Guha, P. and C.A. Clark, "Properties and Applications of High Chromium Duplex Stainless Steels", "Age Hardening in Duplex Stainless Steel", Duplex Stainless Steels, Conf. Proceedings, Ed. R.A. Lula, ASM, Metals Park, Ohio, 1983, p355.

[4] Solomon, H.D. and T.M. Devine, Jr., "Duplex Stainless Steels - A Tale of Two Phases", "Age Hardening in Duplex Stainless Steel", Duplex Stainless Steels, Conf. Proceedings, Ed. R.A. Lula, ASM, Metals Park, Ohio, 1983, p693.

[5] "Fabrication of Ferralium Alloy 255", Technical Information Pamphlet H-2030, Hayes International, Kokomo, Indiana, 1988.

[6] Chance, J., W. Coop and K.J. Gradwell, "Structure-Property Relationships in a 25-Cr, 7-Ni, 2-Mo Duplex Stainless Steel Casting Alloy", "Age Hardening in Duplex Stainless Steel", Duplex Stainless Steels, Conf. Proceedings, Ed. R.A. Lula, ASM, Metals Park, Ohio, 1983, p371.

[7] Unpublished data, Earle M Jorgenson Co Steel, 1992.

[8] "Standard Test Method for Tension Testing of Metallic Materials", Annual Book of ASTM Standards, ASTM E8, Vol. 3.01, ASTM, Philadelphia, PA, 1992, p130.

[9] "Standard Test Method for Notched Bar Impact Testing of Metallic Materials", Annual Book of ASTM Standards, ASTM E23, Vol. 3.01, ASTM, Philadelphia, PA, 1992, p205.

[10] Kanninen, M.F and C.H. Popelar, Advanced Fracture Mechanics, Oxford University Press, New York, New York, 1985.

[11] "Standard Test Method for Plane Strain Fracture Toughness of Metallic Materials", Annual Book of ASTM Standards, ASTM E399, Vol. 3.01, ASTM, Philadelphia, PA, 1992, p506.

[12] Unpublished CVN data, CDNSWC, 1992.

[13] Raju, I.S. and J.C. Newman, Jr., "Stress-Intensity Factor Influence Coefficients for Internal and External Surface Cracks in Cylindrical Vessels", J of Pressure Vessel Technology, Trans ASME, Vol. 104, No. 4, Nov. 1982, pp. 293-299.

Applications

Karl-Heinz Schwalbe[1]

INTRODUCTION OF δ_5 AS AN OPERATIONAL DEFINITION OF THE CTOD AND ITS PRACTICAL USE

REFERENCE: Schwalbe, K.-H., **"Introduction of δ_5 as an Operational Definition of the CTOD and its Practical Use"**, Fracture Mechanics: 26th Volume, ASTM STP 1256, Walter G. Reuter, John H. Underwood, and James C. Newman, Eds., American Society for Testing and Materials Philadelphia, 1995.

ABSTRACT: A number of years ago δ_5 was introduced as an experimental technique for determining the crack tip opening displacement. Experience gained since then has confirmed that δ_5 can be used as an operational definition of the CTOD which has the advantage that due to its direct measurement without the need of calibration functions, it can be measured on any cracked part, be it a test specimen or a structural component. In the case of bend bars δ_5 is closely linked to standardised test methods. It is also shown that δ_5 is uniquely related to the J-integral and that it can be predicted as a driving force parameter with the Engineering Treatment Model, allowing the use of δ_5 in flaw assessments.

KEYWORDS: Crack tip opening displacement, flaw assessment, J-integral, Engineering Treatment Model

The characterisation of crack tip conditions with the J-integral is well established. The J-integral is widely used
- as a fracture parameter for determining the material's fracture resistance
and
- as a parameter describing the loading conditions in a structural component.

Thus, under certain conditions a consistent system can be established for predicting failure events in cracked structural components.

Problems arise, however, when substantial amounts of crack growth have to be handled. Since J can correlate crack growth uniquely only up to a small percentage of the original ligament length, b_0, alternative correlation parameters have been sought for. These are:

The Modified J-Integral, J_M

The modified J-integral, J_M, has been introduced by Ernst [1,2] and represents an extension of the J-integral to the regime beyond J-controlled crack growth. It has been demonstrated [3,4] that J_M is capable of correlating much more crack growth than the J-integral; the figures reported for CT specimens range from 22 to 50 per cent of the original ligament length, b_0, which is substantially larger than the 6 [5] or 10 [6] percent stated for J. Hence, J_M is a parameter for generating extended size independent R-curves, but it has no longer the meaning of a crack field parameter in the spirit of the HRR field. It should be noted that some experimental work, e.g. [7] shows that J correlates crack growth as well as J_M.

[1]Director, Institute of Materials Research, GKSS Research Center, Geesthacht, Germany

Copyright © 1995 by ASTM International www.astm.org

The Crack Tip Opening Displacement

The Standard Method

The crack tip opening displacement (CTOD) is frequently being used as an alternative fracture parameter [8,9]. Standardised test methods [10-12] use a test technique which extrapolates a remotely measured plastic displacement, v_{pl}, to the pre-crack tip. In the equation

$$\delta_{BS} = \frac{K^2\left(1-\upsilon^2\right)}{2R_{p0.2}E} + \frac{r_{pl}\left(W-a_o\right)}{r_{pl}\left(W-a_o\right)+a_o+z} \cdot v_{pl} \qquad (1)$$

the first term on the right hand side represents the small scale yielding contribution to the total CTOD, whereas the second term gives the plastic contribution, based on the assumption that the specimen (bend specimen or CT specimen) rotates about a fixed hinge point, the location of which is given by the plastic rotation factor, r_{pl}. Depending on the individual test standard, r_{pl} takes values from 0.4 to 0.47. In Equ (1) the d was provided with the subscript "BS" to indicate that this CTOD is based on a British Standards method which applies to bend-type specimens. Due to the evaluation formalisms used, the thus determined CTOD loses its well defined physical meaning when the crack grows. The reason for this is that the fixed location of the hinge point becomes meaningless in the event of crack growth. This can be accounted for if one assumes that the hinge point migrates along the ligament after the crack had started to grow [12,13]. The thus modified CTOD, δ^M_{BS}, is then

$$\delta^M_{BS} = \frac{K^2\left(1-\upsilon^2\right)}{2R_{p0.2}E} + \frac{0.6\Delta a + 0.4\left(W-a_o\right)}{0.6\left(a_o+\Delta a\right)-0.4W+z} v_{pl} \qquad (2)$$

By this modification, the CTOD is nominally determined at the original fatigue pre-crack tip.

The δ_5 Method

With this method, the CTOD is measured on the specimen's side surface at gage points located 2.5 mm at either side of the pre-crack tip. Fig. 1 shows a welded centre cracked tensile specimen fully instrumented for determining J-R and δ_5-R curves [14]. It has been used for a number of years for measuring fracture toughness and crack growth resistance, both on laboratory specimens and a set of full scale components. Whilst the δ_5 technique is an empirical method, it is the aim of this communication to present some justification for its suitability. Some unsolved problems will also be mentioned.

EXPERIMENTAL EVIDENCE

δ_5 As a Crack Growth Correlation Parameter

It has been demonstrated in a number of papers [4, 13-18] that δ_5-R curves can be generated which are to a much greater extent independent of size and geometry than

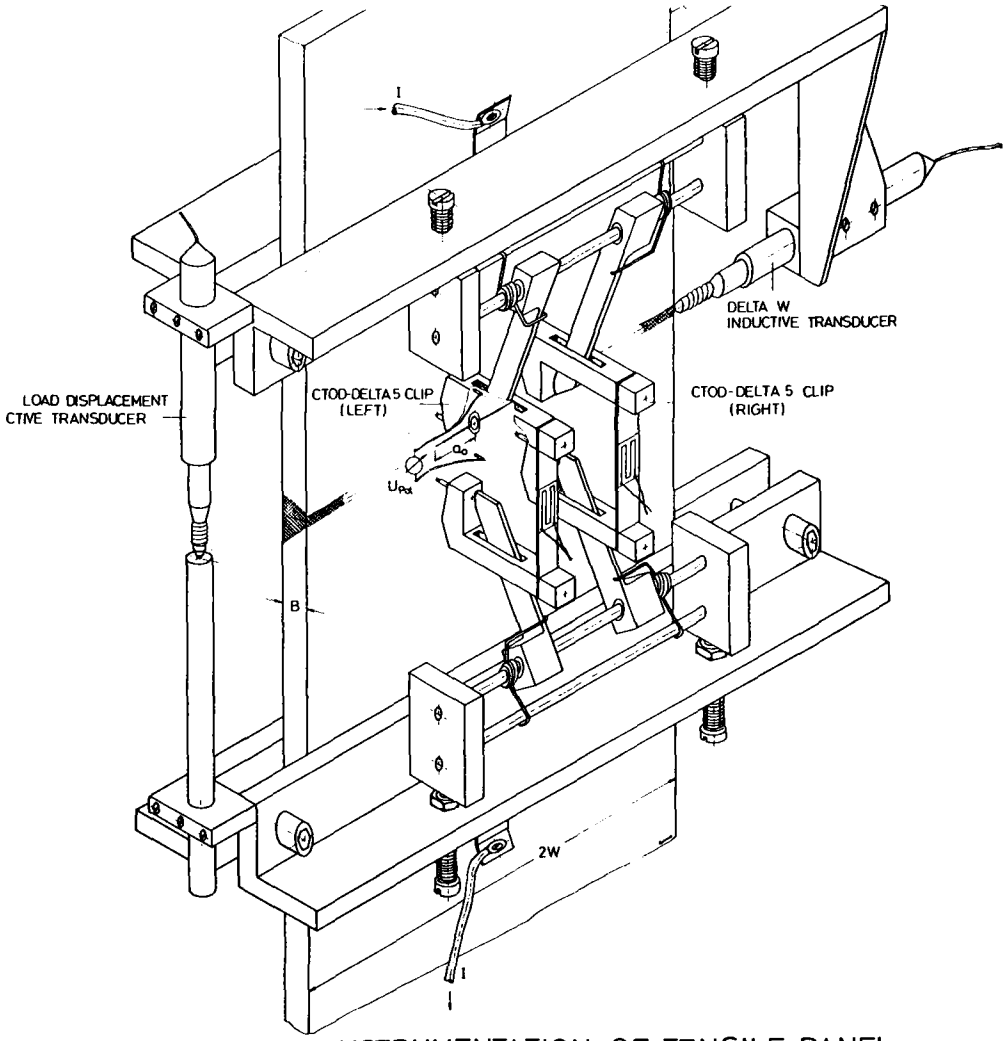


Fig. 1: Experimental setup for measuring δ_5. Two clips are attached to the specimen for measuring δ_5 at both crack tips. The front clip is drawn in a broken fashion to show the crack.

the respective J-R curves. The length of a size independent R curve ranges from 25 per cent of the original ligament size for CT specimens up to over 50 per cent for tension configurations (centre cracked and double edge cracked). The statement for tension configurations is valid only for thin sections with a state of plane stress. Fig. 2 shows δ_5-R-curves obtained on 10 mm thick CT specimens having three different widths [19]. It is clearly seen that δ_5 correlates crack growth uniquely up to about 0.25 b_0.

These empirical findings, based on the comparison of R-curves from various specimen geometries, suggest that δ_5 can be successfully used as a crack growth correlation parameter.

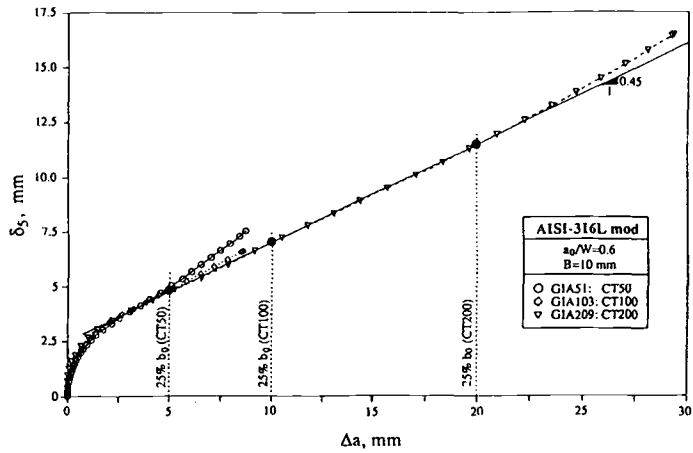


Fig. 2: δ_5-R-curves for 10 mm thick, and 50, 100, and 200 mm wide CT specimens made of the austenic steel 316L mod [19].

Correlation Between δ_5 and Other Parameters

Since the J integral on the one hand is a mechanically founded crack field parameter and δ_{BS} on the other hand is a well established experimental toughness parameter, it is important to know the relationships between δ_5 and these parameters.

Usually all our experiments are equipped such that δ_5, δ_{BS}, and J can be determined on every specimen. This way correlations between these parameters can be easily obtained.

As far as the relationship between δ_5 and J is concerned, the experiments on thin sections in plane stress have shown [14,15,17] that there is a unique, i.e. size and geometry independent relationship between both quantities, as long as J does not exceed its validity limits. An example is shown in Fig. 3: CT and CCT (centre cracked tensile) specimens made of polypropylene exhibit the same δ_5-J correlation.

Fig. 4 shows another example: here the δ_5 values measured on CT specimens with different geometries are plotted versus the respective J values. The relationship between both quantities is unique as long as J is valid according to the validity limit: the curves diverge when crack growth exceeds 5 to 10 percent of the original ligament width, b_0.

Moreover, in both examples as well as in other examples already published [14,15,18], the relationship between δ_5 and J is almost linear, as one would expect from the simple non-hardening relationship

$$CTOD = A\frac{J}{\sigma_Y} \tag{3}$$

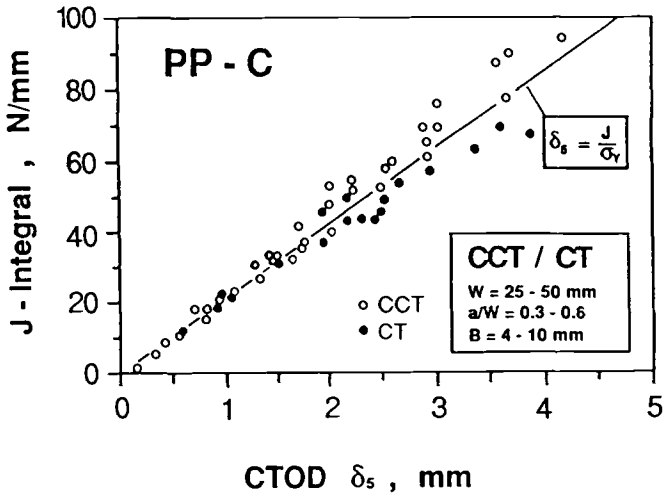


Fig. 3: Relationship between experimentally determined values of δ_5 and J for CT and CCT specimens of polypropylene [17].

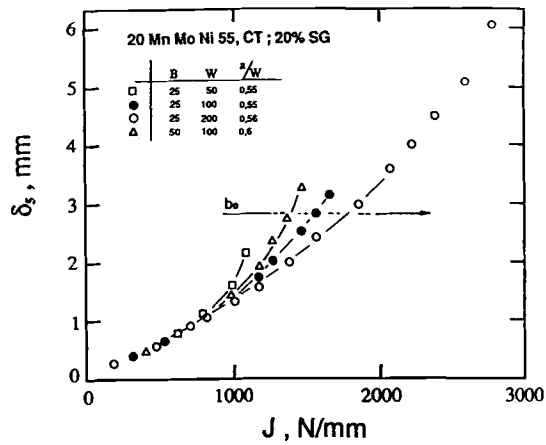


Fig. 4: Correlation between experimental δ_5 and J values, determined on side grooved CT specimens of different size and thickness-to-width ratio; steel 20MnMoNi55 [4].

A further important matter concerns the compatibility of the δ_5 technique with the standard type CTOD, δ_{BS}. Fig 5 shows critical CTOD values for welded joints; it can be seen that both methods agree very well.The effect of crack growth is shown by Fig. 6: δ_5 and δ_{BS} diverge after initiation of crack growth. The difference between both quantities can be reduced by using the modified δ_{BS} parameter as defined by Eq (2); a further reduction can be achieved by taking account of the material dependence of the plastic rotation factor, v_{pl}, as outlined in Ref. [13]. A further example is given in Fig. 7. Inspite of the different definitions of both parameters the vast majority of cases has resulted in reasonable coincidence of δ_5 and δ_{BS} (and δ^M_{BS} for growing cracks).

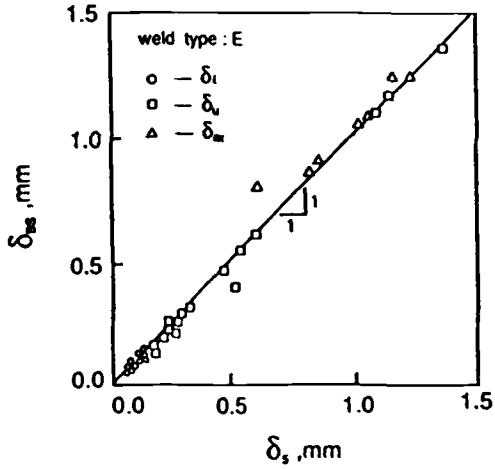


Fig. 5: Comparison of δ_5 with δ_{BS} for a steel weld[19], cracks in heat affected zone, 25 mm thick SENB specimens.

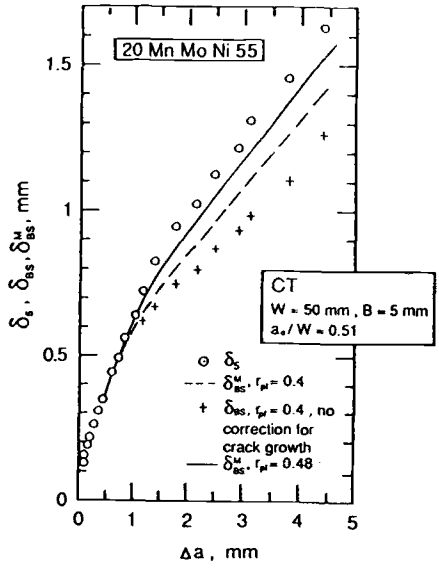


Fig. 6: Crack growth resistance curve for steel 20MnMoNi55 determined on the basis of δ_5, δ_{BS}, and δ^M_{BS} [13].

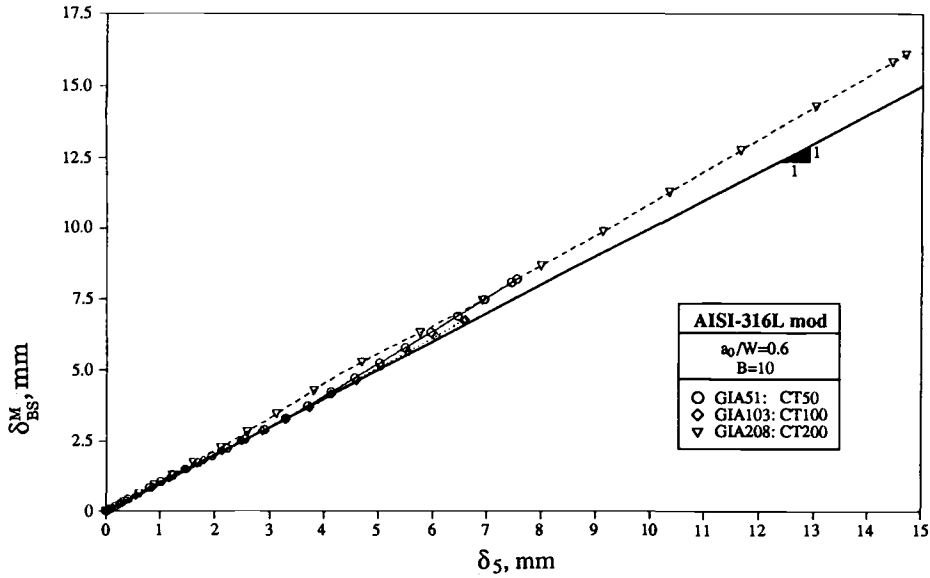


Fig. 7: Correlation between δ_5 and δ_{BS}^{M} for the specimens shown in Fig. 2. CT 50 means CT specimen with W = 50 mm and so on.

THEORETICAL EVIDENCE

Stationary Crack

The empirical finding shown above that for a given material δ_5 is uniquely related to J can be explained if one assumes that the gauge points over which δ_5 is measured are located within the HRR field. According to the HRR field equations the displacements are expected to vary with J in the form

$$\delta_5 \sim J^{\frac{1}{1+N}} \tag{4}$$

where N is the strain hardening exponent of the power law stress-strain curve

$$\frac{\sigma}{\sigma_Y} = \left[\frac{\varepsilon}{\varepsilon_Y}\right]^N \tag{5}$$

The empirical findings related to Eq (3) seem to be in conflict with Eq (4). However, for low N values the magnitued of the exponent in Eq (4) is not so totally different from unity so that a linear fit through the experimental data is a reasonable approximation. A closer examination of experimental data reveals that there is indeed a range in which δ_5 behaves according to Eq (4). Figs. 8 and 9 show two examples. The proportionality between δ_5 and $J^{1/(1+N)}$ tends to cease when the HRR field and hence the J validity breaks down; in case of the steel this corresponds with J values around 1000 N/mm, see Fig. 4. More details on the δ_5-J correlation will be presented in the Section "δ_5 as a driving force parameter".

Growing Crack

In their crack growth analysis Rice et al. [21] related the near-tip opening displacement, d, taken at a small distance, r, from the actual crack tip with a J-like parameter,J_X. With the assumptions: plane strain, small scale yielding, and elastic-ideally plastic materials, they obtained

$$\delta = r\frac{\alpha}{\sigma_Y}\frac{dJ_x}{da} + \beta\frac{\sigma_Y}{E}r\ln\frac{2.718R}{r} \tag{6}$$

where $a \approx 0.65$, $b \approx 5.08$, R is a length parameter related with the plastic zone size. Ernst [22] derived a different formulation in that d can be taken at the original crack tip by setting $r = \Delta a$, and by replacing J_X by the modified J-integral, J_M. Thus, the defined d is taken as a measure of δ_5

$$\delta \rightarrow \delta_5 = \frac{\alpha}{\sigma_Y}J_M + \int_{a_o}^{a}\beta\frac{\sigma_Y}{E}\ln\frac{2.718R}{a-a_o}da \tag{7}$$

Since the Rice et al. analysis was performed for $r \rightarrow 0$,Eq (7) cannot be expected to be valid for large r, e.g. for r large compared with the remaining ligament. If, on the other hand, r or Δa is large enough, the second term in Eq (7) is small compared with the first one, i.e. it can be expected that under certain circumstances δ_5 and J_M are uniquely correlated:

$$\delta_5 \approx \frac{\alpha}{\sigma_Y}J_M \tag{8}$$

Eq(8) will not be compared with experimental data since it is based on a non-hardening material. Although the power 1/(1+N) seems to be appropriate also for J_M it is not clear how strain hardening may affect the constant a so that any comparison with experimental data would be arbitrary.
In conclusion, it can be stated that δ_5 is a unique function of the mechanically founded parameters J and J_M, thus showing the usefulness of its definition.

δ_5 AS A DRIVING FORCE PARAMETER

The Engineering Treatment Model (ETM) has been set up to provide a framework for estimating δ_5 as a driving force parameter as a function of applied load or strain [23]. In short, under contained yielding conditions (applied load, F, lower than or equal to the net section yielding load, F_Y,) δ_5 is given by the well known small scale yielding, non-hardening solution for plane stress

$$\delta_5 = \frac{K_{pl}^2}{E\sigma_Y} = \frac{J}{\sigma_Y} \tag{9}$$

where K_{pl} is the plasticity corrected stress intensity factor. Under net section yielding conditions δ_5 behaves like the stress-strain curve in Eq (5)

$$\frac{\delta_5}{\delta_Y} = \frac{\varepsilon}{\varepsilon_Y} = \left[\frac{F}{F_Y}\right]^{1/N} = \left[\frac{J}{J_Y}\right]^{\frac{1}{1+N}} \tag{10}$$

The normalised form of Eq (10) provides a size and geometry independent formulation of the driving force, expressed in δ_5 or J; δ_Y and J_Y, respectively, designate the "yield values" of δ_5 and J, respectively, evaluated with Eq (10) at $F = F_Y$. The quantities δ_5 and J can be estimated under fully plastic conditions by

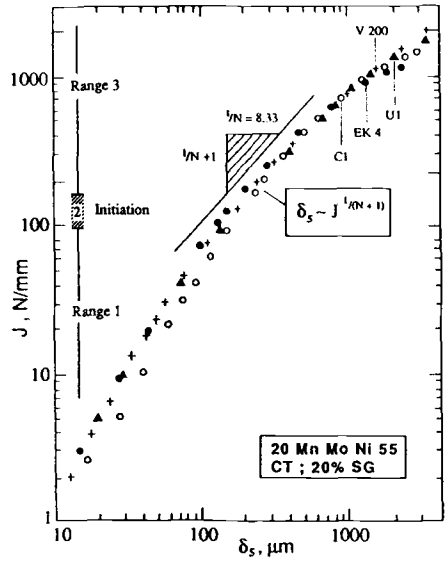


Fig. 8: Data from Fig. 4 in double logarithmic scales in order to reveal power law type behaviour.

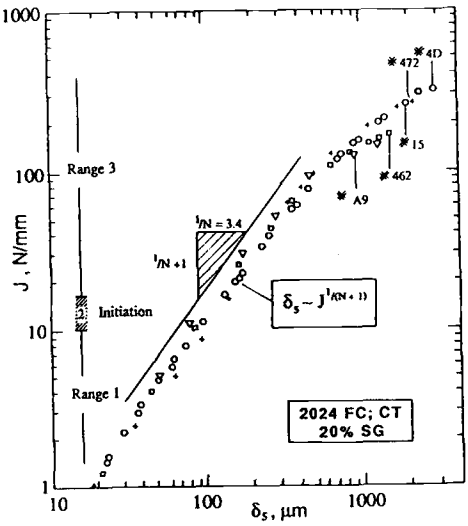


Fig 9: Experimental values of δ_5 and J for an aluminium alloy [4]; side grooved CT Specimens, thickness from 5 to 95 mm, width from 50 to 200 mm.

magnifying the respective yield value with the material's power law hardening characteristics, as expressed by Eq (9). On the background of Eqs (9) and (10) the behaviour of the experimental findings referred to above becomes more transparent: δ_5 varies linearly with J under contained yielding conditions, whereas under net section yielding conditions the material's work-hardening behaviour manifests itself, see Figs. 8 and 9. This will be further substantiated in the following.

In Fig. 10 plane stress finite element calculations are compared with the respective ETM estimates; it can be seen that Eqs (9) and (10) capture the different kinds of behaviour in the regimes of contained yielding and net section yielding quite well.

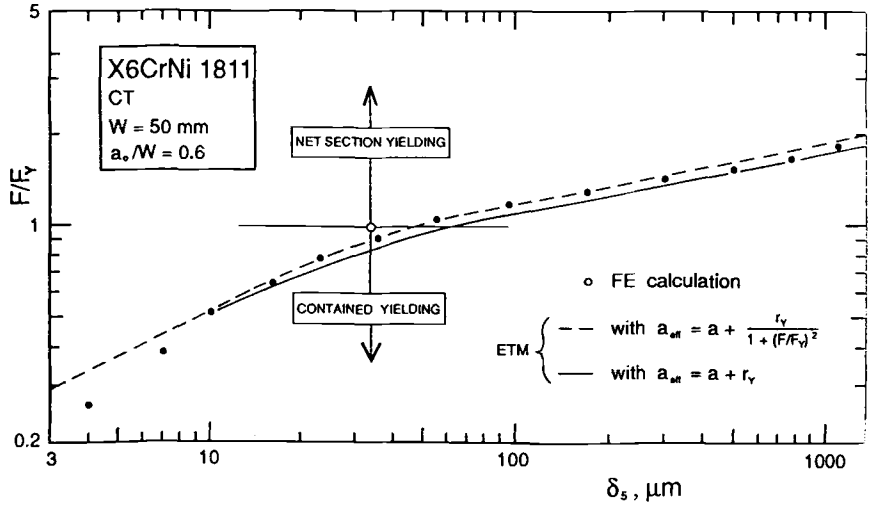


Fig. 10: Comparison of finite element calculations by Amstutz and Seeger [24] with ETM predictions; the background of the two different curves is explained in Ref. [23].

The relationship between δ_5 and J under net section conditions is demonstrated in Fig. 11, where Eq (10) gives an excellent representation of the finite element points.

A further validation of the ETM has been performed by means of finite element calculations [25] on so-called three-hole-specimens [26], Fig. 12. These specimens are supposed to represent stiffened panels, and it is seen that also in this case which is substantially more complex than an ordinary test specimen the predicted δ_5-J correlation is very well confirmed. Absolute values of δ_5 from the same set of finite element calculations are plotted in Fig. 13 versus the applied load.

These examples as well as numerous others reported elsewhere e.g. [27-29] demonstrate clearly that the parameter δ_5 can be estimated as a driving force parameter using the ETM, with an accuracy which should be sufficient for defect assessments.

However, there is a problem which has still to be solved: Figs 10 and 13 show that at loads below $F/F_Y \approx 0.5$ the ETM tends to provide overestimations of δ_5. The reason is probably that at these loads the gauge points are no longer related to the HRR field. A solution to overcome this discrepancy is being worked on.

The flexibility of the method can also be demonstrated by a further application: A crack along the interface between two different materials - for example a crack in the

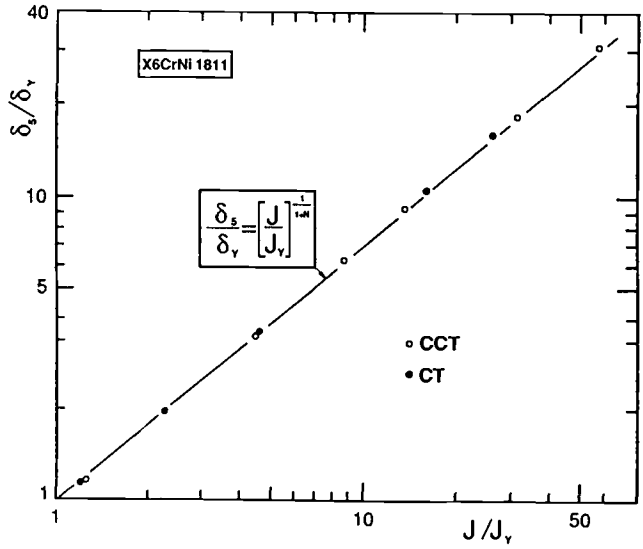


Fig. 11: Comparison of finite element calculations on a CT and a CCT specimen [24] with ETM under net section yielding conditions.

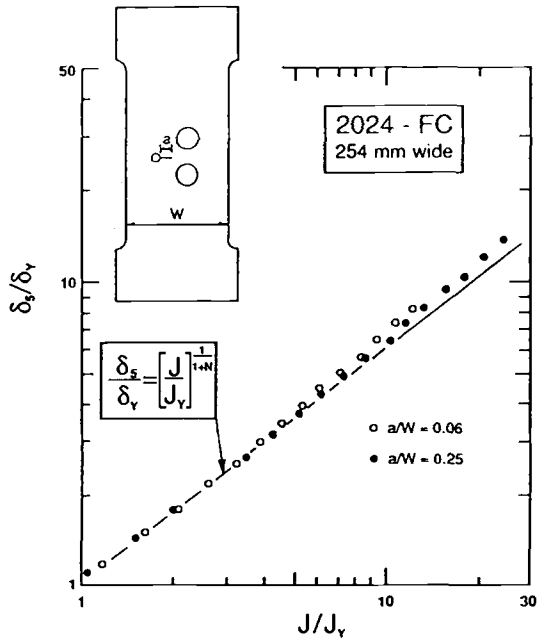


Fig. 12: Normalised δ_5 as a function of normalised J; plane stress FE calculations from Amstutz and Seeger [25] on three-hole-specimens after Newman [26].

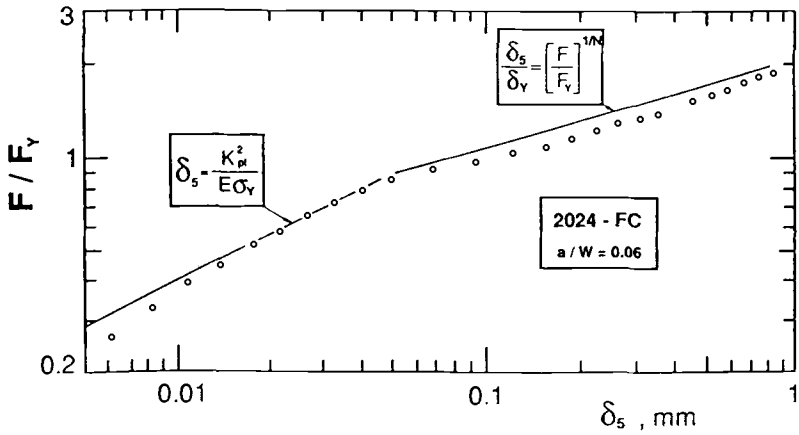


Fig. 13: Finite element calculations of $\delta 5$ from Fig. 12 and ETM predictions as a function of the applied load.

fusion line of a weld - may exhibit a CTOD arising from two contributions from either side of the crack which are different in magnitude. These two contributions can be measured separately with the three-leg-clip shown in Fig. 14, with the centre leg (O in Fig. 14) at the interface.

CONCLUDING REMARKS

Experience has shown that $\delta 5$ can be readily used as an operational definition of the crack tip opening displacement. On the one hand, it provides a means for measuring the material's resistance against initiation and growth of a crack. It is particularly appealing that $\delta 5$ can be measured on any specimen or component geometry with a surface-breaking crack, since this displacement is measured directly. Unlike the experimental determination of the J-integral no calibration function is needed. This way transferability studies can be most easily undertaken, as it has already been done for axial through-cracks in pressurised cylinders [16] and for circumferential through-cracks in pipes under bending [29]. No such flexibility exists for the standardised CTOD, δ_{BS}, which can be used on bend bars (and CT specimens) only. However, as it has been shown above, a good correspondence exists between $\delta 5$ and the standard δ_{BS} for bending. The $\delta 5$ technique can, of course, be used for any specimen or component thickness. If thickness is varied in a test series, then thickness dependent R-curves are obtained [14], similar to J R-curves. Work is in progress for applying the $\delta 5$ technique to part-through surface cracks.

On the other hand, $\delta 5$ can be estimated as a driving force parameter using the simple formalisms of the ETM. Also on the driving force side a successful application has been performed on a structural component [29]. The input information needed is the stress intensity factor, the limit load, the yield stress, and the strain hardening exponent [23].

In conclusion, a complete assessment system can be built on $\delta 5$, comprehending the experimental determination of material properties and an estimation scheme for the driving force, Fig. 15. The latter one has already been formulated in a procedural form [23]. Not only does $\delta 5$ work in a practical sense, it is also related to the crack field parameter, J.

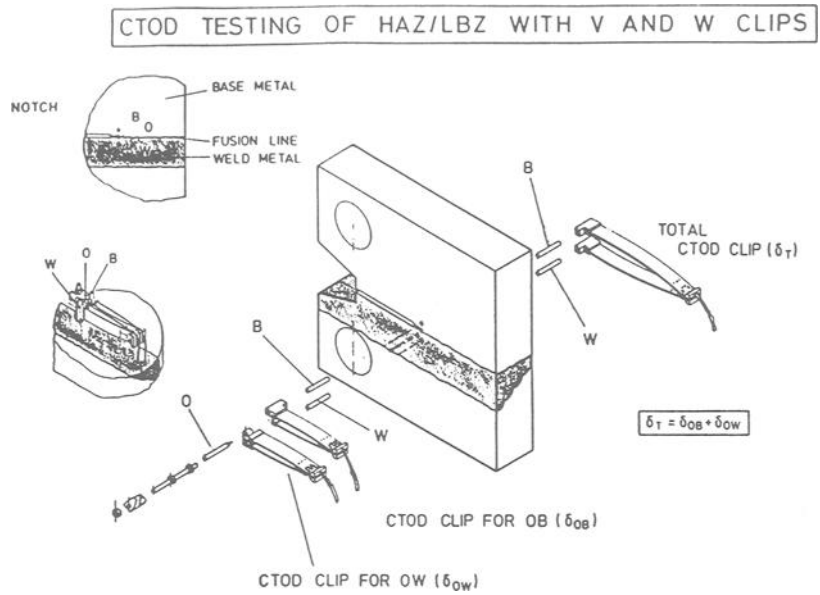


Fig. 14: Three-leg-clip for determining separately the CTOD contributions from either side of an interface crack. Patent pending.

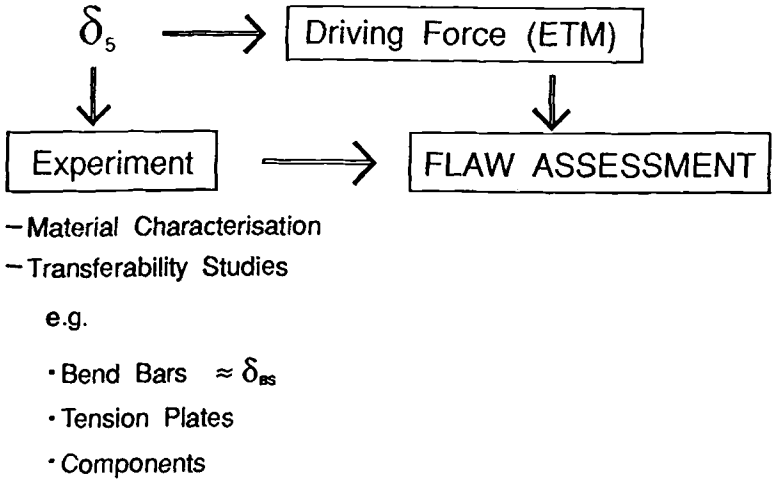


Fig. 15: The crack tip opening displacement, $\delta 5$, can be measured on various configurations. The material properties and driving force estimates from the ETM can be used for flaw assessments.

ACKNOWLEDGEMENTS

Many fruitful descussions with my colleagues Dr. A. Cornec and Dr. J. Heerens helped clarifying the material used for this article.

NOMENCLATURE

a	crack length
a_o	starting crack length
Δa	crack growth
B	thickness of specimen or component
b_o	starting ligament length, $b_o = W-a_o$
E	Young's modulus
F	applied load
J	J-integral
J_M	modified J after H. Ernst
K	stress intensity factor
K_{pl}	plasticity corrected K
N	strain hardening exponent
$R_{p0.2}$	0.2 percent yield strength
r_{pl}	plastic rotation factor of bend bar
v_{pl}	plastic component of mouth opening displacement of bend bar
W	width of specimen or component
z	distance of measurement points for d_{BS} from specimen front face
δ	crack tip opening displacement
δ_5	δ measured at original crack tip according to Fig. 1
δ_{BS}	δ experimentally determined after standardised test procedures
δ^M_{BS}	δ_{BS} taking account of crack growth
e	strain
n	Poisson's ratio
s	stress

Subscript Y: value of respective quantity at incipient net section yielding.

REFERENCES

[1] H. Ernst, Material resistance and instability beyond J-controlled crack growth in: ASTM STP 803, Vol I pp. 191-213, American Society for Testing and Materials, Philadelphia, 1983.

[2] H. Ernst, "Relationship Between Crack Tip Opening Displacement and Jm" in The Crack Tip Opening Displacement in Elastic-Plastic Fracture Mechnaics, K.-H. Schwalbe, Springer Verlag. 1986, pp. 197-206

[3] H. Ernst, K.-H. Schwalbe, D. Hellmann, and D.E. McCabe, Modified J, J_M, resistance curves under plane stress conditions, Int. Journ. of Fracture 37, pp. 83-100, 1988.

[4] J. Heerens, Rißabstumpfung, Spaltbruch im Übergangsbereich und stabiles Rißwachstum - untersucht mit den Methoden der nichtlinearen Bruchmechanik, Ph. D. Thesis, Report GKSS 90/E/31, GKSS Research Centre, Geesthacht, 1990.

[5] C.F. Shih, H.G. de Lorenzi, and W.R. Andrews, Studies on crack initiation and stable crack growth, in ASTM STP 668, pp. 65-120, American Society for Testing and Materials, Philadelphia, 1979.

[6] ASTM E 1152-87, Standard test method for determining J-R curves, in:Annual Book of ASTM Standards, Vol 03.01, American Society for Testing and Materials, Philadelphia, 1990.

[7] J.A. Joyce and E.H. Hackett, Development of an engineering definition of the extent of J-controlled crack growth in: J.G. Blauel and K.-H. Schwalbe, eds., ESIS/EGF 9 Defect Assessment of Components - Fundamentals and Application, Mechanical Engineering Publications, London, 1991.

[8] J.D. Harrison, The "State-of-the-art" in crack tip opening displacement (CTOD) testing and analysis, Report108/1980, The Welding Institute, Abington, U.K., 1980.

[9] K.-H. Schwalbe, ed., The Crack Tip Opening displacement in Elastic-Plastic Fracture Mechanics, Springer, Heidelberg, 1986.

[10] BS 5762:1979, Methods for crack opening displacement (COD) tetsing, The British Standards Institution, 1979.

[11] ASTM E 1290-89, Standard test method for crack-tip opening displacement (CTOD) fracture toughness measurement, in: Annual Book of ASTM Standards, Vol. 03.01, American Society for Testing and Materials, Philadelphia, 1990.

[12] ESIS P1-92, ESIS recommendations for determining the fracture resistance of ductile materials, European Structural Integrity Society (ESIS), Delft, 1992.

[13] D. Hellmann and K.-H. Schwalbe, On the experimental determination of CTOD based R-curves, in: K.-H. Schwalbe, ed., The Crack Tip Opening displacement in Elastic-Plastic Fracture Mechanics, Springer, Heidelberg, 1986.

[14] D. Hellmann and K.-H. Schwalbe, Geometry and size effects on J-R and d-R curves under plane stress conditions, in: ASTM STP 833, pp. 577-605. American Society for Testing and Materials, Philadelphia, 1984.

[15] D. Hellmann and K.-H. Schwalbe, R-cuve behaviour of double edge notched tension specimens in plane stress, Z. Werkstofftechnik, Vol.17, pp. 280-285, 1986.

[16] K.E. Aeberli, D. Schulze, P. Morawietz, H. Fuhlrott, J. Heerens, and K.-H. Schwalbe, Fracture mechanics tests on axially cracked pipe sections subjected to internal pressure, in: K.-H. Schwalbe, Ed., The Crack Tip Opening Displacement in Elastic-Plastic Fracture Mechanics, Springer-Verlag, Heidelberg, 1986.

[17] E. Reese, K.-H. Schwalbe and K. Friedrich, Characterisation of polymer materials by elastic-plastic crack growth resistance curves, in: D. Firrao, ed. ECF8 - Fracture Behaviour and Design of Materials and Structures, Conference Proceedings of the Eighth European Conference on Fracture, Turin, 1991.

[18] K.-H. Schwalbe and D. Hellmann, Correlation of stable crack growth with the J-integral and the crack tip opening displacement, effects of geometry, size, and material, progress report on an investigation of the elastic-plastic R-curve methodology, GKSS 84/E/37, GKSS-Forschungszentrum Geesthacht, Geesthacht, 1984.

[19] M. Koçak, S. Yao, K.-H. Schwalbe, and F. Walter, Effect of crack depth (a/W) on weld metal fracture toughness, in: M. Koçak, ed., Welding-90, IITT International, Gourmay-sur-Marne, 1990.

[20] K. Baustian, A. Cornec and K.-H. Schwalbe, R-Kurven im Rißinitiierungsbereich bei Verwendung der Bruchparameter J-Integral und CTOD, Technical Note GKSS WW/90/1, GKSS-Forschungszentrum Geesthacht, Geesthacht, 1990.

[21] J.R. Rice, W.J. Drugan and T.L. Sham, Elastic-plastic analysis of growing cracks, in: ASTM STP 700, American Society for Testing and Materials, Philadelphia, 1980.

[22] H. Ernst, Relations between the crack tip opening displacement, δ_5, and the modified J, JM, in: K.-H. Schwalbe, Ed., The Crack Tip Opening, Displacement in Elastic-Plastic Fracture Mechanics, Springer-Verlag, Heidelberg, 1986.

[23] K.-H. Schwalbe and A. Cornec, The Engineering Treatment Model (ETM) and its practical application, Fatigue and Fracture of Engineering Materials and Strucutres, Vol. 14, pp. 405-412, 1991.

[24] H. Amstutz and T. Seeger, Bruchmechanische Analyse eines austenitischen Stahles (X6CrNi1811) an zwei Standardrißscheiben mit ebenem Spannungszustand, Report Fl-2/1984, Technische Hochschule Darmstadt, Darmstadt, 1984.

[25] H. Amstutz and T. Seeger, Spannungs-und Verformungszustände einer Dreilochprobe, Report Fl-18/1986, Technische Hochschule Darmstadt, Darmstadt, 1986.

[26] J. Newman, Finite element analysis of initiation, stable crack growth, and instability using a crack tip opening displacement criterion, in ASTM STP 833, American Society for Testing and Materials, Philadelphia, pp. 93-117, 1984.

[27] K.-H. Schwalbe, The prediction of failure situations using the CTOD concept based on the Engineering Treatment Model (ETM), in [9].

[28] K.-H. Schwalbe, A. Cornec and J. Heerens, The Engineering Treatment Model (ETM) - a simple method for estimating the driving force under elastic-plastic and plane stress conditions, in: J.G. Blauel and K.-H. Schwalbe, eds., ESIS/EGF 9 Defect Assessment of Components-Fundamentals and Application, Mechanical Engineering Publications, London, 1991.

[29] K.-H. Schwalbe and L. Grüter, Ductile crack growth under plane stress conditions: size effects and structural assessment - II. Assessment of circumferential through - cracks in austenitic steel pipes using the δ_5 technique and the Engineering Treatment Model, Engng. Fract. Mech. 42, No.2, pp. 221-235, 1992.

Christopher D. Wilson[1]

FRACTURE MECHANICS LIFE PREDICTION COMPUTER CODE VERIFICATION AND VALIDATION

REFERENCE: Wilson, C. D., **"Fracture Mechanics Life Prediction Computer Code Verification and Validation,"** Fracture Mechanics: 26th Volume, ASTM STP 1256, Walter G. Reuter, John H. Underwood, James C. Newman, Jr., Eds., American Society for Testing and Materials, Philadelphia, 1995.

ABSTRACT: The verification and validation (V&V) of a fracture mechanics life prediction computer code is an essential task. The confidence level of results is directly related to the effort invested in the V&V process. The V&V process of life prediction software is broken two major parts: computer code assessment and fracture mechanics assessment. The fracture mechanics assessment is divided into three V&V tasks: fracture mechanics parameters, baseline predictions, and advanced predictions. The details of validating the stress intensity factor solution for a surface crack in a finite plate is discussed. Example V&V results are reported for NASCRAC Version 2.0 and NASA/FLAGRO Version 1.3. NASCRAC has significant errors in implementing a fatigue crack growth algorithm. In addition, the surface crack stress intensity factor solution in NASCRAC does not agree well with established analytical and experimental benchmark results. NASA/FLAGRO has computer coding problems which affect its portability.

KEYWORDS: Software verification and validation, fatigue crack growth, fracture mechanics life prediction, surface cracks, crack shape evolution, local stress intensity factor, average stress intensity factor.

WHY SOFTWARE VERIFICATION AND VALIDATION?

Early fracture mechanics life prediction software was developed by private companies or government agencies for in-house use. Software was informally verified and validated by the software developer. Later fracture mechanics life prediction software was developed for the general structural analysis community. These life prediction computer programs have brought much power to the hands of structural analysts, who often use this power without having expertise in fracture mechanics or access to an in-house expert. These life prediction computer programs must be designed for a large body of users with varying levels of expertise. Software verification and validation (V&V) is a rigorous process which develops software that is both functional and reliable.

[1] Graduate Student, Engineering Science and Mechanics Department, The University of Tennessee, Knoxville, TN 37996-2030. Formerly, aerospace engineer, NASA George C. Marshall Space Flight Center.

Copyright © 1995 by ASTM International www.astm.org

Hornbeck [1] describes software V&V as "One of the most vital and yet most difficult tasks which must be carried out ... In many cases the verification procedure can actually be more expensive and time consuming than obtaining the final desired answer. However, the confidence which one can place in the final results is directly related to the time and care which are invested in the verification process." Fracture mechanics life prediction code V&V is significant because no computer program is perfect and because no user is all-knowing. The unforgiving nature of crack-like defects in structures often leaves no margin for error.

The Institute of Electrical and Electronics Engineers has written several voluntary standards for software V&V. IEEE Std. 1012-1986 Software Verification and Validation Plans should be consulted before any software is developed. This standard implies that engineers and material scientists should work with computer scientists in developing software. Verification is defined as the process of determining whether or not the given phase of the software development cycle meets the requirements developed in the previous phase. Validation is defined as the process of evaluating software at the end of the software development process to ensure compliance with software requirements. Thus, verification occurs during the development process and validation occurs after the development process. Using these definitions, the software developer can perform both verification and validation, while the user can perform only validation.

VERIFICATION AND VALIDATION GUIDELINE

A V&V guideline for life prediction software can broken into two major parts: computer code assessment and fracture mechanics assessment. Computer code assessment should verify and validate the modularity, error trapping, portability, ease of use, and documentation quality of the software. Fracture mechanics assessment should verify and validate solutions for fracture mechanics parameters, physical models for crack growth, and quality of any associated fracture mechanics databases. Computer code assessment asks the question, "Does the computer code function as intended?" Fracture mechanics assessment asks the question, "Is the solution or model reasonable in terms of accuracy and usefulness?"

Computer Code Assessment

AT&T [2] has written a general overview of software design and testing. A sample computer code assessment checklist would include: evaluation of data reference and usage; data declaration, definition, and initialization; general computation; comparison and booleans; iteration; control flow; intraprocess and interprocess interfaces; input and output; project specification and design; achievement of design goals; commentary; coding standards; system resource; and post-compilation checks [2]. In addition, the quality of documentation must be evaluated. Documentation should be consistent with the code and should include statements of accuracy and limitations.

Fracture Mechanics Assessment

The fracture mechanics assessment can be broken into three phases: V&V of fracture mechanics parameters, V&V of baseline predictions made with fracture mechanics parameters and crack growth models, and V&V of advanced predictions made with fracture mechanics parameters and crack growth models. Fracture mechanics parameters, baseline predictions, and advanced predictions should be compared to benchmark solutions. A benchmark solution is a well-defined mathematical analysis or experimental result that can

be used for correlation with a life prediction computer code. Benchmarks should have known accuracy and well-characterized limitations. Examples of benchmark solutions are the K solutions contained in the various ASTM standard tests.

Fracture mechanics parameters—Fracture mechanics parameters should be checked for accuracy and limitations. An indirect approach must be applied to K (or J, C^*) solutions because the fracture mechanics parameters are derived, not basic physical quantities. Solutions should be compared to other existing results and limit cases for consistency. Experimental results for simple crack geometries and loadings can be obtained using photoelasticity, compliance, or strain gages. When no comparisons with existing solutions can be made, new results should be carefully generated using analytical tools such as finite element or boundary integral element analyses. Weight functions should be checked for limiting cases, such as tension, bending, or pressure loads. Although net section stress is not a fracture mechanics parameter, its calculation and use should be checked.

Baseline predictions—Baseline predictions are well-characterized problems with universally accepted solutions. Typically, a baseline prediction would have extensive analytical and experimental results. Baseline predictions often combine the use of fracture mechanics parameters and physical models for crack growth. Unlike the V&V of fracture mechanics parameters, the V&V approach is direct—comparison of predicted and experimentally measured crack size and shape and the time or number of cycles to achieve the crack size and shape. Two examples of baseline predictions are critical flaw size (CFS) and constant amplitude fatigue crack growth (FCG).

The V&V of CFS determination includes two issues: failure condition and the numerical algorithm for root solving used to determine the CFS. Examples of failure conditions include exceedance of single point fracture toughness (K_c or J_{Ic}), resistance curve fracture toughness (J-R), or limit load. The numerical algorithm to determine CFS should be stable and should find any local maxima where the failure condition occurs.

The V&V of constant amplitude FCG includes five issues: FCG rate model and quality of databases provided that use the FCG rate model; numerical integration algorithm; linear elastic fracture mechanics (LEFM) limits and any simple plasticity corrections which extend those limits; algorithm to determine critical initial flaw size (CIFS); and 2-D crack growth models for elliptical part-through and embedded cracks which predict crack shape evolution and life.

Advanced predictions—Advanced predictions are state-of-the-art problems where a universally accepted approach does not exist. Typically, an advanced prediction would not have extensive analytical and experimental results. Advanced predictions often combine the use of fracture mechanics parameters and physical models for crack growth. Four examples of advanced predictions are extensions to LEFM-based FCG; nonlinear time-dependent crack growth; combined mechanism crack growth; and fracture mechanics-based proof test logic. The V&V of advanced predictions should include a direct approach—comparison of predicted and measured crack size and shape and time or number of cycles to achieve the crack size and shape.

Extensions to LEFM-based FCG include short crack effects, contained plasticity, variable amplitude FCG with acceleration and retardation effects, complex uniaxial stress states, crack geometry transitions, multiaxial loading, and mixed-mode crack growth. Nonlinear time-dependent crack growth includes FCG characterized by ΔJ and creep crack growth characterized by C^*. Combined mechanism crack growth includes combined low cycle fatigue-high cycle fatigue, creep-fatigue, and corrosion-fatigue.

Case Study: V&V of Surface Cracks

The V&V of surface crack geometry (Fig. 1) is of primary importance and is chosen as an example of the fracture mechanics assessment part of the V&V process. The discussion is limited to mode I LEFM applied to surface cracks in a finite plate subjected to tension and bending (through the thickness), without finite width corrections. The V&V process for surface cracks addresses the fracture mechanics parameter (K) and baseline predictions using fatigue crack growth (cycles to through crack transition or cycles to failure). Both local and average K are presented. A combined fracture mechanics parameter-baseline prediction scheme based on crack shape evolution during fatigue loading is also presented.

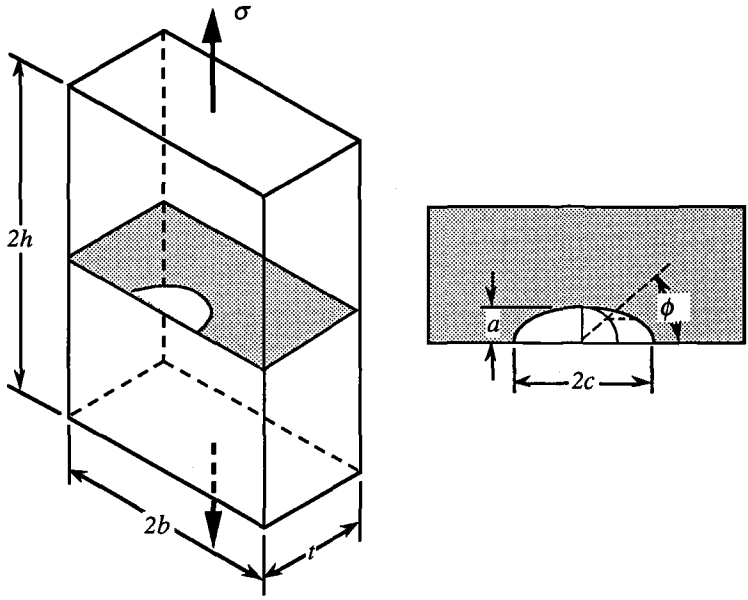


FIG. 1—Surface Crack in a Finite Plate

Local K solution for surface crack—In this work, the Newman-Raju (N-R) solutions for a surface crack in a finite plate subjected to tension and bending are considered benchmark solutions. Newman and Raju [3, 4] used the finite element method to determine correction factors for surface cracks. Their solution for a flat plate loaded in tension (σ_T) and bending (σ_B) is in the form:

$$K = f_W \left(F_T \sigma_T + F_B \sigma_B\right) \sqrt{\frac{\pi a}{Q}}, \tag{1}$$

with the tension correction factor, F_T, and the bending correction factor, F_B, both being functions of a/c, a/t, and ϕ, the angle along the crack front shown in Fig. 1. Newman and

Raju developed a finite width correction factor, f_W, given by:

$$f_w = \sqrt{\sec\left(\frac{\pi c}{2b}\sqrt{\frac{a}{t}}\right)}. \tag{2}$$

Q is the square of the complete elliptical integral of the second kind approximated by the expression:

$$Q = \begin{cases} 1+1.464(a/c)^{1.65} & a/c \le 1 \\ 1+1.464(c/a)^{1.65} & a/c > 1 \end{cases}. \tag{3}$$

The results were developed for $a/t < 1$ and $a/c \le 2$, and $c/b < 0.5$. Newman [5] evaluated a large number of K solutions and found that the N-R solution [3, 4] gave best correlation with experimental results. In 1981, Scott and Thorpe [6] critically reviewed K solutions for the surface crack and also concluded that the N-R solution [3, 4] was the most accurate solution available.

Newman and Raju [7] developed empirical equations based on their finite element results. These empirical equations give answers within 3% of the N-R finite element results [3, 4]. The limits of applicability of the empirical N-R equations are $a/c \le 2$, $c/b < 0.5$, and

$$\frac{a}{t} < \begin{cases} 1.25\left(\frac{a}{c}+0.6\right) & 0 < \frac{a}{c} < 0.2 \\ 1 & \frac{a}{c} \ge 0.2 \end{cases}. \tag{4}$$

Average K solution for surface crack—The N-R K solutions [3, 4, 7] are local values of K along the crack front, typically evaluated at the surface ($\phi = 0$) and at the depth ($\phi = \pi/2$) of the crack. Cruse and Besuner [8] defined average values of K, denoted by $\overline{K}$, and determined by considering crack front extension in one degree of freedom:

$$\overline{K}_i = \left(\frac{1}{\delta A_i}\iint_{\delta A_i} K^2(s)\,dA_i\right)^{1/2}, \tag{5}$$

where δA_i is the change in crack area due to crack front extension in the degree of freedom i, $K(s)$ is the local K at any point along the crack front s, and dA_i is the increase in local crack area at a point on s. As the number of degrees of freedom increases, δA_i decreases and $\overline{K} \rightarrow K$. If two degrees of freedom (x and y) are used, then the average stress intensity factor values for the two degrees of freedom $\overline{K}_x$ and $\overline{K}_y$ should lie between the local stress intensity factor values K ($\phi = 0$) and K ($\phi = \pi/2$). Besuner [9] outlined a procedure to determine $\overline{K}$ using the weight function method.

If a weight function is to be verified and validated, then the average values of the N-R correction factors should be used as benchmark solutions. Oore [10] used Eq 5 and

determined the average values of K in the x and y degrees of freedom to be:

$$\overline{K}_y = \left[\frac{4}{\pi}\int_0^{\pi/2} K^2(\phi)\sin^2(\phi)\ d\phi\right]^{1/2}, \tag{6}$$

and

$$\overline{K}_x = \left[\frac{4}{\pi}\int_0^{\pi/2} K^2(\phi)\cos^2(\phi)\ d\phi\right]^{1/2}. \tag{7}$$

Eqs 6 and 7 were evaluated using the N-R finite element results and Simpson's 1/3 quadrature rule [1]. In general, the local and average values of stress intensity factor will not be equal.

Fatigue crack growth models—The stress intensity factor solution must be coupled with a model describing fatigue crack growth in terms of ΔK. For a fixed load ratio, R, and a wide range of ΔK values, FCG rates can be represented as a straight line on the log-log plot using the Paris equation:

$$\frac{da}{dN} = C(\Delta K)^n, \tag{8}$$

with empirical constants C and n (n is the slope of the fatigue crack growth rate curve) that are determined experimentally for a given material, loading, and environment. For most metallic alloys, the value of n ranges from 2 to 4.

The Modified Forman equation [11] is capable of describing fatigue crack growth rates for a large range of ΔK values:

$$\frac{da}{dN} = \frac{C(1-R)^m(\Delta K)^n(\Delta K - \Delta K_{th})^p}{[(1-R)K_c - \Delta K]^q}, \tag{9}$$

where C, n, p, q are fitting constants. The value of m is determined for each R in the load spectrum using the crack opening stress algorithm of Newman [12]. The critical stress intensity factor, K_C, is used as the crack instability condition:

$$\frac{K_c}{K_{Ic}} = 1 + B_k \exp\left[-\left(\frac{A_k t}{t_0}\right)^2\right], \tag{10}$$

where t_0 is the nominal plane strain thickness:

$$t_0 = 2.5\left(\frac{K_{Ic}}{\sigma_{ys}}\right)^2, \tag{11}$$

and A_k and B_k are fitting constants. For part-through cracks, the part-through fracture

toughness K_{Ie} is used in place of K_C. The threshold stress intensity factor, ΔK_{th}, is modeled by:

$$\Delta K_{th} = (1 - C_0 R)^d \Delta K_0, \tag{12}$$

where ΔK_0 is the threshold stress intensity factor for $R = 0$, and C_0 and d are fitting constants. Forman, et al. [11] has developed a database containing all the Modified Forman fitting constants and necessary material properties for a variety of metals used in the aerospace industry. Both the Paris equation and the Modified Forman equation are used as benchmark models in the examples presented in this paper.

Cycles to failure—The number of cycles to failure predicted by a coupled K and da/dN-ΔK system can be compared to experimental results. This type of V&V was performed by Forman and Mettu [13, 14] for the N-R empirical equations and the Modified Forman equation using the NASA/FLAGRO software. In this paper, past ASTM round-robin results [15-17] for the life of flat plates with surface crack are taken as benchmark results. Results from seven specimens in the second analytical exercise are given in Table 1. All seven specimens had the same crack geometry and loading.

As a further validation of NASA/FLAGRO, the benchmark surface crack problem of the ASTM round-robin was analyzed using the previously validated coupled K and da/dN-ΔK system. The predicted number of cycles to crack breakthrough was 19,100 and the predicted number of cycles to failure was 19,300. The prediction ratio (ratio of predicted life to actual life) was calculated to be 0.92 for both crack breakthrough and failure. These predictions compare very favorably to the benchmark experimental results, yielding a slightly conservative result.

TABLE 1—Cycles to Failure for Second Analytical Exercise [15].

Specimen No.	Test Result	
	breakthrough	failure
23-18	23,000	24,600
37-3	...	20,100
32-2	...	19,900
23-12	22,400	23,000
23-13	19,800	20,000
23-14	20,000	20,400
23-10	18,800	19,400
average value	20,800	21,057

Crack shape evolution—The aspect ratio a/c of a surface crack can change dramatically during loading. Many researchers have used marker bands to map the evolution of the crack front by alternately fatigue cycling and marking using low stress cycling. Corn [18] coined the term "preferred propagation path," abbreviated as PPP, to describe the equilibrium shape that the surface crack tries to grow toward. If the aspect ratio of the crack is not on the PPP, the crack shape will evolve with fatigue cycling in an attempt to join the PPP during later life. For tension, aspect ratios tend to approach unity (semicircular shape). For bending, aspect ratios tend to approach zero (highly elliptical

shape). The approximate PPPs for tension and bending are given in ASTM E740 Fracture Testing with Surface-Crack Tension Specimens:

$$\frac{a}{c} = \begin{cases} 1 - 0.2\left(\frac{a}{t}\right)^2 & \text{tension} \\ 1 - \frac{a}{t} & \text{bending} \end{cases}, \tag{13}$$

for $a/t \le 0.7$. Fig. 2 shows the approximate PPPs and experimental results compiled by Mahmoud [19, 20]. Cracks that start on the PPPs tend to remain on the PPPs. Other cracks tend to evolve to the PPPs as the fatigue life continues.

To develop the evolution of crack shape and a PPP, a K solution must combined with a da/dN-ΔK equation. If the Newman-Raju [7] K empirical solution for tensile loading is combined with the Paris equation, then the change in crack depth Δa is related to the change in crack length Δc by:

$$\frac{\Delta a}{\Delta c} = \left\{ \sqrt{\frac{a}{c}} \left[1.1 + 0.35\left(\frac{a}{t}\right)^2 \right] \right\}^{-n}, \tag{14}$$

for $a/c \le 1$. Similar equations can be written for the bending case.

Implicit in the discussion above is the assumption that the Paris equation constants C and n are the same in the depth direction as in the surface direction. To account for differences in fatigue crack growth rate in the depth and surface directions, Newman and Raju [4] applied a simple crack closure correction that correlated with experimental data:

$$\Delta K(\phi = 0)\big|_{\text{corrected}} = 0.9\ \Delta K(\phi = 0). \tag{15}$$

The correction modifies the equation for crack shape evolution:

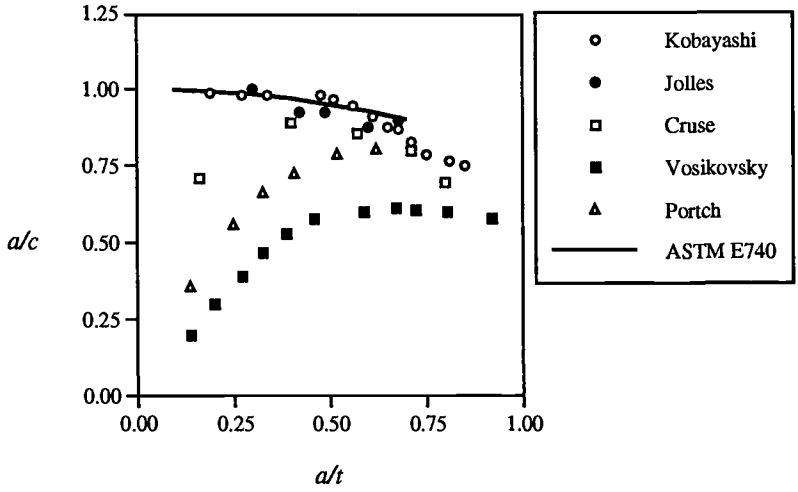
$$\frac{\Delta a}{\Delta c} = \left\{ 0.9\sqrt{\frac{a}{c}} \left[1.1 + 0.35\left(\frac{a}{t}\right)^2 \right] \right\}^{-n}. \tag{16}$$

Forman and Mettu developed a crack closure factor for $\phi = 0$, β_R:

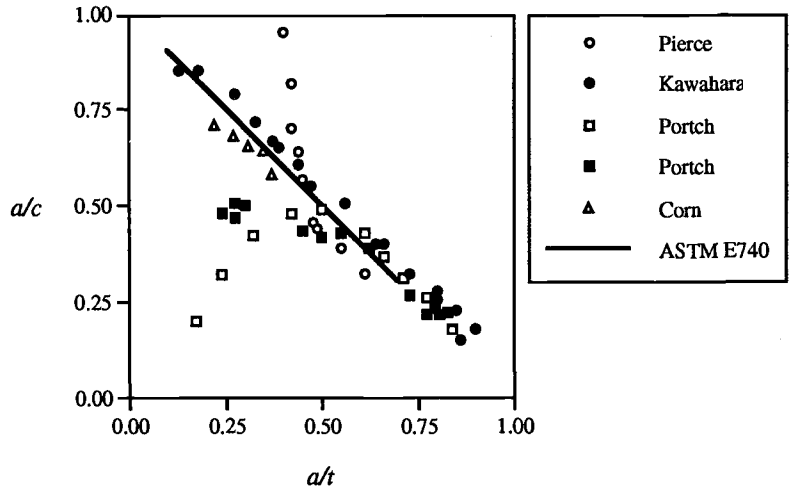
$$\beta_R = \begin{cases} 0.9 + 0.2R^2 - 0.1R^4 & R > 0 \\ 0.9 & R \le 0 \end{cases}. \tag{17}$$

in place of a constant $\beta = 0.9$ used by Newman and Raju. Thus, Eq 17 is a generalization of crack closure factor in Eq 15. A generalization of Eq 16 is given by:

$$\frac{\Delta a}{\Delta c} = \left\{ \beta_R \sqrt{\frac{a}{c}} \left[1.1 + 0.35\left(\frac{a}{t}\right)^2 \right] \right\}^{-n}. \tag{18}$$



(a)



(b)

FIG. 2—Crack Shape Evolution (a) Tension, (b) Bending [19, 20]

If average K values are used in place of local K values, then equation for crack shape evolution using the Paris equation becomes:

$$\frac{\Delta a}{\Delta c} = \left(\frac{\Delta \overline{K}_y}{\Delta \overline{K}_x} \right)^n . \tag{19}$$

Average K values can also be combined with the Modified Forman equation to produce a result analogous to Eq 19.

Müller, et al. [21] used the N-R equations to predict the crack shape evolution for tension and bending with Paris equation exponents of $n = 2$ and $n = 4$. Local K values underpredicted the change in crack aspect ratio a/c. Using average K or using local K with Eq 15 improved the prediction of a/c. Mahmoud [19, 20] statistically examined surface crack growth data in the literature. For tension, Mahmoud found that the N-R equations using local K and closure correction (Eq 16) best fit the experimental results. However, the average K (Eq 19) was almost as good. For bending, Mahmoud found that the local K fit the experimental results much better than the average K. Mahmoud also studied the growth patterns of surface cracks in plates subjected to combined tension and bending. Again, he found the N-R solutions to accurately predict the crack shape evolution. Carter, et al. [22] also concluded that the N-R solutions accurately predicted the crack shape evolution.

Crack shape evolution and predicted PPP can be used to verify and validate the coupled K and da/dN-ΔK system. The N-R solution with crack closure corrections (Eq 15) was again chosen as the benchmark solution. The crack shape evolution and the PPP of a new solution would be compared to the N-R solution coupled with a suitable value of n for the Paris equation or alternatively, the Modified Forman equation.

VERIFICATION AND VALIDATION EXAMPLES

Two V&V examples are presented from the NASCRAC computer program. This computer program employs libraries of K solutions and FCG algorithms to perform life predictions. The NASCRAC computer program is based on the BIGIF computer program developed by Besuner, et al. [23] for the nuclear power industry. The original program has been significantly modified by Harris, et al. [24, 25]. NASCRAC relies heavily on weight functions to calculate K. The NASCRAC version discussed in this paper is Version 2.0, July 1989. Unfortunately, the NASCRAC source code was unavailable to the author.[2] Instead of discussing computer code assessment of NASCRAC as a third V&V example, the author has chosen to discuss computer code assessment of a similar computer program, NASA/FLAGRO. In fact, several NASA/FLAGRO solutions and algorithms were incorporated into NASCRAC. NASA/FLAGRO is based on the EFFGRO program developed by Szamossi [26]. The original program has been significantly modified by Forman, et al. [11, 27, 28]. The NASA/FLAGRO version discussed in this paper is Version 1.3, March 1989.

Modified Forman Equation (NASCRAC)

The Modified Forman equation was included in NASCRAC; however, the algorithm built around the Modified Forman equation was incorrectly coded in NASCRAC, causing two errors to occur. The first error was the omission of Eq 10 relating critical stress

[2] The unavailability of source code is a handicap that the V&V process cannot overcome!

intensity factor, K_C, to thickness and plane strain fracture toughness. Instead of Eq 10, NASCRAC includes a constant value of K_C for each material in the database. The second error was the omission of the algorithm for determining the fitting parameter m in the Modified Forman equation. This parameter should be calculated for each loading block because it is a function of load ratio R. Instead, NASCRAC sets $m = 0$ for all materials in the database. These two errors can greatly affect the accuracy of fatigue life predictions.

If the constant value of K_C included in the NASCRAC database is used for determining fatigue crack growth rates using the Modified Forman equation, then the resulting life predictions may be conservative or unconservative. For example, let $q = 0.5$ and $R = 0$ in the Modified Forman equation. The ratio of *da/dN* as coded to the actual *da/dN* is plotted as a function of normalized stress intensity factor range in Fig. 3. An error in *da/dN* occurs when the K_C value included in the NASCRAC database is different than the K_C value obtained from Eq 10. Two observations can be made from Fig. 3. First, if the value of K_C in the NASCRAC database is within 20% of the actual value of K_C predicted by Eq 10, then the *da/dN* values in NASCRAC will have a factor of 2 difference from the actual *da/dN* values. Second, the difference is not constant—the difference increases with increasing ΔK.

If the constant value $m = 0$ included in the NASCRAC database is used for determining fatigue crack growth rates using the Modified Forman equation, then the resulting life predictions may be conservative or unconservative. For example, fatigue crack growth rate fitting constants for a precipitation-hardened steel PH13-8Mo were determined [29] using NASA/FLAGRO. The calculated values of m were found to vary from -1.53 for $R = -1$ to 0.35 for $R = 0.9$. The ratio of *da/dN* as coded to the actual *da/dN* is plotted as a function of m in Fig. 4. For $0 < R < 0.75$, the fatigue crack growth rates as coded in NASCRAC will underestimate by as much as 40% the actual value of *da/dN* from the Modified Forman equation (an unconservative error). For $R < 0$ and $R > 0.75$, the fatigue crack growth rates in NASCRAC will overestimate by as much as 300% the actual value of *da/dN* from the Modified Forman equation (a conservative error). If the K_C error is also present, then the predicted cycles to failure will be more or less conservative, depending on the whether the K_C in the NASCRAC database is larger or smaller than the actual K_C. These problems with the NASCRAC implementation of the Modified Forman equation are good examples of the errors that can occur when algorithms are borrowed from other sources and used without complete understanding.

Case Study Results: V&V of Surface Cracks (NASCRAC)

NASCRAC uses a weight function solution by Dedhia and Harris [30]. Although the weight function is based on boundary integral element analysis of a circumferential crack in a cylinder, it is used for a surface crack in a finite thickness plate. The weight function solution does not account for finite width. The limits of applicability of the weight function solution are $a/c < 1$ and $a/t < 1$.

The N-R tension correction factors, the averaged N-R correction factors, and the correction factors of the weight function from NASCRAC are plotted in Fig. 5 for $a/c = 0.2$ and 1. As expected, the averaged N-R correction factors fall between the correction factors for $\phi = 0$ and $\pi/2$. At $a/c = 0.2$, the NASCRAC correction factors are consistently between the N-R solutions for $\phi = 0$ and $\pi/2$, except for $a/t = 0.8$. The NASCRAC solution at $\phi = \pi/2$ is close to the averaged N-R solution. For $\phi = 0$, the NASCRAC solution is 5-10% higher than the averaged N-R solutions. At $a/c = 1$, the NASCRAC solution falls inside the

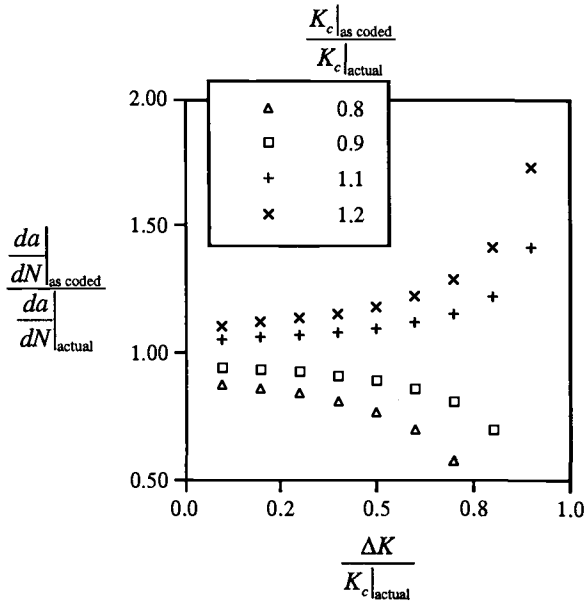


FIG. 3—Example NASCRAC K_c Error in Modified Forman Equation.

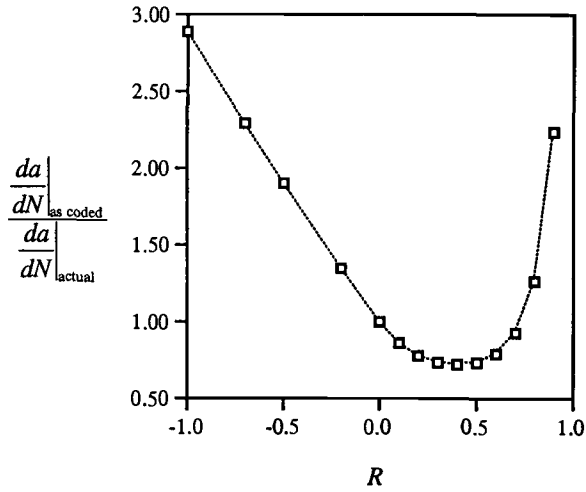


FIG. 4—Example NASCRAC m Error in Modified Forman Equation.

range between the N-R solutions for $\phi = 0$ and $\pi/2$ except for small a/t. The trends in the NASCRAC solution vary greatly from the averaged N-R solution. The NASCRAC solutions for $\phi = 0$ and $\pi/2$ actually cross at $a/t = 0.55$. These trends indicate that the NASCRAC solution is questionable for tensile loading.

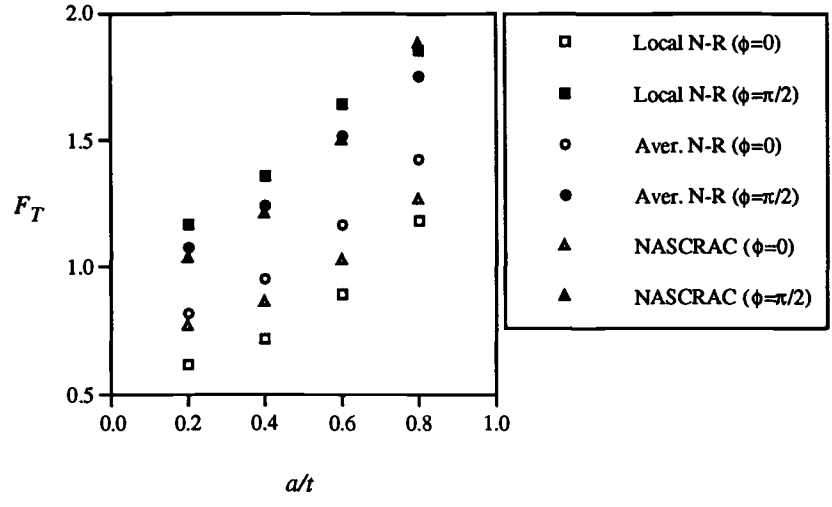
The N-R bending correction factors, the averaged N-R correction factors, and the correction factors of the weight function from NASCRAC are plotted in Fig. 6. For this case, the averaged N-R correction factors vary greatly from the N-R correction factors for $\phi = 0$ and $\phi = \pi/2$. The NASCRAC correction factors have a trend similar to the averaged N-R factors. However, the magnitude of the NASCRAC correction factors and the averaged N-R factors are different, especially at $\phi = 0$. In addition, the NASCRAC solutions falls out of the bounds of the N-R solution for $0.4 < a/t < 0.6$. For $a/c = 1$, the NASCRAC correction factors agree closely to the averaged N-R factors.

NASCRAC was used to predict the life of a flat plates with surface cracks. The previously described errors in the NASCRAC implementation of the Modified Forman equation were uncorrected. Predictions are compared with the ASTM round-robin results in Table 1. NASCRAC predicted failure before crack breakthrough. The NASCRAC prediction ratio for failure was 0.79. The errors in implementing the Modified Forman equation were the cause of the low prediction ratio for NASCRAC. The m error had no effect on the prediction ratio because the load ratio used in the round-robin was close to zero ($R = 0.05$). The K_C error caused NASCRAC to overpredict FCG rates by a factor varying from 1.25 to 2 because K_C in the NASCRAC database was 25% lower than the actual K_C. An additional source for the low prediction ratio is the fact that NASCRAC uses K_{Ic} as the crack instability condition, while the Modified Forman equation uses K_{Ie} for surface cracks. For the round-robin material, K_{Ie} was 50% greater than K_{Ic}. Finally, the initial aspect ratio a/c for the specimens was unity. The weight function correction factors at this value of a/c were identified as questionable because of the crossing trend in Fig. 5.

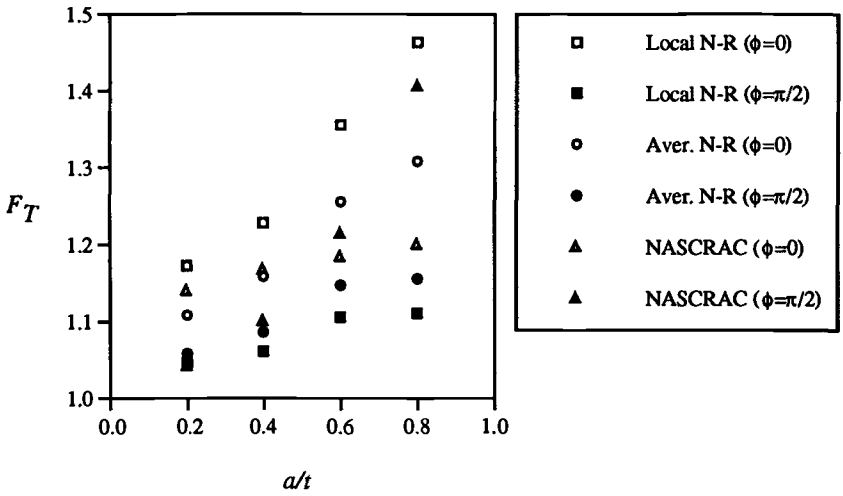
Crack shape evolution and preferred propagation patterns (PPP) for tension and bending of a surface crack in a wide plate with Paris exponent $n = 4$ are shown in Figs. 7 and 8. The Paris equation was used instead of the Modified Forman equation to avoid the effects of previously described errors on the crack shape evolution and PPPs. In Fig. 7, the NASCRAC crack shape evolutions for tension are very inconsistent with N-R crack shape evolutions. For initial $a/c = 1$ and $a/t = 0.1$, a combination starting very close to the PPP, NASCRAC predicts that a/c drops suddenly and then rises back to $a/c = 1$ for $a/t = 0.8$. The NASCRAC crack shape evolutions for tension do not converge to a PPP. In Fig. 8, the NASCRAC crack shape evolutions for bending have a trend that is consistent with the N-R crack shape evolutions. However, the NASCRAC curves overpredict a/c for $a/t > 0.3$.

Coding and Portability Issues (NASA/FLAGRO)

Although NASA/FLAGRO was developed on VAX/VMS computer systems, many users will be running the programs on other computer systems, such as engineering workstations using UNIX. The VAX FORTRAN-77 compiler includes many nonstandard features not supported by other computer systems. Fortunately, many UNIX FORTRAN-77 compilers now include VAX extensions [31]. This inclusion can make porting codes from VAX/VMS to other computer systems easier. Unfortunately, the UNIX FORTRAN-77 compiler follows the ANSI standard more strictly than the VAX FORTRAN compiler. In other words, UNIX FORTRAN is not as forgiving as VAX FORTRAN. Four significant problems were cited when porting NASA/FLAGRO to a UNIX workstation.

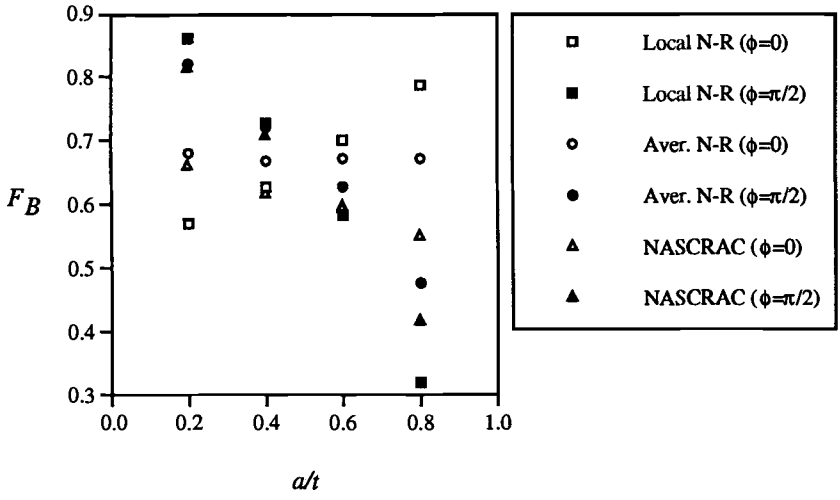


(a)

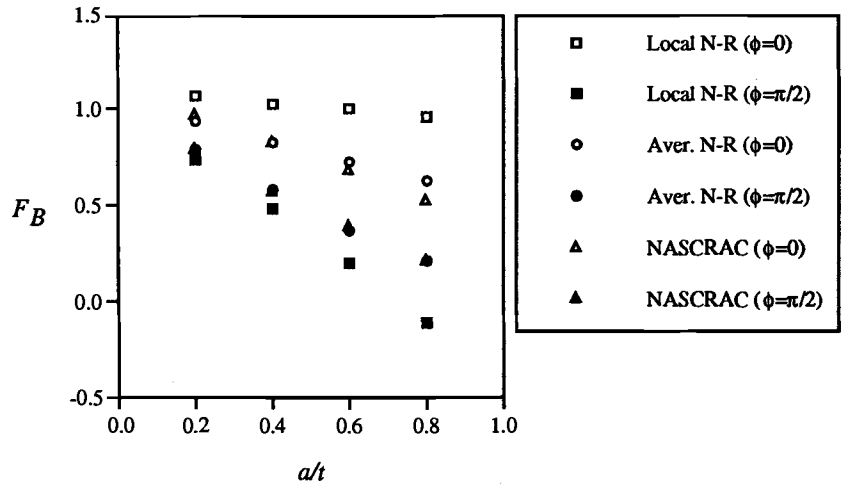


(b)

FIG. 5—Tension Correction Factors for (a) a/c =0.2, (b) a/c = 1.



(a)



(b)

FIG. 6—Bending Correction Factors for (a) a/c = 0.2, (b) a/c = 1.

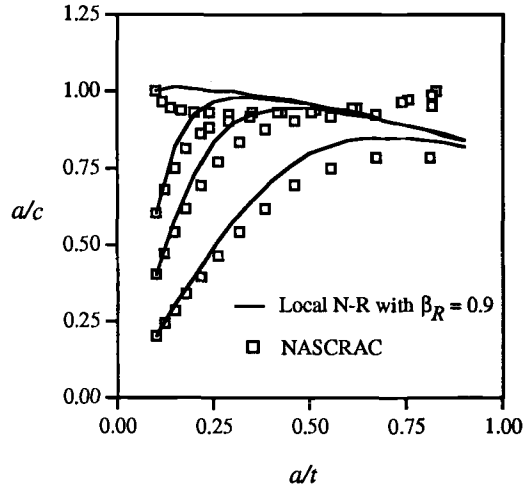


FIG. 7—Tension Crack Shape Evolution for Paris Exponent $n = 4$.

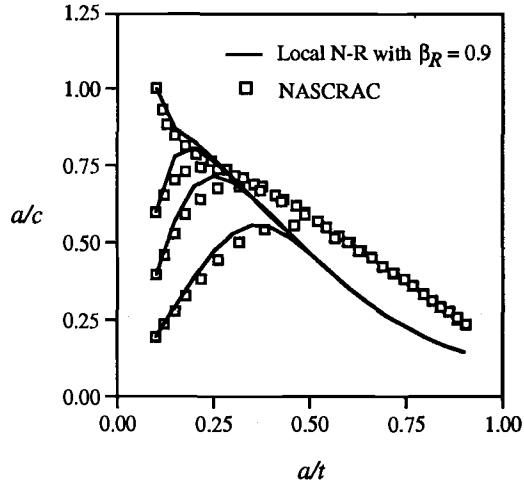


FIG. 8—Bending Crack Shape Evolution for Paris Exponent $n = 4$.

The first significant problem is that NASA/FLAGRO transfers internal data using common blocks containing inconsistent data types and inconsistent lengths. Misaligned common blocks can cause serious performance degradation. This problem can be avoided by using the nonstandard FORTRAN statement "INCLUDE." This statement allows common block declarations to be placed in separate files from the rest of the program. These separate files can be included during compilation, allowing the programmer to repeatedly use the consistent data types and lengths.

The second significant problem is the inconsistency between formal and actual parameters of subroutines. If the inconsistency produces a type mismatch, then erroneous results may occur. Undefined variables can cause a program to behave differently when different compilation (optimization) options are chosen.

The third significant problem is the use of undefined variables in NASA/FLAGRO. The second and third problems can best be avoided by using the nonstandard FORTRAN statement "IMPLICIT UNDEFINED." This statement forces the programmer to declare all variables.

The fourth problem is the heavy use of "GO TO" statements. There are over 900 occurrences of "GO TO" in the 20,000 lines of code. Many of these statements can be avoided using structured "IF/THEN/ELSE/ENDIF" blocks.

CONCLUSIONS

NASCRAC Version 2.0 contains a poorly adapted version of the Modified Forman equation that should not be used. In addition, the NASCRAC solution for a surface crack in a finite plate does not consistently agree with the benchmark solution. NASCRAC predictions for benchmark tests on surface cracks yielded a conservative life prediction ratio of 0.79 for failure before breakthrough. The NASCRAC prediction for crack shape evolution for tension-tension fatigue loading did not converge to a preferred propagation path. The NASCRAC prediction for crack shape evolution for bending fatigue loading did converge to a preferred propagation path, but the path overpredicted *a/c*. The baseline predictions developed with the NASCRAC were better for bending than for tension loading. Overall, it is concluded that the NASCRAC solution for a surface crack in a plate is unreliable. NASA/FLAGRO Version 1.3 contains computer coding which affect its portability to other computer systems. Suggestions to correct these problems were given. Several of the suggestions use nonstandard FORTRAN-77 statements that are included in the newest standard, Fortran 90 [32].

RECOMMENDATIONS

A general recommendation is to develop a comprehensive V&V guideline for life prediction software. This guideline should be developed by a cooperative effort between government, industry, and academia. This guideline would be useful for both software developers and users. A more specific recommendation is to better quantify crack shape evolution of surface cracks experimentally. These tests should record the crack shape evolution of a surface crack in a finite width plate subjected to tension and bending fatigue loading as well as the number of cycles required. The tests should include several different initial values of *a/c*, *a/t*, and *c/b* and should be conducted for at least two different materials and several load ratios *R*.

REFERENCES

[1] Hornbeck, R. W., Numerical Methods, Prentice-Hall, Englewood Cliffs, New Jersey, 1975.

[2] AT&T, Testing to Verify Design and Manufacturing Readiness, McGraw Hill, New York, 1993.

[3] Raju, I. S., and Newman, J. C., Jr., "Stress-Intensity Factors for a Wide Range of Semi-elliptical Surface Cracks in Finite-Thickness Plates," Engineering Fracture Mechanics, Vol. 11, 1979, pp. 817-829.

[4] Newman, J. C., Jr., and Raju, I. S., "Analysis of Surface Cracks in Finite Plates Under Tension or Bending Loads," NASA TP-1578, 1979.

[5] Newman, J. C., Jr., "A Review and Assessment of the Stress-Intensity Factors for Surface Cracks," Part-Through Crack Fatigue Life Prediction, ASTM STP 687, J. B. Chang, Ed., American Society for Testing and Materials, 1979, pp. 16-42.

[6] Scott, P. M., and Thorpe, T. W., "A Critical Review of Crack Tip Stress Intensity Factors for Semi-elliptic Cracks," Fatigue of Engineering Materials and Structures, Vol. 4, No. 4, 1981, pp. 291-309.

[7] Newman, J. C., Jr., and Raju, I. S., "An Empirical Stress-Intensity Factor Equation for the Surface Crack," Engineering Fracture Mechanics, Vol. 15, No. 1-2, 1981, pp. 185-192.

[8] Cruse, T. A., and Besuner, P. M., "Residual Life Prediction for Surface Cracks in Complex Structural Details," Journal of Aircraft, Vol. 12, No. 4, 1975, pp. 369-375.

[9] Besuner, P. M., "Residual Life Estimates for Structures with Partial Thickness Cracks," Mechanics of Crack Growth, ASTM STP 590, American Society for Testing and Materials, 1976, pp. 403-419.

[10] Oore, M., "Assessment of Influence Function for Elliptical Cracks Subjected to Uniform Tension and to Pure Bending," Fracture Mechanics: Twenty-First Symposium, ASTM STP 1074, J. P. Gudas, J. A. Joyce, and E. M. Hackett, Eds., American Society for Testing and Materials, 1990, pp. 490-508.

[11] Forman, R. G., Shivakumar, S., Newman, J. C., Jr., Piotrowski, S. M., and Williams, L. C., "Development of the NASA/FLAGRO Computer Program," Fracture Mechanics: 18th Volume, ASTM STP 945, D. T. Read and R. P. Reed, Eds., American Society for Testing and Materials, 1988, pp. 781-803.

[12] Newman, J. C., Jr., "A Crack Opening Stress Equation for Fatigue Crack Growth," International Journal of Fracture, Vol. 24, 1984, pp. R131-R135.

[13] Forman, R. G., and Mettu, S. R., "Behavior of Surface and Corner Cracks Subjected to Tensile and Bending Loads in Ti-6Al-4V Alloy," NASA TM-102165, Sept. 1990.

[14] Forman, R. G., and Mettu, S. R., "Fatigue Crack Growth Measurements for Surface and Corner Cracks in a Ti-6Al-4V Alloy," JSC-25010, Johnson Space Center, March 1991.

[15] Vroman, G. A., "Life Prediction Analysis of Part-Through Cracks," Part-Through Crack Fatigue Life Prediction, ASTM STP 687, J. B. Chang, Ed., American Society for Testing and Materials, 1979, pp. 89-95.

[16] Peterson, D. E., and Vroman, G. A., "Computer-Aided Fracture Mechanics Life Prediction Analysis," Part-Through Crack Fatigue Life Prediction, ASTM STP 687 , J. B. Chang, Ed., American Society for Testing and Materials, 1979, pp. 129-142.

[17] Chang, J. B., "ASTM Fatigue Life Round-Robin Predictions," Damage Tolerance of Metallic Structures: Analysis Methods and Applications, ASTM STP 842, J. B. Chang and J. L. Rudd, Eds., American Society for Testing and Materials, 1984, pp. 50-68.

[18] Corn, D. L., "A Study of Crack Techniques for Obtaining Partial Thickness Cracks of Pre-selected Depths and Shapes," Engineering Fracture Mechanics, Vol. 3, 1971, pp. 45-52.

[19] Mahmoud, M. A., "Quantitative Prediction of Growth Patterns of Surface Fatigue Cracks in Tension Plates," Engineering Fracture Mechanics, Vol. 30, No. 6, 1988, pp. 735-746.

[20] Mahmoud, M. A., "Growth Patterns of Surface Fatigue Cracks Under Cyclic Bending—A Quantitative Analysis," Engineering Fracture Mechanics, Vol. 31, No. 2, 1988, pp. 357-369.

[21] Müller, H. M., Müller, S., Munz, D., and Neumann, J., "Extension of Surface Cracks During Cyclic Loading," Fracture Mechanics: 17th Volume, ASTM STP 905, J. H. Underwood, R. Chait, C. W. Smith, D. B. Wilhem, W. A. Andrews, and J. C. Newman, Jr., Eds., American Society for Testing and Materials, 1986, pp. 625-643.

[22] Carter, D. K., Canda, W. R., and Blind, J. A., "Experimental Evaluation of Stress-Intensity Solutions for Surface Flaw Growth in Plates," Surface-Crack Growth: Models, Experiments, and Structures, ASTM STP 1060, W. G. Reuter, J. H. Underwood, and J. C. Newman, Jr., Eds., American Society for Testing and Materials, 1990, pp. 215-236.

[23] Besuner, P. M., Davis, C. S., Rogers, G. W., Grover, J. L., and Peters, D. C., "BIGIF - Fracture Mechanics Code for Structures," EPRI NP-1830-CCM, Palo Alto, California, 1981.

[24] Harris, D. O., Eason, E. D., Thomas, J. M., Bianca, C. J., and Salter, L. D., "NASCRAC—A Computer Code for Fracture Mechanics Analysis of Crack Growth." AIAA-87-0847-CP, AIAA/ASME/ASCE/AHS 28th Structures, Structural Dynamics and Materials Conference, Monterey, California, April 6-8, 1987, pp. 662-667.

[25] Failure Analysis Associates, NASCRAC—NASA Crack Analysis Code, Version 2.0, User's Manual, Palo Alto, California, 1989.

[26] Szamossi, M., "Crack Propagation Analysis by Vroman's Model, Computer Analysis Summary, Program EFFGRO," NA-72-74, Rockwell International, Los Angeles, 1972.

[27] Forman, R. G., and Hu, Tianlai, "Application of Fracture Mechanics on the Space Shuttle," Damage Tolerance of Metallic Structures: Analysis Methods and Applications, ASTM STP 842, J. B. Chang and J. L. Rudd, Eds., American Society for Testing and Materials, 1984, pp. 108-133.

[28] Johnson Space Center, "NASA/FLAGRO—Fatigue Crack Growth Program," JSC-22267, Version 1.3, March 1989.

[29] Favenesi, J., Lambert, J., Ingraffea, A. R., Stallworth, R., and Wilson, C., "NASCRAC Fracture Mechanics Computer Code Verification," 1992 Conference on Advanced Earth-to-Orbit Propulsion Technology, Marshall Space Flight Center, May 19-21, 1992.

[30] Dedhia, D. D., and Harris, D. O., "Improved Influence Functions for Part-Circumferential Cracks in Pipes," Circumferential Cracks in Pressure Vessels and Piping, Vol. II, ASME-PVP 95, New York, 1984, pp. 35-48.

[31] Loukides, M., UNIX for FORTRAN Programmers, O'Reilly and Associates, Sebastopol, California, 1990.

[32] Kerrigan, J. F., Migrating to Fortran 90, O'Reilly and Associates, Sebastopol, California, 1993.

J. C. Newman, Jr.[1], J. D. Bland[2] and R. F. Berry, Jr.[1]

FRACTURE TOUGHNESS AND CRITICAL CRACK SIZES FOR THE SPACE SHUTTLE SOLID ROCKET MOTOR D6AC STEEL CASE

REFERENCE: Newman, J. C., Jr., Bland, J. D., and Berry, R. F., Jr., **"Fracture Toughness and Critical Crack Sizes for the Space Shuttle Solid Rocket Motor D6AC Steel Case,"** Fractures Mechanics: 26th Volume, ASTM STP 1256, Walter G. Reuter, John H. Underwood, and James C. Newman, Jr., Eds., American Society for Testing and Materials, Philadelphia, 1995.

ABSTRACT: Fracture toughness and critical crack size tests were conducted on a variety of fracture specimens that were machined from actual Space Shuttle solid rocket motor (SRM) D6AC steel cylindrical case segments. Plane-strain fracture toughness tests were conducted at four temperatures ranging from -30 °C to 55 °C. Average values ranged from a low of 87.6 MPa-$m^{1/2}$ at -30 °C to a high of 120.3 MPa-$m^{1/2}$ at room temperature. Fracture tests were also conducted on seven different crack configurations that simulate details in the SRM field and factory joint locations. These configurations included: surface and through cracks, corner and through cracks at an open hole, and through and corner cracks at a pin-loaded hole. Elastic stress-intensity factors at failure, K_{Ie}, were found to be constant within ± 10 % for the range of crack and specimen sizes tested. The fatigue pre-cracking stress levels were found to have a strong influence on K_{Ie}. An effective elastic fracture toughness, accounting for crack-closure effects, was found to be nearly constant for a wide range of fatigue pre-cracking stress-intensity factor levels.

Fatigue tests were also conducted on simulated SRM case-segment joint leak-check port specimens to determine crack initiation locations, fatigue-crack growth and critical crack sizes. Eddy-current probes, identical to those used in actual hardware, were used to monitor crack growth. Specimens were cycled at either proof-test load or flight-load levels at various temperatures until failure. Critical crack sizes obtained were greater than 25 mm in length and required more than 2,700 cycles to grow from a damage-tolerant crack size (1 mm) to failure.

KEYWORDS: Fracture, cracks, D6AC steel, fatigue, fracture toughness

[1]Senior Scientists, NASA Langley Research Center, Hampton, VA 23681-0001.
[2]Senior Engineer, NASA Marshall Space Flight Center, Huntsville, AL 35812.

Copyright© 1995 by ASTM International www.astm.org

NOMENCLATURE

a	Surface- and corner-crack depth (see Fig. 3), mm
a_i	Initial surface- and corner-crack depth, mm
B	Specimen thickness, mm
C_i	Constants in crack-growth-resistance curve (see eqn. 2), MPa-$m^{1/2}$
c	Length of crack (see Fig. 2 and 3), mm
c_i	Initial length of crack, mm
D	Hole diameter, mm
e	Edge distance from pin-loaded hole (see Fig. 2), mm
F_n	Boundary correction on stress-intensity factor (see refs. 5 and 7)
K_{Ic}	Plane strain fracture toughness, MPa-$m^{1/2}$
K_{Ie}	Elastic stress-intensity factor at failure, MPa-$m^{1/2}$
K^*_{Ie}	Effective cyclic fracture toughness, MPa-$m^{1/2}$
K_F	Fracture toughness in Two-Parameter Fracture Criterion, MPa-$m^{1/2}$
K_{max}	Maximum fatigue stress-intensity factor, MPa-$m^{1/2}$
K_o	Crack opening stress-intensity factor, MPa-$m^{1/2}$
K_R	Stress-intensity factor for crack-growth resistance, MPa-$m^{1/2}$
m	Crack sensitivity factor in Two-Parameter Fracture Criterion
N_f	Number of cycles to failure
P	Applied load, kN
P_{fail}	Maximum load at failure, kN
P_{max}	Maximum cyclic load applied during fatigue crack growth, kN
P_{min}	Minimum cyclic load applied during fatigue crack growth, kN
P_Q	Five-percent offset load (K_{Ic} test), kN
R	Ratio of minimum to maximum cyclic load
S_n	Net-section stress, MPa
T	Test temperature, °C
W	Specimen width (see Fig. 2), mm
α	Fatigue crack growth constraint factor
α_g	Global constraint factor
σ_o	Flow stress (average between σ_{ys} and σ_u), MPa
σ_{ys}	Yield stress, MPa
σ_u	Ultimate tensile strength, MPa

The NASA Space Transportation System involves the shuttle orbiter, an external tank holding the liquid oxygen and hydrogen vessels, and two solid rocket motors (SRM). Each motor operates for about two minutes and delivers over three million pounds of thrust. Because of processing and transportion limitations, the SRM's are made in eight case segments, see Figure 1, that are partially assembled at the factory and completed at the launch site. Segments are joined together by a pin-tang-clevis joint. Each joint has 177 cylindrical pins. There are 180 pin holes, but three holes have slots in the tang end that are used for alignment during assembly and carry no pin loads in motor operation. The joints are sealed with two O-rings placed between the tang and the inner clevis leg in a bore seal configuration. A leak-check-port hole is placed between the two O-rings to check the final assembly for leakage. See reference *1* for more details about the SRM's.

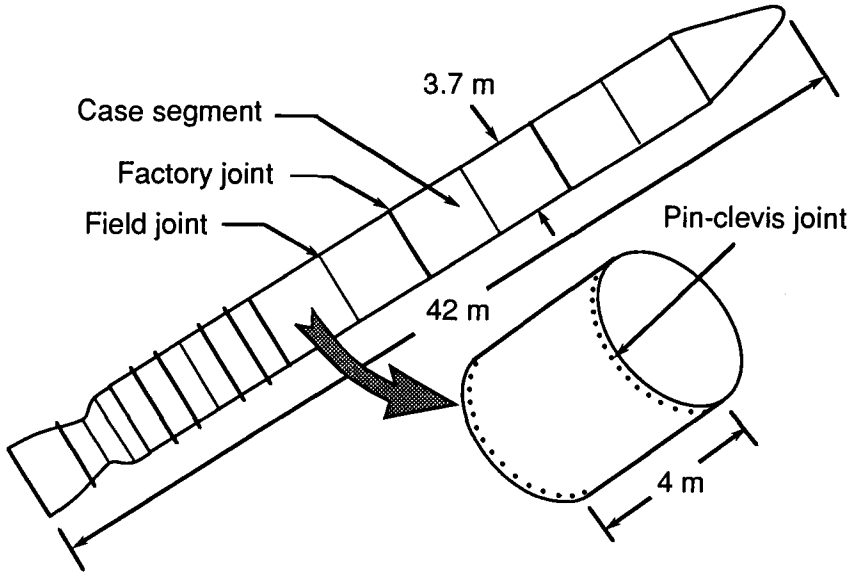


Fig. 1--Space Shuttle Solid Rocket Motor.

The solid rocket motor redesign efforts indicated that a greater understanding of the fatigue and fracture characteristics of the D6AC steel, used to manufacture the cylindrical rocket motor case segments, was needed. To improve the fracture mechanics database for this material, a test program was conducted as a joint program between the NASA Langley Research Center (LaRC) and the Marshall Space Flight Center (MSFC), using a variety of specimens cut from an actual SRM case segment and trim-ring material. Trim-ring material is always cut from the ends of a case segment before heat treatment and trim material will always accompany the case segment during the final heat treatment for fracture toughness testing. The material was provided by the Thiokol Corporation, Brigham City, UT. The details of the NASA program are provided in reference *2*. Parallel to the efforts at NASA, Thiokol Corporation contracted with the

Westinghouse Science and Technology Center, Pittsburgh, PA to conduct J-R curve fracture tests on various thicknesses and temperatures, and fatigue-crack-growth rate tests under cyclic J integral conditions [3].

In the present study, fracture toughness and critical crack size tests were conducted on a variety of fracture specimens. Plane-strain fracture toughness tests were conducted on compact specimens at four temperatures ranging from -30 to 55 °C. Fracture tests were also conducted on seven different crack configurations that simulate details in the SRM field and factory joint locations. The configurations tested and analyzed are shown in Figures 2 and 3. These configurations included: (1) surface and through cracks, (2) corner and through cracks at an open hole, and (3) through and corner cracks at a pin-loaded hole in a plate. The effect of fatigue pre-cracking stress levels on fracture was also studied.

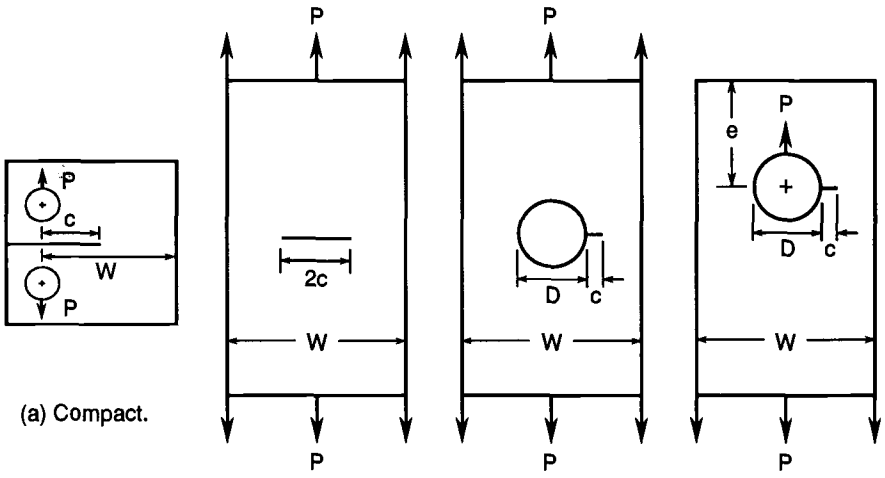


Fig. 2--Fracture specimen configurations tested and analyzed.

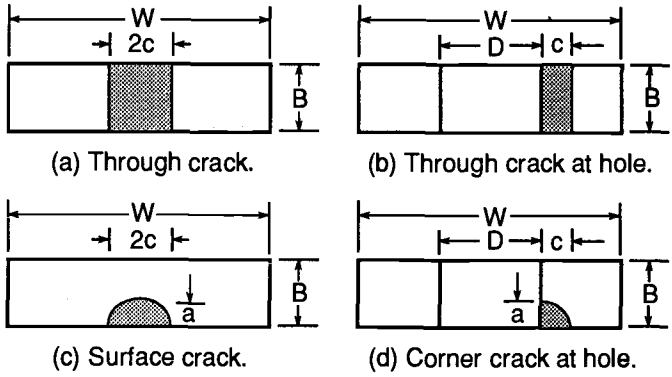


Fig. 3--Crack definitions for fracture specimens.

Fatigue tests were also conducted on simulated SRM case-segment joint leak-check port analog specimens to determine crack initiation locations, fatigue-crack growth and critical crack sizes. The leak-check-port specimen is shown in Figure 4. Eddy-current probes, identical to those used in actual hardware, were used to monitor crack growth. Specimens were cycled at either proof-test load or flight-load levels at various temperatures until failure. Critical crack sizes and cyclic lives were determined.

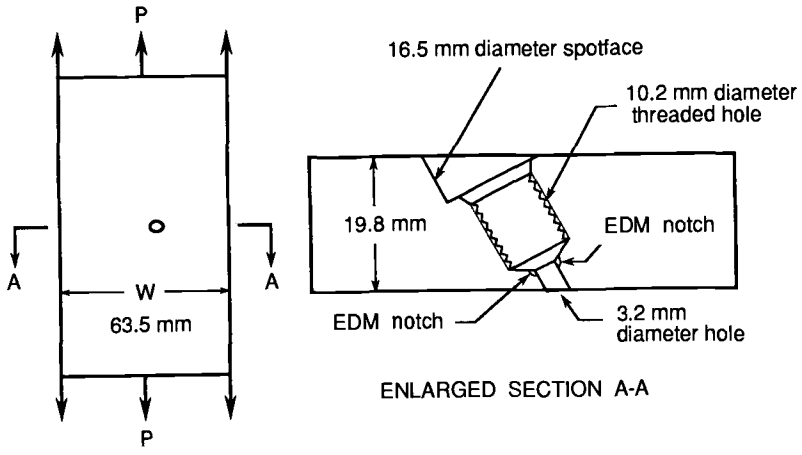


Fig. 4--Leak-check-port analog specimen.

The fracture data generated in the current study was analyzed with several different fracture criteria. Linear-elastic fracture mechanics [*4*,*5*] was applied to all crack configurations whereas a simple crack-growth resistance curve approach [*6*] and the Two-Parameter Fracture Criterion [*5*,*7*] was applied only to the through-the-thickness fracture specimens. An attempt was made to explain the influence of fatigue pre-cracking on fracture toughness by using the crack-closure concept [*8*] and an effective cyclic fracture toughness.

EXPERIMENTAL PROGRAM

Material

The D6AC steel is the prime structural material for the SRM's of the Space Shuttle transportation system. The nominal chemical compositions of the steel in weight percent are 0.42-0.48 C, 0.6-0.9 Mn, 0.4-0.7 Ni, 0.9-1.2 Cr, 0.9-1.1 Mo, 0.15-0.3 Si, 0.01 S (max), 0.01 P (max), 0.05-0.1 V, and balance Fe. Five heats of D6AC steel were used in the present study for the plane-strain fracture toughness tests. Material from an actual SRM case segment (heat treatment number FJS-230) was used in the fracture tests on the other crack configurations and the leak-check-port specimen.

The tensile properties for the five heats of material at room temperature and the tensile properties of material cut from the trim ring of an actual case segment at various temperatures are given in Table 1.

TABLE 1--Tensile and Fracture Toughness Properties for D6AC Steel.

Heat Treat Number	Temperature °C	Yield Stress, MPa	Ultimate Strength, MPa	K_{Ic} MPa-$m^{1/2}$
FYY-74	Room	1387	1485	102.9 (a)
FJL-218	Room	1316	1411	112.0 (a)
FKL-77	Room	1376	1487	112.4 (a)
DYD-42	Room	1391	1456	116.7 (a)
DJA-65	Room	1334	1436	123.3 (a)
FJS-230	Room	1375 (b)	1480 (b)	120.3 (c)
FJS-230	-30	1441 (b)	1557 (b)	87.6 (c)
FJS-230	0	1440 (b)	1556 (b)	114.8 (c)
FJS-230	55	1362 (b)	1475 (b)	117.2 (c)

(a) Data from Thiokol Corporation.
(b) Data from MSFC tests on D6AC case segment material from trim ring (average of 3 tests).
(c) K_Q values (thickness violates ASTM E399 requirement).

Specimen Configurations

Plane strain fracture toughness tests were conducted on compact tension, C(T), specimens with two different thicknesses (B = 23 mm, W = 45.7 mm and B = 11.4 mm, W = 50.8 mm). The planar dimensions for the C(T) specimens were identical to those in ASTM E399 on Plane Strain Fracture Toughness Testing, as shown in Figure 2(a). The thick material was obtained from five different lots of SRM case trim-ring material (four specimens from each lot). The five different lots of material were chosen to represent the widest possible range of material tensile and toughness variations for the SRM's. The thinner material was primarily cut from the membrane portion of a scrapped SRM case segment. Because these specimens were taken from a cylinder, a small amount of material (0.25 mm) was machined from both sides of the specimen to produce a flat surface. Six specimens were cut from case segment (FJS-230) and two specimens were cut from trim material from a different case segment (DJA-65).

The other fracture specimens used in the test program are shown schematically in Figure 2(b) to 2(d). The actual specimen configurations were dog-bone in shape and remotely pin loaded (see ref. *2*) but the test sections were of sufficient length so that the configurations could be approximated by those shown in the figure. The specimens covered a wide range in crack configurations (see Fig. 3) and simulated some of the crack configurations that may be of interest in the redesigned SRM. The as-received case membrane thickness of about 12 mm was retained for these specimens. The long axis of the specimen was cut parallel to the longitudinal axis of the case segment (FJS-230). Because of the approximate 3.7 m diameter of the cylinder, a slight curvature remained in the width direction of the specimen. The effect of this curvature was negligible, especially in the test section which is only 51 mm wide.

To assess the crack initiation, fatigue crack growth and fracture behavior of the leak-check-port region, six specimens were manufactured from trim-ring material of the scrapped SRM case number FJS-230. The specimen is shown in Figure 4. Thiokol Corporation designed and fabricated the specimens and two pairs of grips for mating the specimens in the test stand (see ref. *2*). Each specimen had the same thickness as the SRM tang (19.9 mm), and had a leak-check port machined in the center that was identical to the flight configuration.

Fracture Toughness Testing

Fracture tests were conducted to determine the influence of temperature and fatigue pre-cracking loads on fracture toughness. These series of tests involved only the C(T) configuration.

Temperature--Plane strain fracture toughness (K_{Ic}) values were obtained for D6AC steel at four different temperatures: -30, 0, 20, and 55 °C. This temperature range encompasses all potential SRM case metal temperatures for launch pad conditions. All tests were performed to ASTM E399 standards.

All twenty tests were performed in a 100 kN capacity fatigue test machine and were fatigue pre-cracked at room temperature until the desired crack length was achieved ($c_i/W = 0.5$). The load was cycled from 19.6 kN to 2 kN ($R = 0.1$) at 10 Hz. Typically, about 40,000 cycles were required.

Temperature conditioning was achieved by constructing a fiber-board box around each specimen in the test stand. For the cold tests, a liquid nitrogen supply line entered the box and allowed cold nitrogen gas to circulate around the specimen. A pair of thermocouples were bonded, one to each side of the compact specimen near the crack front, for temperature monitoring and for automatic control of the liquid nitrogen flow rate. The 55 °C tests were performed similarly, using a controlled hot air gun. Each specimen was held to within ± 2 °C for at least 20 minutes before testing. A displacement gage was used to measure the crack-mouth opening and the loading rate was 45 kN/minute. Each specimen was loaded to failure while held at the proper temperature and an X-Y plotter recorded the load-against-displacement trace used to determine the P_Q load and the maximum failure load, P_{fail}.

Fatigue Pre-cracking--A series of tests on eight compact specimens were conducted to study the influence of fatigue pre-cracking loads on fracture toughness. Each specimen was fatigue pre-cracked in the 100 kN fatigue test machine at different load levels until the same final crack length ($c_i/W = 0.5$) was achieved. The specimen was then loaded to failure at 22 kN per minute. The load-against-crack-mouth opening displacement was recorded for each test. All tests were conducted at room temperature.

Critical Crack Size Determination Tests

The fracture tests conducted to determine the critical crack sizes for a variety of crack configurations, see Figures 2(b) to 2(d), were tested in a 1800 kN fatigue test machine. The test machine was fitted with two pairs of high strength steel (4130) adapter plates, each with a 63.5 mm diameter hole. Two high strength steel pins (Vascomax 200) were used to pin the ends of each dog-bone specimen between the adapter plates.

To test the pin-loaded hole specimens, shown in Figure 2(d), a pair of smaller adapter plates with a 25-mm pin were made to apply pin loading in the hole. (The details of the adapter plates and the dog-bone specimen designs are given in reference *2*.)

All specimens had electrical-discharge machined (EDM) notches machined at various locations in the specimens. (The thickness of the EDM shim stock was about 0.25 mm.) The fatigue pre-cracking loads that were used to initiate cracks from the notches in these tests were not intended to represent the operational loads on the SRM. Instead, the loads were selected to produce relatively planar crack fronts with limited plasticity effects. Once the desired crack size was attained, the load was monotonically increased at a rate of 200 kN per minute until the specimen failed. All tests were conducted at room temperature.

Through and Surface Crack Specimens--Five specimens were manufactured from the case segment membrane, Figure 2(b). Two specimens had a semi-circular EDM surface notch in the center of the test section, oriented normal to the loading direction. The notch was about 2.5 mm in radius. A third specimen had an EDM notch in the center that went completely through the thickness. The total notch length was about 6 mm. The remaining two specimens had a 3.2 mm diameter hole drilled completely through the center of the test section. A quarter-circular EDM notch (0.8 mm radius) was placed at one corner of the through hole perpendicular to the loading direction.

Through and Corner Crack at Open Hole Specimens--Six specimens with a 25-mm diameter hole drilled and reamed in the middle of the test section were subjected to remote loading. The specimen is shown in Figure 2(c). Two specimens were machined with an EDM notch completely through the thickness on one side of the hole. The notch was about 2.5 mm in length from the hole surface. The four remaining specimens had a quarter-circular corner notch on one edge of the hole. The corner notch had a radius of about 0.8 mm.

Through and Corner Crack at Pin-Loaded Hole Specimens--Seven specimens with a 25-mm diameter hole drilled and reamed in the middle of the test section were subjected to pin loading. (The actual test specimen was a single dog-bone design with remote pin loading, but the test section was long enough so that a uniform loading could be assumed to exist, see reference *2*.) The specimen configuration is shown in Figure 2(d). The center of the 25-mm hole was located 42 mm from the edge of the specimen. This is the same edge distance (e) from the center of the SRM pin hole to the end of the tang.

The test machine was configured so that a pair of adapter plates with a 63.5 mm diameter hole and pin held one end of the specimen, while the other end was held by smaller adapter plates with 25-mm diameter hole. Each specimen was pinned between the smaller plates by inserting an actual SRM tang-clevis joint pin. Hence, all axial loading was transmitted directly to the specimen via the SRM pin.

Two specimens were machined with an EDM notch through the thickness on one side of the hole. The notch was about 2.5 mm in length. The remaining five specimens had quarter-circular EDM corner notches (0.8 mm in radius).

SRM Leak-Check-Port Analog Tests

The SRM joint leak-check port is the highest stressed location in the motor case. The stress concentration due to the configuration of the port hole, combined with its location adjacent to an alignment slot, causes localized yielding to occur during operating conditions. A case hydroburst test conducted by Thiokol Corporation also revealed that failure of the SRM case segment initiated at this location.

A typical leak-check-port specimen is shown in Figure 4. Again, special adapters were designed by the Thiokol Corporation to carry the extremely high loads required to simulate the proof and operational loads on the analog leak-check-port specimen. Five rows of teeth on each end of the specimen transmit the axial load to each pair of grip plates (see ref. 2). Four of the specimens were EDM notched at the transition from the threaded 10.2 mm diameter hole to the 3.2 mm diameter through hole on the small ligament side, as shown in Figure 4. One specimen was notched on the large ligament side and last specimen was tested without EDM notches.

Each specimen was instrumented with strain gages and aligned in the 1800 kN capacity fatigue test machine so that loading was close to uniaxial. Testing consisted of cycling at maximum loads that corresponded either to flight-load conditions or to proof-pressure test conditions. A maximum load of 832 kN was required to develop flight equivalent stress levels and 930 kN was required for proof-test equivalent stress levels. Most tests were conducted at room temperature but two specimens were cooled to -7 °C or 0 °C to simulate potential flight temperature conditions. The highest cyclic loading frequency attained was 1 Hz.

The test procedure consisted of a series of load cycles, usually 200 at a time, interrupted to check for crack growth or crack initiation. Visual inspections were made by a microscope. In addition, eddy current inspections were performed in the same manner, and with the same equipment as used by Thiokol Corporation to check actual flight hardware. Temporary holds were also made to allow for strain gage data collection. For this purpose, individual cycles were repeated slowly allowing strain gages to be recorded. For most tests, crack-front marker bands (same maximum load with $R \approx 0.8$) were placed, generally at intervals of about 500 cycles. Anywhere from 2,000 to 4,000 cycles at 4 Hz were used to generate each marker band.

RESULTS AND DISCUSSION

Plane-Strain Fracture Toughness

The plane-strain fracture toughness results obtained from the thick compact specimens are shown in Figure 5. The symbols shown the test results and the dashed curve is fitted to the average values at each temperature. The results indicate that the K_{Ic} values for temperatures greater than about -20 °C are higher than the specified minimum design requirements of 100 MPa-$m^{1/2}$. The appearance of the fracture surfaces were similar, except for the size of the resulting shear lips. The shear-lip size for the -30 °C test specimen was about one-half the shear-lip size as that for the 55 °C test specimen.

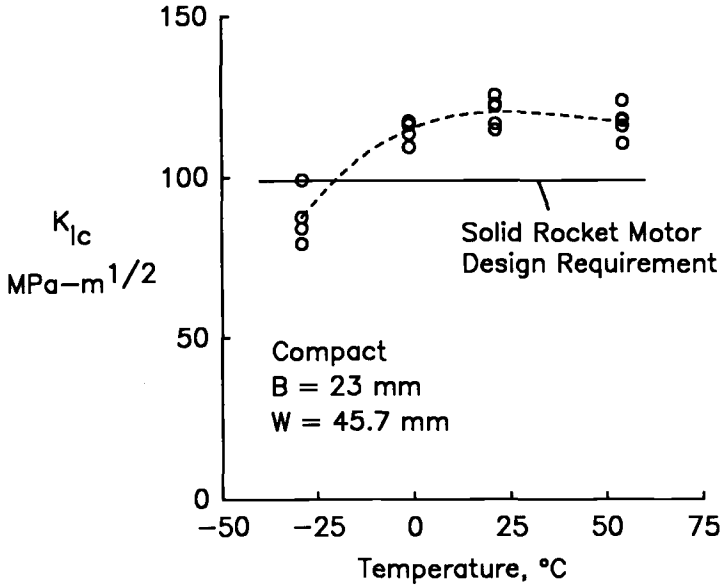


Fig. 5--Plane strain fracture toughness against temperature for compact specimens.

Elastic Stress Intensity Factors at Failure

Fracture tests conducted at low fatigue pre-cracking load levels produced relatively flat crack fronts for all seven crack configurations. This was done to enhance the ability of fracture-analysis methods to correlate the experimental data. One of the first methods attempted was linear-elastic fracture mechanics (LEFM). The elastic stress-intensity factors (SIF) at failure on the wide variety of fracture specimens tested is shown in Figure 6 for the 12-mm thick material. The elastic SIF was calculated from the maximum failure load and the initial crack size, expressed in terms of net-section stress [*4*,*5*], as

$$K_{Ie} = S_n\sqrt{\pi c_i}\, F_n \qquad (1)$$

The solid line is the average K_{Ie} for the three compact specimens and the dashed line is the K_{Ic} value from the 23-mm thick compact specimens. These results demonstrate that LEFM procedures are quite adequate for the crack and specimen sizes tested. K_{Ie} values are constant within about 10 percent. However, as will be shown later, some of the variation in K_{Ie} may be due to a resistance-curve effect.

The fracture data on the compact specimens tested at the low fatigue pre-cracking loads (9.8 kN) are given in Table 2 and the test data from the six other fracture specimens are given in Table 3.

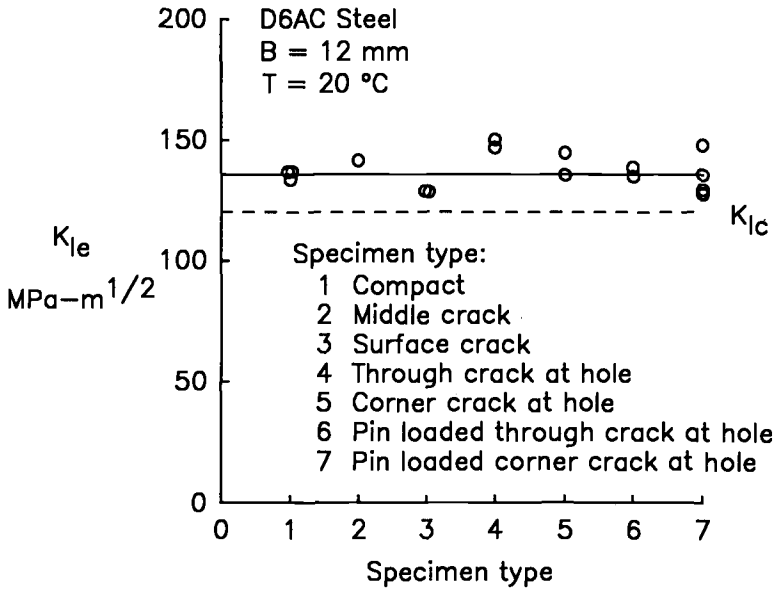


Fig. 6--Elastic stress intensity factor at failure for various fracture specimens.

TABLE 2--Influence of Fatigue Level on Elastic Fracture Toughness.

Specimen	Fatigue Precracking				Fracture	
	P_{max}	N	c_i	K_{max}	P_{fail}	K_{Ie}
Number(a)	kN	Cycles	mm	MPa-$m^{1/2}$	kN	MPa-$m^{1/2}$
SC1A(b)	9.8	87,400	24.4	34.7	38.6	137.0
SC2A(b)	9.8	98,000	26.2	38.5	34.8	136.8
SC1B(c)	9.8	104,000	25.5	36.8	35.6	133.7
SC2B(c)	13.3	45,000	25.5	50.0	34.8	131.9
SC3B(c)	24.0	9,080	26.0	90.1	38.0	147.2
SC4B(c)	27.6	6,430	25.8	103.4	40.9	156.3
SC5B(c)	32.5	3,250	25.9	121.8	44.5	171.8
SC6B(c)	37.8	1,600	26.6	141.8	48.0	185.6

(a) Compact specimens (W = 50.8 mm and B = 11.4 mm) pre-cracked at a stress ratio (R) of 0.1 and pulled to failure at room temperature.
(b) Specimen from trim-ring material (Heat Treat Number: DJA-65).
(c) Specimen from SRM case segment (FJS-230).

TABLE 3--Fracture of Various Cracked Specimen Types from SRM Case.

Specimen Number(a)	Width, W mm	Hole diameter mm	P_{max}(b) kN	Crack depth, a_i mm	Crack length, c_i mm	P_{fail} kN
Surface crack:						
SS2A	50.8	0	311	8.64	9.02	624
SS2B	50.8	0	311	7.37	7.49	674
SS1C (c)	50.8	3.2	400	10.92	6.86	638
Through crack:						
SS2C	50.8	0	222	--	6.22	591
SS1B (c)	50.8	3.2	400	--	11.43	463
Through crack from hole:						
SH1A	63.5	25.6	178	--	7.62	330
SH1B	63.5	25.6	156	--	5.08	358
SH1C (d)	63.5	25.6	278	--	9.91	378
Corner crack from hole:						
SH2A (d)	63.5	25.6	534	7.37	6.10	534
SH2B	63.5	25.6	222	9.65	8.38	390
SH2C	63.5	25.6	178	5.33	4.83	476
Through crack from pin-loaded hole:						
SP3A	63.5	25.6	66.7	--	4.57	329
SP3B	63.5	25.6	66.7	--	4.32	328
Corner crack from pin-loaded hole:						
SP3C	63.5	25.6	111	6.10	4.57	410
SP4A	63.5	25.6	133	7.37	6.10	377
SP4B	63.5	25.6	133	8.38	6.60	379
SP4C	63.5	25.6	133	8.38	6.35	374
SP5A	63.5	25.6	133	2.79	2.29	549

(a) Specimen thickness B = 11.9 mm and tested at room temperature.
(b) Fatigue pre-cracked at P_{max} with P_{min} = 9 kN.
(c) EDM notch was 0.8 mm radius at edge of hole but cracks grew from both sides of hole (see ref. *2*)
(d) Cycled to failure.

Crack Growth Resistance Curves

A simple crack growth resistance curve approach was applied to only the through-the-thickness crack configurations. (Application of the K_R curve approach to surface- and corner-crack configurations was beyond the scope of this investigation.) In 1980, Orange [6], using various semi-empirical fracture criteria, derived K_R curves that would be equivalent to these simple fracture criteria. His analyses showed that, at least, two parameters were required to fit crack growth resistance data. One method in particular was the Two-Parameter Fracture Criterion (TPFC) [5,7]. The functional form of the resistance curve from the TPFC was

$$K_R = C_1 [\Delta c/(\Delta c + C_2)]^{1/2} \quad (2)$$

where C_1 and C_2 are constants related to Newman's two fracture parameters, K_F and m, as $C_1 = K_F$ and $C_2 = (mK_F/\sigma_u)^2/\pi$. In the current application, the constants were used to fit experimental fracture data and to predict failure on other crack configurations using the K_R-curve concept.

Figure 7 shows unpublished test data from Dan Drinan (MSFC) on various size compact specimens. The test specimens were cut from an actual SRM case segment and the large specimen (c_i = 75 mm and W = 152 mm) was tested with the slight curvature. The K_{Ie} values plotted here are based on the P_Q loads (instead of maximum load) to demonstrate the variations in plane-strain fracture toughness that result from using non-standard crack configurations (smaller plate thickness than specified in the ASTM E399 Plane Strain Fracture Toughness Standard). The solid curve is the calculated results with C_1 = 143 MPa-$m^{1/2}$ and C_2 = 0.5 mm. The values of C_1 and C_2 were determined to fit these data using the K_R-curve concept and a least-squares procedure. In the procedure, C_2 was selected by trial-and-error and C_1 was evaluated by minimizing the error between test and analysis.

Similarly, Figure 8 shows test data from the current study on compact and middle-crack specimens. Again, the values of C_1 = 178 MPa-$m^{1/2}$ and C_2 = 0.64 mm were determined to fit the compact specimen data (from Drinan, using the maximum failure loads, and the C(T) results from the current study). The dashed curve is the predicted results for the middle-crack specimen for a 50.8 mm wide specimen. These results show that the K_R-curve approach predicted the M(T) specimen results quite well (within 5 %). Again, the solid and dashed curves were calculated using the K_R-curve concept with equation (2). The calculated net-section failure stress was set equal to the ultimate tensile strength if the stress calculated from the K_R-curve concept exceed the ultimate strength.

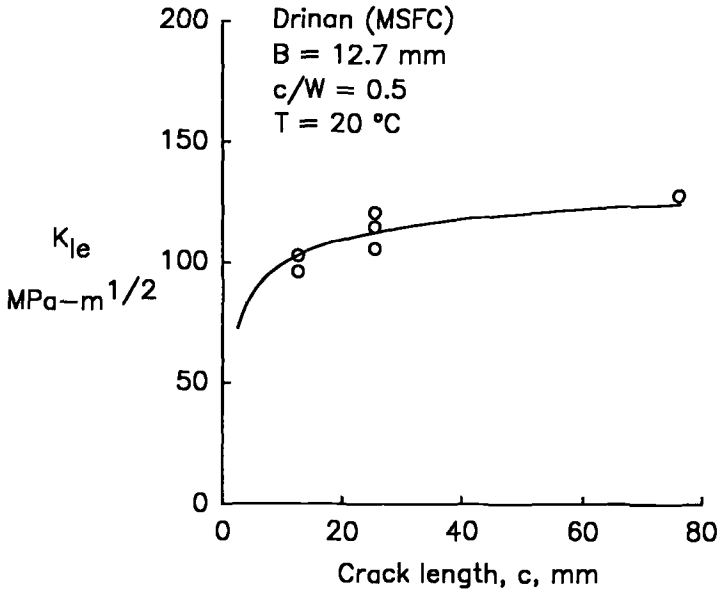


Fig. 7--Elastic stress intensity factor at failure (based on P_Q loads) for various size compact specimens.

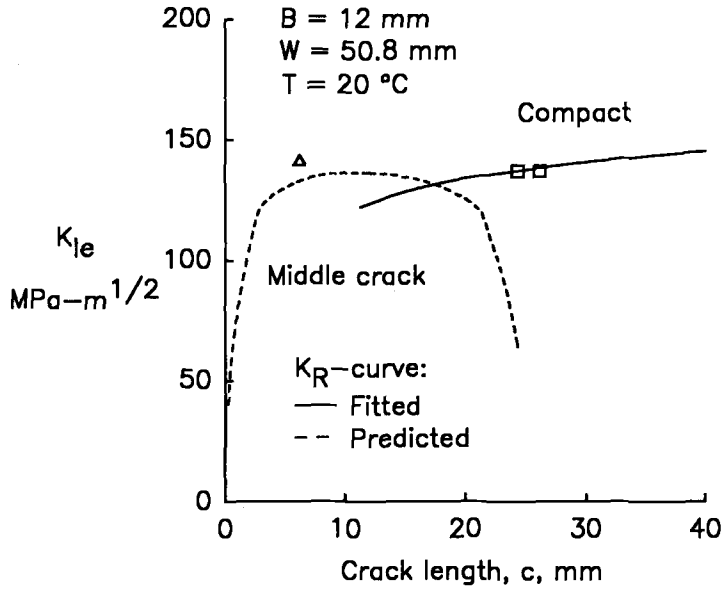


Fig. 8--Comparisons of fitted and predicted K_{Ie} values for two specimen types using the K_R-curve.

To evaluate whether these crack growth resistance curves may be able to predict physical crack extensions, a comparison with crack extension measurements made by Liaw et.al. are shown in Figure 9. (The test data was obtained from an unpublished report by P. K. Liaw, M. G. Peck, G. E. Rudd, and D. W. Sutherland, "Fracture Toughness Behavior of D6AC Space Shuttle Steels, Part I," Westinghouse Science and Technology Center, Pittsburg, PA, 1992.) First, the square symbols show data on 19-mm thick specimens that satisfy the K_{Ic} criteria. The dashed curve shows results predicted from C_1 = 143 MPa-$m^{1/2}$ and C_2 = 0.5 mm that were fit to the fracture data based on the P_Q loads, that is, a plane-strain crack growth resistance curve. The agreement is quite good, especially the peak values, but some discrepancy is observed at the small crack extension values. Crack tunneling in the early stages of crack growth may account for some of this discrepancy.

The circular symbols show crack extension data on 6.4-mm thick compact specimens tested at 0 °C. The solid curve shows the expected crack extension values for a 12-mm thick material tested at room temperature. Although these results can not be directly compared, the trends in the test and predicted results seems reasonable.

Two-Parameter Fracture Criterion

The Two-Parameter Fracture Criterion [5,7] was developed to predict failure loads on various crack configurations, like those tested in the current study. A modified form of the TPFC equation is

$$K_F = K_{Ie}/(1 - m\, S_n/\sigma_u) \tag{3}$$

where K_f and m are two fracture parameters and σ_u is the ultimate tensile strength. This approach is a departure from the traditional TPFC method, in that, the net-section stress is normalized by the tensile strength, σ_u, instead of the plastic-hinge stress (S_u). (For the compact specimen, the net-section stress is calculated from simple beam theory assuming that the uncracked ligament is subjected to tension and bending, and the plastic-hinge stress $S_u = 1.61\ \sigma_u$.) Using the fracture data on the compact specimens, K_F = 190 MPa-$m^{1/2}$ and m = 0.3. The solid curve in Figure 10 was fitted to compact specimen results from Drinan and the current study.

The equation to calculate K_{Ie} for the middle-crack and through crack at a hole specimens from equation (3) was

$$K_{Ie} = K_F/[1 + m\, K_F/(\sigma_u\sqrt{\pi c_i}\, F_n)] \qquad \text{for } S_n < \sigma_u \tag{4}$$

and

$$K_{Ie} = \sigma_u\sqrt{\pi c_i}\, F_n \qquad \text{for } S_n = \sigma_u \tag{5}$$

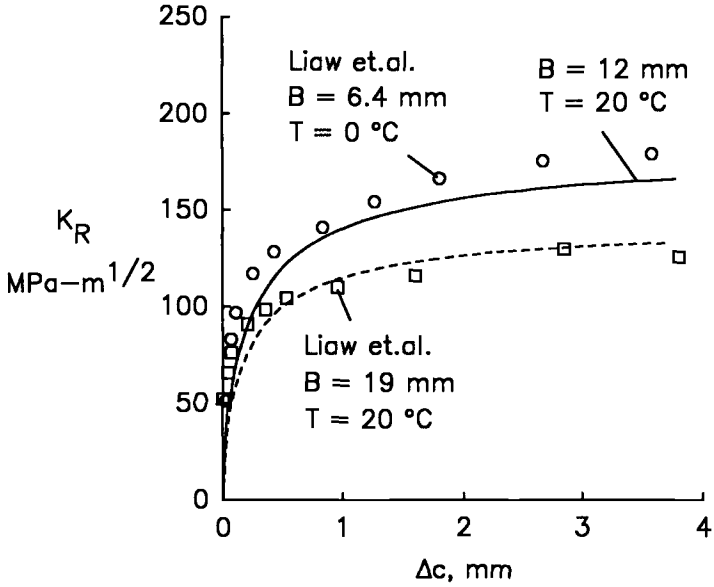


Fig. 9--Crack growth resistance data and curves for various compact specimens and test temperature.

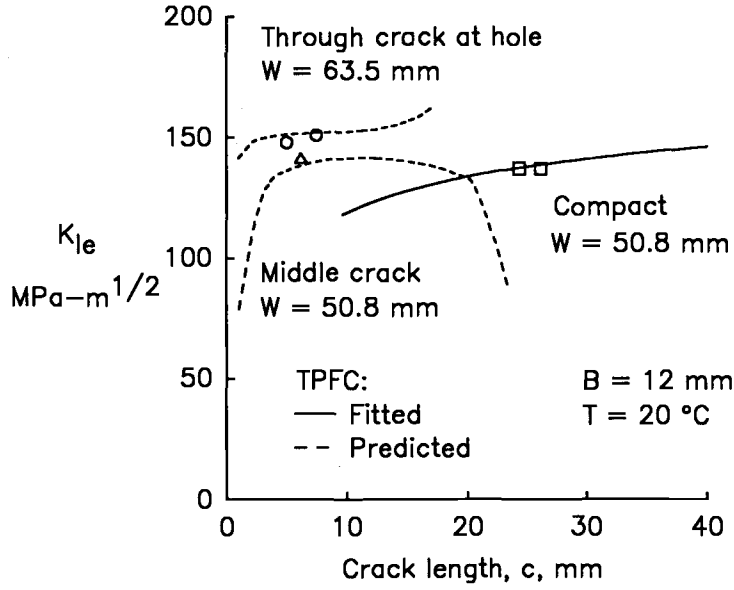


Fig. 10--Comparisons of fitted and predicted K_{Ie} values for three specimen types using the Two-Parameter Fracture Criterion.

where F_n is the usual boundary-correction factor for the crack configurations expressed in terms of S_n instead of gross stress or applied load. The dashed curves in Figure 10 compares the calculated K_{Ie} values with the test results for two other crack configurations. The modified TPFC equations were able to accurately predict the fracture behavior of the through-the-thickness crack configurations.

Influence of Fatigue Pre-cracking or Cycling to Failure

Figure 11 presents the fracture test data obtained on all of the fracture specimens made from the 12-mm thick material as a function of the maximum pre-cracking or cyclic stress-intensity factor, K_{max}. These results indicate that there is a very strong influence of the cyclic crack growth history on fracture toughness. The solid line is the average of the three compact specimens tested at the lowest K_{max} levels and the dashed line is the K_{Ic} value. The lines extend to 60 % of their respective values and supports the ASTM E399 requirement that valid fracture toughness tests should be restricted to K_{max} values less than 60 % of the toughness.

Restricting attention to only the compact specimens, the elastic stress-intensity factors at failure are plotted in Figure 12, as solid symbols. The open symbols are the calculated crack-opening stress-intensity factors, K_o, from a crack-closure model [*8,9*]. Noting that

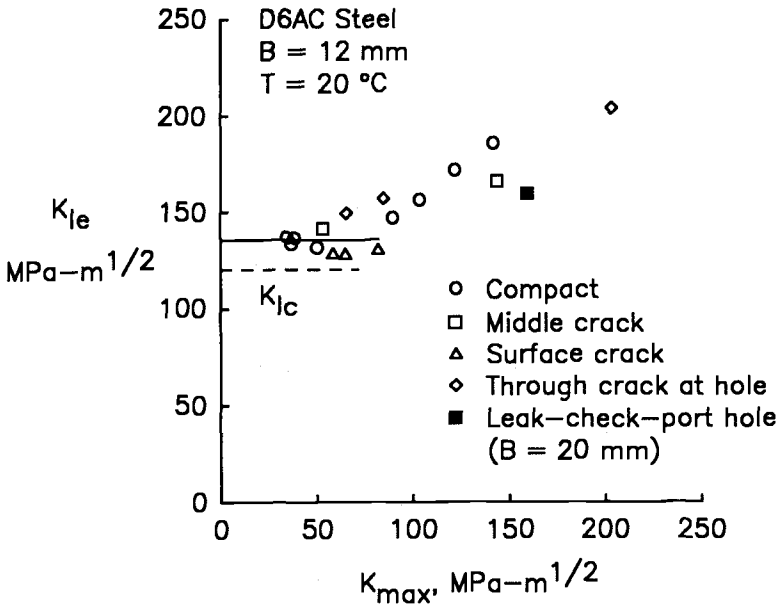


Fig. 11--Elastic stress intensity factor at failure against fatigue pre-cracking levels for various specimen types.

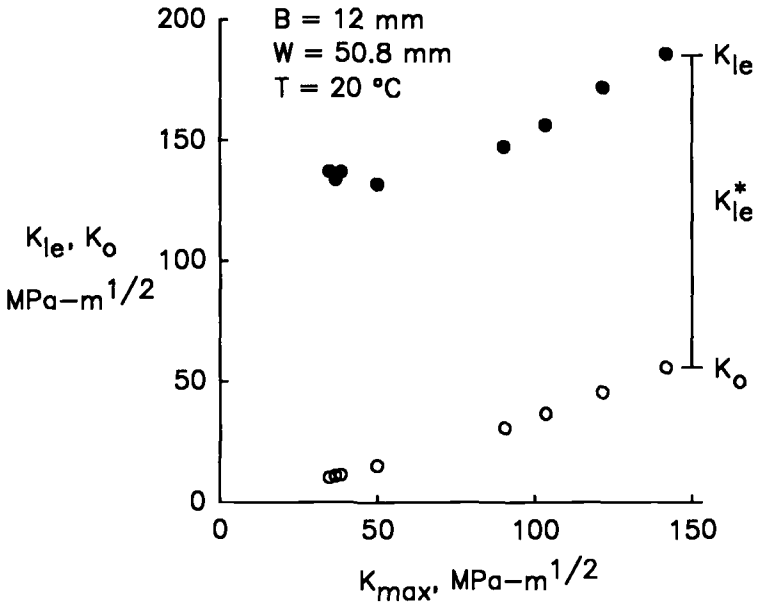


Fig. 12--Fatigue crack opening stress intensity factors, K_o, during pre-cracking and K_{Ie} at failure for compact specimens.

the difference between K_{Ie} and K_o is roughly constant, an effective cyclic fracture toughness, K^*_{Ie}, may be defined.

Before discussing the cyclic fracture toughness, the method used to calculate K_o levels will be presented. From the crack-closure model for a middle-crack specimen, an equation was developed [*9*] to calculate K_o as

$$K_o/K_{max} = A_0 + A_1 R + A_2 R^2 + A_3 R^3 \qquad \text{for } R \geq 0 \tag{6}$$

where $A_i = A_i(S_{max}, \sigma_o, \alpha)$. S_{max} is the remote stress, σ_o is the uniaxial flow stress and α is the constraint factor. Reference *9* gives the equations for A_i. Using K-analogy, K_o/K_{max} from a middle-crack specimen is used to calculate the K_o for a compact specimen. McClung [*10*], using two-dimensional finite-element closure analyses, has also shown that the K-analogy concept may be used for various specimen types.

Recently, the effects of thickness and yielding on a global constraint factor has been studied for finite-thickness plates subjected to tension and bending loads [*11*]. From the three-dimensional, elastic-plastic, finite-element analyses, an average normal stress (opening mode stress) is computed over the plastic zone. The global constraint factor,

α_g, is defined as the average normal stress normalized by the uniaxial flow stress, σ_0. The global constraint factor was developed for use in two-dimensional models to approximate three-dimensional effects. Some typical results for a thickness and specimen size that is similar to the compact specimen tested here is shown in Figure 13. These results are for a middle-crack tension, M(T), and a single edge crack bend, SE(B), specimen. It is assumed that the compact specimen results would lie closer to the bend specimen than the tension specimen. The upper dashed-dot lines show the limiting results for plane-strain conditions; and the dotted line show the lower limit for plane-stress conditions. The solid curve is an equation chosen to fit the finite element results for c/B and b/B ratios greater than 4. But the bend results for c/B = 2 lie quite close to the solid curve. Thus, the constraint equation is

$$\alpha_g = 1.15 + 1.55\ e^{-1.05\ K_n^{1.5}} \tag{7}$$

where $K_n = K/(\sigma_0\sqrt{B})$.

Assuming that α_g is equal to α, equation (6) and (7) were used to calculate K_0/K_{max} for the compact specimens. The K_0/K_{max} value was 0.3 for the specimens with the lowest K_{max} levels and the ratio was about 0.4 for the test with the highest K_{max} value. The effective cyclic fracture toughness K^*_{Ie} is shown in Figure 14 as a function of K_{max}. These results

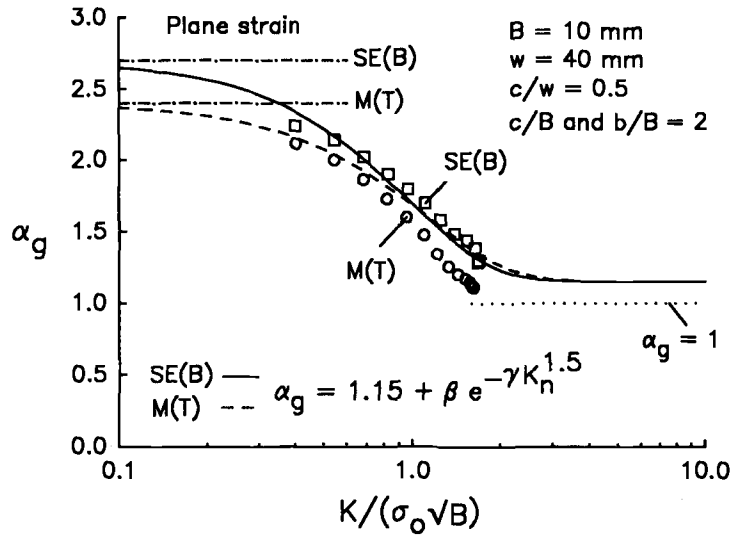


Fig. 13--Global constraint factors for 10-mm thick plates subjected to tension and bending loads.

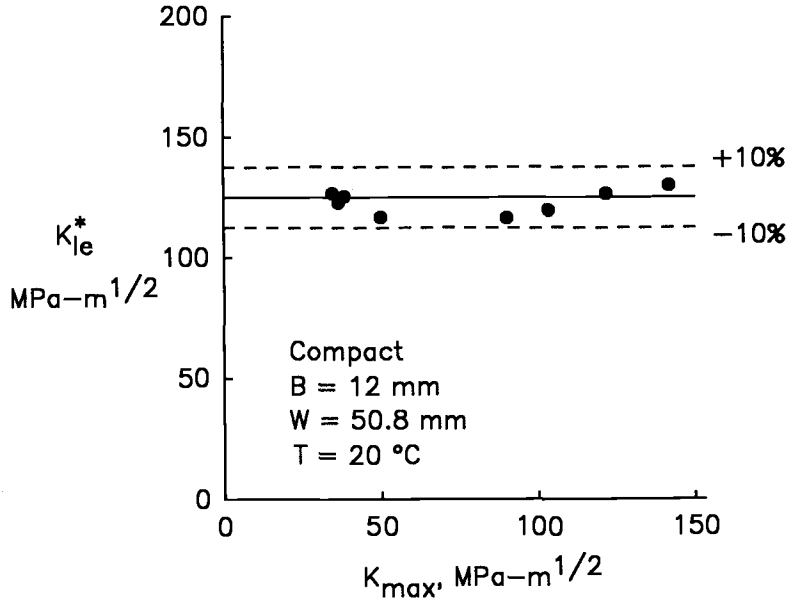


Fig. 14--Effective cyclic fracture toughness, K^*_{Ie}, against fatigue pre-cracking stress intensity factor levels.

indicate that the K^*_{Ie} values are nearly independent of the maximum cyclic stress-intensity factor. Similar to the crack-closure concept applied to fatigue-crack growth, the effective stress-intensity factor appears to account for the effects of cyclic stress history on the fracture process.

Leak-Check-Port Analog Test Results

A summary of the six tests conducted on the leak-check-port specimen is given in Table 4. Specimens FJS-230-01 and FJS-230-03 were fatigue tested at the same load level and temperature. However, specimen 1 had an EDM notch located on the large ligament side (see Fig. 15(a)) and specimen 3 was notched on the small ligament side (for example, see Fig. 15(b)). Despite the different location for the starter notch, the corresponding marker bands and final crack sizes at failure were generally very similar. Even the total number of cycles to failure were very close for the two specimens.

Effects of temperature were demonstrated by specimens 2, 4 and 6. Each of these specimens were notched on the small ligament side and cycled at the same load level. However, specimen 2 and 6 were tested at room temperature while specimen 4 was tested at -7 °C. The results showed that final crack size at failure was smaller for the lower temperature, as would be expected from the lower fracture toughness at the colder temperature. However, the cyclic life was somewhat higher for the colder temperature test because cracks in the D6AC steel tend to grow slower at the lower temperatures based on the marker band results.

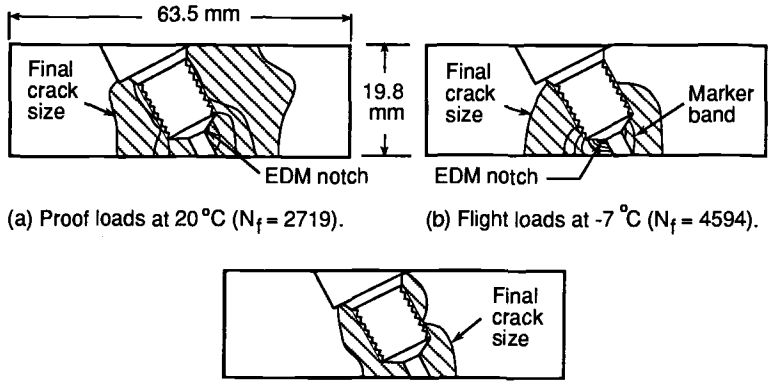
TABLE 4--Leak-Check Port Test Matrix.

Specimen Number	Maximum Cyclic Load, kN (a)	Temperature °C	EDM Notch Location	Cycles to Failure
FJS-230-01	930 (b)	Room	large ligament (d)	2719
FJS-230-02	832 (c)	Room	small ligament (e)	3825
FJS-230-03	930	Room	small ligament (e)	2775
FJS-230-06	832	Room	small ligament (e)	4131
FJS-230-04	832	-7	small ligament (e)	4594
FJS-230-05	930/187	Room/0	none	6718

(a) Minimum load was 13 kN for all specimens.
(b) Proof-test equivalent load.
(c) Flight equivalent load.
(d) EDM notch was about 1.3 mm by 1.3 mm (see ref. *2*).
(e) EDM notch was about 0.8 mm by 1.5 mm (see ref. *2*).
(f) Loading was 350 cycles at proof followed by flight loading.

The results from specimen 5 were interesting because no EDM notch was used to start the crack. This specimen was subjected to 350 cycles at the proof-load condition (room temperature) and then subjected to flight-load conditions (0 °C) until failure. Cracks initiated naturally along the bore of the port hole. An eddy-current measurement technique, identical to that use in the actual SRM hardware, indicated that a crack was present along the threaded region at 200 cycles (during the proof-test equivalent loading).

Figure 15 shows some sketches of the cracking patterns that developed in three of the specimens. This figure shows the EDM notch



(a) Proof loads at 20 °C (N_f = 2719).

(b) Flight loads at -7 °C (N_f = 4594).

(c) Proof and flight loads at 20 °C (N_f = 6718), no EDM notch.

Fig. 15--Typical leak-check-port fatigue, crack growth and fracture results (curves denote fatigue marker bands and fracture).

(dark region), the marker bands, and the final profile of the crack at failure in Figure 15(a) and 15(b). The marker bands were generally easy to see visually and documented the stages of crack growth. The results shown in Figure 15(c) was from the specimen without an EDM notch and no marker loads were applied. In general, crack growth initiated at the EDM notch and grew fastest down the inner surface of the small diameter hole. At failure, all specimens exhibited crack growth to some degree along the threaded region. The un-notched specimen (FJS-230-05) behaved similarly, as mentioned above, except possibly that the crack-initiation site occurred along the threaded hole region. In conclusion, the critical crack sizes for all specimens were large (>25 mm) and required a large numbers of cycles to reach failure (>2,700 cycles).

CONCLUSIONS

Fracture tests have been conducted on a variety of crack configurations made from material taken from Space Shuttle solid rocket motor (SRM) D6AC steel case segments. The tests determined fracture toughness, crack-growth behavior, and critical crack sizes under proof and operational conditions. The results are summarized as follows:

1. Plane strain fracture toughness (K_{Ic}) dropped off rapidly for temperatures less than about 0 °C, but they exceed the SRM design requirements (100 MPa-$m^{1/2}$) down to about -18 °C.

2. Elastic fracture toughness (K_{Ie}) values from seven different crack configurations were constant within ± 10 % for the range of crack and specimen sizes tested.

3. A two-parameter (K_R) resistance curve and a two-parameter fracture criterion (TPFC) predicted the effects of specimen type within 5 % for the through-the-thickness crack configurations.

4. Elastic fracture toughness (K_{Ie}) values were 35 to 50 % higher for specimens that were fatigue pre-cracking at high stress intensity factor levels or cycled to failure.

5. An effective cyclic fracture toughness (elastic fracture toughness minus the crack opening stress intensity factor) was constant within ± 10 % for a wide range of fatigue pre-cracking stress levels.

6. SRM factory joint leak-check port critical crack sizes and cyclic lives were determined for flight and proof pressure test equivalent loads. Six specimens were tested at temperatures ranging from -18 °C to 20 °C. All critical crack sizes were greater than 25 mm in length and required more than 2,700 cycles to grow from a damage-tolerant crack size to failure.

REFERENCES

[1] Webster, R. L., "Challenges Met in Establishing the Structural Integrity of the Space Shuttle Redesigned Solid Rocket Motor," Presented at the AIAA/ASME/ASCE/AHS/ASC Structures, Structural Dynamics and Materials Conference, Hilton Head, South Carolina, April 18-22, 1994.

[2] Bland, J. D., Newman, J. C., Jr., and Berry, R. F., Jr., "Characterization of Fracture Toughness and Critical Crack Sizes for the Space Shuttle Solid Rocket Motor D6AC Steel Case," NASA Technical Memorandum 101524, 1995.

[3] Liaw, P. K., Peck, M. G., and Rudd, G. E., "Fatigue Crack Growth Behavior of D6AC Space Shuttle Steel," Engineering Fracture Mechanics, Vol. 43, No. 3, 1992, pp 379-400.

[4] Tada, H., Paris, P. C., and Irwin, G. R., "The Stress Analysis of Cracks Handbook," Del Research Corporation, 1985.

[5] Newman, J. C., Jr., "Predicting Failure of Specimens with Either Surface Cracks or Corner Cracks at Holes," NASA TN D-8244, June 1976.

[6] Orange, T. W., "A Relation Between Semiempirical Fracture Analyses and R-Curves," NASA TP-1600, January 1980.

[7] Newman, J. C., Jr., "Fracture Analysis of Various Cracked Configurations in Sheet and Plate Materials," Properties Related to Fracture Toughness, ASTM STP 605, American Society for Testing and Materials, 1976, pp 104-123.

[8] Newman, J. C., Jr., "A Crack-Closure Model for Predicting Fatigue Crack Growth under Aircraft Spectrum Loading," Methods and Models for Predicting Fatigue Crack Growth under Random Loading, J. B. Chang and C. M. Hudson, Eds., ASTM STP 748, 1981, pp 53-84.

[9] Newman, J. C., Jr., "A Crack Opening Stress Equation for Fatigue Crack Growth," International Journal of Fracture, Vol. 24, 1984, pp R131-R135.

[10] McClung, R. C., "Finite-Element Analysis of Specimen Geometry Effects on Fatigue Crack Closure," Fatigue and Fracture of Engineering Materials and Structures, Vol. 17, No. 8, 1994, pp 861-872.

[11] Newman, J. C., Jr., Crews, J. H., Jr., Bigelow, C. A., and Dawicke, D. S., "Variations of a Global Constraint Factor in Cracked Bodies under Tension and Bending Loads," Constraint Effects in Fracture: Theory and Applications, ASTM STP 1244, Mark Kirk and Ad Bakker, Eds., American Society for Testing and Materials, Philadelphia, 1994.

L. Hodulak[1], D. Memhard[1], and C. Couterot[2]

VALIDATION OF R6 DEFECT ASSESSMENT METHODOLOGY USING EXPERIMENTS ON PLATES AND PIPES WITH SURFACE CRACKS

REFERENCE: Hodulak, L., Memhard, D., and Couterot, C., "**Validation of R6 Defect Assessment Methodology Using Experiments on Plates and Pipes with Surface Cracks**" Fractures Mechanics: 26th Volume, ASTM STP 1256, Walter G. Reuter, John H. Underwood, and James C. Newman, Jr., Eds., American Society for Testing and Materials, Philadelphia, 1995.

ABSTRACT: Plates and pipes with surface cracks were loaded to a level at which a definite amount of stable crack growth was achieved. Nominal stresses necessary for stable crack extension in depth direction equal to that observed on fracture surfaces were calculated and compared to nominal stresses in experiments. Option 2 of the R6 supplied closer agreement with experiment than Option 1. All results calculated with Option 1 were conservative.

KEYWORDS: defect assessment, R6, stable crack growth, component tests, surface cracks

INTRODUCTION

To verify methods of elastic-plastic fracture mechanics for the assessment of components with defects, experiments were done on steel plates and pipes with surface cracks [1]. All components were loaded to a level at which a definite amount of crack growth was achieved. An assessment of fracture behavior of two of these components using elastic-plastic fracture mechanics and constraint modified J-R curves was reported elsewhere [2]. This paper describes particularly the assessment of eight components using the R6 failure assessment method.

In these calculations crack growth was simulated, using J-R curves measured on compact specimens. Nominal stresses necessary for crack extension in depth direction (through the thickness of plates or pipes), equal to crack extension observed on fracture surfaces were calculated and compared to maximum nominal stresses in experiments. For crack extension in length direction two different assumptions have been adopted: 1. no crack extension in

[1] Fraunhofer-Institut für Werkstoffmechanik, Wöhlerstr. 11, D-79108 Freiburg, Germany
[2] Direction des Etudes et Recherches, Electicité de France, 77250 Moret-sur-Loing, France

Copyright © 1995 by ASTM International www.astm.org

length direction (c = cons.), 2. constant crack shape (a/c = cons.). For some cases, crack extension was evaluated in both depth and length directions using different J-R curves.

For the sake of comparison to experiments a limitation of stable crack growth required in the R6 procedure was not applied. Moreover for some calculations it was necessary to shift the location of the cut-off L_r on the assessment line in order to avoid termination of the crack growth calculation by the plastic collapse cut-off. In most calculations 'Option 1', based on yield stress and 'Option 2', based on stress-strain curve of the material have been used. In one case, where J integral as a function of load was available (FE results), an assessment according to 'Option 3' of the R6 has been used.

MATERIAL AND COMPONENT TESTS

This paragraph describes the data base for the validation of the R6 methodology regarding stable crack growth. In the first part material data obtained from laboratory specimens are summarized. Most of these data are taken from [2]. In the second part component experiments are described.

Material properties

The material is a ferritic steel, German designation X 20 CrMoV 12 1 (DIN No. 1.4992, French standard Z20 CDNV 12.01). The chemical composition and tensile properties are given in Tables 1-3.

Table 1 Chemical composition

C %	Si %	Mn %	P %	S %	Al %	Cu %	Cr %	Ni %	Mo %	V %	As %	Sn %	Nb %	Sb %	N2 %
.22	.23	.52	.013	.01	.014	.006	11.45	.72	.88	.30	.025	.007	.007	.001	.047

Table 2 Tensile properties at 20°C

Yield stress [MPa]	568
Ultimate stress [MPa]	790
Elastic modulus [MPa]	215000
Elongation [%]	18
Reduction in area [%]	61
Charpy energy at 30° [J]	53

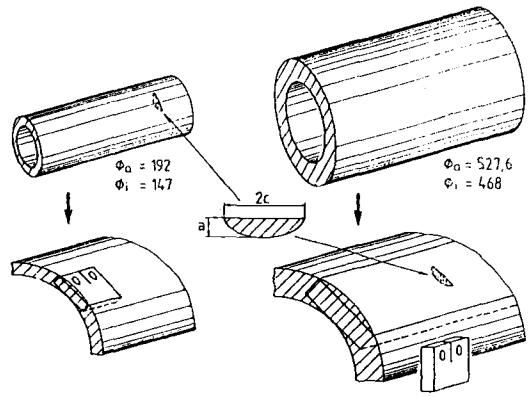


Fig. 1 A scheme of specimen cutting

Table 3 Stress-strain data (at 20° C)

Stress [MPa]	0	568	581	636	710	772	790	790
Strain	0	0.0027	0.005	0.012	0.022	0.04	0.073	0.099

For the crack growth resistance characterization of the material in upper shelf at RT, J-R curves were measured on smooth and side-grooved CT 20/50 specimens cut out from pipes as indicated in Fig. 1. The J-R data are summarized in Table 4.

Table 4 J-R curves (at 20°C): Fracture toughness and coefficients of the power law fit $J = C(\Delta a)^n$. J_{Ic} according to ASTM E 813 (1989), $J_{0.2} = C(0.2)^n$.

Specimen CT	a/W	SG %	C	n	J_{Ic} [kJ]	$J_{0.2}$ [kJ]
RAN 2.1	.56	20	418	.4750	273	195
RAN 2.3	.42	20	492	.4711	336	231
RAN 2.4	.43	20	459	.5152	298	200
RAN 2.5	.72	20	387	.4289	259	166
RAN 2.6	.72	20	409	.4456	273	182
SAN 1.1 (1)	.60	0	584	.4808	427	269
SAN 1.2 (2)	.60	0	600	.4974	431	269

Component tests

Geometry and loading

Four pipes and four plates (dimensions are shown in Table 5) with surface cracks have been tested. Table 6 and Figs. 2-3 give an overview of component geometry, type of loading and size of fatigue cracks. Fig. 4 shows the spans of the 4-point bending equipment. On each pipe, the crack mouth opening displacement (CMOD) was measured with a clip gage during loading as well as strains on the outer pipe surface remote from the crack using strain gages, and the load and displacement of loading points. The experiments were all carried out at room temperature.

Table 5 Dimensions of tested components

Plates	Thickness t [mm]	Width 2W [mm]	Length L [mm]
	20 - 21.2	120	1000
Pipes	Thickness t [mm]	Inner radius R_i [mm]	Length 2L [mm]
	23	73,5	2300

Table 6 Experiments on plates and pipes with surface cracks used in this study for the validation of the R6 method.

Component and loading	Crack type	Case	Crack depth a [mm]	Crack length 2c [mm]	Crack aspect ratio a/c	Thick-ness [mm]
Plate	Surface crack	SAN 2.4	12.7	28.1	0.896	21
under tension		SAN 2.5	13.9	42.0	0.662	20.5
		SAN 2.6	10.5	60.5	0.347	21.2
(Fig. 2)	(Fig. 2)	SAN 2.7	10.9	22.7	0.960	20
Pipe under	Circumferential	RAN 1.41	12.3	24.2	1.01	23
4-point bending	surface crack	RAN 1.42	16.0	40.2	0.80	23
and int. pressure	at outer surface	RAN 1.43	13.0	52.0	0.50	23
(Fig. 3)	(Fig. 3)	RAN 1.44	11.9	24.4	0.98	23

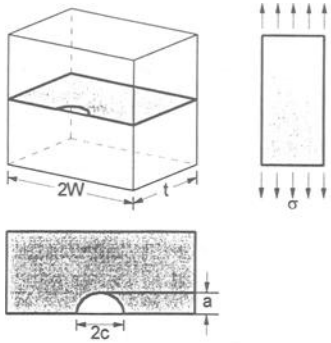


Fig. 2 Cracked plates

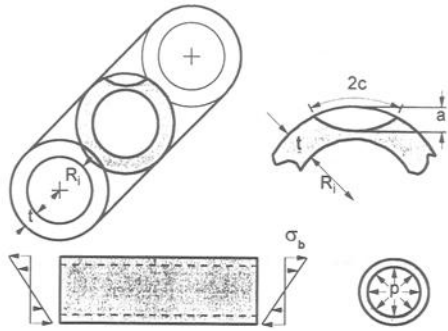


Fig. 3 Cracked pipes

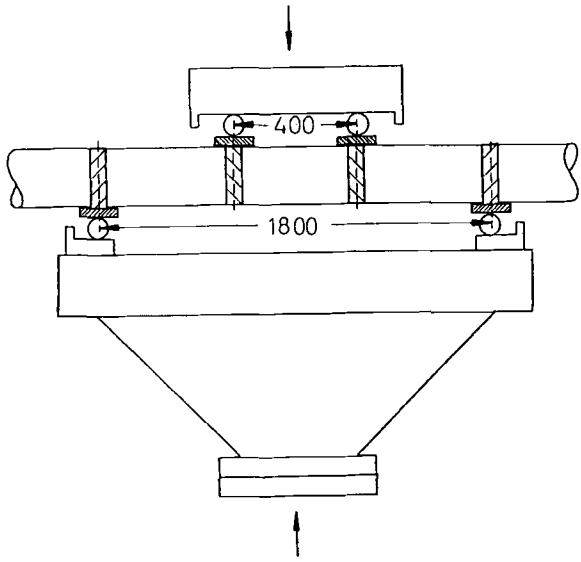


Fig. 4 Scheme of the 4-point bending equipment

Results

Maximum loads and crack extensions for all experiments are summarized in Table 7. The amount of the crack growth was measured on the fracture surface after the experiment. As an example the fracture surface in Fig. 5 shows the notch, the fatigue crack growth area (light gray), the area of the crack growth during the experiment (dark), and the area of the final brittle fracture (produced by breaking the specimen at liquid nitrogen temperature).

Table 7 Maximum load and crack growth in the 8 component tests (values with * obtained by linear-elastic conversion between bending moment and bending stress)

Component and loading	Case	Max. force P [kN]	Uniform or bending stress [MPa]	Crack extension Δa[mm]	Crack extension Δc[mm]
Plate under tension	SAN 2.4	1492	592	0.53	0.28
	SAN 2.5	1384	563	3.2	0.7
	SAN 2.6	1390	546	3.4	0.2
	SAN 2.7	1486	619	0.6	0.2
Pipe under 4-point bending	RAN 1.41	1250	945*	0.89	0.45
	RAN 1.42	1189	899*	2.8	0.6
	RAN 1.43	1191	901*	3.2	0.4
	RAN 1.44	1412	1068*	9	5

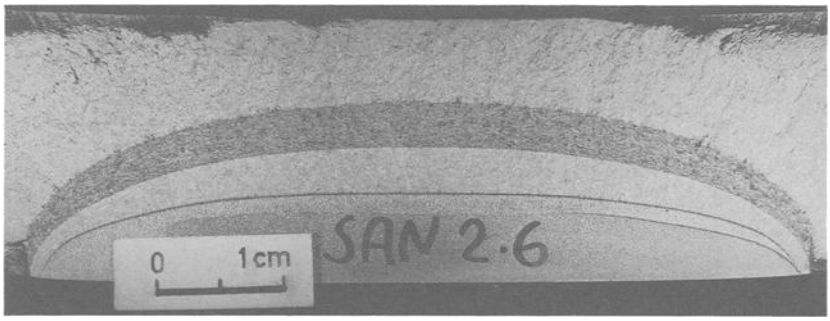


Fig. 5 Fracture surface of the SAN 2.6

POST-TEST CALCULATIONS USING R6

The R6 method

This mainly empirical method [3], based upon J-Integral, uses the concept of a failure assessment diagram to define the boundary between the safe and unsafe operating conditions for a structure. For the application of this method formulae for the stress

intensity factor and the limit load of the component and relevant material, load and geometry input data are required.

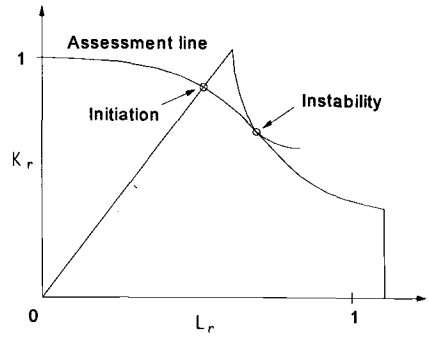


Fig. 6 Failure assessment diagram

The analysis can be performed at different levels of sophistication (e.g. 'Options' 1, 2 and 3 being characterized by different assessment lines). It requires the calculation of the parameters $K_r = K/K_{Ic}$ (stress intensity factor K of the cracked component over the material fracture toughness K_{Ic}) and $L_r = F_{appl}/F_{limit}$ (applied load F_{appl} over plastic yield load F_{limit} of the cracked component). The critical condition (for load or crack size) occurs when the assessment point $[K_r, L_r]$ lies on the assessment line.

For material behavior characterized by J-R curves the failure assessment parameters are

$$K_r = (J_{elastic,\ appl}(a+\Delta a)/J_{material}(\Delta a))^{1/2} \text{ and}$$
$$L_r = F_{appl}/F_{limit}(a+\Delta a).$$

During stable crack growth under increasing load the assessment point $[K_r, L_r]$ moves along the assessment line. Critical conditions are reached at crack instability defined by the condition

$$dJ_{appl}/da > dJ_{material}/da \quad \text{at} \quad J_{appl} = J_{material}.$$

In the analysis various amounts of ductile crack growth are postulated and assessment points $[K_r, L_r]$ are evaluated for each of them. The critical condition (crack instability) occurs when the locus of assessment points touches the failure assessment line at one point only, with all other points on the locus lying outside the area bounded by the axes and the line (see Fig. 6).

Calculation procedure

To demonstrate the applicability of the R6 method especially for situations, in which an appreciable amount of stable or unstable crack growth occurs, post test calculations have the material was available, both Option 1 and Option 2 of R6, and in one case also Option 3, have been used. For the sake of comparison to experiments, restrictions on stable crack growth required in [3] have have not been applied. Nominal stresses (tension and bending been done to experiments described in the first part of this paper. As the stress-strain curve of for plates and pipes, respectively)necessary for crack extension in depth direction equal to that observed on fracture surfaces were calculated and compared to maximum nominal stresses in experiments. For crack extension in length direction two different assumptions

have been adopted: 1. no crack extension in length direction (c = cons.), 2. constant crack shape (a/c = cons.). For some cases stable crack extension was evaluated also in both directions. Calculation results depend on formulae for stress intensity factor and limit load. Formulae used in this study can be found in references [4-7]. Calculation have been performed using the PC program "IWM-VERB" [8].

First calculations

Using the J-R curve measured on 20%-SG CT specimen RAN 2.1 and the assumption, that crack shape a/c does not change during stable crack growth, calculations have been done, in which the crack size was stepwise increased and the crack stability was checked in each step.

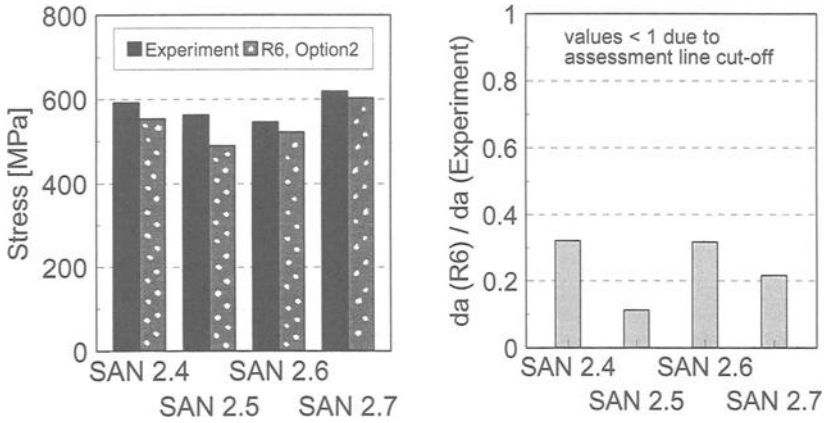


Fig. 7 a, b Plates with surface cracks, Calculation with R6, Option 2 and a/c = cons., J-R curve measured on RAN 2.1

The aim of the calculation was to find the nominal stress, for which the crack depth is equal to final crack depth in experiment. In some cases the program terminated calculations earlier because of crack instability or numerical problems.

Resulting stresses for plates (calculated with R6, Option 2) are compared with measured stresses in Fig. 7 a. For all 4 specimens calculated stresses are lower than the experimental values. All calculations, however, were terminated before the experimental crack extensions have been reached (Fig. 7 b) because of crack instability by plastic collapse (Fig.7 c).

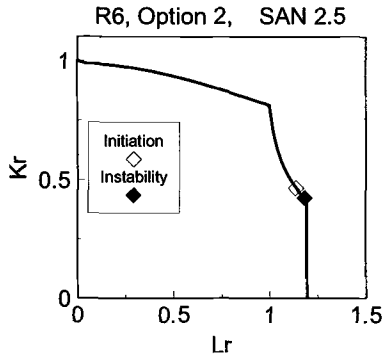


Fig. 7 c FAD for SAN 2.5, regular cut-off

Calculations beyond conventional plastic collapse cut-off

In further calculations for plates with cracks, the cut-off of the R6 assessment line was shifted from $L_r = (\sigma_y + \sigma_u)/(2\sigma_y)$ to $L_r = \sigma_u/\sigma_y$. The resulting stresses are shown in Fig. 8.

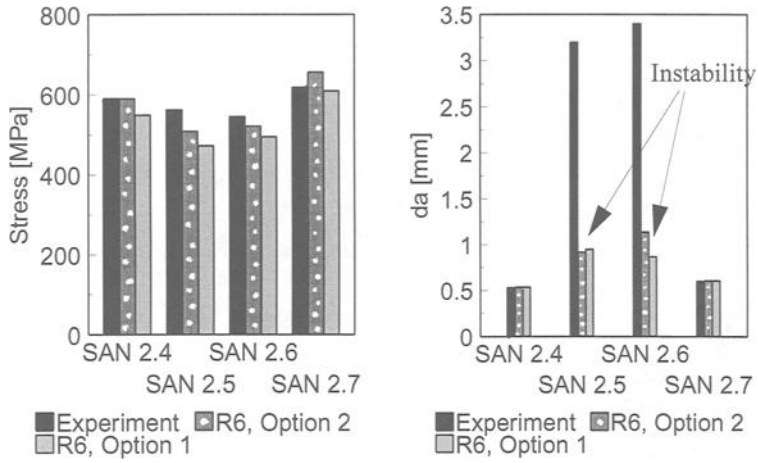


Fig. 8 a, b Plates with surface cracks, calculation with R6, plastic collapse cut-off shifted, a/c = const., J-R curve measured on RAN 2.1

In this case calculations have been terminated at crack extensions smaller than that in the experiments, for 2 specimens - SAN 2.5 and SAN 2.6 - due to crack instability. Experimental load-displacement curves for these plates exhibit actually slight load decrease shortly before the final displacements of loading points (the load in the experiments was displacement controlled). The occurring of the instability for two plates has been determined in R6 calculations correctly, but apparently at smaller crack extensions than observed. With the exception of SAN 2.7 evaluated by Option 2, the calculated stresses for all plates are somewhat lower than measured ones.

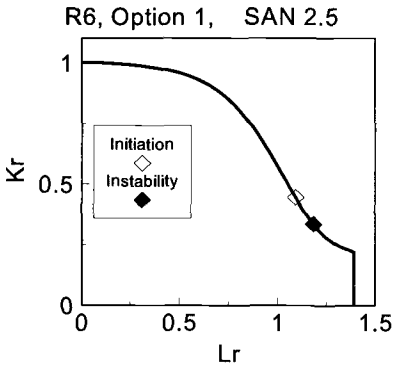


Fig. 8 c FAD for SAN 2.5, shifted cut-off

For cracked pipes under constant internal pressure and increasing displacement of loading points of the bending equipment, similar results have been obtained as for cracked plates under tension (Fig. 9).

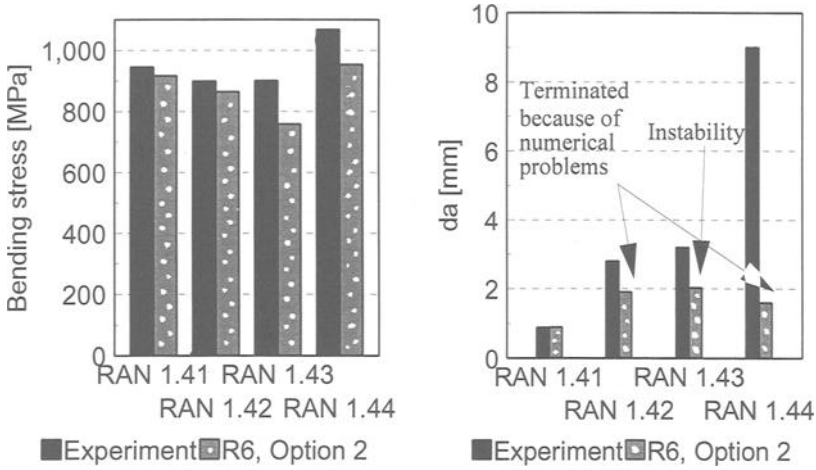


Fig. 9 a, b Pipes with surface cracks, calculations with R6, Option 2, plastic collapse cut-off shifted, a/c = const., J-R curve measured on RAN 2.1

In two cases the calculation was terminated too early due numerical problems at the assessment of crack stability. For pipe RAN 1.43 calculation was terminated at $\Delta a = 2$ mm because of crack instability - earlier than it would actually happen according to force-CMOD curve (Fig. 9c). Only pipe RAN 1.44 was actually loaded beyond the maximum force.

For two cases where numerical problems happened, further calculations have been carried out without checks of the crack stability. It was found that calculated stresses were close to experimental ones and in one case only (SAN 2.7, Option 2, cut-off shifted) the calculated stress was nonconservative (exceeded experimental maximum stress by 5 per cent).

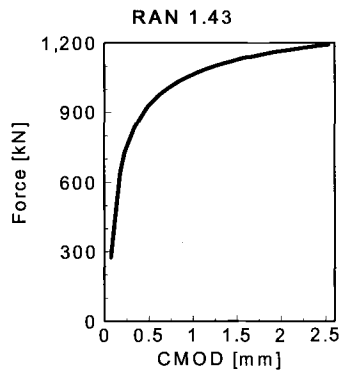


Fig. 9 c Measured force vs. CMOD curve for RAN 1.43

The influence of the crack growth in length direction (c = cons., a/c = cons.) on calculated stresses for cracked plates was found smaller than 4 per cent.

In additional calculations the crack growth in length direction (Δc) has been not assumed, but calculated. For the length direction in the R6 routine the same L_r was used as for depth direction but K_r was calculated using the stress intensity factor for the surface point and the J-R curve obtained from the component SAN 1.2(2). A comparison with measured Δc (surface point value and estimated "mean" value for length direction) for cracked pipes is shown in Fig. 10. The mean value of the crackextension in the length direction has been estimated for the part of the crack front $0 \leq \Phi < 30^{\circ}$. The results for cracked plates were similar to those for pipes, i.e. calculated values were larger than measured ones.

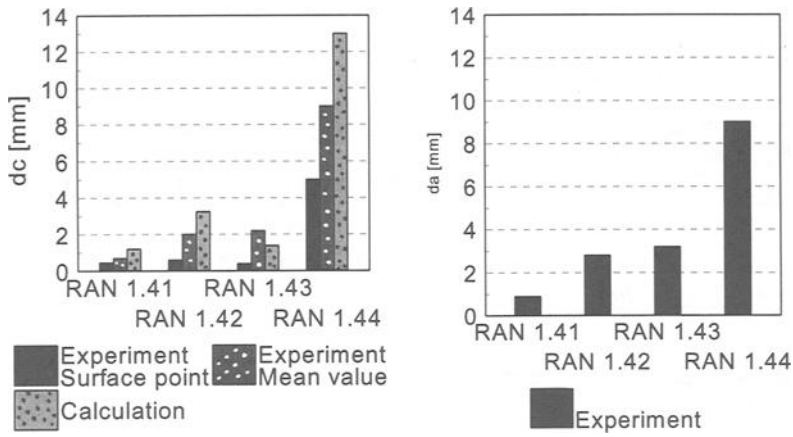


Fig. 10 Pipes with surface cracks: Crack extension Δc in length direction for Δa(calc.) = Δa(exp.), R6, Option 2, J-R curve for Δa: RAN 2.1, J-R curve for Δc: SAN 1.22

Calculations with Option 3 of the R6

The Option 3 was applied to component SAN 2.6, where the J integral as a function of load (for stationary crack) was available [2]. These J data, however, were obtained using a somewhat different stress-strain curve (e.g. yield stress = 514 MPa) and a somewhat smaller crack depth (9.9 mm). In Fig. 11 instability loads for all three R6 options are compared. The best agreement with the experiment was obtained by Option 2. For Option 3 lower yield stress used in FE calculation apparently decreases instability load.

In comparison with the experiment, results for all three options are within the ±10%-band. On the right side of Fig. 11 assessment lines are compared. In the elastic region of the R6 diagram, the curve for Option 3 is greater than 1 as a result of smaller crack depth used in FE calculation. In elastic-plastic region Option 3 curve should allow higher critical load than Option 2. The discrepancies (see left part of Fig. 11) can be explained by the unique yield stress used for calculations of critical loads and the different yield stresses used for normalization of assessment lines.

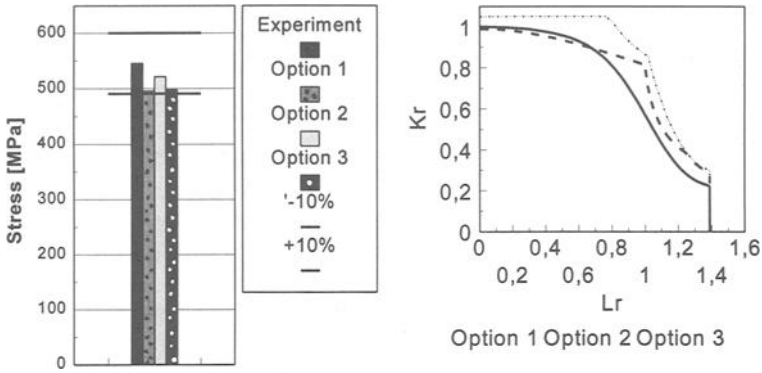


Fig. 11 Instability stresses and assessment lines for component SAN 2.6, calculations with R6, plastic collapse cut-off shifted, a/c = cons., J-R curve measured on RAN 2.1. Input data for Option 3 are not completely compatible with data for other cases.

CONCLUSIONS

The comparison of the experimental results for cracked plates and pipes in the ductile fracture regime with the results of calculations based on the R6 method shows:

Nominal stresses for given stable growth of surface cracks obtained using R6 assessment lines, Option 1 or Option 2 are close to experimental data. Option 2 of the R6 supplied closer agreement with experiment than Option 1.

When the plastic collapse cut-off according to [3] has been used, all results were conservative. In calculations beyond this cut-off, all results, with the exception of one case calculated with Option 2, were conservative.

The influence of the crack growth in the length direction on resulting stresses was almost negligible.

ACKNOWLEDGMENT

These investigations have been funded by the Research and Development Division of Electricité de France (EDF).

REFERENCES

[1] Memhard, D., Klemm, W., Fh-IWM report W4/89, Fraunhofer Institut für Werkstoffmechanik, Freiburg, Germany, 1989.

[2] Klemm, W., Memhard, D., Schmitt, W., "Experimental and Numerical Investigation of Surface Cracks in Plates and Pipes", Fracture Mechanics Verification of Large-Scale Testing, EGF/ESIS8 (Edited by K. Kussmaul), 1991, Mechanical Engineering Publications, London, pp. 139-150.

[3] Milne, I, et al., "Assessment of the Integrity of Structures Containing Defects", Int. J. of Pressure Vessels and Piping 32 (1988), 3-104.

[4] Newman, J.C, Raju, I.S., "Stress-Intensity Factor Equations for Cracks in Three-Dimensional Finite Bodies", ASTM STP 791, 1983, pp. I-238 - I-265.

[5] Harrison, R.P, et al., "Assessment of Structures Containing Defects", CEGB Report R/H/R6-Rev. 2, CEGB, 1980.

[6] Raju, I.S. and Newman, J.C.Jr., "Stress-Intensity Factors for Circumferential Surface Cracks in Pipes and Rods, ASTM STP 905, 1986, pp. 789 - 805.

[7] Kußmaul, K., Blind, D., Roos, E. und Sturm, D.,"Leck-vor- Bruch-Verhalten von Rohrleitungen", VGB Kraftwerkstechnik, Jahrgang 70, Heft 7, Juli 1990, 553-565.

[8] Defect assessment program IWM-VERB, FhG-Software 1941049, Fh-IWM, Freiburg (Germany), February 1993.

Author Index

A

Amstutz, B. E., 256
Ashbaugh, N., 486

B

Baer, W., 361
Bamford, J.-D., 631
Berry, R. F., Jr., 799
Bigelow, C. A., 223
Bland, J. D., 799
Brust, F. W., 461, 673
Bryson, J. W., 430

C

Cordes, J. A., 531
Cornec, A., 336, 376
Couterot, C., 822

D

Daghyani, H. R., 556
Dawes, M. G., 350
Dawicke, D. S., 223, 243, 256
Dodds, R. H., Jr., 107, 715

E

Eidinoff, H. L., 486
Epstein, J. S., 391
Eripret, C., 321
Ernst, H. A., 284

F

Franco, C., 321

G

Ganti, S., 391
Gilles, P., 321
Gross, L. B., 272

H

Hao, S., 336
He, H., 587
Hodulak, L., 417, 822
Hoffman, M. J., 509
Hornet, P., 336, 376

J

Joyce, J. A., 142

K

Kawahara, M., 509
Keeney, J. A., 430
Kim, Y.-J., 199
Kirk, M. T., 126
Kishi, T., 509
Koçak, M., 336, 376
Kortschot, M. T., 486

L

Lambert, D. M., 284
Landes, J. D., 86
Leung, R., 587
Link, R. E., 107, 142
Liu, H. W., 652
Lloyd, W. R., 303, 391, 486

M

Mai, Y.-W., 43, 509, 556, 587
Majumdar, B. S., 461
Maxwell, D. C., 617
McClintock, F. A., 199, 391
Memhard, D., 822
Merkle, J. G., 3
Meyn, D. A., 698
Munz, D., 572
Mutch, Y., 447

Copyright © 1995 by ASTM International www.astm.org

N

Natishan, M. E., 732
Newaz, G. M., 461
Newman, J. C., Jr., 223, 243, 256, 799
Nicholas, T., 617

P

Panontin, T. L., 54
Parida, B. K., 600
Parks, D. M., 199, 391
Piascik, R. S., 303
Porr, W. C., Jr., 107
Prakash, R. V., 600
Pusch, G., 361

R

Reuter, W. G., 391

S

Schwalbe, K.-H., 336, 376, 763
Seth, R. S., 587
Sharobeam, M. H., 86
Sheppard, S. D., 54
Shum, D. K. M., 178
Siegele, D., 417
Sutton, M. A., 243, 256

T

Tregoning, R. L., 732

U

Underwood, J. H.,486

V

VanDerSluys, W. A., 272
Vargas, P. M., 715
Viz, M. J., 631

W

Wade, C. S., 272
Wakayama, S., 509
Wang, Y.-Y., 126
Waskey, J. P., 107
Webb, T. W., 698
Wilson, C. D., 779
Wilson, D. A., 486
Wu, S.-X., 43

X

Xu, J. G., 652

Y

Yang, Y., 572
Yazici, 531
Ye, L., 556
Yoon, K. K., 272

Z

Zehnder, A. T., 631

Subject Index

A

Acoustic emission, 509
Adhesive joints, 556
Aging, strain, 350
Aircraft structure, 631
Aluminum and alloys
  2024-FC, 376
  2024-T3, 223, 243, 256, 303
  2024-T351, 376
  6061-T651, 284
  7075-T651, 652
  aluminum-lithium, 600
  thin sheets, 631
Anisotropy, 600
Applied load, 698
Applied stress, 223, 243
Arcan specimen, 256
ASTM standards
  A 515, 107
  A 516, 54
  A 533, 142, 715
  E 399, 178, 272
  E 813, 178, 587
  E 1152, 178, 272
  E 1290, 126
Asymptotic fields, 673

B

Bending, 284, 391
Bonding, 587
Bond thickness, 556
Bridge indentation method, 447

C

Carbon/epoxy composites, 486
Center-crack tension
    specimens, 284, 336
Ceramics, 447
Charpy tests, 732
Chevron notch method, 447
Cladding, 417
  effects, 600
Cleavage, 199
Compact tension specimens, 43,
    178, 272, 284, 376
Composites
  carbon/epoxy, 486
  lamina, 531, 486
  metal matrix, 461
Computer code verification and
    validation, life prediction,
    779
Constant amplitude loading, 600
Constant extension rate test,
    698
Constraint, 43, 556, 54, 715
  crack tip, 178, 391
  effects, 142, 284, 321
  factor, 223
  loss of, 3, 178
Controlled surface flaw method,
    447
Crack bridging, 509
Crack closure, 509
Crack extension method, 86
Crack face separation profiles,
    284
Crack front tunneling, 303
Crack growth, 199, 223, 391
  creep, 673
  directions, 531
  ductile, 391
  fatigue, 600, 617, 652
  intermittent, 698
  monitors, probes, 799
  rate, 509, 617
  resistance curves, 698
  stable, 256, 447, 531, 822
  theory, 652
Crack initiation stretch, 284
Crack initiation toughness, 43
Crack mouth opening
    displacement, 486
Crack resistance curves, 361
Cracks, 715
  corner, 799
  environmentally assisted, 698
  interfacial, 86
  semielliptical, 430
  shallow, 126

subclad, 417
surface, 86, 107, 779, 799
Crack tip, 3
blunting, 617
constraint, 107, 178, 391
fields, 178, 631
opening angle, 199, 243, 303
opening displacement, 43, 54, 256, 376, 556, 763
E 1290, 126
estimating, 336
three-dimensional, 223
shear decohesion, 652
Crack tunneling, 223
Creep crack growth, 673
Cyclic fatigue, 509
Cyclic loading, 617

D

Damage, notch-tip, 486
Damage zone model, 531
Defect assessment, 336, 822
Deformation, 54
Deformation, nonlinear, 447
Deformation, plastic, 417
Dimple, 652
Disk shaped specimen, 272
Dispersoids, 652
Displacements, 284, 486
Displacement test, rising, 698
Domain integral procedure, 715
Double-edge notched tension specimens, 43, 587
Ductile failure, 86
Ductile fracture, 43, 142
Ductile tearing, 321
Dynamic toughness characterization, 732

E

Eddy current probes, 799
Embrittlement, locally intensified straining and aging, 350
Engineering Treatment Model, 336, 763
Environmentally assisted cracking, 698
Extension rate test, constant, 698

F

Failure assessment method, R6, 822
Fatigue precrack, 447
specimens, 698
Ferralium, 255, 732
Ferrite, 732
Finite element analysis, 272, 531, 572
constraint characterization, 556
Engineering Treatment Model, 336
geometrically nonlinear, 631
modeling, 86
plane-strain, 126
stress triaxiality characterization, 556
three-dimensional, 3, 223
weldment specimen, 391
Flaw assessment, 763
Flaw, finite length, 430
Flight spectrum loading, 600
Four-point bend specimen, 361
Functionally graded material, 572

G

Glass/epoxy panels, 531
Grain boundaries, 652
Graphite/aluminum panels, 531
Graphite morphology parameters, quantitative, 361

H

Hardwood, 587
Hold times, 617
HY-80, 54
HY-100 structural steel, 142

I

Impact loading, 715
Impact toughness, 732
Inclusions, 652
Indentation fracture method, 447
Inertial effects, 715
Inner surface flaws, 430
IN718-STA1, nickel-base superalloy, 284

Integrated Reactor Vessel Material Surveillance Program, 272
Interface, bimaterial, 86, 321, 336, 376
Interlayer, 572
Interleaf specimen, 391
Iron, nodular cast, 361

J

J_{Ic}, 142, 447
E 813, 178, 587
J-integral, 43, 54, 86, 107, 142, 272, 284, 361, 556
modified, 763
Joints, adhesive, 556
Joints, bimaterial, 376, 572
Joints, welded, 361
Joints, mismatched, 336
J-Q methodology, 107, 556
J-R curves, 272, 587
E 1152, 178, 272
J-resistance curves, 284

L

Laminates, 531, 486
Leak-check port specimens, 799
Life prediction computer code, 779
Lithium, aluminum-lithium alloy, 600
Loading, 284
constant amplitude, 600
history dependent conditions, 673
minimum, hold, 617
monotonic, 178, 199
prediction, 531
static, 361
test, rising, 698
unloading compliance technique, 361
Load separation, 86
Loss of constraint, 3, 178

M

Microtopography reconstruction, 303
Mismatching, 361
effects, weld metal, 321
joints, estimate, 336
strength, 336, 376, 391
Modeling
Bodner-Partom viscoplastic constitutive, 715
computerized life prediction, 779
crack tunneling, 223
damage zone, 531
failure prediction, 461
finite element analysis, 54, 86
metal matrix composite system, 461
numerical, 673
three-dimensional crack model, 430
Mode I crack growth, 199
Mode I/Mode II stable crack growth, 256
Morphology parameters, quantitative graphite, 361

N

NASCRAC, 779
Nickel-base alloy, 284
Notch-tip damage, 486
Numerical modeling, 673

O

Orientation, 600

P

Paper, 587
Peak stress location, 572
Plane-strain bending, 391
Plane-strain finite element analysis, 126
Plane-strain fracture toughness
E 399, 178, 272
Plane-strain Mode I crack growth, 199
Plasticity, 461
Plates, thin, 631
Plates, wide, 336, 350
Plate theory, 631
Profiling, 284

Q

Q-stress, 178

R

R6, 822
Radiography, X-ray, 486
Rate sensitivity, 715
R-curves, 376, 447, 509
Reconstruction, microtopography, 303
Recycling, 587
Rolling orientation, 243
Rotation correction, 142

S

Safety analysis, 3
Safety assessment, 417
Scanning electron microscopy, 509, 556
Scatter, 732
Shear decohesion, 652
Single-edge bend specimen, 732
Single-edge notch bend specimens, 126, 376, 715
Single-edge notched tension specimens, 43, 284, 587
Single specimen technique, 86
Small-scale yielding, 178
Softwood, 587
Space shuttle rocket motor, 799
Steel
  A 515, 107
  A 516, 54
  A 533, 142, 715
  D6AC, 799
  HY-80, 54
  HY-100, 142
  stainless, 732
  welded, 350
Strain, critical, stress modified, 54
Strain aging, 199
  locally intensified, 350
Strain hardening, 3
Strain rate sensitivity, 715
Strength mismatch, 391
Stress, 486
  applied, 243
  intensity factor, 417, 430, 509, 631
    average, 779
    local, 779
  level, precracking, 799
  peak, 572
  peak applied, 223
  ratio, 600
  strain curves, 336
  triaxiality, 391, 556
Striation, 652
Structural integrity, welds, 321

T

Tearing, ductile, 321
Tearing modulus, 142
Tearing resistance, 142
Tearing, stable, 223, 303, 391
Tensile loading, 531, 631
Tensile strength, 126
Tensile test, in situ, 361
Thermal shock, 417, 430
Thin sheet, 223
Three-dimensional crack model, 430
Three-dimensional crack tip opening displacement, 223
Three-dimensional finite element analysis, 223
Three-dimensional finite element model, 54, 86
Three-dimensional loss of constraint, 3
Three-dimensional nonlinear dynamic analyses, 715
Three-dimensional transverse constraint, 178
Three-parameter characterization, 199
Three-point bend specimen, 486
Titanium, 391, 461, 617
Toughness, 587
Toughness scaling, 107
Transformation induced dilation, 509
Transition toughening, 509
Transition zone, 256
Translaminar fracture, 486
T-stress, 142

Tunneling, 223
  behavior, 243
  crack, 303
Two-parameter fracture
    mechanics, 107

U

Unloading compliance
    technique, partial, 361
Upper shelf fracture, 142

V

Void growth, 43, 54
Void nucleation, 43

W

Warm prestress, 178
Welds, 321, 336, 361
  electron beam, 376
  geometry, 391
  heat-affected zone, 350
  undermatched, 391
Wide plate tension tests, welded,
    350

Y

Yielding, small-scale, 178
Yield strength, 376, 587

X

X-ray radiography, 486

Z

Zirconia, 509

ISBN 0-8031-1996-8